AFRL-RQ-ED-TR-2020-0026

Supercritical Acoustic Flame Experiments

Alizera Badakhshan
John Bennewitz
Steve Danczyk
Dave Forliti
Ivett Leyva
Mario Roa
Alex Schumaker
Doug Talley
Jeff Wegener

Air Force Research Laboratory (AFMC)
Combustion Devices Branch
AFRL/RQRC
10 E. Saturn Blvd.
Edwards AFB, CA 93524

August 2020

In-House Final Report

DISTRIBUTION STATEMENT A: Approved for public release; distribution unlimited. PA No. 20381

STINFO COPY

AIR FORCE RESEARCH LABORATORY
AEROSPACE SYSTEMS DIRECTORATE

■ Air Force Materiel Command ■ United States Air Force ■ Edwards Air Force Base, CA 93524

- STINFO COPY -
NOTICE AND SIGNATURE PAGE

Using Government drawings, specifications, or other data included in this document for any purpose other than Government procurement does not in any way obligate the U.S. Government. The fact that the Government formulated or supplied the drawings, specifications, or other data does not license the holder or any other person or corporation; or convey any rights or permission to manufacture, use, or sell any patented invention that may relate to them.

This report was cleared for public release by the USAF 412 Test Wing (412 TW) Public Affairs Office (PAO) and is available to the general public, including foreign nationals.

AFRL-RQ-ED-TR-2020-0026 HAS BEEN REVIEWED AND IS APPROVED FOR PUBLICATION IN ACCORDANCE WITH ASSIGNED DISTRIBUTION STATEMENT.

FOR THE DIRECTOR:

//SIGNED//	//SIGNED//
DOUGLAS G. TALLEY, Ph.D. Program Manager	INGRID J. WYSONG, Ph.D. Chief, Combustion Devices Branch

//SIGNED//

Technical Advisor
Rocket Propulsion Division

This report is published in the interest of scientific and technical information exchange, and its publication does not constitute the Government's approval or disapproval of its ideas or findings.

REPORT DOCUMENTATION PAGE

Form Approved
OMB No. 0704-0188

Public reporting burden for this collection of information is estimated to average 1 hour per response, including the time for reviewing instructions, searching existing data sources, gathering and maintaining the data needed, and completing and reviewing this collection of information. Send comments regarding this burden estimate or any other aspect of this collection of information, including suggestions for reducing this burden to Department of Defense, Washington Headquarters Services, Directorate for Information Operations and Reports (0704-0188), 1215 Jefferson Davis Highway, Suite 1204, Arlington, VA 22202-4302. Respondents should be aware that notwithstanding any other provision of law, no person shall be subject to any penalty for failing to comply with a collection of information if it does not display a currently valid OMB control number. **PLEASE DO NOT RETURN YOUR FORM TO THE ABOVE ADDRESS.**

1. REPORT DATE *(MM/DD/YYYY)*	**2. REPORT TYPE**	**3. DATES COVERED** *(From - To)*
08/30/2020	Final Report	11/09/2012 – 06/01/2020

4. TITLE AND SUBTITLE
Supercritical Acoustic Flame Experiments

5a. CONTRACT NUMBER
In-House

5b. GRANT NUMBER

5c. PROGRAM ELEMENT NUMBER

6. AUTHOR(S)
Alizera Badakhshan, John Bennewitz, Steve Danczyk, Dave Forliti, Ivett Leyva, Mario Roa, Alex Schumaker, Doug Talley, Jeff Wegener

5d. PROJECT NUMBER

5e. TASK NUMBER

5f. WORK UNIT NUMBER
Q0YA

7. PERFORMING ORGANIZATION NAME(S) AND ADDRESS(ES)
Air Force Research Laboratory (AFMC)
Combustion Devices Branch (AFRL/RQRC)
10 E. Saturn Blvd.
Edwards AFB, CA 93524

8. PERFORMING ORGANIZATION REPORT NO.

9. SPONSORING / MONITORING AGENCY NAME(S) AND ADDRESS(ES)
Air Force Research Laboratory (AFMC)
AFRL/RQR
5 Pollux Drive
Edwards AFB, CA 93524

10. SPONSOR/MONITOR'S ACRONYM(S)

11. SPONSOR/MONITOR'S REPORT NUMBER(S)
AFRL-RQ-ED-TR-2020-0026

12. DISTRIBUTION / AVAILABILITY STATEMENT
DISTRIBUTION STATEMENT A. Approved for public release; distribution unlimited.

13. SUPPLEMENTARY NOTES
PA Clearance No. 20381 Cleared 9/14/2020

14. ABSTRACT

This report documents a sequence of studies that were performed with a major objective to determine the combustion response of injectors with and without acoustic forcing. A previous project had focused primarily only on the fluid dynamics response without combustion. The experimental facility was extensively redesigned and reconstructed to allow combustion. The main type of injectors considered were shear coaxial injectors flowing liquid oxygen in the center jet and gaseous hydrogen in the annular jet. However an impinging element injector was also examined as was a gas centered swirl coaxial injector flowing gaseous oxygen in the center and swirling liquid kerosene. The project also received a tasking to investigate the effect of energetic additives on the combustion characteristics of single hydrocarbon fuel droplets as a different class of combustion response. The details of all these studies are extensively documented in the Appendix.

15. SUBJECT TERMS

16. SECURITY CLASSIFICATION OF:			**17. LIMITATION OF ABSTRACT**	**18. NUMBER OF PAGES**	**19a. NAME OF RESPONSIBLE PERSON**
					Douglas G. Talley
a. REPORT	**b. ABSTRACT**	**c. THIS PAGE**			**19b. TELEPHONE NO** *(include area code)*
Unclassified	**Unclassified**	**Unclassified**	SAR	715	661 275-6174

Standard Form 298 (Rev. 8-98)
Prescribed by ANSI Std. 239.18

This Page Intentionally Left Blank

TABLE OF CONTENTS

Section	Page
1.0 EXECUTIVE SUMMARY	1
2.0 ACKNOWLEDGEMENTS	3
3.0 REFERENCES	4
APPENDIX	A-1

Abstract

This report documents a sequence of studies that were performed with a major objective to determine the combustion response of injectors with and without acoustic forcing. A previous project had focused primarily only on the fluid dynamics response without combustion. The experimental facility was extensively redesigned and reconstructed to allow combustion. The main type of injectors considered were shear coaxial injectors flowing liquid oxygen in the center jet and gaseous hydrogen in the annular jet. However an impinging element injector was also examined as was a gas centered swirl coaxial injector flowing gaseous oxygen in the center and swirling liquid kerosene. The project also received a tasking to investigate the effect of energetic additives on the combustion characteristics of single hydrocarbon fuel droplets as a different class of combustion response. The details of all these studies are extensively documented in the Appendix.

1.0 EXECUTIVE SUMMARY

This report documents extensive studies that were conducted in response to the problem of combustion instabilities in liquid rocket engines. Combustion instabilities are organized, oscillatory motions in combustion chambers sustained by combustion. They can cause considerable damage to liquid rocket engines. In extreme cases, catastrophic damage can occur in less than a single second. Combustion instabilities are notoriously hard to predict and may be considered to be one of the largest combustion-related risks to developing liquid rocket engines. Good entries into the literature may be found in [1], which reviews developments up to 1972, and [2] which addresses developments subsequently.

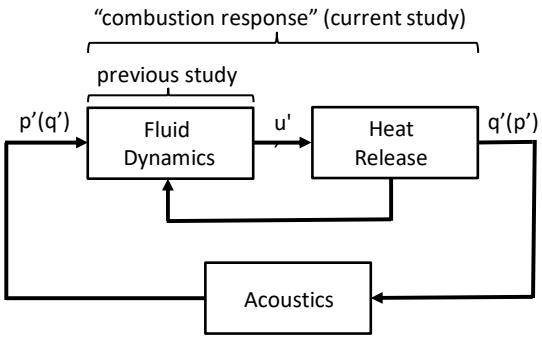

Figure 1. Combustion instability feedback loop

Combustion instabilities are often understood in controls theory terms to be a closed-loop feedback system, as illustrated in Figure 1. Pressure oscillations p' feed forward through the fluid dynamics u' and heat release processes q' along the top of the outer loop to produce heat release fluctuations as a function of the pressure fluctuations, q'(p'). The heat release fluctuations then feed back into chamber pressure fluctuations p'(q') through the chamber acoustics in the bottom part of the outer loop. There is also an inner feedback loop between the fluid dynamics and the heat release as shown. Combustion instabilities are produced if amplification occurs in the outer loop.

In the combustion instability literature, the feed forward part involving the fluid dynamics and the heat release together along the top of the outer loop, including the inner loop, is known as the *combustion response*, that is, q'(p'). The combustion response is usually considered to be the most unknown part of predicting combustion instabilities. A predecessor set of studies [3] focused exclusively on the fluid dynamics part of the feed forward process but not the entire combustion response. It examined the responses of fluid flows to acoustic waves in the absence of heat release. The present set of studies extended this focus to include the entire combustion response by allowing heat release to occur in the form of combustion. In neither set of studies was the feedback from heat release to the chamber acoustics allowed, in order to focus entirely on the forward responses. In the prior set of studies [3], such a feedback was not possible because the heat release was not present. In the present set of studies, the feedback was decoupled by carefully minimizing the ability of the combustion to affect the pressure. In both studies, the acoustics was produced by externally driving the flows in an open loop fashion. In both studies, the flows examined were mainly those of coaxial injectors, a common kind of rocket injector, although there were exceptions as noted below.

Distribution Statement A: TO BE Approved for Public Release; distribution is unlimited. PA Clearance Number

In what follows, the various studies performed under this project are only briefly summarized. However, citations are provided to references where all the details may be found. The cited references are fully reproduced in the Appendix for immediate access to these details.

Some of the present study consisted of further documenting the results of the previous studies [4]. Two comprehensive reviews were written [4-5], one of which appeared as an AIAA Progress Series book chapter [5]. In addition, project personnel contributed to subjecting some of the past data to increasingly more sophisticated data analysis [6-8].

The predecessor study without combustion [3] was performed entirely with inert nitrogen, where liquid nitrogen simulated liquid oxygen and gaseous nitrogen simulated gaseous hydrogen. Expanding the scope to include combustion where actual liquid oxygen and actual hydrogen could be burned required a clean slate redesign and reconstruction of the experimental facilities. The changes are documented in [9] and in the Ph.D. thesis of Wegener [10]. The reconstructed experiment included the invention of a new ignition method using a nano-ignition torch [11-12].

Wegner et al. also performed a study, still without combustion, but simulating the density ratio and multicomponent nature of combustion more closely than the previous pure nitrogen studies by replacing the gaseous nitrogen simulant for hydrogen with gaseous helium [13-14]. They found that the shear flow structures along the inner jet convected at a speed well predicted by theory. They also examined how strong the acoustics had to be in order to interfere with the naturally occurring structures in the jet, a feature called *receptivity*. When the acoustics were at a pressure antinode (PAN), receptivity didn't occur until the acoustic amplitude approached the dynamic pressure of the outer jet ($p' \sim (\rho u^2)_{outer}$). However, at a pressure node (PN), receptivity was found to occur even at very low acoustic amplitudes. Wegener et al. also performed the first preliminary combustion studies using actual liquid oxygen and hydrogen [15].

A series of combustion studies then followed. These began with examinations of single element coaxial liquid oxygen / gaseous hydrogen flames, with and without acoustics [16-17]. These culminated in a recently published journal paper [18] that reported on single elements without acoustics. A companion journal paper that reports on the added effects of acoustics is currently under review [19]. These papers identified and elucidated on a naturally occurring so-called "wave amplification mechanism." This naturally occurring mechanism was found to persist in the presence of acoustic waves, but in a modified form.

Following the single element work, the experiment was further modified to flow three elements simultaneously in a linear arrangement, to allow inter-element effects to be investigated. Of interest was how the center element behaved in the presence of the two outer elements, in comparison with only a single element, and how the outer elements behaved in comparison with the single element. This required some extensive facilitated modifications, particularly with regard to preventing three times the amount of combustion-produced water vapor from condensing on the windows of the experiment. Preliminary results were reported in [20-23], and a journal article is currently being prepared to formally document the final results [24]. Major conclusions included the lack of any lifted flames even as a linear array, and the lack of obvious interactions directly between the liquid cores of the jets. Significant interactions were observed in the gas phase, however, and these served to indirectly transmit information between the liquid cores.

Beyond the study of coaxial liquid oxygen/gaseous hydrogen injectors, the study expanded at times to include other kinds of flows as well. One study was conducted of the effect of acoustic waves on impinging liquid nitrogen jets at high pressures with no combustion [25]. It was observed that impact waves became visually prominent in a narrow range of chamber pressures and jet ve-

locities, particularly when both jet velocity and chamber pressure was low (subcritical for the latter). At supercritical pressures, no droplets or ligaments were ever observed to form; instead the flow field resembled a fine mist. The impact waves also revealed a receptivity behavior. Above a certain amplitude of acoustic forcing, the impact waves were found to disappear. Different behavior was observed for PN and PAN acoustic forcing.

Limited studies were also made on acoustic interactions with the combustion of gas centered swirl coaxial (GCSC) liquid kerosene/gaseous oxygen injectors [26]. GCSC injectors are also of the coaxial class, but in an opposite sense to coaxial injectors for liquid oxygen and gaseous hydrogen, wherein the gas (gaseous oxygen) flows in the center and the liquid (kerosene) flows in the annulus. In addition, the annular liquid kerosene flow is swirled. The results of these studies were partially obscured by window wetting by the kerosene, and also by thick soot layers that formed on the periphery of the swirling liquid sheets in these hydrocarbon flames. It was found that an oleophilic coating on the inner surface of the windows significantly reduced the former problem by causing the liquid kerosene to spread into thin films over the window. Despite these obstacles, it could be observed that these flames are possibly lifting from the injector, as opposed to the H2/O2 flames which always remained attached. In addition, the soot cloud was found to be non-periodic in nature, highly stochastic in its formation, convected slowly compared to the oxygen core and the flame, and tended to rotate around the oxygen core.

Finally, the effect of energetic additives on the combustion characteristics of single hydrocarbon fuel droplets was investigated [27-33]. These studies were conducted at atmospheric pressure, and no acoustic effects were explored. Both burning rate constants and ignition delays were reported, along with qualitative descriptions of other droplet behavior, particularly near the end of droplet life. Two new methods of igniting the droplets were invented for this study [30], as well as a new method of analyzing the surface regression rate [32]. Significant findings included an error analysis addressing the wide variation in reported surface regression rates reported by various authors for the same droplet fuels, and a conclusion that most energetic additives (with a few exceptions) produced little noticeable effect except near the end of droplet life.

In addition to the Distribution A material reported here and in the Appendix, several reports were also written under Distribution C distribution requirements. Distribution C documents cannot be included in a Distribution A document such as this one. However, the Distribution C documents do not contain significant insights in addition to those reported here, so they may be omitted here without detracting from the technical content.

2.0 ACKNOWLEDGEMENTS

The authors would like to acknowledge the indispensable assistance of Mr. Randy Harvey in constructing, maintaining, and operating the experimental facilities. The assistance of Mr. Miguel Placenscia is also gratefully acknowledged. This project was funded by the Air Force Office of Scientific Research, with Dr. Mitat Birkan as the Project Officer. His unwavering support is gratefully acknowledged.

3.0 REFERENCES

The pages in the Appendix where the citations may be found are given in parentheses at the end of each citation, e.g., (A-2). No page number in parentheses means the reference is not included in the appendix.

1. Harrje, D.T., and Reardon, F.H., *Liquid Propellant Rocket Combustion Instability*, NASA SP-194 (1972).
2. Yang, V., and Anderson, W. (editors), *Liquid Rocket Engine Combustion Instability,* AIAA Progress in Astronautics and Aeronautics Series, vol. 169 (1995).
3. Chehroudi, B. Davis, D., Graham, J., Karagozian, A., Leyva, I., Rodriguez, J., Talley, D., and Teshome, S., *Dynamics of Supercritical Flows,* Final Report, AFRL-RZ-ED-TR-2012-0031, Air Force Research Laboratory (2012).
4. Chehroudi, B., "Recent Experimental Efforts on High-Pressure Supercritical Injection for Liquid Rockets and Their Implications," *International Journal of Aerospace Engineering*, Vol. 2012, pp. 1–31, (2012). (A-2)
5. Forliti, D.J., Leyva, I.A., Talley, D.G., Rodriguez, J.I., Teshome, S., Wegener, J.L., Roa, M., and, Karagozian, A.R., "Forced and unforced shear coaxial mixing and combustion at subcritical and supercritical pressures," *High Pressure Flows for Propulsion Applications*, edited by J. Bellan, AIAA Progress in Astronautics and Aeronautics, vol. 260, published online (March 2020). https://doi.org/10.2514/5.9781624105814.0233.0280. (A-33)
6. Hua, J.-C., Gunaratne, G.H., Talley, D.G., Gord, J.R., and Roy, S., "Dynamic-Mode Decomposition Based Analysis of Shear Coaxial Jets With and Without Transverse Acoustic Driving," J. Fluid Mech, vol. 790, pp. 5-32 (2016) doi:10.1017/jfm.2016.2. (A-80)
7. Subramani, H., Saha, A., Reza, M., Meyer, T., Roy, S., Gord, J., and Talley, D., "Spectral Decomposition of Acoustically Excited Nonreacting Cryogenic Coaxial Jets," 14th International Conference on Liquid Atomization and Spray Systems, Chicago IL, 22-26 July (2018). (A-108)
8. Yi, T., Fugger, C., Jensen, R.J., Caswell, A.W., Talley, D.G., Casiano, M.J., and Roy, S., "Fast and Unbiased Determination of the Dominant Frequencies and Amplitude of Thermoacoustic Oscillations," Journal of Propulsion and Power, accepted for publication, 21 Feb (2020). (A-112)
9. Wegener, J. L., Leyva, I. A., Forliti, D. J., and Talley, D. G., "Development of a Facility for Combustion Stability Experiments at Supercritical Pressures," 52nd Aerospace Science Meeting, paper AIAA 2014-0137, National Harbor, Maryland, 13-17 January 2014. (A-125)
10. Wegener, J. L., *Multi-Phase Combustion and Transport Processes Under the Influence of Acoustic Excitation*, Ph.D. Thesis, University of California Los Angeles (2014). (A-144)
11. Badakhshan, A., Danczyk, S., and Talley, D., "Photoignition Torch Applied to Cryo-genic H2/O2 Coaxial Jet," JANNAF Programmatic and Industrial Base Meeting, 11th Modeling and Simulation, 9th Liquid Propulsion, 8th Spacecraft Propulsion Joint Subcommittee Meeting, Phoenix, AZ 5-8 Dec (2016). (A-427)

12. Badakhshan, A., Danczyk, S., Forliti, D., Leyva, I., and Talley, G., "Nano-ignition Torch Applied to Cryogenic H2/O2 Coaxial Jet," 54th AIAA Aerospace Sciences Meeting, paper AIAA 2016-0184, San Diego, CA, 4-8 January 2016. (A-431)
13. Wegener, J.L., Forliti, D.J., Leyva, I.A., and Talley, D.G., "Receptivity of a Cryogenic Coaxial Liquid Jet to Acoustic Disturbances," ILASS Americas 26th Annual Conference on Liquid Atomization and Spray Systems, Portland, OR, May (2014). Marshall Best Paper Award. (A-443)
14. Wegener, J. L., Forliti, D. J., Leyva, I. A., Talley, D. G., "Receptivity of a Cryogenic Coaxial Gas-Liquid Jet to Acoustic Disturbances," AIAA Propulsion and Energy Forum and Exposition, paper AIAA 2014-3487, Cleveland, Ohio, 28-30 July (2014). (A-454)
15. Forliti, D.J., Badakhshan, A., Wegener, J.L., Leyva, I.A., and Talley, D.G., "The Response of Cryogenic H2/O2 Coaxial Jet Flames to Acoustic Disturbances," AIAA SciTech, 53rd AIAA Aerospace Sciences Meeting, paper AIAA-2015-1607, Kissimmee, Florida, 5-9 January 2015. (A-467)
16. Roa, M., Forliti, D., Badakhshan, A., and Talley, D., "Acoustically Forced Coaxial Hydrogen/Liquid Oxygen Jet Flames," ILASS Americas 28th Annual Conference on Liquid Atomization and Spray Systems, Dearborn, MI, May 2016. (A-480)
17. Roa, M., and Talley, D.G., "Vortex Dynamic Mechanisms in Coaxial Hydrogen/ LOX Jet Flames," AIAA SciTech Forum, Aerospace Sciences Meeting, paper AIAA 2018-0677, Kissimmee, FL, 8-12 Jan (2018). doi: 10.2514/6.2018-0677. (A-489)
18. Roa, M., and Talley, D.G., "Wave Dynamic Mechanisms in Coaxial Hydrogen/Liquid-Oxygen Jet Flames," Journal of Propulsion and Power 35(2):369-381, March-April (2019). https://doi.org/10.2514/1.B37079. (A-512)
19. Roa, M., and Talley, D.G., "Acoustic Forcing of Hydrogen / Liquid Oxygen Turbulent Shear Coaxial Flames" Journal of Propulsion and Power, under review (2020).
20. Roa, M., and Talley, D.G., "Preliminary Study of the Reacting Flow from Multi-Element Shear Coaxial Flows," 65th JANNAF Propulsion Meeting, Programmatic and Industrial Base Meeting, 12th Modeling and Simulation, 10th Liquid Propulsion, 9th Spacecraft Propulsion Joint Subcommittee Meeting, Long Beach, CA, 21-24 May (2018). (A-525)
21. Roa, M., and Talley, D.G., "Preliminary Study of Reacting Three-Element Gas/Liquid Shear Coaxial Flows," ILASS-Americas 30th Annual Conference on Liquid Atomization and Spray Systems, Tempe, AZ, May (2019). (A-539)
22. Roa, M., and Talley, D.G., "Unsteady and Transversely Forced Dynamics of Two-Phase Multi-Element Shear Coaxial Flows," AIAA Propulsion and Energy Forum, paper AIAA 2019-4108, Indianapolis IN, 19-22 August (2019). https://doi.org/10.2514/6.2019-4108. (A-551)
23. Roa, M., and Talley, D.G., "Acoustic Forcing and Sensitivity of the Hydrodynamic Instabilities and Flame Dynamics from Hydrogen/LOX Shear Coaxial Flames," AIAA SciTech Forum, paper AIAA-2020-422, Orlando, FL, 6-10 Jan (2020). (A-567)
24. Roa, M., and Talley, D.G., "Multi-Element Effects in Acoustic Forcing of Hydrogen / Liquid Oxygen Turbulent Shear Coaxial Flames," journal paper under preparation (2020).

25. Roa, M., Schumaker, S. A., Talley, D. G., "Cryogenic Impinging Jets Subjected to High Frequency Transverse Acoustic Forcing in a High Pressure Environment," 52nd AIAA/SEA/ASEE Joint Propulsion Conference, paper AIAA 2016-5086, Salt Lake City, Utah, (25-27 July 2016). (A-581)

26. Roa, M., Bennewitz, J.W., Schumaker, S.A., and Talley, D.G., "A Study of Acoustic Forcing on Gas-Centered Swirl-Coaxial Reacting flows," AIAA SciTech Forum, 55th AIAA Aerospace Sciences Meeting, paper AIAA 2015-1335, Grapevine, TX, (9-13 January 2017). (A-591)

27. Badakhshan, A., Bennewitz, J., and Talley, D., "Photoignition for Study of Combustion Characteristics of Hydrocarbon Fuel Droplets," 10th U. S. National Combustion Meeting, College Park, MD April 23-26 (2017). (A-607)

28. Bennewitz, J.W., Badakhshan, A., Schumaker, S.A., and Talley, D.G., "Measurement of the Burning Rate and Ignition Delay for Various Hydrocarbon Fuel Droplets using Photothermal Ignition of Aluminum Nanoparticles," ILASS Americas 29th Annual Conference on Liquid Atomization and Spray Systems, Atlanta, GA May 15-18 (2017). (A-613)

29. Bennewitz, J.W., Badakhshan, A., and Talley, D.G., "Systematic Measurement of Hydrocarbon Fuel Droplet Burning Rate Constants and Ignition Delays," AIAA SciTech Forum, Aerospace Sciences Meeting, paper AIAA 2018-0672, Kissimmee, FL, 8-12 Jan (2018). doi: 10.2514/6.2018-0672. (A-620)

30. Badakhshan, A., Bennewitz, J.W., and Talley, D., "New Ignition Methods for Droplet Combustion Studies," Combustion Science and Technology 190(7)1302-1312 https://doi.org/10.1080/00102202.2018.1445726 (2018). (A-636)

31. Badakhshan, A., Bennewitz, J.W., and Talley, D.G., "Combustion Characteristics of Neat and Nanoparticle Fuels of Hydrocarbon Droplets: Effects of Ignition Method and Nanoparticle Additives," 65th JANNAF Propulsion Meeting, Programmatic and Industrial Base Meeting, 12th Modeling and Simulation, 10th Liquid Propulsion, 9th Spacecraft Propulsion Joint Subcommittee Meeting, Long Beach, CA, 21-24 May (2018). (A-648)

32. Bennewitz, J.W., Badakhshan, A., and Talley, D.G., "Systematic Measurement of Hydrocarbon Fuel Droplet Burning Rate Constants and Ignition Delays," Journal of Propulsion and Power 35(4):690-703 (2019). https://doi.org/10.2514/1.B37195. (A-662)

33. Bennewitz, J.W., Badakhshan, A., and Talley, D.G., "Combustion Characteristics of Suspended Hydrocarbon Fuel Droplets with Various Nanoenergetic Additives," Combustion Science and Technology, https://doi.org/10.1080/00102202.2020.1729756, 24 Feb (2020). (A-676)

APPENDIX

Hindawi Publishing Corporation
International Journal of Aerospace Engineering
Volume 2012, Article ID 121802, 31 pages
doi:10.1155/2012/121802

Review Article

Recent Experimental Efforts on High-Pressure Supercritical Injection for Liquid Rockets and Their Implications

Bruce Chehroudi

Advanced Technology Consultants, Laguna Niguel, CA 92677, USA

Correspondence should be addressed to Bruce Chehroudi, chehroudib@aol.com

Received 6 March 2012; Revised 3 June 2012; Accepted 11 June 2012

Academic Editor: David Greatrix

Copyright © 2012 Bruce Chehroudi. This is an open access article distributed under the Creative Commons Attribution License, which permits unrestricted use, distribution, and reproduction in any medium, provided the original work is properly cited.

Pressure and temperature of the liquid rocket thrust chambers into which propellants are injected have been in an ascending trajectory to gain higher specific impulse. It is quite possible then that the thermodynamic condition into which liquid propellants are injected reaches or surpasses the critical point of one or more of the injected fluids. For example, in cryogenic hydrogen/oxygen liquid rocket engines, such as Space Shuttle Main Engine (SSME) or Vulcain (Ariane 5), the injected liquid oxygen finds itself in a supercritical condition. Very little detailed information was available on the behavior of liquid jets under such a harsh environment nearly two decades ago. The author had the opportunity to be intimately involved in the evolutionary understanding of injection processes at the Air Force Research Laboratory (AFRL), spanning sub- to supercritical conditions during this period. The information included here attempts to present a coherent summary of experimental achievements pertinent to liquid rockets, focusing only on the injection of nonreacting cryogenic liquids into a high-pressure environment surpassing the critical point of at least one of the propellants. Moreover, some implications of the results acquired under such an environment are offered in the context of the liquid rocket combustion instability problem.

1. Introduction

In designs of chemical rocket engines, liquid fuel and oxidizer are often injected as round jets into a hot and elevated-pressure environment of the thrust chamber. The coaxial and impinging jets injectors are two of the well-established designs in liquid rocket engines (LREs). On the other hand, higher specific impulse is a major motivation for operating rocket thrust chambers at progressively higher pressures. Conditions therefore exist in which the injected liquid finds itself near or even above the thermodynamic critical point. Examples are Space Shuttle Main Engine and Vulcain (Ariane 5) with liquid H_2/liquid O_2.

In such cases, major changes occur in some important and key properties of a substance as it approaches the thermodynamic critical point. For example, under thermodynamic equilibrium, the distinction between the liquid and gas phases disappears at and above the critical point and hence it is referred to as a "fluid." Also, large changes in density occur near the critical point. The constant-pressure specific heat becomes very large and surface tension vanishes at and beyond the critical point. As the ambient pressure into which a liquid jet is injected increases, the importance of the solubility of ambient gases into the injected liquid phase increases and one should consider multicomponent phase equilibrium information. For mixtures, determination of the critical conditions, called the "critical mixing temperature or pressure", is a complex process; see Bruno and Ely [1] and Lazar and Faeth [2]. For example, when a pure liquid hydrocarbon fuel drop is introduced into a nitrogen gas, a thin layer on its surface is a mixture of dissolved nitrogen and the fuel which spreads spatially in time; see Umemura [3].

Understanding the behavior of jets under supercritical conditions therefore is critical to design and modeling of the liquid rockets, in particular, cryogenic liquid rockets. For this reason, systematic research programs, both experimental and computations, have been initiated in the past 20 years to understand behaviors of jets under transcritical and supercritical conditions both with and without externally forced (acoustic) excitations. The reason the external excitation is considered stems from the combined experimental/theoretical work suggesting that interaction between

acoustic resonance modes of the chamber and the jets could play an important role in combustion instability. The basic premise here is that when an important dynamic feature, such as the injected jet's dark-core or breakup zone, of an injector design becomes sufficiently sensitive to thermofluid parameters of its environment, it is highly likely that this could strengthen the feedback link thought to be critical in the amplification process and hence push the system into an unstable operating regime.

The purpose of this paper is to present an overview of important experimental achievements, characterizing and understanding nonreacting steady liquid jets injected into supercritical conditions, and offer some implications of these results and potential linkages to production engines. It is not the intention of this work to provide a comprehensive review of the subject, rather to present important findings reported in recent decades.

The coverage of the injectors' experimental data in this paper is divided into three parts: single liquid jets, coaxial jets, and impinging jets. However, the treatment for the impinging jets is comparatively shorter due to limited data available extending to supercritical conditions. Two sections are considered for each part. One focuses on jets injected into an environment devoid of any externally imposed acoustic excitations and the other considers the impact of such excitations on jet characteristics. Most cases reviewed here pertain to cryogenic liquid jets with the environment, into which the jets are injected, existing at thermodynamic supercritical temperatures. This is similar to those experienced in cryogenic liquid rocket engines.

2. Single Jet without External Excitation

In this section, relevant experimental work conducted on a single steady round jet injected into an environment lacking any externally imposed acoustic disturbances is considered. The purpose here is to examine the behavior of such jets under high pressures, specifically supercritical conditions. In the selection of candidate cases, the test matrix is chosen to cover supercritical conditions. However, it is preferred that the matrix spans a broader range encompassing both sub- and supercritical conditions because it generally provides a more comprehensive picture of differences and similarities between the two conditions.

Historically, research on supercritical injection of relevance to liquid rockets started with a published work of Newman and Brzustowski [4]. They used a steady CO_2 jet injected into a chamber of pure N_2 and also into mixtures of CO_2 + N_2 at both sub- and supercritical pressures and temperatures. Obviously, if the chamber is at a supercritical pressure, the injected jet pressure is higher and must also be at a supercritical pressure. They showed that when the chamber pressure approached just above the critical pressure of the CO_2, injection of CO_2 into mixtures of CO_2 + N_2 (varying initial CO_2 concentration to change mixture density) widened the visual appearance of the jet. This was explained to be due to changes in chamber-to-injectant density ratio. At a higher chamber supercritical pressure, injection of CO_2 into a pure nitrogen gas, but varying temperature (from sub- to supercritical), caused shortening of both the jet visible length and width with chamber temperature.

Newman and Brzustowski [4] also investigated and explained effects of increased chamber temperature on jet appearance. They found that such effects were due to progressive reduction in ambient gas density, hence lowering surface tension to zero at critical temperature, and to increase in liquid CO_2 evaporation. In other experiments, CO_2 was injected into a mixture of CO_2 + N_2 with fixed but large initial CO_2 mass fraction in order to reduce jet evaporation. The chamber temperature was fixed at a supercritical value, but its pressure was varied from sub- to supercritical pressures. They hypothesized and conjectured that at supercritical chamber temperatures and pressures the jet may be considered as a variable-density single-phase turbulent submerged gas jet. Finally, assuming self-preserving flow, negligible gravity, zero latent heat of vaporization, ideal gas behavior, and thermal equilibrium between gas and drops, they develop a model for predicting the profile of the outer extent of a supercritical steady jet and its centerline mean axial velocity. Comparison of this model with experiment was very poor near the injector exit area where most important and complex processes take place. Hence, the proposed hypothesis was not backed by this effort and the matter remained unresolved.

After the aforementioned initial study, two organizations (DLR in Germany and AFRL in USA) dominated the field by pursuing systematic research programs to understand jet breakup and dynamics under high chamber pressures at, and specifically exceeding, the critical condition of the injectant. The majority of the experimental works presented here is thus coming from these two organizations plus other satellite universities they collaborated and/or supported. Each organization has constructed a unique facility from which most of the results for nonreacting jets were acquired and presented here. For more details on their facility designs readers are referred to their publications, many of which are listed in the references.

Researchers at DLR began working with the most simplest and fundamental of all cases, that is, the injection of a single nonreacting round jet into a quiescent environment. At AFRL, although initially droplet studies were planned and conducted, a transition to jets at high Reynolds numbers of practical interest was initiated by the author of this paper and his team members; for example, see Chehroudi et al. [5]. The injection of jets were studied at various chamber pressures ranging from subcritical to supercritical (mostly at supercritical temperatures), which included chamber pressures representative of those experienced in typical cryogenic liquid rocket engine (LRE). For safety reasons, and for the H_2/LOX liquid rockets, it was preferred to simulate liquid oxygen with liquid nitrogen. Early studies have shown that at a nonreacting condition the injection behaviors of these two fluids were similar. To avoid complications introduced by mixture effects, however, many of these studies involved injection of cryogenic liquid nitrogen (LN_2) into room temperature gaseous nitrogen (GN_2). Critical pressure and temperature of nitrogen are 3.39 MPa and 126.2 K,

respectively. Injections into other ambient gases were also investigated.

The objective of this section of the paper is to present key findings and discuss representative results. In some cases, key conclusions confirmed independently by both organizations (DLR and AFRL) are highlighted when appropriate and if they add to the reader's understanding. Before delving into details of the results, it worth indicating that Mayer et al. [6] were the first to take active steps towards a large-scale facility investigating both single and coaxial cryogenic jets under cold and fired conditions. They used LN_2 jets at 105 K injected into a GN_2 environment at 300 K, but at varying ambient pressures ranging from sub- to supercritical conditions. They reported drastic changes in the jet structure near and above the critical pressure. The jet behaved similar to the classical atomization of liquid fuels, with ligaments and drops, below the critical pressure. Mayer et al. [6] attributed this behavior to a continual decline of surface tension until it vanished at and beyond the critical point.

2.1. Visualization of the Jet Interface. Figure 1 presents results published in a work led by Chehroudi which shows representative images of cryogenic LN_2 jets injected into gaseous nitrogen at 300 K (supercritical in temperature); see Chehroudi et al. [5]. The initial temperature of the jets was measured in a separate experiment and under identical flow conditions with a very small thermocouple. Depending on the flow condition, the measured initial injection temperature varied from 99 K to 110 K, that is, injected at a subcritical value. Pressures in Figure 1 are reported as reduced pressures (P_r), defined to be the chamber pressure divided by the critical pressure of the injected nitrogen. In frames 1 to 4 (of Figure 1), where the chamber pressure is subcritical, the jets have a classical liquid spray appearance. Figure 2 shows magnified images of the three injection cases under sub-, near-, and super-critical chamber pressures. This software magnification is performed to more clearly show the shear layer structure near the injector exit area. As shown in Figure 1, and consistent with the classical liquid jet breakup regimes described by Reitz and Bracco [7], surface instabilities grow downstream from the injector, and very fine ligaments and drops are ejected from the jet (see also the left image in Figure 2). This behavior corresponds to the second wind-induced liquid jet break-up regime described by Reitz and Bracco [7].

Major structural and interfacial changes occur at about $P_r = 1.03$ as shown in frame 5 of Figure 1. Above this chamber pressure, drops are no longer detected, and as characterized by Chehroudi et al. [5], regular "finger-like" entities are observed at the interface. Rather than breaking up into droplets, the interface appears to dissolve at different distances from the dense and dark core. These structures are illustrated at $P_r = 1.22$ in the middle frame of Figure 2. Such a change in morphology of the mixing layer is evidently due to combined effects of the reduction in the surface tension, as the critical pressure is exceeded, and disappearance of the enthalpy of vaporization because of this transition to supercritical pressures.

As the chamber pressure is further increased, the length and thickness of the dense (and dark) core decrease, and the jet begins to appear similar to a turbulent gaseous jet injected into a gaseous environment. This is illustrated in frames 7 and higher in Figure 1. Any further droplet production, and consequently any additional classical liquid atomization, is completely suppressed. These observations were confirmed by Mayer et al. [6, 8], Chehroudi et al. [5], and Roy and Segal [9]. As mentioned earlier, similar results were also found when injecting liquid oxygen instead of the liquid nitrogen.

It is important to indicate that because of the very large density variations between the jet core and the chamber, Chehroudi et al. [5] investigated whether the evolution of the jet within the region of their measurement was affected by the buoyancy forces. Therefore, they calculated the Froude number values under each test condition. As an example, Chehroudi et al. [5, 10] showed that the Froude number ranged from 42,000 to 110,000. To make sense of these values, they looked at the Chen and Rodi [11] results. Chen and Rodi [11] suggested that the flow is momentum dominated when a defined length scale x_b is less than 0.53, while Papanicolaou and List [12] suggested $x_b < 1$. The length scale is given by $x_b = \mathrm{Fr}^{-1/2}(\rho/\rho_\infty)^{-1/4}(x/d)$, where x is the axial distance, d is the initial jet diameter, and ρ and ρ_∞ are the jet and ambient densities, respectively. The Froude number is defined as $\mathrm{Fr} \equiv \rho U^2/gd|\rho_\infty - \rho|$ where U is the velocity difference and g is the gravitational acceleration. Considering a more conservative estimate by Chen and Rodi [11], the jet used by Chehroudi et al. [5, 10] is momentum dominated for distances less than 30 to 40 mm from the injector exit plane. Pictures presented in Figures 1 and 2 cover up to about 5.5 mm (axial distance/diameter ratio of 21.6) from the injector, and hence buoyancy effects can be ignored in favor of inertial forces.

2.2. Length Scale Investigation. Injection of a single LN_2 jet into gaseous N_2 (at 298 K) has been investigated by Branam and Mayer [13] at ambient pressures of 4 MPa and 6 MPa, corresponding to reduced pressures of 1.17 and 1.76, respectively. The initial injection temperature of the nitrogen was near the critical point. They provided a measure of the length scales by analyzing shadowgraph images and called it as the "visible length scale." More details on their image analysis can be found in Branam and Mayer [13].

Figure 3 shows a typical result of the geometrically averaged length scale (average of radial and axial length scales) measured at the x/D of 10 as a function of the radial position. Results from the k-ε computational method are also shown. This suggests that the measured visible length scale is comparable in magnitude to the Taylor length scale determined by the computational method.

The ratio of the axial to the radial length scales indicates whether the visible structures are spherical or more ellipsoidal in shape. Both length scales are shown in Figure 4 for an injection temperature of 123 K, that is, injection of N_2 at a high density. In the near-injector region, the axial length scales are much larger than the radial ones. Further downstream, however, the visible structures become more

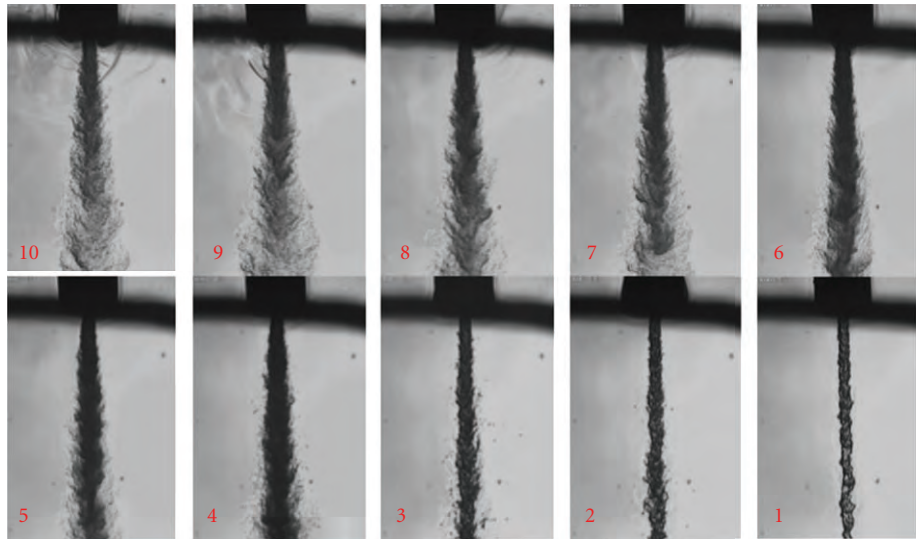

Figure 1: Back-illuminated images of a single nitrogen jet injected into nitrogen at a fixed supercritical temperature of 300 K but varying sub- to supercritical pressures (For N_2: $P_{critical}$ = 3.39 MPa; T_c = 126.2 K). From lower right to upper left: $P_{ch}/P_{critical}$ (frame no.) = 0.23 (1), 0.43 (2), 0.62 (3), 0.83 (4), 1.03 (5), 1.22 (6), 1.62 (7), 2.44 (8), 2.74 (9). Reynolds' number (Re) was from 25,000 to 75,000. Injection' velocity: 10–15 m/s. Froude' number: 40,000 to 110,000. Injectant temperature: 99 to 120 K. Chehroudi et al. [5].

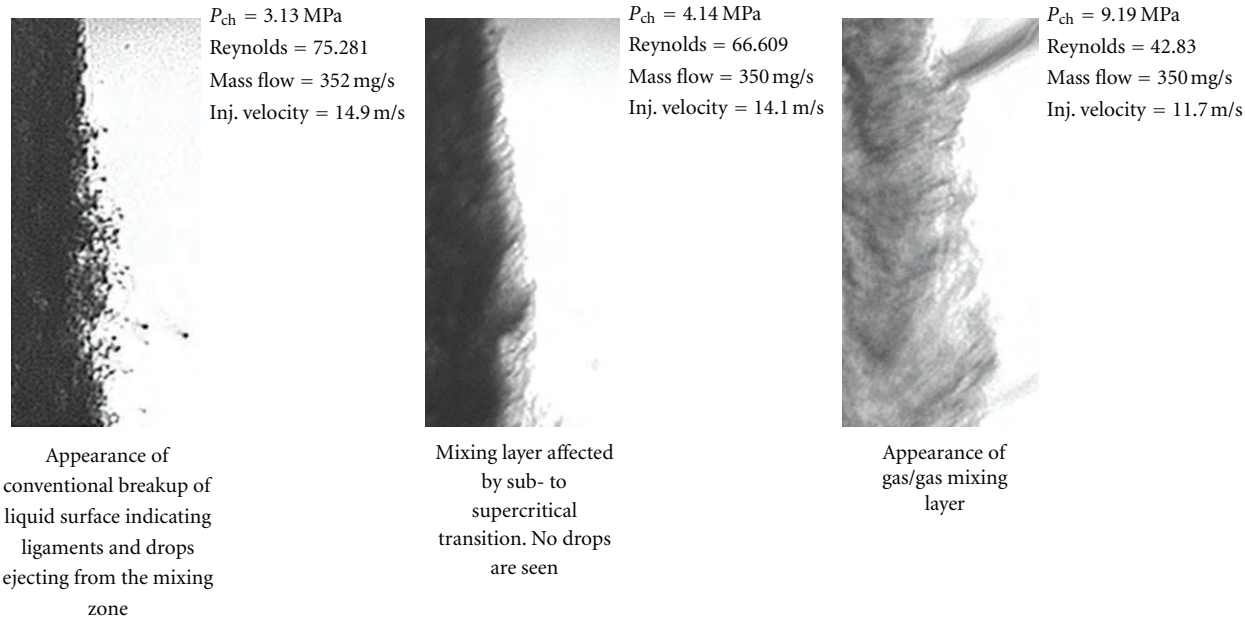

Figure 2: Software magnified images of the jets in Figure 1 at their outer boundaries showing transition to the gas-jet-like appearance starting at just below the critical pressure of the injectant. Images are at fixed supercritical chamber temperature of 300 K. Chehroudi et al. [5].

circular in shape. At a higher injection temperature (132 K), the asymmetry between the radial and axial length scales is not as pronounced as that seen under the lower temperature condition (123 K).

2.3. Jet Spreading Angle or Growth Rate. Measurements and estimations of the growth rate of a jet have been a subject of intense research for years because it provides a primary measure of mixing and development of the jet itself. Chehroudi's group was the first to extract quantitative measurements of this physical parameter using the images taken from a cryogenic N_2 jet injected into GN_2 under both subcritical and supercritical pressures; see Chehroudi et al. [5]. These measurements led to important conclusions regarding the character of the growth rate and the behavior of the jet near the injector and under such conditions, specifically at supercritical chamber pressures.

The spreading angle or growth rate was measured from a field of view within 5.5 mm of the injector exit plane (distance-to-diameter ratio of up to 21.6) and was inertially

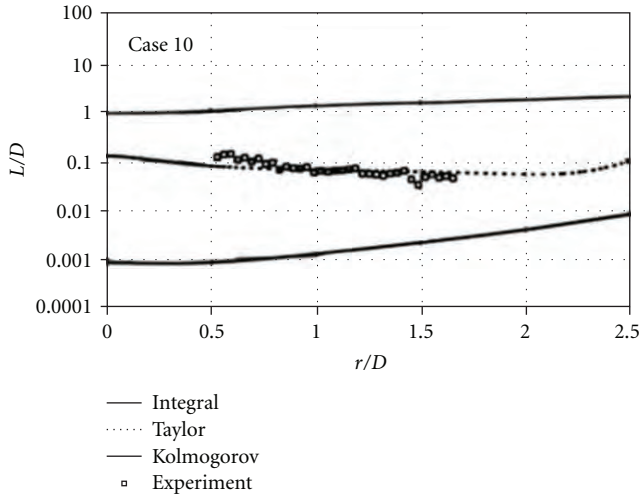

FIGURE 3: Comparison between calculated and experimental length scales for a single jet of LN_2 injected into GN_2 at $x/d = 10$, chamber pressure of 6 MPa, 1.9 m/s, injected temperature of $T = 132$ K. Branam and Mayer [13].

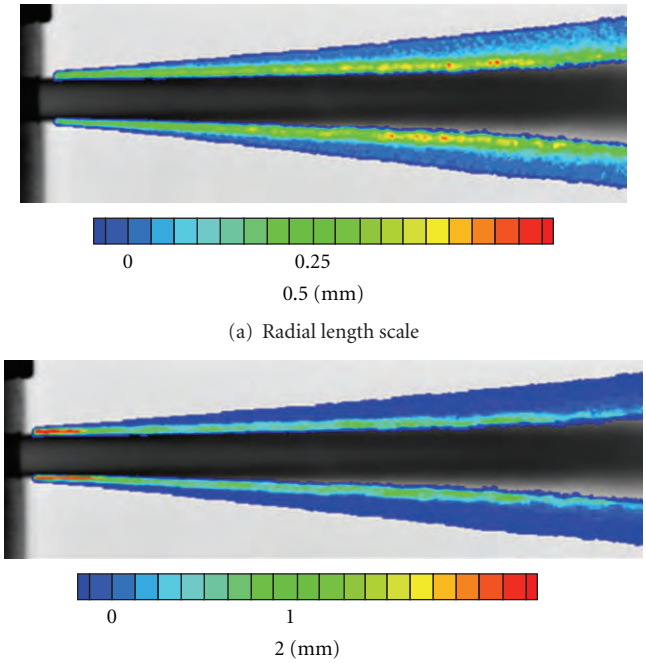

(a) Radial length scale

(b) Axial length scale

FIGURE 4: Experimental length scales for LN_2 into GN_2, chamber pressure of 4 MPa, LN_2 injected temperature of 123 K. Branam and Mayer [13].

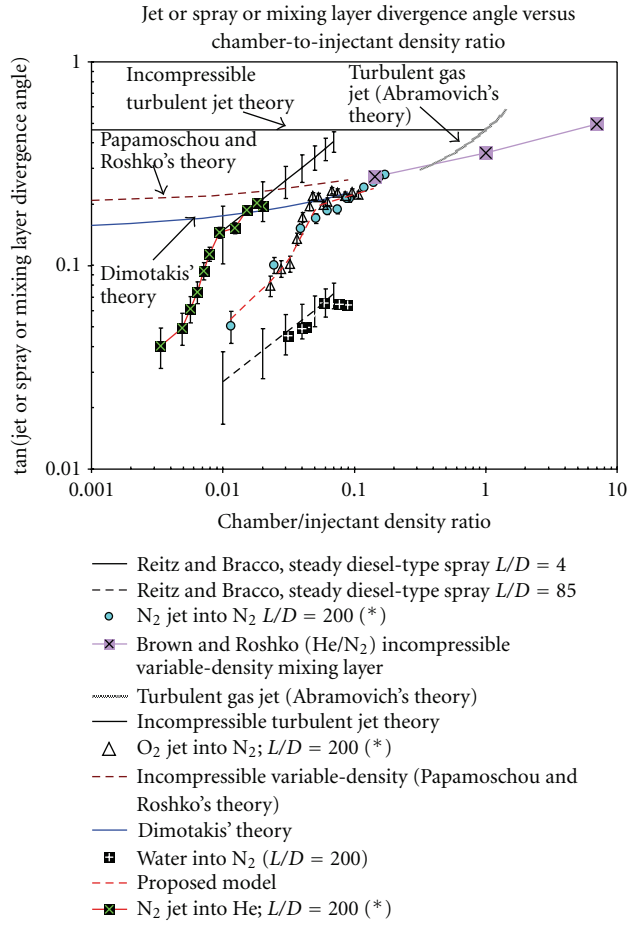

FIGURE 5: Spreading or growth rate of single jets as a tangent of the visual spreading angle versus the chamber-to-injectant density ratio. Data taken by Chehroudi are indicated by an asterisk (*) in the legend. Chehroudi et al. [5].

dominated as discussed earlier. Chehroudi et al. [5] indicated that their data were also taken from the corresponding and appropriate initial region of the jet to ensure existence of a classical mixing layer. The initial jet spreading angle, or its growth rate, was then measured for all acquired images, and results along with those of others are presented in Figure 5. Of importance in this figure is the justification for the selection of the data sets and the nature of their measurements by other researchers. They are elaborated at sufficient detail in earlier papers. In order to gain a deeper appreciation of these selections, the reader is referred to Chehroudi et al. [10]. Therefore, they are only mentioned here in brief.

Because the jets investigated by Chehroudi et al. [5] exhibited both liquid-spray-like and gas-jet-like (two-phase and single-phase, resp.) appearances, depending on pressure (see Figure 1), appropriate comparisons with both liquid sprays (injected into a gas) and gas jets (injected into a gas) were justified and hence these results are presented in Figure 5. The simplest is the prediction of the linear growth or constant spreading angle for the turbulent incompressible submerged jet using the mixing length concept. Following Abramovich [14], a semiempirical equation was used which attempts to incorporate the effects of density variations by an introduction of a characteristic velocity (see Chehroudi et al. [10] for more details).

Brown and Roshko [15] measured spreading angles for a subsonic, two-dimensional, incompressible, turbulent mixing layer in which helium and nitrogen were used. Brown [16] (for a temporally growing mixing layer) and Papamoschou and Roshko [17] proposed a theoretical equation for incompressible variable-density gaseous mixing layers. Finally, Dimotakis [18] used the observation that, in general, the entrainment into the mixing layer from each stream was not the same and, in a system moving with a convection velocity, offered a geometrical argument to derive an equation for two-dimensional incompressible variable-density mixing layers. Chehroudi et al. [5] included predictions from these models as shown in Figure 5. Results by Richards and Pitts [19] for variable-density jets are also included.

Because both liquid-spray-like and gas-jet-like visual behaviors were observed, the growth rate for the liquid sprays produced from single-hole nozzles, typical of the ones used in diesel engines, was also incorporated in this figure. Figure 5 covers a density ratio of four orders of magnitude and is regarded as a unique and new plot in its own right. To some extent, and for comparable cases, disagreements between some results in this figure can be attributed to differences in the definition of the mixing layer thicknesses and the adopted measurement methods. For detailed discussion of this figure, see Chehroudi et al. [5, 10].

The important point which was stressed by Chehroudi et al. [10] is that for a range of density ratios in which images exhibit gas-jet-like appearance, the experimental data agrees well with the proposed theoretical equation by Dimotakis [18] and closely follows the trend of the Brown/Papamoschou and Roshko equation as shown in Figure 5. This can be taken as an important quantitative evidence that at supercritical pressures, the injected jets visually behave like a gas. Chehroudi's work appears to be the first time such a rigorous and quantitative evidence had been developed. The fractal dimension results discussed later provide additional evidence in support of this behavior.

Chehroudi et al. [20] also used the Raman scattering studies to measure density distributions. Initially, the growth rate measurements by them, using results acquired during the Raman scattering work, did not provide the same jet thickness values as those determined by the shadowgraphy approach. Apparently, as discussed by Brown and Roshko [15], different thickness definitions exist, and one can explore their relationship. Similar attempts in the context of supercritical jets showed that within the distances investigated, twice the full-width half-maximum (FWHM) of the Raman intensity radial profiles was equivalent to the thickness values measured through shadowgraphy. Realization of this relationship was very critical to consolidate the results from two different methodologies (Raman versus shadowgraphy). Figure 6 shows the growth rate measured using the Raman data in contrast to those determined through shadowgraph images.

These results were subsequently confirmed and extended by Oschwald and Micci [21] through a similar measurement technique. For example, they showed that when twice the FWHM of the Raman radial intensity profiles is used for

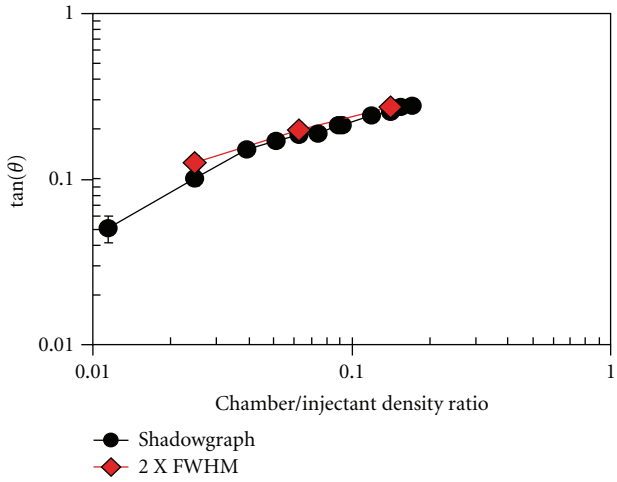

Figure 6: Comparison of the tangent of the spreading angle for a single jet of LN_2 injected into GN_2 measured using shadowgraph and Raman's techniques at twice the FWHM values. Chehroudi et al. [20].

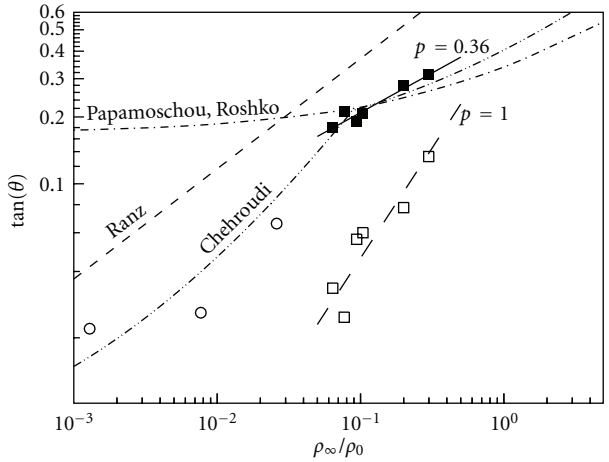

Figure 7: Comparison of the tangent of the spreading angle by Raman's techniques using twice the FWHM values (DLR data). Solid squares are for data from x/D of 15 to 32 whereas hollow squares are from x/D of 0.5 to 14. Chehroudi's model is also shown as dash-dot-dot curve. Single jet LN_2 into GN_2 with injector L/D = 11.6. Data from Oschwald and Micci [21]. Open circles are data points from Reitz and Bracco [7].

x/D values within 15 and 32, a good agreement exists between their results and those by Chehroudi's group (see the case designated as "$p = 0.36$" in Figure 7, where "p" is the exponent of the curve fitted through the data). However, the twice FWHM criterion did not fully agree with shadowgraphs for $x/D < 15$ in the study conducted by Oschwald and Micci [21] (see the case identified as "$p = 1.0$" in Figure 7).

Note that Oschwald and Micci [21] measured a larger range of axial distances and found that the criterion was not universal at extended ranges. There are several reasons why different trends might be observed at different distances.

It has to do with the fact that shadowgraphy and Raman scattering approaches measure different physical properties. The Raman signal is taken to be proportional to density whereas shadowgraphy is sensitive to the gradients of the density distribution. Thus a unique relationship between the results measured by the two methods may only be valid for a limited region and/or perhaps specific configurations. Recall that the data discussed above were obtained from injectors with different L/D ratios. Another potential cause, and hence discrepancies, is errors in attempting to perform Raman's measurements close to the injector inlet where density variations and thus index of refraction variations can be very large.

2.4. Fractal Dimension of the Interface. Fractals are intimately connected to the concept of self-similarity; see Mandelbrot [22]. The fractal dimension of any curve is between 1 and 2. The more wrinkled and space-filling a curve is, the larger the values of its fractal dimension. Natural curves, such as the outline of a cauliflower, are self-similar only to that within a narrow range of scales. The objective of the analysis here was to measure the fractal dimension of the interface of jets injected into the chamber in order to see if any pattern was uncovered.

The fractal dimension of jets at various pressures ranging from subcritical to supercritical was calculated and compared to results by other researchers. Reference results were taken from Sreenivasan and Meneveau [23] who measured the fractal dimensions of a variety of turbulent gaseous jets, mixing layers, and boundary layers. These results indicated a fractal dimension between 1.33 and 1.38. In addition, the fractal dimensions of a turbulent water jet (Dimotakis et al. [18]) and of a liquid jet in the second wind-induced atomization regime (Taylor and Hoyt [24]) were computed from high-resolution scanned images.

The fractal dimensions from the above reference cases are shown as horizontal lines in Figure 8. Overlaid on top of these lines are discrete points indicating the fractal dimension of LN_2 jets injected into GN_2 at various chamber pressures. One sees that at supercritical chamber pressures, the fractal dimension approaches a value similar to gaseous turbulent jets and mixing layers. As the chamber pressure is decreased, the fractal dimension also decreases. Below a reduced pressure of 0.8, the fractal dimension rapidly declines to a value approximately equal to that of liquid sprays in the second wind-induced liquid jet break-up regime.

A detailed discussion of the above results is also found in Chehroudi et al. [25, 26]. The key conclusion reached by Chehroudi's group is that the results from fractal analysis complement and extend the imaging data they acquired for the initial jet growth rate. At supercritical pressures, jets have a fractal dimension similar to turbulent gas jets, and at subcritical pressures, cryogenic jets have a fractal dimension similar to liquid sprays. The transition occurs at about the same chamber pressure as that when the transition in visual appearance and growth rate data discussed in Figure 5 takes place. Such distinctly different behaviors for jets under sub- and supercritical conditions were first demonstrated by

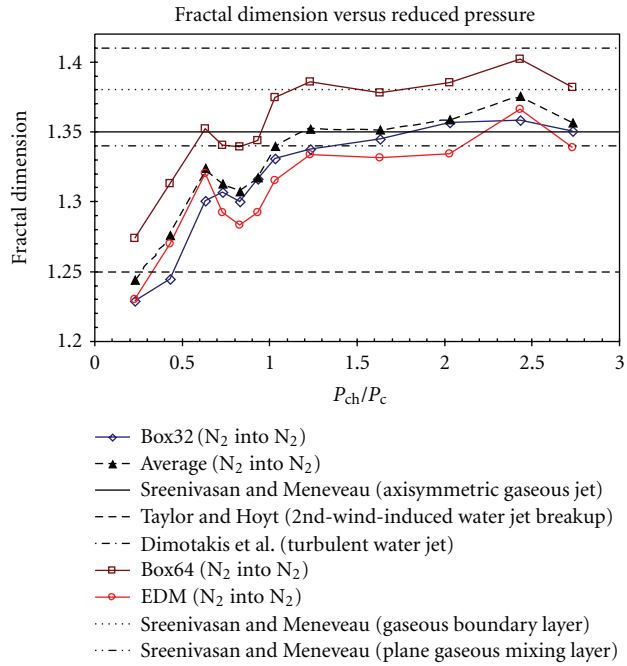

Figure 8: Fractal dimensions of the boundaries of various single jets as a function of reduced chamber pressure (chamber pressure divided by the critical pressure of the jet material). Discrete points are data from Chehroudi et al. [25, 26]. Box 32, Box 64, and EDM are different methods of calculating the fractal dimension, giving an impression of the extent of variability; for details, see Chehroudi et al. [25, 26].

Chehroudi's group in a quantitative manner using fractal analysis.

2.5. Measurement of the Dark-Core Length. Before presenting their results under supercritical conditions, Chehroudi et al. [25, 26] discussed some measurements from (gaseous and liquid) jets at subcritical conditions to set the stage and provide a contrast to their data. It is therefore useful to summarize what they recalled in their work.

According to Abramovich [14], the length of the "potential core" in isothermal uniform-density axisymmetric and two-dimensional jets is estimated to be about 6 to 10 injector diameters; whereas for nonisothermal cold jets injected into hot environments, it can reach up to about 25 injector diameters depending on jet temperature.

Also, according to Chehroudi et al. [27] the "intact core" length of the liquid sprays similar to the ones used in diesel engines is given by the equation $Cd_j(\rho_l/\rho_g)^{1/2}$ where ρ_l and ρ_g are liquid injectant and chamber gas densities, respectively, d_j is an effective jet exit diameter, and C is a constant between 3.3 and 11. This reflects an intact core length between 33 and 110 injector diameters for the chamber-to-injectant density ratio of 0.01 and between 16.5 and 55 diameters for the chamber-to-injectant density ratio of 0.04. These results are presented in Figures 9(a) and 9(b) for better comparison with what is measured for LN_2 injection into both sub- and supercritical GN_2 environment.

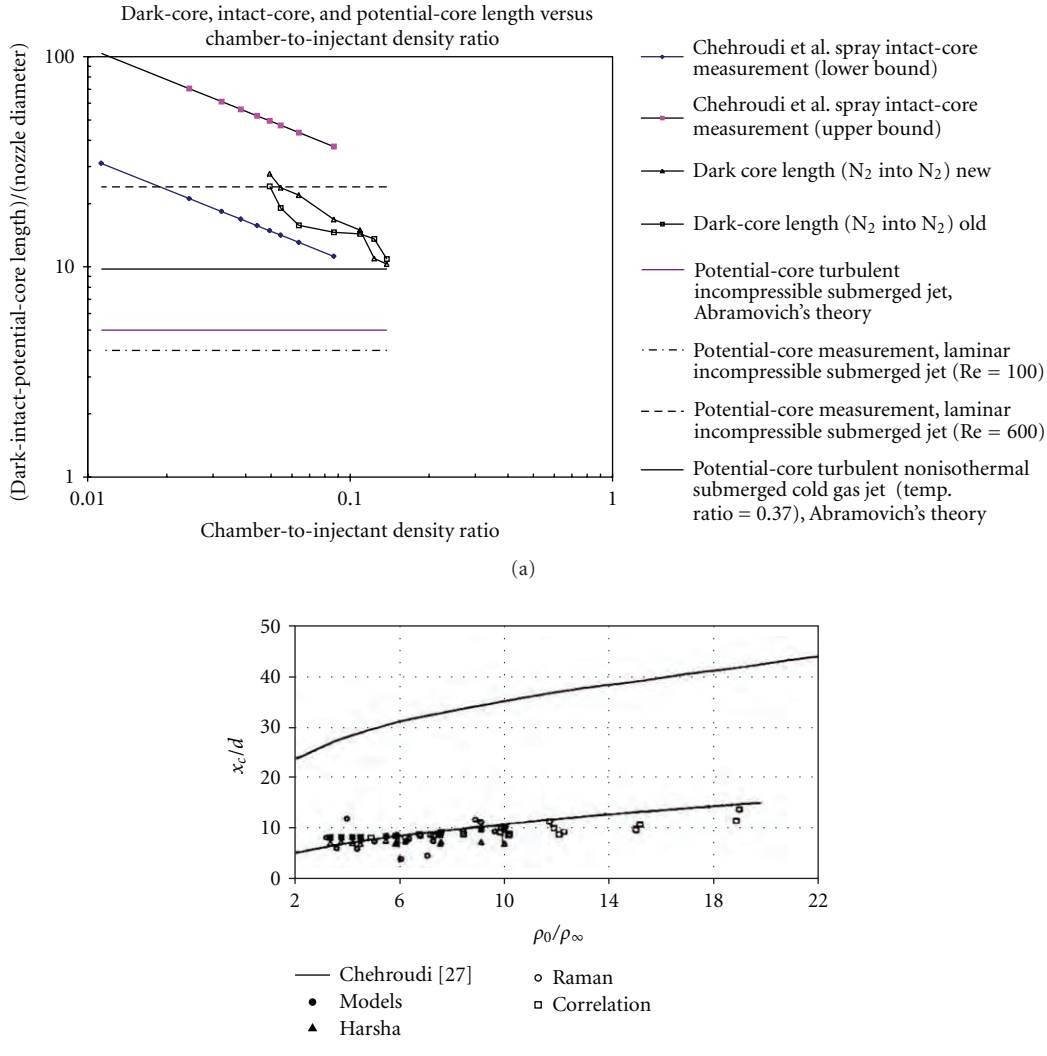

Figure 9: Ratio of either the dark-core, intact-core, or potential-core length, depending on the case, divided by the density ratio for single jets. (a): Chehroudi et al. [10], determined by analysis of shadowgraphs, for an injector $L/D = 200$. (b): Branam and Mayer [13], determined via Raman data, injector $L/D = 40$. Models: determined by computer simulation. Correlation: a correlation using a set of Raman's data by Branam and Mayer [13].

Considering that the classical two-stream mixing layer should start from the injector exit and extends to approximately the end of the potential core (or intact core) of the jet, Chehroudi et al. [5, 10] assumed that the jet "dark-core" region seen in their images played a similar role as the intact core or potential core. Figure 9(a) shows the dark-, intact-, or potential-core lengths normalized by the injector hole diameter plotted versus density ratio. By referring to Figure 9(a), Chehroudi et al. [5, 10] indicated that the growth rate data taken by them, which is presented earlier in Figure 1, was indeed from the corresponding and appropriate initial region to ensure existence of a classical mixing layer. They emphasized that it is only then when a valid comparison can be made (as they did) between their results and the two-stream mixing layers available in the literature. Finally, they found that the core length fluctuation levels at supercritical condition were several times lower than those observed at subcritical chamber pressures.

Complementary results by the Branam and Mayer [13] are also shown in Figure 9(b). These results were determined through a log-log plot of the centerline intensity measured by the Raman scattering to distinguish different flow regions. Note that the horizontal axis for Figures 9(a) and 9(b) are inverse of each other. The Branam and Mayer [13] data are at or below the lower bound of the Chehroudi et al. [27] model (i.e., solid curves in Figure 9(b)) which was proposed based on the liquid spray data in various atomization regimes. For chamber-to-injectant density ratios of less than 0.1 in Figure 9(a) (or injectant-to-chamber ratio of greater than 10 in Figure 9(b)), it appears that the Chehroudi et al. [25, 26]

experimental data shown in Figure 9(a) is larger by about a factor of 1.5 to 2 compared to the "correlation" given by Branam and Mayer [13] in Figure 9(b).

Considering that the raw data used by the two groups are from two different injectors and measurement methodologies, the agreement is considered adequate. However, further investigations are warranted.

2.6. Density and Temperature Fields. The main purpose of the Raman scattering measurements was to provide quantitative information and to enable mapping of the jet density field. Temperatures, for example, were calculated assuming application of a suitable equation of state. Radial density profiles were reported by Oschwald and Schik [28] in a normalized fashion. In this section, the centerline density and/or temperature profiles as functions of the axial distance from the injector exit plane and their self-similarity assessment are discussed.

The test conditions were chosen in order to assess the influence of the thermodynamic state of the injected cryogenic N_2 on the jet disintegration process. For example, above the critical pressure, the specific heat is finite but exhibits a maximum at a particular temperature. At this same point, the thermal diffusivity exhibits a minimum value. Three test cases were therefore investigated as shown in Figure 10(a). In test case A, the initial injection temperature is both above the critical temperature and above the temperature where the specific heat assumes a maximum value, whereas for test cases B and C the initial injection temperatures are both below the critical value and the temperature where the specific heat is at a maximum value.

Figures 10(b) and 10(c) show normalized centerline axial profiles of the density and temperature acquired by Oschwald and Schik [28] at a chamber pressure of 4 MPa (near the critical pressure of nitrogen). Note that the density decay behavior becomes slower as the initial injection temperature is decreased. The temperature profile, however, stays flat for up to a normalized distance (x/D) of about 25 to 30. They indicated that the development of the centerline temperature reflects the thermophysical properties of the nitrogen, being specific to the region where the specific heat reaches a maximum. For initial injection temperatures below the temperature where the specific heat reaches a maximum value, as the jet heats up, the fluid has to pass through a state with a maximum specific heat. The fluid temperature can then reach a value where a large amount of heat can be stored without any noticeable increase in temperature. It appears that the maximum specific heat line in a supercritical fluid results in a behavior similar to a liquid at its boiling point. That is, heat transfer to the nitrogen does not increase its temperature but simply expands the fluid (i.e., increases its specific volume). It is also for this reason that the dashed curves in Figure 10(a) are referred to as "pseudo boiling lines." Note that the density of the fluid varies strongly with temperature in this zone. At 6 MPa ($P_r = 1.76$, data not shown), the maximum of the specific heat is much less pronounced and the effects of the pseudo-boiling line is not as distinct as those seen under chamber pressure of 4 MPa. As shown by Oschwald and Schik [28], however, far downstream, it was observed that the temperature of the disintegrating and mixing supercritical fluid jet approached a value representative of a fully mixed jet but at a slower pace than that for the jet density.

The self-similarity of the density field has also been investigated by Chehroudi et al. [20] and the results are presented in Figure 11. According to Wygnanski and Fiedler [29], a fully self-preserved velocity field of a turbulent air jet should be observed at an x/D of greater than 40 when the Reynolds number is near 100,000. So et al. [30] reported self-preservation for x/D values larger than about 20 in a binary gas jet at Reynolds' number (Re) of about 4300. Although it appears that some inconsistencies exist for this criterion, one can see that for the near-critical and supercritical pressures, the density radial profiles approach the similarity model curve shown in Figure 11. The disagreement increases at subcritical pressures where the model is least applicable. It is worth indicating that results from a modeling and computational simulation by Zong et al. [31] also agrees well with Chehroudi's Raman scattering measurements.

Chehroudi et al. [20] using their Raman scattering data determined the FWHM of the radial density profiles at each axial distance from the injector, and the results, along with data by other investigators, are shown in Figure 12. More information on their experimental conditions is given in Table 1. Note that except for Chehroudi et al. [5, 25] and Oschwald et al. [32], all others performed injection of gaseous fluids into an ambient gas at subcritical pressures (based on the injectant critical pressure). Also, the FWHM was determined using the mass fraction profiles in both So et al. [30] and Richards and Pitts [19]. However, reported FWHM values by So et al. [30] using both density and mass fraction profiles were comparable. Chehroudi et al. [20] data in Figure 12 shows an increasingly larger spreading rate as chamber pressure is raised. The data at the supercritical condition ($P_r = 2.03$) approaches that of Richards and Pitts [19] acquired at a density ratio of 1.56 even though this ratio is substantially smaller than Chehroudi et al. [20] data. Results at larger distances were not available for their jet to enable a more comprehensive comparison between the cases.

Richards and Pitts [19] concluded that if care is exercised to ensure that the flow is free of buoyancy and coflow effects, the spreading rate in variable-density jets was independent of the initial density ratio, velocity profile, and turbulence level and conformed with the constant-density results of others. In addition, they proposed a slope in the range between 0.212 and 0.220 for the linear jet growth rate equation; see Figure 12. However, a linear least-square fit to Chehroudi et al. [20] data at $P_r = 2.03$ gives a slope of 0.102, almost half of that by Richards and Pitts [19]. One possible explanation for this difference is that Chehroudi's data covers a range much closer to the injector exit plane than that by Richards and Pitts [19], leading to a lowered growth rate value. A tendency towards higher growth rates can be seen if only the farthest two data points are considered in Chehroudi's data. However, a solid conclusion cannot be drawn based on these two points. It is also possible that at some high enough injectant-to-chamber density ratio, the spread rate universality indicated by Richards and Pitts breaks down and

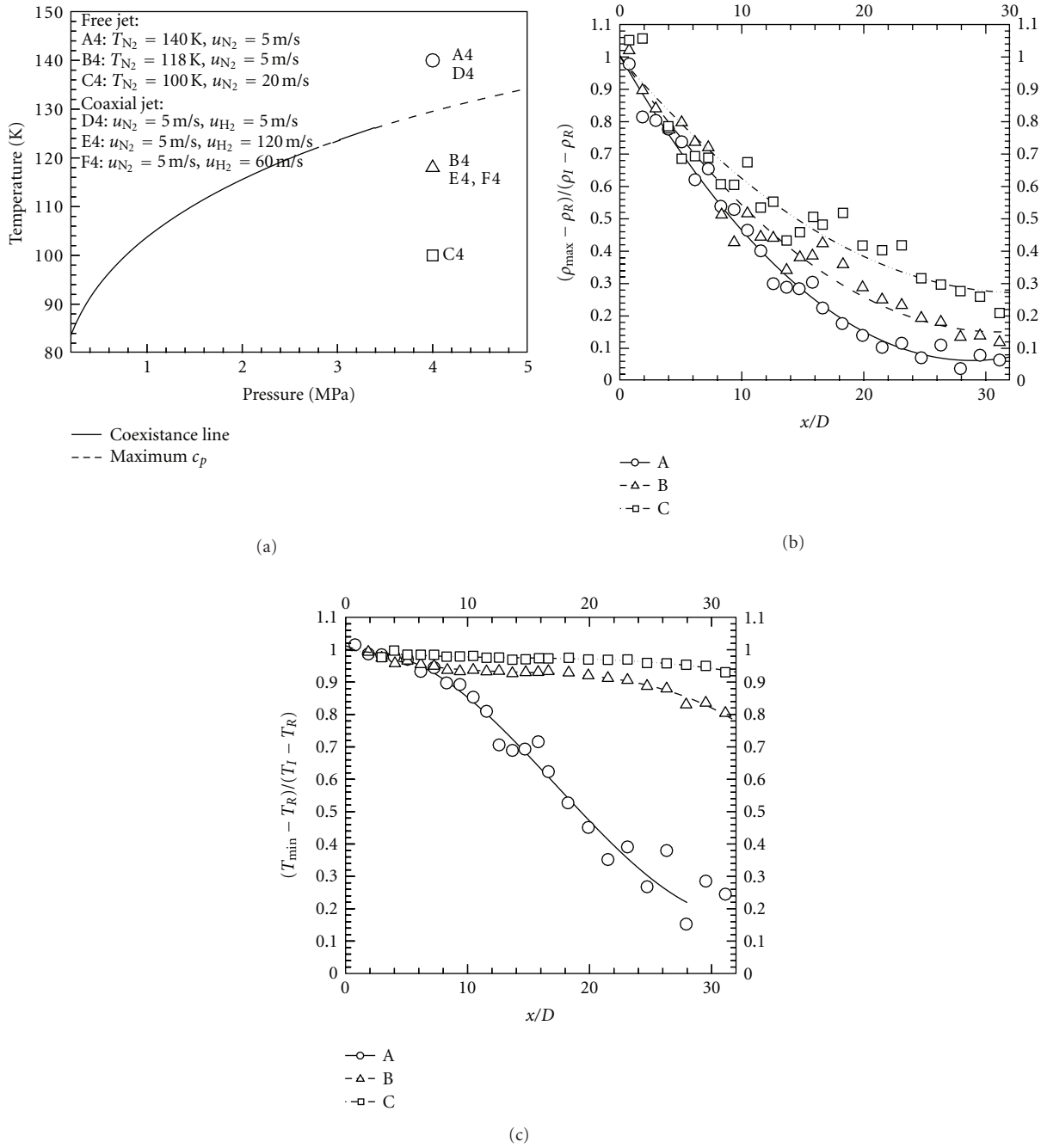

FIGURE 10: Normalized centerline density (b) and temperature (c) axial profiles of LN_2 injected into GN_2 at three different injection temperatures and a chamber pressure of 4 MPa (i.e., near critical pressure). The plot (a) shows the thermodynamic conditions under which test cases A, B, and C are conducted. The dashed line is the pseudoboiling line. Note, A4, B4, and C4 symbols represent A, B, and C cases, respectively. Oschwald and Schik [28].

one observes a somewhat retarded growth rate for variable-density turbulent jets. Some evidence in support of this position was given by Chehroudi et al. [20].

2.7. Phenomenological Model of the Jet Growth Rate. Using the experimental data collected on the growth of a cryogenic jet, a phenomenological model for the growth rate was proposed by Chehroudi et al. [5, 10] for the first time in the literature. Complete details on the development of this equation are to be found in these references. However, the physical reasoning motivating the proposed model equation is outlined below.

It was noticed by Chehroudi that previous expressions for the growth rate of liquid sprays and of turbulent jets have

Table 1: Some information extracted from works by other investigators reported here. T_{inj} and T_{ch} are injection and chamber temperatures. P_{ch} is chamber pressure. L/D is the injector hole-to-diameter ratio, x/D is the normalized distance from injector exit within which measurements were made. Chehroudi et al. [20].

	(Fluid inj./cham.)	T_{inj} K	P_{ch} MPa	T_{ch} K	Reduced pressure P_r	Inj./chamb. density ratio	Diameter D mm	Diameter L/D	Diameter x/D	Raynolds' number Re	Profile used to measure FWHM
Oschwald et al.	N_2/N_2	118	4	298	1.17	3.34	1.9	11.5	8.42	$1.2E+05$	Density
Oschwald et al.	N_2/N_2	140	4	298	1.17	12.5	1.9	11.5	1.05	$1.3E+05$	Density
Chehroudi et al.	N_2/N_2	95	6.9	295	2.03	7.1	0.505	100	4.8 to 24.4	$3.5E+04$	Density
Chehroudi et al.	N_2/N_2	110	1.5	295	0.43	40.6	0.505	100	4.8 to 24.5	$1.2E+04$	Density
So et al.	(He + Air)/Air	275	0.1	275	0.08	0.64	9.5		5.1	$5.0E+03$	Concentration and density
So et al.	(He + Air)/Air	275	0.1	275	0.08	0.64	9.5		6.4	$5.0E+03$	Concentration and density
Richards and Pitts	He into Air	275	0.1	275	0.44	0.138	6.35	~50	20–80	$4.0E+03$	Mass fraction
Richards and Pitts	C_3H_8 into Air	275	0.1	275	0.02	1.56	6.35	~50	40–120	$2.5E+04$	Mass fraction

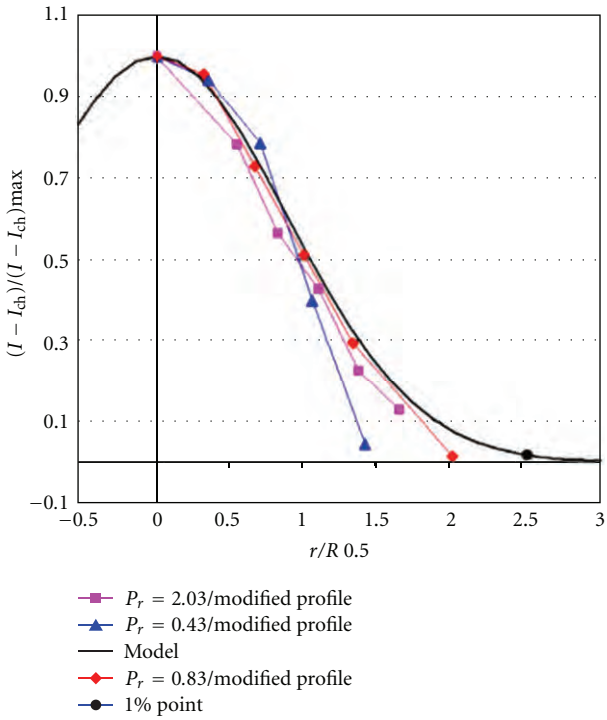

Figure 11: Plots of normalized intensity versus normalized radius for a single LN_2 jet injected into GN_2, at $x/D = 12.2$, at subcritical, near-critical, and supercritical pressures (Chehroudi et al. [20]). The solid curve is the self-similar model that represents data from a gaseous jet injected into a gaseous environment. I and I_{ch} symbols are measured intensities in the jet and in the chamber far away from the jet, respectively. Chehroudi et al. [20].

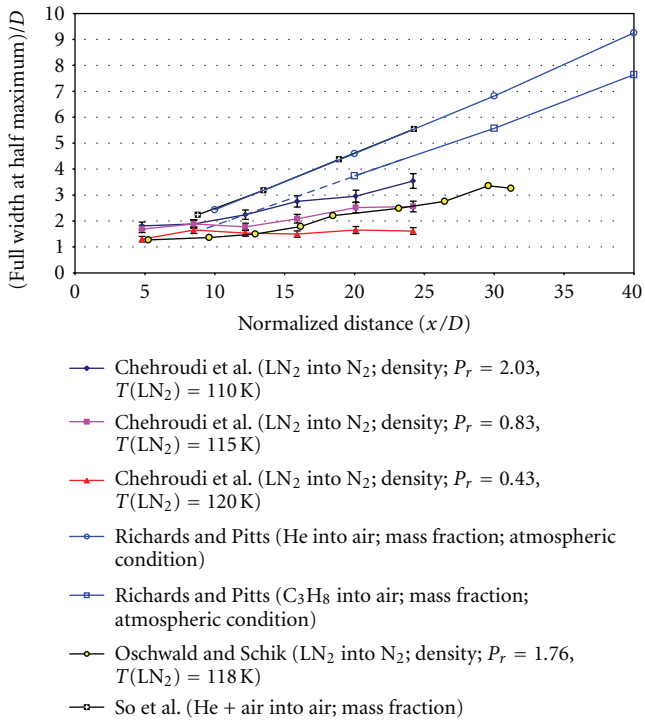

Figure 12: Normalized FWHM of the density-surplus radial profiles of single jets plotted as a function of the normalized axial distance from the injector exit plane. From Chehroudi et al. [20].

a remarkably similar form. For example, Reitz and Bracco [7] proposed that the growth rate of isothermal steady liquid sprays could be expressed as

$$\theta \approx 0.27\left[0 + \left(\frac{\rho_g}{\rho_l}\right)^{0.5}\right]. \quad (1)$$

The first term in the bracket is the number zero. This zero term was purposely kept to enable a comparison with other equations Chehroudi et al. [5, 10] discussed. They also referred to an equation proposed by Papamoschou and Roshko [17] for incompressible, but variable-density, turbulent gaseous jets:

$$\theta \approx 0.212\left[1 + \left(\frac{\rho_g}{\rho_l}\right)^{0.5}\right]. \quad (2)$$

The similarity in the form of these equations is quite astonishing considering vast differences between the cases. Chehroudi then suggested a linkage between the two cases. This is how Chehroudi et al. [5, 10] explained their case.

Imagine a jet that is being injected into a subcritical pressure environment similar to the ones shown in frame 4 of Figure 1 (or the left image in Figure 2). Clearly there are drops, ligaments, and interface "bulges" testifying existence of a surface tension. Chehroudi's group also reported evidence of a thermodynamic phase change under this condition. Hence, one appropriate characteristic time of the problem (at subcritical, $P_r < 1$) is the "bulge" formation/separation time (τ_b) on the interface of the turbulent liquid jet. This time scale, according to Chehroudi et al. [5, 10], characterizes the formation and separation event of bulges from the liquid jet which subsequently produce isolated ligaments and drops. Then they referred to a suggestion made by Tseng et al. [33] that this time scale was equal to $(\rho_l L^3/\sigma)^{1/2}$ for the primary breakup in turbulent liquid jets, where ρ_l, L, and σ are liquid density, characteristic dimensions of turbulent eddies, and surface tension, respectively. The second relevant characteristic time (for subcritical jets) that Chehroudi considered was the gasification time (τ_g). Here, an estimate of this time was calculated through the so-called D-squared law of spherical drop evaporation which is equal to D^2/K, where D and K are drop diameter and vaporization constant, respectively. In addition, Chehroudi also proposed a hypothesis as follows: if the aforementioned characteristic times (calculated for appropriate length scales) were nearly equal in magnitude, then the interface bulges are not able to separate as unattached entities from the jet interface to form ligaments and drops. This is because they are gasified as fast as they desire to be detached. This condition was then defined as the onset of the gas-jet-like behavior. Therefore, the transition between liquid-spray-like and gas-jet-like behaviors would be governed by finding the point at which these characteristic times are approximately equal. The scenario just explained is also supported by the "comb-like" structures seen in the middle image of Figure 2.

Using the above physical description, a model equation was then proposed for the N_2/N_2 system as

$$\theta = 0.27\left[\frac{\tau_b}{(\tau_b + \tau_g)} + \left(\frac{\rho_g}{\rho_l}\right)^{0.5}\right]. \tag{3}$$

In the limit when $\tau_g \gg \tau_b$ and $\tau_g \to \infty$, this equation collapses to the isothermal liquid spray case. This equation agrees well with the Chehroudi et al. [5, 10] experimental data at subcritical pressures for $\tau_b/(\tau_b + \tau_g) < 0.5$. A constant value of 0.5 was used for this term to predict the spreading rate at higher chamber pressures, including supercritical pressures.

For injection of N_2 into N_2, the characteristic time ratio, $\tau_b/(\tau_b + \tau_g)$, was computed from the experimental measurements of bulge and droplet sizes and calculations of the relevant properties. For N_2 injection into other gases, however, reliable information about the mixture properties at the interface, particularly the surface tension, prevented such a calculation from being performed; see Chehroudi et al. [5, 10]. To model these cases though, they further hypothesized that the characteristic time ratio term is a dominant function of the density ratio; that is, $\tau_b/(\tau_b + \tau_g) = F(\rho_g/\rho_l)$. Chehroudi then referred to the work by Brown and Roshko [15] in which they indicated that such a hypothesis is reasonable. This is because at low Mach numbers, there is no distinction between mixing layers where the two streams have different molecular weights, temperatures, or compressibility effects. Measurements and calculations of $\tau_b/(\tau_b + \tau_g)$ provided a shape of the function "F" for the N_2/N_2 system which is given as a plot in Chehroudi et al. [5, 10]. A curve fit of that plot generates the following equation:

$$F\left(\frac{\rho_g}{\rho_l}\right) = 5.325\left(\frac{\rho_g}{\rho_l}\right) + 0.0288 \quad \text{when } \frac{\rho_g}{\rho_l} < 0.0885$$
$$= 0.5 \quad \text{when } \frac{\rho_g}{\rho_l} \geq 0.0885. \tag{4}$$

It was found that the same function, F, calculated from measurements of the N_2/N_2 system could be made to work for other cases, provided that a case-dependent transformation was made to the density ratio at which the function F is evaluated. The final form of the Chehroudi proposed equation is

$$\theta = 0.27\left[F\left(x\left(\frac{\rho_g}{\rho_l}\right)\right) + \left(\frac{\rho_g}{\rho_l}\right)^{0.5}\right], \tag{5}$$

where $x = 1.0$ for N_2 into N_2, $x = 0.2$ for N_2 into He, and $x = 1.2$ for N_2 into Ar.

The quality of the agreement with experimental data is demonstrated in Figure 13. Hence there are no major changes in the form of the proposed model equation, even for an extreme arrangement such as injection of N_2 into He gas. It is also important to indicate that spreading angle

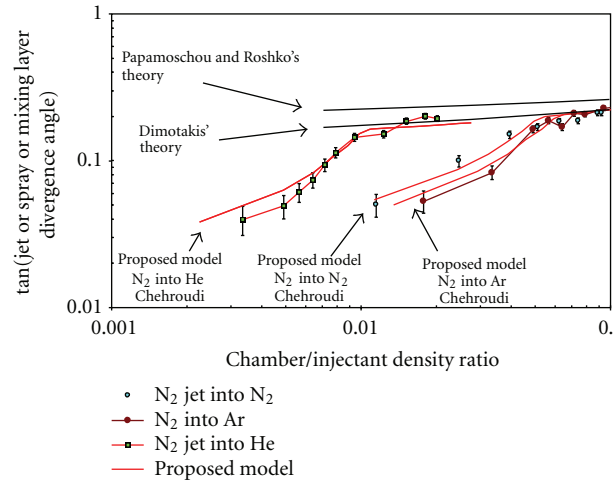

Figure 13: Comparison of the Chehroudi's proposed growth rate model with experimental data for single jets. Chehroudi et al. [5, 10].

under supercritical condition using modeling and computer simulation work by Zong and Yang [34] also agrees with Chehroudi's equation.

3. Single Jet with External Excitation

3.1. Effects of External Acoustic Field. Substantial evidences accumulated in the past attributed combustion instability to a complex interaction of the external acoustic field with the fuel injection processes, leading to incidences of instability in liquid rocket engines. For example, Oefelein and Yang [35] indicated that the near-injector processes in the thrust chamber were generally more sensitive to velocity fluctuations parallel to the injector face than normal to it. For this and other reasons, controlled experimental, analytical, and computational studies have been conducted in the past focusing on the effects of acoustic waves on both gaseous and liquid jets from a variety of injector designs. However, as indicated earlier, with a few exceptions, the scope of this paper is limited to experimental work which covers injection into supercritical conditions.

Chehroudi and Talley [36] used a piezo-siren design capable of generating sound waves with a sound power level (SPL) of up to 180 dB. This was used at three chamber pressures of 1.46, 2.48, and 4.86 MPa (reduced pressures of 0.43, 0.73, and 1.42, resp.). The experimental setup consisted of an acoustic driver and a high-pressure chamber, forming a cavity which resonated at several frequencies. The strongest ones were reported at 2700 and 4800 Hz. This basic setup was also used as the backbone for many of their future studies on coaxial injectors albeit with some improvements in data acquisition and facility plumbing. Chehroudi and Talley [36] injected LN_2 into GN_2 at room temperature under sub- and supercritical chamber pressures. Three different flow rates were considered, and the nature of the aforementioned interaction was documented via a high-speed imaging system using a CCD camera.

Figure 14 shows some sample results from this study where images of the jet are shown at two different perpendicular directions. These pair images at two different angles were taken on different test runs, but the operating conditions were as close as possible to each other. Each composite jet image consists of a mosaic of several images taken from the same test run but at different times and jet axial locations.

Chehroudi and Tally [36] reported that the acoustic field constricted the jet in the wave propagation direction, as seen in Figure 14, and consequently stretched the jet in the direction perpendicular to the propagation. They found that the impact of the acoustic waves on the jet structure was indeed strong at subcritical and near-critical pressures, but weakest at supercritical pressures. This is quite evident in Figure 14. They also observed that the externally imposed acoustic field interacted strongly at low injectant flow rates. The weakest effect was observed at supercritical pressures. This suggests that the mechanisms governing the coupling between acoustic waves and jets may be significantly different for jets injected under supercritical and subcritical conditions. This observation is important and its implications are discussed later in this writing.

To search for a plausible reason for the observed minimal impact at supercritical chamber pressures, Chehroudi and Talley [36] used the information mentioned earlier that at supercritical pressures, the unperturbed-jet spreading rate is the same as that by an incompressible variable-density gaseous jet; see Chehroudi et al. [5, 10]. For this reason, one expects the existence of vortices similar to what has been described, for example, by Rockwell [37] in which transverse disturbances were generated by an externally oscillating plate at a fixed amplitude but different frequencies (1000 to 10000 Hz). A synopsis of Rockwell's conclusions is useful in the context of the discussion here and hence is presented in the next two paragraphs.

A relatively large planar nozzle was designed by Rockwell [37] to inject water and investigate the details of vortex formation and their interactions near the exit area. The effects of the frequency of oscillations on the natural vortex coalescence were classified based on a Strouhal number ($St = fd/U$, where f, d, and U are the externally imposed excitation frequency, jet diameter, and mean jet velocity) versus Reynolds number ($Re = \rho U d/\mu$, where ρ and μ are the injectant density and viscosity) plot, see Figure 15. For the range of Re investigated (1,860 to 10,800), natural breakdown of the jet (i.e., with no external disturbances) was observed to be within a few nozzle widths. The dimensionless frequency (St_N) of natural vortices was found to change with Re number as $St_N = 0.012\ (Re)^{0.5}$. Four regimes were distinguished based on the observed effects of the external disturbance on the nature of the vortex interaction. The reference regime was that which corresponds to the natural breakdown of the jet. The four regimes were named, in order of decreasing St number, as "upper zone," "preservation," "matched excitation," and "forced fusion" regimes. A plot of these regimes is shown in Figure 15 and compared with the values estimated for Chehroudi's study using LN_2 injection into a GN_2 chamber.

In the "upper zone" regime of Figure 15 where the excitation frequencies were higher than about 3 to 4 times the natural breakdown frequency ($St > 3\ St_N$), no effects were observed. In the "preservation" regime, the core flow of the jet tended to be preserved followed by the induction of smaller vortices, the time-averaged velocity profile was narrowed, and the longitudinal turbulence was decreased (relative to undisturbed case). When the excitation frequency was matched with the natural break-down frequency ("matched" regime), the effect was to accelerate the process of vortex formation and growth relative to the undisturbed case. Also, transverse distortion of the jet core was seen due to the vortex growth and coalescence. For the symmetrical jet work of Becker and Massaro [38], symmetrical ring vortices were produced and highest time-averaged widening of the jet has occurred. This was in contrast to the planar jet case in which vortices on the two sides of the jet were 180 degrees out of phase with each other. This regime merges to the "preservation" regime at higher Re number (~10,000). In the "forced fusion" regime (frequencies ~1/3 of natural jet breakdown), the natural break-down vortices were forced to fuse early as a result of the formation of large-diameter applied disturbance vortices. Vaslov and Ginevskiy

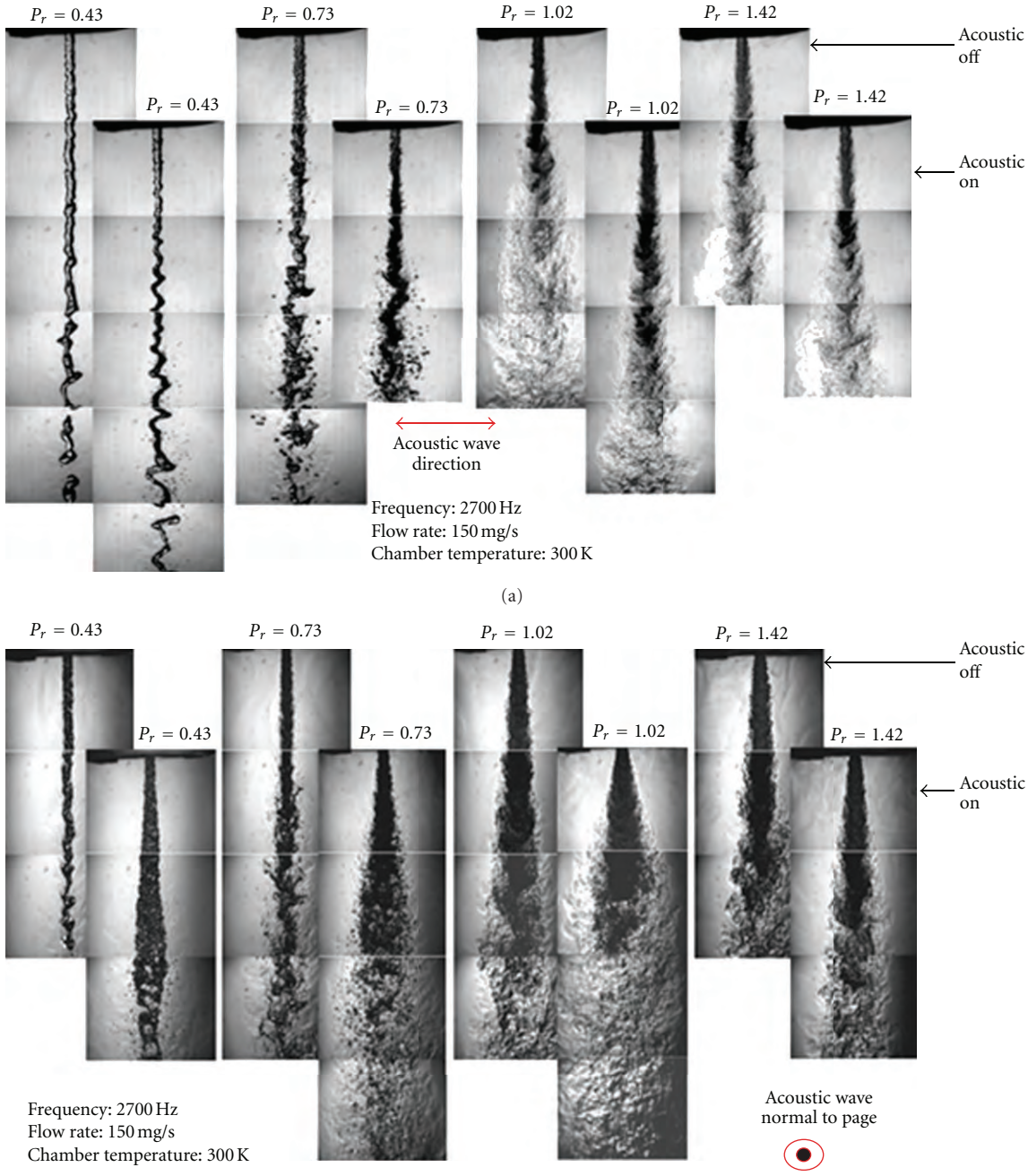

FIGURE 14: Interaction of acoustic waves with a single round liquid nitrogen jet injected into gaseous nitrogen at a range of chamber pressures from sub- to supercritical conditions. (a) Top images show front view; only one acoustic driver located at the left of the jet. The set of images shifted downward are when the acoustic field is turned on as indicated. (b) Bottom images show side views of the same jet (the same acoustic driver is located behind this page). P_r is the reduced chamber pressure (i.e., chamber pressure divided by the critical temperature of the injected nitrogen). Chehroudi and Talley [36].

[39] found that in this regime the time-averaged velocity profile of the jet was broadened. Finally, in the "lower zone" regime (frequencies < 1/10 of natural jet breakdown), the vortex growth was unaffected in their formation region. In the limit, however, as St approaches zero, the jet experienced a quasi-steady deflection process. Rockwell [37] stated that a fallacious averaged jet widening is detected if a time-averaged measurement technique is used downstream the injector, when in reality the jet is being deflected by the applied transverse disturbance.

To see how the results of Chehroudi and Talley [36] relate with Rockwell [37], their supercritical data is superimposed on the plot by Rockwell indicating different regimes discussed in the previous paragraph. Figure 15 shows a

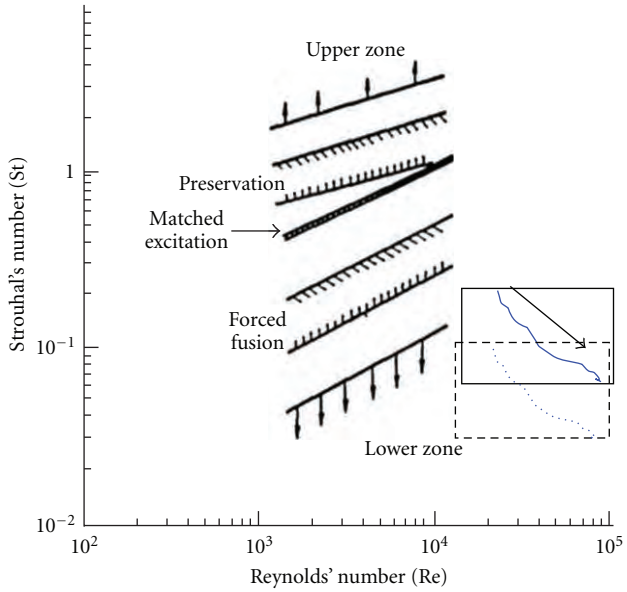

Figure 15: Regimes discussed by Rockwell [37] shown on an excitation Strouhal number versus the jet Reynolds number plot. The small solid rectangle to the right indicates the approximate region in which the Chehroudi LN_2 jet data lies when excitation is at 4800 Hz. The curve within this rectangle shows the approximate path as flow rate is increased from the lowest to the highest values, all at supercritical chamber pressures. Similar region for the 2700 Hz excitation is shown as a dashed rectangle. Chehroudi and Talley [36].

plot of the Strouhal number as a function of the Reynolds number. The curve marked as "matched excitation" is the same equation proposed by Becker and Massaro [38] for the natural breakdown of the jet. It can be seen that results from Chehroudi's study are beyond the regions studied by Rockwell [37]. With the caveats of extrapolating Rockwell's results, Figure 15 suggests that the frequencies used by Chehroudi's group are not expected to bring about noticeably large effects of the acoustic waves on supercritical jet because they lie in the region identified by Rockwell [37] as the "lower zone." No effects of the transverse disturbance on the jet were observed in the studies conducted by Rockwell [37] in this regime as described earlier. Note that the lowest flow rate case studied by Chehroudi's group in Figure 15 tends to enter into the "forced fusion" regime where stronger interaction is expected.

4. Coaxial Jets without External Excitation

Coaxial jets injectors have been used in liquid rocket engines since the 1940s and are found in the present-day hardware such as the Space Shuttle Main Engine (SSME); see Hulka and Hutt [40]. Rocket engines such as the SSME use liquid oxygen (LOX) and hydrogen (H_2) as propellants with the LOX flowing through an inner tube (or a center post) of a coaxial injector design and H_2 through an outer annular region. The inner jet goes through the break-up process after it exits the injector and then mixes in the shear layer between the inner and outer streams. Subsequently, combustion and heat release occur to generate the desired engine thrust.

Often the combustion processes are controlled by, or at least intimately related to, the jet breakup and mixing of the oxidizer and fuel streams. Certain aspects of these processes can safely and inexpensively be studied using chemically inert fuel and oxidizer simulants. Moreover, attempts are made for as many parameters as possible, such as velocity ratio, mass flow rate ratio, density ratio, Reynolds' number (Re), Weber's number (We), and Ohnesorge's number (Oh), to represent similar values obtained in real engines. This scaling exercise, to the extent possible, allows reasonable inferences and evaluation of different injector designs before ever being tested under hot fire conditions.

Investigations targeted at enhanced and fundamental understanding of the injection processes and combustion stability, although desirable to be performed under operating engine conditions, are practically problematic and costly for many reasons, including the need for an optically accessible full-scale liquid rocket engine, special material choices, and optical diagnostic limitations. For example, a single-element noncombusting test rig having as much of the key features of a real cryogenic rocket engine as possible, such as cryogenic temperatures, transcritical temperature ranges, supercritical pressures, realistic velocity ratios, and activation of an acoustic field inside its test chamber, is as close as one can get to the actual engine, yet avoiding indicated complications associated with the combustion in a full-scale setup. Therefore, test rigs have been designed in many studies to have such desired characteristics. Combination of the cryogenic liquid N_2 and gaseous N_2 (to eliminate mixture critical phenomena) and N_2/helium (He) system (to better simulate the LOX/H_2 injection issues) were considered in most of these studies.

4.1. Coaxial LN_2/He Injection. Telaar et al. [41] experimentally investigated the influence of the ambient pressure on the atomization phenomena from subcritical to supercritical pressures in a coaxial LN_2/He injection. They used a coaxial injector design with an inner diameter of $d_{LN_2} = 1.9$ mm for the cryogenic nitrogen flow and an annular slit width of 0.2 mm with an outer diameter of 2.8 mm for helium. Two examples of the flow visualization by shadowgraphy near the injector region are shown in Figure 16. The changes in the break-up mechanism at a reduced surface tension are quite evident. At the low chamber pressure of 1 MPa in Figure 16(A), a liquid spray is formed, whereas at the supercritical pressure of 6 MPa in Figure 16(B), a gas-like turbulent mixing of the dense and light fluids is seen. At 6 MPa, the initial temperature of the center LN_2 jet was 97 K, whereas the critical mixing temperature of He/N_2 mixtures at this pressure is 125.7 K. Thus, in the mixing layer between the LN_2 and He gas, transcritical zones may exist. The visual boundary of the LN_2 jet as shown in this figure is assumed to be the layer at which the temperature reaches the critical mixing temperature. At this interface then, the influence of the surface tension forces as compared to the shear forces appears to be negligible.

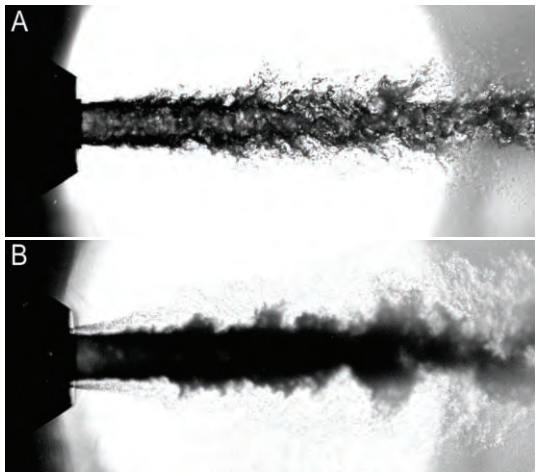

Figure 16: Binary coaxial liquid N_2/GHe system at (A) chamber pressure of 1.0 MPa, (B) chamber pressure of 6.0 MPa. Inner-tube hole diameter, d_{LN_2} = 1.9 mm; liquid nitrogen injection velocity, v_{LN_2} = 5 m/s; helium gas injection velocity, v_{He} = 100 m/s; liquid nitrogen injection temperature, T_{LN_2} = 97 K; gaseous helium injection temperature, T_{He} = 280 K (from Telaar et al. [41]).

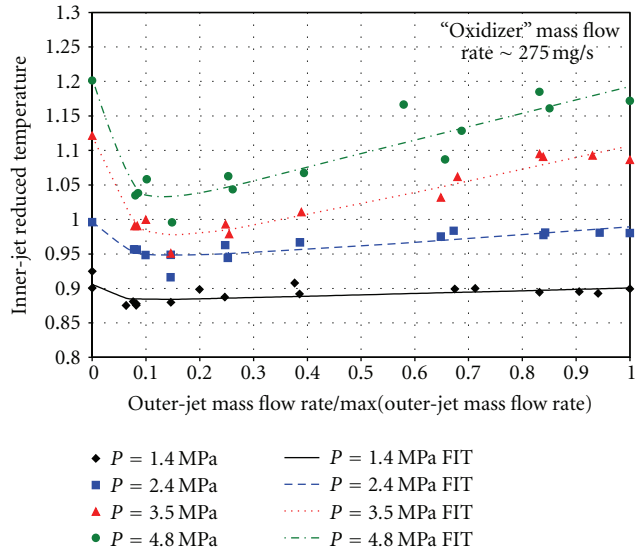

Figure 17: The inner-jet reduced temperature for a coaxial injector plotted versus the annular outer-jet mass flow rate, normalized by its maximum mass flow rate, at four different chamber pressures. Inner-jet mass flow rate is fixed at about 275 mg/s. The lines, called "FIT" on the inset, are curve fits to the raw data. The maximum outer-jet mass flow rates for 1.4, 2.4, 3.5, and 4.8 MPa are 2,995, 2,985, 2,974, and 2,918 mg/s, respectively, Davis and Chehroudi [42].

4.2. Visualization of a Liquid Nitrogen/Gaseous Nitrogen Coaxial Injector. Davis and Chehroudi [42] used a coaxial injector designed to inject a liquid nitrogen, with a coflow of gaseous nitrogen in its annular region, as a part of a program to better understand the nature of the interaction between acoustic waves and liquid fuel jets in cryogenic rocket engines. In their test setup, injection was into a chamber filled with gaseous nitrogen at a supercritical temperature and different pressures spanning from sub- to super critical conditions. However, prior to presenting Davis and Chehroudi's results on acoustic forcing investigations, they provided a wealth of new information on dynamics of the jets (with no acoustic excitations), specifically focusing on the dark-core length of the inner jet in their coaxial injector. This is discussed next.

Davis and Chehroudi [42] argued that in their coaxial injector design, or in any generic one, the outer-jet flow rate played two key roles. First, it assisted the inner-jet breakup at the subcritical condition and enhanced mixing for the supercritical case. Second, because of the temperature differences between the inner jet and the outer jet, there was a heat exchange between the two, both inside and outside the injector. Evidences for the heat transfer behavior were given by examination of the results from jet temperature measurements. Figure 17 shows normalized temperature measurements within the inner jet and at the injector exit plane plotted versus normalized outer-jet mass flow rate at four different chamber pressures covering sub-, near-, and super-critical chamber pressures. Figure 18 shows images indicating typical jet characteristics taken at these same three-chamber reduced pressures. Evidences on the impact of the heat transfer are shown in Figure 17. For instance, at the lowest (subcritical) chamber pressure of 1.4 MPa, Davis and Chehroudi [42] found that the inner-jet exit-plane temperature was fairly insensitive to changes in the annular outer-jet flow rate; see Figure 17. However, at all other elevated pressures, particularly at the supercritical one, an increase in inner-jet exit temperature was measured.

Under zero or no outer-jet flow rate condition in Figure 17, the annular passage of the injector was filled with the warm chamber nitrogen, hence strongly affected the heat transfer not only inside but also outside the injector. Clear evidence for the high heat transfer rate inside the injector was shown from the exit temperature measurements under this no-flow condition; see the y-axis in Figure 17. Here, the observed elevated temperature was reported to be the effects of the warm chamber gases present inside the annular space of the injector. Hence, referring to Figure 18, even though no atomizing (outer-jet) mass flow was at work in frames 11 and 21, one sees a shorter dark-core axial length than those seen in other images presented in frames 13 and 23. A small flow of the colder-than-chamber gaseous nitrogen in the annular passage, though may not assist the jet breakup, lowers the inner-jet exit temperature. Davis and Chehroudi [42] reported that the two processes (i.e., gas-assist liquid atomization and heat transmission) worked in such a way that the net effect was an apparent longer dark core in most cases. For example, compare the images in column one and two (from the left) in the last two rows as shown in Figure 18.

Clearly, the jet behaved differently at different outer-jet mass flow rates. Considering that the outer-jet mass flow rate acted as an atomizing gas, thus accelerating the break-up mechanism, then as the mass flow rate of the outer jet increased slightly (~487 mg/s, frame 3, Figure 18), the inner jet began to break up into relatively large droplets and

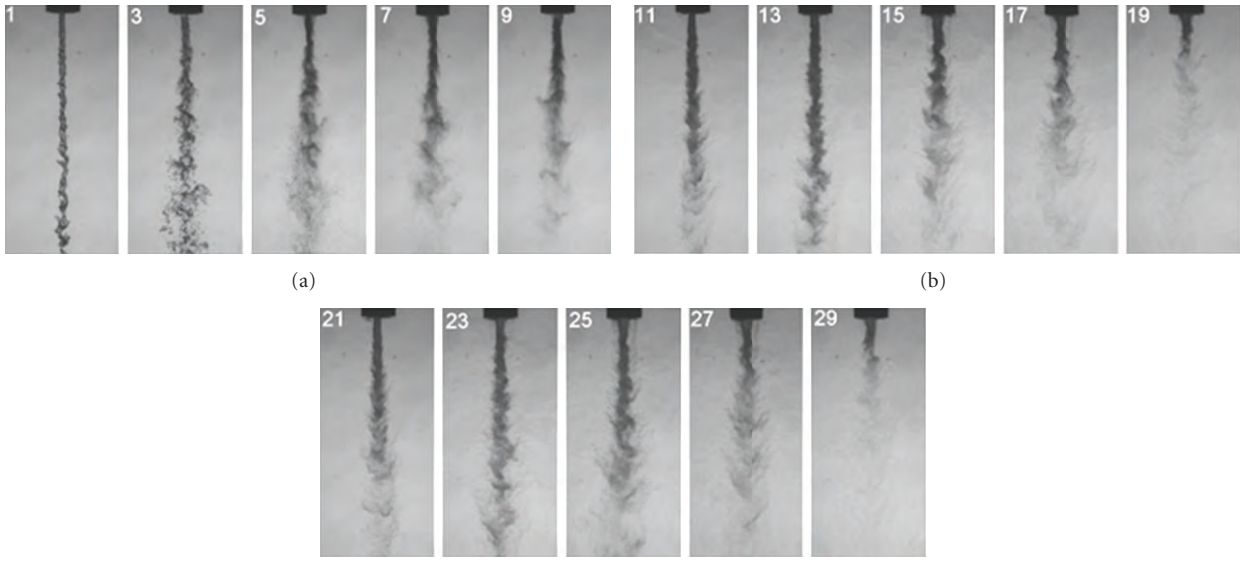

Figure 18: Images of a coaxial jet at approximately the same inner-jet mass flow rates (~275 mg/s). Columns are at about the same outer-annular-jet mass flow rates. For each row, the annular mass flow rate starts at a zero value to 2800 mg/s and increases from the left column to the right. The chamber pressure levels for images 1–9 are subcritical (~1.41 MPa), for 11–19 are near-critical (~3.46 MPa), and for 21–29 are supercritical (~4.77 MPa). Inner-and outer-tube flow average temperatures at injector exit are 170 K and 112 K, respectively. Davis and Chehroudi [42].

ligaments resulting from its interaction with the atomizing outer-jet flow. When the outer-jet flow rate was increased even further, finer droplets and ligaments were reported forming from the inner jet fluid, and more of its mass from the intact core was converted into droplets and ligaments. This consequently produced a shorter and less dark core for the inner jet. Moreover, as the outer flow rate increased, the heat transfer from the outer jet to the inner one intensified outside the injector, thus lowering the average density of the inner core in the injector near-field area. Under the subcritical condition, Davis and Chehroudi [42] reported that this combined outer-jet-assisted atomization of the inner jet and heat transfer processes created a dark core region more susceptible to external excitations.

4.3. Density Measurements in a Coaxial LN_2/GH_2 Jet. Although use of the Raman scattering is straightforward for a liquid N_2 injection into a gaseous N_2, in a mixture of N_2 and H_2 the Raman signals of the N_2 and H_2 are generated at two different wavelengths. Thus, in principle, utilizing an appropriate filtering technique, the signals from both species can be analyzed independently and the partial densities of each species can be determined.

This diagnostic method has been used to investigate the atomization and mixing of coaxial LN_2/H_2 injection at pressures which were supercritical with respect to the critical pressure of pure nitrogen in the inner jet; see Oschwald et al. [32]. During all the tests, the fluids were injected into a flow channel filled with N_2 at near atmospheric temperature and a pressure of 4 MPa ($P_r = P/P_{crit} = 1.17$). Results from a coaxial LN_2/H_2 injection are shown in Figure 19(b) and are contrasted with a single-jet case presented in Figure 19(a). The decrease of the measured densities at large positive r/D values was reported to be due to refraction of the laser beam experienced as a result of density gradients existing at the H_2/LN_2 interface. Similar radial profiles have also been obtained for a range of axial distances from the injector. Based on these data, two-dimensional species distributions were reconstructed for both H_2 and N_2. For the D4 test case described in Figure 19, such a distribution pertaining to the H_2 is shown in Figure 20.

The maximum of the radial nitrogen density distribution at each axial distance was plotted as a function of the normalized distance (x/D) from the injector; see Oschwald et al. [32]. This was then used to ascertain the evolution of the injection process for the LN_2 jet downstream of the injector, as well as to assess the mixing effectiveness between the H_2 and N_2 species. Compared to the test case without the H_2 coflow, the existence of the coflow decreased the measured nitrogen density much faster from its initial injection value near the injector exit area to a plateau which was a value for the far-field background level. The x/D value at which this plateau occurred was then interpreted as representing a complete mixing of the jet with its background gas.

It was shown in Oschwald et al. [32] that when the inner-jet temperature at the injector exit was above the pseudoboiling temperature, it had a shorter decay distance (x/D) than a jet with an injection temperature initially below it. In both cases, the injected nitrogen was at a supercritical pressure. They also reported that the nitrogen inner jet above the pseudoboiling temperature exhibited a gas-like density; whereas below this temperature it possessed a liquid-like density value. Interestingly, their data suggested that

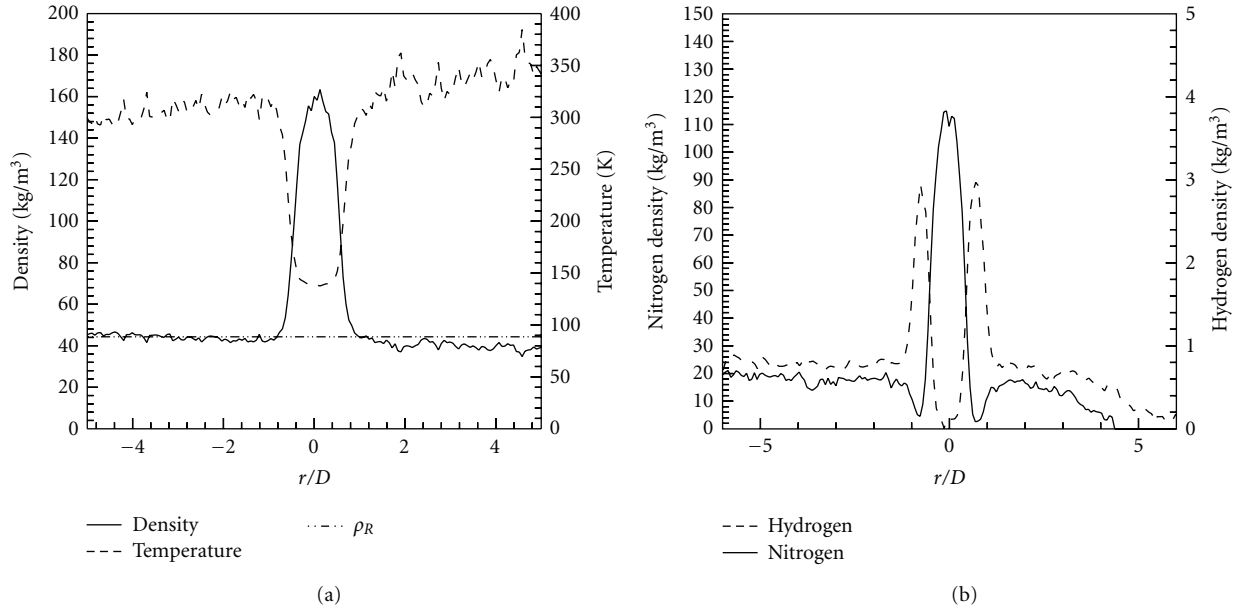

	Test case	V_{N_2} [m/s]	T_{N_2} [K]	V_{H_2} [m/s]	T_{H_2} [K]
single N_2 jet	A4	5	140	—	—
	B4	5	118	—	—
coaxial N_2/H_2 jet	D4	5	140	60	270
	E4	5	118	120	270
	F4	5	118	60	270

FIGURE 19: (a) Radial N_2 density profile for test case A4 (single jet), 2 mm ($x/D = 1.05$) downstream of the coaxial injector exit. (b) Radial N_2 and H_2 density profiles for coaxial LN_2/ H_2 injection for test case D4, 2 mm ($x/D = 1.05$) downstream the injector exit. Laser beam direction is from left to right. Oschwald et al. [32].

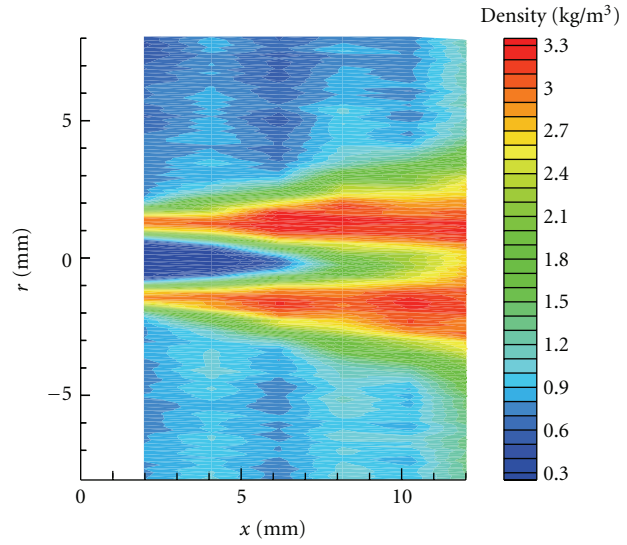

FIGURE 20: Hydrogen density for a coaxial LN_2/H_2 injection for the test case D4 in Figure 19 ($T_{N_2} = 140$ K, $T_{H_2} = 270$ K). Oschwald et al. [32].

the effect of higher H_2 velocity was found not to be as pronounced as this effect of the initial N_2 density.

4.4. Spreading Angle and Core Length Measurements. Two important, and less difficult to measure, geometrical characteristics of such coaxial injectors are the spreading angle of the (combined inner and) outer jet and the length of a dark inner-core of the injected jet. They are readily determined through the high-speed shadowgraphy approach. Both the length of the dark core and the spreading angle provide good measures for mixing characteristic of the jets in coaxial injectors.

Mixing of the propellant streams, if not controlling, is at least intimately related to the combustion process. To a first-order approximation, one measure of the mixing process is the length of the inner jet's liquid and/or dark core, which has been extensively studied by many researchers in the past. For details see Davis and Chehroudi [43]. Experimental core-length correlations, semiempirical theories, and other data for shear coaxial injector studies involving core length were competently summarized by Davis and Chehroudi [42]. Many of the correlations and semiempirical theories

reviewed by them indicated dependencies of the core length with parameters such as outer-jet-to-inner-jet velocity ratio (V_r), outer-jet-to-inner-jet momentum flux ratio (M), density ratio (ρ_o/ρ_i), Reynolds' number (Re), and Weber's number (We). One difficulty Davis and Chehroudi reported with applying these relationships at supercritical pressures is that the predicted core length was very small or zero in magnitude. This is because one of the parameters in the equation was (We) and surface tension diminished greatly or vanishes all together. To overcome the difficulty in core length prediction associated with large (We) number, one group of researchers, proposed that M can be used to describe the scaling of the core length for shear-coaxial injectors and need not include (We) number if it was sufficiently high; see Davis and Chehroudi [42, 43] for details.

But before moving forward, it should be mentioned that confusion does exist in the literature especially when vague definitions are used to characterize the core length. The terms potential-core, potential-cone, intact length, intact-liquid length, and break-up length have all been used along with various measurement techniques. To be clear and to remove any possible ambiguities from the data, the dark-core length was defined as the connected dark fluid region between the injector exit area and the first break in the core as defined by an adaptive thresholding procedure; see Davis [44] or Davis and Chehroudi [42] for more details.

A plot of the dark-core length values for a coaxial injector measured by Davis and Chehroudi [43, 44] versus momentum flux ratio is shown in Figure 21. They used liquid nitrogen (in inner jet) with gaseous nitrogen (in outer annular jet) injected into a chamber filled with gaseous nitrogen at various pressures spanning sub- to supercritical values. The chamber temperature was always at a supercritical value. A clear distinction between the subcritical dark-core length (diamond symbols) and this length at the near-critical and supercritical chamber pressures is seen in Figure 21. Subcritical data suggests a much longer length than that at supercritical pressures for a given momentum flux ratio. Davis and Chehroudi indicated that both the near-critical and supercritical pressure conditions produced an appearance of a single-phase coaxial jet even though liquid nitrogen was injected through the inner tube of the coaxial jet. Recall that earlier in the single-jet part of this paper, Chehroudi and his coworkers [5, 10, 26] also found that two-phase-appearing jets were solely observed at subcritical chamber pressures. However, at supercritical chamber pressures, the spreading rate and fractal dimension values were the same as those seen for gaseous jets injected into a gaseous environment (i.e., single phase); that is, these supercritical single jets can be considered as variable-density, single-phase, gaseous jets. This conclusion presented earlier for the single-jet injection is something Davis and Chehroudi [43, 44] also showed to be mostly valid when it comes to the dark-core length observations in coaxial jet injectors. Evidences in support of such a behavior for coaxial injectors are presented in the next few paragraphs.

The dashed line in Figure 21 is a least-square curve fit to the subcritical data, and the dotted line is a similar

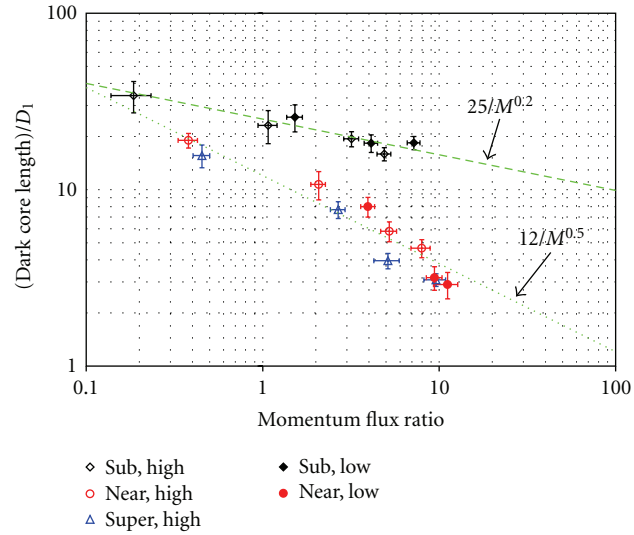

FIGURE 21: Plots of the dark-core length versus momentum flux ratio for a coaxial injector. Liquid nitrogen (inner jet) and gaseous nitrogen (outer annular jet) injected into chamber filled with gaseous nitrogen. The diamond, circle, and up-triangle symbols represent sub-, near-, and supercritical chamber pressure, respectively. The hollow symbols are at a "high" outer-jet temperature (~190 K) and solid symbols are at a "low" outer-jet temperature (~140 K). The dashed line is $25/M^{0.2}$ and the dotted line is $12/M^{0.5}$. Davis and Chehroudi [43, 44].

fit to the near-critical and supercritical data. As indicated by the equations in this figure from Davis and Chehroudi [42, 43], the single-phase-appearing (i.e., at near-critical and supercritical pressures) data has a $M^{-0.5}$ dependence on momentum flux ratio. However, they indicated that the two-phase-appearing subcritical data had a weaker dependence, $M^{-0.2}$, than the single-phase dark-core length at near- and super-critical chamber pressures. Other quantitative differences between the subcritical and supercritical cases have been reported before. They also reported that the $M^{-0.5}$ form of the dependency on M parameter under near- and supercritical pressures is not only valid for gas-gas shear-coaxial jets, but is also for any single-phase (gas-gas or liquid-liquid) shear-coaxial jet.

Figure 22 was constructed by Davis and Chehroudi [42, 43] aiming at a comprehensive comparison of the dark-core length they measured for the LN_2/GN_2 with all other comparable single-phase and two-phase data available in the literature for the potential-core length, intact-core length, and break-up length. This unique figure represents all relevant data in the literature concerning core length spanning 5 orders of magnitude in momentum flux ratio. They also noted that as M approaches zero, one reaches a limit which defines a single round jet configuration because the outer-jet velocity becomes zero. From the information shown in Figure 22, it seems that for $M < 1$, the data points converge and approach the core length range expected for single round jets reported by Chehroudi et al. [27] and Oschwald et al. [45]. The single-phase data by others (i.e., injectants and chamber content all are in one phase, either all gaseous or all liquids) along with the Davis and Chehroudi's

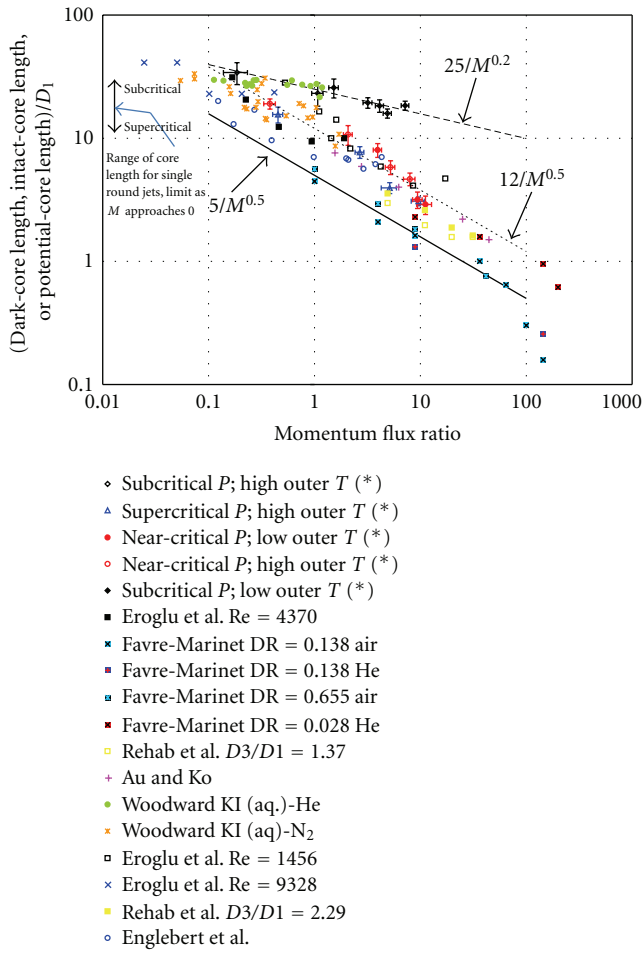

FIGURE 22: This figure shows comparison of the present coaxial-jet dark-core length measurements with all other relevant core length data available in the literature versus momentum flux ratio. Amongst the data reported by others, Eroglu et al. [47], Englebert et al. [48], and Woodward [50] are two-phase flows and the rest are single phase. The range of core length for cryogenic single jet (LN_2/GN_2) is also shown at the left margin. Davis and Chehroudi [42, 43].

LN_2/GN_2 supercritical results are all seen in Figure 22 to follow a dependence close to $L/D_1 = AM^{-0.5}$, where the constant A is between 5 and 12. This information combined with the clear separation of all the two-phase data, including the subcritical core length data seen in Figure 22, essentially suggests a two-phase behavior at subcritical and a single-phase conformance at supercritical chamber pressures.

Even though best efforts were made to use the most relevant data by other investigators, some shortcomings were reported. For example, at $M > 100$ in Figure 22, the experiments of Favre-Marinet and Camano Shettini [46] exhibited a recirculation bubble at the end of the core, and thus the core length decreases as depicted in this figure. The injectors used to produce the two-phase coaxial jets of Eroglu et al. [47] and Englebert et al. [48] had apparently much larger outer-jet gap widths than what is typical of rocket injectors. Additionally, the apparatus of Eroglu et al. [47], reported in Faragó and Chigier [49], did not produce fully turbulent inner jet until $\mathrm{Re} > 10^4$. Davis and Chehroudi [42, 43] explained that the lack of a fully turbulent inner jet and the significant differences between their injector and shear-coaxial ones used in rockets could be the reason why the core length measured by Eroglu et al. [47] is shorter than those observed in their work. Englebert et al. [48] reported that the core length scaled with $M^{-0.3}$. The two-phase core length by Woodward [50] for the water potassium iodide solution with helium, however, obeyed very nearly the trends for the subcritical data points (i.e., $25\,M^{-0.2}$). Considering that the momentum flux ratios near or higher than 10 are of importance for liquid rocket engines (LRE), Davis and Chehroudi [42, 43] indicated that the data for the subcritical (two-phase) case was the only reported information in the neighborhood of the $M = 10$.

Outer-to-inner jet velocity ratio, V_r, has been a design parameter for shear-coaxial injectors, particularly, as a criterion to ensure stable operation of liquid rocket engines (LRE). For LOX/H_2 engines, the design rule of thumb has been to keep the velocity ratio greater than about 10 in order to maintain stable engine operation, as is discussed by Hulka and Hutt [40]. Although this stability criterion has been suggested by the experimental data, no physical explanation has been provided. Related to this is a method to rate a LRE for combustion instability, known as the *temperature ramping*. The temperature ramping of a fired H_2/O_2 LRE is accomplished by lowering the temperature of the H_2 (in the outer jet of the coaxial injector) while maintaining its mass flow rate at a constant value. The lower the H_2 temperature when the onset of the combustion instability is detected, the broader the stability margin of that particular LRE. The temperature ramping is related to and affects the velocity ratio. This is because one of the outcomes of lowering H_2 temperature at constant mass flow rate is the increased density and consequently, lowered injection velocity values. Davis and Chehroudi [42, 43] therefore investigated the impact of the velocity ratio on their nonreacting LN_2/GN_2 coaxial jets, hoping that results may shed some light on the effects of velocity ratio observed in fired production engines. This is explained next.

To determine the effects of the outer-jet temperature (which is GN_2 in Davis and Chehroudi's work) on the coaxial jet, Davis and Chehroudi [42, 43] studied two nominal temperatures of ~190 K and ~140 K, called "high" and "low," respectively. Recognizing that the dark-core length is a dynamic quantity, its basic characterization required measurements of both the average and root mean square (RMS) of length fluctuations. The averaged dark-core lengths were then measured and are shown in Figures 23(a) and 24(a) as a function of velocity ratio for sub-, near-, and super-critical chamber pressures. The RMS of the variations of the dark-core length is also shown in Figures 23(b) and 24(b). Note that Figures 23 and 24 present results for conditions when the external acoustic field is both turned on and off for "high" and "low" outer-jet temperatures. However, it is important to emphasize that in this section only the results when the acoustic field is turned off are discussed, deferring the impact of the externally imposed acoustic field to the next part of this paper.

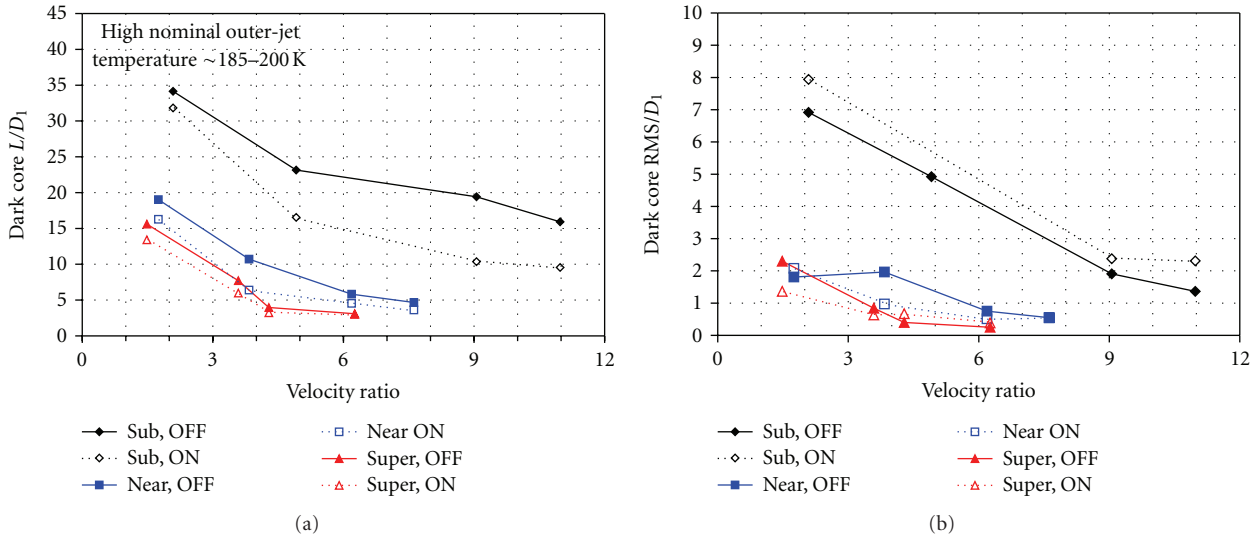

FIGURE 23: Plot of the averaged dark-core length (a) and the root mean square (RMS) of the length variations (b) normalized by the inner diameter of a LN_2/GN_2 coaxial jets injector. The solid symbols and lines represent the data when the acoustic driver is off, and the hollow symbols and dotted lines show the data when the acoustic driver was operated at ~3 kHz. The diamond, square, and up-triangle symbols are sub-, near-, and supercritical chamber pressures, respectively. All cases are for the high nominal outer-jet temperature of ~190 K. In the inset, the words sub, near, and super refer to subcritical, near critical, and supercritical chamber pressures, respectively, and the words OFF and ON refer to the acoustic driver being off and on at ~3 kHz, respectively. Davis and Chehroudi [42, 43].

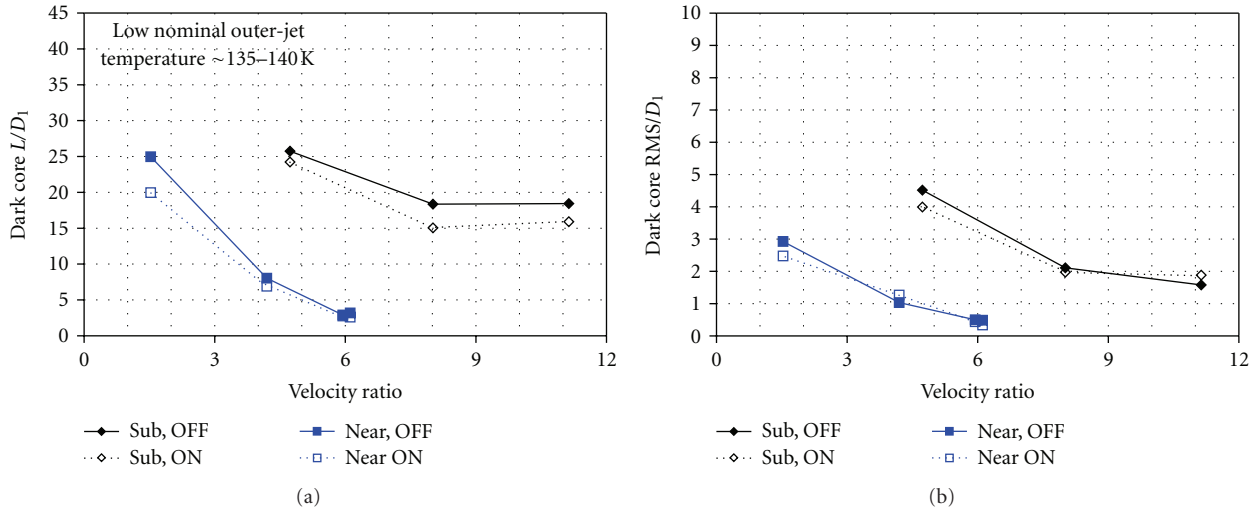

FIGURE 24: Plot of the averaged dark-core length (a) and the root mean square (RMS) of the length variations (b) normalized by the inner diameter of a LN_2/GN_2 coaxial jets injector. The solid symbols and lines represent data when the acoustic driver is off, and the hollow symbols and dotted lines show results when the acoustic driver is operated at ~3 kHz. The diamond and square symbols are for sub- and near-critical chamber pressures, respectively. All cases are for the low nominal outer-jet temperature of ~140 K. In the inset, the words sub and near refer to subcritical and near-critical chamber pressures, respectively, and the words OFF and ON refer to the acoustic driver being off and on at ~3 kHz, respectively. Davis and Chehroudi [42, 43].

Evident in Figures 23(a) and 24(a) is the fact that the length of the dark core decreases as the chamber pressure is increased from sub- to super-critical conditions. The dark core provides an indication of high-density regions of the flow. At a given fixed chamber pressure, as V_r is increased, the length of the dark core decreases and appears approaching a constant value. The RMS values of the dark-core length fluctuations, shown in Figures 23(b) and 24(b), exhibit somewhat similar trends to those seen for the averaged values, that is, substantially lowered at near- and super-critical chamber pressures.

It is known that for a liquid-fueled rocket, atomization and break-up processes, interactions between the propellant jets, droplet formation, and vaporization are all affected by the pressure and, particularly, velocity fluctuations. Also, for any chemically reacting system, it is expected that, to certain

but different degrees, the rate at which energy is released be sensitive to the rate of changes in temperature, density, pressure, and, of course, particularly mixture ratio. It is then intuitive to relate, in some form, the RMS values of the dark-core length fluctuations to mixture ratio variations. On the other hand, a low RMS value can be interpreted as the coaxial jet's "*inherent steadiness*" (or insensitivity to external stimuli) and vice versa. Examination of Figures 23(b) and 24(b) clearly shows that this property is drastically reduced as the velocity ratio is increased. Although these results are for one injector (i.e., no interinjector interaction), Davis and Chehroudi [42, 43] proposed a linkage between these nonreacting results and production-engine combustion instabilities observed at low velocity ratios. They stated that "*it is then quite possible that the observed improvement in combustion stability at higher values of velocity ratio is a result of the inability of the jet to generate large mass flow rate fluctuations under these conditions, thus weakening a key feedback mechanism for the self-excitation process.*"

As indicated earlier, in temperature ramping exercises for stability rating of LOX/H_2 engines, the mass flow rate of the outer-jet hydrogen is maintained at a constant value. Davis and Chehroudi [42, 43] also attempted to provide a linkage between the temperature ramping and their experimental data. They said that as the temperature of the H_2 is decreased during a ramping episode, the H_2 becomes more dense, which decreases the injector velocity ratio at a constant mass flow rate. The RMS plots shown in Figures 23(b) and 24(b) suggest that such a decline in this ratio amplifies the jet's *inherent unsteadiness* (i.e., higher RMS values), providing a possible explanation for the engine's eventual arrival into an unstable zone as a temperature ramping test proceeds.

On the spreading angle or growth rate of the coaxial jets, Figure 25 is a compilation of experimental measurements reported earlier by Chehroudi et al. [5, 10] on single jets along with those newly acquired from a coaxial injector and other data. The tangent of the total jet divergence angle is plotted against the chamber-to-injectant (for single jets) or chamber-to-inner-jet (for coaxial jets) density ratio. The data taken by Chehroudi for single jets in the same facility is marked by (*) in the legend. Note that there are also some theoretical expressions presented in this figure for comparison purposes. The coaxial injector data follows the direction of the arrow as chamber pressure is changed from sub- to near- and to super-critical condition. Interestingly, the data for coaxial injection at subcritical condition conforms with the classical incompressible variable-density shear layer (Dimotakis' theory) which is also what is observed for the single jet, but at supercritical chamber pressures. This suggests that under such a condition the outer jet in Chehroudi's coaxial injector grows similar to a variable-density gaseous jet. Coaxial data, although stays nearly at a constant value, departs from the rest in this figure as chamber pressure is raised towards the supercritical condition.

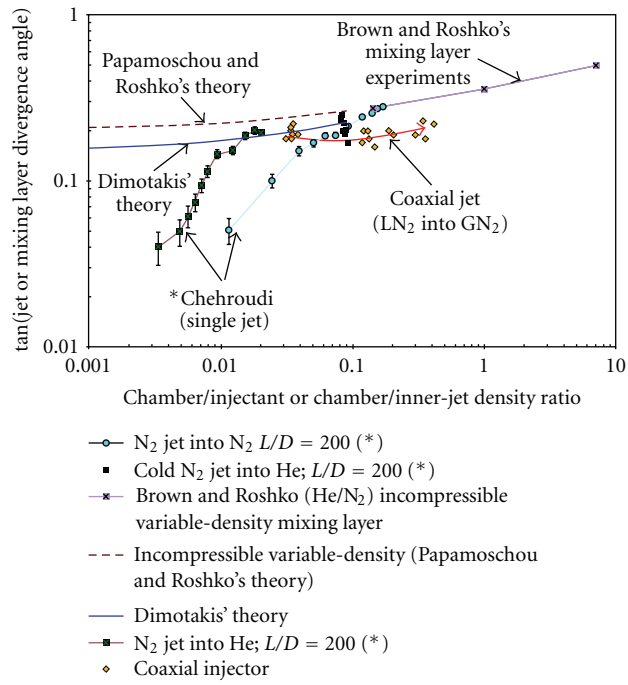

FIGURE 25: Spreading rate of the shear layer versus the chamber/injectant or chamber/inner-jet density ratio for single and coaxial jets compared with different predictions for planar shear layers. For the coaxial data, the chamber pressure increases from sub- to near- and to supercritical conditions in the direction of the arrow.

5. Coaxial Jets with External Excitation

Cold flow studies investigating the interaction of acoustic waves with single-jet injectors have recently been extended to include coaxial injectors by Chehroudi et al. [51], Davis and Chehroudi [42] and Leyva et al. [52]. Their objective was to characterize the coaxial jets response and understand how nonreacting injector results are related to historical liquid rocket engine combustion instability data. As it will be shown in the next few paragraphs, the aforementioned observation that the single-jet interaction with the externally imposed acoustic waves was stronger at subcritical pressures than at supercritical pressures appears to remain generally true for the coaxial-jet injector as well, although some influences of the mass flow ratio and initial temperature were observed. Efforts by Chehroudi's group continue in order to better understand how various parameters control the coupling mechanisms.

Figure 26, taken by Davis and Chehroudi [42], shows a sample of ten consecutive images at sub- (rows one and two from top), near- (rows three and four), and supercritical (rows five and six) chamber pressures from a LN_2/GN_2 coaxial injector. Rows one, three, and five are when the acoustic driver was off and the remaining ones are when it was activated at ~3 kHz. The evolution of the jet in time is from left to right in this figure and the time interval between frames is about 55.6 μs. Prominent in all images of the jet is the existence of a dark central region. After close examination of many images at different magnifications, Davis and Chehroudi [42] reported that the dark core under the unexcited subcritical pressures (Figure 25, row one) can be approximated as a cylinder-like structure with unstable

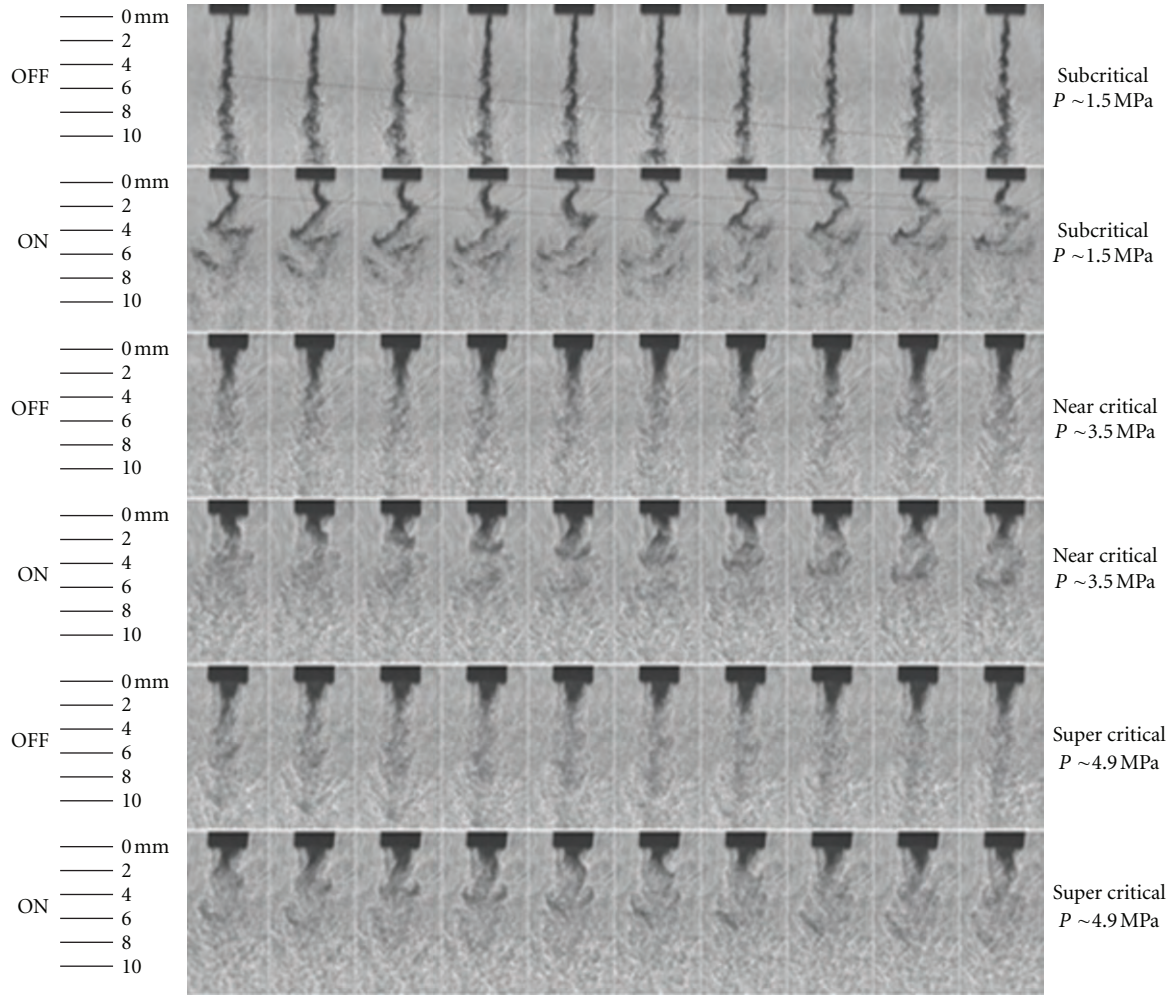

Figure 26: Consecutive frames from high-speed shadowgraph movies or a coaxial injector (LN_2/GN_2 into N_2-filled chamber) with the acoustic driver turned off (in rows 1, 3, and 5) and on (in rows 2, 4, and 6) at ~3 kHz. Time increases from left to right with an interval of 55.6 ms between frames. The first two rows are at a subcritical chamber pressure (~1.5 MPa), the third and fourth rows are at a near-critical chamber pressure (~3.5 MPa), and the fifth and sixth rows are at a supercritical chamber pressure (~4.9 MPa). The acoustic driver is turned off for the first, third, and fifth rows and on for the second, fourth, and sixth at ~3 kHz. The light gray lines in the first and second rows connect fluid structure as they evolve in time. Davis and Chehroudi [42].

surface waves of low amplitudes. However, when they increased the chamber pressure to near- and supercritical pressures (rows three and five), the dark-core length became shorter (as indicated earlier) and the structure changed to a more conical shape near the injector exit area. The conical structure of the dark core has been reported before for single-phase coaxial jets by Lasheras and Hopfinger [53] but not at supercritical conditions.

Excitation of the jet with an acoustic driver yielded significantly different behavior of the dark core compared to that of the unexcited one. The strongest effect was observed under subcritical pressures and made clear in Figure 26. Note that the direction of the acoustically induced velocity oscillations is horizontal (towards left and right) in images presented in Figure 26. It is seen that the core of the jet forms large-scale sinusoidal structures as a result of this imposed velocity field oscillations. From the movies they acquired, Davis and Chehroudi [42, 43] explained an observed dominant pattern which is also shown in Figure 26. They said that as a piece of fluid left the injector tip, the momentum from the acoustically induced motion caused a transverse displacement pushing the core of the jet into the higher-speed annular jet area. Then the dense fluid from the core experienced acceleration in the axial direction, which was caused by the high-speed annular jet motion. Upon reversal of the acoustic field, the dense fluid, which was initially from the core but now in the high-speed annular flow, appeared to maintain its transverse component of the momentum imparted upon leaving the injector and hence the dense fluid particle did not reverse its direction. The dense fluid parcel then slowed (both in the axial and transverse directions) as it arrived at the shear layer between the outer jet and the chamber fluid farther downstream, where a "cusp-shaped" structure was formed from the dense

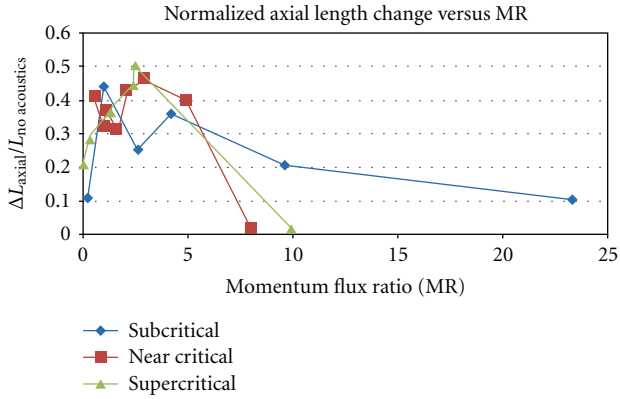

FIGURE 27: Maximum length change between dark-core length without acoustics and dark-core length with acoustics (ΔL_{axial}) divided by the dark-core length without acoustics ($L_{no\ acoustics}$) for each momentum flux ratio case. Results for a coaxial injector. Rodriguez et al. [54].

fluid originating in the core of the jet. Subsequent mixing and heat transfer from the outer-jet to the inner-jet core fluid ultimately cause the fluid parcel to be indistinguishable from the outer-jet fluid.

Figures 23(a) and 24(a) also show the impact of the outer-jet-to-inner-jet velocity ratio (V_r) on the mean dark-core length at three different chamber pressures but under externally imposed acoustic excitation. On an average, when the dark core feels the imposed external acoustic field, its length is shorter than or equal to that when the acoustic driver is turned off. At the near-critical and supercritical chamber pressures, as the V_r increases, the difference between the lengths of the dark core, measured with and without the acoustic field, diminishes. One distinct feature of plots in Figures 23(b) and 24(b) is that, at any given velocity ratio, the RMS of the core fluctuations under subcritical condition is much higher than near- and, particularly, super-critical conditions. And equally important, is that this statement is true with or without the externally imposed acoustic excitation field. Using Davis and Chehroudi's [42, 43] interpretation of the RMS, it appears that the jets under supercritical conditions are more *inherently insensitive* to their environment even when an acoustic field is imposed. Another important feature here is the fact that the magnitude of this RMS of fluctuations drastically declines for all cases, more so for the subcritical case, when velocity ratio is increased. Implications of these unique and important observations for the combustion instability in liquid rocket engines are provided later in this writing.

Rodriguez et al. [54] initiated a set of experiments to analyze the impact of the transverse acoustic wave phase variations on the magnitude of the inner-jet dark-core length. The chosen coaxial jet was exposed to different acoustic conditions by varying the phase between two acoustic sources which faced each other while the jet was located at the midpoint between the two sources, all being inside a high-pressure chamber. The coaxial jet was exposed to a subcritical and a near-critical pressure environment. The measurements were performed on backlit images of the coaxial jet obtained with a high-speed camera. The outer-jet-to-inner-jet momentum flux ratio was varied from 1 to 20 for subcritical conditions and from 0.6 to 5 for near-critical conditions. The resonant frequency of the system was approximately 3 kHz and the maximum pressure variation with respect to total pressure was 3%. Figure 27 shows summary of their results. This figure presents the maximum dark-core length reduction between the case without the external acoustics and that with the acoustics for all phase angles, each normalized with the core length without the acoustics and then plotted as a function of M (momentum flux ratio). The analysis of this data showed a reduction of this length with acoustic excitation within the momentum flux ratio (M) range between 1 and 5 for all chamber pressures, except at the subcritical which extended up to M value of 10. The effect of the acoustic waves at lower or higher M values did not have significant influences on the behavior of the dark-core length.

Rodriguez [55] also examined effects of the injector geometry, specifically the impact of the inner-tube wall thickness on the jet behavior and its interaction with the acoustic field. A new injector design was considered with a thinner inner-tube wall thickness value which consequently produced an inner jet with larger diameter than the original one used in earlier studies. The highest reduction in the dark-core length for the tests with the new coaxial injector geometry took place at moderate M values which supports similar evidence obtained with the original injector possessing a larger inner-tube wall thickness. The results for the new injector also showed that for a given outer-to-inner jet momentum flux ratio, the normalized values of the dark core length between subcritical and nearcritical cases agree reasonably well.

6. Impinging Jets

To the best of this author's knowledge, there is only one impinging jet data set reported under both sub- and supercritical conditions; see Chehroudi [56]. However, the study conducted by Anderson et al. [57] is an example at

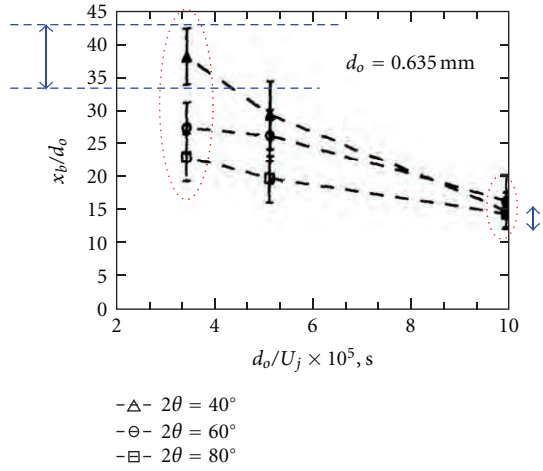

FIGURE 28: This figure shows *sheet break-up length* for an impinging injector as a function of instability parameter at three different impingement included angles. Much higher sensitivity of the *sheet break-up length* is seen with included angle (2θ) at low dn/V ($= d_o/U_j$, in the original article) values. Anderson et al. [57].

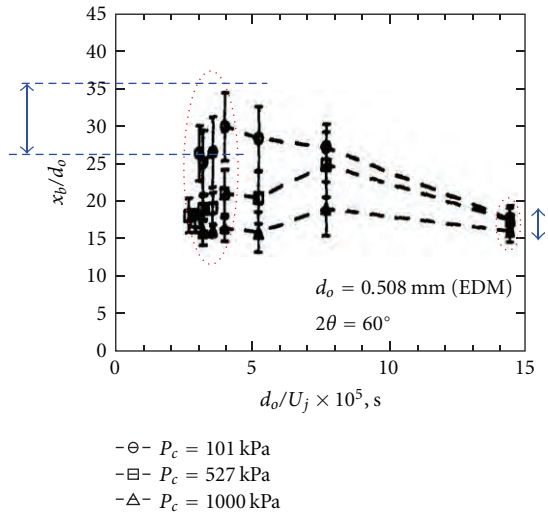

FIGURE 29: This figure shows *sheet break-up length* for an impinging injector as a function of instability parameter at three different chamber pressures. Much higher sensitivity of the *sheet break-up length* is seen with chamber pressure at low dn/V ($= d_o/U_j$, in the original article) values. Anderson et al. [57].

high-pressure subcritical chamber conditions which is of relevance to the discussion in this section.

Figures 28 and 29 taken from Anderson et al.'s [57] studies show measured data for the *sheet break-up* length in a doublet impinging jet injector design plotted against injector-hole-diameter (dn)-to-injection-velocity (V) ratio, that is, dn/V. The dn/V ratio is also called the *stability parameter*. This is because of the dependency of the rocket engine stability region (using this type of injector design) with the dn/V ratio. Large differences between the sheet break-up lengths for different pressures and different impinging-jet included angles (2θ) at low values of the stability parameter are seen in Figure 29. For example, Figure 29 strongly suggests higher sensitivity of the injector when dn/V is reduced through an increase in V (injection velocity) values. This is simply deduced by the enlarged size of the scatter bounds at any given pressure and sensitivity to pressure changes at low dn/V values. Although strictly speaking one should have its frequency response (amplitude and phase) measured, Chehroudi [56] interpreted these results as an indication of injector hypersensitivity under such conditions. At a given pressure or included angle, the *data scatter band* shown in Figures 28 and 29 is also largest at low dn/V values, again and consistently suggesting a more erratic/chaotic dynamic behavior.

The changes in the dark-core (break-up) length were also reported in Figure 30 by Chehroudi [56], showing a progressive increase in chamber pressure up to a supercritical condition for liquid nitrogen injection into gaseous nitrogen environment with no externally imposed acoustic field. The long preimpingement length seen along the jet is expected due to L/dn of about 100 which was intentionally designed to obtain a fully developed condition at the hole exit plane and also to accentuate the effects of chamber pressure on the nature of the impingement. Obviously, shorter dark core is achieved for lower (injector hole) L/dn values used in LRE. It is observed that not only the dark-core length of each individual jet is reduced as supercritical pressures are approached (as before and as expected), but the jet also thickens during this process. Clearly each jet is going through a very similar process discussed earlier in the context of single jet discussion. However, there are important implications as a result of such anatomical changes in an impinging injector which will briefly be discussed in the final part of this paper.

Aside from these results, the author is not aware of any published impinging jet data of relevance under supercritical chamber conditions. The situation is even worse as no systematic investigation or results are available on the impact of external excitation (imposed acoustic field) on impinging-jet injectors.

7. Implications for Combustion Instability

From the review of recent studies presented here, it is clear that our understanding of the jet behavior under transcritical and supercritical conditions has substantially improved in the past 20 years primarily due to pioneering experimental studies reviewed here. Computer simulations have also contributed heavily in the understanding and design process but are not within the scope of this short review. While experimental results have been very valuable for simulations and provided physics-based improvements in computational efforts, the implications of these results towards formulating "*a big-picture*" and efforts in constructing such an image through synergies amongst these pieces of information were needed and are just beginning. One relevant sketch of this *big picture* this author knows is that attempted by Chehroudi [56]. He, in his work, has made an effort to collect pieces of experimental information and offered a compelling

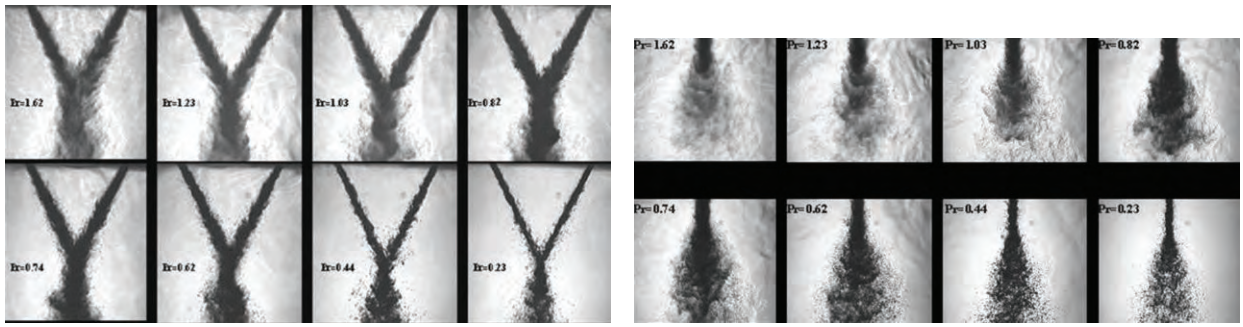

(a) (b)

FIGURE 30: Instant images of sub-, near-, and supercritical impinging jets for LN_2 into GN_2 (room temperature) injection by Chehroudi. The last two rows show the same injector in the first two rows but viewed at a 90-degree angle. P_{ch} = 0.8, 1.5, 2.1, 2.5, 2.8, 3.5, 4.2, 5.5 MPa; from lower right to upper left, P_{ch} = 100, 200, 300, 350, 400, 500, 600, 800 psig. For nitrogen: $P_{critical}$ = 3.39 MPa; $T_{critical}$ = 126.2 K. Re = 25,000 to 70,000; holes' length-to-diameter (L/dn) of ~100; no cavitation; injection velocity: 10–15 m/s. Chehroudi [56].

argument to link nonreacting cold-flow studies (in test rigs) to fired subscale engine information and to what occurs in production engine in the context of combustion instability. Of course, as the history of scientific discovery testifies, such efforts are mostly evolutionary in nature and, while they approach full understanding in time, are incomplete in every step taken. Nevertheless, they are important in order to continuously improve the "sketch" and hopefully soon converge to a colorful big picture. Therefore, in this section, the work by Chehroudi [56] published in such a context is summarized to present a sample of an important attempt to tackle the problem through placement of pieces of jigsaw puzzle. But before doing so, a concise description of the combustion instability in liquid rocket engine is offered to provide a context and sufficient background for Chehroudi's work.

Acoustic combustion instability has been one of the most complex phenomena in liquid rocket engines and therefore difficult to fully understand, control, and predict particularly in the design of high-power rockets. The difficulty arises from the emergence of oscillatory combustion with rapidly increasing and large pressure amplitudes. This leads to local burnout of the combustion chamber walls and injector plates which is caused through extreme heat-transfer rates by high-frequency pressure and gas velocity fluctuations; see Harrje and Reardon [58] and Yang and Anderson [59]. It is thought that resonance acoustic modes of the thrust chamber, amongst them the transverse modes being the most troublesome, are excited through the energy provided by the combustion. The amplification process is thought to include a feedback of information from the acoustic field to the injector or near-injector phenomena which in turn tends to reinforce the combustion-to-acoustic-field energy transfer processes.

This energy transfer reasoning alone is the widely cited general principle by Lord Rayleigh [60]. In essence, he made a phasing argument and stated that the interaction between the combustion heat release and the acoustic field is the strongest if heat is added in a region of space and at the time when the acoustic amplitude is the highest. Although this view has been useful to understand a part of the big picture, evidences gathered by past investigations attributed combustion instability to a complex interaction of the external acoustic field with the fuel injection or near-injector processes as a feedback mechanism, thereby leading to incidences of instability in rocket engines. See, for example, Heidemann and Groeneweg [61], Anderson et al. [57], and Hulka and Hutt [40]. For this and other reasons, controlled studies have been conducted probing into the effects of acoustic waves on gaseous and liquid jets from a variety of injector hole designs. A series of investigations concentrated on disturbances induced from within the injection system. They considered the effects of acoustic fields on many phenomena such as flow structure, vortex pairing, and shear layer growth rate in the initial region of the jet (e.g., see a short review article by Kiwata et al. [62]). More relevant to the work reported here are a few reports and articles on gaseous and (in particular) liquid jets under the influence of external (transverse and longitudinal) acoustic fields. The experimental work under high-pressure supercritical condition has already been reviewed here. More information on this and others can be found in Chehroudi and Tally [39] and Davis and Chehroudi [42, 43].

In Davis and Chehroudi's [63, 64] experimental work on a cryogenic nonfired coaxial injector at sub- and supercritical pressures, they have offered a plausible explanation of why in temperature ramping stability rating exercises an engine becomes unstable. In such tests, which are usually conducted in LOX/H_2 cryogenic liquid rocket engines (LRE), they proposed that a progressive reduction of the propellant (H_2) temperature decreases the outer-to-inner jet velocity ratio for shear coaxial injectors and therefore pushes the engine into an unstable operating zone. As indicated earlier, this velocity ratio was found to be a key parameter defining the stability of the engine; see Hulka and Hutt [40]. But what this velocity ratio does to the jet itself and how the connection to combustion instability comes about are explained in the next paragraph. Moreover, in Chehroudi's work, in which an externally imposed acoustic field was used to simulate certain key aspects of their interaction in real engines, it was shown

that at subcritical conditions the root mean square (RMS) fluctuation values of the dark-core length were much higher than those at near-critical and supercritical conditions by a factor of 4 to 6 at all velocity ratios; see Figures 23(b) and 24(b). Also, as the outer-to-inner jet velocity ratio declined, the RMS value increased from 1-2 to values of about 7-8 inner-jet hole diameters at subcritical pressures.

Chehroudi [56] interpreted the RMS of the dense dark core as a reflection of mass fluctuations to a first-order approximation; combining it with measurements of a core dominant oscillation frequency consistent with the imposed acoustic field's resonant mode frequency, he then suggested that a connection to rocket combustion instability may be obtained from these data through examination of the RMS of the dark-core length fluctuations. Decreases in the dark-core length fluctuation levels (quantified through the RMS) were then interpreted as the *reduced intrinsic sensitivity* of the jet. Chehroudi [56] then stated the possibility that decreases in the dark-core length fluctuation levels could weaken a key feedback mechanism for the self-excitation process that is believed to drive the combustion instability in cryogenic LRE. This was offered as a possible explanation for the combustion stability improvements experienced in production engines under higher outer-to-inner jet velocity ratios (see also Figures 23 and 24). The effect of temperature ramping was linked to its impact on the outer-to-inner velocity ratio and hence was also explained. More details can be found in Davis and Chehroudi [63, 64], Davis [44], and Leyva et al. [65]. In other words, *the dynamic behavior of the dark-core, specifically its axial length, was considered by* Chehroudi [56] *to be the culprit for coaxial jet injectors*.

Chehroudi [56] has then compared some of his results (from nonreacting test rigs) with those taken in single-element fired rocket engines and demonstrated consistency of results pertaining to the dark-core dynamics. For example, he noted that measured mean intact or dark-core length for SSME-like momentum flux ratios by Woodward et al. [66] in a LOX/GH_2-*fired* single-element rocket engine agreed with those of Davis and Chehroudi's [63, 64] nonreacting case. Additionally, Chehroudi [56] referred to the existence of the dark-core length fluctuations reported by Woodward et al. [66]. He also pointed at a recent work by Yang et al. [67] in which they performed tests in a *fired* single-element rocket equipped with a coaxial LOX/CH_4 injector. Their measurements of the dark core length indicated an increasing trend in the level of fluctuations when the outer-to-inner velocity ratio was decreased and the core oscillation spectra showed more high-frequency contents in jet oscillation at lower velocity ratios. Finally, Chehroudi [56], by referring to the work of Smith et al. [68] where subcritical-to-supercritical sweeps were carefully conducted in a *fired* rocket engine, indicated that very low RMS values of the dark-core length at near- and super-critical conditions and high RMS values at subcritical pressures, both measured by Davis and Chehroudi [63, 64] in their *nonreacting* experimental setup, were consistent with the *fired*-engine experimental observations by Smith et al. [68]. Hence, Smith et al. [68] 's reported unstable combustion behavior at subcritical pressures with high core unsteadiness correlates with Davis and Chehroudi's high RMS values at subcritical conditions, which was then interpreted as conditions leading to highly "sensitive" dark-core dynamic response to its surrounding. In short, Chehroudi indicated that these results in such fired engines were consistent with the Davis and Chehroudi [63, 64] conclusions cited above.

Leveraging the observation that some of the key findings in cold nonreacting jets were consistent with subscale fired rocket engine, all using coaxial injectors, Chehroudi [56] then attempted to employ these, particularly the single-jet's, information to offer a compelling argument in addressing the combustion instability in engines using impinging-jet injector designs. Whereas RMS of the core fluctuations was a key factor for coaxial injectors, Chehroudi [56] proposed that both the mean and RMS of the dark core fluctuations in each jet of an impinging-jet injector were key parameters.

On the engine side, Chehroudi [56] used the information that when the so-called stability parameter (dn/V) was reduced in production engines possessing impinging-jet injectors, combustion instability emerged at some point within this change. This stable-to-unstable transition boundary has been discussed in details by Anderson et al. [57] and is referred to as the Hewitt correlation. To offer a possible explanation, Chehroudi [56] had to propose a hypothesis (explained in the next paragraph) which although intuitively acceptable, requires further verification. However, he, by using data from impinging-jet injector designs in production engines and the dark-core lengths measured from single jets reported here (Figure 9), was able to provide some initial support for the hypothesis. Next, the hypothesis itself and some of his supporting information are explained.

For example, Chehroudi [56] showed that a reduction in the dn/V (stability parameter) through changes in either dn or V leads to shortening of the mean dark-core (or break-up) length for each jet in an impinging jet injector. He then stated that it was quite possible that as dn/V was reduced in an engine, the mean dark core length reached a critical value ($L_{C,P\text{th}}$) where one intuitively expects *inherently high sensitivity (high RMS)* for an impinging-jet injector "system" to its environmental acoustic field. *Here,* Chehroudi [56] *hypothesized that the Hewitt stable-to-unstable transition point (or line), which is usually observed as dn/V is reduced, was at or near a condition where the distance from the holes exit plane of the impinging injector to the impinging point (i.e., pre-impingement length) reached a critical value* ($L_{C,P\text{th}}$), *creating a situation somewhat similar to what is shown in Figure 31.* The arrangement shown in this figure was considered to be most sensitive to the ambient acoustic field. Chehroudi [56] also demonstrated that a situation shown in Figure 31 could easily take place in the thrust chamber of production engines during operation considering typical geometrical dimensions of impinging jet injectors for these engines. He also provided experimental evidence by Anderson et al. [57] (Figures 28 and 29) from tests of nonreacting impinging jets conducted at elevated chamber pressures suggesting high level of sensitivity for the arrangement shown in Figure 31.

Considering what was discussed for the coaxial jet injector, one implication of the hypothesis Chehroudi proposed is that an impinging jet injector engine should be more

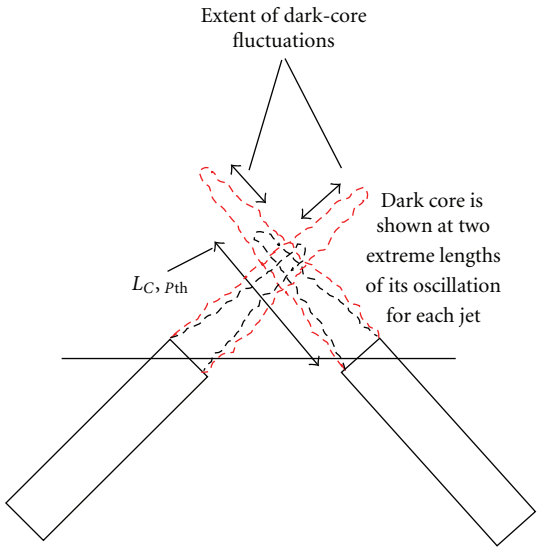

FIGURE 31: This figure shows the extent of the dark-core (or break-up) length fluctuations for individual jets of an impinging injector design for a situation when the average length ($L_{C,Pth}$) is of the same order as (or less than) the distance from each hole to the impinging point. Chehroudi [56].

stable at sufficiently high pressures, such as supercritical conditions. This is because not only the RMS of the core length fluctuations declines substantially (see Figures 23(b) and 24(b)), but also the length of the core may become adequately shorter than the pre-impingement length depending on the geometrical dimensions of the impinger. The changes in the dark-core (break-up) length can also be inferred by examination of Figure 30, showing a progressive increase in chamber pressure up to a supercritical condition for liquid nitrogen injection into gaseous nitrogen environment with no externally imposed acoustic field. The long pre-impingement length seen along the jet is expected due to *L/dn* of about 100 which was intentionally designed to obtain a fully developed condition at the hole exit plane and also to accentuate the effects of chamber pressure on the nature of the impingement. Obviously, shorter dark core is achieved for lower (injector hole) *L/dn* values used in LRE. Not only the dark core length of each individual jet is reduced as supercritical pressures are approached (as before and expected), but the jet also becomes thicker. The impinger is expected to pass through a situation described in Figure 31 as chamber pressure is increased. Hypersensitivity is anticipated at that condition according to Chehroudi's hypothesis. Progressive increase of chamber pressure beyond this point sufficiently thickens each jet and shortens the dark-core length to a situation where the two dark-core lengths are shorter than the preimpingement distance and a gas-like jet is impinging another gas-like jet with enlarged cross-section areas. Based on Chehroudi's hypothesis and given that RMS of the dark core is much lower at supercritical than subcritical conditions, a more robust (targeting and mixing) and less sensitive impinging jet system would be expected at supercritical chamber pressures. However, it is likely that the dynamic behavior of the *potential core* plays a somewhat similar but weaker role under this latter gas-like condition.

Chehroudi's [56] attempt should be considered as the first step, but an important one, towards construction of a "*big picture*" through linkage of the increasing amount of experimental information made available. Essentially he was able to connect pieces of information from nonreacting test rigs, fired subscale engines, and production engines to provide an initial sketch. The sketch proposed by Chehroudi [56] has the advantage, simplicity, and the beauty as well, of identifying the possible weak link in the combustion stability assessment regardless of the design of the injector at least for the two popular cryogenic impinging and coaxial cases described. Much, of course, remains to be investigated, amongst them is the close examination of the historical data on the *dynamic characteristics* of the dark-core (or break-up) length and width for the circular jets forming the impinging injector for the propellant of interest and under the realistic thrust chamber conditions (which are quite rare or nonexistent) to further substantiate that a critical value, $L_{C,Pth}$, is reached when the onset of instability is detected in an engine. Also, the *dynamic* characterization of each jet forming the impinging injector and when the two jets meet, in the presence of an externally imposed acoustic field, is highly desirable to assess sensitivity of the dark-core or break-up length of the jet to relevant design and operating variables.

8. Conclusions

It is evident from this relatively short and targeted review that much has been learned on jet breakup and relevant processes involved in cryogenic liquid propellant injection into high-pressure supercritical condition over the past twenty years. In a quest to understand coaxial jet injectors used in H_2/O_2 cryogenic liquid rocket engines, systematic research efforts have been initiated which consider a logical progression from single jet injected into a quiescent environment to such jets under externally imposed acoustic field and to coaxial injectors with and without acoustic forcing, all under nonreacting conditions.

It is now clear that the impact of progressively lowered surface tension, as environmental pressure approaches the injectant's critical pressure from subcritical and exceeds to supercritical condition, suppresses classical liquid breakup and drop/ligament formation processes and a gas-like jet behavior emerges at or above the critical pressure of the injectant. It is also shown, quantitatively, and for the first time by Chehroudi's group that single liquid jets injected into a supercritical pressure and temperature behave similar to variable-density incompressible jets in visual growth rate. The gas-like nature of these single jets under such conditions has also been demonstrated through fractal analysis of the injected jet boundary. Based on physical arguments and visualizations, an effective model, and the only one known to this author, for the growth rate of such jets was proposed by Chehroudi, a model which mimics the experimental data quite well from sub- to supercritical chamber pressures and for different fluids.

Visual length scales were measured which suggest conformance with the Taylor microscale. The Raman scattering measurements were conducted both for density profiles and growth rates. Based on this information, relationships between the same jet parameters when measured by shadowgraphy and by the Raman scattering were established. Similarity behavior in the radial density profile was demonstrated for the near- and super-critical single jets when the gas-like appearance emerged. Jet growth rates under supercritical pressures, as identified by density profiles, showed tendency to converge with those extrapolated for gaseous jets near the injector exit plane. Temperature estimates from the Raman data suggested existence of a pseudo-boiling behavior when the injection temperature is below the pseudo-boiling line at which the fluid-specific heat becomes very large (mathematical infinity). When the injected liquid possessing temperatures below the pseudo-boiling line warms up under supercritical chamber pressures, it eventually reaches this line, at which time most of the absorbed heat is taken up by the large specific heat value of the fluid, thus exhibiting a pseudo-boiling behavior.

Dark-core length dynamics of cryogenic single jets injected into both sub- and super-critical conditions were measured and compared with those of liquid fuel sprays and single-phase jets. At subcritical conditions, larger fluctuations of this length were reported than those under supercritical chamber pressures. Investigations on the response of the single jets to externally imposed acoustic waves indicated high sensitivity of the jet at subcritical pressures which then substantially diminished at supercritical pressures. Such a lack of response or jet's inherent insensitivity at supercritical pressures was explained through comparison with results extracted from similar studies conducted on single-phase (liquid and gaseous) jets.

Coaxial-jet studies revealed the existence of a dark core originating from the central hole exit area, similar to the single-jet case, but for the coaxial case it was surrounded by a cushion of the outer jet promoting liquid atomization at subcritical and mixing at supercritical pressures. The dark core interface assumed the appearance of a gaseous jet again under supercritical conditions similar to what was observed in a single-jet case. However, the possibility of delay in such a transition exists depending on the solubility of the inner jet and the critical mixing condition.

The mean dark-core length measurements in coaxial injectors with no externally imposed acoustic field exhibited a dual-character behavior depending on whether it experienced subcritical or supercritical chamber pressures. Results for the LN_2 injection to GN_2 were compared with a vast number of pertinent cases from single-phase gaseous and liquid flows to two-phase flows and found that the dark-core length scales with the outer-to-inner jet momentum flux ratio to the power of -0.2, for the subcritical, and to -0.5 for supercritical pressures. Interestingly, as outer-to-inner jet momentum flux ratio approaches zero (i.e., turning into a single jet), the dark-core length approaches values corresponding to the single-jet measurements. The growth rate for the coaxial jets, as measured by the visual spreading angle of the outer (GN_2) jet, agreed with that of supercritical pressures measured for the single jet but then declined below this value as one approached the supercritical pressures.

The impact of the external acoustic forcing on the coaxial jet was seen to be the highest at the subcritical pressures, similar to the single jet and substantially declined when reaching critical and supercritical chamber pressures. Effects of increases in outer-to-inner jet velocity ratio, an important design parameter for stable engine operation and recommended to be greater than 10, were seen to dramatically reduce the mean dark-core length at subcritical pressures while having a minimal impact on this length under supercritical pressures. The dynamic behavior of the core was examined by measurements of the RMS of the core length fluctuations and interpreted as a factor influencing or contributing towards the propellant mass flow oscillations in a rocket thrust chamber. This too behaved very similar to the dark-core length mean value and was distinctively much higher at subcritical pressures than any others. This RMS behavior was then used to offer possible explanations for the empirical observation that stable engine operation required higher outer-to-inner jet velocity ratios (greater than about 10) and also for temperature ramping stability rating tests. Finally, for the injector used, the overall impact of the acoustic field was seen to be important only within a certain region of momentum flux ratios from about 1 to 5.

Implications of a subset of these results were discussed in the context of the rocket combustion instability. Essentially, evidences were shown which suggest that the RMS of the dark-core length and its mean value are important for dynamic behavior of an impinging jet injector. It appears that for the coaxial jets, only RMS values are of relevance in this context.

A hypothesis was proposed that associates the stable-to-unstable transition border in the Hewitt stability plot (for liquid rockets using impinging jets designs) to an event which is defined as an arrangement seen at a moment when the mean core length of one or more of the single jets in an impinging-jet injector design reaches the pre-impingement distance. Some evidences were presented in support of this hypothesis. Essentially, a new alternate and compelling explanation for the Hewitt transition border was offered.

References

[1] T. J. Bruno and J. F. Ely, *Supercritical Fluid Technology: Review in Modern Theory and Applications*, CRC Press, 1991.

[2] R. S. Lazar and G. M. Faeth, "Bipropellant droplet combustion in the vicinity of the critical point," in *Proceedings of the 30th Symposium (International) on Combustion*, p. 801, The Combustion Institute, 1971.

[3] A. Umemura, "Supercritical droplet gasification combustion," in *Proceedings of the IUTAM Symposium on Theories Combustion on Droplets and Sprays*, Taiwan, December 1994.

[4] J. A. Newman and Brzustowski, "Behavior of a liquid jet near the thermodynamic critical region," *AIAA Journal*, vol. 9, no. 8, pp. 1595–1602, 1971.

[5] B. Chehroudi, D. Talley, and E. Coy, "Initial growth rate and visual characteristics of a round Jet into a sub- to supercritical

environment of relevance to rocket, gas turbine, and diesel engines," in *Proceedings of the 37th AIAA Aerospace Science Meeting and Exhibit*, Reno, NV, USA, January 1999, AIAA 99-0206.

[6] W. Mayer, A. Schik, C. Schweitzer, and M. Schaffler, "Injection and mixing processes in high pressure LOX/GH2 rocket combustors," in *Proceedings of the 32nd AIAA/ASME/SAE/ASEE Joint Propulsion Conference & Exhibit*, Lake Buena Vista, Fla, USA, 1996, AIAA Paper no. 96-2620.

[7] R. D. Reitz and F. B. Bracco, "On the dependence of spray angle and other spray parameters on nozzle design and operating condition," in *Proceedings of the SAE International Congress and Exposition*, Detroit, MI, USA, February-March 1979, SAE Paper no. 790494.

[8] W. Mayer, A. Ivancic, A. Schik, and U. Homung, "Propellant atomization in LOX/GH2 rocket combustors," in *Proceedings of the 34th AIAA/ASME/SAE/ASEE Joint Propulsion Conference & Exhibit*, Cleveland, Ohio, USA, July 1998, Paper no. 98-3685.

[9] A. Roy and C. Segal, "Experimental study of subcritical to supercritical jet mixing," in *Proceedings of the 47th AIAA ASM Meeting, Paper AIAA-2009-809*, Orlando, Fla, USA, January 2008.

[10] B. Chehroudi, D. Talley, and E. Coy, "Visual characteristics and initial growth rates of round cryogenic jets at subcritical and supercritical pressures," *Physics of Fluids*, vol. 14, no. 2, pp. 850–861, 2002.

[11] C. J. Chen and W. Rodi, *Vertical Turbulent Buoyant Jets: A Review of Experimental Data*, Pergamon Press, 1980.

[12] P. N. Papanicolaou and E. J. List, "Investigations of round vertical turbulent buoyant jets," *Journal of Fluid Mechanics*, vol. 195, pp. 341–391, 1988.

[13] R. Branam and W. Mayer, "Characterization of cryogenic injection at supercritical pressure," *Journal of Propulsion and Power*, vol. 19, no. 3, pp. 342–355, 2003.

[14] G. N. Abramovich, *The Theory of Turbulent Jets*, MIT Press, Cambridge, UK, 1963.

[15] G. L. Brown and A. Roshko, "On density effects and large structure in turbulent mixing layers," *Journal of Fluid Mechanics*, vol. 64, no. 4, pp. 775–816, 1974.

[16] G. Brown, "The entrainment and large structure in turbulent mixing layers," in *Proceedings of the 5th Australian Conference on Hydraulics and Fluid Mechanics*, pp. 352–359, 1974.

[17] D. Papamoschou and A. Roshko, "The compressible turbulent shear layer: an experimental study," *Journal of Fluid Mechanics*, vol. 197, pp. 453–477, 1988.

[18] P. E. Dimotakis, "Two-dimensional shear-layer entrainment," *AIAA Journal*, vol. 24, no. 11, pp. 1791–1796, 1986.

[19] C. D. Richards and W. M. Pitts, "Global density effects on the self-preservation behaviour of turbulent free jets," *Journal of Fluid Mechanics*, vol. 254, pp. 417–435, 1993.

[20] B. Chehroudi, R. Cohn, D. Talley, and A. Badakhshan, "Raman scattering measurements in the initial region of sub- and supercritical jets," in *Proceedings of the 36th Joint Propulsion Conference*, Huntsville, AL, USA, 2000, AIAA 2000-3392.

[21] M. Oschwald and M. M. Micci, "Spreading angle and centerline variation of density of supercritical nitrogen jets," *Atomization and Sprays*, vol. 12, no. 1–3, pp. 91–106, 2002.

[22] B. B. Mandelbrot, *The Fractal Geometry of Nature*, W. H. Freeman and Company, San Francisco, Calif, USA, 1983.

[23] K. R. Sreenivasan and C. Meneveau, "The fractal facets of turbulence," *Journal of Fluid Mechanics*, vol. 173, pp. 357–386, 1986.

[24] J. J. Taylor and J. W. Hoyt, "Water jet photography—techniques and methods," *Experiments in Fluids*, vol. 1, no. 3, pp. 113–120, 1983.

[25] B. Chehroudi, D. Talley, and E. Coy, "Fractal geometry and growth rate of cryogenic jets near critical point," in *Proceedings of the 35th AIAA/ASME/SAE/ASEE Joint Propulsion Conference*, Los Angeles, Calif, USA, June 1999, AIAA Paper 99-2489.

[26] B. Chehroudi and D. Talley, "The fractal geometry of round turbulent cryogenic nitrogen jets at subcritical and supercritical pressures," *Atomization and Sprays*, vol. 14, no. 1, pp. 81–91, 2004.

[27] B. Chehroudi, S.-H. Chen, F. V. Bracco, and Y. Onuma, "On the intact core of full-cone sprays," SAE Transaction 850126, 1985.

[28] M. Oschwald and A. Schik, "Supercritical nitrogen free jet investigated by spontaneous Raman scattering," *Experiments in Fluids*, vol. 27, no. 6, pp. 497–506, 1999.

[29] I. Wygnanski and H. E. Fiedler, "The two-dimensional Mixing region," *Journal of Fluid Mechanics*, vol. 41, no. 2, pp. 327–361, 1970.

[30] R. M. C. So, J. Y. Zhu, M. V. Ötügen, and B. C. Hwang, "Some measurements in a binary gas jet," *Experiments in Fluids*, vol. 9, no. 5, pp. 273–284, 1990.

[31] N. Zong, H. Meng, S.-Y. Hsieh, and V. Yang, "A numerical study of cryogenic fluid injection and mixing under supercritical conditions," *Physics of Fluids*, vol. 16, no. 12, pp. 4248–4261, 2004.

[32] M. Oschwald, A. Schik, M. Klar, and W. Mayer, "Investigation of coaxial LN_2/GH_2-injection at supercritical pressure by spontaneous raman scattering," in *Proceedings of the 35th AIAA/ASME/SAE/ASEE Joint Propulsion Conference and Exhibit*, Los Angeles, Calif, USA, June 1999.

[33] L.-K. Tseng, G. A. Ruff, P.-K. Wu, and G. M. Faeth, "Continuous- and dispersed-phase structure of pressure-atomized sprays," in *Proceedings of the Progress in Astronautics and Aeronautics: Recent Advances in Spray Combustion*, 1995.

[34] N. Zong and V. Yang, "Cryogenic fluid jets and mixing layers in transcritical and supercritical environments," *Combustion Science and Technology*, vol. 178, no. 1-3, pp. 193–227, 2006.

[35] J. C. Oefelein and V. Yang, "Comprehensive review of liquid-propellant combustion instabilities in F-1 engines," *Journal of Propulsion and Power*, vol. 9, no. 5, pp. 657–677, 1993.

[36] B. Chehroudi and D. Talley, "Interaction of acoustic waves with a cryogenic nitrogen jet at sub- and supercritical pressures," in *Proceedings of the 40th Aerospace Sciences Meeting and Exhibit*, Reno, NV, USA, 2002, AIAA 2002-0342.

[37] D. O. Rockwell, "External excitation of planar jets," *Journal of Applied Mechanics*, vol. 39, no. 4, pp. 883–891, 1972.

[38] H. A. Becker and T. A. Massaro, "Vortex evolution in a round jet," *Journal of Fluid Mechanics*, vol. 31, pp. 435–448, 1968.

[39] Y. V. Vaslov and A. S. Ginevskiy, "Acoustic effects on aerodynamic characteristics of a turbulent jet," Tech. Rep. FTD-MT-24-232-68, Foreign Technology Division, Air Force Systems Command, 1968.

[40] J. Hulka and J. J. Hutt, "Instability phenomena in liquid oxygen/hydrogen propellant rocket engines," in *Liquid Rocket Engine Combustion Instability*, V. Yang and W. E. Anderson,

Eds., AIAA Progress in Astronautics and Aeronautics, pp. 39–71, 1995.

[41] J. Telaar, G. Schneider, and W. Mayer, *Experimental Investigation of Breakup of Turbulent Liquid Jets*, ILASS-Europe 2000, Darmstadt, Germany, 2000.

[42] D. Davis and B. Chehroudi, "The effects of pressure and acoustic field on a cryogenic coaxial jet," in *Proceedings of the 42nd AIAA Aerospace Sciences Meeting and Exhibit*, pp. 10741–10759, January 2004.

[43] D. Davis and B. Chehroudi, "Behaviour of a rocket-Like coaxial injector in an acoustic field, ILAS america," in *Proceedings of the 19th Annual Conference on Liquid Atomization and Spray Systems*, Toronto, Canada, May 2006.

[44] D. W. Davis, *On the behavior of a shear-coaxial Jet, spanning sub- to super-critical pressures, with and without an externally imposed transverse acoustic field [Ph.D. thesis]*, Department of Mechanical and Nuclear Engineering, The Pennsylvania State University, 2006.

[45] M. Oschwald, J. J. Smith, R. Branam et al., "Injection of fluids into supercritical environments," *Combustion Science and Technology*, vol. 178, no. 1–3, pp. 49–100, 2006.

[46] M. Favre-Marinet and E. B. Camano Schettini, "Density field of coaxial jets with large velocity ratio and large density differences," *International Journal of Heat and Mass Transfer*, vol. 44, no. 10, pp. 1913–1924, 2001.

[47] H. Eroglu, N. Chigier, and Z. Farago, "Coaxial atomizer liquid intact lengths," *Physics of Fluids A*, vol. 3, no. 2, pp. 303–308, 1991.

[48] C. Englebert, Y. Hardalupas, and J. H. Whitlaw, "Article usage statistics center," *Proceedings of the Royal Society A*, vol. 451, pp. 189–229, 1995.

[49] Z. Faragó and N. Chigier, "Morphological classification of disintegration of round liquid jets in a coaxial air stream," *Atomization and Sprays*, vol. 2, pp. 137–153, 1992.

[50] R. D. Woodward, *Primary atomization of liquid jets issuing from rocket engine coaxial Injectors [Ph.D. thesis]*, Pennsylvania State University, Department of Mechanical Engineering, University Park, Pa, USA, 1993.

[51] B. Chehroudi, D. Davis, and D. Talley, "Initial results from a cryogenic coaxial injector in an acoustic field," in *Proceedings of the 41st Aerospace Sciences Meeting and Exhibit*, Reno, NV, USA, 2003, AIAA 2003-1339.

[52] I. A. Leyva, J. I. Rodriguez, B. Chehroudi, and D. Talley, "Preliminary results on coaxial jet spread angles and the effects of variable phase transverse acoustic fields," in *Proceedings of the 46th AIAA Aerospace Sciences Meeting and Exhibit*, Reno, Nv, USA, January 2008.

[53] J. C. Lasheras and E. J. Hopfinger, "Liquid jet instability and atomization in a coaxial gas stream," *Annual Review of Fluid Mechanics*, vol. 32, pp. 275–308, 2000.

[54] J. I. Rodriguez, I. A. Leyva, B. Chehroudi, and D. Talley, in *Proceedings of the 21st Annual Conference on Liquid Atomization and Spray Systems (ILASS '08)*, Orlando, Fla, USA, May 2008.

[55] J. I. Rodriguez, *Acoustic excitation of liquid fuel droplets and coaxial jets [Ph.D. thesis]*, University of California at Los Angeles, 2009.

[56] B. Chehroudi, "Physical hypothesis for the combustion instability in cryogenic liquid rocket engines," *Journal of Propulsion and Power*, vol. 26, no. 6, pp. 1153–1160, 2010.

[57] W. E. Anderson, H. M. Ryan, R. J. Santoro, and R. A. Hewitt, "Combustion instability mechanisms in liquid rocket engines using impinging jet injectors," in *Proceedings of the 31st AIAA/ASME/SAE/ASEE Joint Propulsion Conference and Exhibit*, San Diego, Calif, USA, July 1995, Paper AIAA-95-2357.

[58] T. D. Harrje and F. F. Reardon, "Propellant rocket combustion instability," NASA Report, 1972, NASA SP-194.

[59] "Liquid rocket engine combustion instability," in *Proceedings of the AIAA Progress in Astronautics and Aeronautics*, V. Yang and W. E. Anderson, Eds., vol. 169, p. 577, 1995.

[60] L. Rayleigh, "The explanation of certain acoustical phenomena," in *Proceedings of the Royal Institution*, vol. 8, pp. 536–542, London, UK, 1878.

[61] M. F. Heidemann and J. F. Groeneweg, "Analysis of the dynamic response of liquid Jet atomization to acoustic oscillations," NASA Technical Note, 1969, NASA TN D-5339.

[62] T. Kiwata, A. Okajima, and H. Ueno, "Effects of excitation on plane and coaxial jets," in *Proceedings of the 3rd Joint ASME/JSME Fluid Engineering Conference*, pp. 18–22, San Francisco, Calif, USA, 1999.

[63] D. W. Davis and B. Chehroudi, "Measurements in an acoustically-driven coaxial jet under supercritical conditions," *Journal of Propulsion and Power*, vol. 23, no. 2, pp. 364–374, 2007.

[64] D. W. Davis and B. Chehroudi, "Shear-coaxial jets from a rocket-like injector in a transverse acoustic field at high pressures," in *Proceedings of the 44th AIAA Aerospace Sciences Meeting*, pp. 9173–9190, Reno, Nv, USA, January 2006, Paper No. AIAA-2006-0758.

[65] I. A. Leyva, B. Chehroudi, and D. Talley, "Dark core analysis of coaxial injectors at sub-, near-, and supercritical pressures in a transverse acoustic field," in *Proceedings of the 43rd AIAA/ASME/SAE/ASEE Joint Propulsion Conference and Exhibit*, pp. 4342–4359, Cincinnati, Ohio, USA, July 2007.

[66] R. D. Woodward, S. Pal, S. Farhangi, G. E. Jensen, and R. J. Santoro, "LOX/GH2 shear coaxial injector atomization studies: effect of recess and non-concentricity," in *Proceedings of the 45th AIAA Aerospace Sciences Meeting and Exhibit*, pp. 6925–6946, Reno, Nv, USA, January 2007.

[67] B. Yang, C. Francesco, L. Wang, and M. Oschwald, "Experimental investigation of reactive liquid Oxygen/CH4 coaxial sprays," *Journal of Propulsion and Power*, vol. 23, no. 4, pp. 763–771, 2007.

[68] J. J. Smith, M. Bechle, D. Suslov, M. Oschwald, O. J. Haidn, and G. M. Schneider, "High pressure LOx/H2 combustion and flame dynamics preliminary results," in *Proceedings of the 40th AIAA/ASME/SAE/ASEE Joint Propulsion Conference & Exhibit*, Fort Lauderdale, Fla, USA, July 2004, AIAA-2004-3376.

Forced and Unforced Shear Coaxial Mixing and Combustion at Subcritical and Supercritical Pressures

D. J. Forliti
Sierra Lobo, Inc., Edwards Air Force Base, California
The University of St. Thomas, St. Paul, Minnesota

I. A. Leyva
Air Force Office of Scientific Research, Arlington, Virginia

D. G. Talley
Air Force Research Lab, Edwards Air Force Base, California

J. I. Rodriguez, S. Teshome and J. L. Wegener
ERC Inc., Edwards Air Force Base, California
University of California, Los Angeles, California

M. Roa
Sierra Lobo, Inc., Edwards Air Force Base, California

A. R. Karagozian
University of California, Los Angeles, California

Downloaded by Doug Talley on June 5, 2020 | http://arc.aiaa.org | DOI: 10.2514/5.9781624105814.0233.0280 | Book DOI: 10.2514/4.105814

I. INTRODUCTION

Combustion stability has been a pervasive issue for propulsion devices. Combustion in a confined environment may exhibit a feedback-loop phenomenon referred to as a thermoacoustic instability. Acoustic waves within a confined space can alter the mixing process established by the injection system, resulting in a concomitant response in the heat-release process. Unsteady heat release, when in proper phase with the acoustic field, can lead to amplification of the acoustics, closing the feedback loop [1]. Although the description of such a feedback loop appears straightforward, the complexity arises from the coupling among the acoustic field and the propellant mixing and combustion processes.

The objective of the current chapter is to provide an overview of research on the dynamics of multiphase shear coaxial jets at Air Force Research Lab (AFRL), Edwards Air Force Base, California. This flow configuration represents a

This material is declared a work of the U.S. Government and is not subject to copyright protection in the United States.

Distribution Statement A: Approved for Public Release; Distribution is Unlimited. PA Clearance Number 88ABW-2018-3196

Downloaded by Doug Talley on June 5, 2020 | http://arc.aiaa.org | DOI: 10.2514/5.9781624105814.0233.0280 | Book DOI: 10.2514/4.105814

canonical flowfield that has relevance to liquid rocket engine systems [1–3]. Flowfields, both undisturbed and acoustically forced, were characterized over a range of injector geometries and flow conditions. In general, the inner jet is denser (e.g., liquid nitrogen) than the outer jet (e.g., gaseous nitrogen or helium). Five geometries and a comprehensive range of operating pressures (sub- to supercritical) and outer-to-inner jet momentum flux ratios were considered. The objective was to explore as broad an operating space as the facilities allowed with regard to liquid rocket injectors. The overall goal was to provide insight on the mixing of shear coaxial injector flows, especially when exposed to different acoustic environments. The knowledge gained is intended to advance the understanding of combustion instability mechanisms, specifically how acoustic waves alter the mixing dynamics of injector flows, and how geometry and flow conditions influence such interactions.

The chapter is organized as follows. The parameters of multiphase coaxial jets are first described. An overview of the experimental facilities will then be presented. The mixing characteristics of unforced coaxial jets will be quantified and documented to highlight the importance of injector geometry and flow parameters. Characteristic velocity and frequency scales of the unforced coaxial jet will be provided, which culminated in the development of a preferred mode scaling law. The impact of maximum acoustic forcing will then be described for a variety of injector designs. A wide range of injector responses will be presented, exhibiting different symmetries and levels of mixing influence. Receptivity was also studied with respect to acoustic intensity and frequency, which led to an enhanced understanding of the mechanisms responsible for the acoustic-flow interactions. Preliminary results under reacting flow conditions will be presented, indicating behavior that is qualitatively similar to the nonreacting tests.

II. BACKGROUND: COAXIAL JET

The shear coaxial jet has been a subject of study for several decades because of its relevance to propulsion, energy conversion, and other applications [1]. As shown in Fig. 1a, the shear coaxial jet is composed of two concentric jet flows that issue into an ambient environment. Ko and Kwan [4], a pioneer group of researchers in the area of gas-phase coaxial jets, divide the mean flowfield into three spatial zones. The first zone downstream of the jet exit is referred to as the initial merging zone. In this region, both the inner and outer flows have jet cores bound by spatially developing shear layers. Unlike the work of Ko and coworkers [4–10], the initial conditions of the coaxial jet flows studied here are fully developed turbulent flows. The downstream end of the initial mixing zone is defined as the location where the two shear layers begin to merge, which is also where the end of the outer jet turbulent core is located. This leads to the second zone, which is referred to as the intermediate merging zone. It is within this region that the inner and outer shear layers diffuse into one another and begin to

Downloaded by Doug Talley on June 5, 2020 | http://arc.aiaa.org | DOI: 10.2514/5.9781624105814.0233.0280 | Book DOI: 10.2514/4.105814

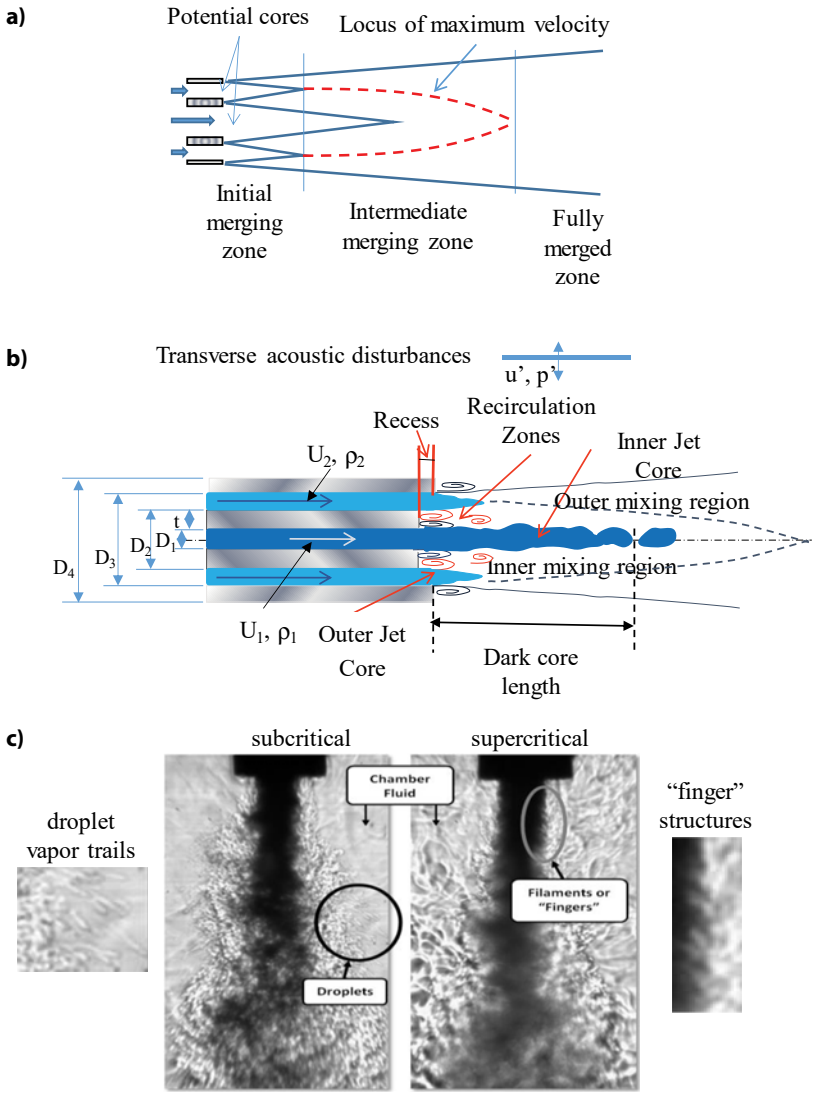

Fig. 1 Structure of the a) single-phase and b) two-phase coaxial jet and c) sub- and supercritical flow visualizations of nitrogen–nitrogen liquid/gas coaxial jets.

transition toward a single, highly disturbed shear layer. In the far-field region, the coaxial jet exhibits a maximum mean velocity on the centerline axis, and the flowfield begins to exhibit the flow properties of a single round jet. Ko and coworkers [4–10] explored this global flowfield over a broad range of operating conditions

where both jet fluids are gases, providing the foundation for the current work. In contrast to these studies, the focus of this chapter is related to coaxial jets in which the inner jet is a denser fluid (or liquid) and the outer jet is a lighter fluid (or gas), as shown in Fig. 1b. This adds additional influences of density gradients and surface tension, although many of the salient features studied by Ko and coworkers [4–10], like parallel and merging shear layers, are still present.

In the context of combustion instability, the initial merging zone is of particular interest because of two factors. First, the presence of steep gradients and inflection points in the mean velocity profiles in this region can lead to hydrodynamic instabilities. Hence this region of the flow tends to be highly receptive to disturbances. A hydrodynamic instability excited by disturbances can lead to local flow oscillations. These local oscillations may also experience spatial amplification and have a greater overall impact in the downstream region. Second, the flame-anchoring process occurs in the near field; often the flame attaches to the inner jet tube. Disturbances, both natural and external, can alter the flame stabilization mechanism, leading to axial or transverse flame motion, local quenching, and flame detachment. Dynamics of the flame stabilization process can play a role in a combustion instability mechanism. Thus, attention has been focused on natural instabilities (i.e., instabilities that emerge because of hydrodynamic instability selection when the flow is exposed to broadband/white noise) in the coaxial jet near field and the response of the flow to external forcing.

Figure 1b is an illustration of the shear coaxial jet configuration studied here. The region between the inner and outer flows is complicated by the presence of an inner jet tube with a wall of finite thickness t, which causes a wake region. Thus, the inner mixing region between the inner and outer jet may exhibit an instability that is either of a shear layer, a wake, or a mixed mode. It is well known that there is a competition between the wake and shear-layer instability mechanisms in this flow region [11–17]. This region is also known to play a key role in flame stabilization in combustion applications [18]. The recirculation zone may also exhibit asymmetry depending on the velocity and density ratio between the two jet flows [19]. The location, size, and instability properties of these recirculation zones are likely to impact both the mixing dynamics and the response of the flow to external forcing. In addition, the inner and outer shear layers can influence one another, leading to coupled dynamics [14]. Although the interaction between the two shear layers has been observed, a detailed understanding of the physics is still lacking, and the conditions under which strong synchronization occurs is not well understood. Another feature indicated in Fig. 1b is the dark core length, which is an estimate of the length of the fluid column associated with the inner jet before it either breaks or is no longer distinguishable, as enough mixing between the inner and outer jets has occurred. More details on how the dark core length is estimated will be given later in the chapter.

The shear coaxial jet flowfield depends on a variety of dimensionless groups based on relevant velocity and length scales as well as fluid properties. Regarding geometry, the coaxial jet has four characteristic diameters, as shown in Fig. 1b.

Downloaded by Doug Talley on June 5, 2020 | http://arc.aiaa.org | DOI: 10.2514/5.9781624105814.0233.0280 | Book DOI: 10.2514/4.105814

Downloaded by Doug Talley on June 5, 2020 | http://arc.aiaa.org | DOI: 10.2514/5.9781624105814.0233.0280 | Book DOI: 10.2514/4.105814

The outer diameter of the outer jet tube, D_4, is expected to have negligible effect unless the coaxial jet is exposed to an external fluid that is moving. With this in mind, the geometry of the injector can be condensed into two parameters, the outer-to-inner jet area ratio (AR) and the dimensionless inner jet post thickness t/D_1. There is an additional geometric parameter if the inner jet tube is recessed. Having the inner jet tube recessed is expected to have an impact on the mixing dynamics [20]. Only injector small area ratio (SAR)–thin was studied, both with no recess and then with approximately $0.5D_1$ recess. The results are discussed in detail in Graham et al. [21] and discussed only briefly in this chapter. In an effort to ensure that the thin inner injector wall for large area ratio (LAR)–thin (which will be defined later) was not visibly vibrating while acoustics were applied, that injector had the inner tube sticking out $0.2D_1$, which was the minimum at which is was still possible to visualize any potential movement. This injector was considered flush for comparison with other injectors because the length that the inner injector was sticking out was not enough to have a significant effect on mixing near the inner jet exit. All other injectors to be discussed in this chapter have recesses that are negligible to the extent that is mechanically possible to assemble the injectors and inspect them. Two key Reynolds numbers may be defined, one each for the inner (based on jet diameter) and outer (based on hydraulic diameter) jet flows. Each shear layer is also known to be sensitive to velocity and density ratios among the inner jet, outer jet, and the ambient fluid [22]. For coaxial jets, asymptotic analysis suggests that a key parameter is the outer-to-inner jet momentum flux ratio J [23–25], which is defined as

$$J = \frac{\rho_2 U_2^2}{\rho_1 U_1^2} \tag{1}$$

where the density ρ and velocity U are as represented in Fig. 1b. The studies by Favre-Marinet and coworkers [26, 27] on variable density coaxial gas jets supported the importance of momentum flux ratio but also showed that outer-to-inner jet density ratio has an additional distinguishable effect. Also shown in Fig. 1b is the presence of transverse acoustic waves, which impose pressure (p') and velocity (u') perturbations on the flowfield, the proper parameterization of which was an aspect of this research.

For subcritical pressure conditions, the inner jet is liquid and the outer jet is gas, and the liquid–gas interface adds surface tension (σ) effects, which may be nondimensionalized to form the aerodynamic Weber number

$$We = \frac{\rho_2 (U_2 - U_1)^2 D_1}{\sigma} \tag{2}$$

The behavior of the multiphase flow of the coaxial jet can be broken into different regimes depending on the liquid jet Reynolds number and the Weber number [28]. Visual results to be shown later will generally represent the fiber regime of atomization. Injector flows at ambient pressures above the fluid critical

pressure result in an infinite Weber number, although surface tension may be present even at high pressure for inhomogeneous mixtures.

The last key bulk parameter of the shear coaxial jet is related to the operating pressure. As the ambient pressure is increased above the thermodynamic critical pressure of the inner jet fluid, the liquid surface tension disappears, as does the sharp interface separating liquid from gas. The mixing of liquids and gases at supercritical pressure begins to behave like single-phase mixing of fluids with extreme density differences [29, 30]. The reduced pressure is defined as the ratio of the ambient pressure to the critical pressure. When the fluids in the inner jet, the outer jet, and the ambient are all of the same composition, for instance in the all-nitrogen cases to be presented in the following, the critical pressure has a single value, and the reduced pressure can be uniquely defined. When the jets and the ambient are composed of different fluids, however, the critical pressure comes to be dependent on the local mixture composition, and therefore can be a quantity that varies in space and time [31–34]. Then a reduced pressure based on a global ambient pressure can no longer be uniquely defined. In part because many of the results that follow are for a single fluid (nitrogen) where the critical pressure is a single value, the reduced pressure is by convention defined here to be the ratio of the ambient pressure to the critical pressure of the pure fluid of the inner jet:

$$P_r = \frac{P}{P_{cr,1}} \tag{3}$$

where P is the ambient pressure where mixing is occurring, and $P_{cr,1}$ is the critical-point pressure of the inner jet fluid. Hence P_r values below unity were considered subcritical and those above unity were considered supercritical. Ribert et al. [35] offer a good summary of high-pressure jet mixing databases.

As an example of the flowfield of interest in this chapter, Fig. 1c shows injector flow images at subcritical ($P_r = 0.44$) and supercritical ($P_r = 1.05$) conditions. These images were taken by Rodriguez [36]. The region in the middle is dark because the inner jet has colder and denser nitrogen, and the high-speed annular flow of cold nitrogen assists in the breakup of the inner jet. The presence of droplets in the subcritical case is clearly evident, particularly in the outer region of the image, where the ejected droplets from the inner jet create a streak trajectory in the shadowgraph image [37]. The supercritical image does not exhibit any regions where droplets or liquid surfaces are present. The inner jet shear layer does show a fingerlike structure where the dense inner jet fluid is pulled into the high-speed outer jet flow. Because the conditions are supercritical, the mixing dynamics represented in the image are associated with single-phase mixing of two fluids of very different densities. Oefelein et al. [38] offer additional details on the differences of coaxial jet mixing at subcritical and supercritical pressures.

Downloaded by Doug Talley on June 5, 2020 | http://arc.aiaa.org | DOI: 10.2514/5.9781624105814.0233.0280 | Book DOI: 10.2514/4.105814

Downloaded by Doug Talley on June 5, 2020 | http://arc.aiaa.org | DOI: 10.2514/5.9781624105814.0233.0280 | Book DOI: 10.2514/4.105814

In addition to bulk parameters, the coaxial jet flowfield is also sensitive to boundary conditions. The injectors used in these studies employed constant area tubes that are sufficient in length to establish fully developed flow in the turbulent regime.

III. EXPERIMENTAL FACILITIES AND INSTRUMENTATION

A. EXPERIMENTAL FACILITIES

A schematic of both experimental test sections used in this study is shown in Fig. 2a. The design employs a "chamber within a chamber" approach, where the inner chamber creates an ideal environment for 1-D acoustic-wave resonance but is not sealed off from the surrounding volume. This surrounding volume is the outer chamber, which has the structural integrity to withstand high-pressure conditions. As shown in Fig. 2, two acoustic sirens capable of operating at high pressure are located transversely offset relative to one another, allowing for the establishment of transverse acoustic resonance in the chamber. The circular piezoelectric sirens connect to the facility through carefully designed waveguides. The sirens operate via structural resonance and thus operate most effectively within

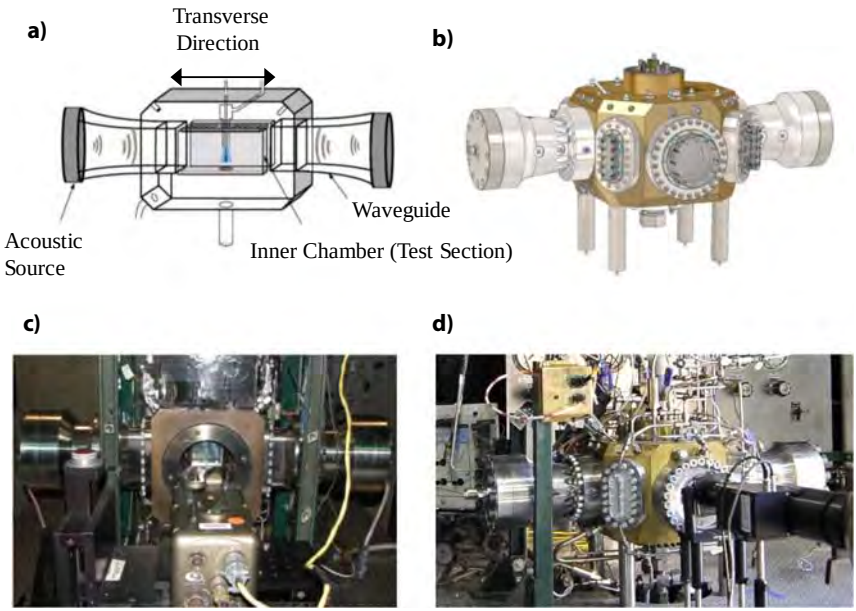

Fig. 2 a) Conceptual experimental facility, b) computer-aided design rendering of the reacting flow facility, and images of the c) nonreacting and d) reacting flow facilities.

Downloaded by Doug Talley on June 5, 2020 | http://arc.aiaa.org | DOI: 10.2514/5.9781624105814.0233.0280 | Book DOI: 10.2514/4.105814

narrow frequency bands. The nominal design resonant frequency for the sirens was ~3 kHz, although a few additional resonant frequency bands are available [39]. Each siren is driven by a dedicated amplified sinuous waveform, with a relative phase shift between the two signals being used to establish different mode shapes within the chamber. For instance, in-phase driving signals can be used to establish a pressure antinode (PAN) at the middle of the chamber, whereas 180 deg out-of-phase driving signals result in a pressure node (PN) at this location. Images of the most recent facility that can be run in nonreacting and reacting modes are shown in Figs. 2b and 2d. More details of the facilities may be found in dissertations by Davis [40], Rodriguez [36], Teshome [41], and Wegener [42].

B. INJECTOR DESIGN

A variety of shear coaxial injector configurations were explored. Figure 3 provides a schematic showing the relative scale of the various injector diameters. Table 1 provides the naming convention and geometry parameters, and Table 2 provides a summary of flow conditions and the length of the imaged domain in terms of inner jet diameter D_1. Injectors will be referred to as either I–V or using a combination of LAR or SAR and thin or thick (with respect to the inner injector post thickness), terms which are defined in Fig. 3. Table 1 provides the two geometry parameters AR and dimensionless post thickness t/D_1 for the five injectors. This combination of geometries allowed us to explore parametric extremes or limit cases in mixing. For example, SAR–thick allowed exploration of the behavior when the flow in the recirculation zone can play a dominant role in mixing. On the other hand, SAR–thin and LAR–thin have the thinnest posts manufacturable so that we

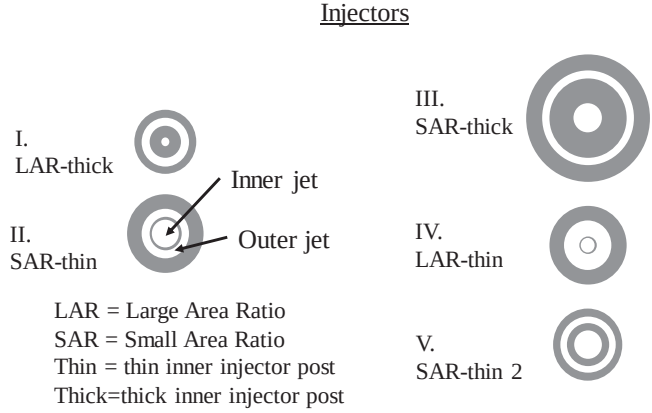

Fig. 3 Schematic representation of the relative scale for different injector exit geometries.

TABLE 1 INJECTOR DESCRIPTION AND GEOMETRIC PARAMETERS

Injector	Description	AR	t/D_1	L_1/D_1	L_2/D_{2H}
I	LAR–thick	12.9	1.05	100	33.5
II	SAR–thin	1.65	0.09	65	52.5
III	SAR–thick	2.90	0.84	52	62
IV	LAR–thin	10.6	0.13	109	29
V	SAR–thin 2	1.68	0.27	100	146

can explore, as close as possible, the limit of concentric shear layers with reduced effects from a recirculation zone. Two distinct AR ranges were considered because we knew from previous literature that the AR can affect mixing, but we also had to contend with manufacturability constraints. Table 1 also includes length and diameter for each flow passage, where hydraulic diameter was used for the outer flow passage. All length-to-diameter ratios were adequate to achieve fully developed turbulent flow conditions.

Table 2 provides the operating conditions and the imaging limits for each injector study. The thermodynamic state of the inner and outer jet streams for each injector are shown as well. The purpose of switching to helium for injector V (SAR–thin 2) was to have improved shadowgraph imaging of the gas-phase dynamics as well as consider a different density ratio between the outer and inner jets. In general, momentum flux ratio was varied by holding the inner jet flow rate constant and changing the outer jet flow, although a few conditions required changes in the inner jet flow rate because of facility limitations. As will be described later, injector V momentum flux ratios were varied by changing both flow rates such that the convection velocity within the inner shear layer was held constant.

C. INSTRUMENTATION

The experiments were fully instrumented with thermocouples and pressure transducers to characterize the condition of the working fluid at various points within the facility. Flow rates were measured using thermal mass flow meters. For nonreacting flows, the injector exit temperatures were measured with a movable thermocouple that could measure temperature profiles near the exit plane of the injector. The thermocouple was withdrawn before jet properties, such as dark core length, were measured. Such profile measurements were not possible under reacting conditions. Instead, exit conditions were based on temperatures measured near the inlet of the injector assembly. Bulk-averaged exit velocities and momentum flux ratios were calculated using the measured mass flow rates, the measured temperatures, and chamber pressure. Uncertainty of the chamber

Downloaded by Doug Talley on June 5, 2020 | http://arc.aiaa.org | DOI: 10.2514/5.9781624105814.0233.0280 | Book DOI: 10.2514/4.105814

Downloaded by Doug Talley on June 5, 2020 | http://arc.aiaa.org | DOI: 10.2514/5.9781624105814.0233.0280 | Book DOI: 10.2514/4.105814

TABLE 2 INJECTOR FLOW CONDITIONS AND IMAGING DOMAIN[a]

Injector	J	P_r	Fluids for $P_r < 1$ (inner jet/outer jet)	Fluids for $P_r = 1.05$ (inner jet/outer jet)	Fluids for $P_r = 1.46$ (inner jet/outer jet)	$(L/D_1)_{\text{image}}$
I	0–20	0.44, 1.05, 1.46	LN_2/GN_2	LN_2 and SN_2/SN_2	SN_2/SN_2	40
II	0–20	0.44, 1.05, 1.46	LN_2/GN_2	LN_2/SN_2	LN_2/SN_2	14
III	0.5–20	0.44, 1.05	LN_2/GN_2	LN_2/SN_2	N/A	12
IV	0.5–20	0.44, 1.05	LN_2/GN_2	LN_2/SN_2	N/A	20
V	2.0, 5.9	0.8	LN_2/GHe	N/A	N/A	13

[a]LN_2 = liquid nitrogen, SN_2 = supercritical nitrogen, GN_2 = gaseous nitrogen.

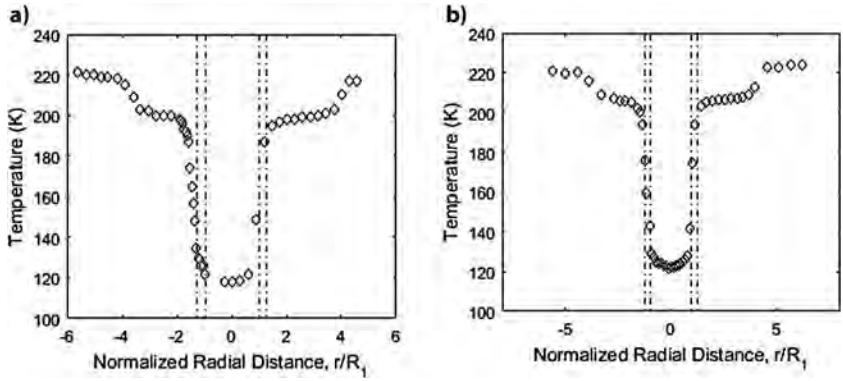

Fig. 4 Temperature profiles taken one D_1 downstream from the exit plane of injector LAR–thin for different J values (running conditions are given in Table 3).

pressure measurement was within 1 and 0.5% for sub- and supercritical operating conditions, respectively.

Two examples of the temperature profiles near the injector exit are shown in Fig. 4 for the operating conditions listed in Table 3. These profiles are for injector LAR–thin using an all-N_2 configuration. An accurate determination of the temperature at the exit of the injector increased the accuracy of jet parameters such as density and momentum flux ratios. Also, having detailed profiles of the temperature gives a qualitative description of how much mixing has occurred between the inner and outer jets, in this case by one D_1 downstream of the exit plane. For example, in the profiles in Fig. 4 there is hardly a uniform region within the temperature profile for the inner jet; mixing has already occurred between the two jets at the measurement location. As documented by Davis et al. [43], these profiles are also influenced by heat transfer between the inner and outer flows within the injector hardware.

Three Kulite differential pressure transducers were placed flush with the inside face of the back acrylic wall of the inner chamber to characterize the acoustic amplitude and mode set up by the two sirens. One transducer was placed at the same transverse location as the injector, and the other two were located equidistant on either side of the center. The acoustic resonance was tuned by ensuring the two side transducers had matched amplitudes and a desired phase; the available resonant frequencies were determined using a frequency sweep procedure described by Wegener et al. [39].

The primary means of studying the coaxial jet flow dynamics was backlit high-speed images. The inner jet, due to high fluid density, appeared as a dark column. The less-dense outer jet was also in many cases distinguishable from the relatively warmer ambient gaseous nitrogen in the chamber. Phantom v7.1 and v710 high-speed cameras (shown in Fig. 2c and 2d) at 20–30-kHz frame rates were used to

Downloaded by Doug Talley on June 5, 2020 | http://arc.aiaa.org | DOI: 10.2514/5.9781624105814.0233.0280 | Book DOI: 10.2514/4.105814

TABLE 3 OPERATING CONDITIONS FOR CASES SHOWN IN FIG. 4

Quantity	Fig. 4a	Fig. 4b
J	1.9	8.5
R	4.1	8.5
S	0.11	0.12
$T_{chamber}$ (K)	221	225
$\rho_{chamber}$ (kg/m^3)	57	56
$P_{chamber}$ (MPa)	3.56	3.56
T_{outer} (K)	200	208
$\dot{m}_{outer}$ (g/s)	3.48	5.14
ρ_{outer} (kg/m^3)	65	61
U_{outer} (m/s)	13.3	20.6
Re_{outer}	9.6×10^4	1.4×10^5
T_{inner} (K)	118	123
$\dot{m}_{inner}$ (g/s)	0.724	0.483
ρ_{inner} (kg/m^3)	577	515
U_{inner} (m/s)	3.3	2.4
Re_{inner}	2.8×10^4	2.4×10^4

capture the jet dynamics. More details on the imaging setup can be found in Rodriguez [36] and Teshome [41].

Various image postprocessing methods were applied to extract information from the data. Estimates for the length of the inner jet and shear-layer spreading rates were measured through contrast-based algorithms [36, 41]. Proper orthogonal decomposition (POD) [1, 44, 45] applied to the image sets for each operating condition facilitated the identification of spatial and temporal behaviors intrinsic to the natural and forced flows. POD is essentially a pattern-recognition tool that extracts orthogonal basis functions that are arranged in decreasing order of importance in how the modes contribute to the overall variance in the data. This algorithm allows for the identification of structures in the data that are otherwise obscured by the presence of simultaneously occurring phenomena and noise.

IV. RESULTS

The results presented here were obtained over many years by a team of researchers who were part of the lab at various times. The overall objective was to characterize

Downloaded by Doug Talley on June 5, 2020 | http://arc.aiaa.org | DOI: 10.2514/5.9781624105814.0233.0280 | Book DOI: 10.2514/4.105814

Downloaded by Doug Talley on June 5, 2020 | http://arc.aiaa.org | DOI: 10.2514/5.9781624105814.0233.0280 | Book DOI: 10.2514/4.105814

the mixing process in shear coaxial jets from subcritical to supercritical pressures. Specific questions to be answered spanning sub- to supercritical pressures were as follows: What are the salient nondimensional numbers dictating the mixing process for shear coaxial jets? What are the effects of geometry on the mixing process? How is the mixing affected by an imposed acoustic field? And finally, what features of the mixing process persist when you go from nonreacting to reacting jets? Of course, implicit in every question was how the answer changes as the pressure increases from sub- to supercritical values. The following section will detail a methodical and comprehensive experimental study dealing with the preceding questions.

A. UNFORCED NONREACTING FLOW BEHAVIOR

1. VISUAL FEATURES

This section will give a brief account of the behavior of the coaxial jets for different injector configurations with varying momentum flux ratios at different chamber pressures. The investigation of the mixing of the inner and outer jets was carried out mostly through the characterization of the inner jet, which is best seen in the images, as well as the identifiable flow structures of the outer jet. Therefore, a method for measuring the inner jet had to be developed. Because the inner jet is always denser than the outer jet, it appears as a dark column or dark core in the flow visualizations (Fig. 1c). The length of the dark core is therefore related to the length of the inner jet, and it can be defined and computed in different ways. Here, it was computed using MATLAB subroutines to delineate the contrast between the inner and outer jets. Dark core length is a measure of the largest continuous center dark column attached to the injector exit. Shorter lengths denote faster mixing between the inner jet and the outer jet, and vice versa. For this study, absolute values of the dark core length are not as important as relative differences measured for different injectors at similar nominal conditions or for different flow conditions with a given injector. In other words, we emphasized capturing trends in mixing vs making quantitative comparisons of inner jet lengths with other measurement techniques because we already know that the actual values will depend on the visualization technique and the definition used [37, 46, 47].

Injectors LAR–thin and SAR–thick will be compared first. Note that the inner jet tube for injector LAR–thin stuck out by about $0.2D_1$ for direct visual confirmation that the inner jet injector tube was not oscillating because of turbulent flow disturbances in the outer jet. As indicated in Table 2, these injectors were operated with nitrogen for the inner and outer jet as well as the ambient fluid.

Let us first look at the unforced behavior of injector LAR–thin, shown in Fig. 5a at various momentum flux ratios at $P_r = 0.44$ [41]. The forced behavior shown in Figs. 5b and 5c will be explained in Sec. IV.B. At $J = 0.1$, the very low

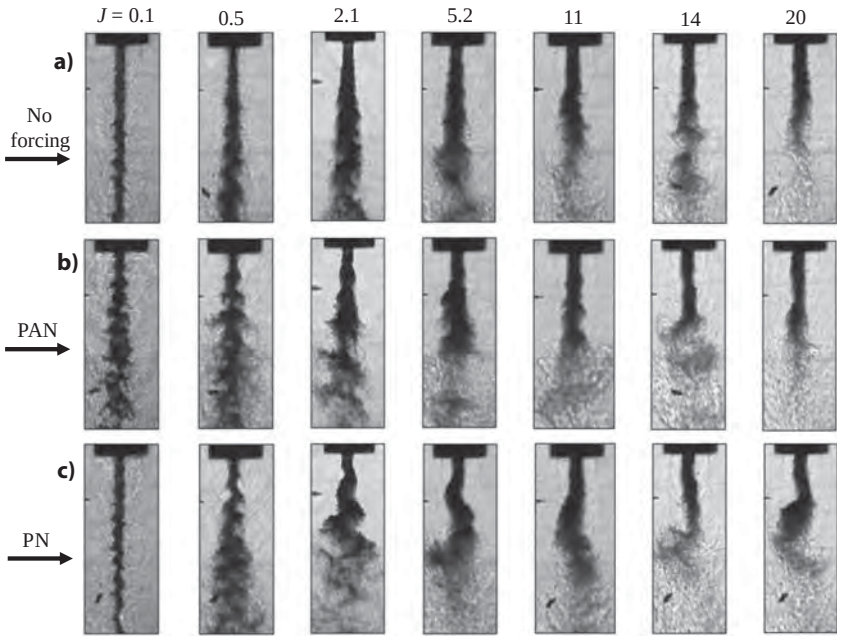

Fig. 5 Visualizations of injector LAR–thin for nitrogen–nitrogen operation at subcritical pressure at momentum flux ratios of 0.1, 0.5, 2.1, 5.2, 11, 14, and 20 under a) no acoustic forcing, b) pressure antinode forcing, and c) pressure node forcing [41].

momentum outer jet flow had minimal impact on the development of the liquid inner jet flow. The low aerodynamic Weber number of approximately 20 enabled the inner jet to maintain integrity for over $20D_1$ downstream of the exit, which is about where the field of view in the image ends. Although small periodic surface wrinkles started forming about $10D_1$ downstream of the exit, they were not large enough to disrupt the continuity of the jet. As the outer jet flow rate was increased, resulting in $J = 0.5$, the dark core region stayed continuous for over $20D_1$. However, surface instabilities were enhanced and occurred earlier than for the lower J case. The widening of the dense core is apparent as it mixes with the outer jet.

As J increased, the dark core region broke up into a fine-droplet spray. The presence of a higher shear force at the inner jet interface aided in the formation of a fine mist of droplets on the periphery of the inner jet flow. Enhanced entrainment of inner jet fluid into the outer flow was evident in the increased spread of the inner jet. Accordingly, the dark core length became shorter with increasing J. For this injector, any influence of the inner jet post is limited to the very near field of the injector, and the mixing is governed by an apparent shear-layer instability.

Downloaded by Doug Talley on June 5, 2020 | http://arc.aiaa.org | DOI: 10.2514/5.9781624105814.0233.0280 | Book DOI: 10.2514/4.105814

Downloaded by Doug Talley on June 5, 2020 | http://arc.aiaa.org | DOI: 10.2514/5.9781624105814.0233.0280 | Book DOI: 10.2514/4.105814

The mixing properties of injector SAR–thick are shown in Fig. 6a as a function of J at subcritical pressure for a nitrogen–nitrogen coaxial jet (see Table 2). It should be noted that the inner jet diameter is nearly twice that of injector LAR–thin. At $J = 0.1$, just as with injector LAR–thin, the inner jet for injector SAR–thick stayed unbroken and relatively undisturbed along the entire field of view, which extends $13D_1$ in length. In contrast to the injector LAR–thin flow, the thick inner jet post of injector SAR–thick causes the formation of an axisymmetric recirculation zone. For the low-J case, the low momentum outer jet fluid predominates in the recirculation zone. The sense of the dominant rotation of the recirculating flow, evident from viewing sequential images, can change with operating conditions. For lower momentum flux ratios, the rotation direction was such that a local counterflow condition was established at the interface of the inner jet and the recirculation zone.

At $J = 0.5$, there was a significant presence of surface irregularities that formed ligaments just a few diameters D_1 downstream of the exit and subsequently broke down and dispersed into droplets. Even so, the dark core region still remained unbroken for the entire field of view. The recirculation zone also consisted of the outer jet fluid with small traces of droplets that came off the surface of the inner flow. The inner jet interface experienced reduced disturbances in the

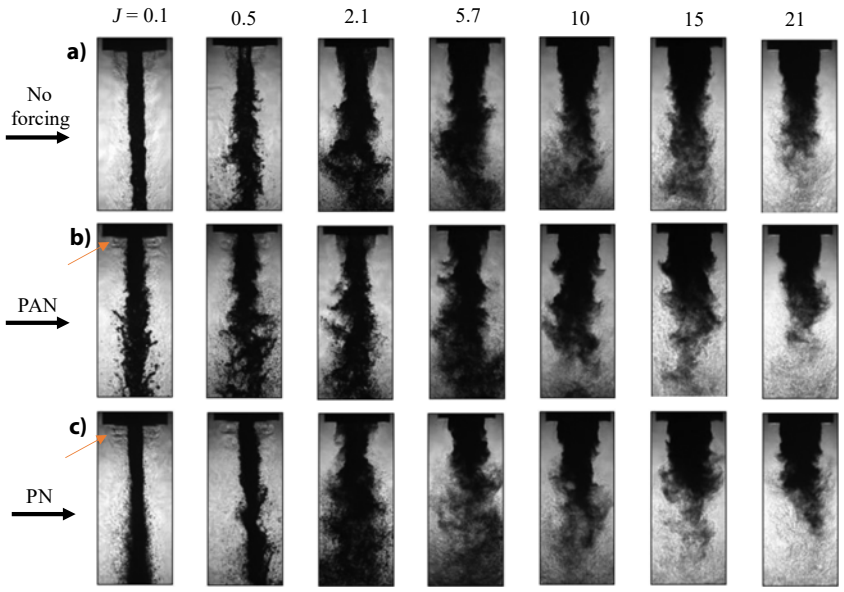

Fig. 6 Visualizations of injector SAR–thick for nitrogen–nitrogen operation at subcritical pressure at momentum flux ratios of 0.1, 0.5, 2.1, 5.7, 10, 15, and 21 under a) no acoustic forcing, b) pressure antinode forcing, and c) pressure node forcing [41].

initial region where the recirculation zone is present. The merging of the outer jet flow to the inner jet interface, which occurs downstream of the recirculation zone, appears to match the location where the inner jet surface experiences enhanced diffusion.

For $J = 2.1$, the fluid inside the recirculation zone mainly consisted of the lower-momentum inner jet fluid, and the predominant sense of rotation changed such that a counterflow existed at the inside boundary of the outer jet. As shown in Fig. 1b, a pair of counter-rotating vortices is expected near the inner jet post exit plane. It is likely that the extreme density and velocity ratios across the post result in asymmetry in the vortex pair, and the imaging indicates dominance of one vortex over the other.

The presence of the dense, dark fluid in the recirculation zone for $J = 2.1$ and several higher momentum flux ratios created a perception of "necking" in the dark core flows. Further downstream, the dark core could no longer maintain continuity and was dispersed into droplets. Small- and larger-scale surface disturbances are observed along the length of the inner jet core. As the momentum flux ratio increased to $J = 5.7$, the recirculation zone was completely obscured with inner jet fluid droplets. The remaining inner jet fluid experienced increased dispersion resulting in a shorter dark core length. Increasing to $J = 15$ and $J = 21$ showed relatively small decreases in the dark core length.

The subcritical mixing behavior presented in Figs. 5a and 6a is generally representative of other injector designs tested in these facilities. The transition of a droplet-laden recirculation zone for LAR–thick occurred at a momentum flux ratio above 2.1, whereas it occurred near 2.1 for injector SAR–thick [36]. For injector SAR–thin 2, no significant droplet presence in the notably smaller recirculation zone was observed up to $J = 6$, but in this case the outer jet was helium.

Injectors LAR–thick, LAR–thin, SAR–thin, and SAR–thick were also tested at supercritical pressure conditions ($P_r = 1.05$) to investigate the mixing process at conditions more representative of liquid rocket engines. Figure 7a shows the flow visualizations for injector LAR–thin at different momentum flux ratios without forcing. These cases employ pure nitrogen in both the inner and outer jets and in the chamber, as was the case in Figs. 5 and 6. The mixing behavior with changing J is qualitatively similar to that observed at subcritical conditions. However, injector flows showed increased spread at supercritical conditions, especially at lower momentum flux ratios, as evident in the thicker inner flow region. This is a manifestation of no surface tension at supercritical conditions. The dark core regions were also shorter compared to the flows with similar J values at subcritical conditions. Although not shown here, the recirculation zone has qualitatively similar behavior at supercritical conditions for injector SAR–thick [41]. The darkening of the recirculation zone, an indicator of higher presence of dense inner jet fluid, occurred at a lower momentum flux ratio of 0.5 at supercritical conditions compared to the subcritical value of 2.1. Thus, it is likely that surface tension inhibits entrainment of inner jet fluid into the recirculation zone.

Downloaded by Doug Talley on June 5, 2020 | http://arc.aiaa.org | DOI: 10.2514/5.9781624105814.0233.0280 | Book DOI: 10.2514/4.105814

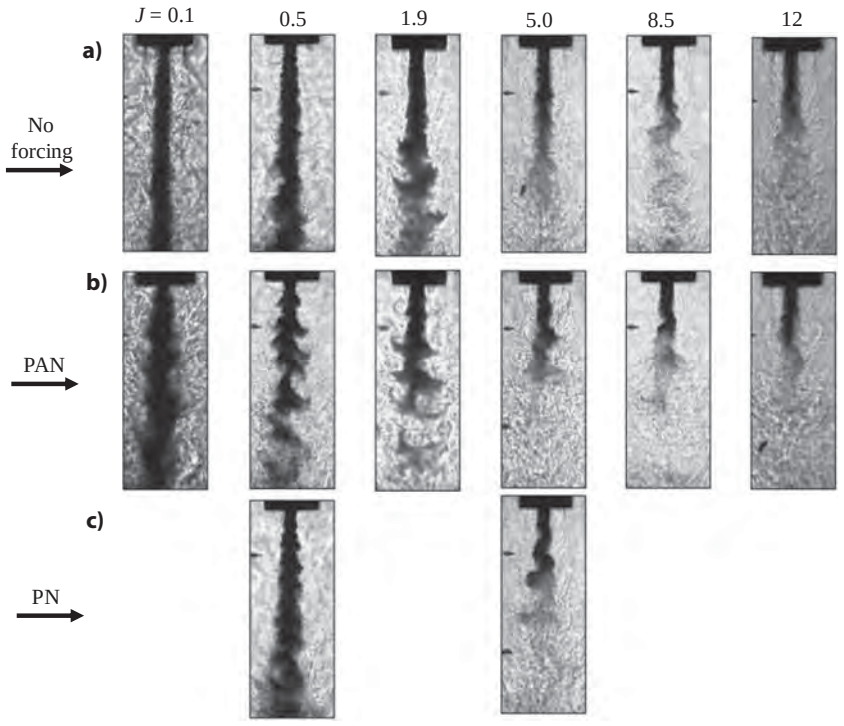

Fig. 7 Visualizations of nitrogen–nitrogen operation of injector LAR–thin at $P_r = 1.05$ and momentum flux ratios of 0.1, 0.5, 1.9, 5.0, 8.5, and 12 under a) no acoustic forcing, b) pressure antinode forcing, and c) pressure node forcing [41].

2. DARK CORE LENGTH TRENDS

The most widely studied injector by this group was LAR–thick. The data for the variation in dark core length with J obtained by Leyva et al. [48] and Davis and Chehroudi [49] for LAR–thick, along with historical data for different injectors at a wide set of operating conditions (first compiled by Davis and Chehroudi [49]), showed good separation into two branches, as shown in Fig. 8. The work by Leyva et al. [48] used 1000–2000 images to calculate the dark core length for each condition, and so it added reliability to the previous work by Davis and Chehroudi [49], who only had high-frequency measurements for a few data points. In fact, that is one of the main reasons why some of the conditions were repeated between the two sets of investigations. The upper branch in Fig. 8 corresponds to two-phase subcritical cases, and the lower branch corresponds to supercritical or single-phase data. It is clear that mixing of two-phase flows at subcritical pressures is slower than mixing for single-phase systems.

Downloaded by Doug Talley on June 5, 2020 | http://arc.aiaa.org | DOI: 10.2514/5.9781624105814.0233.0280 | Book DOI: 10.2514/4.105814

Downloaded by Doug Talley on June 5, 2020 | http://arc.aiaa.org | DOI: 10.2514/5.9781624105814.0233.0280 | Book DOI: 10.2514/4.105814

Also, for the subcritical data, the unsteadiness in the dark core length was much larger; the standard deviation for the dark core length at subcritical conditions was on average 20%, whereas that for the supercritical cases was on average 10%. The subcritical data have an approximate scaling of dark core length with $J^{-0.2}$, and the single-phase data have an approximate relation of $J^{-0.5}$. DeSouza and Segal [50] also offer a dark core analysis of the data they gathered and their own correlations with J. However, as research progressed at AFRL [21, 40, 43, 47, 48, 51] and different injectors were studied, the separation between the two branches seen in Fig. 8 was filled by data taken with injectors SAR–thin, SAR–thick, and LAR–thin, pointing to the importance of other parameters besides J to characterize mixing, as will be shown subsequently. Figure 8 also includes data for single jets for completeness.

A very interesting feature that was observed for the data gathered at supercritical pressures for LAR–thick is the effect of the density of the inner jet. As shown in Fig. 9a, significant scatter was observed in the dark core length data for a given value of J for similar chamber pressures. It was clear that the density of the inner jet varied significantly for the cases studied (ρ_{IJ}/ρ_{cr} varied from 0.5 to 1.8) and that, even though the density ratio of the outer to the inner jet is taken into account in the definition of J, a different parameter was having an effect. Therefore, the data were normalized by the ratio of a reference inner jet density to the density of the jet being measured. The chosen reference density was 190.4 kg/m^3, corresponding to nitrogen at $T = 129$ K and 3.55 MPa, which are the average conditions of the data taken at $\rho_{IJ}/\rho_{cr} = 0.5$–1. As can be seen in

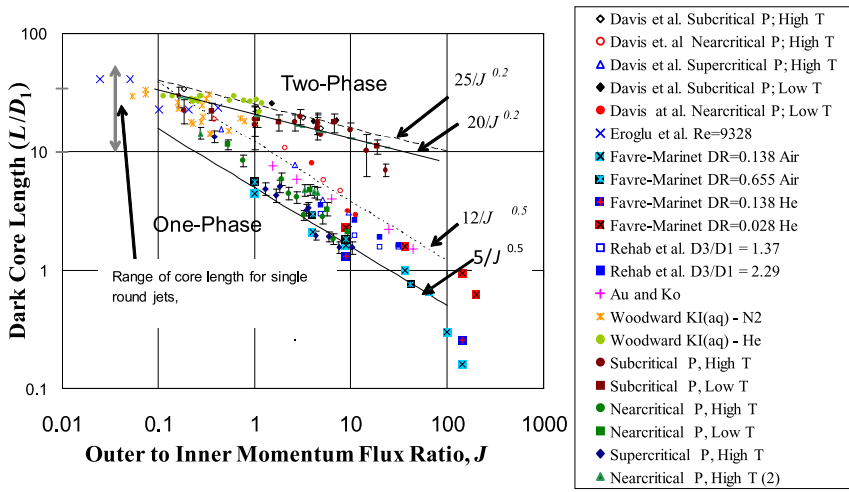

Fig. 8 Comparison of data gathered at AFRL for LAR–thick with historical data, building on compilations by Davis and Chehroudi [49] and Leyva et al. [48].

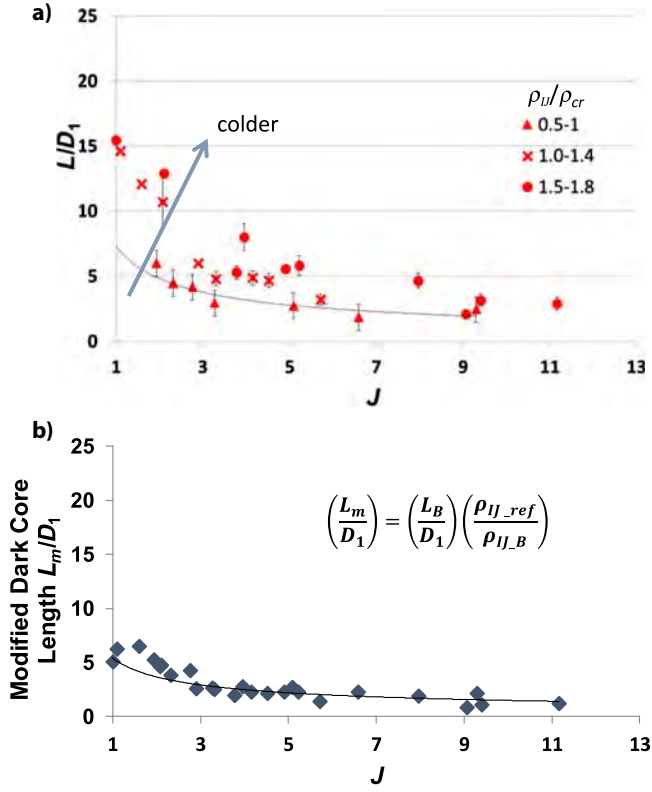

Fig. 9 a) Compilation of dark core data taken for LAR–thick at 3.5–3.7 MPa. b) Collapse of data in a) by normalizing by the inner jet density with a reference density evaluated at 129 K and 3.55 MPa.

Fig. 9b, the resulting collapse is very good, and all the data more or less lie on the same curve. The same normalization was applied to data taken at ~5 MPa, and the collapse was also noticeable. This example is shown in this chapter to indicate that there might be a direct effect of inner jet density on mixing independent of other variables, a possibility that could be explored further in future studies.

To understand the effects of geometry on mixing, all injectors except SAR–thin 2 (Fig. 3) were studied for nitrogen–nitrogen coaxial jets. With these four geometries, the effects of AR and inner jet post thickness could be studied. Injector SAR–thin 2 was nominally designed to be the same as injector SAR–thin, but because of manufacturing constraints, it could not be reproduced identically.

The dark core length results obtained with different injectors for subcritical pressure ($P_r = 0.44$) are shown in Fig. 10. All data are for nominally flush configurations except for some data for SAR–thin, which had a $0.5D_1$ recess of the

Downloaded by Doug Talley on June 5, 2020 | http://arc.aiaa.org | DOI: 10.2514/5.9781624105814.0233.0280 | Book DOI: 10.2514/4.105814

Downloaded by Doug Talley on June 5, 2020 | http://arc.aiaa.org | DOI: 10.2514/5.9781624105814.0233.0280 | Book DOI: 10.2514/4.105814

inner jet tube, and LAR–thin, which had the inner jet sticking out $0.2D_1$ [21]. Because each curve corresponding to a different geometry follows a different trend with J, it is clear that geometry plays a significant role in mixing for the cases studied. The slowest mixing, consistent across the range of J values studied, is for injector LAR–thin, and the fastest mixing is for SAR–thick. However, comparing LAR–thin and LAR–thick, we see that for similar AR values, having a thick post with a pronounced recirculation zone helps mixing, which is intuitive because the structures created in the recirculation zone are very efficient at mixing fluid from the outer and inner jets. The same general trend is true when comparing SAR–thin and SAR–thick, except that, as seen in the figure, the data for SAR injectors show lower values for dark core length than the data for LAR injectors. Observations from Champagne and Wygnanski [52] and Gladnick et al. [53] point to longer potential core lengths with LAR. Overall the data seem to indicate a collapse in L/D values for $J > 10$ except for LAR–thin. Future studies could be conducted at higher J values to see if LAR–thin also collapses with the rest of the curves.

The dark core length trends for the conditions just above the critical pressure ($P_r = 1.05$) shown in Fig. 11 are not as clear as for subcritical cases, although trends look similar to one another. Although the data for the recessed case for SAR–thin collapsed with the data for the same injector with no recess at subcritical pressures (see Fig. 10), this is not the case here. Therefore, the data are included for completeness, but the following description applies only to the flush injectors. It is still the case that the slowest and fastest mixing correspond, respectively, to LAR–thin and SAR–thick, as in the subcritical case. However, the differences between LAR–thin and LAR–thick are much smaller. The dark

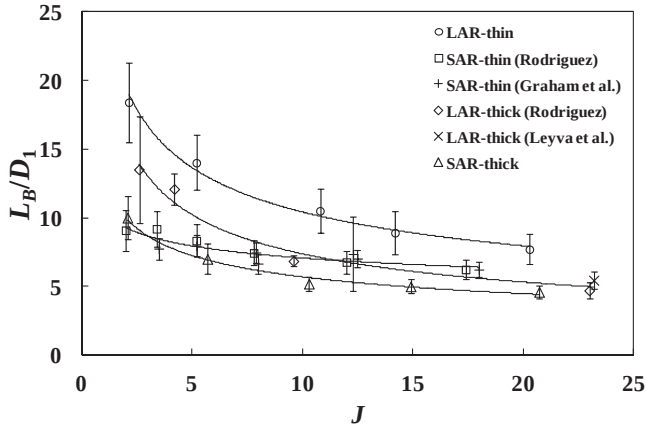

Fig. 10 Baseline normalized dark core length L_B/D_1 for $P_r = 0.44$ for four injector geometries (uncertainty bands are one standard deviation) [41].

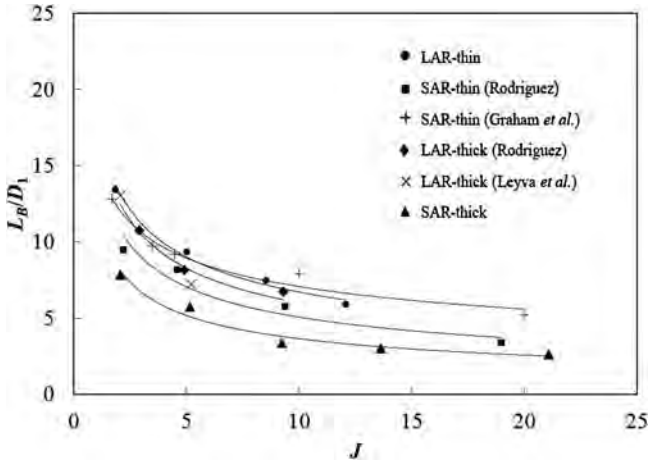

Fig. 11 Baseline normalized dark core length L_B/D_1 for $P_r = 1.05$ for four injector geometries [41].

core lengths for the SAR–thin injector are still consistently longer than those for SAR–thick, as was the case at subcritical pressures.

As a first attempt to capture the behavior and dependence on the dark core length of geometry and J, the data were fitted to a relation of the form

$$\left(\frac{L}{D_1}\right) = c_1 J^{c2} \left(\frac{t}{D_1}\right)^{c3} \left(\frac{A_o}{A_i}\right)^{c4} \tag{4}$$

The fit coefficients were determined using linear regression, and the values for the exponents for the subcritical and near-critical data are shown in Table 4. The form of the equation was chosen to see which exponents each variable would have to assess the most dominant effects.

As can be seen from the exponents, for the subcritical data, the effects of AR and J are comparable but in opposite directions. The effect of the normalized inner jet tube thickness is the smallest. For the supercritical data, the effect of J is strongest, and the effects of the two geometry parameters are comparable

TABLE 4 EXPONENT VALUES FOR EQ. (4) FOR SUBCRITICAL AND SUPERCRITICAL CONDITIONS

P_r	c_1	c_2	c_3	c_4
0.44	9	−0.34	−0.15	0.30
1.05	11	−0.43	−0.12	0.15

Downloaded by Doug Talley on June 5, 2020 | http://arc.aiaa.org | DOI: 10.2514/5.9781624105814.0233.0280 | Book DOI: 10.2514/4.105814

Downloaded by Doug Talley on June 5, 2020 | http://arc.aiaa.org | DOI: 10.2514/5.9781624105814.0233.0280 | Book DOI: 10.2514/4.105814

to each other but in opposite directions. In general, as already explained directly by the plots, there is a negative dependence of the dark core length with normalized thickness of the inner jet tube wall and a positive dependence with AR.

The results of dark core length analysis for nonreactive nitrogen flows provide insight into the development of injector systems that mix well and generate compact and efficient combustion processes. The results can also be used to control the level of intrinsic disturbances that result from hydrodynamic instability in the flow [7, 8, 54]. In general, higher levels of mixing are accompanied by energetic turbulent structures. The presence of such structures will be beneficial, as external disturbances must compete with these intrinsic fluctuations, making the flow less responsive. There is a risk that the naturally occurring hydrodynamic instabilities (seen in Figs. 5–7 without excitation, for example) could be unintentionally tuned to an acoustic mode of the chamber, leading the injector to become the initiator of a combustion instability. Thus, there is a need for spectral information on the injector flowfield.

3. INNER SHEAR-LAYER CONVECTION VELOCITIES

As supported by the previous discussion on dark core length, the evolution of structures on the inner jet boundary plays an important role in the mixing process. Thus, there is a need to understand the properties of these structures—their formation frequency, velocity, and growth rate. One of the key aspects of the coaxial jet is the frequency content associated with the mixing process. Hence, there is a need to establish a frequency scaling law for the coaxial jet. The Strouhal number is defined as

$$St = \frac{f_{\text{nat}} D}{U} \tag{5}$$

where f_{nat} is the natural frequency of the flowfield, D is the characteristic diameter, and U is the characteristic velocity. Independent of the type of flow being studied, the selection of characteristic scales is very important. For the velocity scale, the choice must either represent the velocity of the instabilities or at least be proportional to this velocity.

In this work, we adopted the convection velocity estimated by Dimotakis [55] for planar variable density shear layers, which involves the velocity weighted by the square root of the density,

$$U_{\text{c,th}} = \frac{\rho_1^{1/2} U_1 + \rho_2^{1/2} U_2}{\rho_1^{1/2} + \rho_2^{1/2}} \tag{6}$$

where $U_{\text{c,th}}$ is this theoretical convection velocity. Equation (6) obviously neglects the effects of surface tension, and thus the applicability to multiphase flows is limited. The jet velocities U_1 and U_2 are obtained through measurement of

mass flow rate, the known exit area for each stream, and the temperature and pressure of the fluids.

The appropriateness of Eq. (6) was tested by measuring shear-layer convection velocities via image analysis. Consider an array of pixels as shown by the curve along the right side of the inner jet in Fig. 12a. A piecewise linear trajectory is manually selected along the edge of the inner jet shear layer. For a single pixel lying on this trajectory, the pixel intensity will oscillate in time from low (dark) to high (light) as dense fluid structures convect through. When the entire pixel trajectory is considered rather than a single point, the shear-layer structures will traverse through the array of pixels, creating areas of dark and light intensity that

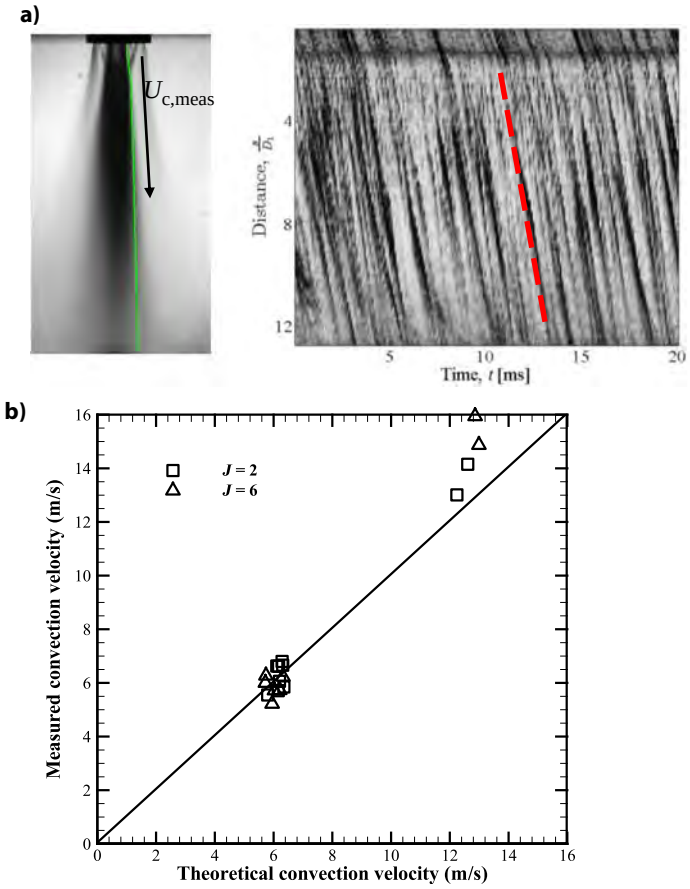

Fig. 12 a) Axial distance $s - t$ pixel intensity history for use in estimating the convection velocity and b) comparison of measured convection velocities to the Dimotakis [55] estimate for variable-density shear layers (injector SAR–thin 2, $P_r = 0.8$) [42].

Downloaded by Doug Talley on June 5, 2020 | http://arc.aiaa.org | DOI: 10.2514/5.9781624105814.0233.0280 | Book DOI: 10.2514/4.105814

change over time. Figure 12a shows this streak pattern created over a sequence of images. On the vertical axis the shear-layer curve coordinate s is nondimensionalized by D_1, and the horizontal axis is time in milliseconds. A diagonal streak represents the convection of a single liquid structure that begins near the injector exit and travels downstream. Very close to the injector, $s/D_1 \approx 1$, a dark horizontal bar in the streak image represents the signature of the end of the recirculation zone. The convection velocity upstream of this dark horizontal feature, represented by the slope of the streaks, is less than the shear-layer convection velocity downstream of the recirculation zone, where the much faster outer jet meets the inner jet. The streaks that appear at $s/D_1 > 1$ are of interest here. The slope of a single streak, $\Delta s/\Delta t$, is the velocity of the coherent structure represented by the streak. A total of eight streaks were analyzed for each case, resulting in eight independent convection velocity samples. The average of this sample set was computed to represent the measured convection velocity $U_{c,meas}$ for each experimental condition. Image distortion due to index-of-refraction gradients along the path of light will cause an error in location of the structures that produce the streaks, which propagates into an error in the convection velocity. Order-of-magnitude analysis using the refraction of the helium–air interface near the jet exit was used to estimate this error in convection velocity to be less than 2%. The uncertainty of the mean due to variance among the eight samples is approximately 5%.

Figure 12b shows theoretical vs measured convection velocities for the two J values employed for injector SAR–thin 2; flow rates were selected to keep the convection velocity predicted using Eq. (6) fixed—hence the overlap of points for both J values. Data were collected for a nominal ($\sim$6 m/s) and a higher ($\sim$12 m/s) convection velocity for both J values. The agreement is quite good, indicating that the Dimotakis [55] model may be employed for the current flow conditions. A deviation observed at the higher convection velocity is evident. An error in temperature due to heat transfer within the injector leads to a direct error in the evaluated fluid density. The velocity is estimated using the calculated density and the measured flow rate, thus creating further error because of temperature uncertainty. An approximate analysis of uncertainty in the theoretical convection velocity due to temperature error is 2%, which would not explain the observed deviation at higher flow rates (i.e., higher convection velocities). The robustness of the theoretical convection velocity to other operating conditions is uncertain; one might expect a deviation for lower Weber number conditions where surface tension effects are enhanced and play a more significant role in the shear-layer instability. The application to thick post injectors is also questionable because the wake region interferes with the establishment of a shear layer.

4. POD OF IMAGE DATA

POD, also known as principal-component analysis (PCA), has proven to be a powerful means for extracting relevant qualitative and quantitative information from otherwise complicated and noise-ridden measurement data. Berkooz et al.

Downloaded by Doug Talley on June 5, 2020 | http://arc.aiaa.org | DOI: 10.2514/5.9781624105814.0233.0280 | Book DOI: 10.2514/4.105814

Downloaded by Doug Talley on June 5, 2020 | http://arc.aiaa.org | DOI: 10.2514/5.9781624105814.0233.0280 | Book DOI: 10.2514/4.105814

[56] and Chatterjee [57] give an in-depth discussion on the fundamentals of POD. The POD algorithm was applied to injector visualization data using the singular value decomposition (SVD) [1, 58].

The POD results isolate a number of modes that capture various phenomena ranging from global flapping, shear-layer type instabilities, and random small-scale dynamics. The emphasis of previous research [49–52] was placed on isolating hydrodynamic instabilities associated with convecting structures on the inner shear layer, as these features are likely drivers of combustion instabilities. Arienti and Soteriou [59] provide criteria for identifying convective modes from POD data.

In this study, the preferred mode is associated with the convective mode having the most energetic POD mode pair (i.e., the mode pair with the highest eigenvalues) [41, 42]. It is likely that multiple convective modes are present in the unforced cases because of the highly turbulent nature of the flow. Other convective modes with lower singular values are not considered as representing preferred modes.

The preferred mode frequency of the coaxial jet was found for a number of data sets for injector SAR–thin 2 for momentum flux ratios of 2 and 6 and for nominal and high flow rates. The choice of a momentum flux ratio of 6 is based on expected values using hydrogen and oxygen in subsequent combustion experiments with the same injector. The average of D_1 and D_2 was used as the characteristic diameter in the Strouhal number defined in Eq. (5). Figure 13 shows the dimensionless frequency as a function of momentum flux ratio for the two different convection velocities. Symbols represent the convection velocity of the shear-layer structures, which is achieved by increasing the flow rate. The measured convection velocity provides a slightly reduced level of scatter compared to results using Eq. (6), in large part because of the deviation that occurs at higher convection velocities indicated in Fig. 12b. The data fall within 25% of a value of 0.3. As stated for the convection velocity correlation, the robustness of the frequency scaling law with respect to different conditions and geometries is unclear. These data were collected for an injector with a relatively thin post thickness in the high-Weber-number regime. Excursions outside this operating domain will likely introduce phenomena such as surface tension and wakes that influence the frequency selection process.

B. FORCED COAXIAL JETS

1. VISUAL FEATURES

An extensive effort at AFRL [21, 41, 43, 47, 49, 51] spanning several investigators explored the response of four injectors to high-amplitude acoustic forcing at sub- and supercritical pressure conditions. These research campaigns employed near-maximum siren amplitude at a frequency of approximately 3 kHz, driven by two amplified sine waves with controlled phase (see Fig. 2). The relative phase between

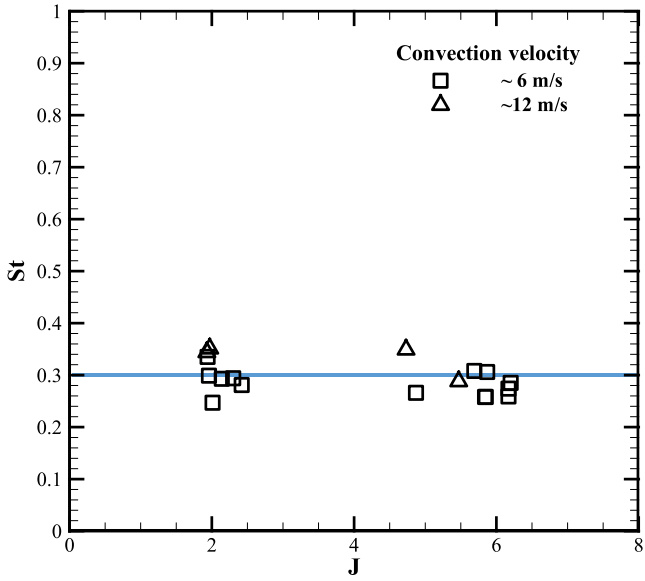

Fig. 13 Strouhal number as a function of momentum flux ratio for subcritical conditions for injector SAR–thin 2 [42].

the two piezoelectric sirens was varied to manipulate the acoustic environment. A phase shift of zero created a PAN and velocity node in the middle of the chamber, and a phase shift of 180 deg created a PN and velocity antinode at the same location.

Figure 14 shows the instantaneous backlit images for injector LAR–thick operating with nitrogen–nitrogen at subcritical pressure for four values of J. For each J, a variety of different phase angles for siren operation are shown, with the first image in the upper left of each ensemble showing the unforced case for reference. For each image ensemble, the phase angle where maximum and minimum pressure fluctuation amplitude was achieved is labeled. Ideally, these conditions would be zero and 180 deg, respectively, but spatial temperature and density variations as well as siren and electronics imperfections are likely responsible for the observed deviations.

Figure 14a corresponds to $J = 0.17$. The overall behavior of the jet does not change substantially with acoustic forcing, but a slight increase in mixing can be observed. For several phase-angle cases, the inner jet experiences slightly enhanced spreading. In contrast, the 135 deg and the baseline conditions show very little spread, and the core only starts to break up toward the bottom of the image. At $J = 2.6$ (Fig. 14b), the effects of the acoustics are very clear. The inner jet dark core has a sinuous response for every phase angle, reaching a

Downloaded by Doug Talley on June 5, 2020 | http://arc.aiaa.org | DOI: 10.2514/5.9781624105814.0233.0280 | Book DOI: 10.2514/4.105814

Downloaded by Doug Talley on June 5, 2020 | http://arc.aiaa.org | DOI: 10.2514/5.9781624105814.0233.0280 | Book DOI: 10.2514/4.105814

minimum dark core length at 180 deg, which corresponds to minimum pressure fluctuation amplitude but maximum velocity amplitude. Mixing is enhanced significantly, with large regions where the dark core segments have almost completely blended with their surroundings. The behavior at 315 deg, the phase angle associated with maximum pressure fluctuations, shows minimum transverse motion of the inner jet due to acoustic forcing. At $J = 9.6$ (Fig. 14c) there is a very thick dark core. This thickness is evidence that the high momentum flux of the outer jet is having a strong effect on the inner jet, allowing it to mix very rapidly across the recirculation region at the exit of the injector, as was shown in Fig. 6a for injector SAR–thick. Transverse motion of the dark inner jet is observed, with no clear influence of the phase angle. In a sense, the dark core is too short to show any bending due to acoustic forcing. However, it is clear from all the acoustically forced images that, downstream of the dark core breakup, the ensuing mixing region is curved, widened, and perturbed by the acoustic forcing. Finally, for $J = 23$ (Fig. 14d), the shape of the dark core does not seem to vary noticeably among the images; the only difference is the slight change in curvature toward the downstream end of the dark core for different acoustic conditions.

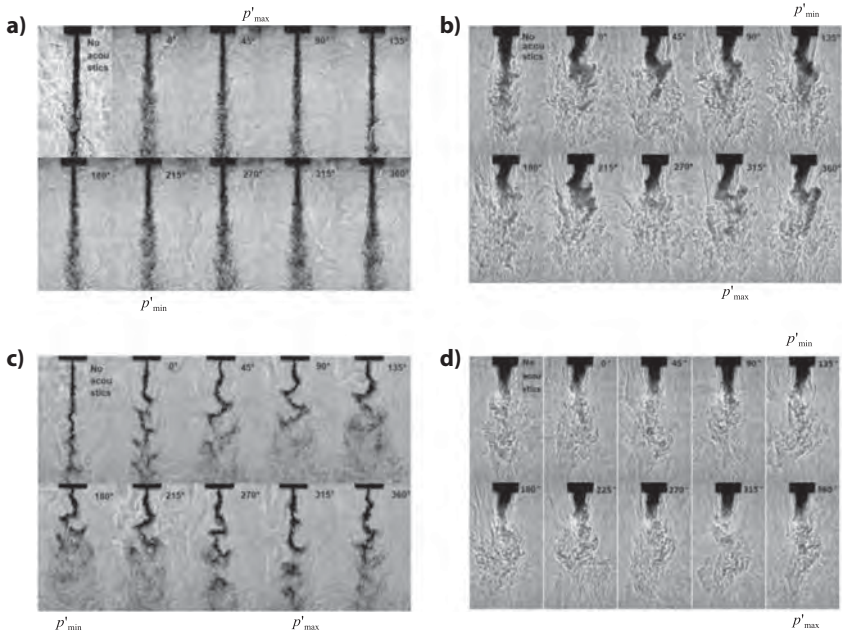

Fig. 14 Visualizations of injector LAR–thick under acoustic forcing conditions at subcritical pressure at momentum flux ratios *J* of a) 0.17, b) 2.6, c) 9.6, and d) 23 [36].

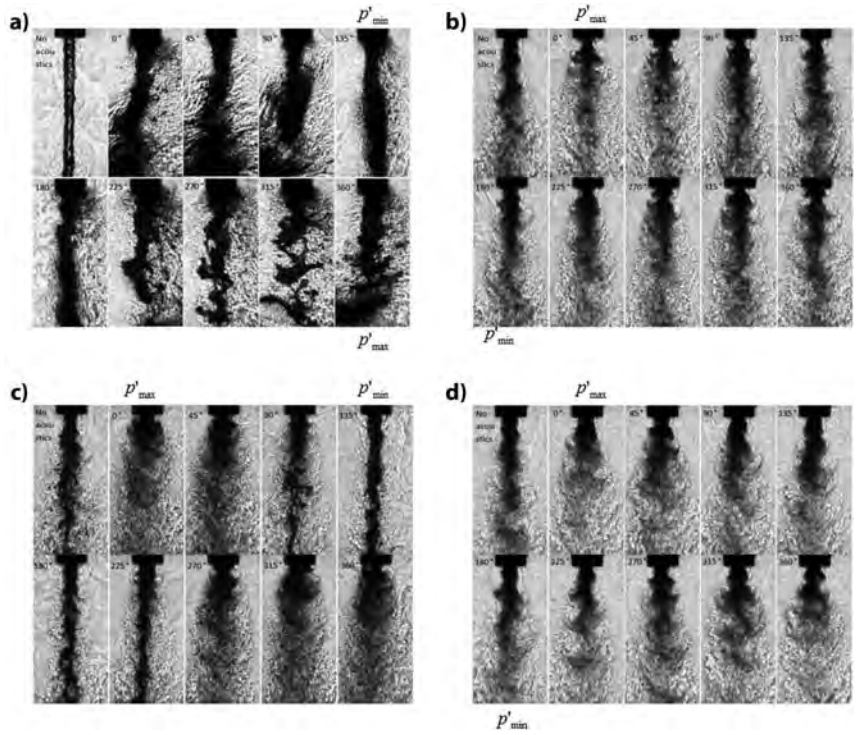

Fig. 15 Visualizations of injector SAR–thin under acoustic forcing conditions at subcritical pressure at momentum flux ratios *J* of a) 0.09, b) 2.0, c) 7.8, and d) 18 [36].

Figure 15 shows the response of the coaxial jet to acoustic forcing at subcritical pressure for injector SAR–thin. The images shown in Fig. 15a correspond to a momentum flux ratio of 0.089. The inner jet can be clearly distinguished from the outer jet and its surroundings. The thickness of the inner jet stays constant throughout the image. This injector has a substantial response to acoustic forcing. For the phase angles from 0 deg to 90 deg, the inner jet bends noticeably and there is strong atomization taking place near the injector exit. The dark core region is somewhat thicker and blurred. The next two phase angles show a perturbed but straight inner jet. The images corresponding to a phase difference between 225 deg and 315 deg show the liquid stream from the inner jet shortened significantly, with large structures of liquid that have been separated from the inner jet. The acoustic response of injector SAR–thin at low momentum flux ratio is significantly different than that of injector LAR–thick (Fig. 14a). Although the percentage of the acoustic pressure to the chamber pressure was about the same for both injectors, the inner jet for injector SAR–thin was operated at approximately half the velocity of injector LAR–thick; thus, the acoustics were

Downloaded by Doug Talley on June 5, 2020 | http://arc.aiaa.org | DOI: 10.2514/5.9781624105814.0233.0280 | Book DOI: 10.2514/4.105814

operated at a much higher relative pressure compared to the dynamic pressure of the inner jet. This could be partly responsible for the enhanced influence of acoustics on the injector SAR–thin at low momentum flux ratio.

At $J = 2.0$ (Fig. 15b), there is a striking response of the coaxial jet to acoustic excitation in this case. The mixing is strongly enhanced near phase angles of zero (i.e., a PAN). Large, apparently coherent, axisymmetric structures are formed near the injector exit. These structures become very large and facilitate rapid mixing and breakdown of the inner jet. A similar behavior has been observed for PAN forcing for injectors LAR–thin [41] and SAR–thin 2 [60]. It is apparent that this behavior is more prevalent when the inner jet post is thin. The acoustic response for phase angles around 180 deg shows a different behavior: There appears to be a lengthening and thinning effect on the inner jet. Although not clear from this viewing angle, PN forcing might have a flattening effect on jets [61] and coaxial jets [62]. Views from the side of the jet would be needed to confirm this. The thinning of the inner jet happens some distance downstream of the exit plane. Note that immediately downstream of the exit plane the thickness of the inner jet is comparable to the baseline. The jet at a PN condition is clearly different from the sinuous motion generated for injector LAR–thick (Fig. 14b). It is currently unclear why an injector flow responds so differently to PN excitation, as highlighted by the differences between Figs. 14b and 15b. Lastly, the image taken at a phase angle of 225 deg shows a very good example of the enhanced mixing between the inner and outer jets forming what appears to be coherent asymmetrical structures with mass from both jets.

Figures 15c and 15d show injector SAR–thin at subcritical pressure at momentum flux ratios of 7.8 and 18, respectively. The results of these two momentum flux ratios are similar. The PAN forcing shows the strongest impact of forcing. Apparent axisymmetric structures are formed on the inner jet surface, and mixing enhancement is observed. The effects of forcing near the PN condition do not manifest in any clear trend.

A look back to Figs. 5b and 5c shows the results for injector LAR–thin at subcritical pressure under PAN and PN forcing, respectively, at a variety of momentum flux ratios. Overall, the behavior is similar to that observed for injectors LAR–thick and SAR–thin. The PAN forcing results in the excitation of axisymmetric structures on the inner jet core. The wavelength of the instabilities, particularly in the lower momentum flux ratio range, increases with momentum flux ratio, which is partially caused by the manner in which the different momentum flux ratios were achieved. Forcing at PAN conditions enhanced mixing, with the effect degrading as momentum flux ratios increased. As with the results of Rodriguez et al. [47], the acoustic forcing amplitude was scaled to the mean chamber pressure. The PN forcing shows an interesting trend with momentum flux ratio. The lowest J case exhibits a modest wrinkling of the liquid surface with no jet deflection. As J is increased to 0.5, the response changes to the sinuous behavior observed with injector LAR–thick. The sinuous response continues at higher momentum flux ratios.

Downloaded by Doug Talley on June 5, 2020 | http://arc.aiaa.org | DOI: 10.2514/5.9781624105814.0233.0280 | Book DOI: 10.2514/4.105814

Downloaded by Doug Talley on June 5, 2020 | http://arc.aiaa.org | DOI: 10.2514/5.9781624105814.0233.0280 | Book DOI: 10.2514/4.105814

The subcritical pressure response of injector SAR–thick to PAN and PN acoustic forcing is shown in Figs. 6b and 6c, respectively. Here the PAN forcing is clearly seen to enhance liquid ligament formation, particularly at lower momentum flux ratios. At the two lowest values of J, the generation of coherent structures in the recirculation zone is clearly seen, as is their entrainment of outer jet mass (see the arrows in Fig. 6). By the third value of J, the recirculation zone is much darker, as mass from the inner jet is now more entrained, and it is more difficult to identify coherent structures near the jet exit plane. In the three highest values of J, the recirculation zone is all dark, giving the appearance of a much thicker inner jet core, and the coherent structures appear as features of the denser inner jet. These structures are likely axisymmetric. PN forcing is different in nature. The lowest momentum flux ratio case appears to be experiencing some thinning in the near field near the center of the image, followed by enhancement of atomization. A similar observation was made by Baillot et al. [62] when viewing PN forcing that caused the aforementioned flattening effect. The lowest momentum flux ratio PN case in fact looks very similar to the PAN case in terms of the structures being generated in the recirculation zone, but qualitatively, the wavelength of each structure is smaller (see the arrows in the figure). The next image is also qualitatively similar to the corresponding one for PAN in the behavior of the recirculation zone, but the outer jet seems to be less disturbed downstream. For the remaining three higher momentum flux ratios, the dark core is shorter than in the corresponding cases for PAN, and there are less pronounced structures in the inner jet, except for the very last case, where structures are observed near the end of the core. However, no large-scale flapping occurred such as that observed for injector LAR–thick (Fig. 14b). There are two substantial differences between injectors LAR–thick and SAR–thick. The first difference is the AR and the second is the scale of the injector (see Fig. 3). The inner jet for injector SAR–thick is nearly three times larger than that for injector LAR–thick. The forcing frequency was held constant near 3 kHz to maintain the highest acoustic amplitudes possible, but the different scale injectors are likely to have different natural mode frequencies; thus, the relative forcing frequency may be substantially different.

The nonreacting flow facility was also used to explore the acoustically forced flow response at supercritical pressure for all injectors except SAR–thin 2. Only one injector will be described in detail here.

Figures 7b and 7c show the acoustic forcing response of injector LAR–thin at supercritical pressure across a range of momentum flux ratios. Only two momentum flux ratios were forced at PN conditions. Overall, the response of injector LAR–thin to acoustic forcing is qualitatively similar to that at subcritical conditions (Fig. 5). Forcing at the PAN condition results in symmetric structure formation on the inner/outer jets, although the structures are highly turbulent and noisy. The image for $J = 1.9$ is a good example of how the structures observed have mass from the inner and outer jets. The structures can be clearly observed as continuous between the two jets, and the most downstream structures seem

Downloaded by Doug Talley on June 5, 2020 | http://arc.aiaa.org | DOI: 10.2514/5.9781624105814.0233.0280 | Book DOI: 10.2514/4.105814

to have less dense fluid than the initial part of the inner jet, as mixing has occurred. Increasing the momentum flux ratio in general leads to degraded impact of acoustics, which may be partially caused by relative amplitude and frequency effects, as stated earlier.

The injectors SAR–thin and SAR–thick forced at supercritical pressure show similar behavior; see Rodriguez [36] and Teshome [41] for details. For fixed momentum flux ratio and fluid temperatures, operating at different chamber pressure influences the density ratio between the two jet streams. This therefore causes a concomitant change in velocity ratio, which can have an effect on the mixed recirculation zone/shear layer developed between the two jets.

2. CONVECTIVE MODES IN FORCED INJECTOR FLOWS

Teshome [41] applied the POD technique for injectors SAR–thick and LAR–thin to elucidate the properties of the strongest convective modes induced through acoustic forcing. Once again, the convective mode pair algorithm described earlier was used to identify the dominant mode. The cross power spectral density (CPSD) function of the POD temporal coefficients for the dominant mode pair for both the forced and unforced cases was computed to show the temporal behavior of the flow.

Figure 16 shows the effects of PAN forcing in terms of the spatial and temporal properties of the dominant convective mode for injector LAR–thin at subcritical conditions at three different momentum flux ratios. At $J = 0.5$ (Fig. 16a), the unforced dominant convective mode shows weak structure in the near field and gradual emergence of a mode that is antisymmetric toward the downstream region as lobes of different signs (black and white) appear in the left and right sides of the image at the same downstream distance from the exit plane. This mode, when superimposed on the mean image, results in a sinuous deformation of the liquid jet column. Forcing strongly at the PAN condition, the flow responds with a coherent symmetric structure formation as shown in the spatial mode shape. This apparent varicose mode is maintained over the full range of the image, with some distortion in the downstream region. The CPSD amplitude shown in the figure includes the spectrum for both the unforced (dashed line) and PAN-forced (solid line) dominant convective mode pairs. For the unforced case, the convective mode pair has a peak near 1.5 kHz. When forced near 3 kHz, a clear peak occurs at the forcing frequency and the first harmonic. Additionally, the broadband peak is seen to shift to center on the forcing frequency. It is clear that the dominant convective mode was dramatically altered by the acoustic forcing, both spatially and temporally.

As shown in Fig. 16b, a different forcing response is observed for $J = 5.2$. The unforced convective mode is seen to be once again antisymmetric with an enhanced spreading rate compared to the lower J case, which is consistent with the dark core length trends with J. With PAN forcing, the spatial mode is neither purely symmetric nor antisymmetric. The CPSDs of the unforced and

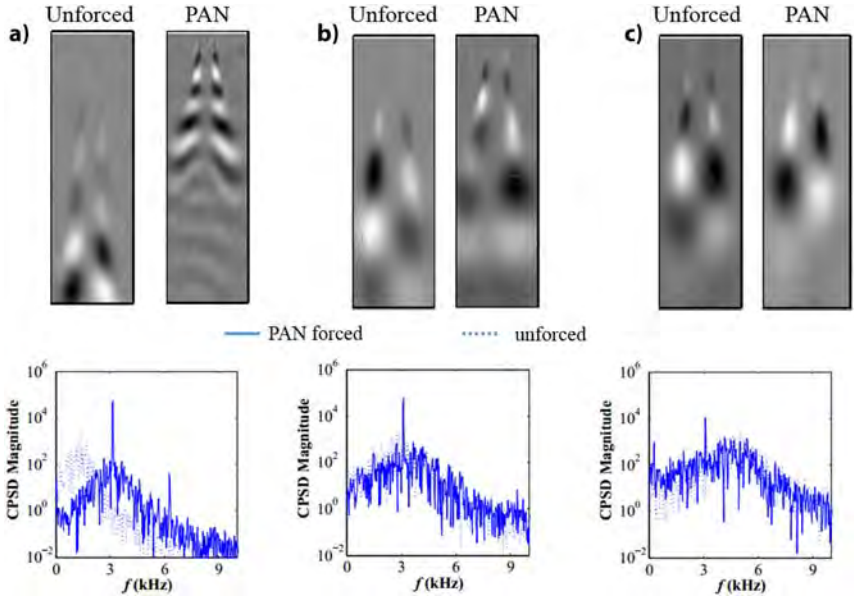

Fig. 16 The unforced and PAN-forced spatial mode of the dominant convective mode for injector LAR–thin at subcritical pressure at momentum flux ratio *J* of a) 0.5, b) 5.2, and c) 11 [41].

PAN-forced cases have strong overlap. It is apparent that the flow is being forced near the peak frequency of the unforced case. The broadband spectra are nominally the same for both the PAN-forced and unforced cases. The flow response to PAN forcing at this *J* value is limited to the forcing frequency, and no apparent harmonics are generated, at least within this spatial mode shape. The spatial mode is also less altered by acoustic forcing compared to the low momentum flux ratio case.

Figure 16c shows the PAN-forcing behavior at $J = 11$. The unforced and PAN-forced spatial mode shapes are similar, and the forced flow is predominantly antisymmetric. The CPSD is very similar for both cases, with a clear peak at the forcing frequency (with no harmonics) emerging with forcing. The preferred mode frequency of the unforced case appears to be ~4.5 kHz, which is higher than for the other two cases; thus, the forcing at 3 kHz is effectively low-frequency forcing. There appears to be some reorganization of spectral content from high to low frequency with the addition of acoustic forcing. The results presented in Fig. 16 show that an increase in J has degraded but not eliminated the coupling between the acoustics and the flowfield.

The PN-forcing response of injector LAR–thin at subcritical pressure shows an overall similar trend with respect to changes in *J* [41]. The PN forcing does

Downloaded by Doug Talley on June 5, 2020 | http://arc.aiaa.org | DOI: 10.2514/5.9781624105814.0233.0280 | Book DOI: 10.2514/4.105814

result in an antisymmetric response, indicating a different interaction mechanism. An increase in J appears to degrade the influence of PN forcing, including a reduction in impact on the changes in spatial mode shape and overall spectral properties.

Figure 17 shows the influence of PAN forcing of injector SAR–thick at subcritical pressure for three J values. As shown in Fig. 17a, the PAN forcing at $J = 2.1$ shows negligible impact. The CPSD unforced case shows a relatively low frequency peak below 1 kHz, and forcing does not impact the distribution, other than a minor peak at the forcing frequency. The spatial mode shape appears to show an antisymmetric structure of similar characteristics for both the unforced and PAN-forcing cases. Forcing at $J = 5.7$ and 15, shown in Figs. 17b and 17c, respectively, shows more manifestation of forcing. Interestingly, the unforced spectrum shows no significant change in the CPSD, unlike the trend shown for injector LAR–thin. All cases involve relatively high-frequency forcing, as the 3-kHz forcing frequency is higher than the peak frequency of the unforced cases for all momentum flux ratios. Peaks occur at the forcing frequency and two harmonics, and in general, energy is shifted from lower frequency to higher frequency. The mode shapes of the forced cases show a small-scale structure that becomes highly symmetric at the maximum momentum flux ratio of 15. The limited impact of increasing J on the unforced spectra is likely caused by the reduced interaction of the inner and outer jet due to the large recirculation region.

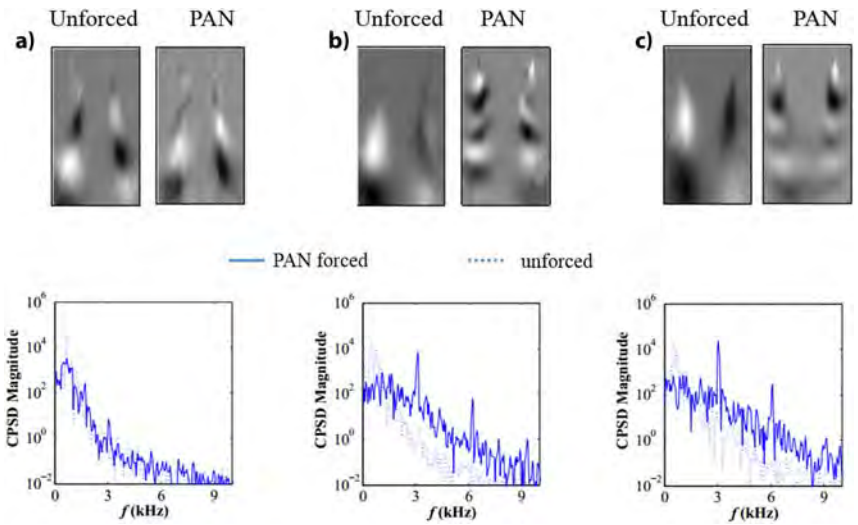

Fig. 17 The unforced and PAN-forced spatial mode of the dominant convective mode for injector SAR–thick at subcritical pressure at momentum flux ratio J of a) 2.1, b) 5.7, and c) 15 [41].

Downloaded by Doug Talley on June 5, 2020 | http://arc.aiaa.org | DOI: 10.2514/5.9781624105814.0233.0280 | Book DOI: 10.2514/4.105814

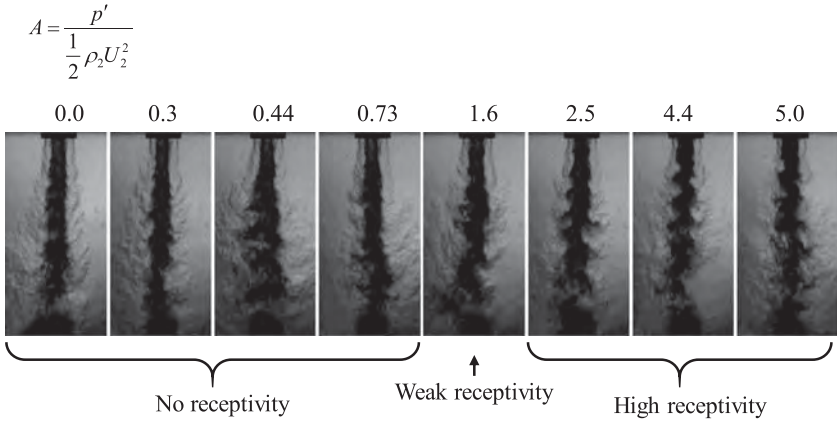

Fig. 18 PAN behavior for injector SAR–thin 2 at a momentum flux ratio of 2.0 as a function of acoustic forcing amplitude at a frequency ratio of 2.6 ($P_r = 0.8$).

The characteristics of the convective modes at supercritical pressure conditions show a trend similar overall to that of subcritical conditions and are thus not included here; see Teshome [41] for further details on the convective modes at supercritical pressure. Similar to the findings for the characteristic frequency and convection velocities, surface tension does not appear to play a predominant role in the range of conditions considered. Density ratio is also influenced by operation at sub- and supercritical conditions, although the density ratio is maintained at $\ll 1$ for all cases.

Wegener [42] conducted a study on the receptivity of injector SAR–thin 2 to acoustic forcing, where emphasis was placed on sensitivity to forcing characteristics. The purpose of this particular study was to document the conditions at which a coupling between the acoustics and flow occurs as a function of acoustic amplitude and frequency (i.e., identify boundaries between no coupling and detected coupling). Acoustic fields impose fluctuations in both pressure and velocity. The acoustic amplitude was varied with the injector located within the PAN and PN regions. Using the preferred mode frequency scaling law shown in Fig. 13, Wegener [42] fixed the forcing to natural mode frequency ratio at values of 1.7, 2.0, and 2.6. The receptivity of injector SAR–thin 2 at two J values, 2 and 6, was also examined. As mentioned, the inner jet in this case is nitrogen, the outer jet is helium, and the chamber ambient is nitrogen.

Figure 18 shows injector SAR–thin 2 forced at a forcing frequency to natural frequency ratio of 2.6 at a PAN location at different amplitudes, with $J \sim 2$ and at high subcritical pressure. The pressure was nondimensionalized using the outer jet dynamic pressure. At low amplitude, there is no measured influence of acoustic forcing on the flowfield. At a particular forcing amplitude, a change may be detected through analysis of the POD of the data set. A new forced POD mode

Downloaded by Doug Talley on June 5, 2020 | http://arc.aiaa.org | DOI: 10.2514/5.9781624105814.0233.0280 | Book DOI: 10.2514/4.105814

Downloaded by Doug Talley on June 5, 2020 | http://arc.aiaa.org | DOI: 10.2514/5.9781624105814.0233.0280 | Book DOI: 10.2514/4.105814

pair is observed, but the ordering of the forced mode is such that the natural mode is still the strongest convective mode. At higher forcing amplitudes, the forced mode is dominant over the flowfield, even though the natural mode is still detectable. Hence, there are two transition points. The first is the lowest amplitude at which detection of a forcing response is observed, and the second is the amplitude at which the forced mode overtakes the naturally present mode. A qualitatively similar transition was observed for $J \sim 6$ [42]. A similar receptivity analysis was conducted for the PN-forcing conditions.

The receptivity trends for injector SAR–thin 2 operated at subcritical pressure are summarized in Fig. 19 for both momentum flux ratios and PN and PAN forcing. The empty squares represent the highest forcing amplitude at which no forced mode was detected, and the solid squares represent the lowest amplitude at which the forced mode dominates the natural mode. Thus, the shaded area represents the range over which the forced mode emerges and takes over as the

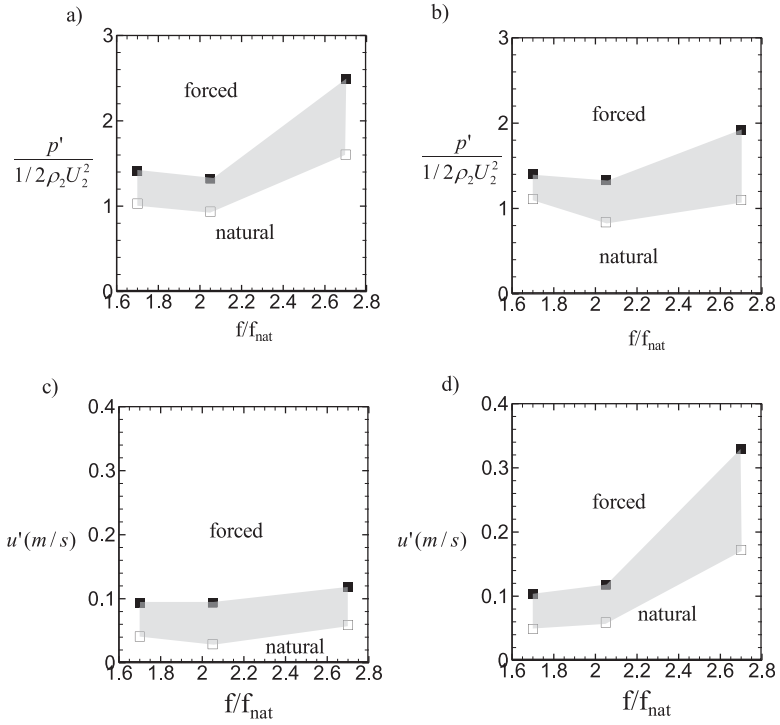

Fig. 19 PAN forcing (top row) and PN forcing (bottom row) receptivity as a function of normalized frequency and normalized acoustic pressure amplitude for injector SAR–thin 2 for $J = 2.0$ (left column) and $J = 5.9$ (right column). From [60]; reprinted by permission of the American Institute of Aeronautics and Astronautics, Inc.)

strongest mode. As shown in Figs. 19a and 19b, both momentum flux ratios indicate that higher forcing amplitudes are required to overtake the natural mode for PAN forcing at higher frequency ratios. It is interesting to note that the inception of receptivity occurs at a nominal dimensionless amplitude of unity. This is consistent with the arguments of Baillot et al. [62] that induced oscillations in the outer gaseous flow drives the flow response.

The PN-forcing receptivity trends for injector SAR–thin 2 at subcritical pressure are shown in Figs. 19c and 19d. The receptivity of the two momentum flux ratios is nominally the same except at the highest frequency ratio. The forcing amplitude was not normalized for the PN cases. A near tripling of the dimensional acoustic velocity is required for the case of a momentum flux ratio of 6 to dominate the preferred mode at the highest forcing frequency. The lower momentum flux ratio case has limited dependence on the range of frequencies considered.

3. PHYSICAL MECHANISMS

It is apparent that the way acoustic disturbances influence coaxial jet flows is very complex, with multiple coupling mechanisms occurring depending on the operating conditions and acoustic environment. Within a liquid rocket engine experiencing a transverse acoustic resonance, the various injectors distributed across the injector face will experience different spatial regions of the acoustic mode shape based on their location. Injectors may be placed near a PAN, near a PN, or in between these regions. Thus, the coupling in these various regions must be fully understood to design an injector distribution on the injection face of the rocket engine properly. Unlike the experimental work presented in this chapter, where the frequency is independently selected, the frequency selection during injector distribution design will be governed by the acoustic resonances associated with the main chamber and any noise sources inside the chamber that align with these frequencies.

The placement of the injector at a PAN exposes the flowfield to an unsteady back pressure. The predominant mechanism, as proposed by Baillot et al. [62], appears to be related to an induced unsteady flow rate in the gaseous outer jet. The pulsing outer jet facilitates the generation of axisymmetric structures on the inner jet boundary, causing an enhancement of mixing. Baillot et al. [62] found that this mechanism appears to become active when the acoustic pressure amplitude is larger than the outer jet dynamic pressure. A similar finding was reported by Wegener [42] and is presented in Fig. 19. In support of this theory, Wegener developed a simple model of the unsteady flow within the injector exposed to a sinuous variation in back pressure and found that the liquid inner jet experiences negligible unsteadiness because of the inertia of the liquid, whereas the gaseous flow experiences significant unsteadiness because of the lower fluid density. In further support of this mechanism, Carpentier et al. [63] found that a single liquid jet (i.e., unassisted by a co-flow of gas) does not respond to high-frequency forcing when placed at a PAN condition.

Downloaded by Doug Talley on June 5, 2020 | http://arc.aiaa.org | DOI: 10.2514/5.9781624105814.0233.0280 | Book DOI: 10.2514/4.105814

Downloaded by Doug Talley on June 5, 2020 | http://arc.aiaa.org | DOI: 10.2514/5.9781624105814.0233.0280 | Book DOI: 10.2514/4.105814

The PN acoustic environment appears to have a more complicated effect on the coaxial jet. There are two effects that have been observed, the first being a flattening of the liquid jet downstream of the exit plane and the second being a flapping of the jet. The mechanism that causes the flattening effect has received recent attention in the research community. Carpentier et al. [63], Baillot et al. [62], and Hoover et al. [64] all found that placement of a liquid jet or liquid/gas coaxial jet at a PN condition results in a flattening of the liquid jet in the plane perpendicular to the acoustic resonance. Chehroudi and Talley [61] also observed the flattening effect. Although flattening was not observed directly in the work of Leyva [48], Rodriguez [36], and Teshome [41], the thinning observed for PN forcing at low momentum flux ratio is indicative of this phenomenon. A recent set of simulations by Hakim et al. [65] studied the unforced and PN-forced coaxial jet flames at supercritical pressure. The simulation at high relative frequency exhibited the same flattening of the inner jet. Thus, the relative frequency appears to play a role in this mechanism.

The mechanism that leads to the deformation of the liquid into a flat sheet is currently under debate. Baillot et al. [62] provide arguments that the radiation pressure force caused by the acoustic field reflecting off the jet column is the cause of the flattening effect. The azimuthal nonuniformity of the pressure distribution due to this force leads to the deformation into a sheet. The authors find that the acoustic field must reach a critical amplitude to overcome the stabilizing effects of surface tension. An alternative explanation to the flattening effect involves the hydrodynamic pressure field surrounding the jet being exposed to an oscillating transverse flow. As the crossflow interacts with the jet column, a local low-pressure region will be established on the sides of the jet, and a stagnation point and low-pressure region will occur on the windward and leeward sides of the jet, respectively. If the transverse flow oscillates at high frequency, the jet will tend to have a mean low pressure on the sides where the transverse flow accelerates around the jet. The static pressure distribution will again lead to a flattening of the jet. If the forcing frequency is sufficiently low, the jet column will experience significant displacement during the forcing cycle, resulting in the flapping of the jet, which appears to interfere with the flattening effect. The simulations by Hakim et al. [65] were analyzed in the context of these two possible explanations for the flattening effect. The authors concluded that the hydrodynamic interaction, as opposed to the acoustic radiation force, was most likely the cause for the flattening effect for their simulations. It should be noted that Baillot et al. [62] did not observe the flattening effect at the PN condition when the injector flow was in the fibrous atomization regime, which is likely related to why flattening was not observed in the AFRL studies at moderate to high momentum flux ratio values.

As mentioned, the PN-forced coaxial jet can also exhibit a response in the form of a transversely distorted jet. An extreme example of this mode of response is shown in Fig. 14b, with a subtler illustration shown in Fig. 5c. The arguments given by Hakim et al. [65] suggest that the interaction is essentially an unsteady crossflow effect. Buffum and Williams [66] studied a high-speed liquid jet

exposed to the PN region of a relatively low-frequency acoustic resonance and found that the jet experienced sinusoidal transverse deflection. They also conducted order-of-magnitude estimates of the various forces on the jet and found that the drag force on the jet due to the acoustic velocity crossflow was the dominant external force.

Last, placement of the injector between the PAN and PN locations adds complexity as a wide range of mechanisms become available, including acoustic radiation forces, unsteady back-pressure fluctuations, and velocity coupling with the augmented drag effects due to unsteadiness. Baillot et al. [62] and Carpentier et al. [63] found that the acoustic radiation force causes a mean deflection of the jet toward the nearest PN. More work is required to investigate the role of the various available coupling mechanisms in regions between nodes and antinodes.

4. REACTING FLOW RESULTS

As mentioned, the reacting flow facility was developed to facilitate the study of acoustically forced rocket injector flames [42]. Studies to date have focused on injector SAR–thin 2 employing liquid oxygen in the core and cooled gaseous hydrogen in the outer jet. The oxygen-to-hydrogen mass flow ratio was nominally 6, and the momentum flux ratio was 2.2. The chamber pressure was approximately 34 bar, which is below the critical-point pressure of oxygen.

Figure 20 shows an instantaneous image of the nonreacting and reacting cases operating with liquid oxygen and gaseous hydrogen as just described. Under combustion conditions, a number of changes are observed. The dark core is substantially shortened by the presence of combustion. The darkening of the lower left region in the image was due to condensation of water vapor on the inner

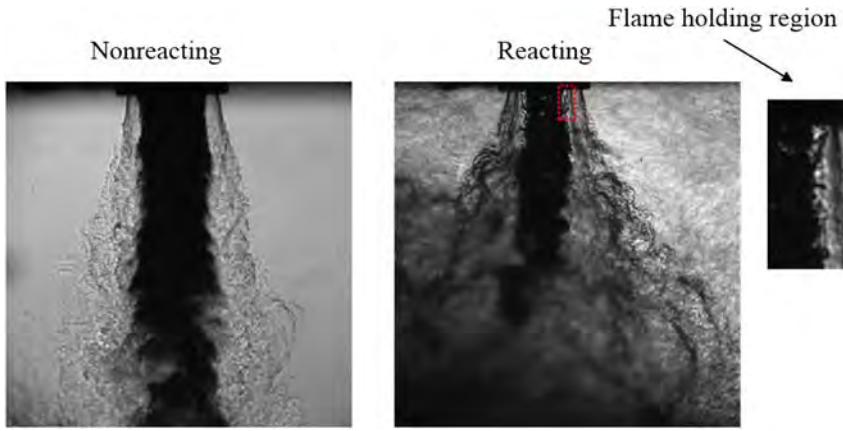

Fig. 20 Backlit images of injector SAR–thin 2 operating with liquid oxygen and gaseous hydrogen for reacting and nonreacting conditions [67].

Downloaded by Doug Talley on June 5, 2020 | http://arc.aiaa.org | DOI: 10.2514/5.9781624105814.0233.0280 | Book DOI: 10.2514/4.105814

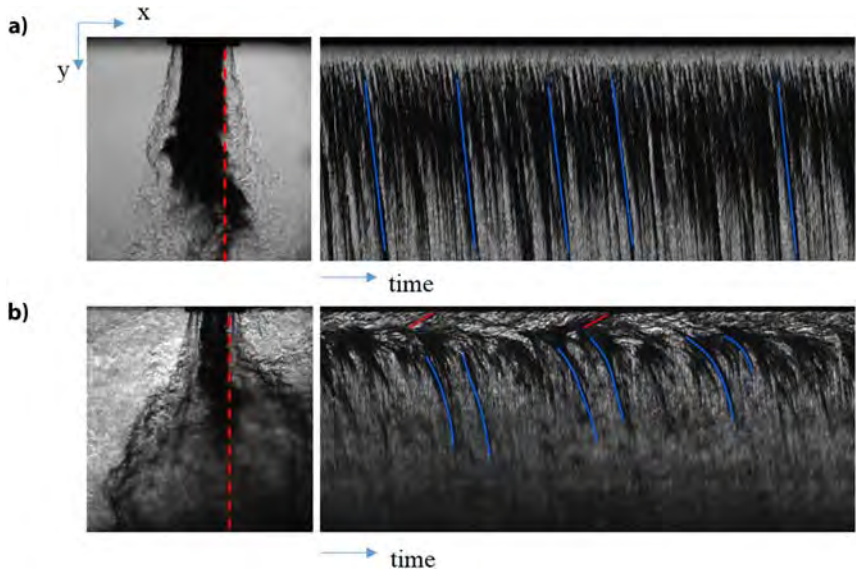

Fig. 21 Pixel array $y - t$ streak diagrams for injector SAR–thin 2 for a) nonreacting and b) reacting conditions [67].

chamber window, an effect that has been subsequently mitigated. The surface of the liquid oxygen core is also less diffused with combustion, which is expected because of the enhanced evaporation associated with the temperature increase in the reacting zone. The combustion also results in a broadening of the jet boundary due to fluid expansion.

The flame is anchored at the inner jet post, as has been verified by unfiltered chemiluminescence images, which is expected for cryogenic oxygen–hydrogen flames [68]. The presence of the flame in the inner jet post wake provides enhanced visual access in this region through evaporation of the liquid droplets. Because of this access, small liquid oxygen structures are seen to enter the recirculation zone and convect upstream to the post (as is supported by Fig. 21). Hence, the predominant rotational sense of the recirculation zone is such that counterflow is applied to the inner edge of the hydrogen flow.

Figure 21 shows inner shear-layer streak imaging to capture the motion of liquid structures in both the reacting and nonreacting cases. For the nonreacting case, the shear-layer structures are seen to emerge downstream of the recirculation zone and convect at a constant velocity; this velocity was shown earlier to be well approximated by the Dimotakis shear-layer convection velocity model [55]. Under reacting conditions, the shear-layer convection velocity is not constant, as indicated by the curvature in the streaks; the structures start at low speed near the end of the recirculation zone and accelerate as they convect downstream.

Downloaded by Doug Talley on June 5, 2020 | http://arc.aiaa.org | DOI: 10.2514/5.9781624105814.0233.0280 | Book DOI: 10.2514/4.105814

The presence of the flame inhibits the momentum transfer between the high-speed outer flow and the lower-speed inner flow. The region within the recirculation zone shows evidence of structures moving upstream.

Localized spectral analysis of pixel intensities was used to provide insight into the effects of the flame on the timescales of the flowfield. Figure 22 shows the time series and spectrum of pixel intensities for a location within the shear layer at two inner jet diameters downstream of the injector exit. The time signals are seen to be complex and contain a range of timescales. The spectra of the two cases do indicate that the presence of combustion tends to shift the intensity fluctuations into a lower frequency range. This is in general agreement with linear stability results, which indicate that a flame in the shear region tends to have a stabilizing effect and shift energy to lower frequencies (e.g., Mahalingam et al. [69]).

Instantaneous shadowgraph images of unforced and acoustically forced cases under both nonreacting and reacting conditions are shown in Fig. 23. The forcing frequency was fixed near 3 kHz for all cases. The nonreacting forced cases show similar qualitative behavior to that which has been described earlier. Under reacting conditions, no local flame extinction was observed regardless of the acoustic forcing amplitude. Overall, the qualitative impact of acoustic excitation under combustion conditions is less than for nonreacting conditions. Forcing the flame at PAN conditions does result in the formation of a small-scale coherent structure on the surface of the inner jet in the near field. This local response does not appear to generate a large alteration in the global mixing behavior. For the PN-forced case, the dark core does not exhibit the large-scale flapping

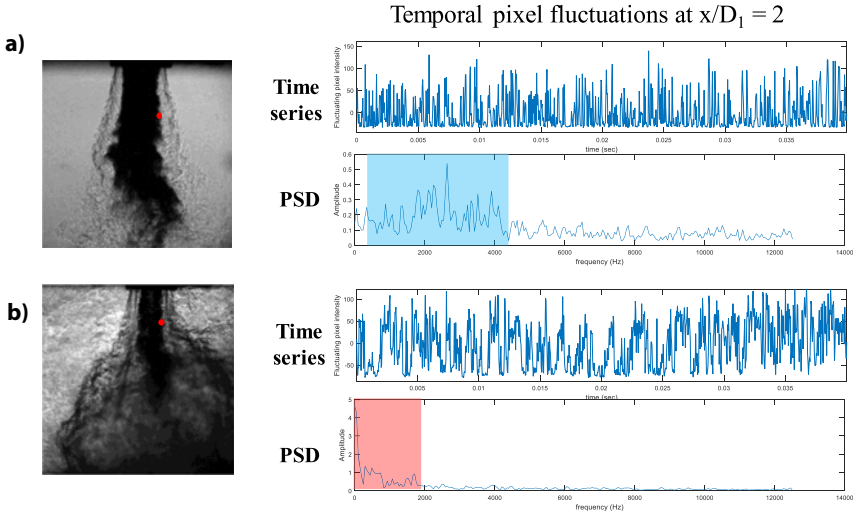

Fig. 22 Temporal and spectral characteristics of pixel intensity fluctuations in the inner shear layer for a) nonreacting and b) reacting flow conditions for injector SAR–thin 2 [67].

Downloaded by Doug Talley on June 5, 2020 | http://arc.aiaa.org | DOI: 10.2514/5.9781624105814.0233.0280 | Book DOI: 10.2514/4.105814

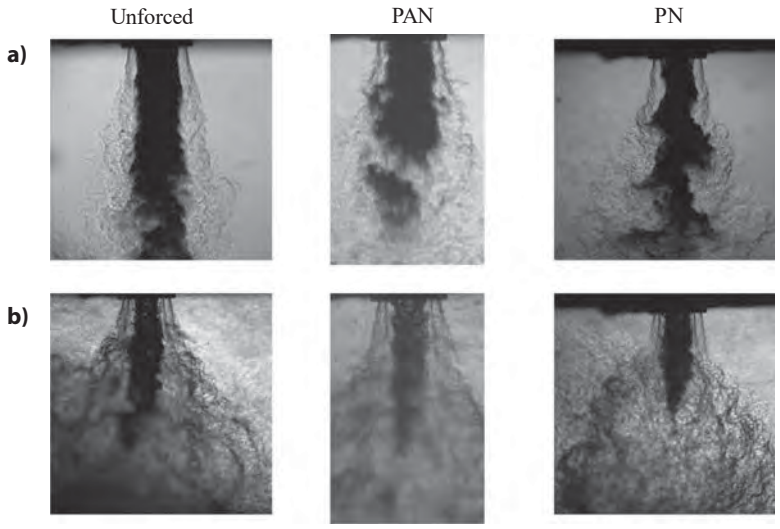

Fig. 23 Backlit images of unforced, PAN-forced, and PN-forced cases for a) nonreacting and b) reacting flow conditions for injector SAR–thin 2 [67].

behavior demonstrated by the nonreacting case. The response of the flame is more subtle and requires more sophisticated signal processing methods for detection. However, it is noticeable how the inner jet thins downstream compared with the nonforced case.

V. CONCLUSIONS

The experimental studies of shear coaxial jets have elucidated many of the salient features of both natural and acoustically forced flows. It was shown that the injector geometry has a large impact on the unforced mixing characteristics, with the general trend being that either an increase in post thickness or a decrease in AR results in enhanced mixing. The thick post facilitates the generation of larger-scale structures that more efficiently mix the two jet flows. The fact that a SAR facilitates enhanced mixing agrees with results from previous studies. Geometry effects appear to be slightly degraded when operating at supercritical conditions, where momentum flux ratio becomes the dominant control parameter. The liquid jet density also has an influence on mixing separate from the momentum flux ratio. Characteristic velocity and frequency scales were also identified for one injector design across a range of conditions, which indicated the importance of shear-layer instabilities.

Acoustic forcing can induce a variety of responses, depending on the characteristics of the injector geometry, flow conditions, and acoustic properties. The

Downloaded by Doug Talley on June 5, 2020 | http://arc.aiaa.org | DOI: 10.2514/5.9781624105814.0233.0280 | Book DOI: 10.2514/4.105814

thin post injectors tend to have relatively strong coupling to the acoustics, whereas injectors with a thicker post demonstrate reduced receptivity under some conditions. The PAN mechanism appears to be driven by flow rate oscillations in the gaseous outer jet, as injector SAR–thin 2 indicated an inability to respond to the acoustic forcing unless the pressure fluctuations were near or above the dynamic pressure of the outer jet flow. For the PN behavior, the jet responds to very low levels of transverse acoustic velocity fluctuations. Interestingly, the critical amplitude at which coupling occurs does not depend on momentum flux ratio. It is apparent that the aerodynamic interaction between the coaxial jet and the weak acoustic velocity oscillation is amplified by unsteady aerodynamics; the jet and crossflow interactions do not have sufficient time during the acoustic cycle to reach a steady state. Jets exposed to PN excitation can also manifest a flattening effect, which has been observed in the literature. The body of evidence regarding whether the jet flattens or exhibits sinuous motion suggests that the relative frequency of the jet to the acoustics determines which response occurs. Further investigation of the role of relative frequency between the acoustics and the flowfield is needed.

The primary influence of operating at either sub- or supercritical pressure appears to be in the unforced mixing behavior. Under supercritical conditions, the surface tension disappears and mixing between the inner and outer jet is promoted, particularly at higher momentum flux ratios. A similar trend is observed in the response of supercritical jets to acoustic forcing with momentum flux ratio compared to the subcritical cases.

Preliminary combustion results with liquid oxygen and cryogenic gaseous hydrogen show that the mechanisms appear to be qualitatively the same. There is a general shift of spectral content in the flow to lower frequencies, and thus keeping the acoustic forcing frequency fixed results in the combustion cases having a higher relative forcing frequency. Further studies to explore the coupling of acoustic waves to cryogenic flames are currently underway [70–72].

REFERENCES

[1] Sardeshmukh, S., Huang, C., Gejji, R., Bedard, M., Hallum, Z., Lucht, R., and Anderson, W., "High-Pressure Experiments Relevant to Rocket Propulsion," *High Pressure Flows for Propulsion Applications*, edited by J. Bellan, Vol. 260, Progress in Astronautics and Aeronautics, AIAA, Reston, VA, 2020, pp. 183–232.

[2] Hulka, J., and Hutt, J. J., "Instability Phenomena in Liquid Oxygen/Hydrogen Propellant Rocket Engines," *Liquid Rocket Engine Combustion Instability*, edited by W. E. Anderson, and V. Yang, Vol. 169, Progress in Astronautics and Aeronautics, AIAA, New York, 1995, pp. 39–71.

[3] Matsuyama, S., Terashima, H., Koshi, M., and Umemura, A., "Detailed Modeling of Supercritical Jets and Flames," *High Pressure Flows for Propulsion Applications*, edited by J. Bellan, Vol. 260, Progress in Astronautics and Aeronautics, AIAA, Reston, VA, 2020, pp. 569–628.

Downloaded by Doug Talley on June 5, 2020 | http://arc.aiaa.org | DOI: 10.2514/5.9781624105814.0233.0280 | Book DOI: 10.2514/4.105814

Downloaded by Doug Talley on June 5, 2020 | http://arc.aiaa.org | DOI: 10.2514/5.9781624105814.0233.0280 | Book DOI: 10.2514/4.105814

[4] Ko, N., and Kwan, A., "The Initial Region of Subsonic Coaxial Jets," *Journal of Fluid Mechanics*, Vol. 73, No. 02, 1976, pp. 305–332.

[5] Kwan, A., and Ko, N., "Coherent Structures in Subsonic Coaxial Jets," *Journal of Sound and Vibration*, Vol. 48, No. 2, 1976, pp. 203–219.

[6] Kwan, A., and Ko, N., "The Initial Region of Subsonic Coaxial Jets. Part 2," *Journal of Fluid Mechanics*, Vol. 82, No. 02, 1977, pp. 273–287.

[7] Ko, N., and Au, H., "Coaxial Jets of Different Mean Velocity Ratios," *Journal of Sound and Vibration*, Vol. 100, No. 2, 1985, pp. 211–232.

[8] Au, H., and Ko, N., "Coaxial Jets of Different Mean Velocity Ratios, Part 2," *Journal of Sound and Vibration*, Vol. 116, No. 3, 1987, pp. 427–443.

[9] Tang, S. K., and Ko, N., "Coherent Structure Interactions in an Unexcited Coaxial Jet," *Experiments in Fluids*, Vol. 17, No. 3, 1994, pp. 147–157.

[10] Tang, S. K., and Ko, N., "Experimental Investigation of the Structure Interaction in an Excited Coaxial Jet," *Experimental Thermal and Fluid Science*, Vol. 8, No. 3, 1994, pp. 214–229.

[11] Bocanegra-Evans, H., and Allen, J. J., "Wake–Shear Layer Interaction Using a Soap Film Tunnel," *Physics of Fluids*, Vol. 17, No. 9, 2005, p. 091112.

[12] Wallace, D., and Redekopp, L. G., "Linear Instability Characteristics of Wake-Shear Layers," *Physics of Fluids A: Fluid Dynamics*, Vol. 4, No. 1, 1992, pp. 189–191.

[13] Boldman, D. R., Brinich, P. F., and Goldstein, M. E., "Vortex Shedding from a Blunt Trailing Edge with Equal and Unequal External Mean Velocities," *Journal of Fluid Mechanics*, Vol. 75, No. 04, 1976, pp. 721–735.

[14] Dahm, W. J., Frieler, C. E., and Tryggvason, G., "Vortex Structure and Dynamics in the Near Field of a Coaxial Jet," *Journal of Fluid Mechanics*, Vol. 241, 1992, pp. 371–402.

[15] Tian, V., McKeon, B., and Leyva, I. A., "Split Stream Flow Past a Blunt Trailing Edge with Appplication to Combustion Instabilities," AIAA Paper 2012–3807, August, 2012.

[16] Segalini, A., and Talamelli, A., "Experimental Analysis of Dominant Instabilities in Coaxial Jets," *Physics of Fluids*, Vol. 23, No. 2, 2011, p. 024103.

[17] Koochesfahani, M., and Frieler, C. E., "Instability of Nonuniform Density Free Shear Layers with a Wake Profile," *AIAA Journal*, Vol. 27, No. 12, 1989, pp. 1735–1740.

[18] Singla, G., Scouflaire, P., and Rolon, J., "Flame Stabilization in High Pressure LO_x/GH_2 and GCH_4 Combustion," *Proceedings of the Combustion Institute*, Vol. 31, No. 2, 2007, pp. 2215–2222.

[19] Oefelein, J. C., "Thermophysical Characteristics of Shear-Coaxial LOX–H_2 Flames at Supercritical Pressure," *Proceedings of the Combustion Institute*, Vol. 30, No. 2, 2005, pp. 2929–2937.

[20] Juniper, M. P., and Candel, S. M., "The Stability of Ducted Compound Flows and Consequences for the Geometry of Coaxial Injectors," *Journal of Fluid Mechanics*, Vol. 482, 2003, pp. 257–269.

[21] Graham, J. J., Leyva, I. A., Rodriguez, J. I., and Talley, D., "On the Effect of a Transverse Acoustic Field on a Flush Shear Coaxial Injector," AIAA Paper 2009–5142, August, 2009.

[22] Brown, G. L., and Roshko, A., "On Density Effects and Large Structure in Turbulent Mixing Layers," *Journal of Fluid Mechanics*, Vol. 64, No. 04, 1974, pp. 775–816.

[23] Villermaux, E., and Hopfinger, E. J., "Self-Sustained Oscillations of a Confined Jet: A Case Study for the Non-Linear Delayed Saturation Model," *Physica D: Nonlinear Phenomena*, Vol. 72, No. 3, 1994, pp. 230–243.

[24] Lasheras, J. C., Villermaux, E., and Hopfinger, E. J., "Break-Up and Atomization of a Round Water Jet by a High-Speed Annular Air Jet," *Journal of Fluid Mechanics*, Vol. 357, 1998, pp. 351–379.

[25] Schumaker, S. A., and Driscoll, J. F., "Mixing Properties of Coaxial Jets with Large Velocity Ratios and Large Inverse Density Ratios," *Physics of Fluids*, Vol. 24, No. 5, 2012, p. 055101.

[26] Favre-Marinet, M., Camano, E. B., and Sarboch, J., "Near-Field of Coaxial Jets with Large Density Differences," *Experiments in Fluids*, Vol. 26, No. 1–2, 1999, pp. 97–106.

[27] Favre-Marinet, M., and Schettini, E. C., "The Density Field of Coaxial Jets with Large Velocity Ratio and Large Density Differences," *International Journal of Heat and Mass Transfer*, Vol. 44, No. 10, 2001, pp. 1913–1924.

[28] Chigier, N., and Farago, Z., "Morphological Classification of Disintegration of Round Liquid Jets in a Coaxial Air Stream," *Atomization and Sprays*, Vol. 2, No. 2, 1992, pp. 137–153.

[29] Chehroudi, B., Talley, D., and Coy, E., "Visual Characteristics and Initial Growth Rates of Round Cryogenic Jets at Subcritical and Supercritical Pressures," *Physics of Fluids*, Vol. 14, No. 2, 2002, pp. 850–861.

[30] Chehroudi, B., "Recent Experimental Efforts on High-Pressure Supercritical Injection for Liquid Rockets and Their Implications," *International Journal of Aerospace Engineering*, Vol. 2012, 2012, pp. 1–31.

[31] Oschwald, M., Smith, J. J., and Branam, R., "Injection of Fluids into Supercritical Environments," *Combustion Science and Technology*, Vol. 178, No. 1–3, 2006, pp. 49–100.

[32] Thol, M., and Bell, I. H., "Empirical Fundamental Equations of State for Pure Fluids and Mixtures," *High Pressure Flows for Propulsion Applications*, edited by J. Bellan, Vol. 260, Progress in Astronautics and Aeronautics, AIAA, Reston, VA, 2020, pp. 365–406.

[33] Giovangigli, V., Matuszewski, L., and Gaillard, P., "High Pressure Flames with Multicomponent Transport," *High Pressure Flows for Propulsion Applications*, edited by J. Bellan, Vol. 260, Progress in Astronautics and Aeronautics, AIAA, Reston, VA, 2020, pp. 483–528.

[34] Matheis, J., Muller, H., Hickel, S., and Pfitzner, M., "Large-Eddy Simulation of Cryogenic Jet Injection at Supercritical Pressures," *High Pressure Flows for Propulsion Applications*, edited by J. Bellan, Vol. 260, Progress in Astronautics and Aeronautics, AIAA, Reston, VA, 2020, pp. 529–568.

[35] Ribert, G., Domingo, P., Petit, X., Vallee, N., and Blaisot, J., "Modeling and Simulations of High-Pressure Practical Flows," *High Pressure Flows for Propulsion Applications*, edited by J. Bellan, Vol. 260, Progress in Astronautics and Aeronautics, AIAA, Reston, VA, 2020, pp. 629–676.

[36] Rodriguez, J. I., "Acoustic Excitation of Liquid Fuel Droplets and Coaxial Jets," Ph.D. Dissertation, The Univ. of California at Los Angeles, Los Angeles, CA, 2009.

[37] Lamanna, G., Steinhausen, C., Weckenmann, F., Weigand, B., Bork, B., Preusche, A., Dreizler, A., Stierle, R., and Gross, J., "Laboratory Experiments of High-Pressure Fluid Drops," *High Pressure Flows for Propulsion Applications*, edited by J. Bellan,

Downloaded by Doug Talley on June 5, 2020 | http://arc.aiaa.org | DOI: 10.2514/5.9781624105814.0233.0280 | Book DOI: 10.2514/4.105814

Vol. 260, Progress in Astronautics and Aeronautics, AIAA, Reston, VA, 2020, pp. 49–110.

[38] Oefelein, J., and Lacaze, G., "Large-Eddy Simulation of Liquid Injection and Combustion Processes in High-Pressure Systems," *High Pressure Flows for Propulsion Applications*, edited by J. Bellan, Vol. 260, Progress in Astronautics and Aeronautics, AIAA, Reston, VA, 2020, pp. 677–728.

[39] Wegener, J. L., Leyva, I. A., Forliti, D. J., and Talley, D. G., "Development of a Facility for Combustion Stability Experiments at Supercritical Pressure," AIAA 2014-0137, January, 2014.

[40] Davis, D. W., "On the Behavior of a Shear-Coaxial Jet, Spanning Sub- to Supercritical Pressures, with and without an Externally Imposed Transverse Acoustic Field," Ph.D. Dissertation, The Pennsylvania State Univ., University Park, PA, 2006.

[41] Teshome, S., "Droplet Combustion and Non-Reactive Shear-Coaxial Jets with Transverse Acoustic Excitation," Ph.D. Dissertation, The Univ. of California at Los Angeles, Los Angeles, CA, 2012.

[42] Wegener, J. L., "Multi-Phase Combustion and Transport Processes under the Influence of Acoustic Excitation," Ph.D. Dissertation, The Univ. of California at Los Angeles, Los Angeles, CA, 2014.

[43] Davis, D. W., Chehroudi, B., and Sorensen, I., "Measurements in an Acoustically Driven Coaxial Jet under Supercritical Conditions," AIAA Paper 2005–736, January, 2005.

[44] Berkooz, G., Elezgaray, J., and Holmes, P., "The Proper Orthogonal Decomposition, Wavelets and Modal Approaches to the Dynamics of Coherent Structures," *Applied Scientific Research*, Vol. 53, No. 3–4, 1994, pp. 321–338.

[45] Holmes, P., Lumley, J. L., and Berkooz, G., *Turbulence, Coherent Structures, Dynamical Systems and Symmetry*, Cambridge Univ. Press, Cambridge, UK, 1998.

[46] Linne, M., Falgout, Z., and Rahm, M., "Optical Diagnostics for Sprays at High Pressure," *High Pressure Flows for Propulsion Applications*, edited by J. Bellan, Vol. 260, Progress in Astronautics and Aeronautics, AIAA, Reston, VA, 2020, pp. 111–156.

[47] Rodriguez, J. I., Leyva, I. A., Graham, J. J., and Talley, D., "Mixing Enhancement of Liquid Rocket Engine Injector Flow," AIAA Paper 2009–5143, August, 2009.

[48] Leyva, I. A., Chehroudi, B., and Talley, D., "Dark Core Analysis of Coaxial Injectors at Sub-, Near-, and Supercritical Pressures in a Transverse Acoustic Field," AIAA Paper 2007–5456, July, 2007.

[49] Davis, D. W., and Chehroudi, B., "Measurements in an Acoustically Driven Coaxial Jet under Sub-, Near-, and Supercritical Conditions," *Journal of Propulsion and Power*, Vol. 23, No. 2, 2007, pp. 366–376.

[50] DeSouza, S., and Segal, C., "Supercritical Coaxial Jet Disintegration," *High Pressure Flows for Propulsion Applications*, edited by J. Bellan, Vol. 260, Progress in Astronautics and Aeronautics, AIAA, Reston, VA, 2020, pp. 157–182.

[51] Teshome, S., Leyva, I. A., Talley, D., and Karagozian, A. R., "Cryogenic High-Pressure Shear-Coaxial Jets Exposed to Transverse Acoustic Forcing," AIAA 2012–1265, January, 2012.

[52] Champagne, F. H., and Wygnanski, I. J., "An Experimental Investigation of Coaxial Turbulent Jets," *International Journal of Heat and Mass Transfer*, Vol. 14, No. 9, 1971, pp. 1445–1464.

Downloaded by Doug Talley on June 5, 2020 | http://arc.aiaa.org | DOI: 10.2514/5.9781624105814.0233.0280 | Book DOI: 10.2514/4.105814

[53] Gladnick, P. G., Enotiadis, A. C., and LaRue, J. C., "Near-Field Characteristics of a Turbulent Coflowing Jet," *AIAA Journal*, Vol. 28, No. 8, 1990, pp. 1405–1414.

[54] Ho, C., and Huerre, P., "Perturbed Free Shear Layers," *Annual Review of Fluid Mechanics*, Vol. 16, No. 1, 1984, pp. 365–422.

[55] Dimotakis, P. E., "Two-Dimensional Shear-Layer Entrainment," *AIAA Journal*, Vol. 24, No. 11, 1986, pp. 1791–1796.

[56] Berkooz, G., Holmes, P., and Lumley, J. L., "The Proper Orthogonal Decomposition in the Analysis of Turbulent Flows," *Annual Review of Fluid Mechanics*, Vol. 25, No. 1, 1993, pp. 539–575.

[57] Chatterjee, A., "An Introduction to the Proper Orthogonal Decomposition," *Current Science*, Vol. 78, No. 7, 2000, pp. 808–817.

[58] Bjornsson, H., and Venegas, S. A., "A Manual for EOF and SVD Analyses of Climatic Data," CCGCR Report 97-1, Feb. 1997.

[59] Arienti, M., and Soteriou, M. C., "Time-Resolved Proper Orthogonal Decomposition of Liquid Jet Dynamics," *Physics of Fluids*, Vol. 21, No. 11, 2009, p. 112104.

[60] Wegener, J. L., Forliti, D. J., Leyva, I. A., and Talley, D. G., "Receptivity of a Cryogenic Coaxial Gas-Liquid Jet to Acoustic Disturbances," AIAA Paper 2014–3487, July, 2014.

[61] Chehroudi, B., and Talley, D., "Interaction of Acoustic Waves with a Cryogenic Nitrogen Jet at Sub- and Supercritical Pressures," AIAA Paper 2002–0342, January, 2002.

[62] Baillot, F., Blaisot, J., and Boisdron, G., "Behaviour of an Air-Assisted Jet Submitted to a Transverse High-Frequency Acoustic Field," *Journal of Fluid Mechanics*, Vol. 640, 2009, pp. 305–342.

[63] Carpentier, J., Baillot, F., and Blaisot, J., "Behavior of Cylindrical Liquid Jets Evolving in a Transverse Acoustic Field," *Physics of Fluids*, Vol. 21, No. 2, 2009, p. 023601.

[64] Hoover, D. V., Ryan, H. M., Pal, S., Merkle, C. L., Jacobs, H. R., and Santoro, R. J., "Pressure Oscillation Effects on Jet Breakup," Heat and Mass Transfer in Spray Systems, HTD-Vol. 187, ASME, New York, NY, pp. 27–36.

[65] Hakim, L., Schmitt, T., and Ducruix, S., "Dynamics of a Transcritical Coaxial Flame under a High-Frequency Transverse Acoustic Forcing: Influence of the Modulation Frequency on the Flame Response," *Combustion and Flame*, Vol. 162, No. 10, 2015, pp. 3482–3502.

[66] Buffum, F. G., and Williams, F. A., "The Response of a Turbulent Liquid Jet to Transverse Acoustic Fields," *Proceedings of the 1967 Heat Transfer and Fluid Mechanics Institute*, Stanford University Press, Stanford, CA, 1967, pp. 247–276.

[67] Roa, M., Forliti, D., and Badakhsahn, A., "Acoustically Forced Coaxial Hydrogen/Liquid Oxygen Jet Flames," *ILASS Americas 28th Annual Conference on Liquid Atomization and Spray Systems*, 2016.

[68] Forliti, D. J., Badakhshan, A., Wegener, J. L., Leyva, I. A., and Talley, D. G., "The Response of Cryogenic H_2/O_2 Coaxial Jet Flames to Acoustic Disturbances," AIAA Paper 2015-1607, January, 2015.

[69] Mahalingam, S., Cantwell, B. J., and Ferziger, J. H., "Stability of Low-Speed Reacting Flows," *Physics of Fluids A: Fluid Dynamics*, Vol. 3, No. 6, 1991, pp. 1533–1543.

[70] Eroglu, H., Chigier, N., and Farago, Z., "Coaxial Atomizer Liquid Intact Lengths," *Physics of Fluids A: Fluid Dynamics*, Vol. 3, No. 2, 1991, pp. 303–308.

Downloaded by Doug Talley on June 5, 2020 | http://arc.aiaa.org | DOI: 10.2514/5.9781624105814.0233.0280 | Book DOI: 10.2514/4.105814

[71] Rehab, H., Villermaux, E., and Hopfinger, E. J., "Geometrical Effects on the Near-Field Flow Structure of Coaxial Jets," *AIAA Journal*, Vol. 36, No. 5, 1998, pp. 867–869.

[72] Woodward, R. D., "Primary Atomization of Liquid Jets Issuing from Rocket Engine Coaxial Injectors," Ph.D. Dissertation, The Pennsylvania State Univ., University Park, PA, 1993.

Downloaded by Doug Talley on June 5, 2020 | http://arc.aiaa.org | DOI: 10.2514/5.9781624105814.0233.0280 | Book DOI: 10.2514/4.105814

CrossMark

J. Fluid Mech. (2016), *vol.* 790, *pp.* 5–32. © Cambridge University Press 2016
doi:10.1017/jfm.2016.2

Dynamic-mode decomposition based analysis of shear coaxial jets with and without transverse acoustic driving

Jia-Chen Hua[1], Gemunu H. Gunaratne[1], Douglas G. Talley[2], James R. Gord[3] and Sukesh Roy[4,†]

[1]Department of Physics, University of Houston, Houston, TX 77204, USA

[2]Aerospace Systems Directorate, Air Force Research Laboratory, Edwards Air Force Base, CA 93524, USA

[3]Aerospace Systems Directorate, Air Force Research Laboratory, Wright-Patterson Air Force Base, OH 45433, USA

[4]Spectral Energies, LLC, Dayton, OH 45431, USA

(Received 26 May 2015; revised 21 October 2015; accepted 30 December 2015)

Modal decompositions of unperturbed and acoustically driven injector flows from shear coaxial jets are implemented using dynamic-mode decomposition, which is a natural approach in the search for collective oscillatory behaviour in nonlinear systems. Previous studies using proper orthogonal decomposition had revealed the most energetic pairs of coherent structures in injector flows. One of the difficulties in extracting lower-energy coherent structures follows from the need to differentiate robust flow constituents from noise and other irregular facets of a flow. The identification of robust features is critical for applications such as flow control as well, since only they can be used for the tasks. A dynamic-mode decomposition based algorithm for this differentiation is introduced and used to identify different classes of robust dynamic modes. They include (1) background modes located outside the injector flow that decay rapidly, (2) injector modes – including those presented in earlier studies – located in the vicinity of the flow, (3) modes that persist under acoustic driving, (4) modes responding linearly to the driving and, most interestingly, (5) a mode whose density exhibits antiphase oscillatory behaviour in the observation plane and that appears only when J, the outer-to-inner-jet momentum flux ratio, is sufficiently large; we infer that this is a projection of a mode rotating about the symmetry axis and born via a spontaneous symmetry breaking. Each of these classes of modes is analysed as J is increased, and their consequences for the flow patterns are discussed.

Key words: jets, low-dimensional models, nonlinear dynamical systems

1. Introduction

Shear coaxial jets, in which a circular jet flows inside an annular jet, are canonical flows found in many applications, for example liquid rocket engines. Despite the

† Email address for correspondence: roy.sukesh@gmail.com

simplicity of the geometry, the flows exhibit very complex dynamical behaviour and non-trivial interactions with the dynamics of their surroundings (Hopfinger 1998; Hong *et al.* 2006), one important interaction being with coherent acoustic waves. They are important, for instance, in combustion chambers experiencing combustion-induced acoustic instabilities (Miesse 1955; Wicker & Eaton 1994; Villermaux, Rehab & Hopfinger 1998; Davis & Chehroudi 2006, 2007; Leyva *et al.* 2007; Teshome 2012). If the acoustic–jet interaction is such that pressure fluctuations become phase coherent with heat-release fluctuations, the acoustics can amplify temperature gradients and cause damage to the combusting system. Thus, it is important to gain an understanding of how different geometries and flow conditions affect the nature of the coupling between acoustic waves and coaxial jets.

Teshome (2012) studied the simplified case of acoustic waves interacting with non-reacting shear coaxial jets. He performed modal decomposition of high-frequency high-resolution shadowgraph imaging. Because applications usually have complex geometries, it is inefficient to perform such decompositions using predetermined basis functions. It is more appropriate to use techniques such as proper orthogonal decomposition (POD) (Lumley 1967; Sirovich 1987*a*,*b*,*c*; Berkooz *et al.* 1993), in which the basis functions are derived as part of the analysis. This approach was used by Teshome (2012); however, only the nature of the primary POD modes in the flows was reported.

In the present study, we extend the analysis of Teshome's data using an alternative decomposition based on Koopman eigenfunctions (Mezic & Banaszuk 2004; Rowley *et al.* 2009; Mezic 2013; Motheau *et al.* 2013). Koopman decomposition (Mezic & Banaszuk 2004; Rowley *et al.* 2009; Budišić, Mohr & Mezić 2012; Mezic 2013) is a natural approach to search for collective oscillatory behaviour and is based on the Koopman operator theory (Rowley *et al.* 2009; Schmid 2010; Mezic 2013), which generalizes eigendecomposition to nonlinear systems. Koopman modes are a generalization of normal modes (Mezic 2013), and each mode represents a global collective motion within a flow. Importantly, spectral properties of the flow will be contained in the spectrum of the Koopman operator (Rowley *et al.* 2009; Mezic 2013). A fast algorithm proposed by Schmid (2010) and referred to as dynamic-mode decomposition (DMD) can be used for computing approximately (a subset of) the Koopman spectrum from the time series of snapshots of the flow.

Each Koopman mode is associated with a complex eigenvalue whose real and imaginary parts represent the growth rate and frequency of the mode respectively. These eigenvalues can be used to address a critical issue in the analysis of nonlinear flows, namely how to differentiate robust features of the flow from noise and other non-robust characteristics. As we contend (Roy *et al.* 2015), comparison of Koopman spectra from nominally identical experiments can be the basis of this differentiation. The starting point is a search for reproducible Koopman modes, i.e. those that persist in different experiments. The differentiation is based on the following conjecture: robust characteristics of the flow can be associated with reproducible Koopman modes. Only robust features are expected to be useful in applications such as flow control.

Injector flows are introduced in § 2, and Koopman mode analysis and the relevant computational techniques are summarized in § 3. The results of the modal decomposition of injector flows for a series of control parameters are presented in § 4. Section 5 contains a discussion of the implications of our results.

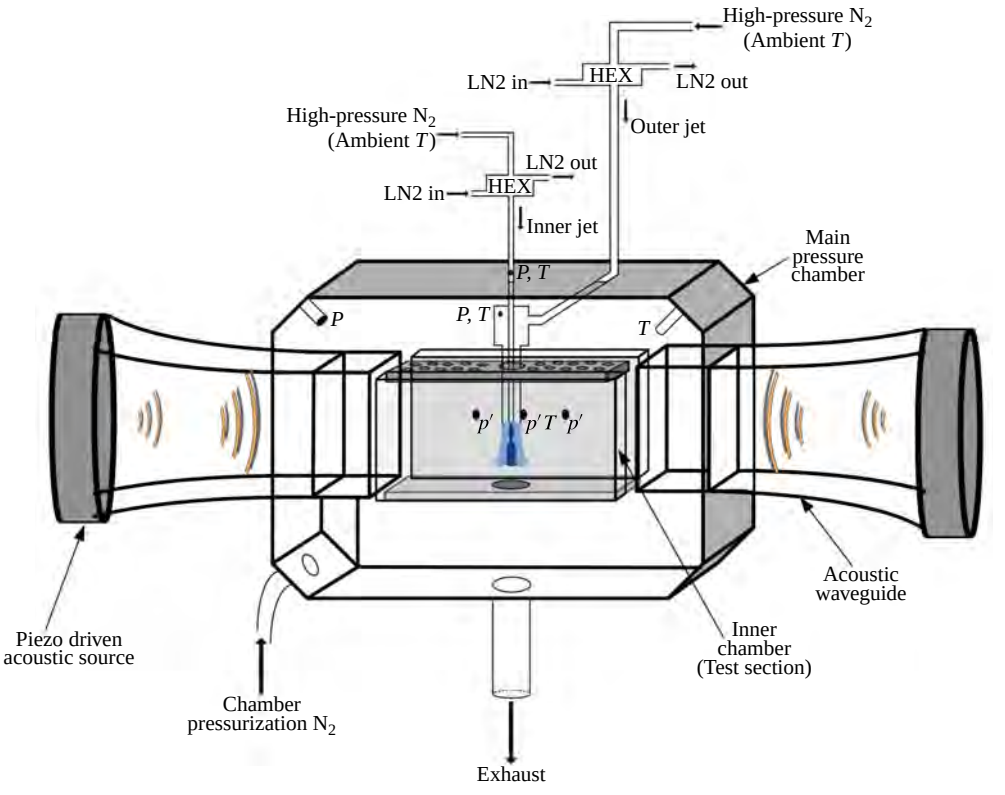

FIGURE 1. (Colour online) Schematic of the chamber and peripheral lines. The light long arrows point to constituents of the device and the heavy short arrows give the flow directions of gasses. Courtesy of Teshome (2012).

2. Injector flows

The experiments in the non-reactive shear coaxial study were conducted in the Cryogenic Supercritical Flow Facility (EC-4) at the Air Force Research Laboratory located at Edwards Air Force Base, CA. The fluid used in these studies was N_2 at ambient conditions tapped from a high-pressure supply line. Liquid N_2 was used for temperature control (Teshome 2012). The pressure within the chamber could be as high as 36 atm. A schematic of the experimental facility is shown in figure 1.

Injector flows were observed with shadowgraph imaging using diffuse backscattering and recorded using Phantom v7.1 and v710 high-speed cameras (Teshome 2012). High-density regions appeared dark. The flow was analysed through a modal decomposition implemented through Koopman mode analysis, described below.

The shear coaxial injector consisted of concentric straight tubes, where the inner jet flowed through the centre tube and the outer jet flowed through the annulus. A schematic of a sectional view of the entire injector assembly is shown in figure 2.

The inner jet was introduced through the top inlet hole of the assembly and entered a small plenum, which served as a settling chamber for the flow. The outer jet was introduced into a settling chamber through two ports located on the side of the assembly. Two parameters were varied for the two types of injectors constructed from 316 stainless steel: (1) the ratio of the inner-jet tube thickness to the diameter of

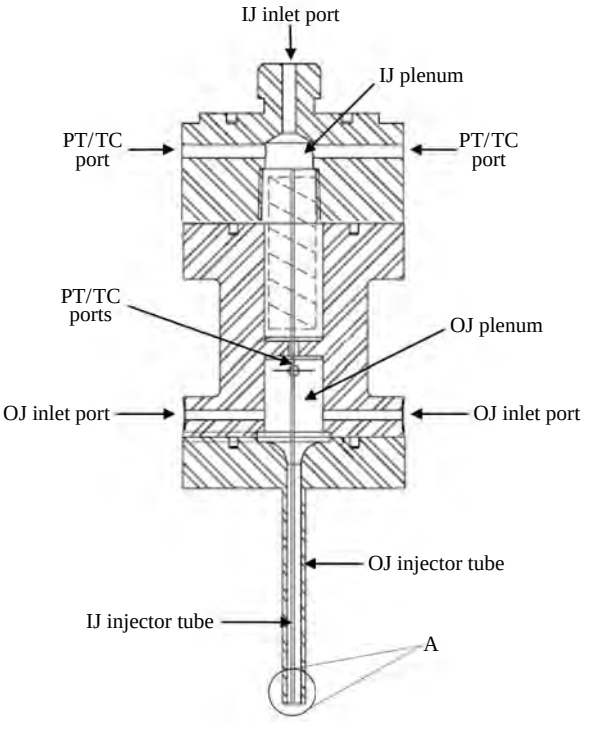

FIGURE 2. Schematic of the shear coaxial injector assembly (for expanded view of A, see figure 3) (from Teshome 2012).

the inner-jet tube and (2) the ratio of the outer-jet to inner-jet cross-sectional areas. Figure 3 is a schematic of the dimensions of the injector exit. The first injector with the large area ratio (LAR) and thin inner-tube post is labelled 'LAR-thin', while the second injector with the small area ratio (SAR) and thick post is labelled 'SAR-thick'. The results reported here are for the LAR-thin configuration; flows in the other injector tube set-up are similar but contain significantly higher levels of noise. For the same reason, we focus on subcritical-chamber-pressure experiments. The dimensions of the injector cross-section for the LAR-thin configuration were $D_1 = 0.70$ mm, $D_2 = 0.89$ mm, $D_3 = 2.44$ mm and $D_4 = 3.94$ mm.

The physical parameters of the coaxial jet flow were based on the injector exit flow properties. They are characterized by J, the outer-to-inner-jet momentum flux ratio, $\rho_o U_o^2/\rho_i U_i^2$, where ρ and U are the density and velocity of the flow respectively. For 'LAR-thin-subcritial' experiments, the available values of J are 0.1, 0.5, 2.1, 5.2, 11, 14 and 20.

The experimental set-up for injector flows in the absence of additional perturbations (referred to as baseline flows) was rotationally invariant about the axis of the flow. We also analysed flows that were subjected to transverse acoustic perturbations imposed using a waveguide attached to each side of a rectangular test section, as shown in figure 1. These perturbations break the rotational symmetry of the experimental configuration. Two types of acoustic driving were performed in the experiments: (1) those where the injector was placed at a pressure antinode (PAN) and (2) those where it was placed at a pressure node (PN). We focus on injector flows subjected to PAN driving; they contain lower levels of noise.

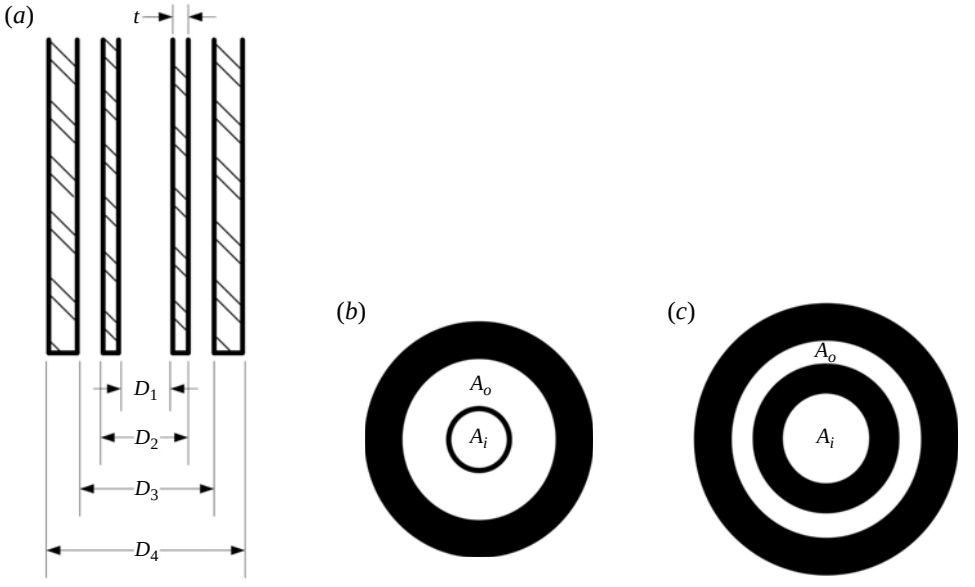

FIGURE 3. Schematic of the shear coaxial injector exit (from Teshome 2012): (*a*) expanded view of A in figure 2; (*b*) LAR-thin; (*c*) SAR-thick.

Each image was recorded on a grid of 192×302 with a resolution of 22 μm; thus the image dimensions are 4.2 mm × 6.6 mm. The image capture began close to the initiation of the injector flow and transients could be observed through the Koopman mode analysis, as seen below. The transients were especially long for smaller values of J.

3. Koopman modes and dynamic-mode decompositions

3.1. *Modal decomposition*

Proper orthogonal decomposition (Lumley 1967; Sirovich 1987*a*,*b*,*c*) has been used to analyse patterns within injector flows (Teshome 2012; Tirunagari *et al.* 2012*a*,*b*). The analyses provide the structure of proper orthogonal modes and the relative contributions to the flow from each mode. Typically, modes with larger contributions are associated with the regular constituents of the underlying flow and those with lower contributions are assumed to be noise and other irregular facets of the flow. However, there has not been a verification of this flow differentiation. Previous DMDs of sprays (Tirunagari *et al.* 2012*b*) have also not addressed the issue. The analysis reported here is motivated by an approach introduced in Roy *et al.* (2015) and outlined below which differentiates robust and non-robust constituents of a flow using Koopman mode analysis (Rowley *et al.* 2009; Schmid 2010; Mezic 2013). As we observe from figures 15 and 24 below, robust and non-robust constituents of injector flows cannot be differentiated using their contributions to the flow alone.

Koopman mode analysis of spatio-temporal fluid density fields is included for completeness and follows Lumley (1967), Sirovich (1987*a*,*b*,*c*), Rowley *et al.* (2009), Schmid (2010) and Mezic (2013). Suppose that the state of a dynamical system is z and that its dynamics is given by

$$\dot{z} = \mathscr{F}(z), \tag{3.1}$$

with constraints and restrictions such as an appropriate set of boundary conditions. The dynamics evolves from the initial state z_0 of the system to $z_t \equiv \boldsymbol{S}^t(z_0)$ at time t. In the case of fluid dynamics of injector flows, $\mathscr{F}$ consists of the Navier–Stokes equations with, perhaps, no-slip boundary conditions. Although this is the most compact representation of the flow, it is difficult to solve the system under realistic conditions, especially for high Reynolds numbers. On the other hand, high-quality empirical data are available on various secondary fields associated with the dynamical system, e.g. the density field of the injector flows. Let us represent one such (observable) secondary field (associated with z) by $u[z](\boldsymbol{x})$, where $\boldsymbol{x}$ represents the grid points on which the observations are made. As the state of the system evolves from z_0 at time $t = 0$ to z_t at time t, the secondary field evolves from $u[z_0](\boldsymbol{x})$ to $u[z_t](\boldsymbol{x})$. When the context is clear, one can simplify the notation by writing $u(\boldsymbol{x}, t)$ for $u[z_t](\boldsymbol{x})$.

Koopman analysis (Mezic & Banaszuk 2004; Rowley *et al.* 2009; Budišić *et al.* 2012; Mezic 2013) of the system is conducted on the 'observable' $\boldsymbol{u}[z](\boldsymbol{x}, t)$. An initial function $\boldsymbol{u}[z_0](\boldsymbol{x}, t = 0)$ evolves to a function $\boldsymbol{u}[z_t](\boldsymbol{x}, t)$ at time t. The transformation between the functions is given by the Koopman (or composition) operator, which is defined as

$$U^t{:}\boldsymbol{u}[z_0](\boldsymbol{x}, t = 0) \rightarrow \boldsymbol{u}[z_t](\boldsymbol{x}, t). \tag{3.2}$$

It should be noted that even when $\boldsymbol{S}^t$ is finite-dimensional and nonlinear, the Koopman operator U^t is infinite-dimensional and linear (Rowley *et al.* 2009; Mezic 2013). Since both $\boldsymbol{S}^t$ and U^t describe the same flow, one expects common features in the descriptions. For example, if the injector flow were uniform in time, z_0 would be a fixed point of $\boldsymbol{S}^t$ and $\boldsymbol{u}[z_0](\boldsymbol{x}, t = 0)$ would be a fixed point of U^t. In periodic flows, the periodicity will be reflected in the spectra of z_t as well as in the spectra of $\boldsymbol{u}[z_t](\boldsymbol{x}, t)$. In fact, it is known that spectral properties of $\boldsymbol{S}^t$ are contained in the eigenspectrum of U^t. Eigenvalues of U^t form the Koopman spectrum, and the corresponding eigenfunctions are referred to as Koopman eigenfunctions. Coefficients in the projection of $\boldsymbol{u}[z_t](\boldsymbol{x}, t)$ to the Koopman eigenfunctions form the Koopman modes of the state (Rowley *et al.* 2009). As the system evolves under $\boldsymbol{S}^t$, the kth Koopman mode evolves as $\mathrm{e}^{\mu_k t}$, where μ_k is the associated eigenvalue. Thus, the Koopman formalism is a generalization of normal form analysis and is a natural approach to searching for collective cyclic behaviour in spatio-temporal data.

Dynamic-mode decomposition (Bagheri *et al.* 2009; Schmid 2009, 2010) is an efficient algorithm for computing approximations for the eigenvalues and eigenvectors of U^t from empirical snapshots collected at uniform time intervals δt. Since $U^{\delta t}$ is independent of the state $u(\boldsymbol{x}, t)$, one can approximate the transformation of the field during the time interval $[t, t + \delta t]$ as

$$u(\boldsymbol{x}, t + \delta t) \approx \boldsymbol{A}u(\boldsymbol{x}, t), \tag{3.3}$$

where $\boldsymbol{A} \equiv \boldsymbol{A}(\delta t)$ is a matrix of size $HW \times HW$ in the case of a field of two spatial dimensions presented on a grid of size $H \times W$. If one denotes by u_k the field corresponding to the snapshot taken at time $t = k\delta t$, (3.3) can be rewritten as $u_{k+1} \approx \boldsymbol{A}u_k$. Thus,

$$\mathbb{U}_1 \equiv [u_1, u_2, \ldots, u_n] \approx \boldsymbol{A}[u_0, u_1, u_2, \ldots, u_{n-1}] \equiv \boldsymbol{A}\mathbb{U}_0. \tag{3.4}$$

With sufficiently large n, singular-value decomposition of $\mathbb{U}_0 = \boldsymbol{V}\boldsymbol{S}\boldsymbol{W}^{\mathrm{T}}$ can be used to compute the spectrum of $\boldsymbol{A}$ (or equivalently of $\boldsymbol{V}^{\mathrm{T}}\boldsymbol{A}\boldsymbol{V}$) by noting that $\boldsymbol{V}^{\mathrm{T}}\boldsymbol{A}\boldsymbol{V} =$

$\boldsymbol{V}^{\mathrm{T}}\mathbb{U}_1\boldsymbol{W}\boldsymbol{S}^{-1}$ (Schmid 2009). Eigenvectors of $\boldsymbol{A}$ are referred to as dynamic modes of the spatio-temporal dynamics (Bagheri *et al.* 2009; Schmid 2009, 2010). Dynamic-mode decomposition provides an approximation to a subset of the Koopman spectrum Λ_n, and the corresponding eigenfunctions $\Phi_n(\boldsymbol{x})$ approximate Koopman modes.

It should be noted that since $\boldsymbol{A}$ is not symmetric, the eigenvalues Λ_n and the eigenfunctions $\Phi_n(\boldsymbol{x})$ are, in general, complex-valued. Furthermore, the eigenfunctions are not orthonormal. Eigenvalues of the Hermitian conjugate $\boldsymbol{A}^{\dagger}$ of $\boldsymbol{A}$ are $\Lambda_n^* t$. The corresponding eigenfunctions $\tilde{\Phi}_n(\boldsymbol{x})$ are orthogonal to the $\Phi_n(\boldsymbol{x})$ – specifically, with an appropriate normalization $\int \mathrm{d}\boldsymbol{x}\, \tilde{\Phi}_m(\boldsymbol{x})\Phi_n(\boldsymbol{x}) = \delta_{mn}$.

The spatio-temporal flow field $u(\boldsymbol{x}, t)$ can be expanded as

$$u(\boldsymbol{x}, t) = \sum a_k(t)\Phi_k(\boldsymbol{x}), \tag{3.5}$$

where the sum is performed over the DMD modes. Variations in $u(\boldsymbol{x}, t)$ can be quantified using $V \equiv \mathbb{E}[(u(\boldsymbol{x}, t))^2]$, where the expectation is over the grid points and snapshots. By the orthonormality introduced above, $a_k(t) = \int \mathrm{d}\boldsymbol{x}\, \tilde{\Phi}_k(\boldsymbol{x})u(\boldsymbol{x}, t)$. If necessary, the field can also be expanded in the basis $\{\tilde{\Phi}(\boldsymbol{x})\}$ as $u(\boldsymbol{x}, t) = \sum \tilde{a}_k(t)\tilde{\Phi}_k(\boldsymbol{x})$. Now the variations in the spatio-temporal dynamics reduce to $V = \sum a_k\tilde{a}_k$, and one can interpret the quantity $L_k = a_k\tilde{a}_k$ as the contribution (or 'energy') from the kth mode. It should be noted, however, that because DMD modes are not orthogonal, L_k is not strictly positive; hence, in defining $\beta_n = \sum_{k=0}^{n-1} L_k / \sum_{k=0}^{HW-1} L_k$, where larger values of β_n correspond to better approximations of the data, one must sum absolute values. It should be noted, however, that with this definition, β_n may exceed 1 in some rare cases.

Prior to computing dynamic modes, the density of each frame is rescaled by removing the mean and setting the standard deviation to 1. Unlike mean subtraction (Chen, Tu & Rowley 2012), this rescaling does not change the DMD eigenvalues or dynamic modes. The intensity of the dynamic modes (i.e. the fluctuations) can be compared with the mean density.

3.2. *Robust modes*

The (nonlinear) Navier–Stokes equations, especially in the presence of many distinct modes, can amplify noise and other irregular facets of the injector flow (Cross & Hohenberg 1993). Consequently, features of a flow may differ among multiple realizations of an experiment or a simulation. Thus, the ability to extract robust characteristics from an injector flow is critically important. We use the following conjecture for the selection: configuration-independent (or robust) features of spatio-temporal dynamics can be captured through dynamic modes that are reproduced in multiple experiments. We also assume that different subgroupings of the full set of snapshots can be used for this purpose. In contrast, dynamic modes representing noise and non-robust flow constituents depend on the specific experimental realization. The corresponding differentiation in POD based methods relies on irregular features having lower energies than the regular flow facets. The results of the injector flow analysis, outlined in the next section, indicate that this differentiation may not be valid (Roy *et al.* 2015). It should also be noted that in constructing reduced-order models or in developing techniques to control the flow, one must focus on the robust features of the flow. Non-robust features cannot be used for this purpose; however, their statistical features or dynamical invariants may be necessary to complete the flow characterization.

In the experiment, injector flows were recorded at 25 kHz; thus, imaginary values of the Koopman spectrum lay in the range $(-2.5\pi \times 10^4, 2.5\pi \times 10^4)$. As discussed earlier, Koopman eigenvalues are either real or appear in complex conjugate pairs. To search for robust modes, we subgrouped the snapshots from each experiment into even-numbered and odd-numbered frames and implemented dynamic-mode computations for these subgroups as well. (Had the data not included transients, it would have been possible to include results from the first and second halves of snapshots as well.) We then searched for (nearly) identical Koopman eigenvalues among the different groups and investigated whether the corresponding Koopman modes were close. Specifically, reproducible dynamic modes of the flow were defined using the following criteria.

(1) The imaginary parts of the eigenvalues from multiple groups should be sufficiently close; specifically,

$$\max_g(|\mathrm{Im}(\Lambda_i) - \mathrm{Im}(\Lambda_j^{(g)})|) \leqslant \delta_I, \tag{3.6}$$

where g represents different subgroupings and δ_I is a cutoff.

(2) The real parts of an eigenvalue identified from the first condition should not vary significantly among the subgroups; specifically,

$$\max_g(|\mathrm{Re}(\Lambda_i) - \mathrm{Re}(\Lambda_j^{(g)})|) \leqslant \delta_R, \tag{3.7}$$

for a cutoff δ_R. Typically, the real parts of the eigenvalues exhibit larger variation; thus, the cutoff δ_R is larger than δ_I. For the work reported here we select $\delta_R \approx 1.5\delta_I$.

(3) Eigenmodes from the different groupings that satisfy the earlier conditions should be close. Specifically, if $\Phi_i(\boldsymbol{x})$ and $\Phi_j^{(g)}(\boldsymbol{x})$ are normalized eigenfunctions associated with proximate eigenvalues, then

$$\max_g\{\min_\theta |\exp(\mathrm{i}\theta)\Phi_i(\boldsymbol{x}) - \Phi_j^{(g)}(\boldsymbol{x})|\} \leqslant \Delta, \tag{3.8}$$

for a cutoff Δ. Here, we have noted that eigenfunctions computed from different experimental realizations may differ in phase.

At this point, we do not have a unique and unambiguous set of cutoff values δ_I, δ_R and Δ for injector flows; in fact, they may depend on the level of experimental and observational noise. Since the left-hand side of (3.8) is known to $\in (0, 2)$, Δ is selected first. For the results reported here Δ was chosen to be near 0.6. Its suitability is validated by visual inspection of modes from the different groups of snapshots. Next, δ_I and δ_R are simultaneously increased from 0 and the number of modes N_m satisfying the three criteria is recorded. We find that N_m increases initially as δ_I and δ_R are increased, and subsequently reaches a plateau. Modes in the plateau are assumed to be robust.

3.3. *Reconstruction of flow constituents*

Dynamic modes are associated with unique eigenvalues Λ_n, the growth rate and the frequency of the nth mode. One can use this observation to address an important issue: a constituent of the injector flow may not be captured by a single dynamic mode; rather, several such modes may be required to reconstruct a typical constituent

(Roy *et al.* 2015). Analysis of simulated and experimental data suggests approaches for identifying multiple modes that may be associated with a single flow constituent. Specifically, their eigenvalues are found to lie on a smooth curve in the complex plane (Bagheri *et al.* 2009; Schmid 2009, 2010). An alternative scheme is as follows. We recall that the primary dynamic mode (i.e. that with the highest energy) has a single frequency -2π times the imaginary part of the corresponding Λ. One may expect dynamic modes with harmonics of this frequency to be associated with the same flow constituent.

Once dynamic modes associated with a flow constituent are identified, the constituent and its evolution can be reconstructed using

$$u_{const.}(\boldsymbol{x}, t) = \sum a_i(t)\Phi_i(\boldsymbol{x}) + \text{c.c.}, \tag{3.9}$$

where 'c.c.' denotes complex conjugation, and the summation is over the modes associated with the constituent.

4. Results

4.1. *A classification of robust dynamic modes*

Analyses of injector flows for J values of 0.1, 0.5, 2.1, 5.2, 11.0, 14.0 and 20.0 show that robust dynamic modes fall into several distinct classes based on their locations, symmetries and dynamics. We outline the classification before presenting the results from the Koopman mode analysis.

(1) *Background modes* are spatially disordered, and their primary features lie outside the injector flow. They are transient and decay for all values of J. The robust mode 4 of the baseline flow at $J = 0.1$, shown in figure 4, is an example of a background mode. As observed here, the spatial structure of a background mode is disordered. Although these modes are robust within subgroupings of the snapshots in a single experiment, we suspect that their spatial structures differ between experiments.

(2) *Injector modes* have a well-defined spatial structure within the injector flow and exhibit high-frequency dynamics. Their coefficients $a(t)$ have sharp spectra. For a given subgrouping, their amplitudes exhibit either slow decay or slow growth; as can be seen from figure 16(*b*), the real part of their eigenvalue is statistically consistent with zero growth. Robust mode 72 of the baseline flow at $J = 0.1$, shown in figure 5, is an example of an injector mode. The projection shown in figure 5(*a*) supports the assertion that the mode contains successive high- and low-density annular regions, and that the planes of these annuli are, in general, not normal to the symmetry axis. (Injector modes that are symmetric about the axis are also found.) The dynamics of the flow in the complex plane, shown in figure 5(*c*), lies on an outward moving spiral.

(3) *Rotating modes* are observed for values of J larger than 5.2. The reconstruction of the dynamics for one such mode (robust mode 7 for $J = 11$) reveals that the densities of points on either side exhibit antiphase oscillatory behaviour, as observed in figure 8. Since the injector and the flow at the inlet are axially symmetric, this observation indicates that the underlying mode is an azimuthally modulated rotating mode generated via spontaneous symmetry breaking.

The stroboscopic depiction creates a visual illusion in figure 6(*c*). The dynamics follows an inward moving spiral and the angular position of the orbit nearly returns to its original value following 93 time steps. Consequently, the set of discrete points on the orbit appears to consist of 93 radial lines. However, joining successive points

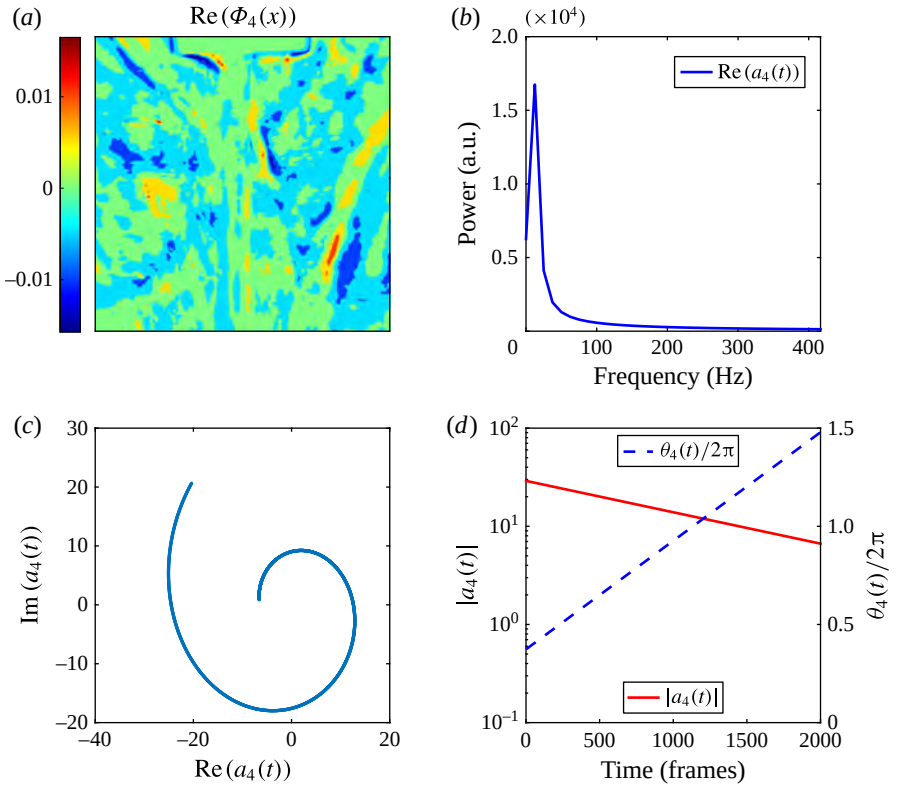

FIGURE 4. (Colour online) Background modes (a) are spatially disordered and located outside the injector flow. (b) Their coefficients $a(t)$ exhibit low-frequency dynamics. The amplitudes of the modes decay exponentially, as can be observed from the dynamics on the complex plane (c) or from $|a(t)|$ (d). The phase of $a(t)$, representing downstream motion of the mode, progresses uniformly, as observed in (d). The remaining figures will be presented in the same format.

during a small time interval, as shown in figure 7, reiterates that the orbit is a single inward moving spiral.

Similarly, the orbit shown in figure 5(c) lies on an outward moving spiral. That the motion is outward is confirmed by the (slow) growth of $|a_{72}(t)|$ in figure 5(d). Following 24 iterations, the angular and radial positions of the orbit have returned to slightly higher values than in their initial state. Consequently, the stroboscopic image appears to consist of 24 equally spaced arcs.

Reconstruction of the dynamics associated with the rotating mode, presented in figure 8, shows a periodic flipping (left to right) of the high-/low-density regions in the viewing plane. It is uncorrelated to any of the injector modes, as can be established using phase dynamics. Experimental noise and irregularities in the flow cause fluctuations in the coefficients of the dynamic modes. Interestingly, angular changes of the phase-space orbit are highly robust, and the irregularities are restricted to the radial component (Roy *et al.* 2015). The phase of the coefficient $a_k(t)$ of a dynamic mode $\boldsymbol{\Phi}_k(\boldsymbol{x})$ is defined as

$$\theta_k(t) = \tan^{-1}[\mathrm{Im}(a_k(t))/\mathrm{Re}(a_k(t))]. \tag{4.1}$$

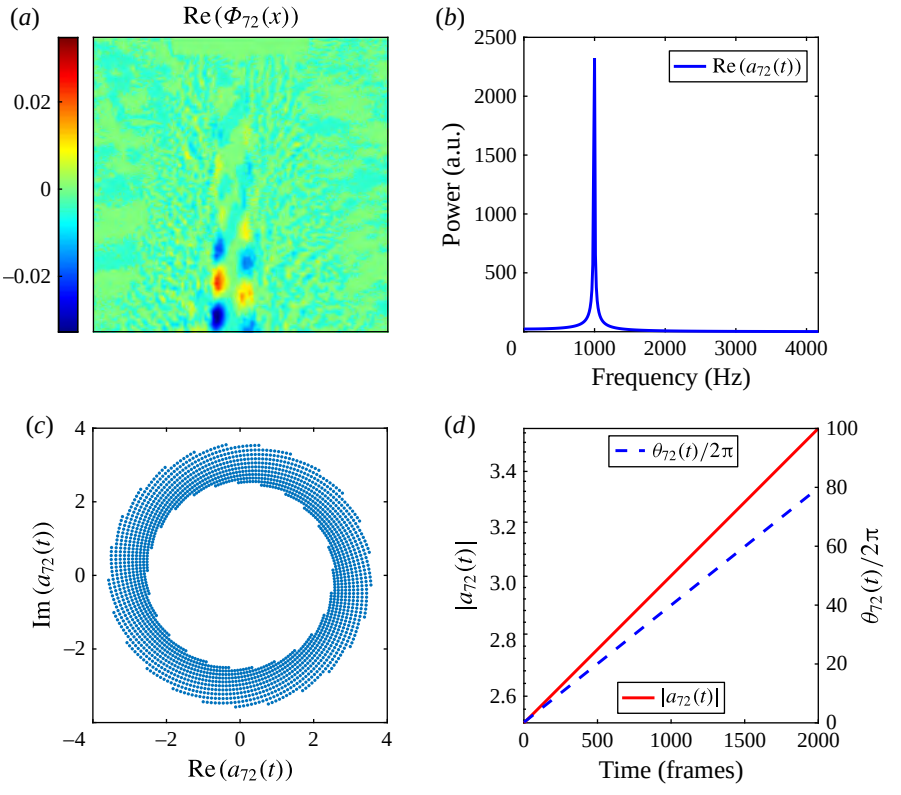

FIGURE 5. (Colour online) Injector modes (*a*) are located primarily within the injector flow, and (*b*) their coefficients $a(t)$ exhibit sharp spectra. As observed in (*c*,*d*), the amplitude of the mode for the selected subgrouping exhibits slow growth, while the phase progresses uniformly. It should be noted that (*c*) shows a single trajectory; the illusion of multiple trajectories is caused by the stroboscopic sampling.

The relationship between the phases of two dynamic modes can be illustrated using Lissajous figures, such as figure 9, which relate phases of a pair of modes through their sine functions (Roy *et al.* 2015). Specifically, when the ratio of angular velocities for two phases θ_i and θ_j is a (low-order) rational number, pairs of points $\{\sin\theta_i(t), \sin\theta_j(t)\}$ lie on a curve; otherwise, the points fill the space. As an example, figure 9 compares the phase dynamics of the rotating mode with one of the injector modes. Their frequencies (figure 9*a*) and phase dynamics (figure 9*c*) are not related, and the motion in the Lissajous figure (figure 9*d*) is space filling. Thus, it is inferred that the modes are uncorrelated.

(4) *Linear response modes* are located primarily in the neighbourhood of the injector flow and have an eigenvalue whose imaginary part is the ratio of the acoustic driving frequency and 2π. Figure 10 contains an example of such a mode.

(5) *Persistent modes* are those observed in PAN driven injector flows that have a structure and period similar to those of corresponding baseline injector modes. For example, as seen from figure 11, mode 83 of the PAN driven flow at $J = 0.1$ has a structure and dynamics qualitatively similar to mode 92 of the baseline flow. However, the amplitude of the latter is nearly unchanged in time while that of the former is found to decay.

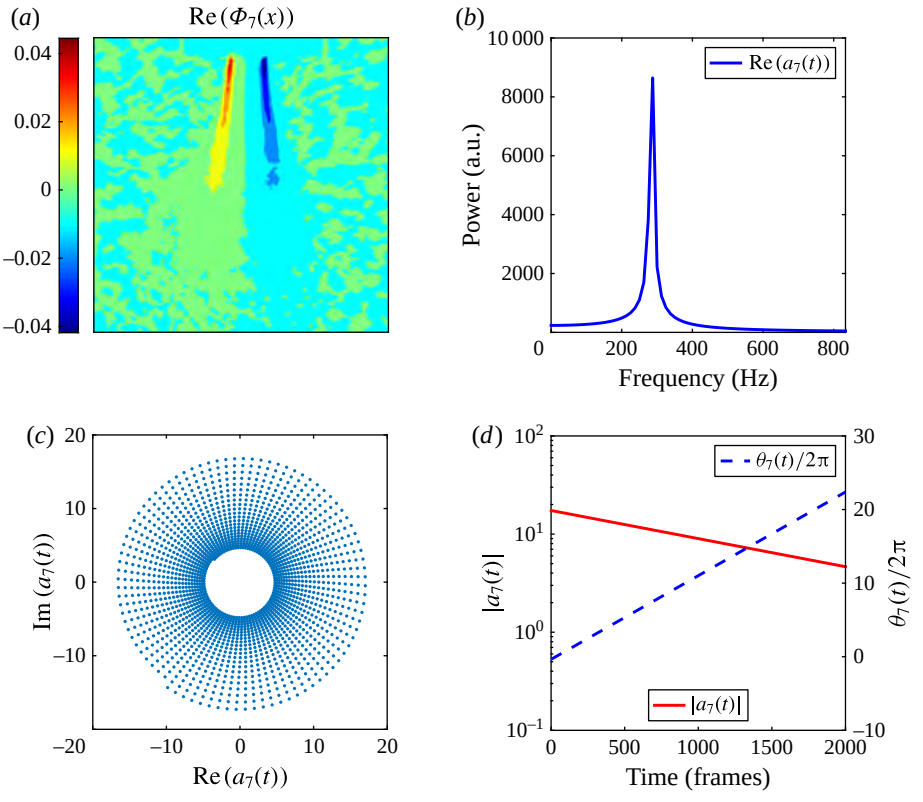

FIGURE 6. (Colour online) Projections of rotating modes (*a*) are asymmetric, and (*b*) their coefficients $a(t)$ have sharp spectra. As observed in (*c*,*d*), they exhibit uniform angular progression. Once again, (*c*) shows a single trajectory; the illusion of multiple (apparently radial) trajectories is caused by the stroboscopic sampling. Their magnitudes $|a(t)|$ exhibit a slow decay. We propose that the underlying three-dimensional flow is an azimuthally modulated rotating mode.

The correlation between persistent modes can be illustrated using their phase dynamics. The frequencies of the time coefficients of the modes (figure 12*a*) and their phase dynamics (figure 12*c*) are identical. The orbit in the Lissajous figure (figure 12*d*) is nearly a closed curve (its width is presumably due to irregularities and experimental noise). Thus, it is inferred that persistent modes are correlated.

The discussion is concluded with a recapitulation (figure 13) of the classes of robust modes identified in injector flows.

4.2. *Injector flows for low J* ($J \leqslant 2.1$)

The major features of the robust modes for injector flows for $J \leqslant 2.1$ are similar, and their characteristics will be illustrated using the results for $J = 0.1$.

4.2.1. *Baseline injector flows for* $J = 0.1$

Figure 14 shows a series of images of the baseline flow at $J = 0.1$. The injector can be seen at the centre near the top of each image. Figure 15 shows the energies of the 100 DMD modes of the injector flow at $J = 0.1$, with energies as defined in

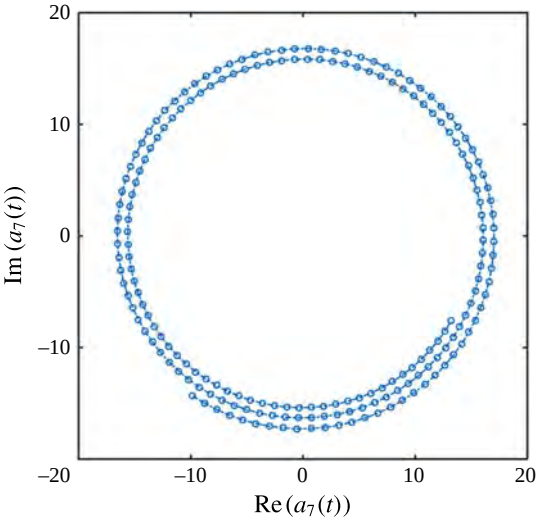

FIGURE 7. (Colour online) The dynamics of $a_7(t)$ in the complex plane follows an inward moving spiral. The corresponding motion for growing modes is on outward moving spirals.

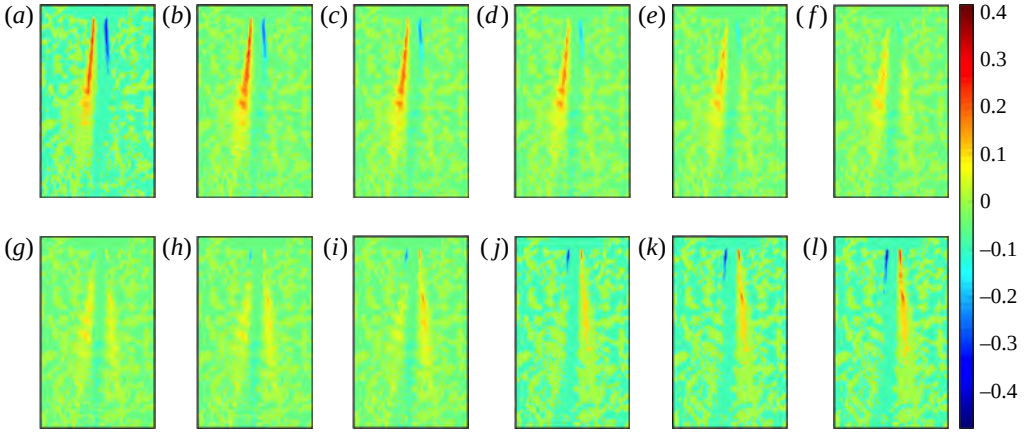

FIGURE 8. (Colour online) Several snapshots of reconstruction of mode 7 for $J = 11$, illustrating the antiphase oscillations of the projection: (*a*) 26.44 ms, (*b*) 26.48 ms, (*c*) 26.52 ms, (*d*) 26.56 ms, (*e*) 26.60 ms, (*f*) 26.64 ms, (*g*) 26.68 ms, (*h*) 26.72 ms, (*i*) 26.76 ms, (*j*) 26.80 ms, (*k*) 26.84 ms, (*l*) 26.88 ms.

§ 3.1. It can be observed, as we have already alluded to, that robust and non-robust modes cannot be partitioned using their energies (associated with DMD). The ability to differentiate robust modes from non-robust modes is one of the more significant advantages of DMD. It can be noticed also that the energy of the 'mean' mode $\Phi_0(\boldsymbol{x})$ is two orders of magnitude larger than the rest. Consequently, the variations of the spatio-temporal velocity field associated with the remaining modes are at least an order of magnitude smaller than those associated with $\Phi_0(\boldsymbol{x})$, as can be deduced from the definition of energy (§ 3.1). Figure 16(*a*) shows the corresponding DMD spectra for modes with non-negative imaginary parts.

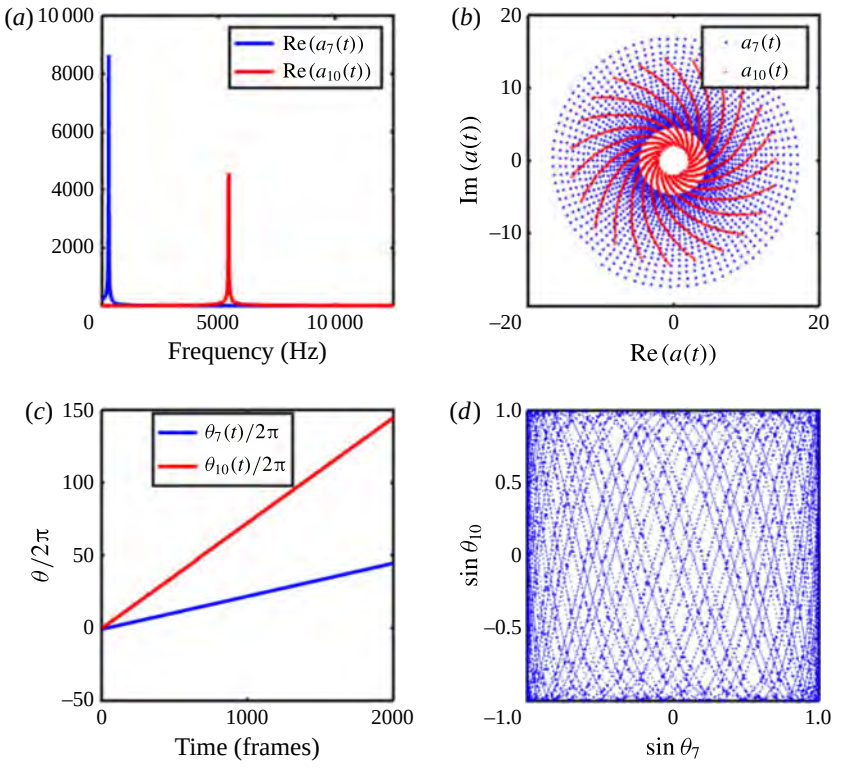

FIGURE 9. (Colour online) Comparison of the dynamics of the rotating mode $\Phi_7(\boldsymbol{x})$ and an injector mode $\Phi_{10}(\boldsymbol{x})$ for injector flow at $J = 11$. Their frequencies (*a*), complex-plane dynamics (*b*) and phase dynamics (*c*) are different. (As in figure 5, (*b*) shows two trajectories for $a_7(t)$ (points) and $a_{10}(t)$ (solid); the illusion of multiple trajectories is caused by the stroboscopic sampling.) (*d*) The orbit in the Lissajous figure appears to be a space filling curve. Here, $\lambda_7 = -16.49 + 1786.03\mathrm{i}$, and $\lambda_{10} = -23.96 + 34127.42\mathrm{i}$.

Reproducible modes of the flow are defined using cutoff values $\delta_I = 36$, $\delta_R = 54$ and $\Delta = 0.58$. The modes are partitioned into two groups according to their frequency (imaginary parts of the eigenvalues) and the location of the eigenfunctions. The low-frequency robust modes ($\mathrm{Im}(\Lambda) \leqslant 2000$), shown in figure 16(*c*), are background modes. They are transient; i.e. their amplitudes decay exponentially, as observed in figure 4. The imaginary parts of almost all of the background modes are observed to be (nearly) integer multiples of $\mathrm{Im}(\Lambda_4)$, suggesting that they are harmonics of $\Phi_4(\boldsymbol{x})$. Together, they will form a single flow constituent. Figure 17 shows several snapshots of the reconstructed spatio-temporal dynamics.

The high-frequency ($\mathrm{Im}(\Lambda_i) > 2000$) robust modes, shown in figure 16(*b*), are located near the injector flow. The dynamic modes associated with each group along with their energies are illustrated in figure 15. The contrast between the background flow and the injector flow (robust mode 48) becomes apparent on comparing the reconstructed flows shown in figures 17 and 18.

For $J = 0.1$, the robust injector modes, whose spectra are shown in figure 16(*b*), decay exponentially and are observed to flow downstream. Symmetric and asymmetric injector modes are found, examples of which are given in figures 19 and 20. Since the

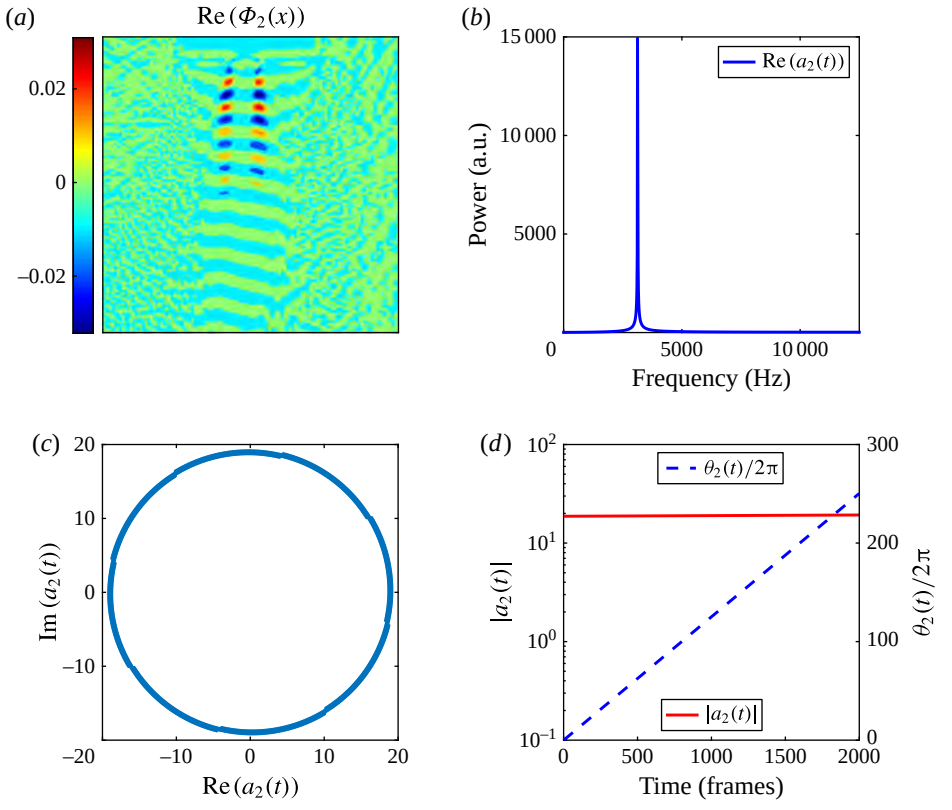

FIGURE 10. (Colour online) Robust mode 2 for $J = 0.1$ of the acoustically driven flow is a linear response mode. The imaginary part of its eigenvalue equals the ratio of the driving frequency and 2π.

amplitudes of the modes shown decay in time, the plot of the real versus imaginary parts follows an inward spiralling path.

4.2.2. *Acoustically driven injector flows for* $J = 0.1$

Figure 21 shows a series of images of the acoustically driven flow at $J = 0.1$ when the injector is placed at a PAN of the acoustic driving. The flow has considerably more structure than the corresponding baseline flow. The DMD spectrum and robust modes are shown in figure 22. Robust modes were selected using the criteria $\delta_I = 23$, $\delta_R = 15$ and $\Delta = 0.4$. The modes in figure 22(*c*) capture the spatio-temporal dynamics of the background flow, while those in figure 22(*b*) represent the injector flow, with some of them having analogues in the baseline flow, as exemplified by the modes shown in figure 11.

A new robust dynamic mode (mode 2) whose frequency is that of the acoustic driving is found. The imaginary part of Λ_2 is the PAN driving frequency divided by 2π, suggesting that it is the linear response of the flow field to the acoustic perturbation. The real part of the eigenvalue is nearly zero, indicating, as seen in figure 10, that $a_2(t)$ maintains its magnitude in time. The wavelength of the linear response mode is similar to the modulation in the flow seen in figure 21, and the

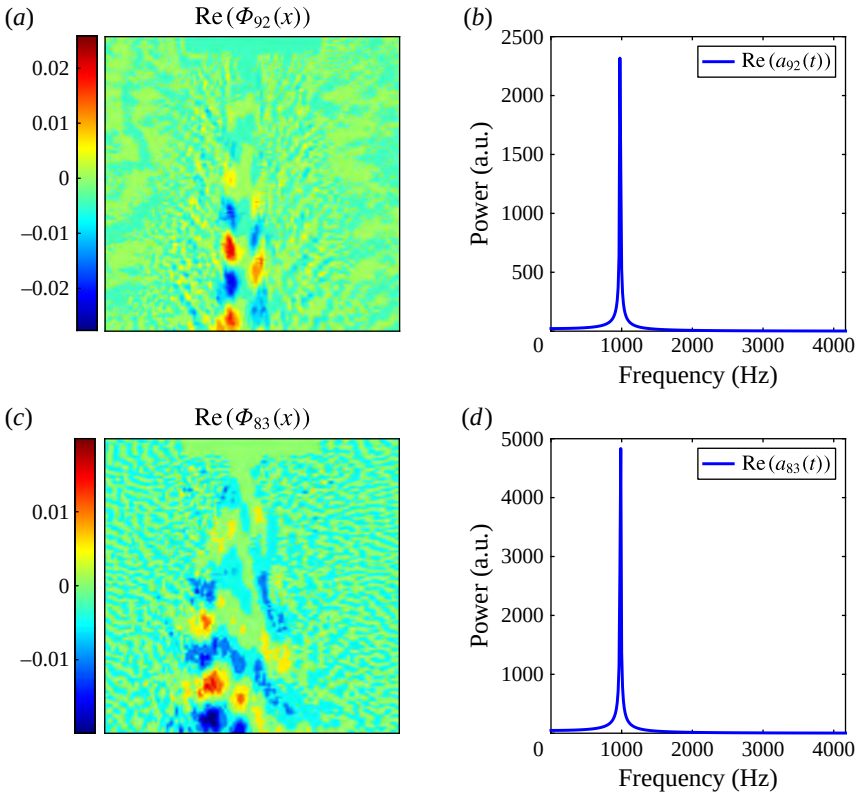

FIGURE 11. (Colour online) Robust mode 83 of the PAN driven flow, shown in (*c*), has a structure similar to the robust baseline mode 92 shown in (*a*). Their spectra, shown in (*d*) and (*b*) respectively, are similar as well.

large energy associated with the mode (seen in figure 22) is related to the large amplitude of the modulation.

It can be noticed that the real part of mode 61 is positive, indicating that it grows for the duration of the experiment. We suspect that it saturates at later times; the expectation needs to be verified in longer experimental runs.

4.3. *Injector flows for large J* ($J \geqslant 5.2$)

The injector flows for $J \geqslant 5.2$ present additional robust modes, which are illustrated through the results analysis of the flow for $J = 11$.

4.3.1. *Baseline injector flows for* $J = 11$

Figure 23 shows several snapshots of the injector flow at $J = 11$. It can be noticed that the high-density injector flows diffuse into the ambient fluid earlier at this high J. Figure 24 shows the 100 dynamic modes of the flow with the highest energies. As in the case of $J = 0.1$, the energy of the mean mode $\Phi_0(\boldsymbol{x})$ is more than two orders of

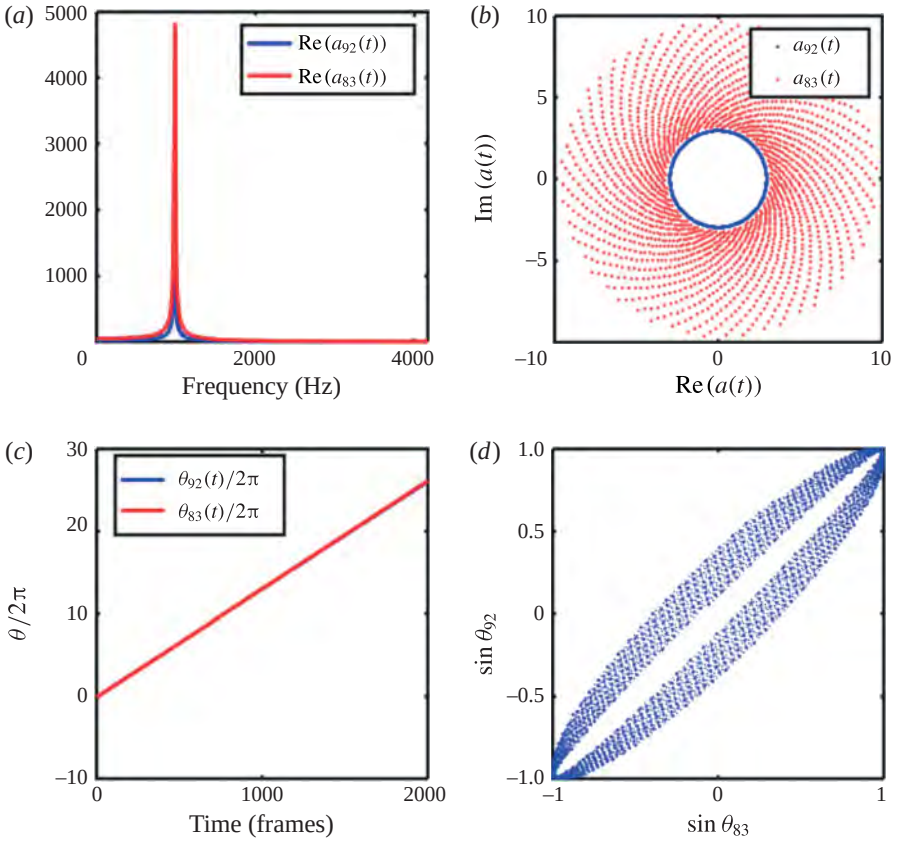

FIGURE 12. (Colour online) The eigenvalues of the two modes compared here are $\lambda = 0.05 + 6155.52\mathrm{i}$ and $\lambda = 13.95 + 6177.75\mathrm{i}$. Comparison of the dynamics of $\Phi_{92}(t)$ for the baseline flow and $\Phi_{83}(t)$ for the PAN driven flow. The (*a*) spectra and (*c*) angular progressions of the dynamics of the two modes are identical. (*b*) The magnitude $|a_{92}(t)|$ of the baseline flow is nearly unchanged (the inner solid line) in time while $|a_{83}(t)|$ for the PAN driven flow decays in time (the inward spiralling points). The Lissajous figure, shown in (*d*), is nearly a closed curve, thus reiterating the correlation between the persistent modes.

magnitude higher than the energies of the remaining modes. It can be observed that there are only a very few robust modes at $J = 11$. This is consistent with the presence of large variations in the flow, as illustrated in figure 23.

Figure 25(*a*) shows the DMD spectrum for the flow and figure 25(*b*) that for the robust modes; as before, the error bars are standard deviations of the set of eigenvalue real parts derived from distinct subgroupings of snapshots selected to represent the same dynamic mode. No robust low-frequency background modes are present in this flow. Furthermore, all injector modes in this flow are asymmetric. As mentioned in § 4.1, when J goes beyond 5.2, a rotating mode emerges in the baseline flow. The projection of this mode and the reconstructed dynamics were shown in figures 6 and 8. In addition, the rotating mode is not correlated with any of the injector modes, as illustrated in figure 9.

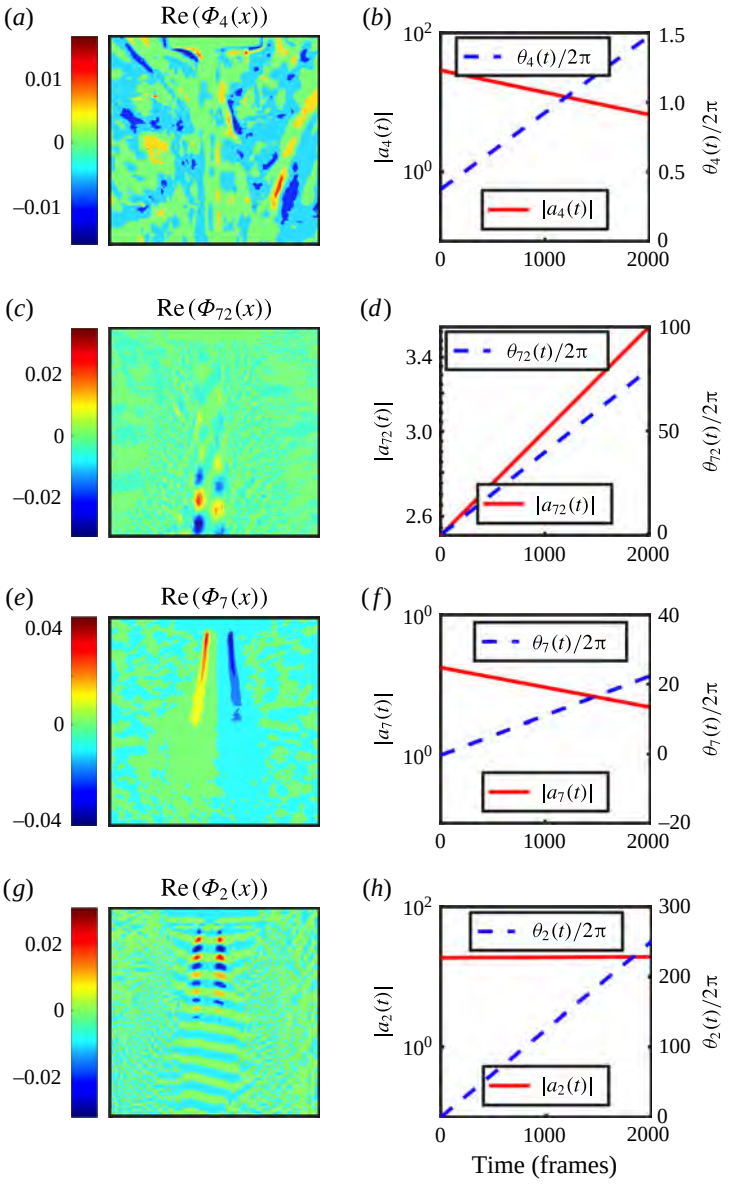

FIGURE 13. (Colour online) The four classes of robust modes found in injector flows and the dynamics of their coefficients: (*a*,*b*) a background mode, (*c*,*d*) an injector mode, (*e*,*f*) a rotating mode and (*g*,*h*) a linear response mode.

4.3.2. *Acoustically driven injector flows for* $J = 11$

Qualitatively, the acoustically driven flow at $J = 11$ is similar to the corresponding baseline flow. As in the case of low J, robust modes of the baseline flow persist when the injector is placed at a PAN of acoustic driving. The driving also initiates a linear response mode, as shown in figure 26. As seen from figure 26(*d*), the amplitude of $a_1(t)$ decays slowly for the selected subgrouping; the dynamics of the real versus imaginary parts of $a_1(t)$ follows an inward spiralling curve.

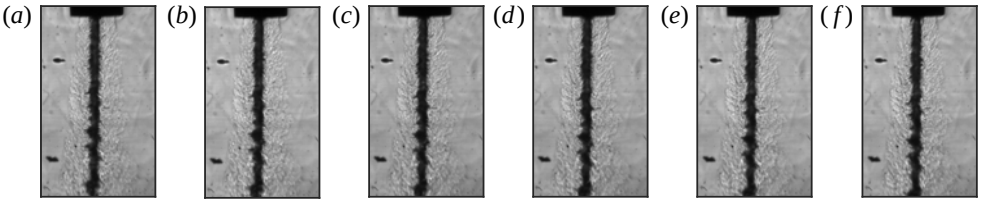

FIGURE 14. Several snapshots of the baseline injector flow at $J = 0.1$: (*a*) 3.96 ms, (*b*) 4.08 ms, (*c*) 4.20 ms, (*d*) 4.32 ms, (*e*) 4.44 ms and (*f*) 4.56 ms.

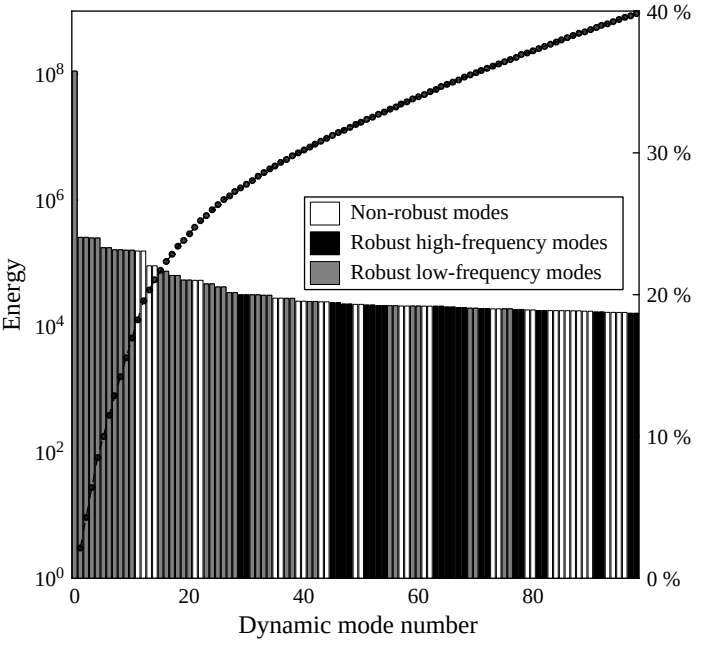

FIGURE 15. Energies of the 100 DMD modes with the highest energies for the full set of snapshots. Non-reproducible modes of the flow are shown in white. Reproducible modes are partitioned into high-frequency and low-frequency modes, shown in black and grey respectively.

5. Conclusions

Despite their apparent simplicity, shear coaxial jets can exhibit highly complex dynamical behaviour. Since theoretical analysis of realistic injector flows is difficult, an alternative approach to unravel the complexity is needed. Here, we proposed the use of modal decompositions of high-resolution high-frequency experimental data to perform this task. Teshome (2012) and Tirunagari *et al.* (2012*a*,*b*) implemented modal decompositions using POD. These studies only reported the most significant modes in the flows.

Strongly driven injector flows appear to be highly disordered and contain significant levels of non-reproducible constituents. One disadvantage of POD is the absence of techniques to differentiate these non-reproducible constituents from the robust dynamical features of the flow. In this paper, we used Koopman mode analysis, a natural approach to search for oscillatory modes (Mezic & Banaszuk 2004; Rowley

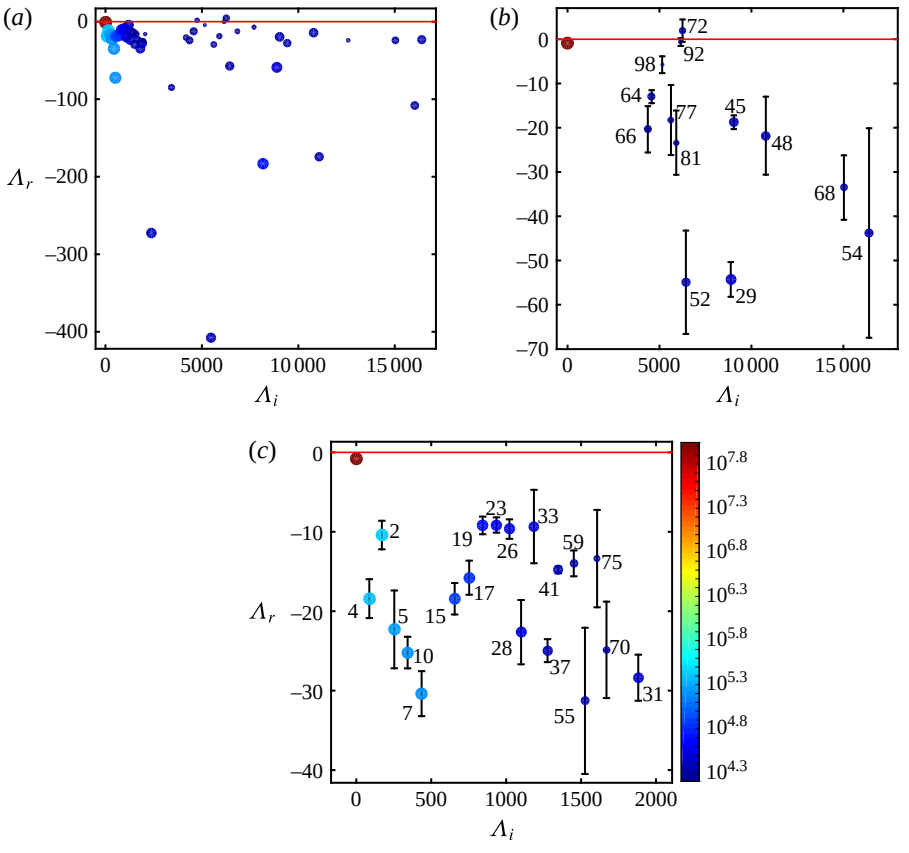

FIGURE 16. (Colour online) The DMD spectrum of $J = 0.1$ baseline flow. (*a*) The 100 modes with the highest energies and positive imaginary parts. The high-frequency ($\mathrm{Im}(\Lambda_i) > 2000$) robust modes, shown in (*b*), are located near the injector flow. The error bars are standard deviations for a set of eigenvalue real parts from different subgroupings that were identified as representing the same eigenmode. Modes 64, 66, 77, 92, 72, 52, 45, 48, 98, 81 and 68 are asymmetric (e.g. figure 20); modes 29 and 54 are symmetric about the axis. (*c*) Low-frequency ($\mathrm{Im}(\Lambda_i) \leqslant 2000$) robust modes that represent the background flow. The colour of the points represents the energies of the modes, according to the colour bar.

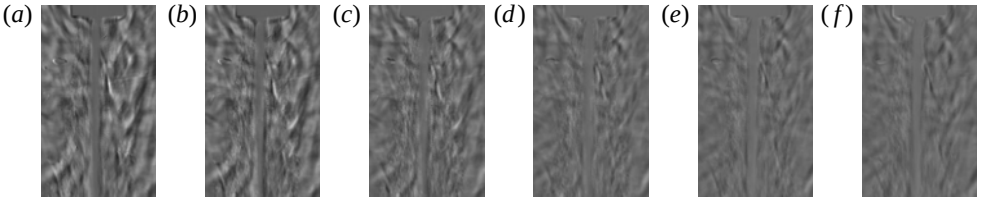

FIGURE 17. Several snapshots of the reconstructed background flow, which lies outside the injector flow and fails to exhibit a well-defined spatial structure: (*a*) 4 ms, (*b*) 6 ms, (*c*) 8 ms, (*d*) 10 ms, (*e*) 12 ms and (*f*) 14 ms.

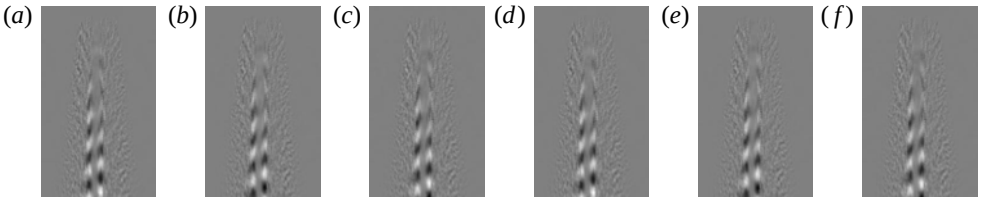

FIGURE 18. Several snapshots of the reconstructed flow for the robust asymmetric mode 48: (*a*) 4 ms, (*b*) 4.2 ms, (*c*) 4.4 ms, (*d*) 4.6 ms, (*e*) 4.8 ms and (*f*) 5 ms. The mode is seen to flow downstream.

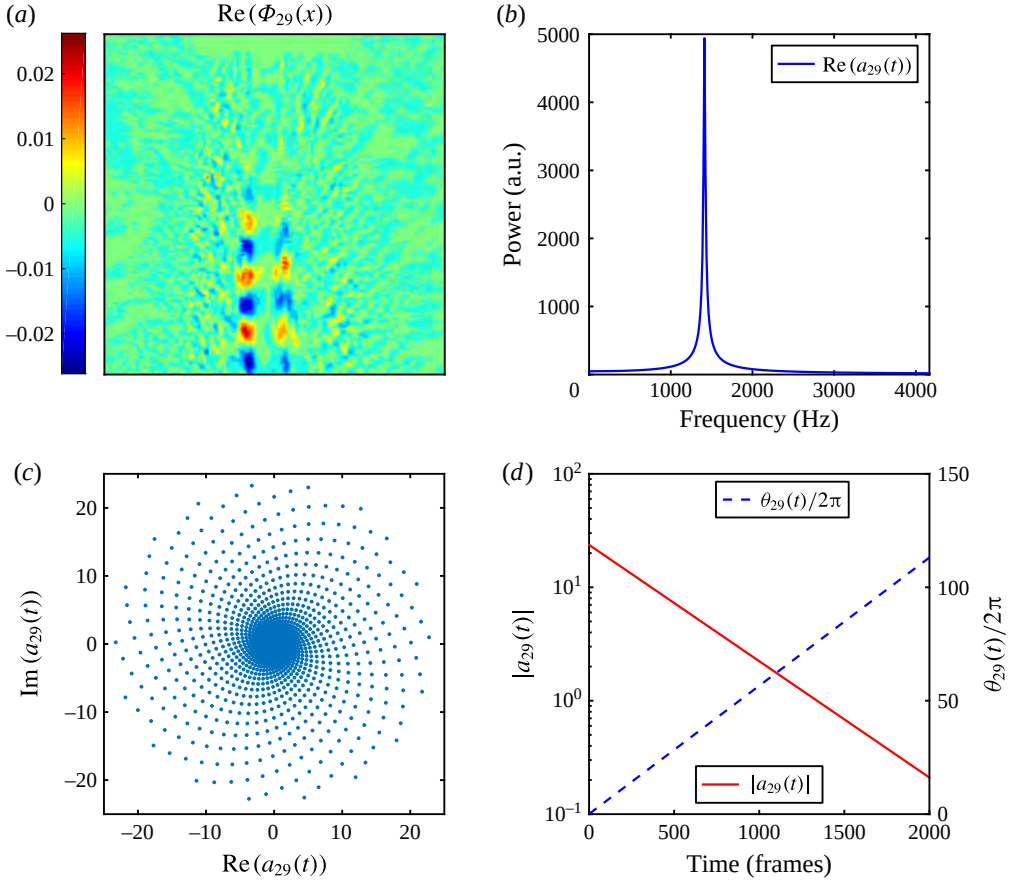

FIGURE 19. (Colour online) Robust symmetric mode Φ_{29}.

et al. 2009; Budišić *et al.* 2012; Mezic 2013), to decompose injector flows. The difficulty was that even non-cyclic and stochastic constituents of a finite data set may be interpreted as a sum of periodic dynamics. However, the deconvolution of these irregular dynamical facets is non-robust, i.e. they depend on the specific data set. Thus, we proposed an approach for differentiating robust and non-robust features in the flow that is based on identifying the former with reproducible Koopman modes, i.e. those that persist in distinct subgroupings of the data (Roy *et al.* 2015). It was

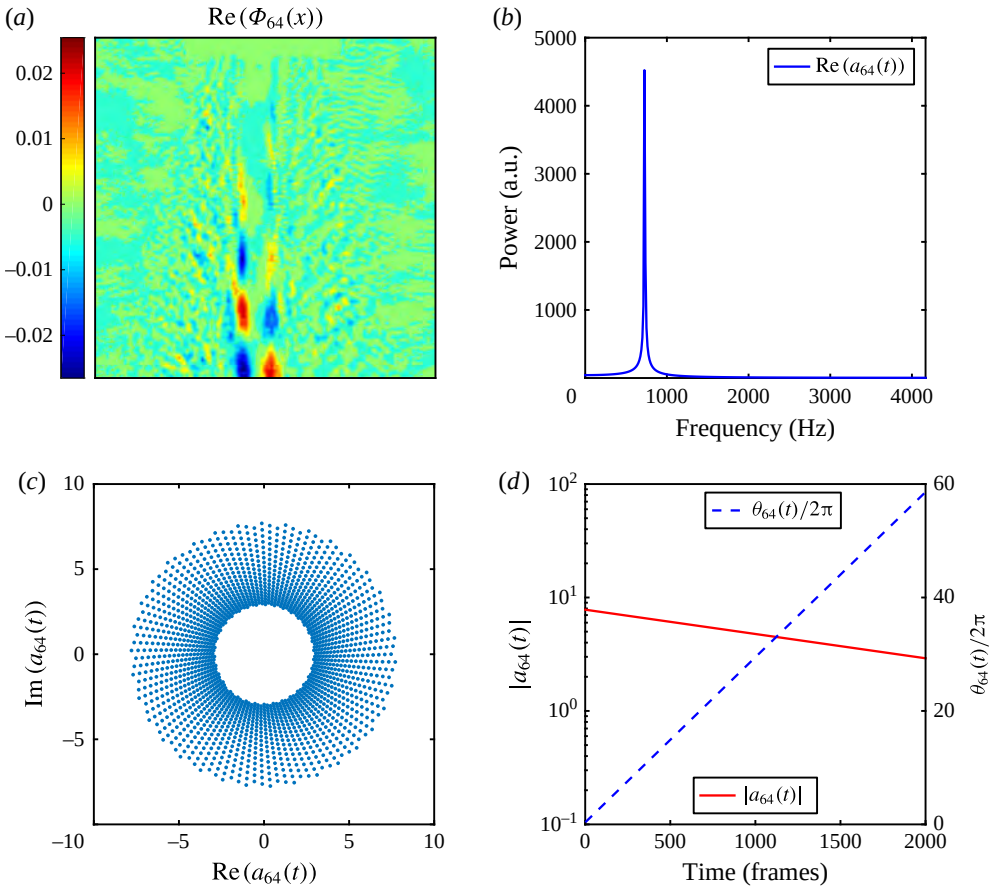

FIGURE 20. (Colour online) Robust asymmetric mode Φ_{64}.

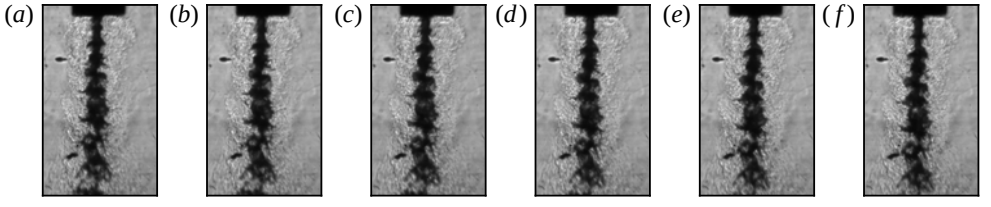

FIGURE 21. Several snapshots of the acoustically driven flow at $J = 0.1$ when the injector is placed at a PAN of the acoustic driving: (*a*) 3.96 ms, (*b*) 4.0 ms, (*c*) 4.04 ms, (*d*) 4.08 ms, (*e*) 4.12 ms and (*f*) 4.16 ms.

thus possible to study all relevant modes of the flow. It is important to note that only these robust features are expected to be useful in applications such as flow control.

The studies reported here were conducted on injector flows of N_2 under high pressure into an ambient N_2 background. The flows were observed with shadowgraph imaging using diffuse backscattering. The high-density injector flows could be observed as darker regions of the visual field. Koopman mode analysis of the density field in baseline flows (those not subjected to additional perturbations) and

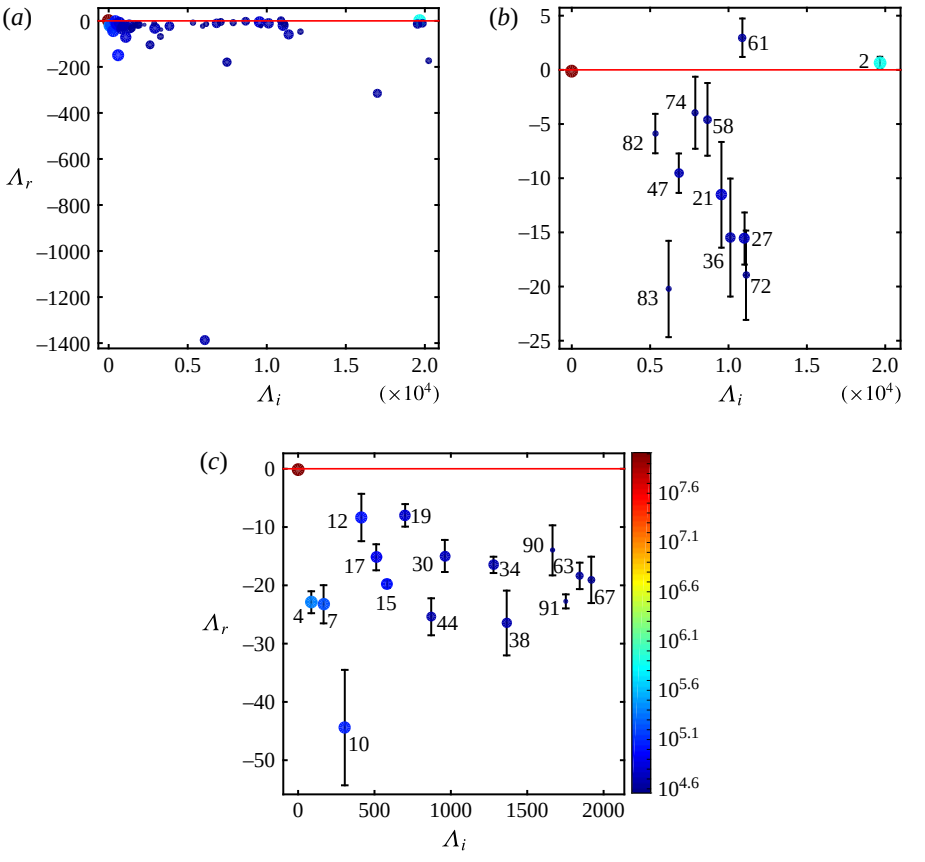

FIGURE 22. (Colour online) The DMD spectrum for the flow at $J = 0.1$ when the injector is placed at a PAN of the acoustic driving. (*a*) The first 100 modes with positive imaginary parts. (*b*) High-frequency ($\mathrm{Im}(\Lambda_i) > 2000$) robust modes with mode number i labelled. The error bars are identical to those defined in figure 16. Mode 2 is the linear response to the driving. (*c*) The low-frequency robust modes ($\mathrm{Im}(\Lambda_i) \leqslant 2000$) represent the background flow.

acoustically excited flows revealed several classes of robust dynamic modes. The modulations of the density field imposed by each of these modes were at least an order of magnitude smaller than the spatial variations in the time-averaged flow.

Several distinct groups of robust dynamic modes characterized by their spatial locations and dynamics were identified in the baseline flows. The first group contained a set of low-frequency excitations located outside the primary injector flow that exhibited rapid decay, as can be observed in figure 4 and the Koopman spectrum in figure 16(*c*). Reconstruction of the flow associated with background modes (figure 17) showed that this flow constituent has no well-defined structure. Although background modes are common between different subgroupings of snapshots in a single experiment, it is expected that they will differ among experiments. Background modes are not found for larger values of the control parameter J, presumably because they have decayed to insignificant levels during the experiment.

The second group of modes are referred to as injector modes because of their location near the primary injector flow. Unlike background modes, they have

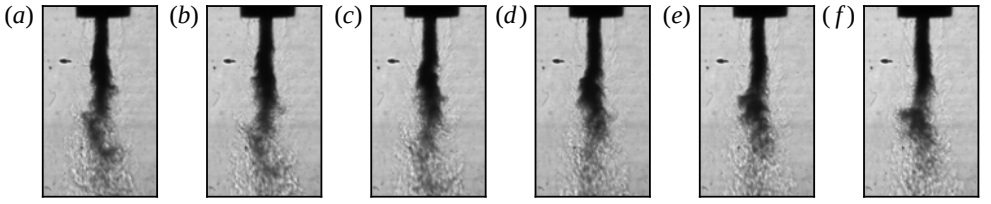

FIGURE 23. Several snapshots of the baseline injector flow at $J = 11$: (*a*) 3.96 ms, (*b*) 4.0 ms, (*c*) 4.04 ms, (*d*) 4.08 ms, (*e*) 4.12 ms and (*f*) 4.16 ms.

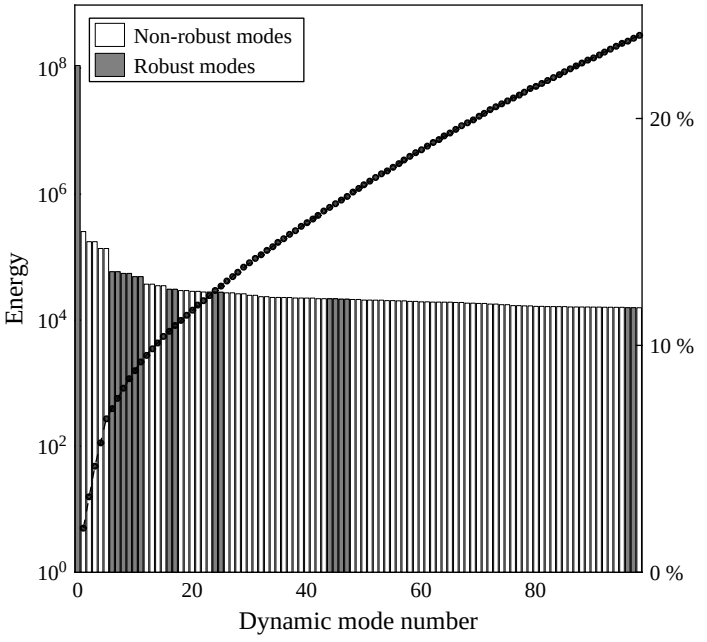

FIGURE 24. The energies of the 100 DMD modes with the highest energies for the full data set of the injector flow for $J = 11$. Non-reproducible modes of the flow are shown in white.

a well-defined structure, an example of which is shown in figure 5; they are high-frequency modes, propagate along the flow (see figure 18) and decay at a significantly slower rate. The wavelength of injector modes is comparable to the modulations of the flow, seen in figure 14, and is likely to be the origin of the latter. The spectrum of injector modes and their error estimates, shown in figure 16(*b*), suggest that some of these may persist beyond the initial transients. This suggestion needs to be validated in longer experimental runs. The broad features of injector modes remain unchanged under acoustic perturbation (figure 22) and for higher values of J (figure 25). While injector modes for small J can be either symmetric (figure 19) or asymmetric (figure 20) in the viewing plane, those for large values of J are antisymmetric. It is possible that the high-/low-density regions in these modes are spirals. They are the only modes reported by Teshome (2012).

Acoustic driving generates additional small-wavelength modulations of the injector flow, as can be seen in figure 21. These appear to be caused by a new robust mode,

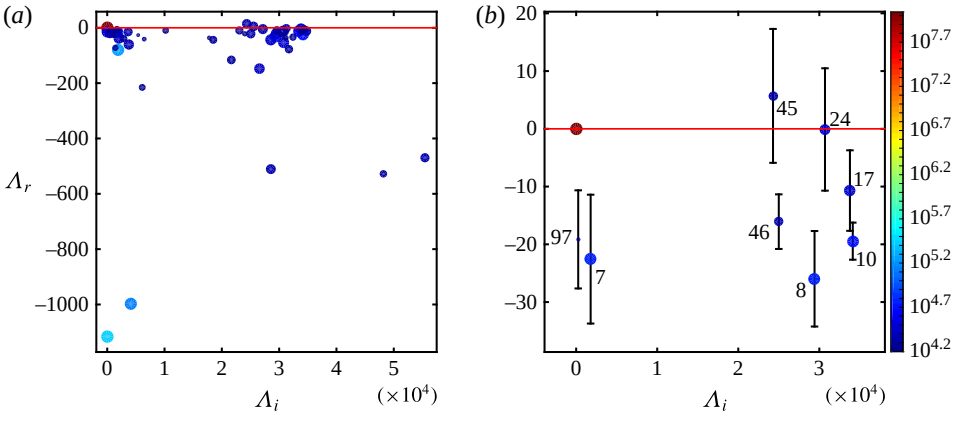

FIGURE 25. (Colour online) The DMD spectrum of $J = 11$ baseline flow. (*a*) The 100 modes with the highest energies and positive imaginary parts and (*b*) robust modes. Mode 7 is the new rotating mode, while modes 45, 46, 8, 24, 17 and 10 are asymmetric injector modes.

which we referred to as a linear response mode; the imaginary part of its eigenvalue is identical to the driving frequency (divided by 2π). Their dynamics exhibits a very sharp spectrum, and their magnitude is (nearly) uniform in time, as seen from figures 10 and 26. For the acoustic driving studied, the spatial periodicity of the linear response mode is smaller than that of injector modes, resulting in the smaller wavelength modulations observed in figure 21. As seen from figure 22, the linear response mode has a large energy, which is correlated with the increased amplitude of modulations of the flow. Linear response modes are found for PAN driven flows at all values of J.

A class of robust dynamic modes of the baseline flow retain their structure and dynamical features under acoustic perturbation. A pair of such modes is shown in figure 11, and the comparison of dynamics of a baseline mode and the corresponding PAN driven persistent mode is shown in figure 12. These modes, referred to as persistent modes, were found for all values of J studied.

The most interesting class of modes was termed rotating modes, as shown in figure 6, and only observed for $J > 5.2$. The projection of their density fields exhibits antiphase oscillatory behaviour. The reconstruction of the spatio-temporal dynamics, illustrated using several snapshots in figure 8, highlights a periodic flipping of the high-/low-density regions. Since the injector and the inlet flow are axisymmetric and the viewing plane has no special stature, the flipping observed in the viewing plane can only be described as a projection of an azimuthally modulated rotating mode, generated via a spontaneous symmetry breaking (Cross & Hohenberg 1993) similar to the rotating modes in uniform flame fronts (Palacios *et al.* 1997). The modes persist under acoustic perturbation, although in this case the system is not axisymmetric, and the symmetry breaking may not be spontaneous.

The roles played by robust modes at different values of J, the outer-to-inner-jet momentum ratio, can be quantified by figures 15 and 24. Injector flows for small values of J (when the outer-jet momentum is relatively large) contain only a few non-robust modes, while those for large values of J consist mostly of non-robust modes. The implication is that large-J flows are more irregular, an observation consistent with

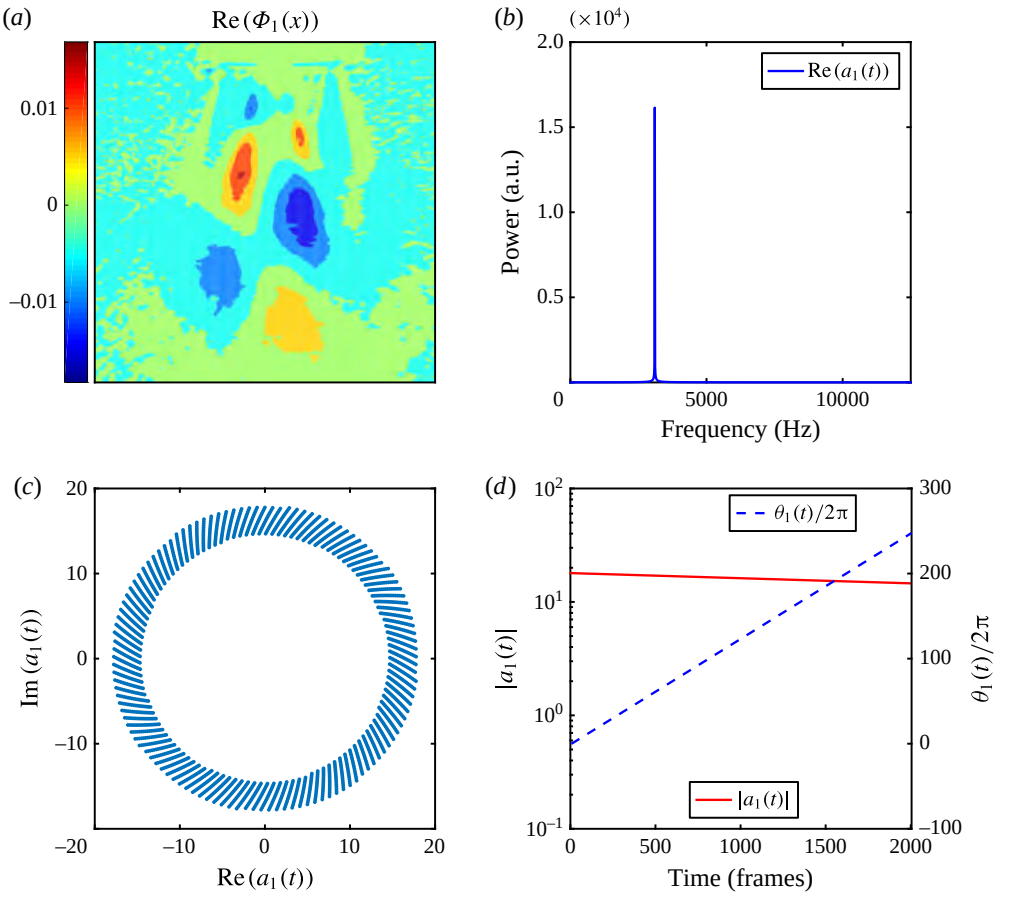

FIGURE 26. (Colour online) Linear response mode (mode 1) for PAN driving of the flow at $J = 11$. The imaginary part of its eigenvalue is identical to the driving frequency divided by 2π.

figures 14 and 23. The energy distributions also reaffirm that it may not be possible to differentiate robust and non-robust flow constituents using their energies alone.

The modal decompositions of injector flows presented here highlight the need for additional investigations. One issue is to identify robust Koopman modes that persist beyond the initial transient stage, i.e. those relevant for long-term flows. For example, our analysis of injector flows suggests that while the background modes are transient, many of the injector modes will persist. The task of differentiating the two groups can be implemented in one of two ways. The first is to conduct and analyse longer experimental runs where transients have decayed. An alternative computational approach is to conduct a sparsity-promoting DMD introduced recently (Jovanovic, Schimid & Nichols 2014). Sparsity-promoting DMD performs the extraction of dynamic modes associated with persistent flows, even when transients have larger energy.

The formation of rotating modes for $J \geqslant 5.2$ is another extremely interesting observation and requires further investigations. It would be especially important to validate the mode with supplementary measurements, study its onset in detail, and

analyse flows appearing in injectors with other geometries and under different classes of acoustic perturbations. Finally, it will be beneficial to determine whether additional classes of dynamic modes are present in the corresponding combustion flows.

Acknowledgement

Funding for this research was provided by the Air Force Research Laboratory under contract nos. FA8650-13-C-2440 and FA9300-13-M-1503. The paper has been cleared for public release by the Air Force Research Laboratory (no. 88ABW-2015-3171).

REFERENCES

BAGHERI, S., SCHLATTER, P., SCHMID, P. J. & HENNINGSON, D. S. 2009 Global stability of a jet in crossflow. *J. Fluid Mech.* **624**, 33–44.

BERKOOZ, G., HOLMES, P. & LUMLEY, J. L. 1993 The proper orthogonal decomposition in the analysis of turbulent flows. *Annu. Rev. Fluid Mech.* **25**, 539–575.

BUDIŠIĆ, M., MOHR, R. M. & MEZIĆ, I. 2012 Applied Koopmanism. *Chaos* **22** (4), 047510.

CHEN, K. K., TU, J. H. & ROWLEY, C. W. 2012 Variants of dynamic mode decomposition: boundary condition, Koopman and Fourier analysis. *J. Nonlinear Sci.* **22**, 887–915.

CROSS, M. C. & HOHENBERG, P. C. 1993 Pattern-formation outside of equilibrium. *Rev. Mod. Phys.* **65** (3), 851–1112.

DAVIS, D. W. & CHEHROUDI, B. 2006 Shear-coaxial jets from a Rocket-like injector in a transverse acoustic field at high pressures. In *44th AIAA Aerospace Sciences Meeting Reno, NV, Jan. 9–12, 2006*.

DAVIS, D. W. & CHEHROUDI, B. 2007 Measurements in an acoustically driven coaxial jet under sub-, near-, and supercritical conditions. *J. Propul. Power* **23** (2), 364–374.

HONG, L., FUSETTI, A., DE ROSA, M. & OSCHWALD, M. 2006 Experimental investigation on the acoustic characteristics of LOZ/CH4 flame. In *ICLASS-2006, 10th International Conference on Liquid Atomization and Spray Systems, Kyoto, Japan, Aug. 27–Sept. 1, 2006*.

HOPFINGER, E. J. 1998 Liquid jet instability and atomization in a coaxial gas stream. In *Advances in Turbulence VII* (ed. U. Frisch), Fluid Mechanics and its Applications, vol. 46, pp. 69–78; *7th European Turbulence Conference (ETC7), St. Jean Cap Ferrat, France, Jun. 30–Jul. 03, 1998*. Springer.

JOVANOVIĆ, M. R., SCHMID, P. J. & NICHOLS, J. W. 2014 Sparsity-promoting dynamic mode decomposition. *Phys. Fluids* **26**, 024103.

LEYVA, I. A., RODRIGUEZ, J., CHEHROUDI, B. & TALLEY, D. 2007 Preliminary results on coaxial jet spread angles and the effects of variable phase transverse acoustic fields. In *46th AIAA Aerospace Sciences Meeting and Exhibit Reno, NV, Jan. 7–10, 2008*.

LUMLEY, J. L. 1967 The structure of inhomogeneous flow. In *Atmospheric Turbulence and Radio Wave Propagation*, pp. 166–176. Publishing House Nauka.

MEZIC, I. 2013 Analysis of fluid flows via spectral properties of the Koopman operator. In *Annual Review of Fluid Mechanics, Vol. 45* (ed. S. H. Davis & P. Moin), Annual Review of Fluid Mechanics, vol. 45, pp. 357–378.

MEZIC, I. & BANASZUK, A. 2004 Comparison of systems with complex behavior. *Physica* D **197** (1), 101–133.

MIESSE, C. C. 1955 The effect of ambient pressure oscillations on the disintegration and dispersion of a liquid jet. *J. Jet Propulsion* **25** (10), 525–530.

MOTHEAU, E., MERY, Y., NICOUD, F. & POINSOT, T. 2013 Analysis and modeling of entropy modes in a realistic aeronautical gas turbine. *Trans. ASME J. Engng Gas Turbines Power* **135** (9), 092602.

PALACIOS, A., GUNARATNE, G. H., GORMAN, M. & ROBBINS, K. A. 1997 Cellular pattern formation in circular domains. *Chaos* **7** (3), 463–475.

ROWLEY, C. W., MEZIC, I., BAGHERI, S., SCHLATTER, P. & HENNINGSON, D. S. 2009 Spectral analysis of nonlinear flows. *J. Fluid Mech.* **641**, 115–127.

ROY, S., HUA, J.-C., BARNHILL, W., GUNARATNE, G. H. & GORD, J. R. 2015 Deconvolution of reacting-flow dynamics using proper orthogonal and dynamic mode decompositions. *Phys. Rev.* E **91** (1), 013001.

SCHMID, P. J. 2009 Dynamic mode decomposition of experimental data. In *Proceedings of 8th International Symposium on Particle Image Velocimetry, PIV09-0141, Melbourne, Victoria*.

SCHMID, P. J. 2010 Dynamic mode decomposition of numerical and experimental data. *J. Fluid Mech.* **656**, 5–28.

SIROVICH, L. 1987*a* Turbulence and the dynamics of coherent structures. 1. Coherent structures. *Q. Appl. Maths* **45** (3), 561–571.

SIROVICH, L. 1987*b* Turbulence and the dynamics of coherent structures. 2. Symmetries and transformations. *Q. Appl. Maths* **45** (3), 573–582.

SIROVICH, L. 1987*c* Turbulence and the dynamics of coherent structures. 3. Dynamics and scaling. *Q. Appl. Maths* **45** (3), 583–590.

TESHOME, S. 2012 Droplet combustion and non-reactive shear-coaxial jets with transverse acoustic excitation. PhD thesis. UCLA Electronic Theses and Dissertations.

TIRUNAGARI, S., HULKKONENE, T., VUORINEN, V., KAARIO, O. & LARMI, M. 2012*a* Proper orthogonal decomposition analysis of cross sectional fuel spray data. In *ICLASS 2012, 12th Triennial International Conference on Liquid Atomization and Spray Systems, Heidelberg, Germany, September 2–6, 2012*.

TIRUNAGARI, S., VUORINEN, V., KAARIO, O. & LARMI, M. 2012*b* Analysis of proper orthogonal decomposition and dynamic mode decomposition on LES of subsonic jets. *CSI J. Comput.* **1** (3), 20–26.

VILLERMAUX, E., REHAB, H. & HOPFINGER, E. J. 1998 Shear instabilities in the near field of coaxial jets. *Phys. Fluids* **10** (9), S2; *15th Annual Fluid Mechanics Photo Contest at the Meeting of the American Physical Society Division of Fluid Dynamics, San Francisco, CA, Nov. 1997*.

WICKER, R. B. & EATON, J. K. 1994 Near-field of a coaxial jet with and without axial excitation. *AIAA J.* **32** (3), 542–546; *AIAA 31st Aerospace Sciences Meeting, Reno, NV, Jan. 11–14, 1993*.

Spectral Decomposition of Acoustically Excited Nonreacting Cryogenic Coaxial Jets

H. Subramani[1,2], A. Saha[2], M. H. Reza[2], T. R. Meyer[2], S. Roy[3], J. R. Gord[4], D. Talley[5]
1. Iowa State University, Department of Mechanical Engineering, Ames, IA
2. Purdue University, School of Mechanical Engineering, West Lafayette, IN
3. Spectral Energies, LLC, Dayton, OH
4. Air Force Research Laboratory, Aerospace Systems Directorate, Wright-Patterson AFB, OH
5. Air Force Research Laboratory, Aerospace Systems Directorate, Edwards AFB, CA

Abstract

In this paper, we detail the dynamics of nonreacting cryogenic coaxial nitrogen jets based on the availability of shadowgraph images sampled at 25 kHz that allows for the investigation of the spatial and temporal characteristics of large scale coherent features present in such flows. Spectral maps computed using the continuous wavelet transform are presented in which the occurrence of multiple frequential patterns can be noted in both space and time. The principal components of wavelet-filtered image sequences are also presented that allows for a lower-dimensional representation of energetically relevant coherent patterns in the dataset.

Keywords: Continuous Wavelet Transform, Proper Orthogonal Decomposition, Spatial-Temporal Data Analysis, High Speed Images

---

Introduction

A deeper understanding of the behavior of shear coaxial jets, i.e. two jets issuing in parallel from a pair of injectors, is necessitated by a continual quest to identify highly efficient combustion regimes within liquid rocket engines. It is, in general, acknowledged that stable combustion regimes strongly depend upon both fluid dynamic parameters such as velocity and density as well as atomizer design parameters such as nozzle area and nozzle thickness. However, such empirical knowledge is often rendered insufficient in the face of increasingly complex design criteria such as the requirements of elevated operating pressures based upon the demand for higher specific impulse. In addition, liquid rocket engines are host to high frequency combustion instabilities, also known as thermoacoustic instabilities, in which an interweaving of fluid dynamics, unsteady heat release and acoustics often results in debilitating consequences. Considering the complexity of the phenomena involved, questions abound with regards to the interplay between the transverse acoustics waves of the chamber and the coaxial jets' shear layer instabilities, and, as to how this relationship is affected by the thermodynamic states of the fluids involved [1-5].

The past decade has seen tremendous progress in terms of the development of research facilities and diagnostic capabilities aimed at exploring the dynamics of coaxial jets. This has resulted in allowing for the inference of the mixing and atomization behaviors through the application of image processing algorithms upon the opulence of data in the form of detailed images acquired at high sampling rates [6]. At the same time, the promulgation of mathematical transformations that cater to the decryption of high dimensional datasets including the proper orthogonal decomposition [7, 8] and dynamic mode decomposition [9-11] has resulted in the characterization of jet behavior in terms of their energetic coherent spatial structures as well as their dominating frequential content. Despite the abundance in literature that has been accumulating over the decade, a noticeable omission has been with regards to the description of the temporal dynamics of these coherent structures. In this paper, we attempt to portray the spatial-temporal trajectories of the shear layer instabilities through the utilization of the continuous wavelet transform [12-14]. The overarching objective is to emphasize the continuous wavelet transform as a necessary complement to the existing data analysis toolkit that includes the above said spectral decompositions as well as the Fourier transformation.

The paper is organized as follows. The next section provides a summary of the experimental facility and the coaxial jet dataset that is the subject of this study. The penultimate section discusses the dynamics of nonreacting coaxial cryogenic Nitrogen jets.

Experimental Setup, Coaxial Jet Dataset and Mathematical Preliminaries

The experiments were conducted at the Edwards Air Force Research Laboratory and a complete description of the facility can be found in [3]. Here we restrict ourselves to describing the essential details for the sake of completeness. Two jets of Nitrogen were injected via a coaxial injector into a chamber wherein they underwent mixing that resulted in the atomization of the inner jet. The inner jet was a liquid (107 - 110 K) and the outer jet was a gas

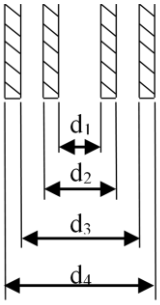

Figure 1: Coaxial injector configuration

(mm)	LAR-Thin
d_1	0.70
d_2	0.89
d_3	2.44
d_4	3.94

Table 1: Configuration dimensions

(192 - 212 K). With light being shot from the rear, the silhouette of the two jets was captured by means of a high-speed camera at a sampling rate of 25000 frames per second. An image is shown in fig. (2a) in which the inner jet appears darker due to the inability of light to traverse the liquid medium. However, the outer jet is barely distinguishable from the ambient which is also gaseous Nitrogen at slightly higher temperatures. The pressure of the chamber was maintained such that a two-phase liquid-vapor coaxial jet mixture was obtained and this condition is referred to herein as a subcritical condition.

Fig. (1) indicates the dimensions of the coaxial injector configuration that was considered over the course of this study. Tab. (1) provides the geometric details concerning this configuration. The design was one in which a thin inner injector post separated unevenly matched exit areas. This condition will be referred to as Large-Area-Ratio-Thin (LAR-Thin). In addition, the experimental apparatus facilitated for the perturbation of the coaxial jets by means of transverse acoustic waves travelling separately from either side via wave guides. Two phase resolved conditions were chosen, the pressure antinode (PAN) and the pressure node (PN) conditions. In the PAN situation, the two acoustic waves impinged on either side of the jets at the same time while there was 180^0 phase offset in the case of the PN condition.

Each experimental run consisted of obtaining 2000 images at a sampling frequency of 25 kHz. Note that we deal with only the subcritical scenario in which the inner jet is a liquid while the outer jet is gaseous. For the LAR-Thin conditions, each image consists of 320 rows and 192 columns of pixel values. These images were recorded on an 8-bit grayscale by means of a Phantom camera. The maximal values near 255 indicate the presence of light and the dark regions valued close to 0 indicate the absence therein. The first preprocessing step involved a linear standardization of values to range between 0 and 1. This was followed by a complement operation using the matlab function *imcomplement*. After this step, high values indicated the presence of both the solid injector corresponding to the top section of the image in fig. (2a) as well as the core of the inner jet. The third and final step involved a subtraction of the temporal mean wherein the mean value computed across the time sequence at each pixel location was subtracted from the corresponding pixel value for each image. The mean-subtracted version of the original image is shown in fig. (2b).

The continuous wavelet transform was performed using the complex-valued Morlet wavelet as the basis. Extensive details concerning the mathematics can be found in [12]. A one-dimensional transformation was computed individually on every time series that could be extracted from each grid point of the image sequence. The total variance of the image sequence was then computed on the wavelet space as detailed in [12] and recast into various forms that will be displayed in the next section.

Results

In this section, we describe the computations involved in the development of spectral maps from the wavelet space that form the basis of our analysis of the coaxial jet dynamics. As an example, consider the LAR-Thin-Subcritical experiment for a momentum flux ratio of J = 00.10 with PAN acoustic forcing at a frequency of 3.13 kHz in which 2000 snapshots were sampled at 25 kHz with each snapshot having 320 rows and 192 columns of pixel values. An illustration of one such snapshot, after subtraction of the mean, has been provided in fig. (2b).

The quantity amounting to the sum of squares of all values of this mean-subtracted sequence accumulated over the entire set of pixel locations can be thought of as the total variance contained in the sequence. This quantity can be recast in the wavelet space as a summation over pixel locations, time instants and scales. Note that this involves the collective computation of the continuous wavelet transform coefficients for time series extracted from each pixel of the mean-subtracted sequence.

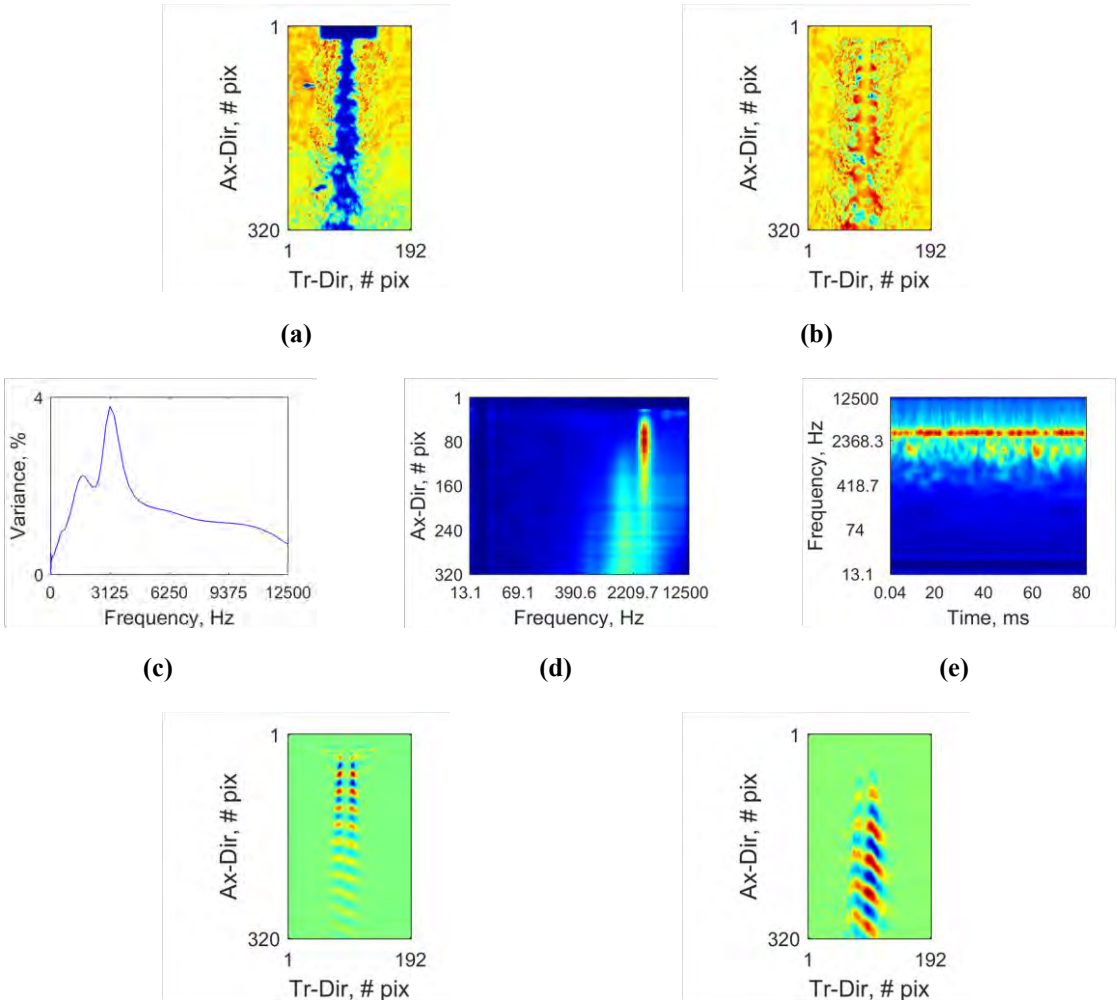

Figure 2: Case study of J = 00.10 PAN LAR-Thin condition forced at 3.13 kHz.

The global variance, defined as the mapping of the total variance as a function of scale, is shown in fig. (2c). The bimodal shape implies the presence of two modes with the frequencies associated to the peaks being 3125.0 Hz and 1674.6 Hz. In a similar manner, the total variance can be recast into the axial variance map shown in fig. (2d) and the temporal variance map shown in fig. (2e). The axial variance map plots the total variance as a function of axial location (in terms of row number) and frequency. With the 3125.0 Hz dominating upstream and the 1674.6 Hz propping up downstream, the bimodal behavior is also evident in this figure. The temporal variance map shows the modifications to the frequency content in time. Based on a cursory glance, the forcing frequency is persistent throughout the entire sequence and the other frequency tends to occur as intermittent events in time.

To associate spatial shapes to the peak frequencies, a reconstruction of the mean-subtracted sequence can be performed in a cumulative fashion across all pixels and at the frequency of interest. This filtered sequence is then projected onto an efficient basis by invoking the singular value decomposition. The energetic SVD modes associated with the two frequencies are shown in figs. (2f) and (2g). Once again, these two modes confirm our previous findings from the plot of the axial variance as with regards to their respective locations.

Conclusions and Future Work

In this paper, we have presented the continuous wavelet transform of coaxial jet image sequences as computed using the complex-valued Morlet wavelet. The total variance has been recast into various forms on the wavelet space

and displayed in the previous section. The modes associated with the dominant singular vectors are also plotted for specific frequencies of interest.

In the future, we will be utilizing the methodology detailed in this paper to extract modes that arise in the immediate wake of a thick-post inner injector. These modes will be referred to as wake modes since we cannot visualize their presence in the case of the thinner post scenarios.

Acknowledgements

This manuscript has been cleared for public release by the Air Force Research Laboratory (No. 88ABW-2018-1187).

References

1. Davis, D.W., On the behavior of a shear-coaxial jet, spanning sub-to supercritical pressures, with and without an externally imposed transverse acoustic field. 2006, PENNSYLVANIA STATE UNIV UNIVERSITY PARK DEPT OF MECHANICAL AND NUCLEAR ENGINEERING.
2. Rodriguez, J.I., Acoustic Excitation of Liquid Fuel Droplets and Coaxial Jets. 2009, AIR FORCE RESEARCH LAB EDWARDS AFB CA PROPULSION DIRECTORATE.
3. Teshome, S., Droplet combustion and non-reactive shear-coaxial jets with transverse acoustic excitation. 2012, AIR FORCE RESEARCH LAB EDWARDS AFB CA ROCKET PROPULSION DIR.
4. Wegener, J.L., Multi-phase combustion and transport processes under the influence of acoustic excitation. 2014: University of California, Los Angeles.
5. Chehroudi, B., Recent experimental efforts on high-pressure supercritical injection for liquid rockets and their implications. International Journal of Aerospace Engineering, 2012. 2012.
6. Leyva, I., B. Chehroudi, and D. Talley. Dark core analysis of coaxial injectors at sub-, near-, and supercritical conditions in a transverse acoustic field.
7. Hua, J.-C., et al., Dynamical-systems analysis and unstable periodic orbits in reacting flows behind symmetric bluff bodies. Physical Review E, 2013. 88(3): p. 033011.
8. Wegener, J.L., et al. Receptivity of a cryogenic coaxial gas-liquid jet to acoustic disturbances.
9. Forliti, D.J., et al. The Response of Cryogenic H2/O2 Coaxial Jet Flames to Acoustic Disturbances.
10. Hua, J.-C., et al., Dynamic-mode decomposition based analysis of shear coaxial jets with and without transverse acoustic driving. Journal of Fluid Mechanics, 2016. 790: p. 5-32.
11. Roy, S., et al., Deconvolution of reacting-flow dynamics using proper orthogonal and dynamic mode decompositions. Physical Review E, 2015. 91(1): p. 013001.
12. Torrence, C. and G.P. Compo, A Practical Guide to Wavelet Analysis. Bulletin of the American Meteorological Society, 1998. 79(1): p. 61-78.
13. Farge, M., Wavelet transforms and their applications to turbulence. Annual Review of Fluid Mechanics, 1992. 24(1): p. 395-458.
14. Farge, M., et al., Wavelets and turbulence. Proceedings of the IEEE, 1996. 84(4): p. 639-669.

Check for updates

Fast and Unbiased Determination of Dominant Frequencies and Amplitude of Thermoacoustic Oscillations

Tongxun Yi,* Christopher Fugger,† and Sukesh Roy‡
Spectral Energies, LLC, Beavercreek, Ohio 45430
Robert J. Jensen§
Sierra Lobo, Inc., Edwards Air Force Base, California 93524
Andrew W. Caswell¶
U.S. Air Force Research Laboratory, Wright–Patterson Air Force Base, Dayton, Ohio 45433
Douglas G. Talley**
U.S. Air Force Research Laboratory, Edwards Air Force Base, California 93524
and
Matthew J. Casiano††
NASA Marshall Space Flight Center, Huntsville, Alabama 35812

https://doi.org/10.2514/1.B37896

Reported is a three-step procedure (also referred to as the observer) for fast and unbiased determination of the dominant frequencies and amplitude of thermoacoustic oscillations. The first step is to determine the rang of the dominant frequency by computing the amplitude at frequency bins uniformly distributed from the lowest possible frequency to the Nyquist frequency (i.e., one-half of the sampling frequency) with a strategically specified, widely spaced frequency-bin separation. The other steps are to refine the estimation. The frequency estimation becomes unbiased after step 2, and the error (or uncertainty) is insensitive to the signal-to-noise ratio. The computational complexity can be orders-of-magnitude lower than the discrete Fourier transform and the fast Fourier transform, and the accuracy is no longer limited by F_s/N, where F_s and N refer to the sampling frequency and the data length, respectively. This Paper recommends that the frequencies and amplitude be estimated every two pressure cycles. Cycle-to-cycle (or short-term) variations in the frequencies and amplitude are well resolved for thermoacoustic oscillations in three different real devices exhibiting quasi-steady oscillations before the onset of combustion instabilities and spontaneous instabilities (i.e., linearly unstable oscillations) with different levels of nonlinearities, respectively.

Downloaded by UNIVERSITY OF CINCINNATI on April 22, 2020 | http://arc.aiaa.org | DOI: 10.2514/1.B37896

I. Introduction

COMBUSTION instabilities, during both the quasi-steady, limit-cycle state and the transient stages (i.e., the onset and decay) exhibit nearly periodic oscillations in pressure and the heat-release rate. Combustion instabilities typically occur around the acoustic resonant frequencies and are initiated and sustained by the positive feedback between pressure and the heat-release rate. The frequencies and amplitude, the key parameters characterizing nearly cyclic oscillations, are known to constantly vary [1–3]. Fast and accurate determination of these parameters with a shortest possible observation window is highly desirable for in-depth characterization and improved understanding of the initiation, saturation and decay of combustion instabilities, energy transfer among acoustic modes, rating of combustion stabilities, online monitoring, and active combustion control [4–9]. Besides combustion instabilities, fast and accurate determination of the dominant frequencies, amplitude, and phases is also relevant to array signal processing, radar signal processing, optical communication, and active noise/vibration control.

Cycle-to-cycle (i.e., short-term) variations in the frequency and amplitude have been investigated by several researchers both experimentally and theoretically. Burnley and Culick [1] modeled the vortical and entropical motion as white noise and theoretically studied the noise effects on thermoacoustic oscillations. They observed that external excitations increased both the amplitude and the variance of pressure oscillations and that parametric excitations resulted in a noise-induced drift in the stability margin and spreading of the probability density function of the pressure amplitude. They also observed a bimodal distribution of the pressure amplitude for a linearly stable system by using the threshold velocity model for the combustion response to acoustic oscillations. Lieuwen [2] captured cycle-to-cycle (i.e., short-term) variations in the frequency with the zero-crossing technique and discussed the role of noise and system nonlinearities on the limiting amplitude and the transition from stable to unstable oscillations. Okuno et al. [3] used cycle networks and phase-space networks to characterize fully developed combustion instabilities and reported the observations of the pseudoperiodicity, high dimensionality, and possible presence of a power-law distribution and small-world-like nature. Yi and Gutmark [10] determined the damping ratio ζ for thermoacoustic oscillations with a least-mean-square algorithm based on the pressure amplitude at a number of frequency bins around the dominant frequency. Lieuwen [11] determined the damping ratio ζ using an autocorrelation-based approach. Both approaches require knowledge of the dominant frequencies, and both investigations show that ζ consistently decreases at the approach of the onset of combustion instabilities.

The techniques for frequency estimation can be classified into three categories. The first category is based on the discrete Fourier transform (DFT) and its variants [12–14]; the second one is based on the adaptive notch filters (ANFs) [15,16]; the second one is based on the adaptive notch filters (ANFs) [15,16]; and the third one is based on the Kalman filters (KFs) [17,18]. The ANFs and KFs must be stable and generally work well with a high signal-to-noise ratio (SNR). The DFT-based approaches have no stability concerns and

Presented as Paper 2005-0123 at the AIAA 43rd Aerospace Sciences Meeting and Exhibit, Reno, NV, January 12–15, 2005; received 15 November 2019; revision received 19 February 2020; accepted for publication 21 February 2020; published online 16 April 2020. This material is declared a work of the U.S. Government and is not subject to copyright protection in the United States. All rights reserved. All requests for copying and permission to reprint should be submitted to CCC at www.copyright.com; employ the eISSN 1533-3876 to initiate your request. See also AIAA Rights and Permissions www.aiaa.org/randp.

*Senior Research Engineer, 4065 Executive Drive. Senior Member AIAA.
†Research Engineer, 4065 Executive Drive. Member AIAA.
‡Senior Research Scientist, 4065 Executive Drive. Associate Fellow AIAA.
§Senior Research Engineer, 4 Draco Drive. Senior Member AIAA.
¶Senior Research Engineer, 2130 Eighth Street. Senior Member AIAA.
**Principal Research Physical Scientist. Associate Fellow AIAA.
††Aerospace Engineer, Propulsion Systems Department, Mailstop ER42. Senior Member AIAA.

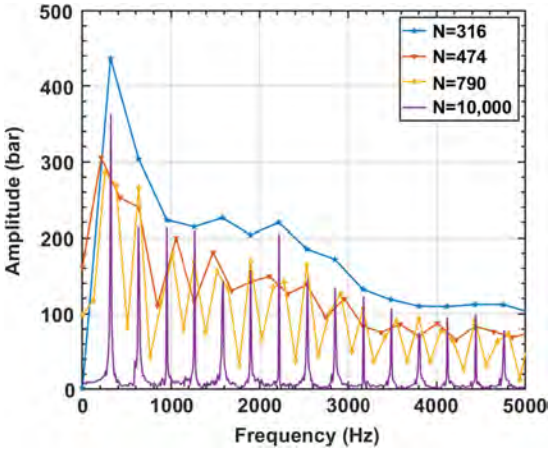

Fig. 1 The spectrum computed with DFT or FFT with $N = 316$, 474, 790, and 10,000.

Downloaded by UNIVERSITY OF CINCINNATI on April 22, 2020 | http://arc.aiaa.org | DOI: 10.2514/1.B37896

work well with low SNRs; however, the computational complexity is rather high, of the order of $\mathcal{O}(N^2)$, where N refers to the data length. The spectral resolution of discrete Fourier transform (DFT) and fast Fourier transform (FFT) is defined as $R_F = F_s/N$, where F_s denotes the sampling frequency (hertz). A higher spectral resolution requires a larger N, which inevitably increases the computational complexity. Assume that the frequency and amplitude need to be estimated every K pressure cycles; then, the spectral resolution becomes $R_F = F_0/K$, where F_0 refers to the signal frequency. Assume $K = 2$; then, the spectral resolution becomes $R_F = F_0/2$, which obviously is too coarse to resolve short-term variations in thermoacoustic oscillations. The frequency-bin separation can be reduced from $\Delta F = F_s/N$ to $\Delta F_z = F_s/(N + M)$ by padding M zeros to the end of the N samples; however, zero padding increases the computational complexity from $C_{\mathrm{DFT}} = \mathcal{O}(N^2)$ to $C_{\mathrm{DFT_z}}\mathcal{O}(NN + MN)$ for DFT and from $C_{\mathrm{FFT}} = \mathcal{O}(N\log(N))$ to $C_{\mathrm{FFT_z}} = \mathcal{O}((N + M)\log(N + M))$ for FFT. Figure 1 shows the pressure spectrum computed with DFT (or FFT) with the data length $N = 316$, 474, 790, and 10,000 for a hydrocarbon-fueled rocket engine. The sampling frequency F_s is 100,000 Hz. Pressure oscillations are highly nonlinear, involving a fundamental mode at 317.2 Hz and more than 60 harmonics below 20,000 Hz. Both the fundamental mode and all harmonics can be adequately resolved with $N = 10{,}000$ (i.e., $R_f = 10$ Hz); only the fundamental mode is identifiable with (i.e., one pressure cycle); quite a number of dominant modes cannot be identified with $N = 474$ (i.e., one pressure cycle and half). Although all modes are identifiable with $N = 790$ (i.e., two pressure cycles and a half), the amplitude and frequencies of most modes cannot be accurately determined because of the large frequency-bin separation of approximately 63 Hz. As reported in the present Paper, the observer is capable of unbiased estimation of the frequencies with the data length N as short as (corresponding to two pressure cycles), with the computational complexity orders-of-magnitude lower that of DFT and also much below that of FFT.

The present Paper is organized as follows. Section II details the observer algorithm. Section III describes the three-step procedure for fast and accurate determination of the dominant frequencies and amplitude, which is an implementation of the observer algorithm. Section IV parametrically examines the effects of the data length and noise on the observer performance (i.e., convergence and accuracy). Section V presents cycle-to-cycle (i.e., short-term) variations in the dominant frequency and amplitude of thermoacoustic oscillations in a premixed channel combustor and two liquid-fueled rocket engines. Section VI concludes the Paper by summarizing the major findings.

II. Observer Algorithm

The observer algorithm reported in this paper is a further development and a significant upgrade from the one previously described in [9] with the primary goal of reconstruction of the dominant modes for active control of combustion instabilities. In the present study, the observer is further developed into a three-step procedure for fast and accurate determination of the dominant frequencies and amplitude, the key parameters characterizing thermoacoustic oscillations. Without loss of generality, we consider a pure (i.e., noiseless), time-invariant sinusoid with the frequency F_0, amplitude A, and the initial phase θ_0. The kth sample is written as

$$a_k = A\cos((k-1)\omega_0 T + \theta_0) = \frac{\tilde{A}\left(e^{-j(k-1)\omega_0 T} + e^{j(k-1)\omega_0 T}\right)}{2} \quad (k = 1, 2, \ldots) \tag{1}$$

where $\omega_0 = 2\pi F_0$, $\tilde{A} = Ae^{j\theta_0}$, and T denotes the sampling period, $T = 1/F_s$. Assume the spectrum is to be determined at a series of frequency bins (say, M) within an interested frequency range. The amplitude at the angular-frequency bin of ω_i $(i = 1, 2, \ldots, M)$ is defined as

$$\begin{aligned} P(e^{j\omega_i}) &= \frac{2}{N}\sum_{k=1}^{N} a_k e^{-j(k-1)\omega_i T} \\ &= \frac{\tilde{A}}{N}\left\{\sum_{k=1}^{N} e^{j(k-1)(\omega_i-\omega_0)T} + \sum_{k=1}^{N} e^{-j(k-1)(\omega_i+\omega_0)T}\right\} \\ &= \frac{\tilde{A}}{N}\left\{\frac{\sin[(TN(\omega_0-\omega_i))/2]}{\sin[(T(\omega_0-\omega_i))/2]} e^{(j(\omega_0-\omega_i)(N-1)T)/2}\right. \\ &\quad \left. + \frac{\sin[TN(\omega_0+\omega_i)/2]}{\sin[T(\omega_0+\omega_i)/2]} e^{-(j(\omega_0+\omega_i)(N-1)T)/2}\right\} \end{aligned} \tag{2}$$

$P(e^{j\omega_i})$ can be further written as

$$P(\omega_i) = \tilde{A}(\overline{P}_{\omega_{-(i)}} e^{j\omega_{-(i)}TN} + \overline{P}_{\omega_{+(i)}} e^{j\omega_{+(i)}TN}) \tag{3}$$

where $\bar{P}_{\omega_{-(i)}} = \sin(TN\omega_-)/N\sin(T\omega_-)$, $\omega_{-(i)} = (\omega_0 - \omega_i)/2$, $\bar{P}_{\omega_{+(i)}} = \sin(TN\omega_+)/N\sin(T\omega_+)$, and $\omega_{+(i)} = (\omega_0 + \omega_i)/2$. The variation of $\bar{P}_{\omega_-}$ with ω_- and that of $\bar{P}_{\omega_+}$ with ω_+ can be examined with the modified sinc function $g(f)$ illustrated in Fig. 2, which is defined as

$$g(f) = \left|\frac{\sin(Nf)}{N\sin(f)}\right| \qquad (-\pi/2 \le f = \omega_{\pm}T \le \pi/2) \tag{4}$$

The function $g(f)$ has the following properties:

1) The modified sinc function $g(f)$ is essentially a bandpass filter with the large gain around the signal frequency F_0.

2) The largest value of $g(f)$ is unity located at $f_0 = 0$.

3) The zeros of $g(f)$ are located at $f_k = k\pi/N$ $(k = 1, 2, \ldots)$. The curve between each neighboring pair of f_k and f_{k+1} is referred to as the kth side lobe, and that between $f_0 = 0$ and $f_1 = \pi/\mathrm{N}$ is referred to as the main lobe.

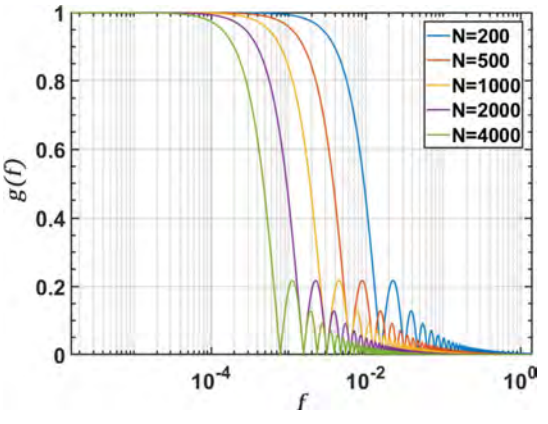

Fig. 2 Magnitude of the modified sinc function $g(f)$.

Downloaded by UNIVERSITY OF CINCINNATI on April 22, 2020 | http://arc.aiaa.org | DOI: 10.2514/1.B37896

4) The widths of both the main lobe and the side lobes are inversely proportional to the data length N.

5) Within the main lobe, $g(f)$ consistently decreases with f until $f_1 = \pi/N$.

6) At the data length N, the peak of $g(f)$ within the kth side lobe is located at $f_{pk} = (k + 0.5)\pi/N$ $(k = 1, 2, \ldots)$, and $g(f_{pk})$ consistently decreases with the index k. At $N = 500$, $g(f_{p0})$: $g(f_{p1})$: $\ldots$: $g(f_{p6}) = 1 : 0.212 : 0.127 : 0.091 : 0.071 : 0.058 : 0.049$.

7) At $N = 500$, the peak of the first side lobe is located at $f_{p1} = 0.0128$ with $g(f_{p1}) = 0.212$.

8) At $N = 500$, within the main lobe, the angular frequency for $g(f) = 0.212$, 0.424, and 0.636 is located at $f_m = 0.0128$, 0.0041, and 0.0031, respectively.

9) By reducing the frequency-bin separation ΔF below $F_s/(2N)$, at least one frequency bin will be located within the main lobe. The amplitude of the frequency bin closest to the signal frequency F_0 within the main lobe will have the largest amplitude $\overline{P}_{\omega_-(i)}$ among all frequency bins, i.e., $\omega_m = \underset{\omega_i(i=1,2,\ldots,M)}{\arg\min} |\omega_i - \omega_0|$ and $\omega_m = \underset{\omega_i(i=1,2,\ldots,M)}{\arg\max} |\overline{P}_{\omega_-(i)=(\omega_0-\omega_i/2)}|$.

10) For the angular-frequency bin ω_m within the main lobe, by increasing the data length N, one can always place $\omega_{+(m)} = (\omega_0 + \omega_m)/2$ several side lobes away from $\omega_{-(m)} = (\omega_0 - \omega_m)/2$, thus rendering $\overline{P}_{\omega_{-(m)}} \gg \overline{P}_{\omega_+(m)}$ and $|\overline{P}_{\omega_{+(m)}}| \to 0$.

11) By simultaneously increasing N and reducing the frequency-bin separation ΔF, one can always ensure that $|\overline{P}_{\omega_-(m)}| \to 1$, $|\overline{P}_{\omega_{+(m)}}| \to 0$, $|P(\omega_m)| > |P(\omega_i)|_{(i\neq m)}$, and $|P_m(\omega_m)| \to A$.

12) The difference between $\omega_{+(m)}$ and $\omega_{-(m)}$ is the angular frequency ω_0 of the signal. A higher ω_0 means that $\omega_{+(m)}$ will be located further away from $\omega_{-(m)}$; thus, a smaller N can be used for accurate determination of the signal frequency and the amplitude. In other words, the observer works better with high-frequency estimation than low-frequency estimation.

13) The observer is globally stable.

14) The complexity of the observer is $\mathcal{O}(NM)$, where N is the data length within the observation window and M is the number of frequency bins within the interested frequency ranges. The frequency ranges within which combustion instabilities occur can be known through developments, operations, and even predictions. In such cases, the number of frequency bins can be significantly reduced (see Sec. III), $M \ll N$.

III. Three-Step Procedure

A three-step procedure is developed for fast and accurate determination of the dominant frequencies and amplitude, which is based on the observer algorithm and properties of the modified sinc function $g(f)$. For the convenience of description, let us exemplify the three-step procedure by estimating the frequency and amplitude for the following noise-contaminated signal:

$$p_k = \sin((k-1)\omega_0 T + \theta_0) + \alpha\mathcal{E}(-1, 1) \quad (k = 0, 1, 2, \ldots) \tag{5}$$

Here, $F_s = 100{,}000$ Hz, and thus $T = 1 \times 10^{-5}$ s. $\mathcal{E}(-1, 1)$ denotes white noise uniformly distributed within $[-1 \quad 1]$. The signal frequency $F_0 = 317.2$ Hz, with the angular frequency $\omega_0 = 2\pi F_0 = 1993$ rad/s. There are 315 samples within each pressure cycle. The lower bound of the interested frequency range F_b is set to be 100 Hz. The three-step procedure is as follows.

The first step is to estimate the dominant frequencies by computing the amplitude at rather widely spaced frequency bins uniformly distributed from the lowest possible frequency F_b to the Nyquist frequency, i.e., one-half of the sampling frequency F_s. With the data length $N \geq F_s/(2F_b)$, i.e., $N \geq 500$, one can make sure that ω_+ for all frequency bins will be located outside the main lobe, i.e., $\omega_{+i} = |(\omega_i + \omega_0)/(2F_s)| \geq \pi/N$ $(i = 1, 2, \ldots, M)$, thus ensuring $P_{\omega_+} \leq g(f_{p1}) = 0.212$. According to property 8 in the item list, at $N = 500$, by specifying the frequency-bin separation ΔF to satisfy $(2\pi\Delta F_1/F_s) < 0.0128$, i.e., $\Delta F_1 < 204$ Hz, one can ensure that $P_{\omega_-} > 0.212$; by specifying ΔF_1 to satisfy $(2\pi\Delta F_1/F_s) < 0.0041$, i.e., $\Delta F_1 < 65$ Hz, one can ensure that $P_{\omega_-} > 0.424$; by specifying ΔF_1 to satisfy $(2\pi\Delta F_1/F_s) < 0.0031$, i.e., $\Delta F_1 < 49$ Hz, one can ensure that $P_{\omega_-} > 0.636$. Note that the signal frequency F_0 is located either between a certain pair of two neighboring frequency bins or at a certain frequency bin, thus ensuring $\omega_- < 2\pi\Delta F_1/F_s$ within this pair of neighboring frequency bins. One can see from Fig. 2 that any angular-frequency bin satisfying $P_{\omega_-} > 0.212$ must be located within the main lobe. By reducing ΔF_1 to satisfy $(2\pi F_1/F_s) \leq 0.0128$, i.e., $\Delta F_1 \leq 0.002F_s$, the pair of neighboring frequency bins within which the signal frequency F_0 resides can be determined, thus ensuring $F_m - \Delta F_1 < F_0 < F_m + \Delta F_1$, where F_m denotes the frequency bin of the largest amplitude. The first (or coarse) estimation of the signal frequency and amplitude is made by developing a second-order, curve-fitting polynomial around F_m in the form of $P_{01} = a_1F_{01}^2 + b_1F_{01} + c_1$, where the three frequency bins are denoted as $F_{01} = [F_{01,1}, F_{01,2}, F_{01,3}] = [F_m - \Delta F_1, F_m, F_m + \Delta F_1]$ and the corresponding amplitude is denoted as $P_{01} = [P_{01,1}, P_{01,2}, P_{01,3}] = [P(F_{m-1}), P(F_m), P(F_{m+1})]$. Note that $F_{m-1} = F_m - \Delta F_1$ and $F_{m+1} = F_m + \Delta F_1$. The dominant frequency and the peak amplitude are estimated to be $\hat{F}_{01} = -b_1/(2a_1)$ and $\hat{P}_{01} = a_1\hat{F}_{01}^2 + b_1\hat{F}_{01} + c_1$, respectively.

The second step is to refine the estimation by computing the amplitude at a number (preferably 5) of frequency bins around the estimated frequency $\hat{F}_{01}$ with a frequency-bin separation of ΔF_2, which should be smaller than ΔF_1, preferably $\Delta F_2 = 0.25\Delta F_1$. Denote the five frequency bins as $F_{02} = [F_{02,1}, F_{02,2}, F_{02,3}, F_{02,4}, F_{02,5}] = [\hat{F}_{01} - 2\Delta F_2, \hat{F}_{01} - \Delta F_2, \hat{F}_{01}, \hat{F}_{01} + \Delta F_2, \hat{F}_{01} + 2\Delta F_2]$ and the corresponding amplitude as $P_{02} = [P_{02,1}, P_{02,2}, P_{02,3}, P_{02,4}, P_{02,5}] = [P(F_{02,1}), P(F_{02,2}), P(F_{02,3}), P(F_{02,4}), P(F_{02,5})]$. A second-order, curve-fitting polynomial is developed for the amplitude at the five frequency bins in the form of $P_{02} = a_2F_{02}^2 + b_2F_{02} + c_2$ from which the dominant frequency and the amplitude are refined to be $\hat{F}_{02} = -b_2/(2a_2)$ and $\hat{P}_{02} = a_2\hat{F}_{02}^2 + b_2\hat{F}_{02} + c_2$, respectively. For step 2, we recommend that a data length of two pressure cycles (based on $\hat{F}_{01}$) be used.

The third step is to further refine the estimation by computing the amplitude at a number of frequency bins (preferably 3) around $\hat{F}_{02}$, namely, $F_{03} = [F_{03,1}, F_{03,2}, F_{03,3}] = [\hat{F}_{02} - \Delta F_3, \hat{F}_{02}, \hat{F}_{02} + \Delta F_3]$, where ΔF_3 denotes the frequency-bin separation for step 3. ΔF_3 should be smaller than ΔF_2, preferably $\Delta F_3 = 0.5\Delta F_2$. Denote the amplitude at the three frequency bins as $P_{03} = [P_{03,1}, P_{03,2}, P_{03,3}] = [P(F_{03,1}), P(F_{03,2}), P(F_{03,3})]$, and develop a second-order, curve-fitting polynomial for the amplitude in the form of $P_{03} = a_3F_{03}^2 + b_3F_{03} + c_3$. The dominant frequency and the amplitude are further refined to be $\hat{F}_{03} = -b_3/(2a_3)$ and $\hat{P}_{03} = a_3\hat{F}_{03}^2 + b_3\hat{F}_{03} + c_3$, respectively. Similar to step 2, we recommend a data length corresponding to two pressure cycles (based on $\hat{F}_{02}$) be used for step 3. The estimation of the frequencies and amplitude typically converges after step 2, as detailed in Sec. IV.

The computational complexity, i.e., the number of multiplications, is 334 for step 1 with $\Delta F_1 = 150$ Hz, 5 for step 2, and 3 for Step 3. The computational complexity for step 1 is higher than that of steps 2 and 3 by almost two orders of magnitude; however, step 1 is no longer needed when the candidate frequency ranges are known, say, through development, testing, and routine operations. The three steps for estimation of the dominant frequencies and amplitude for the sinusoid [Eq. (5)] are shown in Figs. 3a–3c, respectively. Here, $\alpha = 0$ and $N = 334$, corresponding to one pressure cycle. The first estimation gives $\hat{F}_{01} = 321.5$ Hz, and the second estimation gives $\hat{F}_{02} = 316.9$ Hz, i.e., 0.3 Hz below the setting value or the true signal frequency.

IV. Observer Performance

A parametric study using the Monte Carlo method is conducted to examine effects of the data length N and noise on the observer performance, i.e., convergence and the estimation error (or uncertainty). Ten thousand data sequences with the initial phase θ_0 uniformly distributed within $[0\ 2\pi]$ rad/s are generated for the signal defined by Eq. (5) at each data length N and each noise level α.

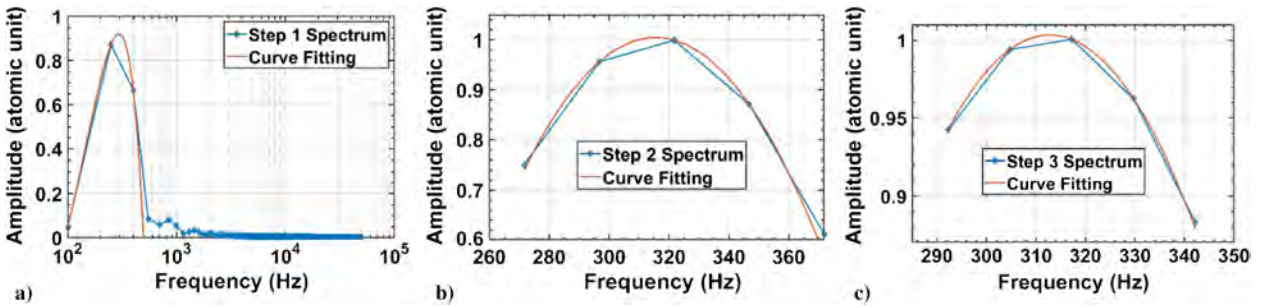

Fig. 3 The three-step procedure for estimation of the frequency and amplitude: a) $F_1 = 150$ Hz, b) $F_2 = 25$ Hz, and c) $F_3 = 12.5$ Hz.

The SNR is 32, 22, 14, 8, 4, 0, −4 and −10 for $\alpha = 0.25$, 0.40, 0.60, 0.80, 1.0, 1.25, 1.50 and 2.0, respectively. The sampling frequency F_s is 100,000 Hz.

A. Convergence

Figures 4a–4c show the mean and the standard deviation of the estimated frequency at $\alpha = 0$, 0.6 and 1.0, respectively. The data length of the observation window is $N = 632$, corresponding to two pressure cycles. The frequency estimation converges to the setting value after step 2. Both the mean and the standard deviation of the estimated frequency change little after step 2. Clearly, the observer is capable of unbiased frequency estimation.

Figures 5a and 5d show the estimated frequency at $\alpha = 0$ for steps 1 and 2, respectively. The data length is $N = 632$, corresponding

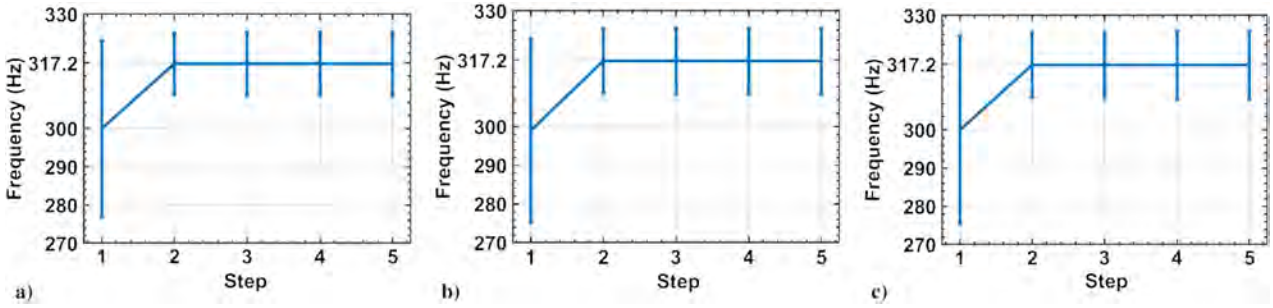

Fig. 4 Frequency estimation at different steps with a) $\alpha = 0$, b) $\alpha = 0.6$, and c) $\alpha = 1.0$.

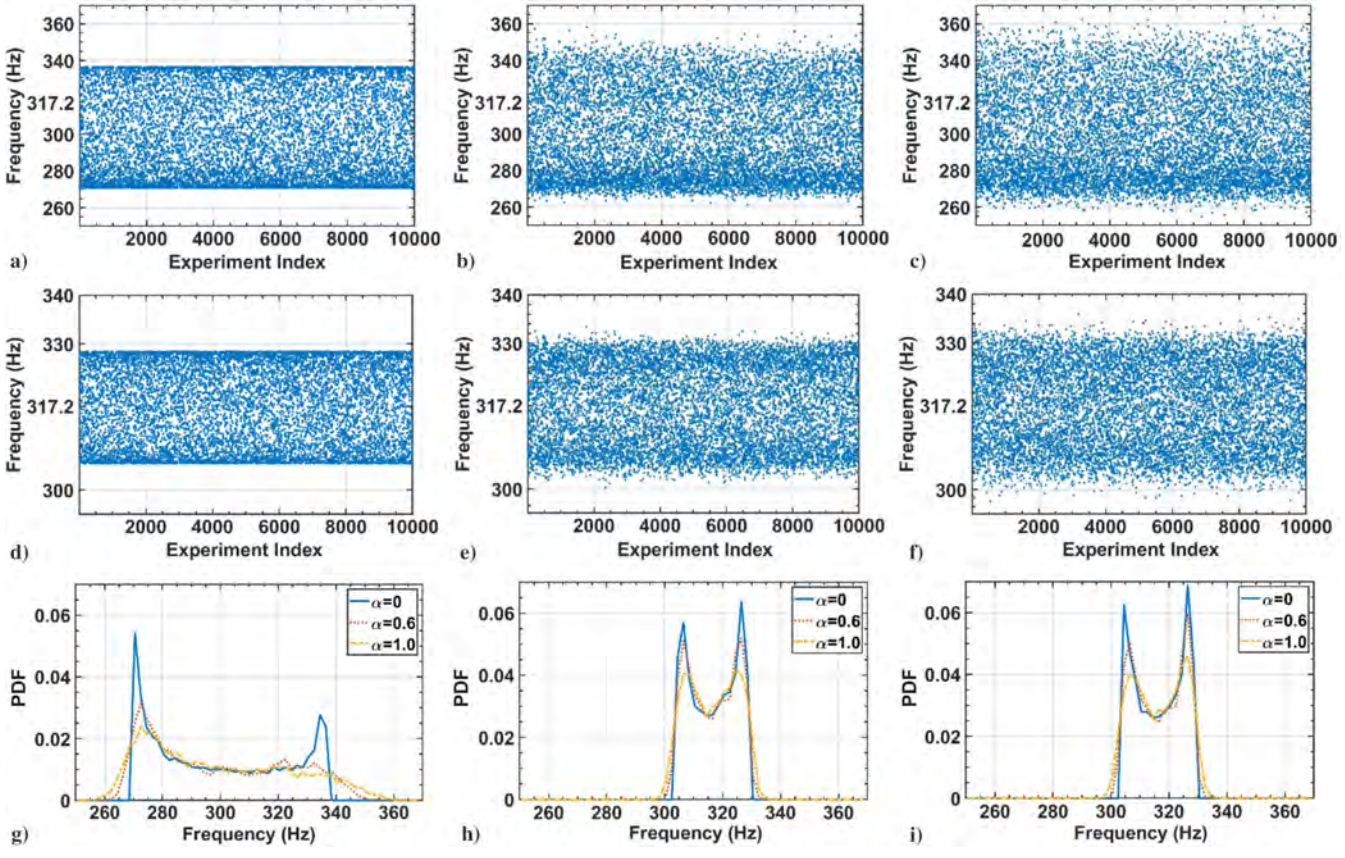

Fig. 5 The estimated frequency for step 1 with a) $\alpha = 0$, b) $\alpha = 0.6$, and c) $\alpha = 1.0$ and for step 2 with d) $\alpha = 0$, e) $\alpha = 0.6$, and f) $\alpha = 1.0$, and the PDF of the estimated frequency for g) step 1, h) step 2, and i) step 3.

Downloaded by UNIVERSITY OF CINCINNATI on April 22, 2020 | http://arc.aiaa.org | DOI: 10.2514/1.B37896

to two pressure cycles. The estimated frequency varies from approximately 270 to approximately 335 Hz for step 1 and from approximately 308 to approximately 328 Hz for step 2, commensurate with the reduction in the standard deviation of the estimated frequency presented in Fig. 4. Substantial reductions in the error (or uncertainty) of the estimated frequency from step 1 to step 2 are also observed at $\alpha = 0.6$ (Figs. 5b and 5e) and $\alpha = 1.0$ (Figs. 5c and 5f). For all three steps, noise only slightly expands the error (or uncertainty) in the estimated frequency. Figures 5g–5i show the probability density function (PDF) of the estimated frequency at the three steps, which obviously are not Gaussian. The PDFs for steps 2 and 3 are quite similar, indicating the convergence in frequency estimation after step 2.

Figures 6a–6c present the mean and the standard deviation of the estimated amplitude at different steps with the noise level $\alpha = 0$, 0.6 and 1.0, respectively. Here, $N = 632$, corresponding to two pressure cycles. Similar to frequency estimation, the amplitude estimation converges after step 2; however, different from frequency estimation, the estimated amplitude exhibits a small bias mainly due to noise. The bias of the estimated amplitude increases with the SNR but is below 0.5% at $\alpha = 1.0$.

Figures 7a and 7d display the estimated amplitude at $\alpha = 0$ for steps 1 and 2, respectively. There is a large shift in the mean amplitude and a dramatic reduction in the estimation error (or uncertainty) from step 1 to step 2. Here, $N = 632$, corresponding to two pressure cycles. A similar observation is made for the amplitude estimation at $\alpha = 0.6$ (Figs. 7b and 7e) and $\alpha = 1.0$ (Figs. 7c and 7f). Different from frequency estimation, the amplitude estimation is considerably broadened by noise, as can be seen from both the scatter plots (Figs. 7a–7f) and the PDFs (Figs. 7g–7i). The PDF changes substantially from step 1 to step 2 but little from step 2 to step 3, which again suggests convergence in the amplitude estimation after step 2. Different from the frequency estimation (Figs. 5g–5i), the PDF of the estimated amplitude appears Gaussian.

B. Effects of Data Length N

The data length is a critical parameter for the observer, which determines the lobe width of the modified sinc function $g(f)$ (see Fig. 2). The three-step procedure is rooted in the variation of $g(f)$ with N. The first step mainly serves to identify the frequency range within which the dominant frequency resides, so a larger lobe width and consequently a smaller N should be used; the other steps serve to refine the estimation of frequencies and amplitude, so a larger N is desirable. Figure 8 shows that the error (or uncertainty) of the

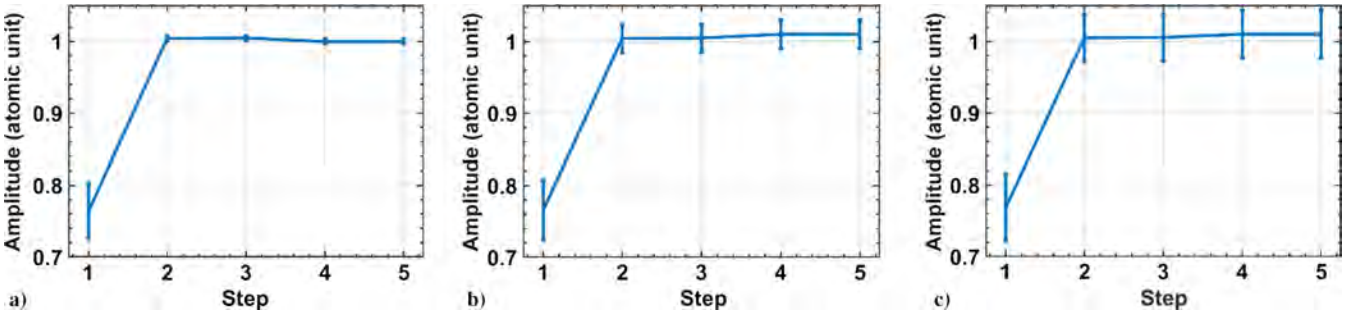

Fig. 6 The amplitude estimation at different steps with a) $\alpha = 0$, b) $\alpha = 0.6$, and c) $\alpha = 1.0$.

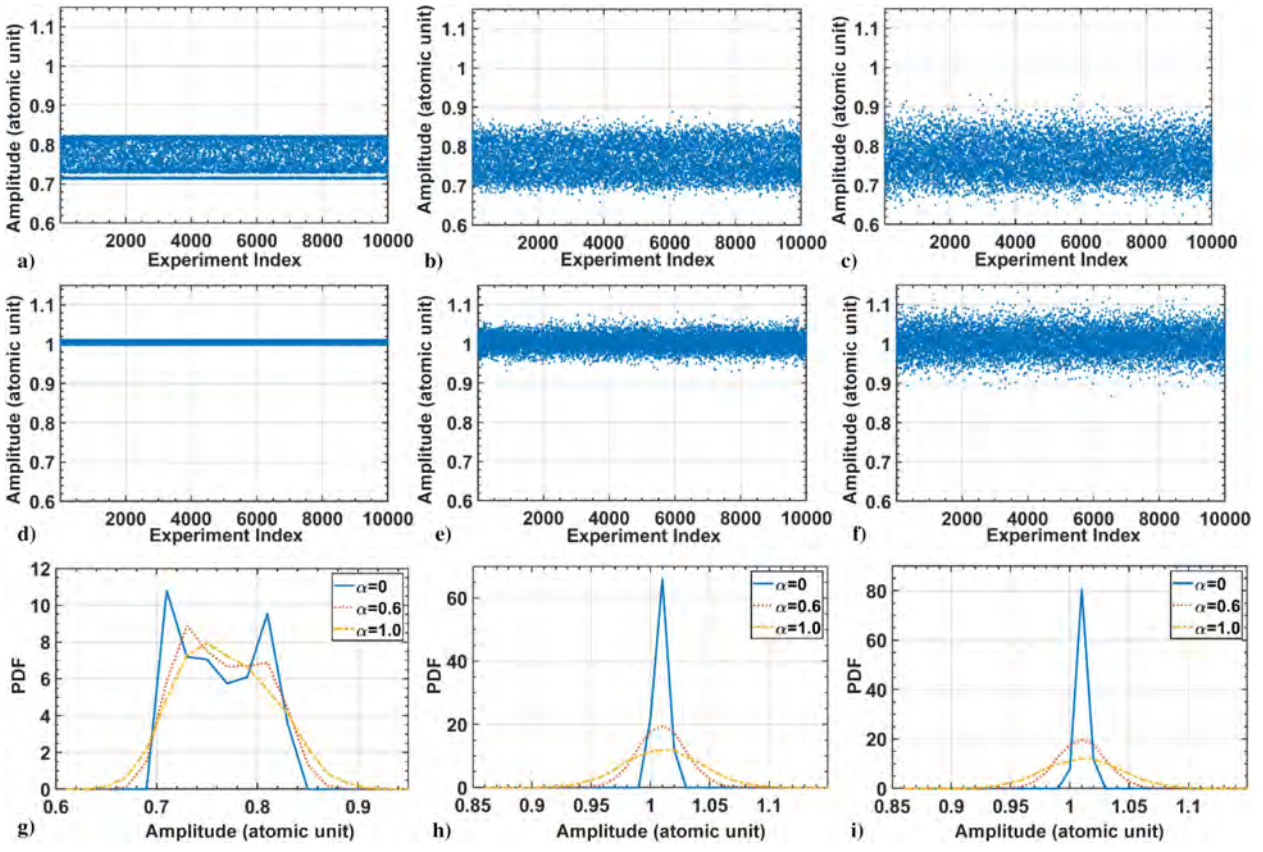

Fig. 7 The estimated amplitude for step 1 with a) $\alpha = 0$, b) $\alpha = 0.6$, and c) $\alpha = 1$, and for step 2 with d) $\alpha = 0$, e) $\alpha = 0.6$, and f) $\alpha = 1.0$, and the PDF of the estimated amplitude for g) step 1, h) step 2, and i) step 3.

Downloaded by UNIVERSITY OF CINCINNATI on April 22, 2020 | http://arc.aiaa.org | DOI: 10.2514/1.B37896

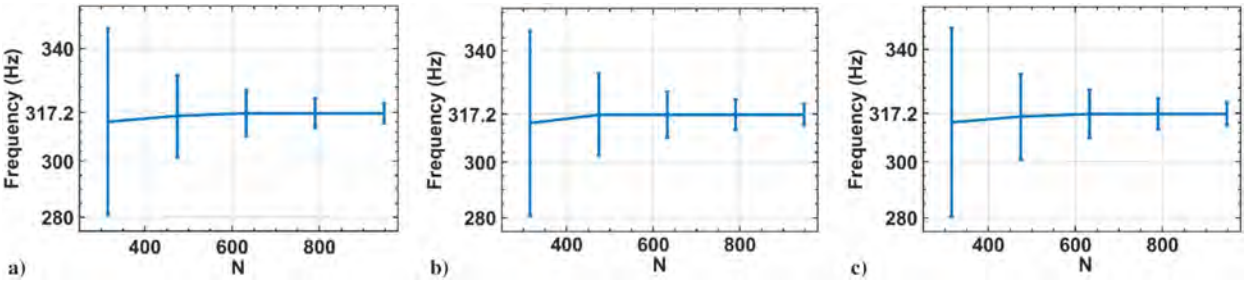

Fig. 8 The frequency estimation after step 2 with a) $\alpha = 0$, b) $\alpha = 0.6$, and c) $\alpha = 1.0$.

estimated amplitude consistently decreases with N. Unbiased frequency estimation is achieved with $N = 632$, corresponding to two pressure cycles.

Figures 9a–9c show the estimated frequency for step 2 at $\alpha = 0$. The error (or uncertainty) of the estimated frequency substantially decreases with N. A similar observation is made for the estimated frequency for step 2 at $\alpha = 1.0$. The substantial reduction in the error (or uncertainty) is also identifiable from the PDFs shown in Figs. 9g–9i. The PDF of the estimated frequency appears bimodal rather than Gaussian; however, it has been found that by reducing the frequency-bin separation below a certain threshold, say, 5 Hz, the PDF does appear Gaussian.

Figures 10a–10c display the mean and the standard deviation of the estimated amplitude at different data length N. The estimated

Downloaded by UNIVERSITY OF CINCINNATI on April 22, 2020 | http://arc.aiaa.org | DOI: 10.2514/1.B37896

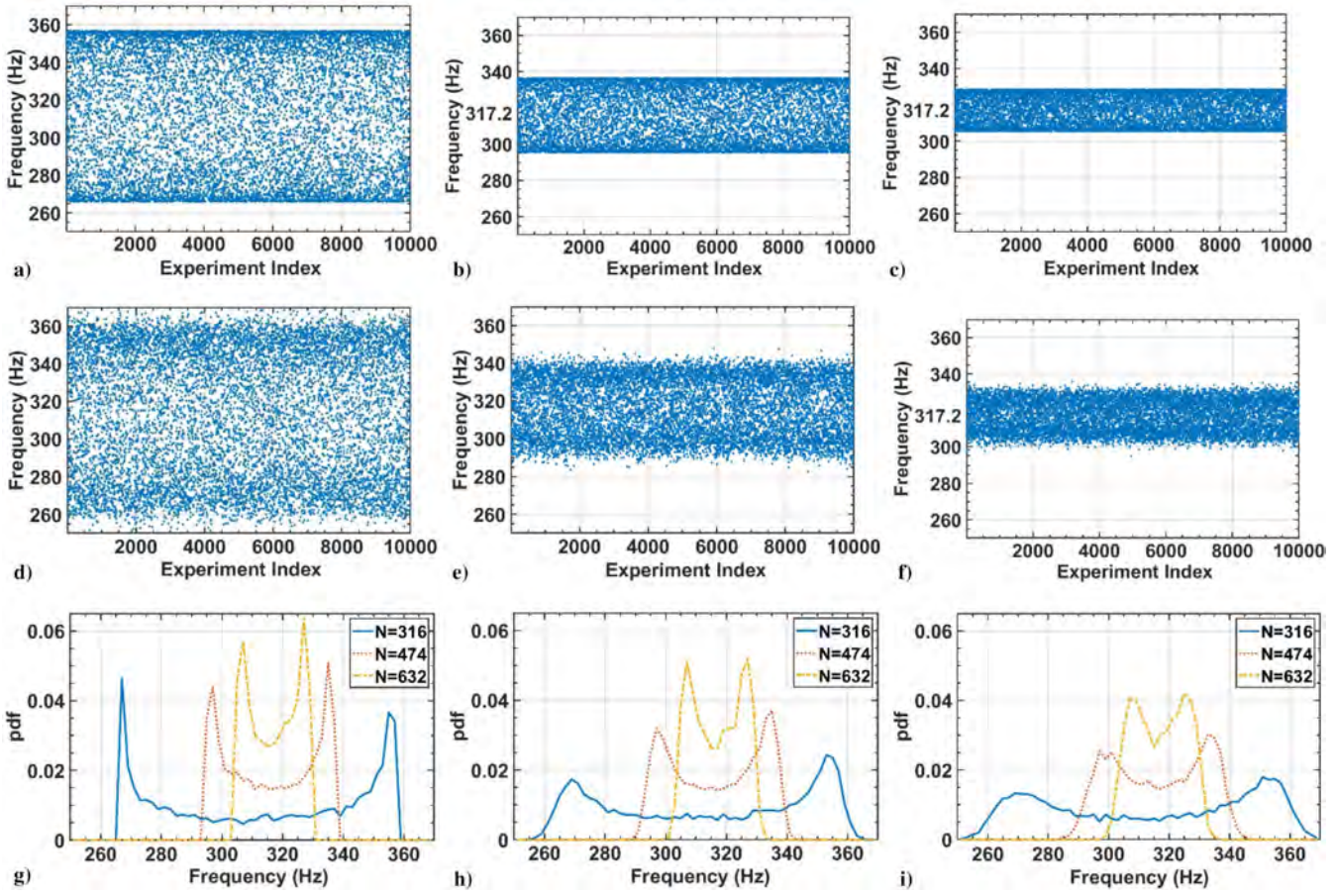

Fig. 9 The frequency estimation for step 2 with $\alpha = 0$ and a) $N = 316$, b) 474, and c) 632 and with $\alpha = 1.0$ and d) $N = 316$, e) 474, and f) 632, and the PDF of the estimated frequency for g) $\alpha = 0$, h) 0.6, and i) 1.0.

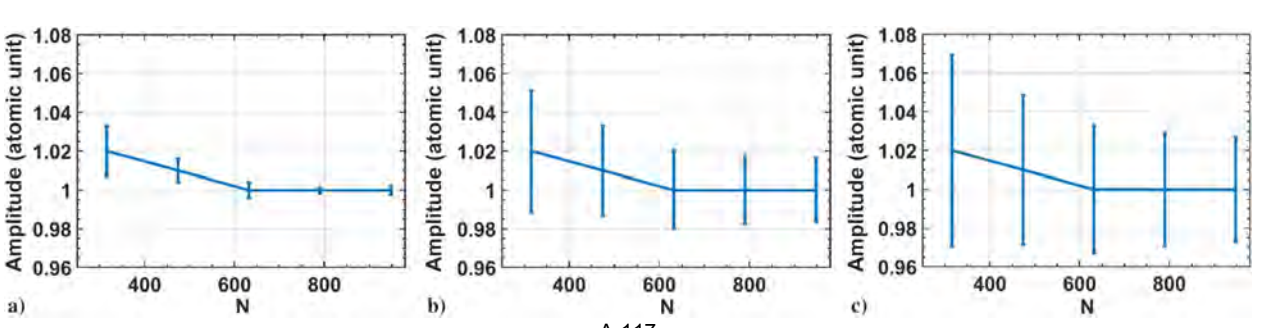

Fig. 10 The estimated amplitude for step 2 with a) $\alpha = 0$, b) $\alpha = 0.6$, and c) $\alpha = 1.0$.

amplitude converges almost exactly to the setting value even in the presence of noise with $N \geq 632$.

Figures 11a–11c show the estimated amplitude for step 2 with $\alpha = 0$. The scattering in the estimated amplitude, an indicator of the estimation error (or uncertainty), consistently decreases with the data length N. A similar observation is made for the estimated amplitude for step 2 at $\alpha = 1.0$, as shown in Figs. 11d–11f. Different from frequency estimation, the uncertainty in the estimated amplitude is substantially broadened by noise. The PDFs of the estimated amplitude appear Gaussian, as one can see from Figs. 11g–11i.

C. Effects of Noise

Figure 12a shows the mean and the standard deviation of the estimated frequency at different noise levels. Unbiased frequency estimation is achieved after step 2. Here, $N = 632$, corresponding to two pressure cycles. The estimation error (or uncertainty) in the frequency estimation is essentially insensitive to noise. Figure 12b shows the mean and the standard deviation of the estimated amplitude at different noise levels for step 2. The bias in the amplitude estimation slightly increases with the noise level α but remains below 0.5% at the SNR as low as 4 dB; however, the standard deviation in the estimated amplitude δP_m considerably increases with α. The error or uncertainty of the amplitude δP_m can be expressed as a second-order, curve-fitting polynomial of α in the form of $\delta P_m = 0.0071\alpha^2 + 0.0222\alpha + 0.0038$, with a fitting error of 3.5%, 3.4%, 1.1%, 0.5%, and 0.4% at $\alpha = 0$, 0.3, 0.6, 0.8, and 1.0, respectively.

V. Applications

The observer is evaluated on three different pressure signals characteristic of pressure oscillations due to combustion instabilities in three different real devices, one from a premixed propane/air channel combustor [19] and one each from two different liquid rocket engines supplied by two of the authors (Casiano and Jensen). Pressure oscillations on the channel combustor (signal 1) are quasi-steady, and the pressure amplitude sharply increases with the equivalence ratio beyond $\phi = 0.91$. It is also found that that the damping ratio ζ consistently decreases with ϕ from 0.70 and drops to the minimum at $\phi = 0.91$ [20]. Thus, we consider $\phi = 0.91$ as the onset of combustion instabilities. Different from thermoacoustic oscillations in

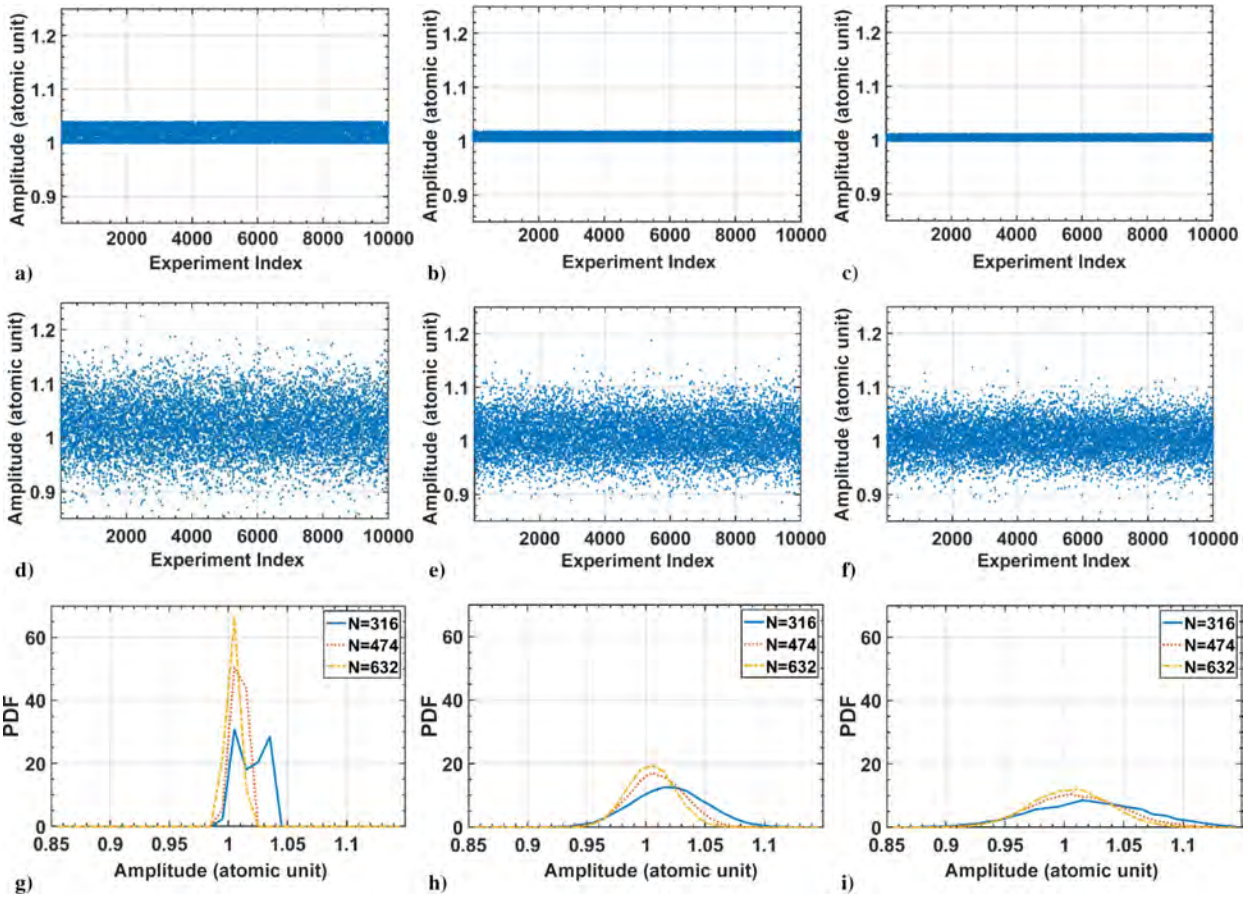

Fig. 11 The estimated amplitude for step 2 with $\alpha = 0$ and a) $N = 316$, b) 474, and c) 632 and with $\alpha = 1.0$ and d) $N = 316$, e) 474, and f) 632, and the PDF of the estimated amplitude for g) $\alpha = 0$, h) 0.6, and i) 1.0.

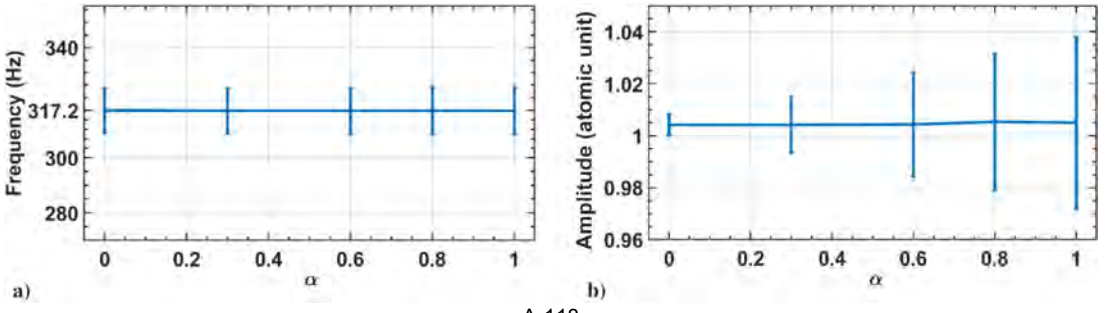

Fig. 12 Effects of noise on a) the frequency estimation and b) the amplitude estimation.

Downloaded by UNIVERSITY OF CINCINNATI on April 22, 2020 | http://arc.aiaa.org | DOI: 10.2514/1.B37896

signal 1, the other two pressure oscillations are linearly unstable; nearly periodic pressure oscillations grow out of low-amplitude, aperiodic background noise with the amplitude consistently increasing with time. The difference is that harmonic oscillations do not appear during the pressure growth of one of the signals (signal 2), while they quickly emerge during the pressure growth of the other (signal 3).

A. Quasi-Steady Pressure Oscillations (Signal 1)

Figure 13 displays pressure oscillations in signal 1 at the equivalence ratio $\phi = 0.91$, corresponding to excitation of the quarter-wave mode of the combustion chamber at approximately 88.8 Hz. The rig was previously described in [19]. The sampling frequency F_s is 20,000 Hz. There are about 225 samples within each pressure cycle. Also shown in Fig. 13 is the pressure amplitude computed with $N = 250$ and 500, respectively, with a 50% overlap between neighboring data segments. The magnified view in Figs. 13b and 13c suggests that the estimated amplitude well captures short-term variations in pressure oscillations.

Figure 14a shows the pressure spectrum computed with different data length N from less than one pressure cycle to six pressure cycles. One can see from Fig. 14b that the estimated frequency changes little with $N \geq 500$ (i.e., two pressure cycles). Figure 14c shows the decrease in the amplitude with N. This is expected as thermoacoustic oscillations do not occur at any single fixed frequency, the bandwidth consistently decreases with N (Fig. 2), and large variations in amplitude are increasingly filtered out with a larger N. To resolve the physical, cycle-to-cycle (or short-term) variations in the dominant frequency and amplitude, the intrinsic error (or uncertainty) of the observer must be kept sufficiently small.

The intrinsic error (or uncertainty) of the observer is parametrically determined by estimating the frequency and amplitude of a noise-contaminated sinusoid,

$$\tilde{p}(t) = P_{mN} \sin(2\pi F_{mN} t + \theta_0) + \alpha \mathcal{E}(-1, 1) \tag{6}$$

where F_{mN} and P_{mN} denote the mean frequency and the mean amplitude of the measured pressure estimated with the data length N. Similar to the parametric study in Sec. IV, 10,000 data sequences of N samples for $\tilde{p}(t)$ with the initial phase θ_0 uniformly distributed within $[0, 2\pi]$ are generated with F_{mN} and P_{mN}, and the frequency and amplitude are estimated for each data sequence. Figure 15 shows that the standard deviation of the estimated frequency (δF_m) is comparable to that of the experimental data at $N = 250$ (i.e., about one pressure cycle) but substantially smaller at $N = 500$ (i.e., about two pressure cycles). There is a 50% overlap between neighboring data segments. Thus, the data length of two pressure cycles, preferably with a 50% overlap between neighboring data segments, is well capable of resolving cycle-to-cycle (or short-term) variations in thermoacoustic oscillations.

Figure 16 shows that the standard deviation of the estimated amplitude (δP_m) for the noise-contaminated sinusoid [Eq. (6)] is more than one time higher than that of the experimental data, which is true even for a data length as short as one pressure cycle. There is a 50% overlap between neighboring data segments. Based on this parametric study, we recommend that for a reasonable balance between accuracy and the fast-tracking requirement the frequency and the amplitude of thermoacoustic oscillations be estimated every two pressure cycles with a 50% overlap between neighboring data segments.

B. Linearly Unstable Oscillations (Signal 2)

Displayed in Fig. 17 are pressure oscillations in signal 2, corresponding to excitation of the first tangential mode of the combustion chamber (approximately 2021 Hz) in a subscale, liquid-oxygen/liquid-hydrogen rocket engine. Pressure oscillations grow out of the broadband background noise at $t = \sim 4.1$ s. The sampling frequency F_s is 50,000 Hz. There are 25 samples within each pressure cycle. Also presented in Fig. 17 is the pressure amplitude computed with $N = 25$ and 50 with a 50% overlap between neighboring data segments. The pressure amplitude faithfully tracks pressure variations. Figure 18a shows the pressure spectrum computed with $N = 25, 50, 75, 100$, and 500 within the time window of [4.5 4.6] s. Within this period, pressure oscillations are quasi-stationary, i.e., free of large increases and decreases. The dominant frequency and the amplitude are accurately identified with $N = 25$, i.e., within one pressure cycle. Although the

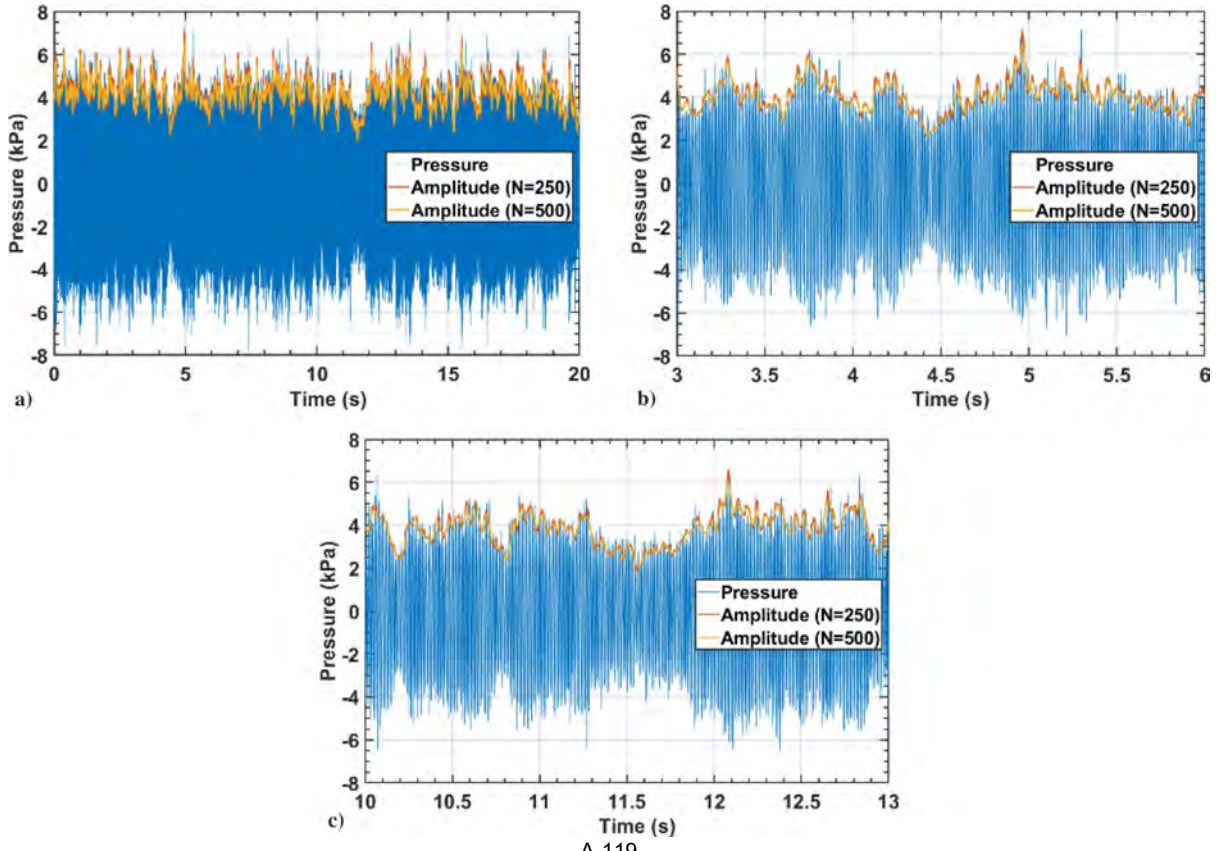

Fig. 13 Pressure and the estimated amplitude for signal 1 within a) [0 20] s, b) [3 6] s, and c) [10 13] s.

Downloaded by UNIVERSITY OF CINCINNATI on April 22, 2020 | http://arc.aiaa.org | DOI: 10.2514/1.B37896

Downloaded by UNIVERSITY OF CINCINNATI on April 22, 2020 | http://arc.aiaa.org | DOI: 10.2514/1.B37896

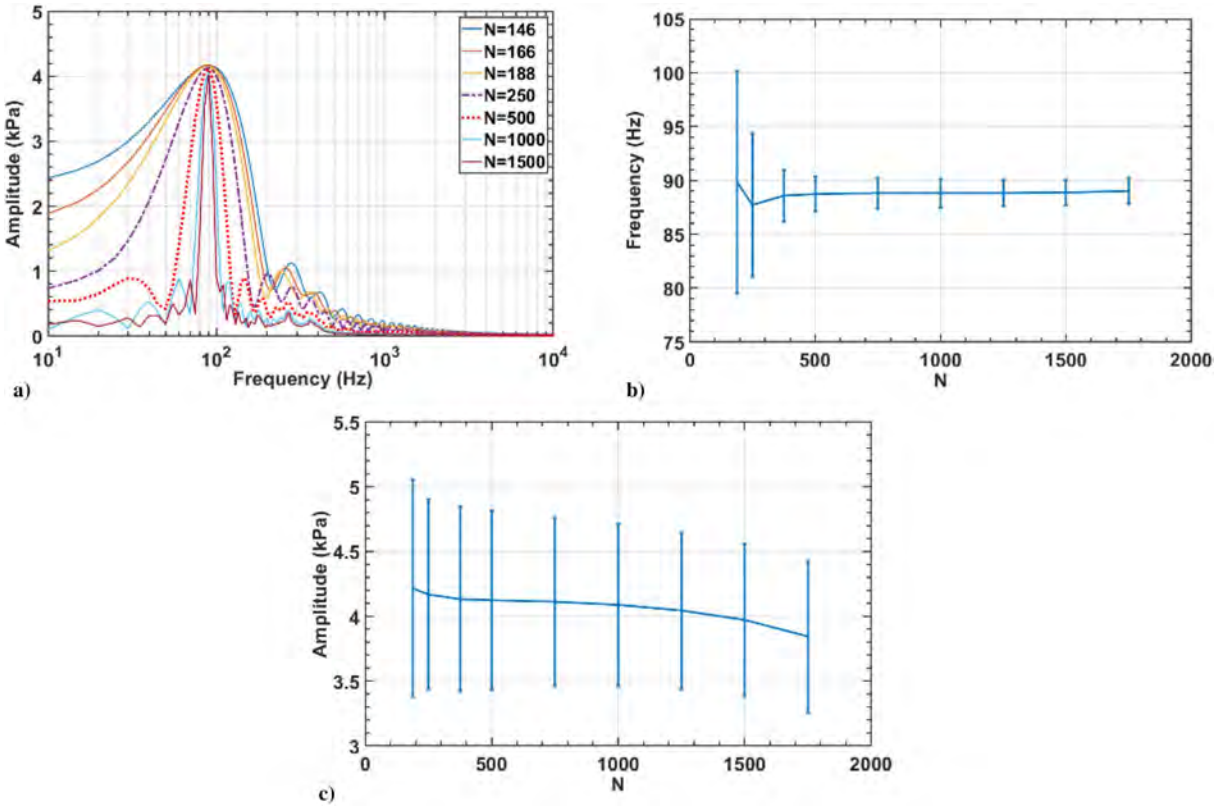

Fig. 14 a) The pressure spectrum, b) the dominant frequency, and c) the amplitude of thermoacoustic oscillations in the channel combustor at $\phi = 0.91$.

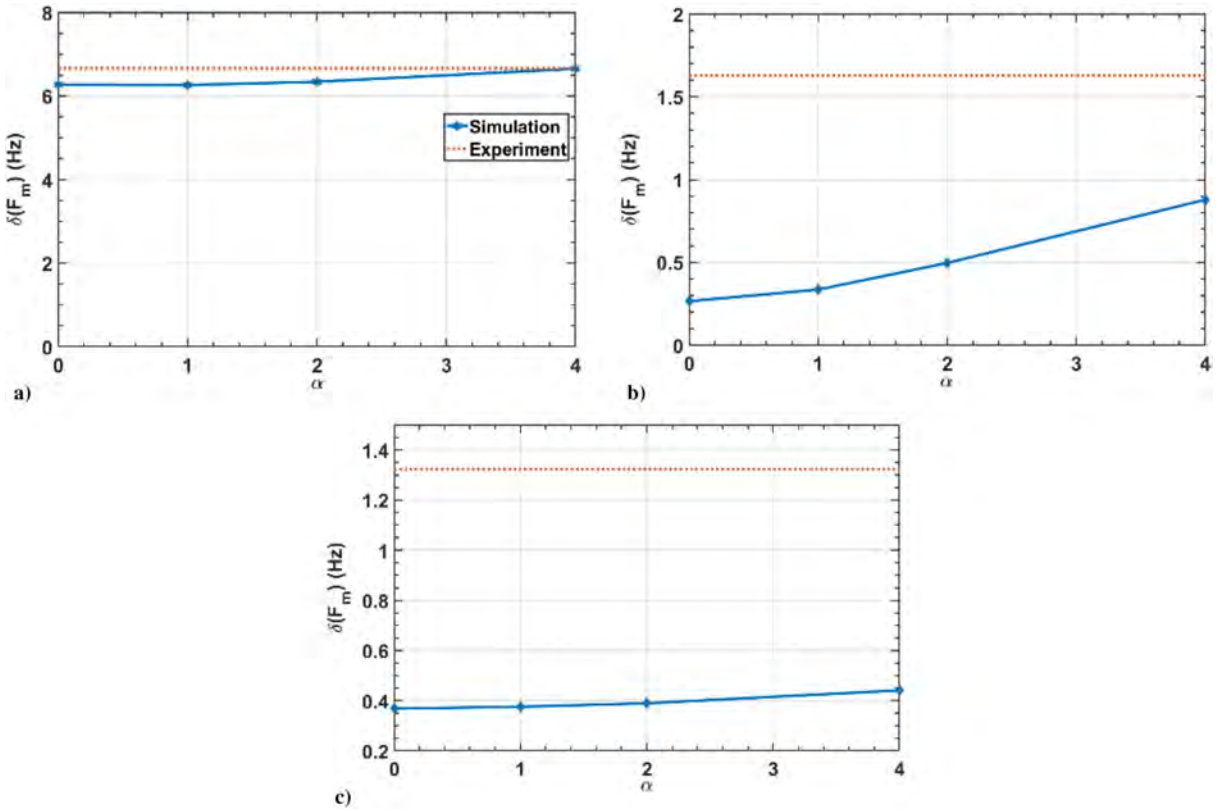

Fig. 15 The standard deviation of the estimated frequency with a) $N = 250$, b) $N = 500$, and c) $N = 1000$.

frequency and the amplitude can be identified within one pressure cycle, the variance in the estimation error is considerably larger than that estimated with $N = 50$, corresponding to two pressure cycles (see Fig. 18a). One can see from Fig. 18b that the large, cycle-to-cycle (i.e., short-term) variations in the frequency which are resolvable with $N = 50$ (i.e., two pressure cycles) are greatly attenuated when N is

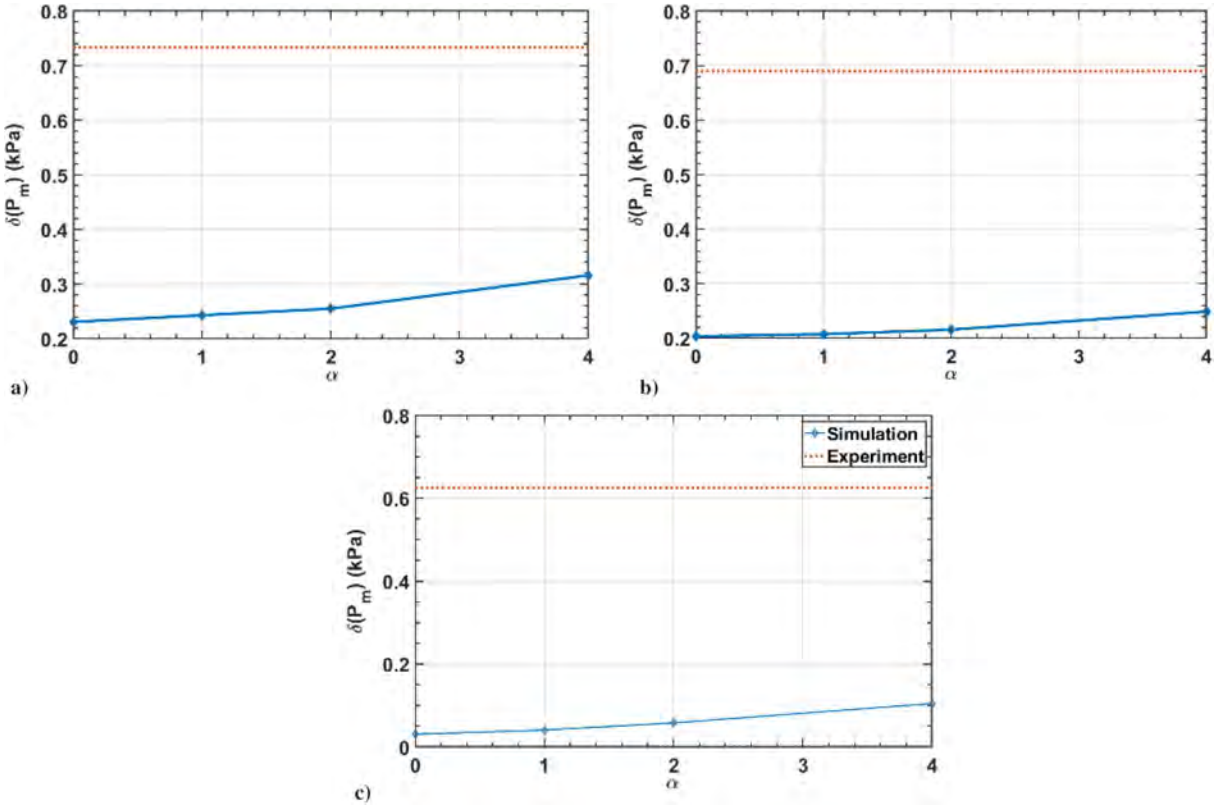

Fig. 16 The standard deviation of the estimated amplitude with a) $N = 250$, b) $N = 500$, and c) $N = 1000$.

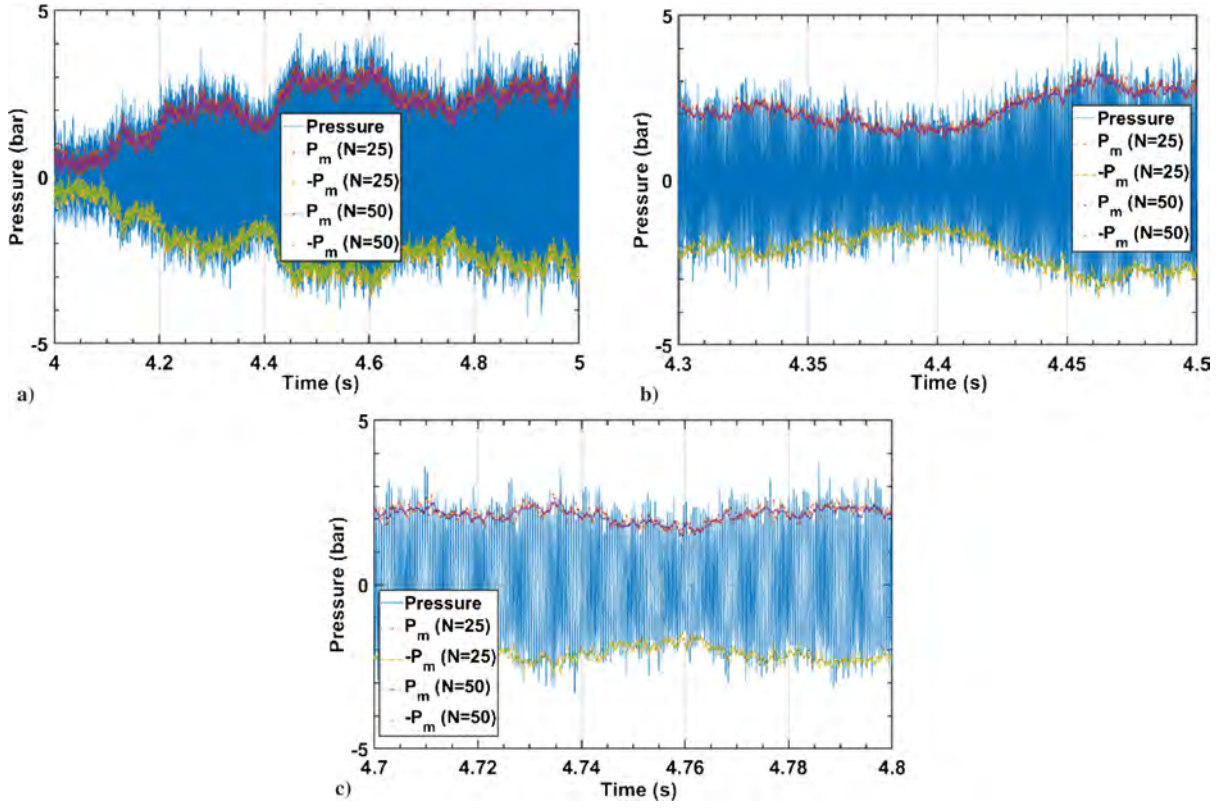

Fig. 17 Pressure oscillations in signal 2 within a) [4.0 5.0] s, b) [4.3 4.5] s, and c) [4.7 4.8] s.

increased to 75 (i.e., three pressure cycles). A similar observation is made on the amplitude estimation, as shown in Fig. 18c. With $N = 500$, corresponding to approximately 20 pressure cycles, only slow variations in pressure oscillations are captured, while short-term variations, which are resolvable with $N = 50$, 75, and 100, are smoothed out.

Downloaded by UNIVERSITY OF CINCINNATI on April 22, 2020 | http://arc.aiaa.org | DOI: 10.2514/1.B37896

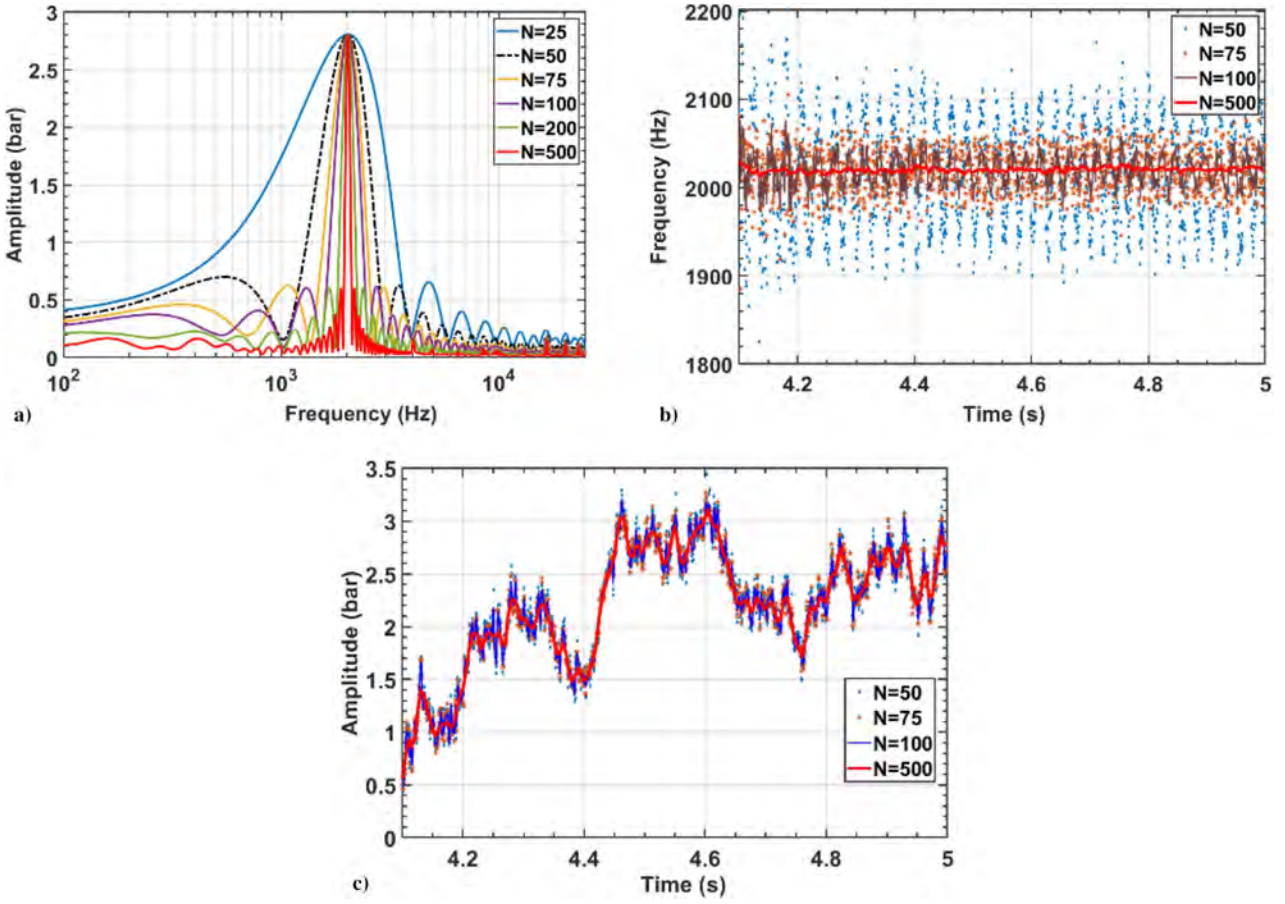

Fig. 18 a) The pressure spectrum computed within the observation window of [4.5 4.6] s, b) the estimated frequency, and c) the estimated amplitude.

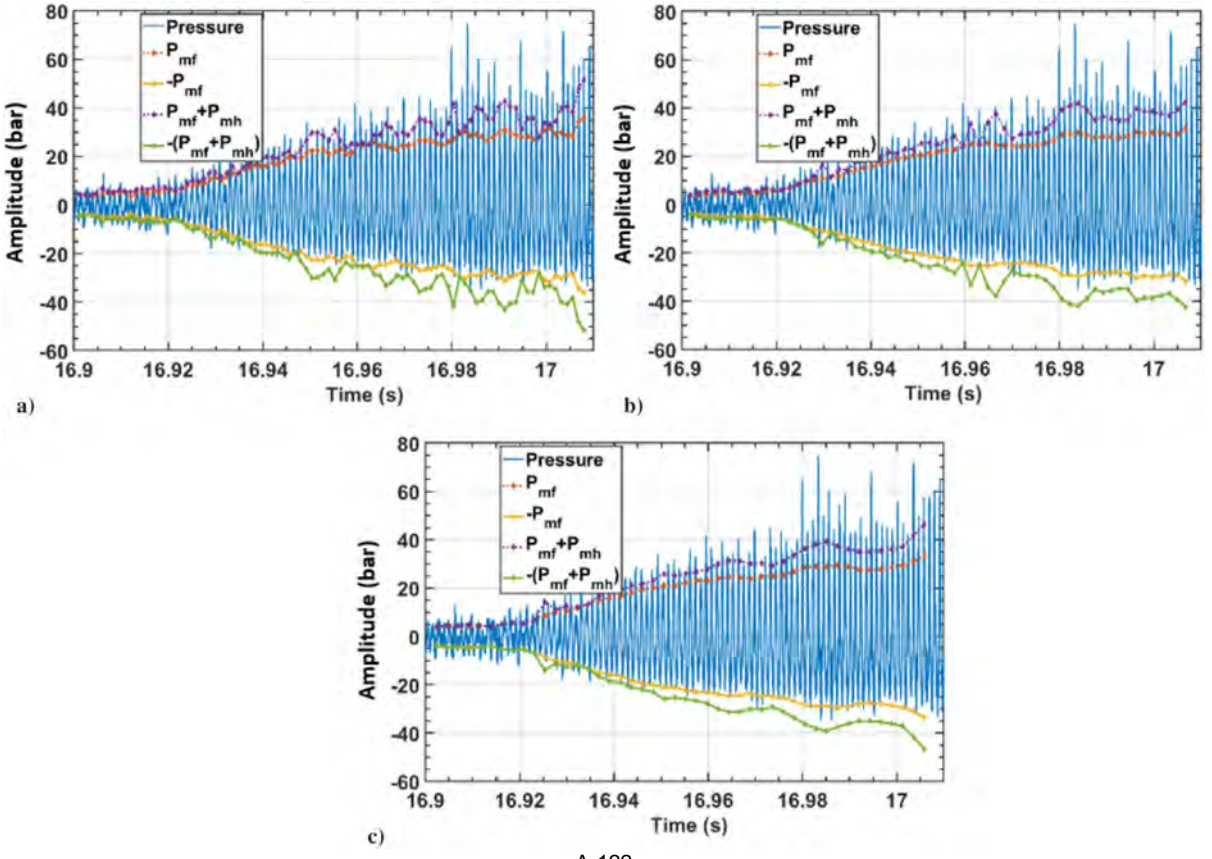

Fig. 19 Pressure for signal 3 and the pressure amplitude computed with a) $N = 240$, b) $N = 350$, and c) $N = 460$.

Downloaded by UNIVERSITY OF CINCINNATI on April 22, 2020 | http://arc.aiaa.org | DOI: 10.2514/1.B37896

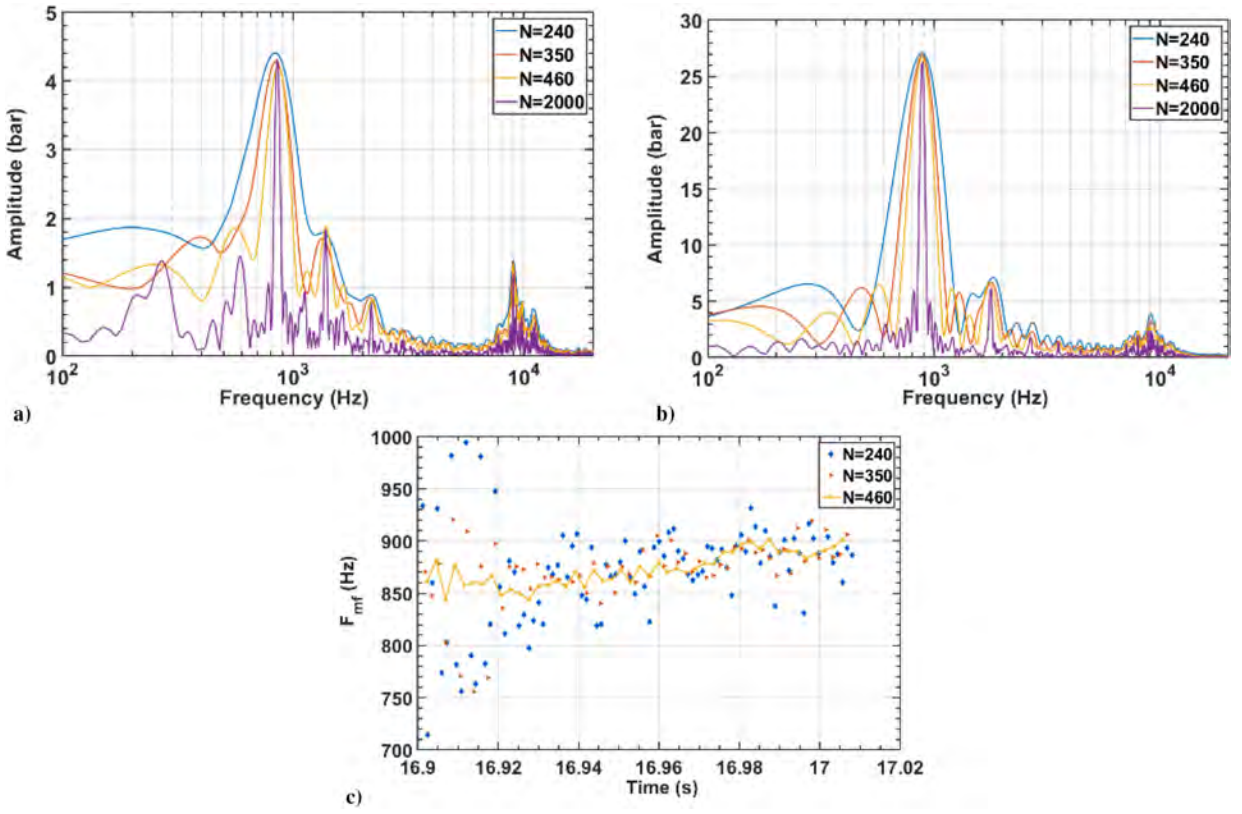

Fig. 20 The pressure spectrum within a) [16.90 16.92] s and b) [16.97 16.99] s, and c) the estimated fundamental frequency.

C. Unstable Oscillations with Harmonic Generation (Signal 3: Hydrocarbon Boost Oxygen-Rich Preburner)

Figure 19 shows pressure oscillations from the test data for the Hydrocarbon Boost Oxygen-Rich Preburner. The Hydrocarbon Boost program conducted tests of the oxygen-rich, staged, subscale preburner at Test Stand 2A at Edwards Air Force Base. The subscale preburner test campaign accomplished the first demonstrations of several key rocket engine technologies. This preburner was a combustion device incorporating the first domestic implementation of a diluent type preburner with an equivalent flow rate of approximately 40k lbf. The sampling frequency F_s is 100,000 Hz. Also displayed in Fig. 19 are P_{mf} and the sum of P_{mf} and P_{mh} (i.e., $P_{mf} + P_{mh}$), where P_{mf} and P_{mh} refer to the amplitude of the fundamental mode and its first harmonic, respectively. From the pressure spectrum shown in Figs. 20a and 20b, one can see that the fundamental frequency increases from approximately 853 Hz at $t = 16.91$ s to approximately 887 Hz at $t = 16.98$ s, with the amplitude from 4.2 to 27 bar. The nonlinearity in pressure oscillations is readily identifiable from the asymmetry in pressure oscillations around zero and the growth of P_{mh}. Figure 20a shows the pressure spectrum within a time window of [16.90 16.92] s, exhibiting a dominant mode at approximately 853 Hz as well as oscillations around 280, 550, 1380, 2180, and 39,000 Hz. By $t = 16.98$ s, the dominant mode at approximately 887 Hz grows to 27 bar with its first harmonic at approximately 1774 Hz to 6.3 bar, and the mode around 1380 Hz has disappeared. Such rapid variations cannot be captured if spectral analysis is conducted over a larger time window, say within [16.90 16.99] s. Figure 20c shows that F_{mf} slightly increases with time. The estimated frequency is substantially smoothed when the data length N is increased from 240 (about two pressure cycles) to 460 (about four pressure cycles).

VI. Conclusions

A three-step procedure (also referred to as the observer) with potentials for real-time applications is developed for fast and accurate determination of the dominant frequencies and amplitude of thermoacoustic oscillations. The observer is capable of much faster and more accurate estimation of the dominant frequencies and amplitude with a much shorter sample length than the discrete Fourier transform and the fast Fourier transform, with the spectral resolution no longer limited by the sampling frequency and the data length. The computational complexity can be orders-of-magnitude lower than that of DFT and much below that of FFT. The computational complexity can be further significantly reduced when the frequency ranges are known. The frequency estimation is unbiased after step 2 and the error (or uncertainty) is essentially insensitive to noise. A parametric study using the Monte Carlo method is conducted to assess effects of the data length and noise on the convergence and the estimation error (or uncertainty). The error (or uncertainty) in frequency estimation consistently decreases with the data length.

We have tested the observer on pressure oscillations of different characteristics of combustion instabilities on three propulsion devices, namely quasi-steady pressure oscillations (signal 1), linearly unstable pressure oscillations (signal 2), and unstable pressure oscillations with harmonic generations (signal 3). For quasi-steady pressure oscillations (signal 1), an estimation with the data length of two pressure cycles with a 50% overlap adequately resolves cycle-to-cycle (or short-term) variations in the frequency and the amplitude, which far exceed the intrinsic error (or uncertainty) of the observer. An unbiased estimation of the dominant frequency can be made with the data length as short as one pressure cycle. The mean frequency remains invariant with the data length, but the root mean square of the estimated frequency consistently decreases. The estimated amplitude decreases with the data length (or the observation window) because of the decreasing width of the main lobe of the modified sinc function and the finite bandwidth of thermoacoustic oscillations. For linearly unstable pressure oscillations (signal 2), the observer faithfully tracks the growth and variations of pressure oscillations with the data length of two pressure cycles. By increasing the data length (or the observation window), the large, cycle-to-cycle (i.e., short-term) variations in the frequency resolvable with a shorter observation window are increasingly attenuated, suggesting the importance of fast estimation with a short time window. For unstable oscillations with harmonic generation (signal 3), the growth of both the fundamental mode and the harmonics is faithfully resolved using the observer with the data

Downloaded by UNIVERSITY OF CINCINNATI on April 22, 2020 | http://arc.aiaa.org | DOI: 10.2514/1.B37896

length as short as two pressure cycles. The observer is capable of accurately resolving fast transience and simultaneous determination of the frequencies and amplitude of a large number of harmonics, making it a particularly useful tool for studying the onset of combustion instabilities, trigger instabilities, and highly nonlinear acoustics.

Acknowledgments

This work was funded, in part, by the U.S. Air Force Research Laboratory under contract numbers FA9300-18-C-2501 and FA8650-15-D-2518. Jensen's time was contributed under contract number FA9300-18-F-9000.

References

[1] Burnley, V. S., and Culick, F. E. C., "Influence of Random Excitations on Acoustic Instabilities in Combustion Chambers," *AIAA Journal*, Vol. 38, No. 8, 2000, pp. 1403–1410. https://doi.org/10.2514/2.1116

[2] Lieuwen, T. C., "Experimental Investigation of Limit-Cycle Oscillations in an Unstable Gas Turbine Combustor," *Journal of Propulsion and Power*, Vol. 18, No. 1, 2002, pp. 61–67. https://doi.org/10.2514/2.5898

[3] Okuno, Y., Small, M., and Gotoda, H., "Dynamics of Self-Excited Thermoacoustic Instability in a Combustion System: Pseudo-Periodic and High-Dimensional Nature," *Chaos: An Interdisciplinary Journal of Nonlinear Science*, Vol. 25, No. 4, 2015, Paper 043107. https://doi.org/10.1063/1.4914358

[4] Culick, F. E. C., *Unsteady Motions in Combustion Chambers for Propulsion Systems*, Research and Technology Organization, AGARDograph AG-AVT-039, 2006.

[5] Lieuwen, T., and Yang, V., *Combustion Instabilities in Gas Turbine Engines: Operational Experience, Fundamental Mechanisms, and Modeling*, Progress in Astronautics and Aeronautics, Vol. 210, AIAA, Reston, VA, 2005.

[6] Candel, S., "Combustion Dynamics and Control: Progress and Challenges," *Proceedings of the Combustion Institute*, Vol. 29, No. 1, 2002, pp. 1–28. https://doi.org/10.1016/S1540-7489(02)80007-4

[7] Dowling, A. P., "Aeroacoustics and Active Noise Control," von Kármán Inst. for Fluid Dynamics, Lecture Series 1997-07, 1997.

[8] Neumeier, Y., Markopoulos, N., and Zinn, B. T., "A Procedure for Real-Time Mode Decomposition, Observation, and Prediction for Active Control of Combustion Instabilities," *Proceedings of the 1997 IEEE International Conference on Control Applications*, IEEE, New York, Oct. 1997, pp. 818–823. https://doi.org/10.1109/CCA.1997.627762

[9] Yi, T., and Gutmark, E. J., "Adaptive Control of Combustion Instability Based on Dominant Acoustic Modes Reconstruction," *Combustion Science and Technology*, Vol. 180, No. 2, 2007, pp. 249–263. https://doi.org/10.1080/00102200701600986

[10] Yi, T., and Gutmark, E. J., "Online Prediction of the Onset of Combustion Instabilities Based on the Computation of Damping Ratios," *Journal of Sound and Vibration*, Vol. 310, Nos. 1–5, 2008, pp. 442–447. https://doi.org/10.1016/j.jsv.2007.07.072

[11] Lieuwen, T., "Online Combustor Stability Margin Assessment Using Dynamic Pressure Data," *ASME Journal of Engineering for Gas Turbines and Power*, Vol. 127, No. 3, 2005, pp. 478–482. https://doi.org/10.1115/1.1850493

[12] Quinn, B. G., "Estimating Frequency by Interpolation Using Fourier Coefficients," *IEEE Transactions on Signal Processing*, Vol. 42, No. 5, 1994, pp. 1264–1268. https://doi.org/10.1109/78.295186

[13] Quinn, B. G., "Estimation of Frequency, Amplitude, and Phase from the DFT of a Time Series," *IEEE Transactions on Signal Processing*, Vol. 45, No. 3, 1997, pp. 814–817. https://doi.org/10.1109/78.558515

[14] Aboutanios, E., and Mulgrew, B., "Iterative Frequency Estimation by Interpolation on Fourier Coefficients," *IEEE Transactions on Signal Processing*, Vol. 53, No. 4, 2005, pp. 1237–1242. https://doi.org/10.1109/TSP.2005.843719

[15] Nehorai, A., "A Minimal Parameter Adaptive Notch Filter with Constrained Poles and Zeros," *IEEE Transactions on Acoustics, Speech, and Signal Processing*, Vol. 33, No. 4, 1985, pp. 983–996. https://doi.org/10.1109/TASSP.1985.1164643

[16] Li, G., "A Stable and Efficient Adaptive Notch Filter for Direct Frequency Estimation," *IEEE Transactions on Signal Processing*, Vol. 45, No. 8, 1997, pp. 2001–2009. https://doi.org/10.1109/78.611196

[17] Routray, A., Pradhan, A. K., and Rao, K. P., "A Novel Kalman Filter for Frequency Estimation of Distorted Signals in Power Systems," *IEEE Transactions on Instrumentation and Measurement*, Vol. 51, No. 3, 2002, pp. 469–479. https://doi.org/10.1109/TIM.2002.1017717

[18] Dash, P. K., Jena, R. K., Panda, G., and Routray, A., "An Extended Complex Kalman Filter for Frequency Measurement of Distorted Signals," *IEEE Transactions on Instrumentation and Measurement*, Vol. 49, No. 4, 2000, pp. 746–753. https://doi.org/10.1109/19.863918

[19] Caswell, A. W., Rankin, B. A., Huelskamp, B., Jiang, N., Lynch, A., Belovich, V., and Gord, J. R., "Spatiotemporal Characterization of Flame-Vortex Interactions in Bluff-Body Stabilized Turbulent Premixed Flames Using Simultaneous High-Repetition-Rate OH-PLIF and PIV," AIAA Paper 2015-0424, Jan. 2015.

[20] Yi, T., Fugger, C., Jensen, R. J., Caswell, A. W., Talley, D. G., Casiano, M. J., and Roy, S., "Characterization of Pressure Oscillations at the Approach of Combustion Instabilities," *AIAA SciTech Forum*, AIAA Paper 2020-0173, Jan. 2020.

J. C. Oefelein
Associate Editor

Downloaded by UNIVERSITY OF CINCINNATI on April 22, 2020 | http://arc.aiaa.org | DOI: 10.2514/1.B37896

AIAA SciTech
13-17 January 2014, National Harbor, Maryland
52nd Aerospace Sciences Meeting

CrossMark
click for updates

Development of a Facility for Combustion Stability Experiments at Supercritical Pressure

Jeffrey L. Wegener[1]
University of California at Los Angeles, CA 90095

Ivett A. Leyva[2]
AFRL/RQRE, Edwards AFB, CA 93524

David J. Forliti[3]
Sierra Lobo, Inc. supporting AFRL/RQRC, Edwards AFB, CA 93524

and
Douglas G. Talley[4]
AFRL/RQRC, Edwards AFB, CA 93524

Downloaded by Doug Talley on September 19, 2016 | http://arc.aiaa.org | DOI: 10.2514/6.2014-0137

Combustion instability in liquid rocket engines can have severe consequences including degraded performance, accelerated component wear, and potentially catastrophic failure. High-frequency instabilities, which are generally the most harmful in liquid rocket engines, can be driven by interactions between disturbances associated with transverse acoustic resonances and the combustion process. The combustion response to acoustic perturbation is a critical component of the instabililty mechanism, and is in general not well understood. The current paper describes an experimental facility at the Air Force Research Laboratory (AFRL) at Edwards Air Force Base that is intended to investigate the coupling between transverse acoustic resonances and single/multiple liquid rocket engine injector flames. Critical aspects of the facility will be described, including the capability to operate at supercritical pressures that are relevant to high-performance liquid rocket engines, accurately-controlled and cryogenically-conditioned propellants, and optical access to facilitate the use of advanced diagnostics. The transverse acoustic resonance is induced through the use of carefully-controlled piezoelectric sirens, allowing monochromatic excitation across a range of amplitudes at a number of discrete frequencies. The location of the flame within the acoustic resonance mode shape can also be varied through relative phase control of the two acoustic sources. The operating space of the facility, for oxygen and hydrogen operation, will be described. Preliminary nonreacting and reacting data will also be presented to demonstrate the quality of operation of this facility. It is anticipated that future results generated using this facility will provide both fundamental insight into the acoustic-flame interactions as well as provide a database useful for validating combustion instability models.

Nomenclature

A	=	area
c	=	speed of sound

[1] Graduate Student, Department of Mechanical and Aerospace Engineering, UCLA, Los Angeles, CA 90095 student member.
[2] Technical Advisor, AFRL/RQRE, 4 Draco Drive, Building 8351, Edwards AFB, CA 93524, Associate Fellow.
[3] Research Scientist, Sierra Lobo, Inc., 4 Draco Drive, Building 8451, Edwards AFB, CA 93524, senior member.
[4] Lead, Combustion Dynamics Group, AFRL/RQRC., 4 Draco Drive, Building 8451, Edwards AFB, CA 93524, Associate Fellow.

Distribution Statement A: Approved for public release; distribution is unlimited.
Public Affairs Case Number: 13550

This material is declared a work of the U.S. Government and is not subject to copyright protection in the United States.

D_1 = inner injector inner diameter
D_2 = inner injector outer diameter
D_3 = outer injector inner diameter
D_4 = outer injector outer diameter
dt = time step
f_F = acoustic frequency
m = waveguide flare constant
p_c = mean chamber pressure
p' = acoustic pressure perturbation amplitude
t = inner post thickness
u' = acoustic velocity perturbation amplitude
x = streamwise (longitudinal) coordinate axis
y = spanwise (transverse) coordinate axis
z = depthwise coordinate axis

Downloaded by Doug Talley on September 19, 2016 | http://arc.aiaa.org | DOI: 10.2514/6.2014-0137

I. Introduction

LIQUID rocket engines exhibit challenging scientific problems which have been the subject of extensive efforts over several decades. A fundamental understanding of these problems remains incomplete for several phenomena, with combustion instability being a critical example. This lack of understanding has caused delays and budget increases in rocket engine development programs. The inability to predict combustion instabilities in particular, requires expensive iterative testing as part of the development cycle.

Physics-based modeling and understanding of the problem have potential to improve the prediction of combustion instability, leading to a simplified design cycle requiring fewer redesign iterations. Verification and validation of numerical models for combustion stability require advanced bench-scale experiments to serve two primary purposes. First, these experiments must improve fundamental knowledge of the underlying physics of combustion instability. Combustion instability has been investigated in a wide range of scenarios and typically involves a coupling between hydrodynamic instabilities, unsteady heat release, and acoustic disturbances[1]. Liquid rocket engine (LRE) injectors create non-premixed flames, relying on turbulent mixing within shear layers which exhibit velocity and heat release oscillations that can couple with chamber acoustics. Characterizing these oscillations in terms of frequencies and amplitudes from detailed experimental measurements and data analysis will improve the ability to predict these values, and indicate the likelihood of an oscillation giving rise to combustion instability. Second, these experiments must provide data for validation of computational models. This requirement drives the need for high-fidelity measurements and well-characterized boundary conditions.

Fundamental experiments exploring combustion stability in conditions similar to that of a liquid rocket engine (LRE) require challenging systems, including cryogenic propellants and supercritical chamber pressure operation, among others. To meet these requirements, a new combustion stability experimental facility was recently constructed at the Air Force Research Laboratory (AFRL) at Edwards Air Force Base. The development of this facility was based on experience gained from an existing nonreactive facility at AFRL[2-4]. Insight was also gained from a small number of existing combustors which create LRE conditions in sub-scale tests. These tests involve total mass flow rates which are often orders of magnitude lower than a typical LRE and contain five or fewer injector elements. But, in order to employ detailed experimental methods, such as high-speed diagnostics and acoustic control systems, a variety of hardware designs have been used. Five modern combustors are particularly relavant for comparison with the new combustion stability facility. These are the Multi-injector Combustor (MIC) and the Very High Amplitude Modulator (VHAM) facility, both operated jointly by ONERA and CNRS, the Common Research Combustor (CRC) operated jointly by CNRS and DLR, the BKH combustor operated by DLR, and the Continuously Variable Resonance Combustor (CVRC) operated by Purdue University.

The CRC originated in 2002 from the efforts of a German-French working group which now operates identical experimental combustors at the Research Institute for Equilibrium Systems (IRPHE) in Marseilles, France and DLR in Lampoldshausen, Germany. The CRC injects propellant from one side of a flat, cylindrically shaped chamber through a single injector which is $1/10^{th}$ scale of a typical LRE injector. With high-speed shadowgraphy and OH* chemiluminescence imaging, the dynamics of a single LOx/H_2 flame were investigated to fundamentally relate spatial and temporal heat release oscillations to pressure oscillations controlled by external acoustic forcing. A single injector element though, provides only partial representation of thermoacoustic instabilities occurring in LREs that contain multiple injectors and interactions between adjacent flames.

The BKH combustor is part of a recently constructed facility at DLR Lampoldshausen, Germany, which focuses on high-frequency combustion instability for LO_x/H_2 conditions[5,6]. This combustor includes five shear coaxial injectors in a cross formation to investigate interactions between neighboring flames. The MIC, located in Paris, France, shares many design features with the BKH combustor. The MIC uses multiple injectors, but in a linear arrangement to isolate interactions between pairs of flames using two-dimensional imaging[7,8]. Unless utilizing laser sheet flame illumination, a cross formation prevents one from distinguishing between foreground and background flames when viewing OH* emission images.

The VHAM facility is a modified version of the MIC which creates much greater acoustic pressure amplitudes in an effort to replicate the high-amplitude oscillations documented in actual LRE combustion instabilities[9]. The VHAM facility uses a toothed wheel to periodically block gas flow through exhaust nozzles, creating high-pressure amplitudes inside the combustion chamber. The toothed-wheel exhaust nozzle technique is also employed in the MIC, BKH, and CRC designs for the same purpose. With this method, the periodic nozzle imposes an acoustic boundary condition on the chamber wall, where the acoustic frequency is controlled by the wheel speed. The resulting pressure perturbation amplitude though, is not independently controlled, and is instead determined by hardware geometry such as nozzle diameter and tooth profile design. In the MIC, BKH, and CRC configurations, the toothed wheel is placed over a secondary exhaust nozzle which is located on the side of the chamber, perpendicular to the primary exhaust nozzle. The VHAM does not use secondary nozzles and two primary exhaust nozzles located at the end of the chamber are periodically blocked by a common toothed wheel. This alternative design was used to create pressure amplitudes as high as 20% of p_{cc} in the VHAM, whereas previous experience with the smaller amplitudes of the MIC design yielded limited flame response[9].

Controlled acoustic excitation in the manner described above allows a partial decoupling of a portion of the combustion instability feedback loop. Without an external acoustic source, chamber pressure perturbations exist due to combustion instabilities alone, and these natural changes in pressure cause further pulsations in combustion and heat release rate via oscillations in propellant flow and mixing rates. This mechanism is best represented in three steps as shown in Fig. 1. As flow oscillations represented by u' create fluctuations in propellant mixing, unsteady heat release is produced, represented by q' in Fig. 1. Then, unsteady heat release induces acoustic pressure perturbations which may resonate within the combustion chamber. Acoustics may influence the propellant mixing process and create a feedback mechanism. In this way, the flame serves as a source. But, when controlled acoustic excitation contributes to chamber acoustics, feedback dependencies are partly disassociated because a second source of acoustics is added. This allows one to investigate the effects of acoustic waves on fluid dynamic instability and unsteady heat release by varying acoustic pressure amplitude and frequency. With this strategy, the degree to which perturbation amplitudes and their inherent frequencies can be varied is highly dependent on the specific design used for external acoustic forcing.

In contrast to the nozzle modulation method used by all four aforementioned combustors, the CVRC of Purdue uses an acoustic control system relying on variable injector geometry[10]. By altering the size of the oxidizer plenum, the resonant frequency of the injector flow is controlled such that chamber pressure amplitudes range from less than 10% to 60% of the chamber pressure were achieved. The highest pressure amplitudes are achieved when the oscillation frequency of the injector matches the chamber pressure oscillation frequency, whereas a mismatch dampens the chamber mode. Thus, the CVRC design forgoes the electro-mechanical system of a typical acoustic source, and instead relies on injector flow oscillations to create heat release oscillations in the reaction zone. A family of chamber geometries can be investigated; some are stable and some are not. This method reliably induces high-amplitude instability, but requires mindful choice of fuel species and propellant flow conditions to indirectly manipulate the preferred frequency and amplitude of the instability.

The current endeavor concentrates on operational flexibility. The importance of variable injector configurations, propellant flow conditions, and acoustic excitation motivated the combustion stability facility design to offer a wide range of conditions in these three areas. A single injector is used in a modular flange, allowing for multiple injectors in future work. Second, propellant temperatures, and thus densities, are widely variable by employing cryogenic heat exchangers to cool ambient temperature gaseous propellants to the desired temperatures. Lastly, a pair of piezoelectric sirens serve as acoustic sources with variable acoustic pressure amplitudes and a range of forcing frequencies. This approach allows for separate control of amplitude and frequency.

II. Experimental Facility

The combustion stability facility takes on the complexities of a complete LRE test stand at subscale. All data acquisition and control system (DACS) hardware and user interfaces are located in a remote control room. Thus, the infrastructure, plumbing, and electrical designs necessary to realize this facility are extensive. This description

Downloaded by Doug Talley on September 19, 2016 | http://arc.aiaa.org | DOI: 10.2514/6.2014-0137

though, will be limited to features having a direct influence on the experimental environment. These include the combustion chamber, cryogenic heat exchangers and propellant supply systems, the acoustic excitation system, and high-speed imaging.

A. Combustion Chamber

Similar to the previously existing chamber used in nonreactive AFRL work[2,11], the chamber is designed as a chamber within another chamber. The inner chamber creates a near ideal environment for one-dimensional acoustic wave resonance, but is not sealed from the surrounding volume. This surrounding volume is the outer chamber, which has the structural integrity to withstand operating pressures of 1500 psi (=10.34 MPa). Thick walls and windows are not necessary for the inner chamber, allowing more freedom for placing injectors and integrating new injector designs. A CAD rendering of the chamber assembly is shown in Fig. 2, and a photograph of the completed facility is shown in Fig. 3 with the chamber integrated into the apparatus.

The outer chamber is fabricated from a forged Naval brass alloy and has an octagon shape to offer optical access from multiple views. The current configuration contains six windows, which includes large windows in the front and rear walls of the chamber and four smaller windows located at each corner of the outer chamber. The large windows are made of sapphire, while the smaller windows are made of quartz. Large opening in the two remaining chamber side walls are used for acoustic excitation attachments. The injector assembly and exhaust port are located at the top and bottom of the outer chamber, respectively, creating downward propellant flows which exit the combustor through a 4.8 mm exhaust orifice, the chamber's only exhaust path.

The central part of the inner chamber, where the injector is located, is a rectangular volume open to transverse acoustic excitation from the left and right. The inner chamber depth is 20.32 mm and the height is 36.07 mm, making room for subscale injectors only. The transverse width is much larger, reaching 0.82 m from the left acoustic source to the right acoustic source. This dimension makes the inner chamber volume large in comparison to the size of the combustion zone. One should also note that although the inner chamber cross sectional area is 20.32 mm × 36.07 mm near the injector, the far left and far right areas of the inner chamber expand to a large circular area in order to house each acoustic driver.Two quartz inner chamber windows separate the inner chamber from the outer chamber, and because these windows need not withstand a large pressure differential, small holes are located throughout the rear inner window. Hence dynamic pressure transducers and thermocouples are placed in these holes to diagnose the region near the flame by way of placement directly through the window. At the upper wall of the inner chamber, a gaseous nitrogen plenum provides two flows parallel to propellant flows. First, window cooling flows enter the inner chamber through slotted holes above the windows. Second, a propellant coflow system provides gaseous nitrogen to the region surrounding the flame by entering the chamber through dozens of 0.48 mm holes in a circular pattern around the injector.

B. Fluid Supply Systems

In a facility where propellant density control is crucial in achieving a set of experimental objectives, propellant temperature and pressure are paramount. In this case, the propellant pressure at the injector exit is treated as equal to the chamber pressure. The propellant temperature, though, is determined by the oxygen and hydrogen supply systems. Liquid rocket engine propellant tanks often hold fuel and oxidizer at cryogenic states, but this facility instead relies on ambient temperature propellant tanks providing high-pressure oxygen and hydrogen. Cryogenic heat exchangers then cool the propellants to the desired state. Thus, fluid supply system descriptions will focus on chamber pressurization techniques and cryogenic heat exchangers in order to understand propellant systems as a whole.

As in an LRE, similar experimental systems[5,9] have relied on combustion for chamber pressurization. But, when using subscale injectors and propellant flow rates of 10 g/s or less, combustion alone will not produce the high pressures seen in actual LREs. The current endeavor indeed maintains low flow rates, and also utilizes a relatively large chamber volume as explained in the previous section. Thus, an added source of mass flow must exist in order to achieve desired pressures and densities, which is a more precise technique to control the mean chamber pressure, rather than with combustion alone. A nitrogen chamber pressurization system serves this purpose by entering the chamber through multiple ports in the outer chamber wall, and chamber pressure is set using a variable control valve in the nitrogen supply system. Flow out of the chamber is restricted by the exhaust orifice. This technique adds freedom for designing a large array experimental conditions, because chamber pressure is controlled independent of propellant flow conditions. The source of chamber pressurization is partly decoupled from the combustion process.

With propellant pressure determined by chamber pressure, propellant flow rate and temperature are left to be controlled by the propellant feed system. First, flow rate is set using a remote needle valve followed by a mass flow meter (Porter 123 series), and both of these components are located upstream from the heat exchangers such that

Downloaded by Doug Talley on September 19, 2016 | http://arc.aiaa.org | DOI: 10.2514/6.2014-0137

these components operate on gaseous propellants at nominal room temperature. Maximum mass flow rates are 0.7 g/s and 10 g/s for hydrogen and oxygen, respectively. Downstream of the flow meters, hydrogen and oxygen pass through individual heat exchangers. Both heat exchangers operate under similar principles where propellant flow passes through a coiled tube which is cooled by liquid nitrogen. The oxygen heat exchanger is shown in Fig. 4 and the hydrogen heat exchanger is shown in Fig. 5. In the case of the oxygen heat exchanger, the propellant tube is coiled inside of a casting which also contains a coiled tube for liquid nitrogen flow. Electric heaters are mounted to the aluminum casting to offer additional energy in the event that the casting is chilled below the target temperature. The heating system consists of six heater elements individually controlled by a closed-loop control system written in LabVIEW. In this way, coolant control valves are set to slightly sub-cool the casting using liquid nitrogen, reducing the process gas to a temperature 2 to 5 K below the target temperature. The heater power is then manually applied and automatically adjusted to hold the process fluid outlet temperature equal to the target temperature with an accuracy of ±1 K. The oxygen heat exchanger was designed and constructed by Sierra Lobo, Inc. For the hydrogen heat exchanger, the propellant tube is immersed directly within a liquid nitrogen bath and heaters are not included. The temperature of the process fluid in each heat exchanger is controlled by individually regulating liquid nitrogen flow rates through each system with separate control valves. Although the propellant heat exchangers offer variable control of temperature, a conditioning process is required to cool plumbing hardware prior to achieving a desired, stable temperature. The temperature conditioning process is performed using nitrogen as a surrogate process fluid in order to minimize propellant usage.

To characterize the capability of each heat exchanger, the minimum achievable temperature was measured for a range of chamber pressures. This was done by utilizing high liquid nitrogen flow rates over a long period of time to cool the hardware of each system. Thus, the injector flow temperature for each process fluid was minimized, representing a low temperature limit on the facility operating space. The results from this effort are shown in Fig. 6 for oxygen, where minimum temperature is shown to have a small dependence on chamber pressure. An oxygen density contour is the background of Fig. 6, showing that a liquid phase is achievable for $p_c < p_{crit,Ox}$, where $p_{crit,Ox}$ = 731 psia (=5.04 MPa). Mass flow rate is shown to have a negative correlation with temperature. Similar measurements were made with the hydrogen propellant system, but to perform these tests safely, helium was used as a surrogate. Minimum helium temperatures are shown in Fig. 7, superimposed on a hydrogen density contour map. For both oxygen and hydrogen, the minimum achievable temperature falls between 110 and 120 K with a primary dependence on propellant flow rate and a minor dependence on chamber pressure.

To formalize a range of possible operating conditions for the new facility, a parametric map of propellant density ratio S versus chamber pressure p_c is shown in Fig. 8. The oxygen and hydrogen density limits required to calculate S were determined using temperature limits from a heat exchanger characterization study. The upper temperature limit was taken as room temperature, while the lower limit is the minimum achievable propellant temperature ascertained from the heat exchanger characterization study, i.e. Figs. 6 and 7. To create Fig. 8, the resulting limits of S were then plotted for two-phase LO_x-GH_2 flow, single-phase GO_x-GH_2 flow, and flows in which $p_c > p_{crit,Ox}$.

The injector consists of a single shear-coaxial element designed for hydrogen flow in the annulus and oxygen flow in the center. In terms of total cross-sectional area, the injector is $1/10^{th}$ scale of the J-2 engine, for example. An injector of this size is challenging to manufacture, but is used here to achieve jet velocities and Reynolds numbers with an order of magnitude similar to an actual LRE while maintaining much smaller propellant mass flow rates. The cross sectional dimensions of the injector are shown in Fig. 9. The outer to inner jet area ratio is 1.68. The inner post thickness to inner diameter ratio t/D_1 has a value of 0.27, which prevents the inner shear layer from behaving purely as the meeting of co-flowing fluids. Instead, a recirculation zone is expected to form at the exit of the injector between the outer and inner jets. The length of the inner and outer injectors are sufficient to create fully developed turbulent flow at the exit for all conditions of interest here.

A comparison of the inner jet Reynolds number Re_{ij} and the outer jet Reynolds number Re_{oj} for similar research combustors is shown in Fig. 10, with operating points of actual oxygen-hydrogen LREs. Operating spaces of four other combustion instability research facilities are shown, including the BKH combustor of DLR, Germany, the Common Research Combustor (CRC) of CNRS, France and DLR, Germany, the Multi-Injector Combustor (MIC) of ONERA and CNRS, France, and the Cryogenic Combustion Laboratory (CCL) of Pennsylvania State University, USA. These facilities were specifically chosen for comparison because detailed flow conditions for oxygen-hydrogen stability experiments for shear-coaxial jets are available in published literature[5,7,8,12,13], but one must be cognizant that apparatuses such as these often see multiple modifications in only a few years time. As a result, Fig. 10 should be considered a general guide for comparison, because Re values for the facility concerned here, as well as the others in Fig. 10, can be revised with simple hardware modifications.

C. Acoustic Characterization

Downloaded by Doug Talley on September 19, 2016 | http://arc.aiaa.org | DOI: 10.2514/6.2014-0137

A challenging task required to complete the facility design was the development of an acoustic excitation system. An ideal design will offer free control of amplitude over a wide range of acoustic frequencies. But, as seen in the acoustic control systems of existing facilities[6], this proves to be difficult. Designs must often sacrifice either control of frequency or amplitude in order to achieve high pressure amplitudes on the order of those manifested by LRE combustion instabilities. This facility utilizes a pair of piezoelectric acoustic sirens, where pressure amplitude is variably controlled with input voltage amplitude until reaching the sirens maximum safe amplitude of approximately 600V. The chamber integrates the sirens using stainless steel waveguides mounted to the left and right sides of the outer chamber as shown in Fig. 2.

The waveguides act as horns which focus acoustic energy from the 100 mm diameter sirens to the smaller rectangular inner chamber. This acoustic horn technique facilitates the production of high pressure amplitudes at the point of interest, the flame. The waveguides' shape must provide a smooth transition from a 11.24 cm diameter circlular flange to a 2.03 cm × 3.61 cm rectangular cross-section. To minimize two-dimensional and three-dimensional waves, the circle-to-rectangle transition must be void of abrupt area changes and sharp corners. This requirement, combined with material stress from high chamber pressures, make design and fabrication challenging.

The area reduction from circle to rectangle follows a quasi-one-dimensional model for sound propagation in a rigid-walled duct, which is derived beginning with the acoustic wave equation,

$$\nabla^2 p - \frac{1}{c^2}\frac{\partial^2 p}{\partial t^2} = 0\,, \tag{1}$$

which is then integrated for acoustic pressure p for a three-dimensional segment of the duct. A coordinate system is adopted where x is the jet streamwise direction, y is the transverse direction, and z is the depthwise direction. Thus, a perfectly-shaped waveguide will prevent acoustic wave propagation in the x and z directions and concentrate 100% of the energy from each siren to produce waves in the y direction. Gauss's theorem is then used to convert the volume integral of $\nabla^2 p$ to a surface integral. Then, apply the boundary condition that $\nabla p \cdot n = 0$ at the inner wall of the waveguide, divide by Δy, and take the limit as $\Delta y \to 0$ ($\Delta y = \partial y$). One obtains

$$\frac{\partial}{\partial y}\iint_A \frac{\partial p}{\partial y}\,dA - \frac{1}{c^2}\frac{\partial^2}{\partial t^2}\iint_A p\,dA = 0\,. \tag{2}$$

With the exception of a thin acoustic boundary layer near the inner wall of the waveguide, p is uniform over any given cross section, i.e. $\frac{\partial p}{\partial x} = \frac{\partial p}{\partial z} = 0$. The equation above then reduces to

$$\frac{1}{A}\frac{\partial}{\partial y}\left(A\frac{\partial p}{\partial y}\right) - \frac{1}{c^2}\frac{\partial^2 p}{\partial t^2} = 0\,, \tag{3}$$

which is known as Webster's horn equation, after Arthur G. Webster[14]. Following Pierce[15], Webster's horn equation can be simplified as

$$\left\{\frac{\partial^2}{\partial y^2} + \frac{1}{4A^2}\left[(A')^2 - 2AA''\right] - \frac{1}{c^2}\frac{\partial}{\partial t^2}\right\}A^{1/2} p = 0\,. \tag{4}$$

This is a nonlinear ordinary differential equation with respect to A which can be used to describe the optimal area of an expanding or constricting waveguide. The general solution is

$$A = A_{th}\left(\cosh my + T\sinh my\right)^2\,. \tag{5}$$

Downloaded by Doug Talley on September 19, 2016 | http://arc.aiaa.org | DOI: 10.2514/6.2014-0137

The specific solution is found for the catenoidal horn shape[15] for $T = 0$ using boundary conditions enforced by the chosen siren diameter, inner chamber area, and waveguide length in order to determine the throat area A_{th} and flare constant m. Finally, the specific solution was used to model the inside wall of each waveguide according to a prescribed area function. The CAD rendering in Fig. 11 shows the left waveguide in a cut-away view. With an identical assembly on the right of the chamber, the acoustic system produces high-amplitude pressure waves, $p'/p_c \sim 0.01$, traveling in the y direction.

Acoustic pressure amplitudes induced by this system are largely governed by the resonant modes of the chamber and the piezoelectric sirens. The chamber geometry will allow resonant modes for a particular set of acoustic frequencies, which are also dependent on the speed of sound for a given thermodynamics state. The sirens, on the other hand, have resonant frequencies of their own. Below 6 kHz, the sirens exhibit only three resonant frequencies and operating far from these three frequencies results in inefficient sound production and low pressure amplitudes. Thus the maximum achievable amplitudes are dependent on frequency as it relates to resonance of two independent phenomena.

Regarding the resonant chamber modes, an analytical examination reveals a broad array of frequencies. The analytical relationship between chamber length L, acoustic frequency f_F, and the speed of sound c follows as

$$L = \frac{n}{2}\lambda = \frac{n}{2}\left(\frac{c}{f_F}\right) \tag{1}$$

where even values of n create resonant conditions for acoustic sources operated in-phase (φ =0°) and odd values of n create resonant conditions for acoustic sources operated out-of-phase (φ =180°). In the same regard, sources operated in-phase will create a pressure antinode (PAN) at the center of the chamber and sources operated out-of-phase will create a pressure node (PN) at the center of the chamber. Due to the waveguides long span, ten transverse resonant frequencies occur at less then 6 kHz. Unlike convective waves, a resonant condition will form acoustic waves which are symmetric with respect to both space and time. Spatially, an isothermal volume subject to transverse resonance will produce evenly spaced PNs and PANs. This places the injector at a location of known acoustic perturbation gradients $\frac{\partial p'}{\partial y}$ and $\frac{\partial u'}{\partial y}$, where $\frac{\partial p'}{\partial y} = 0$ for a PAN condition (φ =0°) and $\frac{\partial u'}{\partial y} = 0$ for a PN condition (φ =180°). Temporally, the acoustic waves reveal a symmetric waveform lacking the abnormalities present when waves of unequal amplitude or phase interact and maintain a traveling wave component.

Second, the resonant frequencies of the sirens must be determined experimentally, as each unique siren will have its own characteristic peak amplitudes. This is best investigated using a frequency sweep method with each siren removed from the chamber. In this way, acoustic pressure is measured without regard to chamber resonance. An experimental frequency sweep was performed for 0 to 6 kHz and two peaks are observed at 3076 Hz and 5200 Hz for the left siren and 3084 Hz and 5101 Hz for the right siren. Wider bands of high sound production also exist at 1638-1915 Hz for the left siren and 1620-1860 for the right siren. These isolated frequencies offer three separate narrow bands of high amplitude acoustic excitation for each siren, while operating outside these bands results in much lower amplitudes.

Finally, a combined acoustic characterization of both sirens mounted inside the chamber must be completed to understand the system's performance. A frequency sweep from 0 to 6 kHz was employed with operation of sirens in-phase. To measure the frequency response of pressure oscillations within the chamber, a dynamic pressure transducer (Kulite model XCE-093-50D) was placed at the center of the chamber. When operating acoustic sources in-phase the chamber's center location represents a PAN, and is an excellent measure of the maximum pressure amplitude for a given frequency. The results of these measurements are shown in Fig. 11 for a chamber pressure of 400 psia (=2.76 MPa). Not all ten transverse chamber modes are identified in Fig. 12, with transverse resonance peaks only located near the sirens' optimum frequency bands. Although 1T and 2T modes exist for the chamber, for example, 1T and 2T modes do not appear in the comprehensive frequency sweep in Fig. 12 due to siren limitations, demonstrating the combined result of chamber and siren resonance.

In conclusion, the acoustic system demonstrates advantages over other techniques, but also has limitations. The piezoelectric sirens are useful only for select frequency bands. The pressure amplitudes achievable within these frequency bands are approximately equal to 1% of the mean chamber pressure. Although the pressure oscillations of LRE combustion instabilities can reach amplitudes far greater than 1% of the mean chamber pressure, the amplitudes obtained by this acoustic system are sufficient for inducing a significant response in the coaxial jet, as will be shown in the results and as shown in previous nonreacting experiments[16,17]. Further, by decoupling the

Downloaded by Doug Talley on September 19, 2016 | http://arc.aiaa.org | DOI: 10.2514/6.2014-0137

source of chamber pressurization from propellant flow rates, it becomes advantageous to scale p' with a the coaxial jet dynamics rather than the mean chamber pressure. For example, p' may be scaled by the jet dynamic pressure. At any rate, the acoustic system provides three key advantages over other techniques. First, by spacing the sirens very far apart (0.82 m), several different T modes can be achieved below 6 kHz. For example, Fig. 12 shows that a mean chamber pressure of 400 psia allows one to produce a resonant mode at 1543 Hz (3T) and also at 3169 Hz (6T). Second, the pressure amplitude is directly controlled by altering the voltage input to the sirens, similar to a traditional loudspeaker. Last, both a PN and a PAN can be located at the jet by operating the sirens out-of-phase and in-phase, respectively.

D. High-Speed Imaging

Jet flow visualization is the primary diagnostic tool for studying nonreactive flow dynamics, provided by back-lit high-speed images. A variable power Newport model 66986 power supply controls a 300 W Xe lamp, which emits light in the near ultraviolet spectrum. This beam is projected through the rear window as a back-light source. Although the beam is not collimated, this back-lighting technique produces sufficient contrast at fluid interfaces. Differences in the refractive index of the jets and the surrounding medium provide the necessary distinction between the fluids of interest. The low temperature, liquid nitrogen inner jet appears as a dark column of fluid as viewed by the high-speed camera placed on the opposite side of the light source.

A Phantom v7.10 high-speed camera is used to visualize the fast dynamical processes inherent to an unforced coaxial jet flow as well as those present during high-frequency acoustic forcing. A 200 mm Nikon MicroNikkor lens is used with a no. 1 close-up lens attachment, giving a spatial resolution of 30 μm per pixel. Image framing rates of 10 kHz or greater are used in order to avoid aliasing up to 5 kHz, which is much greater than the highest forcing frequency used in this study, 2600 Hz. An external trigger from the facility control system is used to start recording the image frames, which are synchronized with all other data using the coordinated universal time (UTC) stamp from an IRIG-B timecode generator.

The reactive imaging set up is designed to capture ultraviolet bands of flame radiation in order to isolate chemiluminescence of excited hydroxyl radicals near a wavelength of 308 nm. An oxygen-hydrogen flame also emits light in the visible spectrum due to photon emission from H_2O radicals, which is blocked using a UV bandpass filter with a center wavelength of 307.2 nm with a FWHM of 11.7 nm and peak transmission of 16.0%. The filter is mounted to a 105 mm Nikon UV-Nikkor lens. After passing through the filter and lens, light is captured using a Lambert Instruments HiCATT image intensifier, and the photocathode of the image intensifier was chosen to have a high quantum efficiency in the UV range. In order to project the intensified light onto the Phantom v7.10 high-speed camera, a relay lens is mounted in between the image intensifier and the camera.

III. Results

Results will be shown that demonstrate the facility capability for both nonreactive and reactive tests at a mean chamber pressure of 400 psia. First, nonreactive tests are performed using liquid nitrogen (LN_2) as the inner jet and gaseous helium (GHe) as the outer jet, which creates a outer-to-inner jet density ratio S similar to an oxygen-hydrogen LRE. The inner and outer jet temperatures are set to be approximately 120 K and 275 K, respectively, which gives $S = 0.009$. Sample images are shown in Fig. 13 for an unforced jet with an outer-to-inner momentum flux ratio J of 2. Fig. 13 demonstrates many shear-coaxial jet features using a series of snapshots which were acquired at a frame rate of 10 kHz, and a small field of view is added to increase the clarity of structures near the injector exit.

At the exit of the injector, a recirculation zone is easily distinguishable. Moving in the radial direction from the center of the jet, one first observes an interface between the liquid nitrogen inner jet and the recirculation zone formed between the inner and outer jets. This feature is labeled as (1) in Fig. 13. The width of the recirculation zone is equal to the inner post thickness t at the exit of the injector and converges to zero as the recirculation zone extends downstream. The recirculation zone results from a finite inner post thickness, separating near-field stability of this geometry from that of classical co-flowing streams (t=0) commonly used in linear stability theory[18,19].

Advancing farther in the radial direction, an outer shear layer is identified between the gaseous helium outer jet and the surrounding gaseous nitrogen. Although this interface is less distinguishable in analogous LN_2-GN_2 jet experiments[3,4], the LN_2-GHe jet shown in Fig. 13 reveals significant contrast between the light outer jet and the more dense ambient nitrogen ($\rho_c \approx 7\rho_{oj}$). At this interface, an outer shear layer instability is formed. Preliminary analysis of LN_2-GHe jets also indicates unique stability characteristics for the inner and outer shear layers, making this imaging technique particularly valuable when accompanied by image analysis techniques such as proper orthogonal decomposition[11,20] and dynamic mode decomposition[21,23].

Downloaded by Doug Talley on September 19, 2016 | http://arc.aiaa.org | DOI: 10.2514/6.2014-0137

Immediately downstream of the recirculation zone, a dynamic interface forms between the inner and outer jets. This interface, labeled as (4) in Fig. 13, is the most important feature of the jet for this particular set of experiments due to its importance in inner jet atomization and mixing. This region may be called the mixing layer or the inner shear layer, and the latter term is used here for continuity with other works. Additionally, the extreme contrast between the liquid inner jet with $\rho_{ij} \approx 500$ kg/m^3 and the light outer jet with $\rho_{oj} \approx 5$ kg/m^3 makes for straightforward image analysis because pixel intensity gradients are most steep at the inner shear layer. Near the recirculation zone, the inner shear layer appears as well-defined interfacial waves. Further downstream, the shear layer thickness increases and these waves develop into vortices.

Regarding coaxial jet behavior in acoustically forced conditions, Figs. 14 and 15 show several image samples for PN and PAN forcing, respectively. Comparing Fig. 14 and Fig. 15 reveals the qualitative differences between forcing a jet located at a PN and PAN, and the value of an experimental facility which can create each condition. A jet located at a PN, when responsive to acoustic forcing, is exposed to a periodic transverse velocity with an amplitude of u'. This caused the jet to take a sinusoidal shape[2,11]. The inner and outer jets are swept to the left during one-half of the acoustic period and then to the right during the remaining half of the acoustic period. A PAN, on the other hand, causes the jet to adopt an axisymmetric instability due to injector pulsation in the outer jet[3,17,23]. Preliminary results show that jets located at a PN are more susceptible to transverse acoustic forcing than jets located at a PAN.

The preliminary results shown in Figs. 13-15 are for $J = 2$, which is also used for preliminary reactive tests to offer a comparison. Reactive tests are performed using liquid oxygen (LO_x) as the inner jet and gaseous hydrogen (GH_2) as the outer jet, with an equivalence ratio φ of 1.36, which is equivalent to a mixture ratio MR of 5.9. As described earlier, a temperature conditioning process is required in order to reach stable, desired inner and outer jet temperatures. To begin a reactive test, this temperature conditioning process is performed using nitrogen as a surrogate in order to conserve propellant.

Fig. 16 shows a time-series plot of a LO_x-GH_2 test which begins after achieving stable temperatures in the inner and outer jet. Remote valves are used to switch from the nitrogen simulant supply to the propellant supply. Due to differences in viscosity, density, and heat conduction constants, alternating between nitrogen simulant flow and propellant flow causes small changes in mass flow rate and temperature. The difference between the process fluid temperature at the injector before and after the species transition was found to be highly dependent on both chamber pressure and mass flow rate. As can be seen by the propellant valve operations in Fig. 16, an oxygen "lead" technique is used at the beginning of the automated test sequence. More than 10 s after the oxygen supply valve is opened, the hydrogen supply valve is opened prior to triggering the ignitor. The time at which each propellant valve is opened is chosen such that each propellant reaches the injector, and thus replaces the nitrogen surrogate, at the desired point in time. Only milliseconds after hydrogen reaches the injector, a torch ignitor is triggered to ignite the propellant mixture. Note that since the chamber pressure is largely determined by a nitrogen chamber pressurization system, propellants are ignited after the chamber is pressurized. To ignite the propellant mixture at elevated pressures, a novel photoignition technique is used, and will be described in subsequent publications. After a burn duration of 6 s, the hydrogen valve is closed first, causing the flame to extinguish.

The test firing represented in Fig. 16 was captured with OH* chemiluminescence imaging, and Fig. 17 includes several image samples acquired near t =19.5 s. These images clearly resolve the evolution of burning structures as they convect downstream. The near-field region produces a non-premixed flame caused by the diffusion of hydrogen and oxygen at the inner shear layer. In the far downstream region, structures may break away from the main body of the flame, as shown in the fourth image of Fig. 17. Of utmost importance in combustion stability studies are the burning structures produced near the exit of the injector, which represent localized pockets of intense OH* chemiluminescence. Although OH* chemiluminsescence has been shown to be proportional to heat release[24], more recent studies highlight sources of inaccuracy when using OH* chemiluminescence to quantify heat release to turbulent flames[25]. Still, Fig. 17 allows one to conclude that unsteady heat release exists, and OH* chemiluminescence such as these may be used to make approximate conclusions regarding flame standoff distance and instability frequencies using image analysis algorithms, for example.

IV. Conclusion

A new facility has been constructed at the Air Force Research Lab at Edwards AFB, CA to experimentally investigate combustion stability for cryogenic propellants at high pressure. A widely variable test matrix may be achieved for nonreactive as well as reactive conditions by utilizing precise control of inner and outer jet temperatures and chamber pressure. Temperatures are controlled with an accuracy of ±1 K in a range spanning from 110 K to room temperature, while the mean chamber pressure is controlled using a secondary chamber

Downloaded by Doug Talley on September 19, 2016 | http://arc.aiaa.org | DOI: 10.2514/6.2014-0137

pressurization flow which partially decouples chamber pressure from combustion. A pair of piezoelectric sirens is used to create acoustic pressure oscillations which simulate the pressure oscillations an LRE combustion instability. Proper control of the phase difference and frequency of the sirens allows one to produce transverse standing waves with a pressure node (PN) or pressure antinode (PAN) located at the coaxial jet. The response of a coaxial jet to this environment is studied using high-speed diagnostics in the form of dynamic pressure transducers, backlit imaging, and OH* chemiluminescence imaging. These experimental capabilities, as well as ongoing facility advancements, will allow researchers to fundamentally investigate combustion instabilities in a manner which is comparable to very few other facilities in existence today.

Acknowledgments

Support was provided by the Air Force Office of Scientific Research, project officer Mitat Birkan, and by AFRL Laboratory Revitalization Funds. Significant technical contributions to the design and construction of the facilty are gratefully acknowleged from Randy Harvey, Al Badakhshan, Foster Beasley, Claudia Heflin, John Hasier, Todd Newkirk, Jeff Muss, and Rory Davis. Advanced Mobile Propulsion Test (AMPT) LLC provided significant expertise in the design and implementation of the data acquisition and control system and Sierra Lobo, Inc on the design and construction of the oxygen heat exchanger.

Downloaded by Doug Talley on September 19, 2016 | http://arc.aiaa.org | DOI: 10.2514/6.2014-0137

References

[1]Schadow, K., and Gutmark, E., "Combustion instability related to vortex shedding in dump combustors and their passive control," *Progress in Energy and Combustion Science* Vol. 18, No. 2, 1992, pp. 117-132.

[2]Leyva, I.A., Chehroudi, B., and Talley, D., "Dark core analysis of coaxial injectors at sub-, near-, and supercritical pressures in a transverse acoustic field," *43rd AIAA/ASME/SAE/ASEE Joint Propulsion Conference and Exhibit*, Vol. 5, 275–282, 2007-5456.

[3]Leyva, I.A., Rodriguez, J.I., Davis, B.W., and Chehroudi, B., "Preliminary results on coaxial jet spread angles and the effects of variable phase transverse acoustic fields," *46nd AIAA Aerospace Sciences Meeting & Exhibit*, Reno, NV, 2008.

[4]Teshome, S., "Droplet Combustion and Non-Reactive Shear-Coaxial Jets with Transverse Acoustic Excitation," PhD thesis, University of California, Los Angeles, Department of Mechanical and Aerospace Engineering, March 2012.

[5]Hardi, J., "Experimental Investigation of High Frequency Combustion Instability in Cryogenic Oxygen-Hydrogen Rocket Engines," PhD thesis, The University of Adelaide, School of Mechanical Engineering, June 2012.

[6]Hardi, J., Oschwald, M., and Dally, B., "Acoustic characterisation of a rectangular rocket combustor with liquid oxygen and hydrogen propellants," *Proceedings of the Institution of Mechanical Engineers, Part G: Journal of Aerospace Engineering*, Vol. 227, No. 3, 2013, pp. 436–446.

[7]Richecoeur, F., "Experiments and numerical simulations of interactions between transverse acoustic modes and cryogenic flames," PhD thesis, Ecole Centrale Paris, November 2006.

[8]Richecoeur, F., Ducruix, S., Scouflaire, P., and Candel, S., "Effect of temperature fluctuations on high frequency acoustic coupling," *Proc. of the Combustion Institute*, Vol. 32, 2009, 1663–1670.

[9]Mery, Y., Hakim, L., Scouflaire, P., Vingart, L., Ducruix, S., and Candel, S., "Experimental investigation of cryogenic flame dynamics under transverse acoustic modulations," *Comptes Rendus Mecanique*, Vol. 341, 2013, 100–109.

[10]Yu, Y.C., Koeglmeier, S.M., Sisco, J.C., and Anderson, W.E., "Combustion instability of gaseous fuels in a continuously variable resonance chamber (CVRC)," 44th Joint Propulsion Conference and Exhibit, AIAA 2008-4657, 2008.

[11]Teshome, S., Leyva, I.A., and Talley, D.G., "Proper orthogonal decomposition analysis of shear-coaxial injector flows with and without transverse acoustic forcing," *JANNAF Joint Subcommittee Meeting*, Huntsville, AL, 2011.

[12]Hulka, J. and Hutt, J.J., Instability phenomena in liquid oxygen/hydrogen propellant rocket engines. V. Yang and W.E. Anderson, editors, *Progress in Astronautics and Aeronautics: Liquid Rocket Engine Combustion Instability*, pages 39–72. AIAA, 1995.

[13]Woodward, R.D., Pal, S., Farhangi, S., Jensen, G.E., and Santoro, R.J., "LOx/GH2 shear coaxial injector atomization studies: effect of recess and non-concentricity," *45th AIAA Aerospace Sciences Meeting and Exhibit*, pp. 1–22, 2007-571.

[14]Webster, A.G., "Acoustical impedence, and the theory of horns and of the phonograph," *Proceedings of the National Academy of Sciences*, Vol. 5, 1919, pp. 275–282.

[15]Pierce, A. D. *Acoustics: An Introduction to Its Physical Principles and Applications*. Acoustical Society of America, 1991.

[16]Graham, J., Leyva, I.A., Rodriguez, J.I., and Talley, D., "On the effect of a transverse acoustic field on a flush shear coaxial injector," AIAA 2009-5142.

[17]Rodriguez, J.I., Leyva, I.A., Graham, J., and Talley, D., "Mixing Enhancement of Liquid Rocket Engine Injector Flow," AIAA 2009-5143.

[18]Jendoubi, S. and Strykowski, P.J., "Absolute and convective instability of axisymmetric jets with external flow," *Physics of Fluids*, Vol. 6, 1994, 3000–3009.

[19]Yecko, P., Zaleski, S., and Fullana, J.-M., "Viscous modes in two-phase mixing layers," *Physics of Fluids*, Vol. 14, No. 12, 2002, 4115–4122.

[20]Arienti, M. and Soteriou, M.C., "Dynamics of free jets submitted to upstream acoustic modulations," *Physics of Fluids*, Vol. 21, No. 112104, 2009.
[21]Schmid, P.J., "Application of the dynamic mode decomposition to experimental data," *Experiments in Fluids*, Vol. 50, 2011, pp. 1123–1130.
[22]Jovanovic, M.R., Schmid, P.J., and Nichols, J.W., "Low-rank and sparse dynamic mode decomposition," *Center forTurbulence Research, Annual Research Briefs,* 2012, pp. 139–152.
[23]Baillot, F., Blaisot, J.-B., Boisdron, G., and Dumouchel, C., "Behaviour of an airassisted jet submitted to a transverse high-frequency acoustic field," *J. of Fluid Mechanics*, Vol. 640, 2009, pp. 305–342.
[24]Marchese, A.J., Dryer, F.L., Nayagam, V., and Colantino, R.O., "Hydroxyl radical chemiluminescence imaging and the structure of microgravity droplet flames," *Twenty-sixth Symposium (International) on Combustion*, 1996, pp. 1219–1226.
[25]Kojima, J., Ikeda, Y., and Nakajima, T., "Spatially resolved measurement of OH*, CH*, and C*2 chemiluminescence in the reactio zone of laminar methane/air premixed flames," *Proc. Comb. Inst.*, Vol. 28, 2000, pp. 1757–1764.

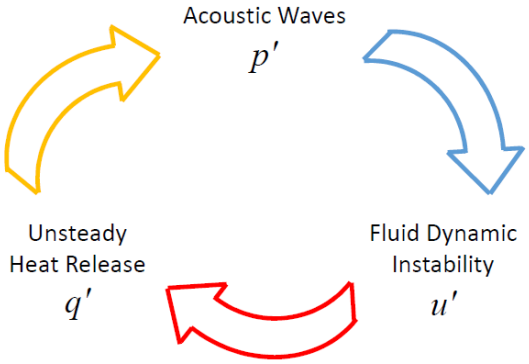

Figure 1. Three-part combustion instability feedback loop.

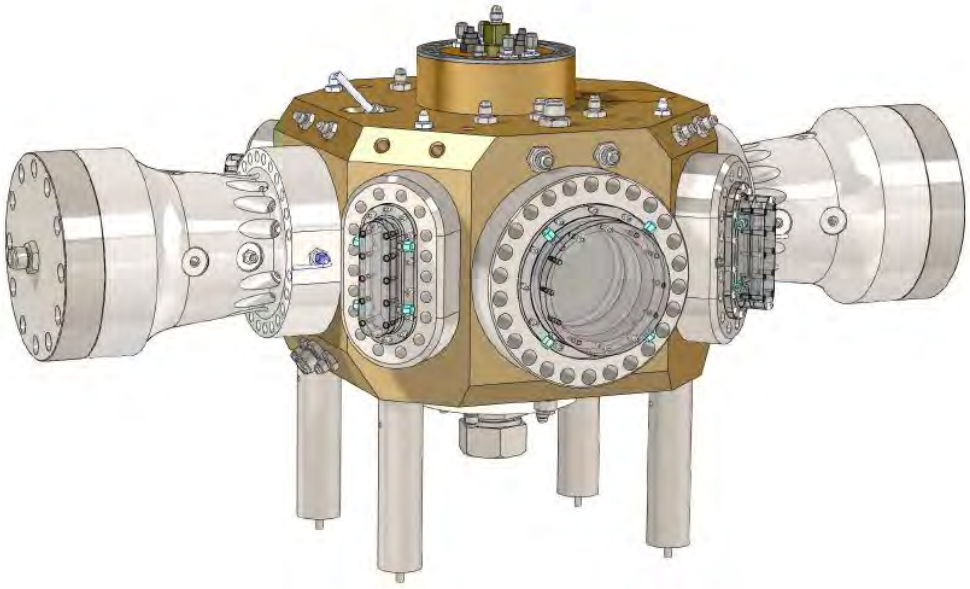

Figure 2. A three-dimensional CAD rendering of the high pressure combustion chamber at Air Force Research Laboratory at Edwards AFB, CA.

Downloaded by Doug Talley on September 19, 2016 | http://arc.aiaa.org | DOI: 10.2514/6.2014-0137

Downloaded by Doug Talley on September 19, 2016 | http://arc.aiaa.org | DOI: 10.2514/6.2014-0137

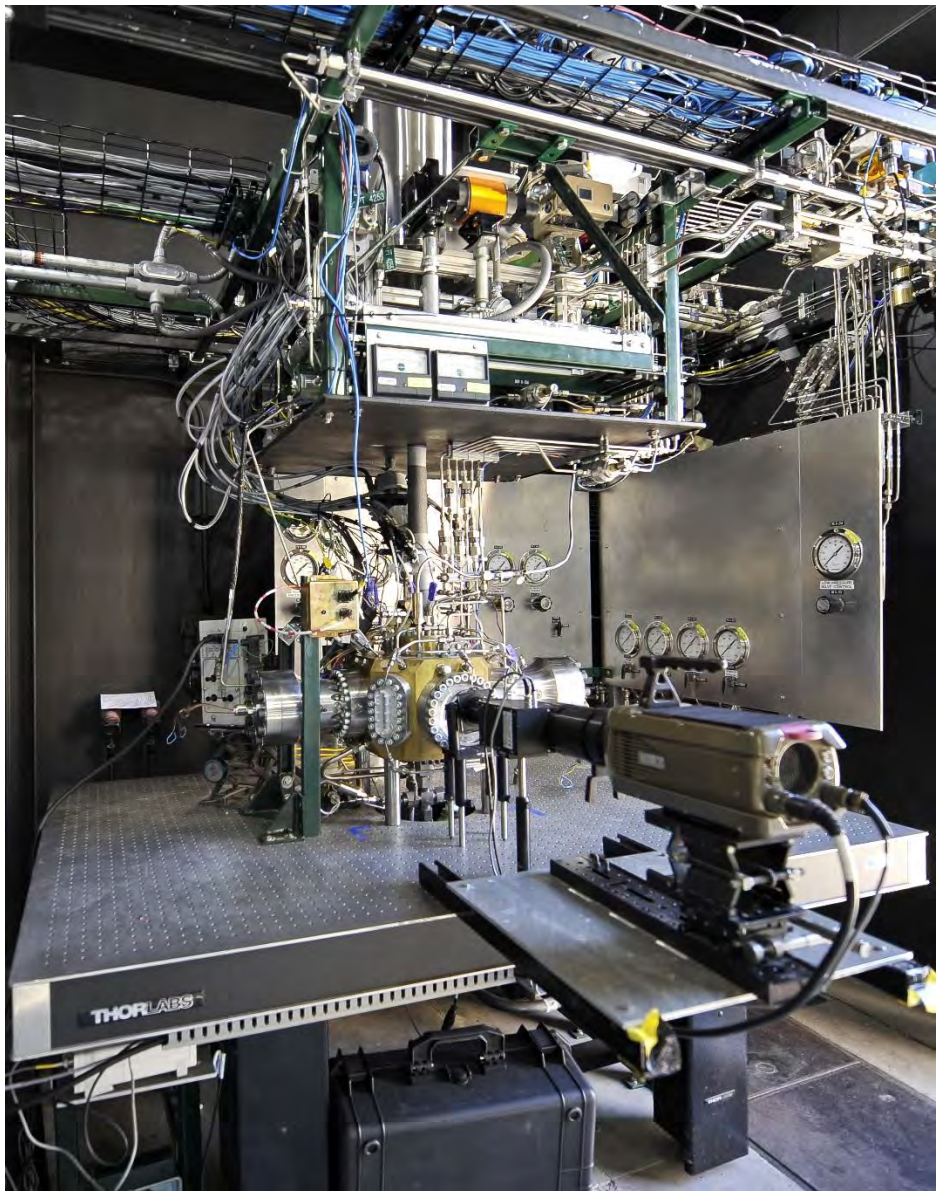

Figure 3. Photograph of the completed apparatus.

Downloaded by Doug Talley on September 19, 2016 | http://arc.aiaa.org | DOI: 10.2514/6.2014-0137

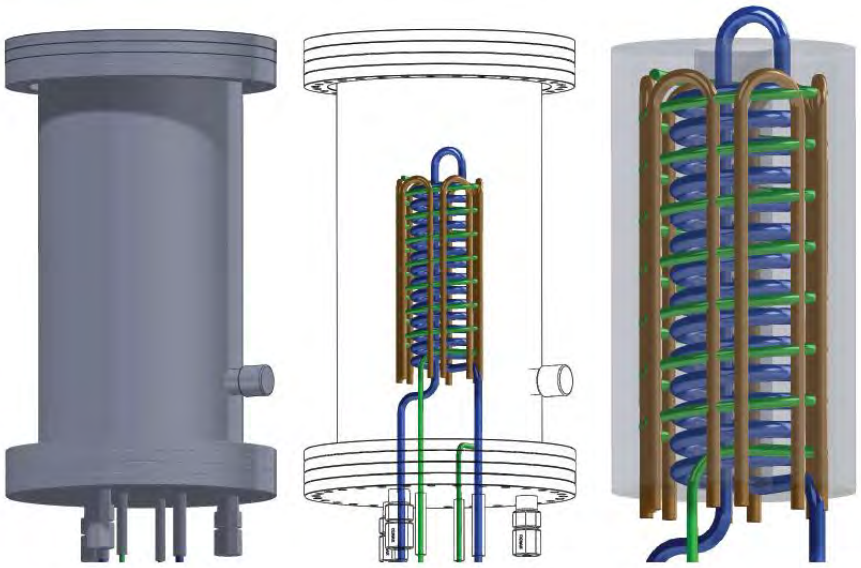

Figure 4. The oxygen heat exchanger cools oxygen gas (green) using liquid nitrogen (blue). Oxygen is cooled below the target temperature and electric heaters (brown) bring oxygen to the target temperature with a control resolution of ±1 K. Insulation is provided by a vacuum jacket (shown in left view, outlined in center view). An aluminum casting surrounds the plumbing assembly (shown in right view, gray).

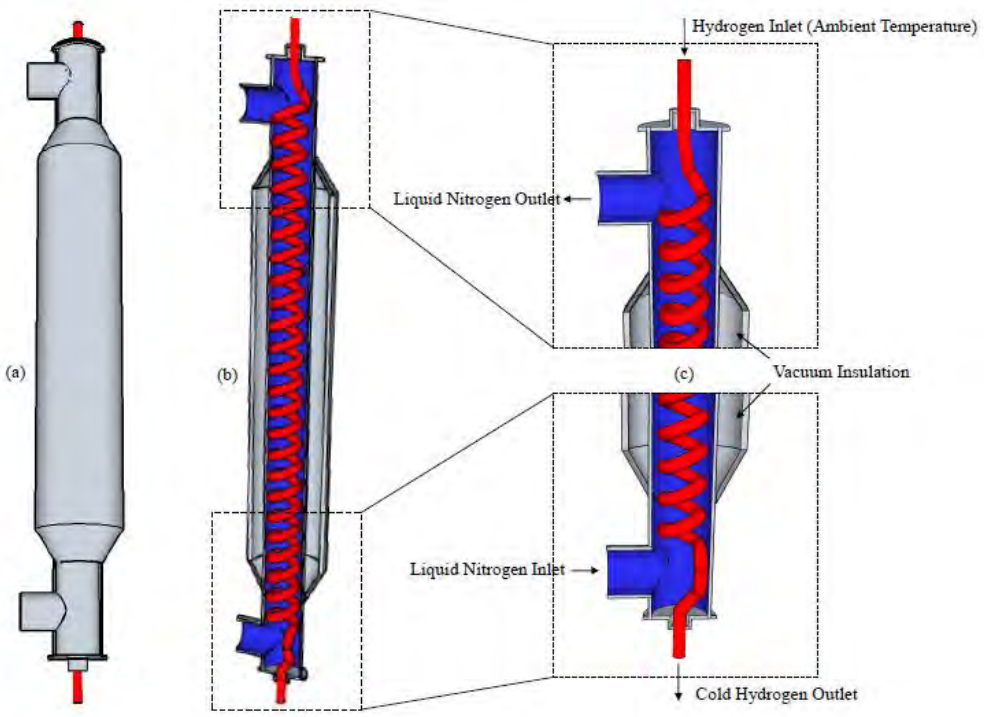

Figure 5. The hydrogen heat exchanger cools hydrogen gas (red) using liquid nitrogen (blue). Insulation is provided by a vacuum jacket.

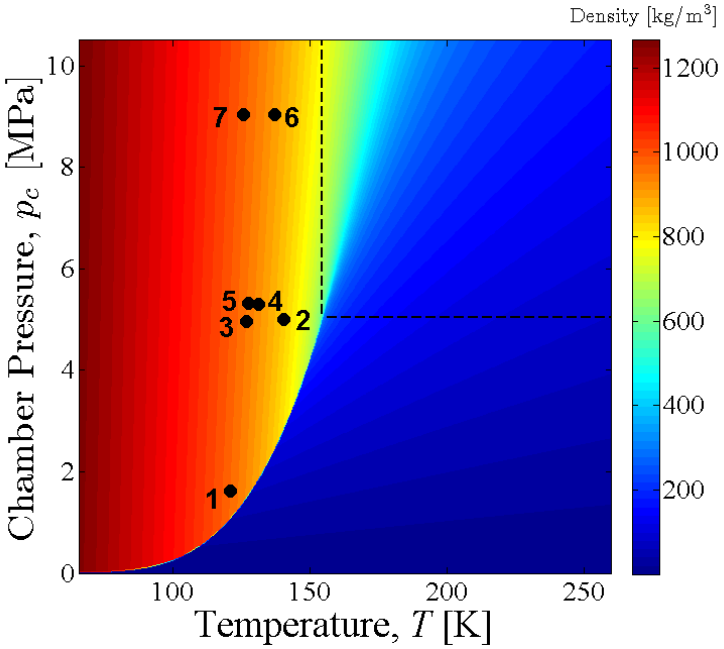

Figure 6. The facility's minimum achievable oxygen temperatures are plotted with an oxygen density contour overlay. Both chamber pressure and mass flow rate are controlled while temperature is measured. (1) 3.7 g/s (2) 2.6 g/s (3) 9.3 g/s (4) 3.0 g/s (5) 11.1 g/s (6) 2.7 g/s (7) 10.4 g/s

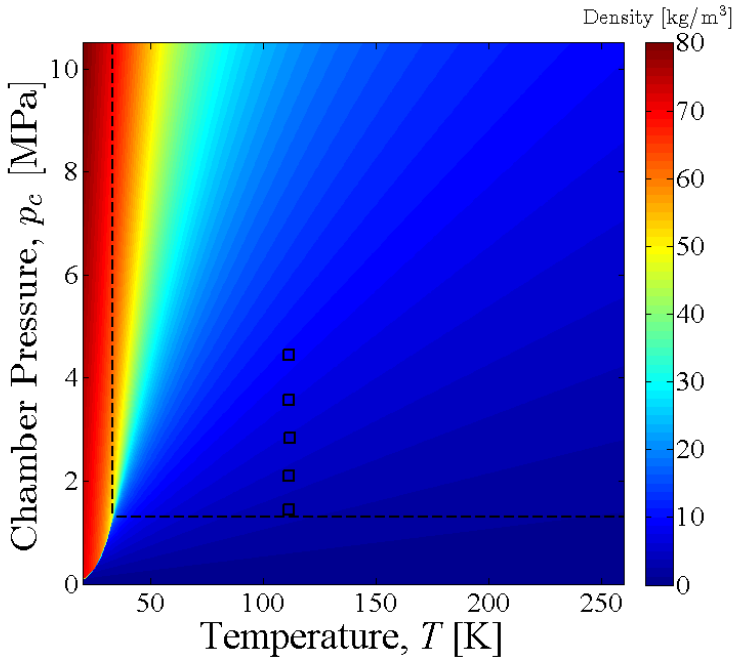

Figure 7. The facility's minimum achievable helium temperatures are plotted with a hydrogen density contour overlay. Helium is used as a surrogate gas, and is representative of minimum hydrogen achievable hydrogen temperatures in the outer jet. The nominal outer jet flow rate is approximately 1.3 g/s.

Downloaded by Doug Talley on September 19, 2016 | http://arc.aiaa.org | DOI: 10.2514/6.2014-0137

Downloaded by Doug Talley on September 19, 2016 | http://arc.aiaa.org | DOI: 10.2514/6.2014-0137

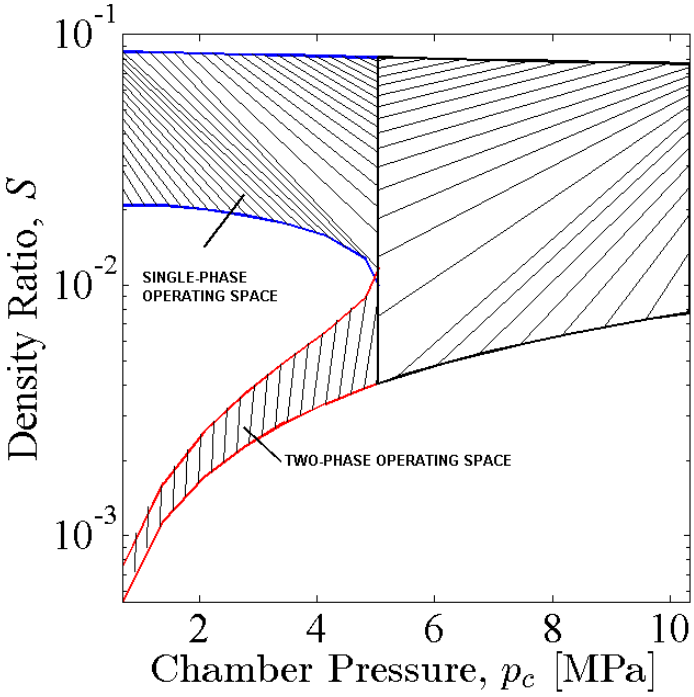

Figure 8. The facility's range of possible density ratios plotted versus chamber pressure.

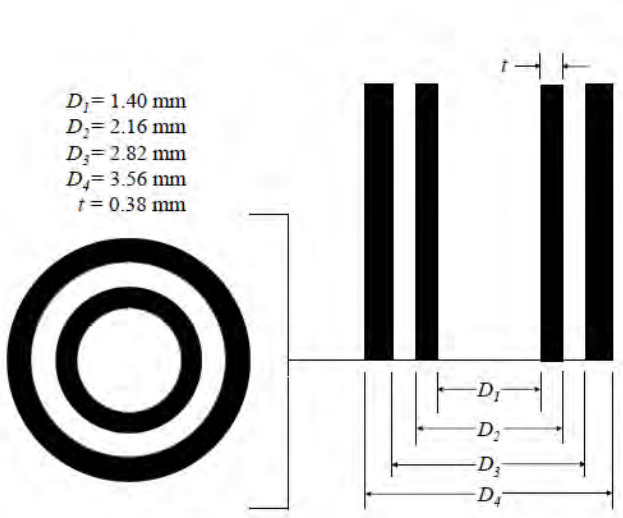

Figure 9. The dimensions of the coaxial injector used for new experiments in this study.

Downloaded by Doug Talley on September 19, 2016 | http://arc.aiaa.org | DOI: 10.2514/6.2014-0137

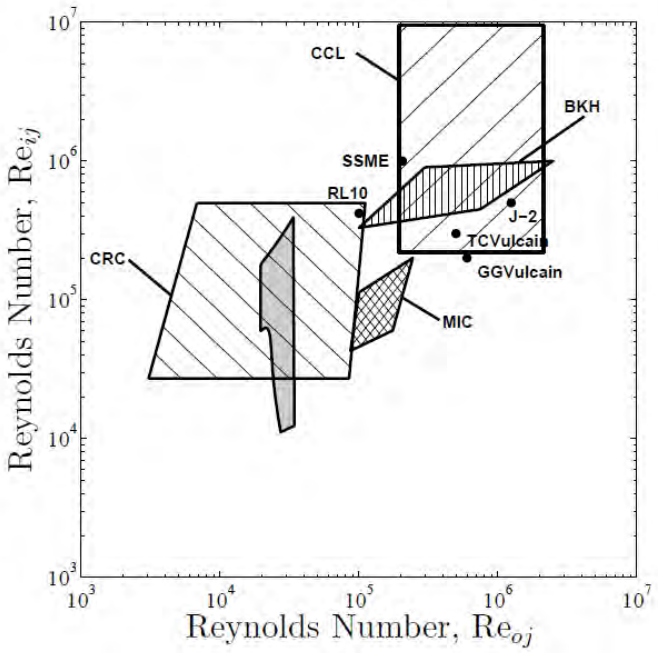

Figure 10. Shear-coaxial injector Reynolds numbers for the combustion stability facility (gray) with a comparison to other experimental facilities and liquid rocket engines with H2-O2 flows. Data is included for the Vulcain Gas Generator (GGVulcain), Vulcain Main Thrust Chamber (TCVulcain), RL10 engine, Space Shuttle Main Engine (SSME), J-2 engine, BKH combustor and Common Research Combustor (CRC) of DLR in Germany, Cryogenic Combustion Laboratory (CCL) of Pennsylvania State Univ., and the Mutli-Injector Combustor (MIC) of ONERA and CNRS in France.

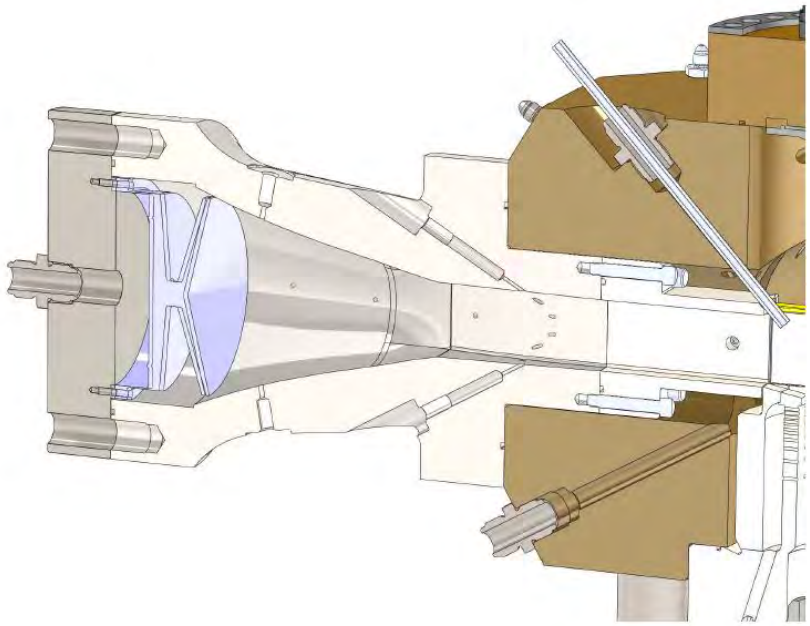

Figure 11. Cross sectional CAD rendering of the left waveguide. The end flange and piezoelectric siren are mounted on the left, and the waveguide assembly is mounted to the brass outer chamber on the right. The ignitor barrel enters through a diagonal port in the top left corner of the outer chamber wall.

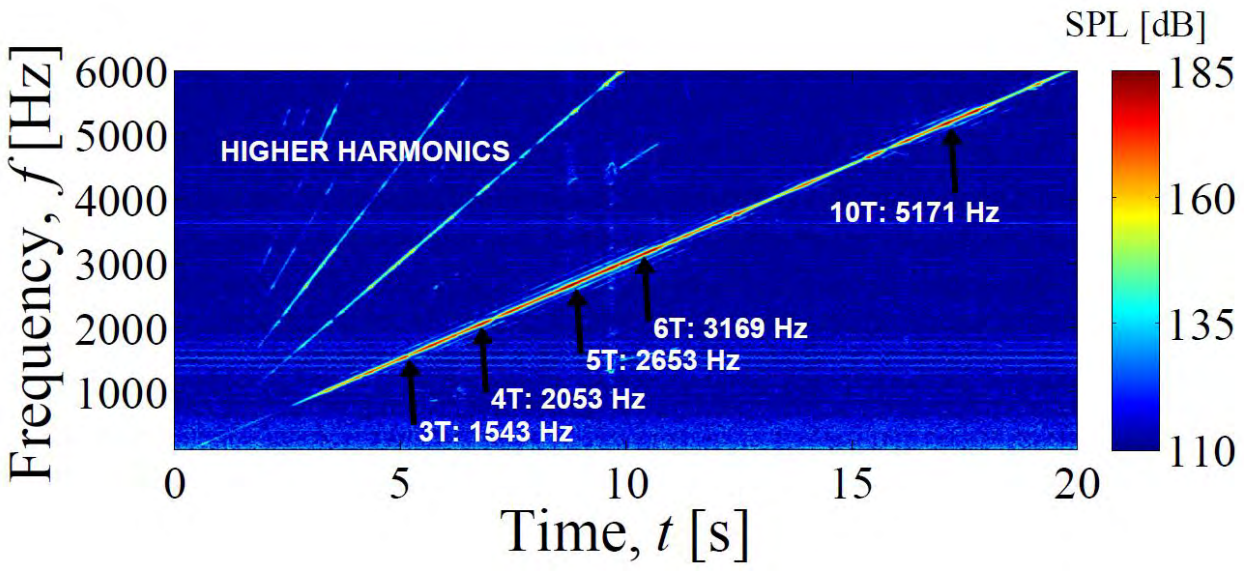

Figure 12. Acoustic pressure spectra results for a PAN condition measured using a pressure transducer in the center of the chamber. Magnitude is scaled with a sound pressure level (SPL) colormap, and key regions of transverse resonance are annotated. 1T, 2T, 7T, 8T, and 9T modes do not create appreciable pressure amplitudes, because these frequencies are outside of the useable frequency bands of the acoustic siresn. This study seeks to use one-dimensional, transverse waves only. Longitudinal modes and longitudinal-transverse mixed modes are ignored in this plot. p_c=400 psia = 2.76 MPa

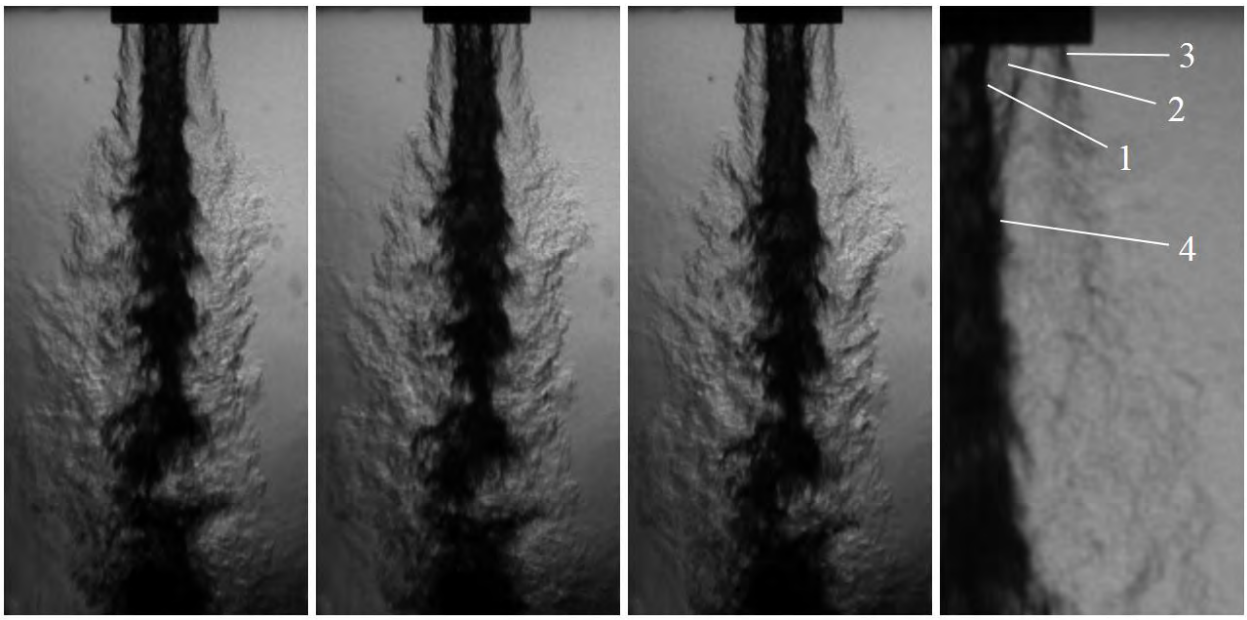

Figure 13. Liquid nitrogen-gaseous helium shear-coaxial jets without acoustic forcing. Three consecutive images are taken from a set of high speed images acquired at 10 kHz. A fourth image is shown with a reduced field of view to show the (1) interface between the inner jet and recirculation zone (2) recirculation zone (3) outer shear layer and (4) inner shear layer.
J = 2, p_c = 400 psia = 2.76 MPa

Downloaded by Doug Talley on September 19, 2016 | http://arc.aiaa.org | DOI: 10.2514/6.2014-0137

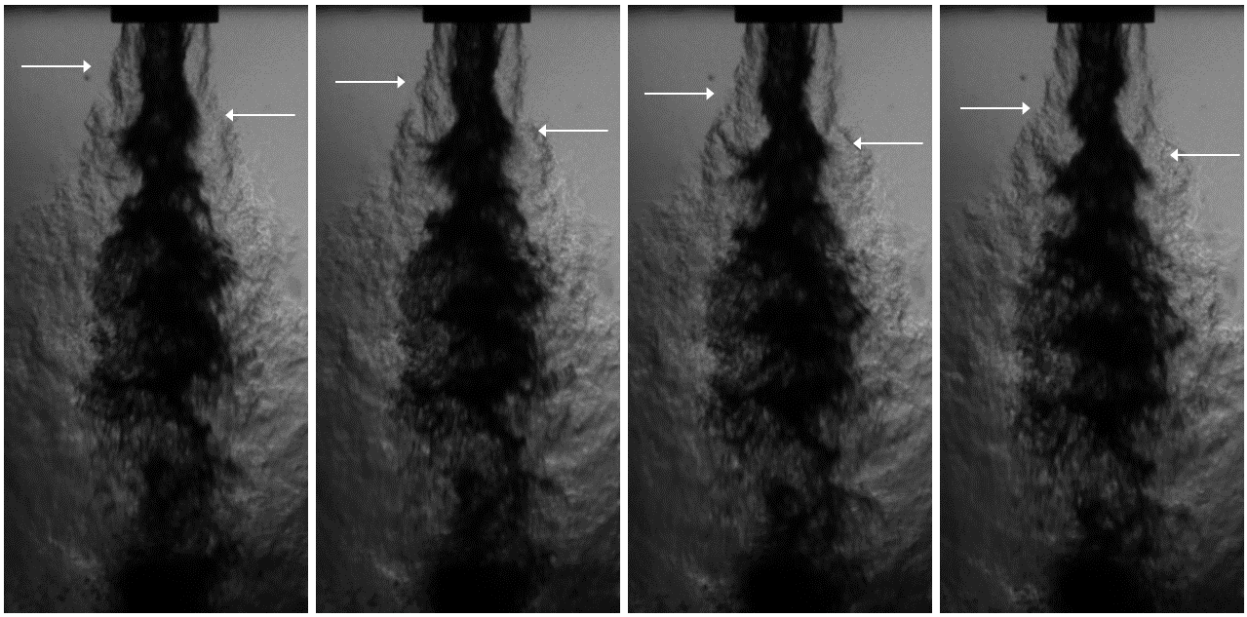

Figure 14. Liquid nitrogen-gaseous helium shear-coaxial jets exposed to external, transverse acoustic forcing at a pressure node. Four consecutive images are taken from a set of high speed images acquired at 10 kHz. An antisymmetric instability forms as periodic spanwise motions caused by the acoustic velocity perturbation u'. $J = 2$, $p_c = 400$ psia = 2.76 MPa, $f_F = 1700$ Hz, $u' = 0.43$ m/s

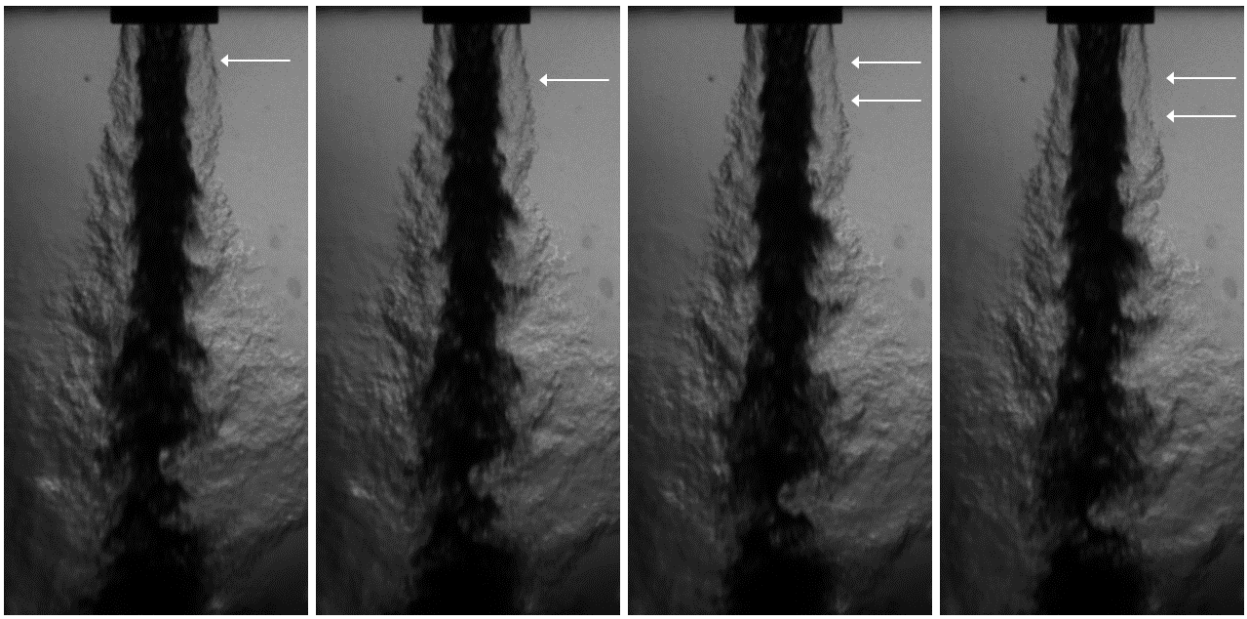

Figure 15. Liquid nitrogen-gaseous helium shear-coaxial jets exposed to external, transverse acoustic forcing at a pressure antinode. Four consecutive images are taken from a set of high speed images acquired at 10 kHz. An axisymmetric instability forms due to outer jet flow pulsations caused by the acoustic pressure perturbation p'. $J = 2$, $p_c = 400$ psia = 2.76 MPa, $f_F = 1700$ Hz, $p' = 1.53$ psi

Downloaded by Doug Talley on September 19, 2016 | http://arc.aiaa.org | DOI: 10.2514/6.2014-0137

Downloaded by Doug Talley on September 19, 2016 | http://arc.aiaa.org | DOI: 10.2514/6.2014-0137

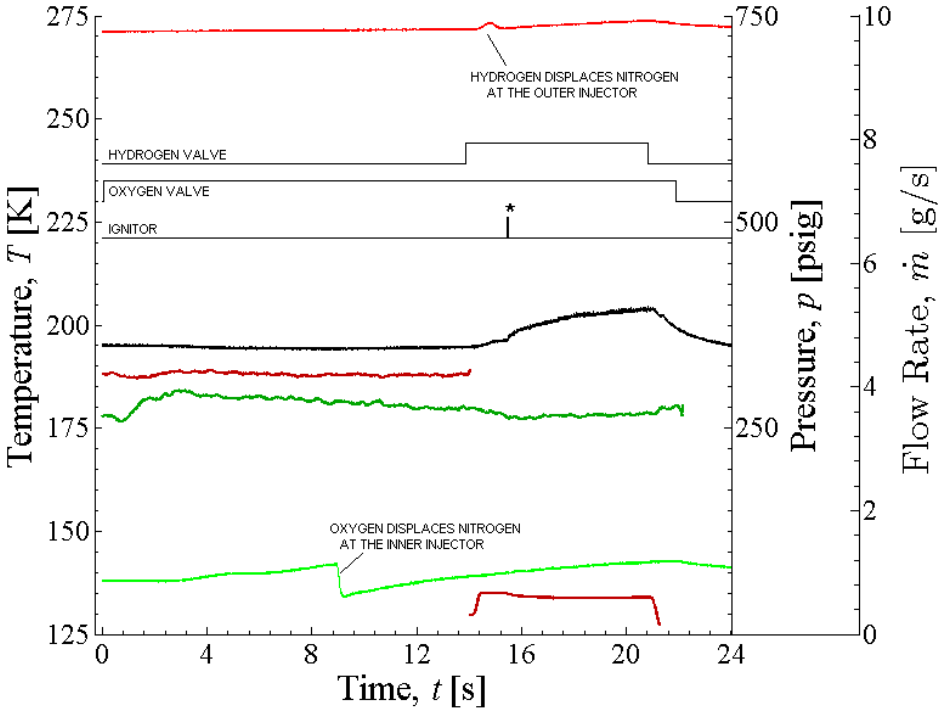

Figure 16. Time series plot of a typical reactive test using oxygen as the inner jet and hydrogen as the outer jet. The transition from a nitrogen simulant to the propellant occurs after the propellant valve is opened. A step change in outer jet mass flow rate occurs near t = 14 s, where nitrogen flow rate of approximately 4.2 g/s changes to a hydrogen mass flow rate of 0.65 g/s (dark red). The inner jet mass flow rate shows a species change near t = 1s, where a nitrogen flow rate of 3.6 g/s is overtaken by an oxygen mass flow rate of approximately 3.9 g/s. Inner jet temperature (light green), outer jet temperature (light red), and chamber pressure (black) are also shown. MR = 5.9 (φ=1.36), J = 2

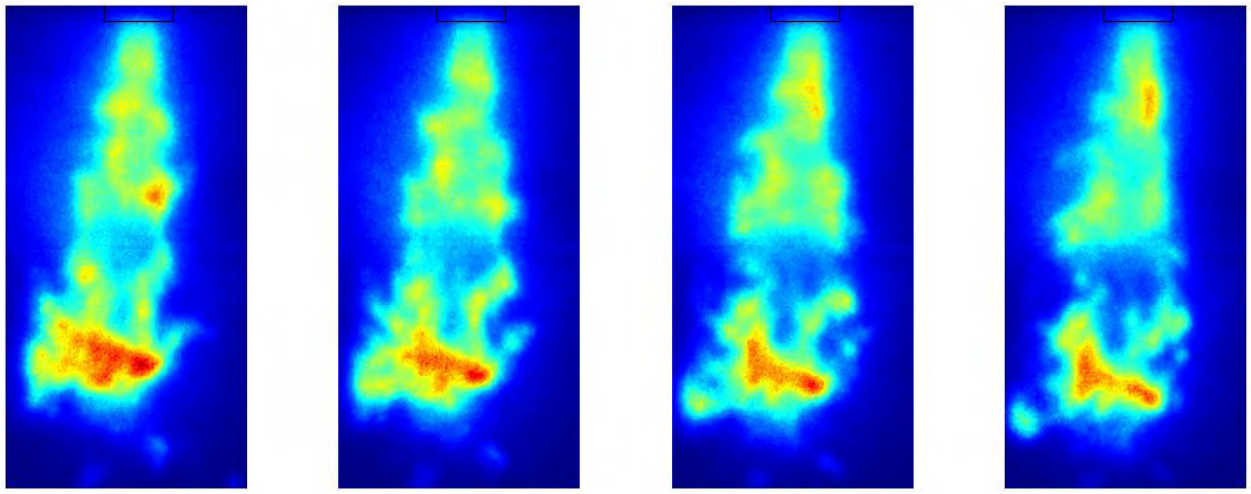

Figure 17. Liquid oxygen-gaseous hydrogen shear-coaxial jet flames without acoustic forcing. Four consecutive images are taken from a set of high speed images acquired at 16 kHz. The intensifier gate duration, which is essentially the camera exposure time, is set to 61 μs. Flame structures form near the injector exit and evolve as they travel downstream.
MR = 5.9, J = 2, $p_c \approx$ 400 psia = 2.76 MPa

University of California

Los Angeles

Multi-phase Combustion and Transport Processes Under the Influence of Acoustic Excitation

A dissertation submitted in partial satisfaction

of the requirements for the degree

Doctor of Philosophy in Mechanical Engineering

by

Jeffrey L. Wegener

2014

Abstract of the Dissertation

Multi-phase Combustion and Transport Processes Under the Influence of Acoustic Excitation

by

Jeffrey L. Wegener

Doctor of Philosophy in Mechanical Engineering

University of California, Los Angeles, 2014

Professor Ann R. Karagozian, Chair

This experimental study examined the coupling of acoustics with reactive multi-phase transport processes and shear flows. The first portion of this dissertation deals with combustion of various liquid fuels when under the influence of externally applied acoustic excitation. For this study, an apparatus at the Energy and Propulsion Research Laboratory, UCLA, used a horizontal waveguide to create a standing acoustic wave, wherein burning fuel droplets were positioned near pressure nodes within the waveguide. Alcohol fuels (ethanol and methonal) as well as aviation fuel replacements (Fischer-Tropsch (FT) synfuel and an FT blend with JP-8) were studied here. During acoustic excitation, the flame surrounding the droplet was observed to be deflected in a manner consistent with the direction of a theoretical acoustic radiation force, analogous to a buoyancy force, acting on the burning system. Based on this degree of deflection, a method was developed for experimentally quantifying the acoustic acceleration and relating it to the theoretical acoustic acceleration. This technique employed phase-locked optical imaging of the flame in the ultraviolet band in order to capture hydroxyl radical (OH*) chemiluminescence as an indication of the flame structure and shape. The flame was observed to be deflected in a bulk manner, but also with micro-scale oscillations in

time. The bulk or mean flame alteration was used to determine an experimental value of the acoustic acceleration for a range of different fuels and excitation conditions. This investigation showed experimentally determined acoustic accelerations which were quite consistent qualitatively with theory, but which were quantitatively inconsistent with theoretical predictions. Observed flame deformations were greatest for a droplet situated immediately next to a pressure node, in contrast to the theory, while milder flame deflections were observed for droplets positioned closer to a pressure antinode. These observations were consistent among all fuels studied, qualitatively and with the same mean qualitative trends. Phase-locked OH* chemiluminescence imaging revealed significant differences in the amplitude of flame oscillation based on the applied frequency and droplet location. Low frequency acoustic excitation and proximity to the pressure node produced higher amplitude flame oscillations, suggesting an enhanced degree of acoustically-coupled combustion that could be responsible for qualitative differences between theory and experimental measurements of acoustic acceleration.

The second portion of this dissertation utilized a similar, but more advanced facility which was recently constructed at the Air Force Research Laboratory, Propulsion Directorate (RQR). These experiments explored the interaction between acoustics and nonreactive shear-coaxial jets under high chamber pressure, acoustically resonant conditions, using liquid nitrogen as the inner jet and gaseous helium as the outer jet. The shear-coaxial jet was placed within the chamber, for which piezoelectric sirens could create a standing wave. The coaxial jet could thus be situated at either a pressure node or a pressure antinode location, and backlit high-speed imaging was used to resolve the naturally unstable mixing layer between the inner and outer jets. For jets with and without exposure to acoustic forcing, two different reduced basis methods were applied to the gray-scale pixel intensity data in order to extract instability frequencies and mode shapes from image sets; these included proper orthogonal decomposition (POD) and dynamic mode decomposition (DMD). A new POD-based method was used to quantify the

susceptibility of coaxial jets to external acoustic forcing by comparing the pixel intensity variance induced by the acoustic mode to the total variance of pixel intensity caused by fluctuations in jet mixing. A novel forcing susceptibility diagram was then created for coaxial jet momentum flux ratios of 2 and 6 for both pressure node and pressure antinode locations. Measurements of the critical forcing amplitude were made to quantify the acoustic perturbation amplitudes required in order for the forced mode to overtake the natural mode as the most dominant instability in the jet, which is generally classified as "lock-in" to the applied mode. It was found that, for forcing frequencies greater than the natural frequency of the jet, an increase in the forcing frequency caused the jet to be less susceptible to applied acoustic disturbances, thus requiring higher acoustic forcing to achieve "lock-in". This relationship held true for both pressure node and pressure antinode conditions. The shear layer instability characteristics of unforced jets were also investigated, and a theoretical convection velocity which depends on inner and outer jet velocities and densities was validated for the range of experimental flow conditions used in this study. An extensive description of the design of the experimental reactive facility is also offered, including preliminary results for oxygen-hydrogen coaxial jet flames acquired using high-speed OH* chemiluminescence imaging.

The dissertation of Jeffrey L. Wegener is approved.

Chris R. Anderson

Jeff D. Eldredge

Ivett A. Leyva

Owen I. Smith

Ann R. Karagozian, Committee Chair

University of California, Los Angeles

2014

to Samantha and Ian

Table of Contents

1 Introduction and Background 1

1.1 Combustion Instabilities 2

1.1.1 Physical Mechanisms 2

1.1.2 Gas Turbine Engines 7

1.1.3 Liquid Rocket Engines 8

1.2 Fuel Droplet Combustion 13

1.2.1 Alternative Fuels 13

1.2.2 Fundamental Droplet Combustion 15

1.2.3 Effects of Acoustics on Fuel Droplet Combustion 16

1.3 Shear-Coaxial Jets 21

1.3.1 Nonreactive Shear-Coaxial Jets 21

1.3.2 Reactive Shear-Coaxial Jets 39

1.4 Present Studies 46

2 Experimental Facility and Methods - Acoustically Coupled Fuel Droplet Combustion 56

2.1 Acoustic Waveguide 56

2.2 Droplet Generation and Ignition 60

2.3 Imaging 60

2.3.1 Optics 61

2.3.2 Image Acquisition 62

2.3.3 Acoustics-Imaging Synchronization 63
2.4 Measurement Methods 64
2.4.1 Burning Rate Constant 64
2.4.2 Acoustic Acceleration 65
2.4.3 Flame Standoff Distance 66
2.5 Experimental Procedure 67
2.6 Measurement Uncertainties 69
2.6.1 Precision Uncertainty 69
2.6.2 Bias Uncertainty 71

3 Results - Acoustically Coupled Fuel Droplet Combustion 86
3.1 Burning Rate Constant 86
3.1.1 Baseline Burning Rate Constant 86
3.1.2 Effect of Acoustics on Burning Rate Constant 87
3.2 Flame Behavior 88
3.2.1 Flame Deflection and Acoustic Acceleration 89
3.2.2 Standoff Distance 92

4 Experimental Facility and Methods - Shear-Coaxial Jets 116
4.1 High Pressure Chamber and Fluid Delivery Systems 117
4.1.1 Chamber 117
4.1.2 Propellant Systems 117
4.2 Inner Chamber 126
4.2.1 Inner Chamber Dimensions and Instrumentation 126

4.2.2 Inner Chamber Nitrogen Flows . . . 127
4.3 Waveguide Design and Characterization . . . 127
4.3.1 Acoustic Drivers . . . 128
4.3.2 Waveguide . . . 129
4.3.3 Resonant Frequencies . . . 132
4.4 Nonreactive Jet Imaging . . . 136
4.5 Reduced Basis Methods . . . 137
4.5.1 Proper Orthogonal Decomposition . . . 137
4.5.2 Application of Proper Orthogonal Decomposition . . . 142
4.5.3 Dynamic Mode Decomposition . . . 146
4.5.4 Application of Dynamic Mode Decomposition . . . 152
4.6 Measurement Uncertainty . . . 155

5 Results - Shear-Coaxial Jets . . . 182

5.1 Qualitative Observations of Liquid Nitrogen-Gaseous Helium Shear-Coaxial Jets . . . 182
5.2 Comparisons of POD and DMD . . . 186
5.3 Susceptibility of Nitrogen-Helium Shear-Coaxial Jets to Acoustic Forcing 191
5.3.1 Unforced Shear-Coaxial Jets . . . 192
5.3.2 Shear-Coaxial Jets Subject to Acoustic Forcing . . . 197

6 Conclusions and Future Work . . . 226

6.1 Studies on Acoustically-coupled Droplet Combustion . . . 226
6.2 Studies on Shear-coaxial Jets . . . 227

A Shear-Coaxial Jet Experimental Methods Details 230

A.1 Acoustic Forcing System 230

A.2 Positive Semidefinite Proof 232

List of Figures

1.1 Bimodal combustion instability feedback loop. 47
1.2 Three-part combustion instability feedback loop. 47
1.3 Photos of the Delta IV and Ariane 5 launch vehicles. 48
1.4 LRE gas generator cycle diagram. 48
1.5 Hydrogen temperature ramping plot for a LRE stability verification test. 49
1.6 Various configurations of the shear-coaxial injector element. 49
1.7 Diagram of the nonreactive shear-coaxial jet. 50
1.8 Liquid core break up images for coaxial jets of the membrane and fibre-type regime. 51
1.9 A convective shear layer diagrammed in the vortex frame of reference. . . 51
1.10 Five regimes of liquid-gas coaxial jet break up plotted with respect to Re and We. 52
1.11 Liquid nitrogen-gaseous helium coaxial jets issuing into subcritical and supercritical environments. 52
1.12 Velocity ratio plotted versus density ratio with absolute-convective instability transition lines. 53
1.13 Flow diagram of a reactive shear-coaxial jet. 54
1.14 Combustion instability feedback with controlled acoustic forcing. 55

2.1 Experimental setup of the acoustic waveguide and feed droplet system. . 76
2.2 Frequency sweep for the speaker-speaker configuration with speakers operated 180^o out-of-phase and a PN occurring at the center of the waveguide. 77

2.3 Frequency sweep for the speaker-speaker configuration with speakers operated in-phase (0^o) and a PAN occurring at the center of the waveguide. 78

2.4 Frequency sweep for the speaker-reflector configuration. 79

2.5 Acoustic pressure amplitude measurements for the speaker-reflector configuration. 80

2.6 Acoustic pressure amplitude measurements for the speaker-speaker configuration ($\phi = 180^o$). 81

2.7 Acoustic pressure amplitude measurements for the speaker-speaker configuration ($\phi = 0^o$). 82

2.8 OH* chemiluminescence optics 83

2.9 Transmission versus wavelength for the optical system. 84

2.10 OH* chemiluminescence image for ethanol under acoustic forcing. 85

2.11 Abel transformed ethanol flame image. 85

3.1 OH* chemiluminescence images of burning droplets in the absence of acoustic forcing. 98

3.2 Pressure perturbations, estimated theoretical and actual acoustic accelerations g_a, and average burning rate constant K as a function of waveguide location for the ethanol droplet burning in the vicinity of a pressure node at a frequency of 332 Hz and $p'_{max} = 150$ Pa. 99

3.3 Pressure perturbations, estimated theoretical and actual acoustic accelerations g_a, and average burning rate constant K as a function of waveguide location for the ethanol droplet burning in the vicinity of a pressure node at a frequency of 898 Hz and $p'_{max} = 150$ Pa. 100

3.4 Pressure perturbations, estimated theoretical and actual acoustic accelerations g_a, and average burning rate constant K as a function of waveguide location for the ethanol droplet burning in the vicinity of a pressure node at a frequency of 1500 Hz and $p'_{max} = 150$ Pa. 101

3.5 Pressure perturbations, estimated theoretical and actual acoustic accelerations g_a, and average burning rate constant K as a function of waveguide location for the methanol droplet burning in the vicinity of a pressure node at a frequency of 332 Hz and $p'_{max} = 150$ Pa. 102

3.6 Pressure perturbations, estimated theoretical and actual acoustic accelerations g_a, and average burning rate constant K as a function of waveguide location for the methanol droplet burning in the vicinity of a pressure node at a frequency of 898 Hz and $p'_{max} = 150$ Pa. 103

3.7 Pressure perturbations, estimated theoretical and actual acoustic accelerations g_a, and average burning rate constant K as a function of waveguide location for the methanol droplet burning in the vicinity of a pressure node at a frequency of 1500 Hz and $p'_{max} = 150$ Pa. 104

3.8 Pressure perturbations, estimated theoretical and actual acoustic accelerations g_a, and average burning rate constant K as a function of waveguide location for the FT droplet burning in the vicinity of a pressure node at a frequency of 332 Hz and $p'_{max} = 150$ Pa. 105

3.9 Pressure perturbations, estimated theoretical and actual acoustic accelerations g_a, and average burning rate constant K as a function of waveguide location for the FT droplet burning in the vicinity of a pressure node at a frequency of 898 Hz and $p'_{max} = 150$ Pa. 106

3.10 Pressure perturbations, estimated theoretical and actual acoustic accelerations g_a, and average burning rate constant K as a function of waveguide location for the FT droplet burning in the vicinity of a pressure node at a frequency of 1500 Hz and $p'_{max} = 150$ Pa. 107

3.11 Pressure perturbations, estimated theoretical and actual acoustic accelerations g_a, and average burning rate constant K as a function of waveguide location for the JP8FT droplet burning in the vicinity of a pressure node at a frequency of 332 Hz and $p'_{max} = 150$ Pa. 108

3.12 Pressure perturbations, estimated theoretical and actual acoustic accelerations g_a, and average burning rate constant K as a function of waveguide location for the JP8FT droplet burning in the vicinity of a pressure node at a frequency of 898 Hz and $p'_{max} = 150$ Pa. 109

3.13 Pressure perturbations, estimated theoretical and actual acoustic accelerations g_a, and average burning rate constant K as a function of waveguide location for the JP8FT droplet burning in the vicinity of a pressure node at a frequency of 1500 Hz and $p'_{max} = 150$ Pa. 110

3.14 Ethanol flame images under the influence of acoustics. Flames are consistently deflected away from the pressure node (PN). 111

3.15 A pair of ethanol flame images acquired at different points within the acoustic cycle. 111

3.16 Horizontal flame standoff distance plotted versus the acoustic pressure phase. All fuels and acoustic frequencies are shown for three select waveguide locations. 112

3.17 Standoff distance oscillation amplitude plotted versus waveguide location. 113

3.18 Time-averaged standoff distance plotted versus waveguide location. . . . 114

3.19 Time-averaged standoff distance plotted versus theoretcal acoustic acceleration. 114

3.20 Time-averaged standoff distance plotted versus nondimensional horizontal velocity 115

4.1 Three-dimensional CAD rendering of the AFRL combustion chamber. . . 161

4.2 Oxygen heat exchanger diagram. 162

4.3 Hydrogen heat exchanger diagram. 163

4.4 Time series plot of a typical firing sequence. 164

4.5 Minimum inner jet temperatures with oxygen flow. 165

4.6 Minimum outer jet temperatures with helium flow. 166

4.7 Minimum inner and outer jet temperatures with nitrogen flow. 167

4.8 Experimental facility parametric mapping of density ratio S vs. chamber pressure p_c. 168

4.9 The dimensions of the coaxial injector used for new experiments in this study. 168

4.10 Cross sectional CAD view of the shear-coaxial injector. 169

4.11 Experimental facility parametric mapping of inner jet Reynolds number Re_{ij} vs. outer jet Reynolds number Re_{oj}. 170

4.12 Shear-coaxial jet velocity profile diagram. 171

4.13 Experimental facility parametric mapping of momentum flux ratio J vs. mixture ratio MR. 172

4.14 Acoustic pressure spectra results for both the left and right piezo sirens when placed outside of the combustion chamber. 173

4.15 Diagram of a rigid-walled duct of variable cross-sectional area $A(y)$. . . . 174

4.16 Chamber cross sectional area plotted versus the transverse direction y, including the left waveguide, inner chamber, and right waveguide. 174

4.17 Acoustic frequency sweep results for PAN conditions at various chamber pressures. 175

4.18 A single row of matrix **A** constructed from an $m \times n$ image for POD analysis. 176

4.19 Matrix **A** constructed from N images and M pixels for POD analysis. . . 176

4.20 Instantaneous, time-averaged, and cropped image samples. 177

4.21 POD singular values computed for $J = 2$ and $f_F = 2050$ Hz at a PN. . . 177

4.22 POD eigenvalues computed for $J = 2$ and $f_F = 2050$ Hz at a PN. 178

4.23 POM images for mode-1 and mode-2 at $J = 2$ and $f_F = 2050$ Hz at a PN. 178

4.24 PSD spectra for POD mode-1 at $J = 2$ and $f_F = 2050$ Hz at a PN. . . . 179

4.25 CPSD spectra for POD modes-1 and mode-2 at $J = 2$ and $f_F = 2050$ Hz at a PN. 180

4.26 Mode frequencies, amplitudes, and growth rates identified by DMD for $J = 2$ and $f_F = 2050$ Hz at a PN. 181

4.27 Reconstructed images of the unstable mode identified by DMD at $J = 2$ and $f_F = 2050$ Hz at a PN. 181

5.1 Enlarge sample of the shear-coaxial jet field of view, accompanied by snapshot samples. 206

5.2 Sample of four consecutive OH* chemiluminescence snapshots. 207

5.3 Cross power spectral density for modes 3 and 4 of an unforced jet at $J = 6$. 208

5.4 POD eigenvalues computed for $J = 2$ without acoustic forcing. 209

5.5 Reconstructed jet images for POMs 1-12 for an unforced jet at $J = 6$. . . 210

5.6 PSD and eigenvector images shown for mode-3 and mode-4, representing the natural mode pair for $J = 6$. 211

5.7 Mode frequencies, amplitudes, and growth rates identified by DMD for $J = 6$ without acoustic forcing. 212

5.8 Instability frequency versus shear layer convective velocity. 213

5.9 Jet Strouhal number versus J using a theoretical convection velocity. . . 214

5.10 Time-average coaxial jet image which defines the inner shear layer curve s.214

5.11 The pixels located on the inner shear layer curve s plotted versus time. . 215

5.12 Measured shear layer convection velocity $U_{c,meas}$ versus a theoretical convection velocity $U_{c,th}$. 216

5.13 Jet Strouhal number versus J using a measured convection velocity. . . . 216

5.14 Forcing susceptibility diagram for a shear-coaxial jet at a PN. 217

5.15 LN_2-GHe shear-coaxial jets exposed to acoustic forcing at a PN. 218

5.16 PSD and eigenvector images shown for mode-2 and mode-3, representing the forced mode pair for $J = 2$ at a PN. 219

5.17 Forced mode variance contribution versus forcing amplitude (PN). 220

5.18 Forcing susceptibility diagram for a shear-coaxial jet at a PN. 221

5.19 LN_2-GHe shear-coaxial jets exposed to acoustic forcing at a PAN. 222

5.20 PSD and eigenvector images shown for mode-1 and mode-2, representing the forced mode pair for $J = 2$ at a PAN. 223

5.21 Forced mode variance contribution versus forcing amplitude (PAN). . . . 224

5.22 Forced mode variance contribution versus a nondimensional forcing amplitude (PAN). 225

A.1 Piezoelectric acoustic siren. 235

A.2 Cross sectional CAD rendering of the left waveguide. 235

A.3 Acoustic forcing flow chart. 236

A.4 Acoustic pressure spectra results for p_c=400 psia. 237

A.5 Facility piping and instrumentation diagram (PID) page 1. 238

A.6 Facility piping and instrumentation diagram (PID) page 2. 239

List of Tables

2.1 Experimental and Theoretical Resonant Frequencies 73

2.2 Fuel Properties 74

2.3 Camera Specifications 75

3.1 Comparison of measured values of burning rate constant K for various fuel droplets in the absence of acoustic excitation. 97

4.1 AFRL injector dimensions. 159

4.2 Pressure transducer uncertainty values. 160

A.1 Data for unforced LN_2-GHe nonreactive experiments. 233

A.2 Data for acoustically forced LN_2-GHe nonreactive experiments. 234

Nomenclature

Symbols or Abbreviations

$\mathbf{A}$	matrix form of pixel intensities for an image set
$\widetilde{\mathbf{A}}$	matrix form of mean pixel intensities for an image set (POD)
a	set of pixel intensities for an image set
c	speed of sound
$\mathbf{D}$	eigenvalue matrix (DMD)
f	frequency
f_F	acoustic forcing frequency
f_{nat}	natural jet instability frequency
g_a	acoustic acceleration
g_o	gravitational acceleration
I	acoustic intensity
J	outer-to-inner jet momentum flux ratio
K	burning rate constant
L	distance between acoustic drivers
M	number of pixels in one image
MR	oxygen-to-fuel mixture ratio
N	number of images
Oh	Ohnesorge number
p_c	mean chamber pressure
p'	pressure perturbation

Symbols or Abbreviations (continued)

Q_v	volumetric flow rate
R	outer-to-inner jet velocity ratio
$\mathbf{R}$	covariance matrix (POD)
Re	Reynolds number
S	outer-to-inner jet density ratio
$\widetilde{\mathbf{S}}$	companion matrix (DMD)
St	Strouhal number
T_∞	ambient temperature
$\mathbf{U}$	orthogonal matrix containing temporal information (POD)
U_∞	bulk flow velocity
U_c	shear layer convection velocity
u_k	vector of temporal amplitude coefficients for mode k (POD)
u'	velocity perturbation
$\mathbf{V}$	orthogonal matrix containing spatial information (POD)
v_k	vector of proper orthogonal mode k (POD)
We	Weber number
z_a	acoustic impedance

Greek Symbols

α	density difference correction factor
ϕ	phase
ϕ_f	flame deflection angle
$\phi_{f/o}$	fuel-to-oxygen equivalence ratio
$\mathbf{\Lambda}$	product of the singular value matrix and its transpose (POD)
λ	acoustic wavelength
ω	complex eigenvalues (DMD)
ρ	density
$\mathbf{\Sigma}$	diagonal matrix singular values (POD)

Subscripts

B	buoyancy
$eqvs$	equivalent volume of a sphere
exp	experimental
f	flame
i	imaginary
ij	inner jet
oj	outer jet
p	hot combustion products
R	acoustic radiation
r	real
s	surface
th	theoretical
II	image intensifier

Acknowledgments

The shear-coaxial jet experimental work was sponsored by the Air Force Office of Scientific Research (AFOSR), Laboratory Task 11RZ07COR, under Dr. Mitat Birkan, program manager, and facility development support was provided by AFRL Commander's Revitalization Funds. AFOSR must also be thanked for the equipment grant that allowed the Energy and Propulsion Laboratory at UCLA to purchase the NanoStar Camera, without which ultraviolet imaging of burning droplet experiments would not be possible. I am also thankful for the departmental fellowship I received from the UCLA Mechanical and Aerospace Engineering Department, which allowed me to begin full-time graduate study in the 2009-2010 academic year. The department also supported me as a Teaching Assistant for the 2010-2011 academic year.

I owe Drs. Doug Talley and Ivett Leyva for this opportunity. I was entrusted with a tremendous amount of responsibility during the construction of this facility, and as a result, I am better prepared for what lies ahead. Many of my tasks involved on-the-job training, which required patience on their part. Much of this on-the-job training occurred under the watch of Randy Harvey. Randy is a technician with the analytical approach of an engineer. Working with Randy, I was confident someone was always watching over me and ready to catch my engineering mistakes. Together, Randy and I built a spectacular machine which will bear fruit for many years. I am also indebted to Dr. David Forliti for emphasizing scientific education and fundamental research where basic engineering and facility validation often took precedence. Thanks to his emphasis, this dissertation contains merit with regard to both scientific research and facility engineering. Finally, I thank Prof. Ann Karagozian for trusting me and my abilities, even when progress was much slower than expected. Her encouragement was a boost of confidence when I needed it the most.

Vita

2003	High School Diploma, Raytown High School, Raytown, MO
2007	B.S. Mechanical Engineering, Missouri Univ. of Science and Technology (ST)
2007-2009	Departmental Fellowship, Mechanical and Aerospace Engineering Department, Missouri ST
2009	M.S. Mechanical Engineering, Missouri ST
2009	Propulsion Research Scientist, Air Force Research Laboratory (AFRL), Edwards AFB, CA
2009-2010	Departmental Fellowship, Mechanical and Aerospace Engineering Department, UCLA
2010	Teaching Assistant, Mechanical and Aerospace Engineering Department, UCLA. MAE 157 - Basic Mechanical Engineering Laboratory
2011	Teaching Assistant, Mechanical and Aerospace Engineering Department, UCLA. MAE 150C - Combustion
2011	M.S. Aerospace Engineering, UCLA
2011-2013	Graduate Student Researcher, AFRL, Edwards AFB, CA
2013	American Institute of Aeronautics and Astronautics (AIAA) Liquid Propulsion Student of the Year

Publications and Presentations

J.L. Wegener, I.A. Leyva, D.J. Forliti, and D.G. Talley, Development of a Facility for Combustion Stability Experiments at Supercritical Pressure, 52nd AIAA Aerospace Sciences Meeting, National Harbor, MD, January 13-17, 2014.

C.I. Sevilla-Esparza, J.L. Wegener, S. Teshome, J.I. Rodriguez, O.I. Smith, and A.R. Karagozian, Droplet Combustion in the Presence of Acoustic Excitation, to be published in Combustion and Flame.

J.L. Wegener, C. Sevilla, J. Smolke, A. Sung, K. Chen, O.I. Smith, and A.R. Karagozian, Transient OH* Chemiluminescence Imaging of Acoustically Coupled Fuel Droplet Combustion, APS/DFD Meeting, Baltimore, MD, November 20-22, 2011.

H. Lan, J.L. Wegener, B.F. Armaly, and J.A. Drallmeier, Simulations and Measurements of 3-D Gravity Driven Liquid Film Flow, J. Fluids Eng., Vol. 132, 081301, 2010.

J.L. Wegener and J.A. Drallmeier, Measurement of Thin Liquid Film Characteristics using Laser Focus Displacement Instruments for Atomization Applications, 22nd Annual ILASS-Americas Conference, Cincinnati, OH, May 16-19, 2010.

J.L. Wegener, M.A. Friedrich, J.A. Drallmeier, and B.F. Armaly, Experimental Validation of a Film Separation Criterion, 11th Triennial ICLASS Conference, Vail, CO, July 26-30, 2009.

CHAPTER 1

Introduction and Background

Acoustic fluctuations are coupled to condensed phase combustion in an array of important power generation and propulsion applications, including liquid rocket engines (LREs), gas turbine engines, and other air-breathing engines. Although each combustion system exhibits unique problems caused by acoustic fluctuations, a broad view of the field reveals an inability to suppress combustion instabilities due to a lack of fundamental knowledge regarding the coupling of combustion and acoustics. The inability to control these instabilities has led to engine and engine component failures in the case of liquid rocket and gas turbine engines, and a consequential increase in combustion instability research.

This study contributes to this field by isolating the problem in two ways. First, a set of alternative fuel combustion experiments performed at the UCLA Energy and Propulsion Research Laboratory investigate the behavior of burning droplets placed within standing acoustic waveforms. Second, a study at the advanced experimental facility of the Air Force Research Laboratory at Edwards AFB, CA explores coaxial, cryogenic non-reactive and reactive jets in the presence of strong acoustic forcing in a high pressure chamber. Each respective study concentrates effort towards behaviors which have a direct impact on the instabilities observed in the predominant applications (gas turbine engines and LREs). Such behaviors include but are not limited to acoustically altered fuel burning rates, droplet flame deformations, and acoustically enhanced jet mixing and atomization. These phenomena hold paramount importance in that they impact

performance, efficiency, and robustness of the system.

1.1 Combustion Instabilities

Combustion instabilities are characterized by large amplitude oscillations of one or more acoustic modes or injector modes of a combustion chamber. The pressure and velocity perturbations produced by these instabilities are problematic because they result in thrust oscillations, severe vibrations that interfere with control system operation, increased heat transfer and thermal stresses to combustor walls, oscillatory mechanical loads that fatigue hardware components, and flame blowoff or flashback [1]. This study provides an overview of combustion instability by first describing the physical mechanisms which fundamentally create the phenomena. The physical mechanisms section is followed by discussion of instability in two primary power systems. A brief background of combustion instabilities in gas turbine engines is given first, due to its relevance to the fuel droplet combustion results in chapter 3. This is followed by a historical summary of LRE combustion instability, which is directly related to the shear-coaxial jet research of chapter 5. A literature review is then presented for fundamental research of fuel droplet combustion and shear-coaxial jets.

1.1.1 Physical Mechanisms

In the most fundamental sense, a system's stability relies on competing mechanisms of driving and damping. The stability of a combustion system and its associated heat release as shown in Fig. 1.1 is determined by acoustic feedback, which can cause driving or damping. The genesis of acoustics though, often lies in unsteady heat release generated by changes in local propellant reaction rates. These changes in reaction rate can also be governed by fuel-oxidizer mixing fluctuations in the flame region. In this case a third

mechanism, fluid mixing, is the origin of unsteady heat release and thus, the production of acoustic energy [2]. A discussion on the combustion instability feedback loop, then, will begin here with a fluid dynamics mechanism.

This physical sequence of events is depicted in Fig. 1.2, which is a detailed version of the more common bimodal representation in Fig. 1.1 [3–5]. The thermoacoustic feedback loop is reduced to three major phenomena, a graphical representation also utilized by Candel [6] and others [7, 8]. These three are represented by oscillations in fluid velocity u', heat release q', and acoustic pressure p' in Fig. 1.2, which are perturbations from the time averaged value, i.e.

$$u = \overline{u} + u' \tag{1.1}$$

$$q = \overline{q} + q' \tag{1.2}$$

$$p = \overline{p} + p' \tag{1.3}$$

Reactive flows can exhibit velocity oscillations due to several perturbation sources, many of which naturally occur in the absence of the acoustic fluctuations. Fluid dynamic instability inherent to a reactive flow instigates the existence of thermoacoustic instability, and only after the onset of acoustic pressure perturbations will acoustic waves act upon the propellant velocity u to complete the instability feedback loop. Natural fluid dynamic instabilities can be provoked by large-scale events such as inlet flow oscillations [9], engendering shear layer instability [10] or vortex development, whereas small scale events like droplet formation and atomization can also have an important role through enhanced mixing and entrainment. High Reynolds number flows supply broadband turbulence to the flame region [11], enhancing molecular mixing processes. Flow instabilities with distinct frequencies often accompany broadband noise, asserting high amplitude velocity fluctuations, and thus mixing oscillations, in the flame region.

Ultimately, these mixing fluctuations will alter flame location and shape via changes in species concentration. This relationship is the link between "Fluid Dynamic Insta-

bility" and "Unsteady Heat Release" in Fig. 1.2. For example, inlet flow oscillations of fuel or oxidizer can globally alter mixture ratio and flame strain rates to the point of extinction [12]; this behavior is shown to be influenced by pressure [13]. Shear flow instabilities produce locally unsteady heat release due to continually changing species mass fractions and densities [14, 15], and heat release fluctuations may adopt the instability frequency naturally occurring in the shear layer. Vortex shedding may result from the puffing behavior of inlet flow oscillations [16] or from shear layer vorticity. In the case of two-phase flow, oscillatory behavior can results from differences in times scales associated with breakup, vaporization, and mixing processes. The extent to which chemical reaction processes and fluid mechanical/mixing processes control combustion is described by the Dahmkohler number

$$Da = \frac{\tau_m}{\tau_{ch}} \tag{1.4}$$

which is a ratio of the characteristic fluid mixing time τ_m and the characteristic reaction time τ_{ch}. For large-scale fluid structures, τ_m is often large in comparison to reaction time scales, hence combustion is limited by reactant mixing of diffusive processes. For small-scale mixing such as that which occurs during droplet atomization and reaction, τ_m is often small compared with reaction rates, and as such are instead limited by kinetics (τ_{ch}). Overall, both fluid mechanics and chemical kinetics must be considered to ascertain the controlling factor in an unsteady combustion system.

In acoustically-coupled combustion, the flame will significantly impact the fluid dynamics, making this interaction two-way coupled. The natural instability frequencies of different types of two-phase shear flows have been shown to be dependent on density, velocity, and viscosity gradients [10], which are manipulated by a flame's temperature distribution when in the presence of a reaction. In addition, the flame's elevated temperatures introduce rapid dilatation and alter the pressure and density distributions which can produce vorticity through baroclinic torque. Subsequently, the interdependence of

fluid dynamics and the flame create a strong coupling which is critical in combustion stability.

As spatio-temporal flame oscillations cause unsteady heat release, thermal expansion and contraction will be concomitant with pressure oscillations which propagate through the surrounding media at the speed of sound. In Fig. 1.2, the enhancement of acoustics by unsteady heat release is represented by the link between "Unsteady Heat Release" and "Acoustic Waves". Increasing pressure perturbations may result when heat release oscillation frequencies equal resonant modes of the combustion chamber. Resonant chamber modes can be radial, tangential, longitudinal, or a mixture of the three, and are determined by geometric chamber dimensions [8, 17–19]. Acoustic pressure oscillations alone may have little direct effect on combustion processes. For example, this is supported by experiments of droplet combustion [20–22] at velocity nodes, i.e. locations of maximum pressure perturbation and zero velocity perturbation in a standing acoustic wave. In this example, there is little coupling between acoustic waves and unsteady heat release, exemplified by minimal changes in burning rate and flame shape.

However, acoustic perturbations in general have an influence on fluid dynamic processes. Both pressure nodes (PNs) ($p' = 0$, $u' = u'_{max}$) and pressure antinodes (PANs) ($p' = p'_{max}$, $u' = 0$) have a unique effect on fluid dynamic processes. Large tangential acoustic velocity oscillations at a PN act to increase mixing and vorticity by inducing additional velocity perturbations within the shear flow, and the natural mode of a shear layer may be overtaken by that of external acoustic forcing [23, 24], especially if the shear layer is convectively unstable [25]. In the case of coaxial jets, a PN condition may also intensify mixing [16, 19, 26] and create a sinuous yet cohesive jet shape [27–30]. If located at a PAN, an incoming flow may be impeded by a periodic rise in chamber pressure [16]. The resulting flow rate pulsations induce a time dependent mixture ratio MR, and large-scale yet relatively symmetric chugging instability. Flow rate pulsations

may also occur for traveling waves which can result in behaviors representative of both a PAN and a PN.

Hence, acoustic feedback serves to amplify or attenuate unsteady heat release through both pressure and velocity perturbations which affect the flow field. Past studies have described this relationship via the well-known the Rayleigh criterion [31]. The Rayleigh criterion addresses the problem using the phase relationship between pressure and heat release oscillations. This two-part approach reduces the complexities described above by including only the pressure oscillation amplitude p' and the heat release oscillation amplitude q', and is often explained using the bimodal diagram in Fig. 1.1 [3–5]. Amplification is said to occur if the pressure perturbation p' occurs in-phase with the heat release perturbation q'. Damping occurs when p' and q' are out-of-phase. The associated Rayleigh index G is given by

$$G(x) = \frac{1}{T}\int_T p'(x,t)q'(x,t)\mathrm{d}t \tag{1.5}$$

which integrates the pressure and heat release oscillations over the time period T to quantify the extent to which the instability is amplified ($G > 0$), or the system experiences damping ($G < 0$). The Rayleigh index is a valuable tool for measuring the coupling of acoustics and combustion or lack thereof, but it does not describe the underlying physics of combustion instability. Utilization of the Rayleigh criterion for measuring the coupling of acoustics and combustion has been used in an experimental dump combustor study by Smith and Zukoski [32] which later inspired more detailed work by Yu *et al.* [33] and Schadow and Gutmark [34] in similar geometries, where low frequency convective modes in the combustion chamber triggered pulsating inlet flow rates which resulted in uncontrolled p' amplification and positive values of the Rayleigh index G. McManus *et al.* [2] and Candel [6] review the Rayleigh criterion's use within other unsteady combustion systems. The Rayleigh criterion is an appropriate quantitative gauge of acoustic-flame coupling, but is particularly valuable in explaining causality when also

accompanied by a investigation of fluid dynamic instability in a three-part approach including heat release, pressure perturbations, and fluid mixing associated with velocity perturbations.

1.1.2 Gas Turbine Engines

The 1980s marked the start of a momentous increase in the importance of instabilities in gas turbine engines. Added attention arose from the challenges of meeting NOx emission standards, chiefly the Gas Turbine New Source Performance Standards (NSPS) in 1979 and the EPA's Best Available Control Technology (BACT) approach in 1987, which were followed by the more broad Clean Air Act Amendments of the 1990s [35, 36]. Formation of nitrogen oxides (NO_x) most commonly has an exponential dependence on temperature via the 'thermal' NO mechanism, and thus NOx reduction requires a decrease in combustor flame temperatures [37]. This is often achieved with leaner fuel-air mixtures [37], which can create lower flame temperatures. Lower flame temperatures bring the combustor closer to the lean blowout condition, where small temporal variations in fuel-air ratio can significantly affect the heat release rate, burning rate, and flame position and shape. Leaner conditions are often associated with pulsations in the flow field. The ensuing combustor pressure oscillations in gas turbines can reach amplitudes as high as 6 psi (rms). Resulting problems have included cracking of combustion chambers, fretting of the outside of the fuel injector, intolerable noise, and other damage [38, 39].

Premixing or partially-premixing of fuel and air has also been employed in gas turbine engines to reduce NOx by eliminating localized high temperatures characteristic of the presence of local diffusion flames. Yet the premixing technique has also shown to contribute to instabilities. Thus, combustion guidelines are being developed for new diffusion flame combustor concepts to eliminate potential instability problems [39]. Consequently, the renewed value of research in non-premixed flames in the presence of acous-

tics calls for salient relationships describing the behavior of jet and droplet/spray flames within acoustic flow fields. These relationships depend on fuel type, which is gaining recognition due to the increasing popularity of alternative fuels for aircraft engines [40].

1.1.3 Liquid Rocket Engines

Historically, only one propulsion method has been used for a vehicle to escape the earth's gravitational field and travel into outer space. Currently and in the near future, this technique remains chemical propulsion. Solid motors, liquid rocket engines (LREs), and hybrid engines, or a combination thereof, have been incorporated into multiple stages to provide the necessary thrust for successful launch vehicles to date [41]. Liquid rocket engines are part of the foundation of any launch vehicle's propulsion system due to their ability to endure long periods of operation with the required levels of thrust. Pairing LREs with high thrust solid rocket boosters to constitute a vehicle's first stage is a common configuration for providing greater acceleration early in flight, followed by disposal of the spent solid motors. For example, the Atlas V uses this technique, as well as the Ariane 5 and the Delta IV, shown in Fig. 1.3.

Liquid rocket engines typically achieve higher specific impulses than their solid and hybrid counterparts, but at the cost of more complexity. An LRE stores propellants as a liquid and uses a system of pipes, valves, manifolds, and injectors to feed fuel and oxidizer into the combustion chamber. In the most simple design, high pressure propellant tanks supply propellants to the chamber. The pressure-fed cycle though, requires thick-walled propellant tanks, limited chamber pressure, or a combination thereof in order to produce the required propellant flow rates. The pressure-fed cycle can be used for upper stage engines, where heavy tanks are acceptable because the upper stage constitutes a relatively small portion of the launch vehicle's total weight at low altitudes. On the other hand, first stage LREs often adopt turbopumps to drive high propellant supply

pressures and combustion chamber pressures while using low pressure tanks. There are exceptions to this rule though, and one example is the upper stage RL10 engine, driven by turbopumps. One type of pump-fed system is the gas-generator engine cycle, which is discussed here as an exemplary illustration of the intricacies within an LRE.

In a gas-generator cycle, a small amount of fuel and oxidizer flow is diverted to produce energy to drive the propellant pumps. The "gas generator" of this engine cycle burns a propellant mixture with a small flow rate and spins a turbine with the hot exhaust products before diverting the exhaust outside the engine. The pre-burner, an alternative to the gas-generator, serves a similar purpose but routes the turbine exhaust into the main combustion chamber. The fuel pump and oxygen pump can be placed on the same shaft such that both propellant pumps are driven by a single turbine, thus minimizing weight and complexity. This configuration is shown in the flow diagram in Fig. 1.4. Alternatively, the gas-generator exhaust can drive two separate turbines, one for each pump. Fuel is commonly used as a chamber and nozzle coolant by routing cold fuel through channels in the chamber and nozzle walls prior to flowing into the injector plenum. In the J-2 engine used in the Apollo program, for example, hydrogen at less than 25 K traveled through tubes welded to the outside of the nozzle wall and was subsequently heated to 110 K before reaching the hydrogen injector distribution dome [42].

These propellant feed systems, as well as the chamber's acoustic modes and the engine structure, can interact with chamber pressure oscillations to sustain instability. The existence of pressure amplitudes exceeding the amplitude of the noise floor is considered combustion instability, and in this sense, a liquid rocket engine is never perfectly smooth. Pressure fluctuations having peak-to-peak magnitudes less that 5% of the chamber pressure, $\frac{p'}{p_c} < 0.05$, are considered "smooth" and larger amplitudes generally designate "rough" combustion [41]. However, payload considerations often can only tol-

erate combustion instabilities having amplitudes much less than 5% of p_c. Furthermore, the nondimensional value of $\frac{p'}{p_c}$ has become the most common method for quantitative evaluation of combustion instability in LREs.

Combustion instabilities are also classified with regard to frequency. Frequencies less than 400 Hz are considered low frequency instabilities, also termed "chugging" instabilities. Interaction between injector feed systems and the combustion chamber is often the cause of low frequency instability [3], whereby chamber pressure momentarily rises above the propellant supply pressure(s), impeding inlet flow and initiating pulsations in propellant flow rate. Frequencies between 400 Hz and 1000 Hz are intermediate frequency instabilities and are commonly related to vibrations of the engine structure, but can also be caused by combustion processes. High frequency instability occurs at frequencies greater than 1000 Hz. Instabilities of this type, called "screeching" instabilities, generally involve excitation of acoustically resonant chamber modes and can rapidly amplify to destructive magnitudes; this makes diagnosis and prevention very challenging.

For LREs, early recognition of combustion instabilities has lead to a vast history of research. By the 1950s, German rocket technology from the Peenemuende program had literally been moved to France, the Soviet Union, and also the United States, where slight modifications to existing German V-2 and V-4 rockets exhibited combustion instability. After changing the concave injector face of the V-4 to a flat injector arrangement for the Navaho engine [43], the Navaho was unstable until injector baffles were added in 1960 [44]. During the same period of time, the X-1 engine was developed strictly for scientific exploration by an experimental engines group in the US Department of Defense. This program identified stability problems during staged startup tests and throttling tests [45], an issue which still occurs in modern engine development programs [44].

One of the first major campaigns in the engine stability discipline occurred in the

1960s, largely motivated to suppress vibrations in human-carrying flights to the moon [46]. Of the 3200 full-scale tests of the Saturn V's F-1 engines from 1962-1966, about 2000 of these tests were principally focused on combustion instability as part of a program called Project First [47]. It was learned that injector design, which controlled interactions between jets of fuel and oxidizer, was of utmost importance. The F-1 engine, in particular, used impinging style injectors where two jets of fuel and two jets of oxygen converge on a single impingement point to atomize and burn. Injector configurations which were originally deemed as producing 'absolutely' stable engine conditions were later shown to have less stability for different fuels and flow conditions [46, 48], revealing an incomplete understanding of the problem.

In parallel, the J-2 engine was also developed in the 1960s, but with key design differences from the F-1 and much better stability characteristics. The J-2 was one of the first successful hydrogen fueled rocket engines, whereas the F-1 used kerosene based fuel (RP-1). The J-2 also utilized shear-coaxial injectors [42]. The engine's first tests resulted in high frequency instability, but was reduced to an acceptable level using radial baffles. Particular conditions also resulted in low frequency chugging, which was eliminated using a metering orifice at the inlet of the oxygen tube. This technique effectively made oxygen flow insensitive to chamber pressure perturbations by increasing the pressure drop across the injector, but did not alter the high frequency instability margin [45]. Thus, although high and low frequency modes coexisted, tolerable high frequency instability endured from its own prevailing cause. This inadequate state of the practice resulted in inefficient approaches involving many expensive tests, often in a trial-and-error method. New programs specifically dealing with combustion instabilities in liquid rockets did not appear again in the U.S. until the 1980s, which coincided with a comprehensive research program in France following the failure of an Ariane vehicle due to combustion instability in a Viking engine [49].

LRE instability testing and abatement empirical techniques have improved since the extensive tests of the F-1, but a lack of reliable design criteria has made use of these techniques a requirement for new engine development programs. As mentioned above, acoustic baffles were an early choice for unstable engines, but additional hardware was avoided due to cost and weight. Instead, engineers adopted the injector, injector plenum geometry, and acoustic cavities as primary variables to control mixing while preventing propellant flow oscillations. Margins of stability were found to be sensitive to small changes in the geometry of shear-coaxial injectors. For example, in a subscale engine study a mild recess of the oxygen tube was found to shift the range of operating conditions in which the engine was stable [50]. Fig. 1.6 shows the numerous ways in which the oxygen tube or "LO_x post" has been manipulated in the past, and one or more of these designs is still used today [45]. Stability testing, on the other hand, has been aimed at identifying three areas of operations: stable, dynamically unstable, and spontaneously unstable. When the engine is subject to an initial, controlled perturbation, or "bomb", measured pressure oscillations will return to original levels if the engine is stable. In such tests, the chamber is required to reach stability within a limited time, which is calculated as a function of frequency. Conversely, a dynamically unstable engine will sustain significant chamber pressure oscillations after the perturbation subsides. An operating point is deemed spontaneously unstable if the engine is self-excited [51]. Finally, hydrogen temperature ramping is a stability testing method that should be mentioned due to its relevance to this study. A range of fuel temperatures is included while testing gas generator cycle and expander cycle LREs, because variables such as run time and throttle set point will determine the amount of heat energy added to the fuel upstream of the injector. Hydrogen temperature ramping has been used extensively in LH_2-LO_x engines, which is reviewed by Hulka and Hutt [45]. Hydrogen temperature variations dynamically alter fuel density, viscosity, and injector feed pressure, which can result in instability for a specific temperature band as shown in Fig. 1.5, for example.

Thus, hardware designs and stability verification tests provide the answers needed, but require a trial-and-error approach. Stability verification tests are intended for engine qualification, not engine development. Results indicate whether an engine is stable or unstable without explaining why, and this information is gathered and applied after engine development is complete. To reduce the number of design iterations and improve computational combustion tools, the community must turn to scientific research of the underlying physics.

1.2 Fuel Droplet Combustion

1.2.1 Alternative Fuels

Rapid rise in the demand for fossil fuels, combined with constricting emission regulations, is resulting in expanded interest in alternative fuel sources. Although long term goals focus on reducing dependence on crude oil, the current infrastructure requires near term solutions which involve hydrocarbons [52]. As a result, the U.S. is witnessing tremendous growth in the use of biofuels in automotive transportation, while the aircraft industry is exploring the use of fuels derived from a range of sources (coal, natural gas, etc.) from the Fischer-Tropsch (FT) process [53].

Ethanol and biodiesel have led the recent expansion of the biofuel industry. Since 2000, global ethanol and biodiesel production has increased by more than 200% and 500%, respectively, with the largest growth occurring in the U.S. [54]. Alcohols, such as ethanol and methanol, serve as gasoline substitutes with less pollutant emissions and higher octane performance [55]. However, the use of pure alcohols is unfeasible without significant changes to current engine designs. Gasoline-biofuel blends, on the other hand, maintain characteristics similar to those of gasoline and can be used in existing internal combustion (IC) engines with zero or few modifications. These blends are effective

in the current transportation infrastructure, which is cultivating a global market for blends of gasoline and 10% ethanol (E10) and 85% ethanol (E85). Thus, there remains an immediate demand for understanding the behavior of these fuels in the presence of acoustic forcing as their usage is increasingly diversified. Although the IC engine, the most popular biofuels application, features acoustic pressure waves in the intake manifold and ports [56], the term "combustion instability" is used in the realm of IC engines to describe unwanted cycle-to-cycle variation in cylinder pressures, temperatures, and species concentrations. Therefore, the effects of sound waves on IC engine combustion are quite different from that of a gas turbine combustor or liquid rocket combustion chamber. Still, suppressing or exploiting acoustics within intake systems is desired for IC engines [57], presenting a need to explore the behavior of biofuels in the presence of acoustic flow fields.

For aircraft propulsion, the use of Fischer-Tropsch (FT) fuels is seeing increased use as an alternative fuel. These synthetic fuels are produced by converting carbon based materials into liquid fuels using the Fischer-Tropsch process [58], and the USAF plans to meet half of domestic fuel needs with FT fuel by 2016. Progress toward this goal is being achieved by using a 50-50% by volume blend of JP-8 and FT fuel, and nearly the entire USAF fleet has been certified for use with this FT blend [53, 59].

Thus, near term progress in the search for alternative fuel sources is being made using multiple fuel types and blends thereof. However, increased use of these fuels must be accompanied by a better fundamental understanding of the fuels' performance in typical engine operating conditions. As discussed previously, typical conditions often involve resonant acoustic waves, which have repercussions unique to the fuel being used. The diffusive, convective, and reactive time scales affiliated with one fuel will differ from another, altering the effects of flow instabilities on the combustion process. Therefore, the successful proliferation of alternative fuels requires studies which define the relationship

between acoustic fluctuations and combustion processes for each fuel.

1.2.2 Fundamental Droplet Combustion

Droplet combustion plays a role in a significant portion of condensed phase combustion applications. Fuel injectors may create dilute sprays of tiny droplets, or instead liquid jets which form free ligaments and then break up into large droplets [60, 61]. In either scenario, the combustion of the field of droplets is largely governed by the combustion of individual droplets. Therefore, fundamental studies of the combustion of a single droplet offer conclusions which apply to a field of many burning droplets in a fuel spray. Such studies involve spherical or semi-spherical droplets, which are placed in quiescent flow or convective flow with slip. A diffusion flame front forms away from the droplet surface where fuel vapor, evaporated from the droplet surface, diffuses into and reacts with the oxidizer, usually air. Aside from sprays, droplet combustion is often used as a model for heterogeneous combustion in general [62].

Droplet sizes and lifetimes for quasi-steady droplet burning are described by the well-known d^2 law [63, 64]:

$$d^2(t) = d^2(t = 0) - Kt \tag{1.6}$$

where the square of the droplet diameter d varies linearly with time t according to the burning rate constant K. The d^2 law has been shown to accurately describe droplet burning for spherical droplets in micro-gravity environments and semi-spherical droplets in normal gravity, but in the latter case the scaled diameter of an equivalent spherical droplet is required [65], as described below.

Micro-gravity droplet burning experiments provide ideal conditions for application of the d^2 law. Without gravitational forces, the droplet and the surrounding flame both maintain a spherical shape. This setting provides for straightforward determination of the droplet diameter d and thus the burning rate constant K. Experimental validation

of the d^2 law in micro-gravity conditions is shown by Law and Faeth [62] and Marchese *et al.* [66, 67], among many others. Work by Marchese *et al.* also includes imaging of electronically excited hydroxyl (OH*) radical chemiluminescence for the flame surrounding the droplet in order to validate the accuracy of a droplet combustion model, but more importantly, to confirm OH* chemiluminescence as an appropriate flame location indicator. For both fuels used, methanol and n-heptane, this is confirmed as an appropriate technique. To the knowledge of the current author, work by Dattarajan *et al.* [22] is the only set of experiments utilizing OH* chemiluminescence imaging for burning droplets in acoustically forced conditions. This technique is used for micro-gravity and normal gravity conditions, and Dattarajan et al. also successfully uses the d^2 law in quantifying burning rate constants for both sets of experiments.

Both micro-gravity and normal gravity environments require additional steps in the application of the d^2 law due to alterations in the shape of the droplet and flame. A more ellipsoidal droplet shape is formed by the balance of weight (for normal gravity) and surface tension, and is addressed by using an equivalent diameter d_{eqvs}, which is determined as the diameter of a sphere with a volume equal to that of the non-spherical droplet [65]. In normal gravity, the natural convection caused by thermal buoyancy creates an elongated flame shape with variations in flame standoff distance. Thus, the droplet combustion phenomena in normal gravity require understanding of steady flow effects even in the absence of forced convection. Still, the d^2 law has shown accuracy for droplets in non-quiescent flows [68, 69] when d_{eqvs} is used.

1.2.3 Effects of Acoustics on Fuel Droplet Combustion

Burning droplets exhibit salient changes in behavior when exposed to acoustic forcing. First and foremost, this has been documented by several experimental works which show burning rate constants increased by surrounding acoustic flow fields. Early observation

of the influence of acoustic forcing on burning rate is documented by Kumagai and Isoda [68], where an increase in the burning rate is thought to occur due to greater mass and heat transfer rates at the droplet surface due to steeper temperature gradients and species concentration gradients. This relationship has since been further explored by several others, including various studies by Saito *et al.* [70, 71]. Saito *et al.* [70, 71] record the effects of burning kerosene droplets in a normal gravity environment when the droplet is positioned near a pressure node (PN) or pressure antinode (PAN) of a standing acoustic wave. Locations of maximum and minimum velocity perturbations coincide with the location of a PN and PAN, respectively. Results show evaporation and burning rate constants of the burning droplet near a PN which are more than twice that of the unforced case, while positions near a PAN yield no significant alteration of these behaviors when compared to the unforced case.

Experiments performed in micro-gravity environments, on the other hand, lack the natural convective flow caused by thermal buoyancy, and thus isolate the effects of acoustic forcing. Burning droplets in zero gravity conditions are examined by several experimentalists [20–22, 72, 73]. Okai *et al.* [72] explore the influence of frequency and oscillation amplitude for n-octane single droplets and droplet pairs. Results show burning rates having a dependence on amplitude, with burning rates increasing with amplitude until flame extinction occurs, which is an event requiring more detailed inspection conducted by others [74, 75]. Experiments by Tanabe *et al.* [20, 21] confirm the burning rate conclusions noted above for both micro-gravity and normal gravity with n-decane droplets. Their studies situate the droplet at a pressure node, or between a pressure node and antinode of a standing acoustic wave. Moreover, their work reveals flame deformations in the presence of acoustic forcing, captured by flame imaging in the visible spectrum, and thus visualization of soot in the flame. Qualitative observations show flame deflections toward a PAN, or away from a PN.

To explain and predict this behavior, Tanabe *et al.* [20] propose an acoustic radiation force theory. Acoustic radiation forces are studied in a multitude of theoretical and experimental works extending back several decades. These forces are theorized and physically manifested by the existence of acoustic streaming, steady flow induced by an oscillating flow. Early experimental and theoretical study of acoustic streaming dates back more than one century [76, 77], which later allowed for theoretical formulations of the acoustic radiation force [78–80]. Expanding acoustic radiation force theory into the realm of combustion, Tanabe *et al.* [20] treat the region of hot products surrounding the droplet as a sphere of density ρ_p, which is less than the density of the gas surrounding the flame ρ_o. This discrimination between lighter and heavier gases permits a formulation from the work of Nyborg [79], where an equation is derived for the acoustic radiation force on a sphere of different density than that of the surrounding gas. Adding the assumption that $\rho_p << \rho_o$, Tanabe et al. reach an expression for the acoustic radiation force, F_R, acting on a sphere of hot products

$$F_R = \alpha(\rho_p - \rho_o)V\frac{\partial\overline{u'^2}}{\partial x} \tag{1.7}$$

where V is the volume of the sphere containing the hot products, x is the displacement of the droplet from the pressure node or pressure antinode location, and $\overline{u'^2}$ is the mean of the square of the local perturbation velocity u'. The coefficient α is defined as

$$\alpha = \frac{3\rho_o}{2(2\rho_p + \rho_o)} \tag{1.8}$$

The formulation in equation (1.7) is remarkably similar to that of a buoyancy force, which led Tanabe *et al.* to treat the acoustic radiation force acting on a burning droplet as analogous to a buoyancy force. In testing this theory, the flame behaviors observed in their imaging experiments affirm the prediction of the direction of flame deflection, where the acoustic radiation force calls for the hot products to shift towards a PAN. These experiments utilize a horizontal waveguide configuration, and thus involve only

horizontal acoustic radiation forces (i.e. parallel with sound wave propagation). The same group also tested this theory in a vertical waveguide configuration, generating forces which act upward, against thermal buoyancy forces [73]. Droplet combustion imaging in this experiment showcases a flame adopting a more spherical shell surrounding the droplet and claims gravitational forces are effectively "cancelled", but further evidence of this behavior is unavailable.

Droplet burning rate and flame orientation are also subject to extensive study in works performed at UCLA with regard to normal gravity [75, 81, 82], and experiments led by the same group in the micro-gravity facility at the NASA Glenn Research Center [22]. These phenomena were experimentally investigated using a horizontally oriented, long cylindrical waveguide, or Kundt's tube, either with a loudspeaker positioned at both ends or with one loudspeaker replaced by a sound reflector. Work by Dattarajan *et al.* [22] used the speaker and reflector configuration to create standing acoustic waves for methanol droplet experiments in micro-gravity. Similar to results discussed above, burning rates measured by Dattarajan et al. exhibit an increase over the unforced case when the droplet is located near a PN. In fact, for sound pressure levels of 135 dB, burning rate constants are as much as 200% greater than the unforced value for droplets situated near a PN. A smaller increase of 75% is shown for droplets near a PAN. For the same apparatus in normal gravity at 138 dB a smaller relative increase of 11-15% is measured for droplet near a PN, and the burning rate shows no alteration for droplets positioned near a PAN. With regard to flame deformation, the same study notes a trend in the direction of flame direction, where flames consistently deflect away from the approximate location of the PN, consistent with the theory of Tanabe *et al.* [20]. This flame deflection behavior is seen for both micro-gravity and normal gravity experiments, but with the micro-gravity conditions revealing a more obvious flame deflection direction due to the absence of thermal buoyancy.

Studies conducted solely in normal gravity by Rodriguez *et al.* [75] and Teshome *et al.* [82] offer results which agree with experiments above over a wider range of acoustic frequencies and for an array of fuels (ethanol, methanol, pure FT, and a JP-8/FT blend), but with more detail concerning the location of the burning droplet relative to the PN. Whether using a speaker-reflector configuration or a speaker-speaker configuration, the speaker assembly was moved as a unit within the waveguide while holding the droplet location constant. In this fashion, the location of the droplet could be varied with respect to the acoustic waveform. Further details on this technique are included in Section 2.1.

This technique exposes a trend of increasing burning rate as the droplet is moved from a PAN to a PN, with increases in the burning rate constant of up to 20%. These studies also give attention to the amount of flame deflection captured by imaging. Flame orientation generally agrees qualitatively with the theory of Tanabe *et al.* and with other pertinent experiments, but quantifying flame deflection brings light to certain unexplainable behavior. Imaging shows the largest deflections immediately next to a PN, with a dramatic switch in flame orientation when comparing results to the left and right of a PN. Teshome *et al.* [82] quantifies these deflections by measuring the flame deflection angle relative to the unforced, vertically oriented flame. To relate deflection angle measurements to the acoustic radiation force of Tanabe *et al.*, Teshome *et al.* balances the acoustic radiation force with the buoyancy force for the flame surrounding the droplet using a technique to be described further in 2.4.2. The resulting comparisons show that although equation (1.7) predicts flame orientation accurately, experimental results show significant quantitative differences. The trends and actual quantities evidenced by experiment are not captured by the same theory, and this is explored further in the present studies.

1.3 Shear-Coaxial Jets

A variety of coaxial jets have been used for injection of reactants in LREs. These include swirl coaxial jets, gas-centered coaxial jets, and impinging coaxial jets (shown in Fig. 1.6), to name a few. Unless otherwise noted, this study focuses hereafter on *parallel* shear-coaxial jets with an outer, annular jet of fuel and an inner jet of oxidizer, or an inert simulant in the inner jet and/or outer jet for a nonreactive configuration. Other coaxial jet types have been successful in LREs to date, but the parallel shear-coaxial jet still offers the most ideal condition for fundamental research due to its simplicity in injector design and exit flow conditions.

1.3.1 Nonreactive Shear-Coaxial Jets

1.3.1.1 General Characterization

The shear-coaxial jet involves three separate bodies of fluid in a concentric arrangement, creating two different shear layers. First, the inner jet and outer jet form the inner shear layer, where the traditionally denser fluid of the inner jet is disturbed by the surrounding outer jet, often at a higher velocity than the inner flow. A mixing layer is formed near the injector exit and increases in thickness in the streamwise direction, entraining more of the two fluids into the inner shear layer. Meanwhile, the outer shear layer forms between the outer jet and the ambient gas having zero bulk velocity. Each shear layer can exhibit large differences in velocity, density, and temperature, and as a result, become separate independent sources of instability which may interact. The two phenomena mentioned here, mixing and instability, are the primary foci of this discussion.

The streamwise development of these two shear layers was characterized in early research by Kwan and Ko [83] as shown in Fig. 1.7. Three zones are used to appropriately differentiate between regions containing an intact outer jet core, inner jet core, or the

existence of a single, fully merged jet. The region near the injector exit consists of both an intact inner jet core and outer jet core, and the downstream end of the outer jet core defines the end of the *initial merging zone*. The *intermediate zone* then, is defined as the region downstream of the outer potential core tip, but where distinguishable outer and inner mixing layers still exist. Primary vortices of the inner shear layer with convective velocity U_{c1} and secondary vortices of the outer shear layer with convective velocity U_{c2} reside in the initial merging zone, and then begin to interact in the intermediate zone. Last, the *fully merged zone* covers the region where the mixed jet behaves and appears as an equivalent singe jet of equal thrust.

Important nondimensional numbers and their definitions include the outer-to-inner density ratio $S \equiv \frac{\rho_{oj}}{\rho_{ij}}$, velocity ratio $R \equiv \frac{U_{oj}}{U_{ij}}$, and the momentum flux ratio $J \equiv \frac{\rho_{oj} U_{oj}^2}{\rho_{ij} U_{ij}^2}$. These three values are the most common measures for mixing and stability relationships and traditionally, $S \ll 1$ due to the jet's denser inner core. Additionally, with comparable mass flow rates ($\dot{m}_{oj} \sim \dot{m}_{ij}$), the outer jet velocity is much greater than that of the inner jet. This is certainly true for LO_x/GH_2 applications, as well as many of the nonreactive experiments of interest in this section. Consequently, at sub-critical pressure the shear forces at the inner shear layer cause a liquid inner jet to break up in a classical cascade of ligament and droplet formation, and finally atomization. For nonreactive jets, the break up process is characterized by J, the inner jet Reynolds number $\mathrm{Re}_{ij} \equiv \frac{U_{ij} D_1 \rho_{ij}}{\mu_{ij}}$, and the gaseous Weber number $We \equiv \frac{\rho_{oj} U_{oj}^2 D_1}{\sigma}$, where D_1 is the inner jet exit diameter and σ is the surface tension. These parameters can be used to identify multiple regimes of recognizably different break up processes [16]. Instantaneous images of inner jet break up for high We flows are shown in Fig. 1.8 due to their direct relevance to this study. More detailed characterization of mixing and stability is still subject to research.

1.3.1.2 Near-field Mixing

The earliest purported experimental study of coaxial jets was done by Forstall and Shapiro [84] for single-phase flow, where firm qualitative trends were established for the mixing of the gas inner and outer jets at atmospheric pressure. As the velocity of the air outer jet was increased, it was shown that the helium-air inner jet was less distinct. The boundary between the two jets eventually became ambiguous with downstream distance, and the streamwise position at which this occurred advanced upstream as the jet's velocity ratio increased.

Chigier and Beer [85] confirmed the general conclusions of Fortall and Shapiro [84] by quantitatively investigating the velocity distributions of air inner and outer jets issuing into quiescent air. Velocities were calculated using differential pressure measurements to give radial velocity distributions at several axial positions from the injector exit to $8D_1$ downstream. The injector used by Chigier and Beer [85] contracted the inner diameter and outer annulus near the exit rather than using a parallel shear-coaxial element. Velocity ratios ranging from 0.024 to ∞ were used to span from conditions nearly equal to a single jet and an annular jet, respectively. For a low velocity ratio, $R = 0.085$, the outer jet completely merged with the inner jet within a distance $D_2 - D_1$ from the exit and the central potential core extended far downstream similar to a single air jet. For a larger velocity ratio, $R = 2.35$, the potential core to end at a distance was just $3D_1$ from the exit.

In the 1970s, several bodies of work investigated near-field mixing of coaxial jets with attention to area ratio $AR \equiv \frac{A_{oj}}{A_{ij}}$ as well as R (Champagne and Wygnanski [86], Ko and Kwan [87], and Ko and Kwan [88]). Again, these experiments used air jets injected from contracting coaxial nozzles into air, with Reynolds numbers as high as 10^5 for each nozzle. Champagne and Wygnanski [86] noted that when increasing the outer diameter of the annulus to increase AR from 1.28 to 2.94 while holding R constant, an

increase in the outer jet potential core length was observed. However, this length was not affected by changes in R for the flow conditions used in their work ($0< R\leq 10$). The inner jet behavior though, depended on both AR and R. In this respect, Champagne and Wygnanski [86] deduced that the outer jet core length acts similar to a single jet in the ambient gas, having little sensitivity to changes in the inner jet. Ko and Kwan [88] also compared the coaxial jet to a single jet, but clearly defined regions for each class of flow. The outer shear layer was called the *secondary mixing region*, which was deemed equivalent to a single jet in potential core length and spreading behavior. The inner shear layer was called the *primary mixing region*, which was said to function like the layer between a single jet in a co-flowing ambient gas as opposed to a co-flowing stream of finite thickness. But, experimental conditions in Ko and Kwan [88] were limited to $R < 1$ (R=0.3, 0.5, 0.7). The results of both groups reaffirmed the finding of previous researchers that the velocity difference ($|U_{oj} - U_{ij}|$) is positively correlated with mixing due to enhanced shear between the inner and outer jets.

An extensive array of analytical derivations and experiments on coaxial jet and two-dimensional shear layer mixing were pursued by Dimotakis [89], and later by Dahm and Dimotakis [90], Dimotakis [91], and Dahm *et al.* [92]. These works aim to describe mixing layers by quantifying mass entrainment, shear layer convection velocity, circulation, and vortex size, to name a few. Dimotakis [89] used empirical relations to derive an expression for the volume flux entrainment ratio E_v and the mean vortex spacing to position ratio $\frac{l}{x}$. More importantly, a relation for shear layer convection velocity was derived by applying the Bernoulli equation to a two-dimensional shear layer. Dimotakis [89] asserted that a stagnation point must exist between vortices when in the Galilean rest frame of the vortices, and thus, Bernoulli's equation would apply along a line through this point. Following this frame of reference in Fig. 1.9, neglecting gravity, and assuming that differences in static pressure can be ignored, then the dynamic

pressures in each free stream were matched, i.e.

$$\rho_1 \left(U_1 - U_c\right)^2 \approx \rho_2 \left(U_c - U_2\right)^2 \tag{1.9}$$

Solving for the convection velocity, as in Dahm *et al.* [92], yields

$$U_c \approx \frac{U_{ij}\rho_{ij}^{\frac{1}{2}} + U_{oj}\rho_{oj}^{\frac{1}{2}}}{\rho_{ij}^{\frac{1}{2}} + \rho_{oj}^{\frac{1}{2}}} \tag{1.10}$$

for a shear-coaxial jet. In contrast to prior studies of isodensity jets, this relation accounts for different densities as well as velocities, and is far more pertinent to bi-propellant applications and research thereof. Other studies have since validated and applied eqn. 1.10 for this reason [92, 93].

Modern coaxial jet research has sought to account for an even larger body of variables to describe mixing and break up, in addition to velocity and density. These include chamber pressure, outer and inner jet temperature, viscosity, and surface tension forces present in two-phase flows. Reactive experiments are often the most holistic approach for research of combustion systems, but construction and maintenance of combustion facilities remains costly, especially for cryogenic applications such as LREs. In terms of scientific value, nonreactive experiments can also simplify the physics of otherwise complex flows, clarifying the results. Therefore, nonreactive experiments have remained an excellent research strategy throughout the 1990s, 2000s, and today.

During this period, a significant effort was made to categorize two-phase coaxial jets according to the break up process of the inner liquid core. Chigier and Farago [94] used Re_{ij} and We to characterize several regimes of inner jet break up, and Lasheras and Hopfinger [95] extended their work to include the effects of J and the Ohnesorge number $Oh \equiv \mu_{ij}/(\rho_{ij}\sigma D_1)^{\frac{1}{2}}$. The culmination of this work is shown in Fig. 1.10, where five regimes of break up for air-water jets at atmospheric pressure are shown to occur according to the values of Re_{ij}, We, J, and Oh. These five regimes are axisymmetric

and nonaxisymmetric Rayeigh break up, shear break up, membrane break up, and fibre-type break up. The latter two regimes are of particular interest here, because LRE flow conditions often exhibit high We values produced by high velocity gas in the outer jet which strips the outer perimeter of the denser inner jet. Membrane and fibre-type break up were characterized in Lasheras and Hopfinger [95] as having an inner core length L_b less than $8D_1$. Under the action of the gaseous jet turbulence, the liquid core breaks into clusters and ligaments near the injector exit and atomization can occur less than $2D_1$ from the exit for $We{\sim}1000$. Their experiments support the correlation

$$\frac{L_b}{D_1} = \frac{6}{\sqrt{J}} \left(\left| 1 - \frac{1}{R} \right| \right)^{-1} \tag{1.11}$$

for use in LREs, but devise a separate relation for low We flows not in the fibre-type regime. Extensive experiments by Baillot *et al.* [16] not only support the numerous regime boundaries in Fig. 1.10, but also support the $L_b{\sim}J^{-\frac{1}{2}}$ relationship, despite using an impinging inner jet shear-coaxial injector (see Fig. 1.6c). However, their experiments also included tests at very slightly elevated chamber pressure. At just 2.16 and 3.6 kPa above atmospheric pressure, the Re_{ij} and We values for break up regime boundaries were clearly altered, revealing the importance of pressure in shear-coaxial jet break up and atomization.

The effects of pressure are particularly important to the LRE community, where high chamber pressures are desired in order increase specific impulse. Although, supercritical pressure introduces less understood physics into the mixing process. The well-known features of liquid jet break up (e.g., ligaments, droplets, and atomization) are replaced with indiscernible fluid interfaces and obscure lumps rather than droplets. The first apparent set of experiments on jets in supercritical environments was done by Newman and Brzustowski [96] in 1971. Their experiments involved backlit shadowgraphy of single jets of liquid CO_2 in a gaseous nitrogen environment. With the chamber pressure above the critical pressure of CO_2 and the temperature below the critical temperature of CO_2,

i.e. $p_c > p_{crit,CO_2}$ and $T_c < T_{crit,CO_2}$, CO_2 droplet sizes were observed. As T_c approached T_{crit,CO_2}, droplets became smaller until the liquid-gas interfaces became unobservable for $T_c \geq T_{crit,CO_2}$. At this point, the flow could no longer be described as heterogeneous two-phase flow.

Since the work of Newman and Brzustowski [96], a large body of work has supported and expanded upon their findings. A number of studies have been done at both the U.S. Air Force Research Laboratory (AFRL) and the German Aerospace Center (DLR), and a thorough review of their advancements prior to 2006 is found in Oschwald *et al.* [97]. Nonreactive, near-critical and supercritical experiments at AFRL began with single liquid nitrogen (LN_2) jets in a quiescent nitrogen environment and later experiments added a nitrogen outer jet in a shear-coaxial configuration. For the single jet, drops at the liquid-gas interface were no longer detected when the chamber pressure reached $\frac{p_c}{p_{crit,N_2}} = 1.03$. Instead, finger-like entities were seen at the interface. Chamber pressures greater than $2.5p_{crit,N_2}$ were eventually tested, and the continuous shrinking of the dense liquid core was observed as pressure increased to and beyond this point, as well as the suppression of droplet production for single jets and coaxial jets [97–99]. Chehroudi *et al.* [98] also showed quantitative evidence of gas jet behavior to support the gas-like appearance of the jet in supercritical environments for a specific range of jet densities.

Meanwhile, nonreactive experiments at DLR by Telaar *et al.* [100] and Mayer and Smith [14] used LN_2 and gaseous helium (GHe) coaxial jets to better replicate the density ratios of LO_x-GH_2 rocket engines. A sample of their shadowgraphy results is shown in Fig. 1.11. These results reinforced the LN_2-GN_2 results noted above, even for species with very different critical pressures and temperatures. The development of the inner jet was said to be dependent on its own fluid properties. Complementary experiments were performed with LN_2-GH_2 flows by Oschwald *et al.* [101] using Raman scattering for quantitative density measurements. This diagnostic technique provided Raman signals of

nitrogen and hydrogen at two different wavelengths and appropriately filtered the signals to effectively measure the species fraction of each. The results were analyzed to measure a streamwise location at which the jet was completely mixed with the background gas, culminating in salient evidence of mixing or lack thereof. This was the first study measuring species fractions in sub and supercritical pressure environments.

Since the composite review by AFRL and DLR in Oschwald *et al.* [97], further backlit image analysis of coaxial jets at AFRL has accumulated strong indications of a correlation to predict inner core length L_b for a wide range of flow conditions. First, Davis and Chehroudi [102] and Davis [103] used low speed imaging (< 1 kHz) to optically measure L_b, and organized a large amount of data from the literature to create a comprehensive review of the dark core length's dependence on chamber pressure. Leyva *et al.* [29] advanced this study to include variations in J and the influence of acoustic forcing, both of which were found to have a significant impact on L_b and jet spread angle. With the use of high speed imaging (> 10 kHz), coherent jet oscillations were also recognized when acoustic forcing was applied. For example, L_b measured for jets at a PN location in the chamber were found to be less than those measured for jets at a PAN location [75, 81]. Rodriguez [75] also included variations in injector area ratio AR in a study which was expanded to include a recessed inner post by Graham *et al.* [104]. In conclusion, an array of variables encompassing injector geometry, density ratio S, velocity ratio R ($J = SR^2$), chamber pressure, and acoustic forcing conditions have been shown by works at AFRL to alter shear-coaxial jet mixing as evidenced by variations in dark core length.

Experimental data from testing of two shear-coaxial injectors, sub and super-critical pressures, and J values ranging from 1 to 23 was used by Teshome [23] to find an empirical correlation for L_b. This new data was supplemented with experimental data from studies mentioned above ([23, 75, 104, 105]) to create an empirical solution to

predict L_b. Injector geometry and momentum flux ratio were combined to create the nondimensional parameter G, which takes the form

$$G = c_1 J^{c_2} \left(\frac{t}{D_1} \right)^{c_3} (AR)^{c_4} \tag{1.12}$$

where t is the wall thickness of the coaxial injector's inner tube. The constants c_1, c_2, c_3, and c_4 were chosen to fit the data of four injectors, all having different combinations of large or small values for $\frac{t}{D_1}$ and AR. Again, this study demonstrated the importance of chamber pressure through the difficulty in producing a correlation applicable both above and below the critical pressure. Teshome [23] was instead forced to choose two unique sets of constants; the first set was chosen to fit L_b vs. G data for sub-critical pressure and a second set was required for super-critical pressure. Although a physics-based approach may identify the missing factors necessary to predict dark core length across a range of pressures in the future, this correlation remains the most comprehensive empirical formula to quantify mixing for LRE-like coaxial injectors by including the majority of the variables identified in the studies cited above. Future work at AFRL will explore the effects of these variables for reactive propellants.

1.3.1.3 Stability Consideration

Early jet turbulence researchers recognized that many combustion systems are diffusion-controlled, having chemical kinetics which are so rapid that the reaction rate is entirely dictated by turbulent mixing [86]. When isolating these mixing processes in nonreactive experiments, these researchers also recognized the existence of high amplitude modes of fluid instability which would completely dominate the mixing processes of a combustion system. Several key studies will be discussed here which give attention to the frequencies and amplitudes of these coherent instabilities rather than chaotic turbulence.

Crow and Champagne [106] characterized the natural instability of single jets according to the Strouhal number St and explored the relationship between instability

amplitude and St. The Strouhal number is a nondimensional measure of frequency f generally defined as

$$St = \frac{fx}{u} \tag{1.13}$$

where x is a characteristic length scale and u is a characteristic velocity scale. Crow and Champagne [106] explored single jets of water, and later air, and defined x as the jet exit diameter D which was held constant while the mean jet exit velocity U_e was controlled. The jet spectra was probed at various positions downstream of the exit, and a natural oscillation was found to occur at $St = 0.30$. This mode was amplified downstream of the exit until reaching a peak amplitude at x/D=9.5. Crow and Champagne then used a loudspeaker upstream of the jet exit to force the jet at a controlled frequency, unequal to the jet's natural frequency. In this way, St was controlled using f and U_e to employ a range of $0.15 < St < 0.60$. They found that the forcing frequency could be measured and controlled in the near-exit region $x/D < 8$, but the natural mode, or "preferred" mode, dominated and saturated in the region $x/D > 8$ regardless of the forcing frequency. This conflicted with existing linear stability theory which failed to predict $St = 0.30$, but rather asserted an increasing instability amplitude for increasing St. A significant conclusion of Crow and Champagne's study was that linear stability theory could not be used to predict the jet's dominant mode because nonlinearity established the preferred mode of $St = 0.30$. This is a classical work in single jet instability due to its clear demonstration that jet instability has a preferred mode which can be scaled using St.

Since the work of Crow and Champagne, single jet preferred modes have been shown to adopt different values of St and definitions thereof. As an example, the systematic experimental study by Birbaud *et al.* [107] defined a preferred mode Strouhal number for both the jet and the shear layer existing between the jet column and the surrounding quiescent gas, St_D and St_θ, respectively. St_D was defined using the jet exit diameter D and St_θ was defined using the initial momentum thickness θ_0, a measured quantity. For low Reynolds number air jets at atmospheric pressure, the jet mode frequency f_D and

the shear layer mode frequency f_θ were measured for natural jets and for jets subject to upstream acoustic forcing at f_0. This study not only asserted that two natural modes can exist in single jets, but also that the values of the preferred Strouhal numbers, St_D^p and St_θ^p, can be used to predict the response of jets to acoustic forcing. Particularly, when f_0 was chosen to be near the preferred mode f_p, the jet adopted and amplified the forced mode as the convective instability moved downstream. When f_0 was much greater than f_p, the jet was insensitive to upstream modulations and did not display evidence of the forced mode. This study represents the field's advancement since the work of Crow and Champagne, demonstrating that even without the added complexities of a coaxial jet, single jet natural modes feature several key behaviors. Mainly, St can be intuitively defined by parameters characteristic of the source of the instability, such as θ_0, and a jet is more likely to amplify a forced mode if the forcing frequency is near that of the natural jet instability.

Coaxial jets may also manifest the same principles as single jets, albeit with more complexity. In early work by Kwan and Ko [83] and Ko and Kwan [88], similar concepts were explored for shear-coaxial jets. Velocity fluctuation measurements revealed two modes in the initial merging zone; a low frequency mode was measured from primary vortices in the inner shear layer and a high frequency mode was measured from secondary vortices in the outer shear layer. In the intermediate zone the low and high frequency vortices merged and one overtook the other to dominate the fully merged zone. Like Crow and Champagne [106], Ko and Kwan [88] described modes according to St and attempted to find one St value to predict the jet's preferred mode over a range of flow conditions. However, Ko and Kwan acknowledged that the complexity of a coaxial jet not only required different length and velocity scales than the single jet, but also called for separate length and velocity scales for the inner shear layer and the outer shear layer.

These two definitions followed as

$$St = \frac{fD_1}{\left[0.6\left(U_{ij} - U_{oj}\right) + U_{oj}\right]/0.6} \tag{1.14}$$

$$St = \frac{fD_3}{U_{oj}} \tag{1.15}$$

where eqns. 1.14 and 1.15 applied to the inner shear layer mode and outer shear layer mode, respectively. Experimental validation in Kwan and Ko [83] and Ko and Kwan [88] supported these definitions. Although the experiments were limited to $R < 1$, this work clearly described two sources of shear layer instability in coaxial jets and stark differences between them. The definition of eqns. 1.14 and 1.15 is the earliest attempt to differentiate multiple sources of coaxial jet instability with individual scaling laws. Other researchers have since defined St to include variables such as jet exit boundary layer thickness and a combined jet mean velocity to reach a St scaling which holds for greater values of R [108, 109].

Advances in stability theory have since isolated additional sources of instability in two-dimensional shear layer mixing, which can provide insight to possible sources of instability in three-dimensional coaxial jets. The field of linear stability theory has seen vast development and application since its ineffectiveness in explaining the results of Crow and Champagne, and could be reviewed to designate flows which are accurately and inaccurately predicted by stability theory. A lengthy review of this kind will not be offered here. However, a few select studies of this kind will be discussed, because despite the shortcomings of linear stability theory when treating LRE-like flows with complex geometry and nonlinear effects, *linear stability results offer intuition for scaling laws such as St.*

A straightforward classification of modes was included in a theoretical stability study by Yecko *et al.* [10], where a two-dimensional, liquid-gas shear layer of unequal density, velocity, and viscosity was subject to temporal stability calculations. The common

A-201

Kelvin-Helmholtz instability was identified resulting from a velocity deficit at the interface, as expected. Inviscid theory will capture this mode, which is said to be the cause of instability in the experiments of Crow and Champagne (Talamelli and Gavarini [108]), but will not capture Tollmien-Schlichting (T-S) type modes. A liquid T-S mode and a gas T-S mode were identified by Yecko *et al.* [10] as the result of Reynolds stress at a liquid-gas or liquid-liquid interface, which cannot be neglected in the cryogenic flows of rocket engines. Later experimental work by Matas *et al.* [93] showed that viscous models often predict higher frequencies in spatial stability calculations though, and a correct estimation of the shear layer convection velocity U_c is more critical for obtaining accurate frequencies. Their own calculations assumed the formula of eqn. 1.10 for U_c from Dimotakis [89]. Lastly, Matas *et al.* [93] noted that instability frequencies between streams with finite thicknesses would be even more difficult to estimate, because the modes of multiple shear layers will communicate.

The presence of global instability in a number of different types of shear flows is well known [25]. As noted by [110], evidence in the spatial evolution of the disturbance amplitude for a nonlinear global mode in an infinite domain consists of a sharp front located at the upstream boundary of the absolute instability region, where the disturbance amplitude abruptly increases and stays high as one moves downstream. Under such conditions the flow behaves as an oscillator rather than a noise amplifier. Flows that can become globally unstable include low density axisymmetric jets in quiescent surroundings below a critical jet-to-surroundings density ratio [111, 112], countercurrent mixing layers above a critical velocity difference [113, 114], and wake flows above a critical Reynolds number [115, 116]. The evidence for such transitions includes phenomena that have already been documented for the transverse jet [117], e.g., (1) clear changes in the spectral character of the shear-layer, with strong oscillations at narrow spectral peaks for global instability, representing pure tones with higher harmonics, (2) a rather dramatic alteration in the value of the Strouhal number associated with the initial insta-

bility as the influencing flow parameter is brought into the range for globally unstable flow, and (3) little spectral alteration of the globally unstable flow in response to low to moderate flow excitation, in contrast to significant spectral alteration of the convectively unstable flow during such excitation. Additional phenomena associated with a transition to globally unstable conditions include: (4) a rather abrupt increase in the amplitude of the disturbance within and near the shear-layer as one approaches the critical flow parameter, consistent with the characteristics of the Landau equation [25, 113], and (5) a reduction in the energy transfer from fundamental to subharmonic frequencies along the shear-layer, and hence a reduction in the strength of subharmonics and corresponding inhibition of the vortex pairing process after the transition. In addition, for the low density free jet it has been shown that very strong external sinusoidal excitation can be used to overcome the fundamental instability mode for globally unstable conditions [118, 119]. These findings are consistent with theoretical work [120] which suggests that for spatially developing flows, external forcing upstream of the transition from convective to absolute instability can overwhelm the naturally occurring absolute instability. The low density jet experiments show that at forcing frequencies f_F that are relatively close to the global instability frequency f_{nat} and/or at very high amplitude forcing, the global frequency is not observed at all, and the forcing frequency dominates the flow's spectral character, with the capacity to either reduce or enhance jet mixing. The excitation amplitude at which the flow "locks" on to the forcing frequency f_F increases in proportion to $\mid f_{nat} - f_F \mid$, consistent with the flow transition to a global mode via a Hopf bifurcation [25, 110]. The capacity for strong sinusoidal forcing to alter the global instability is viewed as a means of controlling the low density jet.

Jendoubi and Strykowski [121] used inviscid, spatio-temporal stability theory to describe the modes created by axisymmetric jets with ambient co-flow and counter-flow. This study focused on the behavior of two particular modes with regard to large changes in the density ratio and velocity ratio. "Mode I" was described as a shear layer insta-

bility, having peak velocity perturbations at the interface which were not felt in the center of the jet nor at a position far from the jet. "Mode II" was deemed a jet column mode, because peak perturbations were located at the shear layer as well as the jet centerline. These two modes were found to not only produce convectively unstable modes, but for a specific range of velocity and density ratios each mode predicted absolute instability. The transition from convective to absolute instability was the focus of Jendoubi and Strykowski [121]. This transition is important because should a mode become absolutely unstable, it becomes time-amplifying in a localized area and basically self-excited, whereas convective modes develop as the waves are conveyed downstream. If an LRE, for example, sustained absolutely unstable propellant flows, then the self-excited mixing of reactants may become insensitive to acoustic feedback. To explore this possibility, a plot from Jendoubi and Strykowski [121] is presented in Fig. 1.12, showing convective-absolute transition lines calculated as a function of the velocity and density ratio. The operating conditions of a typical LO_x-GH_2 LRE are added, showing that absoulte instability brought on by these particular modes is unlikely.

Absolute instability is especially relevant to combustion instability when considering its resistance to external forcing. This feature has been investigated experimentally for single jets by Getsinger *et al.* [122], among others [115, 118, 123]. For low density jets in crossflow, Getsinger *et al.* [122] found an absolutely unstable jet to be resistant to upstream forcing in a way which was dependent on the jet-to-crossflow momentum flux ratio and the forcing frequency. It was observed that as the forcing amplitude increased, a "lock-in" amplitude was eventually reached such that the formerly absolutely unstable jet adopted a convective instability with a frequency equal to the forcing frequency. The lock-in amplitude was found to be dependent on momentum flux ratio and linearly dependent on the nondimensional forcing frequency F, defined as a ratio of the forcing frequency f_F to the jet's natural frequency f_0. Other lock-in experiments of single jets have also observed this relationship, namely nonreactive work by Sreenivasan *et al.* [123]

and nonreactive and reactive experiments recently presented in Juniper *et al.* [118]. To the author's knowledge, the first experimental evidence of the lock-in phenomenon was shown in Provansal *et al.* [115] for the wake behind a cylinder. If applied to coaxial jets, this concept could aid investigators when diagnosing an acoustically forced flow condition as absolutely or convectively unstable or when classifying flows according to their resistance to said forcing, which is the foremost objective of the present study.

From a theoretical standpoint, to predict absolute or convective instability for coaxial jet flow conditions requires that the results of Jendoubi and Strykowski [121] be supplemented with an analysis specific to coaxial jets. The analysis must account for sources of instability in the outer shear layer and the inner post wake, both of which were not present in Jendoubi and Strykowski's study. Their results indicate that LRE coaxial jets are far from the convective-to-absolute transition due to high speed co-flow and dense inner jets, preventing both the jet column and shear layer modes from reaching absolute instability. This is supported by Fig. 1.12. But, a finite thickness inner post creates a potential source of absolute instability in the wake region.

In a more recent theoretical study by Talamelli and Gavarini [108], the outer shear layer as well as a finite inner post thickness were included in an effort to explore these two regions as possible sources of absolute instability. Three unstable modes were identified: one in the outer shear layer and two associated with the inner post wake. For a small but nonzero wake velocity, one of the wake modes was shown to become locally absolutely unstable. It is also notable that the absolutely unstable mode could be described by $St \approx 0.24$ when St was calculated using the wake thickness and mean free stream velocity, i.e. $(U_{ij} + U_{oj})/2$. Further inspection of this mode showed that the absolute instability exists for a limited range of R, and the extent of this range depended on the assumed momentum thickness θ and the wake velocity. Specifically, a significant amount of reverse flow in the wake increased the likelihood of absolute instability. As

will be shown later, wake induced modes are particularly important in the present study due to the injector's finite inner post thickness t, which creates a visually identifiable recirculation zone in the near-field.

Although inviscid and incompressible assumptions were made in Talamelli and Gavarini's analysis, LRE coaxial jets may manifest the absolutely unstable wake mode described above. Teshome [30] extended the previously discussed work at AFRL [75, 81, 104, 105] by measuring natural and acoustically forced coaxial jet instability frequencies for sub- and near-critical chamber pressures, simulating the cryogenic propellants of LREs in a nonreactive LN_2-GN_2 configuration. Images from high-speed shadowgraphy were used to determine the frequencies most representative of a range of flow conditions, both acoustically forced and unforced. This was achieved by extracting spectral information from image sets using a partial orthogonal decomposition (POD) algorithm to reconstruct modes with a high energy content garnered from fluctuating image intensities. Separate spectra plots were obtained for each flow condition. It was observed that for high J and $AR(\equiv \frac{A_{oj}}{A_{ij}})$ the jet appeared to sustain its natural instability frequency even when acoustically forced, displaying absolutely unstable behavior. Conversely, low J and AR conditions were sensitive to forcing, adopting a instability frequency equal to f_F. In this study, high amplitudes of acoustic forcing were used to replicate the severity of an actual engine instability rather than the low level forcing technique of Getsinger *et al.* [122], for example. Thus, an absolutely unstable wake mode may be present in the experiments of Teshome [30], and a more detailed alteration of forcing amplitudes to confirm frequency lock-in could be performed as reinforcement.

Due to the limited amount of experiments regarding forcing of absolutely unstable coaxial jets, it is difficult to anticipate the appearance of this phenomenon. The behavior of convectively unstable jets though, is well documented for experiments where these flows are subject to transverse acoustic forcing, and a short list of studies will be discussed

here to classify the expected results. The earliest experiments of this kind were reported by Miesse [124] and Buffum and Williams [27], both of which involved two-phase flow. Miesse [124] recorded a definite jet response to external acoustic forcing, regardless of whether wave propagation was parallel (longitudinal) or perpendicular (transverse) to the jet axis. Buffum and Williams [27] focused on single water jets exposed to transverse, standing acoustic waves. When placed at a pressure node (PN) for frequencies less than 500 Hz, a whipping motion was observed which is analogous to a jet injected into an oscillating crossflow. For SPL>161 dB, increased atomization was also recorded. Subsequent studies focused on the increased break up and atomization caused by acoustic forcing. For example, Carpentier *et al.* [26] also studied single liquid jets in transverse acoustic fields, but noted steady jet flattening for acoustic frequencies ranging from 500 to 1864 Hz. The jet was constricted in the wave propagation direction and stretched in the direction perpendicular to wave propagation, a phenomenon also reported for high pressure in Chehroudi *et al.* [98]. However, Carpentier *et al.* [26] did not observe the sinuous jet motions as in Buffum and Williams [27], and used a simple analytical model to explain the existence of both regimes of jet response, primarily categorized by frequency. In conclusion, their model mathematically explained that if the values of the acoustic velocity u' and $1/(f_F D_1)$ are large, then sinuous jet forms can result. Otherwise, an acoustic radiation force F_R similar to that discussed in section 1.2.3 induces steady flattening and fanning in the plane of the PN.

When tested for coaxial jets, these conditions produce quite different results. Baillot *et al.* [16] tested liquid-gas coaxial jets with regard to the relationships stated by Carpentier *et al.* and discerned different behaviors at PNs and PANs. At a PN, Baillot *et al.* [16] also observed jet flattening, but noted that for a sufficient amount of outer jet flow no flattening occurred. Again, this phenomenon was also observed by Leyva *et al.* [29] and Chehroudi *et al.* [98] for elevated pressures. At a PAN, jet break up was only influenced by acoustics if in the presence of outer jet flow, which is a feature that

emerged as a result of outer jet flow pulsations. By periodically impeding outer jet flow with chamber pressure fluctuations at a PAN, acoustics increased mixing and breakup via the formation of axisymmetric vortices. Although the nonreactive experiments cited above exclude the effects of speed of sound gradients inherent in high temperature combustion systems, many of these rules hold true for acoustic forcing of reactive flows, as discussed below.

1.3.2 Reactive Shear-Coaxial Jets

1.3.2.1 General Characterization

The flame of a reactive coaxial jet adds complexity to fluid instability and mixing, but many key features are retained from nonreactive jets. As shown in Fig. 1.13, the vortex structures at the inner shear layer manipulate the reaction zone, creating a wrinkled flame. A ring shaped flame forms a distance x_f downstream from the inner post, and its flame thickness δ_f grows in the streamwise direction x until the flame merges to become a single, broad flame downstream of the liquid core tip. An attached flame corresponds to $x_f = 0$. Near the reaction zone, steep temperature gradients promote a rapid density reduction of both the liquid oxygen core and the outer gaseous fuel, a process controlled by convective transport of hot gases. Thus, the state of the dense inner jet is significantly altered by the wrinkled flame, and if reaction rates are controlled by mixing or liquid vaporization then this can generate combustion instability. Analysis by Snyder *et al.* [125] confirmed that combustion of LO_x-GH_2 coaxial jets in LREs is indeed a oxygen vaporization limited process, because the characteristic vaporization time scale t_v is longer than both the characteristic chemical and mixing time scales, t_c and t_m, i.e. $t_c < t_m < t_v$ (see also Candel *et al.* [126]). Therefore, the interfacial instabilities of the liquid oxygen core and measure of its length, L_b, are paramount for understanding combustion instability.

As a direct result of the added heat release of a combustion system, fluid mixing and instability cannot be easily isolated as in the nonreactive flows discussed heretofore. Measures of mixing such as L_b are consequently studied concurrent with instability, because fluid mechanics are difficult to decouple from unsteady heat release and the ensuing chamber acoustics of a combustion instability feedback loop, shown in Fig. 1.2. Suitably, the following section reviewing reactive coaxial jet research is ameliorated by discussing mixing and stability phenomena together in light of their close coupling in reactive flows.

1.3.2.2 Propellant Mixing and Stability Consideration

Although LO_x-GH_2 engines were thoroughly tested by engineers as early as the 1950s and '60s, little fundamental research was done during this period. At the Lewis Laboratory (now the NASA Glenn Research Center) in 1958, Baker and Steffen [127] used a bench scale thrust chamber with multiple propellant combinations to measure high frequency pressure chamber pressure fluctuations for various chamber lengths. Little high frequency instability was observed for hydrogen-oxygen propellants in particular, and in experiments with coaxial injectors no instability was present. Other propellant combinations brought about significant longitudinal modes.

Early experiments of this kind were limited to direct probe measurements as opposed to optical techniques. A later set of experiments from Heidmann [128] at the same laboratory in 1965 included some of the first images with evidence of mixing alterations caused by combustion instability. For a small shear-coaxial injector ($D_1 = 0.7$ mm) LO_x-GH_2 combustion images resolved the outline of the liquid core, and the core length L_b was shown to respond to transverse waves. Their imaging technique could not resolve break up and vaporization, but clearly displayed a reduced L_b in the presence of transverse acoustic modes, a behavior likened to a liquid jet in gaseous cross-flow.

Numerous other experiments of small-scale thrust chambers by NASA in the 1960s confirmed Baker and Steffen's conclusion that LO_x-GH_2 coaxial jets produce stable conditions relative to their marginally stable LO_x-Hydrocarbon counterpart. In fact, it was the Apollo program's difficulty with combustion instability in the kerosene based F-1 engine that largely motivated the surge in research during this period. Meanwhile, the J-2 engine, a hydrogen fueled upper stage engine flown during Apollo missions, exhibited minor instabilities which were quickly abated (see section 1.1.3). Oxygen-hydrogen coaxial jets were being adopted as a stable configuration by both the engineering and the scientific communities. At the conclusion of NASA's subscale campaign of experiments at the Lewis Laboratory, it was even stated that ". . . all liquid oxygen-hydrogen staged combustion tests in the U.S. have been stable at high frequency." [45] The knowledge acquired up to this time was consolidated in NASA SP-194, *Liquid Rocket Engine Combustion Instability.*

Motivation for fundamental research in this area then subsided until two in-flight incidents of combustion instability occurred for engines of the European Ariane rocket [3]. These unexpected events renewed research activity in the field, and several key research groups have developed new test facilities to experimentally replicate the complex flows of LREs while using modern imaging techniques. These facilities attempt to reproduce the hazardous, high-pressure conditions of LREs at subscale while also applying novel concepts for high-fidelity acoustic control. Below, this review highlights the diverse experiences of five modern combustors which are particularly relevant to this study. These are the Multi-injector Combustor (MIC) and the Very High Amplitude Modulator (VHAM), both operated jointly by the French Aerospace Research Agency (ONERA) and the French National Center for Scientific Research (CNRS), the Common Research Combustor (CRC) operated jointly by CNRS and DLR, the BKH combustor operated by DLR, and the Continuously Variable Resonance Combustor (CVRC) operated by Purdue University.

The CRC originated in 2002 from the efforts of a German-French working group which now operates identical experimental combustors at the Research Institute for Equilibrium Systems (IRPHE) in Marseilles, France and DLR in Lampoldshausen, Germany. The CRC injects propellants from one side of a flat, cylindrically shaped chamber through a single injector which is 1/10th scale of a typical LRE injector. With high-speed shadowgraphy and OH* chemiluminescence imaging, the dynamics of a single LO_x/GH_2 flame can be isolated to fundamentally relate spatial and temporal heat release oscillations to pressure oscillations controlled by external acoustic forcing from a secondary nozzle. A single injector element though, provides only partial representation of thermoacoustic cycles occurring in LREs with multiple injectors and interactions between adjacent flames.

The BKH combustor is part of a recently constructed facility at DLR Lampoldshausen, Germany which focuses on high frequency combustion instability for LO_x/GH_2 and LO_x/LH_2 combustion. Simultaneous high speed backlit shadowgraphy and OH* chemiluminescence imaging was used to measure liquid core length L_b in addition to flame shape, both of which had a strong response to external acoustic forcing. Dark core length L_b values were reduced by up to 70% when forced at resonant chamber frequencies, and a curve-fit between L_b/D_1 and a nondimensional acoustic pressure amplitude predicted core length with reasonable accuracy for the conditions used in Hardi [24]. The pressure amplitude p' was nondimensionalized by the chamber pressure, i.e. p'/p_c, in one attempt to collapse L_b data into a single relationship. A second nondimensionalization method used the dynamic pressure of the outer jet, which followed as

$$\frac{\rho_c u'^2}{\rho_{oj} u_{oj}^2} \tag{1.16}$$

where ρ_c is the chamber gas density and the acoustic velocity amplitude u' is calculated from p' measurements. Both attempts to scale acoustic perturbation amplitudes with dark core length showed promise.

Hardi [24] also describes linear and nonlinear instability events which occurred during high frequency acoustic excitation. First, pressure measurements of unforced coaxial jet combustion confirmed the system's natural excitation of the first longitudinal (1L) and first transverse (1T) modes via small increases in p' values at those frequencies. Second, transverse forcing at the 1T frequency (≈4 kHz) strongly excited this mode while also creating low frequency chugging far from the excitation frequency. A similar event occurred when forcing at the 1L1T frequency. The chugging mode only occurred during high frequency excitation of transverse modes, and was said to occur due to nonlinear effects.

The BKH combustor also includes five shear-coaxial injectors in a cross formation to investigate interactions between neighboring flames. Although Hardi [24] was unable to give flame interaction detailed attention, this feature is expected to be investigated in future work. The MIC, located in Paris, shares many design features with the BKH combustor. The MIC also uses multiple injectors, but always in a linear arrangement to isolate interactions between pairs of flames when using two-dimensional imaging. Unless utilizing laser sheet flame illumination as in OH-PLIF, a cross injector formation prevents one from distinguishing between foreground and background flames when viewing OH* emission images. But, even OH-Planar Laser Induced Fluorescence (PLIF) imaging in these configurations has been challenging because it is difficult to penetrate the dense oxygen jet with a laser sheet [129, 130].

The VHAM is a modified version of the MIC which creates much greater acoustic pressure amplitudes in an effort to replicate the high amplitude oscillations documented in actual LRE combustion instabilities. The VHAM uses a toothed wheel to periodically block gas flow through exhaust nozzles, creating high pressure amplitudes inside the combustion chamber. The tooth wheel exhaust nozzle technique is also employed in the MIC, BKH, and CRC designs for the same purpose [18, 131]. With this method, the

periodic nozzle imposes an acoustic boundary condition on the chamber wall, where the acoustic frequency is controlled by the wheel speed. The resulting pressure perturbation amplitude though, is not controlled, and is instead determined by hardware geometry such as nozzle diameter and tooth shape. In the MIC, BKH, and CRC configurations, the toothed wheel is placed over a secondary exhaust nozzle which is located on the side of the chamber, perpendicular to the primary exhaust nozzle. In the VHAM though, zero secondary nozzles exist and two primary exhaust nozzles located at the end of the chamber are excited by a single toothed wheel. The VHAM design was recently used to create pressure amplitudes as high as 20% of p_c in Mery *et al.* [19]. Consequently, the VHAM induced a strong flame response whereas previous tests with smaller amplitudes in the MIC design yielded very little flame response.

The MIC used LO_x-GH_2 propellants in early experiments but quickly moved to LO_x-CH_4 propellants in an effort to achieve a more dramatic flame response to acoustic forcing. Again, this was linked to low amplitude acoustic pressure created by the single toothed wheel. Eventually, LO_x-CH_4 tests of subcritical and supercritical chamber pressure revealed a notable flame response to external forcing. A Ph.D. thesis by Richecoeur [8] presents results with similarity to Heidmann [128], mainly an increased spread angle caused by a shortened mixing region. Also, the combustor's five element injector arrangement showed evidence of interaction of adjacent flames. The VHAM is expected to produce a substantial flame response, even with LO_x-GH_2 propellants, and these results may be publicized in the future.

Controlled acoustic excitation in the manner described above allows experimentalists to partially decoupled a portion of the combustion instability feedback loop. Without an external acoustic source, chamber pressure perturbations exist due to combustion instabilities alone. But, when user-controlled acoustic excitation contributes to chamber acoustics, dual feedback dependencies exist as shown in Fig. 1.14. This configuration

allows one to isolate the effects of acoustic waves on fluid dynamic instability and heat release by controlling acoustic pressure amplitude and frequency. With this strategy, the degree to which perturbation amplitudes and their inherent frequencies can be varied is highly dependent on the specific hardware design used for external acoustic forcing. However, if the flame is self-excited then added acoustic forcing will compete with naturally occurring modes, and the experimentalist forfeits *complete* control over chamber acoustics. An analytical comparison of the excited acoustic energy and combustion energy was made by Rey *et al.* [132] and this relationship will be considered for the chamber used in the present study.

In contrast to the nozzle modulation method used by all four aforementioned combustors, the CVRC of Purdue uses an acoustic control system relying on variable injector geometry [17]. By altering the size of the oxidizer plenum, the resonant frequency of the injector flow is controlled such that chamber pressure amplitudes range from less than 10% to 60% of the chamber pressure. The highest pressure amplitudes are achieved when the oscillation frequency of the injector matches a chamber resonant frequency, whereas a mismatch dampens the chamber mode. Thus, the CVRC design forgoes the electro-mechanical system of a typical acoustic source [8, 23, 24], and instead relies on injector flow oscillations to create unsteady heat release. This method reliably induces high amplitude instability, but requires mindful choice of fuel species and propellant flow conditions to manipulate the preferred frequency and amplitude of the instability.

The lessons learned from the experimental facilities described above were instrumental in the design and construction of the shear-coaxial jet combustion facility used in this study. Many concepts introduced here are revisited in section 4.3, with new observations regarding the stability of O_2-H_2 flames.

1.4 Present Studies

The goal of the present studies is to explore acoustically-coupled combustion and transport processes in two fundamental configurations. One involves a continuously burning liquid fuel droplet exposed to acoustic excitation in a cylindrical waveguide at background atmospheric pressure. These experiments have been conducted at UCLA in the Energy and Propulsion Research Laboratory. The other configuration involves a coaxial jet of transcritical fluid injection into a high pressure (2.75 MPa) chamber at AFRL, also with exposure to acoustic excitation, and with the ultimate goal of exploring reactive flow. A detailed exploration of each system helps to shed light on important phenomena associated with acoustically-coupled combustion instabilities.

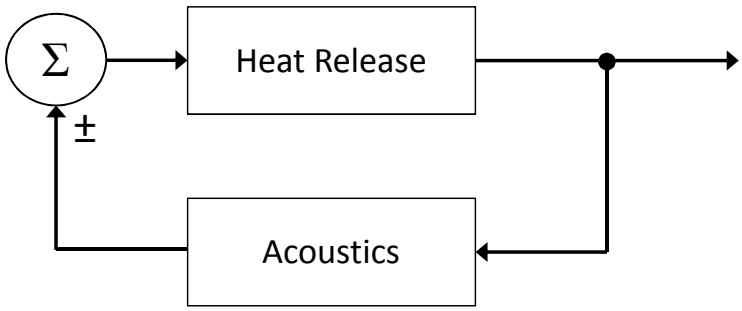

1.1: The bimodal combustion instability feedback loop [4, 5].

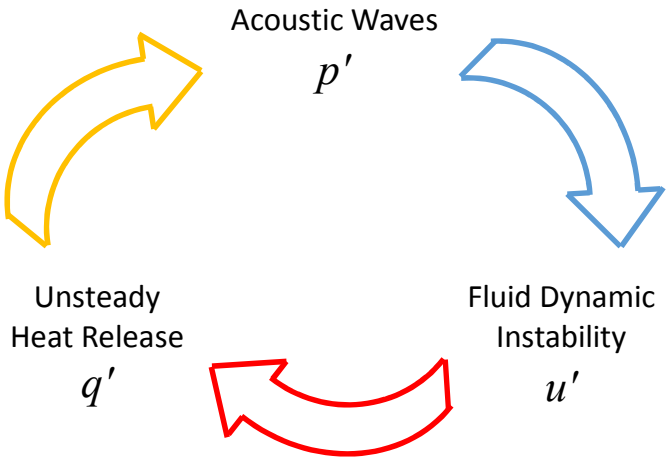

1.2: Three-part combustion instability feedback loop.

1.3: Modern launch vehicles using O_2-H_2 LREs. Delta IV (left, ULA 2011) Ariane 5 (right, ESA 2013)

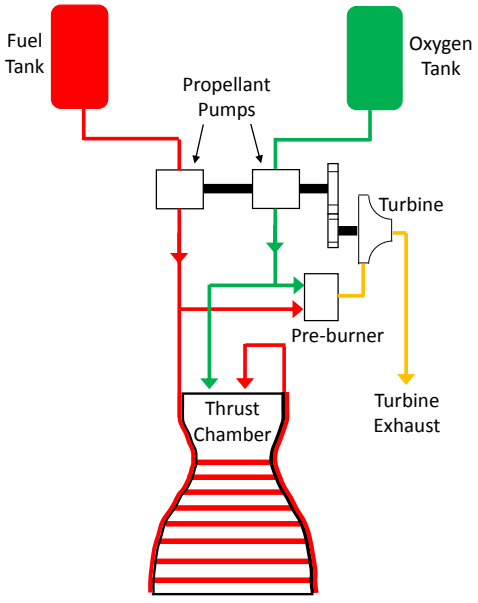

1.4: Diagram of the gas generator cycle in a liquid rocket engine.

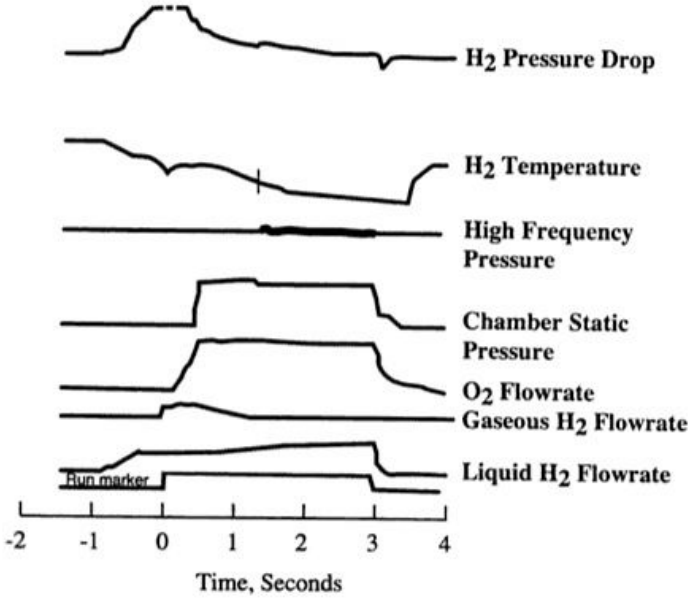

1.5: Fuel temperature ramping has been a common technique for verifying LRE stability for a wide range of fuel properties in hydrogen-oxygen engines. This plot, taken from Hulka and Hutt [45], reveals an instability occurring after a temperature drop engendered a lower hydrogen supply pressure.

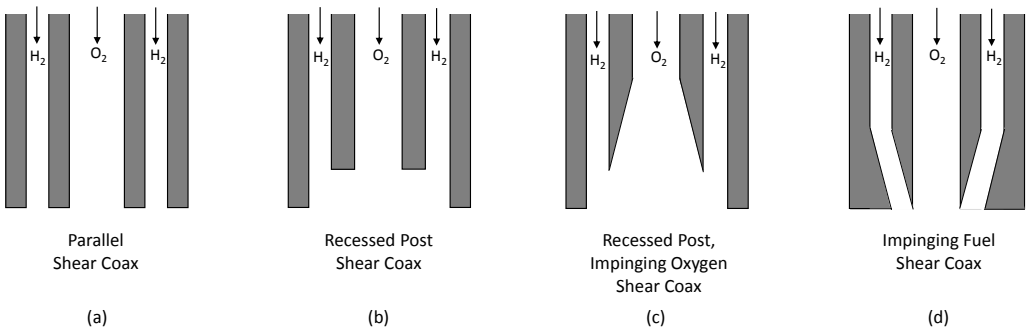

1.6: As early as the 1960s, multiple configurations of the shear-coaxial injector had been used to enhance mixing and prevent instability in hydrogen-oxygen LREs.

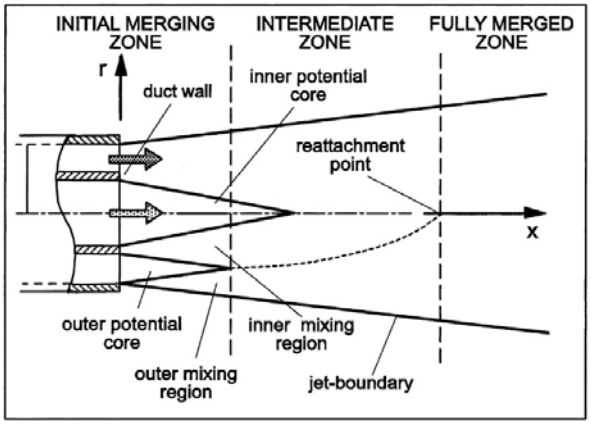

1.7: The mixing of the nonreactive shear-coaxial jet is characterized by three merging zones and two mixing regions. (diagram by Talamelli and Gavalini [108], adopted from Ko and Kwan [88])

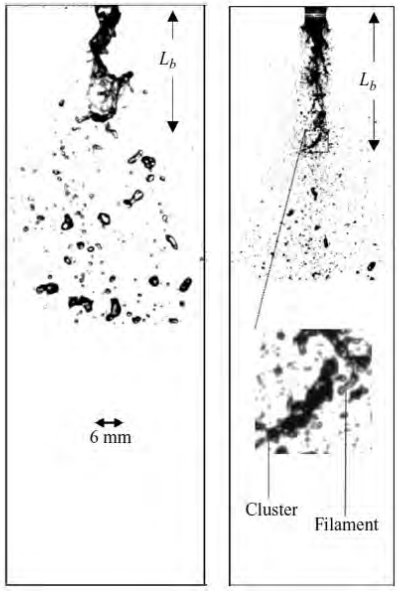

1.8: Coaxial jet images from Baillot *et al.* [16] show the membrane break up regime (left) and the fibre-type break up regime (right).

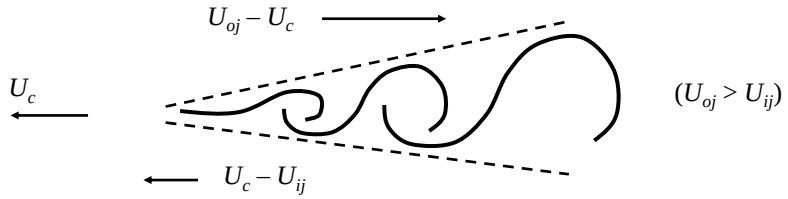

1.9: A convective shear layer diagram drawn in the vortex frame of reference.

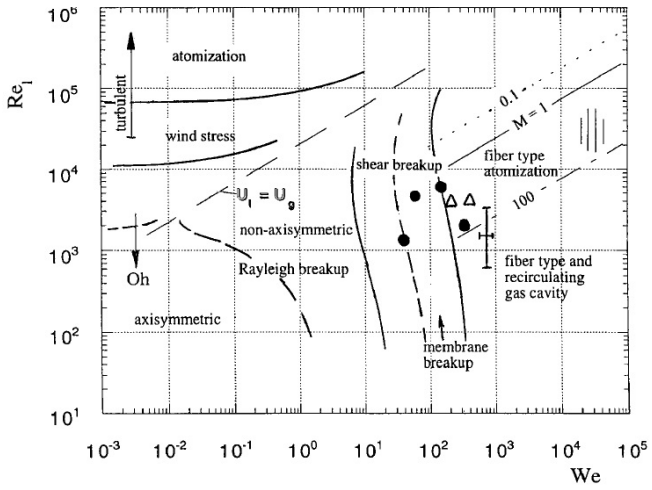

1.10: Break up characteristics of liquid-gas coaxial jets separated into five regimes (axisymmetric Rayleigh, antisymmetric Rayleigh, shear, membrane, and fibre-type break up) according to liquid Reynolds number and Weber number. M is the momentum flux ratio. (plot from Lasheras and Hopfinger [95])

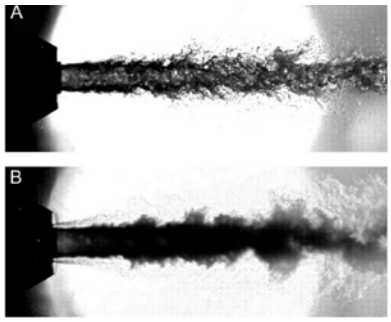

1.11: Shear-Coaxial jets of liquid nitrogen and gaseous helium issuing into high pressure chambers. $D_1 = 1.9$ mm, $U_{ij} = 5$ m/s, $U_{oj} = 100$ m/s, $T_{ij} = 97$ K, $T_{oj} = 280$ K (A) 1.0 MPa (B) 6.0 MPa (Mayer and Smith [14])

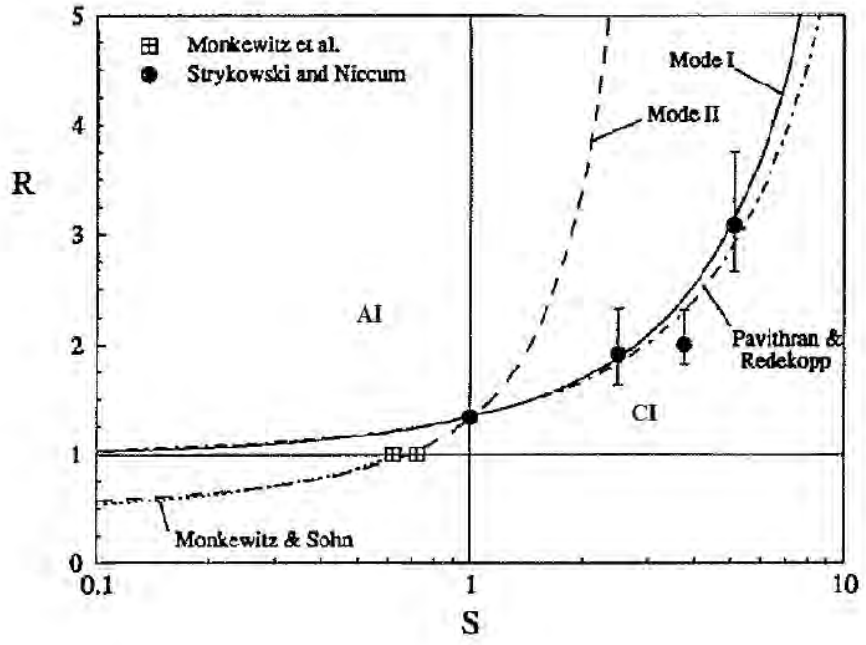

1.12: Absolute-convective instability transition lines from Jendoubi and Strykowski [121] with results from several others [113, 114, 133, 134]. The upper left region represents absolutely unstable operating space, and the lower right region represents convectively unstable operating space. Following the definitions of [121] for the x and y axes, $R > 1$ represents ambient counter-flow and $R < 1$ represents co-flow ($R \equiv (U_1 - U_2)/(U_1 + U_2)$). $S > 1$ represents jets *heavier* than the surrounding fluid, and $S < 1$ represents jets *lighter* than the surrounding fluid ($S \equiv \rho_1/\rho_2$). The typical conditions of a LO_x-GH_2 shear-coaxial jet lie in the convective instability operating space for $R < 0$, not shown here.

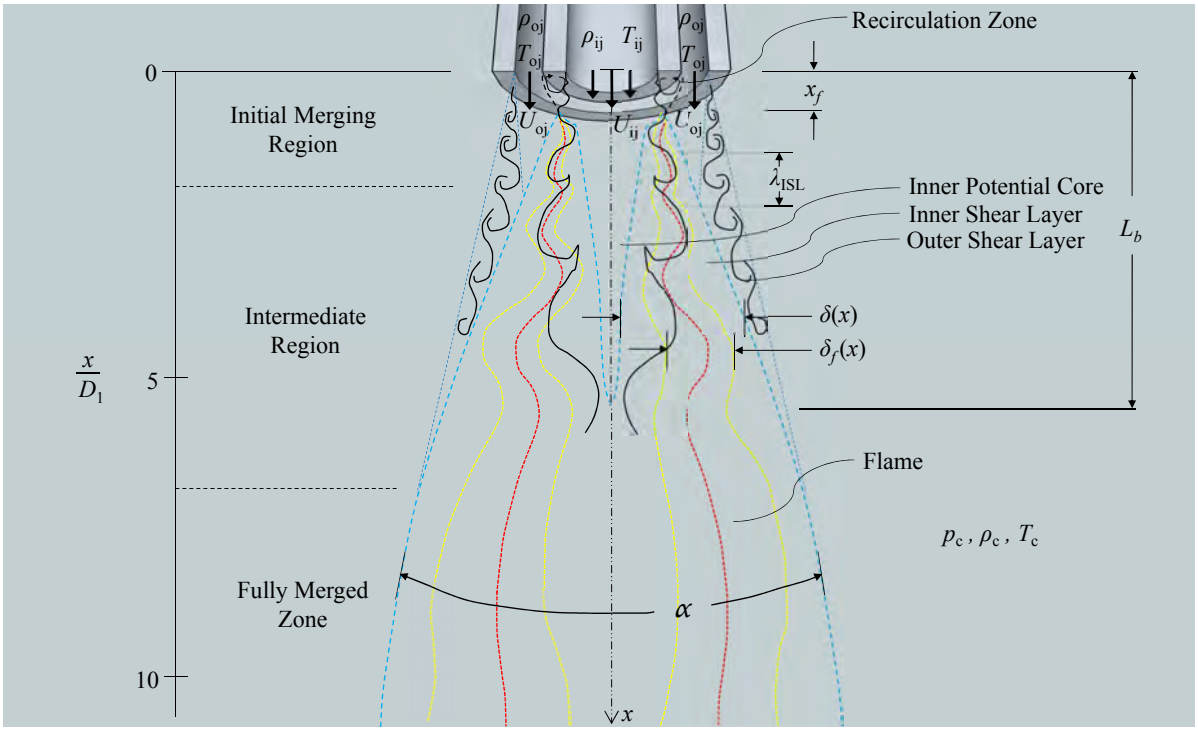

1.13: Flow diagram of a reactive shear-coaxial jet.

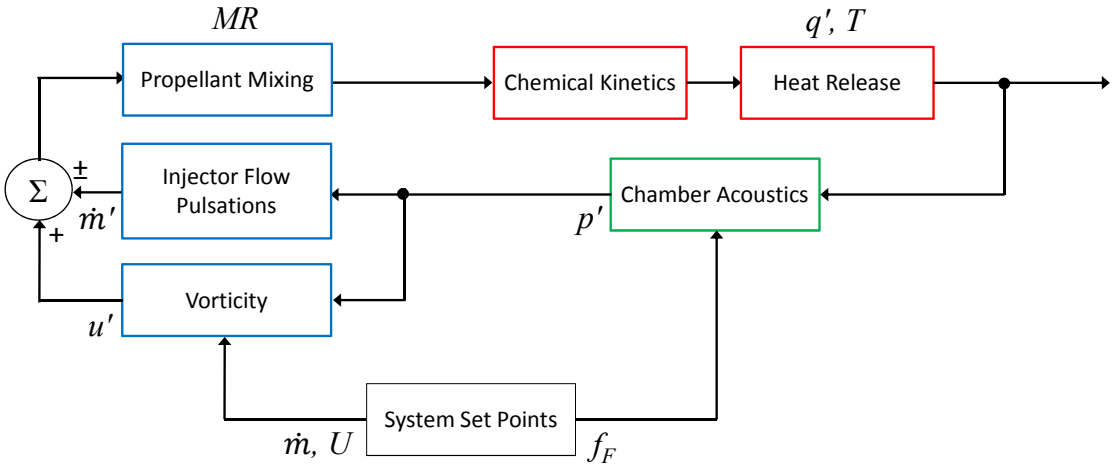

1.14: An expanded portrayal of the three part combustion instability feedback loop showing fluid mechanical features in blue, reactive features in red, and acoustic pressure oscillations in green. User-controlled acoustic forcing acts as an additional input to chamber pressure oscillations. Injector exit flow conditions act as a potential control of shear layer vortex structures.

CHAPTER 2

Experimental Facility and Methods - Acoustically Coupled Fuel Droplet Combustion

The experimental apparatus in these studies is the same as that used by Dattarajan *et al.* [22] and Rodriguez *et al.* [75], with several modifications. Modifications include, but are not limited to, the pressure perturbation measurement system and the flame imaging system, both of which will be described in this chapter.

2.1 Acoustic Waveguide

A long, cylindrical waveguide, similar to a Kundt's tube, was used to create standing acoustic waves by placing a loudspeaker at each end. The system was operated at atmospheric background pressure and room temperature. A continuosly fed, burning fuel droplet was situated at the center of the waveguide. The waveguide was made of aluminum tubing with an inner diameter of 11.4 cm and a full length of 90 cm, and quartz windows placed in the side of the waveguide nearest the droplet allowed for optical access. The 8 Ω woofer loudspeakers were connected using three long rods, allowing the pair to be moved as an assembly while remaining a constant distance apart. The same apparatus was also used in a speaker-reflector configuration by replacing one speaker with an aluminum reflector plate. The complete apparatus is shown in Figure 2.1.

Using a function generator, a sinusoidal signal was sent to each loudspeaker with

the two signals in-phase ($\Delta\phi = 0°$) or out-of-phase ($\Delta\phi = 180°$). Due to a constant waveguide length L the loudspeaker frequency, or acoustic frequency f_a, is the controlling parameter in creating a resonant standing waveform within the waveguide. Theoretically, f_a can be chosen such that the waveguide length L is an integral multiple of half the acoustic wavelength, $\lambda/2$, that is,

$$L = \frac{n}{2}\lambda = \frac{n}{2}(\frac{c}{f_a}), \tag{2.1}$$

where c is the speed of sound. Regardless of the value of the f_a and n, speakers operated out-of-phase ($\Delta\phi = 180°$) will create a PN at the center of the waveguide and speakers operated in-phase ($\Delta\phi = 0°$) will create a PAN at the center [135]. But, to create an acoustically resonant condition with maximum pressure perturbations, then f_a must take on a value such that n is an integer. More specifically, for speakers operated out-of-phase, if f_a is chosen to give an odd value of n then the pressure amplitude is maximized in the waveguide. For speakers operated in-phase, if f_a is chosen to give an even value of n then the pressure amplitude is maximized in the waveguide. Thus, resonant conditions hold for a select few frequencies, but for any frequency the center of the waveguide will take on a PN or PAN condition for $\Delta\phi = 180°$ and $\Delta\phi = 0°$, respectively. These conclusions assume the perturbation amplitudes created by the speakers to be identical. In the special case where one speaker is instead replaced with a rigid wall, eqn. (2.1) still holds true. Theoretically, in this speaker-reflector configuration odd values of n produce a PN at the waveguide center, and even values of n produce a PAN at the waveguide center.

Experimental acoustic characterization relied on point-like pressure measurements made using a Kulite XCE-093-50D miniature pressure transducer with an output resolution 0.29 mV/kPa and diameter of 2.4 mm. The sinusoidal pressure transducer output signal was amplified and then used to find the pressure perturbation amplitude p'. With the sensor placed at the center of the waveguide, the most ideal f_a was determined by

sweeping through a wide range of frequencies in search of p' minima (PN) for $\Delta\phi = 180°$ or p' maxima (PAN) for $\Delta\phi = 0°$. The result of this frequency sweep technique is shown in Figures 2.2 and 2.3 for $\Delta\phi = 180°$ and $\Delta\phi = 0°$, respectively. Pressure measurements at the speaker are also shown, which will exhibit maxima for all resonant frequencies. Along these lines, a speaker-reflector frequency sweep was performed with a pressure sensor located at the reflector, and results are shown in Figure 2.4. All three frequency sweeps presented here can be used to extract experimental resonant wave frequencies, which can then be compared to theoretical resonant frequencies calculated using eqn. (2.1). This comparison is shown in Table 2.1.

Experiments by Dattarajan *et al.* [22] and Rodriguez *et al.* [75] employed a speaker-reflector configuration, but Teshome *et al.* [82] improved upon this by instead using the speaker-speaker configuration, citing a more symmetric pressure distribution about the center. This claim is explored more thoroughly here by measuring p' throughout the axial length of the waveguide for each frequency of interest. The resulting collection of pressure versus waveguide location plots is divided into speaker-reflector conditions in Figure 2.5, speaker-speaker out-of-phase conditions in Figure 2.6, and speaker-speaker in-phase conditions in Figure 2.7. Comparison with theoretical pressure distributions are also shown, with the pressure maximum based on matching of theory and experiment at the closest peak to the waveguide center.

First considering the speaker-reflector pressure distributions, the amplitudes are shown to be generally symmetric for frequencies near the theoretical values of Table 2.1. Figure 2.7 includes two frequencies which produce a PN at the waveguide center, 308 Hz and 784 Hz, and one other frequency which produces a PAN at the center, 562 Hz. Upon closer inspection though, the pressure distribution is mildly asymmetric for the lowest frequency, 308 Hz. The correspondingly longer wavelength associated with 308 Hz appears to exacerbate any asymmetric speaker boundary conditions, having a

greater impact on the distribution at the center. Moreover, previous work has shown conditions producing a distinct PN at the waveguide center to also produce a quite asymmetric velocity distribution according to hot wire measurements [75].

For the speaker-speaker results shown in Figure 2.6, operating the speakers 180^o out-of-phase creates standing waves at the waveguide center regardless of acoustic frequency. For five different frequencies ranging from 332 Hz to 1500 Hz the primary difference is instead the maximum measured pressure amplitude. Similar plots are found in Figure 2.7 for speakers in-phase, which produces a PAN near the center for all five frequencies explored here. Also, when comparing two conditions with an equal speaker input voltage but different frequencies, choosing a frequency close to the resonant frequency will provide a larger pressure amplitude. For example, contrasting Figures 2.7(c) for 898 Hz and 2.7(d) for 1088 Hz shows a much larger amplitude for 1088 Hz. This principle holds true for all frequencies explored here, such that the difference in sound pressure level between a resonant and non-resonant flow condition could be easily detected by the human ear. The same body of work revealing asymmetric velocity distributions for the speaker-reflector configuration measured a very symmetric velocity distribution for the speaker-speaker configuration, largely motivating previous [82] and current experiments to employ a two speaker configuration. With this established, one must also note that additional hot wire measurements are needed to complete the current acoustic characterization and confirm the assumption that VAN locations indeed coincide with PN locations and vise versa. Hotwire measurements in Teshome *et al.* [82] were uncalibrated and preliminary, but did show a symmetric velocity profile with a VAN at the waveguide center.

2.2 Droplet Generation and Ignition

The fuel delivery system consisted of a hollow borosilicate glass capillary and a KDS Model 100 syringe pump. The fuel droplet was suspended within the waveguide at the tip of the glass capillary of approximately 0.37 mm outer diameter. Liquid fuel was delivered to the capillary during droplet combustion at a constant volumetric flow rate Q_v, set by the syringe pump. The volumetric flow rate and the droplet size were used to determine the burning rate constant K, as will be described below. A protective copper shroud was placed above the end of the glass capillary in order to prevent vaporization of the fuel within the glass capillary just above the droplet. The distance between the end of the shroud and the end of the tip of the capillary was fixed at 3.2 mm, a regime for which the droplet burning rate constant did not depend on this length [22]. The droplet was ignited by means of a resistive heating Ni-Cr wire mounted on a push-type solenoid. A TattleTale Model 8 data logger/controller board was used to synchronize the extenstion of the solenoid arm and the passage of current in the ignitor wires. This mechanism created an efficient means for igniting the droplet remotely without having to open, manually ignite, and close the waveguide. After ignition, the flame remained intact unless extinguished by strong convective flow or by a fuel vapor jet formed at the capillary exit due to overheated incoming fuel. This ignition technique was identically performed for all fuels, which are listed in Table 2.2 with their respective properties.

2.3 Imaging

Flame imaging was performed using an intensified camera and image acquisition system designed to capture OH* chemiluminescence at various instants within an acoustic cycle. This imaging system is discussed in several parts. First, the optical train assembled to capture OH* chemiluminescence is described, including a quantitative estimation of

transmission versus wavelength. Second, a description of the components, communications, and controls required to coordinate image acquisition will include equipment specifications and variables set by the user, with justification. Last, a timing system based upon the acoustic pressure cycle is explained.

2.3.1 Optics

There are several well-documented reactions occurring within hydrocarbon flames which produce chain carriers in route to the final combustion products. If sufficiently energetic, such reactions will produce radicals in electronically excited states which then undergo deexcitation through one of two mechanisms. More specifically, hydrocarbon flames commonly exhibit the reaction

$$CH(^2\Pi_u) + O_2(^3\Sigma_g) \rightarrow CO(^1\Sigma^+) + OH^*(^2\Sigma^+) \tag{2.2}$$

where electronically excited hydroxyl radicals (OH*) then experience spontaneous radiative deexcitation (chemiluminescence) or collisional deexcitation (quenching). The exact proportions of quenched OH* and OH* which produces chemiluminescence are governed, for example, by fuel type (e.g. carbon to hydrogen ratio) and flow conditions (e.g. pressure). Regardless of these precise quantities though, regions of OH* chemiluminescence are shown to coincide with primary reaction zones and lie close to, if not coincide with, maximum temperature [66, 136]. This correlation between OH* chemiluminescence and flame topology has limitations with turbulent premixed flames or flames near extinction [137], but is quite sufficient for laminar diffusion flames in steady state conditions. Thus, for droplet combustion this study tracks light emission created via the deexcitation reaction

$$OH^*(^2\Sigma^+) \rightarrow OH(^2\Pi) + h\nu \tag{2.3}$$

which is observed in the ultraviolet (UV) band at approximately 308 nm.

The optical arrangement passes a span of UV wavelengths to isolate this particular source of chemiluminescence. Figure 2.8 shows the receiving optics from the flame to the camera. The quartz waveguide window and the UV lens (UV-Nikkor 105 mm f/4.5) pass with over 70% transmission for low UV to high infrared (IR) wavelengths, while the camera photocathode is designed for best capture with low wavelengths. The UV bandpass filter provides 88% maximum transmission centered around 320 nm, and also transmits 20-50% of IR light. The camera photocathode (NanoStar S20 type) achieves greatest quantum efficiencies for 200-450 nm. The combined transmission of the receiving optics is quantified in Figure 2.9. To confirm capture of OH* chemiluminescence and blocking of other sources of chemiluminescence, results from the work of Kojima *et al.* [138] are shown for comparison. The transmission range is consistent with this prior work for methane.

2.3.2 Image Acquisition

Acquiring and storing flame images for specific parts of an acoustic cycle is made possible by the interconnection of image acquisition equipment shown in Figure 2.1. The function generator which controls loudspeakers sends a second signal, equal to the first in phase and frequency, to a Programmable Timing Unit (PTU) for camera control. This parallel control of the acoustic and imaging systems by a single function generator permits image capture which is phase-locked to a short span of time within the acoustic cycle.

The PTU sends a signal to the camera which can be custom manipulated within LaVision's software interface, but always maintains a frequency equal to the acoustic frequency. Custom manipulations include specifying the image intensifier gate width, image intensifier gain, number of intensifier pulses within one image frame (burst count), and the phase angle marking the start of the intensifier gate. For all imaging in this study, the gate width time is set equal to 1/64 of the acoustic period, $T_a/64$, while the

intensifier gain and burst count must be varied to ration the total intensity captured by the CCD sensor. For example, high luminosity flames such as JP-8 require a lower intensifier gain and burst count than low luminosity flames such as methanol. Otherwise, the CCD sensor will be damaged by over-exposure. Depending on fuel type, the intensifier gain and burst count range from 30/100 to 80/100 and 20 to 200, respectively. Other specifications are listed in Table 2.3. Last, the phase angle marking the start of the intensifier gate is specified by a repeating loop of 18 different phase angles, $\phi_{II} = 20 : 20 : 360$. However, this phase angle sequence is in reference to the PTU output signal, which is not in phase with the acoustic pressure cycle due to time delays caused by components within both the acoustic system and the imaging system. Thus, these time delays, or phase delays, must be measured in order to convert ϕ_{II} to its equivalent value referenced by the acoustic pressure cycle ϕ_p.

2.3.3 Acoustics-Imaging Synchronization

Reformatting ϕ_{II} in terms of ϕ_p is possible by comparing two signals and their associated phase delays. First, the pressure perturbation signal is measured by a pressure transducer and observed via oscilliscope, creating phase delays due to the transducer unit and pressure transducer amplifier. Second, the camera produces a TTL output pulsed with the image intensifier gate, thus providing a pulsed signal corresponding to the actual time period captured by the camera. Relating these two signals allows one to identify the exact slice of time within the acoustic pressure cycle which is captured by the camera. Moreover, this technique strategically avoids individual measurement of the phase delays associated with each individual compenent within the acoustic and imaging systems (e.g. speaker amplifier, loudspeakers, sound travel, PTU, etc.).

Specifically, the problem is represented as $\phi_p = \phi_{II} + \Delta\phi$. Setting $\phi_{II} = 0$ and measuring $\Delta\phi$ gives a solution for ϕ_p. $\Delta\phi$ is uniquely determined for each forcing

frequency as the difference between the two signals listed above plus pressure transducer and pressure transducer amplifier phase delays, as listed above. The pressure transducer phase delay is $< 1^o$, and negligible. The pressure transducer amplifier phase delay is measured as part of a complete frequency response measurement, thus recording both the amplifier gain and phase delay as a function of frequency. The camera's TTL output representing the image intensifier gate is delayed by 20 ns and the delays associated with all wiring are ~ 1 ns, both negligible.

2.4 Measurement Methods

2.4.1 Burning Rate Constant

From continuity for a spherical droplet of diameter d, the instantaneous burning rate constant K may be evaluated as

$$K = \frac{4Q_v}{\pi d(t)} - 2d\dot{d} \tag{2.4}$$

A constant volumetric flow rate Q_v provided by the syringe pump was chosen in order to maintain a roughly constant droplet size. This technique makes the first term in eqn. (2.4) the dominant term, while the second term is close to zero. This is the opposite of the typical "non-fed" burning droplet governed by the d^2 law when $Q_v = 0$ [63, 64]. Due to the normal gravity environment of the present experiments, eqn. (2.4) required a droplet diameter equivalent to that of a sphere with volume equal to the oblong droplet volume, as done by Struk *et al.* [65] and described in section 1.2.2. A custom image processing MATLAB^{TM} algorithm was used to fit an ellipse to the droplet in each image, thus providing the data needed to calculate d_{eqvs} for each image and $\dot{d}_{eqvs}$ for a set of images. Additional LED back-lighting provided ample contrast between the liquid fuel and the back-light in order for the image processing algorithm to detect the silhouette of the droplet. Time-averaged K values were then computed according to eqn. (2.4)

for a complete flow condition. The same calculation could be performed for a given acoustic phase angle within a flow condition, but this task reveals fuel droplet sizes to be independent of phase and thus K values also independent of phase. Investigation of burning rate versus acoustic phase could instead require utilizing chemiluminescence intensity variations with respect to acoustic phase, which has not been explored in previous works.

2.4.2 Acoustic Acceleration

In the absence of acoustic forcing the only net force is the buoyancy force, acting on the volume V of hot products with density ρ_p. When surrounded by a cooler gas of density ρ_o the buoyancy force follows as $F_B = (\rho_p - \rho_o)Vg_o$, which results in a vertically oriented, symmetric flame. With acoustic excitation, the flame orientation became aligned with the resultant force due to buoyancy and an analogous acoustic radiation force, $F_R = (\rho_p - \rho_o)Vg_a$, where g_a is the acoustic acceleration. This type of behavior is shown in Figure 2.10. According to the theory suggested by Tanabe *et al.* [21], based on the work of Nyborg [79], the acoustic acceleration g_a depends on the position of the droplet with respect to the PN or PAN. In light of the preceding relationship, this study experimentally determines acoustic acceleration as done by Teshome *et al.* [82]. The actual acoustic acceleration at the location of the droplet is estimated using the measured deflection angle ϕ_f and gravitational acceleration

$$g_{a,exp} = g_o \tan \phi_f \tag{2.5}$$

The degree of flame deflection ϕ_f was estimated by measuring the average change in angle between the tangent lines of an unforced and forced flame edge, as shown in Figure 2.10. For extreme cases of flame deflection where the flame is nearly horizontal, more uncertainty can be attributed to ϕ_f because the plume region turns upward in the far wake of the flame.

2.4.3 Flame Standoff Distance

A burning droplet in normal gravity is encompassed by a quasi-ellipsoidal flame front as shown by Figure 2.10, an image for the special case of an acoustically excited burning droplet. For both unforced and forced burning droplets, the flame standoff distance δ_f is clearly a function of the angle θ measured from the positive x-axis in the x-y plane. One should also deduce that unlike the unforced case, the acoustically forced flame is not axisymmetric because δ_f is also a function of the out-of-plane angle ϕ. But, for the two-dimensional standoff distance measurements discussed here, this descrimination will not bear importance.

Flame standoff distance is defined as the difference between the flame and droplet radii, $\delta_f = r_f - r_s$, each of which is measured by image analysis algorithms. First, r_s is defined as a function of θ using the droplet ellipse fit technique identical to that employed in d_{eqvs} measurements. Second, r_f is defined as the distance from the center of the droplet to the location of maximum OH* chemiluminescence intensity for a given value of θ. This particular definition of the "flame" is common to many experimental works in the fields of both diffusion and premixed flames [66, 67, 137, 138]. Several other definitions have been used as a reliable measure of flame topology, including the point of maximum temperature, maximum C_2* or CH* chemiluminescence, or maximum HCO mole fraction. Moreover, different flame measurement methods can provide conflicting results in the realm of turbulent premixed flames or flames near the extinction strain limit. Extinction studies have actually revealed shortcomings in the traditional OH* chemiluminescence technique when carbon-based chain carriers sustain reaction where a lack of OH* chemiluminescence would otherwise predict extinction [137]. The questions arising from these inconsistencies are highly motivated by combustion instability research and imply a loss of robustness for this study's r_f definition. But, the set of results analyzed here avoid extinction for even the strongest convective and oscillating

flows. In conclusion, the maximum OH* chemiluminescence flame definition is imperfect, but quite effective for a diffusion flame in the current flow conditions, where a lack of extinction and turbulent flame structure provide for an unbroken flame front in all flame images.

Finally, δ_f data analysis will focus attention on the upstream side of the flame, the location of which is determined by acoustic flow conditions. For example, Figure 2.10 shows a stagnation point on the flame's right side. A different droplet position though, can switch flame orientation and move the stagnation point, thus moving the area of interest. Therefore, it is important to clarify that δ_f is measured on the upstream side only. These measurements include $\delta_f(\theta = 0^o)$ and $\delta_f(\theta = 180^o)$, depending on flame orientation. Other valuable analysis includes minimum standoff distance created by natural convection $\delta_f(\theta = 270^o)$ and standoff distance at the stagnation point $\delta_f(\theta = \alpha_f)$, but little study of these points is included in this body of work.

2.5 Experimental Procedure

Upon beginning a set of experiments, a clean syringe was loaded with the desired fuel and connected to the glass capillary by a rubber tube. The flow rate maintained by the syringe pump was chosen to achieve quasi-steady droplet burning for a given fuel and flow condition. For all experiments in this study, fuel flow rate fell within the range 53.3 mL/hr $< Q_v <$ 63.3 mm^3/s. The acoustic amplitude for a given condition was identified using p' measured at the PAN with the smallest positive x location, which required knowledge gained from pressure distributions shown in Section 2.1. This amplitude is represented as p'_{max}, i.e. $p'_{max}(f_a = 332 \text{ Hz}) = p'(x = 28 \text{ cm})$, $p'_{max}(f_a = 898 \text{ Hz}) = p'(x = 10 \text{ cm})$, $p'_{max}(f_a = 1500 \text{ Hz}) = p'(x = 5 \text{ cm})$. Finally, before each ignition, the waveguide was purged with air to remove combustion products from prior experiments.

Droplet ignition was performed using the heater wire and push-type solenoid assembly, and ignition was immediately followed by initiating the acoustics. Under the steady conditions used here, burning droplets could be sustained for as long as 10 minutes without flame extinction. Within this burning period an image recording loop cycled through 18 different phase-locked acoustic phase angles, $\phi_{II} = 20 : 20 : 360$, acquiring 5 images at each phase before proceeding to the next. This method of capturing 90 images was performed 4 times to complete 1 recording session, which required 2 to 5 minutes of recording. Each image was immediately digitized in .im7 file format with an associated clock time. The imaging procedure was completed by acquiring a set of 50 background images with the capillary and shroud removed from the field of view, and thus the LED creating the only source of light and variations thereof.

The experiment was followed by two steps of image processing. First, a flame image was processed using LaVision's DaVis software, where the average of 50 background images was subtracted from the flame image. Second, the resulting pair of flame images (original and background subtracted) were reoriented and analyzed using a MATLAB^{TM} algorithm. The original image was utilized only to detect the droplet edge, and then calculate the position and dimensions of an ellipse coinciding with the droplet silouette. Using the pixel coordinates of the ellipse center, the background subtracted image was converted from cartesian coordinates to cylindrical coordinates with an origin at the ellipse center, and this final image was used for all remaining flame analysis. It should be noted that imperfections in the background subtraction technique arise because although the shroud, capillary, and droplet shield backlighting, the backlight is still subtracted from these areas, creating biased regions in the final flame image. The pixel intensities of these regions are lower than actual intensities, but this bias error does not interfere with the conclusions of this study.

2.6 Measurement Uncertainties

2.6.1 Precision Uncertainty

The sources of precision uncertainty in the measured values of the burning rate constant K in eqn. (2.4) stem from uncertainties in the fuel volumetric flow rate Q_v and determining the equivalent sphere diameter d_{eqvs} for the droplet. The technique for calculating the uncertainty in d_{eqvs} is similar to the method used by Dattarajan *et al.* [22] which utilizes the principles of uncertainty propagation in Mills and Chang [139], but with improved resolution due to a reduced pixel view. First, the equivalent sphere diameter is found in terms of the major and minor axes of the droplet ellipse, resulting in $d_{eqvs} = 2a^{\frac{2}{3}}b^{\frac{1}{3}}$. Then, if the uncertainty in the axes lengths, a and b, are equal, then the method cited above follows as

$$\begin{aligned}
\Delta d_{eqs} &= \sqrt{\left(\frac{\partial d_{eqs}}{\partial a}\Delta a\right)^2 + \left(\frac{\partial d_{eqs}}{\partial b}\Delta b\right)^2} \\
&= \sqrt{\left(\frac{2}{3}\frac{2b^{\frac{1}{3}}}{a^{\frac{1}{3}}}\Delta a\right)^2 + \left(\frac{1}{3}\frac{2a^{\frac{2}{3}}}{b^{\frac{2}{3}}}\Delta b\right)^2} \\
&= \sqrt{\left(\frac{4}{3}\Delta a\left[\frac{b}{a}\right]^{\frac{1}{3}}\right)^2 + \left(\frac{2}{3}\Delta b\left[\frac{a}{b}\right]^{\frac{2}{3}}\right)^2} \\
&= \Delta ab\sqrt{\frac{16}{9}\left[\frac{b}{a}\right]^{\frac{2}{3}} + \frac{4}{9}\left[\frac{b}{a}\right]^{-\frac{4}{3}}}
\end{aligned} \tag{2.6}$$

where it is assumed $\Delta a = \Delta b = \Delta ab$. Uncertainty in d_{eqvs} is then calculated using $d_{eqvs} \approx 1.5$ mm, $\Delta ab \approx 0.05$ mm, and $\frac{b}{a} \approx 1.5$, giving an uncertainty of $\frac{\Delta d_{eqvs}}{d_{eqvs}} \approx 5.4\%$. Uncertainty in Q_v though, is based solely in the precision uncertainty of the syringe pump. Thus, the manufacturer's rating of 0.1% is used for $\frac{\Delta Q_v}{Q_v}$.

The resulting uncertainties in K follow as

$$\begin{aligned}\Delta K &= \sqrt{\left(\frac{\partial K}{\partial Q_v}\Delta Q_v\right)^2 + \left(\frac{\partial K}{\partial d_{eqs}}\Delta d_{eqs}\right)^2} \\ &= \sqrt{\left(\frac{4\Delta Q_v}{\pi d_{eqs}}\right)^2 + \left(-\frac{4Q_v}{\pi d_{eqs}^2}\Delta d_{eqs}\right)^2} \\ &= \sqrt{\left(K\frac{\Delta Q_v}{Q_v}\right)^2 + \left(-K\frac{\Delta d_{eqs}}{d_{eqs}}\right)^2} \\ &= K\sqrt{\left(\frac{\Delta Q_v}{Q_v}\right)^2 + \left(\frac{\Delta d_{eqs}}{d_{eqs}}\right)^2}\end{aligned} \tag{2.7}$$

Therefore, $\frac{\Delta K}{K} = 5.4\%$ when $\frac{\Delta d_{eqvs}}{d_{eqvs}} \approx 5.4\%$ and $\frac{\Delta Q_v}{Q_v} = 0.1\%$, and the influence of fuel flow uncertainty has a negligible affect on total uncertainty in K. The transient term in eqn. (2.4) also has a negligible affect in this analysis and is not included here. Last, the precision uncertainty of time-averaged K values, which is of primary importance in this study, can be found by accounting for the minimum number of experimental points used to encompass the burning rate constant for one flow condition, 30. The resulting precision uncertainty in average K values is estimated to be $5.4\%/\sqrt{30} \approx 0.99\%$.

The source of precision uncertainty for pressure perturbation measurements, on the other hand, lies only in the accuracy rating of the pressure transducer. The XCE-093-50D has an output signal reproducibility of 0.5% of the full scale output, $\Delta V = (0.005)(\text{FSO}) = (0.005)(100\text{ mV}) = 0.5\text{ mV}$. With a signal resolution of 0.292 mV/kPa and a signal amplifier gain of 495, the calculation follows as

$$\begin{aligned}\Delta p' &= \sqrt{\left(\frac{\partial p'}{\partial V}\Delta V\right)^2} \\ &= \frac{\partial p'}{\partial V}\Delta V \\ &= \frac{\partial}{\partial V}\left(\frac{V}{\delta G}\right)\Delta V \\ &= \frac{0.5\text{ mV}}{\left(0.292\frac{\text{mV}}{\text{kPa}}\right)(495)} = 3.5\text{ Pa}\end{aligned} \tag{2.8}$$

For the pressure amplitude used most in this study, $p' = 150$ Pa, the precision uncertainty is $\frac{\Delta p'}{p'} \approx 2.31\%$.

2.6.2 Bias Uncertainty

Concerning K, sources of bias uncertainty include a 1% accuracy rating for Q_v, quoted from the syringe pump manufacturer, and bias due to pixel representation of the droplet edge. The latter form of uncertainty is present in all experiments where image analysis algorithms are used for edge detection. For this particular study, the camera's high spatial resolution results in a pixel view of 7.3 μm and therefore, droplet edge detection bias is negligibly small when compared to precision uncertainties and error from the droplet ellipse fit process. This ellipse fit technique, the third source of bias uncertainty discussed here, is largely connected to errors from equating the diameter of the droplet ellipse with the diameter of a sphere of equivalent diameter. Extensive analysis is included in Dattarajan *et al.* [22], where other techniques for choosing an appropriate droplet diameter d are quantitatively compared. Additional attention though, could be given to the accuracy of the ellipse fit itself. Surface tension and gravitational forces cause the droplet to form a teardrop-like shape, where an ellipse fit consistently matches the lower edge of the droplet, but over estimates the volume in the upper portion of the droplet. Ultimately, the burning rate constant K is under estimated by an enlarged droplet volume. Flame standoff distance measurements are uninfluenced by this effect because this study is interested in standoff distance for the lower hemisphere of the droplet, where the majority of burning occurs.

Although, the standoff distance measurement technique contains a second source of bias uncertainty. Droplet flame images represent a 3-D reaction zone in a 2-D manner, which misrepresents flame curvature. Well documented deconvolution methods, such as the Abel transform [140], can transform an axisymmetric image of a 3-D field into an

image representing a 2-D plane view. For example, an Abel transformed image of an unforced droplet flame is shown in Figure 2.11. Adversely, acoustically forced flames are non-axisymmetric, leaving the vast majority of images analyzed in this study subject to line-of-sight error. When defining the flame as the point of peak OH* chemiluminescence, as described in section 2.4.3, the measured flame standoff distance is less than the actual distance. Correction requires a value for flame curvature perpendicular to the image plane, which is unknown and unequal to the known flame curvature within the image plane for acoustically forced flames.

2.1: Experimental and Theoretical Resonant Frequencies

Speaker-Speaker				Speaker-Reflector			
$\Delta\phi = 0^o$ (PAN)		$\Delta\phi = 180^o$ (PN)		PN		PAN	
f_{exp} [Hz]	f_{th} [Hz]	f_{exp} [Hz]	f_{th} [Hz]	f_{exp} [Hz]	f_{th} [Hz]	f_{exp} [Hz]	f_{th} [Hz]
154		332	281.2	562	527.9	308	263.9
558	562.5	898	843.7	1108	1055.7	796	791.8
1132	1125.0	1500	1406.2		1583.6	1370	1319.7

2.2: Fuel Properties (alcohol fuels [64]; hydrocarbon fuels [141])

Fuel	Chemical Formula	Specific Heat Capacity c_p [kJ/kg·K]	Thermal Conductivity k [W/m·K]	Heat of Vaporization h_{fg} [kJ/kg]	Lower Heating Value LHV [kJ/kg]
Ethanol	C_2H_5OH	2.815	0.0533	841	26952
Methanol	CH_3OH	2.531	0.0616	1104	19930
Pure FT	$C_{12}H_{25}$	2.793	0.00935	339	44136
JP-8/FT	$C_{11}H_{22}$	2.01	0.0134	297	43745

A-243

2.3: Camera Specifications

Maximum Frame Rate	8 Hz
Dynamic Range	4096
Active Image Area	1280 x 1024 pixels
Pixel Size	6.7 μm x 6.7 μm
Field of View	9.3 mm x 7.4 mm
Pixel View	7.3 μm x 7.3 μm
Depth of Field	2 mm
CCD Readout Noise	< 2 counts (RMS)

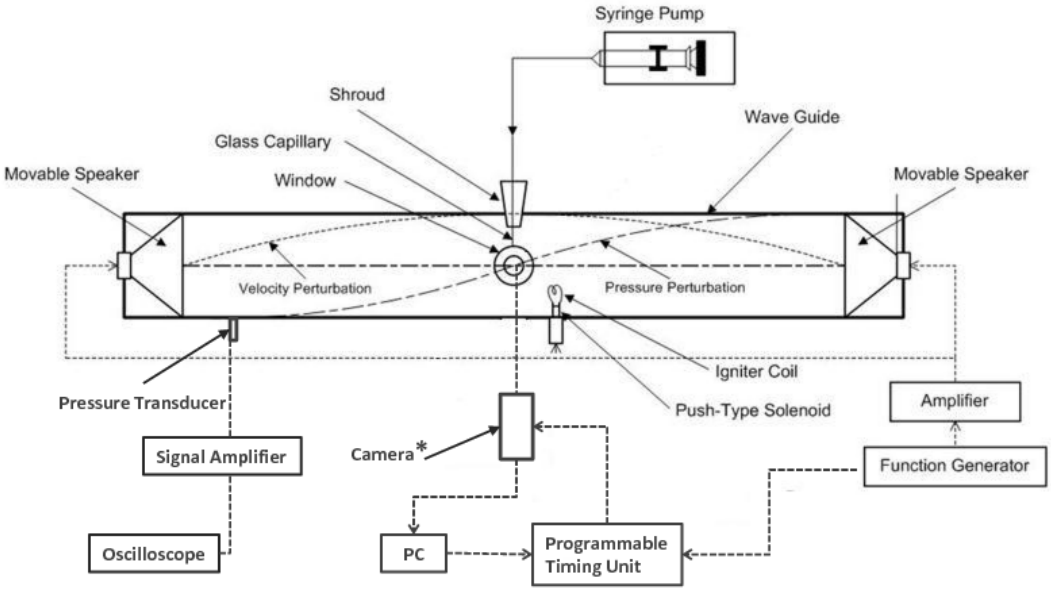

2.1: Experimental setup of the acoustic waveguide and feed droplet system.

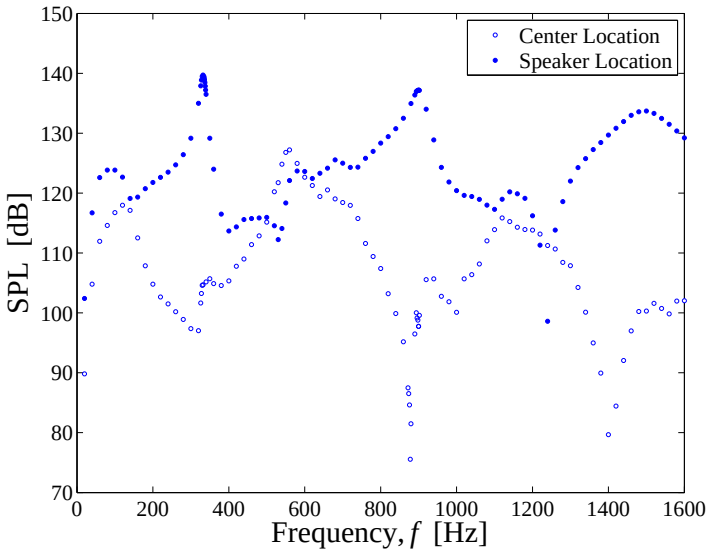

2.2: Frequency sweep for the speaker-speaker configuration with speakers operated 180^o out-of-phase and a PN occurring at the center of the waveguide. The distance between speakers is approximately 61 cm. Resonant frequencies are shown to occur near 332 Hz, 898 Hz, and 1500 Hz.

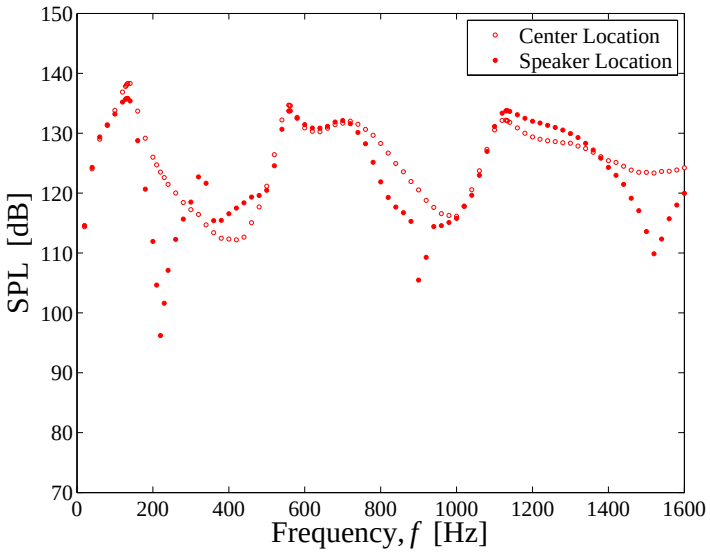

2.3: Frequency sweep for the speaker-speaker configuration with speakers operated in-phase (0^o) and a PAN occurring at the center of the waveguide. The distance between speakers is approximately 61 cm. Resonant frequencies are shown to occur near 134 Hz, 558 Hz, and 1132 Hz.

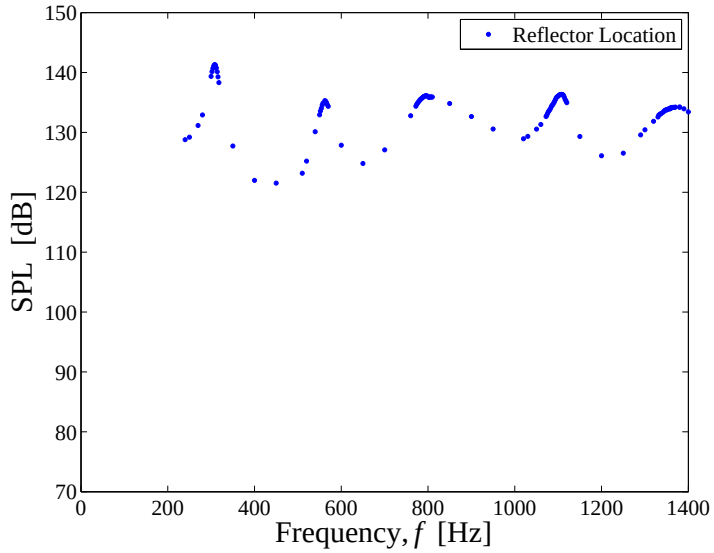

2.4: Frequency sweep for the speaker-reflector configuration. The distance between speaker and reflector is approximately 65 cm. Resonant frequencies are shown to occur near 562 Hz and 1108 Hz for a PAN occurring the waveguide center and 308 Hz, 796 Hz, and 1370 Hz for a PN occurring at the waveguide center.

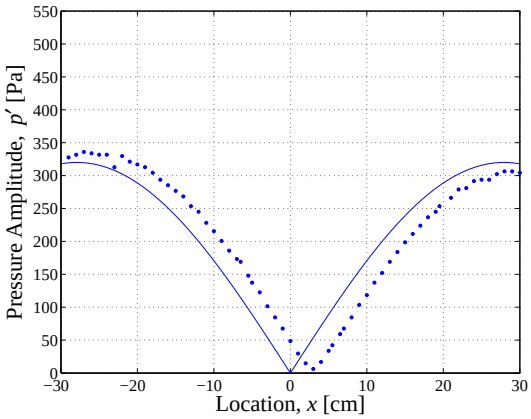

(a) 308 Hz PN (200 mV input)

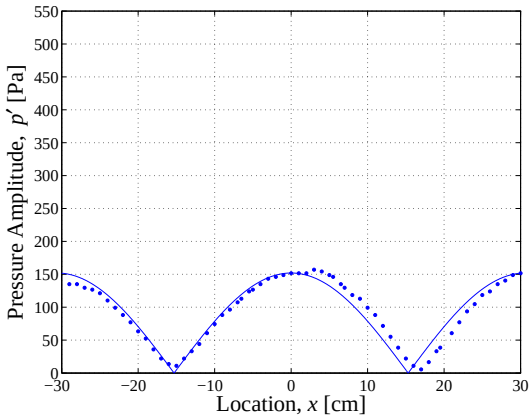

(b) 562 Hz PAN (200 mV input)

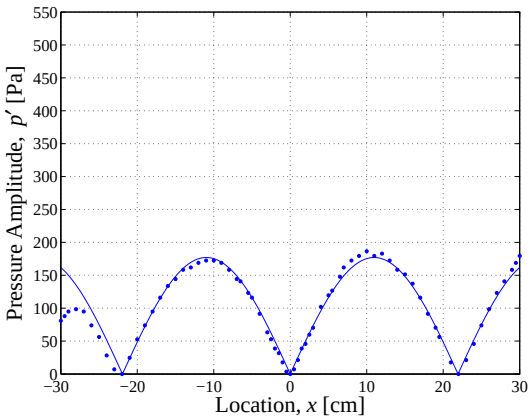

(c) 784 Hz approximate PAN (400 mV input)

2.5: Acoustic pressure amplitude measurements for the speaker-reflector configuration. The distance between speaker and reflector is approximately 65 cm, and the reflector is located at the positive end of the waveguide.

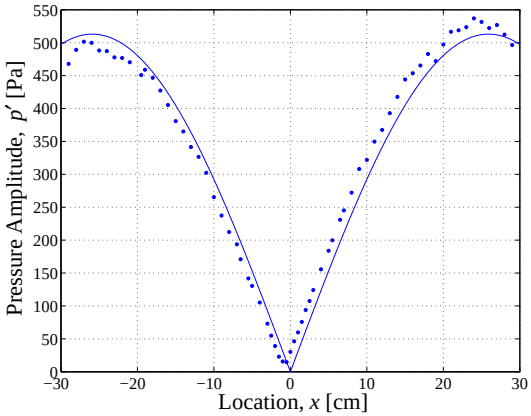

(a) 332 Hz PN

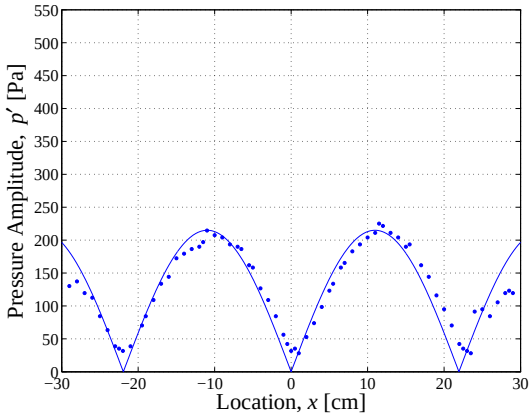

(b) 784 Hz

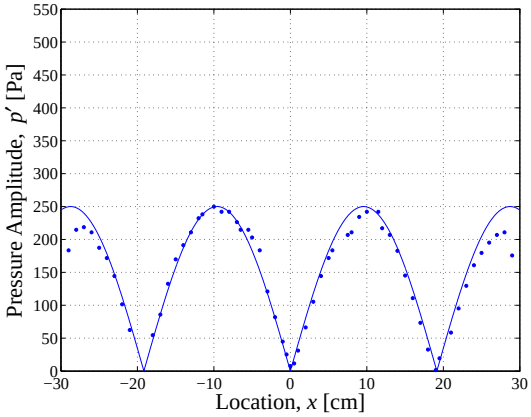

(c) 898 Hz PN

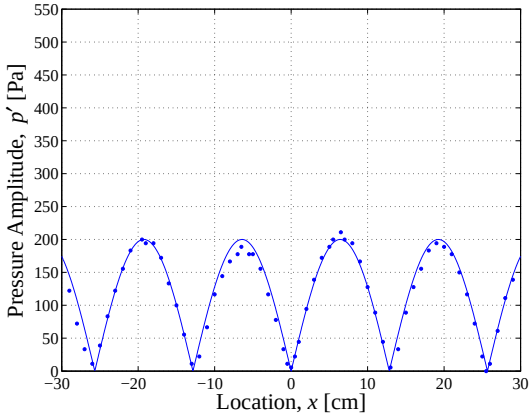

(d) 1340 Hz

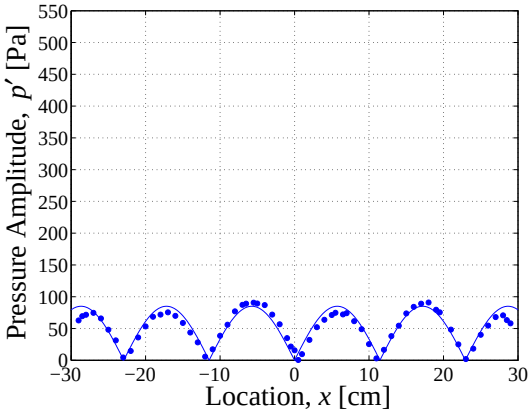

(e) 1500 Hz PN

2.6: Acoustic pressure amplitude measurements for the speaker-speaker configuration ($\phi = 180^o$). The distance between the speakers is approximately 61 cm. (200 mV speaker input)

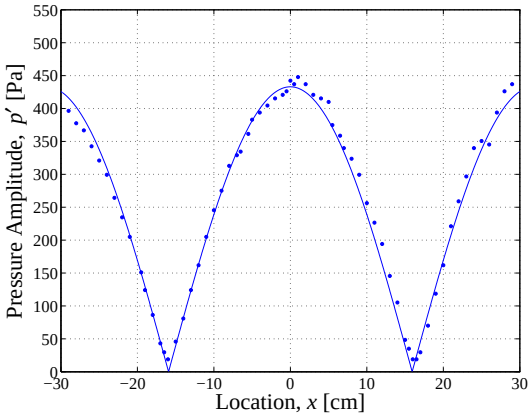

(a) 540 Hz PN

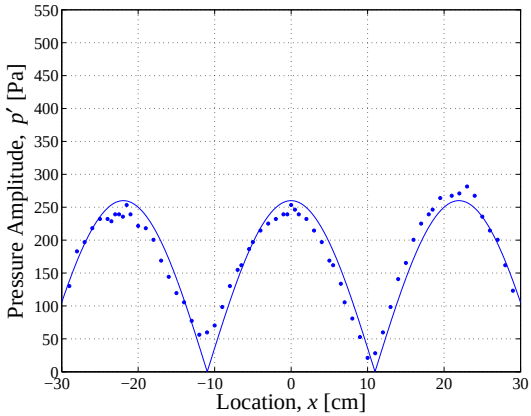

(b) 784 Hz

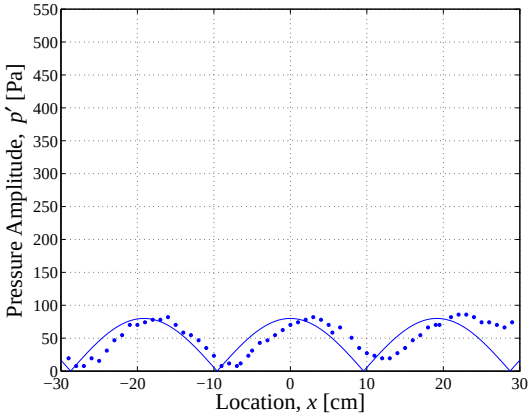

(c) 898 Hz PN

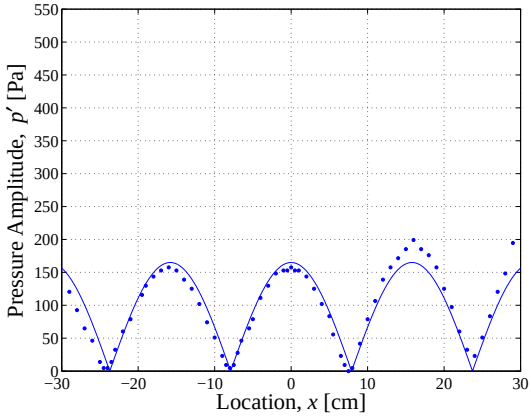

(d) 1088 Hz

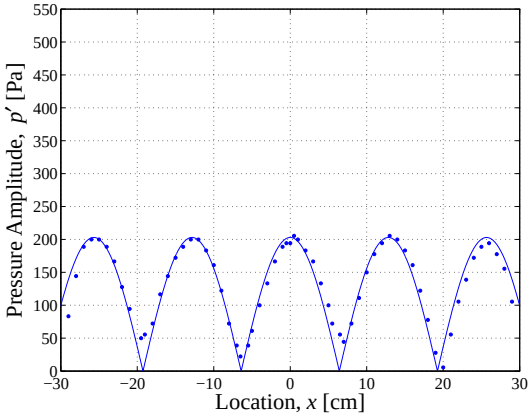

(e) 1340 Hz PN

2.7: Acoustic pressure amplitude measurements for the speaker-speaker configuration ($\phi = 0^o$). The distance between the speakers is approximately 61 cm. (200 mV speaker input)

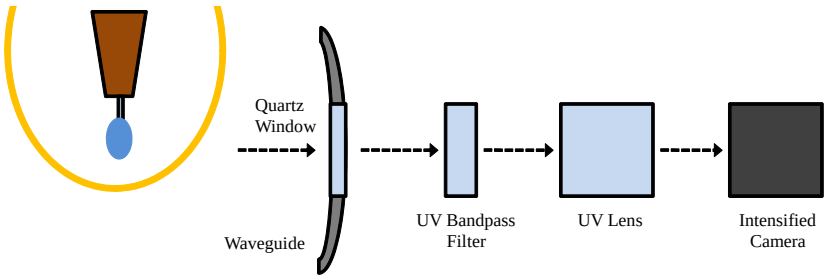

2.8: OH* chemiluminescence optics showing the path of light transmission from the flame source to the photocathode of the intensified camera.

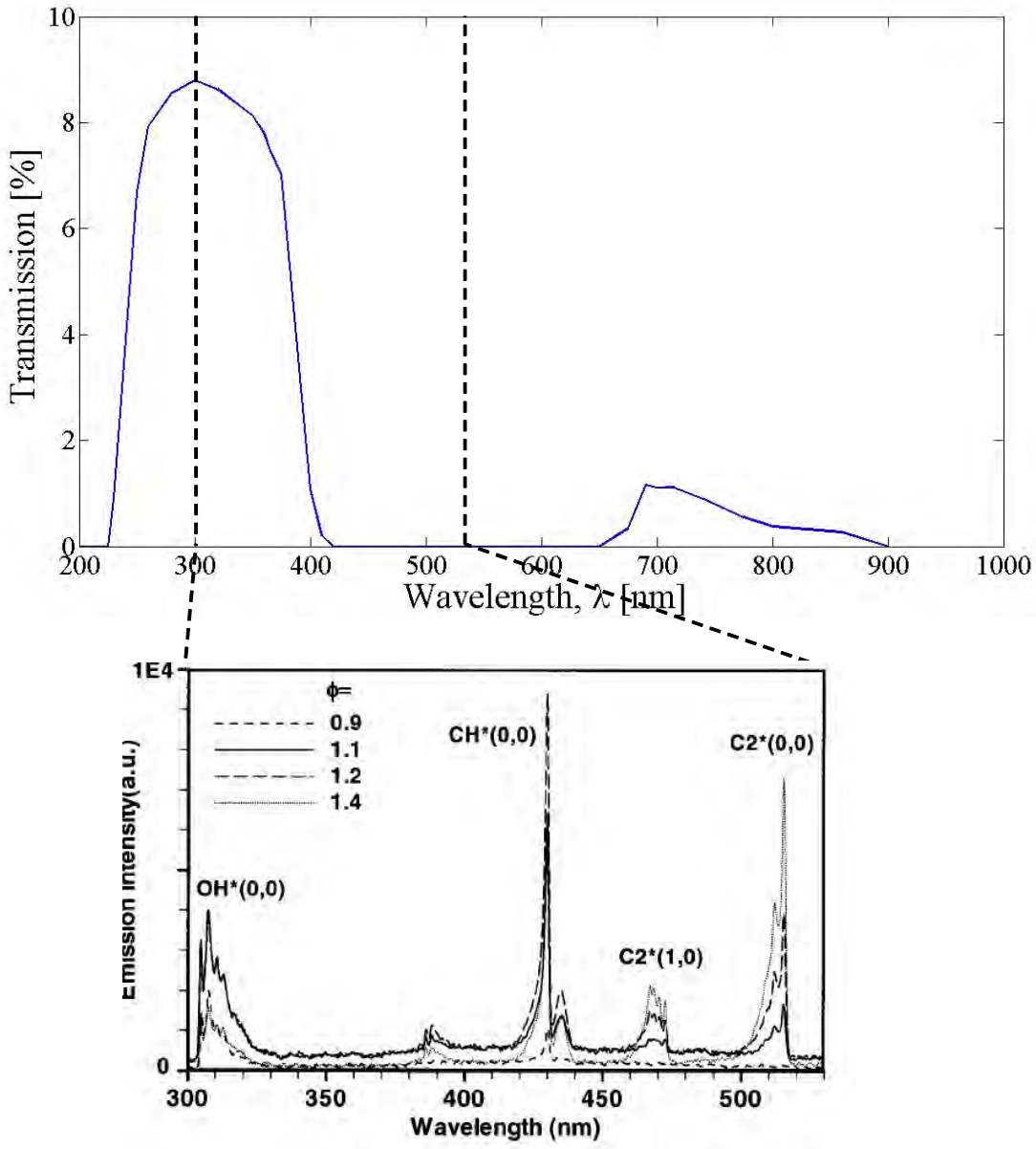

2.9: To confirm the isolation of OH* chemiluminescence, total light transmission was calculated for the complete optical arrangement. A comparison with experimentally measured excitation wavelengths of methane combustion from Kojima *et al.* [138] affirms the current bandpass range.

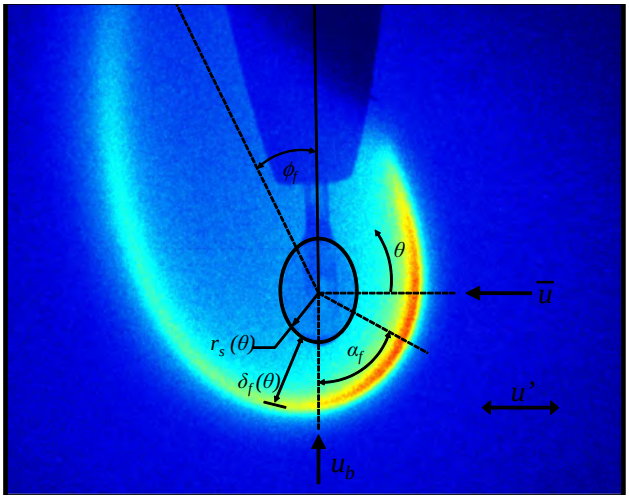

2.10: OH* chemiluminescence image for ethanol under acoustic forcing. The droplet radius r_s and flame radius r_f are dependent on the angle θ defined in a cylindrical coordinate system with an origin at the center of the droplet. Maximum chemiluminescence intensity occurs near the stagnation point, which is located at an angle α_f from the negative y-axis.

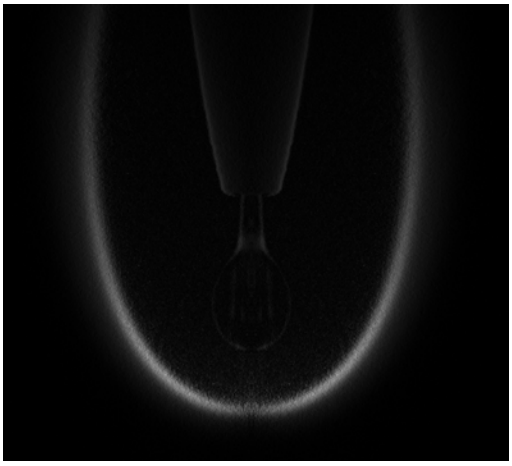

2.11: An ethanol flame in the absence of acoustic forcing is imaged by capturing light emitted from three-dimensional space, which can then be deconvoluted using the Abel transform [140] to create the image above, representing a two-dimensional slice of the axisymmetric flame.

CHAPTER 3

Results - Acoustically Coupled Fuel Droplet Combustion

3.1 Burning Rate Constant

Concerning the burning rate constant K, the primary interests are in the difference in K between unforced and acoustically forced conditions and the effect of various acoustic flow conditions on K. This portion of the study first presents baseline (unforced) burning rate constant measurements and comparisons with established values, then presents measurements for acoustically forced cases.

3.1.1 Baseline Burning Rate Constant

A sample image of chemiluminescence for the unforced burning droplet is shown in Figure 3.1 for each of the four fuels of interest. Gravitational forces give the fuel droplet an oblong shape and produce an elongated flame shape due to natural convection. Although not shown by UV chemiluminescence images, the alcohol and hydrocarbon fuels vary greatly in visible color. The alcohols, due to oxygenated chemical compounds, emit radiative energy mostly in lower wavelengths and appear blue. The hydrocarbons, on the other hand, appear bright yellow due to chemiluminescence in longer wavelengths dominated by electronically excited CH and C_2 radicals.

Baseline burning rate constants for all four fuels used in this study were measured

and compared with other available data, as shown in Table 3.1. Although not quantitatively discussed here, K decreased over long periods of time due to increasing product concentrations surrounding the reaction zone. A reduction in reaction rate can be expected for regions with concentrations saturated by hot products and thus a reduction in oxidizer mass fraction, and this process is especially significant for unforced conditions. For the acoustically excited case, forced convection prevents a large build up of products surrounding the flame and burning rate constants have negligible long term reductions within the time spans used here. To prevent adverse influence by this phenomenon, burning rate constants for unforced conditions were determined using only the first 30 seconds after ignition.

3.1.2 Effect of Acoustics on Burning Rate Constant

Burning droplets were placed at various locations relative to a PN within a standing wave, which allows one to investigate the difference between the forced and unforced K values as well as the changes which occur for different forced conditions. As discussed earlier, applying acoustic perturbations to the field surrounding the droplet will increase the burning rate constant [20–22, 72, 75, 82], but the following results aim to further quantify the increase occurring for various locations relative to the PN as done only by recent studies at UCLA [75, 82].

For acoustic frequencies of 332 Hz, 898 Hz, and 1500 Hz, PNs were located at the center of the waveguide by speakers 180^o out-of-phase. All results presented within this chapter were produced from these three frequencies, but nearly two hundred different acoustic flow conditions were tested by positioning the droplet in different locations within these three waveforms (see Figure 2.6a,c,e). Figures 3.2-3.13 present K values measured at these different locations, along with acoustic acceleration values, as discussed below.

The complete set of acoustically excited K measurements show values greater than or equal to baseline measurements. More specifically, positioning a droplet near the PN consistently produces burning rate constants higher than baseline values, while moving towards the PAN ($x \approx \pm\lambda/4$) produces burning rate constants closer to baseline values. These trends are manifested by three different frequencies and four different fuels, with a select few conditions producing burning rate constants as high as 20% greater than the baseline value near the PN. The higher frequency results show K values extending to PANs in both the positive and negative directions, which are precisely the locations where burning droplets consistently behave similar the unforced burning droplet. Much like previous works have shown, there is no appreciable difference in K at these locations [70, 71, 75, 82]. The increase in K towards the PN though, is believed to occur due to decreased flame standoff distance, causing steeper temperature gradients near the droplet surface and thus greater fuel evaporation rates. These topics are discussed in more detail with flame behavior results.

3.2 Flame Behavior

The imaging system provides the ability to measure flame behavior in multiple ways, ranging from deflection of the flame's plume to chemiluminescence intensity in the reaction zone. Using phase-locked imaging techniques described earlier, acoustic forcing is shown to alter the flame both in a constant manner and a time-dependent manner. In fact, examining flame front location with respect to acoustic phase reveals flame oscillation frequencies equal to the acoustic frequency f_a. These observations and others are illustrated in the following sections, including an interpretation of flame behaviors in terms of the acoustic radiation force.

3.2.1 Flame Deflection and Acoustic Acceleration

The most prevalent flame alteration induced by acoustic forcing is the deflection of the flame to one side. Deflection occurs primarily in the plume of the flame, and examples of this behavior are shown for ethanol in Figure 3.14. The observed deflections are independent of the micro-scale changes in time within each acoustic cycle. Instead, any infrequent changes in flame deflection occur throughout long periods, ~ 1 s. Recent experimental work at UCLA quantifies flame deflection to evaluate an acoustic radiation force theory [20] which has previously been validated qualitatively [21, 75, 82]. Further quantitative comparisons are presented here using the flame deflection measurement techniques of Teshome *et al.* [142].

For a standing wave, the acoustic radiation force equation can be expressed per the analysis of Tanabe *et al.* [20]:

$$F_R = (\rho_p - \rho_o)V[\pm 4\alpha(\frac{I}{z_a})(\frac{2\pi f_a}{c})\sin(\frac{2\pi x}{\lambda})\cos(\frac{2\pi x}{\lambda})] \tag{3.1}$$

Here I represents the acoustic intensity, which depends on the maximum sound pressure level (SPL) inside the waveguide, $z_a = \rho c$ is the acoustic impedance, and c represents the speed of sound. The term in square brackets represents an equivalent acoustic acceleration term, $g_a = \alpha\frac{\partial\overline{u'^2}}{\partial x}$, for a condition where a standing wave is present in the waveguide. The coefficient α defined in eqn. 1.8 is approximated as one in subsequent analyses. Concerning the plus-minus sign in eqn. 3.1, the minus sign corresponds to the case where a PN or VAN was positioned at the center of the waveguide, $x = 0$, whereas the plus sign corresponds to a PAN or VN at that location. Thus, the minus sign is used to calculate theoretical acoustic acceleration $g_{a,th}$ for the waveguide and flow conditions in this study. Inspecting eqn. 3.1, one observes that a burning droplet located to the left ($x < 0$) or right ($x > 0$) of the PN will experience a finite acoustic radiation force F_R due to a nonzero acoustic acceleration g_a. Then, Tanabe *et al.* concludes that the physical consequence of this force on a burning droplet would be flame deflection/deformation in

the opposite direction of F_R, assuming that the hot products with density ρ_p occupy a volume V and are separated from the surrounding gas with density ρ_o.

Noting the analogy between thermal buoyancy and the acoustic radiation force formulated above, Teshome *et al.* [142] utilize well known flame behaviors when buoyant from gravitational acceleration g_o in order to experimentally determine acoustic acceleration g_a. The two accelerations are interpreted as similar in effect, whereas gravitational acceleration is vertically orientated and acoustic acceleration is horizontal (i.e. in the direction of sound propagation). Using the definition of flame deflection angle shown in Figure 2.10, an experimental acoustic acceleration can be calculated as $g_{a,exp} = g_o \tan(\phi_f)$. The flame deflection angle ϕ_f is measured between the vertical axis and the semi-major axis of an ellipse which is fit to the elongated flame shape. In this way, $\phi_f = 45^o$ corresponds to an experimental acoustic acceleration equal to gravitational acceleration, while ϕ_f tending towards 90^o corresponds to an infinitely large experimental acoustic acceleration.

Figures 3.2-3.13 compare theoretical and experimental g_a values, including the absolute value of each ($|g_{a,exp}|$ and $|g_{a,th}|$) juxtaposed with burning rate constants for illustration. Both experimental and theoretical values exhibit a switch in sign near the PN, where experimental images reveal a distinct switch in deflection from leftward orientation for $x < 0$ and rightward orientation for $x > 0$ as shown in Figure 3.14. In this regard, the acoustic radiation force theory consistently agrees with experiments across a wide range of flow conditions and fuel types. These results confirm that acoustically forced flames will deflect away from the nearest PN, or towards a PAN. But, although theoretical values predict a maximum absolute acceleration at $x = \pm\lambda/8$, centered between a PN and PAN, $|g_{a,exp}|$ values reveal maximums closer to the PN. In fact, maximum flame deflections often occur immediately adjacent to the PN, engendering acoustic acceleration values which exceed 9.8 m/s^2 and are much larger than maxima estimated by

Tanabe's theory. If acoustic and gravitational acceleration constants are indeed similar mechanisms for deforming a volume of low density products, then $g_a > 9.8$ m/s^2 would presumably produce acoustic radiation forces which are greater than buoyancy forces. Tanabe *et al.* [21, 73] cite this relationship when producing droplet flames in a vertically oriented waveguide such that the acoustic radiation force and buoyancy force oppose one another, causing the flame to form a sphere-like shape similar to burning droplets in micro-gravity. This effective "cancellation" of gravity has not been reproduced by other experimentalists though, including several attempts by droplet combustion experiments at UCLA.

There are particular flow conditions though, where the location of flame switch does not coincide with a PN. Specifically for the lowest acoustic frequency, $f_a = 332$ Hz, flame switch occurs somewhat far from the PN. For all fuels tested in this study, this lower forcing frequency provides a less distinct flame switch and concurrently, the observed deflections are generally larger when oriented in the negative direction (i.e. leftward). Pressure distributions in Figure 3.2 show a waveform which is slightly asymmetric with a PN favoring the left side of the waveguide, which may contribute to the asymmetries evidenced by burning droplets. The same pressure distribution also shows maximum pressure perturbations which are nearly 10% larger on the waveguide's positive side. Therefore, acoustic pressure asymmetries combined with a lack of acoustic velocity measurements warrant further investigation to verify the absence of traveling waves, and in addition, determine the true waveform characteristic which causes flame switch. One should also note that all acoustic pressure fluctuations were measured at room temperature without combustion, but the temperature and species distribution alterations caused by a burning droplet may not be negligible.

3.2.2 Standoff Distance

3.2.2.1 Standoff Distance Oscillation

Using the phase-locked imaging techniques discussed in Section 2.3, the flame front position can be investigated as a function of acoustic phase. The resulting behavior is best understood by first viewing Figure 3.15, which shows a pair of flame images acquired at two different points within an acoustic cycle. Acoustic excitation manifests a difference in flame position between such a pair of images, and moreover, the flame position is found to oscillate at a frequency equal to the acoustic frequency f_a. In fact, the entire flame appears to maintain a constant global shape while moving horizontally in a sine-like manner, changing position relative to the droplet. Again, the acoustic waveforms used here are assumed to be one-dimensional, which is supported by a lack of vertical flame movement within microscale changes in time.

The flame standoff distance δ_f, defined in Figure 2.10, is dependent on the coordinate angle θ. As a result of the one-dimensional oscillation of the flame, the maximum standoff distance oscillation amplitude δ'_f occurs near $\theta = 0^o$ or $\theta = 180^o$. For example, Figure 3.15 shows a case where $\delta'_{f,max} = \delta'_f(\theta = 0^o)$. Note that the flame's wake region is not examined when investigating standoff distance. Rather, the hemisphere centered around the flame's stagnation point is of paramount interest because it is believed that maximum temperatures and mass burning rates occur in this hemisphere [61]. Then, focusing on the upstream side of the droplet, Figure 3.16 shows $\delta_f(\theta = 0^o)$ versus ϕ_p for each fuel and acoustic frequency at a select few locations within the waveguide. Four acoustic periods worth of phase-locked images show four distinct oscillation cycles for δ_f. The oscillation amplitude δ'_f varies with respect to position within the waveguide though, with effectively zero oscillation for droplets near a PAN (VN). Near a PN (VAN) on the other hand, high amplitudes are observed due to greater velocity perturbations. A greater velocity amplitude u' causes large changes in the total velocity $u = \overline{u} + u'$,

and thus greater changes in mass diffusion rates of air. Physically, these perturbations of oxidizer mass fraction within the reaction zone cause the fuel-air equivalence ratio to change, and the heart of the reaction zone, or flame, must move in order to maintain the prescribed mixture composition for peak reaction rates.

However, the chemical kinetics processes exhibit their own frequency response. Lower acoustic frequencies permit longer periods before flow is reversed at the minimum or maximum of u', and as a result, these lower frequencies (e.g. Figure 3.16a for $f_a = 332$ Hz) allow for greater values of δ'_f. Meanwhile, higher frequencies (e.g. Figure 3.16c for $f_a = 1500$ Hz) with a similar value of u' will prohibit large values of δ'_f due to shorter diffusion time scales relative to the kinetics time scale. Figure 3.17 demonstrates this relationship in a comprehensive manner in a plot of δ'_f versus waveguide location x. This broader perspective reveals a direct relationship between the acoustic period $T_a (= \frac{1}{f_a})$ and δ'_f for the acoustic intensities and frequencies used here, where a three-fold increase in T_a results in approximately the same relative increase in δ'_f. But, this relationship cannot hold for all frequencies. Also, amplitudes as high as 275 μm are observed for $f_a = 332$ Hz at a PN ($x = 0$), while amplitudes are approximately zero for droplets placed at a PAN ($x = \pm\lambda/4$). Thus, trends observed in δ'_f roughly coincide with the trends observed in the burning rate constant K, experimental acoustic acceleration $g_{a,exp}$, and the assumed trend in u', all of which exhibit maximum values at or near a PN. In contrast, there is not a correlation between flame oscillation amplitude and the theoretical acoustic acceleration $g_{a,th}$ of Tanabe *et al.* [20, 21, 73], which predicts a maximum effect mid-way between a PN and PAN, $x = \pm\lambda/8$.

3.2.2.2 Mean Standoff Distance

Acoustic radiation force theory [78, 79] descibes the time-averaged forces caused by acoustic fluctuations. Therefore, a more direct validation of the theory of Tanabe *et al.*

should inspect time-averaged flame behaviors rather than flame alterations occurring throughout microscale changes in time. The mean standoff distance $\overline{\delta_f}$ could offer a better correlation than the analysis above. If indeed the acoustic radiation force should act to displace or deform the droplet's surrounding flame as though it were a sphere of hot products, then the flame front will presumably shift towards the droplet surface on one side of the droplet and away from the droplet on the other side. This concept is partially captured in Section 3.2.1 by using flame deflection angle as a representation of the constant displacement generated by the combined forces of thermal buoyancy and the acoustic radiation force. Instead, a different flame angle can be produced by mean standoff distance measurements which focus on the time-averaged deformations occurring in the stagnation point region of the flame as opposed to the deflection angle of the flame's plume. The aforementioned technique, as well as other comparisons, will be discussed below in an effort to more confidently evaluate the theory of Tanabe *et al.*

First, consider Figure 2.10, where acoustic forcing has altered the location of the flame's stagnation point. The stagnation point is defined here as the location of minimum flame standoff distance and occurs at an angle α_f from the negative y-axis. Thus, $\alpha_f = 0^o$ for the unforced flame, which is governed only by natural convection represented by u_b in Figure 2.10. A second velocity component $\overline{u}$ is also shown, representing horizontal steady flow induced by the fluctuating component u'. In this discussion, the horizontal steady component $\overline{u}$ will be interpreted in two ways. First, this bulk flow can represent flow caused by an acoustic radiation force similar to buoyancy. In other words, high flame temperatures cause the surrounding gases to expand due to increasing temperature, then these low density gases are swept into the reaction zone at a velocity $\overline{u}$ by a buoyancy-like acoustic radiation force. The second interpretation considers $\overline{u}$ as an acoustic streaming velocity [80, 143, 144]. Acoustic streaming is not a result of temperature or density differences, but instead occurs throughout the entire waveguide as a result of wave attenuation near boundaries and dissipation in open space. Both interpretations call for

an increase in $\overline{u}$ as acoustic intensity increases, and therefore a decrease in $\overline{\delta_f}$ as more air diffuses into the reaction zone.

If the acoustic radiation force in eqn. (3.1) is indeed valid, then the minimum flame standoff distance $\overline{\delta_f}_{,min}$ will occur at $x = \pm\lambda/8$. Whether the flame front is displaced by a shift of the entire sphere of hot gases contained within the flame or by a rise in oxidizer diffusion rates via $\overline{u}$, $\overline{\delta_f}_{,min}$ will coincide with maximum $|g_{a,th}|$ if Tanabe *et al.*'s application of acoustic radiation force theory to flames is valid. The exact quantities one expects are obfuscated by gradual variations in temperature and density, but the qualitative expectations are clear. Figure 3.18 shows the relationship between $\overline{\delta_f}$ and waveguide location x when $\overline{\delta_f}$ is measured at either $\theta = 0^o$ or $\theta = 180^o$, depending on flame orientation. $\overline{\delta_f}_{,min}$ is shown to occur near the PN ($x = 0$), as opposed to the predicted value of $x = \pm\lambda/8$ from eqn. (3.1). As the droplet is positioned closer to the PAN, $\overline{\delta_f}_{,min}$ adopts the unforced value shown by dashed lines. This relationship disagrees with that of the prescribed theory, and this point is ameliorated by Figure 3.19. Figure 3.19 confirms a contradicting correlation between flame displacement and theoretical acoustic acceleration, where standoff distance increases with an increase in acoustic acceleration as calculated per the bracketed term in eqn. (3.1). It is thus clear that flame oscillations, which are not represented in the Tanabe theory, may in part be responsible for the discrepancy between theoretical and experimental values of acoustic acceleration.

For future work, a separate technique for comparing the effects of acoustic excitation to those of thermal buoyancy is proposed here. Utilizing the measured angle of minimum standoff distance α_f, a simple nondimensional velocity estimation is proposed

$$\frac{\overline{u}}{u_b} = \tan\alpha_f \tag{3.2}$$

where it is assumed that the steady flow velocity into the flame is equal to the combined magnitude of a vertical vector u_b and a horizontal vector $\overline{u}$. A preliminary plot of $\overline{\delta_f}$ ver-

sus the nondimensional velocity $\frac{\overline{u}}{u_b}$ can be found in Figure 3.20. Briefly, this comparison shows a relationship between standoff distance and convective velocity very similar to that predicted by the classical droplet combustion model with forced convection [61, 64]. In light of the shortcomings of the acoustic radiation force theory discussed above, this calculation is suggested for future analysis of this and similar burning droplet data with more focus allocated to predicting steady flow velocities such as $\overline{u}$, which could better explain the flow fields manipulating flame behavior.

3.1: Comparison of measured values of burning rate constant K for various fuel droplets in the absence of acoustic excitation.

Fuel	K, present (mm^2/s)	K, established (mm^2/s)
Ethanol	0.87-0.96	0.81-0.86 [60]
Methanol	0.94-1.04	0.85-1.2 [145, 146]
Pure FT	0.96-1.05	-
JP-8/FT	0.98-1.05	-

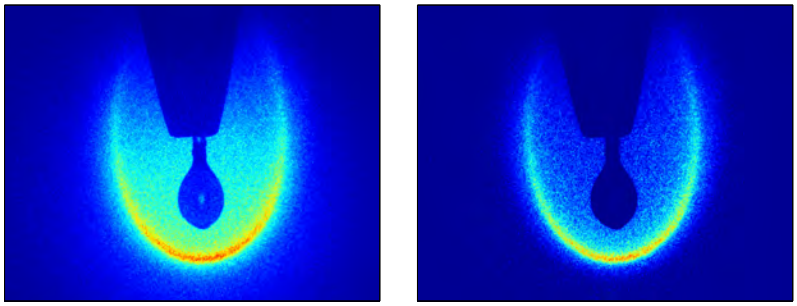

(a) Ethanol

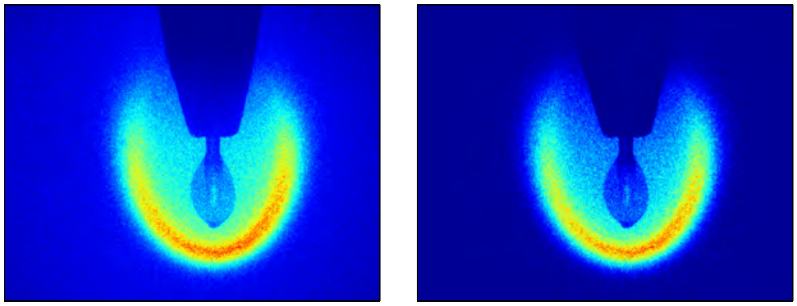

(b) Methanol

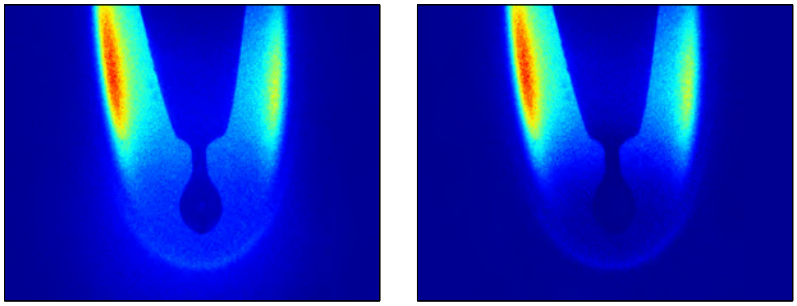

(c) Pure FT

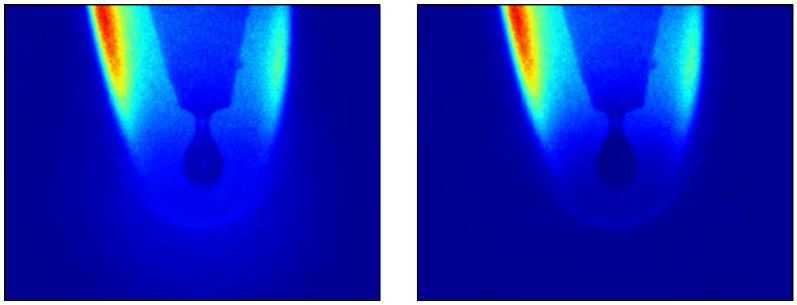

(d) JP-8/FT Blend

3.1: OH* chemiluminescence images of burning droplets in the absence of acoustic forcing. The left column shows an image as captured. The right column shows the same image after background light subtraction.

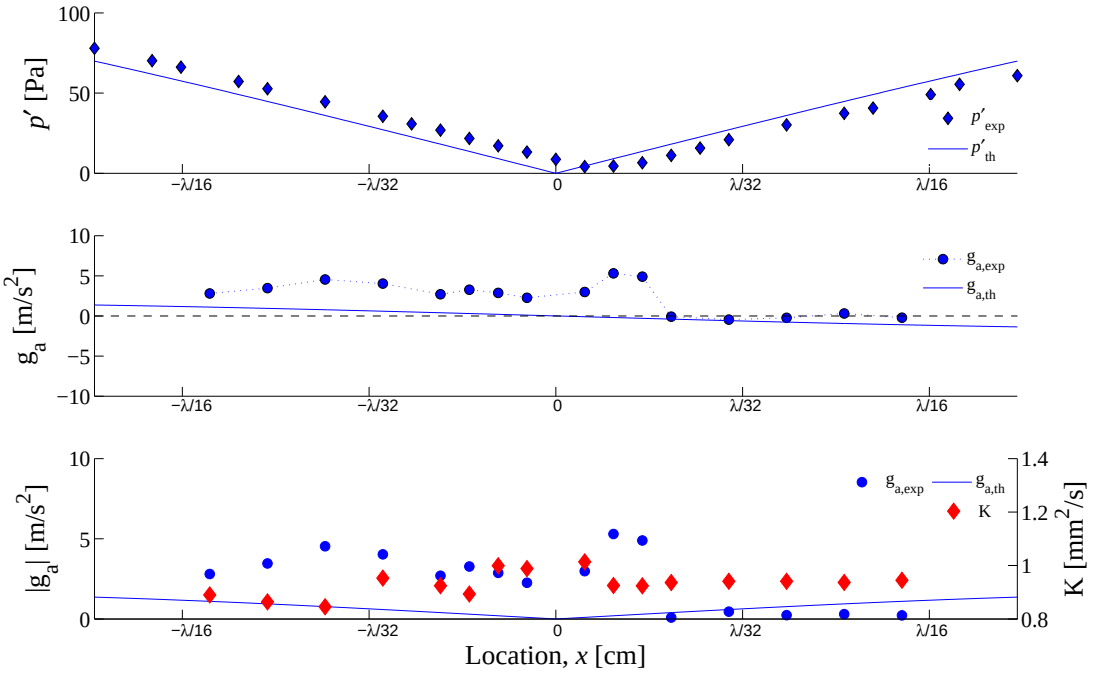

3.2: Pressure perturbations, estimated theoretical and actual acoustic accelerations g_a, and average burning rate constant K as a function of waveguide location for the ethanol droplet burning in the vicinity of a pressure node at a frequency of 332 Hz and $p'_{max} = 150$ Pa.

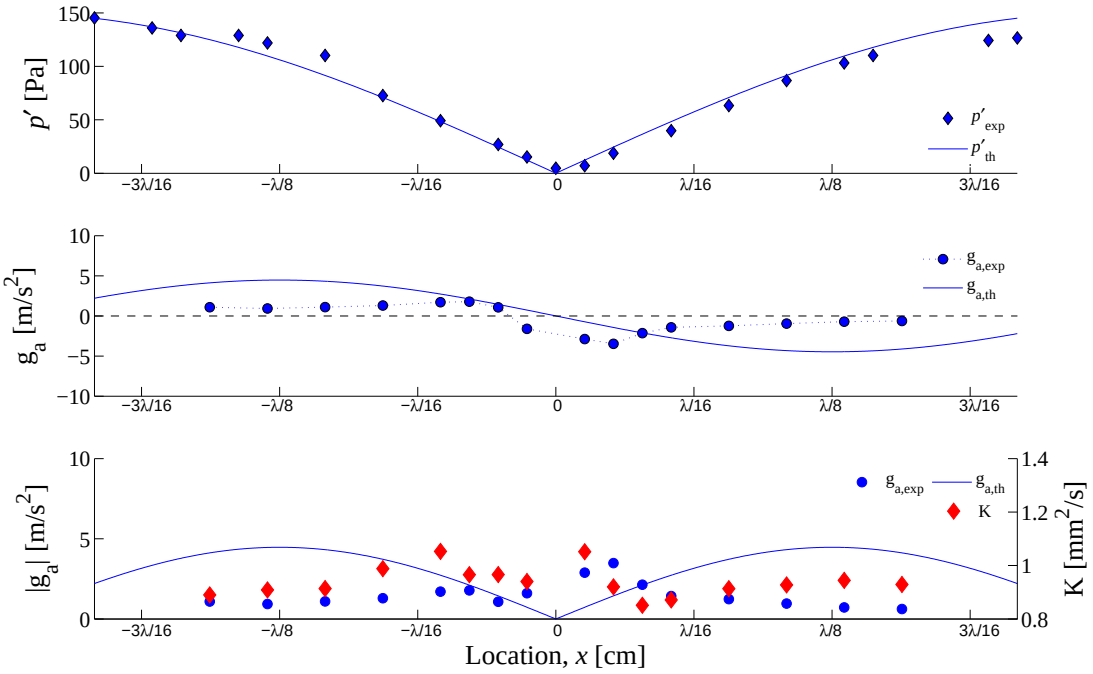

3.3: Pressure perturbations, estimated theoretical and actual acoustic accelerations g_a, and average burning rate constant K as a function of waveguide location for the ethanol droplet burning in the vicinity of a pressure node at a frequency of 898 Hz and $p'_{max} = 150$ Pa.

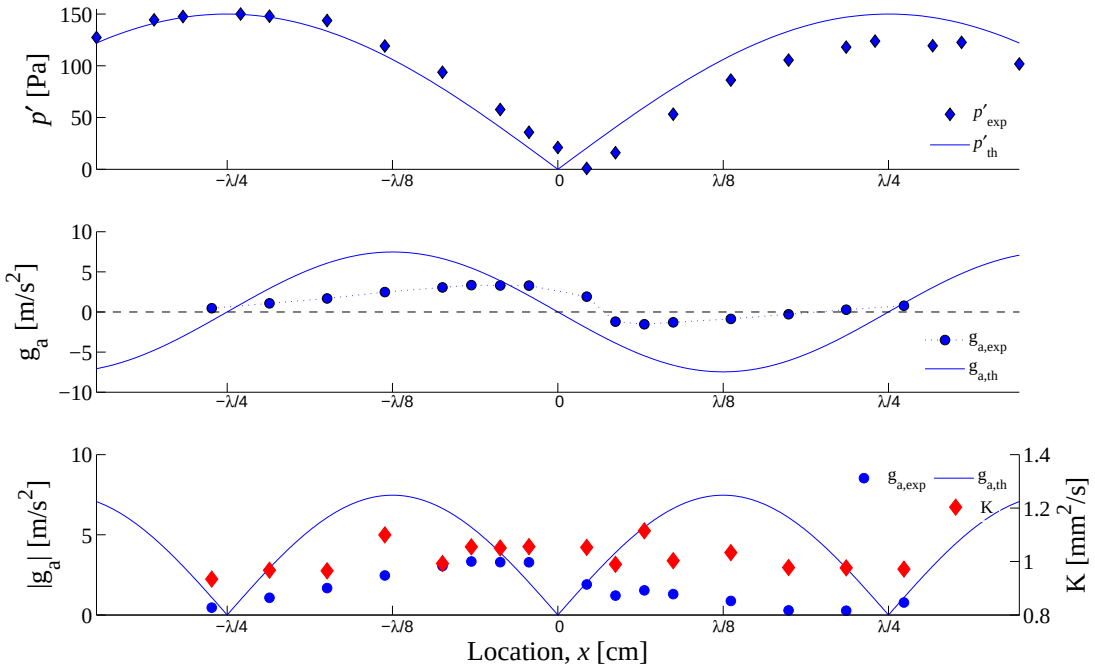

3.4: Pressure perturbations, estimated theoretical and actual acoustic accelerations g_a, and average burning rate constant K as a function of waveguide location for the ethanol droplet burning in the vicinity of a pressure node at a frequency of 1500 Hz and $p'_{max} = 150$ Pa.

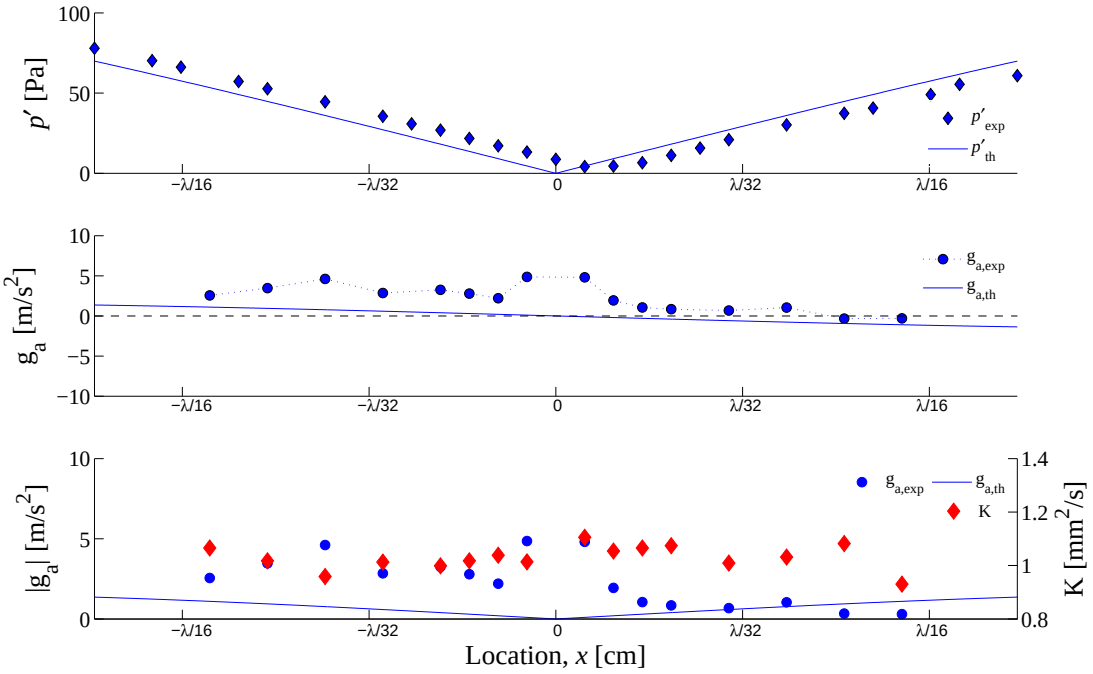

3.5: Pressure perturbations, estimated theoretical and actual acoustic accelerations g_a, and average burning rate constant K as a function of waveguide location for the methanol droplet burning in the vicinity of a pressure node at a frequency of 332 Hz and $p'_{max} = 150$ Pa.

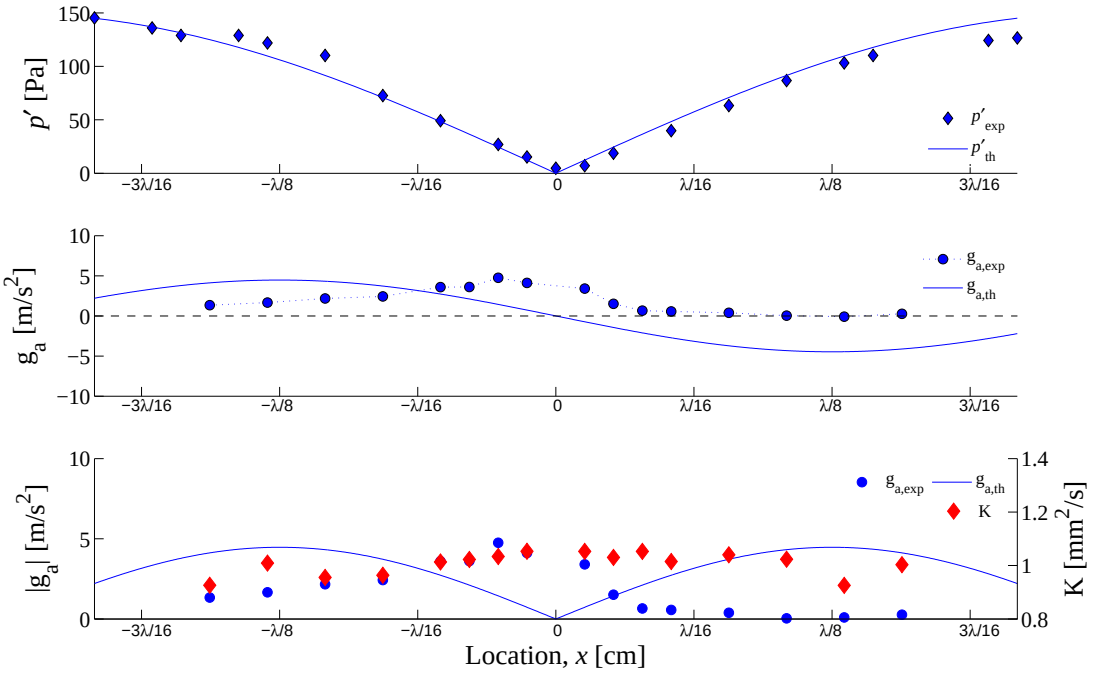

3.6: Pressure perturbations, estimated theoretical and actual acoustic accelerations g_a, and average burning rate constant K as a function of waveguide location for the methanol droplet burning in the vicinity of a pressure node at a frequency of 898 Hz and $p'_{max} = 150$ Pa.

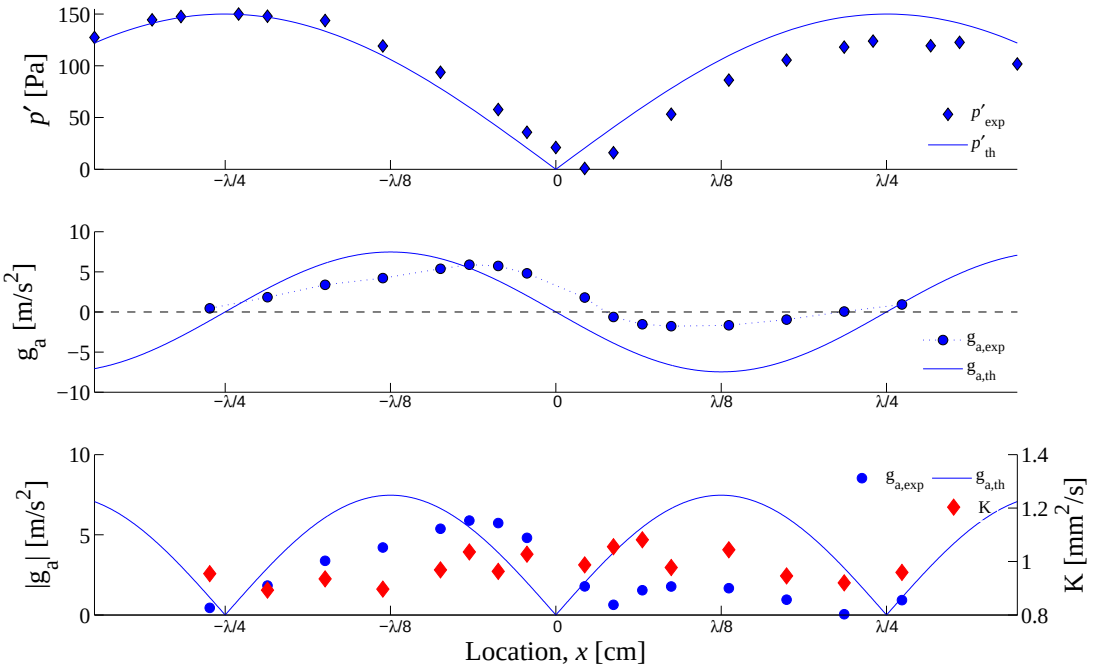

3.7: Pressure perturbations, estimated theoretical and actual acoustic accelerations g_a, and average burning rate constant K as a function of waveguide location for the methanol droplet burning in the vicinity of a pressure node at a frequency of 1500 Hz and $p'_{max} = 150$ Pa.

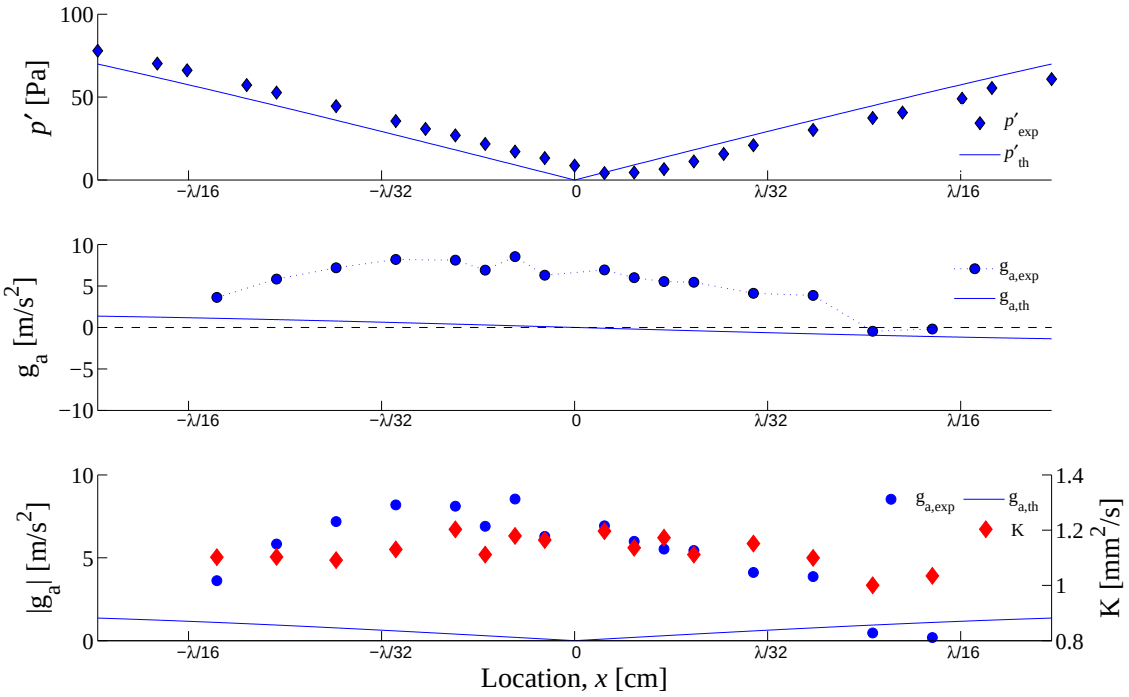

3.8: Pressure perturbations, estimated theoretical and actual acoustic accelerations g_a, and average burning rate constant K as a function of waveguide location for the FT droplet burning in the vicinity of a pressure node at a frequency of 332 Hz and $p'_{max} = 150$ Pa.

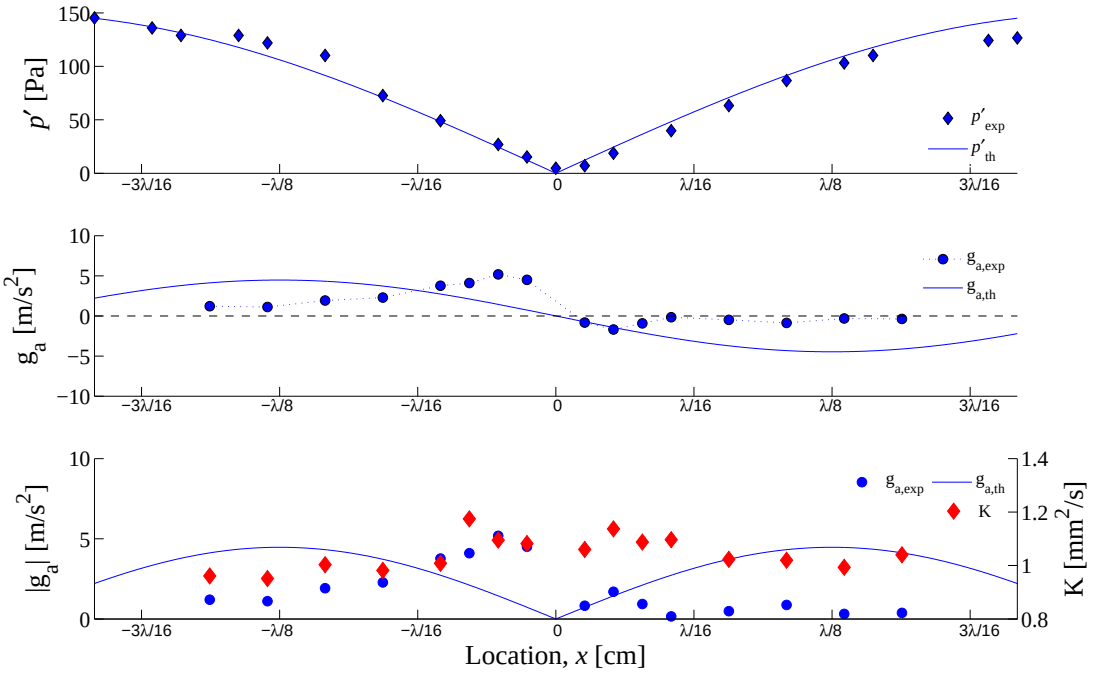

3.9: Pressure perturbations, estimated theoretical and actual acoustic accelerations g_a, and average burning rate constant K as a function of waveguide location for the FT droplet burning in the vicinity of a pressure node at a frequency of 898 Hz and $p'_{max} = 150$ Pa.

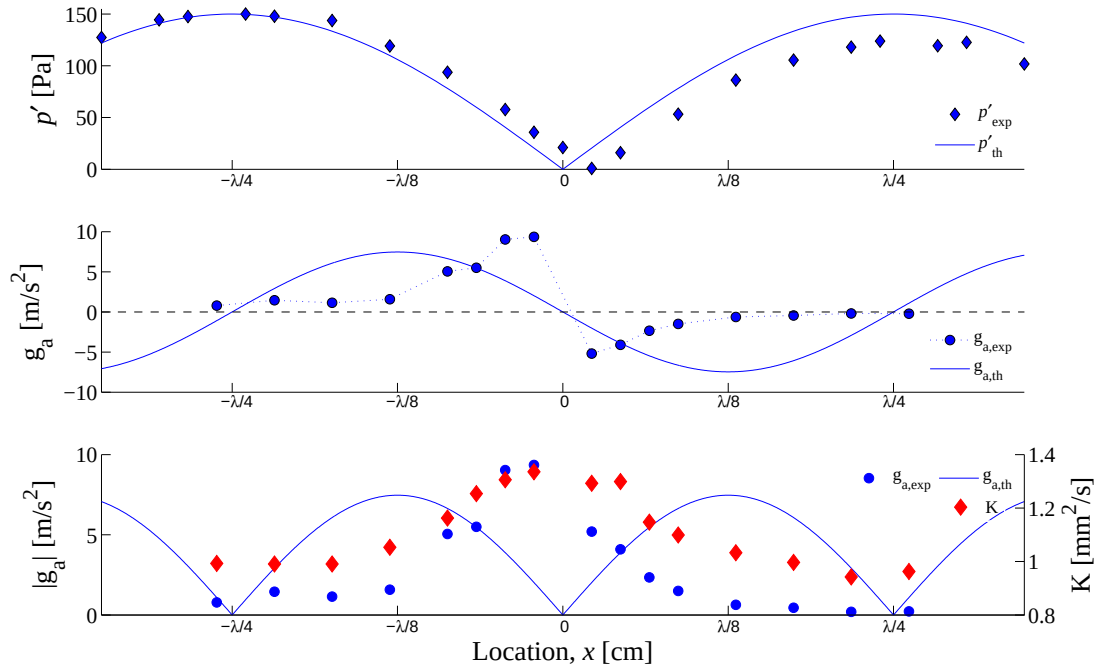

3.10: Pressure perturbations, estimated theoretical and actual acoustic accelerations g_a, and average burning rate constant K as a function of waveguide location for the FT droplet burning in the vicinity of a pressure node at a frequency of 1500 Hz and $p'_{max} = 150$ Pa.

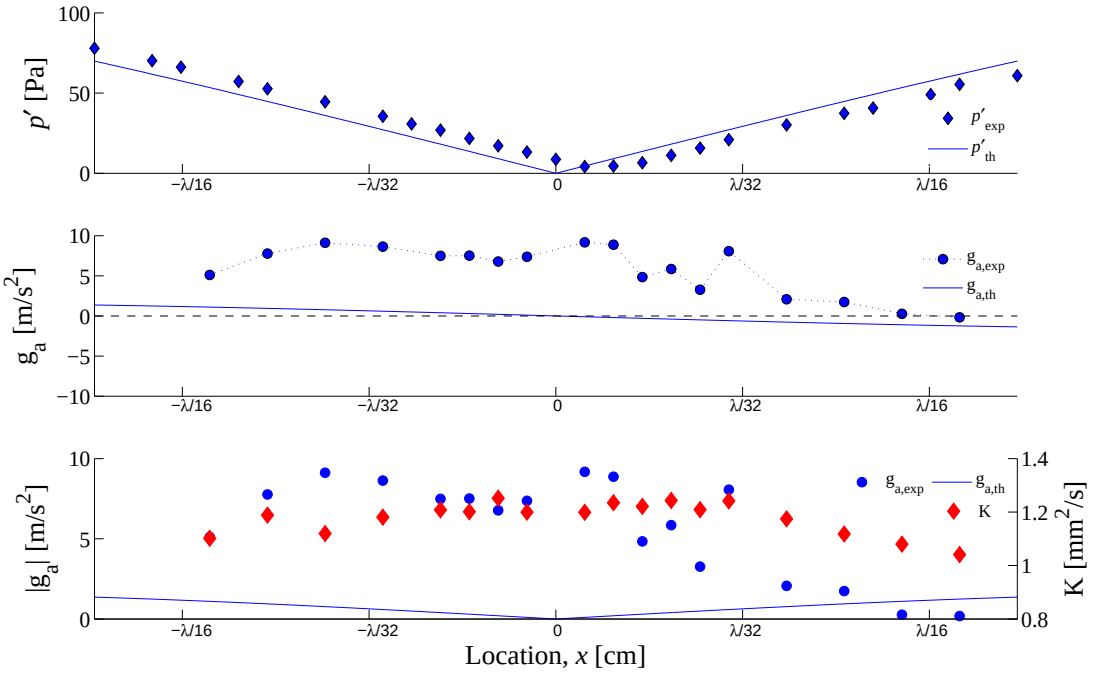

3.11: Pressure perturbations, estimated theoretical and actual acoustic accelerations g_a, and average burning rate constant K as a function of waveguide location for the JP8FT droplet burning in the vicinity of a pressure node at a frequency of 332 Hz and $p'_{max} = 150$ Pa.

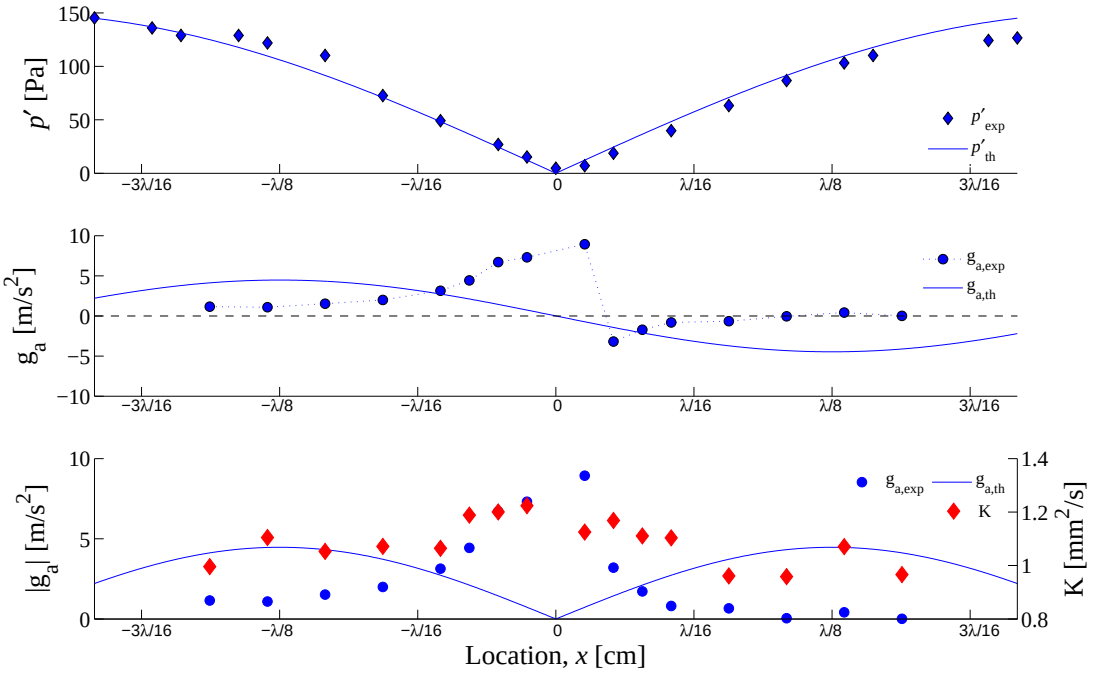

3.12: Pressure perturbations, estimated theoretical and actual acoustic accelerations g_a, and average burning rate constant K as a function of waveguide location for the JP8FT droplet burning in the vicinity of a pressure node at a frequency of 898 Hz and $p'_{max} = 150$ Pa.

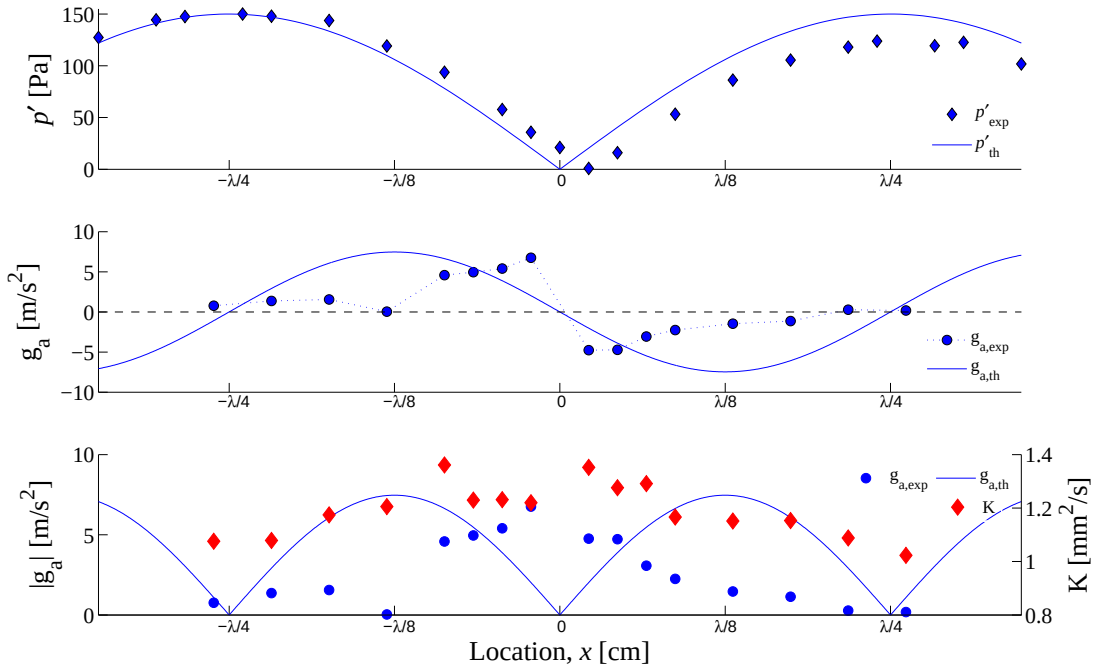

3.13: Pressure perturbations, estimated theoretical and actual acoustic accelerations g_a, and average burning rate constant K as a function of waveguide location for the JP8FT droplet burning in the vicinity of a pressure node at a frequency of 1500 Hz and $p'_{max} = 150$ Pa.

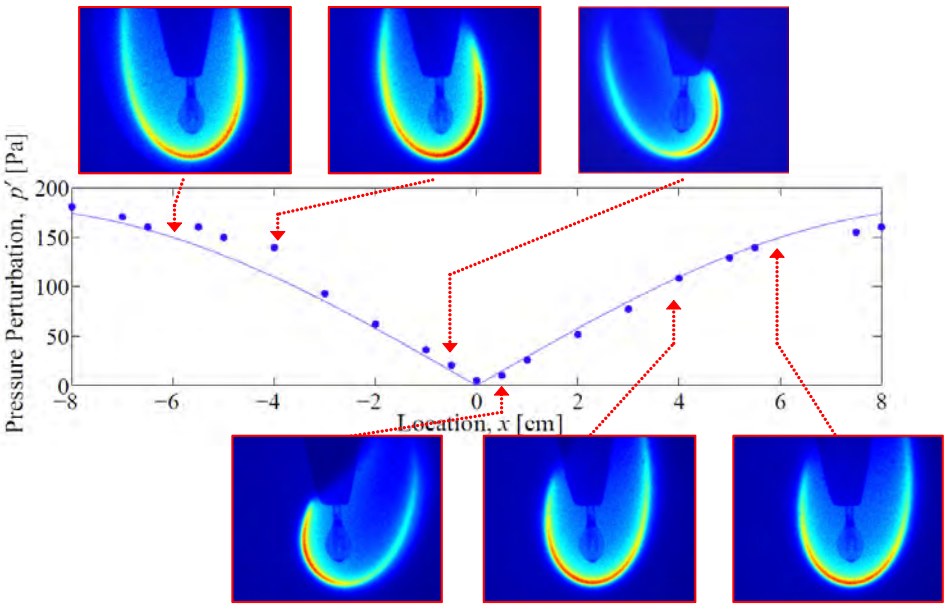

3.14: Ethanol flame images under the influence of acoustics. Flames are consistently deflected away from the pressure node (PN) with a flame "switch"' occurring near the PN.

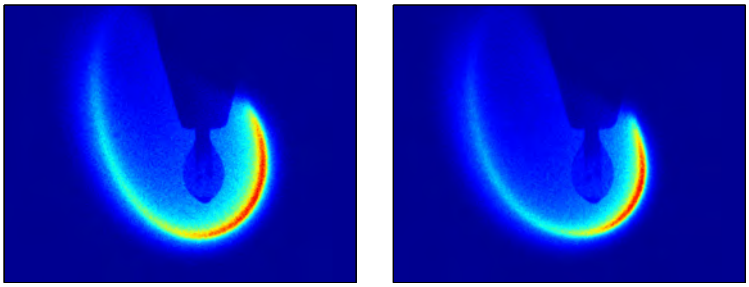

(a) (b)

3.15: A pair of ethanol flame images acquired at different points within the acoustic cycle. ((a) $\phi_p = 80^o$ (b) $\phi_p = 260^o$) Horizontal flame standoff distance δ_f oscillations cause the flame to exhibit a maximum δ_f in (a) and a minimum δ_f in (b) when viewing the right side of the flame.

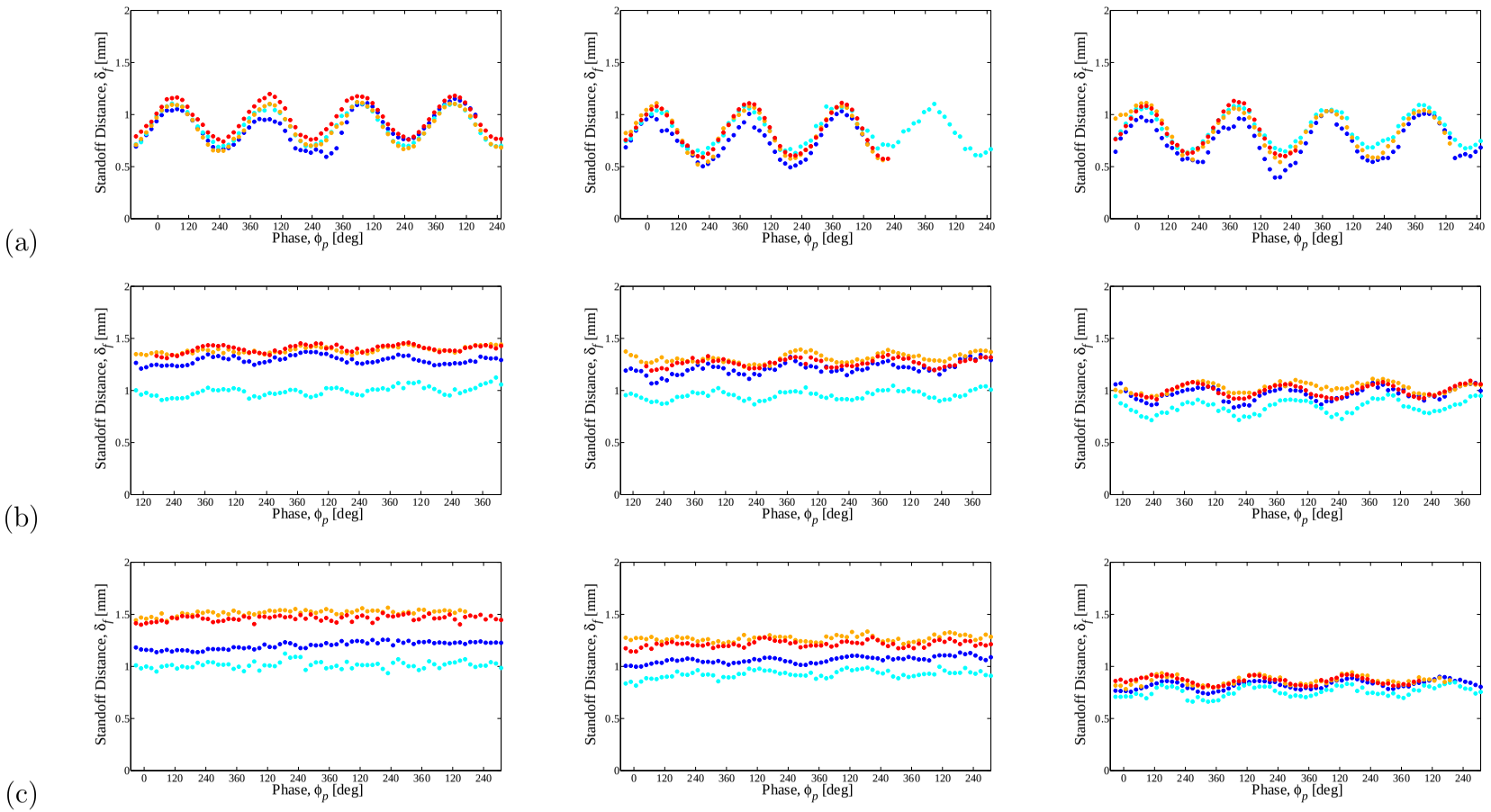

3.16: Horizontal flame standoff distance plotted versus the acoustic pressure phase. All fuels and acoustic frequencies are shown for three select waveguide locations. (rows: (a) $f_a = 332$ Hz (b) $f_a = 898$ Hz (c) $f_a = 1500$ Hz; columns: (left) $x = -6$ cm (middle) $x = -4$ cm (right) $x = -2$ cm; fuels: ( ) ethanol ( ) methanol ( ) FT ( ) JP-8/FT blend).

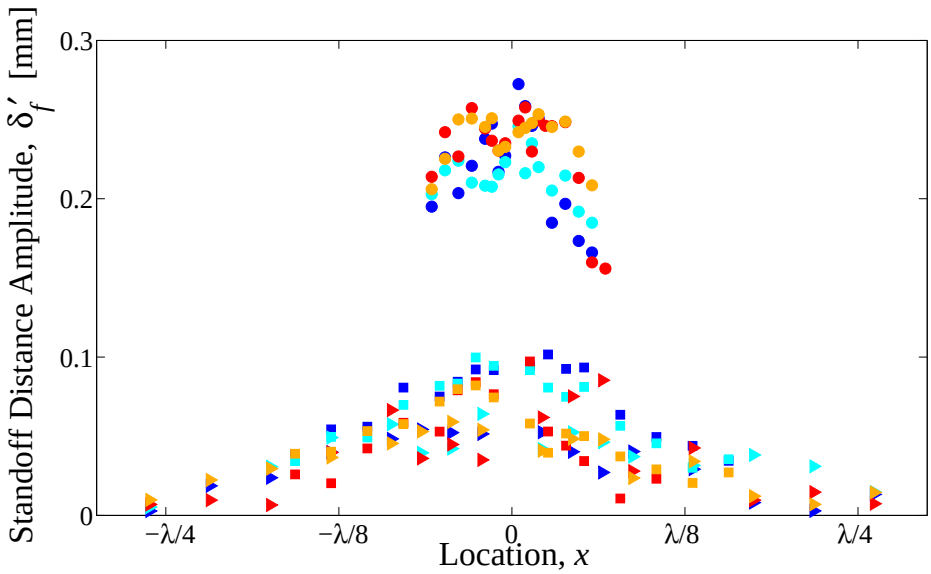

3.17: Standoff distance oscillation amplitude plotted versus waveguide location. (fuels: (●) ethanol (●) methanol (●) FT (●) JP-8/FT blend; frequencies: (●) $f_a = 332$ Hz (■) $f_a = 898$ Hz (▶) $f_a = 1500$ Hz).

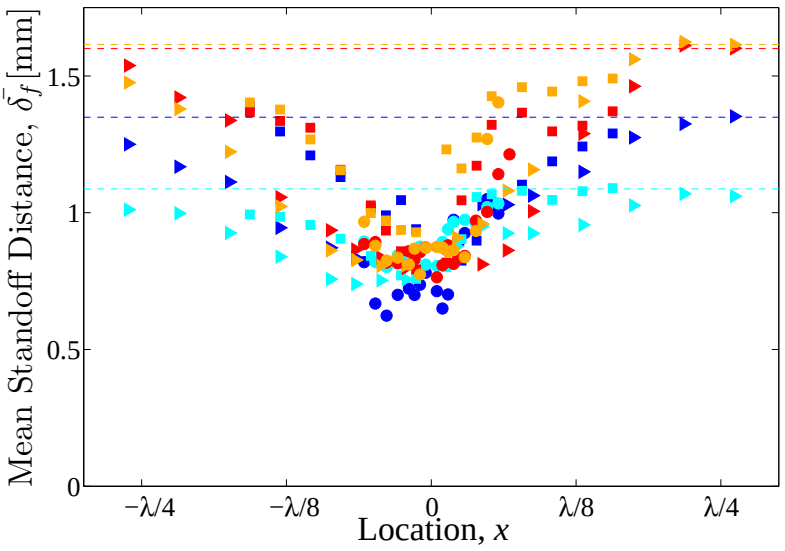

3.18: Time-averaged standoff distance plotted versus waveguide location. (fuels: (●) ethanol (●) methanol (●) FT (●) JP-8/FT blend; frequencies: (●) $f_a = 332$ Hz (■) $f_a = 898$ Hz (▶) $f_a = 1500$ Hz).

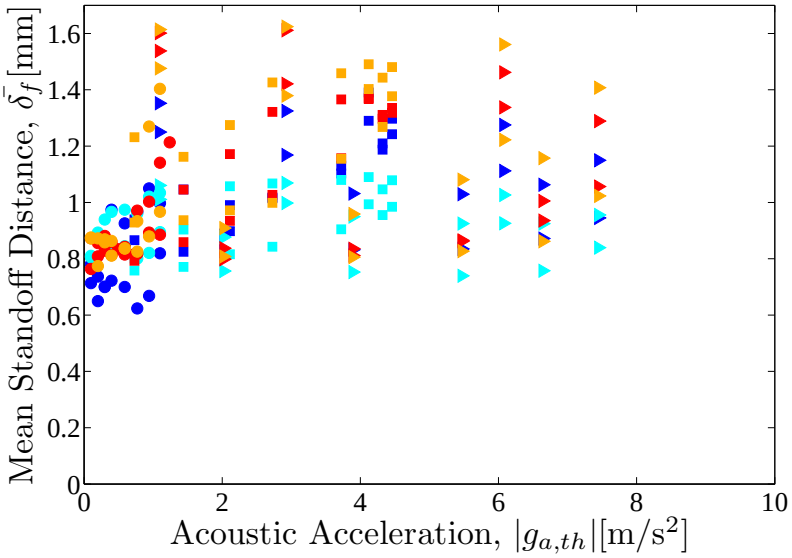

3.19: Time-averaged standoff distance plotted versus theoretcal acoustic acceleration. (fuels: (●) ethanol (●) methanol (●) FT (●) JP-8/FT blend; frequencies: (●) $f_a = 332$ Hz (■) $f_a = 898$ Hz (▶) $f_a = 1500$ Hz).

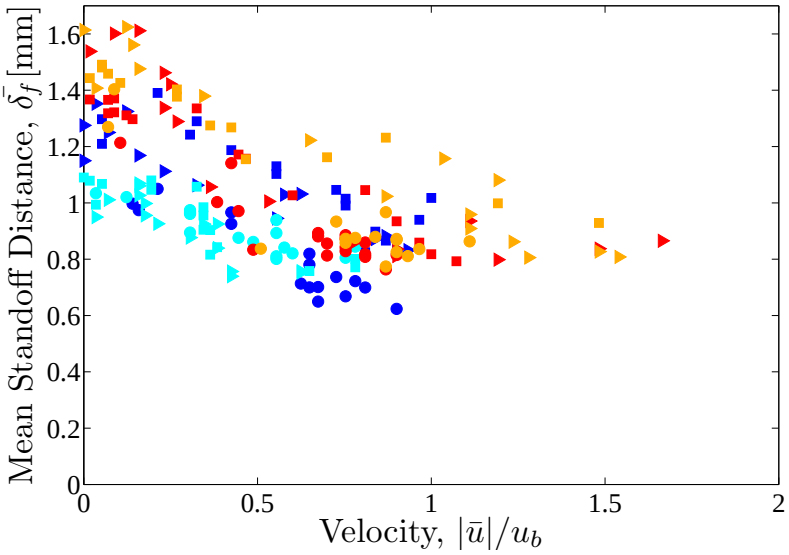

3.20: Time-averaged standoff distance plotted versus nondimensional horizontal velocity calculated using eqn. (3.2). (fuels: (●) ethanol (●) methanol (●) FT (●) JP-8/FT blend; frequencies: (●) $f_a = 332$ Hz (■) $f_a = 898$ Hz (▶) $f_a = 1500$ Hz).

CHAPTER 4

Experimental Facility and Methods - Shear-Coaxial Jets

To best describe the newly-constructed experimental facility used for the study on shear-coaxial jets at high pressures, the nonreactive apparatus used for previous super-critical jet experiments at AFRL must be mentioned. The two chambers lie on opposite sides of a single test cell, and in fact, the reactive chamber adopted many features from the existing nonreactive chamber in order to utilize experience gained from extensive nonreactive testing over many years. These features include the separation of inner and outer chamber volumes, heat exchangers to control propellant temperature, and generating sound using acoustic horns as waveguides. Unlike the nonreactive facility, the reactive facility must address the hazards associated with high pressure combustion of cryogenic oxygen and hydrogen, which requires remote control and sensing of the apparatus. The data acquisition system monitors over 200 sensors and the control system operates over 60 control devices. Thus, the complete system rivals the complexity of a rocket engine test stand, and navigating the intricacies of the entire facility is outside the scope of this chapter. To describe the complete capabilities of the facility though, parametric maps are provided which reach well beyond the experimental conditions explored in chapter 5.

4.1 High Pressure Chamber and Fluid Delivery Systems

4.1.1 Chamber

Similar to the previously existing apparatus used in nonreactive AFRL work [23, 75, 104], the chamber is designed as a chamber within a chamber. The inner chamber creates a near ideal environment for one-dimensional acoustic wave resonance, but is not sealed from the surrounding volume. This surrounding volume is the outer chamber, which has the structural integrity to withstand operating pressures of 1500 psi (10.34 MPa). Thick walls and windows are not necessary for the inner chamber, allowing more freedom when placing instrumentation and integrating new injector designs. A CAD rendering of the chamber assembly is shown in Fig. 4.1.

The outer chamber is fabricated from a forged naval brass alloy and has an octagon shape to offer optical access from multiple views. The current configuration contains six windows in the outer chamber wall, which includes large sapphire windows in the front and rear walls and four smaller quartz windows located at each corner. Large openings in the two remaining chamber side walls (left and right) are used for acoustic excitation sources. The injector assembly and exhaust port are located at the top and bottom of the outer chamber, respectively, creating downward propellant flows which exit the outer chamber through a cylindrical exhaust manifold. The exhaust manifold serves as a dilution and cooling point for the combustion products, and the resulting mixture exits the pressurized volume though a variable diameter exhaust orifice which is set to 4.8 mm, and is the chamber's only exhaust path.

4.1.2 Propellant Systems

To properly compose propellant density and velocity ratios, the oxygen and hydrogen feed systems must control the pressure, temperature, and flow rate of each. In this con-

text, the differential pressure between the injector exit and the chamber is assumed to be small, and the propellant pressure is simply taken as the chamber pressure. Temperature and flow rate though, are actively controlled upstream of the injector.

4.1.2.1 Propellant Flow Rate

Propellants are pressure fed by high pressure tanks located outside of the experimental cell, and flow rate is controlled by a remote needle valve for each propellant at ambient temperature. The needle valve often acts as a sonic nozzle, whereby flow rate remains constant although small changes in the downstream pressure occur, e.g. a rise in chamber pressure following ignition. To gather reliable propellant flow rates a Porter 123 series thermal mass flow meter is used in both the inner and outer jet systems, allowing maximum flow rates of 0.71 g/s, 2.02 g/s, 9.90 g/s, and 10.79 g/s for hydrogen, helium, nitrogen, and oxygen, respectively. Unique calibration data for each gas species is used when converting voltage output to mass flow rate for hydrogen, nitrogen, and oxygen, while helium mass flow rates are calculated using conversion factors published by Porter. These propellant flow rates, albeit low, create a flame similar to that of an O_2-H_2 LRE environment when used in conjunction with a sub-scale injector (see section 4.1.2.3) and considerable gaseous nitrogen flow to produce high chamber pressures (see section 4.1.2.4).

4.1.2.2 Heat Exchangers

Concerning temperature, LRE propellant tanks often hold fuel and oxidizer as a liquid, storing large masses of propellants within small cryogenic tanks. This is the case for many sub-scale test facilities as well [8, 24], and appropriate plumbing insulation allows propellants to be injected at temperatures only slightly above storage temperatures. For example, the BKH combustor maintains low hydrogen temperatures by submerging the

hydrogen supply lines in a liquid nitrogen bath between the liquid hydrogen tank and the test article [24]. Instead, this facility relies on ambient temperature propellant tanks storing gaseous oxygen and hydrogen at pressures exceeding 2000 psi (13.8 MPa). Thus, downstream of the flow meters, hydrogen and oxygen pass through separate cryogenic heat exchangers which cool propellants to the desired temperature.

Both heat exchangers operate under similar principles where propellant passes through a coiled tube which is cooled by liquid nitrogen. Liquid nitrogen is supplied from a 1500 gallon (5680 L) vacuum jacketed vessel pressurized to 90 psig (0.6 MPa). Approximately 9 m of vacuum jacketed tubing transfers liquid nitrogen from the vessel to the experimental cell, where the supply is split to deliver coolant to each individual heat exchanger. With this arrangement, the temperature of the process fluid is controlled by individually regulating liquid nitrogen flow rates through each system with separate control valves. A detailed drawing of the components and instrumentation of the heat exchangers can be found in the complete piping and instrumentation diagram in appendix A.

For the oxygen heat exchanger, which was designed and constructed by Sierra Lobo Inc., 2.82 m of inconel tubing is coiled on a vertical axis near the perimeter of an aluminum casting to carry process fluid. The casting also contains approximately 2 m of coiled tubing in the center of the casting for liquid nitrogen flow. In this way, heat energy from room temperature process gas enters the outer perimeter of the casting and transmits heat inward via conduction, where liquid nitrogen flow continually removes energy via convection. A vacuum jacket surrounds the assembly and is maintained at 10-100 mTorr. In its simplest form, this design can result in inaccurate control of fluid temperature, because liquid nitrogen flow rate control may be too coarse to obtain the desired process fluid temperature. For a test matrix in which propellant density ratio control is imperative, oxygen temperatures near the saturation point require accurate control to avoid large changes in density, caused by a large $\frac{\partial \rho}{\partial T}$. Inaccurate oxygen

temperatures also influence heat transfer phenomena in the flame region where propellant temperatures, as well as other thermodynamic variables such as chamber pressure, will engender a specific flame location and temperature.

As a direct result of these factors, the oxygen heat exchanger contains additional features to improve temperature control. First, a second coolant control valve is installed in parallel with the larger main control valve such that initial liquid nitrogen flow rates are set using the main control valve. Then, fine adjustments in liquid nitrogen flow rate are made with the small control valve as the process fluid outlet temperature approaches the target temperature. The flow capacity rating C_v is 2.0 for the main control valve and 0.075 for the small control valve. Second, electric heaters are mounted to the aluminum casting to offer additional energy in the event that the casting is chilled below the target temperature. The heating system consists of six heater elements individually controlled by a closed-loop control system written in LabVIEW. In this way, coolant control valves are set to slightly sub-cool the casting, reducing the process gas to a temperature 2 to 5 K below the target temperature. The heater power is then manually applied and automatically adjusted to hold the process fluid outlet temperature equal to the target temperature with an accuracy of ± 1 K. To achieve optimal accuracy, the heaters are used unless the target temperature is equal to the system's minimum possible temperature. Only four of the six heaters were used for the results shown in this study. A three-dimensional rendering of the oxygen heat exchanger is shown in Fig. 4.2.

The hydrogen heat exchanger, on the other hand, lacks many of these additional features. As shown in Fig. 4.3, the hydrogen heat exchanger consists of 2.5 m of process fluid tubing directly submerged in a liquid nitrogen bath. In this configuration, the flow direction of coolant is opposite that of the process fluid. This arrangement ensures a minimum process fluid temperature at the outlet region by encompassing said region with unheated coolant. Liquid nitrogen flow is regulated using a single control valve

downstream of the heat exchanger, and the position of this valve is the only variable directly controlled by the user for achieving the desired process fluid temperature. Process fluid outlet temperature then, is actively controlled by the user rather than employing an automatic control loop. Similar to the oxygen heat exchanger, the nitrogen bath is insulated by a vacuum jacket.

Although the propellant heat exchangers offer variable control of temperature, a cooling process is required to condition plumbing hardware prior to achieving a desired, stable temperature. The temperature conditioning process requires approximately 30 minutes and is performed using nitrogen not only as the coolant, but also as the process fluid in order to preserve propellant. When a stable temperature and flow rate are reached, remote valves are used to switch from the nitrogen simulant supply to the propellant supply. Due to differences in viscosity, density, and heat conduction constants, alternating between nitrogen simulant flow and propellant flow causes significant changes in mass flow rate and temperature. A time series plot of the transition from nitrogen simulant to propellant is shown for oxygen and hydrogen in Fig. 4.4. The difference between the process fluid temperature at the injector before and after the species transition was found to be highly dependent on both chamber pressure and mass flow rate.

To characterize the capability of each heat exchanger, the minimum achievable temperature was measured for a range of chamber pressures. This was done by utilizing high liquid nitrogen flow rates over a long period of time to cool the hardware of each system. Thus, the injector flow temperature for each process fluid was minimized, representing a limiting temperature condition for the facility. The results from this effort are shown in Fig. 4.5 for oxygen, where minimum temperature is shown to have a small dependence on chamber pressure. An oxygen density contour is the background of Fig. 4.5, showing that a liquid phase is achievable for $T_{ij} < T_{sat,ox}$ and $p_c < p_{crit,ox}$ and supercritical fluid

for $p_c > p_{crit,Ox}$. Temperature is shown to have a negative correlation with mass flow rate. Similar measurements were made with the hydrogen propellant system, but to perform these tests safely, helium was used as a surrogate. Minimum helium temperatures are shown in Fig. 4.6, superimposed on a hydrogen density contour map.

To quantify the heat exchangers capability for nonreactive experiments, minimum temperatures for nitrogen are plotted for both the inner and outer jets in Fig. 4.7. A nitrogen density contour is also shown. Reviewing temperature limitations for the outer and inner jets, one observes that two-phase flows can be realized for both reactive (LO_x-GH_2) and nonreactive (LN_2-GN_2) tests. Single-phase conditions can also be achieved with subcritical gas-gas jets where $T_{ij} > T_{sat,ox}$ for reactive tests and $T_{ij} > T_{sat,N_2}$ for nonreactive tests. If desired, liquid-liquid conditions can also be achieved for nonreactive tests where $T_{ij} < T_{sat,N_2}$ and $T_{oj} < T_{sat,N_2}$. Although heat exchanger performance is also dependent on process fluid mass flow rate, which is not characterized in Figs. 4.7, these results are a valuable tool for the design of experiments with known facility limitations.

The significance of propellant temperature limits is best understood by mapping the possible values for densitiy ratio S. For oxygen-hydrogen flows, Fig. 4.8 shows the range of achievable values for S as a function of chamber pressure. For $p_c < p_{crit,ox}$, single-phase flows allow for density ratios as high as 0.1. Two-phase LO_x-GH_2 flows though, restrict density ratios to a small range of values less than 0.01, which is comparable to a oxygen-hydrogen engine with regenerative nozzle cooling. Supercritical oxygen flows are characterized by a region with pressures greater than 5.04 MPa (731 psia), where oxygen is a supercritical fluid and a distinct phase change does not exist for oxygen.

4.1.2.3 Injector

The injector consists of a single shear-coaxial element designed for hydrogen flow in the annulus and oxygen flow in the center. In terms of total cross-sectional area, the injector

is $1/10^{th}$ scale of the J-2 engine, for example. An injector of this size is challenging to manufacture, but is used here to maintain jet velocities and Reynolds numbers with orders of magnitude similar to an actual LRE while maintaining much smaller propellant mass flow rates. This technique was also employed in the design of shear-coaxial injectors for the Common Research Combustor of CNRS and DLR. The cross-sectional dimensions of the injector are shown in Fig. 4.9, and dimensions for all recent AFRL injectors are shown in Table 4.1 for comparison. In comparison with previous AFRL shear-coaxial injectors, the current injector has a small area ratio, $\frac{A_{oj}}{A_{ij}} = 1.68$. The inner post thickness to inner diameter ratio $\frac{t}{D_1}$ has a value of 0.27, which prevents the inner shear layer from behaving purely as that of co-flowing fluids. Instead, a recirculation zone is expected to form at the exit of the injector between the outer and inner jets. A CAD image of the injector and top flange assembly is shown in Fig. 4.10.

A comparison of Re_{ij} and Re_{oj} for similar research combustors is shown in Fig. 4.11, with operating points of actual oxygen-hydrogen LREs. Operating spaces of four other combustion instability research facilities are shown, including the BKH combustor of DLR, Germany, the Common Research Combustor (CRC) of CNRS, France and DLR, Germany, the Multi-Injector Combustor (MIC) of ONERA and CNRS, France, and the Cryogenic Combustion Laboratory (CCL) of Pennsylvania State University, USA. These facilities were specifically chosen for comparison because detailed flow conditions for oxygen-hydrogen stability experiments for shear-coaxial jets are available, but one must be cognizant that apparatuses such as these often see multiple modifications in only a few years time. As a result, Fig. 4.11 should be considered only a general guide for comparison, because Re values for the facility concerned here, as well as the others in Fig. 4.11, can be revised with simple hardware modifications.

For all conditions shown in Fig. 4.11, two-phase flows lie in the membrane type breakup regime or the fibre-type breakup regime, characteristic of high Re and high

We flows as discussed in section 1.3.1.2. Reynolds numbers of this magnitude are often considered to create fully-developed turbulent conditions at the injector exit. Fully-developed flow at the injector exit is particularly advantageous for establishing a known and canonical velocity profile, imparting momentum boundary conditions for shear layer studies and providing a boundary layer thickness approximately equal to half of the diameter for a range of mean velocities. Rather than matching the design of a particular LRE injector where the fully-developed turbulence assumption may or may not be valid, the current injector design places priority on ensuring fully-developed turbulent flow for the entire effective range of Re values to provide confidence in experimental boundary conditions. A minimum injector length is required to make this assumption valid. According to the development length criterion of Munson *et al.* [147] the minimum nondimensional development length required for fully-developed turbulent flow is

$$\frac{L}{D} \geq 4.4 Re^{\frac{1}{6}} \tag{4.1}$$

where D is taken as D_1 for the inner jet and $D_3 - D_2$ for the outer jet. Using the complete range of values for Re_{ij} and Re_{oj} from Fig. 4.11, $\frac{L}{D} > 4.4 Re^{\frac{1}{6}}$ for all conditions and the fully-developed turbulence assumption is valid. One particular flow condition is represented by the diagram in Fig. 4.12, where the $1/7^{th}$ power law [148] is used to plot fully-developed velocity profiles for the inner and outer jets.

The injector design chosen here also deviates from popular LRE injector designs, because the inner jet lacks a recessed exit plane. A recessed inner post, as shown in Fig. 1.6b and 1.6c, is commonly used in LREs in order to enhance mixing in the initial merging zone via an increased transverse velocity of either the inner jet, outer jet, or both. The J-2 and SSME engines both used recessed inner posts for LO_x-GH_2 combustion, for example [45]. Thus, both the injector length and the exit geometry deviate from practical designs in order to create more well-known boundary conditions at the injector exit. This design also serves as a baseline geometry that could be used

for comparison with recessed injectors in the future.

A parametric map of the facility can be obtained by combining the density ranges discussed above with injector dimensions and propellant mass flow rates, but first a range of propellant mixture ratios must be defined to constrain the operating space. For oxygen-hydrogen mixtures, the stoichiometric mixture ratio is 8 and actual LREs operate fuel-rich in the range $4.5 < MR < 7.2$. In terms of the fuel-oxidizer equivalence ratio $\phi_{f/o} = \frac{\dot{m}_f/\dot{m}_o}{\left(\dot{m}_f/\dot{m}_o\right)_{st}}$, this range corresponds to $1.11 < \phi_{f/o} < 1.78$. A minimum MR of 2 is used here to capture the lower limit of mixture ratios for a practical specific impulse [149]. A maximum of 8 is taken to include stoichiometric conditions. Using a wide range of mixture ratios offers an expanded range of momentum flux ratios without changing the injector element, as shown in a parametric map of J versus MR in Fig. 4.13.

4.1.2.4 Exhaust

Rather than passing through a single exhaust nozzle, the chambers' exhaust path is staged. Upon exiting the inner chamber through a rectangular hole, the combustion products, which are mixed with nitrogen from the inner chamber, will enter a small manifold. This exhaust manifold serves as a dilution and cooling volume. The exhaust manifold is separated from the outer chamber by a cylindrical wall. Throughout the wall, 3.18 mm diameter holes allow gaseous nitrogen from the outer chamber to flow into the exhaust manifold. Thus, the combustion products are initially cooled and diluted by nitrogen present in the inner chamber and then experience further cooling and dilution due to additional nitrogen in the exhaust manifold.

Consequently, a supplementary flow system introduces gaseous nitrogen into the outer chamber to provide a positive pressure differential between the outer chamber and the exhaust manifold. In turn, this produces a continuous flow of exhaust dilutant into the product mixture. The ensuing nitrogen-rich mixture then exits the exhaust manifold

through a tube with a 22.1 mm inner diameter prior to being choked through a 4.8 mm diameter restricting orifice. Without altering the orifice size, the chamber pressure can be controlled independent of propellant flow rate by adjusting one of several nitrogen flow rates, and the orifice size was chosen to create the desired p_c for a given nitrogen mass flow rate. Assuming that inner chamber nitrogen flows, to be described below, are set according to the experimental needs of the scientifically sensitive region near the flame, the supplementary outer chamber nitrogen flow rate is appropriately used for adjusting the mean chamber pressure. Therefore, this supplementary nitrogen system is termed the chamber pressurization flow system although it also serves as an exhaust dilutant and coolant.

4.2 Inner Chamber

4.2.1 Inner Chamber Dimensions and Instrumentation

The inner chamber is a rectangular volume open to transverse acoustic excitation from circular acoustic drivers on the left and right. The inner chamber depth is 20.32 mm and the height is 36.07 mm, making room for sub-scale injectors only. The width is much larger, reaching 0.82 m from the left acoustic source to the right acoustic source, making the inner chamber volume large in comparison to the injector. One should also note that although the inner chamber cross-sectional area is 20.32 mm $\times$ 36.07 mm near the injector, the far left and far right areas of the inner chamber expand to a large circular area in order to house each acoustic driver. The waveguide design which is used to smoothly transition from a rectangular shape to a circular shape will be described in section 4.3.2. Two quartz inner chamber windows separate the inner chamber from the outer chamber, and because these windows need not withstand a large pressure differential, nine small holes are located throughout the rear inner window at an axial distance

of $12D_1$ from the injector exit, but at various spanwise locations. Three of these nine holes are occupied by dynamic pressure transducers; one of which is spanwise centered in the rear window ($p_{dyn,2}$), while two others are located 25.4 mm to the left and right of the center pressure transducer ($p_{dyn,1}$ and $p_{dyn,3}$). Thermocouples are located 6.35 mm to the left and right of each pressure transducer, totaling six thermocouples measuring temperature at the inside surface of the rear window. Hence, these instruments diagnose the region near the flame at $x = 12D_1$, and one final thermocouple is suspended in the center of the inner chamber exit to measure the flame temperature at $x = 30D_1$. By placing a thermocouple at $x = 30D_1$, the temperature near the end of the flame is measured without disturbing the region captured by high-speed imaging.

4.2.2 Inner Chamber Nitrogen Flows

At the top of the inner chamber, a nitrogen plenum provides two flows parallel to propellant flows. First, window cooling flows enter the inner chamber through slotted holes located immediately inside the top edge of the inner windows. Second, a propellant co-flow system provides gaseous nitrogen to the region surrounding the flame by entering the chamber through dozens of 0.48 mm diameter holes in a circular pattern around the coaxial injector. This co-flow system decreases coaxial jet recirculation in the inner chamber, and will be referred to as the flow straightener flow. The nitrogen used for both the window cooling and flow straightener systems is supplied at ambient temperature.

4.3 Waveguide Design and Characterization

The acoustic system design meets several key requirements. Most importantly, acoustic fluctuations in the transverse direction are maximized and fluctuations in the longitudinal and depth-wise directions are minimized to create approximately one-dimensional

waves. Second, it is possible to create acoustic pressure amplitudes with the same order of magnitude as an actual LRE combustion instability while still maintaining the ability to control and sustain low amplitudes, e.g. $p' < 0.01 p_c$. Last, the acoustic system allows for reliable establishment of standing waveforms with pressure nodes or velocity nodes located at the coaxial jet.

4.3.1 Acoustic Drivers

Similar to both the droplet combustion apparatus and the aforementioned nonreactive facility at AFRL, twin acoustic drivers are used in concordance with the general principles of a Kundt's tube. However, in the case of the system described here and the nonreactive facility at AFRL, drivers with a total area more than twice that of the inner chamber's cross sectional area are used. This feature establishes pressure amplitudes much higher than a traditional Kundt's tube when the waveguide shape is designed as a sound amplifying horn, which will be described in the following section. High acoustic pressure amplitudes are also enabled by using circular piezoelectric sirens as acoustic sources. The sirens are made entirely of aluminum, and the contruction of which is described further in appendix A.1. The sirens enable much higher amplitudes than classical loudspeakers, but piezoelectric sirens have one drawback to mention here.

As a result of their geometric form, the piezoelectric sirens exhibit a few resonant frequencies. Within the narrow bands located at each resonant frequency, high oscillation amplitudes occur in the siren's cone, and high-amplitude coherent sound is produced. Operating the sirens outside of these narrow bands of efficiency results in much lower amplitudes.

To quantify this limitation, sound pressure measurements were made with the sirens mounted outside of the chamber. In this manner, chamber resonance is avoided by allowing waves to propagate into an open room. Each siren was mounted firmly using

the same technique which is used when mounting the siren inside the chamber, and a dynamic pressure transducer (Kulite model XCE-093-50D) was placed 5 cm from the siren's diaphragm. A frequency sweep over a duration of 15 s was used to ramp the oscillation frequency of the siren from 100 Hz to 6000 Hz while acquiring data at a rate of 80 kHz. Results are shown in Fig. 4.14, revealing three frequency bands of peak performance for both the left and right sirens. A wideband at relatively low frequency occurs at 1638-1915 Hz for the left siren and 1620-1860 Hz for the right siren. Then, two distinct peaks occur at 3076 and 5200 Hz for the left siren, and 3083 Hz and 5100 Hz for the right siren. These resonant frequencies will indeed limit the usable range of chamber acoustic frequencies, but this factor must be considered hand in hand with chamber resonance to fully characterize the acoustic system.

4.3.2 Waveguide

As described above, the sirens have a circular shape while the inner chamber is rectangular. Thus, the waveguide's shape must provide a smooth transition from a 11.24 cm diameter circle to a 2.03 cm $\times$ 3.61 cm rectangular cross-section. To minimize two-dimensional and three-dimensional waves, the circle-to-rectangle transition must be void of abrupt area changes and sharp corners. This requirement, combined with material stress from high chamber pressures, make design and fabrication challenging.

The area reduction from circle to rectangle follows a quasi-one-dimensional model for sound propagation in a rigid-walled duct, which is derived beginning with the acoustic wave equation,

$$\nabla^2 p - \frac{1}{c^2}\frac{\partial^2 p}{\partial t^2} = 0, \tag{4.2}$$

which is then integrated for acoustic pressure p for a three-dimensional segment of the duct shown in Fig. 4.15. In agreement with the coaxial jet diagram in Fig. 1.13, x is the jet streamwise direction, y is the transverse direction, and z is the depthwise direction.

Thus, a perfectly shaped waveguide will prevent acoustic wave propagation in the x and z directions and concentrate 100% of the energy from each siren to produce waves in the y direction ($\frac{\partial^2 u}{\partial x^2} = \frac{\partial^2 u}{\partial z^2} = 0$). Gauss's theorem is then used to convert the volume integral of $\nabla^2 p$ to a surface integral, i.e.

$$\iiint_V (\nabla^2 p) dV = \oiint_S (\nabla p \cdot \hat{n}) dS. \tag{4.3}$$

Then, apply the boundary condition that $\nabla p \cdot \hat{n} = 0$ at the inner wall of the waveguide, divide by Δy, and take the limit as $\Delta y \to 0$ ($\Delta y = \partial y$). One obtains

$$\frac{\partial}{\partial y} \iint_A \frac{\partial p}{\partial y} dA - \frac{1}{c^2} \frac{\partial^2}{\partial t^2} \iint_A p dA = 0. \tag{4.4}$$

With the exception of a thin acoustic boundary layer near the inner wall of the waveguide, p is uniform over any given cross section, i.e. $\frac{\partial p}{\partial x} = \frac{\partial p}{\partial z} = 0$. The equation above then reduces to

$$\frac{1}{A} \frac{\partial}{\partial y} \left(A \frac{\partial p}{\partial y} \right) - \frac{1}{c^2} \frac{\partial^2 p}{\partial t^2} = 0, \tag{4.5}$$

which is known as Webster's horn equation, after Arthur G. Webster [150]. Following Pierce [151], Webster's horn equation can be simplified as

$$\left\{ \frac{\partial^2}{\partial y^2} + \frac{1}{4A^2} \left[(A')^2 - 2AA'' \right] - \frac{1}{c^2} \frac{\partial^2}{\partial t^2} \right\} A^{\frac{1}{2}} p = 0. \tag{4.6}$$

This is a nonlinear ordinary differential equation with respect to A which can be used to describe the optimal shape of an expanding or constricting waveguide as shown in Fig. 4.15. The general solution is

$$A^{\frac{1}{2}} = A_{th}^{\frac{1}{2}} (\cosh my + T \sinh my), \tag{4.7}$$

where $A_{th} = A(y = 0)$ and $A_{th}^{\frac{1}{2}} Tm = \frac{\partial (A^{\frac{1}{2}})}{\partial y}(y = 0)$. The specific solution is found for the catenoidal horn shape for $T = 0$ [151]:

$$A = A_{th} (\cosh my)^2. \tag{4.8}$$

The throat area A_{th} and flare constant m are unique constants which are found according to the boundary conditions of the waveguide. First, the throat area is set equal to the cross-sectional area of the inner chamber,

$$A_{th} = (\Delta x)\,(\Delta z) = (36.1 \text{ cm})\,(2.03 \text{ cm}) = 7.33 \text{ cm}^2, \tag{4.9}$$

and finally, constraining the solution for a specific waveguide length L and siren area gives a value of 0.0910 cm^{-1} for m. Thus, the completed solution for a catenoidal horn area distribution is

$$A(y) = 7.33 \cosh^2(.091y)\,. \tag{4.10}$$

This formula for $A = f(y)$ was used to calculate an appropriate transverse area distribution in square centimeters for the acoustic waveguides to the left and right of the chamber. The area distribution according to equation 4.10 is plotted in Fig. 4.16 with the inner chamber included in between the left and right waveguides. Thus, Fig. 4.16 represents the area distribution of the completed chamber.

However, Webster's horn equation is limited when applied to waveguides in this way. Effective use of waveguides as sound amplifiers requires an acoustic frequency above a minimum operating frequency, or cutoff frequency f_c, which is a function of the speed of sound c and the flare constant m. According to Pierce [151],

$$f_c = \frac{mc}{2\pi}, \tag{4.11}$$

which can be used to estimate an appropriate minimum acoustic frequency. This cutoff frequency is less important for horns with $mL \leq 1$ [151], but mL=3.3 for the waveguides used here. As an example, nitrogen at T=300 K gives f_c=511.5 Hz and f_c=552.0 Hz for p_c=0 psig and p_c=1500 psig (10.34 MPa), respectively. Although temperature variations may also alter the speed of sound, and large temperature variations exist near the jet, the temperature of gas in the waveguides was found to have a negligible effect on f_c. Therefore, the cutoff frequency criterion will be adhered to for the experiments in this study.

4.3.3 Resonant Frequencies

4.3.3.1 Acoustic Forcing Strategy and Analytical Consideration

Paired with the resonant modes of the acoustic drivers, the resonant modes of the chamber cavity are imperative in determining a useable set of frequencies for experiments involving high amplitude acoustics. A straightforward calculation predicting several transverse chamber modes is described below. Following theoretical discussion, experimental resonant frequencies are presented for a range of chamber pressures.

Akin to the cavity resonance analysis for the cylindrical waveguide discussed in section 2.1, the resonant frequencies of the more complex chamber geometry addressed here can be predicted by eqn. 2.1, which is listed here for convenience.

$$L = \frac{n}{2}\lambda = \frac{n}{2}(\frac{c}{f_F}) \tag{4.12}$$

Again, regardless of the value of f_F and n, speakers operated out-of-phase ($\Delta\phi = 180°$) will create a PN at the center of the chamber and speakers operated in-phase ($\Delta\phi = 0°$) will create a PAN at the center. To achieve maximum acoustic pressure and velocity amplitudes, f_F must take on a value in accordance with 2.1 where n is a positive integer. But, additional phenomena cause increased error when applying the following assumptions. First, the area changes within each waveguide are neglected when applying one-dimensional theory. Second, the speed of sound c is not constant, but rather is altered by chamber pressure and temperature. Thus, as a result of repeated cooling and firing cycles near the injector, the speed of sound for each experimental test should be considered unique. Temperature, for example, is a minimum at the center of the chamber where cryogenic flows cool the region after long periods of temperature conditioning prior to ignition. During this period, the chamber's maximum temperature is located at ends of each respective waveguide. After ignition though, a sharp temperature rise occurs in the flame region and a small pressure rise occurs due to combustion. Speed of

sound is a function of both time and space as a result of these variations in temperature and pressure.

A second phenomenon which increases error when applying the assumptions of eqn. 2.1 is a result of three-dimensional geometry variations in the waveguides. Although the shape of the internal waveguide walls was carefully designed according to the derivations in Section 4.3.2, resonant modes may occur in three different dimensions. These three are the transverse direction y spanning from the left waveguide to the right waveguide, the secondary transverse direction z spanning from the front window of the inner chamber to the rear window of the inner chamber, and the longitudinal direction x spanning from the upper wall of the inner chamber to the exhaust orifice. Each of these three mode types will be addressed differently.

The transverse modes occurring in the y direction navigate only smooth area changes within the waveguides. Thus, the transverse mode, or "T" mode, will be described using the approximate calculations of eqn. 2.1 using a value of c for pure nitrogen at the mean chamber pressure p_c and the mean chamber temperature T_c. By design, a transverse span of $L = 0.82$ m offers multiple frequencies less than 6000 Hz at which transverse resonance may occur. This mode type will be the focus of all acoustic forcing results presented in this study.

The secondary transverse modes occurring in the z direction will resonate within a very small span created by the depth of the inner chamber. This geometric boundary, created by the front and rear inner windows, is only 20.32 mm in length. Consequently, only very high frequencies are capable of producing resonant conditions in the z direction. A speed of sound of c=344 m/s and n=1, for example, will result in an acoustic resonant frequency of 8465 Hz. This frequency is far greater than the useable range of the piezoelectric sirens. Thus, secondary acoustic modes in the z direction are assumed to be negligible.

The longitudinal modes occurring in the x direction maneuver a series of abrupt area changes between the inner chamber and the exhaust tube. The inner chamber's exit is a rectangular exhaust gap which connects the rectangular inner chamber with the exhaust manifold. The exhaust manifold introduces additional gaseous nitrogen into the exhaust mixture, cooling the mixture before it exits the outer chamber through a 22.1 mm diameter hole, and then the 4.8 mm exhaust orifice. Thus, three interconnected volumes create a longitudinal space in which "L" modes may exist, but cannot be accurately predicted with brief analytical techniques due to two substantial area changes joining the inner chamber, exhaust manifold, and exhaust tube. For a three-dimensional computational analysis of chamber acoustics, ANSYS and COMSOL have been used to successfully resolve the influence of complex geometry and speed of sound variations [18, 24, 131]. Such an analysis is outside the scope of this work and will be considered in future analysis.

4.3.3.2 Experimental Characterization

Using a single dynamic pressure transducer within the inner chamber, acoustically resonant conditions can be identified for both PAN and PN conditions at the center of the chamber. This type of experimental characterization conveys the final result of merging acoustic resonance attributed to each siren with acoustic resonance attributed to chamber geometry. Due to the sirens' ability to produce high pressure amplitudes for only three limited frequency bands, it is expected that p' measurements will be high for a limited number of transverse chamber modes. Other transverse modes may be resonant, but acoustic chamber modes far from the effective frequency bands of the sirens will create low, unusable amplitudes. To demonstrate this balance, a frequency sweep was performed for PAN conditions.

To experimentally determine resonant PAN conditions, p' was measured at the center

of the chamber using a pressure transducer located in the center of the rear inner window, a distance $12D_1$ below the injector. The pressure measured at this point is $p_{dyn,2}$. A PAN condition was produced at this location by operating the sirens in-phase, i.e. $\Delta\phi = 0°$. Over a time span of 20 s, the sirens were linearly swept from an acoustic frequency of 100 to 6000 Hz while sampling pressure at a rate of 40 kHz. This procedure was repeated for ten different mean chamber pressures from 100 to 1000 psia (6.9 MPa) while at room temperature.

To provide a comparative representation of PAN frequency sweep results, time series data are transformed into a periodogram power spectral density estimate using a Hamming window function. Fig. 4.17 includes the results from each chamber pressure set point, and also includes theoretical lines calculated using eqn. 2.1 for comparison. For $f < 1400$ Hz, amplitudes remain negligible regardless of chamber pressure due to the sirens' ineffective sound production in this range. The 1T and 2T modes cannot be identified. For 1400 Hz $< f <$ 4000 Hz, several modes can be identified throughout the sirens' effective frequency range. When comparing the performance of the left and right sirens in Fig. 4.14 with the theoretical transverse resonance values, it is clear that an additional factor must be engendering other peak frequencies shown in Fig. 4.17 for 1400 Hz $< f <$ 4000 Hz. The additional factor may be a result of chamber resonance unaccounted for by transverse resonance calculations, such as longitudinal resonance. Unexpected spectral results may also be manifested by imperfect siren operation. For example, although the phase relationship of each siren control channel is set to zero ($\Delta\phi = 0°$), deviations in $\Delta\phi$ can occur over wide variations in frequency. For $\Delta\phi \neq 0°$, perfect resonance cannot be achieved and the PAN deviates from the center of the chamber [135]. These deviations result from the uniqueness of each siren signal amplifier, amounting to a phase difference of several degrees between each amplifier. Variations in $\Delta\phi$ were not corrected during the frequency sweep represented in Fig. 4.17. In conclusion, although significant amplitudes can be achieved near the 3T, 4T,

5T, 6T, and 7T modes, the exact frequency of each mode cannot be determined as a result of unidentifiable frequency peaks, and thus, Fig. 4.17 alone is an imperfect indication of transverse standing waves. Using the acoustic forcing system requires standing wave verification for each individual experimental condition, and this procedure will be described in appendix A.1.

4.4 Nonreactive Jet Imaging

Jet flow visualization was the primary diagnostic tool for studying LN_2-GHe flow dynamics, provided by back-lit high-speed images. A variable power Newport model 66986 power supply controlled a 300 W Xe lamp, which emitted light in the near ultraviolet spectrum. This beam was projected through the rear window as a back-light source. Although the beam was not collimated, this back-lighting technique produced sufficient contrast at fluid interfaces. Differences in the refractive index of the jets and the surrounding medium provided the necessary distinction between the fluids of interest. The low temperature, liquid nitrogen inner jet appeared as a dark column of fluid as viewed by the high-speed camera placed on the opposite side of the light source. The less dense gaseous helium outer jet was also distinguishable from the heavier gaseous nitrogen surrounding the coaxial jet.

A Phantom v7.10 high-speed camera was used to visualize the fast dynamical processes inherent to an unforced coaxial jet flow as well as those present during high frequency acoustic forcing. A 200 mm Nikon MicroNikkor lens was used with a no. 1 close-up lens attachment, giving a spatial resolution of 30 μm per pixel. Image framing rates of 10 kHz were used in order to avoid aliasing up to 5 kHz, which is much greater than the highest forcing frequency used in this study, 2600 Hz. An external trigger from the facility control system was used to start recording the image frames, which were synchronized with all other data using the coordinated universal time (UTC) stamp

from an IRIG-B timecode generator.

4.5 Reduced Basis Methods

Reduced basis methods are growing in popularity as a computational procedure to reduce the complexity of flow systems exhibiting periodic, coherent structures. For computational fluid dynamicists, reduced basis methods have been used to provide inlet flow boundary conditions which capture important flow instabilities without representing all, and thus insignificant, modes in order to increase computational efficiency [152]. For experimentalists, reduced basis methods have been particularly useful image analysis tools. In a study by Arienti *et al.* [153] the shape and instability frequencies of a jet in crossflow were captured using just a few modes which contain the highest energy contribution. Where experimental systems pose installation challenges for direct probing and sensing instruments, which may cause unwanted flow disturbances, reduced basis methods extract spatial and temporal information from images alone. This study uses proper orthogonal decomposition (POD) to determine the spectral content of the most significant modes in a shear-coaxial jet, and uses the same set of results to describe the qualitative shape of these modes. Also, a brief comparison is made between POD and a second reduced basis method, dynamic mode decomposition (DMD).

4.5.1 Proper Orthogonal Decomposition

When used as an image analysis algorithm for flow instability, POD uses high-speed imaging results to reconstruct an approximate representation of a flow using proper orthogonal modes (POMs) which are ranked according to their pixel intensity variations relative to the time-average. This method has been used by Arienti *et al.* [153] and Arienti and Soteriou [154] to determine the dominant vortex shedding frequencies in

jets in crossflow, and Teshome *et al.* [30] have been the first researchers to apply POD to shear-coaxial jet instabilities. In Teshome *et al.* [30], the natural jet instability and the acoustically forced jet instability was identified by truncating the resulting set of POMs to the highest ranked POM conjugate pair with the goal of representing the jet with a single mode. The present study holds a similar approach, and this section serves to describe POD accordingly.

First, the pixel intensity values for a set of images can be represented in continuous form as

$$a(x,t) = \sum_{k=1}^{N} u_k(t) v_k(x), \tag{4.13}$$

where u_k are vectors of temporal amplitude coefficients, v_k are vectors of proper orthogonal modes, k is the mode number, and N is the number of modes. In order to implement this method, the pixel intensities are arranged into a single aggregate data array for all image frames, giving a a single spatial dimension having a length M equal to the total number of pixels in a single $m \times n$ image. Thus, $M = mn$. First, this is achieved by forming a row vector consisting of all pixel intensity values of each image frame. The row vector is formed in order of increasing pixel columns followed by increasing pixel rows, as shown in Fig. 4.18. Row vectors are then combined for a sequence of N image frames, resulting in the complete matrix $\mathbf{A}$ consisting of N rows by M columns of intensity values. Thus, $\mathbf{A}$ is an array of N sets of M pixel intensities in a single matrix, as shown in Fig. 4.19.

In order to isolate the periodic fluctuations of coherent structures, the intensity fluctuations should be considered rather than the mean. Thus, the time-average of each pixel intensity is subtracted from the mean to produce a matrix of intensity fluctuations $\widetilde{\mathbf{A}}$. That is,

$$\widetilde{\mathbf{A}}_{ij} = \mathbf{A}_{ij} - \frac{1}{N} \sum_{i} \mathbf{A}_{ij} \tag{4.14}$$

where $i = 1...N$, $j = 1...M$. Figure 4.20a shows a single image frame, and Fig. 4.20b

shows the corresponding time-averaged image for $N = 100$ frames. Since a single image contains more than 100,000 pixels and the number of images is ∼1000, then $\widetilde{\mathbf{A}}$ is a rectangular matrix where $N < M$. A singular value decomposition (SVD) can be readily computed for this non-square matrix as opposed to eigenvalue decomposition, which is an alternative to SVD for computing a POD solution, but requires $\widetilde{\mathbf{A}}$ to be a square matrix. According to SVD, $\widetilde{\mathbf{A}}$ can be represented with the form

$$\widetilde{\mathbf{A}} = \mathbf{U}\mathbf{\Sigma}\mathbf{V}^T \tag{4.15}$$

This decomposition is used within POD to divide the complete matrix into a matrix containing temporal information $\mathbf{U}$, a matrix containing spatial information $\mathbf{V}$, and a scaling matrix $\mathbf{\Sigma}$. The product of $\mathbf{U}$ and $\mathbf{\Sigma}$ is representative of u_k in eqn. 4.13, and $\mathbf{V}$ is the matrix form of v_k. After removing unused rows in $\mathbf{U}$ in an economic SVD scheme, $\mathbf{U}$ is an $N \times N$ orthogonal matrix taking the form

$$\mathbf{U} = \begin{bmatrix} u_{11} & u_{12} & & \\ u_{21} & u_{22} & & \\ & & \ddots & \\ & & & u_{NN} \end{bmatrix}, \tag{4.16}$$

$\mathbf{V}^T$ is an $M \times M$ orthogonal matrix taking the form

$$\mathbf{V}^T = \begin{bmatrix} v_{11} & v_{21} & & & & \\ v_{12} & v_{22} & & & & \\ & & \ddots & & & \\ & & & \ddots & & \\ & & & & \ddots & \\ & & & & & v_{MM} \end{bmatrix}, \tag{4.17}$$

and $\mathbf{\Sigma}$ is an $N \times M$ diagonal matrix taking the form

$$\mathbf{\Sigma} = \begin{bmatrix} \sigma_1 & 0 & & & & \\ 0 & \sigma_2 & & & & \\ & & \ddots & & & \\ & & & \sigma_N & 0 \cdots & 0 \end{bmatrix} \tag{4.18}$$

which contains non-negative, real diagonal elements. With row operations, the structure of $\mathbf{\Sigma}$ was enforced to have the ranking $\sigma_1 \geq \sigma_2 \geq \ldots \geq \sigma_N \geq 0$. Thus, POD enforces not only that the singular values of $\mathbf{\Sigma}$ are arranged in descending order, but also enforces orthogonality in $\mathbf{U}$ and $\mathbf{V}$.

To explain why SVD is an appropriate method for completing POD, the following derivation will show that by enforcing orthogonality in $\mathbf{U}$ and $\mathbf{V}$ we have solved a simplified form of a covariance eigenvalue problem. Thus, this method allows one to approximate the eigenvalues and eigenvectors of the covariance which exists in the acquired data. Each eigenvalue and eigenvector will together represent a single mode of fluctuation which exists in $\mathbf{A}$. As will be discussed below, the constraints of SVD allow for an optimal reconstruction of $\mathbf{A}$ according to the covariance of each mode, which is a representation of the energy contribution of the spatio-temporal fluctuations of each mode present in the image. This estimate of energy contribution is with regard to pixel intensity variations only, and is not quantitatively correlated with energy. Therefore, this study will use singular values and eigenvalues as a measure of pixel intensity variance for a single mode rather than a measure of energy. First, consider the $M \times M$ covariance matrix $\mathbf{R} = \widetilde{\mathbf{A}}^T \widetilde{\mathbf{A}}$, or in continuous form

$$\mathbf{R}_{ij} = \sum_{k=1}^{N} a_{ki} a_{kj}. \tag{4.19}$$

$\mathbf{R}_{ij}$ is the product of the intensity fluctuations of the i^{th} pixel and the j^{th} pixel, hence $\mathbf{R}$ is the covariance of intensity throughout the image. When used within a POD algorithm,

the orthogonality constraint of SVD allows one to solve an eigenvalue problem for $\mathbf{R}$ with real, non-negative eigenvalues.

With $\widetilde{\mathbf{A}} = \mathbf{U}\mathbf{\Sigma}\mathbf{V}^T$, the covariance matrix can be rewritten as

$$\mathbf{R} = \mathbf{V}\mathbf{\Sigma}^T\mathbf{U}^T\mathbf{U}\mathbf{\Sigma}\mathbf{V}^T. \tag{4.20}$$

If we assume that $\mathbf{U}$ is orthogonal then $\mathbf{U}^T\mathbf{U}$ is equal to the identity matrix and

$$\mathbf{R} = \mathbf{V}\mathbf{\Sigma}^T\mathbf{\Sigma}\mathbf{V}^T. \tag{4.21}$$

Now, define $\mathbf{\Lambda}$ as the product of the singular value matrix and its transpose ($\mathbf{\Lambda} = \mathbf{\Sigma}^T\mathbf{\Sigma}$), which by definition is the diagonal matrix

$$\mathbf{\Lambda} = \begin{bmatrix} \sigma_1^2 & & & & & & \\ & \sigma_2^2 & & & & & \\ & & \ddots & & & & \\ & & & \sigma_N^2 & & & \\ & & & & 0 & & \\ & & & & & \ddots & \\ & & & & & & 0 \end{bmatrix}, \tag{4.22}$$

where $\mathbf{\Lambda}_{ij} = 0$ for $i > N$ or $j > N$ and the same form is reached by dropping zero columns from $\mathbf{\Sigma}$ to increase computational efficiency. Multiplying both sides of eqn. 4.21 by $\mathbf{V}$ and enforcing orthogonality in $\mathbf{V}$ leads to the desired eigenvalue problem

$$\mathbf{R}\mathbf{V} = \mathbf{V}\mathbf{\Lambda}, \tag{4.23}$$

which is the general form of an eigenvalue problem. An eigenvalue problem defines a non-zero vector that, when multiplied by a square matrix, yields a constant multiple of the non-zero vector. Here, the constant multiplier is $\mathbf{\Lambda}$, and the vector is $\mathbf{V}$. In other words, $\mathbf{V}$ contains the eigenvectors of $\mathbf{R}$ and $\mathbf{\Lambda}$ contains the eigenvalues. By the

definition of the covariance matrix ($\mathbf{R} = \widetilde{\mathbf{A}}^T\widetilde{\mathbf{A}}$), $\mathbf{R}$ is both real and symmetric, because $\widetilde{\mathbf{A}}$ contains real data. Also, following the proof in appendix A.2, $\mathbf{R}$ is positive semidefinite. For any eigenvalue problem where the square matrix $\mathbf{R}$ is real, symmetric, and positive semidefinite, the eigenvector solutions will be orthogonal, i.e. $\mathbf{V}$ is orthogonal. In addition, this state requires that the eigenvalues σ_i^2 are real and non-negative. Finally, this gives real, non-negative values for σ_i and allows rows of $\mathbf{\Sigma}$ to be ranked such that $\sigma_1 \geq \sigma_2 \geq \ldots \geq \sigma_N \geq 0$. The above derivation of the covariance eigenvalue problem is not part of the POD algorithm employed in this study, but can be used in other POD schemes which do not utilize SVD. The derivation is given here to explain why SVD provides a valid reconstruction of the data matrix $\widetilde{\mathbf{A}}$. By enforcing $\mathbf{U}$ and $\mathbf{V}$ to be orthogonal, SVD reaches a solution equivalent to the solution of the covariance eigenvalue problem, thus computing eigenvalues and eigenvectors of the covariance matrix.

4.5.2 Application of Proper Orthogonal Decomposition

Proper orthogonal decomposition was applied to shear-coaxial jet high speed image sets with three objectives:

- qualify the appearance of the most dominant mode
- quantify the frequency of the most dominant mode
- quantify the relative significance of the natural mode and the forced mode occurring within a single acoustically forced flow condition

To reach these objectives, a POD algorithm written in MATLAB was used to reach a solution for the orthogonal matrices $\mathbf{U}$ and $\mathbf{V}$ and the diagonal matrix of singular values $\mathbf{\Sigma}$ for a pixel data matrix $\mathbf{A}$. For a given flow condition, a set of back-lit images was reduced to capture only the pertinent portion of the field of view. The 320×640 field of view was reduced in width and height to only include the jet, thus decreasing

the number of columns M in the aggregate matrix $\mathbf{A}$ and reducing computational time. Figure 4.20 shows a snapshot example, as well as the cropped field of view. The image acquisition rate and duration were chosen to create instability frequency spectra for an appropriate frequency range and resolution. First, the image sampling rate was 10 kHz, which provides a Nyquist frequency of 5 kHz. Second, the number of rows N in matrix $\mathbf{A}$, i.e. the number of images, was 2000. This was chosen to maintain acceptable computational efficiency while providing sufficient frequency resolution, which was 2.5 Hz (=5000Hz/2000). After subtracting the average image from each instantaneous image frame as in eqn. 4.14, SVD was applied to $\widetilde{\mathbf{A}}$ to determine $\mathbf{U}$, $\mathbf{\Sigma}$, and $\mathbf{V}$, which must be analyzed further to obtain mode shapes and frequencies.

Following SVD of $\widetilde{\mathbf{A}}$, additional data reductions were applied to further reduce computational time. Since $N << M$, only the first N diagonal elements of $\mathbf{\Sigma}$ and the first N columns of $\mathbf{V}$ are non-zero. Consequently, $\mathbf{\Sigma}$ and $\mathbf{V}$ were reduced to $N \times N$ and $M \times N$ matrices, respectively. By convention, since the singular values are arranged in descending order of magnitude, the columns of $\mathbf{U}$ and $\mathbf{V}$, which represent an orthonormal bases set of the column and row space of $\widetilde{\mathbf{A}}$, respectively, were arranged to match the order of $\mathbf{\Sigma}$.

Moreover, each column of $\mathbf{Q} = \mathbf{U\Sigma}$, equivalent to $u_k(t)$ in eqn. 4.13, is a vector of time-dependent amplitude coefficients, while the columns of $\mathbf{V}$ are the proper orthogonal modes. The columns of $\mathbf{V}$ are eigenvectors, or can also be called eigenfunctions. Therefore, the first column of $\mathbf{Q}$ contains the temporal characteristics of the coherent flow structure of the first mode, which contained the highest variance contribution to the flow. Meanwhile, the first column of $\mathbf{V}$ contains the spatial distribution of the first mode, and so on, for subsequent columns of $\mathbf{Q}$ and $\mathbf{V}$. As an example, Fig. 4.21 shows a plot of the singular values for all modes in the image set of an acoustically forced flow. The set of eigenvalues for this flow condition is calculated as $\Lambda_i = \sigma_i^2$, and is plotted

in Figure 4.22, which can also be regarded as the energy spectrum for the image set, because each eigenvalue is a representation of variance magnitude for a single mode. For this case, the spatial distribution of the flow was reconstructed using only the first mode, corresponding to the mode with the maximum eigenvalue in Fig. 4.22. The reconstruction of mode-1 is shown in Fig. 4.23b using the first column of $\mathbf{V}$; this is called the proper orthogonal mode (POM) image, or eigenvector. The spatial distributions of subsequent modes could be constructed similarly from the remaining columns of $\mathbf{V}$. For example, the second column of $\mathbf{V}$ is used to reconstruct mode-2, and the POM image is shown in Fig. 4.23c. By subtracting out the average pixel intensities prior to SVD processing, POM images will reveal lobes of dark and light regions to indicate locations where fluid was present and absent as it emanated from the dense inner jet flow. The uniform regions colored gray indicate a mean level in a gray-scaled image. Intuitively, the POM images will provide qualitative results regarding symmetry or asymmetry for a given mode. A jet located at a PN, for example, adopts an antisymmetric instability as shown in Fig. 4.23.

Analysis of the time-dependent amplitude coefficients found in $\mathbf{Q}$ can be used to produce power spectral density (PSD) plots corresponding to each POM. Fig. 4.24 shows a PSD plot for mode-1 obtained from the first column of $\mathbf{Q}$. This is the same mode as shown in Fig. 4.23a. Similar to the measurement of experimental velocity oscillation frequencies using a hot-wire anemometer, Fig. 4.24 provides an indication of flow fluctuations, but only for a single mode. Rather than using an intrusive probe, POD allows one to study oscillations in flow as manifested by density gradients visualized in shadowgraph images. A peak in PSD denotes a recurring flow structure that originates from the inner shear layer with the associated peak frequency.

After forming POM images and PSD plots for a set of high-speed images, one must use both of these outcomes to find the most dominant, *convective* mode in the flow. To

be labeled as the most dominant mode, a solution must meet two requirements. First, its eigenvalue must be greater than those of other modes. In the most simple case, the first eigenvalue is the largest, and therefore the corresponding mode would be the most dominant. Although, a second requirement adds complexity and even subjectivity to the process of determining the most dominant mode. A convective shear-layer instability, or traveling vortex, will be represented by a conjugate POM pair rather than a single POM. Arienti and Soteriou [154] define conjugate mode pairs as any two modes whose cross power spectra magnitude peaks near a phase of 90° and are represented by similar lobe patterns. Following Arienti and Soteriou [154], the cross power spectral density (CPSD) of a conjugate mode pair with temporal amplitude coefficients, a_k and b_k was computed as

$$\text{CPSD} = \sum_{s=0}^{N-1} \text{corr}\left(a_k, b_k\right) e^{-i\omega s} \tag{4.24}$$

where $\text{corr}(a_k, b_k)$ represents the cross-correlation of a_k and b_k. For the same acoustically forced condition shown in Fig. 4.24, the CPSD magnitude of mode-1 and mode-2 is shown in Fig. 4.25 along with the phase difference. The magnitude spectra reveals a peak instability at the forcing frequency, $f_F = 2050$ Hz, and a phase difference of 90° also occurs at 2050 Hz. When choosing to pair mode-1 and mode-2 as a single flow instability, Fig. 4.23 can also be used to add confidence. In Fig. 4.23, the reconstructed POM images of mode-1 and mode-2 show the same visual features simply shifted $90'$ in direction of convection, supporting the pairing of these modes as a single flow phenomenon. In conclusion, because this study seeks to describe convective waves within the jet, an instability having a large energy contribution to the flow must consist of a conjugate mode pair in addition to highly ranked eigenvalues.

Using the post-processing methods described above, the mode identified as most dominant will be described qualitatively by using the POM images from $\mathbf{V}$ and quantitatively by using the PSD of the conjugate mode pair. To meet the final objective

of comparing the significance of natural jet modes and acoustically forced jet modes, a measure of variance contribution will be calculated using the entire collection of N singular values. The pixel intensity variance contribution of a POM pair is calculated as

$$\Psi = \frac{\sigma_{k_1}^2 + \sigma_{k_2}^2}{\sum_{k=1}^{N} \sigma_k^2} \tag{4.25}$$

where $\sigma_{k_1}^2$ and $\sigma_{k_2}^2$ are the eigenvalues of mode-k_1 and mode-k_2 and the denominator is the sum of all eigenvalues. As noted earlier, the eigenvalue of a mode is equal to the square of the singular value for that mode ($\Lambda = \sigma^2$). Mode-k_1 and mode-k_2 are not necessarily mode-1 and mode-2. In conclusion, this method is used for comparing co-existing modes. In an acoustically forced flow system, a natural instability can maintain an energy contribution greater than or less than the mode asserted by forcing, and Ψ quantifies their relative importance.

4.5.3 Dynamic Mode Decomposition

Like POD, DMD allows one to reconstruct a data matrix in an approximate form, projecting large-scale motions onto a solution which neglects noise and maintains significantly fewer degrees of freedom. In eqn. 4.13, the pixel intensity values contained in a are organized to create an ordinary differential equation with temporal and spatial information separated in the variables u and v, respectively. To best describe DMD, a is written in a similar fashion, but with an amplitude coefficient included, i.e.

$$a(x,t) = \sum_{k=1}^{N} a_k' d_k(t) \phi_k(x). \tag{4.26}$$

In this form, d_k contains the temporal information, ϕ_k contains the spatial information or dynamic modes, and a_k' is the amplitude of each mode k. Note that the amplitude coefficient is only dependent on the mode number. The time-dependent function d_k takes a sinusoidal form as $d_k = \exp(\omega_k t)$, where ω_k represents the complex frequency of

mode k. ($\exp(ix) = \cos x + i\sin x$) Since sines and cosines are orthogonal, this form of d_k makes a DMD reconstruction orthogonal in *time*, whereas a POD reconstruction is orthogonal in *space* [152].

Dynamic mode decomposition proceeds by assuming that if $\mathbf{A}$ represents a series of snapshots $\mathbf{a}$ where $\mathbf{a}_1 = \mathbf{a}(x_1, t_1)$ from image 1 to image N. We can write $\mathbf{A}$ as

$$\mathbf{A} = \mathbf{A}_1^N = \{\mathbf{a}_1, \mathbf{a}_2, \mathbf{a}_3, \ldots, \mathbf{a}_N\}, \tag{4.27}$$

then a linear mapping $\mathbf{S}$ connects any flow field $\mathbf{a}_i$ to a subsequent flow field $\mathbf{a}_{i+1}$, that is,

$$\mathbf{S}\mathbf{a}_i = \mathbf{a}_{i+1}. \tag{4.28}$$

In complete form, eqn. 4.28 follows as

$$\begin{bmatrix} s_{11} & s_{12} & \cdots & s_{1M} \\ s_{21} & s_{22} & \cdots & s_{2M} \\ \vdots & & \ddots & \vdots \\ s_{M1} & s_{M2} & \cdots & s_{MM} \end{bmatrix} \begin{bmatrix} a_{1i} \\ a_{2i} \\ \vdots \\ a_{Mi} \end{bmatrix} = \begin{bmatrix} a_{1(i+1)} \\ a_{2(i+1)} \\ \vdots \\ a_{M(i+1)} \end{bmatrix}. \tag{4.29}$$

This linear mapping is assumed to be the same over the entire sampling interval $0 < t \leq (N-1)\Delta t$, which is a linear tangent approximation. If we apply the linear tangent approximation to the next flow field, then $\mathbf{a}_{i+2} = \mathbf{S}\mathbf{S}\mathbf{a}_i = \mathbf{S}^2\mathbf{a}_i$, or for all $i \geq 2$ we have $\mathbf{a}_i = \mathbf{S}^{i-1}\mathbf{a}_1$. Using this method for the entire sequence of N flow fields gives a Krylov sequence for $\mathbf{A}_1^N$,

$$\mathbf{A}_1^N = \left\{\mathbf{a}_1, \mathbf{S}\mathbf{a}_1, \mathbf{S}^2\mathbf{a}_1, \ldots, \mathbf{S}^{N-1}\mathbf{a}_1\right\}. \tag{4.30}$$

This formula allows one to predict an entire sequence of flow fields using only a single snapshot $\mathbf{a}_1$, but requires a known $\mathbf{S}$ ($M \times M$), which is a complete and exact mapping of the flow field. Although, when applying reduced basis methods to experimental imaging results, $\mathbf{S}$ is unknown. On the other hand, the entire flow field sequence $\mathbf{A}_1^N$ is known. Thus, rather than determining $\mathbf{A}_1^N$ using a complete $\mathbf{S}$ and a limited amount of data as

in eqn. 4.30, DMD determines a limited form of $\mathbf{S}$ using the known data matrix $\mathbf{A}_1^N$. To this end, eqn. 4.30 is rewritten to better utilize the data matrix and factor out the unknown $\mathbf{S}$. Namely,

$$\begin{aligned} \mathbf{A}_2^N &= \{\mathbf{a}_2, \mathbf{a}_3, \ldots, \mathbf{a}_N\} &&= \left\{\mathbf{S}\mathbf{a}_1, \mathbf{S}^2\mathbf{a}_1, \ldots, \mathbf{S}^{N-1}\mathbf{a}_1\right\} \\ &= \mathbf{S}\left\{\mathbf{a}_1, \mathbf{S}\mathbf{a}_1, \ldots, \mathbf{S}^{N-2}\mathbf{a}_1\right\} \\ &= \mathbf{S}\mathbf{A}_1^{N-1}, \end{aligned} \tag{4.31}$$

which is the reduced form of the linear tangent approximation for the entire sequence of images. A DMD algorithm aims to extract the eigenvalues (time-dependent magnitudes), eigenvectors (spatial distributions), and amplitudes from the dynamical process described by $\mathbf{S}$ based on the pixel data contained in $\mathbf{A}_1^N$.

In addition to the linear tangent assumption, a second assumption is made. If the physical process represented by an experimental image set, or represented by a numerical flow field in the case of computational fluid dynamics, is periodic and steady in the mean, then after a critical number of flow field snapshots have been acquired there will not be new information presented in any of the following snapshots. Additional images will only contain phenomena already captured in the previous set of images. Mathematically, a critical number of snapshots $N-1$ is reached such that $\mathbf{a}_N$ is linearly dependent on the previous $N-1$ snapshots. Thus, each of the vectors $\mathbf{a}_1, \mathbf{a}_2, \ldots, \mathbf{a}_{N-1}$ are linearly independent, but $\mathbf{a}_N$ can be written as a linear combination of those vectors when the correct mapping is applied, i.e.

$$\mathbf{a}_N = g_1\mathbf{a}_1 + g_2\mathbf{a}_2 + \ldots + g_{N-1}\mathbf{a}_{N-1}. \tag{4.32}$$

Since the mapping coefficients $g_1, g_2, \ldots, g_{N-1}$ are scalars, eqn. 4.32 can written in

matrix form as

$$\begin{bmatrix} a_{1N} \\ a_{2N} \\ \vdots \\ \vdots \\ a_{MN} \end{bmatrix} = \begin{bmatrix} a_{11} & a_{12} & \cdots & a_{1(N-1)} \\ a_{21} & a_{22} & \cdots & a_{2(N-1)} \\ \vdots & & & \vdots \\ \vdots & & & \vdots \\ a_{M1} & a_{M2} & \cdots & a_{M(N-1)} \end{bmatrix} \begin{bmatrix} g_1 \\ g_2 \\ \vdots \\ g_{N-1} \end{bmatrix}, \tag{4.33}$$

or simply

$$\mathbf{a}_N = \mathbf{A}_1^{N-1}\mathbf{g}. \tag{4.34}$$

Note that the vector $\mathbf{g}$ is on the right of $\mathbf{A}_1^{N-1}$. Further, if we create a matrix $\widetilde{\mathbf{S}}$ then $\mathbf{A}_2^N$ can be written as

$$\begin{aligned} \mathbf{A}_2^N &= \{\mathbf{a}_2, \mathbf{a}_3, \mathbf{a}_4, \ldots, \mathbf{a}_N\} \\ &= \left\{\mathbf{a}_2, \mathbf{a}_3, \mathbf{a}_4, \ldots, \mathbf{A}_1^{N-1}\mathbf{g}\right\} \\ &= \mathbf{A}_1^{N-1}\widetilde{\mathbf{S}}, \end{aligned} \tag{4.35}$$

which is the reduced form of the linear combination assumption. This form may only be used when $\widetilde{\mathbf{S}}$ is taken as a companion matrix, meaning that all columns of $\widetilde{\mathbf{S}}$ serve as placeholders except for the last column containing the linear combination coefficients of $\mathbf{g}$. The complete companion matrix is

$$\widetilde{\mathbf{S}} = \begin{bmatrix} 0 & & & & g_1 \\ 1 & 0 & & & g_2 \\ & \ddots & \ddots & & \vdots \\ & & 1 & 0 & g_{N-2} \\ & & & 1 & g_{N-1} \end{bmatrix}. \tag{4.36}$$

where the coefficients $\{g_1, g_2, \ldots, g_{N-1}\}$ are unknown. The matrix form of 4.35 is

$$\begin{bmatrix} a_{12} & a_{13} & \cdots & a_{1N} \\ a_{22} & a_{23} & \cdots & a_{2N} \\ \vdots & & & \vdots \\ \vdots & & & \vdots \\ a_{M2} & a_{M3} & \cdots & a_{MN} \end{bmatrix} = \begin{bmatrix} a_{11} & a_{12} & \cdots & a_{1(N-1)} \\ a_{21} & a_{22} & \cdots & a_{2(N-1)} \\ \vdots & & & \vdots \\ \vdots & & & \vdots \\ a_{M1} & a_{M2} & \cdots & a_{M(N-1)} \end{bmatrix} \begin{bmatrix} 0 & & & & g_1 \\ 1 & 0 & & & g_2 \\ & \ddots & \ddots & & \vdots \\ & & 1 & 0 & g_{N-2} \\ & & & 1 & g_{N-1} \end{bmatrix}. \tag{4.37}$$

Finally, joining the linear combination assumption with the linear tangent approximation, $\widetilde{\mathbf{S}}$ is clearly an approximated version of the complete mapping $\mathbf{S}$, because

$$\mathbf{S}\mathbf{A}_1^{N-1} = \mathbf{A}_2^N = \mathbf{A}_1^{N-1}\widetilde{\mathbf{S}}. \tag{4.38}$$

With $\mathbf{A}_2^N$ as the single-stepped advancement of $\mathbf{A}_1^{N-1}$, the i^{th} column of $\mathbf{A}_2^N$ is equal to the $(i+1)^{th}$ column of $\mathbf{A}_1^{N-1}$ for $i = 1, 2, \ldots, N-2$. These two data matrices are used to find the last column of $\widetilde{\mathbf{S}}$, whose eigenvalues approximate some of the eigenvalues of $\mathbf{S}$. Hence, it is our objective to determine an approximate mapping $\widetilde{\mathbf{S}}$ which serves as a reduced version of $\mathbf{S}$.

At this point in the derivation, the remaining steps vary depending on the specific DMD algorithm employed. Regardless, the objective is to formulate and solve an eigenvalue problem for the approximate mapping matrix. The general version described here utilizes a proper orthogonal decomposition basis, whereas other DMD methods use entirely different steps in order to define an eigenvalue problem for the companion matrix $\widetilde{\mathbf{S}}$. Proceeding with the general method described by Jovanovic *et al.* [155], the displaced data matrix $\mathbf{A}_2^N$ and a singular value decomposition of the initial matrix $\mathbf{A}_1^{N-1}$ are used to evaluate a transformed arrangement of $\widetilde{\mathbf{S}}$. By definition, the SVD of $\mathbf{A}_1^{N-1}$ is

$$\mathbf{A}_1^{N-1} = \mathbf{U}\boldsymbol{\Sigma}\mathbf{V}^H, \tag{4.39}$$

where $\mathbf{U}$ and $\mathbf{V}$ are orthogonal and $\boldsymbol{\Sigma}$ represents the energy content for each mode, i.e.

singular values. Then, the right-hand portion of eqn. 4.38 can be written as

$$\mathbf{A}_2^N = \mathbf{U}\mathbf{\Sigma}\mathbf{V}^H\widetilde{\mathbf{S}}. \tag{4.40}$$

Multiplying eqn. 4.40 by $\mathbf{U}^H$ on the left and $\mathbf{V}\mathbf{\Sigma}^{-1}$ on the right gives

$$\mathbf{U}^H\mathbf{A}_2^N\mathbf{V}\mathbf{\Sigma}^{-1} = \mathbf{\Sigma}\mathbf{V}^H\widetilde{\mathbf{S}}\mathbf{V}\mathbf{\Sigma}^{-1}, \tag{4.41}$$

This equation is a new form of $\mathbf{A}_2^N = \mathbf{A}_1^{N-1}\widetilde{\mathbf{S}}$ which includes the singular value decomposition of $\mathbf{A}_1^{N-1}$. For this reason, the general version of DMD can be described as application of the POD modes of $\mathbf{A}_1^{N-1}$ onto the dynamic mode decomposition of $\mathbf{A}_1^N$.

Along these lines, the general version continues by redefining the approximate map, which was defined as $\widetilde{\mathbf{S}}$, as a transformation of $\widetilde{\mathbf{S}}$ using the POD modes of $\mathbf{A}_1^{N-1}$. Remember, $\widetilde{\mathbf{S}}$ is known from eqn. 4.37. As done in Jovanovic *et al.* [155], the transformed companion matrix is equivalent to the right hand side of 4.41, and will be called $\widetilde{\mathbf{S}}'$. In other words,

$$\widetilde{\mathbf{S}}' = \mathbf{\Sigma}\mathbf{V}^H\widetilde{\mathbf{S}}\mathbf{V}\mathbf{\Sigma}^{-1}. \tag{4.42}$$

Eqn. 4.42 provides a known $\widetilde{\mathbf{S}}'$ which allows one to readily formulate a general eigenvalue problem for $\widetilde{\mathbf{S}}'$ which is similar to the eigenvalue problem for $\mathbf{R}$ formulated for POD. The eigenvalue problem for $\widetilde{\mathbf{S}}'$ follows as

$$\widetilde{\mathbf{S}}'\mathbf{X} = \mathbf{X}\mathbf{D}, \tag{4.43}$$

where $\mathbf{D}$ is a matrix of the eigenvalues $d_k(t)$ as in eqn. 4.26. The matrix $\mathbf{X}$ contains eigenvectors which are used to form the dynamic modes $\phi_k(x)$. One can readily solve the eigenvalue problem to determine the time-dependent function $d_k(t)$ and the spatially dependent function $\phi_k(x)$, which are the outputs desired to complete a limited reconstruction of the flow field. To reach this point, constraints have not been placed on the eigenvectors and eigenvalues; both can be negative, imaginary, and need not be orthogonal. Instead, several other assumptions were made to obtain the correct form in eqn.

4.43. First, the linear tangent assumption was made to relate $\mathbf{A}_1^{N-1}$ with $\mathbf{A}_2^N$ using the linear mapping $\mathbf{S}$. Second, the mapping $\mathbf{S}$ was approximated as the companion matrix $\widetilde{\mathbf{S}}$ by way of the linear combination of a critical number of images N. Last, the initial data matrix $\mathbf{A}_1^{N-1}$ was decomposed using SVD as in the POD algorithm of the previous section. Since $\mathbf{S}\mathbf{A}_1^{N-1} = \mathbf{A}_2^N$, this step is referred to as a projection of the linear operator $\mathbf{S}$ onto a POD basis, which is advantageous for reasons discussed in section 4.5.4.

The preceding derivation of DMD is only one possible procedure for completing the decomposition. A second method of DMD, the full-rank method, utilizes a QR decomposition, $\mathbf{A}_1^{N-1} = \mathbf{QR}$, rather than SVD. Here, $\mathbf{Q}$ and $\mathbf{R}$ should not be confused with the nomenclature of section 4.5.1. The full-rank method though, does not provide an order to the identified modes. A magnitude of energy content is not distinguished in QR decomposition as in SVD. As will be shown in the following section, the computation of singular values in the general method enables the ranking of flow instability amplitude: a paramount objective of this study.

4.5.4 Application of Dynamic Mode Decomposition

Dynamic mode decomposition was employed with the same three objectives as the application of POD. Rather than use this algorithm to analyze all experimental flow conditions, a limited number of cases were analyzed using DMD with the primary purpose of comparing the effectiveness of DMD with that of POD. The conclusions gained from this comparison are offered in Section 5.2.

Similar to POD, an algorithm was written in MATLAB to process high speed image sets captured at a frame rate of 10 kHz and store the pixel intensity data in $\mathbf{A}$. In contrast to POD, DMD uses the raw gray-scale intensities to form $\mathbf{A}_1^{N-1}$ and $\mathbf{A}_2^N$ directly rather than subtracting the mean [152]. Then, the matrix $\widetilde{\mathbf{S}}'$ was found using eqns. 4.39 and 4.42, in that order. With a known $\widetilde{\mathbf{S}}'$, the eigenvalue problem in eqn. 4.43 was solved

using a MATLAB built-in function, giving the complex eigenvector matrix

$$\mathbf{X} = \begin{bmatrix} x_{r11} + ix_{i11} & x_{r12} + ix_{i12} & & \\ x_{r21} + ix_{i21} & x_{r22} + ix_{i22} & & \\ & & \ddots & \\ & & & x_{rnn} + ix_{inn} \end{bmatrix} \tag{4.44}$$

and complex eigenvalue matrix

$$\mathbf{D} = \begin{bmatrix} d_{r1} + id_{i1} & 0 & & \\ 0 & d_{r2} + id_{i2} & & \\ & & \ddots & \\ & & & d_{rn} + id_{in} \end{bmatrix}, \tag{4.45}$$

where $\{d_{r1} = d_{r2}, d_{r3} = d_{r4}, \ldots, d_{r(n-1)} = d_{rn}$ and $\{d_{i1} = -d_{i2}, d_{i3} = -d_{i4}, \ldots, d_{i(n-1)} = -d_{in}$. These two matrices are processed to form the complex frequencies and images which represent each mode.

As stated earlier, the matrix $\mathbf{D}$, made up of the individual eigenvalues d_k for each mode, is a periodic form of the frequency of mode k such that

$$d_k = \exp\left(\omega_k \Delta t\right). \tag{4.46}$$

Consequently, the complex frequency ω_k was calculated as

$$\omega_k = \omega_r + i\omega_i = \frac{\ln(d_k)}{2\pi\Delta t}, \tag{4.47}$$

and $\Delta t = 1/(10 \text{ kHz}) = 0.1$ ms. The real component ω_r is the mode growth rate and the imaginary component ω_i is the mode frequency in Hertz. As depicted by the preceding calculation of ω_i, each mode is marked with a single frequency (a scalar) rather than a frequency spectrum (a vector). Meanwhile, the dynamic mode matrix $\mathbf{\Phi}$, made up of the dynamic modes ϕ_k for each mode, is determined using the eigenvector matrix $\mathbf{X}$ and $\mathbf{U}$. Simply stated,

$$\mathbf{\Phi} = \mathbf{UX}. \tag{4.48}$$

Each column of $\mathbf{\Phi}$ is a spatial distribution of the flow field for a single mode, and a linear combination of several columns of $\mathbf{\Phi}$ manifests a simplified reconstruction of the flow field neglecting all other modes and insignificant noise.

As a demonstration of this DMD algorithm, the same set of images used to create the POD results in Section 4.5.2 was analyzed with DMD. Because the flow field subject to analysis was acoustically forced, DMD is expected to reveal a coherent mode with $\omega_i = f_F$. In the top plot of Fig. 4.26 the wave growth rate ω_r is plotted versus ω_i for an LN_2-GHe flow condition coupled with acoustic forcing at a PN for $f_F = 2050$ Hz. The mode resulting from acoustic forcing is easily identified at 2050 Hz, with a slightly positive growth rate, identifying an unstable mode. With the exception of the mean flow represented by a point at the origin, all other modes are stable and are analogous to modes with low-ranked singular values as computed using POD. The spectrum of Fig. 4.26 is symmetric about the $\omega_i = 0$ axis, because all pixel intensity data contained real values. Complex data will generally result in an asymmetric appearance about the $\omega_i = 0$ axis.

For this study though, a measure of amplitude of pixel intensity fluctuations, or energy contribution, is more useful for identifying the significance of a given mode. Accordingly, amplitude was calculated using the method by Schmid [156], which follows as

$$\mathbf{a} = \frac{1}{\left\|\mathbf{V}\mathbf{\Sigma}^{-1}\mathbf{X}\right\|}, \tag{4.49}$$

which can be interpreted as a matrix containing magnitudes of each vector in the two-dimensional space created by the product $\mathbf{V}\mathbf{\Sigma}^{-1}\mathbf{X}$. The value of $\mathbf{a}$ is proportional to a'_k in eqn. 4.26. Most importantly, amplitude relies on the singular values created by SVD, a step not included in the full-rank version of DMD. Further, the foundation of DMD does not include a ranking of modes in the linear tangent approximation, nor in the linear combination assumption of eqn. 4.32. Thus, multiple mode ranking techniques

for DMD algorithms have been explored in an effort to simplify flows using only the most important modes. Singular values alone though, impart the energy contribution of an entire spectra as in Fig. 4.24, not the magnitude at a distinct frequency. Thus, eqn. 4.49 relates the energy contributions held in $\mathbf{\Sigma}$ to a single eigenvector in $\mathbf{X}$. As shown in the lower plot of Fig. 4.26, DMD results convey the highest amplitude for the mean flow, a result which is in agreement with other DMD studies [152, 156, 157]. High amplitudes are also observed at $|\omega_i| = f_F = 2050$ Hz. This is expected for an acoustically forced jet in which the shear layer adopts the acoustic instability as the dominant mode.

A final form of verification lies in the realm of visualization. Like the POM images created using POD, the dynamic mode images of DMD are used for qualitative conclusions, such as jet symmetry or lack thereof. As an example, Fig. 4.27 displays the reconstructed images of one unstable mode shown by the cyan point in Fig. 4.26 where $[\omega_i, \omega_r] = [2050, 6.022]$. Characteristic of PN forcing, Fig. 4.27 shows an antisymmetric jet [29, 30]. The real and imaginary eigenvector images corresponding to ϕ_r and ϕ_i, respectively, are shown to be inherently conjugate by the location of lobes in each image in Fig. 4.27, which are 90° out-of-phase. This pairing occurs for the real and imaginary values found in each column of $\mathbf{\Phi}$, and thus results from the algorithm rather than a choice made by the user. This is one of many differences between DMD and POD, as will be discussed in chapter 5.

4.6 Measurement Uncertainty

The experimental results presented in this study derive from three measured quantities: pressure, temperature, and mass flow rate. These three measurements determine density ρ, velocity U, momentum flux M, and the ratios thereof (S, R, J). Although injector geometry is also used to determine velocity and momentum flux, the uncertainty of injector dimensions was made negligible by using the "as machined" dimensions with

an uncertainty of 0.013 mm (0.0005 in). Also, the precision error of pressure, temperature, and mass flow rate will be ignored due to their small relevance in comparison to bias error. This simplification is valid for two reasons. First, high signal-to-noise ratios were maintained by constructing well-shielded data transfer cables. Second, this study's reported measurements are time-averaged for steady flow conditions. Unsteady measurements, mainly dynamic pressure, were phase-averaged to obtain a mean p' value over more than 10,000 acoustic cycles.

For the inner and outer jets, exit velocities were determined using the relation

$$U_k = \frac{\dot{m}_k}{\rho_k A_k}, \tag{4.50}$$

where k is ij for the inner jet and oj for the outer jet. Following propagation of uncertainty principles of Mills and Chang [139], the uncertainty of U_k can be calculated as

$$\delta U_k = U_k \sqrt{\left(\frac{\delta \dot{m}_k}{\dot{m}_k}\right)^2 + \left(\frac{\delta \rho_k}{\rho_k}\right)^2 + \left(\frac{\delta A_k}{A_k}\right)^2} = U_k \sqrt{\left(\frac{\delta \dot{m}_k}{\dot{m}_k}\right)^2 + \left(\frac{\delta \rho_k}{\rho_k}\right)^2} \tag{4.51}$$

and the uncertainty of the momentum flux, $M_k = \frac{\dot{m}_k^2}{\rho_k A_k}$, is

$$\delta M_k = M_k \sqrt{4\left(\frac{\delta \dot{m}_k}{\dot{m}_k}\right)^2 + \left(\frac{\delta \rho_k}{\rho_k}\right)^2 + \left(\frac{\delta A_k}{A_k}\right)^2} = M_k \sqrt{4\left(\frac{\delta \dot{m}_k}{\dot{m}_k}\right)^2 + \left(\frac{\delta \rho_k}{\rho_k}\right)^2}. \tag{4.52}$$

A combination of vendor calibrations and on-site calibrations provide the measurement uncertainties for each instrument. Temperatures measured with both type E and type R thermocouples will be reported with uncertainties according to data published by the manufacturer, Omega. For the range of temperatures measured here, type E thermocouples have a bias uncertainty of ± 1 K while the bias uncertainty of type R thermocouples is ± 1.5 K. The Porter mass flow meters had a nonlinearity error of 1% full scale output (FSO) and a repeatability error of .2% FSO, as reported by Porter calibrations. This creates a combined nonlinearity and repeatability (CNLR) rating of

1.02%, which is the square root of the sum of squares of each source of error. With only negligible error present due to thermal effects, the CNLR is the total error of the mass flow meters. The CNLR and CNLRH ratings are standard methods for determining the static accuracy of an instrument for data without and with hysteresis, respectively. Thus, a mass flow rate uncertainty was chosen as the total error for the gas species of interest, because the FSO of each mass flow meter, and thus the total error, is altered by a change in species. The uncertainties for oxygen, nitrogen, helium, and hydrogen are 0.130 g/s, 0.119 g/s, 0.024 g/s, and 0.009 g/s, respectively. CNLRH ratings for all GP:50 static pressure transducers and Kulite dynamic pressure transducers were determined in calibrations performed on-site with a high pressure Ruska calibrator. Three different pressure transducer models were used for the pressure data reported in this study, each being used for separate purposes. Acoustic pressure fluctuations were measured with the Kulite Model XCE-093-50D, static pressures at room temperature were measured with the GP:50 Model 7200-8475, and static pressures at cryogenic temperatures were measured with the GP:50 Model 7720-JA-8474. For each of these three classifications of pressure measurement and corresponding sensor model, the total error applied to each category was drawn from calibration results of the *least accurate* single pressure transducer within that group. Values are listed in Table 4.2.

The inner and outer jet densities were evaluated based on chamber pressure and temperatures measured immediately upstream of the injector, using NIST REFPROP tables [158]. As shown in Fig. 4.5, density is primarily dependent on temperature when operating away from the saturation temperature. In this region, since density has a much weaker dependence on pressure than on temperature, the uncertainty in density due to pressure variation was deemed negligible. Thus, for measurement error analysis in this study, $\rho(p,T) \approx \rho(T)$.

Lastly, the uncertainties in momentum flux ratio and velocity ratio were calculated

as

$$\delta J = J\sqrt{\left(\frac{\delta M_{ij}}{M_{ij}}\right)^2 + \left(\frac{\delta M_{oj}}{M_{oj}}\right)^2} \tag{4.53}$$

and

$$\delta R = R\sqrt{\left(\frac{\delta U_{ij}}{U_{ij}}\right)^2 + \left(\frac{\delta U_{oj}}{U_{oj}}\right)^2}, \tag{4.54}$$

respectively. In chapter 5, error bars are included in several key plots to ameliorate clarity as one measures the accuracy of conclusions in this study. Conclusions are reached with an awareness of imperfect measurement techniques, and these error bars serve to quantify imperfections for the reader.

4.1: Dimensions of shear-coaxial injectors* used in AFRL experiments [23, 75].

Inj.	t [mm]	D_1 [mm]	$\frac{t}{D_1}$	D_2 [mm]	D_3 [mm]	D_4 [mm]	D_{eff} [mm]	$\frac{A_{oj}}{A_{ij}}$
I	0.53	0.51	1.05	1.59	2.42	3.18	1.05	12.9
II	0.13	1.40	0.09	1.65	2.44	3.94	1.53	1.65
III	1.24	1.47	0.84	3.96	4.70	6.35	2.72	2.90
IV	0.09	0.70	0.13	0.89	2.44	3.94	0.80	10.6
V	0.38	1.40	0.27	2.16	2.82	3.56	1.78	1.68

* Injector V is used for new experimental results presented in this study, while injectors I-IV were used in previous nonreactive experiments at AFRL.

4.2: Pressure transducer uncertainty values*.

Mfr.	Model	Nonlinearity	Repeatability	Hysteresis	Static Accuracy	Thermal Error	Total Error
Kulite	XCE-093-50D	.09%	.16%	.12%	.22%	-	.22%
GP:50	7720-JA-8474	.05%	.12%	.10%	.16%	.37%	.53%
GP:50	7200-8475	.06%	.12%	.12%	.18%	-	.18%

* Uncertainty values are taken as the total error of the instrument, listed here for each of the three transducer models used in this study. Static accuracy is the CNLRH rating calculated using the square root of the sum of squares method, and is the total error in the absence of significant error due to changes in temperature. For example, CNLRH= $\sqrt{(.06\%)^2 + (.12\%)^2 + (.12\%)^2} = .18\%$, which is the total error of pressures measured with the GP:50 7200-8475 at room temperature.

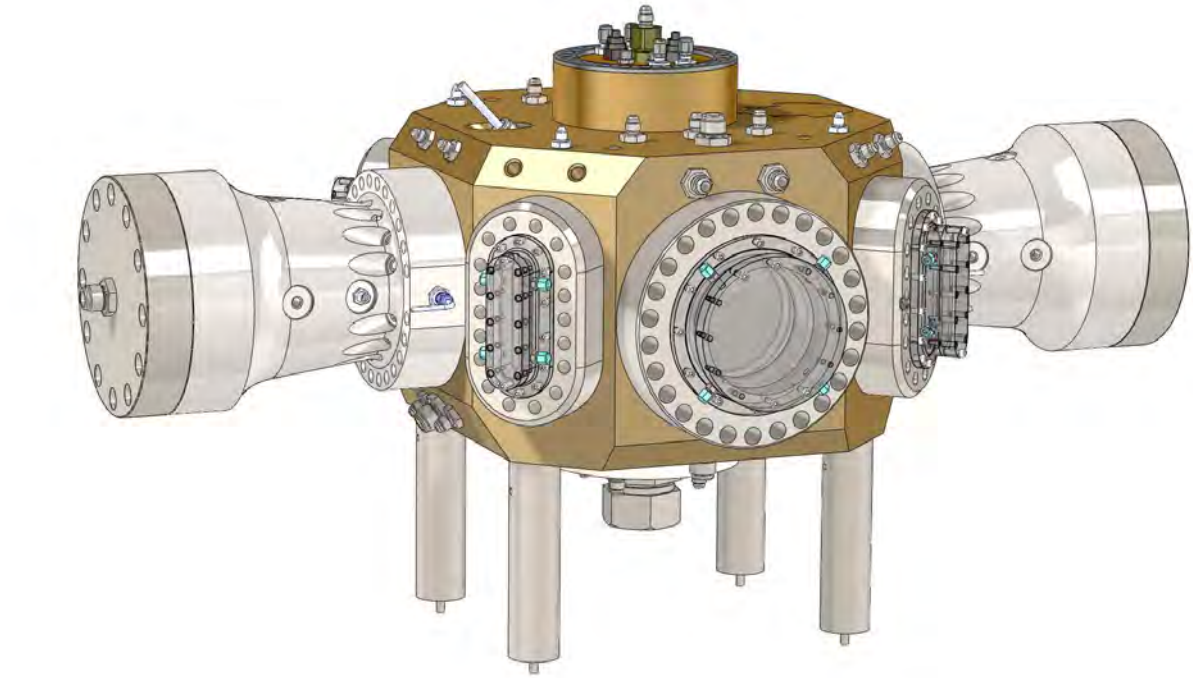

4.1: A three-dimensional CAD rendering of the high pressure combustion chamber at Air Force Research Laboratory at Edwards AFB, CA.

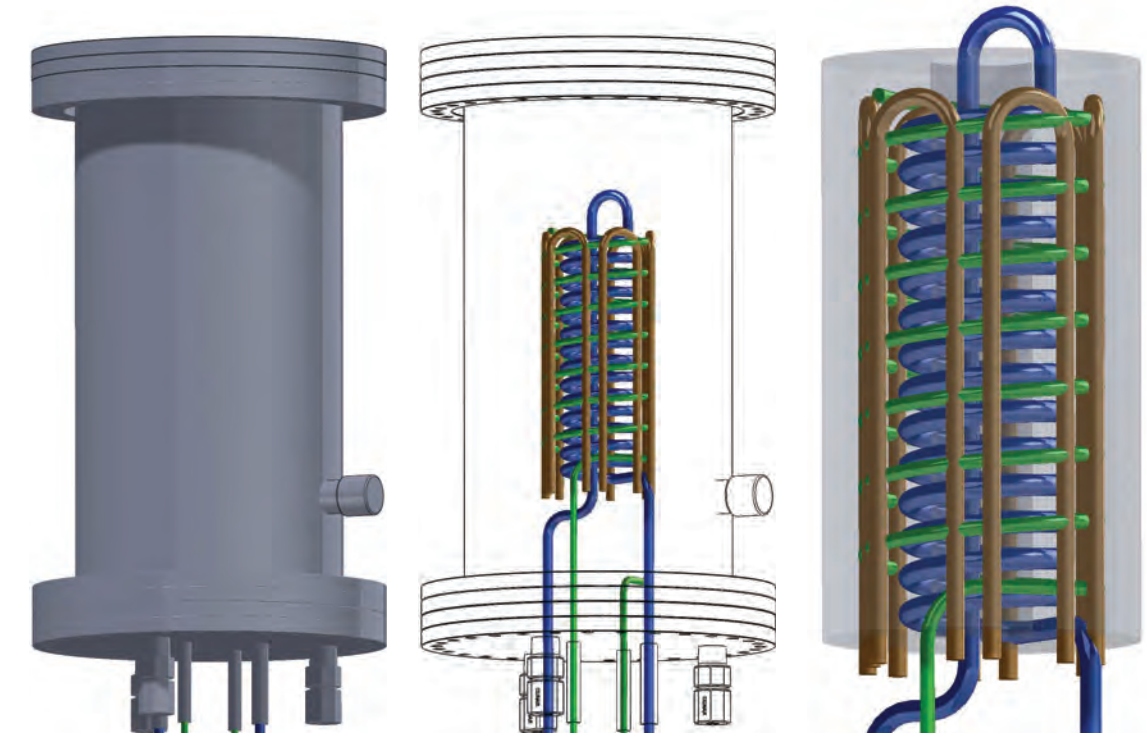

4.2: The oxygen heat exchanger cools oxygen gas (green) using liquid nitrogen (blue). Oxygen is cooled below the target temperature and electric heaters (brown) increase oxygen to the target temperature with a control resolution of ±1 K. Insulation is provided by a vacuum jacket (shown in left view, outlined in center view). An aluminum casting surrounds the plumbing assembly (shown in right view, gray). Courtesy of Sierra Lobo Inc.

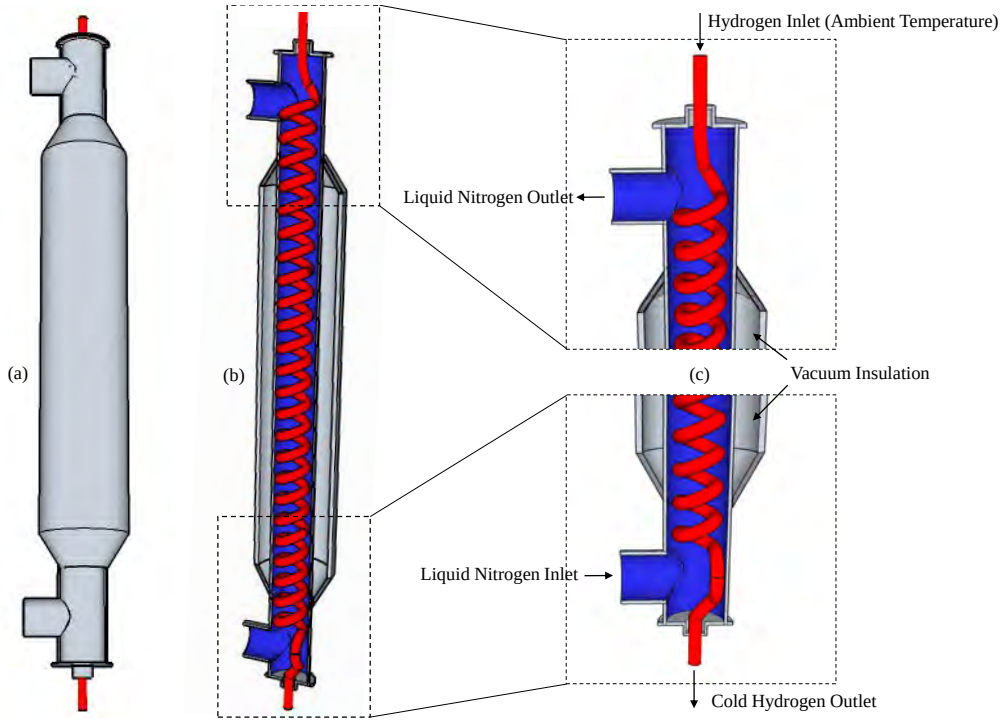

4.3: The hydrogen heat exchanger cools hydrogen gas (red) using liquid nitrogen (blue). Insulation is provided by a vacuum jacket.

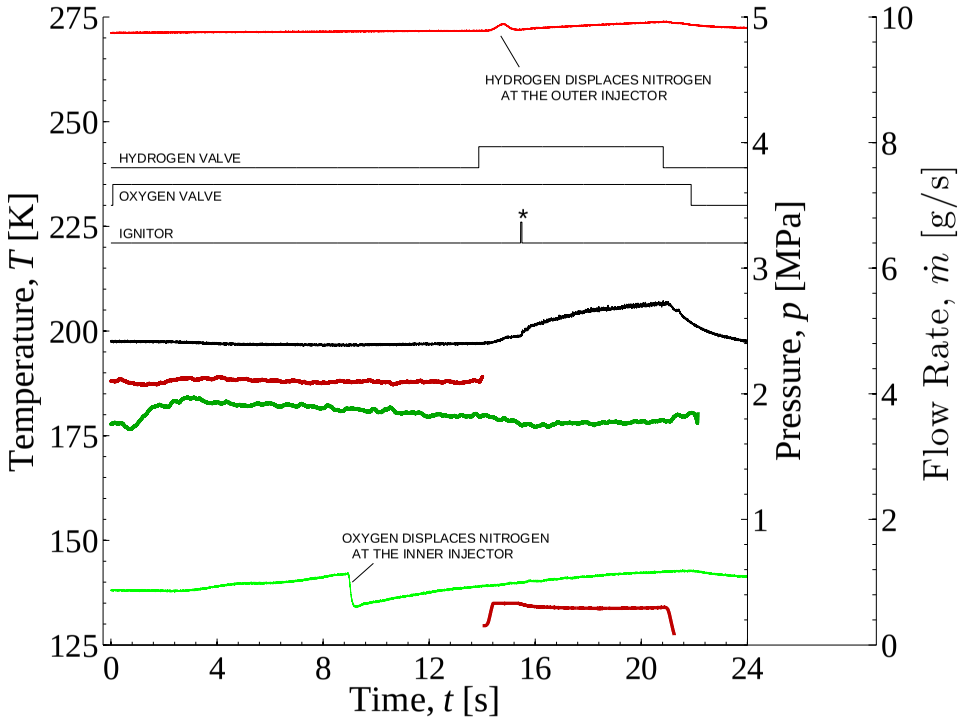

4.4: Time series plot of a reactive test using an oxygen and hydrogen. The transition from nitrogen simulant to propellant occurs after the propellant valve is opened. A step change in outer jet mass flow rate occurs near $t = 14$ s, where a nitrogen flow rate of ≈4.2 g/s changes to a hydrogen mass flow rate of 0.65 g/s (dark red). The inner jet mass flow rate shows a species change near $t = 1$ s, where a nitrogen flow rate of 3.6 g/s is overtaken by an oxygen mass flow rate of ≈3.9 g/s. Inner jet temperature (light green), outer jet temperature (light red), and chamber pressure (black) are also shown. $MR = 5.9$ ($\phi_{o/f} = 1.36$), $J = 2$

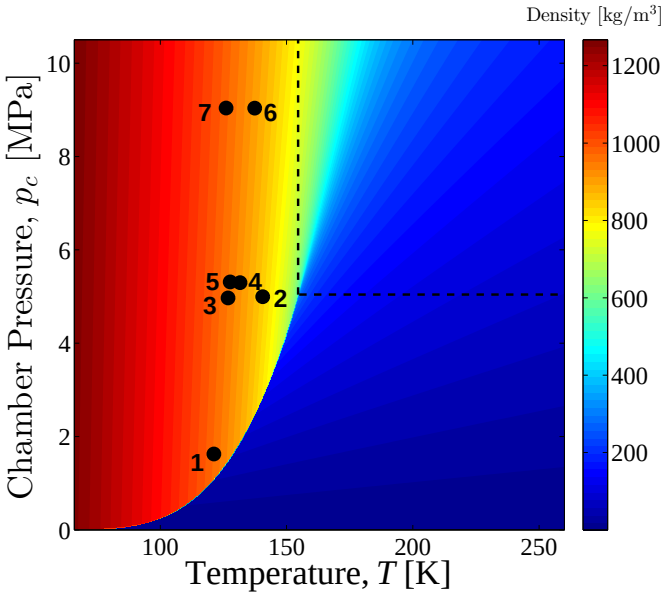

4.5: The facility's minimum achievable oxygen temperatures are plotted with an oxygen density contour overlay. A vertical line and a horizontal line represent the critical temperature and pressure, respectively. Both chamber pressure and mass flow rate are controlled while temperature is measured. (1) 3.7 g/s (2) 2.6 g/s (3) 9.3 g/s (4) 3.0 g/s (5) 11.1 g/s (6) 2.7 g/s (7) 10.4 g/s

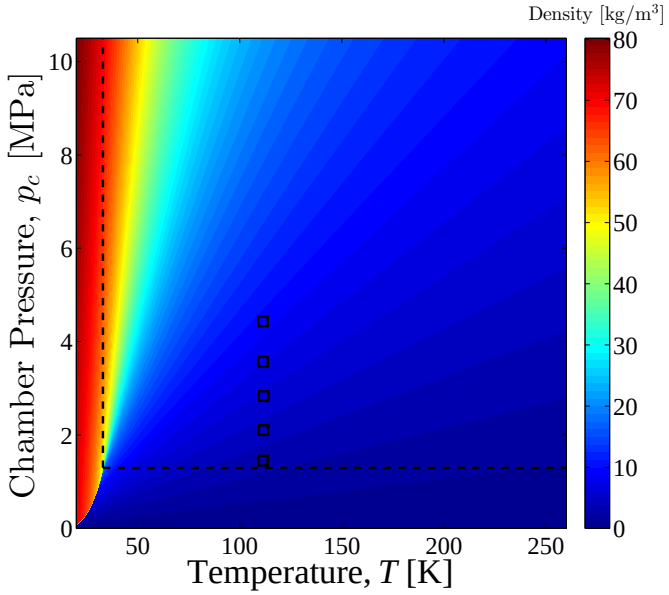

4.6: The facility's minimum achievable helium temperatures are plotted with a hydrogen density contour overlay. A vertical line and a horizontal line represent the critical temperature and pressure, respectively. Helium is used as a surrogate gas, and is representative of minimum hydrogen achievable hydrogen temperatures in the outer jet. The nominal outer jet flow rate is approximately 1.3 g/s.

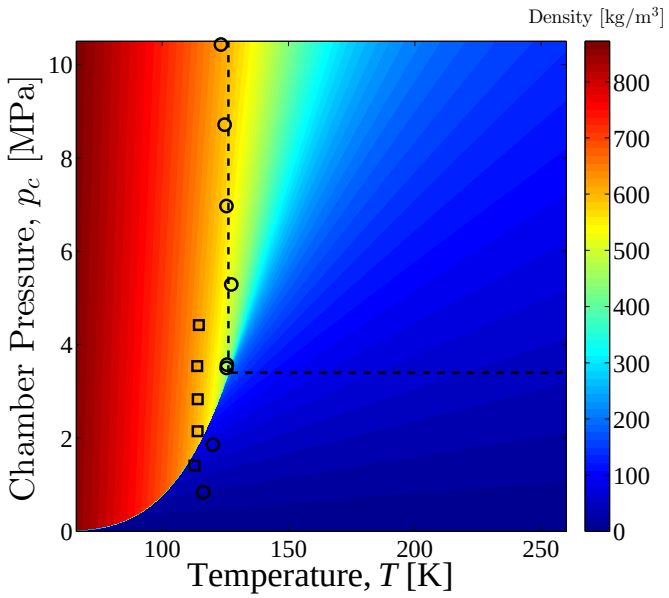

4.7: The facility's minimum achievable nitrogen temperatures for the inner and outer jets are plotted with an nitrogen density contour overlay. A vertical line and a horizontal line represent the critical temperature and pressure, respectively. Both chamber pressure and mass flow rate are controlled while temperature is measured. Flow rates of the inner and outer jets are approximately 9 g/s and 3 g/s, respectively. (○) Inner jet (□) Outer jet

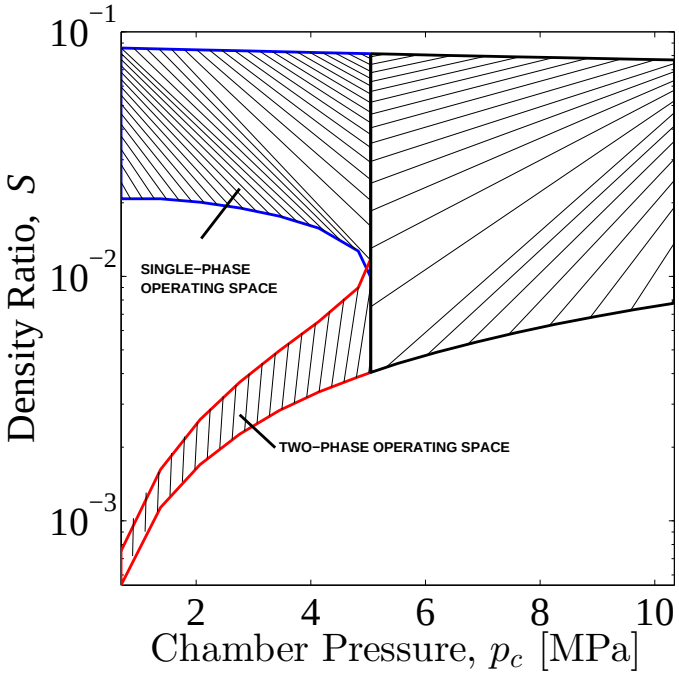

4.8: The facility's range of possible density ratios plotted versus chamber pressure for oxygen and hydrogen propellants.

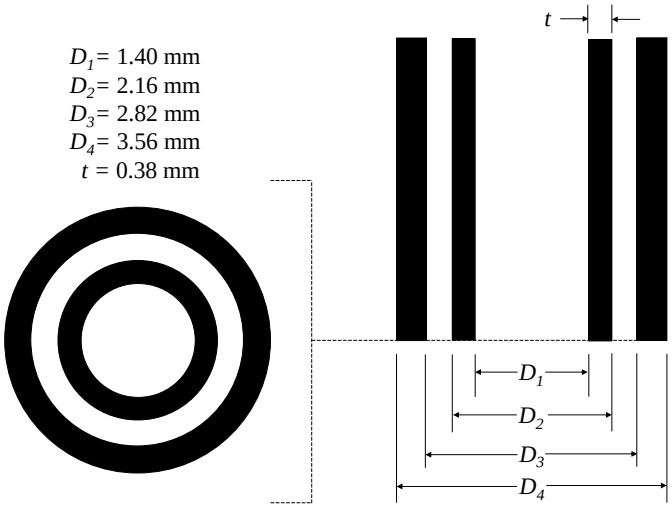

4.9: The dimensions of the coaxial injector used for new experiments in this study.

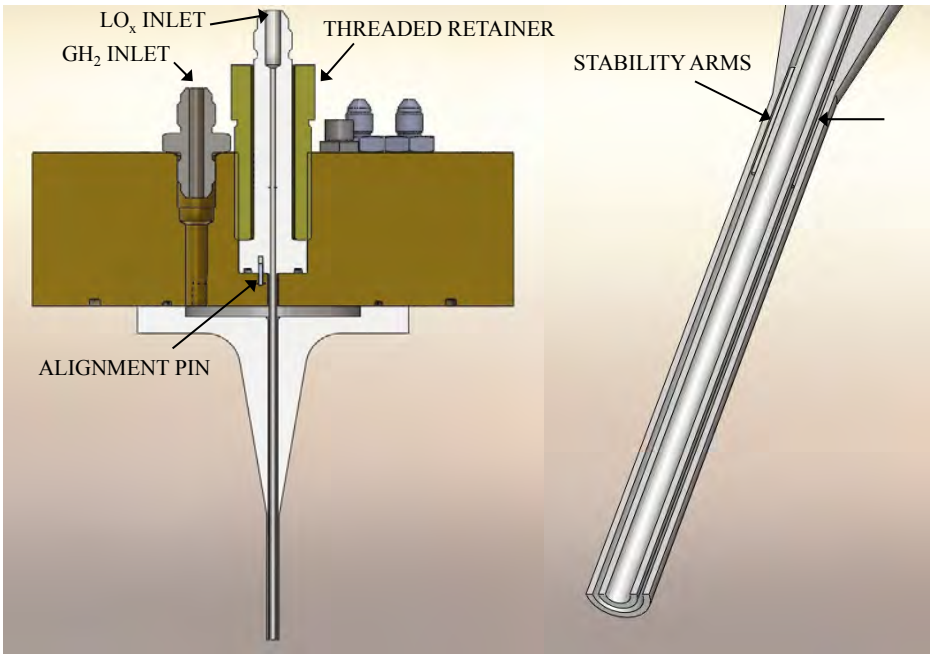

4.10: The inner injector body passes through the center of the brass top flange and is held in place using a retainer. For angular consistency between removal and re-installment, the inner injector is aligned with a dowel pin which is pressed into the top flange. To achieve concentricity between the inner and outer injectors, three stability arms are located on the outside surface of the inner tube (right). The outer injector fastens to the lower surface of the top flange, and an outer jet plenum is located between these two parts. Both the inner and outer injectors are machined from Monel 400 alloy.

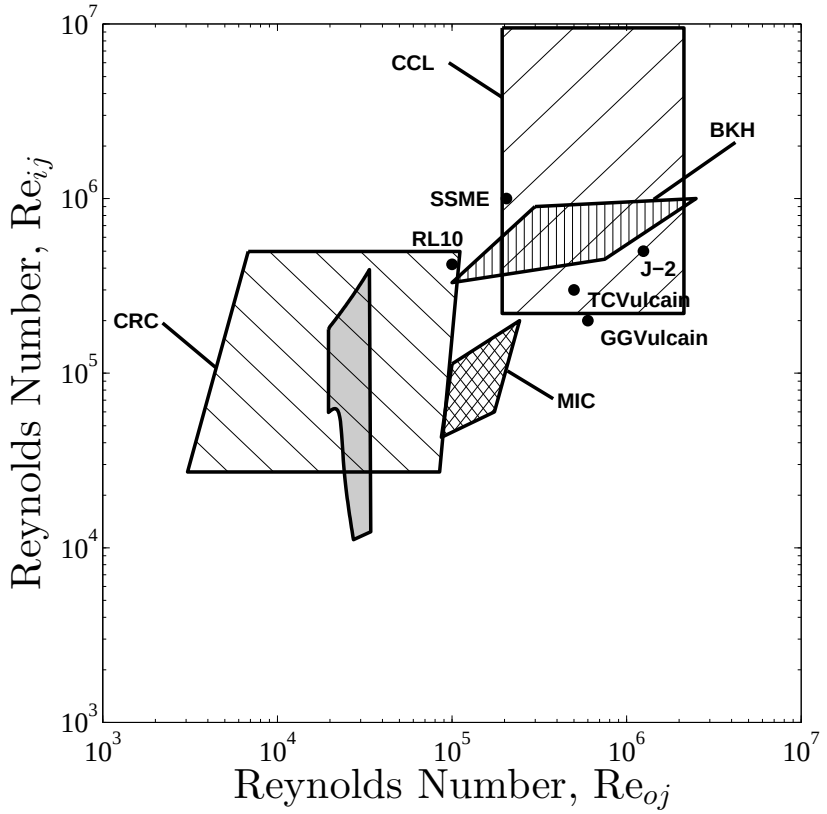

4.11: Shear-coaxial injector Reynolds numbers for the AFRL Combustion Stability Laboratory (gray) with a comparison to other experimental facilities and liquid rocket engines with H_2-O_2 flows. Data is included for the Vulcain Gas Generator (GGVulcain), Vulcain Main Thrust Chamber (TCVulcain), RL10 engine, Space Shuttle Main Engine (SSME), J-2 engine, BKH combustor and Common Research Combustor (CRC) of DLR in Germany, Cryogenic Combustion Laboratory (CCL) of Pennsylvania State Univ., and the Multi-Injector Combustor (MIC) of ONERA and CNRS in France [8, 24, 45, 131, 159].

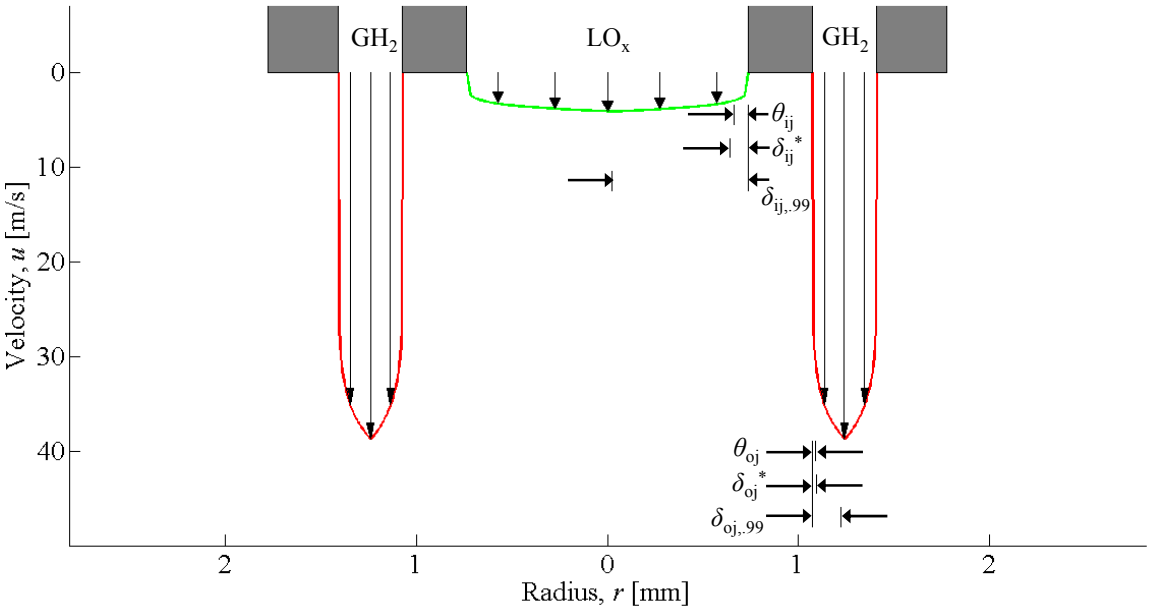

4.12: In a fully-developed turbulent flow, the exit velocity boundary layers of both the outer and inner jets are approximately equal to half the channel width. This particular diagram is an example of the fully-developed turbulent flow of gaseous hydrogen (outer jet) and liquid oxygen (inner jet) where $MR = 7$ ($\phi_{f/o} = 1.14$), $T_{oj} = T_{ij} = 145$ K, $p_c = 700$ psia (4.8 MPa), $\dot{m}_{oj} = 0.65$ g/s, and $\dot{m}_{ij} = 4.55$ g/s.

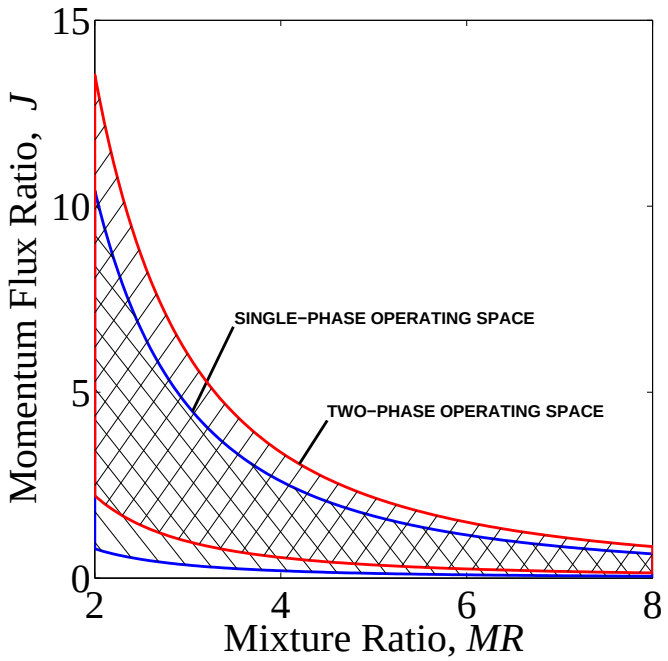

4.13: The facility's range of possible J values is best represented by a parametric map with MR. Single-phase flows (GO_x-GH_2) are bounded by blue lines and two-phase flows (LO_x-GH_2) are bounded by red lines. For reference, the stoichiometric condition for oxygen-hydrogen combustion occurs at $MR = 8$ and the fuel-oxidizer equivalence ratio $\phi_{f/o}$ for $MR = [2,4,6,8]$ is $\phi_{f/o} = [4,2,1.33,1]$.

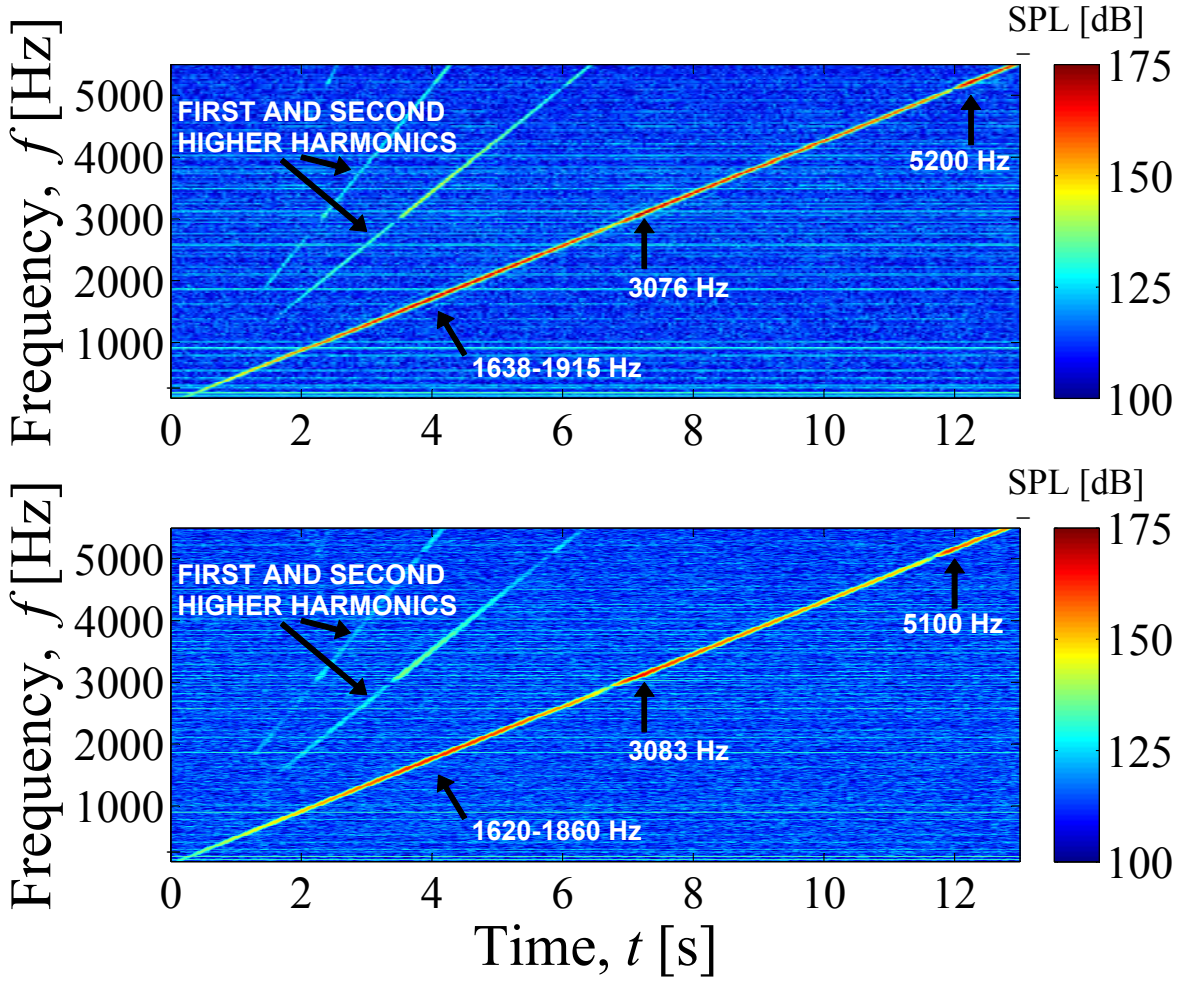

4.14: Acoustic pressure spectra results for the left piezo siren (top) and the right piezo siren (bottom). Magnitude is scaled with a sound pressure level (SPL) colormap, and key regions of piezo siren efficiency are annotated.

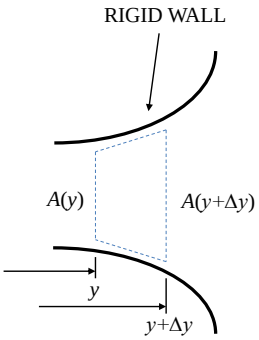

4.15: Area is a function of the transverse coordinate y, and this function is optimized for the design of acoustic waveguides such that wave amplitudes in the x and z directions are minimized while maximizing amplitudes in the y direction.

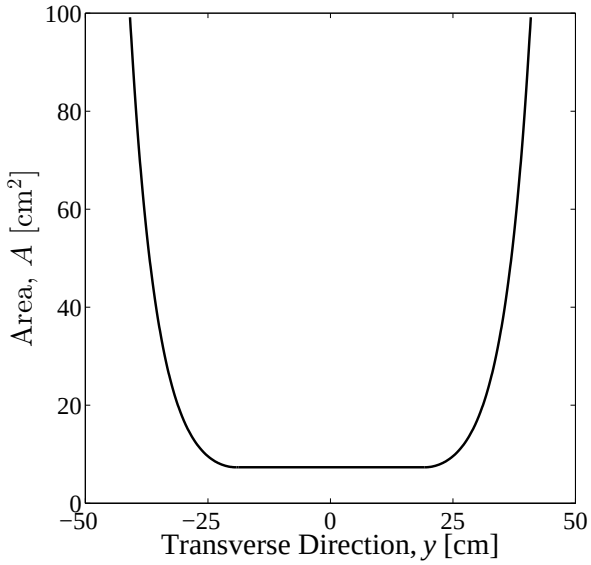

4.16: The left and right waveguides were fabricated according to the area distribution of a catenoidal horn [151]. The waveguides reduce a circular area of 99.18 cm^2 to a rectangular area of 7.33 cm^2 to match the inner chamber. The piezoelectric sirens are located at ±40 cm.

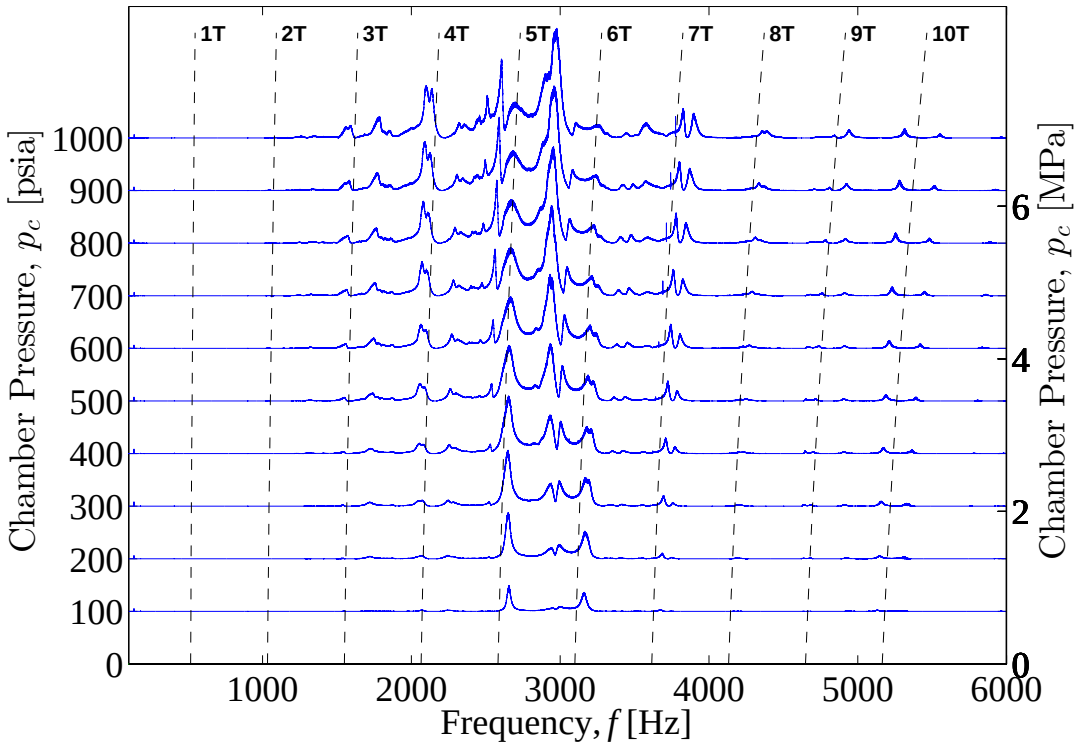

4.17: Acoustic frequency sweep results are plotted as power spectral density for PAN conditions at chamber pressures ranging from 100 to 1000 psia (6.9 MPa). Transverse modes 1T through 10T are identified with theoretical lines which transcend to higher frequency as the chamber pressure increases.

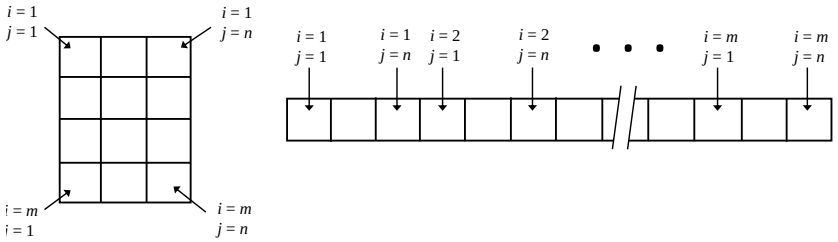

4.18: A single row of matrix **A** constructed from an $m \times n$ image for POD analysis.

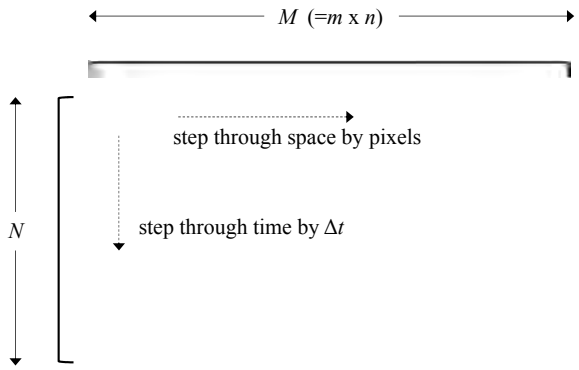

4.19: Prior to applying the POD algorithm, a complete set of images was conditioned to form a single data matrix **A** using N images and M pixels. Each row of **A** was formed by appending consecutive rows from the top row of pixels to the bottom row of pixels.

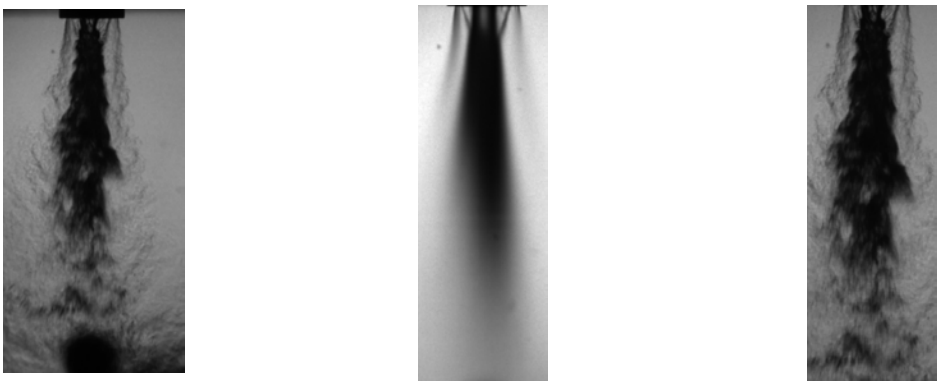

(a) (b) (c)

4.20: Sample images of a LN_2-GHe shear-coaxial jet for $J = 6$ without acoustic forcing. (a) instantaneous image (b) time-averaged image (c) cropped image used for data processing

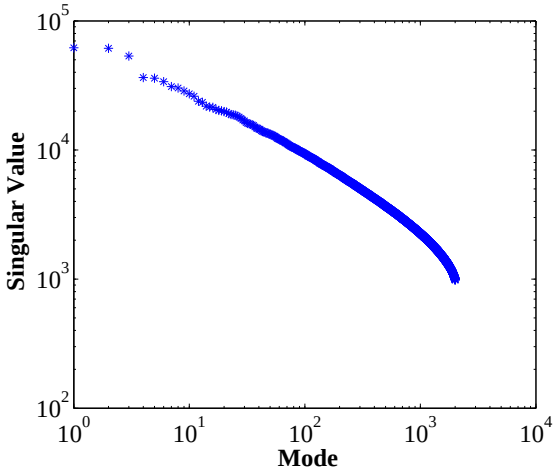

4.21: Singular values for an acoustically forced LN_2-GHe jet with $J = 2$ and $f_F = 2050$ Hz at a PN.

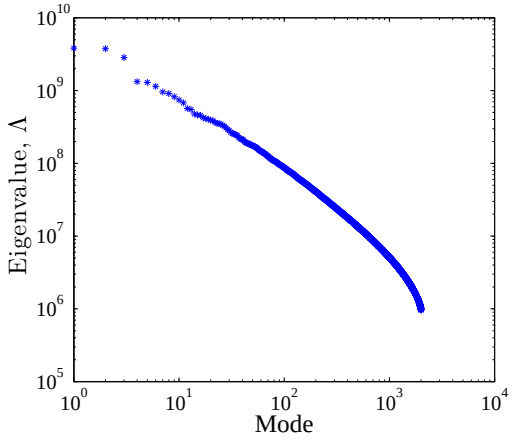

4.22: Eigenvalues for an acoustically forced LN_2-GHe jet with $J = 2$ and $f_F = 2050$ Hz at a PN. $\Lambda = \sigma^2$

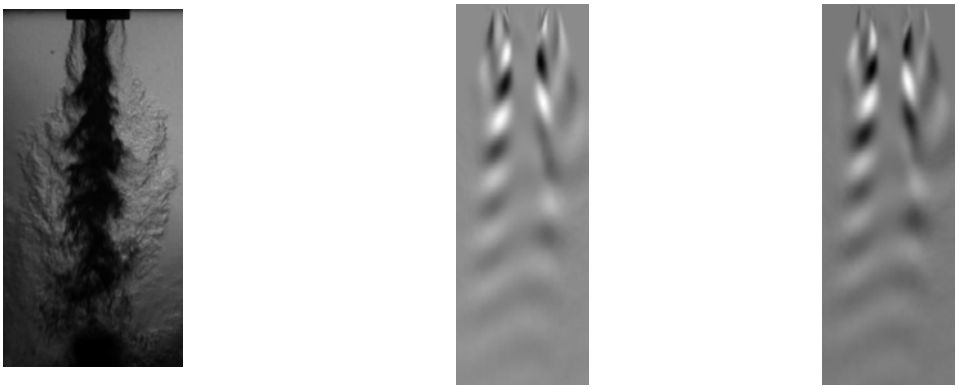

(a) (b) (c)

4.23: A snapshot of an acoustically forced LN_2-GHe jet with $J = 2$ and $f_F = 2050$ Hz at a PN is shown in (a), and reconstructed POM images are shown for POD (b) mode-1 and (c) mode-2.

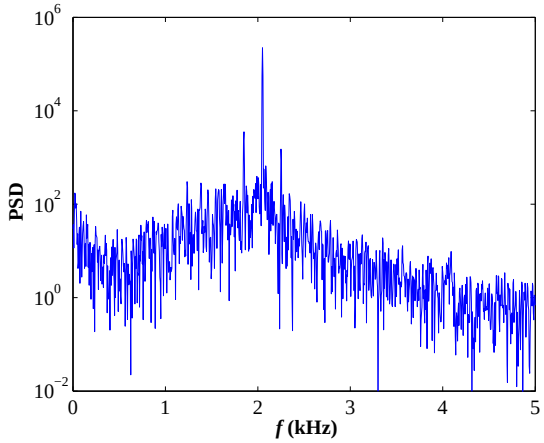

4.24: Power spectral density for mode-1 for an acoustically forced LN_2-GHe jet with $J = 2$ and $f_F = 2050$ Hz at a PN.

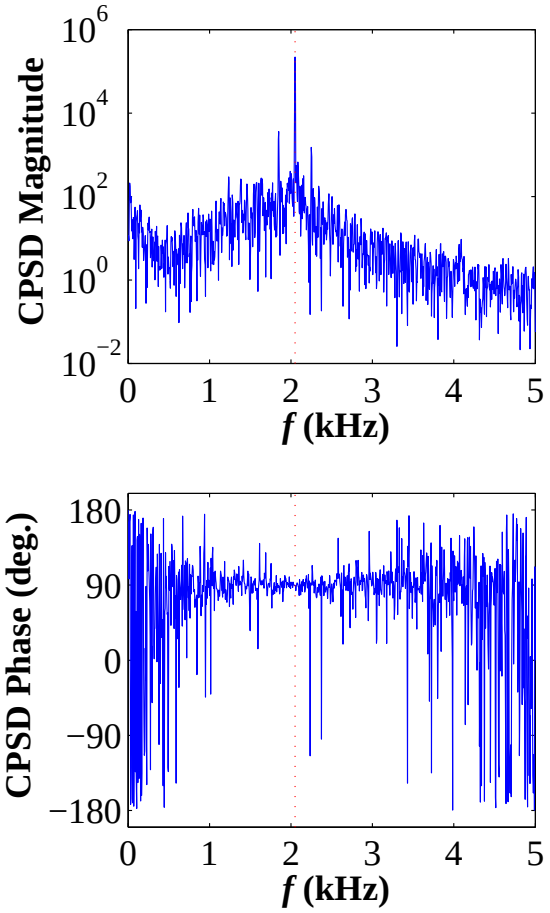

4.25: Cross power spectral density magnitude (top) and phase (bottom) for POD mode-1 and mode-2 for an acoustically forced LN_2-GHe jet with $J = 2$ and $f_F = 2050$ Hz at a PN. The vertical red line located at $f = 2050$ Hz represents the characteristic instability frequency for this condition.

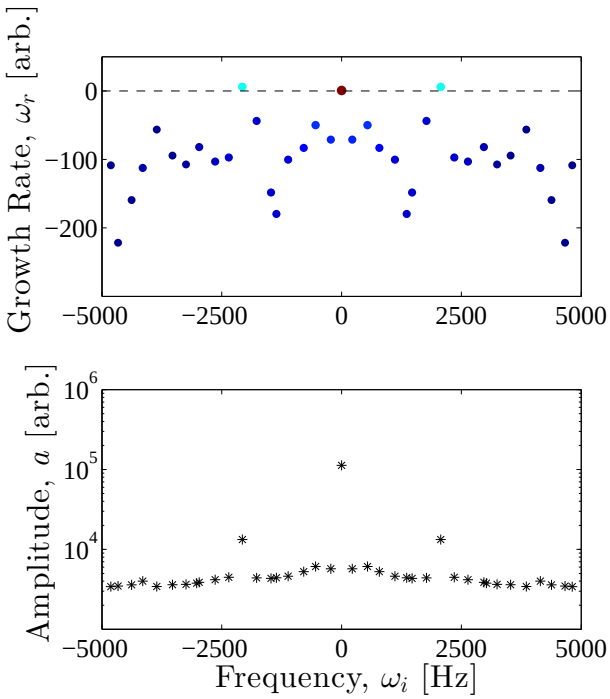

4.26: Top: Real eigenvalues ω_r (growth rate) and imaginary eigenvalues ω_i (frequency) plotted for DMD results computed for an acoustically forced LN_2-GHe jet with $J = 2$ and $f_F = 2050$ Hz at a PN. Each point represents a single mode identified by DMD, and the color and size of each point is scaled with the amplitude of each mode as calculated using eqn. 4.49. Bottom: Mode amplitudes plotted versus ω_i.

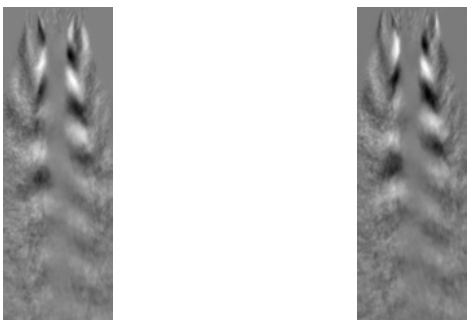

4.27: The DMD eigenvectors ϕ_r (left) and ϕ_i (right) for the unstable mode identified by cyan color in Fig. 4.26. $\lambda_i = f_F = 2050$ Hz

CHAPTER 5

Results - Shear-Coaxial Jets

5.1 Qualitative Observations of Liquid Nitrogen-Gaseous Helium Shear-Coaxial Jets

Prior to establishing quantitative conclusions from high-speed imaging results, several key qualitative observations must be mentioned. Figure 5.1 demonstrates many shear-coaxial jet features in a single snapshot, and a reduced field of view is used to increase the clarity of structures near the injector exit. Phenomena previously observed in other research studies appear in this snapshot, and are described below in order to bring to light the possible sources of shear-coaxial jet instability.

At the exit of the injector, a recirculation zone is easily distinguishable. Moving in the radial direction from the center of the jet, one first observes an interface between the liquid nitrogen inner jet and the recirculation zone formed between the inner and outer jets. This feature is labeled as (1) in Fig. 5.1. The width of the recirculation zone is equal to the inner post thickness t at the exit of the injector and converges to zero as the recirculation zone extends downstream. The recirculation zone results from a finite inner post thickness, separating the near-field features of this geometry from that of classical co-flowing streams ($t = 0$) commonly used in linear stability theory [10, 121] and other experimental studies of coaxial jets and shear layers. Note that a different injector geometry or range of flow conditions will result in a recirculation zone shape different from that observed here. Earlier work at AFRL has more thoroughly

explored the influence of t and the behavior of the recirculation zone [23, 81, 104] in nonreactive coaxial jets. As discussed earlier, when a finite value of t is used, the stability computations of Talamelli and Gavarini [108] predict not only that a wake instability can be produced, but also that the wake instability will be absolutely unstable for a small but nonzero wake velocity. Although wake velocity estimations are not included in this study and the results of Talamelli and Gavarini may not be directly applied, the existence of a recirculation zone gives potential for absolute instability.

Farther out in the radial direction, an outer shear layer is identified between the gaseous helium outer jet and the surrounding gaseous nitrogen. Although this interface is less distinguishable in analogous LN_2-GN_2 jet experiments [23, 29], the LN_2-GHe jet shown in Fig. 5.1 reveals significant contrast between the light outer jet and the more dense ambient nitrogen ($\rho_c \approx 7\rho_{oj}$). At this interface, an outer shear layer instability is formed. Since the outer and inner jets are fully turbulent at the exit, this would generally be expected to disrupt the coherence of large-scale structures in the shear layers. Early experimental conclusions by Ko and Kwan [88] found the outer shear layer to take on a different wavelength and instability frequency than those of the inner shear layer, and two different St definitions were used accordingly for the inner and outer shear layers. Far downstream, the shear layers are interact and merge, but they behave as isolated shear layers near the exit, as described by the separate St definition of Ko and Kwan. In support of defining a unique scaling law for each shear layer, preliminary POD analysis of LN_2-GHe jets also indicates different instability frequencies exist in each shear layer. This study focuses on the inner shear layer due to its direct relevance to fuel-oxidizer mixing and unsteady heat release, but a low-density outer jet provides the ability to track the outer shear layer with high-speed imaging, which is a valuable feature for future work.

Immediately downstream of the recirculation zone, a dynamic interface forms be-

tween the inner and outer jets. This interface, labeled as (4) in Fig. 5.1, is the most important feature of the jet for this particular set of experiments due to its importance in inner jet atomization and mixing. This region may be called the mixing layer or the inner shear layer, and the latter term is used here for continuity with other works. The extreme contrast between the liquid inner jet with $\rho_{ij} \approx 500\ kg/m^3$ and the light outer jet with $\rho_{oj} \approx 5\ kg/m^3$ makes for straightforward image analysis because pixel intensity gradients are most steep at the inner shear layer. Near the end of the recirculation zone, the inner shear layer appears as well-defined interfacial waves. Further downstream, the shear layer thickness increases and these waves develop into vortices. A vortex may form a ligament and break away from the dark core of the inner jet, or remain attached until reaching the end of the dark core ($x = L_b$) where large clumps and ligaments break up in the fully-merged zone. As will be shown by reduced basis methods results, these events occur within a broadband of frequencies accompanied by random noise, but a single characteristic frequency is adopted as the most significant natural instability.

An important observation was also made regarding jet symmetry. When viewing time-averaged images such as that in Fig. 4.20b, asymmetry is seen in the dark core. Upon close inspection of the injector, it was concluded that the observed jet asymmetry results from a lack of concentricity between the inner and outer streams either at the injector exit or in the upstream pathways of the injector. Following a series of efforts to achieve a perfectly symmetric jet, it was concluded that injector hardware adjustments were only sufficient to improve symmetry, but not completely eliminate the problem. Concerning application to LREs, injector asymmetry is considered a challenge, especially for propellant injection systems with dozens of injectors subject to high-volume manufacturing. Manufacturing variability is a likely cause of unpredictable behavior in LREs. Concerning the present research study, small asymmetries may be deemed acceptable if unavoidable and if asymmetric jet structures do not disrupt behaviors relevant to the scientific conclusions of the study. To this end, a verification test was performed to

inspect instability frequencies for the right and left sides of the jet. This study focused specifically on natural instability frequencies determined by POD, and compared f_{nat} for the mixing layer on the left side of the image with f_{nat} for the mixing layer on the right side of the image. For the range of conditions used in this study, the frequency difference was less than 80 Hz and the broadband spectra of each natural mode inhabited approximately the same range of frequencies. (The band of naturally excited frequencies was approximately 200 Hz, and was always found within the range from 720 Hz to 1140 Hz.) It was concluded that differences in spectral behavior are small, and further, these differences are not expected to have a significant effect on the susceptibility of the jet to external acoustic forcing. Future injector configurations should explore improved techniques for maintaining concentric inner and outer injectors without sacrificing the desired injector geometry, but the current injector configuration was accepted for this test campaign.

The natural instabilities of nonreactive shear-coaxial jets discussed above are subject to intense study due to their relevance to coaxial jet flames. As shown in Fig. 5.2, an unforced O_2-H_2 coaxial jet produces pockets of intense heat release rather than an evenly distributed flame. The images shown in Fig. 5.2 represent chemiluminescence of electronically excited OH radicals captured by blocking visible wavelengths using an optical bandpass filter. The bandpass filter was centered near 308 nm, which is the wavelength of peak radiation for OH* chemiluminescence. As discussed in chapter 2, OH* chemiluminescence is a good indication of heat release. Thus, from the sequence of high-speed images in Fig. 5.2, one can conclude that an unforced O_2-H_2 flame produces heat release which is highly dependent on both time and space, and which may experience natural acoustic coupling and/or absolutely unstable shear layer behavior [118] even in the absence of external excitation. Although the qualitative scientific conclusions of this study are limited to nonreactive jets, this sample of high-speed flame images reinforces the need to research naturally occurring instabilities in coaxial jets.

5.2 Comparisons of POD and DMD

Both proper orthogonal decomposition and dynamic mode decomposition are employed to extract organized structure from the visualization data. Although this study applies DMD to coaxial jet images for the first time, both methods have been used for a number of nonreactive and reactive experimental flows where optical techniques are the primary diagnostic tool. The following comparison weighs the advantages and disadvantages of each method such that future application of these methods may be done with specific limitations in mind.

To start the comparison, an argument should be made regarding simplicity. Although the derivations and procedures included in chapter 4 include lengthy details, the resulting code for both POD and DMD can be straightforward. In particular, POD is easier to implement in several ways. When written using singular value decomposition, the mathematical steps of POD are not as complicated as DMD, and creating a POD algorithm simply requires subtracting the time-averaged image from the image set and performing a SVD of the resulting image set. Alternatively, DMD requires separating the image set into $\mathbf{A}_1^{N-1}$ and $\mathbf{A}_2^N$, performing a SVD of $\mathbf{A}_1^{N-1}$, calculating the approximate mapping $\widetilde{\mathbf{S}}'$, solving the eigenvalue problem of $\widetilde{\mathbf{S}}'$, and finally one must use the eigenvalues and eigenvectors to calculate useful frequencies and mode shapes. This lengthy procedure is caused by a more extensive mathematical derivation, and results in DMD codes which are several steps longer than their POD counterpart. In addition, DMD requires more computational time. Using MATLAB, for example, several thousand images can be decomposed with POD in tens of minutes, but with DMD, the same image set will require hours. If instead only a few hundred images are deemed necessary to reconstruct the important modes, then either algorithm can be completed in minutes. But, interpreting the results of each tool brings to light more important differences between POD and DMD.

The most evident difference between POD and DMD is the solution of multi-frequency versus single-frequency results. Proper orthogonal decomposition describes the temporal dynamics of a mode using frequency spectra, whereas DMD represents each mode with a single frequency [152]. Dynamic mode decomposition is more advantageous in this regard. To identify the frequency of a coherent instability, the cross power spectral density from POD obfuscates the mode of interest by including magnitudes for an entire array of frequencies. Figure 5.3 shows the cross power spectral density magnitude and phase for the natural POM pair of an unforced condition at $J = 6$. The vertical red line in Fig. 5.3 is the frequency which best represents the natural mode, because this frequency has the greatest magnitude for a phase near 90°. Thus, this POM pair has a characteristic frequency of 945 Hz and is conjugate according to phase. But, this POM pair exhibits a broadband nature. The spectrum of the natural mode is broadband, and the POM pair also includes the energy of broadband turbulence, or noise, at higher frequencies. Thus, although cross power spectral density calculations were used to determine a single characteristic frequency for the dominant POM pair, each POM encompasses an array of frequencies by definition. Correctly pairing POMs and labeling pairs with a single characteristic frequency is a process which allows for user error in choosing two POMs to make a pair, and again allows for error when determining a single frequency from spectra. Some conditions pose more difficulty than the condition shown in Fig. 5.3. Several cases produced POMs which were particularly challenging to interpret, because a combination of natural and acoustically forced peaks created a spectra of "mixed" modes in a single POM. Dynamic mode decomposition, on the other hand, represents each mode with a single frequency.

As mentioned above, one disadvantage of POD lies in the potential error which results from choosing a pair of conjugate modes to form a single, physical mode. This issue is particularly relevant for unforced conditions or conditions with low levels of forcing, where the natural mode is the most dominant shear layer mode. In such a case,

although the natural mode variance is greater than that of lower ranked modes, the variance contribution is not as large as a forced mode variance contribution from high amplitude acoustic forcing, for example. Figure 5.4 shows a plot of the eigenvalues for the POD modes of an unforced jet; this plot represents the same condition as Fig. 5.3. With the exception of mode-1, there is a gradual decrease in the eigenvalue when viewing the log-log scale in Fig. 5.4. Remember, the eigenvalue of a single mode is proportional to the pixel intensity variance of that mode, as determined by POD ($\Lambda = \sigma^2$). For a very strong natural mode, a mode *pair* would appear with significantly higher eigenvalues which separate the coherent natural mode from other less significant modes. Instead, Fig. 5.4 shows only a single mode with a very large eigenvalue, and this mode merely contains low frequency (<5 Hz), steady-like motion without a conjugate mode pair. Although a coherent natural mode exists, this natural mode did not exhibit particularly strong dominance over other background modes and noise, making it challenging to identify the natural POM pair. One is left to analyze modes two and higher in search of a conjugate mode pair, rather than simply choosing a pair of highly ranked modes which stand out in an eigenvalue plot, such as mode-1 and mode-2 for the acoustically forced case in Fig. 4.22. For the experiments in this study, broadband turbulence contributes a significant amount of energy to the flow field of unforced jets, making the natural mode less distinctive.

In addition to eigenvalue plots, one must also utilize the eigenvector images and the power spectral density for each mode when searching for the conjugate mode pair. As an example, Fig. 5.5 displays the twelve highest ranked eigenvector images for the same unforced condition as Figs. 5.3 and 5.4. The POM ranking is based on eigenvalues, and therefore, is a ranking based on the variance content of each POM as defined using pixel intensity fluctuations from high-speed images sets. Since any mode pair creating a significant pixel intensity variance will be found within the highest ranked modes, Fig. 5.5 will contain the natural mode distributed between two images which have lobe

structures 90° out-of-phase in the direction of convection. The user must find the natural mode pair among these twelve POMs, as opposed to using the twenty highest ranked modes, for example. For the conditions of this study, exploring more than twelve modes was shown to consistently decrease efficiency without altering results. Although mode-1 and mode-2 contain the highest variance contribution, their eigenvector images in Fig. 5.5 do not show flow structures which are 90° out of phase, from simple qualitative inspection. Mode-1 and mode-2 represent two different phenomena. In fact, mode-1 represents low frequency (¡5 Hz) jet flapping, rather than a mixing instability. Mode-3 and mode-4, on the other hand, look very similar in lobe structure. Both contain a slightly antisymmetric inner shear layer instability manifested as dark and light lobes and mode-4 appears to be slightly shifted from mode-3. Indeed, these two modes share the same peak frequency, whereupon the pair has 90° phase difference. The PSD and eigenvector images for both mode-3 and mode-4 are shown side by side in Fig. 5.6. Upon reaching this conclusion, modes 5 through 12 need not be inspected for this particular case. Mode-3 and mode-4 represent the natural instability for $J = 6$ at $f_{nat} = 945$ Hz, and although secondary coherent modes may lie in modes 5 through 12, any other modes produce less pixel intensity variance and leave 945 Hz as the most significant natural instability in the jet. Further, a mode with a high pixel intensity variance is presumed to be a mode having a high energy contribution to the flow. A more difficult case requires CPSD inspection of many mode pairs in order to determine the natural instability mode pair. Clearly, this conclusion required thorough inspection and post-processing of the initial POD results.

In comparison, DMD does not require the pairing of modes in post-processing. Rather, the real and imaginary eigenvectors are inherently 90° out of phase, as was shown in Fig. 4.27, for example. As discussed earlier, the dynamic mode decomposition allows eigenvectors and eigenvalues to be negative and complex, whereas proper orthogonal decomposition constrains these matrices to be real and non-negative by en-

forcing orthogonality in $\mathbf{V}$. In DMD, the eigenvectors standalone as coherent modes by containing both real and imaginary components within a single dynamic mode $\mathbf{\Phi}$ which is tied to a single frequency ω. For this reason, many recent demonstrations of DMD [152, 156, 157] support the use of DMD in place of POD because instability information is often not known *a priori*, and one cannot discern the appropriate pairing of conjugate modes. This study supports the same conclusion.

Finally, for the same unforced condition presented in Figs. 5.3 - 5.5, DMD results are shown in Fig. 5.7. The x-axis is the frequency ω_i in Hertz while the y-axis is the growth rate ω_r and the amplitude a for the upper and lower plots, respectively. Each point in Fig. 5.7 represents a single mode which could be visualized by real and imaginary eigenvector images. As stated earlier, since the mean is not subtracted from the image set prior to implementing DMD, then the highest amplitude is a point at $\omega_i = 0$, which represents the mean. A point at $[\omega_i, \omega_r] = [0, 0]$ also represents the mean flow. Otherwise, significant amplitudes are not observed for any other modes. A significant amplitude could be expected at a frequency near f_{nat}, but obvious peaks in amplitude do not exist. Fig. 5.7 should also be compared to Fig. 4.26, where peak amplitudes were observed for an acoustically forced condition. For an unforced condition though, DMD is unable to clearly identify the significant amplitude of a natural mode for the conditions investigated here. If the natural mode consisted of a larger portion of the aggregate flow energy then perhaps a high value of a would be observed near f_{nat}, but such a condition does not exist for the current test matrix. This may be interpreted as an advantage of POD, whereby a mode characterized by a broadband peak from 800 to 1000 Hz is indiscernible in the single frequency dynamics of DMD, but the same natural mode is captured by a POD mode with broadband spectra. Further analysis is recommended prior to concluding that DMD cannot identify coherent structures with broadband frequencies.

In conclusion, the added complexity of DMD offers an algorithm better suited for identifying the dynamic modes in experimental image data. The *individual* modes of POD do not offer dynamic information, but only mode shapes. The eigenvectors of POD only contain a real component. The complex form of the eigenvectors of DMD inherently contains real and imaginary components which describe a single mode with two different points in phase, thus providing dynamic information regarding a single mode. Additionally, this mode is represented by a single frequency, making DMD more useful for experimental studies seeking to compare the amplitudes of different instability frequencies rather than compare the energy of complete frequency spectra, which includes random turbulence and background noise. When input data is in the form of experimental images, background turbulence is expected for high Re coaxial jets of this kind, and will indeed contribute to the result. Further investigation is needed to determine the proper technique for analyzing this flow regime. If the natural mode of interest is broadband, POD may be preferred in order to capture the complete spectra. Detailed refinement of the user inputs may also improve the performance of both DMD and POD. For example, noise filters may be applied as a pre-processing step or an ideal number of images may be shown to optimize identification of real flow dynamics. POD was sufficient for the objectives of this study, but a future implementation of DMD may offer more clarity to the results.

5.3 Susceptibility of Nitrogen-Helium Shear-Coaxial Jets to Acoustic Forcing

Utilizing the proper orthogonal decomposition, nonreactive shear-coaxial jet results are analyzed with respect to three variables at both a pressure antinode (PAN) and a pressure node (PN). These variables are the acoustic forcing amplitude, nondimensional forcing frequency $F = f_F/f_{nat}$, and outer-to-inner jet momentum flux ratio J. Low

and high values of J are used. An effort is made to separately investigate the influence of each of the these variables on the susceptibility of jets to external acoustic forcing. Specifically, for a given F and J, how will the jet respond to various amplitudes of acoustic forcing? What is the critical forcing amplitude required for the forced mode to overtake the natural mode and become the most dominant jet instability? If J is altered, will the critical forcing amplitude change? A test matrix which aims to answer these questions requires isolated control of each variable. In order to achieve this, unforced jets were first characterized for a range of flow conditions.

5.3.1 Unforced Shear-Coaxial Jets

To explore the influence of momentum flux ratio on shear-coaxial jet instabilities, the values $J = 2$ and $J = 6$ were chosen to span a range which is applicable to LREs and comparable to J values in analogous O_2-H_2 combustion experiments. To best isolate the effects of J, the dimensionless forcing frequency F should be held constant while J is varied. For the present experiments with limitations on applied frequencies associated with standing wave conditions, for a given set of acoustic forcing frequencies, the natural jet frequency f_{nat} for $J = 2$ would optimally be equal to that of $J = 6$. This is particularly challenging, because altering J requires a change in the velocities of the inner jet, outer jet, or both. Thus, shear layer instabilities may adopt different natural frequencies as a result of a modified velocity step $U_{oj} - U_{ij}$ and shear layer convective velocity U_c. Since F is dependent on f_{nat}, individually controlling J and F is challenging.

If the jet adopts a single value of St, as in the work of Birbaud *et al.* [107], Ko and Kwan [88], and others [83, 86, 87, 106], then St can be used to predict f_{nat}. When choosing characteristic velocity and length scales to define St, one must be mindful of the source of instability in a way similar to Ko and Kwan [88]. As done in eqns. 1.14 and 1.15, a Strouhal number which scales with an outer shear layer instability could

be defined with $D_h(=D_3 - D_2)$ and U_{oj}, for example. Conversely, a Strouhal number which scales with an inner shear layer instability should use a smaller diameter, such as D_1, and velocities such as U_{ij} or $(U_{ij} + U_{oj})/2$, which better characterize the inner shear layer region. As shown by works in linear stability theory [10, 121], a change in jet velocities or densities is likely to produce a change in f_{nat}. Thus, to use St as a tool for predicting f_{nat} of the inner shear layer the characteristic definition of St must account for the velocities *and* densities of both the inner and outer jets. Consequently, the shear layer convection velocity of eqn. 1.10 from Dimotakis [89] was chosen as a characteristic velocity for defining St and will be labeled as $U_{c,th}$ hereafter. The formula is included here for convenience.

$$U_{c,th} = \frac{U_{ij}\rho_{ij}^{\frac{1}{2}} + U_{oj}\rho_{oj}^{\frac{1}{2}}}{\rho_{ij}^{\frac{1}{2}} + \rho_{oj}^{\frac{1}{2}}}. \tag{5.1}$$

The dramatically different densities of liquid nitrogen and gaseous helium are included as ρ_{ij} and ρ_{oj}, respectively. By including ρ_{ij} and ρ_{oj}, the shear layer convection velocity better characterizes the present set of experiments. This approach aims to describe the velocity of inner shear layer instabilities represented by vortices which are observed as the most significant structures in the mixing region. For an isodensity shear layer, the convection velocity may be approximated by velocities alone. For example, the mean velocity $U_M = (U_{ij} + U_{oj})/2$ is a more appropriate approximation of U_c in that case, which is found by simply applying eqn. 5.1 for $\rho_{oj} = \rho_{ij}$. Instead, the two-phase flows of interest here ($\rho_{ij} \approx 100\rho_{oj}$) are expected to produce shear layer convection velocities dependent on the density difference as well as the velocity difference. Equation 5.1 is presumed to be an appropriate velocity scale if indeed the natural jet instability frequency matches that of the inner shear layer rather than another source of instability, e.g. the outer shear layer. If the preferred mode of the jet is produced at the outer shear layer or the wake of the recirculation zone, then a different definition of St will be required.

Finally, a definition of St requires a characteristic length scale. Again, to define St for natural jet instability which originates at the inner shear layer, the characteristic length scale is chosen to be approximately equal to the diameter at which the inner and outer jet meet. The exact location at which the outer and inner streams meet is dependent on flow conditions, thus an approximation is required. This characteristic length scale is taken as the average of the inner and outer diameters of the inner injector, D_1 and D_2, respectively, i.e.

$$D_{eff} = \frac{D_1 + D_2}{2}. \tag{5.2}$$

Traditionally, the most important length scale in shear layer instability is the shear layer thickness at the trailing edge, which is dictated by boundary layer thickness at the injector exit. For the present experimental conditions though, fully developed turbulence creates a boundary layer thickness which is approximately equal to the jet radius, making the diameter an appropriate length scale for this particular St definition. The Strouhal number is then defined as

$$St = \frac{f_{nat} D_{eff}}{U_{c,th}}. \tag{5.3}$$

With the assumption that this experimental configuration manifests a constant, preferred value of St for the unforced jet, this scaling law is used to predict f_{nat} values which will be adopted in experiments at $J = 2$ and $J = 6$. In principle, f_{nat} can be controlled by $U_{c,th}$ as one moves from $J = 2$ to $J = 6$.

The validity of this experimental approach and the assumption of constant Strouhal number is assessed by plots in Figs. 5.8 and 5.9. First, a plot of natural frequency versus $U_{c,th}$ is shown in Fig. 5.8. The values of f_{nat}, as determined by the most dominant POM pair, are shown to increase with $U_{c,th}$ as expected. A series of experiments were conducted for $U_{c,th} \approx 6$ m/s which produced $f_{nat} \approx 1$ kHz, and four additional cases were conducted for $U_{c,th} \approx 12$ m/s which produced a range of f_{nat} from 2 kHz to 3 kHz. More importantly, one must note that half of the points in Fig. 5.8 have a nominal

momentum flux ratio of $J = 2$, while half possess a nominal value of $J = 6$. Specifically, $U_{c,th}$ was held constant at 6 m/s while adjusting both the inner and outer jet velocities to achieve $J = 2$ and $J = 6$. This step was repeated for $U_{c,th} \approx 12$ m/s. Refer to appendix A for a table of results for all cases. Due to the repeatability achieved at 6 m/s, this condition was chosen for all acoustically forced flow conditions presented in the following section, where f_{nat}, and thus F, can be held constant while isolating the effects of J on the susceptibility of jets to acoustic forcing.

For the same data as in Fig. 5.8, a plot of St versus J is shown in Fig. 5.9. Although the collection of points has a calculated mean Strouhal number of 0.30, there is a significant amount of scatter, especially among cases where $U_{c,th} \approx 12$ m/s. Therefore, $St = 0.30$ may be a reasonable constant for the preferred mode, but an improved estimate of a characteristic velocity may reduce scatter in St and increase accuracy when predicting f_{nat}.

To test the validity of eqn. 5.1, shear layer convection velocities were experimentally measured via image analysis. Consider an array of pixels shown by the green curve in Fig. 5.10. The set of pixels along the green curve are chosen to represent the inner shear layer region, where vortices are located on the outer edge of the dark core. For a single pixel lying on the green curve, the pixel intensity will oscillate from low (dark) to high (light) as a pocket of dense fluid leaves the area. The oscillating behavior will continue as vortices pass this point in space over a duration in time. When the entire green curve is considered rather than a single point, then vortices will transcend through the array of pixels, creating areas of dark and light pixels which move in time. Fig. 5.11 demonstrates this concept. On the y-axis the shear layer curve coordinate s is nondimensionalized by D_1, while the x-axis is time in milliseconds. A diagonal streak illustrates the convection of inner shear layer vortices, or waves, which begin near the injector exit and travel downstream as time advances from one image to the next, and so on. Very close to

the injector, $\frac{s}{D_1} \approx 1$, a dark horizontal bar in Fig. 5.11 results as the signature of the end of the recirculation zone. The convection velocity upstream of this dark horizontal feature is less than the shear layer convection velocity downstream of the recirculation zone, where the much faster outer jet meets the inner jet. The streaks which appear at $\frac{s}{D_1} > 1$ are of interest here. The slope of a single streak, $\Delta s/\Delta t$, is the velocity of the coherent structure represented by the streak. To make an experimental estimate of the shear layer convection velocity $U_{c,meas}$, a collection of eight structures represented by dark diagonal lines in Fig. Fig. 5.11 were randomly chosen and their velocities were averaged to find a single estimate of $U_{c,meas}$ for each experimental condition.

Fig. 5.12 shows a plot of the experimental and theoretical convection velocities. For reference, a dashed line is plotted for $U_{c,meas} = U_{c,th}$. For low convection velocities, $U_{c,th}$ is an excellent approximation of the actual velocity. For a limited amount of data acquired for higher convection velocities though, $U_{c,th}$ under-predicts the velocity which is actually observed. This discrepancy may explain the scatter observed in St when defined using $U_{c,th}$. To confirm this, Fig. 5.13 shows a plot of St versus J using only experimentally measured values. The deviation previously caused by low estimates of U_c has been reduced, and the preferred mode of $St = 0.30$ is seen for both $J = 2$ and $J = 6$. Although Crow and Champagne [106] investigated single jets, they also observed a preferred mode of $St = 0.30$. This mode identified by their measurements may be analogous to the natural instability observed in this study, be it with different velocity and length scales used to define St. Further inspection would be required to reach a conclusion in this regard. Regardless, the LN_2-GHe shear-coaxial jet maintains a preferred instability scaling of $St \cong 0.30$ for the range of flow conditions explored in this study, and may be used to predict the most dominant natural jet instability frequency when an accurate inner shear layer convection velocity is used.

5.3.2 Shear-Coaxial Jets Subject to Acoustic Forcing

To explore the influence of acoustic forcing amplitude, nondimensional forcing frequency, and momentum flux ratio, results are organized to portray two important concepts. First, similar to lock-in diagrams created in Getsinger *et al.* [122] and Sreenivasan *et al.* [123], diagrams will be used to show the minimum forcing amplitude required for the natural instability of a given flow condition to be overtaken by external acoustic forcing. Second, the same diagrams will quantify the significance of the forced mode via the forced mode pixel intensity variance contribution Ψ as determined by eqn. 4.25. Two such diagrams will be presented, one with results for jets located at a PN and one for jets located at a PAN.

5.3.2.1 Jets Located at a Pressure Node

The first forcing susceptibility diagram is shown in Fig. 5.14, including 36 points for jets located at a PN. The x-axis is the nondimensional forcing frequency F determined using experimental values of f_F and f_{nat}. Three different values of the forcing frequency, $f_F = [1700, 2050, 2600]$ Hz, and two different values of the natural jet frequency $f_{nat} = [921, 970]$ Hz, are included, creating six different values of F shown in Fig. 5.14. Nondimensional forcing frequencies of 1.85, 2.23, and 2.82 correspond to $J = 2$, where the mean natural frequency is 921 Hz. Nondimensional forcing frequencies of 1.75, 2.11, and 2.68 correspond to $J = 6$, where the mean natural frequency is 970 Hz. Although it is desired to include cases where $F < 1$, F was maintained above unity due to facility constraints. The y-axis is the acoustic forcing amplitude represented by u' rather than the measured p'. This is done to describe amplitude with a variable which is more pertinent to a PN, where pressure amplitudes are approximately zero and the jet is instead perturbed by acoustic velocity fluctuations. The acoustic velocity perturbation is

estimated using

$$u' = \frac{p'_{max}}{\rho_c c}, \tag{5.4}$$

where p' is the average of the maximum pressure perturbation amplitudes at the adjacent PANs located at $y = \lambda/4$ and $y = -\lambda/4$. Equation 5.4 requires that acoustic waves are linear and one-dimensional, which is supported by experimental observation for the amplitudes employed in this study. After assuming that a perfectly sinusoidal wave takes shape in the transverse direction, p' at adjacent PANs were calculated by interpolation using pressure amplitude measurements at a point between a PN and a PAN, e.g. $y = \lambda/8$ and $y = -\lambda/8$. The ambient chamber density ρ_c and speed of sound are determined as functions of the measured chamber pressure and temperature following REFPROP fluid properties. Finally, the forcing susceptibility diagram utilizes different symbol sizes to illustrate the forced mode variance contribution Ψ. For example, a large, black-filled symbol represents a high value of Ψ, common in conditions with high levels of acoustic forcing. Conversely, low forcing amplitudes often result in small values of Ψ. In fact, conditions with low levels of forcing often cause the naturally occurring instability to remain dominant, and this type of result is represented by unfilled symbols and symbols filled with an $\times$.

First and foremost, Fig. 5.14 shows that an increase in u' increases the likelihood that the forced mode will overtake the natural jet instability as the most dominant mode. This should be expected, and will remain true for all results presented in this study. Next, as u' is increased beyond the point where the forced mode overtakes the natural mode, the variance contribution from the forced mode continues to increase, giving the forced mode greater and greater dominance over the natural behavior of the jet. There are exceptions to this relationship though. For $F = 2.68$ and $J = 6$, increasing the forcing amplitude beyond $u' = 0.3$ m/s did not result in a greater variance contribution from the forced mode.

Secondly, Fig. 5.14 reveals that the susceptibility of the jet to acoustic forcing at a PN is dependent on F. This is readily apparent for $J = 6$. For $J = 6$, the forced mode overtakes the natural mode at $u' \approx 0.1$ m/s for the lowest forcing frequency, but an equivalent amplitude at the highest frequency does not produce a jet response. In fact, the forced mode for the highest frequency was not detected within the twelve highest ranked POMs determined by POD analysis until the forcing amplitude was increased to $u' = 0.17$ m/s. An even greater amplitude was necessary for the forced mode to overtake the natural mode. This result corresponds directly to that of absolute instability lock-in experiments [118, 122, 123], whereby increasing F from unity causes greater resistivity to forcing. While this phenomenon alone does not allow one to conclude that absolute instability exists, it does indicate that naturally occurring instabilities are more difficult to overcome with forcing at higher frequencies, consistent with absolutely unstable behavior [25, 118].

If the natural jet instability is only convectively unstable though, a separate explanation for the results in Fig. 5.14 could possibly exist. Since the work of Buffum and Williams [27], it has been known that transverse acoustic forcing can induce sinusoidal whipping motions in a jet column. An instability of this type is not strictly a shear layer instability, but is instead a bulk column mode resulting from periodic changes in transverse momentum. This behavior is shown in the snapshot sequence in Fig. 5.15 for $J = 2$, and is also supported by the eigenvector images of the forced mode in Fig. 5.16. More recently, Carpentier *et al.* [26] and Baillot *et al.* [16] recognized that side-to-side or sinuous motions observed by Buffum and Williams are highly dependent on frequency, and that a short acoustic period will prevent a jet from gaining significant spanwise momentum prior to a reverse in the transverse acoustic velocity which occurs at a PN. Not only do the qualitative results of this study demonstrate antisymmetric, sinusoidal jet motions, but Fig. 5.14 supports the principle established by Carpentier *et al.*, stating that at a fixed amplitude, increasing f_F will decrease the amplitude of transverse jet

motions. A similar relationship with f_F was also observed in experiments by Graham *et al.* [104] and Rodriguez *et al.* [81], where a higher f_F caused a degraded sensitivity to transverse acoustic forcing. The observation of sinuous or antisymmetric shear-coaxial jet motion in the vicinity of a PN actually shares some similarities with the droplet combustion experiments described in Chapters 2 and 3 of this dissertation. For all fuels explored and for virtually all amplitudes of acoustic excitation, burning droplets situated precisely at a PN during excitation did not have stable, uni-directionally oriented flames. As described in section 3.2.2, the flames under these circumstances switched back and forth in time, and did not stabilize to an orientation to one direction or the other. This asymmetric, sinuous-like distortion of the flame may have similarities to the sinuous motions quantified for shear-coaxial jets situated at a PN.

Lastly, to show the effect of J, Fig. 5.17 shows a plot of Ψ versus u' for $J = 2$ and $J = 6$. For both momentum flux ratios, low values of u' result in negligible variance contribution from the forced mode as determined by the twelve highest ranked POMs. Although it is not clear that J influences the level of forcing necessary to overtake the natural mode, Fig. 5.17 shows that J influences receptivity to acoustic forcing by viewing the magnitudes of Ψ for each case, consistent with absolutely unstable behavior. The forced mode variance contribution values for $J = 6$ reach magnitudes which are generally larger than those for $J = 2$. For $J = 2$, it appears that a form of saturation has occurred when reaching $u' \approx 0.4$ m/s; higher forcing amplitudes do not excite a greater variance contribution from the forced mode. Conversely, $J = 6$ creates more receptive conditions and values of Ψ which are nearly twice as large as their $J = 2$ counterpart.

5.3.2.2 Jets Located at a Pressure Antinode

A second forcing susceptibility diagram is shown in Fig. 5.18, including 41 points for jets located at a PAN. The y-axis is the acoustic forcing amplitude represented by p' as

measured by the dynamic pressure transducer located directly behind the jet as viewed from the camera. This measurement, named $p_{dyn,2}$, is most important when the jet is located at a PAN. At this location, $u' \approx 0$, making p' the primary cause of acoustically induced jet dynamics.

As shown in Fig. 5.18, p' values of approximately 3.5 kPa are required in order to observe the forced mode in the jet dynamics. When viewing the twelve highest ranked POMs, acoustically forced cases with $p' < 3.5$ kPa did not produce any evidence of the forced mode. A further increase in p' produces a POM pair for the forced mode among the highest POMs, but an amplitude of $\sim$7 kPa is necessary for the forced mode to overtake the natural mode. This is true for both momentum flux ratios and all nondimensional frequencies shown in Fig. 5.18. For example, results for $J = 6$ and $F = 1.75$ show that a forcing amplitude of $p' = 6.27$ kPa asserts significant forced mode dynamics in the jet, but increasing the amplitude to $p' = 7.58$ kPa caused the forced mode to overtake the natural mode as the most dominant instability.

To best explain the influence of acoustic forcing frequency on jet dynamics, the jet's qualitative behaviors may first reveal the mechanism by which pressure fluctuations induce a forced mode instability. Jets located at a PN exhibit transverse side-to-side motion, while jets located at a PAN were observed to have axisymmetric vortex rings at the inner shear layer. This behavior is shown in the snapshot sequence in Fig. 5.19 for $J = 2$, and is also supported by the eigenvector images of the forced mode in Fig. 5.20. These vortex rings, or "puffs", are produced at the injector exit and become the most dominant mode for $p' \gtrsim 7$ kPa. Vortex rings have also been observed in previous experiments at AFRL [81, 104, 105]. Baillot *et al.* [16] observed similar axisymmetric instability for shear-coaxial jets at atmospheric pressure, and concluded that vortex rings result from outer jet gas pulsations. A momentary rise in chamber pressure at the beginning of an acoustic pressure cycle was said to impede the flow of the gas annulus,

followed by an increase in jet velocity due to the subsequent decline in pressure in the latter part of the acoustic cycle. Pulsations were not observed for the dense, liquid inner jet [16]. Using the following analytical derivation, the PAN jet pulsation phenomenon is shown to indeed be dependent on jet density as well as acoustic forcing frequency.

Consider Newton's Second Law when applied to the mass of fluid inside an injector. The downstream end of this mass of fluid is subject to a periodic force with an amplitude of F'_{PAN} at the injector exit, due to a pressure fluctuation p'. The mass of the body of fluid is equal to the product of density ρ and volume V, and the body of fluid has a periodic acceleration a which results from a periodic force applied at the exit of the injector. To obtain the streamwise u' resulting at the exit of an injector at a PAN location, Newton's second law is applied to one quarter of an acoustic cycle which yields

$$\begin{aligned} F_{PAN} &= ma \\ \int_0^{\frac{1}{4f_F}} F_{PAN}\mathrm{d}t &= \int_0^{\frac{1}{4f_F}} ma\mathrm{d}t \\ \int_0^{\frac{1}{4f_F}} F'_{PAN}\sin\left(2\pi f_F t\right)\mathrm{d}t &= \rho V \int_0^{\frac{1}{4f_F}} \frac{\mathrm{d}u}{\mathrm{d}t}\mathrm{d}t. \end{aligned} \tag{5.5}$$

Carrying out the integration of force and acceleration results in

$$\begin{aligned} F'_{PAN}\left[-\frac{1}{2\pi f_F}\cos\left(2\pi f_F t\right)\right]_0^{\frac{1}{4f_F}} &= m\left[u\right]_0^{\frac{1}{4f_F}} \\ F'_{PAN}\left[-\frac{1}{2\pi f_F}\left(\cos\frac{\pi}{2}-\cos 0\right)\right] &= m\left[0-(-u')\right] \\ \frac{F'_{PAN}}{2\pi f_F} &= mu', \end{aligned} \tag{5.6}$$

which can be simplified further by writing F'_{PAN} as the product of the injector exit area A and the pressure amplitude at the jet p' and by writing V as the product of A and the injector length l. These substitutions give a straightforward solution for the injector

fluid velocity fluctuations u' induced by the chamber pressure oscillations p' at a PAN,

$$u' = \frac{p'}{2\pi f_F \rho l} \tag{5.7}$$

This solution may be applied to the inner or outer jet by using ρ_{ij} and l_{ij} or ρ_{oj} and l_{oj}, respectively. If integration is performed over one-half an acoustic cycle rather than one-quarter of an acoustic cycle, then the same solution is reached. Eqn. 5.7 is a relation for injector-acoustic interactions occurring at a PAN, but should be treated as an approximate solution, as it does not account for the geometry of an injector plenum upstream of the constant area section l, nor does it account for potential acoustic resonance in the injector. Eqn. 5.7 also treats the fluid in the injector as a single body with constant mass, neglecting compressibility. Although, the assumptions made to reach this solution limit its applicability, the solution advocates that for a constant p' the pulsation velocity u' is inversely proportional to f_F and ρ.

Therefore, the derivation of the injector pulsation velocity and the results shown in Fig. 5.18 support the conclusions of Baillot *et al.* [16] by asserting an inverse relationship between both f_F and ρ and the amplitude of resulting outer jet pulsations. For the injector of interest here, l_{ij} and l_{oj} are of the same order of magnitude ($l_{ij} = 1.8 l_{oj}$), and differences in the pulsation amplitude u' are caused by a difference in ρ_{ij} and ρ_{oj}. Since $\rho_{ij} \approx 100 \rho_{oj}$, pulsations in the liquid nitrogen inner jet will be negligible in comparison to those in the gaseous helium outer jet. Therefore, one should expect the forced mode will influence the inner shear layer instability when the outer jet pulsations reach a significant velocity amplitude. Meanwhile, inner jet pulsations can be ignored. The inner jet may be indirectly effected by axisymmetric vortex rings which form at the exit of the outer jet and convect downstream, but will be less effected by chamber pressure fluctuations directly. As a result, the outer jet pulsation phenomenon will control the susceptibility of the jet to acoustic forcing. This concept is reenforced by two conclusions of this study. First, Fig. 5.18 shows that increasing the nondimensional forcing frequency F requires

an increase in p' in order for the forced mode to overtake the natural mode. Second, a critical PAN forcing amplitude will be shown to depend solely on outer jet conditions, because the forced mode is manifested specifically via the outer jet.

Concerning forcing frequency, comparing the minimum and maximum values of F for both $J = 2$ and $J = 6$ reveals the salient effect of F. Fig. 5.18 shows that for $J = 2$, at $F = 1.85$ a forcing amplitude of $p' = 6.00$ kPa caused the forced mode to overtake the natural mode, but at $F = 2.82$ an increased forcing amplitude of $p' = 7.93$ kPa was insufficient and the natural instability remained most dominant. For $J = 6$, at $F = 1.75$ a forcing amplitude of $p' = 4.55$ kPa and $p' = 6.27$ kPa caused the forced mode to appear within the twelve highest ranked POMs, an indication that the forced mode is nearly as significant as the natural mode in terms of pixel intensity variance. Further increasing the amplitude to $p' = 7.58$ kPa caused the forced mode to overtake the natural mode. Conversely, for $J = 6$ and $F = 2.68$, $p' = 0.95$ did not produce a significant forced mode, as the forced mode POM pair did not appear within the twelve highest ranked POMs.

Note that although the critical amplitude increases with F, one cannot estimate that this relationship holds for $F < 1$ or near $F = 1$. The current test matrix does not include the forcing frequencies necessary to make this conclusion. In a traditional lock-in diagram for absolute instability [122, 123] the minimum amplitude necessary for lock-in forms the well-known "V" shape, and requires an increase in the minimum amplitude as F is decreased below unity. The results in Fig. 5.18 do not precisely assert this type of behavior, but data at lower forcing frequencies are not available to study the phenomenon in detail. Nevertheless, the fact that there are forcing conditions that preclude lock-in does seem to suggest the appearance of absolutely unstable shear layers.

To understand the influence of J, Fig. 5.21 shows a plot of Ψ versus p' for $J = 2$ and $J = 6$ at a PAN. Similar to Fig. 5.17, low values of p' result in approximately zero

variance contribution from the forced mode as determined by the twelve highest ranked POMs. Significant forced mode variance occurs when p' is increased to a value between 3.5 kPa and 7.0 kPa, depending on J and F. Higher amplitudes cause increased values of Ψ, but this relationship is more pronounced for $J = 6$ than $J = 2$. Similar to a PN condition, forced mode variance contributions for $J = 6$ reach values nearly twice as large those for $J = 2$. Thus, holding all other variables approximately constant, $J = 6$ exhibits greater susceptibility to external acoustic forcing than $J = 2$ when the jet is located at a PAN.

Finally, to emphasize the importance of outer jet pulsations at a PAN, an effort is made to collapse the data in Fig. 5.21 using a nondimensional forcing amplitude on the x-axis rather than the measured quantity p'. If indeed the forced mode infiltrates the inner shear layer by manipulating the outer jet flow, then outer jet pulsations must rival natural turbulence levels which are introduced into the inner shear layer by the outer jet. These natural fluctuations in the outer jet will be proportional to the dynamic pressure of the outer jet $\frac{1}{2}\rho_{oj}u_{oj}^2$, while the forced pulsations at the outer injector exit are shown to be directly proportional to p' in eqn. 5.7. As a result, $p'/\frac{1}{2}\rho_{oj}u_{oj}^2$ was chosen as a nondimensional forcing amplitude and is the new x-axis in Fig. 5.22. When compared with the dimensional plot in Fig. 5.21, Fig. 5.22 shows a more meaningful distribution at $p'/\frac{1}{2}\rho_{oj}u_{oj}^2 = 1$, where both $J = 2$ and $J = 6$ result in positive values of the forced mode variance contribution Ψ. When $p' < \frac{1}{2}\rho_{oj}u_{oj}^2$ the acoustic forcing induces a negligible effect on the jet. In conclusion, when the liquid-gas coaxial jet was acoustically forced at a PAN condition, the forced mode began to influence the inner shear layer instability when the acoustic pressure perturbation p' was nearly equal to or greater than the outer jet dynamic pressure.

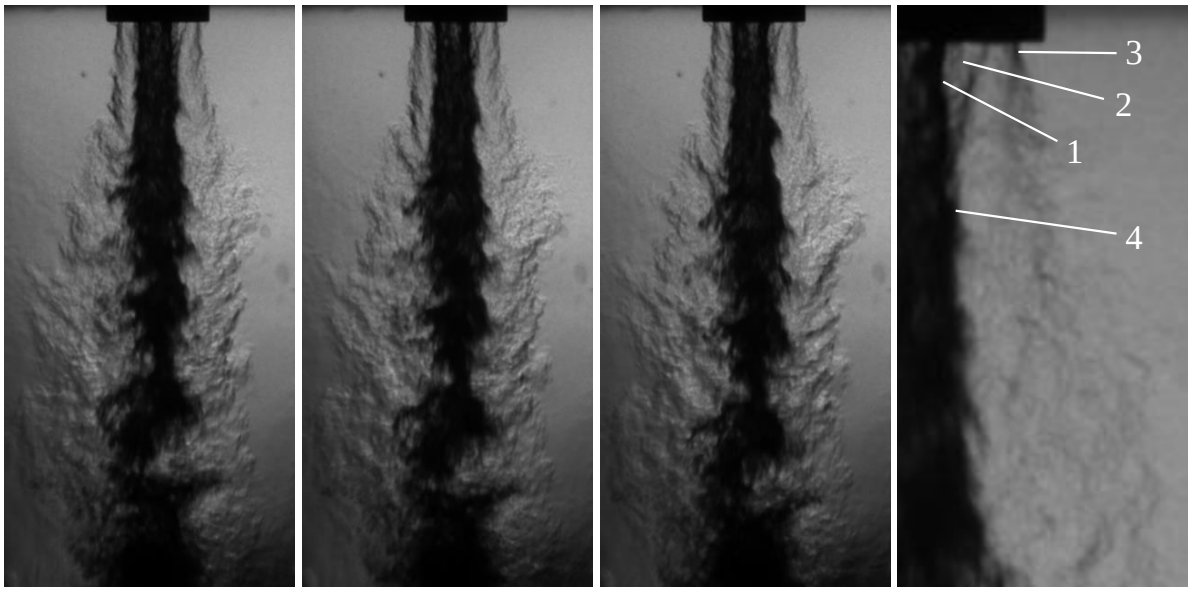

5.1: A sequence of unforced LN_2-GHe jet images acquired at a frame rate of 10 kHz, accompanied by a reduced field of view to show the (1) interface between the liquid nitrogen inner jet and the recirculation zone (2) recirculation zone (3) outer shear layer (4) inner shear layer forming at the downstream end of the recirculation zone.

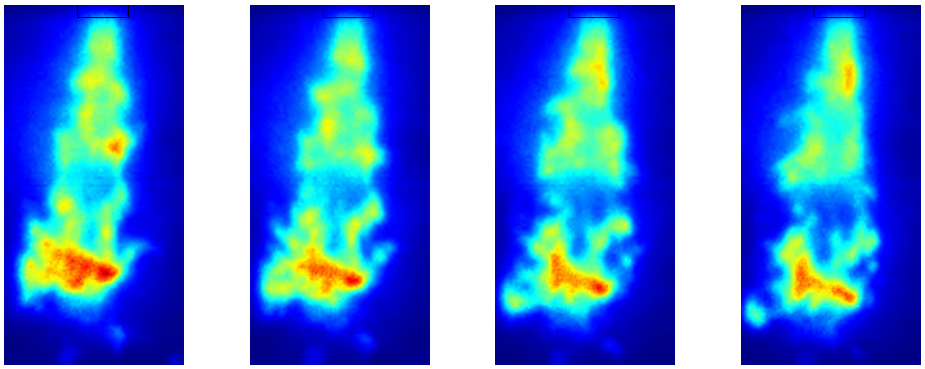

5.2: A consecutive sequence of unforced O_2-H_2 flame images acquired at a frame rate of 16 kHz. The intensifier gate duration, which is essentially the camera exposure time, is set to 61 s. Flame structures form near the injector exit and evolve as they travel downstream. $MR = 5.9$ ($\phi_{f/o} = 1.36$), $J = 2$, p_c≈400 psia = 2.76 MPa.

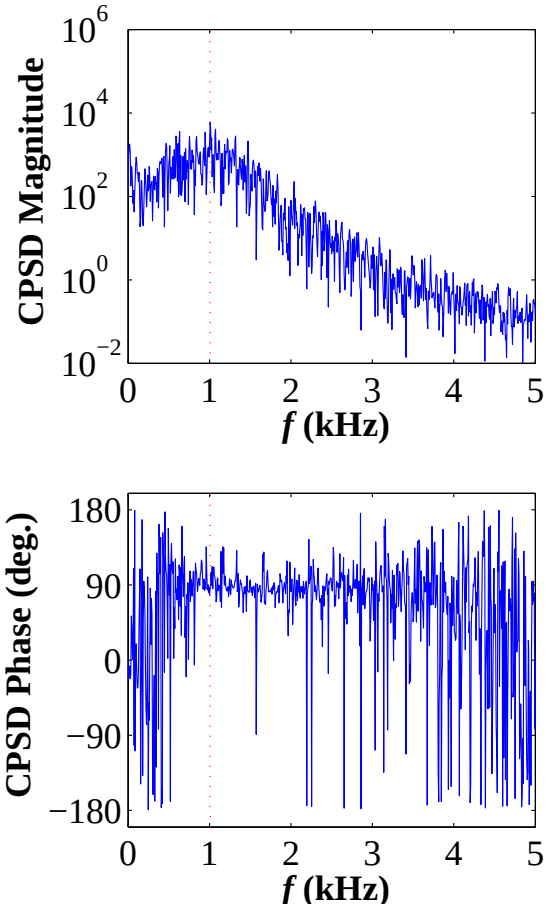

5.3: Cross power spectral density magnitude (top) and phase (bottom) for POD modes 3 and 4 for an unforced LN_2-GHe jet with $J = 6$. A vertical red line is located at $f = 945$ Hz represents the characteristic instability frequency for this particular case.

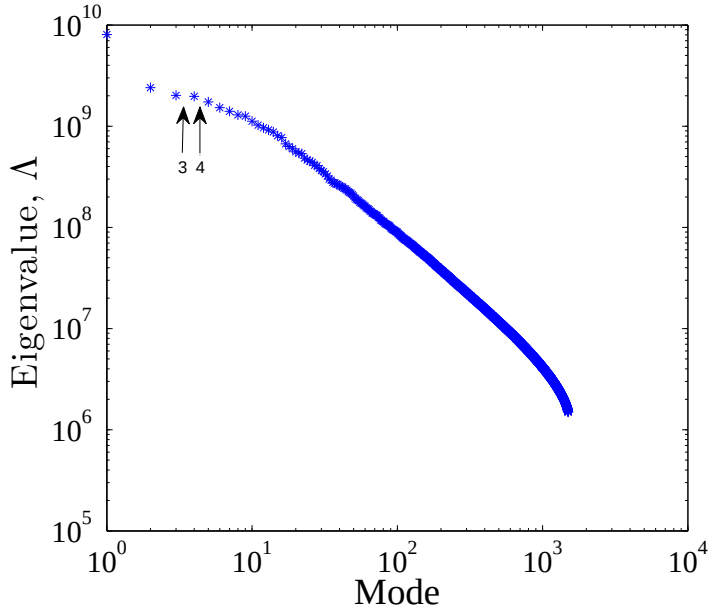

5.4: POD eigenvalues ranked according to magnitude show that although modes 3 and 4 have been chosen to assert the natural instability of the jet, the eigenvalues of modes 5-8 are nearly as high as the eigenvalues of 3 and 4. ($\Lambda = \sigma^2$)

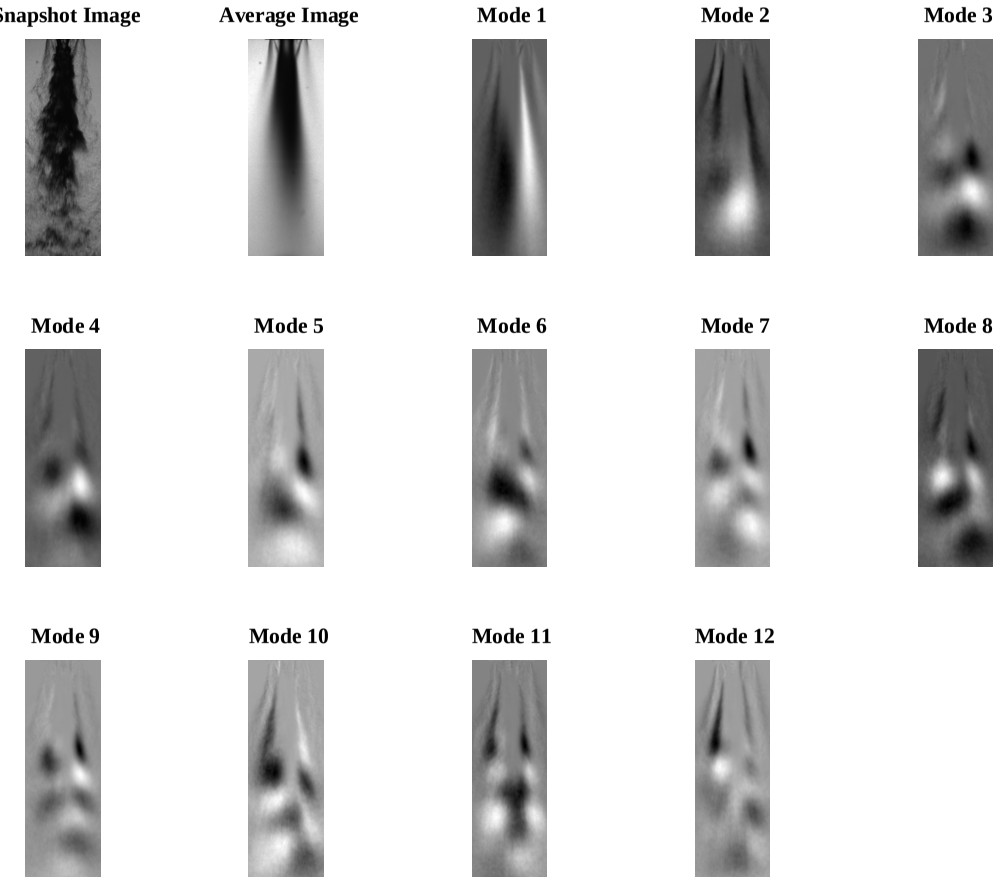

5.5: POM images 1-12 are shown for an unforced LN_2-GHe jet at $J = 6$. Modes 3 and 4 are the highest ranked conjugate mode pair, together demonstrating a natural jet frequency of 945 Hz. The eigenvalues of modes 1 and 2 are greater than 3 and 4, but do not display coherent structures having a 90° phase difference.

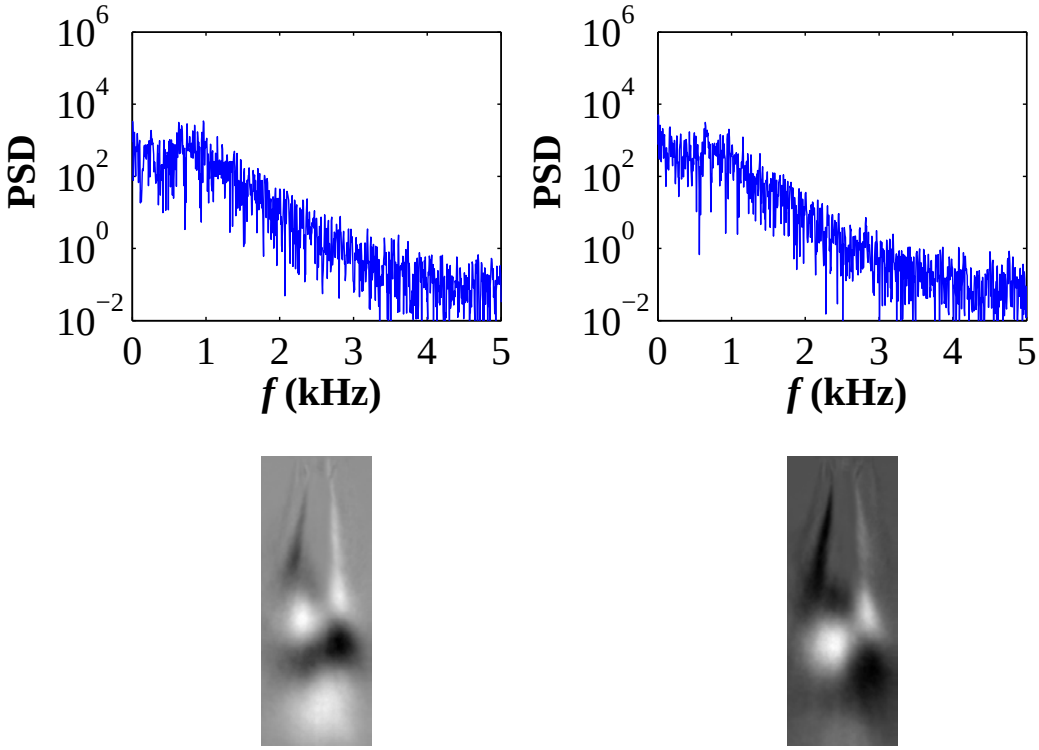

5.6: The naturally occurring mode for $J = 6$ is represented by the POM pair which consists of mode-3 (left) and mode-4 (right). Power spectral density plots are shown (top) with each corresponding eigenvector image (bottom). The natural mode is antisymmetric, and likely a helical instability. The eigenvector images of mode-3 and mode-4 appear to be 90° out-of-phase in the streamwise direction.

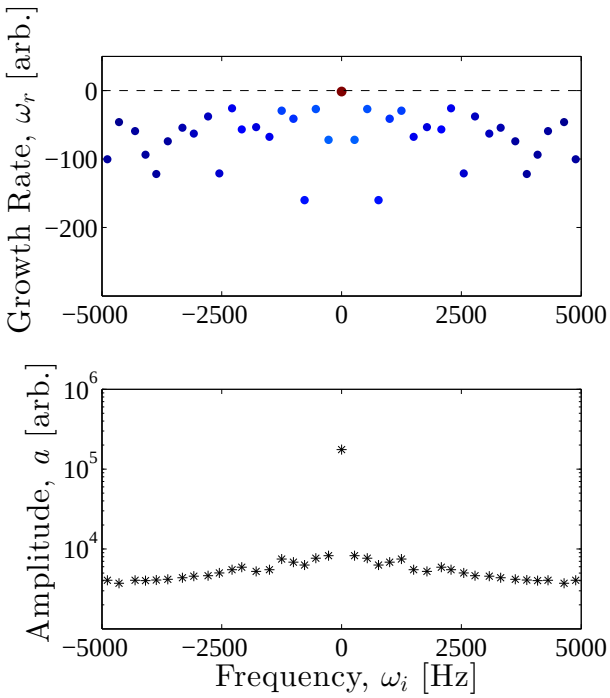

5.7: Top: Real eigenvalues ω_r (growth rate) and imaginary eigenvalues ω_i (frequency) plotted for DMD results computed for an unforced LN_2-GHe jet with $J = 6$. Each point represents a single mode identified by DMD, and the color and size of each point is scaled with the amplitude of each mode as calculated using eqn. 4.49. Bottom: Mode amplitudes plotted versus ω_i. A significant natural mode cannot be identified.

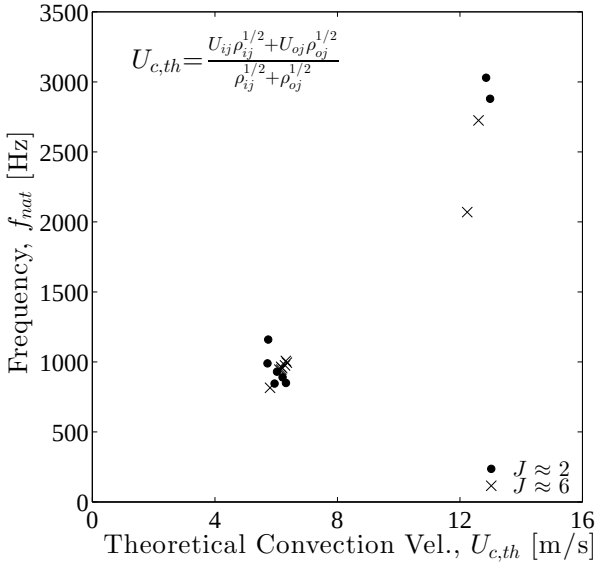

5.8: LN_2-GHe jet instability frequency, as measured by POD, plotted versus shear layer convective velocity. J is nominally maintained between 2 and 6. Each point corresponds to a point in Fig. 5.9 and exact values can be found in appendix A.

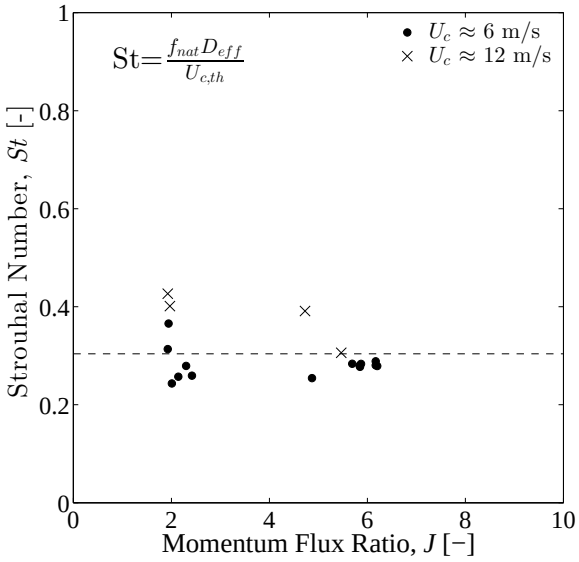

5.9: LN_2-GHe jet Strouhal number plotted versus J based on data in Fig. 5.8, using a theoretical shear layer convection velocity $U_{c,th}$.

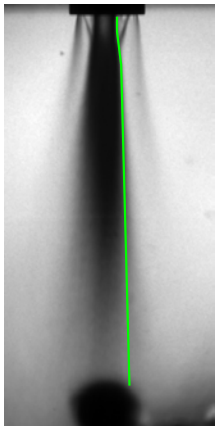

5.10: A time-averaged image of the LN_2-GHe shear-coaxial jet with the location of the inner shear layer curve s in green.

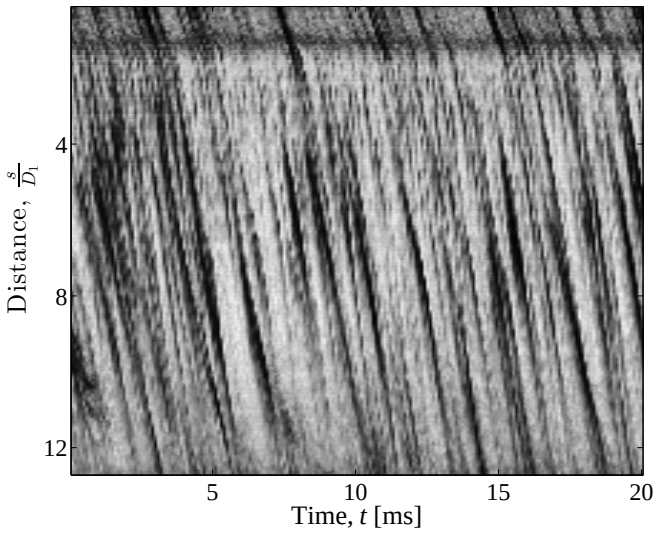

5.11: The pixels located on the shear layer curve s, defined in Fig. 5.10, shown for a period of time spanning 20 ms. Diagonal streaks are the convection of fluid structures of the inner shear layer, and the velocity of each structure is equal to the slope of each respective streak, $\Delta s/\Delta t$.

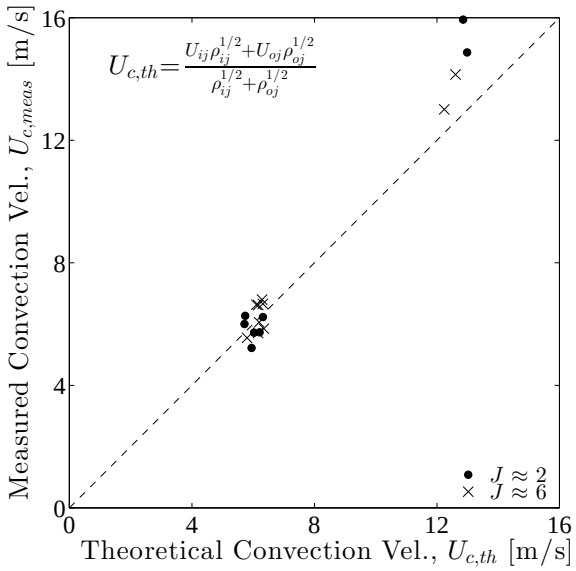

5.12: Measured shear layer convection velocities plotted versus theoretical values.

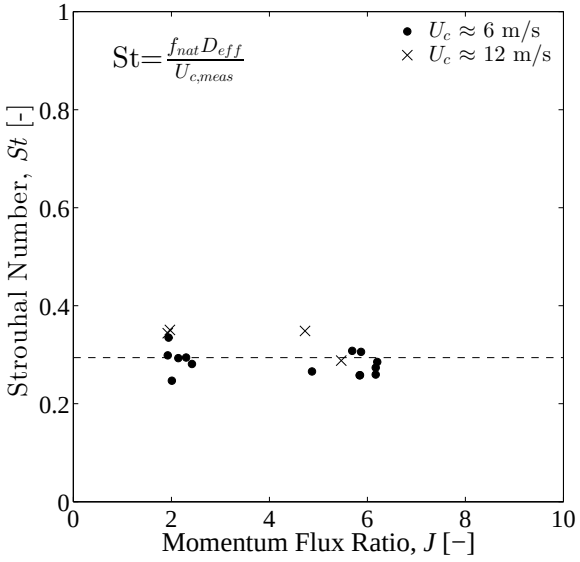

5.13: LN_2-GHe jet Strouhal number plotted versus J, using a measured shear layer convection velocity $U_{c,meas}$.

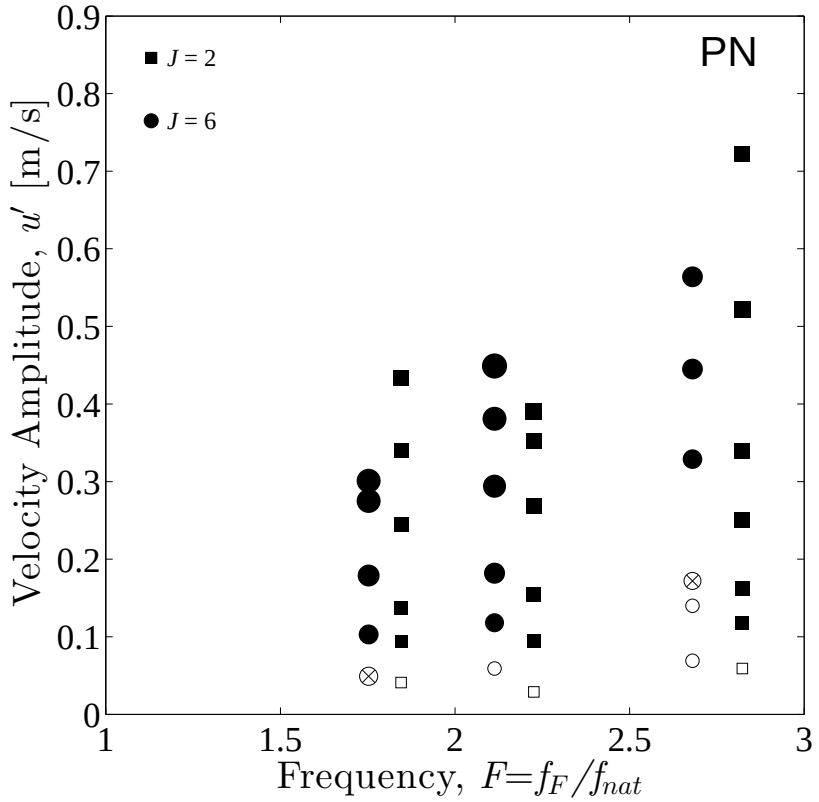

5.14: The acoustic forcing amplitude u' is plotted versus the nondimensional frequency for $J = 2$ and $J = 6$ for a jet located at a PN. Open symbols represent conditions in which the natural mode of the jet was most significant. Closed symbols represent conditions in which the natural mode was overtaken by the forced mode. The size of each symbol is scaled with the forced mode's variance contribution to the flow as determined by POD eigenvalues, e.g. large, filled symbols represent a condition where the forced mode has a large contribution to the total energy of the flow. Very small, open symbols represent a case in which the forced mode did not appear in the POD results. Symbols with an $\times$ represent cases in which the forced mode appeared in the POD results, but did not overtake the natural mode.

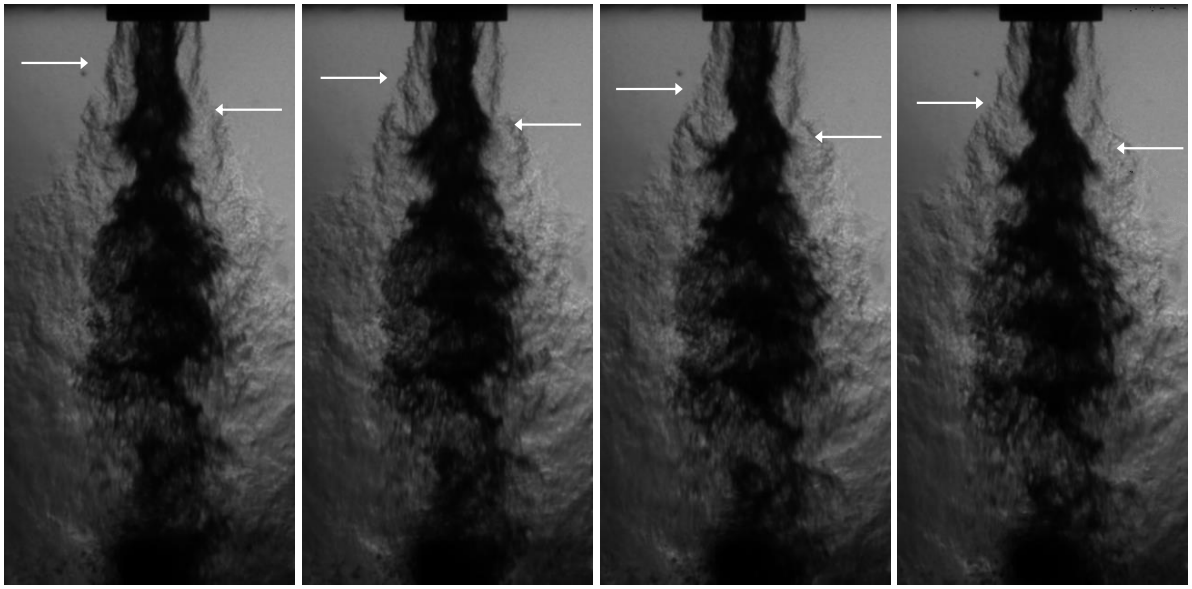

5.15: LN_2-GHe shear-coaxial jets exposed to external, transverse acoustic forcing at a pressure node. Four consecutive images are taken from a set of high-speed images acquired at 10 kHz. An antisymmetric instability forms as periodic spanwise motions caused by the acoustic velocity perturbation u'. $J = 2$, $p_c = 400$ psia $= 2.76$ MPa, $f_F = 1700$ Hz, $u' = 0.43$ m/s

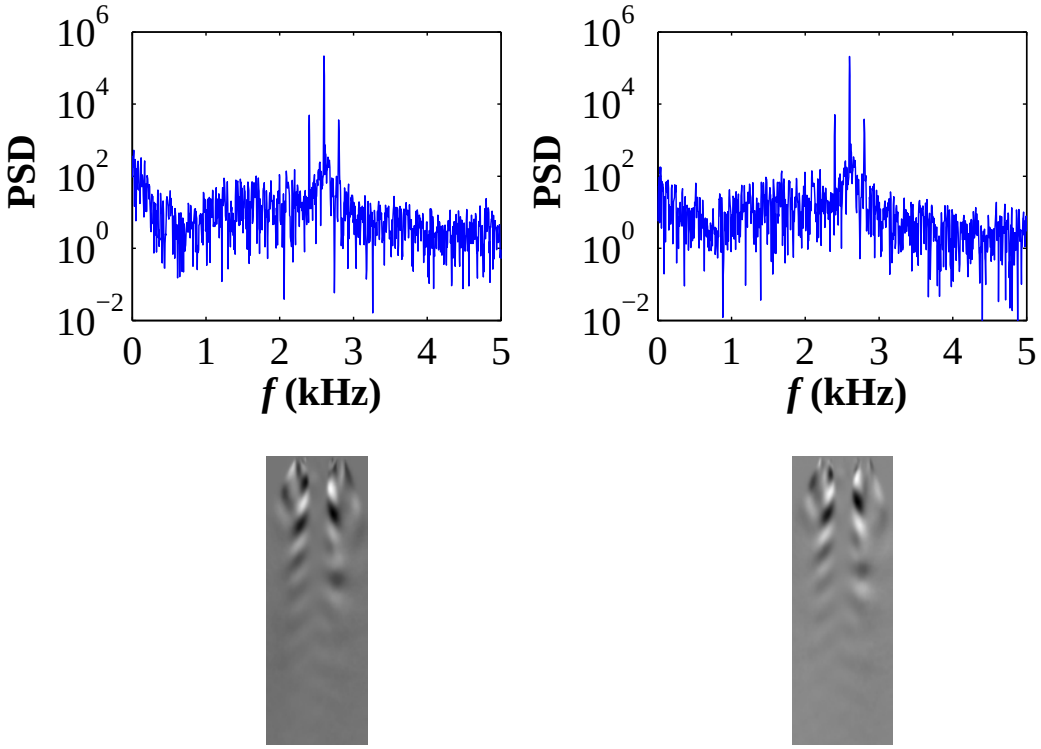

5.16: The forced mode for $J = 2$ at a PN is represented by the POM pair which consists of mode-2 (left) and mode-3 (right). Power spectral density plots are shown (top) with each corresponding eigenvector image (bottom). The forced mode occurring at a PN takes on an antisymmetric appearance. The eigenvector images of mode-2 and mode-3 appear to be 90° out-of-phase in the streamwise direction.

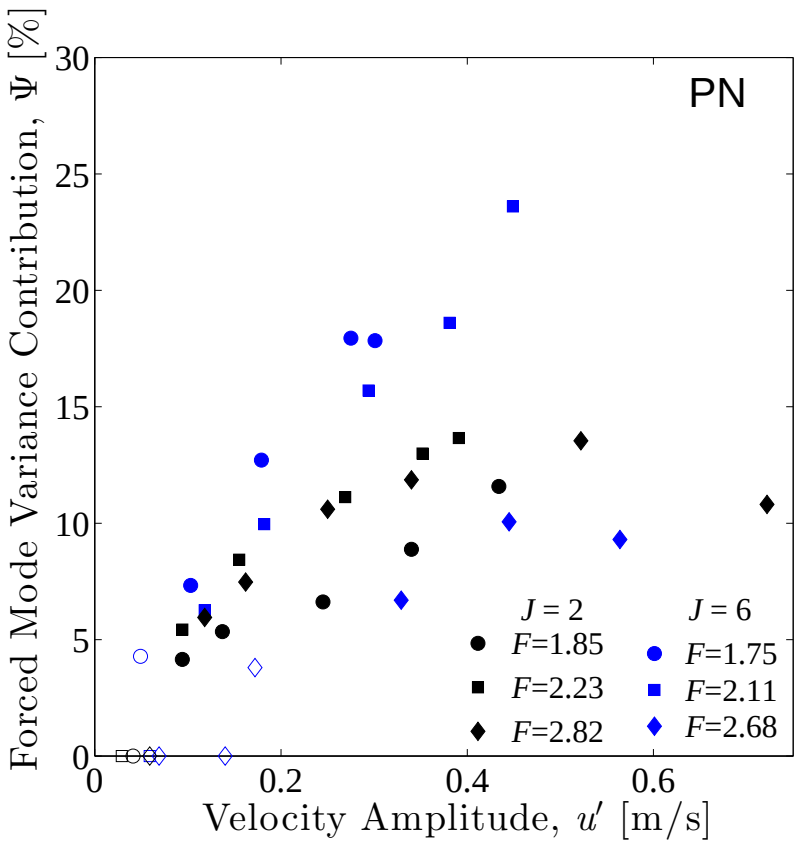

5.17: The forced mode variance contribution is plotted versus the acoustic velocity perturbation amplitude u' for $J = 2$ and $J = 6$ for a jet located at a PN. The nominal natural frequency for $J = 2$ and $J = 6$ is 921 Hz and 970 Hz, respectively. Open symbols represent conditions in which the natural mode of the jet was most significant. Closed symbols represent conditions in which the natural mode was overtaken by the forced mode.

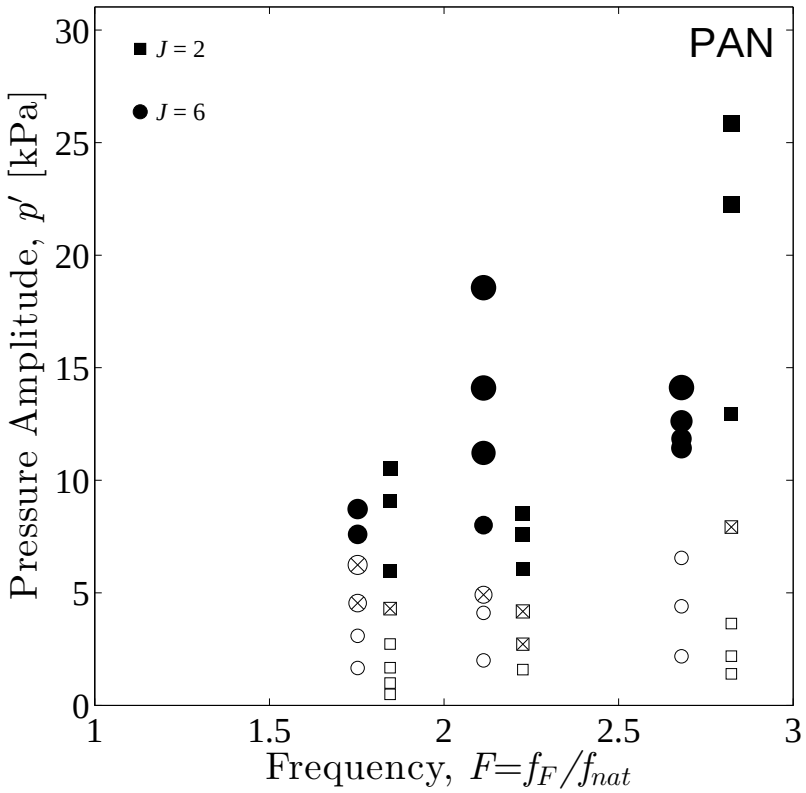

5.18: The acoustic forcing amplitude u' is plotted versus the nondimensional frequency for $J = 2$ and $J = 6$ for a jet located at a PAN. Open symbols represent conditions in which the natural mode of the jet was most significant. Closed symbols represent conditions in which the natural mode was overtaken by the forced mode. The size of each symbol is scaled with the forced mode's variance contribution to the flow as determined by POD eigenvalues, e.g. large, filled symbols represent a condition where the forced mode has a large contribution to the total energy of the flow. Very small, open symbols represent a case in which the forced mode was not exhibited in the POD results. Symbols with an $\times$ represent cases in which the forced mode appeared in the POD results, but did not overtake the natural mode.

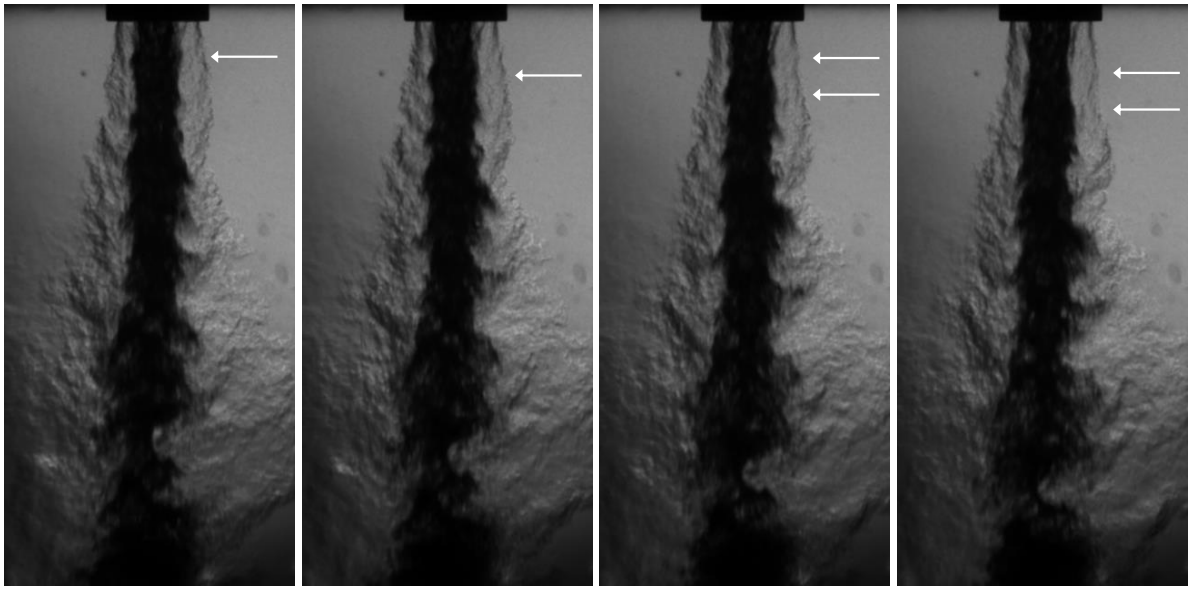

5.19: LN_2-GHe shear-coaxial jets exposed to acoustic forcing at a pressure antinode. Four consecutive images are taken from a set of high-speed images acquired at 10 kHz. An axisymmetric instability forms due to outer jet flow pulsations caused by the acoustic pressure perturbation p'. $J = 2$, $p_c = 400$ psia $= 2.76$ MPa, $f_F = 1700$ Hz, $p' = 1.53$ psi $= 10.55$ kPa

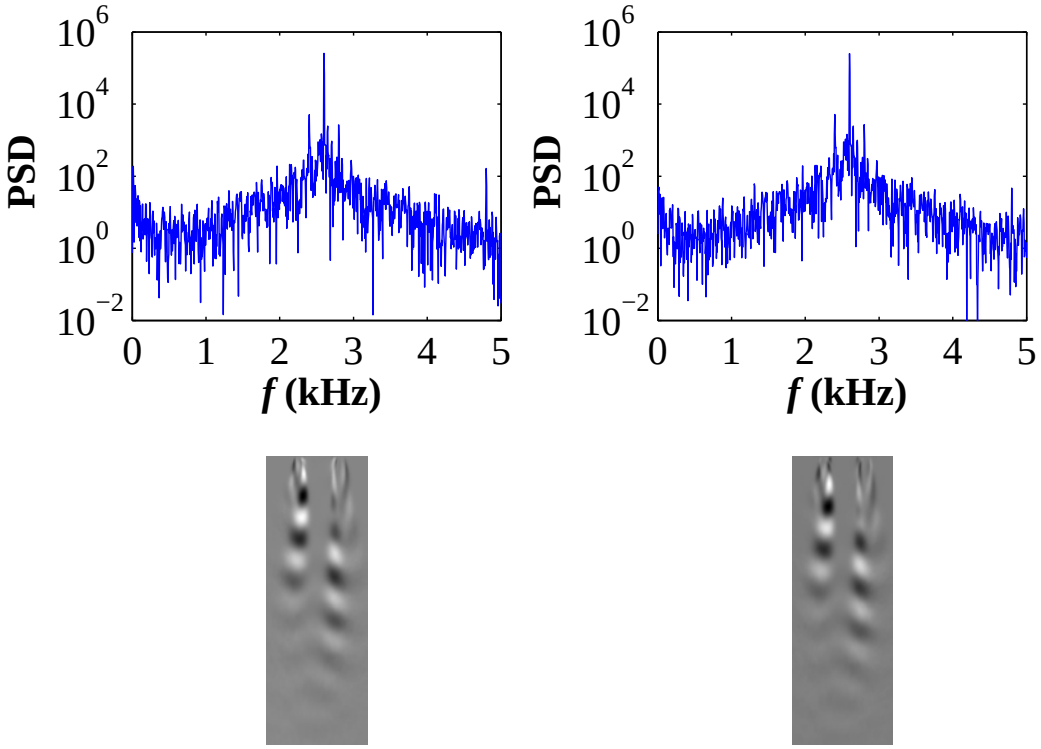

5.20: The forced mode for $J = 2$ at a PAN is represented by the POM pair which consists of mode-1 (left) and mode-2 (right). Power spectral density plots are shown (top) with each corresponding eigenvector image (bottom). The forced mode occurring at a PAN takes on an axisymmetric appearance. The eigenvector images of mode-1 and mode-2 appear to be 90° out-of-phase in the streamwise direction.

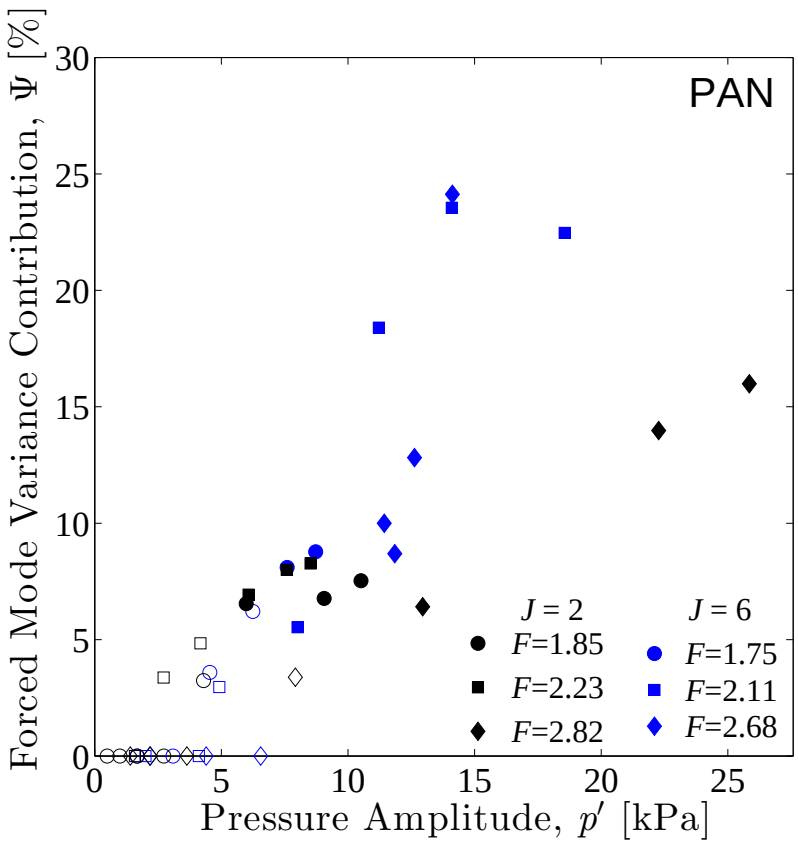

5.21: The forced mode variance contribution is plotted versus the acoustic pressure perturbation amplitude p' for $J = 2$ and $J = 6$ for a jet located at a PAN. The nominal natural frequency for $J = 2$ and $J = 6$ is 921 Hz and 970 Hz, respectively. Open symbols represent conditions in which the natural mode of the jet was most significant. Closed symbols represent conditions in which the natural mode was overtaken by the forced mode.

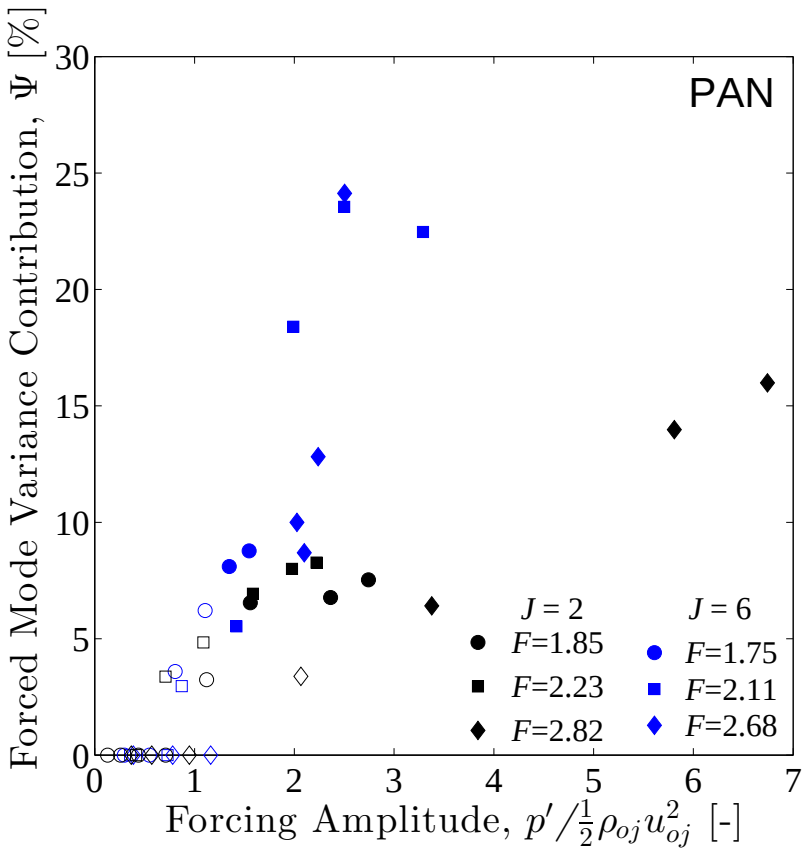

5.22: The forced mode variance contribution is plotted versus the acoustic pressure perturbation amplitude p' nondimensionalized by the outer jet dynamic pressure for $J = 2$ and $J = 6$, for a jet located at a PAN. The nominal natural frequency for $J = 2$ and $J = 6$ is 921 Hz and 970 Hz, respectively. Open symbols represent conditions in which the natural mode of the jet was most significant. Closed symbols represent conditions in which the natural mode was overtaken by the forced mode.

CHAPTER 6

Conclusions and Future Work

This dissertation has described extensive experiments relevant to acoustically-coupled combustion and transport processes. While both studies (on acoustically excited droplet combustion at UCLA and acoustically-coupled coaxial jets at AFRL) have helped to answer a number of fundamental scientific questions, there remain a number of issues on which future studies should focus.

6.1 Studies on Acoustically-coupled Droplet Combustion

The results in Chapter 3 on the fuel droplet combustion studies present strong evidence that the acoustic radiation force theory of Tanabe *et al.* [21, 73] does not properly account for the dynamic interactions between condensed phase combustion and acoustic excitation. Quantitatively, the amount of flame deformation and the locations of maximum flame deformation disagree with the prescribed theory. Qualitatively though, the location of flame switch is predicted fairly well, implying that acoustic radiation force theory plays a role in droplet combustion, but perhaps leaves essential combustion phenomena unaccounted for. Thermochemical relationships vital to condensed phase combustion may hold primary influences, rather than secondary influences, on the flame behaviors observed here.

To capture these effects, future work should explore the chemical kinetics frequency response in detail. First, the spatiotemporal relationship between flame standoff dis-

tance and acoustic phase could be enlightening. This relationship was not discussed in detail here, and could reveal a reaction phase delay which is frequency dependent. Any interdependency between chemical kinetics and frequency could contribute to the fact that Tanabe's theory is more accurate for higher frequencies than lower frequencies. Second, the well known Rayleigh criterion may predict different levels of instability for different acoustic flow conditions. The Rayleigh index, a transfer function calculated using the difference in phase between the pressure fluctuation p' and the heat release fluctuation q', can be found for each flow condition by synchronizing p' measurements with q' measurements, which can be inferred from global or local OH* chemiluminescence intensity. Should these studies provide illuminating results, a revised acoustic radiation force theory could provide a more comprehensive and accurate model of acoustic excitation coupled to condensed phase combustion, giving insight to the field of burning droplets as well as an array of other combustion instability problems.

6.2 Studies on Shear-coaxial Jets

To explore the susceptibility of shear-coaxial jets to external acoustic forcing, this study quantifies the amplitude at which the acoustically forced mode will overcome the naturally occurring mode as the most significant instability in the jet. It is evident that a critical forcing amplitude can indeed be identified, and its value will depend on the nondimensional forcing frequency F and jet flow conditions, such as the momentum flux ratio J. The critical forcing amplitude's dependence on F shares features with V-shaped lock-in diagrams common in absolute instability studies, where values of F which diverge from unity require increasingly large forcing amplitudes in order for the forced mode to overtake the natural mode. Indeed, a potential wake instability may produce absolute instability at the recirculation zone near the injector exit, but further theoretical work is required to determine the likelihood of absolute instability for the range of flow con-

ditions used here. An expanded test matrix to include $F < 1$ is also required to verify a V-shaped curve and confirm this relationship.

Alternatively, the results contain several indications that the natural mode of the jet instability is different from the typical absolutely unstable shear layer. The sinusoidal whipping of jets located at a PN and the streamwise pulsations of jets located at a PAN both are associated with periodic momentum fluctuations, whereby a long acoustic cycle encourages the production of a significant change in fluid momentum. As explained above, this mechanism will prohibit large amplitudes of momentum from being produced if the acoustic cycle is short, and thus an increase in f_F will cause an increase in the critical forcing amplitude for all F. Such a relationship has not been observed in prior studies of absolute instability, although in most studies of lock-in and associated phenomenon, a range of forcing frequencies can be studied without the requirement of creation of a standing wave. Again, an expanded test matrix can verify these relationships. The qualitative behavior of the jet after the acoustically forced mode overtakes the natural mode consistently revealed co-existing modes, whereby the forced mode became most dominant and the natural mode remained a significant mode within the mixing layer. While this is typically observed in absolutely unstable shear layers, there are some differences. The broadband nature of the natural instabilities observed have contrast to that of absolutely unstable flows, which are known to exhibit sharp peaks at a single frequency and higher harmonics. For the range of conditions explored in this study, it is believed that the naturally occurring jet instability is convectively unstable rather than absolutely unstable.

Reduced basis methods were successfully applied using a novel approach which compares the forced mode pixel intensity variance contribution Ψ from one case to another. In this way, quantitative measures of susceptibility to external forcing were obtained. Although qualitative conclusions were a valuable portion of this study, this quantita-

tive method shows great potential for future studies. Dynamic mode decomposition and proper orthogonal decomposition both showed advantages and disadvantages with regard to analyzing experimental images, and future work should continue to utilize and refine these algorithms where harsh environments make it difficult to use intrusive sensors alone. Although proper orthogonal decomposition was used for the majority of post-processing in this study, dynamic mode decomposition is recommended where specific frequencies must be extracted from dynamic flow structures.

The techniques noted above will prove to be powerful when applied to reactive combustion instability experiments, which is a paramount objective of this research campaign. To quantify the susceptibility of oxygen-hydrogen flames to acoustic forcing, reduced based methods will draw spectral information from high-speed images without requiring delicate instrumentation to be placed in a high pressure, high temperature combustion chamber. Ultimately, Strouhal number scaling laws will be refined for reactive conditions and forcing susceptibility diagrams will shine light on the inter-dependencies of the combustion instability feedback loop.

Appendix A

Shear-Coaxial Jet Experimental Methods Details

A.1 Acoustic Forcing System

The acoustic frequency sweeps conducted when characterizing the resonant freqencies of the acoustic system only approximately determined the frequency, amplitude, and phase difference of the sirens necessary to produce transverse standing waves. In order to achieve a more exact PN or PAN condition at the center of the inner chamber, a meticulous set of operations was carried out prior to each acoustically forced flow condition. Each of these operations is manual, and the complete procedure is itemized below.

- *Achieve a steady thermodynamic condition.* Prior to adjusting any acoustic parameters, the chamber speed of sound c must be nominally constant. This is done by setting p_c, $\dot{m}_{ij}$, $\dot{m}_{oj}$, T_{ij}, and T_{oj} according to a predetermined test matrix. The correct mean chamber pressure p_c is achieved by setting the chamber pressurization nitrogen flow accordingly. The mass flow rates $\dot{m}_{ij}$ and $\dot{m}_{oj}$ are set by adjusting needle valves in the supply lines, and as expected, T_{ij} and T_{oj} are adjusted separately using each heat exchanger.

- *Set the desired acoustic frequency f_F.* The signal generator, shown by the wiring diagram in Fig. A.3, is used to set f_F on output channels 1 and 2.

- *Set the desired siren phase difference* $\Delta\phi$. The phase difference $\Delta\phi_{SG}$ of signal generator channels 1 and 2 should be set to 0° and 180° to achieve PAN and PN conditions, respectively.

- *Set the pressure perturbation* p' *to a value approximately equal to the desired level.* The voltage output of signal generator output channels 1 and 2 are set independently.

- *Activate the acoustic sirens.* After activating channels 1 and 2, the sirens will produce an acoustic field which not a standing wave. Inner chamber pressure sensors located on the rear wall provide $p_{dyn,1}$, $p_{dyn,2}$, and $p_{dyn,3}$, which must be actively viewed on the graphical user interface of the data acquisition system. These sensors will reveal an asymmetric condition between the dynamic pressure left of the jet $p_{dyn,1}$ and the dynamic pressure right of the jet $p_{dyn,3}$. This asymmetric condition results from phase delays which are unique to each amplifier and are dependent on both frequency and amplitude.

- *Finalize the siren phase difference* $\Delta\phi$. This step requires the user to view the amplifier output monitor channels. Again, this is performed using the graphical user interface of the data acquisition system. The amplifier output monitor channels will reveal that $\Delta\phi_{AMP} \neq \Delta\phi_{SG}$. Then, $\Delta\phi_{SG}$ must be adjusted until $\Delta\phi_{AMP}$ has reached the desired value according to the data acquisition system. Following this step, the fluctuations observed with $p_{dyn,1}$ and $p_{dyn,3}$ will be nearly equal (symmetric), but output amplitude must often be adjusted to reach true symmetry.

- *Finalize the pressure perturbation* p' *to obtain symmetry.* Again, due to unequal amplifier frequency responses, equal signal generator output amplitudes may not result in equal amplifier output amplitudes. Thus, the signal generator output

amplitudes must be independently adjusted until the acoustic field of the chamber is symmetric, i.e. $p_{dyn,1} = p_{dyn,3}$. If acoustic drivers do not produce equal amplitudes, then standing waves are theoretically impossible. A successful procedure will result in a maximum p' at $p_{dyn,2}$ for a PAN condition, or will result in $p_{dyn,2} \approx 0$ for a PN condition.

A.2 Positive Semidefinite Proof

Where $\mathbf{R}$ is the covariance matrix of $\widetilde{\mathbf{A}}$ and $\mathbf{z}$ is any $m \times 1$ vector,

$$\mathbf{z}^T\mathbf{R}\mathbf{z} = \mathbf{z}^T\widetilde{\mathbf{A}}^T\widetilde{\mathbf{A}}\mathbf{z} = \left(\widetilde{\mathbf{A}}\mathbf{z}\right)^T\left(\widetilde{\mathbf{A}}\mathbf{z}\right) \equiv \mathbf{b}^T\mathbf{b} \geq 0. \tag{A.1}$$

Here, $\mathbf{b} \equiv \widetilde{\mathbf{A}}\mathbf{z}$, which makes $\mathbf{b}$ an $m \times 1$ vector with a magnitude equal to $\mathbf{b}^T\mathbf{b}$. Thus, $\mathbf{b}^T\mathbf{b}$ is non-negative and

$$\mathbf{z}^T\mathbf{R}\mathbf{z} \geq 0. \tag{A.2}$$

By definition, this makes the covariance matrix $\mathbf{R}$ *positive semidefinite*.

A.1: Data for unforced LN_2-GHe nonreactive experiments. Natural frequencies are determined using proper orthogonal decomposition. St_{th} is calculated using $U_{c,th}$. St_{meas} is calculated using $U_{c,meas}$.

J	R	S	T_c [K]	ρ_c [kg/m^3]	p_c [psia]	T_{oj} [K]	m_{oj} [g/s]	ρ_{oj} [kg/m^3]	U_{oj} [m/s]	Re_{oj} (x10^{-4})	T_{ij} [K]	m_{ij} [g/s]	ρ_{ij} [kg/m^3]	U_{ij} [m/s]	Re_{ij} (x10^{-4})	f_{nat} [Hz]	$U_{c,th}$ [m/s]	$U_{c,meas}$ [m/s]	St_{th}	St_{meas}
2.42	16.42	0.0090	287.9	32.7	402.7	274.8	0.55	4.8	43.67	0.92	120.0	2.43	534.5	2.66	1.81	890	6.21	5.73	0.259	0.281
2.30	16.18	0.0088	287.8	32.7	402.5	276.7	0.53	4.8	42.39	0.88	119.5	2.42	541.3	2.62	1.76	930	6.03	5.72	0.279	0.294
2.01	14.45	0.0096	287.7	32.7	402.6	274.6	0.52	4.8	41.46	0.87	121.9	2.44	497.8	2.87	2.09	850	6.32	6.23	0.243	0.247
2.14	15.54	0.0089	287.5	32.7	402.5	274.4	0.52	4.8	41.03	0.87	119.6	2.43	540.4	2.64	1.78	845	5.95	5.22	0.257	0.293
1.93	14.48	0.0092	269.7	36.7	421.4	277.0	0.50	5.0	37.98	0.83	119.7	2.42	541.8	2.62	1.76	990	5.72	6.00	0.313	0.299
1.94	14.57	0.0091	269.8	36.8	421.9	277.7	0.50	5.0	38.28	0.83	119.6	2.43	543.5	2.63	1.75	1160	5.74	6.27	0.366	0.335
4.87	23.40	0.0089	287.0	31.9	391.1	281.6	0.55	4.6	46.34	0.91	121.5	1.72	512.7	1.98	1.49	815	5.80	5.55	0.254	0.266
6.17	25.88	0.0092	286.8	32.6	399.3	274.0	0.64	4.8	51.24	1.08	120.8	1.75	518.8	1.98	1.38	975	6.29	6.80	0.281	0.259
5.84	25.11	0.0093	286.7	32.5	398.7	273.0	0.62	4.8	49.22	1.04	120.9	1.73	516.7	1.96	1.37	945	6.11	6.63	0.280	0.258
5.87	25.25	0.0092	286.7	32.5	398.5	275.4	0.62	4.7	49.74	1.03	121.1	1.72	512.5	1.97	1.39	965	6.16	5.71	0.283	0.306
5.85	25.11	0.0093	286.7	32.8	402.0	277.5	0.62	4.7	49.71	1.03	121.2	1.73	512.7	1.98	1.40	945	6.17	6.62	0.277	0.258
6.17	25.50	0.0095	288.6	32.7	402.6	277.3	0.64	4.8	50.75	1.06	121.7	1.70	502.5	1.99	1.44	1007	6.31	6.66	0.289	0.274
5.69	24.33	0.0096	288.4	32.7	403.9	274.0	0.64	4.8	50.11	1.06	121.7	1.76	501.4	2.06	1.48	995	6.35	5.85	0.284	0.308
6.20	25.43	0.0096	288.3	32.7	403.6	272.9	0.63	4.8	49.58	1.06	121.6	1.68	505.4	1.95	1.40	955	6.20	6.06	0.279	0.285
1.97	14.66	0.0092	272.2	34.9	404.3	274.3	1.10	4.8	86.78	1.84	120.5	5.30	525.4	5.92	4.09	2880	12.99	14.87	0.401	0.351
1.93	14.60	0.0090	271.5	35.0	404.2	275.6	1.08	4.8	86.07	1.81	120.2	5.34	531.2	5.90	4.04	3030	12.86	15.94	0.427	0.344
5.47	24.88	0.0088	270.3	35.4	407.3	275.0	1.27	4.8	99.79	2.12	119.0	3.75	548.8	4.01	2.65	2070	12.24	13.01	0.306	0.288
4.73	21.92	0.0098	269.8	37.1	425.8	275.5	1.27	5.1	95.69	2.12	121.5	3.82	513.7	4.37	3.07	2725	12.61	14.15	0.391	0.349

A.2: Data for acoustically forced LN_2-GHe nonreactive experiments. Data is presented for in units of psi (left) and kPa (right). For jets located at a PAN, the p' value is taken as the pressure perturbation at the jet. For jets located at a PN, the p' value is taken as the average of the pressure perturbations occurring at the PANs to the left and right of the jet. The velocity perturbation u' at a PN is calculated using eqn. 5.4, which relies on the p' values of the adjacent PANs.

J	f_F [Hz]	p' [psi]	
		PN	PAN
2	1700	0.05	0.07
		0.12	0.14
		0.17	0.24
		0.30	0.39
		0.42	0.62
		0.53	0.87
		-	1.31
		-	1.53
	2050	0.04	0.23
		0.13	0.39
		0.22	0.61
		0.38	0.88
		0.50	1.10
		0.55	1.24
	2600	0.10	0.20
		0.19	0.32
		0.26	0.53
		0.41	1.15
		0.55	1.88
		0.84	3.23
		1.17	3.75
6	1700	0.06	0.24
		0.12	0.45
		0.20	0.66
		0.31	0.91
		0.34	1.10
		-	1.27
	2050	0.08	0.29
		0.15	0.60
		0.24	0.71
		0.38	1.16
		0.50	1.63
		0.58	2.04
		-	2.69
	2600	0.10	0.32
		0.21	0.64
		0.26	0.95
		0.49	1.66
		0.67	1.72
		0.84	1.83
		-	2.05

J	f_F [Hz]	p' [kPa]	
		PN	PAN
2	1700	0.35	0.49
		0.80	0.99
		1.17	1.67
		2.08	2.72
		2.89	4.29
		3.69	5.98
		-	9.06
		-	10.52
	2050	0.28	1.59
		0.92	2.72
		1.51	4.17
		2.62	6.08
		3.43	7.58
		3.81	8.52
	2600	0.66	1.40
		1.31	2.18
		1.80	3.64
		2.79	7.92
		3.79	12.95
		5.82	22.27
		8.05	25.85
6	1700	0.38	1.66
		0.81	3.09
		1.40	4.55
		2.14	6.24
		2.34	7.60
		-	8.72
	2050	0.53	2.00
		1.05	4.11
		1.63	4.91
		2.64	8.00
		3.42	11.22
		4.03	14.10
		-	18.56
	2600	0.71	2.18
		1.45	4.40
		1.78	6.55
		3.40	11.43
		4.59	11.85
		5.82	12.62
		-	14.12

A.1: Piezoelectric acoustic siren, of aluminum construction.

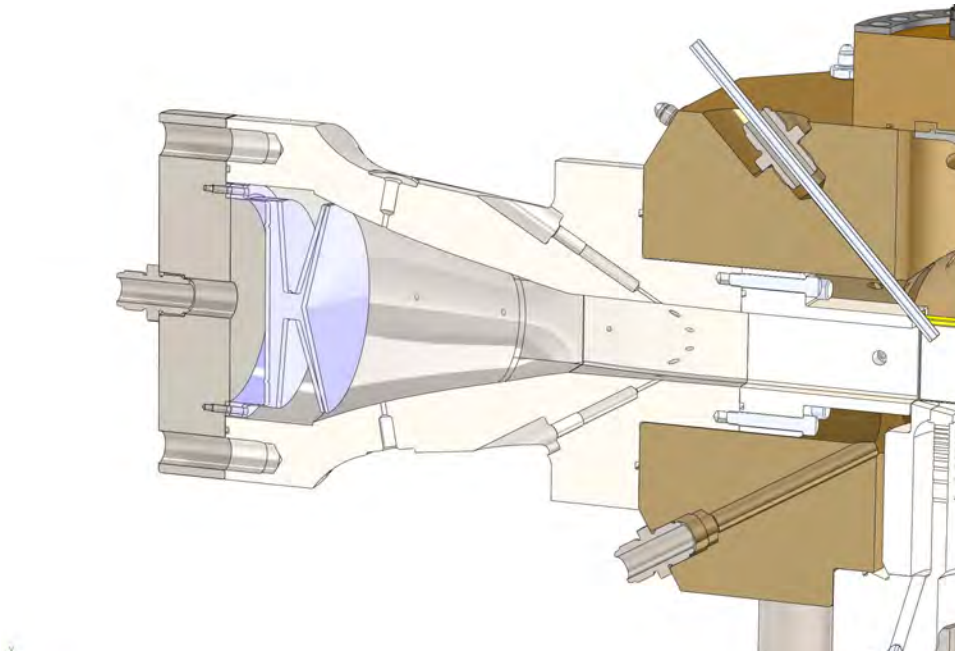

A.2: Cross sectional CAD rendering of the left waveguide.

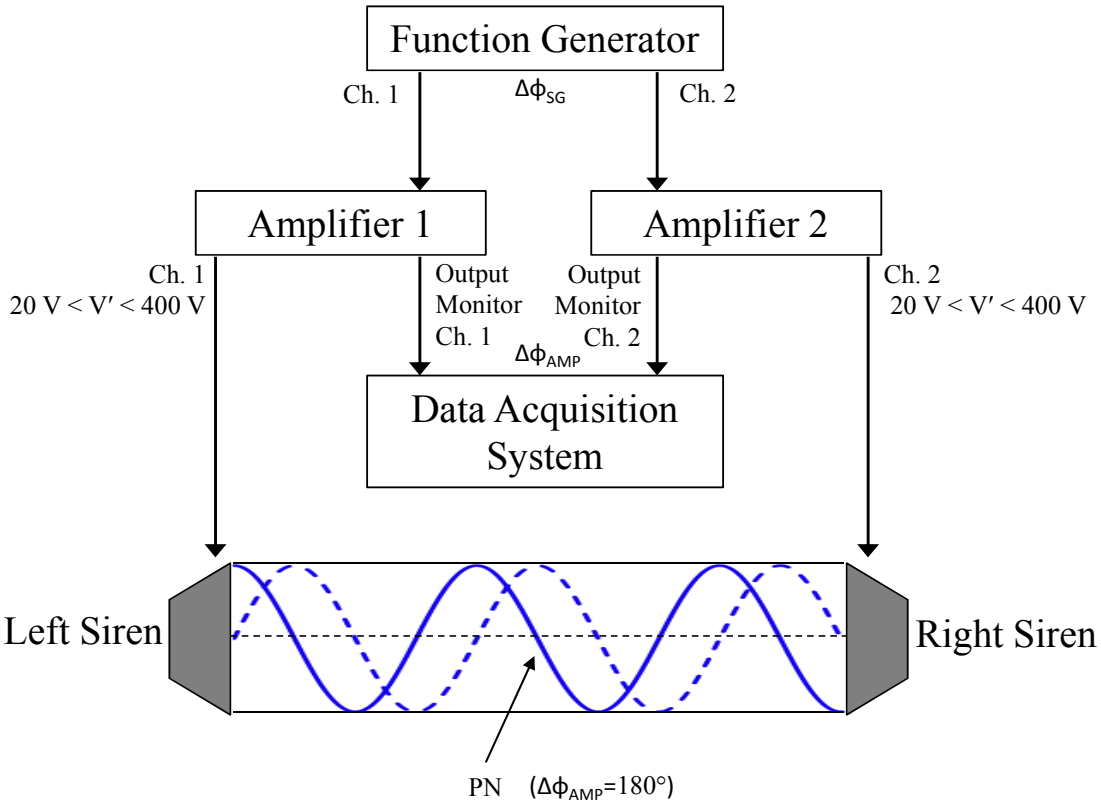

A.3: Acoustic wiring flow chart. The acoustic piezoelectric sirens are controlled using a dual-channel signal generator. Each of the two channels are controlled to have equal frequency, but unequal phase ϕ. Separate amplifiers produce high voltage signals for each siren, and the amplifiers also send an equivalent low voltage signal to the data acquisition system. The siren phase difference, then, is equal to $\Delta\phi_{AMP}$, which must be 0° to create a PAN at the center of the chamber and 180° to create a PN at the center. As a result of unique phase delays applied by each amplifier, the signal generator phase difference $\Delta\phi_{SG}$ must be dynamically adjusted for each acoustic condition in order to achieve a standing wave, i.e. for $\Delta\phi_{AMP} = 0°$ $\rightarrow$ $\Delta\phi_{SG} \neq 0°$, and for $\Delta\phi_{AMP} = 180°$ $\rightarrow$ $\Delta\phi_{SG} \neq 180°$

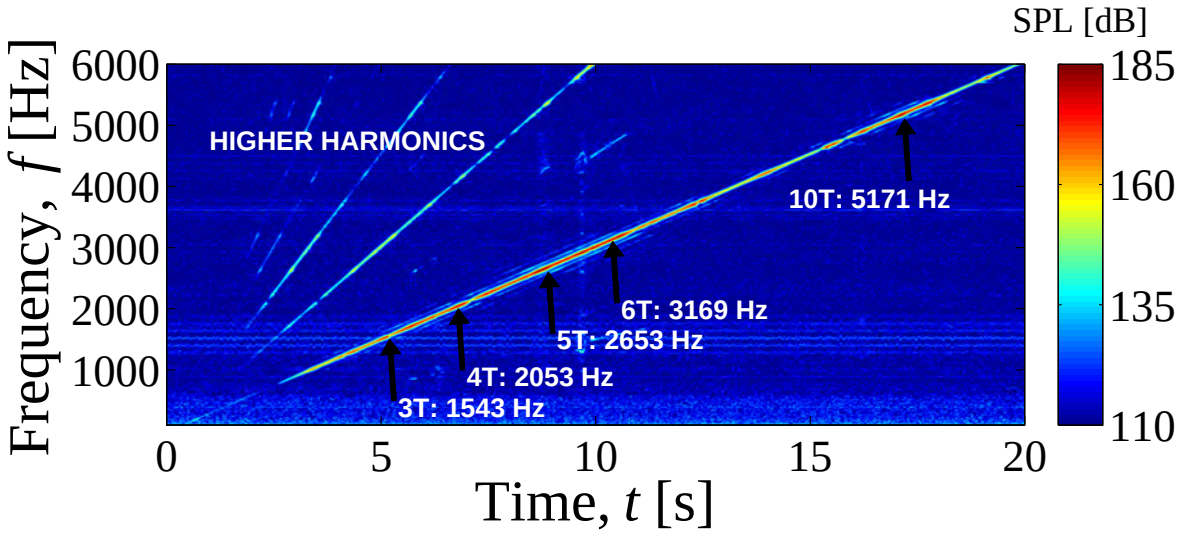

A.4: Acoustic pressure spectra results for a PAN condition measured using a pressure transducer in the center of the chamber. Magnitude is scaled with a sound pressure level (SPL) colormap, and key regions of transverse resonance are annotated. p_c=400 psia

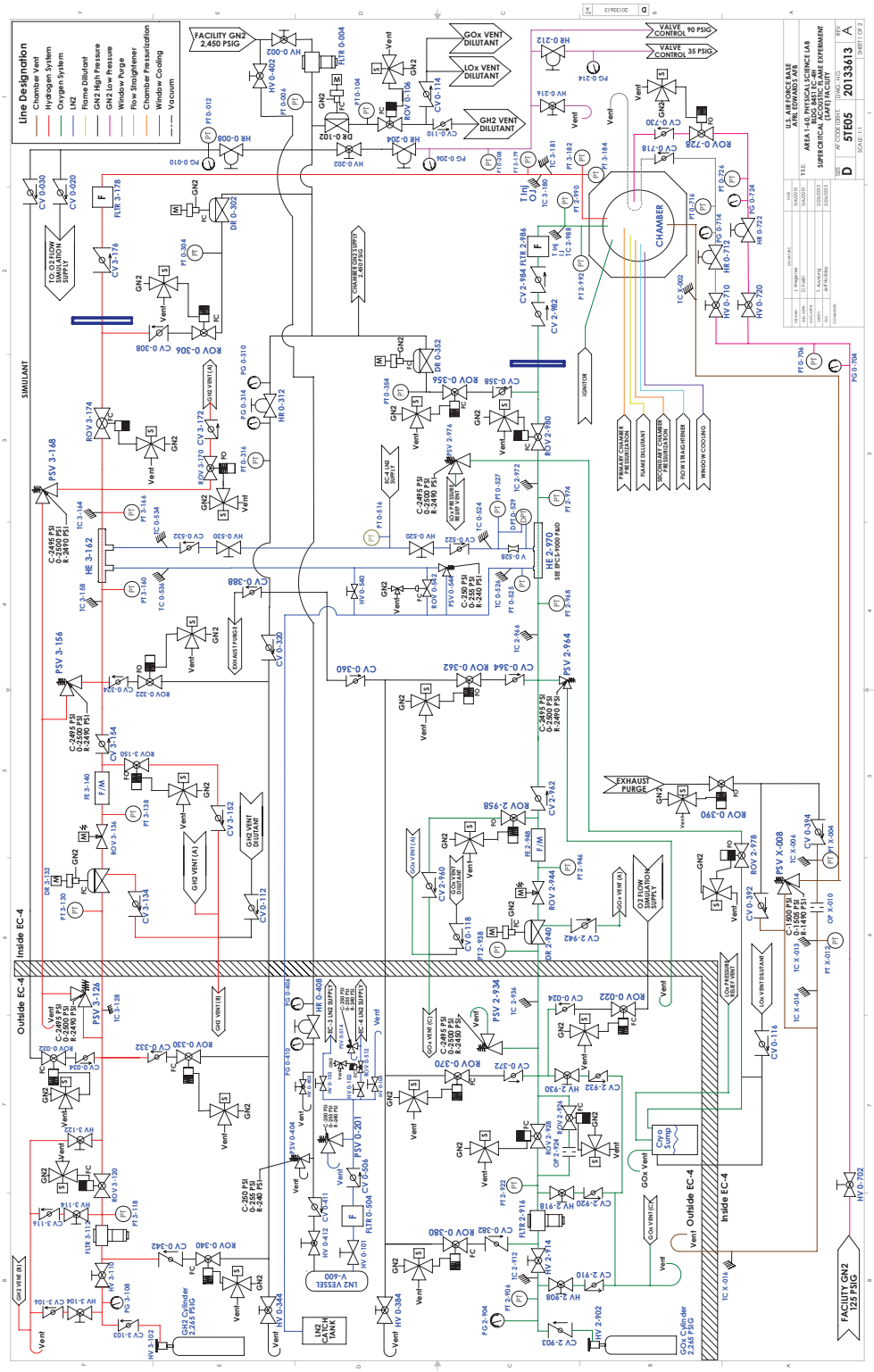

A.5: Facility PID page 1.

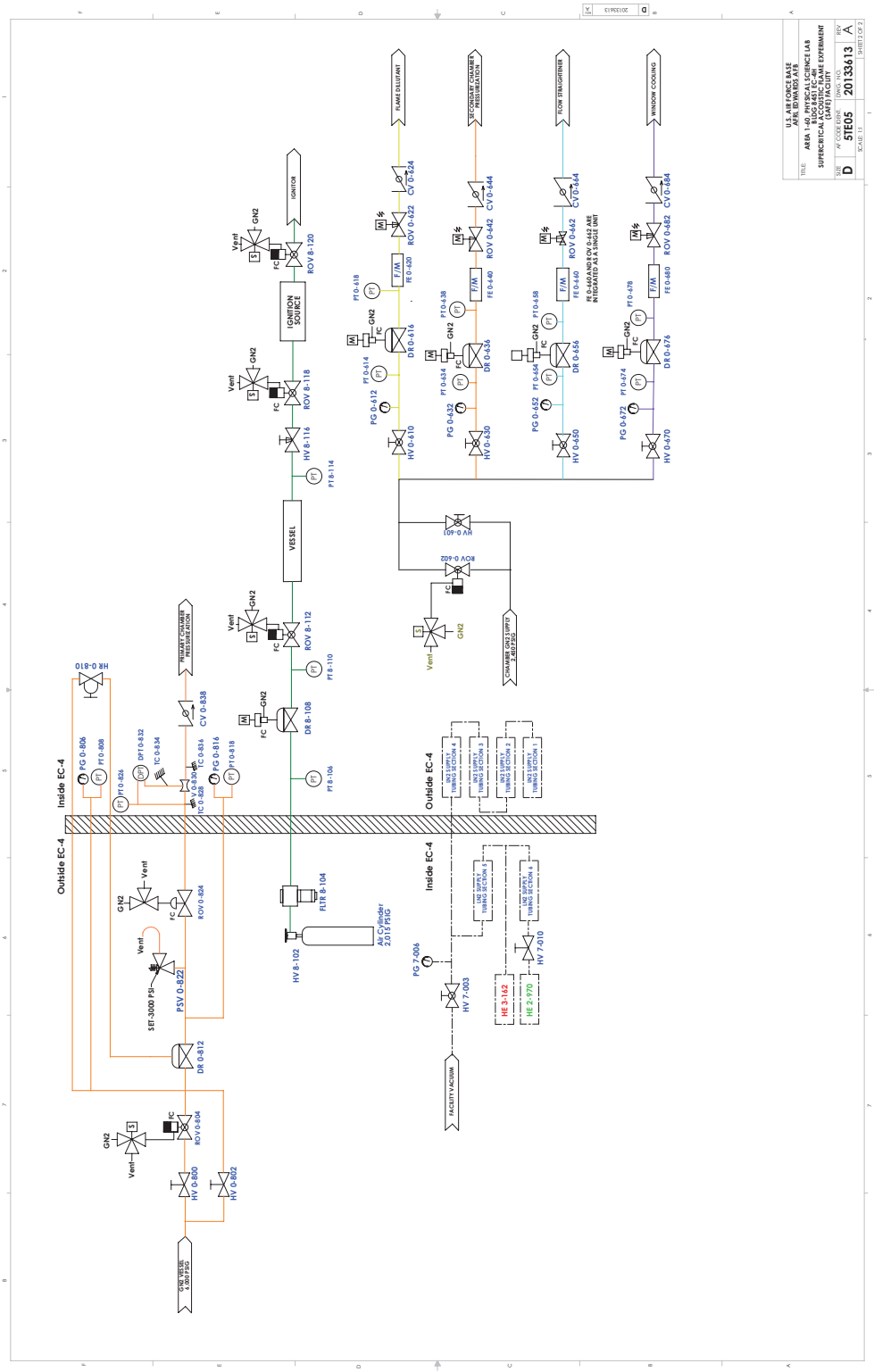

A.6: Facility PID page 2.

Bibliography

[1] T. C. Lieuwen and V. Yang. *Progress in Astronautics and Aeronautics: Combustion Instabilities in Gas Turbine Engines: Operational Experience, Fundamental Mechanisms, and Modeling*. AIAA, 2006.

[2] K. R. McManus, T. Poinsot, and S. M. Candel. A review of active control of combustion instabilities. *Progress in Energy and Combustion Science*, 19:1–29, 1993.

[3] F.E.C. Culick and V. Yang. Overview of combustion instabilities in liquid rocket engines. In V. Yang and W.E. Anderson, editors, *Progress in Astronautics and Aeronautics: Liquid Rocket Engine Combustion Instability*, pages 3–38. AIAA, 1995.

[4] A. M. Annaswamy and A. F. Ghoniem. Active control of combustion instability: Theory and practice. *Control Systems*, 22(6):37–54, 2002.

[5] Q. Diao. *Propellant injection strategy for suppressing acoustic combustion instability*. PhD thesis, University of Maryland, College Park, Mechanical and Engineering Department, June 2010.

[6] S. Candel. Combustion dynamics and control: progress and challenges. Number 29 in Proceedings of the Combustion Institute, pages 1–28, 2002.

[7] T. Lieuwen, H. Torres, C. Johnson, and B.T. Zinn. A mechanism for combustion instability in lean premixed gas turbine combustors. *J. of Engineering for Gas Turbines and Power*, 123:182–189, 2001.

[8] F. Richecoeur. *Experiments and numerical simulations of interactions between*

transverse acoustic modes and cryogenic flames. PhD thesis, Ecole Centrale Paris, November 2006.

[9] Y.C. Yu, S.M. Koeglmeier, J.C. Sisco, and W.E. Anderson. Combustion instability of gaseous fuels in a continuously variable resonance chamber (cvrc). 44th Joint Propulsion Conference and Exhibit, 2008. AIAA 2008-4657.

[10] P. Yecko, S. Zaleski, and J.-M. Fullana. Viscous modes in two-phase mixing layers. *Physics of Fluids*, 14(12):4115–4122, 2002.

[11] K.C. Kim and R.J. Adrian. Very large-scale motion in the outer layer. *Physics of Fluids*, 11(2):417–422, 1999.

[12] P. Givi, W.-H. Jou, and R.W. Metcalfe. Flame extinction in a temporally developing mixing layer. *Twenty-First Symposium (International) on Combustion*, pages 1251–1261, 1986.

[13] H.K. Chelliah, C.K. Law, T. Ueda, M.D. Smooke, and F.A. Williams. An experimental and theoretical investigation of the dilution, pressure and flow-field effects on the extinction condition of methane-air-nitrogen diffusion flames. *Twenty-Third Symposium (International) on Combustion*, pages 503–511, 1990.

[14] W.O.H. Mayer and J.J. Smith. Fundamentals of supercritical mixing and combustion of cryogenic propellants. In et al. Yang, V., editor, *Progress in Astronautics and Aeronautics: Liquid Rocket Engine Thrust Chambers*, page 339367. AIAA, 2004.

[15] Q. Diao, A. Ghosh, and K. H. Yu. Suppression of GO2/GH2 combustion instability using CH4 addition. Number AIAA-2008-1000 in 46th AIAA Aerospace Sciences Meeting, Reno, NV, January 2008.

[16] F. Baillot, J.-B. Blaisot, G. Boisdron, and C. Dumouchel. Behaviour of an air-assisted jet submitted to a transverse high-frequency acoustic field. *J. of Fluid Mechanics*, 640:305–342, 2009.

[17] J.C. Sisco, Y.C. Yu, V. Sankaran, and W.E. Anderson. Examination of mode shapes in an instable model combustor. *Journal of Sound and Vibration*, 330: 61–74, 2011.

[18] J.S. Hardi, M. Oschwald, and B. Dally. Acoustic characterisation of a rectangular rocket combustor with liquid oxygen and hydrogen propellants. *Proceedings of the Institution of Mechanical Engineers, Part G: Journal of Aerospace Engineering*, 227(3):436–446, 2013.

[19] Y. Mery, L. Hakim, P. Scouflaire, L. Vingart, S. Ducruix, and S. Candel. Experimental investigation of cryogenic flame dynamics under transverse acoustic modulations. *Comptes Rendus Mecanique*, 341:100–109, 2013.

[20] M. Tanabe, T. Morita, K. Aoki, K. Satoh, T. Fujimori, and J. Sato. Influence of standing sound waves on droplet combustion. *Proc. Comb. Inst.*, 28:1007–1013, 2000.

[21] M. Tanabe, T. Kuwahara, S. Kimiyoshi, T. Fujimori, J. Sato, and M. Kono. Droplet combustion in standing sound waves. *Proc. Comb. Inst.*, 30:1957–1964, 2005.

[22] S. Dattarajan, A. Lutomirski, R. Lobbia, O.I. Smith, and A.R. Karagozian. Acoustic excitation of droplet combustion in microgravity and normal gravity. *J. Combustion and Flame*, 144:299–317, 2006.

[23] S. Teshome. *Droplet Combustion and Non-Reactive Shear-Coaxial Jets with Trans-*

verse Acoustic Excitation. PhD thesis, University of California, Los Angeles, Department of Mechanical and Aerospace Engineering, March 2012.

[24] J. Hardi. *Experimental Investigation of High Frequency Combustion Instability in Cryogenic Oxygen-Hydrogen Rocket Engines*. PhD thesis, The University of Adelaide, School of Mechanical Engineering, June 2012.

[25] P. Huerre and P. A. Monkewitz. Local and global instabilities in spatially developing flows. *Annual Review of Fluid Mechanics*, 22:473–537, 1990.

[26] J.-B. Carpentier, F. Baillot, J.-B. Blaisot, and C. Dumouchel. Behavior of cylindrical liquid jets evolving in a transverse acoustic field. *Physics of Fluids*, 21(2): 1–15, 2009.

[27] F.G. Buffum and F.A. Williams. The response of a turbulent jet to transverse acoustic fields. Proceedings of the 1967 Heat Transfer and Fluid Mechanics Institute, pages 247–276, 1967.

[28] B. W. Davis and B. Chehroudi. The effects of pressure and acoustic field on a cryogenic coaxial jet. *42nd AIAA Aerospace Sciences Meeting & Exhibit*, 2004. Washington, D.C.

[29] I. A. Leyva, J. I. Rodriguez, B. W. Davis, and B. Chehroudi. Preliminary results on coaxial jet spread angles and the effects of variable phase transverse acoustic fields. *46nd AIAA Aerospace Sciences Meeting & Exhibit*, 2008. Reno, NV.

[30] S. Teshome, I.A. Leyva, and D.G. Talley. Proper orthogonal decomposition analysis of shear-coaxial injector flows with and without transverse acoustic forcing. *JANNAF Joint Subcommittee Meeting*, 2011. Huntsville, AL.

[31] J.W.S. Rayleigh. *The Theory of Sound*. vol. 2, New York: Dover, 1945.

[32] D.A. Smith and E.E. Zukoski. Combustion instability sustained by unsteady vortex combustion. *Twenty-first Joint Propulsion Conference*, AIAA-85-1248, 1985.

[33] K.H. Yu, A. Trouve, and J.W. Daily. Low-frequency pressure oscillations in a model ramjet combustor. *J. Fluid Mechanics*, 232:47–72, 1991.

[34] K.C. Schadow and E. Gutmark. Combustion stability related to vortex shedding in dump combustors and their passive control. *Progress in Energy and Combust. Sci.*, 18:117–132, 1992.

[35] H.C. Mongia, T.J. Held, G.C. Hsiao, and R.P. Pandalai. Incorporation of combustion instability issues into design process: General electric aeroderivative and aero engines experience. In *Progress in Astronautics and Aeronautics: Combustion Instabilities in Gas Turbine Engines: Operational Experience, Fundamental Mechanisms, and Modeling*, pages 89–107. AIAA, 2006.

[36] Standards of Performance for Stationary Gas Turbines Environmental Protection Agency, Standards of Performance for New Stationary Sources. Title 40. 2011. Sections 60.330-60.335, http://www.epa.gov/region7/air/nsps/nspsstandardcontacts.htm.

[37] C.T. Bowman. Control of combustion-generated nitrogen oxide emissions: Technology driven by regulation. volume 24 of *Twenty-Fourth Symposium on Combustion*, pages 859–878, 1992.

[38] K. O. Smith and J. Blust. Combustion instabilities in industrial gas turbines: Solar turbines' experience. In *Progress in Astronautics and Aeronautics: Combustion Instabilities in Gas Turbine Engines: Operational Experience, Fundamental Mechanisms, and Modeling*, pages 29–41. AIAA, 2006.

[39] T. Scarinci. Combustion instability and its passive control: Rolls-royce aeroderivative engine experience. In *Progress in Astronautics and Aeronautics: Combustion Instabilities in Gas Turbine Engines: Operational Experience, Fundamental Mechanisms, and Modeling*, pages 65–88. AIAA, 2006.

[40] B. Wassener. Airlines weigh the advantages of using more biofuel. 2011. The International Herald Tribune, October 10.

[41] G.P. Sutton and O. Biblarz. *Rocket propulsion elements*. John Wiley and Sons, 2001.

[42] NASA. J-2 engine fact sheet. *Saturn V News Reference*, December, 1968. retrieved by NASA 22 February 2012.

[43] D. Haeseler. Peenemuende roots and lessons. In *Liquid Propulsion History I: LOX/HC Propulsion I: Goddard - Peenemuende - Sputnik (8K71PS/8A91 R-7), Vanguard, Juno 1 to Titan, Atlas, Falcon and Beyond*. AIAA Joint Propulsion Conference Presentation Series, July 16, 2013.

[44] S. Bouley and B. Anderson. Rs-27, md-1, ma-5a-7, lr-89-105, h-1, f-1, s-3d, rs-84 (atlas, delta, thor, saturn 1b and v, jupiter. In *Liquid Propulsion History I: LOX/HC Propulsion I: Goddard - Peenemuende - Sputnik (8K71PS/8A91 R-7), Vanguard, Juno 1 to Titan, Atlas, Falcon and Beyond*. AIAA Joint Propulsion Conference Presentation Series, July 16, 2013.

[45] J. Hulka and J.J. Hutt. Instability phenomena in liquid oxygen/hydrogen propellant rocket engines. In V. Yang and W.E. Anderson, editors, *Progress in Astronautics and Aeronautics: Liquid Rocket Engine Combustion Instability*, pages 39–72. AIAA, 1995.

[46] F. E. C. Culick. Unsteady motions in combustion chambers for propulsion systems. 2006. AGARDograph, NATO/RDO-AG-AVT-039.

[47] J. C. Oefelein and V. Yang. Comprehensive review of liquid propellant combustion instabilities in F-1 engines. *Propulsion and Power*, 9(5):657–677, 1993.

[48] G. A. Dressler and J. M. Bauer. Trw pintle engine heritage and performance characteristics. Number AIAA-2000-3871 in 36th AIAA/ASME/SAE/ASEE Joint Propulsion Conference and Exhibit, July 2000.

[49] M. Habiballah, D. Lourme, and F. Pit. Numerical model for combustion stability studies applied to the ariane viking engine. *Propulsion and Power*, 7(3):322–329, 1991.

[50] H.E. Scott, H.E. Bloomer, and A.H. Mansour. M-1 engine subscale injector tests. *NASA Lewis Research Center*, TN D-4053, 1967.

[51] S.C. Fisher, F.E. Dodd, and R.J. Jensen. Scaling techniques for liquid rocket combustion stability testing. In V. Yang and W.E. Anderson, editors, *Progress in Astronautics and Aeronautics: Liquid Rocket Engine Combustion Instability*, pages 545–564. AIAA, 1995.

[52] A. R. Karagozian, W. J. A. Dahm, E. Glasgow, R. Howe, I. Kroo, R. Murray, and H. Shyu. Technology options for improved air vehicle fuel efficiency. 2006. Air Force Scientific Advisory Board Report, Technical Report SAB-TR-06-04.

[53] SrA Jason Hernandez. SECAF certifies synthetic fuel blends for B-52H. *Edwards Air Force Base, CA*, 2007. Edwards Air Force Base, CA. http://www.safie.hq.af.mil/news/story.asp?id=123064095.

[54] A. D. Sagar and S. Kartha. Bioenergy and sustainable development. *Annual Rev. of Environmental Resources*, 32:131–167, 2007.

[55] G. A. Mills and E. E. Ecklund. Alcohols as components of transportation fuels. *Annual Review of Energy*, 12(1):47–80, 1987.

[56] P. M. Morse, R. H. Boden, and H. Schecter. Acoustic vibrations and internal combustion engine performance, i. standing waves in the intake pipe system. *Applied Physics*, 9:16–23, 1938.

[57] D. E. Winterbone and R. J. Pearson. *Theory of Engine Manifold Design: Wave Action Methods for IC Engines*. Professional Engineering Publishing, London, 2000.

[58] F. Fischer. *The Conversion of Coal*. Ernst Benn, Ltd., 1925.

[59] 1st Lt Amanda Ferrell. Air force energy initiatives focus on fuel, beyond. *Edwards Air Force Base, CA*, 2007. http://www.af.mil/news/story.asp?id=123069617.

[60] G.A.E. Godsave. Burning of fuel droplets. Combustion and Flame, pages 818–830, 1953. Baltimore, MD. Williams and Wilkins.

[61] A. Williams. Combustion of droplets of liquid fuels - a review. *Combustion and Flame*, 21, 1973.

[62] C. K. Law and G. M. Faeth. Opportunities and challenges of combustion in microgravity. *Progress in Energy and Combustion Science*, 20, 1994.

[63] C. K. Law. Recent advances in droplet vaporization and combustion. *Progress in Energy and Combustion Science*, 8(3):171–201, 1982.

[64] S. R. Turns. *An Introduction to Combustion*. McGraw Hill, 2000.

[65] P. M. Struk, M. Ackerman, V. Nayagam, and D. L. Dietrich. On calculating burning rates during fibre supported droplet combustion. *Microgravity Science and Technology*, 11, 1998.

[66] A.J. Marchese, F.L. Dryer, V. Nayagam, and R.O. Colantino. Hydroxyl radical chemiluminescence imaging and the structure of microgravity droplet flames. Twenty-sixth Symposium (International) on Combustion, pages 1219–1226, 1996.

[67] A.J. Marchese, R.O. Colantino, F.L. Dryer, and V. Nayagam. Microgravity combustion of methanol and methanol/water droplets: Drop tower experiments and model predictions. Twenty-sixth Symposium (International) on Combustion, pages 1209–1217, 1996.

[68] S. Kumagai and H. Isoda. Combustion of fuel droplets in a vibrating air field. Fifth Symposium (International) on Combustion, 1955.

[69] J. Blaszczyk. Acoustically disturbed fuel droplet combustion. *Fuel*, 70(3):1023–1025, 1973.

[70] M. Saito, M. Sato, and I. Suzuki. Evaporation and combustion of a single fuel droplet in acoustic fields. *Fuel*, 73, 1994.

[71] M. Saito, M. Hoshikawa, and M. Sato. Enhacement of evaporation/combustion coefficient of a single fuel droplet by acoustic oscillation. *Fuel*, 75, 1996.

[72] K. Okai, O. Moriue, M. Araki, M. Tsue, M. Kono, J. Sato, and D. L. Dietrich. Combustion of single droplet and droplet pairs in a vibrating field under microgravity. *Proc. Comb. Inst.*, 28, 2000.

[73] M. Tanabe. Drop tower experiments and numerical modeling on the combustion-induced secondary flow in standing acoustic fields. *J. Microgravity Sci. Technol.*, 22:507–515, 2010.

[74] D.J. McKinney and D. Dunn-Rankin. Acoustically driven extinction in a droplet stream flame. *Combust. Sci. and Tech.*, 161:27–48, 2000.

[75] J.I. Rodriguez. *Acoustic Excitation of Liquid Fuel Droplets and Coaxial Jets.* PhD thesis, University of California, Los Angeles, Department of Mechanical and Aerospace Engineering, June 2009.

[76] M. Faraday. On a peculiar class of acoustical figures; and on certain forms assumed by groups of particles upon vibrating elastic surfaces. *Phil. Trans. R. Soc. Lond.*, 121:229, 1831.

[77] J.W.S. Rayleigh. On the pressure of vibrations. *Philos. Mag.*, 10:364–374, 1902.

[78] L.P. Gor'kov. On the forces acting on a small particle in an acoustical field in an ideal fluid. *Soviet Phys.-Doklady*, 6(9):773–775, 1962.

[79] W.L. Nyborg. Radiation pressure on a small rigid sphere. *J. Acoust. Soc. Am.*, 16 (1):947–952, 1967.

[80] C.P. Lee and T.G. Wang. Acoustic radiation pressure. *J. Acoust. Soc. Am.*, 94 (2):1099–1109, 1993.

[81] J.I. Rodriguez, S. Teshome, H.-S. Mao, A. Pezeshkian, O.I. Smith, and A.R. Karagozian. Acoustically driven droplet combustion with alternative liquid fuels. *46th AIAA Aerospace Sciences Meeting and Exhibit*, 2008.

[82] S. Teshome, A. Pezeshkian, O.I. Smith, and A.R. Karagozian. Influence of standing acoustic waves on combustion of alternative fuels. *Proc. Am. Phys. Soc.*, 2008.

[83] A.S.H. Kwan and N.W.M. Ko. Coherent structures in subsonic coaxial jets. *Journal of Sound and Vibration*, 48:203–219, 1976.

[84] W. Forstall and A.H. Shapiro. Momentum and mass transfer in coaxial gas jets. Massachusetts Institute of Technology, Guided Missiles Program, 1949.

[85] N.A. Chigier and J.M. Beer. The flow region near the nozzle in double concentric jets. *Journal of Basic Engineering*, 86:797–804, 1964.

[86] F.H. Champagne and I.J. Wygnanski. An experimental investigation of coaxial turbulent jets. *International Journal of Heat and Mass Transfer*, 14:1445–1464, 1971.

[87] N.W.M. Ko and A.S.H. Kwan. Experimental investigation of sub sonic coaxial jets. *Proceedings of the 5th Australian Conference on Hydraulics and Fluid Mechanics, University of Canterbury, New Zealand*, 1974.

[88] N.W.M. Ko and A.S.H. Kwan. The initial region of subsonic coaxial jets. *Journal of Fluid Mechanics*, 73:305–332, 1976.

[89] P.E. Dimotakis. Two-dimensional shear-layer entrainment. *AIAA Journal*, 24: 17911796, 1986.

[90] W.J.A. Dahm and P.E. Dimotakis. Mixing at large schmidt number in the self-similar far field of turbulent jets. *Journal of Fluid Mechanics*, 217:299–330, 1990.

[91] P.E. Dimotakis. *Turbulent free shear layer mixing and combustion.* AIAA, 1991.

[92] W.J.A. Dahm, C.E. Frieler, and G. Tryggvason. Vortex structure and dynamics in the near field of a coaxial jet. *Journal of Fluid Mechanics*, 241:371–402, 1992.

[93] J.-P. Matas, S. Marty, and A. Cartellier. Experimental and analytical study of the shear instability of a gas-liquid mixing layer. *Physics of Fluids*, 23:094112, 2011.

[94] N. Chigier and Z. Farago. Morphological classification of disintegration of round liquid jets in a coaxial air stream. *Atomization and Sprays*, 2:2, 1992.

[95] J.C. Lasheras and E.J. Hopfinger. Liquid jet instability and atomization in a coaxial gas stream. *Annual Review of Fluid Mechanics*, 32:275–308, 2000.

[96] J.A. Newman and T.A. Brzustowski. Behavior of a liquid jet near the thermodynamic critical region. *AIAA Journal*, 9:1595–1602, 1971.

[97] M. Oschwald, J. J. Smith, R. Branam, J. Hussong, A. Schik, B. Chehroudi, and D. Talley. Injection of fluids into supercritical environments. *Combustion Science and Technology*, 178, 2006.

[98] B. Chehroudi, D. Talley, and E. Coy. Visual characteristics and initial growth rates of round cryogenic jets at supercritical and supercritical pressures. *Physics of Fluids*, 14:850861, 2002.

[99] B. Chehroudi and D. Talley. Fractal geometry of a cryogenic nitrogen round jet injected into sub- and super-critical conditions. *Atomization and Sprays*, 14:81–91, 2004.

[100] J. Telaar, G. Schneider, and W. Mayer. Experimental investigation of breakup of turbulent liquid jets. *ILASS-Europe Conference*, 2000. Darmstadt, Germany.

[101] M. Oschwald, A. Schik, M. Klar, and W. Mayer. Investigation of coaxial ln2-gh2-injection at supercritical pressure by spontaneous raman scattering. *AIAA 99-2887, 35th Joint Propulsion Conference*, 1999. Los Angeles, CA.

[102] B. W. Davis and B. Chehroudi. Shear-coaxial jets from a rocket-like injector in a transverse acoustic field at high pressures. *44nd AIAA Aerospace Sciences Meeting & Exhibit*, 2006. Reno, NV.

[103] DW Davis. *On the Behavior of a Shear-Coaxial Jet Spanning Sub-to Supercritical Pressures With and Without an Externally Imposed Acoustic Field*. PhD thesis, PhD Thesis, Dept. of Mech. and Nuc. Eng., the Pennsylvania State University, 2006.

[104] J.J. Graham, I.A. Leyva, J.I. Rodriguez, and D. Talley. On the effect of a transverse acoustic field on a shear coaxial injector. *45th AIAA/ASME/SAE/ASEE Joint Propulsion Conference and Exhibit*, 2009-5142.

[105] I.A. Leyva, B. Chehroudi, and D. Talley. Dark core analysis of coaxial injectors at sub-, near-, and supercritical pressures in a transverse acoustic field. *43rd AIAA/ASME/SAE/ASEE Joint Propulsion Conference and Exhibit*, 5:275–282, 2007-5456.

[106] S.C. Crow and F.H. Champagne. Orderly structure in jet turbulence. *Journal of Fluid Mechanics*, 48:547–591, 1971.

[107] Anne-Laure Birbaud, Daniel Durox, Sébastien Ducruix, and S Candel. Dynamics of free jets submitted to upstream acoustic modulations. *Physics of Fluids*, 19: 013602, 2007.

[108] A. Talamelli and I. Gavarini. Linear instability characteristics of incompressible coaxial jets. *Flow Turbulence Combust*, 76:221–240, 2006.

[109] A. Segalini and A. Talamelli. Experimental analysis of dominant instabilities in coaxial jets. *Physics of Fluids*, 23:024103, 2011.

[110] J.-M. Chomaz. Global instabilities in spatially developing flows: Non-normality and nonlinearity. *Annual Review of Fluid Mechanics*, 37:357–392, 2005.

[111] P. A. Monkewitz, D. W. Bechert, B. Barsikow, and B. Lehmann. Self-excited oscillations and mixing in a heated round jet. *Journal of Fluid Mechanics*, 213: 611–639, 1990.

[112] D. M. Kyle and K. R. Sreenivasan. The instability and breakdown of a round variable-density jet. *Journal of Fluid Mechanics*, 249:619–664, 1993.

[113] P.J. Strykowski and D.L. Niccum. The stability of countercurrent mixing layers in circular jets. *Journal of Fluid Mechanics*, 227:309, 1991.

[114] P.J. Strykowski and D.L. Niccum. The influence of velocity and density ratio on the dynamics of spatially developing mixing layers. *Physics of Fluids*, 4:770, 1992.

[115] M. Provansal, C. Mathis, and L. Boyer. Benard-von karman instability: transient and forced regimes. *Journal of Fluid Mechanics*, 182:1–22, 1987.

[116] D. Hammond and L. Redekopp. Global dynamics of symmetric and asymmetric wakes. *Journal of Fluid Mechanics*, 331:231–260, 1997.

[117] S. Megerian, J. Davitian, L. S. de B. Alves, and A. R. Karagozian. Transverse jet shear-layer instabilities. part 1. experimental studies. *Journal of Fluid Mechanics*, 593:93–129, 2007.

[118] M.P. Juniper, L.K.B. Li, and J.W. Nichols. Forcing of self-excited round jet diffusion flames. *Proceedings of the Combustion Institute*, 32:1191–1198, 2009.

[119] M. P. Hallberg and P. J. Strykowski. Open-Loop Control of Fully Nonlinear Self-Excited Oscillations. *Physics of Fluids*, 20:041703, 2008.

[120] B. Pier. Open-Loop Control of Absolutely Unstable Domains. *Royal Society of London Proceedings Series A*, 459(2033):1105–1115, 2003.

[121] S. Jendoubi and P.J. Strykowski. Absolute and convective instability of axisymmetric jets with external flow. *Physics of Fluids*, 6:3000–3009, 1994.

[122] D.R. Getsinger, C. Hendrickson, and A.R. Karagozian. Shear layer instabilities in low-density transverse jets. *Exp Fluids*, 53:783–801, 2012.

[123] K.R. Sreenivasan, S. Raghu, and D. Kyle. Absolute instability in variable density round jets. *Exp Fluids*, 7:309–317, 1989.

[124] C.C. Miesse. The effect of ambient pressure oscillations on the disintegration and dispersion of a liquid jet. *Jet Propulsion*, 25:525–530, 1955.

[125] Ray Snyder, Gerald Herding, JUAN CARLOS ROLON, and Sébastien Candel. Analysis of flame patterns in cryogenic propellant combustion. *Combustion science and technology*, 124(1-6):331–370, 1997.

[126] S. Candel, G. Herding, R. Synder, P. Scouflaire, C. Rolon, D. Stepowski, A. Cessou, and P. Colin. Experimental investigation of shear coaxial cryogenic jet flames. *J. of Propulsion and Power*, 14(5):826–834, 1998.

[127] Louis Baker and Fred W Steffen. *Screaming Tendency of the Gaseous-hydrogen-Liquid-oxygen Propellant Combination.* National Advisory Committee for Aeronautics, 1958.

[128] Marcus F Heidmann. *Oscillatory combustion of a liquid-oxygen jet with gaseous hydrogen.* National Aeronautics and Space Administration, 1965.

[129] G. Singla, P. Scouflaire, C. Rolon, and S. Candel. Planar laser-induced fluorescence of oh in high-pressure cryogenic LOx/GH2 jet flames. *Combustion and Flame*, 144: 151–169, 2006.

[130] G. Singla, P. Scouflaire, C. Rolon, S. Candel, and L. Vingert. Oh planar laser-induced fluorescence and emission imaging in high-pressure LOx/Methane flames. *J. of Propulsion and Power*, 23(3):593–602, 2007.

[131] F. Richecoeur, S. Ducruix, P. Scouflaire, and S. Candel. Effect of temperature fluctuations on high frequency acoustic coupling. *Proc. of the Combustion Institute*, 32:1663–1670, 2009.

[132] Cédric Rey, Sébastien Ducruix, Franck Richecoeur, Philippe Scouflaire, Lucien

Vingert, and Sébastien Candel. High frequency combustion instabilities associated with collective interactions in liquid propulsion. *AIAA Paper*, 3518:11–14, 2004.

[133] S. Pavithran and L.G. Redekopp. The absolute-convective transition in subsonic mixing layers. *Physics of Fluids*, 1:1736, 1989.

[134] P.A. Monkewitz, D.W. Bechert, B. Barsikow, and B. Lehmann. Self-excited oscillations and mixing in a heated round jet. *Journal of Fluid Mechanics*, 213:611, 1990.

[135] J. Eldredge. Private communications. *UCLA*, 2009.

[136] K.T. Walsh, M.B. Long, M.A. Tanoff, and M.D. Smooke. Experimental and computational study of CH, CH*, and OH* in an axisymmetric laminar diffusion flame. Twenty-sixth Symposium (International) on Combustion, pages 615–623, 1998.

[137] H.N. Najm, P.H. Paul, C.J. Mueller, and P.S. Wyckoff. On the adequacy of certain experimental observables as measurements of flame burning rate. *Combustion and Flame*, 113:312–332, 1998.

[138] J. Kojima, Y. Ikeda, and T. Nakajima. Spatially resolved measurement of OH*, CH*, and C^*_2 chemiluminescence in the reactio zone of laminar methane/air premixed flames. *Proc. Comb. Inst.*, 28:1757–1764, 2000.

[139] A. F. Mills and B. H. Chang. Error analysis of experiments. *UCLA, Los Angeles, CA*, 2004.

[140] C. J. Dasch. One-dimensional tomography: a comparison of abel, onion-peeling, and filtered backprojection methods. *J. Applied Optics*, 31(8):1146–1152, 1992.

[141] L. Hoogterp-Decker and P. Schihl. The use of synthetic jp-8 fuels in military engines. 2009. RDECOM-TARDEC, Warren, MI.

[142] S. Teshome, O.I. Smith, and A.R. Karagozian. Droplet combustion in the presence of altered acceleration fields via acoustic excitation. *Western States Sections of the Combustion Institute*, 2009.

[143] W.L. Nyborg. Acoustic streaming due to attenuated plane waves. *J. Acoust. Soc. Am.*, 25(1):68–75, 1953.

[144] W.L. Nyborg. Acoustic streaming near a boundary. *J. Acoust. Soc. Am.*, 30(4): 329–339, 1958.

[145] A. L. Smith and C. C. Graves. Drop burning rates of hydrocarbon and nonhydrocarbon fuels. In *NACA RME 57*. F11, 1957.

[146] B. Vielle, C. Chauveau, X. Chesneau, A. Odeide, and I. Gokalp. High pressure droplet burning experiments in microgravity. *Proc. Combustion Inst.*, 26, 1996.

[147] B.R. Munson, A.P. Rothmayer, T.H. Okiishi, and W.W. Huebsch. *Fundamental Fluid Mechanics*. Wiley, 5th edition, 2005.

[148] Frank M White. *Viscous Fluid Flow 3e*. Tata McGraw-Hill Education, 1974.

[149] O.J. Haidn. Advanced rocket engines. In *Advances on Propulsion Technology for High-Speed Aircraft, Educational Notes RTO-EN-AVT-150*, pages 6–1 6–40. Neuilly-sur-Seine, France: RTO, 2008.

[150] A.G. Webster. Acoustical impedence, and the theory of horns and of the phonograph. *Proceedings of the National Academy of Sciences*, 5:275–282, 1919.

[151] A. D. Pierce. *Acoustics: An Introduction to Its Physical Principles and Applications*. Acoustical Society of America, 1991.

[152] P.J. Schmid. Dynamic mode decomposition of numerical and experimental data. *Journal of Fluid Mechanics*, 656:5–28, 2010.

[153] M. Arienti, M. Corn, G.S. Hagen, R.K. Madabhushi, and M.C. Soteriou. Proper orthogonal decomposition applied to liquid jet dynamics. *21st Annual ILASS-Americas Conference*, 2008. Orlando, FL.

[154] M. Arienti and M.C. Soteriou. Dynamics of free jets submitted to upstream acoustic modulations. *Physics of Fluids*, 21:112104, 2009.

[155] MR Jovanovic, PJ Schmid, and JW Nichols. Low-rank and sparse dynamic mode decomposition. pages 139–152, 2012.

[156] P.J. Schmid. Application of the dynamic mode decomposition to experimental data. *Experiments in Fluids*, 50:1123–1130, 2011.

[157] P.J. Schmid, L. Li, M.P. Juniper, and O. Pust. Applications of the dynamic mode decomposition. *Theor. Comput. Fluid Dyn.*, 25:249–259, 2011.

[158] National Institute of Standards and Technology. Thermophysical properties of fluid systems, 2011.

[159] R.D. Woodward, S. Pal, S. Farhangi, G.E. Jensen, and R.J. Santoro. LOx/GH2 shear coaxial injector atomization studies: effect of recess and non-concentricity. *45th AIAA Aerospace Sciences Meeting and Exhibit*, pages 1–22, 2007-571.

Photoignition Torch Applied to Cryogenic H_2/O_2 Coaxial Jet

Alireza Badakhshan
ERC Inc., Edwards AFB, CA 93524
Stephen Danczyk
Air Force Research Lab, Edwards AFB, CA 93524
and
Douglas Talley
Air Force Research Lab, Edwards AFB, CA 93524

Abstract

A compact high pressure photoignition torch was developed and used to ignite a H_2/O_2 cryogenic coaxial jet at about 130 K and 500 psi. The photo-activated ignition torch takes advantage of the photoignition properties of carbon nanotubes as it is ignited by a low power camera flash. The basic system consists of a 200 mg capsule containing no more than 70 mg of a single-walled carbon nanotube (SWNT)-based "solid fuel mixture". We have shown that by mixing SWNT with other nano-materials, the ignition parameters such as burn temperature, burn duration, and the ignition byproducts can be tailored to meet different ignition requirements. This approach provides a novel method for initiation of combustion at pressures up to ~1000 psi. The small and light-weight ignitor is suitable for certain thrusters and liquid rocket engines. This ignition system is scalable for applications in different combustion chambers such as gas turbines, gas generators, liquid rocket engines, and multi grain solid rocket motors.

Key Words: photoignition, fuel spray ignition, high pressure ignition,

I. Introduction

An ideal ignition system needs to be robust, efficient, reliable, simple, low cost, and flexible. It should also initiate combustion under a broad range of conditions in order to maximize the operational flexibility of energy and propulsion systems. There is no ignition system that meets all of these criteria. Thus there is a need for novel ignition technologies that satisfy specific requirements while maintaining low cost and simplicity. Ajayan et al. first reported the photoignition of single-wall carbon nanotubes (SWNTs) by a compact camera flash in 2002.[1] Subsequently, others reproduced some of the aforementioned results[2,3] and we suggested that SWNTs could be used as an ignition agent for a variety of fuels, including those of interest in liquid rocket engines.[4-6] More recently, research on the photoignition of gaseous fuel and air mixtures showed distributed ignition.[7,8] Photoignition of graphene oxide for fuel burning applications has also been demonstrated.[9]

We have reported on the development of a high pressure ignition torch that is based on the photoignition of carbon nanotubes recently and explained the ignition of liquid fuel sprays in a subscale rocket engine by the torch.[10] In this report, we will describe the most important aspects of this ignition system, including the results for photoignition of a simple fuel spray in air as well as ignition of a coaxial injector flow with cryogenic propellants. The most obvious application for the current effort is in liquid rocket engines, but the reported photoignition torch has a range of other possible applications beyond propulsion systems.

II. Methodology

Samples of SWNT with different nanoparticle Fe content used in this study were obtained from Unidym Inc., Houston, Texas. The samples were as-grown SWNTs with a high concentration of impurities as byproducts of CNT syntheses. The as-grown samples typically contain substantial impurities, (about 50% by weight in the reported samples) mostly Fe nanoparticles and amorphous carbon.[3,11] The term CNT is used for the samples in this report in order to indicate that they were as-grown SWNT samples and they were not purified in any way. However, purified samples show considerably higher photoignition threshold

as tested, thus ill-suited for photoignition applications. In most cases some solid additives (to be described later) were used along with CNTs, which are collectively referred to as a "CNT mixture."

The ignition light source was a modified version of the compact Xe-flash that is used in a disposable camera. This type of light source proved to be quite reliable and the Xe-flash bulb was found to have sufficient structural integrity for high pressure applications, and it survived many pressure cycles between 1 to 135 atm (15-2000 psi). Figure 1 shows the preferred configuration of a self-contained Xe-flash light source, the related electronics, and a transparent ignition capsule that is partially filled with the CNT mixture. Similar ignition capsules were used in all of the configurations reported here. When used within a pressure vessel, the Xe-flash and the ignition capsule were usually placed next to each other under high pressure and connected through sealed feed-through electrical wires to the rest of the electronics outside.

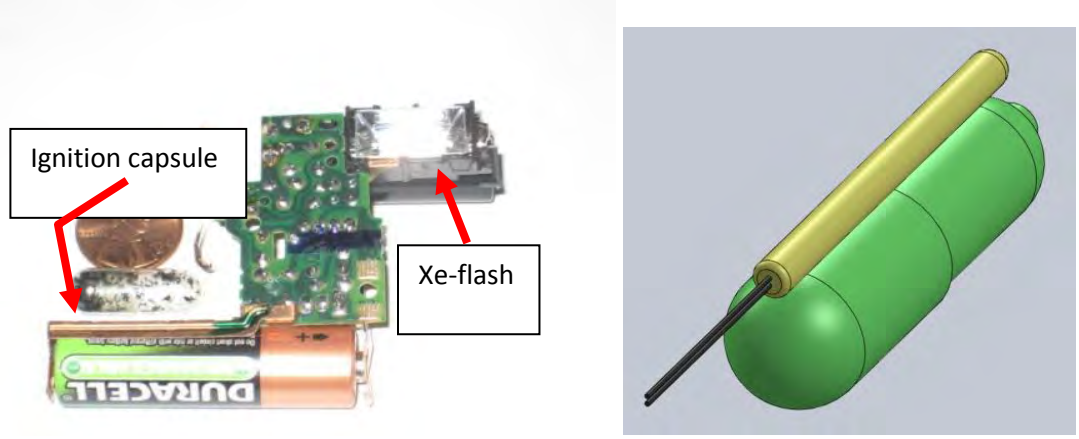

Figure 1 – The photographic image of a complete hardware of a self-contained photoignition device that was used in most of the reported ignition systems and torches. The ignition capsule that is shown below the penny is 5-10% filled with 30-70 mg of the nanostructured solid fuel mixture. Normally the capsule is placed alongside of the Xe-flash that is shown at the top right where it receives the maximum exposure.

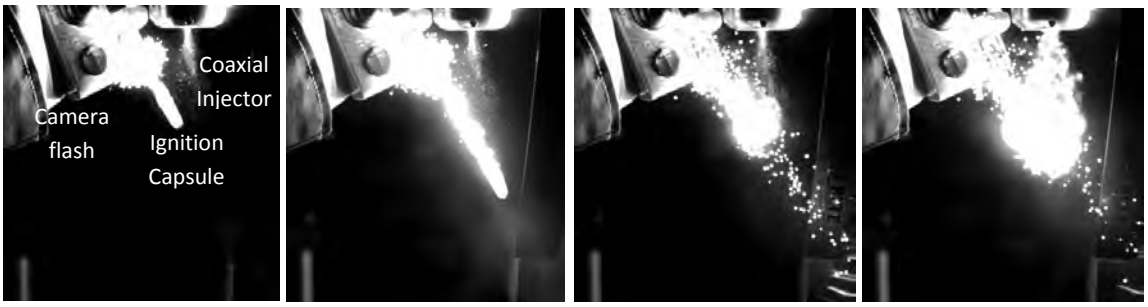

Figure 2 – Photoignition of RP1 spray by a nano-ignition capsule containing about 5 mg of CNT shows the process through the sequence of images. In this case the ignition capsule is taped on the flash of a disposable camera that is also shown. The time reference of t=0 indicates the peak of the illumination of the disposable camera flash with a duration of about 1 ms. The fuel injector is the customized ultrasonic atomizer. These images were captured at 2000 fps.

Experimental Setup for Fuel Spray Ignition

Three different setups were utilized for the fuel ignition experiments. The first one was used for observation of the dynamics of the photoignition process at atmospheric pressure with an unhindered view of the ignition source and the ignition process. The same fuel injector was used in a second setup, a mid-pressure test chamber that was utilized to observe the torch function up to about 30 atm. The third

setup was a compact high-pressure ignition torch (HPIT) chamber that was made of brass and was designed for photoignition experiments up to about 135 atm of pressure. The details of these systems is described elsewhere.[10]

III. Findings

The motivation for this project was to use CNTs as photoignition agents for initiation of combustion at elevated pressures in subscale liquid rocket fuel injectors. The general approach is to take advantage of the exothermic photoignition of carbon nanotubes to initiate combustion within reactants mixed with the nanotubes. The current approach goes beyond the general practice and involves an ignition chamber which is separate from but connected to the combustion chamber and it creates ignition through a stream of hot gas and burning particles.

Table 1 – MIE for different nanostructured materials and their corresponding burn temperatures

nanoparticle samples	**particle size/ smallest dimensional size**	**Min. ignition Energy/area, Fluence (mJ/cm^2)**	**ignition/burn temperature* (^0C)**
CNT(51% Fe)	< 30 nm	64 ± 8	490 ± 30
CNT(18% Fe)	< 30 nm	182 ± 13	420 ± 50
Graphene Oxide Foam/Nanoplatelets	< 30 nm thick platelets	500 ± 60	370 ± 100
Al-nanoparticles	18 nm	290 ± 50	1100 ± 150
Fe, Carbon coated	~ 40 nm	220 ± 35	250 ± 30
Fe powder	~ 30 nm	150 ± 25	220 ± 30
Pd powder	~ 12 nm	530 ± 60	320 ± 40

*the temperature of a focused spot on the sample

We studied ignition characteristics of CNT and a number of other nanoparticles or nanostructured materials in order to identify those parameters that are particularly useful in photoignition process, as listed in Table 1. We also studied photoignition properties of other materials such as multi-walled CNT, C60 fullerenes and metallic and nonmetallic fine particles, among others. Table 1 only includes materials that are well characterized and showed a more consistent photoignition effect. The stated error figures are the measured statistical variations for the first four samples and they are the estimated uncertainty for the last three samples.

Realization of the Photoignition Torch

In preliminary tests, nano-ignition capsules were used to ignite a fuel spray by allowing the two-part capsule to burst open in the vicinity of the fuel spray. The setup of Figure 2(a), an ignition capsule was positioned close to the path of fuel spray from the ultrasonic atomizer, such that upon ignition and rupture of the nano-ignition capsule the fuel and the burning particles impinge upon one another. The camera flash was located very close to the ignition capsule so that it received sufficient energy from the flash to induce photoignition of the CNT mixture. Further investigations of fuel ignition process revealed that a 2-3 mm size hole in an ignition capsule would make it to discharge burning byproducts and burning particles directly through the hole as the pressure is built up in the capsule. Hence it produces a miniature ignition torch.

In order to use a photoignition torch for high pressure applications, a high-pressure ignition torch (HPIT) with a separate ignition chamber was designed and built. HPIT is capable of sending hot/reacting gases and burning particles beyond 35 cm from the ignition capsule. The entire system was housed in an explosion proof facility with the remote operation capability that provided control signals for the different remotely operated values and electrical firing sequence with millisecond accuracy.[10] We have

successfully applied the HPIT system to generate ignition of an O_2/H_2 coaxial shear injector flow at elevated pressures up to ~35 atm (520 psi).[10]

IV. Conclusions

A miniature photo-activated ignition torch utilizing an encapsulated CNT-based fuel mixture was created. The photoignition torch has been tested up to about 70 atm (1000 psi) of pressure and its suitability for spray ignition demonstrated up to ~40 atm (~600 psi). Application of the photoignition torch for initiation of combustion in a cryogenic H2/O2 shear coaxial flame at high pressure was demonstrated at an oxygen temperature of about ~130 K and a pressure of ~35 atm (~520 psi). The photoignition torch as described is quite suitable for high pressure ignition applications and it offers specific advantages. The battery operated ignition system is light weight and compact with a typical mass of less than 25 g (without the battery). The optically coupled photoignition torch offers superior electrical safety so that there are no electrical contacts between the ignition source and the ignition charge or fuel. This makes a photoignition system relatively insensitive to electromagnetic interference and electrostatic discharge. The photoignition torch is based on the mature technology of a compact battery operated Xe-flash lamp and ignition of solid propellants, which makes it quite reliable. While the photoignition torch has been demonstrated only at small scales, the photoignition system can be easily scaled up to much larger sizes with a relatively small penalty in the ignition delay.

References

1. Ajayan PM, et al. “Nanotubes in a Flash: Ignition and Reconstruction”, *Science* 296, pp 705, (2002).
2. Braidy N, Botton GA, and Adronov A, Nanoletters 2 (11), pp. 1277-1280, (2002).
3. Smits J, and Wincheski B, “Response of Fe powder, purified and as-produced HiPCo SWNT to flash exposure”, Materials Science and Engineering A, 358, pp. 384-389, (2003).
4. Chehroudi B, Danczyk S, Morgan C, and Badakhshan A, “Ignition Characteristics of Single-Walled Carbon Nanotubes (SWNTs) Utilizing a Camera Flash for Distributed Ignition of Liquid Sprays”, Tech. Rep. DTIC, Online Information for Defense Community, ADA511240, Oct 2008.
5. Badakhshan A, Danczyk S, Wirth D, and Pilon L, “Ignition of Liquid Fuel Spray and Simulated Solid Rocket Fuel by Photoignition of Carbon Nanotube Utilizing a Camera Flash”, Conf. paper, DTIC, Online Information for Defense Community, ADA571240, Dec 2011.
6. Badakhshan A, and Danczyk, “Photo-ignition of Carbon Nanotube for Ignition of Liquid Fuel Spray and Solid Fuel” Conf. paper, DTIC, Online Information for Defense Community, ADA573322, Mar 2012.
7. Berkowitz AM, and Oehlschlaeger MA, "The PhotoInduced Ignition of Quiescent Ethylene/Air Mixtures Containing Suspended Carbon Nanotubes," *Proceeding of the Combustion Institute*, 33, pp. 3359-3366 (2011).
8. Loomis MP, Lee JG, Yetter RA, “Characterization of photoignition of single walled carbon nanotubes”, Fall Technical Meeting of the Eastern States Section of the Combustion Institute, University of Maryland, October 18-21, (2009).
9. Gilje S, et al., “Photothermal Deoxygenation of Graphene Oxide for Patterning and Distributed Ignition Applications”, Adv Mat, 22, pp. 419–423, (2010).
10. Badakhshan A, Danczyk, Forliti, D, Leyva, I, and Talley, D, "Nano-ignition Torch Applied to Cryogenic H2/O2 Coaxial Jet", 54th AIAA Aerospace Sciences Meeting, AIAA SciTech, (AIAA 2016-0184).
11. See for example http://www.nano-c.com/nanoprod.html, more detailed images of SWNT and impurities are found at: Safarova et al., *Modern Res. Educ. Topics in Microscopy* **2007**, A. Méndez-Vilas and J. Díaz (Eds.).

AIAA SciTech
4-8 January 2016, San Diego, California, USA
54th AIAA Aerospace Sciences Meeting

Nano-ignition Torch Applied to Cryogenic H2/O2 Coaxial Jet

A. Badakhshan[1]
ERC Inc., Edwards AFB, CA 93524
Stephen Danczyk[2]
Air Force Research Lab, Edwards AFB, CA 93524
David Forliti[3]
Sierra Lobo Inc., Edwards AFB, CA 93524
Ivett Leyva[4] and Douglas Talley[5]
Air Force Research Lab, Edwards AFB, CA 93524

Downloaded by Doug Talley on September 19, 2016 | http://arc.aiaa.org | DOI: 10.2514/6.2016-0184

Abstract

A high-pressure photoignition torch has been developed which takes advantage of the photoignition properties of single wall carbon nanotubes (SWNTs). The goal was to initiate combustion in a cryogenic O_2-H_2 coaxial injector at about 35 atm (~520 psi) at O_2 temperature of about 130 K with SWNT-based "solid fuel mixtures". Our investigation includes the effects of chamber pressure, the presence of different solid oxidizers such as $BKNO_3$ and $KMnO_4$, as well as solid fuels and solid propellants, on the functionality of the photoignition torch. We have shown that the ignition parameters such as burn temperature, burn duration and the ignition byproducts can be tailored to meet different ignition requirements. It is anticipated that photoignition provides a suitable method for ignition of systems that require the start of combustion at a high pressure up to about 135 atm (2000 psi) as well as ignition of certain thrusters and liquid rocket engines that require an extremely small and light weight torch igniter. This ignition method can be applied to large combustion chambers such as gas turbines, gas generators, liquid rocket engines and possibly multi grain solid rocket motors.

I. Introduction

THERE are a number of properties that are desirable for an ignition system. Ideally an ignition system should be robust, efficient, reliable, simple, low cost, and flexible. Ideally, an ignition system should initiate combustion under a broad range of conditions in order to maximize the operational flexibility of energy and propulsion systems. When ignition systems rely on high reactivity additives, such as hypergolic or pyrophoric reactants, handling and storage of these specialized chemicals

[1] Research Scientist, ERC Inc., Combustion Devices Group, 10 Saturn Blvd., Edwards AFB, CA 93524
[2] Research Scientist, RQRC, Combustion Devices Group, 10 Saturn Blvd., Edwards AFB, CA 93524
[3] Research Scientist, Sierra Lobo Inc., Edwards AFB, CA 93524
[4] Aerothermodynamics PO, AFOSR/RTE, 875 N Randolph St, Arlington, VA 22242, AIAA Associate Fellow
[5] Research Scientist, Combustion Devices Group, 10 Saturn Blvd., Edwards AFB, CA 93524, AIAA Fellow

This material is declared a work of the U.S. Government and is not subject to copyright protection in the United States.

may be complicated by safety and health concerns. Thus there is a need for novel ignition technologies that satisfy the numerous requirements while maintaining simplicity.

Ajayan et al. first reported the photoignition of single-wall carbon nanotubes (SWNTs) by a camera flash in 2002.[1] It was suggested that Fe nanoparticles within SWNTs play an important role in the photoignition process.[2] Subsequently, others reproduced some of the aforementioned results[3] and we suggested that SWNTs could be used as an ignition agent for a variety of fuels, including those of interest in liquid rocket engines.[4-6] Other applications of photoignition of SWNTs have also been reported.[7-10] More recently, research on the photoignition of gaseous fuel and air mixtures showed distributed ignition.[11,12] Photoignition of graphene oxide for fuel burning applications has also been demonstrated.[13]

An ignition torch that is based on the photoignition of carbon nanotubes was developed and ignition of liquid fuel sprays by the torch has been achieved. In this report, we will describe the experimental procedure for producing ignition that is induced by a compact Xe-flash, including the results for photoignition of a simple fuel spray in air as well as ignition of a coaxial injector flow with cryogenic propellants. The application for the current effort is liquid rocket engines, but the reported photoignition torch has a range of other possible applications beyond propulsion systems.

Downloaded by Doug Talley on September 19, 2016 | http://arc.aiaa.org | DOI: 10.2514/6.2016-0184

II. Experimental Setup

Samples of SWNT with different nanoparticle Fe content used in this study were obtained from Unidym Inc., Houston, Texas. The samples were as-grown SWNTs with a high concentration of impurities as byproducts of CNT syntheses. Based on the evidence presented by the vendor the carbon nanotubes believed to be predominantly SWNT. The as-grown samples typically contain substantial impurities, (about 50% by weight in the reported samples) mostly Fe nanoparticles and amorphous carbon.[3,14] The term CNT is used for the samples in this report in order to indicate that they were as-grown SWNT samples and they were not purified in any way. Contrary to photoignition, most applications of CNTs require high concentration of CNTs and low concentration of Fe, which explains the need for the often elaborate purification process. However, purified samples show considerably higher photoignition threshold as tested, thus ill-suited for photoignition applications. The same batch of CNT was used for all photoignition experiments reported here, the CNT samples with nanoparticle Fe content of 51 wt.%, as stated by the vendor. In most cases some solid additives (to be described later) were used along with CNTs, which are collectively referred to as a "CNT mixture."

The ignition light source was a modified version of the compact Xe-flash that is used in a disposable camera. This type of light source proved to be quite reliable and the Xe-flash bulb was found to have sufficient structural integrity for high pressure applications, and survived many pressure cycles between 1to 135 atm. Also, the same Xe-flash unit was repeatedly used for ignition at elevated pressures up to about 50 atm.

Figure 1 shows the preferred configuration of a self-contained Xe-flash light source, the related electronics, and a transparent ignition capsule that is partially filled with the CNT mixture. Similar ignition

capsules were used in all of the configurations reported here. When used within a pressure vessel, the Xe-flash and the ignition capsule were usually placed next to each other under high pressure and connected through sealed feed-through electrical wires to the rest of the electronics outside.

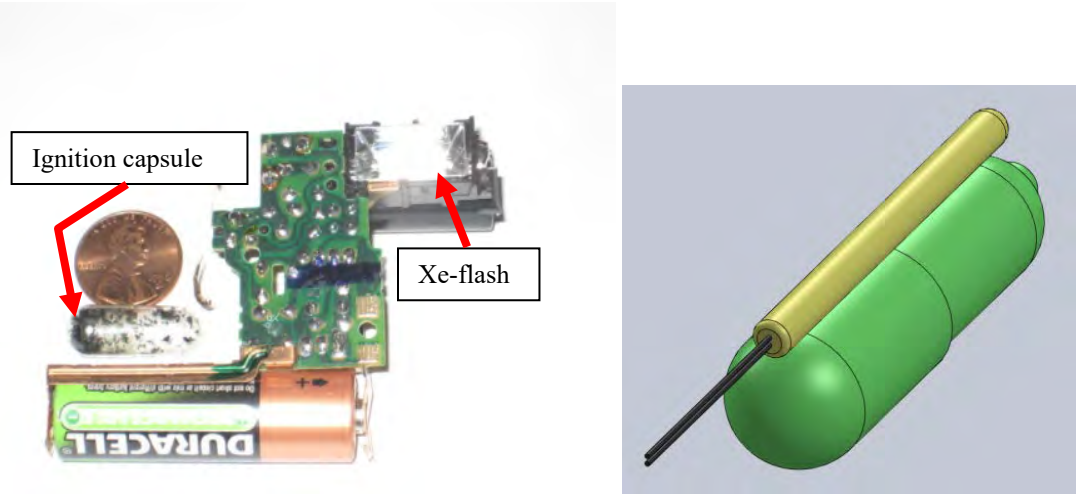

Figure 1 – The photographic image of a complete hardware of a self-contained photoignition device that was used in most of the reported ignition systems and torches. The ignition capsule that is shown below the penny is 5-10% filled with 30-70 mg of the nanostructured solid fuel mixture. Normally the capsule is placed alongside of the Xe-flash that is shown at the top right where it receives the maximum exposure.

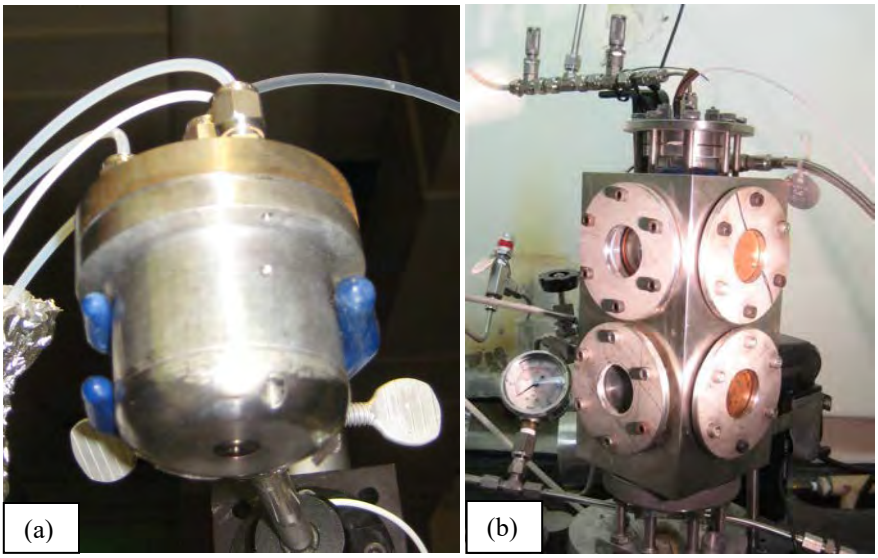

Figure 2 – (a) The customized ultrasonic atomizer (OD=6 cm) that was used as the fuel injector at atmospheric pressure and at an intermediate pressure up to about 30 atm (~450 psi). (b) The mid-pressure combustion chamber for photoignition test up to about 30 atm (440 psi) of pressure with the ultrasonic fuel injector at the top of it. . In this case the light source is located outside of the chamber aginst the lower back window (D=5 cm, L=2.5 cm) and the ignition torch sits inside the chamber and aginst the same window.

Downloaded by Doug Talley on September 19, 2016 | http://arc.aiaa.org | DOI: 10.2514/6.2016-0184

Experimental Setup for Fuel Spray Ignition

Three different setups were utilized for the fuel ignition experiments. The first one was used for observation of the dynamics of the photoignition process at atmospheric pressure with an unhindered view of the ignition source and the ignition process. Figure 2 shows a picture of the ultrasonic atomizer that was used to produce an injector flow for some of the ignition studies. It also shows the second fuel ignition setup, a mid-pressure test chamber that was utilized to observe the torch function up to about 30 atm. The pressurizing gas was N_2, air, or a combination of the two for reduced oxidation capability, and it included both stagnant and flowing conditions.

The third setup was a compact high-pressure ignition torch (HPIT) chamber that was made of brass and was designed for photoignition experiments up to about 135 atm of pressure. Figure 3 shows a schematic diagram of HPIT along with photographic image of the HPIT as it is attached to high pressure combustion chamber that uses HPIT through a 30 cm long connecting tube. The HPIT was utilized to ignite the O_2-H_2 at different pressures and temperatures.

Downloaded by Doug Talley on September 19, 2016 | http://arc.aiaa.org | DOI: 10.2514/6.2016-0184

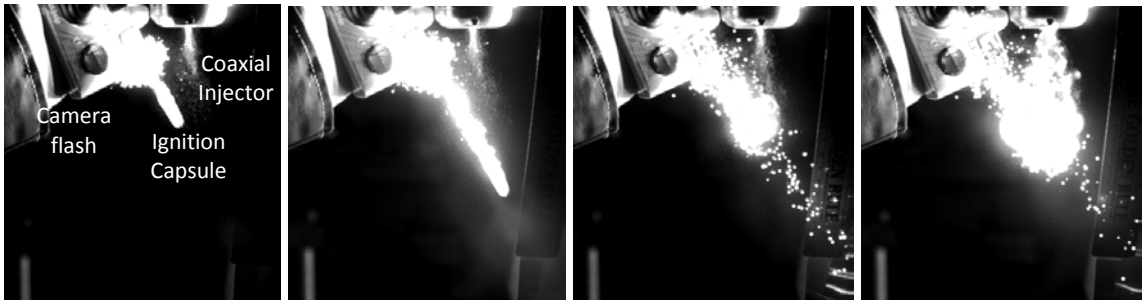

Figure 3 – Photoignition of RP1 spray by a nano-ignition capsule containing about 5 mg of CNT shows the process through the sequence of images. In this case the ignition capsule is taped on the flash of a disposable camera that is also shown. The time reference of t=0 indicates the peak of the illumination of the disposable camera flash with a duration of about 1 ms. The fuel injector is the customized ultrasonic atomizer that is shown in Figure 2(a). These images were captured at 2000 fps.

III. Instrumentation

A high-speed pyrometer, model KGA 740 HS from Mikron Infrared Inc., covering a temperature range from 300-2300 C was used to determine the instantaneous temperature of the sample during the process leading to photoignition of the CNTs, as well as for measuring burn temperature of other ingredients such as aluminum nanoparticles and solid rocket fuel particles. It should be noted that the pyrometer produces a curve of the instantaneous temperature of a focused spot of the sample that is about 2 mm in diameter that also provides a reasonable estimate of the maximum burn temperature of the sample. As such the reported values are a rough measure of maximum burn temperature of the spot on the surface of the sample and they may not represent the true temperature of the entire sample.

A high-speed Phantom V7.1 camera from Vision System capable of capturing up to 4800 frames/s (fps) at full-frame (800x600) was utilized in most of the experiments to record the sequence of ignition events, including fast moving photoignition byproducts. In the HPIT experiments, a different high-speed camera, model Phantom V710 from Vision System (7500 fps at 1280x800) was utilized.

IV. Experimental Procedure

The motivation for this project was to use CNTs as photoignition agents for initiation of combustion in subscale liquid rocket fuel injectors. The general approach is to take advantage of the exothermic photoignition of carbon nanotubes to initiate combustion within reactants mixed with the nanotubes. The current approach goes beyond the general practice and involves an ignition chamber which is separate from but connected to the combustion chamber.

Downloaded by Doug Talley on September 19, 2016 | http://arc.aiaa.org | DOI: 10.2514/6.2016-0184

A. The Need for Encapsulated CNT

Previous proof-of-concept experiments indicated that this could be a viable approach. However, it was observed that samples that were partially wet due to exposure to the mist from the liquid fuel spray required a substantially higher light fluence (energy per unit area) for photoignition. The high fluence requirement made photoignition of fuel sprays very difficult to implement for most applications, because the CNT sample is usually located close to the fuel spray in order to induce ignition.

In order to overcome the problem two methods were devised to keep the CNT samples dry. The first method was encapsulation of CNT mixture in a transparent container/capsule, and the second one was lamination of CNTs along with a solid oxidizer in thin layers of a transparent polymer. Both methods proved to be effective, but the encapsulation is more reproducible and it is easier to implement for high-pressure applications. Thus encapsulation of CNTs along with solid energetic additives, referred to as CNT mixture was employed as the method of choice for igniting liquid fuel/oxidizer flows. Examples of CNT mixtures are presented in Table 1 and a detailed description of the purpose and properties of different CNT mixtures will be discussed later in this report.

The ignition capsules were prepared by placing CNT mixtures in a transparent gel cap size 00 (about 0.75 cm^3 in volume, D=7 mm and L=20 mm). Figure 1shows a typical ignition capsule partially loaded with CNT mixture. Numerous tests indicated that if there was sufficient material in the container, typically a few milligrams, the gaseous byproducts of the photoignition of CNT (mostly CO_2 and CO) would pressurize the capsule beyond its 2 atm (~30 psi) limit, causing it to burst and release its burning contents to ignite the fuel spray.

V. Results and Discussions

Photoignition of Different Materials

We studied ignition characteristics of CNT and a number of other nanoparticles or nanostructured materials in order to identify those parameters that are particularly useful in photoignition process. The parameters of interest are minimum ignition energy (MIE) and burn temperature for different materials, as

listed in Table 1. We also studied photoignition properties of other materials such as multi-walled CNT, C60 fullerenes and SWNT and multiwall carbon nanotubes from different vendors as well as carbon black, metallic and nonmetallic fine particles, and ball milled metallic thermites with mixed results. Table 1 only includes materials that are well characterized and showed a more consistent photoignition effect. The stated error figures are the measured statistical variations for the first four samples and they are the estimated uncertainty for the last three samples.

Table 1 – MIE for different nanostructured materials and their corresponding burn temperatures

nanoparticle samples	**particle size/ smallest dimensional size**	**Min. ignition Energy/area, Fluence (mJ/cm^2)**	**ignition/burn temperature* (^0C)**
CNT(51% Fe)	< 30 nm	64 ± 8	490 ± 30
CNT(18% Fe)	< 30 nm	182 ± 13	420 ± 50
Graphene Oxide Foam/Nanoplatelets	< 30 nm thick platelets	500 ± 60	370 ± 100
Al-nanoparticles	18 nm	290 ± 50	1100 ± 150
Fe, Carbon coated	~ 40 nm	220 ± 35	250 ± 30
Fe powder	~ 30 nm	150 ± 25	220 ± 30
Pd powder	~ 12 nm	530 ± 60	320 ± 40

*this is the temperature of a focused spot on the sample and may not be representative of the entire sample

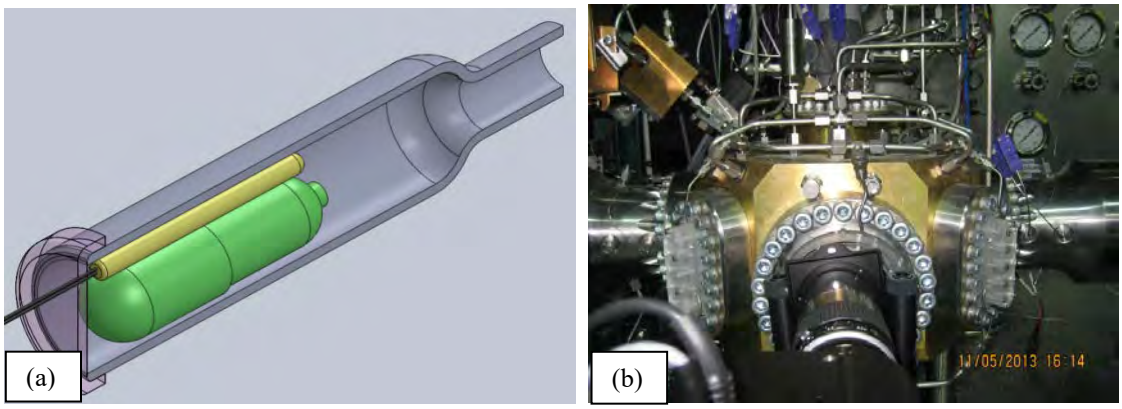

Figure 4 – (a) The schematic diagram of the drop-in 135 atm (2000 psi) ignition torch. The ignition capsules are loaded from the back and hot gas and burning particles rush through the tube (OD=6 mm) in front of the torch. (b) The O_2-H_2 combustion chamber that is designed for combustion instability studies at pressures up to about 100 atm. The high-pressure ignition torch, the brass cube on the top left corner of this photographic image is coupled to the combustion chamber via a 35 cm long tube with OD=6mm.

Realization of the Photoignition Torch

In preliminary tests, nano-ignition capsules were used to ignite a fuel spray by allowing the two-part capsule to burst open in the vicinity of the fuel spray. In this report the term fuel spray is used in its most general sense so that it includes injector flow as well, though from technical point of view they may not be the same as it is related to the presence or flow of the oxidizer. Further investigations of fuel ignition process revealed that a 2-3 mm size hole in an ignition capsule may prevent it from exploding due to over pressurization, if the burn rate was kept sufficiently

Downloaded by Doug Talley on September 19, 2016 | http://arc.aiaa.org | DOI: 10.2514/6.2016-0184

low. In such cases the capsule would discharge burning byproducts and burning particles directly through the hole as the pressure is built up in the capsule. Hence it produces a miniature ignition torch. An example of the application of photoignition torch for fuel spray is shown in Figure 4.

At atmospheric pressure, a typical photoignition torch may burn close to 0.5 second depending on the burn rate and the amount of fuel in the capsule, and it typically discharges a combination of hot gas, flame, and burning particles that extends 15-30 cm away from the ignition capsule. As the ambient pressure is increased beyond about 10 atm, the burn rate gradually increases and the burn duration decreases, so that at about 30 atm the burn duration is no more than half of what it is at 10 atm for most CNT mixtures. This trend is expected to continue as the pressure is increased beyond 30 atm.

Table 2 – Ingredients for a photoignition torch for different chamber pressures.

CNT, main Photoignition Agent (Wt%)	Fuel Al_NP 18/80nm (Wt%)	Fuel SRF (Wt%)	Oxidizer $BKNO_3$ (Wt%)	Oxidizer $KMnO_4$ (Wt%)	Observations and Comments On the Relative Effects of Additives
Sample 0 100%					Short burn duration & low burn Temp. (~800K)
Sample 1 10%			90%		Improved ignition reliability & burn Temp.
Sample 2 10%				90%	Reliable ignition only ≥10 atm
Sample 3 ~3%		~97%			Unreliable ignition of SRF associated with a long ignition delay (ratio doesn't matter)
Sample 4 3%	7-12%	85-90%			More reliable ignition, burns at higher T & is more energetic than samples 2 & 3
Sample 5 3%	7%	45%		45%	Less reliable ignition than the above unless the chamber Pres. ≥10 atm
Sample 6 3%	7%	50%	40%		Improved flash sensitivity & ignition + generate a lot of gas & smoke
Sample 7 1%	9%	80%	10%		Best ignition sensitivity, reliability & burn duration for chamber Pres. ≥7 atm
Sample 8 2%	8%	70%		20%	Comparable to sample 7 only for chamber Pres. ≥15 atm
Sample 9 2%	8%	70%	20%		Improved ignition reliability and burn duration
Sample 10 1%	15%	75%	9%		As good as the above at atmospheric pressure, but burns too fast ≥ 15 atm

B. Fuel Mixtures for a Photoignition Torch

While we were able to ignite a fuel spray with an ignition capsule that contained only CNTs, such an ignition capsule exhibited a number of drawbacks. These are due to the fact that CNTs do not burn long and hot enough and the amount of gas generated may not be sufficient for an effective ignition torch for most applications. The solution was to add small amounts of granulated solid fuel/propellants and oxidizers to the ignition capsule. The CNTs would ignite these additives and then the much more robustly burning

Downloaded by Doug Talley on September 19, 2016 | http://arc.aiaa.org | DOI: 10.2514/6.2016-0184

additives could be used to ignite something else. Table 2 shows examples of ingredients of a typical ignition capsule along with the weight percentage of each of the ingredients in the capsule. Comments about the relative advantages and possible disadvantages of each specific mixture are also stated in Table 2.

It should be mentioned that each material in Table 2 is from the same batch and the total content of the photoignition torches were typically 30-70 mg. CNT samples with no add material as well as samples with added energetic materials such as aluminum nanoparticles (Al-NP) solid rocket fuel (SRF) and solid oxidizers were used as fuel for the photoignition torch. The different CNT mixtures exhibited different ignition properties depending on their ingredients. A rough measure of burn temperature and qualitative burn duration of various CNT mixtures were determined through the pyrometer as described previously. The burn duration of most photoignition torches were also measured by the high-speed camera, which is a more reliable approach.

Downloaded by Doug Talley on September 19, 2016 | http://arc.aiaa.org | DOI: 10.2514/6.2016-0184

All of the ingredients that are listed in Table 2 are commercially available except for the solid rocket fuel (SRF), also known as solid propellant, which is formulated and prepared in-house. The SRF is typically 87% solid loaded composite propellant composed of hydroxyl-terminated polybutadiene (HTPB) as a binder, ammonium perchlorate as an oxidizer and aluminum powder as a fuel. The granulated SRF was used in the ignition capsules that are reported here and they were made from rubber-like solid chunks of SRF that is mixed from solid powders and polymerized through a proprietary process at the Air Force Research Lab, Edwards AFB. It is possible to use commercially available model rocket fuels (MRF) instead of SRF. While MRF is easier to ignite and it typically produces more gas than SRF, it also produces black smoke and leaves behind a film residue on the nearby surfaces. Moreover, MRF in powdered form burns too fast at elevated pressures and it may be hard to produce properly sized particles from this material if it is not polymerized.

At elevated pressures, it may be necessary to push the photoignition byproducts from the ignition chamber into the combustion chamber with pressurized air/gas before they burn out. This is not necessary when the photoignition torch is placed inside the combustion chamber. In ignition experiments with HPIT, an air pressure of 2-4 at above the combustion chamber pressure was used in order to carry ignition byproducts to the high-pressure combustion chamber before they were extinguished. The best photoignition torch for 20-50 at pressure has been generated by samples 7 through 10 in Table 1, respectively.

A typical nano-ignition capsule has a total mass of no more than 200 mg, of which about 130 mg is due to the empty capsule and the rest is the CNT mixture. The amount of CNT in the mixture is typically 1-3 mg. The function of the solid oxidizer is to speed up the propagation of ignition to other solids. For the solid oxidizer, boron–potassium nitrate ($BKNO_3$) and potassium permanganate ($KMnO_4$) were used. While technically BKNO3 is not merely an oxidizer, but a mix of fuel (boron) and oxidizer (KNO3), we used it as an oxidizer.

The role of Al-NP is to make sure that the temperature increases rapidly enough and gets high enough (exceeding 1500 K) to ignite the SRF. We used Al-NP in powdered form with nominal sizes of 18 nm and 80 nm and found both of them to be equally effective as additives for the reported application. The only

notable difference between the two is that the former exhibits photoignition without CNT and latter does not show such a property up to the maximum fluence that was available to us, about 3 J/cm^2. SRF is the main ingredient that provides a burn duration beyond 200 ms and burn temperature well beyond 2000 K. We were able to achieve burn durations approaching 1 s at atmospheric pressure by utilizing the same capsule size of Figure 1 and the same ingredients of Table 2 with no more than 150 mg of CNT mixture. A typical photoignition torch has about 30-70 mg of CNT mixture and burns for 200-400 ms at atmospheric pressure and for 50-100 ms at about 50 atm.

C. Fuel Spay Ignition at Ambient Condition

The setup of Figure 2(a) was used for fuel spray ignition in open air under a fume hood. In the liquid fuel burning experiments, an ignition capsule was positioned close to the path of fuel spray from the ultrasonic atomizer, such that upon ignition and rupture of the nano-ignition capsule the fuel and the burning particles impinge upon one another. The camera flash was located very close to the ignition capsule so that it received sufficient energy from the flash to induce photoignition of the CNT mixture. The photoignition and subsequent fuel ignition and burning process were captured by a high-speed camera, at a rate of 500-2000 frames/second (fps). Figure 3 shows still images of a fuel burning experiment at atmospheric pressure after the activation of the camera flashed. Within 10 ms the combustion of the fuel spray is in progress through the expanding fireball that is about 4 cm in diameter. The flame speed is several meters per second, depending on the fuel and within 15 ms the entire combustible mixture is in flame.

D. Ignition Torch for Combustion of Injector Flow at Elevated Pressures

The setup of Figure 2(b) was used to study photoignition at an elevated pressure up to about 30 atm. In this case, the compact Xe-flash light source was outside of the chamber and the ignition capsule was inside, and the light coupling was made available through a 5 cm wide quartz window at a bottom port opposite to the high-speed camera. The byproducts of the ignition were directed upward toward the fuel spray and the injector flow. The ultrasonic atomizer was modified to accept a pressurized fuel line. The pressure in the chamber was provided by a high pressure air bottle. The exhaust port was at the bottom of the chamber directing the flow and hot gas through a cold trap. Ignition of different types of fuels with this set up was demonstrated including isopropyl alcohol (IPA), methanol and RP1, a category of aerospace fuel similar to kerosene.

In order to use a photoignition torch for high pressure applications, a high-pressure ignition torch (HPIT) with a separate ignition chamber was designed and built. Figure 4 shows a schematic diagram of a HPIT that is capable of sending hot/reacting gases and burning particles beyond 35 cm from the ignition capsule. The body of HPIT is made of brass in order to safely operate at high pressure in an oxygen-rich environment up to about 135 atm (2000 psi). High pressure air is introduced to the HPIT from a K-bottle through an inlet such that the pressure within the ignition chamber stays 2-3 atm above the pressure in the combustion chamber. This excess pressure provides a continuous gas flow in order to carry the hot photoignition byproducts into the combustion chamber and provide the opportunity for fuel ignition at the

Downloaded by Doug Talley on September 19, 2016 | http://arc.aiaa.org | DOI: 10.2514/6.2016-0184

combustion chamber. The entire system was housed in an explosion proof facility with the remote operation capability that provided control signals for the different remote operated values and electrical firing sequence with millisecond accuracy.

We have successfully applied the HPIT system to generate ignition of an O_2-H_2 coaxial shear injector flow at elevated pressures up to ~35 atm. The coaxial shear flow had liquid oxygen in the center tube and gaseous hydrogen in the annular outer tube. Figure 5 shows an example of initiation of O_2-H_2 combustion that is made possible by a photoignition torch. In a typical high-pressure O_2-H_2 combustion experiment, the timing sequence is controlled such that the burning particles arrive at the coaxial jet region within a few milliseconds before H_2 enters the chamber in order to prevent the accumulation of unburned fuel within the chamber. Typically the combustion of fuel happens within a few milliseconds after burning particles first show up in the combustion chamber and the combustion is typically limited to a few seconds in order to avoid overheating and possible melt down of the injector. However combustion can be sustained as long as it is needed for the study, up to 12 s as tested, with no sign of any damages to the injector.

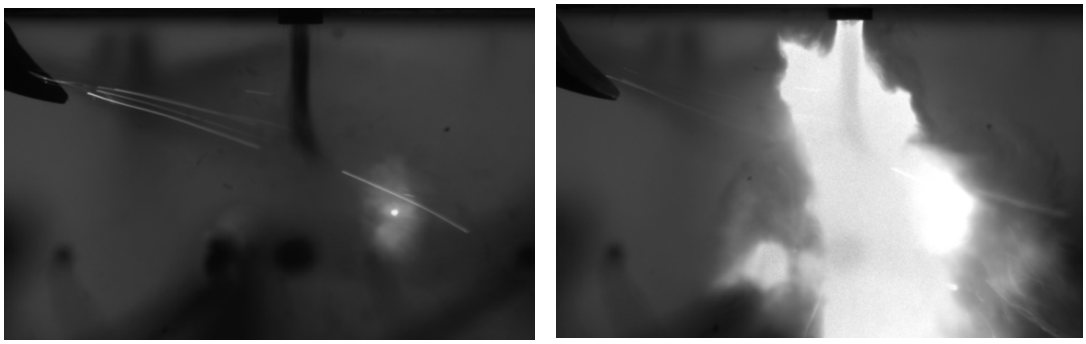

Figure 5 – Snapshots of combustion in LOX/H_2 coaxial jet that was induced by a photoignition torch at ~32 atm and ~133K. The exit point of the burning particles from the 35 cm long tube of the ignition torch is located at the top left corner of the image. These images show t= T+1 ms and T+2 ms after firing of a Xe-flash that has a pulse duration of 1 ms, where T=25-30 ms is the delay between ignition signal and the burning particles entering the combustion chamber. The field of view is about 7 cm across and the images are captured at 1000 fps.

E. Tailoring Ignition Parameters for Fuel Ignition Applications

The function of CNTs is to provide photoignition at a low light level (less than 0.1 J/cm^2), while producing substantial amount of gas to pressurize the capsule.[6.15] This event sets off a chain reaction that ruptures the two part capsule that typically bursts open at about 2 atm of static pressure. Aluminum nanoparticles (Al-NP) in the fuel was easily ignited by burning CNTs (about 800 K) and it produced a high burning temperature (exceeding 1500 K), which lasted more than 100 ms.[15] It is worth mentioning that 18 nm Al-NPs showed photoignition at high enough fluence (> 0.6 J/cm^2) without any CNTs.[15] However Al-NPs produce very little gaseous byproducts, certainly not enough to contribute to the pressure build up within the ignition capsule.

Aluminum nanoparticles burn much longer than CNTs and burn at a high enough temperature to ensure the ignition of SRF particles. In turn SRF particles burn at a very high temperature, well above 2000 K,

Downloaded by Doug Talley on September 19, 2016 | http://arc.aiaa.org | DOI: 10.2514/6.2016-0184

they produce a substantial amount of gas and burn for a substantially longer time, exceeding 500 ms, depending on their size and their surface to volume ratio. Through many tests, it was verified that a combination of the ingredients in Table 1 provides the capability of tailoring the burn temperature, pressure ramp up and burn duration for different applications.

A 200 mg photoignition torch can release numerous burning particles at the exit tube of the torch that is 35 cm away from the ignition capsule. The smallest torch that was able to produce consistent ignition contained about 10 mg of fuel mixture and was able to introduce hot/reacting gases and burning particles 10-15 cm away from the ignition capsule. Burn duration of an ignition capsule is adjustable between 50-1000 ms at atmospheric pressure depending on the type and the amount of its ingredients. A noticeable reduction in burn duration has been observed at elevated pressures beyond 10 atm.

Downloaded by Doug Talley on September 19, 2016 | http://arc.aiaa.org | DOI: 10.2514/6.2016-0184

VI. Conclusions

A miniature photoignition torch using an encapsulated CNT-based fuel mixture was created. The photoignition torch has been tested up to about 135 atm (2000 psi) of pressure and its suitability for spray ignition demonstrated up to ~50 atm (~735 psi). Application of the photoignition torch for initiation of combustion in a cryogenic O_2-H_2 shear coaxial flame at high pressure was demonstrated at an oxygen temperature of about ~130 K and a pressure of ~32 atm (~470 psi). The photoignition torch as described is suitable for high pressure ignition applications. It also offers the following advantages:

-Light weight and compact: A typical self-contained ignition system has a mass of less than 25 g without the battery and it occupies less than 30 cm^3 of space. The ignition capsule is about 200 mg and it contains 50-70 mg of fuel.

-Safety: The photoignition torch is battery operated and optically coupled so that there is no electrical contact between the ignition source and the ignition charge or fuel. This makes a photoignition system relatively insensitive to electromagnetic interference and electrostatic discharge.

-Reliability: The photoignition torch is based on the mature technology of a compact battery operated Xe-flash lamp and ignition of solid propellants. Over the course of 4 years of testing, the Xe-flash has shown no reliability problem.

-Scalability: While the photoignition torch has been demonstrated here only at small scales, the photoignition system can be easily scaled up to much larger sizes with a relatively small penalty in the ignition delay.

Acknowledgements:

Funding support for this work was made possible by a grant from the Nanoscience and Technology program of the Air Force Office of Scientific Research (SFOSR). We would like to thank Dr. Scott Gilje and Dr. Bruce Chehroudi for the helpful discussions.

References

1. Ajayan PM, et al. “Nanotubes in a Flash: Ignition and Reconstruction”, *Science* 296, pp 705, (2002).
2. Braidy N, Botton GA, and Adronov A, Nanoletters 2 (11), pp. 1277-1280, (2002).
3. Smits J, and Wincheski B, “Response of Fe powder, purified and as-produced HiPCo SWNT to flash exposure”, Materials Science and Engineering A, 358, pp. 384-389, (2003).
4. Chehroudi B., Danczyk S, Morgan C, and Badakhshan A, “Ignition Characteristics of Single-Walled Carbon Nanotubes (SWNTs) Utilizing a Camera Flash for Distributed Ignition of Liquid Sprays”, Tech. Rep. DTIC, Online Information for Defense Community, ADA511240, Oct 2008.
5. Badakhshan A, Danczyk S, Wirth D, and Pilon L, “Ignition of Liquid Fuel Spray and Simulated Solid Rocket Fuel by Photoignition of Carbon Nanotube Utilizing a Camera Flash”, Conf. paper, DTIC, Online Information for Defense Community, ADA571240, Dec 2011.
6. Badakhshan A, and Danczyk, “Photo-ignition of Carbon Nanotube for Ignition of Liquid Fuel Spray and Solid Fuel” Conf. paper, DTIC, Online Information for Defense Community, ADA573322, Mar 2012.
7. Manaa R, Mitchell A, and Garza R, “Flash ignition and initiation of explosives−nanotubes mixture”, Journal of the American Chemical Society 127 (40), pp. 13786-13787, (2005).
8. Tseng S, et al., **“**Ignition of carbon nanotubes using a photoflash”, Carbon, 45, pp. 958-964 (2007).
9. Abboud, J., Jiang, N., Zhang, Z., Roy S., Gord, J.R., *Comb and Flame* **2013,** 160 (9), 1842–1847.
10. Ohkura, Y, Weisse J. M., Cai L, and Zheng X., *Nano Lett.*, **2013**, *13* (11), 5528–5533.
11. Berkowitz AM, and Oehlschlaeger MA, "The PhotoInduced Ignition of Quiescent Ethylene/Air Mixtures Containing Suspended Carbon Nanotubes," *Proceeding of the Combustion Institute*, 33, pp. 3359-3366 (2011).
12. Loomis MP, Lee JG, Yetter RA, “Characterization of photoignition of single walled carbon nanotubes”, Fall Technical Meeting of the Eastern States Section of the Combustion Institute, University of Maryland, October 18-21, (2009).
13. Gilje S, et al., “Photothermal Deoxygenation of Graphene Oxide for Patterning and Distributed Ignition Applications”, Adv Mat, 22, pp. 419–423, (2010).
14. See for example http://www.nano-c.com/nanoprod.html, more detailed images of SWNT and impurities are found at: Safarova et al., *Modern Res. Educ. Topics in Microscopy* **2007**, A. Méndez-Vilas and J. Díaz (Eds.).

Downloaded by Doug Talley on September 19, 2016 | http://arc.aiaa.org | DOI: 10.2514/6.2016-0184

Receptivity of a Cryogenic Coaxial Liquid Jet to Acoustic Disturbances

J. L. Wegener
Department of Mechanical Engineering
University of California at Los Angeles
Los Angeles, CA 90095 USA

D. J. Forliti*
Sierra Lobo, Inc.
Edwards AFB, CA 93524 USA

I.A. Leyva
AFRL/RQRE
Edwards AFB, CA 93524 USA

and
D.G. Talley
AFRL/RQRC
Edwards AFB, CA 93524 USA

Abstract

The receptivity of cryogenic coaxial gas-liquid jet flows to transverse acoustic disturbances has been explored experimentally. Liquid nitrogen in the inner jet and cooled helium in the outer annular jet were used to simulate an oxygen/hydrogen liquid rocket engine injector. The flow is submerged in a chamber that experiences a transverse acoustic resonance. The shear coaxial jet is exposed to a variety of acoustic conditions including different frequencies, amplitudes, and locations within the resonant mode shape. High-speed back-lit images were captured to record the behavior of the natural (unforced) and forced coaxial jets. Proper orthogonal decomposition and spectral analysis were used to extract natural and forced modes. Convective modes are extracted, and a new Strouhal number is used to characterize the strongest natural convective mode that is analogous to the preferred mode in free jets. The threshold of receptivity was found for a number of different injector flows and acoustic forcing conditions. The results indicate that the dimensionless frequency plays an important role, and there exists a finite forcing amplitude at which the threshold of receptivity occurs. The receptivity threshold provides useful insight on the suitability of a given injector design for specific rocket combustion chamber conditions.

*Corresponding author: david.forliti.ctr@us.af.mil

Approved for public release; distribution unlimited
PA case number 14132

Introduction

Combustion instability remains one of the key challenges in the development of robust and high-performance propulsion and energy systems. In liquid rocket engines (LREs), combustion instability can lead to degraded performance, severe wear, and catastrophic damage to the propulsion system. Unfortunately, combustion instability phenomena are not sufficiently understood to allow solution at the design stage. Thus full-scale testing and potentially multiple design cycle iterations may be required to satisfy the stability requirements. The development of high-fidelity design tools offers much promise in this regard, although data under a variety of relevant conditions are still needed to validate emerging computational tools.

The Air Force Research Laboratory (AFRL) at Edwards AFB has investigated the mixing properties of cryogenic single and coaxial jets under both sub- and supercritical thermodynamic pressure operating conditions.[1-3] These flows have also been exposed to a range of transverse acoustic forcing conditions.[4-6] A new experimental facility for reacting coaxial jet flows has been developed and is described in detail by Wegener et al.[7] The present paper describes nonreacting data that was collected with this new facility. Although a large quantity of data has been collected in the past for nonreacting conditions, the current effort considers a new framework for characterizing the forcing response of coaxial jets. Past studies have generally placed emphasis on investigating different injector conditions, including injector geometry, momentum flux ratio, and chamber pressure. The current study focuses on a single injector geometry in a two-phase (i.e. subcritical) regime, and focuses on the role of forcing frequency and amplitude.

Background

Single and coaxial jets at high Reynolds number are known to be spectrally broadband. Near the nozzle exit, shear layer instabilities and turbulent initial conditions will in general develop high-frequency oscillations. As the shear layers grow with increasing downstream distance, the spectra shifts to lower frequency.[8] Further downstream, the shear layers have grown to a point where a merger occurs, and typically the most intense fluctuations are encountered in this region. In single free jets, the fluctuations at the shear layer merging location, also referred to as the end of the potential core, are of global relevance and these fluctuations are referred to as the jet preferred mode.[8-11] Crow and Champagne conducted a classic study on forced free jets, and observed that the flow response was highly sensitive to the forcing frequency relative to the preferred mode frequency. More recently, Birbaud et al.[12] conducted a flow control study of a single free jet and considered the dependency of the forcing frequency relative to two characteristic frequencies; the initial high frequency associated with the initial shear layer and the low frequency preferred mode associated with the fluctuations at the end of the potential core. Having one (or more) characteristic frequency provides a useful reference in which to examine the effects of forcing, as different relative frequencies will influence the jet/shear layer structure through different mechanisms.

The coaxial jet contains more spatial and spectral complexity than the single jet, due to the presence of additional length and velocity scales. Figure 1(a)

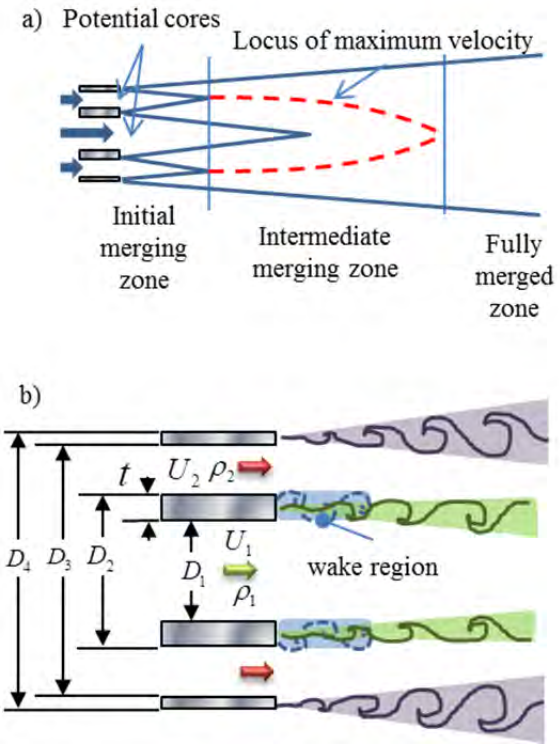

Figure 1. The a) global and b) near-field features of the coaxial jet.

shows the spatial development of the coaxial jet as described by Ko and Kwan.[13] There are a number of fluctuation sources including multiple shear layers and potential core zones. A schematic of the near-field region is shown in Fig. 1(b). The injector geometry is characterized by a set of diameters that can be non-dimensionalized to form two parameters, the area ratio *AR* and dimensionless post thickness t/D_1. Several near-field instabilities may be present, including an inner and outer shear layer, and a potential wake instability associated with the flow downstream of the inner post. The inner shear layer and wake modes overlap and thus these instabilities compete with one another. The acoustic disturbances are likely to couple with the

flow field in the near-field region where the flow is most unstable and sensitive to perturbations.

The coaxial jet flow is dependent on a large number of dimensionless groups. As mentioned above, the geometry can be characterized by the outer-to-inner area ratio *AR*, and the normalized post thickness t/D_1. There are two Reynolds numbers, one for the inner and outer flow. The momentum flux ratio *J*, defined outer to inner, is generally considered the primary independent parameter of the coaxial jet. Each of the two flows have characteristic velocities and densities, allowing the ability to define the velocity and density ratio across each shear layer. The shear flow is also very sensitive to the injector exit conditions, including profiles of mean and fluctuating velocity, and spectral characteristics of turbulence or other background disturbances. If the two streams differ in phase, then the Weber number is also a parameter of importance.

The behavior of the acoustically-excited coaxial jet will depend on all of the parameters mentioned above, in addition to the characteristic scales of the forcing conditions. The forcing can be characterized by the forcing frequency and amplitude; the amplitude may be measured by the magnitude of the pressure and/or velocity fluctuations. The interaction mechanisms differ when the coaxial jet is placed in a fluctuating pressure environment versus a fluctuating velocity environment. Thus the response of a given coaxial jet flow to acoustic perturbations will depend on the relative frequency, relative amplitude, and location within the acoustic resonance mode shape.

The purpose of the current study was to explore the receptivity of cryogenic two-phase coaxial jets to acoustic disturbances in the form of a transverse resonance; a flow is considered to be receptive to perturbations if detectable changes occur in the flow field. This study considered new parameters, the normalized frequency and amplitude. The conditions at which forcing dominates the natural coaxial jet behavior was documented.

Experimental Facility

The experiments were conducted in the Combustion Stability Lab at the Air Force Research Laboratory (AFRL) at Edwards Air Force base. A new facility, capable of high-pressure reacting flows, was used in the current study. Figure 2 shows both a schematic and three-dimensional rendering of the test chamber. Two acoustic sources, piezo sirens from Piezo Systems, Inc., are located symmetrically offset from the injector region. Waveguides shown in Fig. 2(a) are used to excite transverse resonances within the chamber. The acoustic frequency and amplitude are controlled via a signal generator/amplifier combination that drives the sirens. The sirens operate either in phase or with 180° shift to generate the pressure antinode (PAN) and pressure node (PN), respectively; the pressure node case is associated with an acoustic velocity antinode, but will be referred to as pressure node.

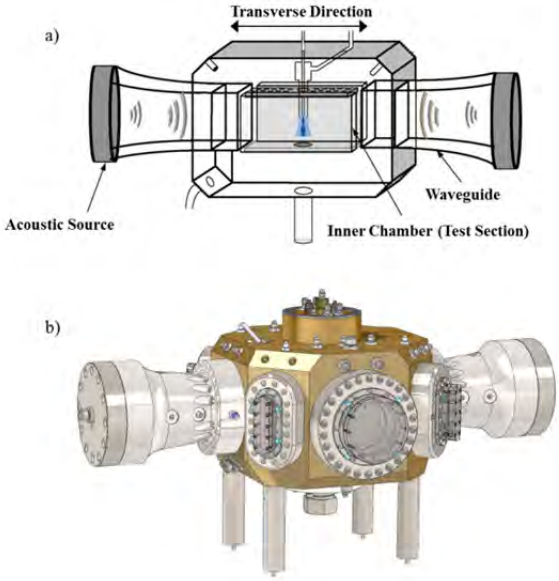

Figure 2. a) Conceptual and b) schematic of the Combustion Stability Lab experimental facility.

The chamber is divided into inner and outer chambers that are not sealed relative to one another. A high flow of gaseous nitrogen in the outer chamber is used to cool the combustion products under combustion conditions, and the combined flow is choked through an exit orifice. The gaseous nitrogen flow is used to set the chamber pressure. The facility is equipped with heat exchangers to allow cooling of the inner and outer injector flows. Further details on the experimental facility can be found in Wegener et al.[7]

A single coaxial jet injector was used for the experiments. The dimensions of the injector are summarized in Table 1. The outer-to-inner area ratio *AR* is

Parameter	Value (mm)
D_1	1.40
D_2	2.16
D_3	2.82
D_4	1.68

Table 1. Geometry of the injector.

1.68 and the dimensionless post thickness t/D_1 is 0.27; both parameters are within the lower range of previous studies at AFRL.[5, 6] The injector flow passages are sufficiently long to ensure fully-developed turbulent flow at the exit of the injector. Similar to previous work, the inner jet is liquid nitrogen. The outer jet in

the current study is cooled helium. The use of helium allows for a closer match to the density ratio as would occur for oxygen/hydrogen operation in a cryogenic rocket engine. The chamber pressure was 2.8 MPa (400 psi) for all experiments. Further details on the experimental conditions are given in Table 2.

Parameter	Values
T of inner jet (N_2)	~ 120 K
T of outer jet (He)	~ 275 K
J	2, 6
Re_1	~ 1.5×10^4
Re_2	~ 1.0×10^4
We	>100

Table 2. Injector operating parameters.

As shown in the table, two momentum flux ratios were considered. Due to the unique combination of fluids and conditions, surface tension values are not available to the authors' knowledge. Based on the visualizations shown later and the results of Farago and Chigier[14], the current experiments appear to be in the fiber-type regime and the Weber number is expected to be approximately 100 or higher.

The primary diagnostic of the coaxial jet involves high-speed backlit imaging. A Phantom v7.10 camera was used to capture images at 10 kHz. The acoustic resonance is characterized through several high-speed Kulite pressure sensors flush mounted in the test section area including the waveguides. A pressure sensor located in the center of the test section and coincident with the axis of the coaxial jet is used to measure the peak pressure fluctuation for the PAN cases. For the PN operation, the peak pressure fluctuation is estimated from measurements at off-node locations using an assumed mode shape, and the maximum acoustic velocity magnitude is estimated from the linear acoustics equation,

$$u' = \frac{p'}{\rho_c c} \tag{1}$$

where u' is the magnitude of the velocity fluctuation in the velocity antinode region, p' is the magnitude of the pressure fluctuation in the pressure antinode region, ρ_c is the density of the ambient gas in the chamber, which is nominal room temperature nitrogen, and c is the speed of sound. The injector flow species and temperatures will definitely alter the properties of the acoustic resonance, thus Eq. 1 is an approximation. The acoustic sirens were used to drive a transverse acoustic resonance ranging from the 3rd to 7th mode. See Wegener et al. for more details on the acoustic characteristics.[7]

Results

The first phase of the research was focused on understanding the properties of the unforced coaxial jets.

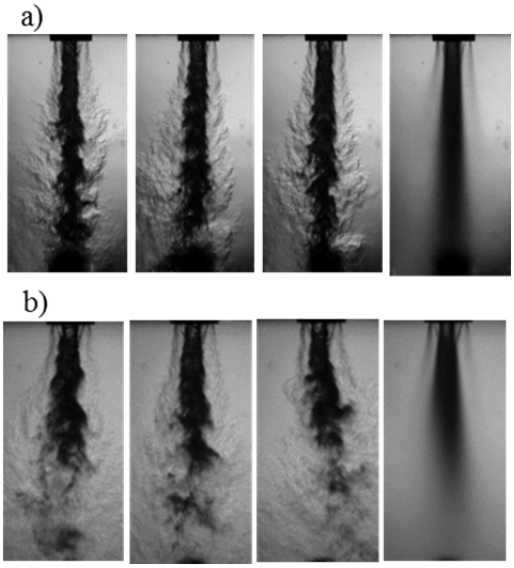

Figure 3. Instantaneous and mean backlit images of the coaxial jet for momentum flux ratio J of a) two and b) six.

Figure 3 shows instantaneous and mean images of the cryogenic coaxial jets at the two momentum flux ratios J of two and six. Although there are frequencies present in both the inner and outer shear layer, the strong contrast between the liquid inner flow and gaseous outer flow dominates the images. One can see some structure within the inner shear layer, although the turbulent inflow conditions result in a highly disturbed interface between the liquid and gas. As expected, the higher momentum flux ratio case has a shorter dark core length.[3] The triangular feature near the injector exit, more readily seen in the $J = 6$ case, is the recirculation zone downstream of the inner tube post. Some asymmetries are also apparent and are caused by manufacturing tolerances and the small scale of the injector components. Separate analyses of each side of the injector indicate similar spectra content (see Wegener[15] for details). It is thus expected that the general trends of the current results are representative of the symmetric case, although this will be validated in future studies.

As mentioned earlier, there is a need to identify the preferred mode of the coaxial jet. A frequency scaling variable, the Strouhal number, may be developed for use in a preferred mode scaling law. There are a number of choices available in defining the length and velocity scale for the Strouhal number. The length scale is a relatively straightforward choice of jet diameter as used for the single jet. In the case of a coaxial jet with

finite (or large) post thickness t/D_1, previous studies show, at least for moderate to high J, that the shear layer will more or less be centered near the middle of the post.[6] Thus the average of D_1 and D_2 are used as the length scale. Further data would need to be considered for different geometries to find the length scale that provides the best collapse across different injector designs.

The velocity scale is more subjective. For the free jet, the convention is to use the mean jet exit velocity. Guidance for an alternative choice is provided through studies of shear layers. Huerre and Monkewitz conducted a linear stability study of variable velocity ratio shear layers.[16] They found that the most unstable frequencies nominally collapse on a single value when the frequency is normalized by the mean velocity of the two streams. For variable density shear layers, the frequency of the most unstable mode will more likely scale with the convection velocity. Thus the convection velocity is proposed as an appropriate velocity scale.

The convection velocity of the coherent structures in a shear layer may be estimated in a variety of ways. Linear stability analysis may be used, for instance. Dimotakis developed a model for the spreading rate of planar shear layers, and included in the model development is an estimate of the convection velocity based on freestream conditions [17]. The model uses the assumption that in the reference frame of the shear layer structure, the dynamic pressure of the two freestreams is equal. This leads to a form of the convection velocity of

$$U_{c,\,Dimotakis} = \frac{\rho_1^{1/2} U_1^2 + \rho_2^{1/2} U_2^{1/2}}{\rho_1^{1/2} + \rho_2^{1/2}}, \qquad (2)$$

where ρ and U are the density and velocity of the freestreams. It should be mentioned that this expression was defined for single-phase shear layers.

In order to evaluate the validity of the Dimotakis model, the convection velocity is directly measured from the time-resolved images. Figure 4(a) shows the mean image for the $J = 6$ case. A line along the middle of the inner shear layer is defined through user input, and the intensities of these pixels are plotted as a function of time as shown in Fig. 4(b). As inner fluid structures convect along this trajectory, they trace diagonal lines in the s/D_1 versus time domain. This technique has been used in the past to visualize organized motion in jets.[18] The slope of the diagonal line represents the mean convection velocity; s is the distance along the shear layer ray. Ten samples are extracted and the mean convection velocity determined. The change in slope near s/D_1 of unity is coincident with the end of the triangular recirculation zone associated with the post wall thickness. As expected, the convection velocity increases downstream of the recirculation zone due to the presence of the high-speed coflow of the outer jet fluid; the outer-to-inner velocity ratio for this case is 25. This convection velocity analysis was conducted

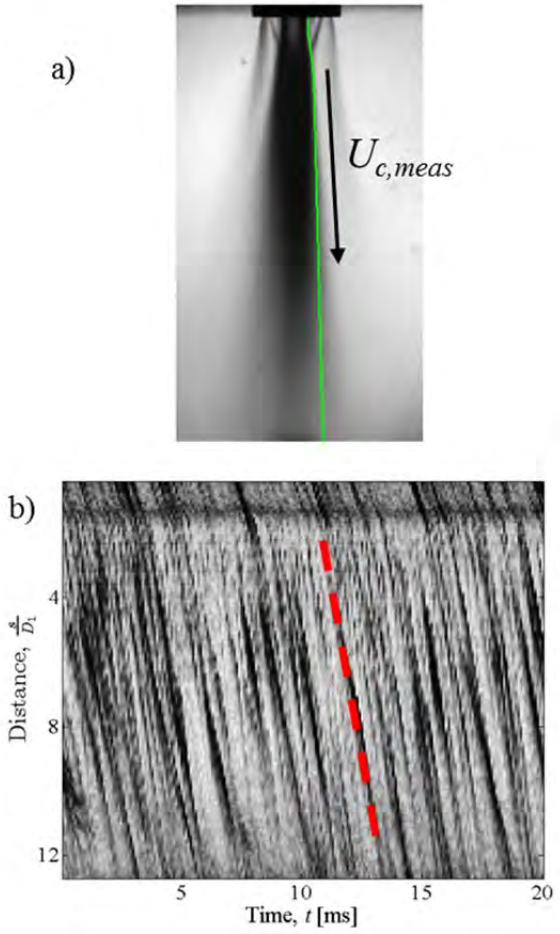

Figure 4. The (a) piecewise linear domain used to construct the (b) axial versus time maps for evaluating the convection velocity.

for several sets of data for the two momentum flux ratios and for two flow rates.

Figure 5 shows predicted versus measured convection velocities for the two momentum flux ratios. Data was collected for nominal and a higher flow rate for both momentum flux ratios. The conditions for the two momentum flux ratios were selected to keep the convection velocity predicted using Eq. 2 fixed, hence the overlap of points for both momentum flux ratios. The agreement is quite good, indicating that the Dimotakis model may be employed for the current flow conditions. A deviation is observed at higher flow rates (high convection velocities) and is likely due to heat transfer within the injector. Measurement of temperature upstream of the injector is used to evaluate density,

thus errors in temperature will result in errors in density. The velocity is estimated using the calculated density and the measured flow rate, thus creating further error due to temperature uncertainty. The subsequent measurements were all done at the lower flow rate associated with a convection velocity near 6 m/s.

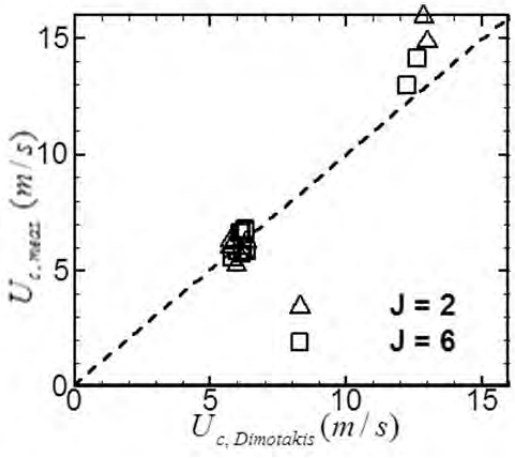

Figure 5. Measured versus predicted convection velocity.

In order to calculate the Strouhal number, the natural frequency of the jet must be extracted from the data. As would be expected for a spreading shear flow, the spectra depend on axial position. The global frequency of the jet is evaluated using the proper orthogonal decomposition (POD) of the image data. This approach places more emphasis on the larger-scale organized motions which make higher contributions to the total variance of the data. The POD is calculated for an image that spans an axial distance of approximately $12D_1$. The POD is calculated using singular value decomposition (SVD), the details of which can be found in Wegener.[15] The POD is applied to sets of 2000 images.

The application of POD to 2000 images yield the same number of variance-contributing modes, thus the POD spectrum is inherently broadband, especially for highly-turbulent flows of the type in the present study. Thus a criteria must be defined for extracting important dynamics from the POD results. Arienti and Soteriou provide a criteria for identifying convective modes from POD data.[19] First the POD spectrum, meaning the eigenvalues as a function of mode number, is constructed and pairs of modes with similar eigenvalues are sought. Once a candidate mode pair is identified, the cross-power spectral density (CPSD) and phase difference is calculated between the temporal coefficients of the mode pair. Once this has been done, the mode pair can be determined to be representing a convecting mode if:

1. the peak in the CPSD is coincident with a region of ± 90° phase shift;
2. the spatial distribution of the POD eigenfunctions are similar with features that are shifted nominally half a wavelength in the convection direction.

If a mode pair satisfied these conditions, a convective dynamic mode has been identified and the frequency of the particular convective mode is associated with the peak in the CPSD. In this study, the preferred mode is associated with the convective mode having the most energetic POD mode pair (i.e. has the highest eigenvalues). The singular values from the SVD process are used to evaluate the variance, as the singular values are equal to the square root of the eigenvalues. It is likely that multiple convective modes are present in the unforced cases of the present study. Other convective modes with lower singular values are not considered as representing preferred modes.

Figure 6(a) shows an example of a POD spectrum (in terms of singular values) as a function of mode number. The most energetic mode pair with similar

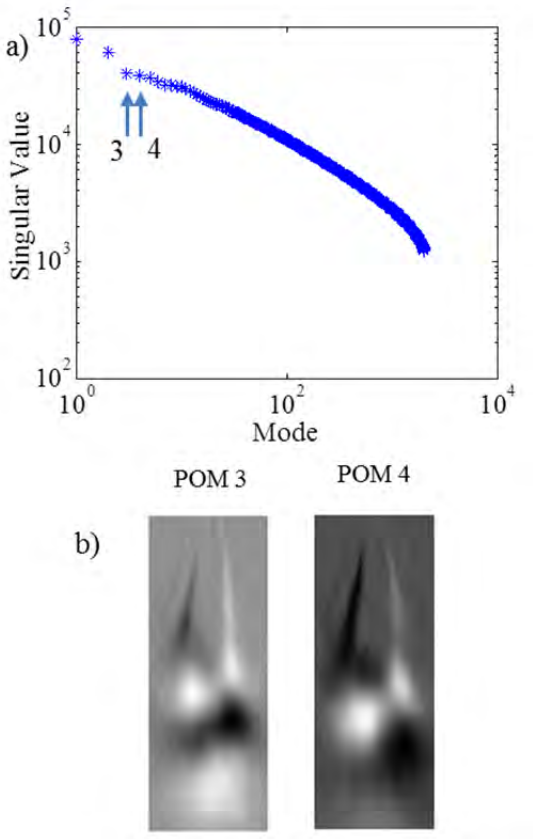

Figure 6. Proper orthogonal decomposition a) spectrum and b) eigenfunctions of mode pair candidate proper orthogonal modes (POM) 3 and 4 for $J = 2$.

singular values is associated with modes three and four. Figure 6(b) shows the proper orthogonal modes (POMs), or eigenfunctions, associated with the mode pair. This figure shows that the spatial distribution is similar, while mode four appears to have features that are slightly shifted downstream relative to mode three. Reconstructing these two modes with the temporal coefficients will represent a convective process. It may be seen that modes seven through nine also have similar singular values, thus a second convective mode may be present. This mode was not evaluated due to the lower variance contribution.

Figure 7 shows the CPSD and phase difference for

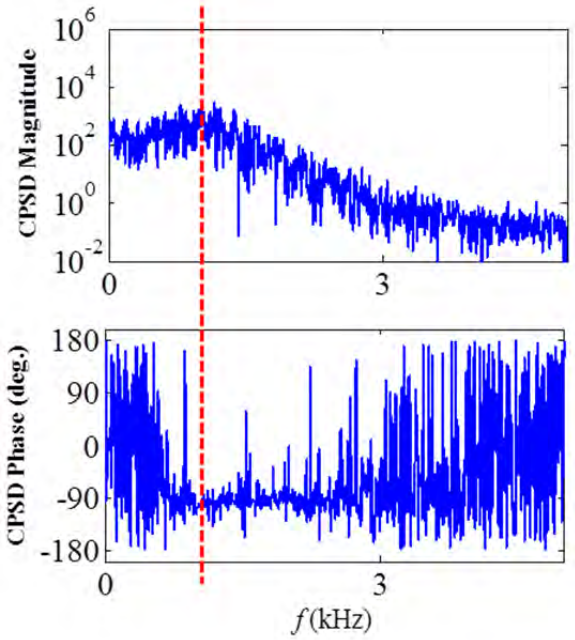

Figure 7. Cross-power spectral density amplitude and phase for modes three and four for $J = 2$.

modes three and four shown in Fig. 6. There is a broad peak on the low-frequency side of the spectrum. The peak is defined within the broad CPSD peak but also requires the phase to be near ± 90°. The frequency is near 1 kHz.

The process described above to identify the preferred mode frequency of the coaxial jet was applied to a number of data sets for both momentum flux ratios and nominal and high flow rates. The Strouhal number defined as

$$St = \frac{f_{nat}(D_1 + D_2)/2}{U_{c,meas.}}, \qquad (3)$$

where f_{nat} is the preferred mode frequency, was calculated for all data sets. The Strouhal number as a function of momentum flux ratio is shown in Fig. 8. The measured convection velocity provides a slightly reduced level of scatter compared results using Eq. 2. The trend represents a nominally constant value for *St* of 0.3. Spectra near the potential core end for

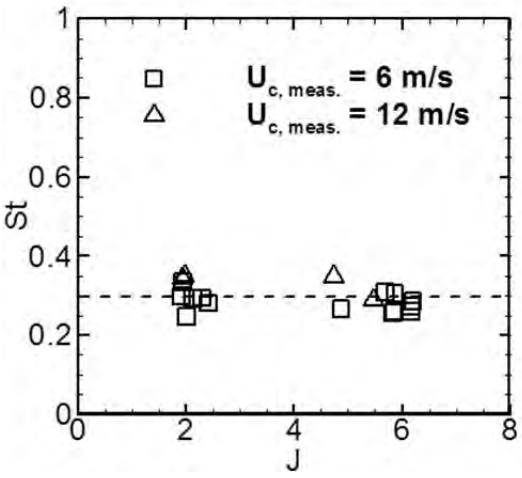

Figure 8. Strouhal number versus momentum flux ratio *J*.

the free jet data of Ko and Davies[20] and coaxial jet data of Ko and Kwan[13], when recast in the form of Eq. 3, fall within the scatter around 0.3. Both nominal and higher flow conditions (i.e. higher convection velocities) fall nominally near 0.3.

The scaling law in Fig. 8 was used to define baseline flow conditions for a predetermined frequency. Since the geometry is fixed, the preferred mode is determined by the convection velocity. For the present study, the unforced flow conditions were defined to result in a preferred mode frequency of approximately 1 kHz. One of the primary forcing parameters is the frequency ratio *F*, defined as

$$F = \frac{f_{forcing}}{f_{nat}}, \qquad (4)$$

where $f_{forcing}$ is the forcing frequency and f_{nat} is the natural preferred mode of the coaxial jet. The current study considered frequency ratios near 1.7, 2.0, and 2.6. The amplitude normalization will be discussed for both the PAN and PN forcing conditions.

Figure 9 shows instantaneous images of the $J = 2$ case for baseline and max PAN/PN forcing. The outer flow and inner shear layer are clearly perturbed under forcing conditions. In particular, the PN forcing results in highly antisymmetric structure in the outer annular flow with antisymmetric structures on the inner jet boundary. The instantaneous image for the PAN case

shows large-scale structures on the inner jet surface, while it is not apparent whether the structure is symmetric or antisymmetric.

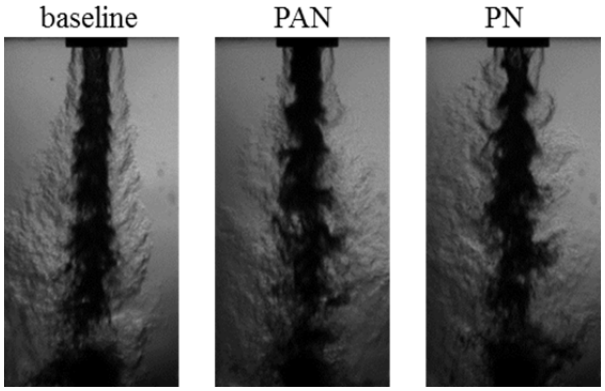

Figure 9. Instantaneous images for the baseline and maximum forced cases for PAN and PN, $J = 2$.

One of the primary goals of the research was to identify the conditions of forcing receptivity as a function of dimensionless forcing frequency and amplitude. The POD technique is used to detect the receptivity and relative importance of the forced and natural modes. Figure 10 shows the first eight POMs for the baseline,

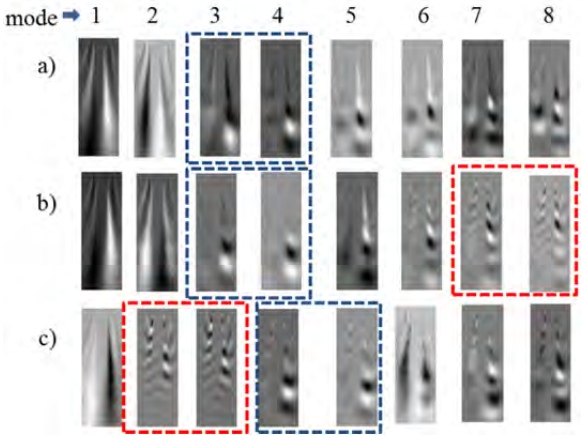

Figure 10. Proper orthogonal modes for $J = 2$, PAN, and $F = 2.7$ for a) unforced, b) $p' = 1.15$ psi, and c) $p' = 1.88$ psi.

and two forcing amplitudes of 1.15 and 1.88 psi for the PAN case for $J = 2.0$ and $F = 2.6$. The dashed blue box represents the natural preferred mode, which is present for all cases. The $p' = 1.15$ psi case shows the emergence of a new high frequency convective mode pair for modes 7 and 8. This force mode is highlighted by the red dashed box. When the amplitude was increased to 1.88 psi, the forced mode contributes more to the image variance as indicated by the order within the POD array. For the forced dominated case in Fig. 10(c), the natural mode persists but is somewhat contaminated with small scale instabilities from the forcing.

For PAN forcing, the injector is essentially exposed to an unsteady back pressure. Thus the coupling is likely to be related to unsteady flow rates caused by a fluctuating pressure drop across the injector. Due to the high density of the inner jet, the impact of the unsteady pressure drop is reduced because of the inertia of the mass within the injector passage. The outer jet is much more responsive to the unsteady back pressure due to the lower mass in the outer jet passage. Thus fluctuating back pressure drives a fluctuating flow rate in the outer jet. The accompanying velocity pulsations will disturb both the inner and outer shear layer. This description is consistent with the explanation given by Baillot et al.[21]

The above mechanism provides for some guidance for normalization of the forcing amplitudes for PAN conditions. The unsteadiness generated in the outer flow will depend on the ratio of the unsteady back pressure to the dynamic pressure of the flow. The magnitude of the induced velocity fluctuation will also depend on the frequency (see Wegener[15] for analysis). For a fixed pressure drop across the injector passage, high-frequency fluctuations have shorter periods in which the fluid can accelerate. Thus it is expected that higher-frequency fluctuations are less likely to couple for PAN forcing, although the hydrodynamic stability considerations also play a factor in how velocity fluctuations of a particular frequency lead to wrinkling of the inner jet column.

Figure 11 shows the inception and dominance boundaries of the PAN forcing conditions for both momentum flux ratios at the three frequency ratios. The empty symbols represent the conditions in which a new forced POM mode pair was observed, but was lower in variance contribution than the natural mode. The filled symbol represents the condition in which the forced mode is dominant over the natural mode. The grey shaded area has not been sampled, although the transition between natural and forced dominance occurs in this region.

It is interesting to note that the inception of receptivity occurs at a nominal dimensionless amplitude of unity. This is consistent with the arguments of Baillot et al.[21] It is unclear why the $J = 2$ case appears to be less receptive to high-frequency fluctuations.

Figure 12 shows the receptivity behavior for the PN forcing conditions. Here the amplitude of the forcing is given in units of m/s. The perturbation velocity is estimated using Eq. 1. The general trend of increasing receptivity with amplitude is once again demonstrated. The mechanism for the response is less evident. The velocity perturbation magnitude is much lower than the outer jet velocity (~ 40 m/s). It is thus unlikely that the

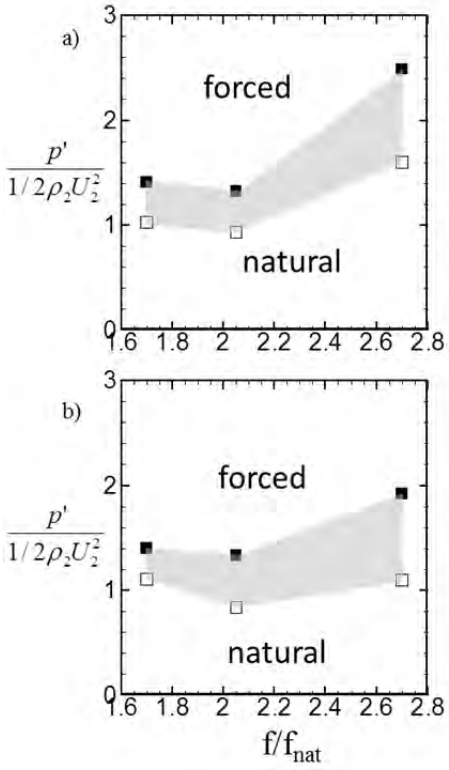

Figure 11. Receptivity regimes for PAN forcing as a function of frequency ratio for a) $J = 2$ and b) $J = 6$.

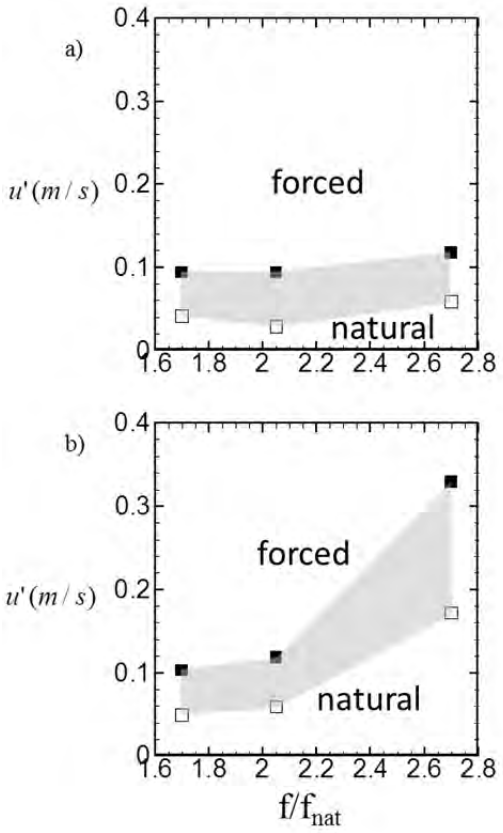

Figure 12. Receptivity regimes for PN forcing as a function of frequency ratio for a) $J = 2$ and b) $J = 6$.

perturbations are directly disturbing the inner jet surface as these low-level disturbances would be insignificant relative to the inflow turbulence.

Further insight may be gained through analysis of the images in the first few diameters of the coaxial jet. In this region, the flow is very unstable due to the high velocity gradients, thus this is the most likely region where the acoustic perturbations can disturb the flow. Figure 13 shows the near field of the coaxial jet for the baseline unforced case as well as highly-forced PAN and PN cases. These images are also representative for the results at $J = 6$. The near field of the dominant convective mode is also shown on the right of the figure. The PAN mode, as supported by the POM, is symmetric (although the thickness and intensity is not symmetric). This would be supportive of the pulsed outer flow mechanism, although this is not nearly as clear in the instantaneous images. The PN case shows very dramatic effects in the near field. In particular, the outer jet appears to be experiencing intense transverse motions that are out of phase. The antisymmetric nature is also supported by the POM. Recall from Fig. 12

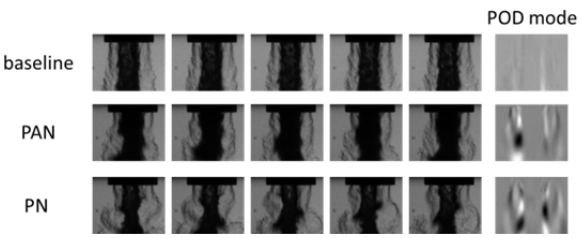

Figure 13. Instantaneous images of the near field of the coaxial jet under forced and unforced conditions for $J = 2$.

that the estimated acoustic velocity is much smaller than the outer jet velocity. The flapping nature of the jet, and the involvement of the jet as a whole, suggests the possibility of excitation of a helical jet column mode. The transverse velocity disturbance is not of sufficient magnitude to cause a drag force leading to such dramatic motion. Future analysis will be required to gain further insight into the coupling mechanism for PN conditions.

Conclusions

An experimental study has investigated the receptivity of two-phase coaxial jet flows to transverse acoustic perturbations. It was found, over the range of conditions considered, that the shear flow structures along the inner jet convect at a speed well predicted by the model developed by Dimotakis.[17] A new Strouhal number definition is proposed that appears to provide reasonable collapse of the frequency of convective modes as extracted from POD analysis of the potential core region of the coaxial jet. Coaxial jets at two different momentum flux ratios were subsequently forced through exposure to variable frequency and amplitude acoustic environments, including PN and PAN conditions.

The PAN forcing appears to generate a pulsation in the outer jet flow rate that subsequently excites instabilities in the flow. The receptivity of the flow field to PAN forcing occurs near the condition where $p' \sim 1/2 \rho_2 U_2^2$, independent of momentum flux ratio. This mechanism will also be sensitive to the inertance properties of the injector design, and therefore sensitive to frequency.

The PN forcing results in a strong coupling even at very low acoustic velocities. The relative magnitudes of the acoustic velocity to the characteristic velocities of the coaxial jet make it unlikely that the acoustics directly generate disturbances in the shear flow. A potential mechanism involves the coherent transverse velocity fluctuations in the acoustic field exciting a helical mode in the outer jet. Further research will be required to further explore the coupling mechanism for PN forcing.

Nomenclature

AR	outer-to-inner area ratio
c	speed of sound
D	diameter
f	frequency
F	normalized frequency
J	outer-to-inner momentum flux ratio
m	mass
p	pressure
p'	pressure fluctuation amplitude
St	Strouhal number
t	inner jet post thickness
U	mean velocity
u'	velocity fluctuation amplitude
ρ	density

Subscripts

c	convection
1	inner jet fluid
2	outer jet fluid

References

1. Chehroudi, B., D. Talley, and E. Coy, *Visual characteristics and initial growth rates of round cryogenic jets at subcritical and supercritical pressures.* Physics of Fluids, 2002. **14**(2): p. 850-861.
2. Oschwald, M., et al., *Injection of fluids into supercritical environments.* Combustion Science and Technology, 2006. **178**(1-3): p. 49-100.
3. Leyva, I., B. Chehroudi, and D. Talley, *Dark Core Analysis of Coaxial Injectors at Sub-, Near-, and Supercritical Conditions in a Transverse Acoustic Field*, in *43rd AIAA/ASME/SAE/ASEE Joint Propulsion Conference & Exhibit.* 2007, American Institute of Aeronautics and Astronautics: Cincinnati, OH.
4. Davis, D.W., *On the behavior of a shear-coaxial jet, spanning sub-to supercritical pressures, with and without an externally imposed transverse acoustic field*, in *Mechanical Engineering*. 2006, The Pennsylvania State University: University Park, PA.
5. Rodriguez, J.I., *Acoustic excitation of liquid fuel droplets and coaxial jets*, in *Aerospace Engineering*. 2009, University of California, Los Angeles: Los Angeles, CA.
6. Teshome, S., *Droplet Combustion and Non-Reactive Shear-Coaxial Jets with Transverse Acoustic Excitation*, in *Mechanical Engineering*. 2012, University of California, Los Angeles: Los Angeles, CA.
7. Wegener, J., et al., *Development of a facility for combustion stability experiments at supercritical pressure*, in *52nd AIAA Aerospace Sciences Meeting*. 2014: National Harbor, MD.
8. Yule, A., *Large-scale structure in the mixing layer of a round jet.* Journal of Fluid Mechanics, 1978. **89**(3): p. 413-432.
9. Crow, S. and F. Champagne, *Orderly structure in jet turbulence.* Journal of Fluid Mechanics, 1971. **48**: p. 547-591.
10. Gutmark, E. and C.M. Ho, *Preferred modes and the spreading rates of jets.* Physics of Fluids (1958-1988), 1983. **26**(10): p. 2932-2938.
11. Drubka, R.E. and H.M. Nagib, *Instabilities in near field of turbulent jets and their dependence on initial conditions and Reynolds number*, in *AFOSR Scientific Report AFOSR-TR-0962*. 1981.

12. Birbaud, A.-L., et al., *Dynamics of free jets submitted to upstream acoustic modulations.* Physics of Fluids, 2007. **19**: p. 013602.
13. Ko, N. and A. Kwan, *The initial region of subsonic coaxial jets.* Journal of Fluid Mechanics, 1976. **73**: p. 305-332.
14. Chigier, N. and Z. Farago, *Morphological classification of disintegration of round liquid jets in a coaxial air stream.* Atomization and Sprays, 1992. **2**(2).
15. Wegener, J., *Multi-phase Combustion and Transport Processes Under the Influence of Acoustic Excitation*, in *Mechanical Engineering*. 2014, University of California, Los Angeles: Los Angeles, CA.
16. Monkewitz, P.A. and P. Huerre, *Influence of the velocity ratio on the spatial instability of mixing layers.* Physics of Fluids, 1982. **25**: p. 1137.
17. Dimotakis, P.E., *Two-dimensional shear-layer entrainment.* AIAA Journal, 1986. **24**(11): p. 1791-1796.
18. Dahm, W.J. and P.E. Dimotakis, *Mixing at large Schmidt number in the self-similar far field of turbulent jets.* Journal of Fluid Mechanics, 1990. **217**: p. 299-330.
19. Arienti, M. and M.C. Soteriou, *Time-resolved proper orthogonal decomposition of liquid jet dynamics.* Physics of Fluids (1994-present), 2009. **21**(11): p. 112104.
20. Ko, N. and P. Davies, *The near field within the potential cone of subsonic cold jets.* Journal of Fluid Mechanics, 1971. **50**(01): p. 49-78.
21. Baillot, F., et al., *Behaviour of an air-assisted jet submitted to a transverse high-frequency acoustic field.* Journal of Fluid Mechanics, 2009. **640**: p. 305-342.

Propulsion and Energy Forum
July 28-30, 2014, Cleveland, OH
50th AIAA/ASME/SAE/ASEE Joint Propulsion Conference

Receptivity of a Cryogenic Coaxial Gas-Liquid Jet to Acoustic Disturbances

Jeffrey L. Wegener[1]
University of California at Los Angeles, CA 90095

David J. Forliti[2]
Sierra Lobo, Inc. supporting AFRL/RQRC, Edwards AFB, CA 93524

Ivett A. Leyva[3]
AFRL/RQRE, Edwards AFB, CA 93524

and
Douglas G. Talley[4]
AFRL/RQRC, Edwards AFB, CA 93524

Downloaded by Doug Talley on July 29, 2014 | http://arc.aiaa.org | DOI: 10.2514/6.2014-3487

An experimental study has been conducted at the Air Force Research Laboratory at Edwards Air Force Base to explore the receptivity of cryogenic coaxial jet flows to transverse acoustic disturbances. The shear coaxial jet flow employed liquid nitrogen in the inner jet and cooled helium in the outer annular jet to represent the nominal fluid dynamical conditions of an oxygen/hydrogen liquid rocket engine injector. The injector flow is submerged in a chamber that experiences a monotonic transverse acoustic resonance characteristic of a rocket chamber in the presence of combustion instability. The coaxial jet is exposed to a variety of acoustic conditions including different frequencies, amplitudes, and locations within the resonant mode shape. High-speed back-lit images were captured to record the behavior of the natural (unforced) and forced coaxial jets. Proper orthogonal decomposition and spectral analysis were used to extract natural and forced modes. Convective modes are extracted, and a new Strouhal number is used to characterize the dominant natural convective mode that is analogous to the preferred mode in free jets. The threshold of receptivity was found for a number of different injector flows and acoustic forcing conditions. The results indicate that the dimensionless frequency plays an important role, and there exists a finite forcing amplitude at which the threshold of receptivity occurs. The receptivity threshold and post receptivity response provides useful insight on the suitability of a given injector design for specific rocket combustion chamber conditions.

[1] Graduate Student, Department of Mechanical and Aerospace Engineering, UCLA, Los Angeles, CA 90095 student member. Currently at Physical Sciences, Inc., Andover, MA 01810.
[2] Research Scientist, Sierra Lobo, Inc., 10 E. Saturn Blvd, Building 8451, Edwards AFB, CA 93524, senior member.
[3]Technical Advisor, AFRL/RQRE, 4 Draco Drive, Building 8351, Edwards AFB, CA 93524, Associate Fellow.
[4] Lead, Combustion Dynamics Group, AFRL/RQRC., 10 E. Saturn Blvd, Building 8451, Edwards AFB, CA 93524, Associate Fellow.

DISTRIBUTION STATEMENT A. Approved for public release; distribution unlimited. PA case number 14311.

This material is declared a work of the U.S. Government and is not subject to copyright protection in the United States.

Nomenclature

AR	=	outer-to-inner area ratio
c	=	speed of sound
D	=	diameter
f	=	frequency
F	=	normalized frequency
J	=	outer-to-inner momentum flux ratio
m	=	mass
p	=	pressure
p'	=	pressure fluctuation amplitude
St	=	Strouhal number
t	=	inner jet post thickness
U	=	mean velocity
u'	=	velocity fluctuation amplitude
ρ	=	density

Subscripts

c	=	convection
meas	=	measured
Dimotakis	=	the Dimotakis[1] convection velocity model
1	=	inner jet fluid
2	=	outer jet fluid

Downloaded by Doug Talley on July 29, 2014 | http://arc.aiaa.org | DOI: 10.2514/6.2014-3487

I. Introduction

COMBUSTION instability phenomena has been and remains one of the key challenges in the development of robust and high performance propulsion and energy systems. In the liquid rocket engine (LRE) application, combustion instability can lead to degraded performance, severe wear, and rapid catastrophic damage to the propulsion system. Unfortunately, combustion instability phenomena are not sufficiently understood to allow solution at the engine design stage. Thus full-scale testing and potential multiple design iterations may be required to satisfy the stability requirement. The development of high-fidelity design tools offers much promise in this respect, although data under a variety of relevant conditions are still needed to validate emerging computational tools.

The Air Force Research Laboratory (AFRL) at Edwards AFB has extensively investigated the mixing properties of cryogenic single and coaxial jets under both sub- and supercritical thermodynamic pressure operating conditions.[2, 3] These flows have also been exposed to a range of transverse acoustic conditions.[4-6] A new experimental facility for reacting coaxial jet flows has been developed as described by Wegener et al.[7] The present paper describes preliminary nonreacting data that was collected using this new facility. Although a large quantity of data has been collected in the past for nonreacting conditions, the current data considers a new framework in which to explore the forcing response of coaxial jets. Past studies have generally placed emphasis on investigating different injector conditions, including injector geometry, momentum flux ratio, and chamber pressure. The current study focuses on a single injector geometry in a two-phase (i.e. subcritical) regime, and focuses on the role of forcing frequency and amplitude.

II. Background

The free jet is known to contain a broad range of frequencies, ranging from the shear layer instabilities near the nozzle exit, to the large-amplitude fluctuations near the end of the potential core, and continuing into the weak far field fluctuations.[8-11] Although the global spectral features of the free jet are extremely broad band, the peak frequencies near the end of the potential core are generally selected as being a representative characteristic of the jet.[8] The approach adopted by Birbaud et al. is also highly appropriate in selecting two frequencies that represent the near field ranging from the nozzle trailing edge to the end of the potential core.[12] Having one (or more) characteristic frequency provides a useful reference in which to examine the effects of forcing, as different relative frequencies will influence the jet/shear layer structure through different mechanisms.

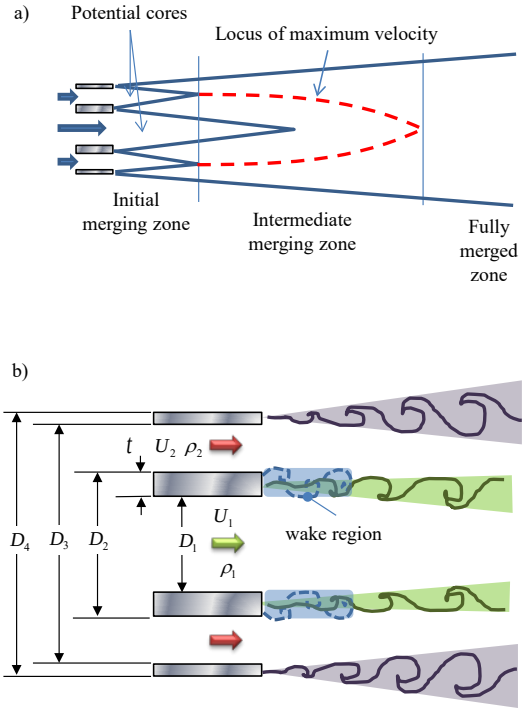

Figure 1. The a) spatial regions of the coaxial jet flow field and b) the potential unsteady structure in the initial merging zone.

The coaxial jet is a highly complex flow due to the presence of multiple shear layers and potentially a splittler plate wake instability in the near field as shown in Fig. 1. Figure 1(a) shows the spatial development of the coaxial jet as described by Ko and Kwan.[13] Figure 1(b) shows the potential shear flow regions in the initial merging zone including an inner and outer shear layer, and a possible wake instability associated with the flow downstream of the inner nozzle trailing edge. This wake instability has been found to occur within certain velocity ratio ranges for coaxial jets and shear layers.[14-20] The role of density ratio on the competition between the shear layer and wake modes has not been thoroughly explored, in particular in the small density ratio (outer to inner stream) regime associated with the conditions of interest at AFRL.

Ko and coworkers have studied the flow and spectral properties of coaxial jets spanning a broad range of conditions.[13, 21-23] They employed two different Strouhal number definitions for the inner and outer shear layer. The inner shear layer Strouhal number definition compensates for the presence of the outer flow, which has a tendancy to increase the frequency through a higher instability convection velocity. For the application of interest at AFRL, the frequencies in the inner shear layer region are of primary interest, as this will be the location of the flame under reacting flow conditions. Thus hydrodynamic instabilities in this region are most likely to generate coherent heat release fluctuations that are known to participate in thermoacoustic instability mechanisms. In this context, a representative preferred mode of the coaxial jet would be be based on the frequency of the inner shear layer structures (which may be dominated by the wake instability) near the end of the inner jet potential core where fluctuations are most intense. Although this preferred mode is likely to generate heat release fluctuations, one must remain cognizant that higher frequency fluctuations closer to the injector trailing edge might play a very key role in driving combustion instability. This aspect will be a subject of future reacting flow research at AFRL.

The coaxial jet flow is dependent on a large number of dimensionless groups. The geometry can be characterized by the outer-to-inner area ratio *AR*, and the normalized post thickness t/D_1. There are two Reynolds numbers, one each for the inner and outer flow. The momentum flux ratio *J*, defined outer to inner flow, is generally considered the primary independent flow parameter of the coaxial jet. Each of the two flows have characteristic velocities and densities, allowing the ability to define the velocity and density ratio across each shear layer. The shear flow is also very sensitive to the injector exit conditions, including profiles of mean and fluctuating velocity, and spectral characteristics of turbulence or other background disturbances. If the two streams differ in phase, then the Weber number is also a parameter of importance.

The behavior of the acoustically-excited coaxial jet will depend on all of the parameters mentioned above, in addition to the characteristic scales of the forcing conditions. The forcing can be characterized by the acoustic frequency and amplitude; the amplitude may be measured by the magnitude of the pressure and/or velocity fluctuations. The interaction mechanisms differ when the coaxial jet is placed in a fluctuating pressure environment versus a fluctuating velocity environment.[24] Thus the response of a given coaxial jet flow to acoustic perturbations will depend on the relative frequency, relative amplitude, and location within the acoustic resonance mode shape.

The purpose of the current study was to explore the receptivity of cryogenic two-phase coaxial jets to disturbances of the form of an acoustic transverse resonance; a flow is considered to be receptive to perturbations if detectable changes occur in the flow field. This study considered new parameters, the normalized frequency and amplitude. The conditions at which forcing dominates the natural coaxial jet behavior were documented.

III. Experimental facility and methods

Downloaded by Doug Talley on July 29, 2014 | http://arc.aiaa.org | DOI: 10.2514/6.2014-3487

The experiments were conducted in the Combustion Stability Lab at the Air Force Research Laboratory (AFRL) at Edwards Air Force base. A new facility, capable of high-pressure reacting flows, was used for the current study. Figure 2 shows both a schematic and three-dimensional rendering of the test chamber. Two acoustic sources, piezo sirens from Piezo Systems, Inc., are located symmetrically offset from the injector region. Waveguides shown in Fig. 2(a) are used to connect the acoustic sources to the injector flow region. The acoustic frequency and amplitude are controlled via a signal generator/amplifier combination that drives the sirens. The sirens operate either in phase or with 180° shift to generate the pressure antinode (PAN) and pressure node (PN) at the middle of the chamber; the pressure node case is associated with an acoustic velocity antinode, but will be referred to as pressure node.

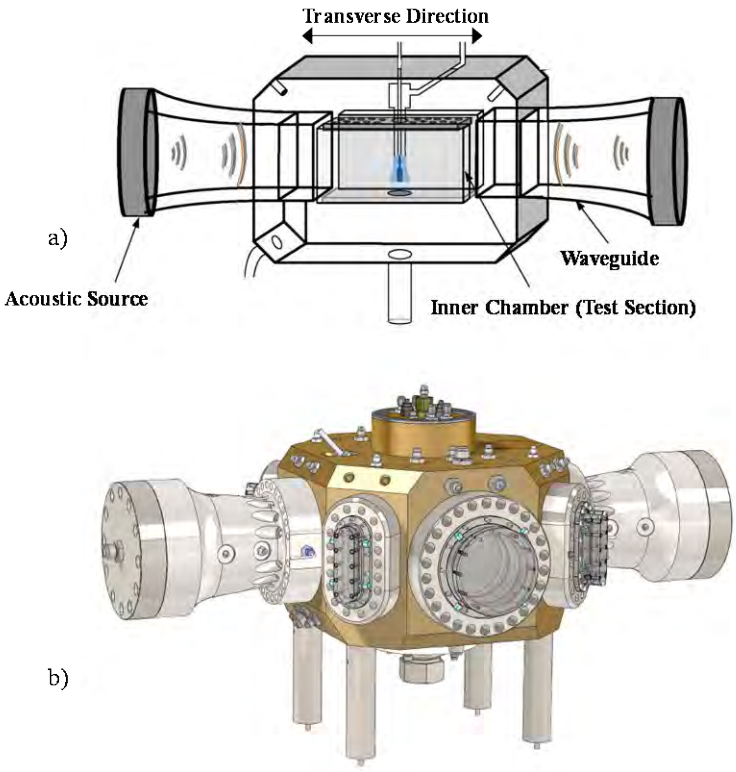

Figure 2. a) Conceptual and b) schematic of the Combustion Stability Lab experimental facility.

The chamber is divided into inner and outer chambers that are not completely sealed relative to one another. A high flow of gaseous nitrogen in the outer chamber is used to cool the combustion products under reacting flow conditions, and the combined flow is choked through an exit orifice. The gaseous nitrogen flow is used to control the chamber pressure. The facility is equipped with heat exchangers to allow cooling of the inner and outer injector flows. Further details on the experimental facility can be found in Wegener et al.[7]

A single coaxial jet injector was used for the experiments. The dimensions of the injector are summarized in Table 1. The outer-to-inner area ratio *AR* is 1.68 and the dimensionless post thickness t/D_1 is 0.27; both parameters are within the lower range of previous studies at AFRL.[4, 6] The injector flow passages are sufficiently long to ensure fully-developed turbulent flow at the exit of the injector. Similar to previous work at AFRL, the inner jet is liquid nitrogen. The outer jet in the current study is cooled helium. The use of helium allows for a closer match to the density ratio as would occur for oxygen/hydrogen operation in a cryogenic rocket engine. The chamber pressure was 2.8 MPa (400 psi) for all experiments. Further details on the experimental conditions are given in Table 2.

Table 1. Geometry of the injector.

Parameter	Value (mm)
D_1	1.40
D_2	2.16
D_3	2.82
D_4	3.56

Table 2. Injector operating parameters.

Parameter	Values
T of inner jet (N_2)	~ 120 K
T of outer jet (He)	~ 275 K
J	2, 6
Re_1	~$1.5x10^4$
Re_2	~ $1.0x10^4$
We	> 100

As shown in the table, two momentum flux ratios were considered. Due to the unique combination of fluids and conditions, surface tension values are not available to the authors' knowledge. Based on the visualizations shown later and the results of Farago and Chigier[25], the current experiments appear to be in the fiber-type regime and the Weber number is expected to be approximately 100 or higher.

The primary diagnostic of the current experimental study involves high-speed backlit imaging. A Phantom v7.10 camera was used to capture images at 10 kHz. The acoustic resonance is characterized through several high-

Downloaded by Doug Talley on July 29, 2014 | http://arc.aiaa.org | DOI: 10.2514/6.2014-3487

speed Kulite pressure sensors flush mounted in the test section area including the waveguides. A pressure sensor located in the center of the test section and coincident with the axis of the coaxial jet is used to measure the peak pressure fluctuation for the PAN cases. For the PN operation, the peak pressure fluctuation is estimated from measurements at off-node locations using an assumed mode shape, and the maximum acoustic velocity magnitude is estimated from the linear acoustics equation,

$$u' = \frac{p'}{\rho_c c} \tag{1}$$

where u' is the magnitude of the velocity fluctuation in the velocity antinode region, p' is the magnitude of the pressure fluctuation in the pressure antinode region, ρ_c is the density of the ambient gas in the chamber, which is nominally room temperature nitrogen, and c is the speed of sound. The injector flow species and temperatures will definitely alter the properties of the acoustic resonance, thus Eq. (1) is an approximation. The acoustic sirens were used to drive a transverse acoustic resonance ranging from the 3rd to 7th mode. See Wegener et al. for more details on the acoustic characteristics.[7]

IV. Results

The first phase of the research was focused on understanding the properties of the unforced coaxial jet. Figure 3 shows instantaneous and mean images of the cryogenic coaxial jet at the two momentum flux ratios J of two and six.

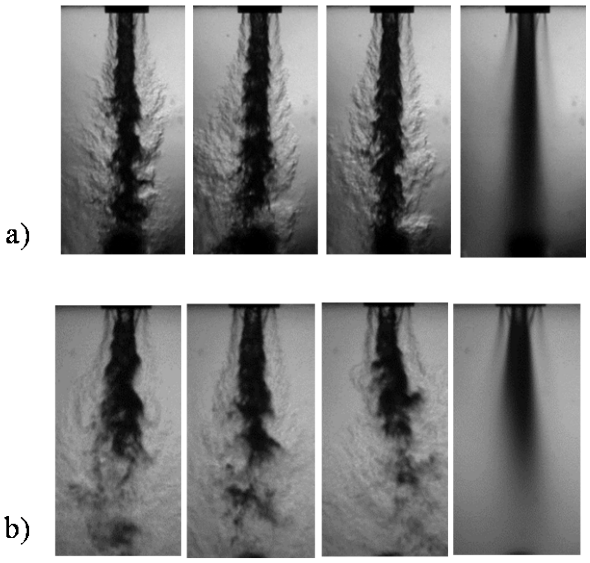

Figure 3. Instantaneous and mean (far right) backlit images of the coaxial jet for momentum flux ratio *J* of a) two and b) six.

Although there are dynamics present in both the inner and outer shear layers, the strong contrast between the liquid inner flow and gaseous outer flow dominates the images. One can see some structure within the inner shear layer, although the turbulent inflow conditions result in a highly disturbed interface between the liquid and gas. As expected, the higher momentum flux ratio case has a shorter dark core length.[26] The triangular feature near the injector exit, more readily seen in the $J = 6$ case, is the recirculation zone downstream of the inner tube post. Some asymmetries are also apparent and are caused by manufacturing tolerances and the small scale of the injector components. Separate analyses of each side of the injector flow field indicate similar spectra content (see Wegener[27] for details). It is thus expected that the general trends of the current results are representative of the symmetric case, although this will be validated in future studies.

As mentioned earlier, there is a need to identify the preferred mode of the coaxial jet. A frequency scaling variable, the Strouhal number, may be developed for use in a preferred mode scaling law. There are a number of choices available in defining the length and velocity scale for the Strouhal number. The length scale is a relatively straightforward choice of jet diameter as used for the single jet. In the case of a coaxial jet with finite (or large) post thickness t/D_1, previous studies show, at least for moderate to high J, that the shear layer will more or less be centered near the middle of the post.[6] Thus the average of D_1 and D_2 are used as the length scale. Further data would need to be considered for different geometries to find the length scale that provides the best collapse across different injector designs.

The velocity scale is more subjective. For the free jet, the convention is to use the mean jet exit velocity. Guidance for an alternative choice is provided through studies of shear layers. Huerre and Monkewitz conducted a linear stability study of variable velocity ratio shear layers.[28] They found that the most unstable frequencies nominally collapse on a single value when the frequency is normalized by the mean velocity of the two streams. For variable density shear layers, the frequency of the most unstable mode will more likely scale with the convection velocity. Thus the convection velocity is proposed as an appropriate velocity scale.

Downloaded by Doug Talley on July 29, 2014 | http://arc.aiaa.org | DOI: 10.2514/6.2014-3487

The convection velocity of the coherent structures in a shear layer may be estimated in a variety of ways. Linear stability analysis may be used, for instance. Dimotakis developed a model for the spreading rate of planar shear layers, and included in the model development is an estimate of the convection velocity based on freestream conditions.[1] The model uses the assumption that in the reference frame of the shear layer structure, the dynamic pressures of the two freestreams are equal. This leads to a form of the convection velocity of

$$U_{c,\,Dimotakis} = \frac{\rho_1^{1/2} U_1^2 + \rho_2^{1/2} U_2^{1/2}}{\rho_1^{1/2} + \rho_2^{1/2}}, \tag{2}$$

where ρ and U are the density and velocity of the freestreams. It should be mentioned that this expression was derived for single-phase shear layers.

In order to evaluate the validity of the Dimotakis model, the convection velocity is directly measured from the time-resolved images. Figure 4(a) shows the mean image for the $J = 6$ case. A line along the middle of the inner shear layer is defined through user input, and the intensities of these pixels are plotted as a function of time as shown in Fig. 4(b). As inner fluid structures convect along this trajectory, they trace diagonal lines in the s/D_1 versus time domain. This technique has been used in the past to visualize organized motion in jets.[29] The slope of a particular diagonal line represents the convection velocity for that structure; s is the distance along the shear layer ray. Ten samples are extracted and the mean convection velocity determined. The change in slope near s/D_1 of unity is coincident with the end of the triangular recirculation zone associated with the blunt post wall. As expected, the convection velocity increases downstream of the recirculation zone due to the presence of the high-speed coflow of the outer jet fluid; the outer-to-inner velocity ratio for this case is 25. This convection velocity analysis was conducted for several sets of data including two momentum flux ratios and two flow rate combinations.

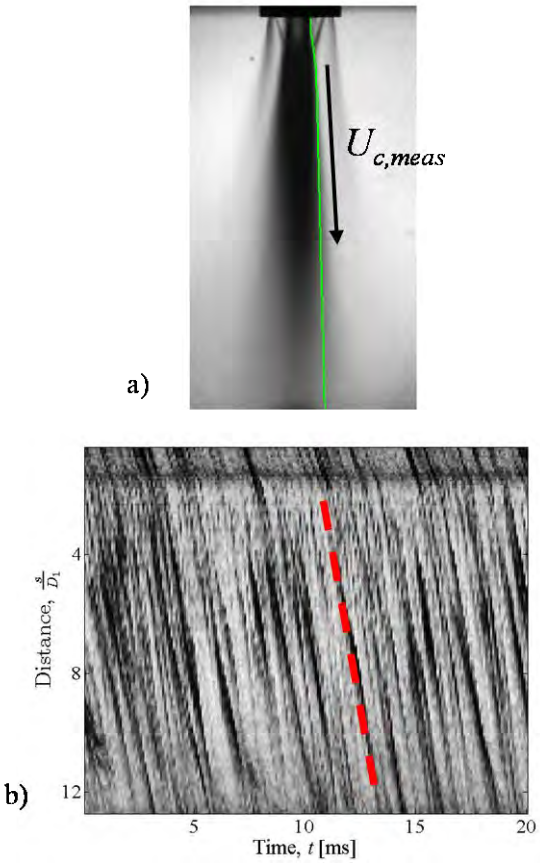

Figure 4. The (a) piecewise linear domain used to construct the (b) axial versus time maps for evaluating the convection velocity.

Figure 5 shows predicted versus measured convection velocities for the two momentum flux ratios. Data was collected for nominal and a higher flow rate for both momentum flux ratios. The conditions for the two momentum flux ratios were selected to keep the convection velocity predicted using Eq. (2) fixed, hence the overlap of points for both momentum flux ratios. The agreement is quite good, indicating that the Dimotakis model may be employed for the current flow conditions. A deviation is observed at higher flow rates (i.e. high convection velocities) and is likely due to heat transfer within the injector. Measurement of temperatures upstream of the injector is used to evaluate density for both flows, thus errors in temperature will result in errors in density. The velocity is estimated using the calculated density and the measured flow rate, thus creating further error due to temperature uncertainty. The subsequent measurements were all done at the lower flow rate associated with a convection velocity near 6 m/s.

In order to calculate the Strouhal number, the characteristic frequency of the jet must be extracted from the data. As would be expected for a spreading shear flow, the spectra depend on axial position. The global frequency of the jet is evaluated using proper orthogonal decomposition (POD) of the image data. This approach places more emphasis on the larger-scale organized motions which make higher contributions to the total variance of the data, thus will be biased towards dynamics in the downstream region. The POD is calculated for an image that spans an

Downloaded by Doug Talley on July 29, 2014 | http://arc.aiaa.org | DOI: 10.2514/6.2014-3487

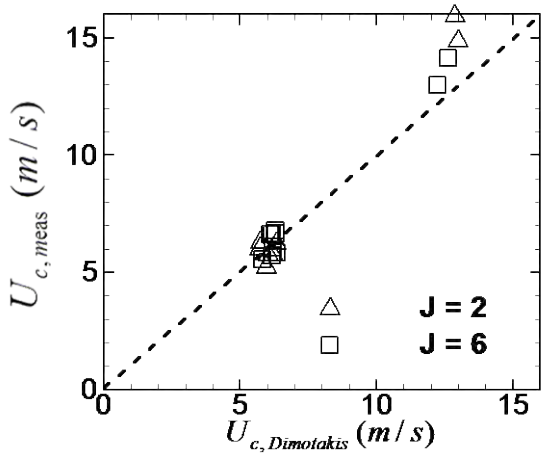

Figure 5. Measured versus predicted convection velocity.

axial distance of approximately $12D_1$. The POD is calculated using singular value decomposition (SVD), the details of which can be found in Wegener.[27] The POD is applied to sets of 2000 images.

The application of POD to 2000 images yield the same number of variance-contributing modes, thus the POD spectrum is inherently broadband, especially for highly-turbulent flows of the type in the present study. Thus a criteria must be defined for isolating important dynamics from the POD results. Arienti and Soteriou provide a criteria for identifying convective modes from POD data.[30] First, the POD spectrum, meaning the eigenvalues as a function of mode number, is constructed and pairs of modes with similar eigenvalues are sought. Once a candidate mode pair is identified, the cross-power spectral density (CPSD) amplitude and phase are calculated for the temporal coefficients of the mode pair. Once this has been done, the mode pair can be determined to be representing a convecting mode if:

1. the peak in the CPSD is coincident with a region of ± 90° phase shift;
2. the spatial distribution of the POD eigenfunctions are similar with features that are shifted nominally half a wavelength in the convection direction.

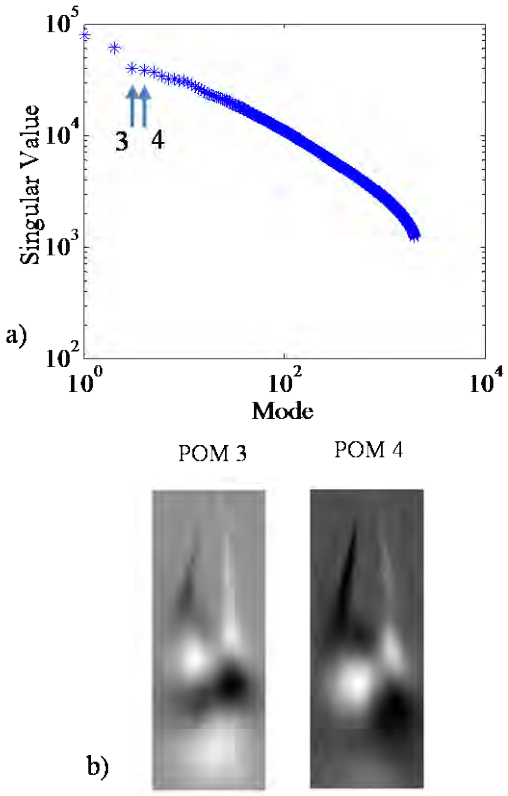

Figure 6. Proper orthogonal decomposition a) spectrum and b) eigenfunctions of mode pair candidate proper orthogonal modes (POM) three and four for $J = 2$.

If a mode pair satisfies these conditions, a convective dynamic mode has been identified and the frequency of the particular convective mode is associated with the peak in the CPSD. In this study, the preferred mode is associated with the convective mode having the most energetic POD mode pair (i.e. has the highest eigenvalues). The singular values from the SVD process are used to evaluate the variance, as the singular values are equal to the square root of the eigenvalues. It is likely that multiple convective modes are present in the unforced cases of the present study. Other convective modes with lower singular values are not considered as representing preferred modes.

Figure 6(a) shows an example of a POD spectrum (in terms of singular values) as a function of mode number. The most energetic mode pair with similar singular values is associated with modes three and four. Figure 6(b) shows the proper orthogonal modes (POMs), or eigenfunctions, associated with the mode pair. This figure shows that the spatial distribution is similar, while mode four appears to have features that are slightly shifted downstream relative to mode three. Reconstructing these two modes with the temporal coefficients will represent a convective process. It may be seen that modes seven through nine also have similar singular values, thus a second convective mode may be present. This mode was not evaluated due to the lower variance contribution.

Figure 7 shows the CPSD and phase difference for modes three and four shown in Fig. 6. There is a broad peak on the low-frequency side of the spectrum. The peak is defined within the broad CPSD peak but also requires the phase to be near ± 90°. The frequency is near 1 kHz.

Downloaded by Doug Talley on July 29, 2014 | http://arc.aiaa.org | DOI: 10.2514/6.2014-3487

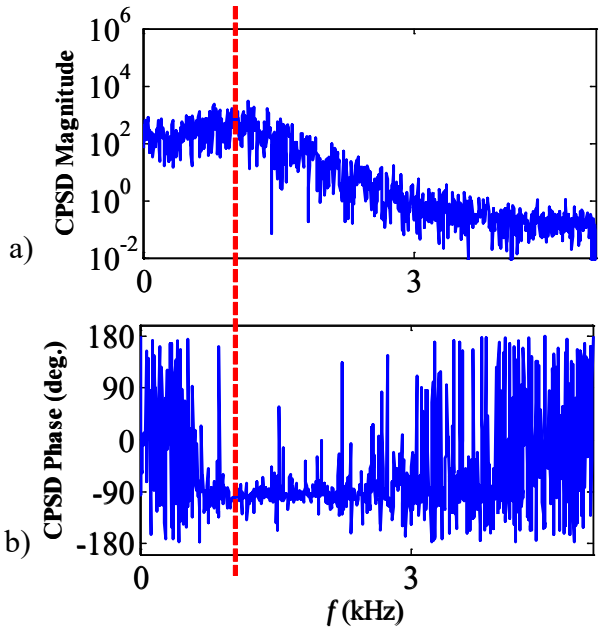

Figure 7. Cross-power spectral density a) amplitude and b) phase for modes three and four for $J = 2$.

The process described above to identify the preferred mode frequency of the coaxial jet was applied to a number of data sets for both momentum flux ratios and nominal and high flow rates. The Strouhal number defined as

$$St = \frac{f_{nat}(D_1 + D_2)/2}{U_{c,meas}}, \tag{3}$$

where f_{nat} is the preferred mode frequency, was calculated for all data sets. The Strouhal number as a function of momentum flux ratio is shown in Fig. 8. The measured convection velocity provides a slightly reduced level of scatter compared results using Eq. (2). The trend represents a nominally constant value for *St* of 0.3. Spectra near the potential core end for the free jet data of Ko and Davies[9] and coaxial jet data of Ko and Kwan[13], when recast in the form of Eq. (3), fall within the scatter around 0.3. Both nominal and higher flow conditions (i.e. higher convection velocities) fall nominally near 0.3.

The scaling law in Fig. 8 was used to define baseline flow conditions for a predetermined frequency. Since the geometry is fixed, the preferred mode is governed by the convection velocity. For the present study, the unforced flow conditions were defined to result in a preferred mode frequency of approximately 1 kHz.

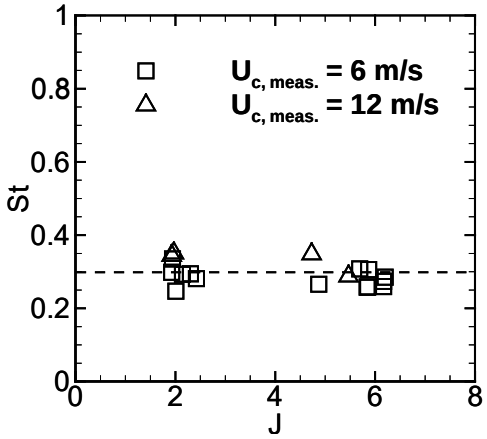

Figure 8. Strouhal number versus momentum flux ratio J.

One of the primary forcing parameters is the frequency ratio *F*, defined as

$$F = \frac{f_{forcing}}{f_{nat}}, \tag{4}$$

where $f_{forcing}$ is the forcing frequency and f_{nat} is the natural preferred mode. The current study considered frequency ratios near 1.7, 2.0, and 2.6. The amplitude normalization will be discussed for both the PAN and PN forcing conditions.

Figure 9 shows instantaneous images of the $J = 2$ case for baseline and max PAN/PN forcing. The outer flow and inner shear layer are clearly perturbed under forcing conditions. In particular, the PN forcing results in highly antisymmetric structure in the outer annular flow with antisymmetric structures on the inner jet boundary. The instantaneous image for the PAN case shows large-scale structures on the inner jet surface, while it is not apparent whether the structure is symmetric or antisymmetric.

One of the primary goals of the research was to identify the conditions of forcing receptivity as a function of dimensionless forcing frequency and amplitude. The POD technique is used to detect the receptivity and relative importance of the forced and natural modes. Figure 10 shows the first eight POMs for the baseline unforced case, and two forcing amplitudes of 1.15 and 1.88 psi for the PAN case for $J = 2.0$ and $F = 2.6$. The dashed blue box represents the natural preferred mode, which is present for all cases. The $p' = 1.15$ psi case shows the emergence of a new high frequency convective mode pair for modes 7 and 8. This force mode is highlighted by the red dashed box. When the amplitude was increased to 1.88 psi, the forced mode contributes more to the image variance as indicated by the order within the POD array. For the forced dominated case in Fig. 10(c), the natural mode persists but is somewhat contaminated with small-scale instabilities from the forcing.

For PAN forcing, the injector is essentially exposed to an unsteady back pressure. Thus the coupling is likely to be related to unsteady flow rates caused by a fluctuating pressure drop across the injector. Due to the high density

Downloaded by Doug Talley on July 29, 2014 | http://arc.aiaa.org | DOI: 10.2514/6.2014-3487

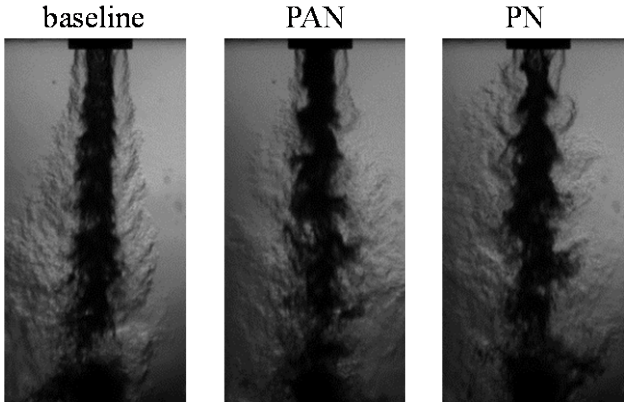

Figure 9. Instantaneous images for the baseline and maximum forced cases for PAN and PN, $J = 2$.

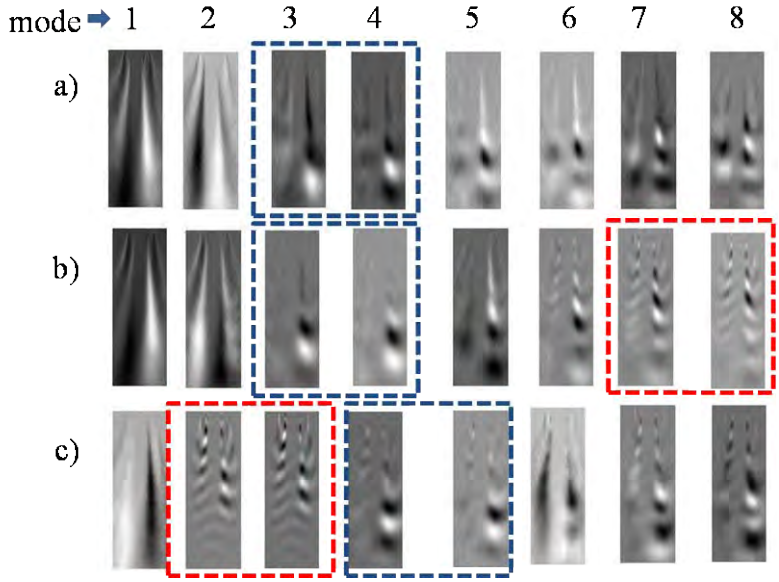

Figure 10. Proper orthogonal modes for $J = 2$, PAN, and $F = 2.7$ for a) unforced, b) $p' = 1.15$ psi, and c) $p' = 1.88$ psi.

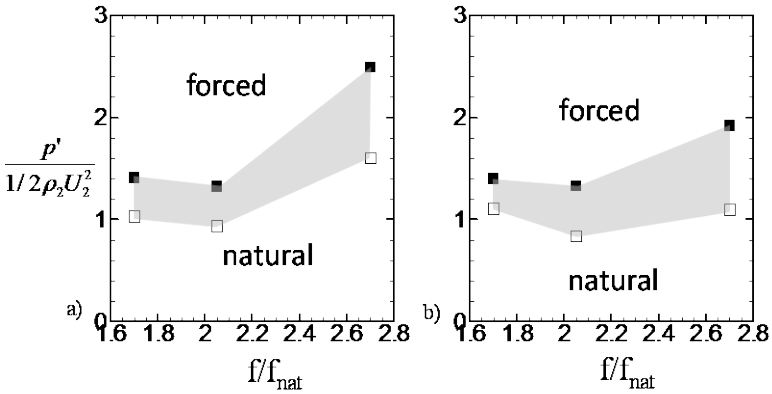

Figure 11. Receptivity regimes for PAN forcing as a function of frequency ratio for a) $J = 2$ and b) $J = 6$.

of the inner jet, the impact of the unsteady pressure drop is reduced because of the high inertia within the injector passage. The outer jet is much more responsive to the unsteady back pressure due to the lower mass in the outer jet passage. Thus fluctuating back pressure drives a fluctuating flow rate in the outer jet. The accompanying velocity pulsations will disturb both the inner and outer shear layer. This description is consistent with the explanation given by Baillot et al.[24]

The above mechanism provides for some guidance for normalization of the forcing amplitudes for PAN conditions. The unsteadiness generated in the outer flow will depend on the ratio of the unsteady back pressure to the dynamic pressure of the flow. The magnitude of the induced velocity fluctuation will also depend on the frequency (see Wegener[27] for analysis). For a fixed pressure drop across the injector passage, high-frequency fluctuations have a shorter time period in which the fluid can accelerate. Thus it is expected that higher-frequency fluctuations are less likely to couple for PAN forcing, although the hydrodynamic stability considerations also play a factor in how velocity fluctuations of a particular frequency lead to wrinkling of the inner jet column.

Figure 11 shows the inception and dominance boundaries of the PAN forcing conditions for both momentum flux ratios at the three frequency ratios. The empty symbols represent the conditions in which a new forced POM mode pair was observed, but was lower in variance contribution than the natural mode. The filled symbol represents the condition in which the forced mode is dominant over the natural mode. Other test points above and below these points are not included for clarity. Between five and seven amplitudes were tested for each frequency ratio. The grey shaded area has not been sampled, although the transition between natural and forced dominance occurs in this region.

It is interesting to note that the inception of receptivity occurs at a nominal dimensionless

Downloaded by Doug Talley on July 29, 2014 | http://arc.aiaa.org | DOI: 10.2514/6.2014-3487

amplitude of unity. This is consistent with the arguments of Baillot et al.[24] It is unclear why the $J = 2$ case appears to be less receptive to high-frequency fluctuations, both in terms of initial detection of receptivity and the amplitude required for the force mode to dominate the natural mode. The $J = 6$ case appears to be less sensitive to frequency ratio in the range explored.

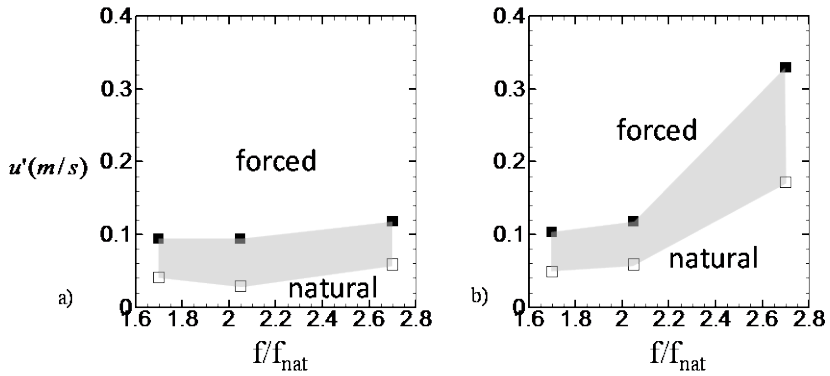

Figure 12. Receptivity regimes for PN forcing as a function of frequency ratio for a) $J = 2$ and b) $J = 6$.

Figure 12 shows the receptivity behavior for the PN forcing conditions. Here the amplitude of the forcing is given in units of m/s. The perturbation velocity is estimated using Eq. (1). The general trend of increasing receptivity with amplitude is once again demonstrated. The mechanism for the response is less evident. The velocity perturbation magnitude is much lower than the outer jet velocity (~ 40 m/s). It is thus unlikely that the perturbations are directly disturbing the inner jet surface as these low-level disturbances would be insignificant relative to the inflow turbulence. Interestingly, the higher momentum flux ratio case exhibits stronger frequency dependence including degraded receptivity at high frequency.

Further insight may be gained through analysis of the images in the first few diameters of the coaxial jet. In this region, the flow is very unstable due to the high velocity gradients, thus this is the most likely region where the acoustic perturbations can disturb the flow. Figure 13 shows the near field of the coaxial jet for the baseline

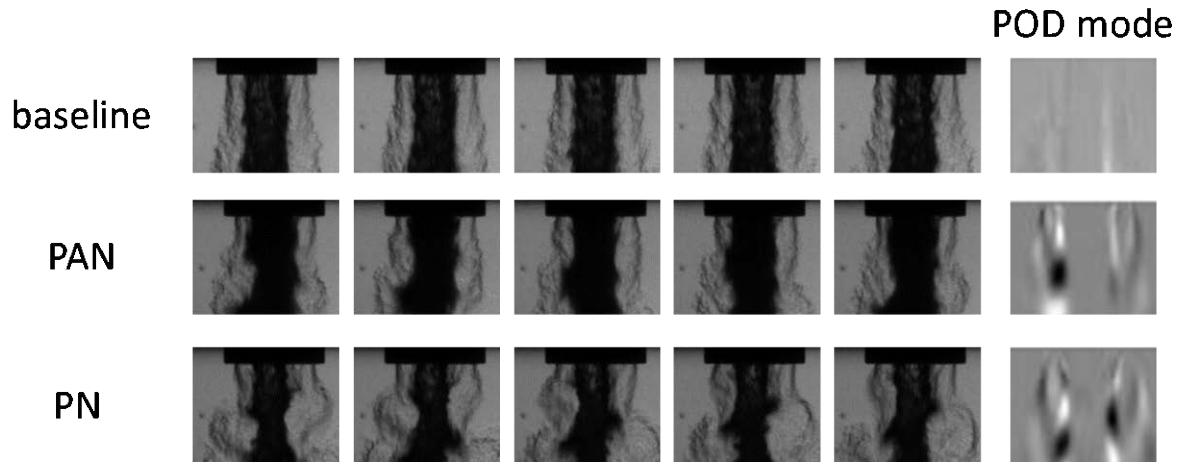

Figure 13. Instantaneous images of the near field of the coaxial jet under forced and unforced conditions for $J = 2$.

unforced case as well as highly-forced PAN and PN cases. These images are also representative for the results at $J = 6$. The near field of the dominant convective POM modes are also shown on the right of the figure. The PAN mode, as supported by the POM distribution, is symmetric (although the thickness and intensity is not symmetric). This would be supportive of the pulsed outer flow mechanism, although this is not nearly as clear in the instantaneous images. The PN case shows very dramatic effects in the near field. In particular, the outer jet appears to be experiencing intense transverse motions that are out of phase. The antisymmetric nature is also supported by the POM. Recall from Fig. 12 that the estimated acoustic velocity is much smaller than the outer jet velocity. The flapping nature of the jet, and the involvement of the jet as a whole, suggests the possibility of excitation of a helical jet column mode (or multiple modes). The transverse velocity disturbance is not of sufficient magnitude to cause a

Downloaded by Doug Talley on July 29, 2014 | http://arc.aiaa.org | DOI: 10.2514/6.2014-3487

drag force leading to such dramatic motion. Future analysis will be required to gain further insight into the coupling mechanism for PN conditions.

V. Conclusions

An experimental study has investigated the receptivity of two-phase coaxial jet flows to transverse acoustic perturbations. It was found, over the range of conditions considered, that the shear flow structures along the inner jet convect at a speed well predicted by the model developed by Dimotakis.[1] A new Strouhal number definition is proposed that appears to provide reasonable collapse of the frequency of convective modes as extracted from POD analysis of the potential core region of the coaxial jet. Coaxial jets at two different momentum flux ratios were subsequently forced through exposure to variable frequency and amplitude acoustic environments, including pressure node and pressure antinode conditions.

The pressure antinode forcing appears to generate a pulsation in the outer jet flow rate that subsequently excites instabilities in the flow. The receptivity of the flow field to pressure antinode forcing occurs near the condition where $p' \sim 1/2 \rho_2 U_2^2$, independent of momentum flux ratio, with the exception of highest frequency case for $J = 2$. This mechanism will also be sensitive to the inertance properties of the injector design, and therefore sensitive to frequency. The receptivity charactersitics are different for the two momentum flux ratios, even though the frequency of the preferred modes were the same. This suggests more subtle differences in the hydrodynamics between the two momentum flux ratios play a role in the receptivity characteristics.

The pressure node forcing results in a strong coupling even at very low acoustic velocities. The relative magnitudes of the acoustic velocity to the characteristic velocities of the coaxial jet make it unlikely that the acoustics directly generate disturbances in the shear flow. A potential mechanism involves the coherent transverse velocity fluctuations in the acoustic field exciting one or multiple helical modes in the outer jet. Further research will be required to further explore the coupling mechanism for pressure node forcing. Once again, the receptivity trends were different for the two momentum flux ratios, suggesting again the presence subtle hydrodynamic effects in the receptivity mechanism. Interestingly, the lower momentum flux ratio case is less receptive at high frequency for the pressure antinode forcing while the higher momentum flux ratio case is less receptive for the pressure node forcing.

Acknowledgments

Support was provided by the Air Force Office of Scientific Research, project officer Mitat Birkan, and by AFRL Laboratory Revitalization Funds. The authors thank Randy Harvey and Todd Newkirk for their assistance in conducting the experiments.

References

1. Dimotakis, P. E., "Two-dimensional shear-layer entrainment," *AIAA Journal,* Vol. 24, No. 11, 1986, pp. 1791-1796.

2. Chehroudi, B., Talley, D., and Coy, E., "Visual characteristics and initial growth rates of round cryogenic jets at subcritical and supercritical pressures," *Physics of Fluids,* Vol. 14, No. 2, 2002, pp. 850-861.

3. Oschwald, M., Smith, J., Branam, R., Hussong, J., Schik, A., Chehroudi, B., and Talley, D., "Injection of fluids into supercritical environments," *Combustion Science and Technology*, Vol. 178, No. 1-3, 2006, pp. 49-100.

4. Davis, D. W., "On the behavior of a shear-coaxial jet, spanning sub-to supercritical pressures, with and without an externally imposed transverse acoustic field," Ph.D., Mechanical Engineering, The Pennsylvania State University, 2006.

5. Rodriguez, J. I., "Acoustic excitation of liquid fuel droplets and coaxial jets," Ph.D., Aerospace Engineering, University of California, Los Angeles, 2009.

6. Teshome, S., "Droplet Combustion and Non-Reactive Shear-Coaxial Jets with Transverse Acoustic Excitation," Ph.D., Mechanical Engineering, University of California, Los Angeles, 2012.

Downloaded by Doug Talley on July 29, 2014 | http://arc.aiaa.org | DOI: 10.2514/6.2014-3487

7. Wegener, J., Leyva, I., Forliti, D., and Talley, D., "Development of a facility for combustion stability experiments at supercritical pressure," 52nd AIAA Aerospace Sciences Meeting, National Harbor, MD, 2014.

8. Crow, S., and Champagne, F., "Orderly structure in jet turbulence," *Journal of Fluid Mechanics,* Vol. 48, 1971, pp. 547-591.

9. Ko, N., and Davies, P., "The near field within the potential cone of subsonic cold jets," *Journal of Fluid Mechanics,* Vol. 50, No. 01, 1971, pp. 49-78.

10. Yule, A. J., *Two-dimensional self-preserving turbulent mixing layers at different free stream velocity ratios*, Aeronautical Research Council 1972.

11. Drubka, R. E., and Nagib, H. M., "Instabilities in near field of turbulent jets and their dependence on initial conditions and Reynolds number," *AFOSR Scientific Report AFOSR-TR-0962*. 1981.

12. Birbaud, A.-L., Durox, D., Ducruix, S., and Candel, S., "Dynamics of free jets submitted to upstream acoustic modulations," *Physics of Fluids,* Vol. 19, 2007, p. 013602.

13. Ko, N., and Kwan, A., "The initial region of subsonic coaxial jets," *Journal of Fluid Mechanics,* Vol. 73, 1976, pp. 305-332.

14. Boldman, D., Brinich, P., and Goldstein, M., "Vortex shedding from a blunt trailing edge with equal and unequal external mean velocities," *Journal of Fluid Mechanics,* Vol. 75, 1976, pp. 721-735.

15. Segalini, A., and Talamelli, A., "Experimental analysis of dominant instabilities in coaxial jets," *Physics of Fluids,* Vol. 23, No. 2, 2011, pp. 024103-1-024103-7.

16. Talamelli, A., and Gavarini, I., "Linear instability characteristics of incompressible coaxial jets," *Flow, Turbulence and Combustion,* Vol. 76, No. 3, 2006, pp. 221-240.

17. Talamelli, A., Segalini, A., Örlü, R., and Buresti, G., "A note on the effect of the separation wall in the initial mixing of coaxial jets," *Experiments in Fluids,* Vol. 54, No. 3, 2013, pp. 1-7.

18. Tian, V., McKeon, B., and Leyva, I. A., "Split stream flow past a blunt trailing edge with application to combustion instabilities," 46th AIAA/ASME/SAE/ASEE Joint Propulsion Conference and Exhibit, 2012.

19. Wallace, D., and Redekopp, L., "Linear instability characteristics of wake-shear layers," *Physics of Fluids A: Fluid Dynamics,* Vol. 4, No. 1, 1992, pp. 189-191.

20. Sarpotdar, S., and Raman, G., "Investigation of the Inner Nozzle Wake on Kelvin Helmholtz Instabilities in a Coannular Jet," *International Journal of Flow Control,* Vol. 3, No. 2, 2011, pp. 67-86.

21. Kwan, A., and Ko, N., "The initial region of subsonic coaxial jets. Part 2," *Journal of Fluid Mechanics,* Vol. 82, 1977, pp. 273-287.

22. Ko, N., and Au, H., "Coaxial jets of different mean velocity ratios," *Journal of Sound Vibration,* Vol. 100, 1985, pp. 211-232.

23. Au, H., and Ko, N., "Coaxial jets of different mean velocity ratios. II," *Journal of Sound Vibration,* Vol. 116, 1987, pp. 427-443.

24. Baillot, F., Blaisot, J.-B., Boisdron, G., and Dumouchel, C., "Behaviour of an air-assisted jet submitted to a transverse high-frequency acoustic field," *Journal of Fluid Mechanics,* Vol. 640, 2009, pp. 305-342.

25. Chigier, N., and Farago, Z., "Morphological classification of disintegration of round liquid jets in a coaxial air stream," *Atomization and Sprays,* Vol. 2, No. 2, 1992.

26. Leyva, I., Chehroudi, B., and Talley, D., "Dark Core Analysis of Coaxial Injectors at Sub-, Near-, and Supercritical Conditions in a Transverse Acoustic Field," 43rd AIAA/ASME/SAE/ASEE Joint Propulsion Conference & Exhibit, Cincinnati, OH, 8-11 July, 2007.

27. Wegener, J., "Multi-phase Combustion and Transport Processes Under the Influence of Acoustic Excitation," Ph.D., Mechanical Engineering, University of California, Los Angeles, 2014.

Downloaded by Doug Talley on July 29, 2014 | http://arc.aiaa.org | DOI: 10.2514/6.2014-3487

28. Monkewitz, P. A., and Huerre, P., "Influence of the velocity ratio on the spatial instability of mixing layers," *Physics of Fluids,* Vol. 25, 1982, p. 1137.

29. Dahm, W. J., and Dimotakis, P. E., "Mixing at large Schmidt number in the self-similar far field of turbulent jets," *Journal of Fluid Mechanics,* Vol. 217, 1990, pp. 299-330.

30. Arienti, M., and Soteriou, M. C., "Time-resolved proper orthogonal decomposition of liquid jet dynamics," *Physics of Fluids (1994-present),* Vol. 21, No. 11, 2009, p. 112104.

Downloaded by Doug Talley on July 29, 2014 | http://arc.aiaa.org | DOI: 10.2514/6.2014-3487

AIAA SciTech
5-9 January 2015, Kissimmee, Florida
53rd AIAA Aerospace Sciences Meeting

The Response of Cryogenic H2/O2 Coaxial Jet Flames to Acoustic Disturbances

David J. Forliti[1]
Sierra Lobo, Inc. Edwards AFB, CA 93524

A. Badakhshan[2]
ERC Inc. Edwards AFB, CA 93524

Jeffrey L. Wegener[3]
Physical Sciences Inc., Andover, MA 01810

Ivett A. Leyva[4]
AFOSR/RTE Arlington, VA 22203

and

Douglas G. Talley[5]
AFRL/RQRC, Edwards AFB, CA 93524

Downloaded by Doug Talley on February 25, 2015 | http://arc.aiaa.org | DOI: 10.2514/6.2015-1607

An experimental study has been conducted to explore the coupling between a coaxial gaseous hydrogen / liquid oxygen jet flame and transverse acoustic perturbations. A variety of chamber conditions including acoustic frequency, amplitude, and the location of the pressure node / antinode with respect to the flame were examined. The flame response was documented using high-speed imaging including backlit visualization and unfiltered chemiluminescence. Dynamic mode decomposition was used to isolate the spatial structure of the flame response at the forcing frequency. The results indicate that the flame response to forcing is qualitatively similar to previous results of nonreacting coaxial jet flows; the pressure node forcing appears to generate in-plane flapping of the flame while pressure antinode forcing induces a helical structure in the flame.

I. Introduction

COMBUSTION instability is one of the critical phenomena that impacts the design, performance, and robustness of energy and propulsion systems. Due to the extreme conditions, liquid rocket engines (LREs) suffer from potentially extreme consequences under unstable conditions, including rapid wear of components and catastrophic failure. Combustion instability is governed by a coupling between propellant injection and mixing, subsequent chemical reaction, and pressure fluctuations. There are multiple coupling mechanisms that are possible, which leads to a variety of combustion instability classifications.[1] Accounting for all combustion instability mechanisms during the engine development process is currently not possible, due in part to a lack of knowledge of the fundamental interactions between fluid dynamics, combustion, and pressure fluctuations. The purpose of the current research is to contribute to this understanding for injector types and operating conditions relevant to LREs. The research, which is

[1] Research Scientist, Sierra Lobo, Inc., 10 E. Saturn Blvd, Building 8451, Edwards AFB, CA 93524, senior member.
[2] Research Scientist, RQRC, Combustion Devices Group, 10 Saturn Blvd., Edwards AFB, CA 93524.
[3] Former Graduate Student, Department of Mechanical and Aerospace Engineering, UCLA, Los Angeles, CA 90095 student member.
[4] Aerothermodynamics PO, AFOSR/RTE,875 N Randolph St, Arlington, VA 22203, Associate Fellow.
[5] Lead, Combustion Dynamics Group, AFRL/RQRC., 10 E. Saturn Blvd, Building 8451, Edwards AFB, CA 93524, Associate Fellow.
Approved for public release; distribution unlimited.

This material is declared a work of the U.S. Government and is not subject to copyright protection in the United States.

experimental in nature, will also generate a database that is needed to validate both low- and high-fidelity rocket engine design tools.

Previous work at AFRL has made major contributions towards understanding the coupling between acoustic waves and rocket injector flows in a *nonreacting* regime.[2-9] These experiments employed a high-pressure test facility that allowed for investigation of coaxial jets flowing inert surrogates, generally gaseous,liquid, and supercritical nitrogen, and exposing this shear flow to a variety of acoustic conditions that are representative of a transverse resonance that would occur in a rocket engine. In subcritical conditions, the center flow of the coaxial jet is cooled to a liquid condition, while the outer annular flow is chilled but maintained as a gas. This configuration is relevant to coaxial jet injectors for O_2/H_2 LREs such as the Space Shuttle Main Engine (SSME). The fluid surrogates were selected and conditioned to have relevance to LRE conditions in terms of the momentum flux ratio, density ratio, velocity ratio, and thermodynamic state (subcritical or supercritical). The geometry of the coaxial injectors was also varied. At sufficiently-elevated pressure, the fluids may experience supercritical behavior where no phase transition between the the liquid-like and gas-like regions exist. The subcritical and supercritical behavior is easily characterized for single component mixures because the critical point is fixed. When a multi-component system is considered, the description of the flow regime is more complicated because the critical point now depends on the composition of the mixture which varies in space and time.[3] The results of this large body of work highlights the manner in which the mixing can be modulated through a one-way coupling between the acoustic field and the fluid mechanics. This provides some insight on the combustion instability mechanism as this interaction plays an important role in the feedback mechanism. What is unclear is how the presence of heat release contributes to the interaction between the fluid mechanics and the acoustics. Additionally, the resultant combustion dynamics which are driven by the fluid mechanics and the acoustics plays a role as unsteady heat release can feed back and amplify the acoustic field. Thus the natural evolution of this research campaign is to introduce heat release into the physics.

The present research employs a new experimental facility at AFRL that is capable of investigating the coupling between acoustic waves and rocket injector flames. The results are preliminary and exploratory, and consider the response of a flame to a variety of acoustic environments, including acoustic frequency and location within the mode shape. The qualitative features of the flames both with and without acoutics are presented, and dynamic mode decomposition (DMD) was applied to isolate the response of the flame at the forcing frequency.

II. Background

The last decade has seen a variety of efforts exploring rocket injector flame dynamics in the presence of tuned or induced acoustic resonance. Anderson and coworkers have been investigating longitudinal combustion instabilities in the Continuously Variable Resonance Chamber (CRVC), with parallel computational efforts.[10-12] Anderson's group has also been exploring transverse instabilities using a linear array of injectors with the outer-most injectors designed to be unstable to drive a transverse mode in the combustion chamber.[13-15] These efforts have focused on swirl-coaxial injectors operating with various oxidizer/hydrocarbon combinations. High-amplitude pressure fluctuations were observed for these experiments.

Experiments in Europe have also focused on exploring the flame response of rocket chambers experiencing different types of induced acoustic modes.[16-22] These studies employed a common methodology for establishing acoustic resonance that involved periodic blocking of a secondary exhaust nozzle. The periodic flow through the secondary nozzle results in chamber pressure fluctuations that when properly tuned can drive an acoustic resonance in the chamber. Dramatic large-scale flame motions have been observed in most of these studies.

The current work complements these efforts in exploring the coupling mechanisms between rocket injector flames and an acoustic resonance. The current effort considers a single shear coaxial injector with cryogenic oxygen in the inner flow and cooled gaseous hydrogen in the outer annular flow. This conserves tracability to the large body of work done over the past decade at AFRL under nonreacting conditions, which will allow insight on the role of heat release in the flow response. This tracability also helps frame the manner in which nonreacting data scales to reacting flow conditions. Unlike many of the efforts cited above, focus is not placed on highly forced conditions (where pressure flucutations scale with the mean chamber pressure), but instead on identifying the conditions where the coupling is first detectable as well as exploring the coupling sensitivity to forcing parameters.

III. Experimental Details

A schematic and design rendering of the facility is shown in Fig. 1. A single injector element is considered in the present study, and is located in the middle of a rectangular test section. A gaseous nitrogen coflow and window cooling flow are used to condition the test area and protect the chamber windows, respectively. Two piezoelectric sirens from Piezo Systems, Inc. are located laterally with respect to the combustion zone and are used to establish

Downloaded by Doug Talley on February 25, 2015 | http://arc.aiaa.org | DOI: 10.2514/6.2015-1607

transverse acoustic standing waves. These sirens are excited through the use of an amplified signal generator. The exhaust of the inner chamber mixes with gaseous nitrogen flow in the outer chamber, and the combined flow passes through an exhaust orifice that controls the chamber pressure. The propellants are supplied from compressed gas tanks at ambient temperature. An oxygen heat exchanger, designed and fabricated by Sierra Lobo, Inc., along with a hydrogen heat exchanger designed in-house are used to cryogenically condition each propellant flow. Ignition is achieved via a novel ignition system that will be described in future publications due to patent-related issues. Further background on the facility is described by Wegener et al.[7]

A variety of coaxial jet injector models have been investigated at AFRL under nonreacting flow conditions.[9, 23] The coaxial jet injector geometry and near field flow dynamics are illustrated in Fig. 2. For H_2/O_2 reactants at typical injection velocities, the flame is expected to be stabilized downstream of the blunt trailing edge between the inner and outer flows (referred to as the LOx post tip or just post tip).[24-28] The various length scales of the subject injector indicated in Fig. 2 are tabulated in Table 1. These dimensions can be converted into two dimensionless groups, the outer-to-inner area ratio AR of 1.68, and the dimensionless post thickness t/D_1 of 0.27. The injector flow passages are sufficiently long to ensure fully-developed turbulent flow at the injector exit.

High framerate images were captured using a Phantom 7.10 camera at a frame rate of 20 kHz. Backlit flow visualization and unfiltered chemiluminescence were employed to characterize the natural and forced reacting flow response. Filtered chemiluminscence will be employed in future studies to isolate OH* emission. A statistical analysis of the images allows for exploration of the spatial and temporal structure of the reacting flow field. Dynamic mode decomposition[31] was employed to extract the flame response to the acoustic forcing. The relative amplitude of the forced mode to the remaining modes of the decomposition are used as a qualitative indicator of relative strength of the forcing response.

A single set of nominal injector operating conditions was considered for the present study. Table 2 summarizes the nominal operating conditions, including propellant temperatures, momentum flux ratio, oxygen to fuel mixture ratio MR, and Reynolds numbers. The chamber pressure was 3.4 kPa (500 psi) which is thermodynamically subcritical for oxygen; thus two-phase flow behavior is expected. The acoustic forcing is characterized by the frequency in kHz, the location of the injector, being either at a pressure node or a pressure antinode, and the driving voltage amplitude (prior to amplification). Acoustic pressure measurement was not possible during the current set of tests, but will be done in future studies.

IV. Results

One of the primary objectives of the current project is to understand the impact the flame imposes on the flow field. Figure 3 shows a series of images of both the nonreacting and reacting flows without acoustic forcing. The images shown in Fig. 3a are backlit images showing the liquid oxygen core and the annular hydrogen flow. In these studies, the backlighting was reduced to avoid contamination of the chemiluminesence for reacting cases. The nonreacting case represents a situation where the flow was not ignited. The dark region in the bottom half of the image is due to nonuniformities in the backlighting. The qualitative features of the inner jet topology are generally representative of past nonreacting flow studies. This particular sequence shows the breaking and downstream convection of a liquid oxygen section at the end of the dark core. This breaking off of a liquid segment is appears to occur in an aperiodic manner. The unfiltered chemiluminescence images shown in Fig. 3b that the emission from the first few diameters is relatively weak compared to the downstream region. This is in part due to fogging of the test chamber window, fogging which does not exist in the downstream region potentially due to heat from the flame. The sequence of images suggests that unsteady burning is present, as would be expected due to the turbulent operating condictions associated with fully-developed flow, and the evolution of the flame topology is resolved. Burning structures appear to move slowly downstream with increasing time. The presence of liquid oxygen within the flame is unclear for the unforced case. Future high-intensity spark backlit shadowgraph imaging will be used to identify the topology of the liquid oxygen inner core.

Over 2000 images were collected for each test case at a frame rate of 20 kHz. Thus the sequence of images can be analyzed to extract spatial and temporal content. For the nonreacting case, spectral analysis was done on the temporal signals from the pixels located near the interface between the liquid oxygen and gaseous hydrogen. This measures the frequencies present in the inner shear layer region. Figure 4 shows the local spectra for the nonreating case shown in Fig. 3a. The figure shows the axial evolution of the spectra of the images as a function of downstream distance. Although noisy, some spectral peaks are evident; the noise is due to the fact that the temporal data is limited to only 2000 samples. The peak indicated by the vertical blue line at x/D_1 of four and seven is likely to be the signature of structures in the inner shear layer. This peak persists to x/D_1 of seven, but dissappears at eight, which is downstream of the dark core. Although the contrast is weaker in the downstream region, the image fluctua-

Downloaded by Doug Talley on February 25, 2015 | http://arc.aiaa.org | DOI: 10.2514/6.2015-1607

tions still represent the presence of structures that contain density differences. The preferred mode of the coaxial jet, based on the scaling law of Wegener[29], is shown on the figure as the red vertical line and is near 1 kHz. The preferred mode estimate of 1 kHz is generally representative of lower frequency peaks at x/D_1 of seven and eight.

Figure 5 shows the spectral content of the chemiluminescence signals for the flame shown in Fig. 3b at the same axial locations shown in Fig. 4 for the nonreacting case. The power spectral density (PSD) plots show both the reacting (blue line) and nonreacting (gray) cases. The spectral peak of 2.5 kHz observed at $x/D_1 = 4$ for the nonreacting case is no longer evident, while a moderate peak has emerged at approximately 3.5 kHz; the new apparent shear layer frequency is indicated by the blue vertical line. This indicates a possible frequency shift of the shear layer mode, indicated by the arrow on the figure, from lower to higher frequency due to the presence of the flame. Although there is no obvious flame signature present in the images at this axial location, there is a low-level light signal detected. This potential frequency shift will be explored further in future work.

The PSDs at the x/D_1 of seven and eight show some strong peaks that are below 2 kHz. For the reacting cases, there are multiple peaks at about 850 Hz and 1300 Hz, as well as a lower frequency that emerges at the downstream location. These peaks are in the same general range as the nonreacting preferred mode of 1 kHz. There is a peak at approximately 400 Hz, that emerges at $x/D_1 = 8$. This new peak may be a discrete phenonmenon or may be the result of nonlinear interaction between the two higher frequencies. The evolution of the spectra further downstream is shown in Fig. 6. The spectra span a range of x/D_1 from nine to thirteen. The spectral trend shows a general shift to lower frequencies with increasing downstream distance, which is expected due to growth of the reacting structure length scales. A consistent peak around 500 Hz and indicated by the red vertical line is seen in the downstream region. The tilted green line shows the broadband energy-containing spectral range is shifting to lower frequency with increasing downstream distance.

Overall, the spectral analysis suggests that the frequency content in the coaxial jet flame is in the same range as found in the nonreacting case, although some potential frequency shifting may be present. Future analysis, which will include proper orthogonal decomposition (POD) and linear stability analysis, will be used to identify dominant (i.e. preferred mode) frequencies and improve our understanding of how flames alter the flow field spectra.

A variety of forced flames were established and studied. Figure 7 shows instantaneous images of both the nonreacting and reacting coaxial jet flame. The forcing frequency was 1.95 kHz, and the forcing amplitude based on the driving voltage was 1.5 V (maximum forcing for the present study was 2.0 V). These results are associated with the injector being located at the pressure node. For the nonreacting case shown in Fig. 7a, the velocity forcing results in a transverse flapping of the liquid core. This has been observed extensively in past nonreacting studies. The pressure node is also associated with an acoustic velocity antinode, which in this case would be a transverse velocity fluctuation in the same direction as the observed jet flapping. The mechanism responsible for this response is not yet clear. Wegener et al. showed that the momentum flux ratio based on transverse velocity fluctuation is not sufficient to explain the jet deflection.[30] A strong helical mode may exist, which is difficult to discern when using a line of sight. Further work is required to understand the coupling mechanism for the pressure node regime.

Figure 7b shows the same injector flow and acoustic conditions with a flame present. The flame is seen to be much larger in axial length, in part due to a reduction in fog buildup on the window. Unlike the unforced flame images shown in Fig. 3(b), the liquid core is easier to see and is seen to exhibit transverse wiggles. Intense burning regions at the transverse sides of the flame are seen to evolve and convect downstream. It is very apparent that the presence of acoustic disturbances has had a significant impact on the qualitative features of the flame.

Dynamic mode decomposition was used to extract the spatial structure of flame response at the forcing frequency. The amplitude of the modes may be extracted using the algorithm of Schmid.[31] The DMD is applied to the image data over the first $10D_1$, to eliminate the lower frequency content in the downstream region. Figure 8 shows the DMD amplitude spectra as a function of frequency for the case with the flame forced at 1.95 kHz, 2.0 V, and a pressure node location. One mode is seen to be dominant over the other modes as is associated with the forcing frequency. Figure 8b shows the real and imaginary components of the spatial mode shape associated with the forcing frequency. The modes clearly represent antisymmetric behavior by the presence of lobes of like sign (red is positive, blue is negative) that are misaligned with respsect to the left and right sides of the jet. The real and imaginary components are very similar, although positive (red) and negative (blue) lobes appear to be shifted half a wavelength in the imaginary component relative to the real component. Thus when added together in the reconstruction, a convective process is produced. A similar convective mode may be reconstructed with a pair of POD modes that have certain statistical properties.[23] The relative amplitude of the forced mode compared to the "background" modes is an indicator of strength of the mode in relation to other modes.

Figure 9 shows the DMD decomposition results for the pressure node case at a higher forcing frequency of 3.05 kHz at a forcing amplitude of 2.0 V. The general trend is the same as found for the 1.95 kHz forcing case. The relative amplitude of the forced mode is closer to the background modes, suggesting the forcing response at 3.05 kHz is

Downloaded by Doug Talley on February 25, 2015 | http://arc.aiaa.org | DOI: 10.2514/6.2015-1607

somewhat degraded compared to 1.95 kHz. The spatial distribution of the modes is also similar, although as expected, the spatial length scales are smaller for the case forced at a higher frequency.

The forced flames located at the pressure antinode experienced a somewhat degraded response. Figure 10 shows the natural and maximum forcing amplitude cases of a flame located at the pressure antinode. Although very subtle, the images in Fig. 10b exhibit a somewhat organized spiral-like structure in the middle of the images that is not evident in the unforced case. Neither of the cases shown in Fig. 10 exhibit the clear dark jet core as shown for the pressure node forced flame shown in Fig. 7b. The dark core is likely obscured by a more intense flame along the coaxial jet centerline compared to the pressure node forced cases.

The spiral-like nature of the pressure antinode forced flames is further elucidated in the DMD results of Figs. 11 and 12; Figs. 11 and 12 are associated with forcing frequencies of 1.9 and 2.95 kHz, respectively. In both pressure antinode cases, the forced mode amplitude is closer to the background levels relative to the pressure node forcing results. This suggests that the forcing response is someone degraded for the pressure antinode case, a trend that is congruent with visual observations of the flame. As found for the pressure node cases, the wavelength of the modes decrease with increasing frequency.

It is interesting to note that the pressure antinode exhibits an apparent helical-like structure. Past results by Teshome[23] and Wegener[29] show that the pressure antinode tends to result in symmetrical structures for nonreacting studies. The pressure antinode forcing mechanism as described by Wegener[29] and Wegener et al.[30] that produces axisymmetric puffing of the outer jet flow would tend to preferentially force an axisymmetric response. Whether these flames have a near field that is axisymmetric or not (that eventually develops into a helical mode) will be explored in future studies.

Unlike the pressure antinode results, the pressure node images show the dark core. This suggests that the flame enhancement for the pressure node does not occur near the injector axis, which would lead to a potential optical interference with respect to viewing the dark core. This suggests that the flapping motion is not axisymmetric but is moving in the plane containing the transverse direction and the axial coordinate.

V. Conclusions

An experimental study was conducted on liquid O_2 / gaseous H_2 coaxial jet flames exposed to transverse standing acoustic waves. The placement of the flame at the pressure node region of the mode shape results in a robust coupling at both frequencies considered. The pressure node excitation results suggest that the flame deflects laterally in the spanwise-axial plane in response to the ambient acoustic velocity perturbations. The response of the flame when placed at the pressure antinode appears to be somewhat reduced compared to the pressure node response. The time-resolved chemiluminescence measurements and dynamic mode decomposition (DMD) of the pressure antinode results indicate a helical-like structure to the flame topology. The forcing mechanism, which is expected to result in axisymmetric pulsing of the annular gas flow, has been found in nonreacting studies to induce axisymmetric structure. The competition/transition between the axisymmetric and helical modes in pressure antinode forced flames will be considered in future work.

References

1. Harrje, D. T., and Reardon, F. H., "Liquid Propellant Rocket Combustion Instability. NASA SP-194," *NASA Special Publication,* Vol. 194, 1972.

2. Chehroudi, B., Talley, D., and Coy, E., "Visual characteristics and initial growth rates of round cryogenic jets at subcritical and supercritical pressures," *Physics of Fluids,* Vol. 14, No. 2, 2002, pp. 850-861.

3. Oschwald, M., Smith, J., Branam, R., Hussong, J., Schik, A., Chehroudi, B., and Talley, D., "Injection of fluids into supercritical environments," *Combustion Science and Technology,* Vol. 178, No. 1-3, 2006, pp. 49-100.

4. Leyva, I., Chehroudi, B., and Talley, D., "Dark Core Analysis of Coaxial Injectors at Sub-, Near-, and Supercritical Conditions in a Transverse Acoustic Field," 43rd AIAA/ASME/SAE/ASEE Joint Propulsion Conference & Exhibit, Cincinnati, OH, 8-11 July, 2007.

5. Leyva, I., Rodriguez, J., Chehroudi, B., and Talley, D., "Preliminary Results on Coaxial Jet Sprean Angles and the Effects of Variable Phase Transverse Acoustic Fields," 46th AIAA Aerospace Sciences Meeting and Exhibit, Reno, NV, 7-10 January, 2008.

Downloaded by Doug Talley on February 25, 2015 | http://arc.aiaa.org | DOI: 10.2514/6.2015-1607

6. Teshome, S., Leyva, I. A., Talley, D., and Karagozian, A. R., "Cryogenic high-pressure shear-coaxial jets exposed to transverse acoustic forcing," 50th AIAA Aerospace Sciences Meeting Including the New Horizons Forum and Aerospace Exposition, Nashville, TN, 2012.

7. Wegener, J., Leyva, I., Forliti, D., and Talley, D., "Development of a facility for combustion stability experiments at supercritical pressure," 52nd AIAA Aerospace Sciences Meeting, National Harbor, MD, 2014.

8. Davis, D. W., "On the behavior of a shear-coaxial jet, spanning sub-to supercritical pressures, with and without an externally imposed transverse acoustic field," Ph.D., Mechanical Engineering, The Pennsylvania State University, 2006.

9. Rodriguez, J. I., "Acoustic excitation of liquid fuel droplets and coaxial jets," Ph.D., Aerospace Engineering, University of California, Los Angeles, 2009.

10. Yu, Y., Koeglmeier, S., Sisco, J., and Anderson, W., "Combustion instability of gaseous fuels in a continuously variable resonance chamber (CVRC)," 44th AIAA/SAE/ASEE Joint Propulsion Conference & Exhibit, Hartford CT, 21-23 July, 2008.

11. Yu, Y., O'Hara, L., Sisco, J., and Anderson, W., "Experimental study of high-frequency combustion instability in a continuously variable resonance combustor," 47th AIAA Aerospace Sciences Meeting Including The New Horizons Forum and Aerospace Exposition, Orlando, FL, 5-8 January, 2009.

12. Harvazinski, M., Talley, D., and Sankaran, V., "Influence of boundary condition treatment on longitudinal mode combustion instability predictions," 49th AIAA/ASME/SAE/ASEE Joint Propulsion Conference, San Jose, CA, 14-17 July, 2013.

13. Pomeroy, B., Lamont, W., and Anderson, W., "Subscale tool for determining transverse combustion response," 45th AIAA/ASME/SAE/ASEE Joint Propulsion Conference & Exhibit, Denver, CO, 2-5 August, 2009.

14. Wierman, M., Nugent, N., and Anderson, W., "Characterization of an unstable rocket combustor with He addition," 46th AIAA/ASME/SAE/ASEE Joint Propulsion Conference & Exhibit, Nashville, TN, 25-28 July, 2010.

15. Pomeroy, B., Morgan, C., and Anderson, W., "Response of a gas-centered swirl coaxial injector to trasnverse instabilities," 47th AIAA/ASME/SAE/ASEE Joint Propulsion Conference and Exhibit, San Diego, CA, 31 July-3 Aug, 2011.

16. Rey, C., Ducruix, S., Richecoeur, F., Scouflaire, P., Vingert, L., and Candel, S., "High frequency combustion instabilities associated with collective interactions in liquid propulsion," 40th AIAA/ASME/SAE/ASEE Joint Propulsion Conference and Exhibit, Fort Lauderdale, FL, 11-14 July, 2004.

17. Richecoeur, F., Scouflaire, P., Decruix, S., and Candel, S., "Interactions between propellant jets and acoustic modes in liquid rocket engines: experiments and simulations," 42nd AIAA/ASME/SAE/ASEE Joint Propulsion Conference & Exhibit, Sacramento, CA, 9-12 July, 2006.

18. Richecoeur, F., Scouflaire, P., Ducruix, S., and Candel, S., "High-frequency transverse acoustic coupling in a multiple-injector cryogenic combustor," *Journal of Propulsion and Power,* Vol. 22, No. 4, 2006, pp. 790-799.

19. Richecoeur, F., Ducruix, S., Scouflaire, P., and Candel, S., "Experimental investigation of high-frequency combustion instabilities in liquid rocket engine," *Acta Astronautica,* Vol. 62, No. 1, 2008, pp. 18-27.

20. Hardi, J., Oschwald, M., and Dally, B., "Flame response to acoustic excitation in a rectangular rocket combustor with LOx/H 2 propellants," *CEAS Space Journal*, 2011, pp. 1-9.

21. Hardi, J. S., Oschwald, M., and Dally, B., "Acoustic characterisation of a rectangular rocket combustor with liquid oxygen and hydrogen propellants," *Proceedings of the Institution of Mechanical Engineers, Part G: Journal of Aerospace Engineering*, 2012.

22. Hardi, J., Martinez, H., Oschwald, M., and Dally, B., "Response of a reacting LOx jet to a transverse acoustic oscillation," Space Propulsion 2012, Bordeaux, France, 7-10 May, 2012.

23. Teshome, S., "Droplet Combustion and Non-Reactive Shear-Coaxial Jets with Transverse Acoustic Excitation," Ph.D., Mechanical Engineering, University of California, Los Angeles, 2012.

Downloaded by Doug Talley on February 25, 2015 | http://arc.aiaa.org | DOI: 10.2514/6.2015-1607

24. Juniper, M., Sé, and Candel, b., "Edge diffusion flame stabilization behind a step over a liquid reactant," *Journal of Propulsion and Power,* Vol. 19, No. 3, 2003, pp. 332-341.

25. Mayer, W., Schik, A., Sch-aring, M., ffler, and Tamura, H., "Injection and mixing processes in high-pressure liquid oxygen/gaseous hydrogen rocket combustors," *Journal of Propulsion and Power,* Vol. 16, No. 5, 2000, pp. 823-828.

26. Singla, G., Scouflaire, P., Rolon, J.-C., and Candel, S., "Flame stabilization in high pressure LO_x/GH_2 and GCH_4 combustion," *Proceedings of the Combustion Institute,* Vol. 31, No. 2, 2007, pp. 2215-2222.

27. Yang, B., Cuoco, F., and Oschwald, M., "Atomization and flames in LOX/H2-and LOX/CH4-spray combustion," *Journal of Propulsion and Power,* Vol. 23, No. 4, 2007, pp. 763-771.

28. Herding, G., Snyder, R., Scouflaire, P., Rolon, C., and Candel, S., "Flame stabilization in cryogenic propellant combustion," Symposium (International) on Combustion, 1996, pp. 2041-2047.

29. Wegener, J., "Multi-phase combustion and transport processes under the influence of acoustic excitation," Ph.D., Mechanical Engineering, University of California, Los Angeles, 2014.

30. Wegener, J., Forliti, D., Leyva, I., and Talley, D., "Receptivity of a cryogenic coaxial gas-liquid jet to acoustic disturbances," 50th AIAA/ASME/SAE/ASEE Joint Propulsion Conference, Cleveland, OH, 2014.

31. Schmid, P., "Application of the dynamic mode decomposition to experimental data," Experiments in Fluids, V. 50, 2011, pp. 1123-1130.

Downloaded by Doug Talley on February 25, 2015 | http://arc.aiaa.org | DOI: 10.2514/6.2015-1607

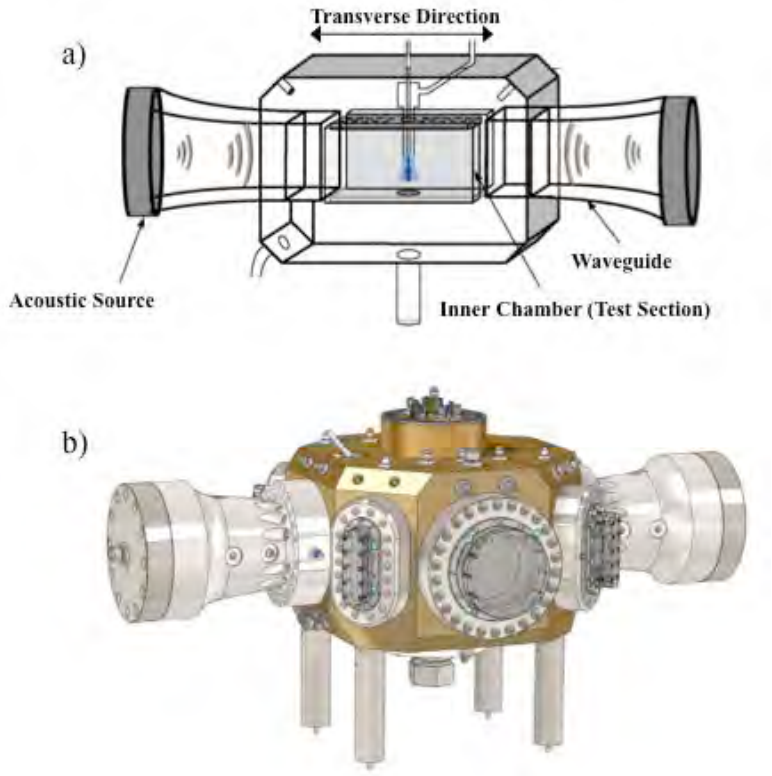

Figure 1. a)Conceptuation and b) schematic of the combustion stability reacting flow facility.

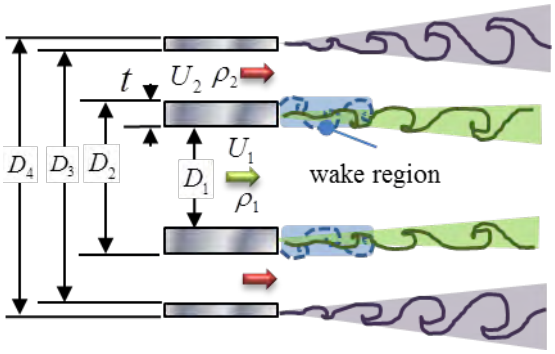

Figure 2. Coaxial jet injector geometry and near field shear flow instabilities.

Downloaded by Doug Talley on February 25, 2015 | http://arc.aiaa.org | DOI: 10.2514/6.2015-1607

Table 1: Injector geometry parameters

Parameter	Value (mm)
D_1	1.40
D_2	2.16
D_3	2.82
D_4	1.68

Table 2: Injector flow conditions

Parameter	Values
T of inner jet (O_2)	130 K
T of outer jet (H_2)	250 K
J	2.7
MR	6
Equivalence ratio	1.33
Chamber pressure	3.4 MPa (500 psi)
O_2 Re	4.7×10^4
H_2 Re	2.2×10^4

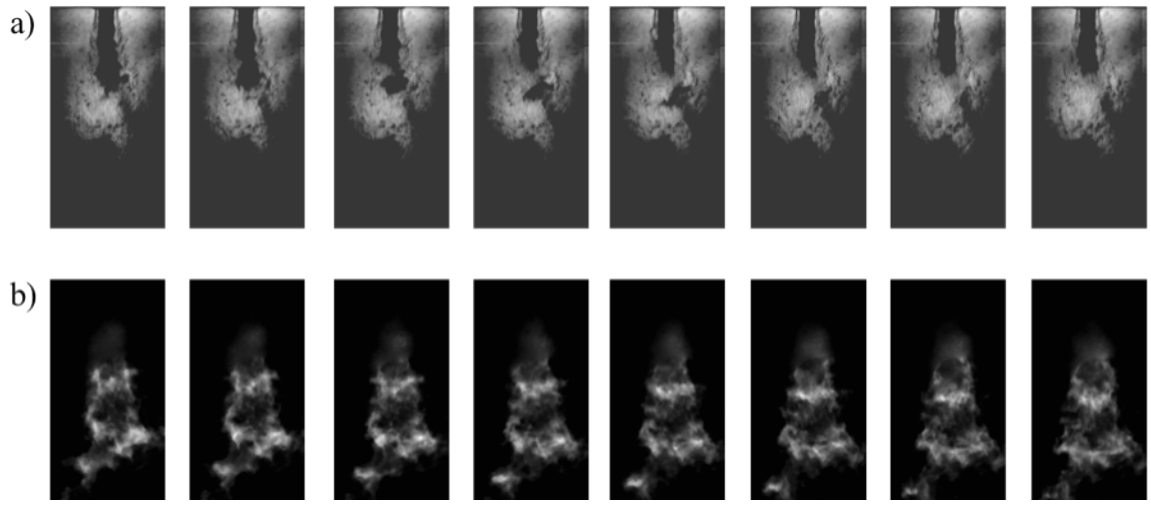

Figure 3. Instantaneous a) backlit and b) unfiltered chemiluminescence images for the unforced condition.

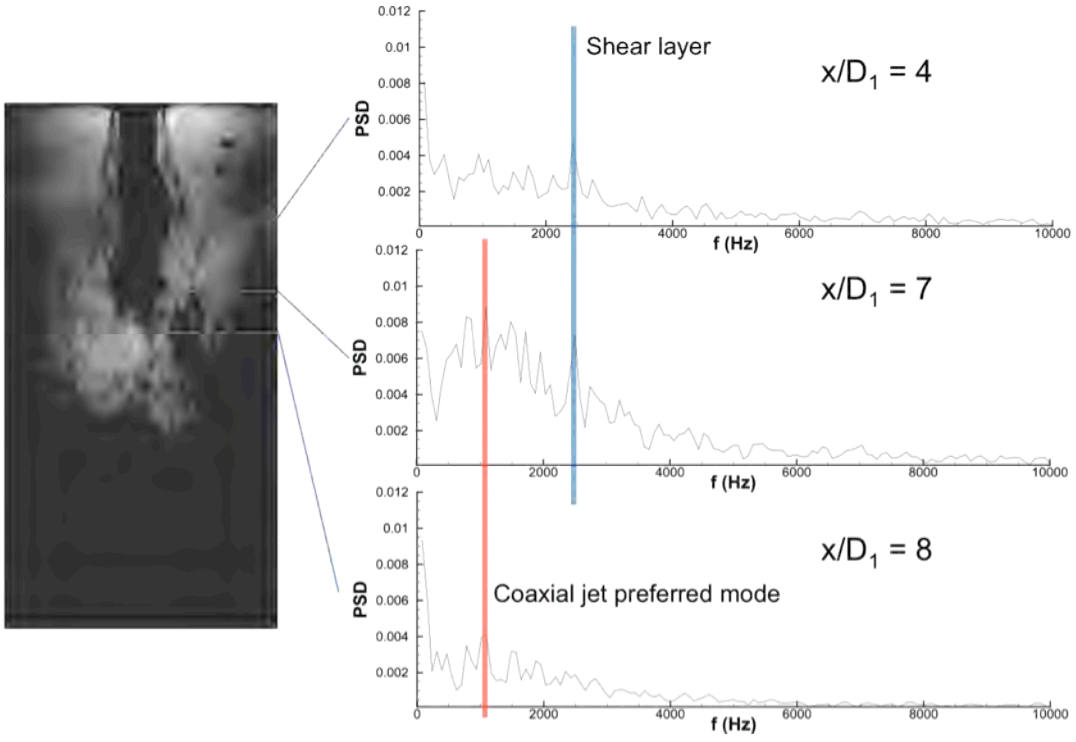

Figure 4. Spectra of the inner shear layer region for the nonreacting unforced flow.

Downloaded by Doug Talley on February 25, 2015 | http://arc.aiaa.org | DOI: 10.2514/6.2015-1607

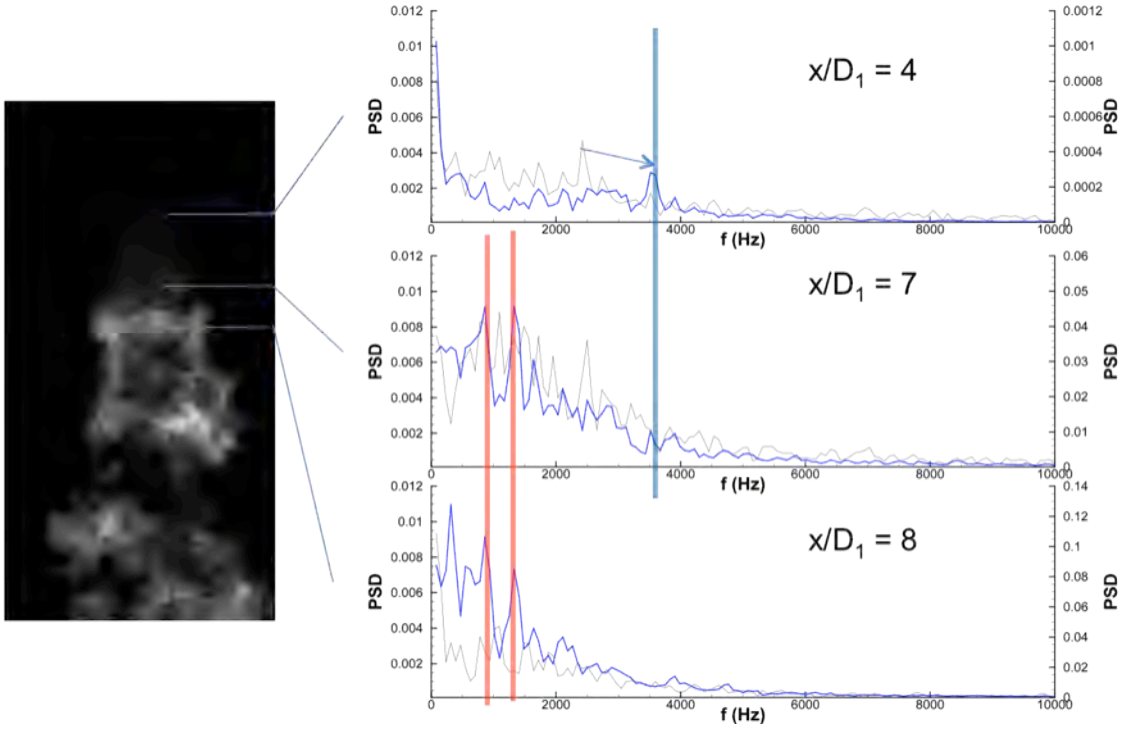

Figure 5. Spectra of the flame region for the reacting unforced flow.

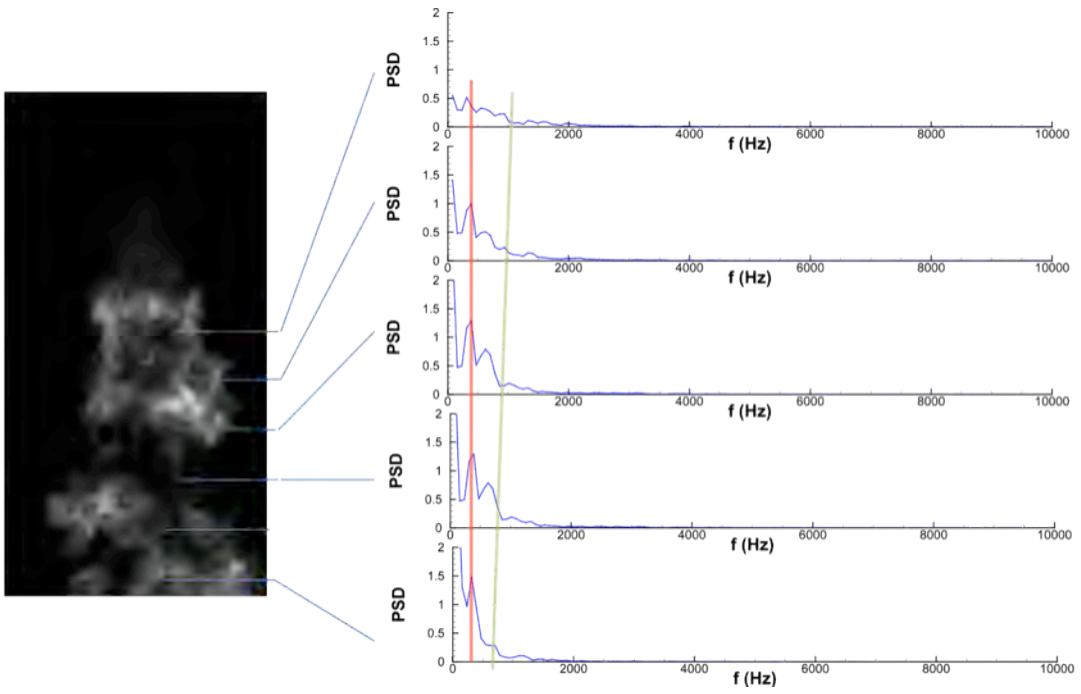

Figure 6. Downstream spectra of the flame region for the reacting unforced flow.

Downloaded by Doug Talley on February 25, 2015 | http://arc.aiaa.org | DOI: 10.2514/6.2015-1607

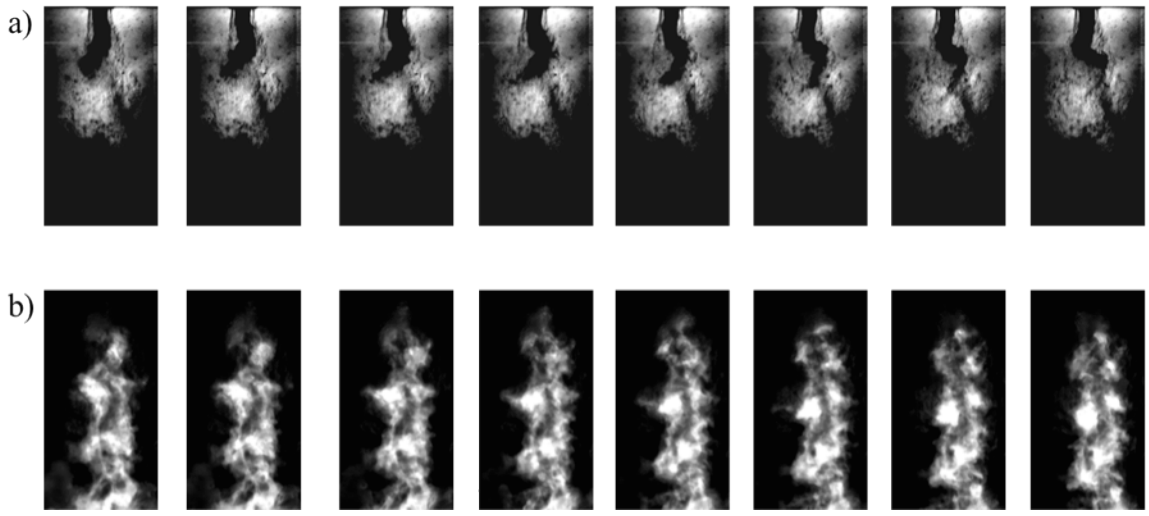

Figure 7. Instantaneous a) backlit and b) unfiltered chemiluminescence images for the pressure node forced condition.

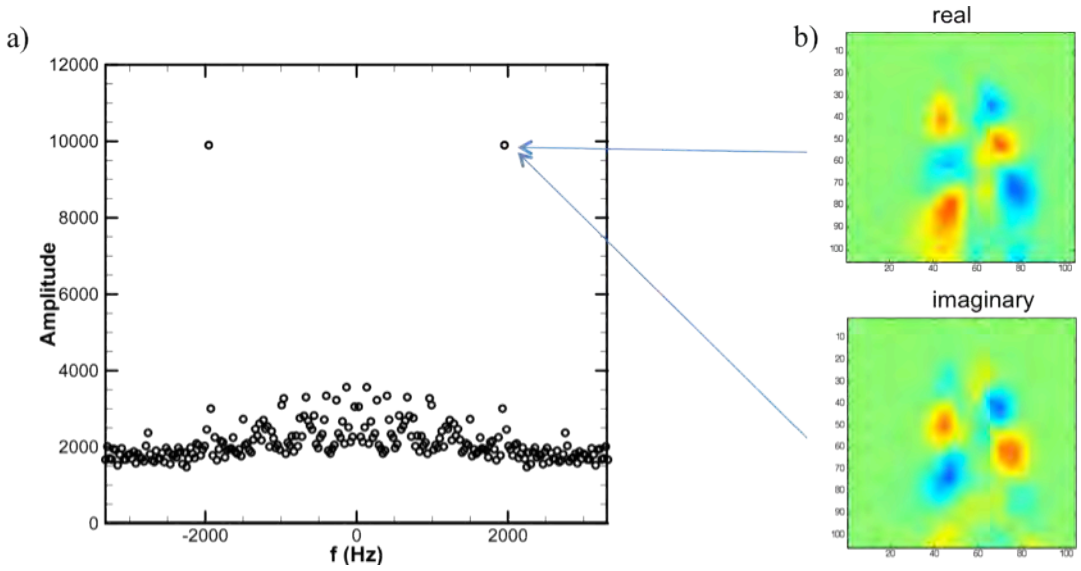

Figure 8. The a) dynamic mode decomposition spectrum and b) forced mode spatial distribution for the maximum pressure node forced flame at 1.95 kHz.

Downloaded by Doug Talley on February 25, 2015 | http://arc.aiaa.org | DOI: 10.2514/6.2015-1607

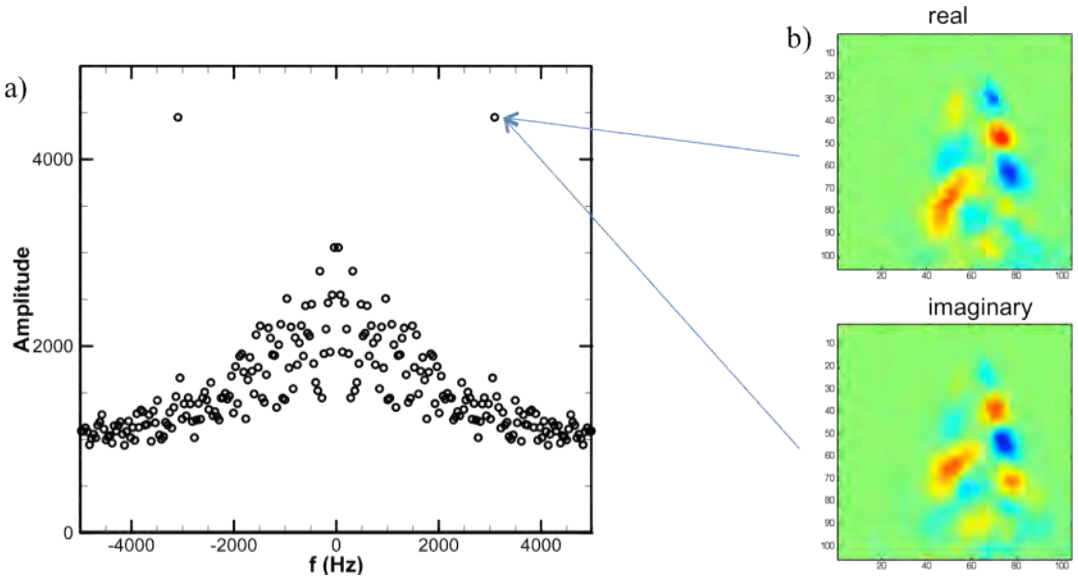

Figure 9. The a) dynamic mode decomposition spectrum and b) forced mode spatial distribution for the maximum pressure node forced flame at 3.05 kHz.

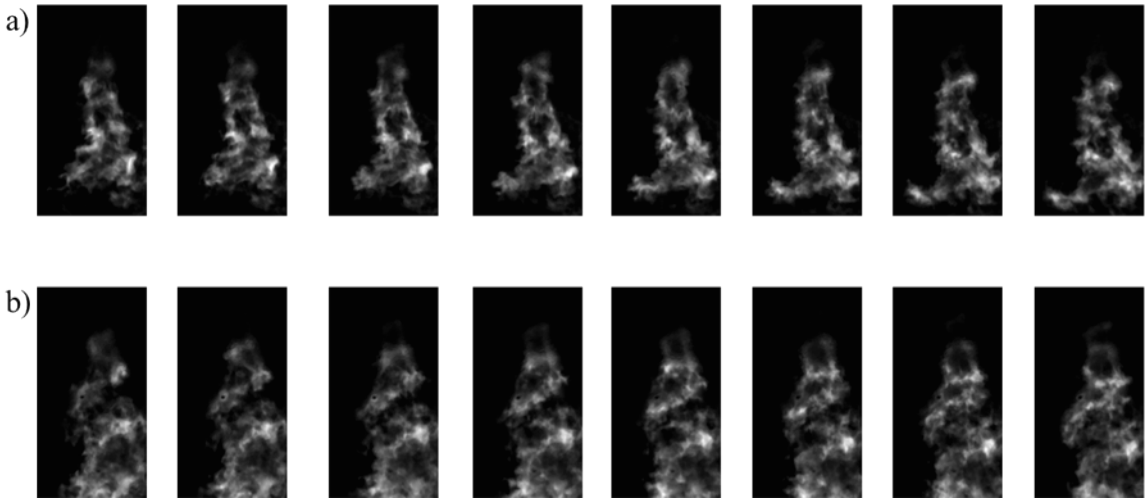

Figure 10. Instantaneous unfiltered chemiluminescence images for the a) unforced and b) pressure anti-node forced condition.

Downloaded by Doug Talley on February 25, 2015 | http://arc.aiaa.org | DOI: 10.2514/6.2015-1607

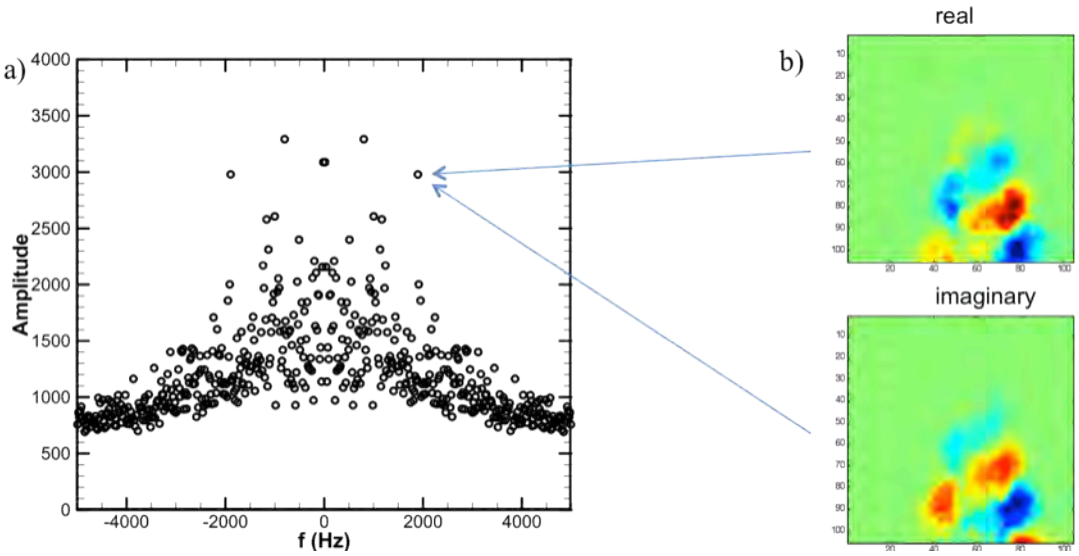

Figure 11. The a) dynamic mode decomposition spectrum and b) forced mode spatial distribution for the maximum pressure antinode forced flame at 1.9 kHz.

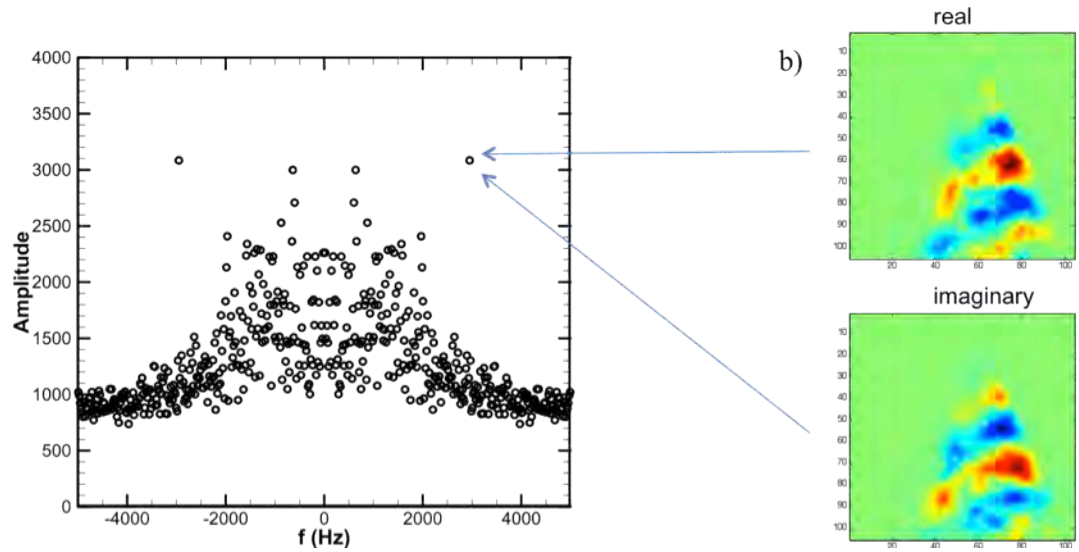

Figure 12. The a) dynamic mode decomposition spectrum and b) forced mode spatial distribution for the maximum pressure antinode forced flame at 2.95 kHz.

Downloaded by Doug Talley on February 25, 2015 | http://arc.aiaa.org | DOI: 10.2514/6.2015-1607

Acoustically Forced Coaxial Hydrogen / Liquid Oxygen Jet Flames

M. Roa* and D. Forliti[1]
Sierra Lobo, Inc.
Edwards, Ca 93524 USA

Al Badakhshan
ERC Inc.
Edwards AFB, CA 93524 USA

Doug Talley
Air Force Research Laboratory
Edwards AFB, CA 93524 USA

Abstract

Combustion instabilities can pose serious problems in the development of liquid rocket engines. In order to understand and predict them, it is necessary to understand how representative liquid rocket injector flames react to acoustic waves. In this study, a representative coaxial gaseous hydrogen / liquid oxygen (LOX) jet flame is visualized for both reacting and nonreacting cases. The jet flame was studied unforced, without acoustics, and forced, with transverse acoustic waves in a pressure node and a pressure antinode configuration. For unforced flames, reactions are found to cause a significantly more expanded plume due to the vaporization and expansion of the LOX. Flame holding is established at the lip with a particularly dominant LOX recirculation zone. Nonreacting convective structures propagate downstream at relatively constant velocity, while reacting structures start at a slow speed and gradually accelerate with downstream distance. These structures never reach the velocity of the nonreacting structures. Reactions shift the spectral content to lower frequencies, consistent with trends observed in the linear stability literature. For forced flames, acoustics do not appear to affect the flame holding. Dynamic mode decomposition detects jet response not only at the fundamental frequency but at higher harmonics as well. Reactions produce inconsistent trends in the harmonics: reactions promote harmonics at a pressure antinode while they damp harmonics at a pressure node.

*Corresponding author: Mario.roa.ctr@us.af.mil
[1]Now at University of St. Thomas, St. Paul, Minnesota

DISTRIBUTION A. Approved for public Release; distribution unlimited. PA 16168

Introduction

Combustion instability associated with liquid rocket engines has been responsible for degradation of engine performance, increase in engine component stresses, and under extreme conditions, catastrophic engine failure. High-frequency instabilities, which are generally the most harmful in liquid rocket engines, can be driven when the disturbances associated with transverse acoustic resonances couple with the combustion process to form a feedback loop. In order to understand and predict combustion instabilities, it is necessary to understand how representative liquid rocket injector flames react to acoustic waves. In general, the thermoacoustic instability phenomenon is understood to be an interaction between acoustic waves and unsteady combustion. The unsteady heat release can amplify the acoustic field if the conditions are favorable. Due to the broadband nature of hydrodynamic instabilities, avoiding a detrimental coupling between acoustics and fluid dynamic mixing is challenging.

One way to try to mitigate the instabilities is to design an injector that does not couple with acoustic perturbation while it still provides the necessary mixing to sustain combustion. One such injector, used extensively for liquid rocket applications, is the shear coaxial injector [1-5]. In this injector configuration liquid oxidizer is injected surrounded by a gaseous fuel, as shown in Figure 1. The aerodynamic interactions at both fluid interfaces bring about hydrodynamic instabilities and atomize the liquid oxidizer into small droplets. These droplets evaporate and mix with the surrounding fuel and react.

There have been many models and efforts [6-9] to describe the atomization process with most being linear in nature and supported with empirical approximations to existing data. The models provide approximate liquid core lengths, time scales associated with growth rates of small disturbance, and droplet sizes and distributions. Due to the highly nonlinear nature of atomization, these models are limited in their range application and do not take reactions and the effects of high pressures into consideration. Accurate predictions of nonlinear, reacting high pressures atomization are left for intense computational studies.

In an effort to further understand high pressure atomization and combustion of a shear coaxial injector, experimental efforts have been carried at academic and national laboratories [10-12]. From these studies, there have been several proposed models of the breakup and dynamics of the liquid core of the shear coaxial injector under relevant rocket engine conditions. One such model is the classical phenomenological break up mod-

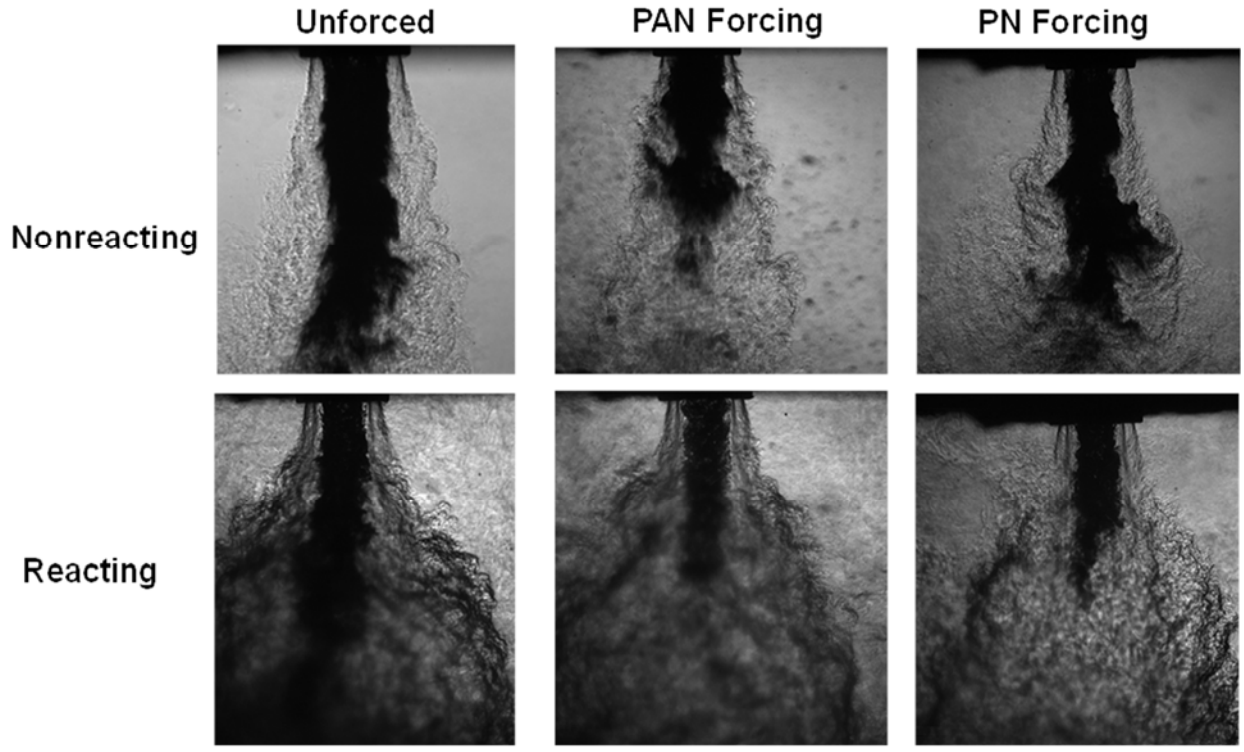

Figure 1. The shear coaxial flow of a LOX center surrounded by gaseous hydrogen. The first row shows the unreacting condition under same acoustic amplitude (0.34 bar) in a PAN and PN configuration. The second row shows the same conditions but reacting.

DISTRIBUTION A. Approved for public Release; distribution unlimited. PA 16168

el by Reitz and Bracco [6]. In this model, the intact liquid core has ligaments and droplets continually shed due to surface instabilities, with the rate of liquid atomization dependent on momentum flux and velocity ratios between the liquid and the gas. This model has been typically used for rocket applications. Experimental and computational results have since raised questions of Reitz and Bracco model on its applicability to coaxial jets at rocket relevant conditions [13-15]. Another model is the core fragmentation model [16] where helical instabilities distort and breakup the liquid core. It is this helical mode that is responsible for some the large scale breakup of the LOX core observed for this investigation.

Since the LOX core has been observed to be the most prominent feature of shear coaxial injectors and with studies suggesting that combustion instabilities couple with LOX-post acoustics [17], an experimental effort was undertaken to study LOX core dynamics and breakup using a shear coaxial configuration subjected to high frequency acoustic forcing. A near field view at the injector exit was studied, limited to 6 LOX diameters, to capture the onset of the LOX core instabilities. The shear coaxial injector was studied both at reacting and nonreacting conditions. High frequency pressure anti-node (PAN) and a pressure node (PN) acoustic forcing was applied at the injector exit. Dynamic mode decomposition (DMD) was used to extract frequencies and spatial modal shape of the LOX response to the acoustic forcing under reacting and nonreacting conditions. There were differences in LOX core convective speeds and LOX core length between the reacting and nonreacting conditions for the acoustically unforced conditions. The LOX core behaved similarly under reacting and nonreacting conditions for the PAN acoustic forcing. A coupling of hydrogen (GH2) and LOX core shear layers occurred and a LOX core helical model was observed for the PN acoustic forcing for both reacting and nonreacting cases.

Figure 2. The experimental chamber and high speed camera.

Experimental Setup and Conditions

The experimental facility at the Air Force Research Laboratory (AFRL) at Edwards Air Force Base was used to investigate the coupling of transverse acoustic resonances with a single, shear coaxial, LOX/GH2 flow with varying acoustic perturbation amplitudes. Figure 2 shows the experimental chamber. The features of this facility were documented by Wegener et al. [12]. The injector geometry was the same as studied by Wegener et al [12]. Experiments were done at a mean chamber pressure of 34.45 bars (500 Psia). Nominal flow rates of liquid oxygen and hydrogen were 4.2 and 0.7 g/s, respectively, with a jet momentum ratio (GH2 to LOX) of 2.2. Both fluids had a Reynolds number on the order of 10^4. The LOX core had a Weber number on the order of 10^4. The LOX core was kept at constant temperature of 140 K and the GH2 at 250 K. The transverse acoustic resonance was induced through the use of carefully-controlled piezo-sirens, allowing excitation across a range of pressure amplitudes for discrete resonant chamber frequencies. The amplitude of the acoustic perturbations was varied incrementally from 0 bar (i.e. no acoustic forcing) to 0.34 bar (5 Psi). The pressure fluctuations were measured via Kulite high-speed pressure transducers (model XCL -100) located at different transverse locations, including the middle of the chamber which is the location of the injector. The mode shape of the acoustic field was altered through the phase relationship between the two acoustic drivers. The control of the mode shape allows for the PAN and PN regions of the acoustic mode to be placed at the exit of the injector. Resonant chamber frequencies of 3060Hz for PAN forcing and 2890 Hz for PN were selected. Previous studies on nonreacting experiments have shown a dramatic difference in the coupling mechanism depending on the local acoustic environment [18].

Shadowgraphy was selected as the basis of flow visualization due to the focus on the LOX core dynamic response to the acoustics, while providing an indirect view of the flame through the locations of density variations. A collimated light source and Vision Research v710 Phantom camera were used to acquire the high-speed shadowgraph images. The images were acquired at a 25 kHz frame rate with an exposure of 5 microseconds. The high-speed shadowgraph images were then analyzed using dynamic mode decomposition (DMD), similar to that described by Schmid [19], to identify when and how the LOX core and its shear flow responded to acoustic perturbations with and without heat release.

Results

Figure 1 shows instantaneous shadowgraph images of unforced and acoustically-forced cases under both unreacting and reacting conditions. The presence of the

flame has a dramatic effect on the topology of the LOX surface. For nonreacting, unforced conditions, the interface is highly blurred and appears to be in a fibrous atomization regime, consistent with Farago and Chigier [20] diagram of fiber type of atomization for the given Reynolds and Weber numbers. Evidence of large scale breakup of the LOX core length for the nonreacting and unforced condition, shown on the upper left in Figure 1, is evident 6 diameters away from the exit. Although the breakup is evident, a frequency cannot be determined nor a breakup length since the core extended beyond 6 diameters for the majority of shadowgraph images collected.

The shape of the acoustic forcing is shown in figure 3, with PAN forcing having the maximum pressure oscillations and the PN having the maximum velocity oscillations. For the acoustic forcing conditions, the same blurred and fibrous atomization was observed for both the PAN and PN conditions at the LOX shear layer, but a dramatic reduction of the LOX core length was observed, as shown in Figure 1. Massflow variations were observed of the LOX core subjected to PAN forcing. PN forcing resulted in a helical mode of the LOX core. For the PAN condition, the massflow variations are due to the increase and decrease of back pressure the injector experiences. In the PAN forcing, the shear coaxial flow is subjected to large pressure fluctuations. Using a simple Bernoulli argument, as the back pressure raises there is reduction in mass flowrate out of the injector and as the pressure dips an increase in LOX flowrate is achieved. These pressure fluctuations results in periodic surges of LOX mass flowrates, with large intact LOX fragments shedding away from the main core at the same acoustic forcing of 3060 Hz. For the PN condition the velocity perturbations are at their maximum. These velocity perturbations impart a helical movement on the LOX core given by the wavy or snake-like pattern of the LOX core. This wavy pattern has been reported previously by Boniface et al [10] and Woodward et al [21]. It is this instability that is responsive for the breakup of the LOX core closer to the nozzle exit under PN forcing compared to the acoustically unforced condition.

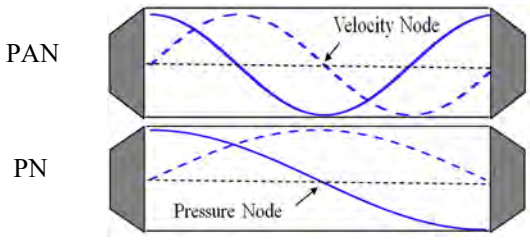

Figure 3. An instant in time of PAN and PN forcing. The solid line is the pressure fluctuations and the dash line is the velocity fluctuations. In PAN forcing, the injector experiences maximum and minimum pressure fluctuations. In PN forcing, the velocity fluctuations are maximum.

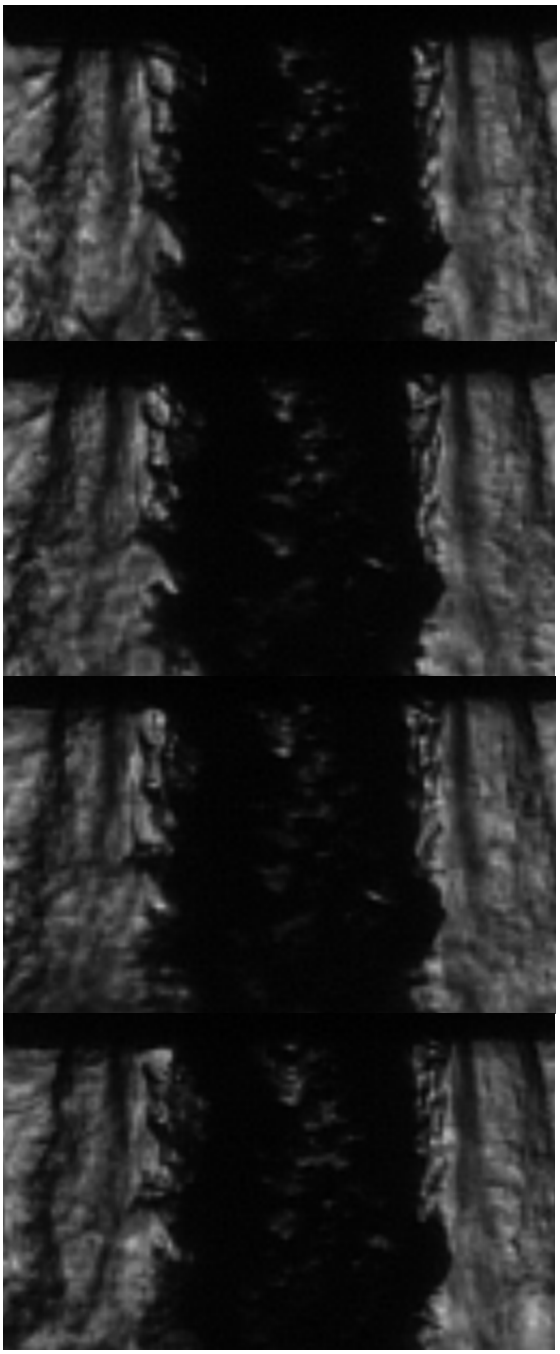

Figure 4. Sequential shadowgraph images demonstrating ligaments being shed off the LOX core for reacting cases. The time step between each image is 0.04 ms.

For the reacting conditions the presence of the flame results in a dramatic reduction in the fibrous nature of the surface, as expected, due to evaporation pro-

cesses as shown in closed up images in figure 4. The presence of the flame also shortens the length of the LOX core, which is again driven in part by the enhanced vaporization regardless of the acoustic forcing. Similarly, an expanded plume exists downstream due to the vaporization and expansion of the LOX, as shown in Figure 1. In the reacting flow cases, small ligaments were observed to be shed off the LOX core near the exit. These small ligaments are then entrained into a recirculation zone established below the LOX post. The ligament shedding close to the nozzle exit can be observed in figure 4, where the sequential images show ligaments on the either side of the LOX core being shed off. These ligaments get entrained into the LOX post recirculation zone if they are shed off within one LOX diameter. If shed past one LOX diameter, the ligaments convect with the rest of the LOX core. Figure 4 also shows an attached flame to inner lip of the GH2 exit.

No local flame extinction was observed regardless of the acoustic forcing amplitude. It has been experimentally observed when the strain rates associated with acoustic forcing is high enough [22], local extinction of the flame and the flame holding regions can occur. The extinction and re-ignition of the flame produces a flow field with uneven heat release that can couple with acoustic forcing, leading to a combustion instability limit cycle. Flame extinction and re-ignition events were not observed for any of the acoustic forcing conditions.

By extracting a column of pixels at each time step along the shear layer edge, dark streaks lines with constant slope represent convecting liquid structures can been seen in figure 5. These dark streaks, which are LOX core structures were observed to be traveling at constant velocity. For the unreacting case with no acoustic forcing, the shear layer between the LOX and the GH2 was approximate to Dimotakis [23] shear layer velocity. In the reacting condition, the shear layer velocity is not constant. Since the flame is attached to inner lip of the GH2 exit, there is a reduction in density between the interface between the LOX core and GH2. This reduced density pulls less on the LOX core, thus

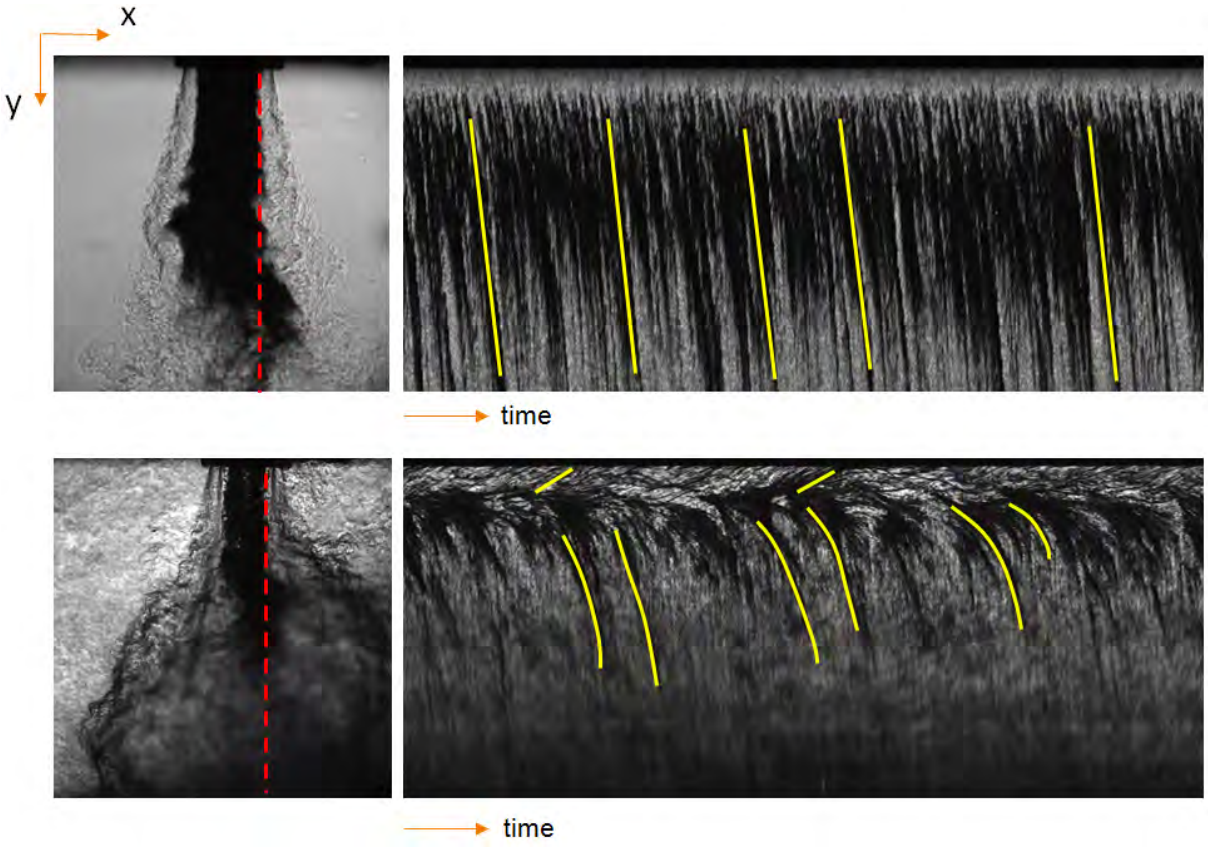

Figure 3. Extracted column of pixels at each time step along shear layer edge as a function of time. The dark streaks, traced with yellow lines, represent convecting liquid structures. The top is the unreacting condition and the bottom is the reacting condition. LOX core structures convect at a constant velocity for the nonreacting, acoustically unforced case. For the reacting condition, the LOX core exits at a low velocity and accelerates after one LOX core diameter away from the exit. The shear layer for the reacting condition never attains the same velocity as the unreacted condition.

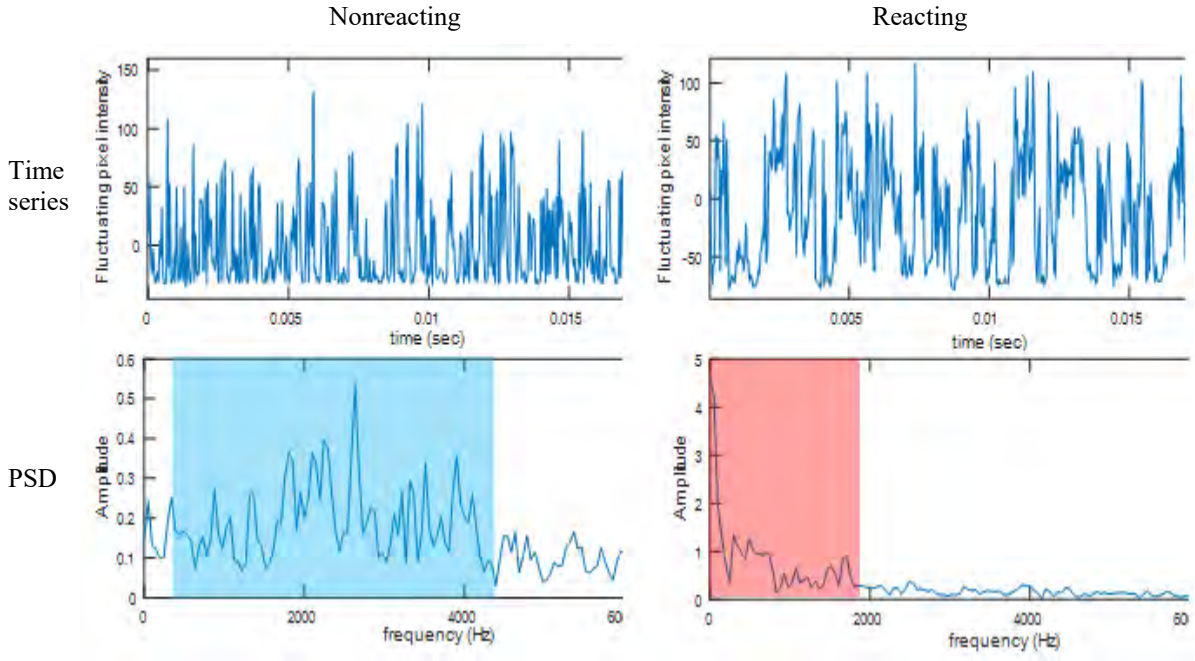

Figure 4. The pixel intensity of a pixel 2 diameters away from the exit along the shear layer, with its corresponding PSD. There is general shift to lower frequencies when the flame is present, consist with linear stability theory.

effectively convects slower compared to the nonreacting LOX core. Beyond the first diameter though, the LOX core starts to accelerate, as shown in figure 5 with the curved dark streaks, but never achieves the same convective velocity as the nonreacting condition. When the acoustic forcing was present the LOX core shape was too distorted to extract velocity information. Figure 5 also shows streaks with opposite flow orientation, illustrating the recirculation of the ligaments that were shed off within the first diameter as demonstrated in figure 4.

Although the trend in spectral content is highly dependent on the specific velocity and heat release profile, the presence of a flame is, in general, expected to result in a stabilizing effect and a shift to lower frequencies (e.g. Mahalingam et al. [24]). Spectral analysis of the measured intensity fluctuations in the near field of the inner shear layer (between the LOX core and GH2) shows there is a general shift of spectral content to lower frequencies when the flame is present. By analyzing the intensity fluctuations at a point 2 diameters away from the nozzle exit along the shear layer and performing a power spectral density, the general shift towards lower spectral content is observed, as shown in figure 6.

Dynamic mode decomposition (DMD) was used to identify the spectral content of both the forced and unforced cases. For the nonreacting case without acoustic perturbations, good agreement was found between the frequency associated with a convective mode and established scaling laws for shear coaxial jets [25]. For the

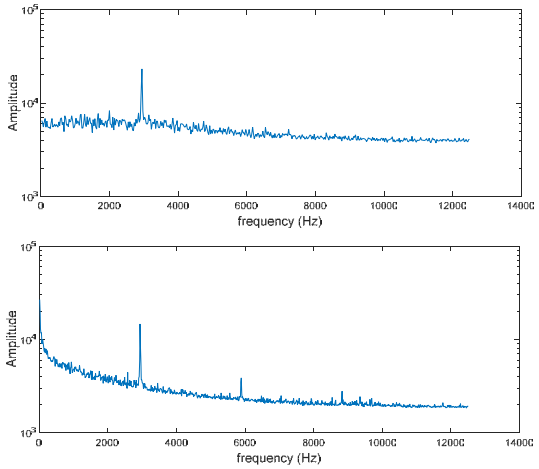

Figure 5. The DMD spectrum for the PAN nonreacting (top) and reacting (bottom) conditions. For the reacting condition, higher harmonics are present in the DMD analysis.

reacting condition without acoustic perturbations, there was no significant dominant mode, although a weak coupling between the inner and outer shear layers was observed at high frequencies.

Figure 7 shows the DMD spectrum for the maximum amplitude forcing condition with the injector placed at the PAN. It is evident from the DMD analysis that physical flow is coupled with the acoustic perturbation at the same driving frequency of 3060Hz. The case shown in figure 7 is for both reacting and nonreacting

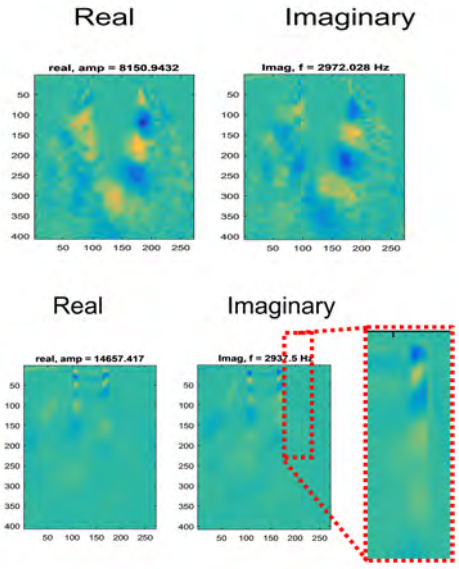

Figure 9. The DMD shape mode of the PAN unreacting (top) and reacting (bottom) condition.

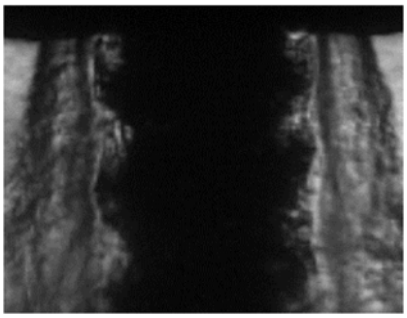

Figure 10. Organized motion of the LOX core under PAN perturbations and reacting.

conditions. The peak-to-peak pressure amplitude for this case was approximately 0.36 bar (5.3 psi). For the reacting condition there is a clear indication of coupling between the acoustics and the inner shear layer instability, including coupling at higher harmonic frequencies, but this coupling is not evident in the nonreacting case. Figure 8 shows the DMD spatial modes. The DMD spatial mode illustrates a symmetric shear layer response of the LOX core, as indicated by the axially aligned positive (yellow) and negative (blue) intensity fluctuations in the DMD spatial mode shapes. This symmetry is expected as the mechanism that is associated with PAN forcing relates to azimuthally-coherent mass flow fluctuations in the LOX core flow as discussed earlier. Although the LOX core response is symmetric, the scales of the axisymmetric structures are not the same. For the reacting case these structures are smaller compared to the nonreacting condition shown in Figure 1. Figure 10 shows a shadowgraph image of

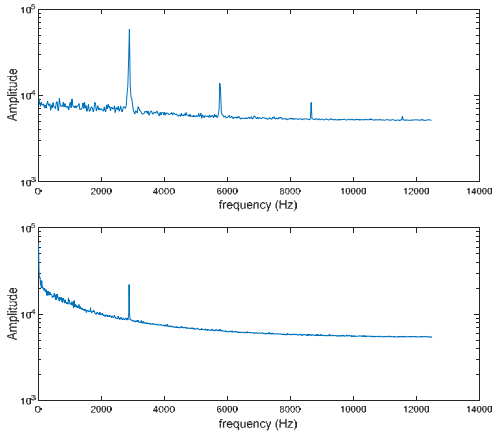

Figure 11. The DMD spectrum for the PN nonreacting (top)and reacting conditions (bottom). For the unreacting condition, higher harmonics are present in the DMD analysis.

the injector near field, and a vertical row of shear layer structures can be seen at the LOX core boundary. These structures are thought to be smaller because the LOX core velocity is slower compared to the nonreacting case, resulting in reduced massflow variations. The LOX core also experiences roll-up motion that is in the opposite direction then would be expected based on the presence of the high-speed GH2 flow. The LOX core rollup travels upstream, opposite of the both the GH2 and LOX core flow, into the wake and recirculation region underneath the LOX post. The observed vorticity orientation suggests the inner shear layer is interacting with the LOX post's low-speed wake region. The combination of the reduced interfacial density, as discussed earlier, and the low-speed wake region effectively slows the LOX core resulting in a decrease in massflow variations subjected PAN forcing. The PAN interactions are first detected when the acoustic perturbation amplitude is approximately 0.13 bar (2 psi). The coherent organized motion, shown in figure 10, at the surface of the LOX core is also first observed at this amplitude.

Figure 11 shows the DMD spectrum for the maximum forcing amplitude PN forcing, similar to figure 7. Similar to the PAN condition, a coupling of the shear layers at a frequency of 2890 Hz was observed for the PN acoustic forcing. There is a reversal of the harmonics detected for the nonreacting and reacting conditions. For the nonreacting condition subjected to PN forcing higher harmonics are detected. The higher harmonics are dampen for the reacting condition. This results is opposite of the PAN results. Figure 12 shows the DMD spatial modes associated with the peak frequencies in figure 11. In the figure 12, the large alternating blue and yellow pattern shows a helical mode excitation of the LOX core when perturbed by PN forcing. A coupling between the inner and outer shear layers, as observed

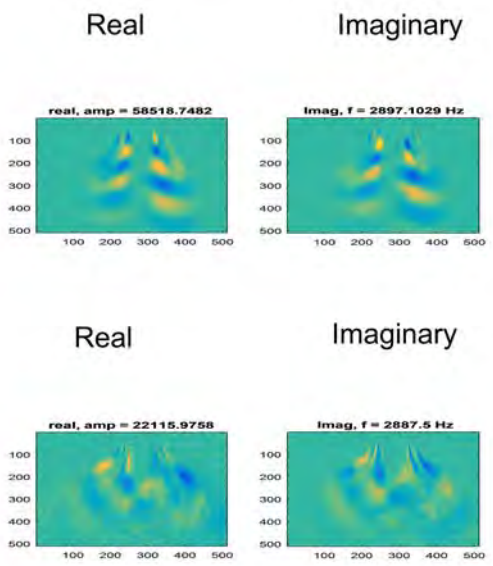

Figure 12. The DMD shape mode of the PN nonreacting (top) and reacting (bottom) condition.

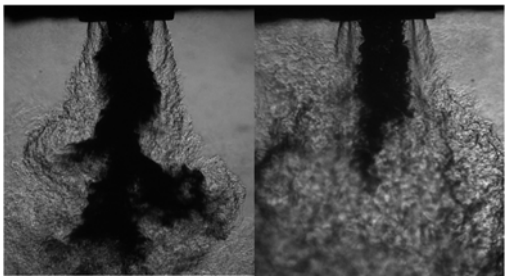

Figure 13. Full field images of the nonreacting (left) and reacting (right) PN forced condition. For the reacting condition there is very little LOX core motion.

by Dahm et al [26], is present when the flow is unreacting, with the LOX core shear layer dominating. The slim alternating blue and yellow streaks to either side of the LOX core illustrate the coupling of GH2 shear layer to the LOX core shear layer. This coupling between the inner and outer shear layer was not observed for PAN conditions when no reaction was present. A coupling was observed when a flame was present. For the reacting condition, an anti-symmetric structure with coherent coupling between the outer and inner shear layers was present.

Figure 13 shows side by side images of the nonreacing and reacting PN forced conditions. For the nonreacting condition, the LOX core responses dramatically to the PN forcing and a helical mode is observed in figure 13. For the reacting condition, the LOX core is slow to respond to the PN forcing. It was observed that GH2 shear layer was in phase with acoustic forcing and LOX core was out of phase with the respect to the incoming acoustic wave. From figure 13 the helical shape of the nonreacting LOX core begins close to the nozzle exit, unlike reacting condition where helical turning starts further away from the nozzle exit compared to nonreacting case. It is believed that the anchored flame at the exit of the nozzle dampens the velocity perturbation at the nozzle exit for the PN forcing, but not for the pressure perturbations in the PAN conditions. The higher harmonics are believed to be dampen because of the LOX core delayed reaction to PN perturbations and the helical shape is not as pronounced under reacting conditions.

Conclusion

The near field of shear LOX/GH2 coaxial flow was investigated under relevant rocket conditions; both reacting and nonreacting conditions were subjected to acoustic forcing. Under reacting conditions, the rapid expansion and vaporization of the LOX core caused an expanded plume that was presented for all acoustic forcing conditions. A LOX recirculation zone was present downstream of the LOX post. In the reacting condition, ligaments where shed off from the LOX core and entrained into the LOX post recirculation zone. Flame holding was established at the inner lip of the GH2 exit. Convective velocities of the LOX core were constant under nonreacting conditions but not in the reacting conditions, where the flow started at a slow speed and gradually accelerated. A shift of spectral content to lower frequencies occurred when a flame was present.

Dynamic mode decomposition captured the physical response of the LOX core under different acoustic forcing. For PAN forcing the LOX core experienced variations of the mass flowrates for both nonreacting and reacting conditions, but the liquid structures differed greatly in size. For PN forcing the nonreating case, a LOX core helical mode was present and the inner outer shear layer coupled together. For the reacting case, the LOX core response was out of phase with respect to the acoustic forcing. Given the physical differences and responses of the nonreacting flows compared to the reacting flows to low amplitude, high frequency acoustic perturbation, it is vital these differences be understood to better control combustion instabilities.

Nomenclature

DMD	Dynamic mode decomposition
GH2	Gaseous Hydrogen
LOX	Liquid Oxygen
PAN	Pressure Anti-node
PN	Pressure Node

Acknowledgements

This work was funded by Airforce Office of Scientific Research.

References

1. Juniper, M.P., and Candel, S.M., *Journal of Fluid Mechanics* 482:257-269 (2003)
2. Hakim, L., Schmitt, T., Ducruix, S., and Candel, S., *Combustion and Flame* 162:3482-3502 (2015)
3. Ibraim, E.A., Kenny, R.J., and Walker, N.B., 42nd *AIAA/ASME/SAE/ASEE/ Joint Propulsion Conference,* Sacramento, Ca, USA, July 2006
4. Puissant, C., and Glogowski, M.J., *Atomization and Sprays* 7:467-478 (1997)
5. Yang, V., and Anderson, W., *Liquid Rocket Engine Combustion Instability*, American Institute of Aeronautics and Astronautics, Inc. 1995, p. 46.
6. Reitz, R.D., and Bracco, F. V., *Physics of Fluids* 25:1730-1742 (1982)
7. Lin, S.P., and Lian, Z.W., *AIAA Journal* 28:120-126 (1990)
8. Mohanta, L., Cheung, F., and Bajorek, S.M., *Physica A*443:333-346 (2016)
9. Lin, S.P., and Ibrahim, E.A., *Journal of Fluid Mechanics* 218:641-658 (1990)
10. Boniface, Y., Reeb, A., Woodard, R., Pal, S., and Santoro, R. J., *Proceedings of the 11th Annual PERC Symposium on Propulsion,*University Park, PA, USA, November 1999,. pp 110-119
11. Pal, S., Moser, M.D., Ryan, H.M., Foust, M.J., and Santoro, R.J., *Atomization and Sprays* 6:227-244 (1996)
12. Wegener, J.L., Leyva, I.A., Forliti, D.J., and Talley, D.G., *52nd AIAA Aerospace Sciences Meeting*, National Harbor, MD, USA, January 2014
13. Oefelein, J.C., and Yang, V., *Journal of Propulsion and Power*, (14): 843-857 (1998)
14. Yang, V., *Symposium (International) on Combustion*, (28) :925-941 (2000)
15. Zong, N., and Yang, V., C*ombustion Science and Technology*, (178): 193-227 (2006)
16. Andrews, M. J., *Atomization and Sprays* 3:29-54 (1993)
17. Locke, J.M., Pal, S, Woodard, R.D., and Santoro R.J, 46th *AIAA/ASME/SAE/ASEE/ Joint Propulsion Conference,* Nashville, TN, USA, July 2010
18. Forliti, D.J., Badakhshan, A., Wegener, J.L., Leyva, I.A., and Talley, D.G *53rd AIAA Aerospace Sciences Meeting,* Kissimmee, FL, USA January 2015.
19. Schmid, P. J., *Journal of Fluid Mechanics* (656):5-28 (2010)
20. Farago, Z., and Chigier, N., *Atomization and Sprays* 2:137-153 (1992)
21. Woodard, R.D, Pal, S., Farhangi, S., and Santoro, R.J., 42nd *AIAA/ASME/SAE/ASEE/ Joint Propulsion Conference,* Reno, NV, USA, January 2001
22. Chaouki, G, Smith, O. I., and Karagozain, A. R,. 39th *AIAA Aerospace Science Meeting S*acramento, Ca, USA, July 2006
23. Dimotakis, P.E., *Am. Inst. Aeronaut. Astronaut. J.* 24(11):1791-1796
24. Mahalingam, S., Cantwell, B.J. and Ferziger. J.H., *Physics of Fluids A: Fluid Dynamics* (3):1533-1543 (1991)
25. Schumaker, S, A., *An experimental investigation of reacting and nonreacting coaxial jet mixing in laboratory rocket engine,* Thesis, (2009)
26. Dahm, W.J.A, Frieler, C.E. and Tryggvason, G., *J. Fluid Mech*.(241):371-402 (1992)

AIAA SciTech Forum
8–12 January 2018, Kissimmee, Florida
2018 AIAA Aerospace Sciences Meeting

10.2514/6.2018-0677

Check for updates

Vortex Dynamic Mechanisms in Coaxial Hydrogen/ LOX Jet Flames

Mario Roa[1]
Sierra Lobo, Inc., Air Force Research Laboratory, Building 8451, Edwards AFB, CA, 93524

Douglas G. Talley[2]
Air Force Research Laboratory, Building 8451, Edwards AFB, CA, 93524

Coaxial gaseous hydrogen / liquid oxygen jet flames were studied experimentally as a function of the outer-to-inner momentum flux ratio *J* using high speed shadowgraphy and OH* chemiluminescence imaging at 25 kHz. Particular attention was paid to vortex dynamic mechanisms that could be observed. It was found that vortices generated at the exit of the annular flow created a chain of events that had a strong effect on the flame. These vortices were found to impinge on the LOX core and create local increases in OH* emission, interpreted as a combustion waves, local troughs in the LOX core caused by increased vaporization, and waves composed of expansion gases, all of which convect downstream at different velocities with the combustion wave propagating the fastest. The combustion waves were found to sometimes merge, sometimes spontaneously disappear, or sometimes continue to propagate as pairs. Earlier results had shown the importance of vortex dynamics in the outer flow to simpler non-reacting coaxial flow. These results confirm their importance also in combusting flows.

I. Introduction

Coaxial jets have been investigated extensively because of their great many uses in engineering applications. Coaxial jets have a simple geometry of concentric flows, where an outer, annular jet of one fluid encircles an inner round jet of another, and the two streams are introduced at generally different flow rates. The shear forces between the two fluids can then produce effective mixing between the fluids. Despite their relative geometric simplicity, coaxial jets have been observed to exhibit a complex range of behaviors depending on their configuration. An experimental investigation is made in this paper of the particular configuration of a burning gaseous hydrogen annular flow and a liquid oxygen central jet with relevance to liquid rocket engines. Particular attention is paid to the role of vortex dynamics in this flow. A more detailed literature review is presented next.

II. Literature Review

In simpler coaxial jet configurations, both fluids are of the same phase, either both gas or both liquid. Early investigations by Ko and Kwan[1] of coaxial gaseous jets showed that far enough downstream, the flow has similar mean velocity profiles to that of single jets, and can be treated as a single jets. They also identified a near nozzle region within the outer jet where high frequency vortices are present, exhibiting similar vortex shedding frequencies as single jets. Dahm *et al* [2] further investigated the vortex behavior emerging from the nozzle exit with detailed images for uniform density liquid coaxial jets. The outer and inner jets and their vortices were visualized with two-color planar laser induced fluorescence, with each jet's fluorescence different to help distinguish both jets. By varying the velocity ratio between both streams, Dahm *et al* observed changes in the vortex pattern emerging from the nozzle exit. They observed changes in the size of the vortices shed and their orientation, and they also observed a "lock-in" phenomenon between the inner and outer vortices. Dahm *et al* also investigated the influence of the jets' absolute velocities while keeping the velocity ratio unchanged, and observed dramatic differences of the vortex structures formed by the inner jet. They argued that the changes to the emerging vortex pattern is the origin of instability, where the instability can be due shear, similar to Kelvin-Helmholtz, or wake-like instability of vortices shedding into a wake. In the case of the coaxial jets, the wake-like instability occurs when vortices are shed due to a velocity inflection point associated with the recirculation zone behind a bluff body, or in this case the recirculation zone downstream of the finite-thickness tube separating the inner jet from the outer jet. Dahm *et al* also observed that regardless of the inner shear vortices formed, the outer vortices appear to govern the downstream flow dynamics. Later flow visualization experiments of

[1] Research Scientist, Sierra Lobo, Inc. 10 E. Saturn Blvd, Building 8451, Edwards, CA 93524, Member
[2] Lead, Combustion Dynamic Group, AFRL/RQRC., 10 E. Saturn Blvd, Building 8451, Edwards, CA 935324, Associate Fellow

Distribution A: Approved for public release; distribution unlimited.

Copyright © 2018 by Mario Roa and Douglas G. Talley. Published by the American Institute of Aeronautics and Astronautics, Inc., with permission.

Downloaded by Doug Talley on January 10, 2018 | http://arc.aiaa.org | DOI: 10.2514/6.2018-0677

gas on gas coaxial jets performed by Wicker and Eaton [3], would show similar vortex behavior and the governing nature of the outer jet vortex. Wicker and Eaton showed that the initial vortex development occurs independently for both the outer and inner shear layer, but when an outer large-scale vortex structure forms, it will ultimately govern the flow downstream. Experiments performed by Rehab *et al* [4], showed that the vortex topology emerging from the nozzle exit is strongly influenced by the nozzle geometry, since different nozzle geometries induce variations in the shape of the shear layers. Direct numerical simulations by Balarac and Métas [5] studied the nozzle geometry effect on the vortex behavior by changing the momentum thickness between both jets and arrived at similar results to Rehab. Mixing studies performed by Villermaux [6 and 7] showed that destabilization of the outer jet is responsible for entraining and mixing with the inner jet. Villermaux *et al* shows that the shape of the velocity profile, precisely the size of the vorticity thickness between the shear layers, sets the size of the annular vortex or the instability.

Experimental studies and linear stability analysis performed by Talamelli et al [8 – 11] explored these vortex instabilities in gaseous coaxial jets. The early experiments performed by Talamelli *et al* , would show that the central jet wall thickness has a role in the vortex shedding behavior. They showed that when the central wall thickness is decreased, the vortex shedding is dominated by shear layer instabilities and not wake-like instabilities for thick walls. Talamelli and Gavarini [11] used a family of hyperbolic tangent velocity profiles, similar to Michalke [12], in their linear stability analysis. They showed that there are three unstable modes present in coaxial jets. The first mode pertains to the outer jet and has an instability similar to Kelvin-Helmholtz instability. The other two modes are wake-like. The wake-like instabilities are formed due to the presence of a physical barrier between jets or the central jet wall thickness. In later experimental work, Segalini and Talamelli [11] systematically varied the velocity ratio between both jets to investigate the instabilities previously predicted. They observed that for high outer to inner velocity ratios (> 1.6), the inner shear layer vortices 'lock-in' to the shedding frequency of the large outer shear vortices, similar to Dahm *et al*. For the intermediate velocity ratios, between 0.75 and 1.6, a Von Kármán street is formed in the inner shear layer behind the inner wall.

A more complex variant of coaxial jets is the case when the two fluids are introduced having different thermodynamic phases, one a liquid and one a gas. A further complexity is introduced when chemical reactions occur between the fluids, as in combustion. The particular configuration of concern here is relevant to liquid rockets, where the outer flow is a gaseous fuel and the inner flow is a liquid oxidant. Gaseous hydrogen (GH2) is considered here as the gaseous fuel and liquid oxygen (LOX) is considered as the liquid oxidant.

Relative to this configuration, Mayer *et. al*.[13-18] experimentally investigated reacting cryogenic oxygen (LOX) and gaseous hydrogen shear coaxial flows at chamber pressures up to 10 MPa. He observed that when chamber pressures approaches and exceeds the oxygen's critical pressure, there were remarkable differences between the subcritical and supercritical physical flow features. For pressures exceeding oxygen's critical pressure of 5 MPa, LOX droplets that would otherwise form due the shearing forces and other hydrodynamics instabilities in subcritical flows were no longer present. Instead, at supercritical pressures, the interface between the center LOX jet and the annular hydrogen jet is highly diffuse. Mayer also observed the formation of a recirculation zone downstream from the LOX tube wall, and that it served as the flame-holding region.

Research efforts at Penn State [19- 22] explored the atomization and droplet velocities from reacting and nonreacting LOX/GH2 coaxial flows at high pressure using phase Doppler particle analyzer. Their results showed that axial distance of 11.1 LOX diameter from the injector face for the reacting conditions, they measured a limited number of LOX droplets (≤ 10 droplets). It was until the probe volume was located at an axial distance of 18.5 LOX diameter downstream, is where they measured enough LOX droplets for statistical comparison to non-reacting conditions. Their results show that the LOX droplet sizes were on average larger for reacting condition when compared to the non-reacting conditions. They would confirm the lack of LOX droplets with high speed imaging of the LOX core. Major species and temperature profiles were also measured using Raman spectroscopy 37 LOX diameter away from the nozzle exit. They measured relative constant hydrogen and water mole fractions and temperatures radially across the coaxial flow for the when the Raman single shots were averaged.

A significant amount of work was performed at the Air Force Research Laboratory [23-27]. That research proceeded from single jet non-reacting flow using liquid nitrogen (LN2) as a simulant for LOX, non-reacting coaxial jets using LN2 and gaseous nitrogen (GN2) as a simulant for hydrogen, to reacting coaxial GH2/LOX jets. The majority of that work, however, concerned non-reacting flows but did investigate the effect of subcritical and supercritical pressure and effect of acoustic waves. Their most recent work has considered reacting flows, however [24,27]. From their experimental effort, different flow dynamics were observed when the flame was present and when it was not. By performing spectral analysis along the LOX/hydrogen shear layer, a shift to a lower frequency was observed when a flame was present. When a flame was present, it was observed that waves in the near nozzle region the LOX jet would travel slower velocities than when a flame was not present. Beyond the LOX post recirculation zone, the waves would accelerate. The acceleration of the LOX jet waves were not observed when the flame was absent. Then they convected

Downloaded by Doug Talley on January 10, 2018 | http://arc.aiaa.org | DOI: 10.2514/6.2018-0677

at a uniform velocity. Acoustic receptivity studies performed demonstrated that the reacting flow could couple with low amplitude acoustic perturbations. It was found that the flame will physically respond to lower acoustic forcing amplitudes when driven at flame's natural frequency. Otherwise, at other than natural frequencies, it would have to driven at high pressure amplitudes for the flame to exhibit any response. Dynamic mode decomposition of the high-speed shadowgraph and unfiltered chemiluminescence captured the physical flame's response to the acoustic forcing. When the flame was subjected to acoustic pressure node (velocity anti-node) forcing, the flame had an in plane flapping response. It had a symmetric puffing response when subjected to pressure anti-node (velocity node) forcing.

Modeling efforts were included in the work of Candel et al [25-33], Yang et al [34-36], and Bellan et al [37-39]. Candel *et. al*. computational and experimental studies on reacting, cryogenic shear coaxial flows identified features of the flame's stability and dynamics. Candel *et al*. also showed that there is a minimum LOX post wall thickness necessary to achieve a stable, anchored flame that would be largely unaffected by instabilities the coaxial flow may exhibit. These results were arrived at, through a series of simulations where the effect of the Damköhler number on the flame stability was investigated be varying the annular hydrogen temperature and exit velocity, and the LOX post thickness. These simulations demonstrated that flame stability is relatively unaffected by the exit hydrogen velocity if the flame is allowed to anchor in the slow recirculation zone downstream from the LOX post. It was not until the post thickness was decreased below the hydrogen/oxygen flame thickness and the hydrogen injection temperature decreased below 100 K that the flame extinguished. Yang *et. al.* performed computations on LOX/GH2 coaxial flows under liquid rocket engine conditions. In order to account for thermodynamic properties near and above the critical point for these types of flows, they employed a Benedict-Webb-Rubin equation of state near the critical point and Soave-Redlich-Kwong otherwise in their large eddy simulations. In their simulations under trans-critical conditions, mixing between the hydrogen and LOX induces a vortical structure within the hydrogen jet that is analogous to a vortex produced by a backward facing step. When chamber pressure is increased in their simulations, vortex structures are still prevalent in the interface between both streams. They also performed simulations using methane instead of hydrogen as fuel, and vortical structures still had a large role in propellant mixing. Bellan *et. al.*[37-39] also performed studies mainly without chemical reactions, and focused mainly on temporally evolving shear layers rather than spatially evolving flows for oxygen/ hydrogen at supercritical conditions. They performed their temporal stability analysis for 1-D, two-dimensional, and three-dimensional shear layer flows. In their work, they examined each term in the vorticity equation at the oxygen/hydrogen shear layer to understand the rotational characteristics of the layer. Their results indicate that little vorticity was created on the heavier, oxygen side of the shear layer. Most of the vorticity is created was found within the hydrogen stream.

Despite the extensive work referenced above, much of which included observation of the combustion dynamics of the reacting coaxial jets, relatively little attention was paid specifically to the vortex dynamics. For the single phase coaxial flows, two types of vortices are formed, the outer annular vortex and a wake-like vortex from the inner jet. The vortices formed and their shapes are largely dependent on the velocity ratio between both streams. The initial vortex development occurs independently for both streams, but the downstream coaxial flow is controlled by the larger annular vortex. This has been argued by several researchers, where the wake-like vortices shed by the inner jet "lock-in" to the shedding frequency of the outer annular vortex. For the two-phase coaxial flows, the large annular vortices are identified as essential flow structures that enhance atomization and mixing between the light gas and the dense, heavier inner jet or core. Their role and the influence they have on reacting coaxial flow downstream is largely missing.

Thus, relatively few observations have been made specifically of the vortex dynamics in reacting multiphase coaxial jet flows. This leads one to question whether the effect of the outer shear flow vortex dynamics is as dominant in these more complex combustion flows as they are in the simpler flows. The results presented herein indicate that they can be. In this paper, high speed visible and OH* chemiluminescence imaging was used to experimentally study the unsteady aspects of LOX hydrogen coaxial jet flames at a subcritical pressure and at various momentum flux ratios. Particular attention was paid to the role of vortex dynamics and vortex/flame interactions. The experimental setup is described next.

III. Experimental Setup

The shear coaxial injector was tested in the high-pressure, windowed combustion chamber shown in figures 1 and 2. Figure 1 shows an assembly drawing of the outer chamber. The main body of the outer chamber is shown in orange. Mounted on the orange chamber are a total of six windows, consisting of two large 101 mm (4 in) diameter round sapphire windows and four oblong windows angled at 45 degree offsets. The chamber was symmetric about the vertical center plane, so only three of the windows are shown in Figure 1. Only the two (diametrically opposed) round

Downloaded by Doug Talley on January 10, 2018 | http://arc.aiaa.org | DOI: 10.2514/6.2018-0677

windows were used in this study; the oblong windows were not used. The round windows were used for high speed shadowgraphy and OH* chemiluminescence imaging, described further below. The injector flow enters from the grey flange on top and exits from the green flange on the bottom. Pressurizing nitrogen is introduced from the two grey angled attachments on the sides (see further below). On either side of the main chamber are high pressure acoustic channels shown in yellow, which are connected to and held at the same pressure as the main chamber. Piezoelectric acoustic drivers are attached internally to the grey flanges on either end. There is no flow in the channels other than the flow induced by the acoustics. In this study, the acoustic drivers were not used, so the flow in the acoustic channels was nominally stagnant. The volume of the acoustic channels was however a part of the volume into which the flows in this study were introduced, so a minimum description of the overall dimensions of the channels is provided herein for that reason.

Figure 2 shows a schematic of the internal details of the chamber. The acoustic channels constitute an inner chamber. The inner chamber is connected to and is at the same pressure as the outer chamber and cannot itself sustain any pressure difference with the outer chamber. It does, however, focus the acoustics (when present) and limits hot combustion gases from exiting into the main chamber. The outer chamber and associated pressure-containing windows and window seals are therefore not exposed to potentially damaging high temperature combustion gases. The coaxial injector is located in the center of this inner chamber and at the top. Centered around the injector are two opposed flat windows in the walls of the acoustic channel for visualization, measuring 76.2 mm (3 in) wide by 41.4 mm (1.63 in) high. A hint of these inner windows can be seen inside the round window in Figure 1. Dynamic pressure transducers can be located as shown in the rectangular inner windows to measure acoustic pressure fluctuations. These transducers were not installed for this study. In the vicinity of the coaxial injector, the inner cross section of the acoustic channel normal to the page is rectangular, 20.5 mm (0.81 in) wide (or 6.8 inner LOX post diameters) and 35.5 mm high. The end-to-end length of the acoustic channel is 0.375 m or 268 LOX post diameters. There is a round-to-rectangular transition from the acoustic drivers to the channel, but the transition is far enough away from the coaxial injector that the geometric details are not important for this study. The total volume of the inner chamber is approximately 2.7×10^6 mm^3.

The combustion chamber is pressurized using nitrogen gas from the two side inlets (which are shown in Figure 2) and does not rely on the combustion process to provide chamber pressure. This is accomplished by keeping the volume occupied by the flame small compared to the combined volume of the inner and outer chambers. This was done in order to maintain accurate control of the chamber pressure. Combustion gases exit the inner chamber through a hole in the bottom of the inner chamber and these gases together with pressurizing gases exit the outer chamber through a metering orifice (not shown) at the bottom of the outer chamber. A mixing fitting at the exit, also not shown, dilutes the combustion gas with the exiting pressurizing gas, so that the metering orifice only experiences relatively cool temperatures.

In addition to the fuel and oxidant and pressurizing nitrogen, a separately controlled nitrogen bleed is introduced through round holes in a face plate surrounding the coaxial injector on the upper wall of the inner chamber. The bleed suppresses the formation of a hot gas recirculation zone near the injector that can otherwise influence the dynamics of the reacting flow. The faceplate with the bleed holes is illustrate in Figure 3. The coaxial injector is located in the center of the plate. The inner diameter of the center LOX jet is 1.4 mm, with a LOX post thickness of 0.38 mm. The outer diameter of the hydrogen flow is 2.82 mm, giving an exit area ratio of 1.68. The diameter of the bleed holes is 0.5 mm. The nitrogen bleed is regulated to a velocity of 0.05 m/s. Also in the faceplate were slots next to the windows for window cooling. The window cooling was also nitrogen, also separately controlled, to a velocity of 0.05 m/s.

The purge and window cooling manifolds were analyzed to determine the possible presence of resonances that might affect the dynamic results reported in this paper. The resonant frequencies were found to be many times lower than the frequencies associated with these results. The gas circuit of the annular fuel manifold (hydrogen) was similarly analyzed and also found not to be acoustically active for these experiments.

All flows were regulated and metered as high pressure gases using off-the-shelf components. Following regulation and metering, the flows were subsequently chilled to the desired temperatures, for example to liquefy the oxygen, using heat exchangers cooled with liquid nitrogen. The pressurizing ambient gases were not temperature regulated and were supplied at room temperature. However, the presence of the LOX and the cooling liquid nitrogen usually produced chamber ambient temperatures that were somewhat below the room temperature. Chilling due to Joule-Thompson expansion effects was also observed.

The coaxial injector was designed to have straight passages resulting in fully developed flows at the exit, per the length criterion of Munson *et. al.* [40], namely $\frac{L}{D} \geq 4.4Re^{1/6}$. The Reynolds numbers of the fuel and oxygen exceeded 10^4 for the entire range tested, hence an L/D of over 100 was used for both propellant circuits (the annular gap thickness was used as the length scale for the coaxial hydrogen). The pressure and temperature for both LOX and hydrogen

Downloaded by Doug Talley on January 10, 2018 | http://arc.aiaa.org | DOI: 10.2514/6.2018-0677

were measured before entering the injector. The LOX jet was kept roughly at 140 K, and the hydrogen gas was chilled to 285 K prior to entering the injector. Some heat exchange occurred inside the injector internal passages due to the temperature difference. In order to minimize this heat exchange, the injector was pre-chilled. Before the hydrogen and LOX entered the injector, chilled gaseous nitrogen ran through the hydrogen circuit and liquid nitrogen ran through the LOX fed circuit for 30 minutes prior to combustion.

The chamber pressure used in these studies was 3.4 MPa (500 psia). This is considerably below the critical pressure of oxygen, so the oxygen was initially a liquid. Igniting the flows at this pressure proved to be non-trivial as most spark ignition methods do not work when a high pressure is established prior to ignition as in this experiment. The approach used was a hydrogen-air torch, ignited using a photoignition technique. See Badkahshan *et al* [42] for details about the photoignition technique.

The reacting flow was visualized with simultaneous high speed shadowgraphy and OH* chemiluminescence. The imaging arrangement is illustrated in Figure 4. The imaging systems captured the unsteadiness of the reacting flow at a framing rate of 25 kHz. The high speed shadowgraph optics were composed of a 7.6cm (3 inch) collimated light source, formed with a ThorLabs SL S202 broadband light source and a spherical 152 mm lens, imaged onto a Phantom Research v 710 with an Infinity K2 long distance microscope lens. The shadowgraph setup allows for droplets down to roughly 100 μm to be resolved. Simultaneously, OH* chemiluminescence was captured with Lambert Instruments HICATT imaged directly onto a Phantom Research v1210 camera. An UV lens (F/2.8 Cerco 2178) with a Semrock (PN FF02-320/40) optical filter were used to image the OH* emission at 308nm. An IRIG time signal synchronized the high-speed imaging and data acquisition systems. A dichroic mirror was used to reflect the UV OH* emission from the flame onto the intensifier, while allowing the visible light to pass through for the shadowgraph images. The shadowgraph camera imaged the first eight LOX diameters from the nozzle exit and the OH* chemiluminescence was imaged 14 LOX diameters from the nozzle exit. Figure 5 shows an instantaneous example image of the OH* chemiluminescence and shadowgraph image with the viewing area of the shadowgraph images compared with OH* viewing area.

The gas-to-liquid momentum flux ratio ($J = \frac{\rho U_{Gas}^2}{\rho U_{Liquid}^2}$) has been identified as a global parameter that controls the atomization and breakup a liquid jet in two phase coaxial flows [41]; hence an investigation on the dynamic mechanism of reacting hydrogen/LOX coaxial jets was principally studied by varying J. The momentum flux ratio was varied primarily by varying the hydrogen gas flow rate through the injector, while the oxygen flow rate was kept relatively constant. Momentum flux ratios ranging from 0.15 to 6 were tested. Other flow parameters are presented in table 1. Densities and surface tensions in this table were obtained from NIST Refprop thermodynamic values [43].

IV. Results and Discussions

A. Shadowgraph Features and Vortex Dynamics

Figure 6 shows a time series of the of shadowgraph images for J values of 0.15, 0.5, 2.2, and 6, arranged in columns with increasing J from left to right. Time increases from top to bottom in each figure at a time step of 40μs. Vertical shadows of various features are evident immediately downstream of the exit, as identified by the white arrows across the top. The outer shadow is the shear layer between the outer annular hydrogen flow and the nitrogen ambient. The next inner shadow is the shadow of the flame, which is attached to the LOX post. The inner dark core is that of the LOX jet itself. A gap exists between the LOX jet and the flame at the injector exit. Immediately at the exit, this is the LOX post thickness, and it can be seen that the flame anchors at the outer rim of the post, as has been reported by others [16 and 32]. Immediately downstream of the exit, the gap is occupied by a recirculation zone between the outer and inner LOX post flows. The recirculation zone is not seen in these images but has been visualized elsewhere [26]. The recirculation zone extends downstream for approximately one LOX diameter for all J's. Farther downstream of the recirculation zone, the gap is not always distinct and when present it is caused by the gaseous oxygen vaporizing from the LOX jet. These shadows become convoluted as the flow moves downstream, often losing visibility altogether. Far enough downstream, the outer layer between the hydrogen gas and the ambient nitrogen becomes replaced by the layer between the expanding hot gases from the flame and the ambient nitrogen.

The entire flow is highly unsteady, but a regular dynamic structure to the flow may be observed. Attention is drawn to the large vortex that tends to be formed in the outer annular hydrogen flow immediately downstream of the exit. The vortex is indicated by the yellow dashed arrows in the images for J = 0.15. The vortex engages both the outer shear layer and the flame and tends to grow as it evolves downstream. It also tends to be larger as J increases, or in this study, as the annular hydrogen flow rate increases. Only single formation events are shown in the high speed videos in Figure 6; in fact the vortices are regularly formed, but only quasiperiodically at frequencies ranging from 4

Downloaded by Doug Talley on January 10, 2018 | http://arc.aiaa.org | DOI: 10.2514/6.2018-0677

to 9 kHz, depending on J. The vortices are energetic enough that when they pinch in, they penetrate inside the average location of the flame and appear to impact on the LOX jet directly. When this happens a trough is observed to appear in the waves on the LOX jet, evidently caused by the locally increased vaporization rate caused by the impinging hot gases in the vortices. The trough formation is indicated by the red arrows in figure 6. Immediately after the trough is formed, an expansion wave of hot gases appears and overcomes the initial unsteady vortex. The expansion wave in the outer flow is then observed to propagate downstream slower than the trough propagates downstream in the LOX jet. It was also observed that for each test condition, the hydrogen jet would at times form smaller vortices that would convect faster. The resulting disparity in the convecting vortex velocities was observed to sometimes lead to vortex coalescence and sometimes to a vortex vanishing altogether. This behavior and its influence on the flame structures is discussed further below.

These large unsteady vortices are initially formed due to hydrodynamics instabilities in the annular hydrogen jet, and share similar dynamic and physical characteristics to that of single jets. In figure 6, the formation of the unsteady annular hydrogen vortex and its subsequent shedding begins when the outer most shear layer of the hydrogen jet curls towards the LOX jet, as discussed above. Several researchers have identified the curling of the hydrogen jet towards the LOX jet as a Kelvin-Helmholtz instability of outer shear layer. This hydrodynamic instability has been theoretically studied and experimentally investigated. Talamelli and Gavarini [11] performed linear stability analysis and their results showed that there is indeed an unstable mode associated with the annular flow and two other wake-like instabilities located at the recirculation downstream of the LOX post. Segalini and Talamelli [9] would later experimentally show that the outer shear layer demonstrated Kelvin-Helmholtz instabilities. A direct numerical simulation study by da Silva *et al* [44] showed that Kelvin-Helmholtz instabilities are responsible for the annular vortex with Strouhal numbers ranging between 0.24 and 0.5.

For the high aerodynamic Weber number$\left(\frac{\rho_{LOX}(U_{H_2}-U_{Lox})^2 D_{Lox}}{\sigma_{Lox}}\right)$ and Reynold's number of the LOX jet, the coaxial flow should have fine droplets and ligaments which may be highly fiberous in appearance [45]. The current shadowgraph optic setup allows for droplets of roughly 100 μm to be resolved, but instead the LOX jet looks glassy and smooth. No droplets or ligaments were present beyond one LOX diameter downstream of the nozzle exit. However, it was observed separately [26] that droplets and ligaments were indeed present within the recirculation zone downstream of the LOX post. These results are consistent with Mayer *et a*l [13, 16, 17], where the smoothness of the LOX jet and the lack of ligaments and droplets was attributed to the rapid vaporization of any LOX structures.

B. Vortex/Flame Interactions

Figure 7 shows the flame behavior corresponding to figure 6, taken from the simultaneous high speed OH* chemiluminescence videos. The OH* emission images are false colored to aid in visualizing the OH* emission intensity. The flame near the exit closely encircles the LOX jet and is continuous with pockets or bands of high OH* emission. As discussed further next, these bands of higher OH* chemiluminescence tend to be locations where vortex/flame interactions occur.

Visualizing the shadowgraph and the OH* images simultaneously allows the vortex/flame interactions to be examined in detail. Two different methods were used to visualize them both simultaneously in the same image. In the first method, the images are overlapped. To produce the overlapped images, the OH* chemiluminescence image was superimposed onto the shadowgraph image by controlling the transparency of the OH* image. The transparency was set by using the individual pixel counts from the OH* image, where the higher the pixel counts or brighter the pixel is, the more opaque that pixel from OH* image becomes. Hence the dimmer that pixel, the more transparent the pixel of the OH* image is. This image decomposition allows for direct comparison of the annular hydrogen vortex behavior with the increase OH* emissions, but obscures the annular vortex effects on the LOX jet. The other method, the wavelet decomposition, allows for study the effect the annular vortex/flame interaction have the LOX core. Wavelet decomposition has been previous used in the medical imaging community [46], where different imaging techniques like Computer Aided Tomography or Magnetic Resonance Imaging can be combined into a single image, while retaining important physical features of both. A wavelet transform, using a Symlet wavelet as the kernel for the decomposition, of the original shadowgraph and the original OH* chemiluminescence image were taken. The individual components from the wavelet transforms from both images were then average together and then an inverse wavelet transform was taken to produce a synthesized single image.

Overlapped and wavelet decompositions of both shadowgraphs and OH* images are shown in Figure 8 (for J = 0.15) and Figure 9 (for J = 6). The left images in each column are the overlapped image, while the right images are the wavelet decompositions. The images show the formation of the vortex in the outer hydrogen jet, and the impingement on the LOX core as it curls and pinches in. Almost immediately after impingement, within a single 40 μs frame, there is a localized increase in OH* emission. Within 1-3 frames after that, a wave trough appears in the

Downloaded by Doug Talley on January 10, 2018 | http://arc.aiaa.org | DOI: 10.2514/6.2018-0677

LOX jet due to an increased local consumption of the LOX. In the works of Mungal *et al* [47] and Breidenthal [48] they identified that the chemical reactions occur mainly in the cores of the rolled-up vortices that were formed in the shear layers. Since vortex roll-up entrains equal volumes of the propellants [49], they argue that the large scale vortices increase propellant mixing. Results presented by Savas and Gollahalli [50] and Ahn and Yu [51], showed that depending on the equivalence ratio and the Damköhler number, chemical reactions don't necessarily need to occur in the center of a vortex but can occur on the along their periphery. Candel *et al* [29, 33] showed numerically that the vaporization rate of the LOX jet is slower than that of the oxygen gas consumption by the flame. Candel *et al* [33] also showed numerically that the latent heat of vaporization of LOX has little effect on the flame and the flame cannot be quenched at the LOX surface; instead the flame moves closer to the LOX surface to increase the local vaporization of the LOX. These observations of other authors is consistent with the present results. It was also observed that the size of the trough is dependent on the size of the annular vortex formed and can lead to the breakup of the LOX jet. Figure 9 shows a large vortex breaking apart the LOX jet as it travels downstream.

C. Wave trajectories

The convection velocities of these large structures: annular hydrogen vortex, the high intensity OH* bands, the trough on the LOX jet, and the hot gas expansion waves, are on average different relative to each other. It is notable that the OH* bands convect faster than either the expansion waves or the LOX jet troughs, probably because the gaseous fuel velocity is larger than that of the LOX, while the expansion waves are confined more to the outer ambient gas. This is confirmed in figures 8 and 9.

Since they are the fastest, accordingly the trajectories of the OH* bands are analyzed here. The velocity of OH* bands or flame structures can be deduced by tracking OH* emission intensity between high speed frames. In order to track the flame structures, the pixel locations were taken along the maximum value of the standard deviation for each separate condition, as shown for example in figure 10. The raw pixel values were first subtracted by their time average and divided by the standard deviation. This ensured that if the flame structure is present, it will be represented as a peak. An example of the peak tracking is shown in figure 11 where the individual peaks and their location with respect to the flame are present. Tracking individual peaks started at 1.5 LOX diameters from the nozzle and continued to 15 LOX diameters. If individual peaks dipped below a certain threshold, they were no longer tracked. This tracking was done for 5000 images or 0.2 seconds of OH* chemiluminescence images.

By tracking the flame structures from frame to frame their unsteady behavior could be analyzed. Tracking flame structure pairs yield a set of three distinct behaviors, similar to the behaviors of the annular vortices. It was observed that a pair of flame structures can either convect together at similar velocities, coalescence when a high velocity trailing flame structure overtakes a slower one, or sometimes one flame structure in the pair completely vanishes. A chart demonstrating this behavior is shown in figure 12. Tracking the localized increases in OH* emissions as a function of time vs distance, the three flame structure pair behaviors are observed. The merging pair occurs when the vortices shed from the hydrogen jet are different sizes, with large vortices convecting slower initially. It should also be recalled that these are analyses from high-speed videos, where 10 flame structures can be observed within 2 milliseconds.

The unsteady flame structures exhibited a broad velocity range that led to the previously discussed behaviors. Velocity histograms for the OH* structure for each condition in table 1 are shown in figure 13. The vertical red and green linesin the histograms presented are the bulk averaged hydrogen and oxygen velocities, respectively, from table 1. For the lower J or low hydrogen velocity conditions, there is a narrow spread of flame structure velocities compared to the higher J conditions. Normalizing the average OH* velocity by the mean of the bulk hydrogen and LOX jet velocities per the below equation

$$V^* = \frac{\overline{V_{OH^*}}}{\frac{V_{H2,Bulk}+V_{LOX,Bulk}}{2}},$$

it can be seen that V* falls within a narrow range of 0.52 to 0.66 for all J, as plotted in Figure 14. In other words, figure 14 shows that arithmetic mean of the bulk velocity of both propellants is a good measure of the flame propagation velocity regardless of J.

A distance or wavelength between flame structures can also be deduced by tracking the distance between two flame structures convecting downstream. Discounting vortices coalescenceing or one vortex vanishing altogether, the separation or wavelength between a convecting vortex pair is roughly constant for their lifetimes, as shown in figure 12. The average the wavelength between flame structures from 4 LOX diameters to 15 LOX diameters are presented in the histograms in figure 15. The shapes of the distribution of the wavelengths in the histograms have similar shapes regardless of J. From the histograms, the majority of the convecting pairs are on average between 2 to 5 mm in

Downloaded by Doug Talley on January 10, 2018 | http://arc.aiaa.org | DOI: 10.2514/6.2018-0677

wavelength. Using these average wavelength (λ) values and the average velocity (V) from flame structure histograms from figure 13 and $V = f \lambda$, the flame structure frequency (f) are centered from 3.8 to 10 kHz, similar to the quasiperiodic frequency of the annular vortex shedding, reinforcing the connection between the annular vortex and its influence on the flame and the downstream flow.

V. Conclusions

The vortex dynamics of a liquid oxygen, gaseous hydrogen coaxial jet was investigated as a function of the outer-to-inner momentum flux ratio J. High speed shadowgraphs and OH* chemiluminescence images of the flow were taken at 25kHz. The results showed a large effect of vortices formed at the exit of the injector in the outer annular flow. These vortices formed quasiperiodically around a broad range of frequencies ranging from 4 to 9 kHz. The mechanism following vortex formation was observed to be as follows: as the outer vortex curls toward the LOX jet, it is energetic enough to penetrate past the average flame location and impinge on the LOX jet. The close presence of the hot gases next to the LOX jet causes a nearly immediate increase in OH* emission, within one frame. A few frames later, a trough in the LOX jet appears, indicating a local increase in LOX vaporization by the hot gases. A wave of expanding hot gases also appears at the same time. This outer vortex is sometimes energetic enough to sever the LOX jet entirely. All these wave structures convect downstream at different velocities, with the OH* chemiluminescence or combustion wave propagating the fastest. Measurement of the combustion wave trajectories revealed three main classes of behaviors: wave pairs that propagate together at similar velocities, wave pairs that propagate at different velocities and eventually coalesce into one wave, and wave pairs where one of the waves appears to spontaneously vanish entirely. Histograms of the wave velocities reveal a spread of velocities somewhere between the bulk velocity of the initial outer hydrogen flow and the bulk velocity of the initial inner LOX flow. The average wave velocities normalized by the average of the two initial bulk velocities were found to be independent of J to within a narrow range, between 0.52 to 0.66. Tracking the wavelengths between flame structures after the initial vortex dynamics steady out, the wavelengths between two flame structures are relatively constant between 4 to 15 LOX diameters. Using the OH* velocity and wavelength histograms, result in the similar quasiperiodic frequency observed for the annular vortex shedding. These results confirm earlier results for simpler coaxial flows without combustion that the outer flow vortex dynamics can still have a significant effect on the flow.

Downloaded by Doug Talley on January 10, 2018 | http://arc.aiaa.org | DOI: 10.2514/6.2018-0677

Acknowledgement

This work was funded by the Air Force Office of Scientific Research and conducted at the AFRL Combustion Stability Laboratory, Edwards AFB, CA. A special thanks is owed to Mr. Randy Harvey for his help during data collection

References

[1] N.W. M. Ko and A. S. H. Kwan, "The initial subsonic coaxial jets," *Journal of Fluid Mechanics*, Vol.73, 1976, pp. 305-332

[2] W. J. A. Dahm, C. E Frieler, and G. Tryggvason, "Vortex structure and dynamics in the near field of a coaxial jet," *Journal of Fluid Mechanics*, Vol. 24, 1992, pp. 371-402

[3] R. B. Wicker and J. K. Eaton, "Near Field of a Coaxial Jet With and Without Axial Excitation," *AIAA Journal*, Vol. 32, No. 3, 1994, pp. 542-546

[4] H. Rehad, E. Villermaux, and E. J. Hopfinger, "Flow regimes of large-velocity-ratio coaxial jets," *Journal of Fluid Mechanics*, Vol 345, 1997, pp. 357-381

[5] G. Balarac and O. Métais, "The near field of coaxial jets: A numerical study," *Physics of Fluids*, 2005, Vol. 17, Issue 6

[6] E. Villermaux, "Mixing and Spray Formation in Coaxial Jets," *AIAA Journal of Propulsion and Power*, Vol. 14, No. 5, 1998, pp. 807-817

[7] E. Villermaux and H. Rehad, "Mixing in coaxial jets," *Journal of Fluids Mechanics*, Vol. 425, 2000, pp. 161-185

[8] R. Örlü, A. Segalini, P. H. Alfredsson, and A. Talamelli, "Turbulence enhancement in coaxial jet flows by means of vortex shedding." *Progress in Turbulence III* , 2009, pp. 235-238.

[9] A. Segalini and A. Talamelli. "Experimental analysis of dominant instabilities in coaxial jets." *Physics of fluids* Vol. 23, no. 2, 2011

[10] A. Talamelli, A. Segalini, R. Örlü, and G. Buresti. "A note on the effect of the separation wall in the initial mixing of coaxial jets." *Experiments in fluids,* Vol. 54, no. 3 2013

[11] A. Talamelli, and I. Gavarini. "Linear instability characteristics of incompressible coaxial jets." *Flow, turbulence and combustion,* Vol .76, no. 3, 2006, pp. 221-240

[12] A. Michalke "Survey on jet instability theory." *Progress in Aerospace Sciences* Vol. 21, 1984, pp. 159-199.

[13] W. Mayer, A. Schik, M. Schäffler, and H. Tamura. "Injection and mixing processes in high-pressure liquid oxygen/gaseous hydrogen rocket combustors." *Journal of Propulsion and Power* Vol. 16, no. 5, 2000, pp. 823-828.

[14] W Mayer, A. H. Schik, B. Vielle, C. Chauveau, I, Gökalp, D, G. Talley, and R, D. Woodward. "Atomization and breakup of cryogenic propellants under high-pressure subcritical and supercritical conditions." *Journal of Propulsion and Power* Vol. 14, no. 5, 1998, pp. 835-842.

[15] W. Mayer, "Coaxial atomization of a round liquid jet in a high speed gas stream: a phenomenological study." *Experiments in Fluids* Vol. 16, no. 6, 1994, pp. 401-410.

[16] W. Mayer and H. Tamura, "Flow Visualization of Supercritical Propellant Injection in a Firing LOX/GH2 Rocket Engine," 31st AIAA/ASME/SAE/ASEE Joint Propulsion Conference, July 1995, San Diego, Ca

[17] W. Mayer and G. Krülle, "Rocket Engine Coaxial Injector Liquid/Gas Interface Flow Phenomena," 28th AIAA/ASME/SAE/ASEE Joint Propulsion Conference, July 1992, Nashville, TN

[18] W. Mayer, A. Schik, C. Schweitzer, and M. Schaeffler, " Injection and mixing processes in high pressure LOX/GH2 rocker combustors," 32nd AIAA/ASME/SAE/ASEE Joint Propulsion Conference, July 1996, Lake Buena Vista, FL

[19] S. Yeralan, S. Pal, and R. J. Santoro, "Experimental Study of Major Species and Temperature Profiles of Liquid Oxygen/Gaseous Hydrogen Rocket Combustion," *AIAA Journal of Propulsion and Power*, Vol. 17, No. 4, 2001, pp.788 - 793

[20] S. Yeralan, S. Pal, and R. J. Santoro, "Experimental Investigation of Oxygen Rich LOX/GH2 Combustion Using Linewise Raman Imaging," 36th AIAA Aerospace Sciences Meeting, 1997, Reno, NV

[21] J. M. Locke, S. Pal, R. D. Woodwards, and R. J. Santoro, "High Speed Visualization of LOX/GH2 Rocket Injector Flowfield: Hot-Fire and Cold-Flow Experiments," 46th AIAA/ASME/SAE/ASEE Joint Propulsion Conference, July 2010, Nashville, TN

[22] S. Pal, M. D. Moser, H. M. Ryan, M. J. Foust, and R. J. Santoro, "Shear Coaxial Injector Atomization Phenomena for Combusting and Non-Combusting Conditions," *Atomization and Sprays*, Vol. 6, 1996, pp. 227-244

[23] B. Chehroudi, "Recent Eperimental Efforts on High-Pressure Supercritical Injection for Liquid Rockets and their Implications," *International Journal of Aerospace Engineer*, 2012

[24] D. J Forliti, I. A. Leyva, D. G. Talley, J. I. Rodriguez, S. Teshome, J. L. Wegener, M. Roa, A. R. Karagozian," Forced and unforced shear coaxial mixing and combustion at subcritical and supercritical pressures," AIAA Book Chapter, Submitted 2017

[25] J. L. Wegener, D. J. Forliti, I. A. Leyva, and D. G. Talley, " Receptivity of a Cryogenic Coaxial Liquid jet to Acoustic Disturbances," 26th ILASS Americas, May 2014, Portland, OR

[26] M. Roa, D. J. Forliti, A. Badakhshan, and D. Talley, "Acoustically Forced Coaxial Hydrogen/Liquid Oxygen Jet Flames," 28th ILASS Americas, May 2016, Dearborn, MI

[27] D.J. Forliti, A. Badakhshan, J. L. Wegener, I. A. Leyva, and D. G. Talley," The Response of Cyrogenic H2/O2 Coaxial Jet Flames to Acoustic Disturbances," 53rd AIAA Aerospace Sciences Meeting, Kissimmee, FL.

[28] M. Juniper, A. Tripathi, P. Scouflaire, J-C. Rolon, and S. Candel, "Structure of Cryogenic Flames at Elevated Pressures," Proceedings of the Combustion Institute, Vol. 28, 2000, pp. 1103-1109

[29] R. Snyder, G. Herding, J-C, Rolon, and S, Candel, "Analysis of Flame Patterns in Cryogenic Propellant Combustion," *Combustion Science and Technology*, Vol 124, 1997, pp. 331-370

[30] S. Candel, G. Herding, R. Synder, P. Scouflaire, C. Rolon, L. Vingert, M. Habiballah, F. Grisch, M. Péalat, P. Bouchardy, D. Stepowski, A. Cessou, and P. Colins, " Experimental Investigation of Shear Coaxial Cryogenic Jet Flames," *AIAA Journal of Propulsion and Power*, Vol. 14, No. 5, 1998, pp. 826-834

[31] G. Singla, P. Scouflaire, C. Rolon, and S. Candel, "Planar laser-induced fluorescence of OH in high-pressure cryogenic Lox/GH2 jet flames," *Combustion and Flame*, Vol. 144, 2006, pp. 151-169

[32] G. Herding, R. Synder, P. Scouflaire, C. Rolon, and S. Candel, "Flame Stabilization in Cryogenic Propellant Combustion," 26th Symposium on Combustion, 1996, pp. 2041-2047

[33] M. Juniper and S. Candel, "Edge Diffusion Flame Stabilization Behind a Step over a Liquid Reactant," *AIAA Journal of Propulsion and Power*, Vol. 19, No. 3, 2003, pp.332-341

[34] N. Zong, and V. Yang, " A numerical study of High-Pressure Oxygen/Methane Mixing and Combustion of a Shear Coaxial Injector," 43rd AIAA Aerospace Sciences Meeting, Reno, NV

Downloaded by Doug Talley on January 10, 2018 | http://arc.aiaa.org | DOI: 10.2514/6.2018-0677

[35] J. C. Oefelein and V. Yang, " Modeling High-Pressure Mixing and Combustion Processes in Liquid Rocket Engines," *AIAA Journal of Propulsion and Power*, Vol. 14, NO. 5, 1998, pp.843-857

[36] N. Zong and V. Yang, "Cyrogenic Fluid Jets and Mixing Layers in Transcritical and Supercritical Environments," *Combustion Science and Technology*, Vol 178, 2006, pp. 193-227

[37] N. Okong'o, K. Harstad, and J. Bellan, " Direct Numerical Simulations of O2/H2 Temporal Mixing Layers Under Supercritical Conditions," *AIAA Journal*, Vol. 40, No.5, pp. 914 -926

[38] N. Okong'o and J. Bellan, " Real-Gas Effects on Mean Flow and Temporal Stability of Binary-Species Mixing Layers," *AIAA Journal*, Vol. 41, No. 12, 2003, pp. 2429-2443

[39] N. Okong'o and J. Bellan, " Turbulence and fluid-front area production in binary-species, supercritical, transitional mixing layers," *Physics of Fluids*, Vol. 16, 2004

[40] B. R. Munson, A. P. Rothmayer, T. H. Okiishi, and W.W. Huebsch. **Fundamental Fluid Mechanics**. Wiley, 5th edition, 2005.

[41] M. F. Marinet and E. B. C. Schettini, "The density field of coaxial jets with large velocity ratio and large density differences," *International Journal of Heat and Mass Transfer*, Vol. 44, 2001, pp. 1913-1924

[42] A. Badakshan and S. Danczyk, "Ignition of Nanoparticles by a Compact Camera Flash," DTIC http://www.dtic.mil/dtic/tr/fulltext/u2/a614547.pdf

[43] Standard Reference Data, NIST Reference Fluid Thermodynamic and Transport Properties Database (Refprop), Matlab Verison

[44] C. da Sailva, G. Balarac, and O. Métais, "Transition in high velocity ratio coaxial jets analysed from direct numerical simulations," *Journal of Turbulence*, Vol. 4, 2003

[45] J. C. Lasheras and E. J. Hopfinger, "Liquid Jet Instability and Atomization in a Coaxial Gas Stream," *Annual Review of Fluid Mechanics,* 2000

[46] G. Pajares and J. M. de la Cruz, " A wavel-baed image fusion tutorial," *The Journal of Pattern Recognition Society*, Vol. 37, 2004, pp.1855-1872

[47] M. G. Mungal and P. E. Dimotakis, "Mixing and Combustion with Low Heat Release," *Journal of Fluid Mechanics*, Vol. 148, 1984, pp. 349-382

[48] J. E. Broadwell and R. E. Briedenthal, "A Simple Model of Mixing and Chemical Reaction in a Turbulent Shear Layer," *Journal of Fluid Mechanics*, Vol. 125, 1982, pp. 397-410

[49] P. E. Dimotakis, "Two-Dimensional Shear-Layer Entrainment," *AIAA Journal*, Vol. 24, No. 11, 1986, pp. 1791-1796

[50] Ö. Savas and S. R. Gollahalli, "Flow Structue in Near-Nozzle Regiong of Gas Jet Flames," *AIAA Journal,* Vol. 24, No. 7, 1986, pp. 1137-1140

[51] K. Ahn and K. H Yu, "Effects of Damköhler number on vortex-flame interactions," *Combustion and Flame*, Vol. 159, 2012, pp. 686-696

Downloaded by Doug Talley on January 10, 2018 | http://arc.aiaa.org | DOI: 10.2514/6.2018-0677

Images, Tables, and Charts

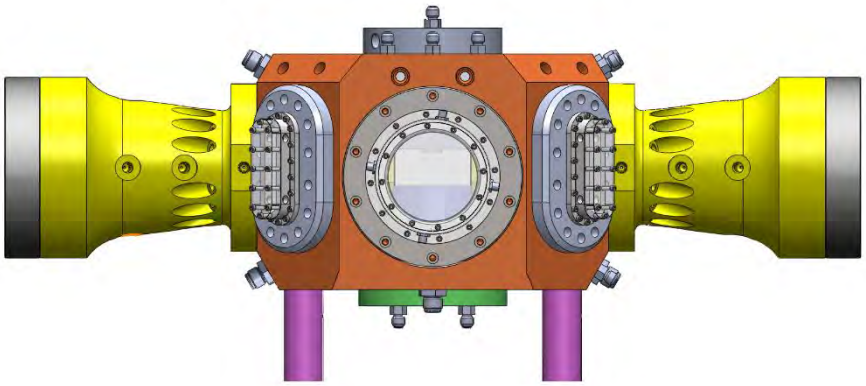

Figure 1. Assembly drawing of the combustion chamber.

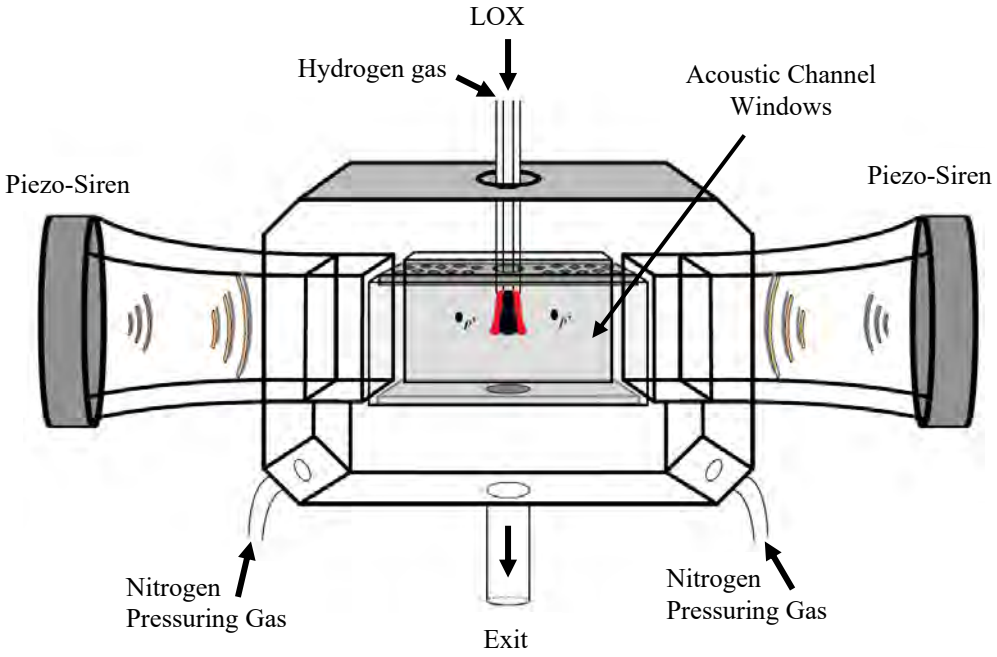

Figure 2. Inner details of the combustion chamber.

Downloaded by Doug Talley on January 10, 2018 | http://arc.aiaa.org | DOI: 10.2514/6.2018-0677

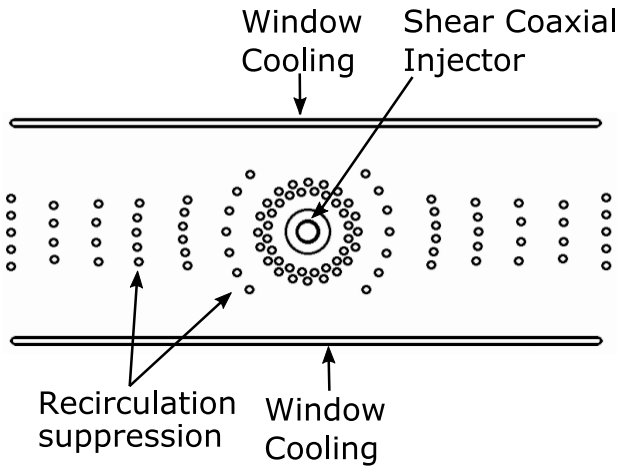

Figure 3 The injector faceplate including bleed ports.

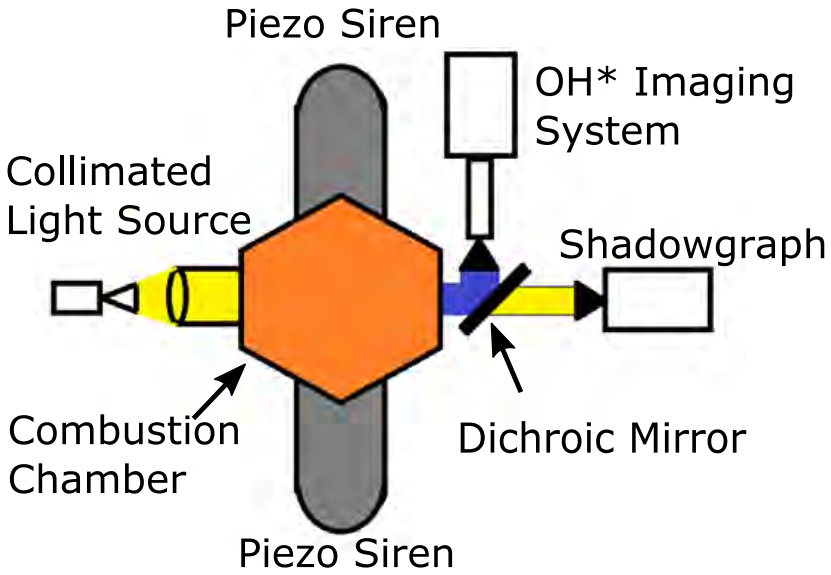

Figure 4 High speed, simultaneous imaging system layout.

Downloaded by Doug Talley on January 10, 2018 | http://arc.aiaa.org | DOI: 10.2514/6.2018-0677

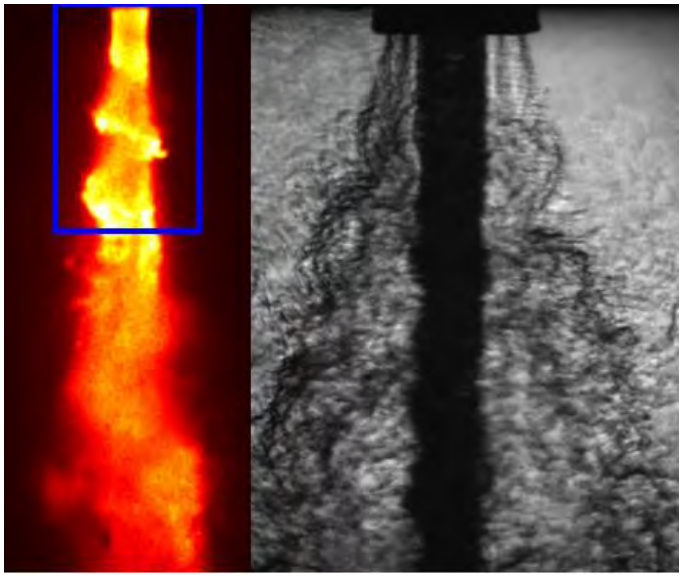

Figure 5 An instantaneous OH* emission image with its corresponding shadowgraph image. The box is the viewing area of shadowgraph compare to the OH* image.

Table 1 Operating Conditions

J	LOX Injection Temp [K]	GH2 Injection Temp [K]	LOX Injection Bulk Velocity (m/s)	GH2 Injection Bulk Velocity (m/s)	Aerodynamics Weber # $We = \frac{\rho_{LOX}(U_{H2} - U_{Lox})^2 D_{Lox}}{\sigma_{Lox}}$
0.15	140	287	4.7	27.5	8000
0.5	143	287	4.9	57.5	40700
1	144	282	5.5	94	115000
2.2	138	287	3	82	108000
4	144	287	3.2	89	120500
6	144	288	2.4	89	115000

Downloaded by Doug Talley on January 10, 2018 | http://arc.aiaa.org | DOI: 10.2514/6.2018-0677

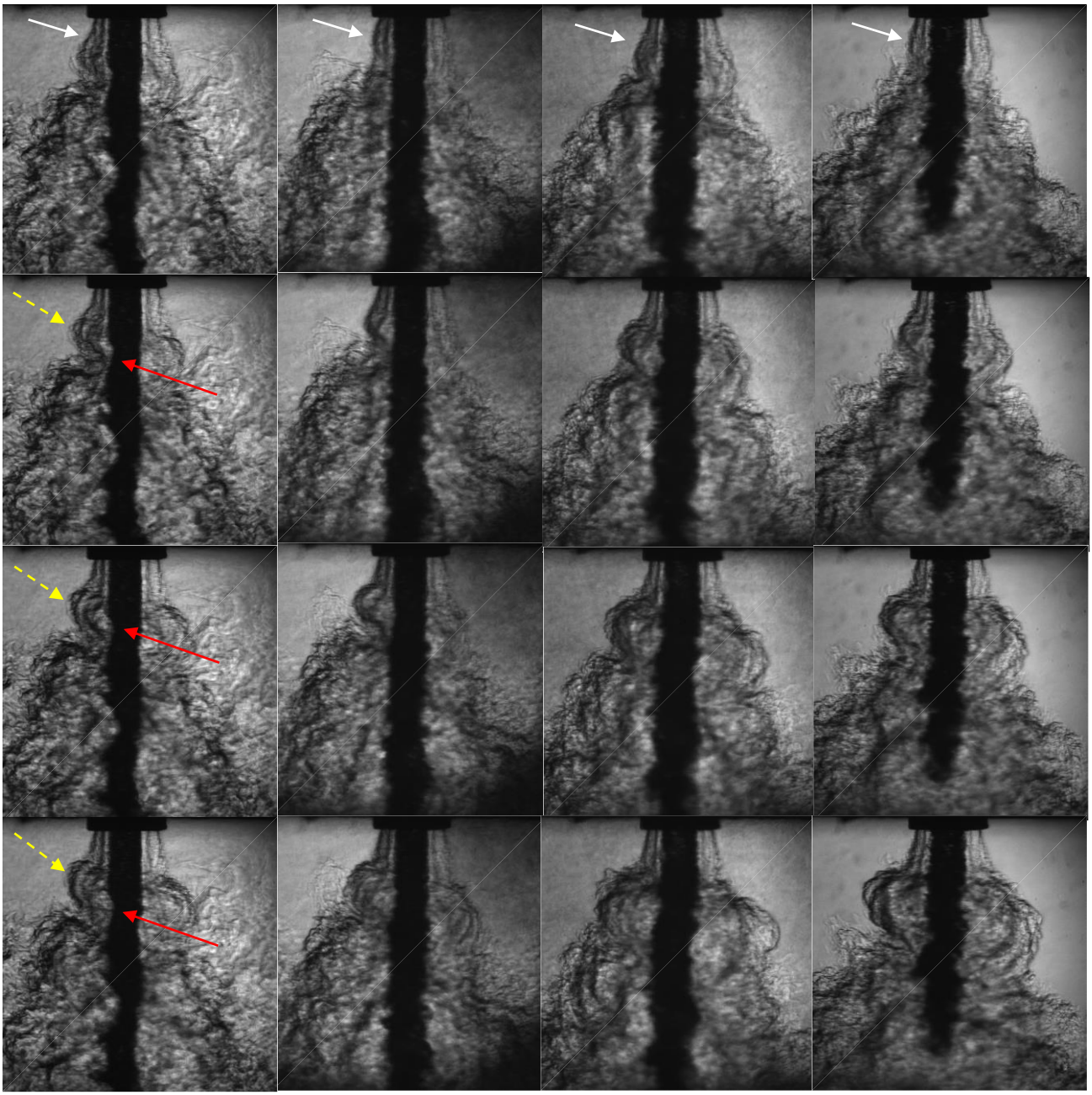

Figure 6 Instantaneous shadowgraphs of the coaxial flames. Each column corresponds to a different J of 0.15, 0.5, 2.2, and 6 from left to right. Time progresses from top to bottom in each column at an interval of 40 μs. The white arrow near the injector exit points to the two shadows formed by density gradient from the outer hydrogen jet with the surrounding nitrogen and an inner one where the flame is located. The dashed-yellow arrows points to the developing annular vortex. The red arrows point to the trough developed on the LOX core due to the outer shear layer pinching in and the developing vortex.

Downloaded by Doug Talley on January 10, 2018 | http://arc.aiaa.org | DOI: 10.2514/6.2018-0677

Downloaded by Doug Talley on January 10, 2018 | http://arc.aiaa.org | DOI: 10.2514/6.2018-0677

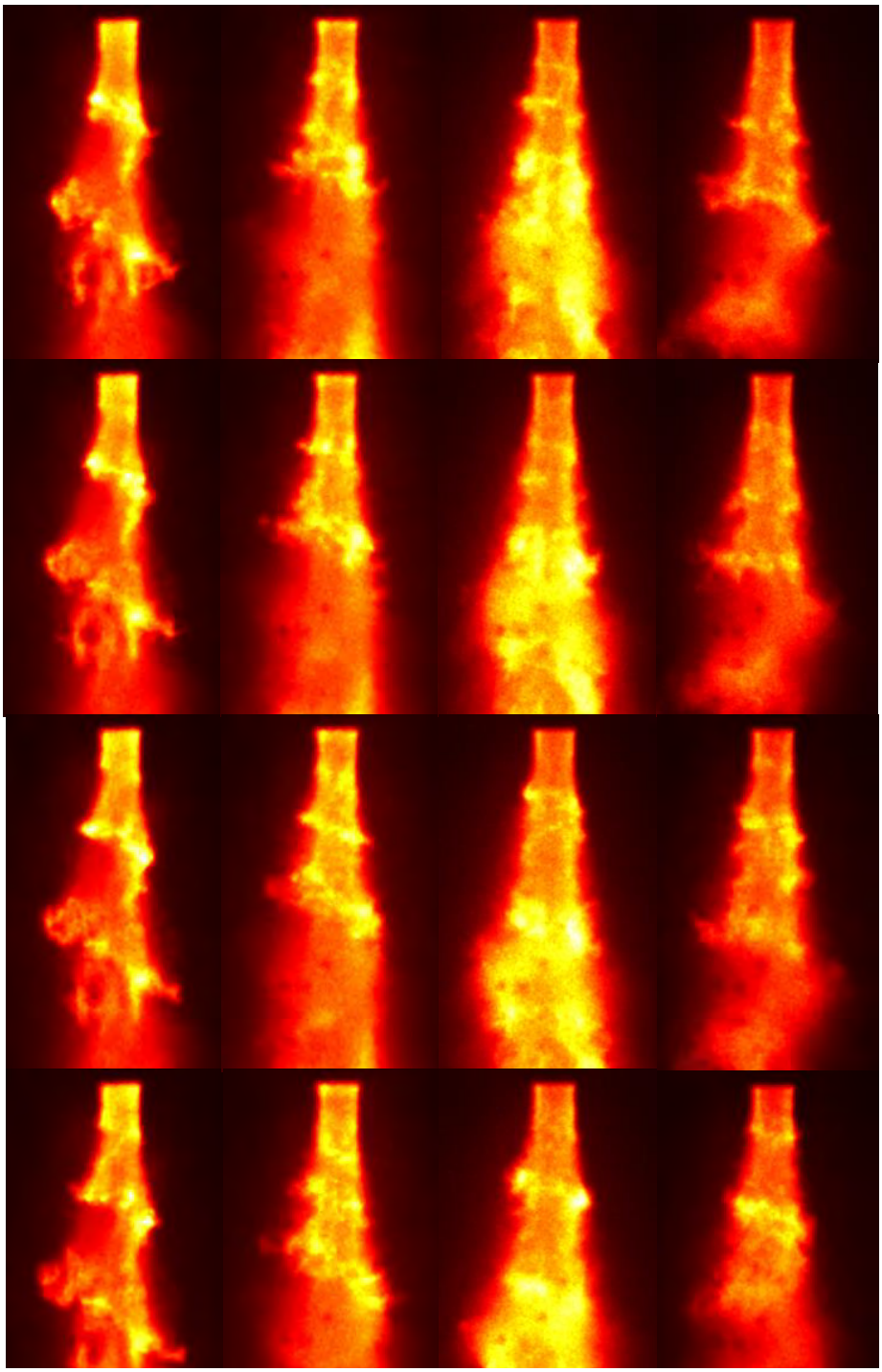

Figure 7 OH* chemilimunescence images corresponding to Figure 6. Yellower regions indicate relative increased in OH* emission.

Downloaded by Doug Talley on January 10, 2018 | http://arc.aiaa.org | DOI: 10.2514/6.2018-0677

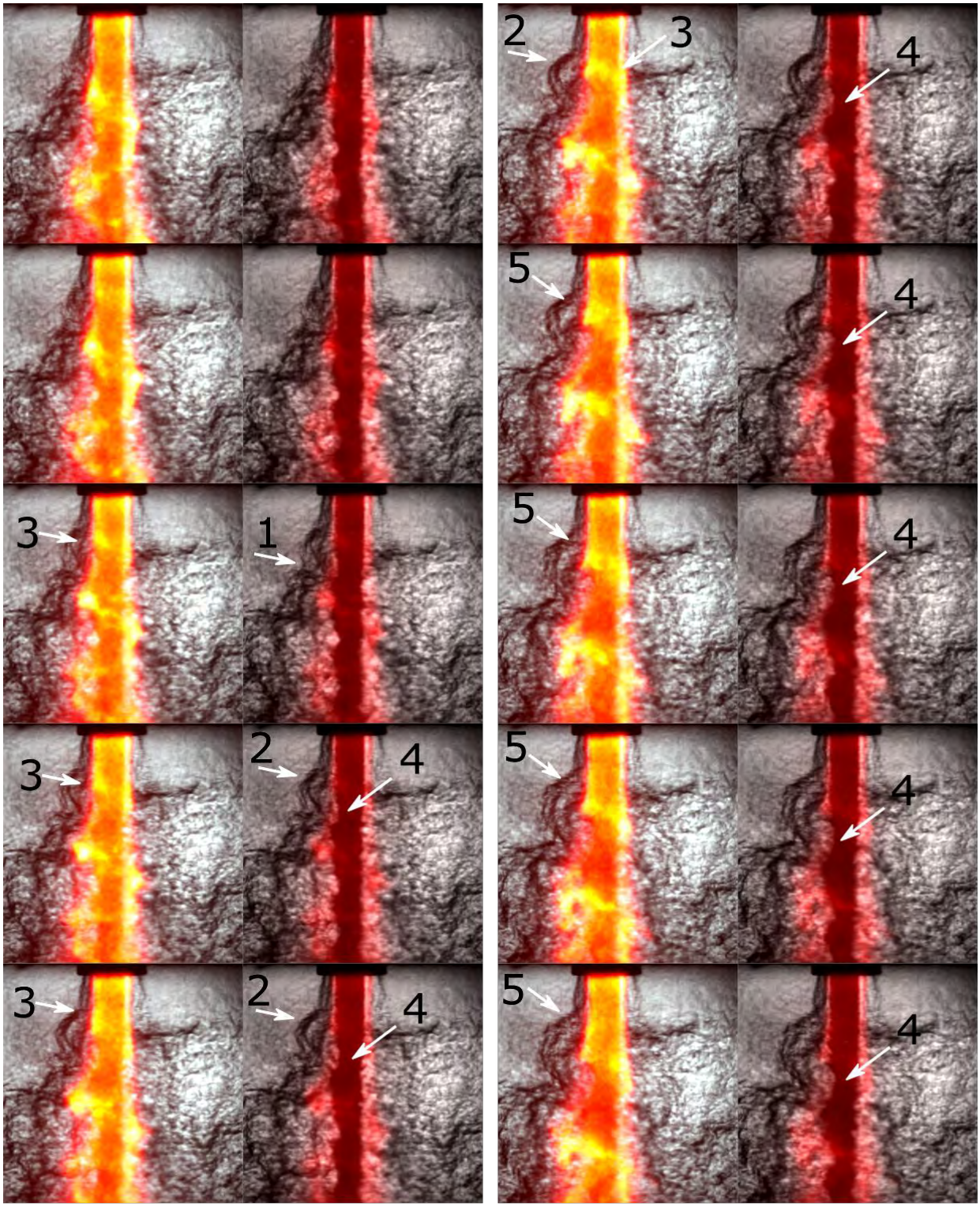

Figure 8 Overlapped (left) and wavelet fused (left) images of the shadowgraph and OH* emission for the J = 0.15 . Time increases from top to bottom, first in the left column and then the right column. The makers indicate (1) impingement on the LOX jet, (2) the formation of the annular hydrogen vortex, (3) the almost immediate local increase in OH* emission, (4) formation of a trough in the LOX jet, and (5) the combustion gas expansion wave.

Downloaded by Doug Talley on January 10, 2018 | http://arc.aiaa.org | DOI: 10.2514/6.2018-0677

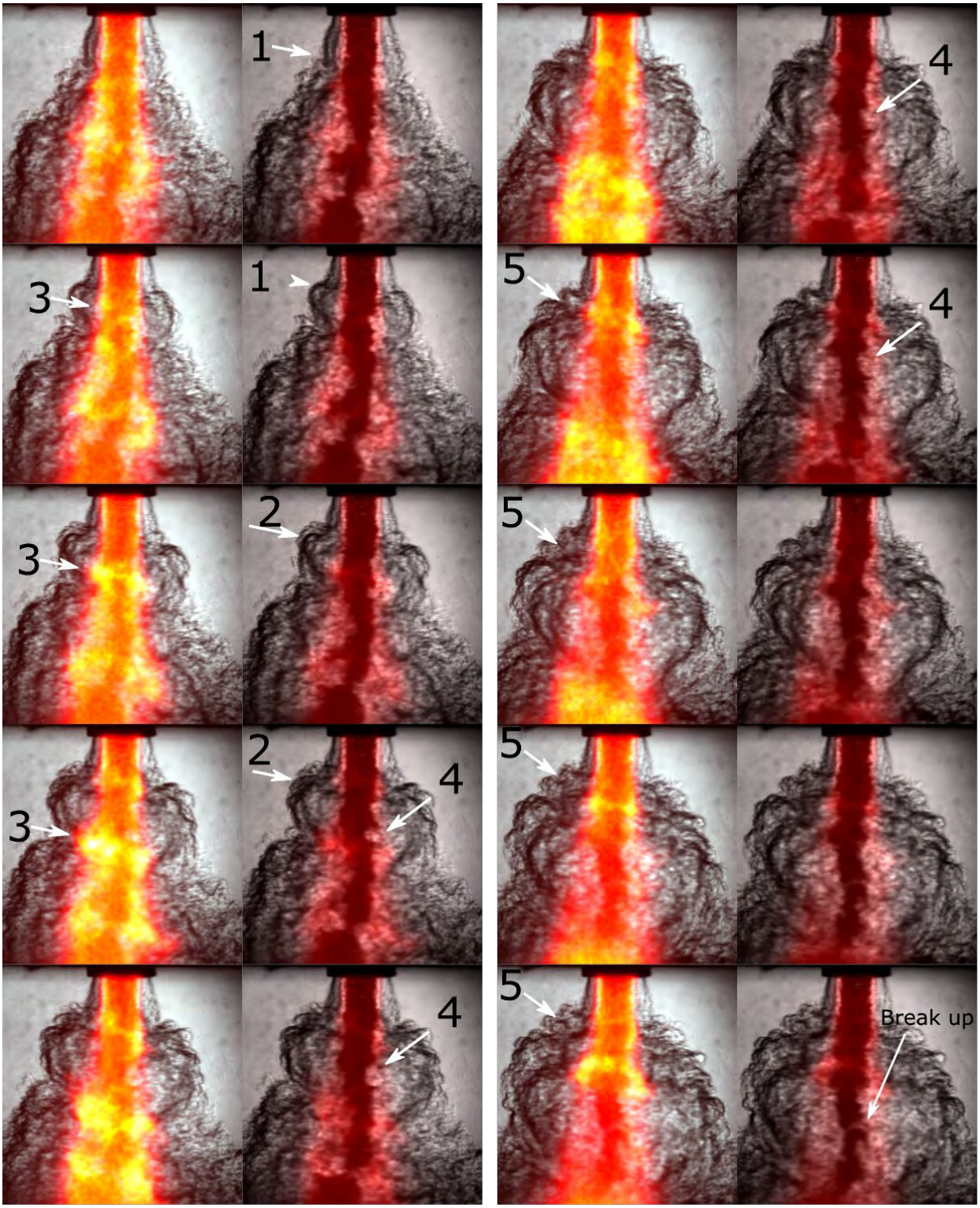

Figure 9 Overlapped (left) and wavelet fused (right) images of the shadowgraph and OH* emission for the J = 6. See caption from Figure 8. The breakup of the LOX jet is also indicated.

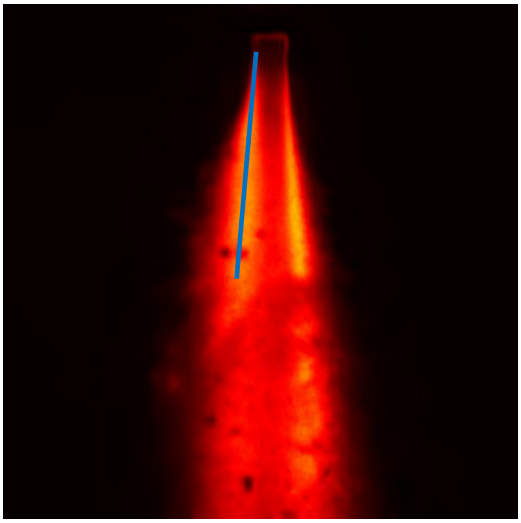

Figure 10 The standard deviation image for J of 0.15 with respect to time. The pixel locations for instantaneous velocity measurements were taken along the blue line plotted over the maximum value of the standard deviation.

Downloaded by Doug Talley on January 10, 2018 | http://arc.aiaa.org | DOI: 10.2514/6.2018-0677

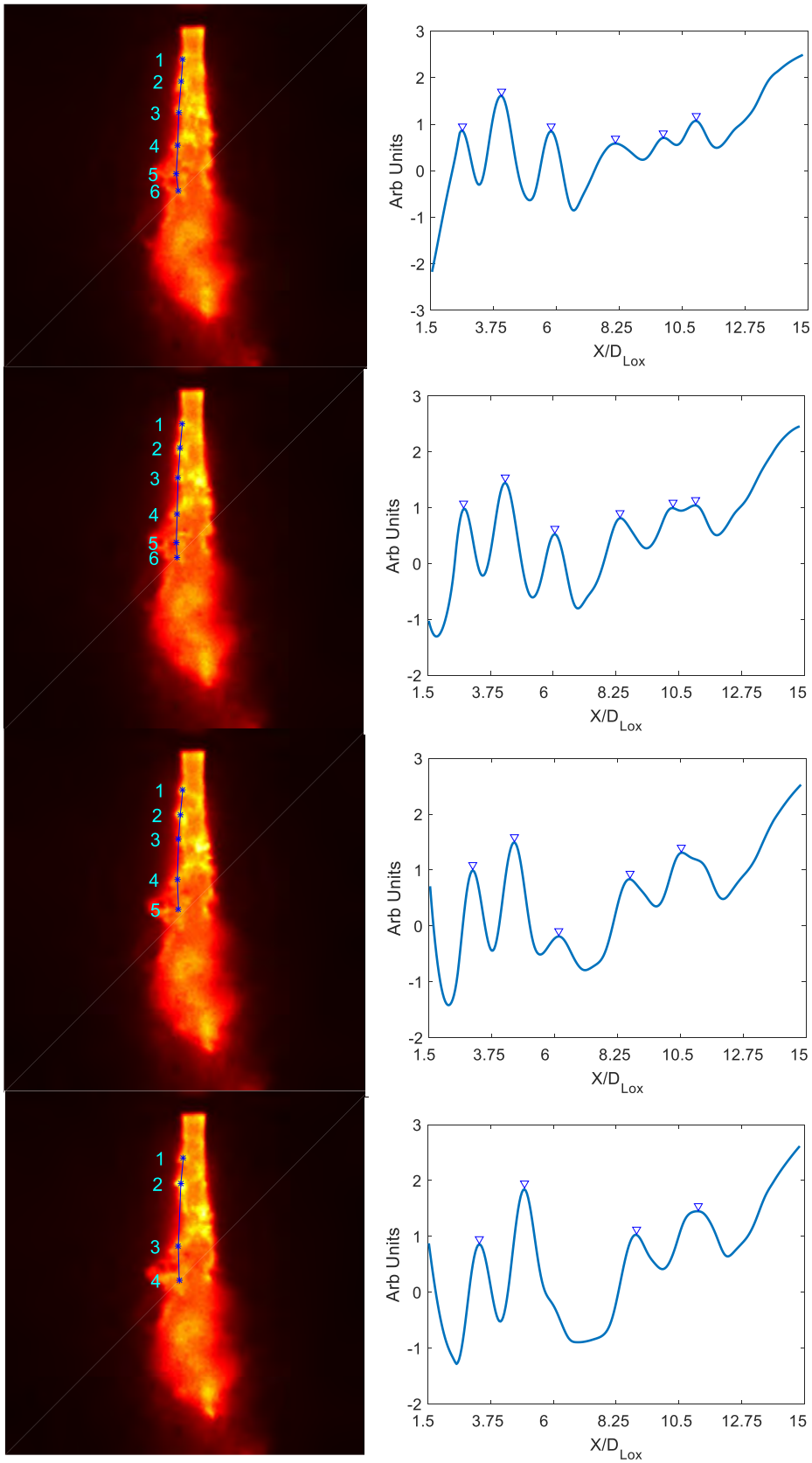

Figure 11 An example of tracking method employed to locate the localized increase of OH* emission. The column on the left are sequential images with the OH* emission peaks located by the developed method with each OH* emission peak labeled. To the right are intensity values of the OH* emission and the location of the peaks. The peaks demonstrate that the vortex flame structure moves downstream, merge, and randomly vanish.

Downloaded by Doug Talley on January 10, 2018 | http://arc.aiaa.org | DOI: 10.2514/6.2018-0677

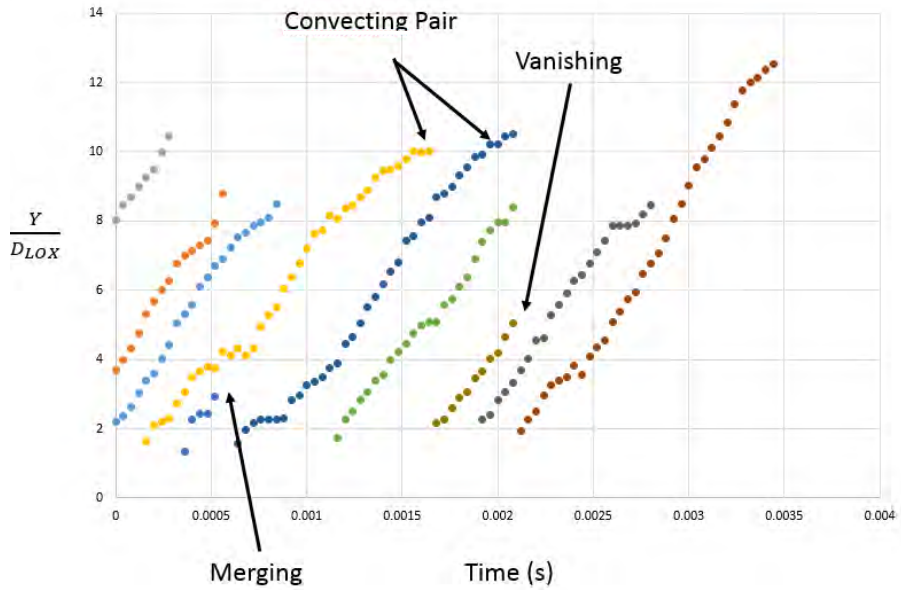

Figure 12 Individual vortices for the J of 0.15 condition are tracked by localized OH* emission increase. The position of each vortex is plot as a function of time. The three vortex pair behavior are present of convecting pair, merging pair, and a single vanishing vortex

Downloaded by Doug Talley on January 10, 2018 | http://arc.aiaa.org | DOI: 10.2514/6.2018-0677

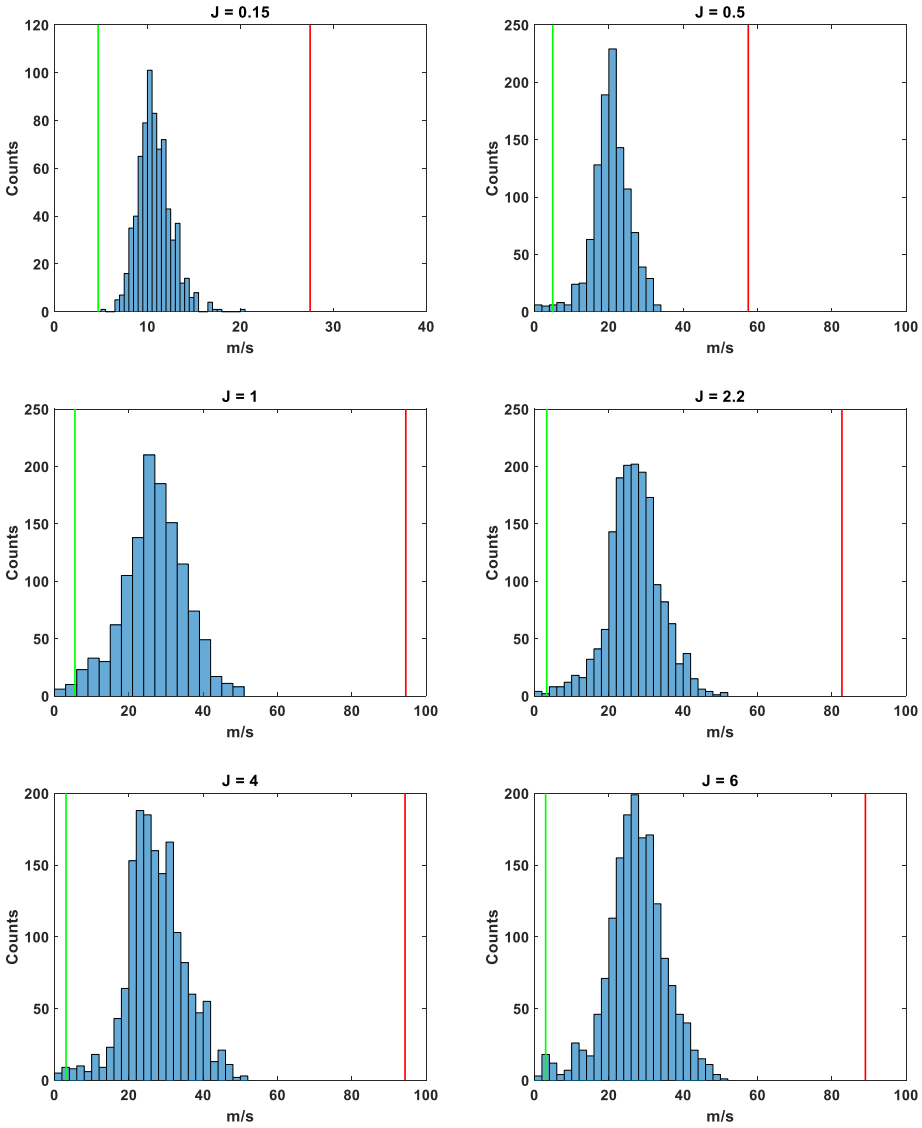

Figure 13 The velocity distributions of the OH* flame structures. The vertical green and red lines are bulk oxygen and hydrogen velocity, respectively, on table 1. The average speed of these flame structures is less than half of the bulk hydrogen velocity.J of 0.15 is not on the same scale as the rest of the J conditions.

Downloaded by Doug Talley on January 10, 2018 | http://arc.aiaa.org | DOI: 10.2514/6.2018-0677

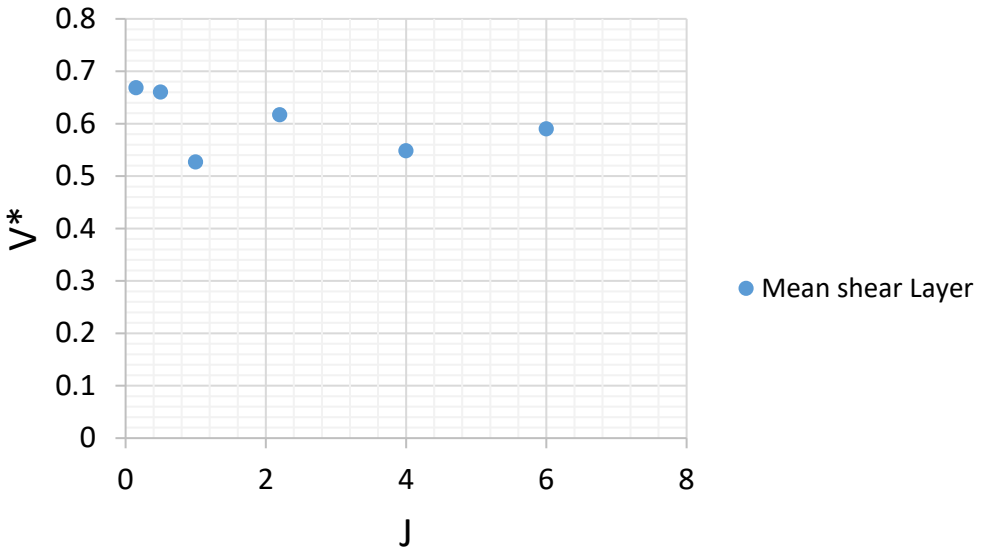

Figure 14 The OH* velocity normalized by the mean of the bulk hydrogen and LOX jets.

Downloaded by Doug Talley on January 10, 2018 | http://arc.aiaa.org | DOI: 10.2514/6.2018-0677

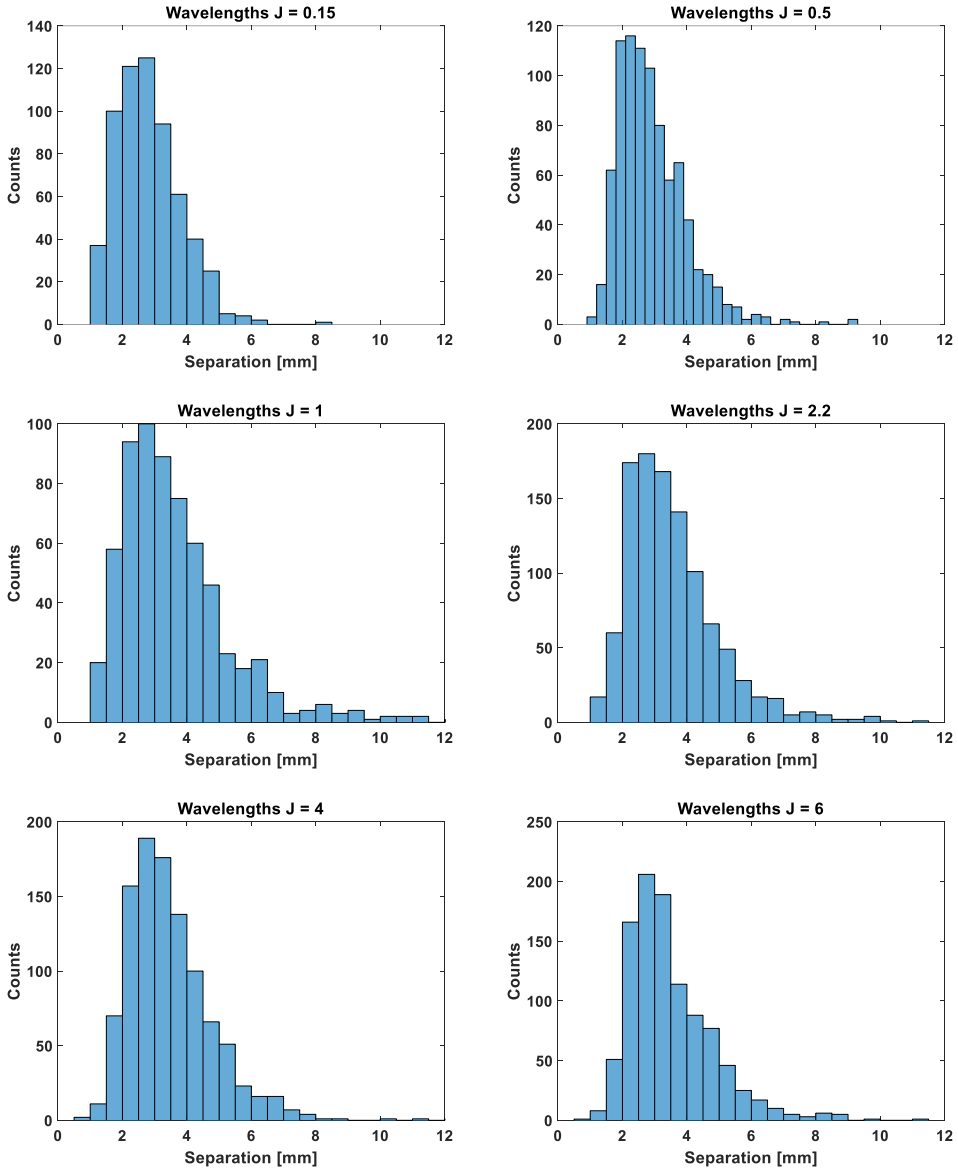

Figure 15The wavelength between OH* emission bands or the average distance between flame structures.

Downloaded by Doug Talley on January 10, 2018 | http://arc.aiaa.org | DOI: 10.2514/6.2018-0677

JOURNAL OF PROPULSION AND POWER
Vol. 35, No. 2, March–April 2019

Wave Dynamic Mechanisms in Coaxial Hydrogen/Liquid-Oxygen Jet Flames

Mario Roa*
Sierra Lobo, Inc., Edwards Air Force Base, California 93524
and
Douglas G. Talley†
U.S. Air Force Research Laboratory, Edwards Air Force Base, California 93524

DOI: 10.2514/1.B37079

Coaxial gaseous hydrogen/liquid-oxygen jet flames were studied experimentally as a function of the outer-to-inner momentum flux ratio J using high-speed shadowgraphy and hydroxyl radical (OH*) chemiluminescence imaging at 25 kHz. Particular attention was paid to wave dynamic mechanisms that could be observed. It was found that large structures generated at the exit of the annular flow created a chain of events that had a strong effect on the flame. These structures were found to impinge on the liquid-oxygen core and created local increases in OH* emission (interpreted as combustion waves), local troughs in the liquid-oxygen core caused by increased vaporization, and waves composed of expansion gases: all of which convected downstream at different velocities, with the combustion wave propagating the fastest. The combustion waves were found to sometimes merge, sometimes spontaneously disappear, or sometimes continue to propagate as pairs. Earlier results had shown the importance of large-scale structure dynamics in the outer flow to simpler nonreacting coaxial flow. These results also confirmed their importance in combusting flows.

Downloaded by Doug Talley on April 16, 2019 | http://arc.aiaa.org | DOI: 10.2514/1.B37079

Nomenclature

D	=	diameter
f	=	frequency, Hz
J	=	momentum flux ratio; outer jet to inner jet momentum flux
l	=	length
Re	=	Reynolds number
U	=	velocity, m/s
We	=	Weber number
Λ	=	wavelength, m
ρ	=	density, kg/m^3
σ	=	surface tension, N/m

I. Introduction

COAXIAL jets have been investigated extensively because of their great many uses in engineering applications. Coaxial jets have a simple geometry of concentric flows, in which an outer, annular jet of one fluid encircles an inner round jet of another, and the two streams are introduced at generally different flow rates. The shear forces between the two fluids can then produce effective mixing between the fluids. Despite their relative geometric simplicity, coaxial jets have been observed to exhibit a complex range of behaviors, depending on their configuration. An experimental investigation is made in this paper of the particular configuration of a burning gaseous hydrogen annular flow and a liquid-oxygen central jet with relevance to liquid rocket engines. Particular attention is paid to the role of large structures formed by the outer hydrogen jet on this flow. A more detailed literature review is presented next.

Presented as Paper 2018-0677 at the 2018 AIAA Aerospace Sciences Meeting, AIAA SciTech Forum, Kissimmee, FL, 8–12 January 2018; received 30 January 2018; revision received 24 September 2018; accepted for publication 3 October 2018; published online 24 December 2018. This material is declared a work of the U.S. Government and is not subject to copyright protection in the United States. All requests for copying and permission to reprint should be submitted to CCC at www.copyright.com; employ the ISSN 0748-4658 (print) or 1533-3876 (online) to initiate your request. See also AIAA Rights and Permissions www.aiaa.org/randp.

*Research Scientist, 10 E. Saturn Blvd. Member AIAA.
†Research Physical Scientist, 10 E. Saturn Blvd. Member AIAA.

II. Literature Review

In simpler coaxial jet configurations, both fluids are of the same phase: either both gas or both liquid. Early investigations by Ko and Kwan [1] of coaxial gaseous jets showed that, far enough downstream, the flow had similar mean velocity profiles to that of single jets. They also identified a near-nozzle region within the outer jet in which high-frequency vortices were present, exhibiting similar vortex shedding frequencies as single jets. Dahm et al. [2] further investigated the vortex behavior emerging from the nozzle exit with detailed images for uniform density liquid coaxial jets. The outer and inner jets and their vortices were visualized with two-color planar laser-induced fluorescence, with each jet's fluorescence different to help distinguish both jets. By varying the velocity ratio between both streams, Dahm et al. observed changes in the vortex pattern emerging from the nozzle exit for the inner jet. They observed changes in the sizes of the vortices shed and their orientations; they also observed a "lock-in" phenomenon between the inner and outer vortices. Dahm et al. also investigated the influence of the jets' absolute velocities while keeping the velocity ratio unchanged, and they observed dramatic differences of the vortex structures formed by the inner jet. They argued that the changes to the emerging vortex pattern were the origin of instability where the instability could be due to shear, similar to Kelvin–Helmholtz, or wakelike instability of vortices shedding into a wake. In the case of the inner jet for a coaxial configuration, the wakelike instability occurred when vortices were shed due to a velocity inflection point associated with the recirculation zone behind a bluff body or, in this case, the recirculation zone downstream of the finite-thickness tube separating the inner jet from the outer jet. Dahm et al. also observed that, regardless of the inner shear vortices formed, the outer vortices appeared to govern the downstream flow dynamics. Later flow visualization experiments of gas-on-gas coaxial jets performed by Wicker and Eaton [3] would show similar vortex behavior and the governing nature of the outer jet vortex. Wicker and Eaton showed that the initial vortex development occurred independently for both the outer and inner shear layers; but, when an outer large-scale vortex structure formed, it would ultimately govern the flow downstream. Experiments performed by Rehab et al. [4] showed that the vortex topology emerging from the nozzle exit was strongly influenced by the nozzle geometry because different nozzle geometries induced variations in the shapes of the shear layers. Direct numerical simulations by Balarac and Métais [5] studied the nozzle geometry effect on the vortex behavior by changing the momentum thickness between both jets and arrived at

similar results to those of Rehab et al. [4]. Mixing studies performed by Villermaux [6] and Villermaux and Rehab [7] showed that destabilization of the outer jet was responsible for entraining and mixing with the inner jet. Rehab et al. [4] showed that the shape of the velocity profile, specifically the size of the vorticity layer thickness between the shear layers, set the growth rate of the vortex.

Experimental studies and a linear stability analysis performed by Örlü et al. [8], Segalini and Talamelli [9], Talamelli et al. [10], and Talamelli and Gavarini [11] explored these vortex instabilities in gaseous coaxial jets. The early experiments performed by Talamelli et al. [10] would show that the central jet wall thickness had a role in the vortex shedding behavior. They showed that, when the central wall thickness was decreased, the vortex shedding was dominated by shear-layer instabilities and not wakelike instabilities for thick walls. Talamelli and Gavarini [11] used a family of hyperbolic tangent velocity profiles, similar to Michalke [12], in their linear stability analysis. They showed that there were three unstable modes present in coaxial jets [11]. The first mode pertained to the outer jet and had an instability similar to the Kelvin–Helmholtz instability. The other two modes were wakelike. The wakelike instabilities were formed due to the presence of a physical barrier between the jets or the central jet wall thickness. In later experimental work, Segalini and Talamelli [9] systematically varied the velocity ratio between both jets to investigate the instabilities previously predicted. They observed that, for high outer to inner velocity ratios (greater than 1.6), the inner shear-layer vortices locked into the shedding frequency of the large outer shear vortices, which was similar to the work of Dahm et al. [2]. For the intermediate velocity ratios, between 0.75 and 1.6, a von Kármán street was formed in the inner shear layer behind the inner wall.

A more complex variant of coaxial jets is the case in which the two fluids are introduced and have different thermodynamic phases: one a liquid, and one a gas. A further complexity is introduced when chemical reactions occur between the fluids, as in combustion. The particular configuration of concern here is relevant to liquid rockets, in which the outer flow is a gaseous fuel and the inner flow is a liquid oxidant. Gaseous hydrogen (GH2) is considered here as the gaseous fuel and liquid oxygen (LOX) is considered as the liquid oxidant.

Relative to this configuration and this study, Mayer et al. [13–15], Mayer and Tamura [16], Mayer and Krülle [17], and Mayer et al. [18] experimentally investigated reacting cryogenic oxygen (LOX) and GH2 shear coaxial flows at chamber pressures up to 10 MPa. They observed that, when the chamber pressure approached and exceeded the oxygen's critical pressure, there were remarkable differences between the subcritical and supercritical physical flow features. For pressures exceeding oxygen's critical pressure of 5 MPa, which are typical for liquid rocket engines, LOX droplets that would otherwise form due the shearing forces and other hydrodynamics instabilities in subcritical flows were no longer present. Instead, at supercritical pressures, the interface between the center LOX jet and the annular hydrogen jet was highly diffuse. They also observed the formation of a recirculation zone downstream from the LOX tube wall, and that it served as the flameholding region.

Research efforts at Pennsylvania State University [19–22] explored the atomization and droplet velocities from reacting and nonreacting LOX/GH2 coaxial flows at high pressure using a phase Doppler particle analyzer. Their results show that for an axial distance of 11.1 LOX diameters away from the injector face for reacting conditions, they measured a limited number of LOX droplets ($\leq$10 droplets). Their results showed that the LOX droplet sizes were, on average, larger for the reacting condition when compared to the nonreacting conditions. They would confirm the lack of LOX droplets with high-speed imaging of the LOX core. Major species and temperature profiles were also measured using Raman spectroscopy 37 LOX diameters away from the nozzle exit. They measured the relative constant average hydrogen and water mole fractions and temperatures radially across the coaxial flow. Missing from their experimental results were temporally resolved observations of how the hydrodynamics and flame interacted, which this study addresses.

A significant amount of work was performed at the U.S. Air Force Research Laboratory [23–27]. The majority of the research was performed on a single coaxial jet using liquid nitrogen and gaseous nitrogen as propellant stimulants for rocket injector studies. The majority of that work, however, concerned nonreacting flows; but, it did investigate the effects of subcritical and supercritical pressures and effects of acoustic forcing. The most recent work considered reacting flows, however [24,27]. From the experimental efforts, different flow dynamics were observed when the flame was present and when it was not. By performing spectral analysis along the LOX/hydrogen shear layer, a shift to a lower frequency was observed when a flame was present. When a flame was present, it was observed that waves in the near-nozzle region of the LOX jet would travel at slower velocities than when a flame was not present. Beyond the LOX post recirculation zone, the waves would accelerate. The acceleration of the LOX jet waves was not observed when the flame was absent. Then, they convected at a uniform velocity. The acoustic receptivity studies performed demonstrated that the reacting flow could couple with low-amplitude acoustic perturbations. It was found that the flame would physically respond to lower acoustic forcing amplitudes when driven at the flame's natural frequency. Otherwise, at other than natural frequencies, it would have to be driven at high-pressure amplitudes for the flame to exhibit any response. Dynamic mode decomposition of the high-speed shadowgraph and unfiltered chemiluminescence captured the physical flame's response to the acoustic forcing. When the flame was subjected to acoustic pressure node (velocity antinode) forcing, the flame had an in-plane flapping response. It had a symmetric puffing response when subjected to pressure antinode (velocity node) forcing. These past studies were limited to a single imaging technique. The current work combines hydroxyl radical (OH*) filtered chemiluminescence with a shadowgraph for a wider range of acoustically unforced, subcritical conditions.

Modeling efforts were included in the work of Juniper et al. [28], Snyder et al. [29], Candel et al. [30], Singla et al. [31], Herding et al. [32], Juniper and Candel [33], Zong and Yang [34], Oefelein and Yang [35], Zong and Yang [36], Okong'o et al. [37], and Okong'o and Bellan [38,39]. Candel et al.'s computational and experimental studies on reacting, cryogenic shear coaxial flows identified features of the flame's stability and dynamics [30]. Candel et al. also showed that there was a minimum LOX post wall thickness necessary to achieve a stable, anchored flame that would be largely unaffected by instabilities the coaxial flow might exhibit. These results were arrived at through a series of simulations in which the effect of the Damköhler number on the flame stability was investigated by varying the annular hydrogen temperature and exit velocity, as well as the LOX post thickness. These simulations demonstrated that flame stability was relatively unaffected by the exit hydrogen velocity if the flame was allowed to anchor in the slow recirculation zone downstream from the LOX post. It was not until the post thickness was decreased below the hydrogen/oxygen flame thickness and the hydrogen injection temperature decreased below 100 K that the flame extinguished. Yang et al. [35,36] performed computations on LOX/GH2 coaxial flows under liquid rocket engine conditions. To account for thermodynamic properties near and above the critical point for these types of flows, they employed a Benedict–Webb–Rubin [35] equation of state near the critical point and a Soave–Redlich–Kwong equation [35] otherwise in their large-eddy simulations. In their simulations under transcritical conditions, mixing between the hydrogen and LOX induced a vortical structure within the hydrogen jet that was analogous to a vortex produced by a backward-facing step. When the chamber pressure was increased in their simulations, vortex structures were still prevalent in the interface between both streams. They also performed simulations using methane instead of hydrogen as fuel, and vortical structures still had a large role in propellant mixing. Okong'o et al. [37] and Okong'o and Bellan [38,39] also performed studies mainly without chemical reactions, and they focused mainly on temporally evolving shear layers rather than spatially evolving flows for oxygen/hydrogen at supercritical conditions. They performed their temporal stability analysis for one-dimensional, two-dimensional, and three-dimensional shear-layer flows. In their work, they examined each term in the vorticity equation at the oxygen/hydrogen shear layer to understand the rotational characteristics of the layer. Their results

Downloaded by Doug Talley on April 16, 2019 | http://arc.aiaa.org | DOI: 10.2514/1.B37079

indicated that little vorticity was created on the heavier, oxygen side of the shear layer. Most of the vorticity created was found within the hydrogen stream.

Despite the extensive work referenced previously, much of which included observation of the combustion dynamics of the reacting coaxial jets, relatively little attention was paid specifically to the role of hydrodynamic instabilities on the reacting flow. For the single phase coaxial flows, the hydrodynamic instabilities have been identified as vortices. There were two types of the vortices formed: the outer annular vortex, and a wakelike vortex from the inner jet. The vortices formed and their shapes were largely dependent on the velocity ratio between both streams. The initial vortex development occurred independently for both streams, but the downstream coaxial flow was controlled by the larger annular vortex. This has been argued by several researchers, for which the wakelike vortices shed by the inner jet lock in to the shedding frequency of the outer annular vortex. For the two-phase coaxial flows, the large annular structures that have been speculated to be vortices were identified as essential flow features that enhanced atomization and mixing between the light gas and the dense, heavier inner jet or core. The role and the influence of these large structures have on reacting coaxial flow downstream are largely unknown.

Thus, relatively few observations have specifically been made of the large annular structures in reacting multiphase coaxial jet flows. This leads one to question whether the effect of the outer shear flow dynamics and the structures formed by it are as dominant in these more complex combustion flows as they are in the simpler flows. The results presented herein indicate that they can be. In this paper, high-speed shadowgraph and OH* chemiluminescence imaging was used to experimentally study the unsteady aspects of LOX hydrogen coaxial jet flames at a subcritical pressure and at various momentum flux ratios. Particular attention was paid to the role of annular jet structure dynamics and its flame interactions. The experimental setup will be described next.

III. Experimental Setup

The shear coaxial injector was tested in the high-pressure optically accessible combustion chamber shown in Figs. 1 and 2. Figure 1 shows an assembly drawing of the outer chamber. The main body of the outer chamber is shown in orange. Mounted on the chamber was a total of six windows, consisting of two large 101 mm (4 in.) diameter round sapphire windows and four oblong windows angled at 45 deg offsets. The 101-mm-diam round sapphire windows were attached to either end of the combustion chamber's 0.127 m (5 in.) circular channel that was 0.38 m (15 in.) in length. The chamber was symmetric about the meridian plane, and so only three of the windows are shown in Fig. 1. Only the two (diametrically opposed) round windows were used in this study; the oblong windows were not used. The round windows were used for high-speed shadowgraphy and OH* chemiluminescence imaging, which will be described further in the following. The injector flow entered from the gray flange on top and exited from the green flange on the bottom. Pressurizing nitrogen was introduced from the two gray angled attachments on the sides (see further in the following). On either side of the main chamber were high-pressure acoustic channels (shown in yellow), which were connected to and held at the same pressure as the main chamber. Piezoelectric acoustic drivers were attached internally to the gray flanges on either end. There was no flow in the channels other than the flow induced by the acoustics. In this study, the acoustic drivers were not used, and so the flow in the acoustic channels was nominally stagnant. The volume of the acoustic channels was, however, a part of the volume into which the flows in this study were introduced, and so a minimum description of the overall dimensions of the channels is provided herein for that reason.

Fig. 1 Assembly drawing of the combustion chamber. The 101-mm-diam center window is shown for size reference.

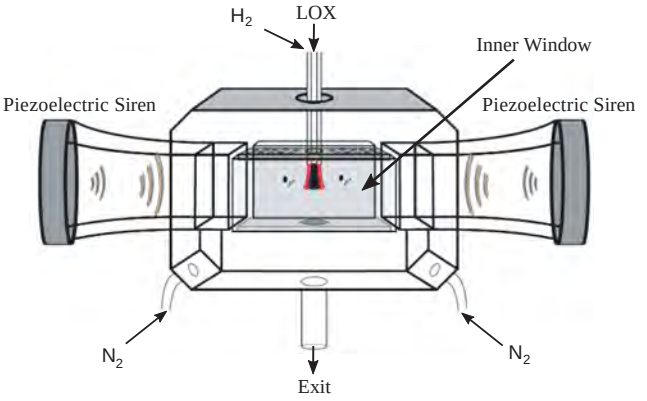

Fig. 2 Inner details of the combustion chamber.

Figure 2 shows a schematic of the internal details of the chamber. The acoustic channels constitute an inner chamber. The inner chamber is connected to and is at the same pressure as the outer chamber and cannot itself sustain any pressure difference with the outer chamber. It does, however, focus the acoustics (when present) and limits hot combustion gases from exiting into the main chamber. The outer chamber and associated pressure-containing windows and window seals are therefore not exposed to potentially damaging high-temperature combustion gases. The coaxial injector is located in the center of this inner chamber and at the top. Centered around the injector are two opposed flat windows in the walls of the acoustic channel for visualization, measuring 76.2 mm (3 in.) wide by 41.4 mm (1.63 in.) high. A hint of these inner windows can be seen inside the round window in Fig. 1. Dynamic pressure transducers can be located as shown in the rectangular inner windows to measure acoustic pressure fluctuations. These transducers were not installed for this study. In the vicinity of the coaxial injector, the inner cross section of the acoustic channel normal to the page is rectangular: 20.5 mm (0.81 in.) wide (or 6.8 inner LOX post diameters) and 35.5 mm high. The end-to-end length of the acoustic channel is 0.375 m or 268 LOX post diameters. There is a round-to-rectangular transition from the acoustic drivers to the channel, but the transition is far enough away from the coaxial injector that the geometric details are not important for this study. The total inner volume of the chamber is approximately 3×10^6 mm^3.

The combustion chamber is pressurized using nitrogen gas from the two side inlets (which are shown in Fig. 2) and does not rely on the combustion process to provide chamber pressure. This is accomplished by keeping the volume occupied by the flame small as compared to the combined volume of the inner and outer chambers. This is done in order to maintain accurate control of the chamber pressure. Combustion gases exit the inner chamber through a hole in the bottom of the inner chamber, and these gases together with pressurizing gases exit the outer chamber through a metering orifice (not shown) at the bottom of the outer chamber. A mixing fitting at the exit, also not shown, dilutes the combustion gas with the exiting pressurizing gas so that the metering orifice only experiences relatively cool temperatures.

In addition to the fuel, oxidant, and pressurizing nitrogen, a separately controlled nitrogen bleed is introduced through round holes in a face plate surrounding the coaxial injector on the upper wall of the inner chamber. The bleed suppresses the formation of a hot-gas recirculation zone near the injector that can otherwise influence the

Downloaded by Doug Talley on April 16, 2019 | http://arc.aiaa.org | DOI: 10.2514/1.B37079

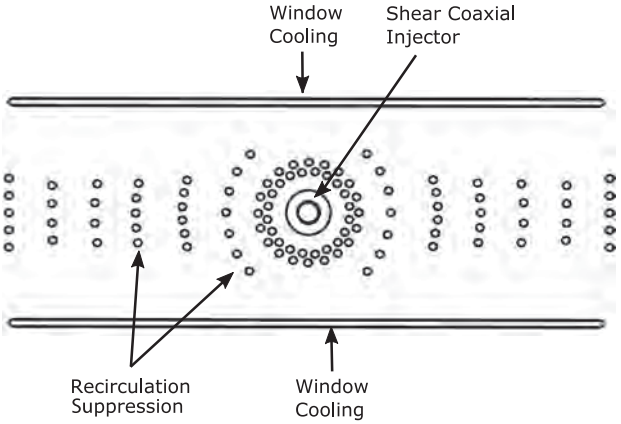

Fig. 3 Injector faceplate including recirculation suppression holes.

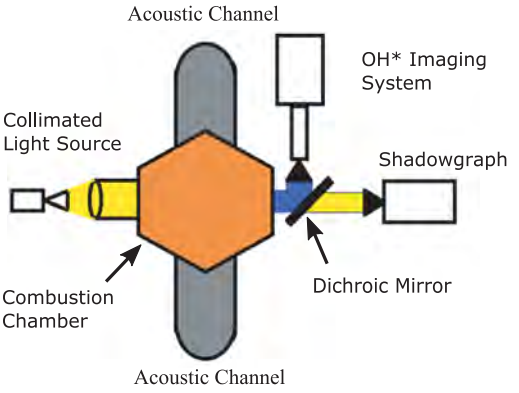

Fig. 4 High-speed simultaneous imaging system layout.

dynamics of the reacting flow. The faceplate with the bleed holes is illustrated in Fig. 3. The coaxial injector is located in the center of the plate. The inner diameter of the center LOX jet is 1.4 mm, with a LOX post thickness of 0.38 mm. The outer diameter of the hydrogen flow is 2.82 mm, giving an exit area ratio of 1.68. The diameter of the bleed holes is 0.5 mm. The nitrogen bleed is regulated to a velocity of 0.05 m/s. Also, in the faceplate are slots next to the windows for window cooling. The window cooling is also nitrogen, which is also separately controlled to a velocity of 0.05 m/s.

The purge and window cooling manifolds were analyzed to determine the possible presence of resonances that might affect the dynamic results reported in this paper. The resonant frequencies were found to be many times lower than the frequencies associated with these results. The gas circuit of the annular fuel manifold (hydrogen) was similarly analyzed and also found not to be acoustically active for these experiments.

All flows were regulated and metered as high-pressure gases using off-the-shelf components. Following regulation and metering, the flows were subsequently chilled to the desired temperatures (for example, to liqufy the oxygen) using heat exchangers cooled with liquid nitrogen. The pressurizing ambient gases were not temperature regulated and were supplied at room temperature. However, the presence of the LOX and the cooling liquid nitrogen usually produced chamber ambient temperatures that were somewhat below the room temperature. Chilling due to Joule–Thompson expansion effects was also observed.

The coaxial injector was designed to have straight passages resulting in fully developed flows at the exit, per the length criterion of Munson et al. [40], namely, $L/D \geq 4.4Re^{1/6}$. The Reynolds numbers, based on the exit diameter of the fuel and oxygen, are presented in Table 1. Using the length criterion, an L/D of over 100 was used for both propellant circuits (the annular gap thickness was used as the length scale for the coaxial hydrogen). The pressure and temperature for both LOX and hydrogen were measured before entering the injector. The LOX jet was kept roughly at 140 K, and the hydrogen gas was chilled to 285 K before entering the injector. Some heat exchange occurred inside the injector internal passages due to the temperature difference. To minimize this heat exchange, the injector was prechilled. Before the hydrogen and LOX entered the injector, chilled gaseous nitrogen ran through the hydrogen circuit and liquid nitrogen ran through the LOX fed circuit for 30 min before combustion.

The chamber pressure used in these studies was 3.4 MPa (500 psia). This is considerably below the critical pressure of oxygen, and so the oxygen was initially a liquid. Igniting the flows at this pressure proved to be nontrivial because most spark ignition methods do not work when a high pressure is established before ignition, as in this experiment. The approach used was a hydrogen–air torch, ignited using a photoignition technique. See the work of Badkahshan and Danczyk [41] for details about the photoignition technique.

The reacting flow was visualized with simultaneous high-speed shadowgraphy and OH* chemiluminescence. The imaging arrangement is illustrated in Fig. 4. The imaging systems captured the unsteadiness of the reacting flow at a framing rate of 25 kHz. The high-speed shadowgraph optics were composed of a 7.6 cm (3 in.) collimated light source, formed with a ThorLabs SL S202 broadband light source and a spherical 152 mm lens, imaged onto a Phantom Research v 710 with an Infinity K2 long-distance microscope lens. The shadowgraph setup allows for droplets down to roughly 100 μm to be resolved. Simultaneously, OH* chemiluminescence was captured with Lambert Instruments high-speed intensified camera attachment imaged directly onto a Phantom Research v1210 camera. An UV lens (F/2.8 Cerco 2178) with a Semrock (PN FF02-320/40) optical filter was used to image the OH* emission at 308 nm. The high-speed cameras and data acquisition systems were synchronized using the signal from the GPS inter-range instrumentation group time, also known as IRIG signal. A dichroic mirror was used to reflect the UV OH* emission from the flame onto the intensifier while allowing the visible light to pass through for the shadowgraph images. The shadowgraph camera imaged the first eight LOX diameters from the nozzle exit, and the OH* chemiluminescence was imaged 14 LOX diameters from the nozzle exit. Figure 5 shows an instantaneous example image of the OH* chemiluminescence and shadowgraph image with the viewing area of the shadowgraph images compared with the OH* viewing area.

The gas-to-liquid momentum flux ratio ($J = \rho U^2_{\text{Gas}}/\rho U^2_{\text{Liquid}}$) has been identified as a global parameter that controls the atomization and breakup of a liquid jet in two-phase coaxial flows [42]; hence, an investigation on the dynamic mechanism of reacting hydrogen/LOX coaxial jets was principally studied by varying J. The momentum flux ratio was varied primarily by varying the hydrogen gas flow rate

Table 1 Operating Conditions

J	LOX injection temperature, K	GH2 injection temperature, K	LOX injection bulk velocity, m/s	GH2 injection bulk velocity, m/s	Aerodynamics Weber number	LOX Reynolds number ($\times 10^3$)	GH2 Reynolds number ($\times 10^3$)
0.15	140	287	4.7	27.5	8,000	87	3.1
0.5	143	287	4.9	57.5	40,700	95	6.8
1	144	282	5.5	94	115,000	110	12
2.2	138	287	3	82	108,000	47	10
4	144	287	3.2	89	120,500	47	10
6	144	288	2.4	89	115,000	45	10

Downloaded by Doug Talley on April 16, 2019 | http://arc.aiaa.org | DOI: 10.2514/1.B37079

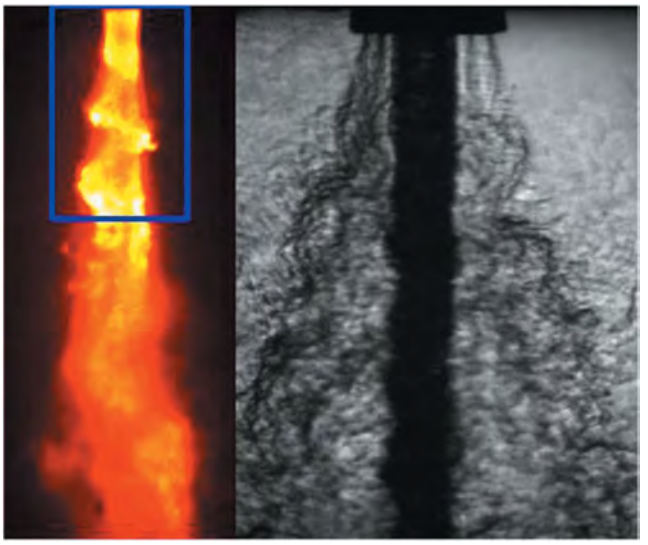

Fig. 5 An instantaneous OH* emission with its corresponding shadowgraph image. The box is the viewing area of the shadowgraph image compared to the OH* image.

through the injector, whereas the oxygen flow rate was kept relatively constant. Momentum flux ratios ranging from 0.15 to 6 were tested. Other flow parameters are presented in Table 1. Densities and surface tensions in this table were obtained from the National Institute of Standards and Technology's Refprop thermodynamic values [43].

IV. Results and Discussions

A. Shadowgraph Features and Annular Structure Dynamics

Figure 6 shows a time series of the of shadowgraph images for J values of 0.15, 0.5, 2.2, and 6, which are arranged in columns with increasing J from left to right. Time increases from top to bottom in each column at a time step of 40 μs. Vertical shadows of various features are evident immediately downstream of the exit, as identified by the white arrows across the top. The white arrow near the injector exit points to the two shadows formed by density gradients from the outer hydrogen jet with the surrounding nitrogen and an inner one where the flame is located. The outer shadow is the shear layer between the outer annular hydrogen flow and the nitrogen ambient. The next inner shadow is the shadow of the flame, which is attached to the LOX post. The inner dark core is that of the LOX jet itself. A gap exists between the LOX jet and the flame's shadow at the injector exit. Immediately at the exit, this is the LOX post thickness, and it can

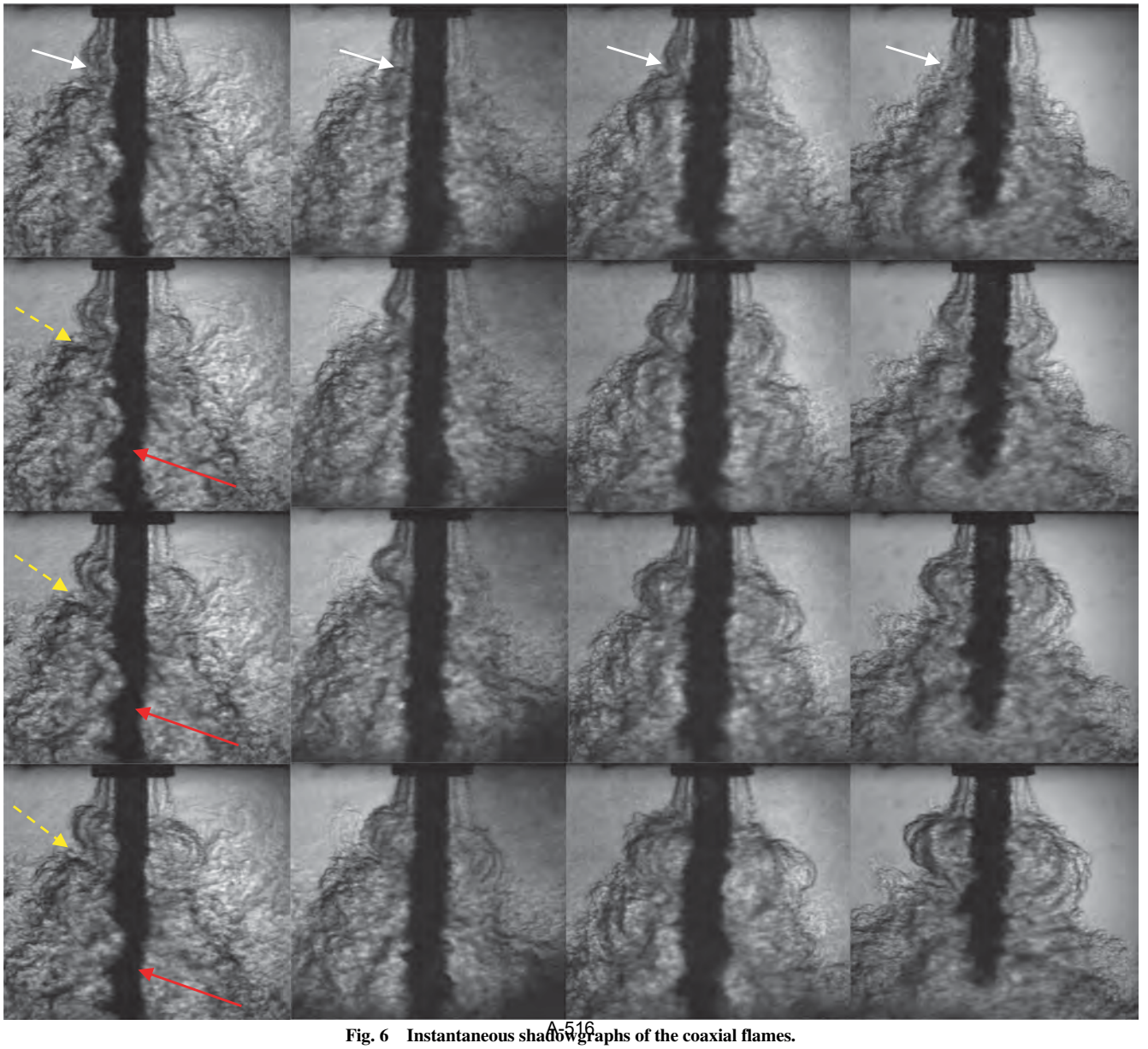

Fig. 6 Instantaneous shadowgraphs of the coaxial flames.

Downloaded by Doug Talley on April 16, 2019 | http://arc.aiaa.org | DOI: 10.2514/1.B37079

be seen that the flame anchors at the outer rim of the post, as has been reported by others [16,32]. Immediately downstream of the exit, the gap is occupied by a recirculation zone between the outer and inner LOX post flows. The recirculation zone is not seen in these images but has been visualized elsewhere [26]. The recirculation zone extends downstream for approximately one LOX diameter for all J. Farther downstream of the recirculation zone, the gap between the flame's outermost shadow and the LOX jet is not always distinct. These shadows become convoluted as the flow moves downstream, often losing visibility altogether. Far enough downstream, the outer layer between the hydrogen gas and the ambient nitrogen becomes replaced by the layer between the expanding hot gases from the flame and the ambient nitrogen.

The entire flow is highly unsteady, but a regular dynamic structure to the flow may be observed. Attention is drawn to the large annular structure that is formed by the outer hydrogen jet immediately

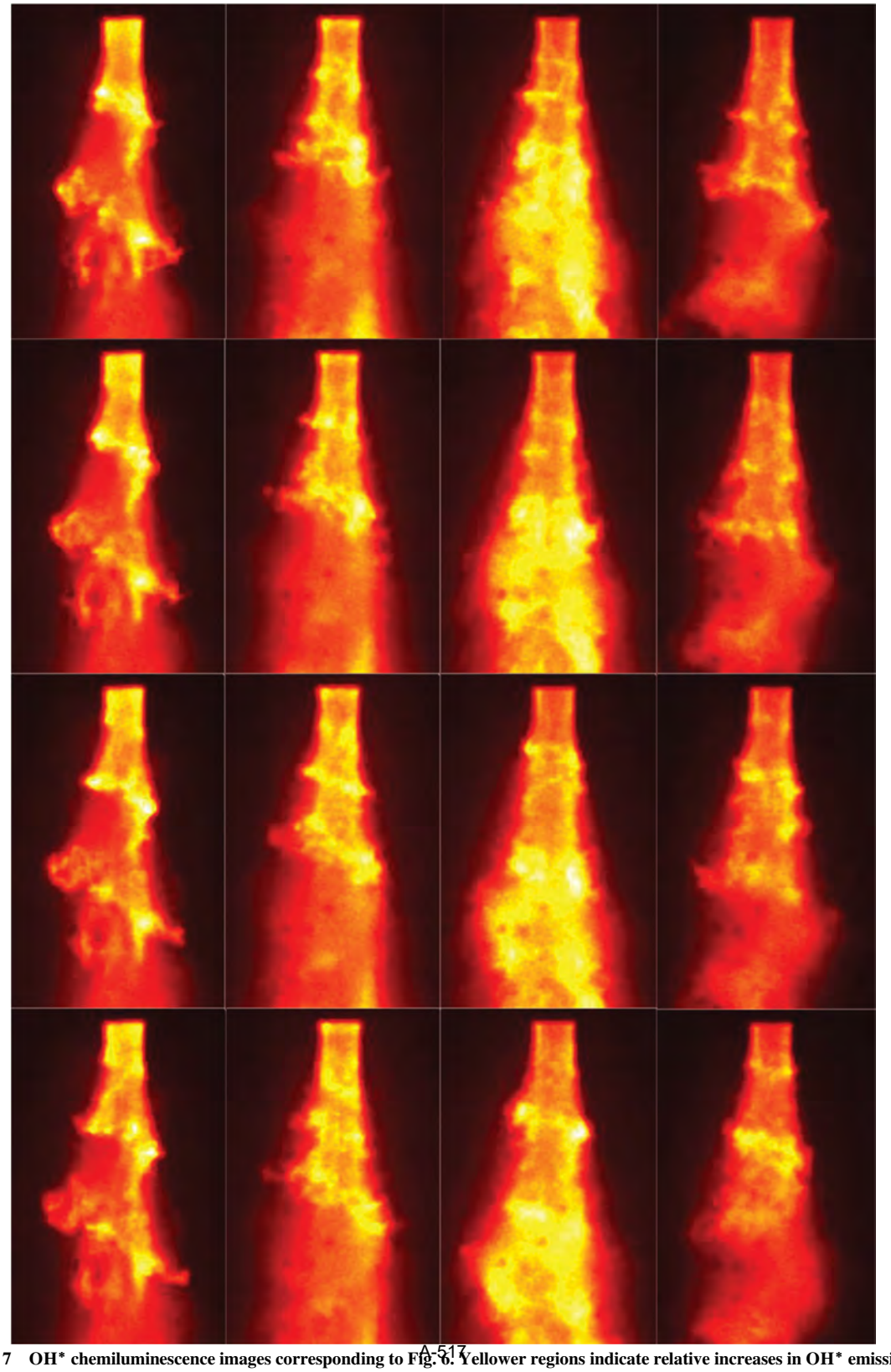

Fig. 7 OH* chemiluminescence images corresponding to Fig. 6. Yellower regions indicate relative increases in OH* emission.

Downloaded by Doug Talley on April 16, 2019 | http://arc.aiaa.org | DOI: 10.2514/1.B37079

downstream of the exit. The developing annular structure is indicated by the yellow dashed arrows in the images for $J = 0.15$. The annular structure engages both the outer shear layer and the flame, and it tends to grow as it evolves downstream. It also tends to be larger as J increases or, in this study, as the annular hydrogen flow rate increases. Only single formation events are shown in the high-speed videos in Fig. 6; in fact, the annular structures are regularly formed, but only quasi periodically, at frequencies ranging from 4 to 9 kHz, depending on J. From Fig. 6, the annular structures can be observed to form initially asymmetrically across all conditions. The asymmetry is probably due to a slightly nonconcentric center LOX post, in which the inner LOX jet is skewed slightly left from the center. The annular structure also exhibits a rollup behavior. The initial rollup is also observed to start to the left of the LOX jet, where the gap between the LOX jet and the hydrogen jet is minimal due to not being concentric. The asymmetry might also be due to the hydrogen jet exhibiting a helical mode and causing the annular structure to be shed in a slanted fashion. The helical mode has been observed Dahm et al. [2] for coaxial jets and Michalke [12] for single jets. Although a hydrogen jet helical mode might be present, it is not believed to be responsible for the asymmetry because the initial rollup event is never observed to alternate on either side of the LOX jet and the slanted orientation of the shed annular structure is always in the same sense. Another possible interpretation of the asymmetry, given by Yoda et al. [44], is the presence of two helical vortex structures, which they argue are just as equally likely to occur as a single helical vortex. However, further studies will require a stereo-optical setup to identify if a single- or double-hydrogen jet helical structure is indeed present.

Regardless of the orientation of the annular structure formed, the structures are observed to be energetic enough that, when they pinch in, they penetrate inside the average location of the flame and appear to impact on the LOX jet directly, as shown in Fig. 6. When this

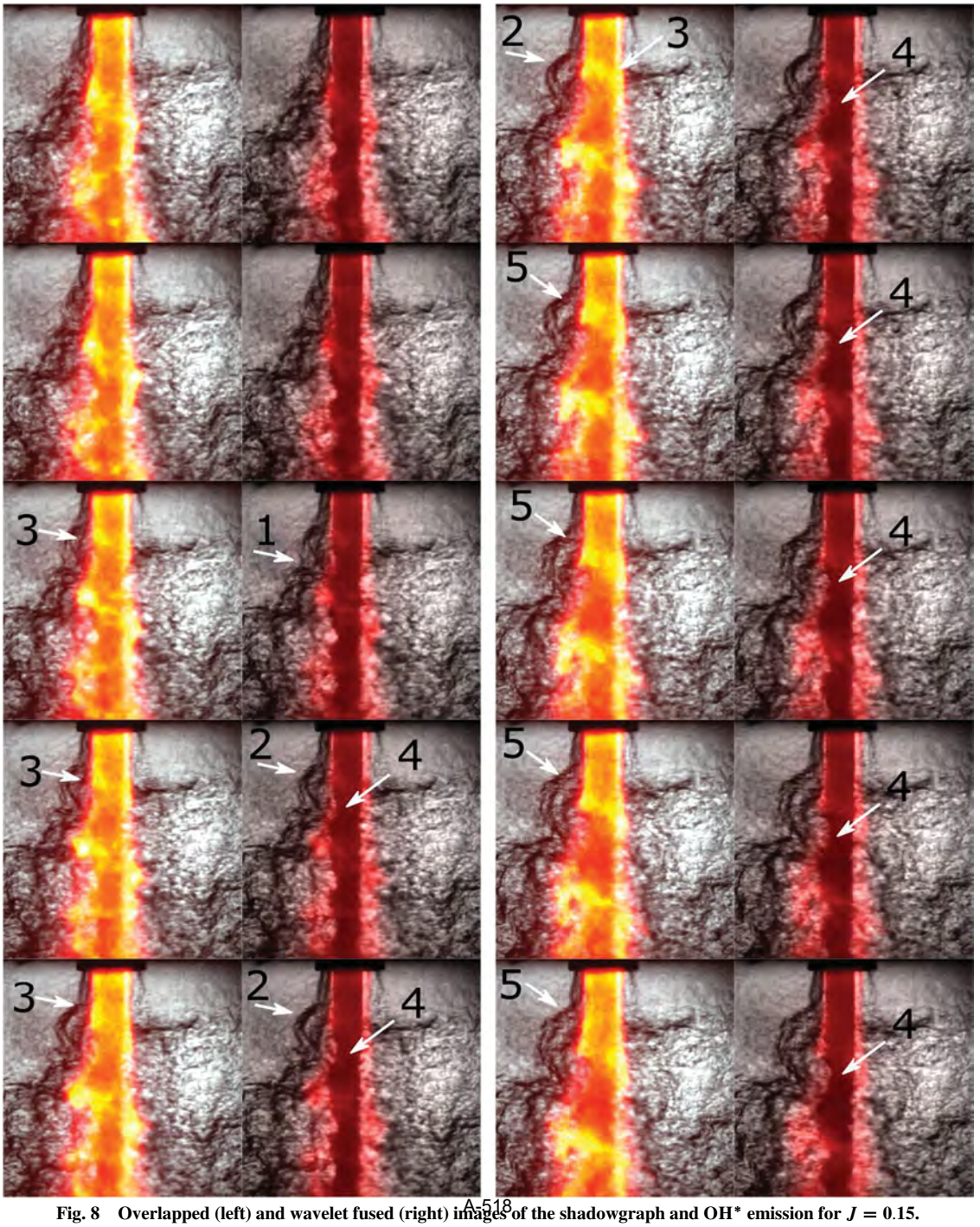

Fig. 8 Overlapped (left) and wavelet fused (right) images of the shadowgraph and OH* emission for $J = 0.15$.

Downloaded by Doug Talley on April 16, 2019 | http://arc.aiaa.org | DOI: 10.2514/1.B37079

happens, a trough is observed to appear in the waves on the LOX jet, evidently caused by the locally increased vaporization rate caused by the impinging hot gases. The trough formation on the LOX core due to the outer shear layer pinching in and the developing annular structure is indicated by the red arrows in Fig. 6. Immediately after the trough is formed, an expansion wave of hot gases appears and overcomes the initial unsteady annular structure. The expansion wave in the outer flow is then observed to propagate downstream slower than the trough propagates downstream in the LOX jet. It is also observed that, for each test condition, the hydrogen jet will at times form smaller structures that will convect faster. The resulting disparity in the convecting annular structures velocities is observed to sometimes lead to structure coalescence and sometimes to the annular structure vanishing altogether. This behavior and its influence on the flame structures are discussed further in the following.

These large unsteady annular structures are initially formed due to hydrodynamic instabilities in the annular hydrogen jet, and they share similar dynamic and physical characteristics to that of single jets and to that of vortices. In Fig. 6, the formation of the unsteady annular hydrogen structure and its subsequent shedding begins when the outermost shear layer of the hydrogen jet curls toward the LOX jet, as discussed previously. Several researchers have identified the curling of the hydrogen jet toward the LOX jet as a Kelvin–Helmholtz instability of the outer shear layer. This hydrodynamic instability has been theoretically studied and experimentally investigated. Talamelli and Gavarini [11] performed a linear stability analysis, and their results showed that there was indeed an unstable mode associated with the annular flow and two other wakelike instabilities located at the recirculation downstream of the LOX post. Segalini and Talamelli [9] would later experimentally show that the outer shear layer

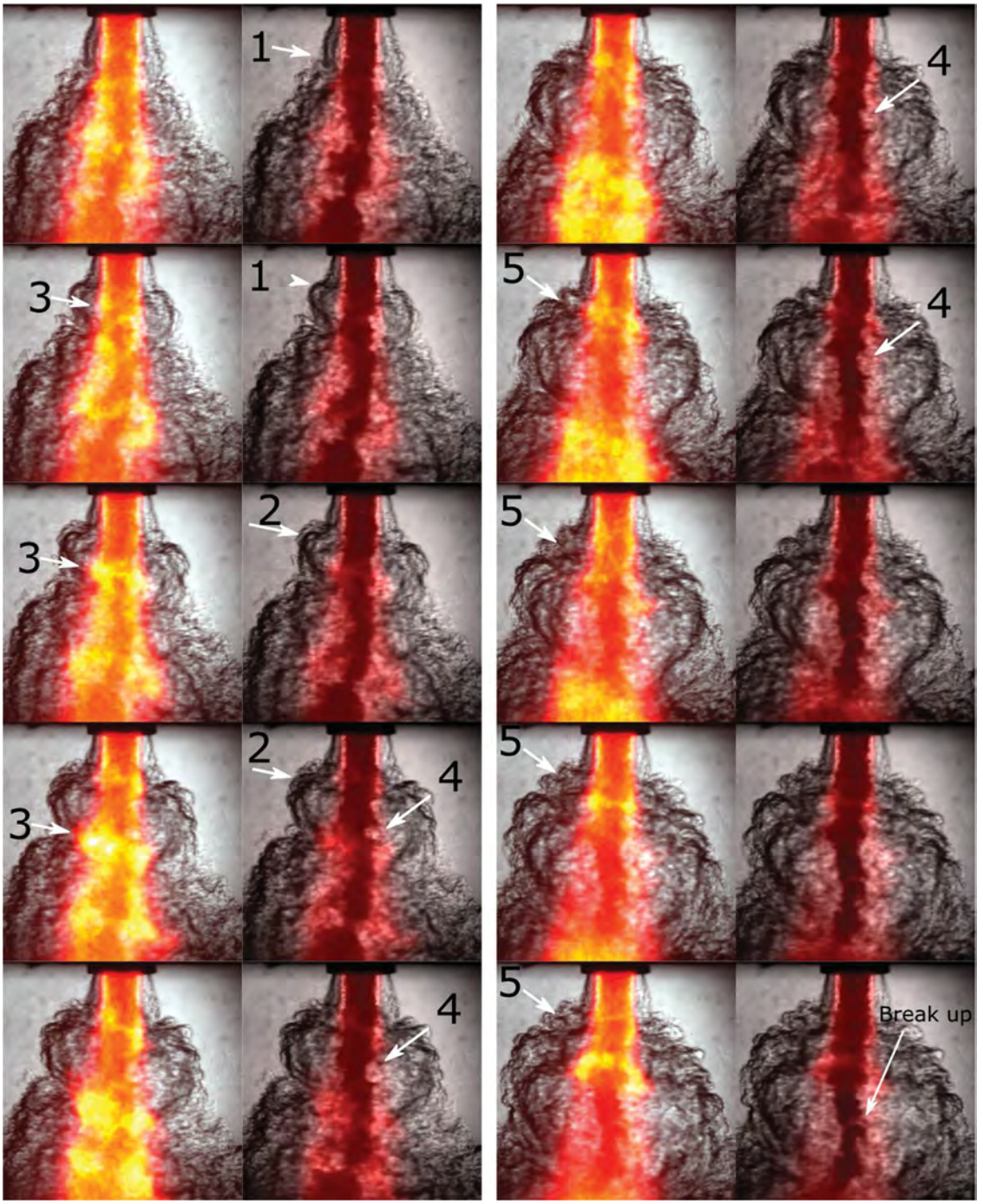

Fig. 9 Overlapped (left) and wavelet fused (right) images of the shadowgraph and OH* emission for $J = 6$. See caption from Fig. 8. The breakup of the LOX jet is also indicated.

Downloaded by Doug Talley on April 16, 2019 | http://arc.aiaa.org | DOI: 10.2514/1.B37079

demonstrated Kelvin–Helmholtz instabilities. A direct numerical simulation study by da Silva et al. [45] showed that Kelvin–Helmholtz instabilities were responsible for the annular structures present in coaxial flows, with Strouhal numbers ranging between 0.24 and 0.5.

For the high aerodynamic Weber number ($\rho_{LOX}(U_{H2} - U_{LOX})^2 D_{LOX}/\sigma_{LOX}$) and Reynolds number of the LOX jet, the coaxial flow should have fine droplets and ligaments that may be highly fibrous in appearance [46]. The current shadowgraph optic setup allows for droplets of roughly 100 μm to be resolved; but, instead, the LOX jet looks smooth. No droplets or ligaments were present beyond one LOX diameter downstream of the nozzle exit. However, it was observed separately [26] that droplets and ligaments were indeed present within the recirculation zone downstream of the LOX post. These results are consistent with the work of Mayer et al. [13–15] Mayer and Tamura [16], and Mayer and Krülle [17], in which the smoothness of the LOX jet and the lack of ligaments and droplets were attributed to the rapid vaporization of any LOX structures.

B. Annular Structure/Flame Interactions

Figure 7 shows the flame behavior corresponding to Fig. 6, taken from the simultaneous high-speed OH* chemiluminescence videos. The OH* emission images are false colored to aid in visualizing the OH* emission intensity. The flame near the exit closely encircles the LOX jet and is continuous with pockets or bands of high OH* emission. As discussed further next, these bands of higher OH* chemiluminescence are used here as markers of flame behavior, although they do not strictly correspond to regions of maximum heat release. The conclusions drawn in the following are not affected by this somewhat inexact interpretation.

Visualizing the shadowgraph and the OH* images simultaneously allows the annular structure/flame interactions to be examined in detail. Two different methods are used to visualize them both simultaneously in the same image. In the first method, the images are overlapped. To produce the overlapped images, the OH* chemiluminescence image is superimposed onto the shadowgraph image by controlling the transparency of the OH* image. The transparency is set by using the individual pixel counts from the OH* image in which, the higher the pixel counts or brighter the pixel, the more opaque that pixel from OH* image becomes. Hence, the dimmer that pixel, the more transparent the pixel of the OH* image. This image decomposition allows for direct comparison of the annular hydrogen vortex behavior with the increase OH* emissions, but it obscures the annular structure effects on the LOX jet. The other method, which is the wavelet decomposition, allows for studying the effect the annular structure/flame interaction has on the LOX core. Wavelet decomposition has been previously used in the medical imaging community [47], in which different imaging techniques like computer-aided tomography or magnetic resonance imaging can be combined into a single image while retaining important physical features of both. A wavelet transform, using a Symlet wavelet as the kernel for the decomposition, of the original shadowgraph and the original OH* chemiluminescence image are taken. The individual components from the wavelet transforms from both images are then averaged together, and then an inverse wavelet transform is taken to produce a synthesized single image.

Overlapped and wavelet decompositions of both shadowgraphs and OH* images are shown in Fig. 8 (for $J = 0.15$) and Fig. 9 (for $J = 6$). The left-side images in each column are the overlapped images, whereas the right-side images are the wavelet decompositions. Time increases from top to bottom: first in the left column, and then in the right column. The numbered markers indicate 1) impingement on the LOX jet, 2) formation of the annular hydrogen structure, 3) the almost immediate local increase in OH* emission, 4) the formation of a trough in the LOX jet, and 5) the combustion gas expansion wave. The images show the formation of the annular structure in the outer hydrogen jet and the impingement on the LOX core as it curls and pinches in. Almost immediately after impingement, within a single 40 μs frame, there is a localized increase in OH* emission. Within one to three frames after that, a wave trough appears in the LOX jet due to an increased local consumption of the LOX. In the works of Mungal and Dimotakis [48] and Broadwell and Breidenthal [49], they identified that the chemical reactions occurred mainly in the cores of the rolled-up vortices that were formed in the shear layers. Because vortex rollup entrains equal volumes of the propellants [48,49], they argued that the large-scale vortices increased propellant mixing. Results presented by Savas and Gollahalli [50] and Ahn and Yu [51] showed that, depending on the equivalence ratio and the Damköhler number, chemical reactions did not necessarily need to occur in the center of a vortex but could occur along their periphery. Snyder et al. [29] and Juniper and Candel [33] showed numerically that the vaporization rate of the LOX jet was slower than that of the oxygen gas consumption by the flame. Juniper and Candel [33] also showed numerically that the latent heat of vaporization of LOX had little effect on the flame and the flame could not be quenched at the LOX surface; instead, the flame moved closer to the LOX surface to increase the local vaporization of the LOX. These observations of other authors were consistent with the present results of the annular structure interactions with the flame. It was also observed that the size of the trough was dependent on the size of the annular structure formed and could lead to the breakup of the LOX jet. Figure 9 shows a large annular structure breaking apart the LOX jet as it travels downstream.

C. Combustion Wave Trajectories

The convection velocities of these large structures (annular hydrogen structure, the high-intensity OH* bands/combustion waves, the trough on the LOX jet, and the hot-gas expansion waves) are on average different relative to each other. As indicated previously, OH* bands will be referred to as combustion waves from on now because they are observed to be created when the hydrogen structure impinges on the LOX jet. It is notable that the combustion waves convect faster than either the annular structures or the LOX jet troughs. This is probably the case because the combustion wave is being swept along by the high-velocity hydrogen jet near the LOX jet, although this phenomenon will have to be examined further. This is confirmed in Figs. 8 and 9.

Because they are the fastest, accordingly, the trajectories of the combustion waves are analyzed here. The velocity of the combustion wave can be deduced by tracking OH* emission intensity between high-speed frames. To track the combustion wave, the pixel locations are taken along the maximum value of the standard deviation for each separate condition, as shown, for example, in Fig. 10. The raw pixel

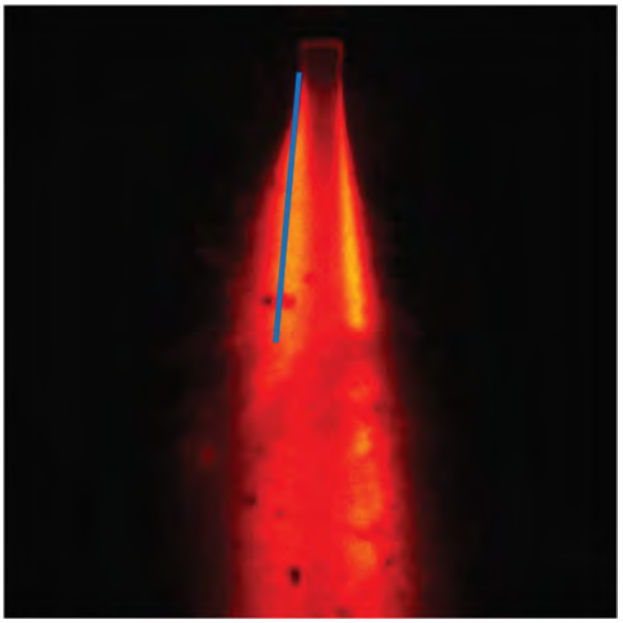

Fig. 10 Standard deviation image for J of 0.15 with respect to time. Pixel locations for instantaneous velocity measurements were taken along the blue line plotted over the maximum value of the standard deviation.

Downloaded by Doug Talley on April 16, 2019 | http://arc.aiaa.org | DOI: 10.2514/1.B37079

values are first subtracted by their time average and divided by the standard deviation. This ensures that, if the combustion wave is present, it will be represented as a peak. An example of the peak tracking is shown in Fig. 11, in which the individual peaks and their locations with respect to the flames are present. The column on the left shows sequential images with the OH* emission peaks. The column on the right shows those OH* peak locations. The peaks demonstrate the mentioned combustion wave behaviors, with two flame structures merging (peaks 5 and 6 to form 5') and one randomly vanishing (peak 3). Tracking individual peaks starts at 1.5 LOX diameters from the nozzle and continues to 15 LOX diameters. If individual peaks dip below a certain threshold, they are no longer tracked. This tracking is done for 5000 images or 0.2 s of OH* chemiluminescence images.

By tracking the combustion wave from frame to frame, their unsteady behavior can be analyzed. Tracking combustion wave pairs yields a set of three distinct behaviors, similar to the behaviors of the annular hydrogen structures. It is observed that a pair of combustion waves can either convect together at similar velocities; coalescence

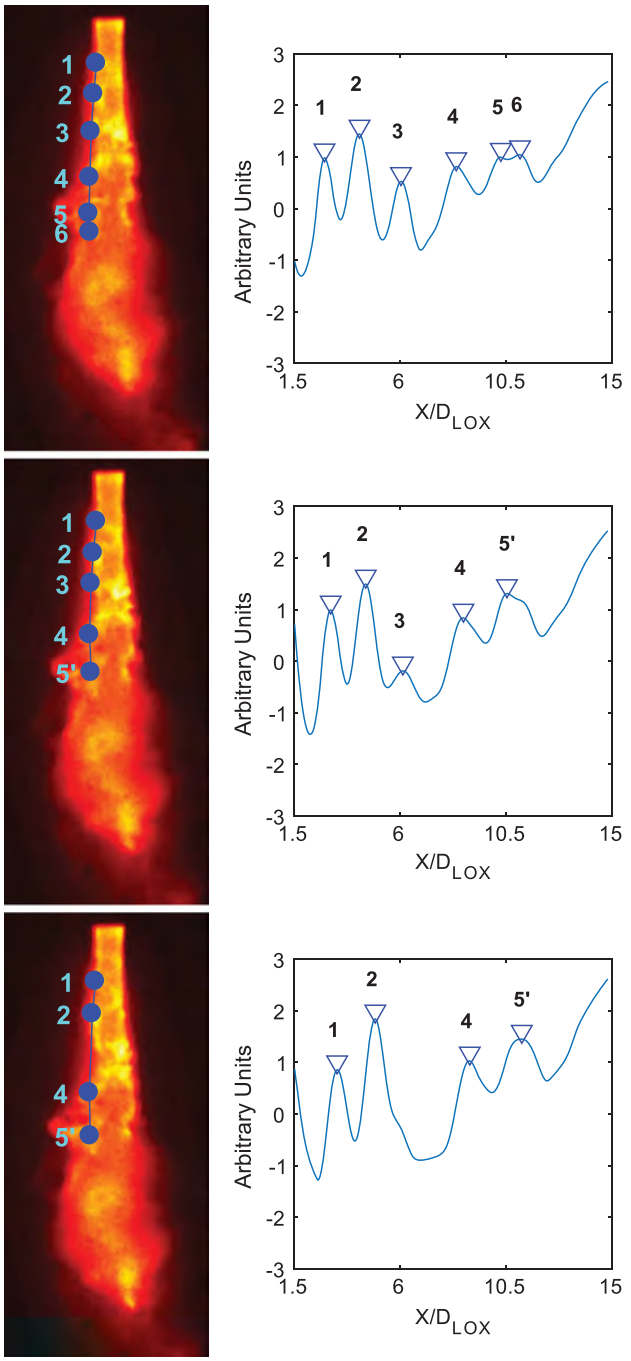

Fig. 11 Examples of tracking methods employed to locate localized increases of OH* emission.

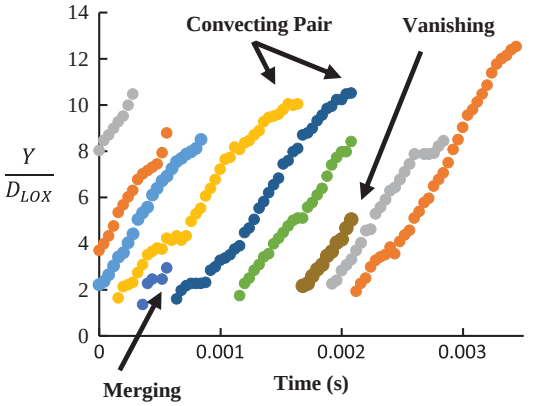

Fig. 12 Individual combustion waves for $J = 0.15$ condition tracked by localized OH* emission increase, with the position of each combustion wave plotted as a function of time.

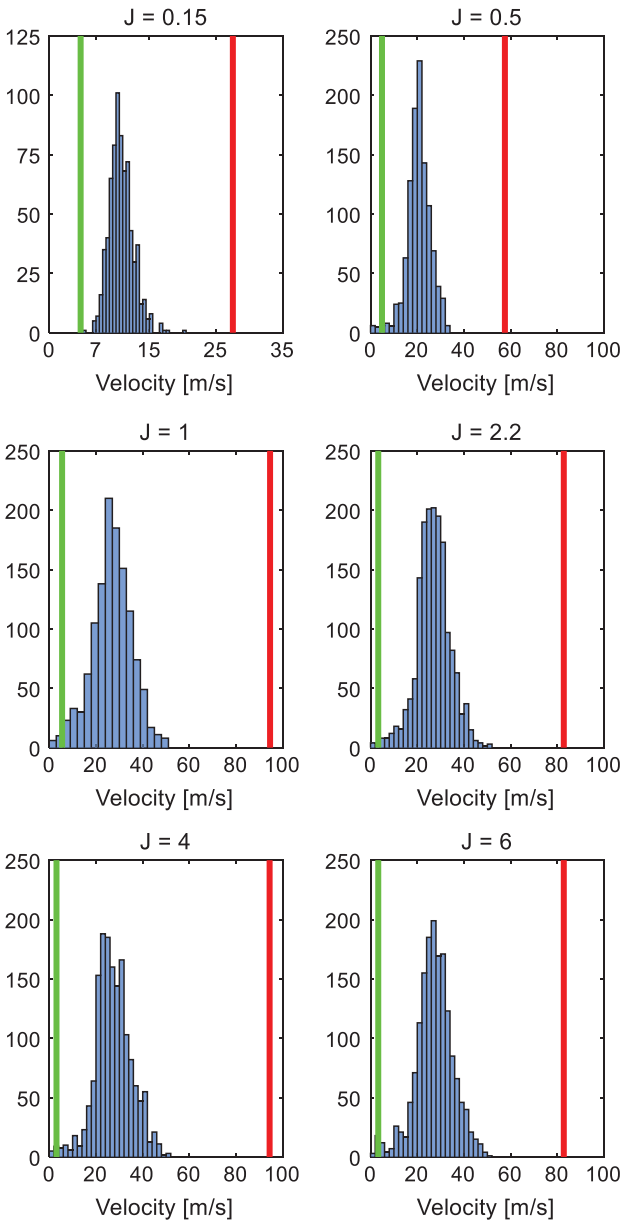

Fig. 13 Velocity distributions of the OH* flame structures.

Downloaded by Doug Talley on April 16, 2019 | http://arc.aiaa.org | DOI: 10.2514/1.B37079

when a high-velocity trailing flame structure overtakes a slower one; or, sometimes, one flame structure in the pair completely vanishes. A chart demonstrating this behavior is shown in Fig. 12. Tracking the localized increases in OH* emissions as a function of time vs distance,

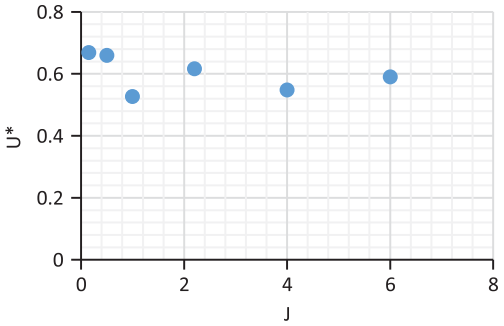

Fig. 14 OH* wave velocity normalized by the mean of the bulk hydrogen and LOX jet velocity.

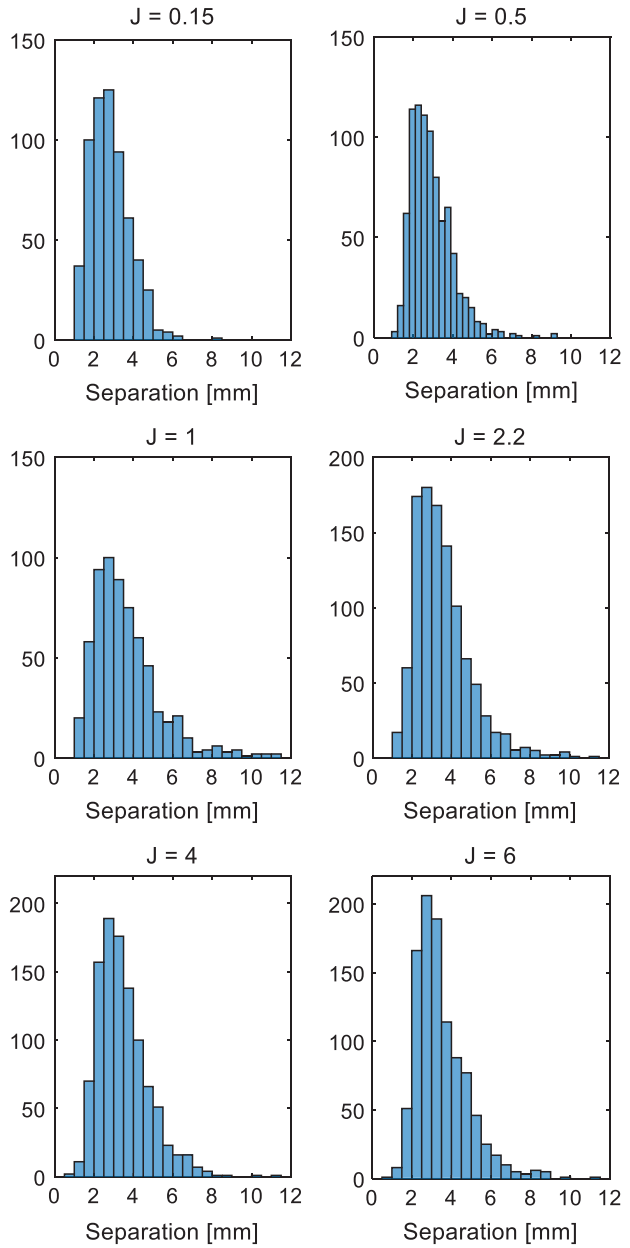

Fig. 15 Average wavelength between combustion waves or the average distance between combustion waves: ordinate number of counts of combustion wave pairs.

the three combustion wave pair behaviors are observed: the convecting pair, the merging pair, and the single vanishing combustion wave. The merging pair occurs when the annular hydrogen structures shed from the hydrogen jet are different sizes, with the large annular structure convecting slower initially. It should also be recalled that these are analyses from high-speed videos, in which 10 combustion waves can be observed within 2 ms, as shown in Fig. 12.

The unsteady combustion waves exhibited a broad velocity range that led to the previously discussed behaviors. Velocity histograms for the OH* flame structure for each condition in Table 1 are shown in Fig. 13. The vertical red and green lines in the histograms presented are the bulk-averaged hydrogen and oxygen velocities, respectively, from Table 1. The average speed of these combustion waves is less than half the bulk hydrogen velocity. The ordinate for each histogram was the number of counts or combustion waves. Note that the $J = 0.15$ condition did not have the same scale. For the lower J or low hydrogen velocity conditions, there was a narrow spread of combustion wave velocities as compared to the higher J conditions. Normalizing the average OH* velocity, indicated by a bar, by the mean of the bulk hydrogen and LOX jet velocities per the following equation

$$U^* = \frac{\overline{U_{\mathrm{OH}^*}}}{(U_{\mathrm{H2,Bulk}} + U_{\mathrm{LOX,Bulk}})/2} \tag{1}$$

it can be seen that U^* falls within a narrow range of 0.52 to 0.66 for all J, as plotted in Fig. 14. In other words, Fig. 14 shows that the arithmetic mean of the bulk velocity of both propellants is a good measure of the OH* flame structure velocity, regardless of J.

A distance or wavelength between combustion waves can also be deduced by tracking the distance between two flame structures convecting downstream. Discounting combustion waves that coalescence or the ones that vanish altogether, the separation or wavelength between a convecting combustion waves pair is roughly constant for their lifetimes, as shown in Fig. 12. The averages of the wavelengths between combustion waves from 4 LOX diameters to 15 LOX diameters are presented in the histograms in Fig. 15. The shapes of the distribution of the wavelengths in the histograms are similar, regardless of J. From the histograms, the majority of the convecting pairs are on average between 2 to 5 mm in wavelength. Using these average wavelength λ values and the average velocity U from flame structure histograms from Fig. 13 and $U = f\lambda$, the flame structure frequencies f are centered from 3.8 to 10 kHz, which are similar to the quasi-periodic frequency of the annular structure shedding, reinforcing the connection between the annular structure and its influence on the flame and the downstream flow.

V. Conclusions

The annular structure dynamics of a liquid-oxygen/gaseous hydrogen coaxial jet was investigated as a function of the outer-to-inner momentum flux ratio J. High-speed shadowgraphs and OH* chemiluminescence images of the flow were taken at 25 kHz. The results show the influence of the annular hydrogen jet structures, formed at the exit of the injector, has the flame and liquid-oxygen (LOX) jet. These annular structures were quasi periodically around a broad range of frequencies ranging from 4 to 9 kHz. The mechanism following large annular structure formation was observed to be as follows: as the annular structure curled toward the LOX jet, it was energetic enough to penetrate past the average flame location and impinge on the LOX jet. The close presence of the hot gases next to the LOX jet caused a nearly immediate increase in OH* emission, within one camera frame. A few frames later, a trough in the LOX jet appeared, indicating a local increase in LOX vaporization by the hot gases. A wave of expanding hot gases also appeared at the same time. This annular structure was sometimes energetic enough to sever the LOX jet entirely. All these wave structures convected downstream at different velocities, with the OH* chemiluminescence or combustion wave propagating the fastest. Measurement of the combustion wave trajectories revealed three main classes of behaviors: combustion wave pairs that propagated together at similar velocities, combustion

Downloaded by Doug Talley on April 16, 2019 | http://arc.aiaa.org | DOI: 10.2514/1.B37079

waves that propagated at different velocities and eventually coalesced into one, and combustion wave pairs in which one of the waves spontaneously vanished entirely. Histograms of the combustion wave velocities revealed a spread of velocities somewhere between the bulk velocity of the initial outer hydrogen flow and the bulk velocity of the initial inner LOX flow. The average wave velocities normalized by the average of the two initial bulk velocities were found to be independent of J to within a narrow range of between 0.52 to 0.66. Tracking the wavelengths between combustion waves after the initial annular structure formed, the wavelengths between two combustion waves were relatively constant between 4 to 15 LOX diameters. Using the OH* velocity and wavelength histograms resulted in a similar quasi-periodic frequency observed for the annular structure shedding. These results confirmed earlier results for simpler coaxial flows without combustion that the outer flow large structure dynamics, which were speculated to be annular vortices because they exhibited the same vortex behavior and orientation but could not be verified with the given optical systems, could still have a significant effect on the flow.

Acknowledgments

This work was funded by the U.S. Air Force Office of Scientific Research and conducted at the U.S. Air Force Research Laboratory's Combustion Stability Laboratory at Edwards Air Force Base in California. A special thanks is owed to Randy Harvey for his help during data collection.

References

[1] Ko, N. W. M., and Kwan, A. S. H., "The Initial Subsonic Coaxial Jets," *Journal of Fluid Mechanics*, Vol. 73, No. 2, 1976, pp. 305–332. doi:10.1017/S0022112076001389

[2] Dahm, W. J. A., Frieler, C. E., and Tryggvason, G., "Vortex Structure and Dynamics in the Near Field of a Coaxial Jet," *Journal of Fluid Mechanics*, Vol. 241, Aug. 1992, pp. 371–402. doi:10.1017/S0022112092002088

[3] Wicker, R. B., and Eaton, J. K., "Near Field of a Coaxial Jet with and Without Axial Excitation," *AIAA Journal*, Vol. 32, No. 3, 1994, pp. 542–546. doi:10.2514/3.12019

[4] Rehab, H., Villermaux, E., and Hopfinger, E. J., "Flow Regimes of Large-Velocity-Ratio Coaxial Jets," *Journal of Fluid Mechanics*, Vol. 345, Aug. 1997, pp. 357–381. doi:10.1017/S002211209700637X

[5] Balarac, G., and Métais, O., "The Near Field of Coaxial Jets: A Numerical Study," *Physics of Fluids*, Vol. 17, No. 6, 2005, Paper 065102. doi:10.1063/1.1900786

[6] Villermaux, E., "Mixing and Spray Formation in Coaxial Jets," *Journal of Propulsion and Power*, Vol. 14, No. 5, 1998, pp. 807–817. doi:10.2514/2.5344

[7] Villermaux, E., and Rehab, H., "Mixing in Coaxial Jets," *Journal of Fluid Mechanics*, Vol. 425, Dec. 2000, pp. 161–185. doi:10.1017/S002211200000210X

[8] Örlü, R., Segalini, A., Alfredsson, P. H., and Talamelli, A., "Turbulence Enhancement in Coaxial Jet Flows by Means of Vortex Shedding," *Progress in Turbulence III. Springer Proceedings in Physics*, Vol. 131, Springer, Berlin, 2009, pp. 235–238. doi:10.1007/978-3-642-02225-8

[9] Segalini, A., and Talamelli, A., "Experimental Analysis of Dominant Instabilities in Coaxial Jets," *Physics of Fluids*, Vol. 23, No. 2, 2011, Paper 024103. doi:10.1063/1.3553280

[10] Talamelli, A., Segalini, A., Örlu, R., and Buresti, G., "A Note on the Effect of the Separation Wall in the Initial Mixing of Coaxial Jets," *Experiments in Fluids*, Vol. 54, No. 3, March 2013, Paper 1483. doi:10.1007/s00348-013-1483-9

[11] Talamelli, A., and Gavarini, I., "Linear Instability Characteristics of Incompressible Coaxial Jets "Flow," *Turbulence and Combustion*, " Vol. 76, No. 3, 2006, pp. 221–240. doi:10.1007/s10494-006-9015-9

[12] Michalke, A., "Survey on Jet Instability Theory," *Progress in Aerospace Sciences*, Vol. 21, 1984, pp. 159–199. doi:10.1016/0376-0421(84)90005-8

[13] Mayer, W., Schik, A., Schäffler, M., and Tamura, H., "Injection and Mixing Processes in High-Pressure Liquid Oxygen/Gaseous Hydrogen Rocket Combustors," *Journal of Propulsion and Power*, Vol. 16, No. 5, 2000, pp. 823–828. doi:10.2514/2.5647

[14] Mayer, W., Schik, A. H., Vielle, B., Chauveau, C., Gökalp, I., Talley, D. G., and Woodward, R. D., "Atomization and Breakup of Cryogenic Propellants Under High-Pressure Subcritical and Supercritical Conditions," *Journal of Propulsion and Power*, Vol. 14, No. 5, 1998, pp. 835–842. doi:10.2514/2.5348

[15] Mayer, W., "Coaxial Atomization of a Round Liquid Jet in a High Speed Gas Stream: A Phenomenological Study," *Experiments in Fluids*, Vol. 16, No. 6, 1994, pp. 401–410. doi:10.1007/BF00202065

[16] Mayer, W., and Tamura, H., "Flow Visualization of Supercritical Propellant Injection in a Firing LOX/GH2 Rocket Engine," *31st AIAA/ASME/SAE/ASEE Joint Propulsion Conference*, AIAA Paper 1995-2433, 1995. doi:10.2514/6.1995-2433

[17] Mayer, W., and Krülle, G., "Rocket Engine Coaxial Injector Liquid/Gas Interface Flow Phenomena," *Journal of Propulsion and Power*, Vol. 11, No. 3, 1995, pp. 513–518. doi:10.2514/3.23872

[18] Mayer, W., Schik, A., Schweitzer, C., and Schaeffler, M., "Injection and Mixing Processes in High Pressure LOX/GH2 Rocket Combustors," *32nd AIAA/ASME/SAE/ASEE Joint Propulsion Conference*, AIAA Paper 1996-2620, 1996. doi:10.2514/6.1996-2620

[19] Yeralan, S., Pal, S., and Santoro, R. J., "Experimental Study of Major Species and Temperature Profiles of Liquid Oxygen/Gaseous Hydrogen Rocket Combustion," *Journal of Propulsion and Power*, Vol. 17, No. 4, 2001, pp. 788–793. doi:10.2514/2.5834

[20] Yeralan, S., Pal, S., and Santoro, R. J., "Experimental Investigation of Oxygen Rich LOX/GH2 Combustion Using Linewise Raman Imaging," *36th AIAA Aerospace Sciences Meeting*, AIAA Paper 1998-0152, 1998. doi:10.2514/6.1998-152

[21] Locke, J. M., Pal, S., Woodwards, R. D., and Santoro, R. J., "High Speed Visualization of LOX/GH2 Rocket Injector Flowfield: Hot-Fire and Cold-Flow Experiments," *46th AIAA/ASME/SAE/ASEE Joint Propulsion Conference*, AIAA Paper 2010-7145, 2010. doi:10.2514/6.2010-7145

[22] Pal, S., Moser, M. D., Ryan, H. M., Foust, M. J., and Santoro, R. J., "Shear Coaxial Injector Atomization Phenomena for Combusting and Non-Combusting Conditions," *Atomization and Sprays*, Vol. 6, No. 2, 1996, pp. 227–244. doi:10.1615/AtomizSpr.v6.i2

[23] Chehroudi, B., "Recent Experimental Efforts on High-Pressure Supercritical Injection for Liquid Rockets and their Implications," *International Journal of Aerospace Engineering*, Vol. 2012, 2012, Paper, 121802. doi:10.155/2012/121802

[24] Forliti, D. J., Leyva, I. A., Talley, D. G., Rodriguez, J. I., Teshome, S., Wegener, J. L., Roa, M., and Karagozian, A. R., "Forced and Unforced Shear Coaxial Mixing and Combustion at Subcritical and Supercritical Pressures," *High Pressure Flows for Propulsion Applications, Progress in Astronautics and Aeronautics*, AIAA, Reston, VA (to be published).

[25] Wegener, J. L., Forliti, D. J., Leyva, I. A., and Talley, D. G., "Receptivity of a Cryogenic Coaxial Liquid Jet to Acoustic Disturbances," *50th AIAA/ASME/SAE/ASEE Joint Propulsion Conference*, AIAA Paper 2014-3487, 2014. doi:10.2514/6.2014-3487

[26] Roa, M., Badakhshan, A., and Talley, D. G., "Acoustically Forced Coaxial Hydrogen/Liquid Oxygen Jet Flames," *28th ILASS Americas*, Inst. of Liquid Atomization and Spray Systems, Dearborn, MI, 2016.

[27] Forliti, D. J., Badakhshan, A., Wegener, J. L., Leyva, I. A., and Talley, D. G., "The Response of Cryogenic H2/O2 Coaxial Jet Flames to Acoustic Disturbances," *53rd AIAA Aerospace Sciences Meeting*, AIAA Paper 2015-1607, 2015. doi:10.2514/6.2015-1607

[28] Juniper, M., Tripathi, A., Scouflaire, P., Rolon, J.-C., and Candel, S., "Structure of Cryogenic Flames at Elevated Pressures," *Proceedings of the Combustion Institute*, Vol. 28, No. 1, 2000, pp. 1103–1109. doi:10.1016/S0082-0784(00)80320-3

[29] Snyder, R., Herding, G., Rolon, J.-C., and Candel, S., "Analysis of Flame Patterns in Cryogenic Propellant Combustion," *Combustion*

Downloaded by Doug Talley on April 16, 2019 | http://arc.aiaa.org | DOI: 10.2514/1.B37079

Science and Technology, Vol. 124, Nos. 1–6, 1997, pp. 331–370. doi:10.1080/00102209708935651

[30] Candel, S., Herding, G., Synder, R., Scouflaire, P., Rolon, C., Vingert, L., Habiballah, M., Grisch, F., Péalat, M., Bouchardy, P., et al., "Experimental Investigation of Shear Coaxial Cryogenic Jet Flames," *Journal of Propulsion and Power*, Vol. 14, No. 5, 1998, pp. 826–834. doi:10.2514/2.5346

[31] Singla, G., Scouflaire, P., Rolon, C., and Candel, S., "Planar Laser-Induced Fluorescence of OH in High-Pressure Cryogenic Lox/GH2 Jet Flames," *Combustion and Flame*, Vol. 144, Nos. 1–2, 2006, pp. 151–169. doi:10.1016/j.combustflame.2005.06.015

[32] Herding, G., Synder, R., Scouflaire, P., Rolon, C., and Candel, S., "Flame Stabilization in Cryogenic Propellant Combustion," *Symposium (International) on Combustion*, Vol. 26, No. 2, 1996, pp. 2041–2047. doi:10.1016/S0082-0784(96)80028-2

[33] Juniper, M., and Candel, S., "Edge Diffusion Flame Stabilization Behind a Step over a Liquid Reactant," *Journal of Propulsion and Power*, Vol. 19, No. 3, 2003, pp. 332–341. doi:10.2514/2.6134

[34] Zong, N., and Yang, V., "A Numerical Study of High-Pressure Oxygen/Methane Mixing and Combustion of a Shear Coaxial Injector," *43rd AIAA Aerospace Sciences Meeting*, AIAA Paper 2005-0152, 2005. doi:10.2514/6.2005-152

[35] Oefelein, J. C., and Yang, V., "Modeling High-Pressure Mixing and Combustion Processes in Liquid Rocket Engines," *Journal of Propulsion and Power*, Vol. 14, No. 5, 1998, pp. 843–857. doi:10.2514/2.5349

[36] Zong, N., and Yang, V., "Cryogenic Fluid Jets and Mixing Layers in Transcritical and Supercritical Environments," *Combustion Science and Technology*, Vol. 178, Nos. 1–3, 2006, pp. 193–227. doi:10.1080/00102200500287613

[37] Okong'o, N., Harstad, K., and Bellan, J., "Direct Numerical Simulations of O2/H2 Temporal Mixing Layers Under Supercritical Conditions," *AIAA Journal*, Vol. 40, No. 5, 2002, pp. 914–926. doi:10.2514/2.1728

[38] Okong'o, N., and Bellan, J., "Real-Gas Effects on Mean Flow and Temporal Stability of Binary-Species Mixing Layers," *AIAA Journal*, Vol. 41, No. 12, 2003, pp. 2429–2443. doi:10.2514/2.6842

[39] Okong'o, N., and Bellan, J., "Turbulence and Fluid-Front Area Production in Binary-Species, Supercritical, Transitional Mixing Layers," *Physics of Fluids*, Vol. 16, No. 5, 2004, Paper 1467. doi:10.1063/1.1688326

[40] Munson, B. R., Rothmayer, A. P., Okiishi, T. H., Huebsch, W. W., and Rothmayer, A. P., "Viscous Flow in Pipes," *Fundamental Fluid Mechanics*, 7th ed., Wiley, Hoboken, NJ, 2013, p. 405.

[41] Badakshan, A., and Danczyk, S., "Ignition of Nanoparticles by a Compact Camera Flash," U.S. Air Force Research Lab. TR AFRL-RQ-ED-TR-2014-0029, Sept. 2014.

[42] Marinet, M. F., and Schettini, E. B. C., "The Density Field of Coaxial Jets with Large Velocity Ratio and Large Density Differences," *International Journal of Heat and Mass Transfer*, Vol. 44, No. 10, 2001, pp. 1913–1924. doi:10.1016/S0017-9310(00)00240-4

[43] "NIST Reference Fluid Thermodynamic and Transport Properties Database (REFPROP)," Software Package, Ver. Matlab 2010b, National Inst. of Standards and Technology, Gaithersburg, MD, 2011.

[44] Yoda, M., Hesselink, L., and Mungal, M. G., "Instantaneous Three-Dimensional Concentration Measurements in the Self-Similar Region of a Round High-Schmidt-Number Jet," *Journal of Fluid Mechanics*, Vol. 279, Nov. 1994, pp. 313–350. doi:10.1017/S0022112094003927

[45] da Sailva, C., Balarac, G., and Métais, O., "Transition in High Velocity Ratio Coaxial Jets Analysed from Direct Numerical Simulations," *Journal of Turbulence*, Vol. 4, No. 24, 2003, pp. 1–18.

[46] Lasheras, J. C., and Hopfinger, E. J., "Liquid Jet Instability and Atomization in a Coaxial Gas Stream," *Annual Review of Fluid Mechanics*, Vol. 32, No. 1, 2000, pp. 275–308. doi:10.1146/annurev.fluid.32.1.275

[47] Pajares, G., and de la Cruz, J. M., "A Wavelet-Based Image Fusion Tutorial," *Pattern Recognition*, Vol. 37, No. 9, 2004, pp. 1855–1872. doi:10.1016/j.patcog.2004.03.010

[48] Mungal, M. G., and Dimotakis, P. E., "Mixing and Combustion with Low Heat Release in a Turbulent Shear Layer," *Journal of Fluid Mechanics*, Vol. 148, Nov. 1984, pp. 349–382. doi:10.1017/S002211208400238X

[49] Broadwell, J. E., and Briedenthal, R. E., "A Simple Model of Mixing and Chemical Reaction in a Turbulent Shear Layer," *Journal of Fluid Mechanics*, Vol. 125, Dec. 1982, pp. 397–410. doi:10.1017/S0022112082003401

[50] Savas, Ö., and Gollahalli, S. R., "Flow Structure in Near-Nozzle Region of Gas Jet Flames," *AIAA Journal*, Vol. 24, No. 7, 1986, pp. 1137–1140. doi:10.2514/3.9404

[51] Ahn, K., and Yu, K. H., "Effects of Damköhler Number on Vortex-Flame Interactions," *Combustion and Flame*, Vol. 159, No. 2, 2012, pp. 686–696. doi:10.1016/j.combustflame.2011.07.021

R. D. W. Bowersox
Associate Editor

Downloaded by Doug Talley on April 16, 2019 | http://arc.aiaa.org | DOI: 10.2514/1.B37079

PRELIMINARY STUDY OF THE REACTING FLOW FROM MULTI-ELEMENT SHEAR COAXIAL FLOWS

Mario Roa
Sierra Lobo, Inc.
Edwards AFB, CA

Douglas. G. Talley
Air Force Research Laboratory
Edwards AFB, CA

ABSTRACT

The reacting flow dynamics from a linear array of three shear coaxial injectors operating under sub-critical pressures was investigated. High-speed images recorded the center injector's response and behavior under the influence of its neighboring injectors for both acoustically unforced and forced conditions. The injectors employed liquid rocket engine relevant propellants of gaseous hydrogen and liquid oxygen. High-speed shadowgraph images along with OH* chemiluminescence captured the hydrodynamic instabilities for each injector and the flame interactions. Overlapping OH* chemiluminescence on top of the shadowgraph images, similar vortex/flame interactions were observed as were observed for a single jet for each individual jet from the injector. Spectral analysis on the OH* chemiluminescence in the near field shows that the individual flames share similar frequency fluctuations when the multi-element array was not subjected to acoustic forcing. These frequencies were also present in the dynamic mode decomposition of the shadowgraph and OH* chemiluminescence images used to investigate the modal structures of both the LOX jet and flame, respectively. Under acoustic forcing, the modal structures of both the LOX jet and flame are the same from each injector.

INTRODUCTION

Liquid rocket engines have been plagued with high frequency combustion instability from their inception [1]. Combustion instabilities in liquid rocket engines arise from complex interactions of acoustic waves coupling and causing oscillatory fluctuation of the volumetric heat release from the combustion process. Combustion instabilities can couple with the combustion chamber acoustics that can directly influence propellant atomization, mixing, flame interactions, and thus, heat release. Combustion instabilities can otherwise also be injector-coupled, where the acoustics from the chamber, propellant feed lines, or injector design drive mass-flow variations into the combustion chamber, causing periodic heat release and pressure fluctuations within the combustion chamber. The complexity of combustion instabilities, and the several potential origins from which they can arise, has usually required expensive trial and error testing to mitigate the severity of the instability in developing new engines [2]. Current efforts in predicting and designing future liquid rocket engines are being developed with computationally expensive models and validating them by using sub-scale liquid rocket engine experiments. This is a more favorable approach since it can potentially limit the amount of expensive development testing. In this effort, a detailed physical and dynamical understanding of the reacting flow from multiple injectors operating at the extreme liquid rocket engine environment is being sought.

Early experiments into understanding combustion instabilities have been documented progressively throughout the years [1-9], and so only the most recent research efforts are reviewed here. The current experimental efforts aimed at studying combustion instabilities are performed by constructing sub-scale combustion chambers that are naturally unstable [10-12] or by the actively driving the reacting forcing with flow modulation [13-15] or speakers. Less extensively investigated is how a single injector's reacting flow field responds physically and dynamically in the presence of neighboring injectors. The few academic studies that have tried are limited in scope to measurements that are possible at such extreme environments. In those studies where optical access is integrated into the experiment, the results typically consist of species selective emission from the flame and time resolved pressure measurements to deduce acoustic/flame interactions. More limited in these studies are quantitative measurements (e.g. Temperature,

velocity, density field, etc…) and a detailed temporal and spatial observations of how the shear flows from multiple injectors and flames interact under acoustic forcing. All of these are vital for the development of future computer models.

Purdue University [10-12] studies combustion instabilities with naturally unstable combustors. Both the transverse instability combustor and the continuously variable resonance combustor are capable of producing self-sustaining transverse and longitudinal combustion instabilities, respectively. The transverse instability combustor is a rectangular combustion chamber with multiple injectors that is capable of producing high-amplitude 1T-mode instability. This is done by locating gas-centered swirl coaxial injectors on either side of a center injector, which is optically accessible. Using high speed backlit imaging with CH* chemiluminescence, they observed CH* emission from the center injector was impeded when the pressure wave was maximum at the center injector. Comparing CFD results with the experimental CH* chemiluminescence, they observed that locations with the highest heat release corresponded well with an increase in the CH* emission both temporally and spatially. This is also the case with the continuously variable resonance combustor, where the combustion instabilities were driven by changing the oxidixer tube length during experimental runs.

Hardi *et. al*. [13-15] employed flow modulation to study high frequency combustion instabilities. This experimental method produces pressure wave excitation of the acoustic resonance modes of the combustion chamber by periodically blocking the exhaust nozzle using a toothed wheel. The location of the toothed wheel determines if transverse or longitudinal instabilities are created for the experimental setup. Hardi *et. al*. studied flame displacement from a multi-element gaseous hydrogen/liquid oxygen shear coaxial to the pressure waves created by the flow modulation. Using the OH* emission from the flame, they employed a flame tracking technique to observe the flame displacement by a transverse acoustic forcing. They attributed the flame displacement to acoustic forcing is probably due to the displacement of the propellants. Even though they collected back-lit imaging from the experiment, due to the vast amounts of density gradients in the reacting flow, few observation were made on the propellant displacement behavior.

Concurrent computational studies performed by Candel *et al*. [16-20], Juniper *et. al.* [21], Sirignano [22,23] and at Edwards AFRL [24] have focused on matching experimental results with their computational models and identifying flow features and physics that lead to combustion instabilities that are missing from the experimental results. Using large eddy simulations of liquid oxygen with a gaseous fuel (Hydrogen or Methane) Candel *et. al.* studied the effects acoustic forcing had on the flame and liquid oxygen jet geometry. Similar to previous experimental results, the liquid oxygen jet shortened and flattened due to the acoustic forcing. They also observed that depending on the acoustic forcing frequency, the flame would have a flag flapping motion or be displace in a bulk fashion. Juniper *et. al.* studied the stability and sensitivity of a coaxial flow using linear models. This was accomplished by varying time and spatial scales for hydrodynamic response to acoustic forcing. They observed that varying the degree of hydrodynamic instabilities greatly influences the regions of heat release and hence the overall thermo-acoustic instability cycle. Sirignano *et. al.* used linear models to study coaxial diffusion flames with and without acoustic forcing. This method used less costly computations to perform a parametric study on varying flow parameters (e.g. injector dimensions) and to observe trends within the flow field. Using a hybrid RANS/LES formulation, researchers at Edwards AFRL studied coupling between acoustics, hydrodynamics, and heat release of Purdue's continuously variable resonance combustor. They investigated the injector's exit conditions under stable and unstable conditions. The physical interactions of the hydrodynamic response of the injector to the acoustic forcing that led to the unsteady heat release are detailed in [24]. They observed that under unstable conditions, vortex shedding from the injector would carry with it unburned propellants and would react when it encounters the incoming pressure wave.

Recent experimental single element studies from Edwards AFRL [25-26] have highlighted several physical interactions between the hydrodynamics instabilities and acoustic forcing that have been missing from the previous experimental studies. Unlike the naturally unstable combustors or the flow modulated combustors, piezo-sirens are used to acoustically drive the reacting flow. The volume occupied by the reacting flow is kept small relative to the volume of the chamber. This ensures that heat release from the combustion is not allowed to from a feed-back loop and become naturally unstable. This method allows for direct observation of how a varying amplitude levels of acoustic pressure influences the reacting flow from a single shear coaxial injector. Using high speed images with OH* emission to study a gaseous hydrogen/liquid oxygen shear coaxial flame, they detailed the influence that shear layer hydrodynamics have on the downstream flow. They observed that when a vortex is formed on the outer shear layer, the vortex would locally consume the liquid oxygen jet at a rapid rate. Spatially at the same location, there will be an increase in OH* emission, where they argued that the vortex would increase the rate of mixing and hence locally consume the liquid oxygen jet. When the same single element was subjected to acoustic forcing, they observed that the outer shear layer vortices would "lock in" to the acoustic forcing frequency when the forcing amplitude was sufficiently high enough.

Using the same experimental chamber at Edwards AFRL, a three element, linear array of shear coaxial injectors were investigated operating at one condition. The linear injector array was studied with and without acoustic forcing. Using high speed shadowgraph and OH* chemiluminescence, this preliminary investigation focuses on the influence the two neighboring elements have on the center injector. This preliminary study is aimed at identifing the spectral behavior and physical interactions between the acoustics and flow features in the near nozzle region that can influence the center injector. Spectral analysis of OH* emission and dyanmic mode decomposition on the high speed images were performed in order to identify the physical flow features that are influencing behavior of the center injector.

EXPERIMENTAL SETUP

The 3 element linear array of shear coaxial injectors was tested at the Stability Lab's high-pressure, windowed combustion chamber at the Edwards AFRL. Figure 1 shows an assembly drawing of the windowed chamber. The main body of the outer chamber is shown in orange. Mounted on the orange chamber are a total of six windows, consisting of two large 101 mm (4 in) diameter round sapphire windows and four oblong windows angled at 45 degree offsets. The chamber is symmetric about the vertical center plane, so only three of the windows are shown in Figure 1. Only the two (diametrically opposed) round windows were used in this study; the oblong windows were not used. The round windows were used for high speed shadowgraphy and OH* chemiluminescence imaging, described further below. The gaseous hydrogen and liquid oxygen enter settling plenums that feed the linear injector array from the grey flange on top. The combustion gases would exit from the green flange on the bottom. Pressurizing nitrogen is introduced into sides of the combustion chamber, as shown in figure 2, hence the combustion process is not used to pressurize the chamber. On either side of the main chamber are high pressure acoustic channels shown in yellow in figure 1, which are connected to and held at the same pressure as the main chamber. Piezoelectric acoustic drivers are attached internally to the grey flanges on either end. There is no flow in the channels other than the flow induced by the acoustics when they are being operated.

Figure 2 shows a schematic of the internal details of the chamber acoustic channel. The acoustic channel constitutes an inner chamber. The inner chamber is connected to and is at the same pressure as the outer chamber and cannot itself sustain any pressure difference with the outer chamber. It does, however, focus the acoustics and limits hot combustion gases from exiting into the main chamber. The outer chamber and associated pressure-containing windows and window seals are therefore not exposed to potentially damaging high temperature combustion gases. The multi-element injector is located in the center of this inner chamber and at the top. The injector issues into the acoustic channel where two opposed flat windows are used as walls of the acoustic channel for visualization, measuring 76.2 mm (3 in) wide by 41.4 mm (1.63 in) high. Three dynamic pressure transducers are located in the rectangular inner windows to measure acoustic pressure fluctuations, as shown in figure 2. In the vicinity of the multi-element coaxial injector, the inner cross section of the acoustic channel normal to the page is rectangular with 20.5 mm (0.81 in) wide (or 13 inner liquid oxygen injector diameters) and 35.5 mm high. The end-to-end length of the acoustic channel or piezo-siren to piezo-siren is 0.75 m or 473 inner liquid oxygen post diameters. There is a round-to-rectangular transition from the acoustic drivers to the channel, but the transition is far enough away from the multi-element injector to not be of any influence.

The combustion chamber is pressurized using nitrogen gas from the two side inlets (which are shown in Figure 2) and does not rely on the combustion process to provide chamber pressure. This is accomplished by keeping the volume occupied by the flame small compared to the combined volume of the inner and outer chambers. This was done in order to maintain accurate control of the chamber pressure and de-couple any thermo-acoustic interactions. Combustion gases exit the inner chamber through a hole in the bottom of the inner chamber and these gases together with pressurizing gases exit the outer chamber through a metering orifice (not shown) at the bottom of the outer chamber. A mixing fitting at the exit, also not shown, dilutes the combustion gas with the exiting pressurizing gas, so that the metering orifice only experiences relatively cool temperatures.

In addition to the fuel and oxidant and pressurizing nitrogen, a separately controlled nitrogen bleed is introduced through round holes in a face plate surrounding the coaxial injector on the upper wall of the inner chamber. The bleed suppresses the formation of a hot gas recirculation zone near the injector that can otherwise influence the

dynamics of the reacting flow. The faceplate with the bleed holes is illustrate in Figure 3. The linear array of coaxial injectors are located in the center of the plate. The inner diameter of each liquid oxygen jet is 1.58 mm (0.0625in), with a LOX post thickness of 0.39 mm. The outer diameter of the hydrogen flow is 2.82 mm (0.11in). The center of each coaxial injector are separated 2.8 inner liquid oxygen diameters away from each other. The diameter of the bleed holes is 0.5 mm. The nitrogen bleed is regulated to a velocity of 0.08 m/s. Also in the faceplate are slots next to the windows for window cooling. In order to avoid steam condensation that would otherwise obstruct the optical view to the reacting flow, the window cooling was also fed gas nitrogen fed with an exit velocity of 5.7 m/s. Although, the velocity from the window purge is high, the momentum flux ratio from the linear injector when compared to the bleed port and the window cooling is well over 10^4 and 15, respectively. Hence, the flow at least in the near nozzle region, the linear injector flow is expected to dominate the downstream flow.

The bleed ports and window cooling manifolds were analyzed to determine the possible presence of resonances that might affect the dynamic results reported in this paper. The resonant frequencies were found to be many times lower than the frequencies associated with these results. The gas circuit of the annular fuel manifold (hydrogen) was similarly analyzed and also found not to be acoustically active for these experiments.

All flows were regulated and metered as high pressure gases and calibrated orifices. Following regulation and metering, the flows were subsequently chilled to the desired temperatures, for example to liquefy the oxygen, using heat exchangers cooled with liquid nitrogen. The pressurizing nitrogen gas and the other nitrogen flows were heated to 305 K to overcome the chilling effects due to Joule-Thompson expansion effects. Each element of the linear injector was designed to have straight passages resulting in fully developed flows at the exit. The internal passages for the linear injector was designed to have injector length to exit diameter (L/D) of over 100. The Reynolds numbers of the fuel and oxygen exceeded 10^4 and are assumed to be turbulent. The pressure and temperature for both LOX and hydrogen were measured before entering the injector. The LOX jet was kept at 140 K, and the hydrogen gas was chilled to 295 K prior to entering the injector. Some heat exchange occurred inside the injector internal passages due to the temperature difference. In order to minimize this heat exchange, the injector was pre-chilled. Before the hydrogen and LOX entered the injector, chilled gaseous nitrogen ran through the hydrogen circuit and liquid nitrogen ran through the LOX fed circuit for 30 minutes prior to combustion.

The chamber pressure used this study was 3.4 MPa (500 psia). This is considerably below the critical pressure of oxygen, so the oxygen was initially a liquid. When the acoustics were present a standing wave was formed at a frequency of 2750 Hz with a wavelength of 0.13 m, which is much larger than the diameter of the injector. The phase of the standing wave was adjusted to correspond to a pressure node at the injector exit. To form the standing wave, a waveform generator, Keysight 33500B, was used to driven high voltage amplifiers, Trek PZD2000A, connected to individual piezo-sirens. A constant pressure amplitude of 13.78 kPa (2 Psi) was used for this study. The pressure amplitude and phase of the standing wave were measured and adjusted using differential pressure transducers, Kulite XCL-100D, prior to ignition. Igniting the flows at this pressure proved to be non-trivial as most spark ignition methods do not work when a high pressure is established prior to ignition as in this experiment. The approach used was a hydrogen-air torch, ignited using a photoignition technique. See Badkahshan et al [27] for details about the photoignition technique.

The reacting flow was visualized with simultaneous high speed shadowgraphy and OH* chemiluminescence. The imaging arrangement is illustrated in Figure 4. The imaging systems captured the unsteadiness of the reacting flow at a framing rate of 25 kHz for 5000 frames or 0.2seconds. The high speed shadowgraph optics were composed of a 7.6cm (3 inch) collimated light source, formed with a ThorLabs SL S202 broadband light source and a spherical 152 mm lens, imaged onto a Phantom Research v 710 with an Sigma Hyperzoom lens. Simultaneously, OH* chemiluminescence was captured with Lambert Instruments HICATT imaged directly onto a Phantom Research v1210 camera. An UV lens (F/2.8 Cerco 2178) with a Semrock (PN FF02-320/40) optical filter were used to image the OH* emission at 308nm. Both cameras have a setup to have a resolution of 0.08mm/pixel. An IRIG time signal synchronized the high-speed imaging and data acquisition systems. A dichroic mirror was used to reflect the UV OH* emission from the flame onto the intensifier, while allowing the visible light to pass through for the shadowgraph images. The both imaging systems captured the over 14 liquid oxygen diameters from the nozzle exit.

The gas-to-liquid momentum flux ratio $\left(J = \frac{\rho U_{Gas}^2}{\rho U_{Liquid}^2}\right)$ has been identified as a global parameter that controls the atomization and breakup a liquid jet in two phase coaxial flows [28]. From previous researchers, it has been observed that if the momentum ratio is too high, then the center liquid is severely shorten and the dynamics and flow physics downstream are highly turbulent and difficult to analyze. In order to understand the impact that neighboring injector's shear layers have on the center injector, a momentum ratio hydrogen to liquid oxygen of 0.5 was selected for this preliminary study.

RESULTS

A sequential series of the instantaneous shadowgraph and OH* emission images is shown in figure 5. In figure 5 the shadowgraph is wavelet fused (left columns) and overlaid (right columns) with its corresponding false colored OH* image. Present in the background of these images are many density gradients from the reacting flow, making it difficult to visualize the hydrogen jet emanating from the linear injector array. Although, the hydrogen jet is difficult to observe, the liquid oxygen jet is clearly visible. From figure 5, each flame envelopes the liquid oxygen jet in the near nozzle region and does not interact with the neighbor until further downstream. In the results observed by Roa *et. al.*[25] for a single injector and using the same propellants, bands of high intensity OH* emission were observed. When the hydrogen jet rolled up into a vortex, it would locally consume the liquid oxygen jet and form a crest on the liquid column. Similar high intensity OH* emission bands are observed in figure 5 for each flame, along with the crests on the liquid oxygen jet.

One way that the center flame can be influenced by its neighbors is through these hydrogen vortex shedding events. As stated earlier, the exact shedding event is difficult to observed directly due to the all density gradients in the background, but the high intensity OH* emission bands, which indicate the presence of an outer shear layer hydrogen vortex, can be tracked for each jet. This can be seen indirectly by tracking the OH* emission fluctuations along a given position of the flame. In figure 5, the interrogation area used to record the OH* emission fluctuations is shown in the green boxes for the left, middle, and right jet flames, for which for now on will be referred to as Jet1, Jet 2, and Jet 3, respectively. The interrogation area is chosen to be one inner liquid oxygen jet diameter away from the nozzle exit and half an inner liquid oxygen diameter in length. Within the interrogation area the OH* emission was integrated for each frame with the temporal mean subtracted. Using a cross spectral density calculation, the OH* emission fluctuations signal of Jet 2 (central injector element or the study element) can be compared with those of the other two.

Figure 6 shows the cross spectral density (CPSD) plots of Jet 2 analyzed with Jet 1 and Jet 3. From the CSPD plots, the frequency with the highest spectral energy among all three jets are close, with 2637 Hz between Jet 2 and Jet 1 and 2647 Hz between Jet 2 and Jet 3. Examining the phase difference from the CPSD plots, the OH* emission fluctuations from the central jet is almost out of phase with its neighboring flames. The phase difference, in degrees, between Jet 2 and 1 is 154˚ and 170.5˚ between Jet 2 and 3. This phase differences corresponds to a time lag of 0.16 milliseconds between Jet 2 and 1 and 0.18 milliseconds between Jet 2 and 3. This indicates that in the near nozzle region, within one inner liquid oxygen diameter, the Jet 2 flame is interacting and being influenced by its neighbors. Specifically, Jet 2 flame's fluctuations are on average out of phase with respect to Jet 1 and 3.

Further investigating the out of phase relationship that the Jet 2 has with its neighbors, dynamic mode decomposition (DMD) was applied on both OH* emission and shadowgraph images. Dynamic mode decomposition is a numerical procedure for extracting dynamical features from flow data. In the DMD applied in this study, the high speed images were decomposed into spatial modes, with each spatial mode having a unique frequency and amplitude. These spatial modes are associated with physical features of the flow field oscillating at a fixed frequency [29]. The larger the mode amplitude of the associated spatial mode, the more dominant that spatial feature is to the flow field being interrogated. The window of interrogation for the DMD analysis for the OH* emission and shadowgraph started at the nozzle exit and extended 5.8 inner liquid oxygen diameters and 10 inner liquid oxygen diameters, respectively. The interrogation area is shown in figure 5. The difference in the interrogation areas is because it assumed that if one hydrogen jet sheds a vortex close to the nozzle, it produces a flow disturbance downstream, causing the other two jets to also shed a vortex lagging the initial vortex. This leads to a convective instability that can manifest itself as the crest on the liquid oxygen jets traveling downstream, due to the flame/vortex interactions previously detailed by Roa *et. al.* The power spectral density of the OH* emission of Jet 2 is shown in figure 7. Plotted on the power spectral density is a shaded region with the frequencies associated with 25% of the total energy from the OH* emission fluctuations.

Comparing this frequency range to the DMD amplitudes, a cluster of DMD amplitude peaks are observed to fall within this frequency range, as shown in figure 8.

Analyzing the spatial modes within this frequency range provides information as to how the flame and the liquid oxygen jet are dynamically and spatially behaving. Figure 9 is the spatial mode associated with the max frequency of 2635 Hz from cross spectral density in figure 7. Figure 9 demonstrates the out of phase relationship Jet 2 has with its neighbors. The alternating red and blue bands in figure 9 are locations where there are changes in OH* emission and surface crests on the liquid oxygen jet. For the OH* emission spatial mode along a fixed distance away from the nozzle, the bands alternate and are nicely organized and degrade the further downstream. This is representative of how the almost 180˚ phase between the jet flame is manifested itself spatially. What is physically occurring is when one hydrogen vortex sheds and produces an OH* emission band across the jet, the other two jet flames response likewise at an almost constant time lag. A comparable offset is present on the shadowgraph spatial mode, but further downstream where the crests on the liquid oxygen surface have enough time grow.

The dynamics the spectral features of the linear injector array were also investigated when subjected to acoustic forcing for the same condition investigated earlier. The linear array was subjected to an acoustic standing wave at a frequency of 2750 Hz and a pressure amplitude of 13.78 kPa (2 Psi). The phase of the standing wave was adjusted so the injector array would be subjected to pressure-node forcing. In a pressure-node the velocity fluctuations are maximum, hence the injector array was subjected to an oscillating velocity field. Figure 10 shows instantaneous images of the reacting flow subjected to acoustic forcing. The liquid oxygen jet is drastically different compared to the unforced case in figure 5. From figure 10 the liquid oxygen jet has developed periodic lobes. The flame also takes on a similar shape near the nozzle exit with high intensity OH* emission located between the lobes of the liquid oxygen jet. It was shown previously [26] that when a single coaxial jet is subjected to pressure-node forcing, the jet takes on an S-shape. This S-shape is consistent in Jets 1, 2, and 3, with the lobes on individual liquid oxygen jets being slanted.

Theoretically, when these types of flows are subjected to a transverse acoustic velocity, this causes improved mixing of the propellants. What occurs is that with each passing acoustic wave, propellants are transported or displaced. This displacement brings unreacted fuel or oxidizer closer or impinges one on its counterpart, resulting in increased mixing of the propellants. This unreacted mixture then releases its energy in phase with acoustic pressure, forming a feedback loop towards a combustion instability limit cycle. This appears to be occurring for all three flames in this study.

Dynamic mode decomposition of the OH* emission and shadowgraph images when subjected to pressure node forcing shows the flame and its effect on the downstream flow. The DMD analysis was applied at the same locations as the unforced condition, as shown in figure 5. Figure 11 shows the DMD amplitude along with the spatial mode at the forcing frequency 2750 Hz. The DMD amplitude for both set of images shows strong frequency peaks at the forcing frequency along with higher harmonics, indicating the flow field has strongly coupled with the acoustic forcing. The DMD spatial mode for 2750 Hz, shows that the alternating OH* emission pattern is slanted unlike the unforced condition. This slanted alternating pattern is representative of changes in OH* emission intensity. It is suspected that as the transverse velocity field pushes on one side of the hydrogen jet and brings it closer to the liquid oxygen jet. This increases local equivalences ratios on the side that forcing and/or displaced occurs and consumes the liquid oxygen, resulting in the lobes shown in figure 10. The DMD spatial mode from the shadowgraph images shows an offset alternating pattern, representative of the lobes on the liquid oxygen jet. The lobe pattern is observed to fully develop further downstream, hence the displacement of the flame in the near nozzle region influences the shape of the liquid oxygen jet downstream. Given that the physical features of the flame and liquid oxygen jet are the same across linear array, Jet 2 does not seem to be greatly influenced by its neighbors. Instead, all three jets appear to have coupled with the acoustic forcing, minimizing their interactions among each unlike the unforced condition.

CONCLUSION

The reacting flow dynamics from a linear array of three shear coaxial injectors operating under sub-critical pressures was investigated with and without acoustic forcing. High-speed shadowgraph and OH* chemiluminescence mages recorded the center injector's response and behavior under the influence of its neighboring injectors. In the unforced condition, all three jet flames were coupled within a narrow frequency band and were almost completely out of phase with each other. This indicated that when one jet produced a flow disturbance, such as vortex shedding, the other two responsed in kind with a time lag. Dynamic mode decomposition of the unforced condition, showed that the physical features from each jet were indeed out of the phase with each other. When the linear array was subjected to

a transverse acoustic velocity field, all three jets had the same response coupling with the acoustic forcing, with little observed inter-jet interactions. It was observed that in all the jets, the liquid oxygen jet developed altenrating lobes on either side, which was picked up by the DMD analysis. The DMD analysis also revealed that the flame had slanted lobes that is consistent with transverse acoustic field displacing the outer hydrogen jet closer to the liquid oxygen jet. These results elucidate the the flow-flame interactions that occur when driving non-premixed rocket flames by transverse acoustic.

REFERENCES

[1] Ross, C. C., and Datner, P. P., "Combustion Instability in Liquid-Propellant Rocket Motors–A Survey," Selected Combustion Problems, edited by Hawthorne, W. R., Fabri, J., and D. B., Spalding, Butterworths Scientific, London, 1954, pp. 352–380.

[2] Oefelein, J. C., and Yang, V., "Comprehensive Review of Liquid- Propellant Combustion Instabilities in F-1 Engines," Journal of Propulsion and Power, Vol. 9, No. 5, 1993, pp. 657–677.

[3] Anderson, W. E., Ryan, H. M., and Santoro, R. J., "Combustion Instability Phenomena of Importance to Liquid Bi-Propellant Rocket Engine," 28th JANNAF Combustion Subcommittee Meeting, edited by Gannaway, M. T., Chemical Propulsion Information Agency (CPIA), Columbia, MD, 1991, pp. 99–112.

[4] Crocco, L., and Cheng, S.I., Theory of Combustion Instability in Liquid Propellant Rocket Motors, AGARDograph 8, Princeton Univ., Princeton, NJ, 1956, pp. 1–24.

[5] Harrje, D. T., and Reardon, F. H., "Liquid Propellant Rocket Combustion Instability," NASA Special Publ. SP-194, 1972.

[6] Culick, F. E. C., "Combustion Instabilities in Liquid-Fuelled Propulsion Systems," AGARD Conference Proceedings, NATO Paper 450, Neuilly sur Seine, France, 1988.

[7] Culick, F. E. C., "Unsteady Motions in Combustion Chambers for Propulsion Systems,"NATOAGARDograph AG-AVT-039, California Inst. of Technology, Pasadena, CA, 2006.

[8] Yang, V., and Anderson, W. E. (eds.), Liquid Rocket Engine Combustion Instability, Vol. 169, Progress in Astronautics and Aeronautics, AIAA, Washington, D.C., 1995.

[9] Natanzon, M. S., Combustion Instability, Vol. 222, Progress in Astronautics and Aeronautics, AIAA, Washington, D.C., 2008.

[10] Morgan C. J., Shipley, K. J., and Anderson, W. E., "Comparative Evaluation between Experiment and Simulation for a Transverse Instability," Journal of Propulsion and Power, Vol. 31, No. 6, 2015

[11] Pomeroy, B. R., Morgan, C., and Anderson, W. E., "Response of a Gas Centered Swirl Coaxial Injector to Transverse Instabilities," 47th AIAA/ ASME/SAE/ASEE Joint Propulsion Conference & Exhibit, AIAA Paper 2011-5698, 2011

[12] Yu. Y. C., Sisco, J. C., Rosen, S., Madhav, A., and Anderson W. E., "Spontaneous Longitudinal Combustion Instability in a Continuously Variable Resonance Combustor," Journal of Propulsion and Power, Vol. 28, No.5, 2012

[13] Hardi. J. S., Beinke, S. K., Oschwald, M.., and Dally, B. B., "Coupling of Cryogenic Oxygen-Hydrogen Flames to Longitudinal and Traverse Acoustic Instabilities," Journal of Propulsion and Power, Vol. 30, No. 4, 2014

[14] Gröning, S., Hardi. J. S., Suslov. D., and Oschwald. M., "Injector-Driven Combustion Instabilities in a Hydrogen/Oxygen Rocket Combustor," Journal of Propulsion and Power, Vol. 32, No. 3, 2016

[15] Hardi. J. S., Oschwald. M., and Dally, B. B., "Study of Lox/H2 Spray Flame Response to Acoustic Exictation in a Rectangular Rocket Combustor," 49th AIAA/ ASME/SAE/ASEE Joint Propulsion Conference & Exhibit, AIAA Paper 2013-3781, 2013

[16] Hakim. L., Schmitt. T., Ducruix, S., and Candel S., "Dynamics of a Transcritical Coaxial Flame under High-Frequency Transverse Forcing: Influence of the Modulation Frequency on the Flame Response," Combustion and Flame, 162, 2015

[17] Urbano, A., Selle, L., Staffelbach, G., Cuenot, B., Schmitt, T., Ducruix, S., and Candel, S., "Exploration of Combustion Instability Triggering using Large Eddy Simulation of a Multiple Injector Liquid Rocket Engine," Combustion and Flame, 169, 2016

[18] Richecoeur, F., Ducriox, S., Scouflaire, P., and Candel, S., "Experimental Investigation on High-Frequency Combustion Instabilities in Liquid Rocket Engines," Acta Astronautica, 62, 2008

[19] Rey, C., Ducruix, S., Richecoeur, F., Scouflaire, P., Vingert, L., and Candel, S., "High Frequency Combustion Instabilities Associated with Collective Interactions in Liquid Propulsion," 40th AIAA/ ASME/SAE/ASEE Joint Propulsion Conference & Exhibit, AIAA Paper 2004-3518, 2004

[20] Richecoeur, F., Scouflaire, P., Ducruix, S., and Candel, S., "High-Frequency Transverse Acoustic Coupling in a Multiple-Injector Cryogenic Combustor," Journal of Propulsion and Power, Vol. 22, No. 4, 2006

[21] Magri. L., See, Y. C., Tammisola, O., Ihme, M., and Juniper, M. P., "Multiple-Scale Thermo-Acoustic Stability Analysis of a Coaxial Jet," Proceedings of the Combustion Institute, 36, 2017

[22] Popov, P. P., Sideris, A., and Sirignano, W. A., "Low-Probability Events Leading to Rocket Engine Combustion Instability," Journal of Propulsion and Power, Vol. 55, No. 3, 2017

[23] Sirignano, W. A., and Krieg, J., "Coaxial Jet Flame Subject to Long-Wavelength Acoustic Oscillations," Journal of Propulsion and Power, Vol. 32, No. 3, 2016

[24] Harvazinski, M. E., Huang, C., Sankaran, V., Feldman, T. W., Anderson, W. E., Merkle, C. L., and Talley, D. G., "Coupling Between Hydrodynamics, Acoustics, and Heat Release in a Self-Excited Unstable Combustor," Physics of Fluids, 27, 2015

[25] Roa, M., and Talley, D. G., "Vortex Dynamic Mechanisms in Coaxial in Hydrogen/LOX Jet Flames," Submitted to Journal of Propulsion and Power, 2018

[26] Roa, M., Forliti, D., Badakhshan, A., and Talley, D. G., "Acoustically Forced Coaxial Hydrogen/ Liquid Oxygen Flames," ILASS Americas 28th Annual Conference, 2016

[27] Badakshan, A., and Danczyk, S., "Ignition of Nanoparticles by a Compact Camera Flash," DTIC http://www.dtic.mil/dtic/tr/fulltext/u2/a614547.pdf

[28] Marinet, M. F., and Schettini, E. B. C.,"The density field of coaxial jets with large velocity ratio and large density differences," International Journal of Heat and Mass Transfer, Vol. 44, 2001

[29] Schmid, P. J., "Dynamic Mode Decomposition of Numerical and Experimental Data," Journal of Fluid Mechanics, Vol 656, 2010

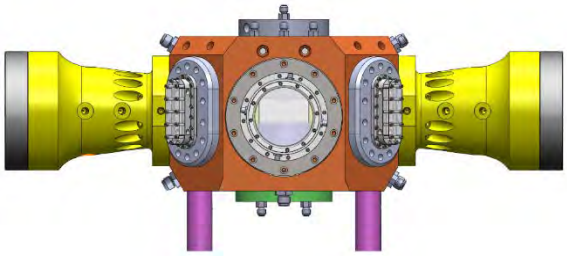

Figure 1. Assembly drawing of the combustion chamber.

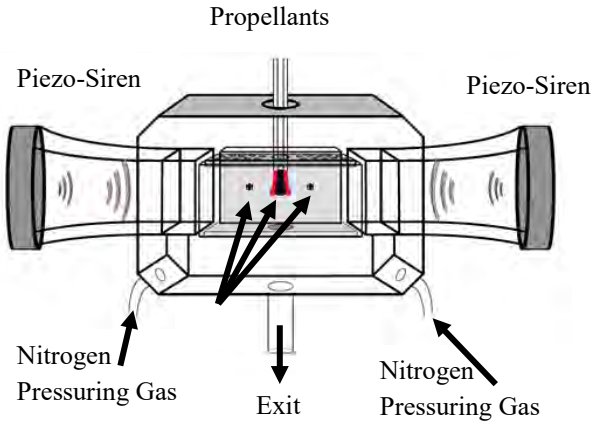

Figure 2. Inner details of the combustion chamber. P' is the location of the differential pressure transducers. The gray section in the middle is the optical windows used to complete the acoustic channel.

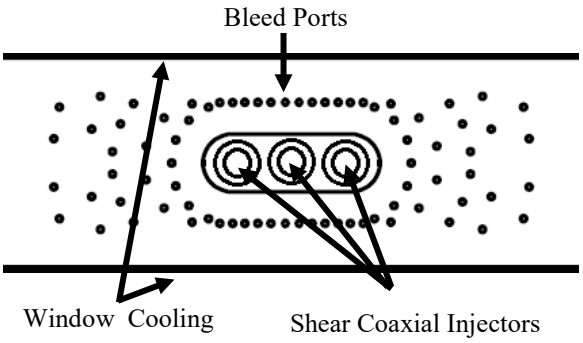

Figure 3. The injector faceplate with bleed ports, window film cooling, and linear array injector in the center.

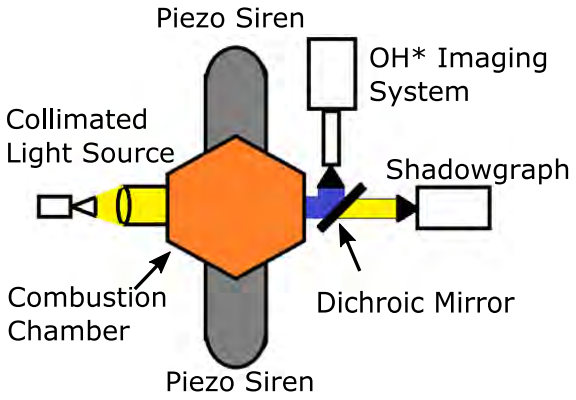

Figure 4. High speed, simultaneous imaging system layout.

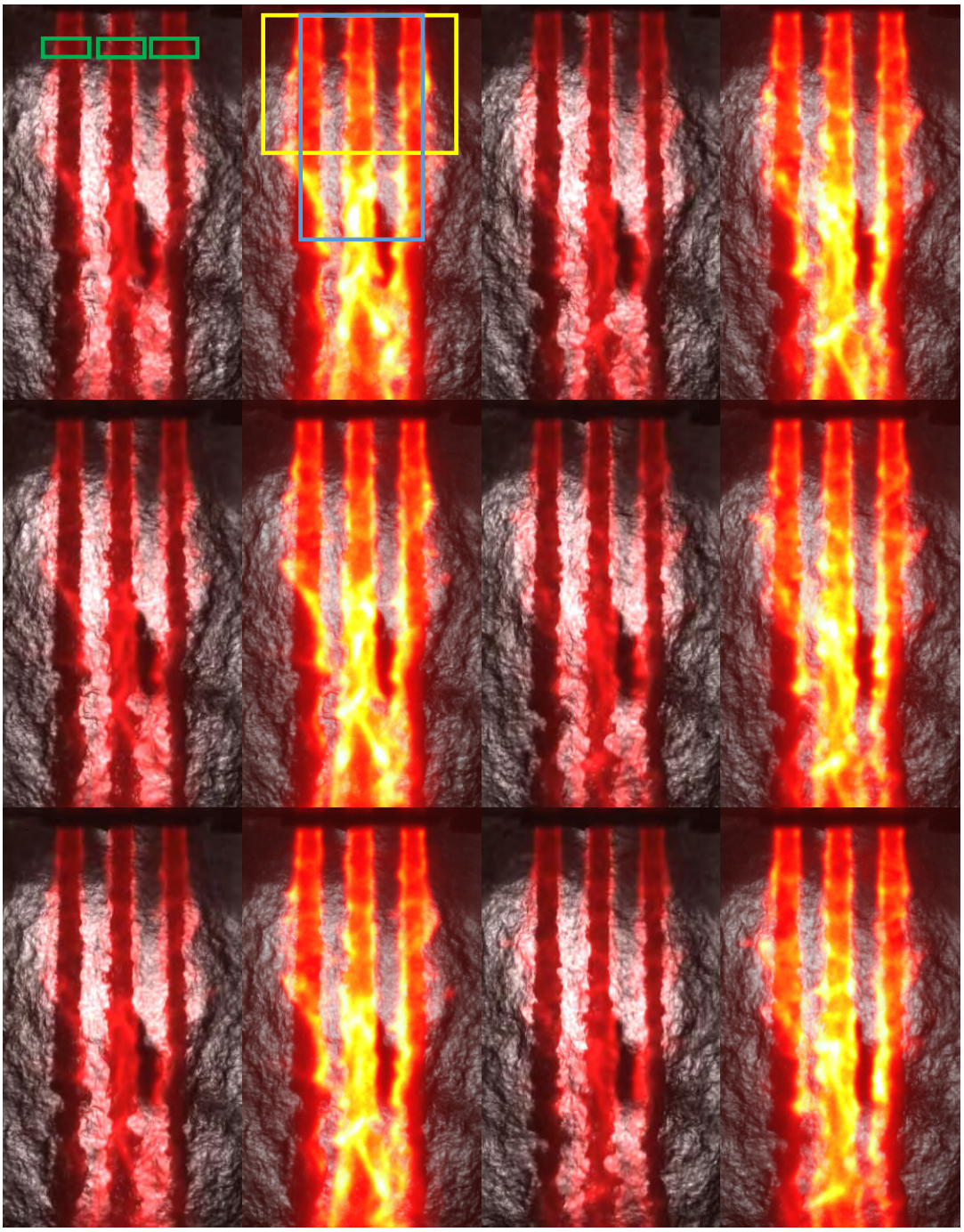

Figure 5. Instantaneous images of the shadowgraph with OH* emission wavelet fused and overlapped (Left column then immediate right, respectively). The time separation between each frame is 0.16 milliseconds. The flame in the near nozzle region don't merge or interact. Each flame surrounds its corresponding liquid oxygen jet. At the locations of high OH* emission, waves form on the liquid oxygen jet. The images are sequential from top to bottom, left to right. The green rectangles are the locations where the OH* emission fluctuations were recorded. The yellow and blue squares is where the DMD snapshots were taken for the OH* emission and shadowgraph, respectively.

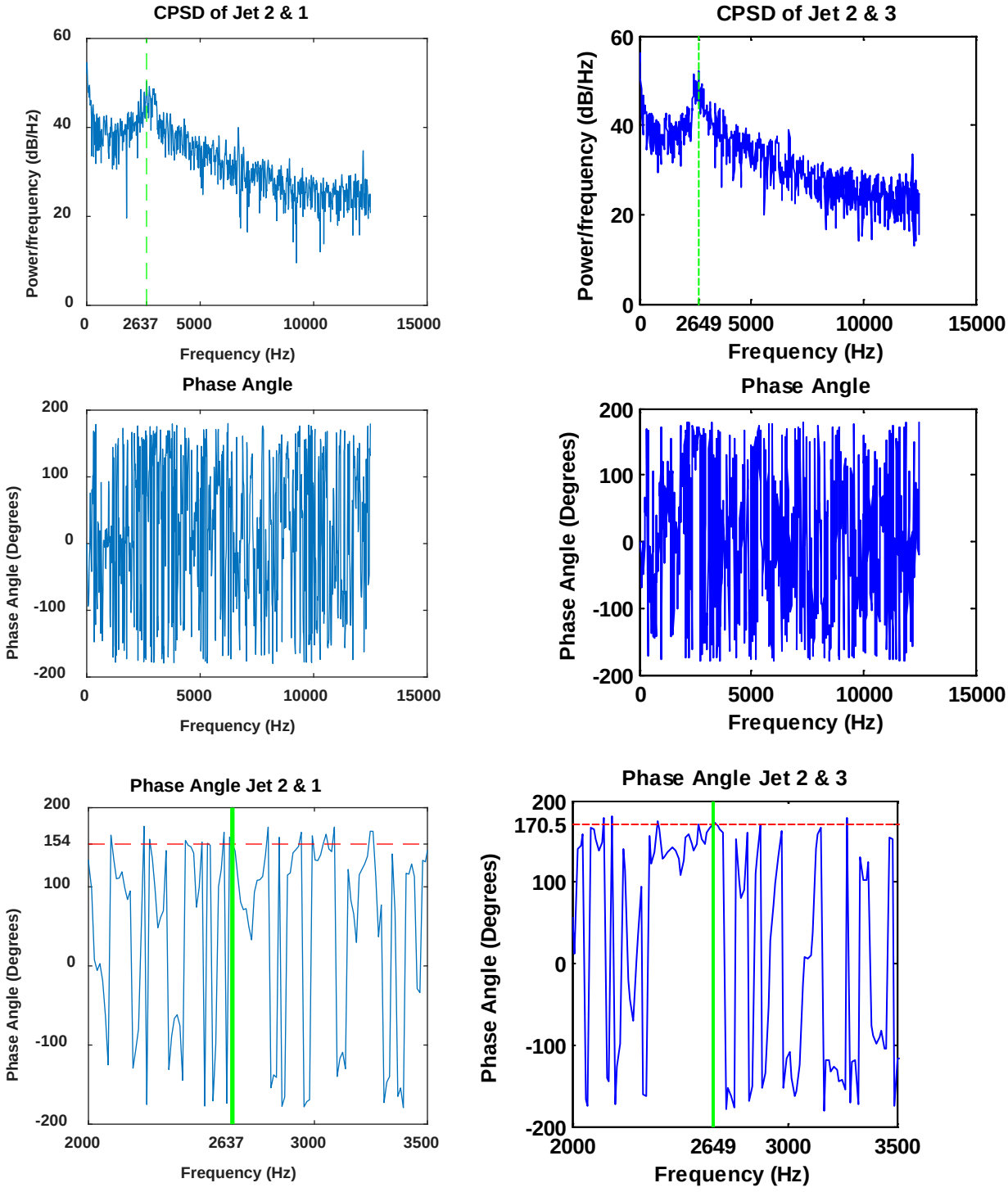

Figure 6 The cross spectral density estimates (CSPD) of the OH* fluctuations between, left column, Jet 2 and Jet 1, and the right column is between Jet 2 and Jet 3. Below each CPSD is the phase between both signals, along with a narrow frequency window. The green line is the dominate frequency and the red dash line is the corresponding phase between both signals.

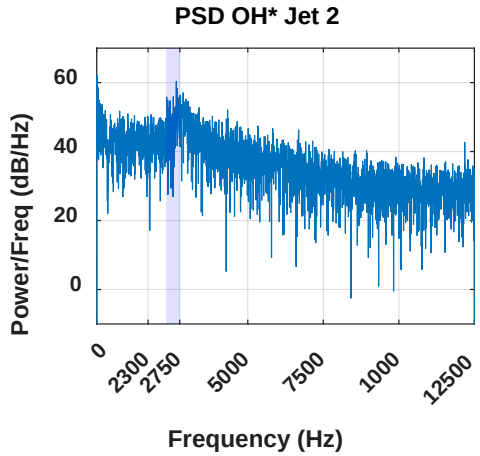

Figure 7. Power spectral density plot of Jet 2, with a shaded region that occupies 25% of the total energy. Between frequencies 2306 and 2756 Hz.

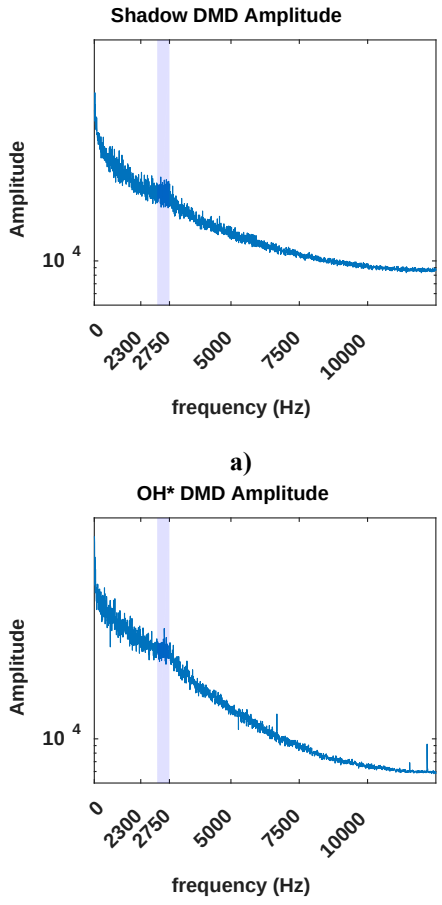

Figure 8. The DMD Mode Amplitude vs Frequency. The shaded region is the 25%occupied frequency from Jet2 for a) Shadowgraph and b) OH* emission.

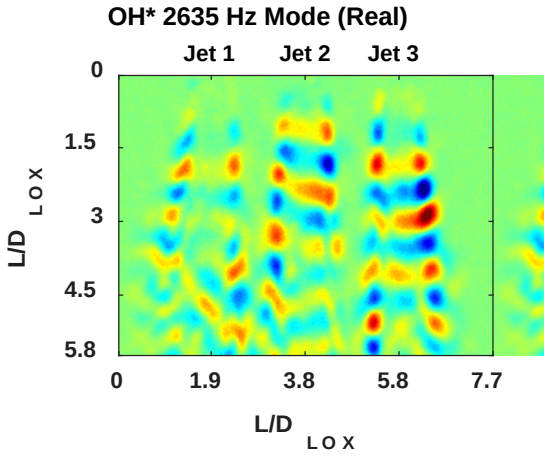

a)

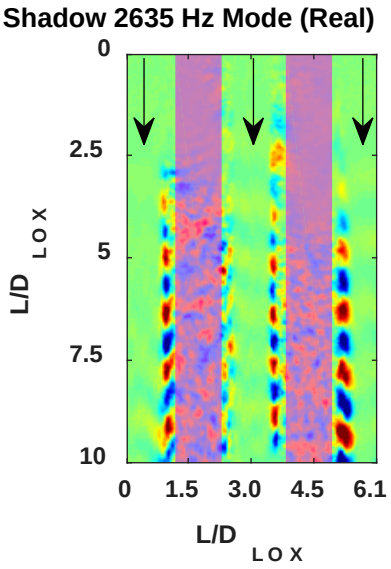

b)

Figure 9. The DMD spatial mode corresponding to the 2635 Hz frequency for: a) OH* emission and b) the shadowgraph. The alternating pattern are indicative of flame shedding events and surface wave on the liquid oxygen surface. The purple is the inter-injector spacing and the arrows point in the direction of the liquid oxygen jet flow.

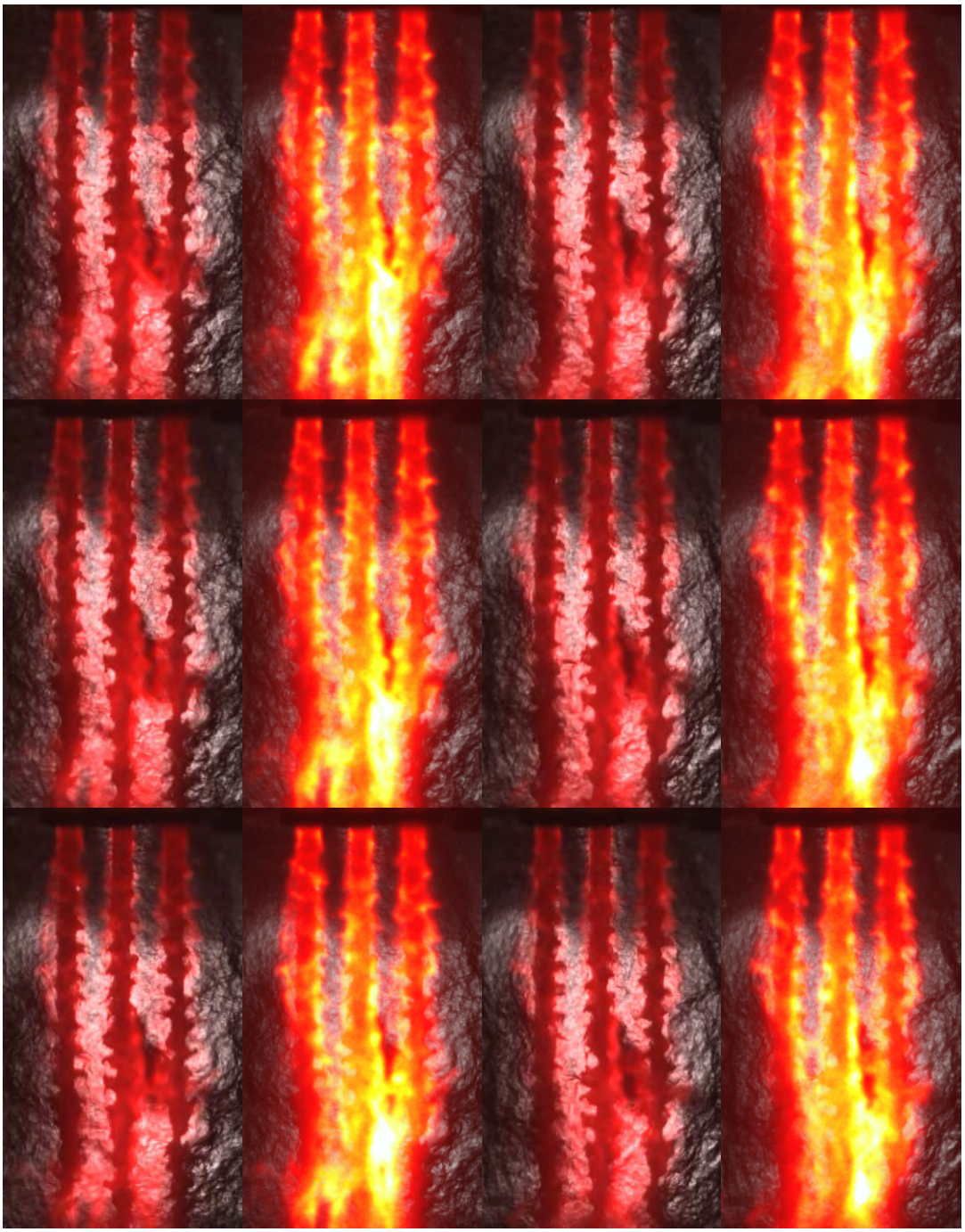

Figure 10 Instantaneous images of the shadowgraph with OH* emission wavelet fused and overlapped (Left column then immediate right, respectively). Subjected to pressure node forcing. The flame still surrounds its liquid oxygen jet in the near nozzle region. All three liquid oxygen jets have developed lobes at the same spatial location where there are high OH* emission. The flame has also take on the lobe shape near the injector exit. The time separation between each frame is 0.16 milliseconds. The images are sequential from top to bottom, left to right.

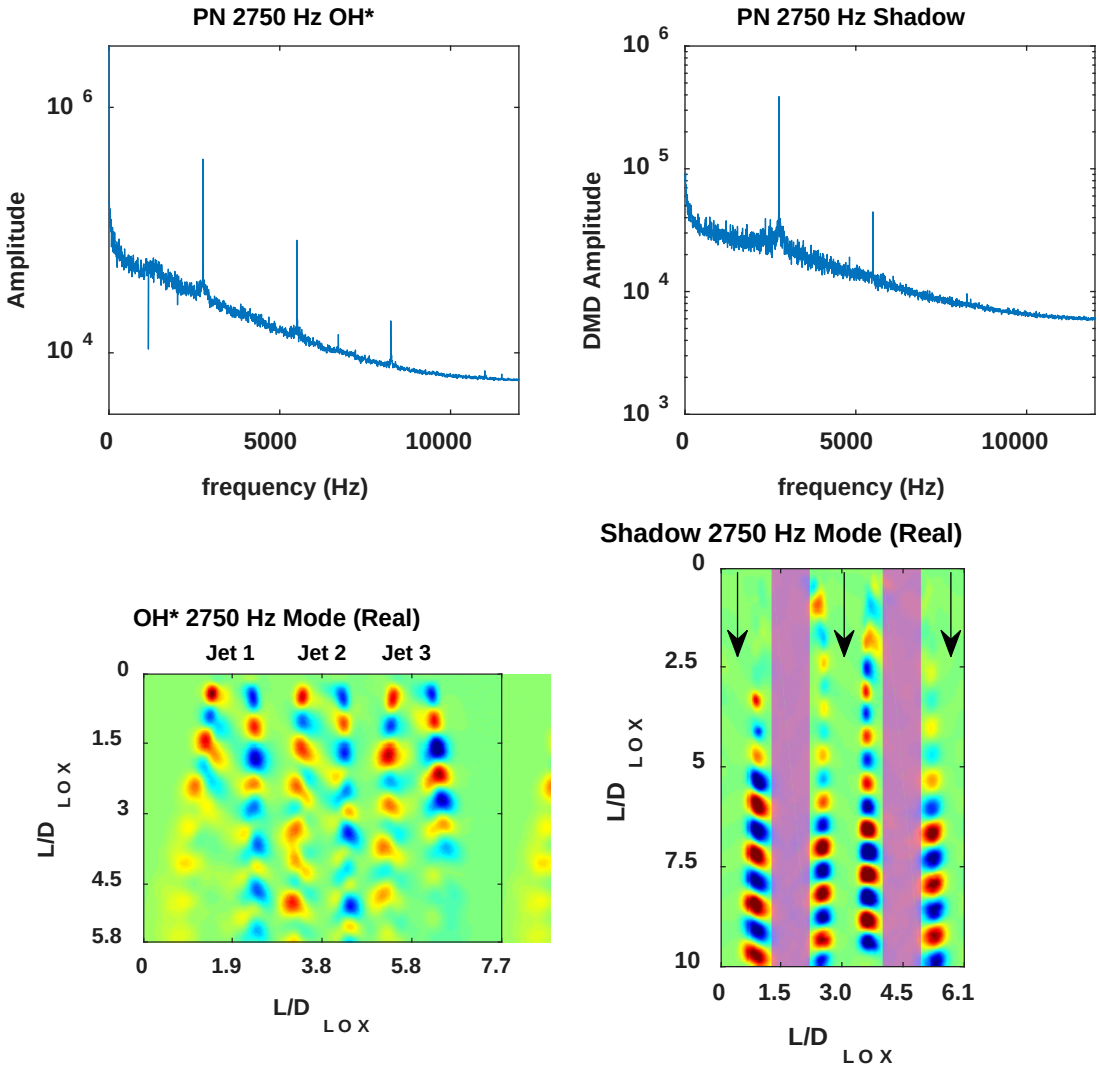

Figure 11. The OH* and shadowgraph DMD amplitude for the acoustic forcing condition at 2750 Hz. The corresponding spatial mode for each shows a slanted lobe pattern and offset alternating pattern for the OH* and shadow graph, respectively. The adjacent shear layers next to Jet 2 are out of phase with each other. The purple is the inter-injector spacing and the arrows point in the direction of the liquid oxygen jet flow.

Preliminary Study of Reacting Three-Element Gas/Liquid Shear Coaxial Flows

Mario Roa
Sierra Lobo, Inc
Edwards AFB, CA, 93524, USA

Douglas G. Talley
Air Force Research Laboratory
Edwards AFB, CA, 93524, USA

Abstract

The average behavior and the flow dynamics from a linear array of three shear coaxial injectors operating under sub-critical pressures was investigated. High speed images captured the unsteady behavior of the annular gaseous hydrogen and liquid oxygen shear coaxial flows, revelant for liquid rocket engine applications. High-speed shadowgraph images along with OH* chemiluminescence captured the hydrodynamic instabilities and their subsequent flame interactions. The behavior of the center injector's response relative to its neighbors' influences are compared to the flow from single injector studies operating under the same conditions. The high speed shadowgraph images show a dramatic difference of the break up length of the liquid oxygen jet from the three-element injector compared to the single element injector. The average of the high speed shadowgraph images show that the break up length is significantly shorter for the single element. Spectral analysis of the OH* chemiluminescence flucuations in the near field shows that the individual flames share a common frequency and the center flame's fluctuations are out of phase with its neighbors. This frequency and out of phase nature is also present in the dynamic mode decomposition of the shadowgraph and OH* chemiluminescence images used to investigate the modal structures for the liquid oxygen jets and the flames, respectively. Overlaying the OH* chemiluminescence images on top of the shadowgraph images showed that the locations of high OH*chemiluminescence lie on the same locations where surface waves are observed on the center liquid oxygen jet.

Introduction

The highest performing liquid rocket engines to date employ a variation on the coaxial gaseous/liquid propellant injector design [1]. The coaxial injector of interest here features a central liquid jet, in this case liquid oxygen, surround circumferentially by a gaseous annular flow, in this case gaseous hydrogen. The annular flow can be tailored to influence the atomization, mixing, and flame stabilization by increasing the aerodynamic forces on the liquid propellant via imparting a swirl on the liquid propellant prior to injection or increasing the shear stresses with a large velocity difference between the gas and liquid propellants.

In the case of shear coaxial flows, past investigations, experimental and theoretical, have revealed a large variety of dynamic behavior governed by a relatively few global parameters, namely the momentum flux ratio (J), velocity ratio (R), and density ratio (S) [2-13]. Lasheras [14] showed an experimental correlation where the center liquid jet break up length is proportional to J^X. This form was found to hold up in Woodward et al. [7], who experimented on gaseous hydrogen and liquid oxygen coaxial jets above atmospheric pressure. Linear stability analysis showed that for a narrow range of velocity ratios a "wake-like" instability forms in the inner shear between the center and annular flow. However, the relative importance of the global parameters was strongly dependent on the injector exit conditions, physical propellant properties, and local flow velocities [15-16].

For any industrial and propulsion applications, the annular gas flow is injected at high velocities relative to the center liquid jet. At the corresponding high Reynolds and Weber numbers, the coaxial jet's dynamics are then governed by the annular flow dynamics. As observed by Dahm at al [17] and Wicker and Eaton [18], as the annular flow velocity is increased, the vortices shed by the annular flow come to dominate the downstream flow. The resulting hydrodynamic instability is largely responsible for the downstream atomization and mixing [14, 19-26]. The same has also been observed to influence the flame dynamics [27]. Hence, and as usual, understanding the break-up and atomization of the liquid jet is fundamental to understanding combustion of the two-phase flow from a coaxial jet.

In an effort to further understand high pressure atomization and combustion from a single shear coaxial injector, experimental efforts have been carried at academic and national laboratories [28-38] under relevant rocket engine conditions and with relevant propellants. Investigating the effects of chamber pressure for gaseous hydrogen/liquid oxygen shear coaxial flow, Mayer at al [32-38] observed that phenomenological differences in the spray occurred depending whether the chamber pressure was below or above the critical pressure of the liquid oxygen. At sub-critical pressures and at low annular hydrogen jet velocity and chamber pressures, Mayer et al. observed that large scale structures will form on the liquid oxygen jet. An increase in either chamber pressure or annular hydrogen velocity decreased the size of the surface structures that shed finer droplets, and resulted in shorter break up lengths of liquid oxygen jet. At supercritical pressures, Mayer et al observed that the liquid oxygen was no longer a spray, and that droplets ceased to exist. The latter was true even in the absence of chemical reactions. Under reacting conditions, Mayer et al. still observed the absence of surface structures and droplets even at subcritical pressures, which was attributed to rapid vaporization. Experimental results from other groups [28] observed the same trends. Also observed was a decrease in break up length of the liquid oxygen jet as J increased.

Although the experimental and computational literature for single coaxial jets is vast and the major physical findings pertaining to liquid rocket engine applications were previously reviewed, investigations into multi-element injection are more limited. Hardi et al. [39-40] investigated the effects the transverse forcing on the atomization of the liquid oxygen for a five element combustor. The results showed that the break-up length of the liquid oxygen jet would shorten up to 30% when subjected to acoustic forcing. Large eddy simulations and experimental work performed Candel et al [41-44] showed the influence annular vortices have on the liquid oxygen jet for multi-element injector schemes under reacting conditions, but little was observed on the spray dynamics. Simulations performed for a linear array of three shear coaxial injectors by Masquelet et al. [45] showed that the vortex shedding from the annular hydrogen jet and the flame are intrinsically linked. In particular, the breakup of the liquid oxygen jet by the shear forces gave rise to flame's unsteady nature.

In this study, a preliminary investigation was carried out at AFRL on a three element, linear array of shear coaxial injectors at relevant liquid rocket engine conditions. The linear injector array was imaged using high speed shadowgraph and OH* chemiluminescence. Attention was focused on the influence the two neighboring elements have the center injector. This preliminary study is aimed at identifying the spectral behavior and physical interactions between the unsteadiness and the flow features in the near nozzle region that can influence the center injector. Spectral analysis of OH* emission and dynamic mode decomposition on the high speed images were performed in order to identify the physical flow features that are influencing the behavior of the center injector.

Experimental Setup and Conditions

The experimental investigation was carried out in a high-pressure, windowed combustion chamber. Three identical shear coaxial injectors were arranged in a linear array. Figure 1 shows an assembly drawing of the windowed chamber. The main body of the outer chamber is shown in orange. Mounted on the orange chamber are a total of six windows, consisting of two large 101 mm (4 in) diameter round sapphire windows and four oblong windows angled at 45 degree offsets. The chamber is symmetric about the vertical center plane, so only three of the windows are shown in Figure 1. Only the two (diametrically opposed) round windows were used in this study; the oblong windows were not used. The round windows were used for high speed shadowgraphy and OH* chemiluminescence imaging, described further below. The gaseous hydrogen and liquid oxygen enter setting plenums that feed the three-element injector array from the grey flange on top, as shown in Figure 1. The combustion gases exit from the green flange on the bottom. On either side of the main chamber are high pressure piezo-sirens housed in the yellow sections shown in Figure 1, which are connected to and held at the same pressure as the main chamber. The piezo-sirens are acoustic drivers that are attached internally to an inner acoustic channel used to set up a standing wave that can be used to investigate acoustic forcing on the injector flow. There is no flow in the channels other than the flow induced by the acoustics when they are being operated.

Figure 2 shows a schematic of the internal details of the combustion chamber's acoustic channel. The acoustic channel constitute an inner chamber. The inner chamber is connected to and is at the same pressure as the outer chamber and cannot itself sustain any pressure difference with the outer chamber. It does, however, focus the acoustics and limits hot combustion gases from exiting into the main chamber. The outer chamber and associated pressure-containing windows and window seals are therefore not exposed to potentially damaging high temperature combustion gases. The three-element injector is located in the center of this inner chamber and at the top. The injector issues into the acoustic channel where two opposed flat windows are used as walls of the acoustic channel for visualization, measuring 76.2 mm (3 in) wide by 41.4 mm (1.63 in) high. Three dynamic pressure transducers are located in the rectangular inner windows to measure acoustic pressure fluctuations, as shown in Figure 2. The end-to-end length of the acoustic channel or piezo-siren to piezo-siren is 0.75 m or 473 inner liquid oxygen post diameters. There is a round-to-rectangular transition from the acoustic drivers to the channel, but the transition is far enough away from the three-element injector to be of any influence. For this investigation the piezo-sirens were not used.

Nitrogen gas is used to pressure the combustion chamber. The pressurizing nitrogen is introduced into sides of the combustion chamber, as shown in Figure 2, hence the combustion process is not used to pressurize the chamber. This is accomplished by keeping the volume occupied by the flame / injector flow small compared to the combined volume of the inner and outer chambers. This was done in order to maintain accurate control of the chamber pressure and de-couple any thermo-acoustic interactions. Combustion gases exit the inner chamber through a hole in the bottom of the inner chamber, where the hot combustion gases mixes with the ambient pressurizing nitrogen prior to exiting the chamber through a metering orifice (not shown) at the bottom of the outer chamber. Mixing the hot combustion gases with the ambient pressurizing nitrogen ensures that the metering orifice only experiences relatively cool temperatures.

In addition to the fuel and oxidant and pressurizing nitrogen, a separately controlled nitrogen bleed is introduced through round holes in a face plate surrounding the coaxial injector on the upper wall of the inner chamber. The bleed suppresses the formation of a recirculation zones from the combustion gases near the injector that can otherwise influence the dynamics of the reacting flow. The faceplate with the bleed holes is illustrate in Figure 3. The linear array of coaxial injectors are located in the center of the plate. The inner diameter of each liquid oxygen jet is 1.58 mm (0.0625in), with a LOX post thickness of 0.38 mm. The outer diameter of the hydrogen flow is 2.82 mm (0.11in). The center of each coaxial injector are separated 2.8 inner liquid oxygen diameters away from each other. The diameter of the bleed holes is 0.5 mm. The nitrogen bleed is regulated to a velocity of 0.08 m/s. Also in the faceplate are slots next to the acoustic chamber windows for window cooling. These slots were used to prevent steam condensation that would otherwise obstruct the optical view to the reacting flow. The window film cooling was also fed gaseous nitrogen with an exit velocity of 5.7 m/s. Although, the velocity from the window film cooling is high, the momentum flux ratio from the linear injector when compared to the bleed port and the window cooling is well over 104 and 15, respectively. Hence, the flow, least in the near nozzle region, from the linear injector is expected to dominate the downstream flow.

The bleed ports and window cooling manifolds were analyzed to determine the possible presence of resonances that might affect the dynamic results reported in this paper. The resonant frequencies were found to be many times lower than the frequencies associated with these results. The gas circuit of the annular fuel manifold (hydrogen) was similarly analyzed and also found not to be acoustically active for these experiments.

The single element studies uses a similarly designed faceplate, but with only one shear coaxial injector. The internal passages for the single element are kept over 100 L/D to ensure fully developed turbulent flow and operates at the same Reynolds as a single element from the three-element injector. The exit diameter of the liquid oxygen jet for the single element studies is slightly smaller at 1.4 mm compared to the 1.71 mm for the three-element injector, but both have the same liquid oxygen post thickness. The hydrogen exit diameter is the same for both injectors. Table 1 lists the exit conditions for each individual jet. Note the temperatures for liquid oxygen and hydrogen are measured in the manifold just prior to entering the injector. The true exit temperatures will be somewhat different due to heat transfer between the liquid oxygen and the gaseous hydrogen in the injector passages, but should be close to the reported value.

All flows were regulated and metered using calibrated orifices. Following regulation and metering, the flows were subsequently chilled to the desired temperatures, for example to liquefy the oxygen, using heat exchangers cooled with liquid nitrogen. The pressurizing nitrogen gas and the other nitrogen flows were heated to 295 to 300 K to overcome chilling due to Joule-Thompson expansion effects. Each element of the linear injector was designed to have straight passages of sufficient length (L/D>100) to produce fully developed turbulent flow at the exit. The individual Reynolds numbers of the fuel and oxygen jets exceeded 10^3 and were therefore turbulent. The liquid oxygen jet was kept near 135 K, but the hydrogen gas temperature was ambient. As indicated above, some heat exchange can and will occur inside the injector's internal passages due to this temperature difference. In order to minimize this heat exchange, the injector was pre-chilled. Prior to combustion, liquid nitrogen ran through the liquid oxygen circuit for several minutes to ensure the internal passage's wall temperatures were at desire temperature.

The chamber pressure used this study was 3.4 MPa (500 psia). This is considerably below the critical pressure of oxygen; hence the oxygen is in a liquid phase. Three high speed differential pressure transducers, Kulite XCL-25D, were used to measure pressure disturbances from the combustion process. Igniting the gaseous hydrogen and liquid oxygen from the three-element injector at this pressure is non-trivial, since spark ignition methods do not work in a high pressure environment. A hydrogen-air flame torch, ignited using a nichrome wire, was used to ignite the propellant mixture.

The reacting flow was visualized with simultaneous high speed shadowgraphy and OH* chemiluminescence. The imaging arrangement is illustrated in Figure 4. The imaging systems captured the unsteadiness of the reacting flow at a framing rate of 25 kHz and 50 kHz for the shadowgraph and OH* chemiluminescence, respectively. A total of 0.2 seconds of images were collected, which was sufficiently long to reveal the average behavior of the flows. For the single injector studies, both imaging systems were set to 25 kHz and recorded for 0.2 seconds. The high speed shadowgraph optics were composed of a 7.6cm (3 inch) collimated light source, formed with a ThorLabs SL S202 broadband light source and a spherical 152 mm lens, imaged onto a Phantom Research v 1210 with an Nikon ED Nikkor 200 mm lens. Simultaneously, OH* chemiluminescence was captured with Lambert Instruments HICATT imaged directly onto a Phantom Research v2511 camera. A UV lens (F/2.8 Cerco 2178) with a Semrock (PN FF02-320/40) optical filter were used to image the OH* emission. The cameras frame rates were set using a BNC model 555 pulse generator and an IRIG time signal was used to synchronize the high-speed imaging and data acquisition systems. A dichroic mirror was used to reflect the UV OH* emission from the flame onto the intensifier, while allowing the visible light to pass through for the shadowgraph images, as shown in Figure 4. Both imaging systems viewed over 14 liquid oxygen diameters from the nozzle exit, with the exception of the shadowgraph for the single element studies where the first 8 liquid oxygen diameters where imaged.

As mentioned previously, the gas-to-liquid momentum flux ratio J has been identified as a global parameter that controls the atomization and breakup of the liquid jet in two phase coaxial flows. An initial survey of the effects of J for liquid rocket engine applications was performed for the tree-element linear array injector. In order to understand the influence that the neighboring elements have on the center injector average behavior and dynamics, the results are compared to single element studies operating at the same conditions.

Results

A comparison between non-reacting and reacting flow from the three-element injector is shown in Figure 5. In Figure 5 the left and right column correspond to J=0.5 and J=4.0, respectively. For the non-reacting conditions, gaseous hydrogen and liquid oxygen are flowing. The gaseous hydrogen can be seen flowing around the liquid oxygen jet and the hydrogen flows are seen to merge with each other between 1 and 2 liquid oxygen diameters downstream. For the J=0.5 non-reacting condition, fine structures are observed at the edges of liquid oxygen jets giving them a fibrous appearance. This is unlike the J=4.0 condition where the liquid oxygen jets appear to be fainter and further downstream droplets are present. In addition, for both conditions the liquid oxygen jets have a wavy appearance, being more pronounce

in the J=4.0 condition. This appearance of the fine structures on the liquid oxygen jets is consistent with the fiber type atomization regime reported by Farago and Chigier [46] for single element coaxial jets. However, when the non-reacting images are compared to reacting conditions, the liquid oxygen jets appear to be smoother and thinner in the near nozzle region. The smoother appearance in the near nozzle region is attributed to the vaporization of the fibrous structures, as has been observed by past researchers. It is not until further downstream that the liquid oxygen jets begin to appear fibrous again. For J=4.0, droplets are also observed further downstream.

Averaging the shadowgraph images from the single- and three-element studies, there is a noticeable difference in the liquid oxygen break up. For the single element studies, a different lens was used to focus on the dynamics in the near nozzle region, within the first 8 liquid oxygen diameters from the injector exit. A red box shown in Figure 6 represents the viewing area for the single element compared to field of the view for the three-elements, which is almost twice the length of the single element studies. The single element studies follows expected trends with the liquid oxygen jet shortening as J is increased. This was not observed for three elements. Large eddy simulations on a linear array of three shear coaxial injectors performed by Matsuyama et al. [31] observed a similar trend. They attributed the phenomenon to a decrease in vorticity and turbulence magnitude when the outer shear flows from each jet collide and merge.

The simultaneous dynamics of the merging/colliding outer hydrogen shear flows, the flames, and the liquid oxygen jets is shown in Figure 7. See the figure caption for further details regarding what is present in the figure. Present in the background of these images are many density gradients from the reacting flow, making it difficult to visualize the hydrogen jet emanating from the linear injector array. However, whereas the hydrogen jet are difficult observe, the liquid oxygen jets are clearly visible. Each flame is shown to envelop its own liquid oxygen jet in the near nozzle region and appears not interact with the neighbor until further downstream. In the results observed by Roa et al. [27] for a single injector using the same propellants, it was observed that bands of high intensity OH* emission occurred when the hydrogen jet curled towards the liquid oxygen jet. The curl would then shed a vortex that continuously impinges on the liquid oxygen jet where the high intensity OH* bands would form. At the same location where the high intensity OH* bands would occur, the liquid oxygen jet would be locally consumed and form a crest on the liquid oxygen column. Similar high intensity OH* emission bands are observed in Figure 7 for each flame, along with the crests on the liquid oxygen jet.

One way that the center flame can be influenced by its neighbors is through the shear layer interactions and annular hydrogen vortex shedding events, as noted by Masquelet et al. [45]. As stated earlier, due to the high number of density gradients present in the background of the reacting flow, the exact shedding event is difficult to observe directly, but the high intensity OH* emission bands, which indicate of the presence of an outer shear layer hydrogen vortex, can be tracked for each jet.

In Figure 7, the interrogation area used to record the OH* emission fluctuations discussed below is shown in the green boxes for the left, middle, and right jet flames. These will be referred to subsequently as Jet 1, Jet 2, and Jet 3, respectively. The interrogation area is chosen to begin one liquid oxygen jet diameter downstream from the nozzle exit and extend for one half an inner liquid oxygen jet diameter in axial length. This location is where the outer annular shear layers are observed to initially come in contact based on the non-reacting images. Within each interrogation window, the total OH* emission was determined for each frame, and afterwards the temporal mean was subtracted. A cross spectral density (CPSD) is then used to estimate the OH* emission fluctuation of Jet 2 (central jet) compared with those of the other two.

Figure 8 shows the CPSD plots of Jet 2 analyzed with Jet 1 and Jet 3 for J=0.5. From the CPSD plots, the frequency with the highest spectral energy among all three jets are close, at 2637 Hz between Jet 2 and Jet 1 and 2647 Hz between Jet 2 and Jet 3. Examining the phase difference from the CPSD plots, the OH* emission fluctuations from the central jet is almost out of phase with its neighboring flames. The maximum phase difference, in degrees, between Jet 2 and 1 is 154˚ and 170.5˚ between Jet 2 and 3. This phase differences corresponds to a time lag of 0.16 milliseconds between Jet 2 and 1 and 0.18 milliseconds between Jet 2 and 3. This is indicative that in the near nozzle region, within one inner liquid oxygen diameter, the Jet 2 flame is interacting and being influenced by its neighbors, but out of phase on average with respect to its neighbors.

To further investigate the out of phase relationship that Jet 2 has with its neighbors, dynamic mode decomposition (DMD) was applied on both the OH* emission and shadowgraph images. Dynamic mode decomposition is a numerical procedure for extracting dynamical features from flow data. For the DMD applied in this study, the high speed images were decomposed into spatial modes, with each spatial mode having a unique frequency and amplitude. These spatial modes are associated with physical features of the flow field oscillating at a fixed frequency [47]. The larger the mode amplitude of the associated spatial mode, the more dominant that spatial feature is to the flow field being interrogated. The window interrogation for the DMD analysis for the OH* emission and shadowgraph images started at the nozzle exit and extended 5.8 inner liquid oxygen diameters and

10 inner liquid oxygen diameters, respectively. The interrogation areas are shown in Figure 7. The interrogation areas are different because it assumed that if one hydrogen jet sheds a vortex close to the nozzle, it produces a flow disturbance downstream, to which the other two jets also shed a vortex lagging the initial vortex. This leads to a convective instability that can manifest itself as the crest on the liquid oxygen jets traveling downstream, due to the flame/vortex interactions previously detailed by Roa et. al. The longer interrogation window for the shadowgraphs attempts to capture this.

The power spectral density of the OH* emission of Jet 2 is shown in Figure 9. Plotted on this figure is a shaded region containing the frequencies associated with 25% of the total energy from the OH* emission fluctuations. Comparing this frequency range to the DMD amplitudes shown in Figure 10, a cluster of DMD amplitude peaks are observed to fall within this region.

Analyzing the spatial modes within this frequency range provides information as to how the flame and the liquid oxygen jet are dynamically and spatially behaving. Figure 11 is the spatial mode associated with the maximum frequency of 2635 Hz from the cross power spectral density in Figure 9. Figure 11 demonstrates the out of phase relationship Jet 2 has with its neighbors. The alternating red and blue bands in Figure 11 are locations where there are changes in OH* emission and surface crests on the liquid oxygen jet. For the OH* emission spatial mode, bands are nicely organized in an alternate pattern and degrade as distance downstream increases. This is representative of how the out of phase relationship between the jet flames manifests itself spatially. It is speculated that what is physically occurring is when one annular hydrogen vortex sheds, it produces an OH* emission band across the jet, to which afterwards the other two jet flames response likewise at an almost constant time lag. A comparable offset is present on the shadowgraph spatial mode, but it manifests itself further downstream after the crests on the liquid oxygen surface have enough time to grow.

Discussion and Conclusions

The reacting flow dynamics from a linear array of three shear coaxial injectors operating under sub-critical pressures was investigated and compared to single element results. High-speed shadowgraph and OH* chemilumiescence images recorded the center injector's response and behavior under the influence of its neighboring injectors. Comparing the single injector and three-element reacting flows, the time average shadowgraph images revealed longer intact liquid oxygen jets for the three-element reacting flow.

Although the imaging techniques performed in this study are not suited to measure turbulence or vorticity strengths, it speculated that the merging shear layers dampen the turbulence and vorticity strength. Analysis of the flame dynamics showed that all three jet flame intensities fluctuated in the near nozzle region similar to the single element studies. The fluctuations in the near nozzle region were coupled at a similar frequency and the individual jet flame fluctuations were out of phase with each other. This indicated that when one jet produced a flow disturbance, such as a vortex shedding event, the other two responded in kind with a time lag. Dynamic mode decomposition showed that the physical features from each jet were indeed out of the phase with each other.

References

1. Yang, V., and Anderson, W. E., *Liquid Rocket Combustion Instability*, Vol. 169, Progress in Asotrnautics and Aeronautics, AIAA, 1995
2. Hua, J. C., Gurarratne, G. H., Talley, D. G., Gord, J. R., and Roy, S., *Journal of Fluid Mechanics*, Vol. 790, 5-32 (2016)
3. Teshome, S., Leyva, I. A., Talley, D. G., Karagozian, A. R., *50th AIAA Aerospace Sciences Meeting,*Nashville, Tennesse, USA, January 2012
4. Forliti, D. J., Badakhshan, A., Wegener, J. L., Leyva, I. A., and Talley, D. G., *53rd AIAA Aerospace Sciences Meeting*, Kissimmee, Florida, USA, January 2015
5. Juniper, M. P., and Candel, S. M., *Journal of Fluid Mechanics*, Vol. 482, 257-269 2003
6. Huang, R. F., and Lin, C. L., *AIAA Journal*, Vol. 35, No. 5, 1997
7. Woodward, R. D., Pal, S., Farhangi, Jensen, G. E., and Santoro. R. J., *45th AIAA Aerospace Sciences Meeting,* Reno, Nevada, USA, January 2007
8. Tani, H., Teramoto. S., and Okamoto, K., *Experiments in Fluids*,56-85 (2015)
9. Delon, A., Cartellier, A., and Matas, J. P., *Physical Review Fluids*, 3 (2018)
10. Kumar, A., and Sahi, S., *International Journal of Spray and Combustion Dynamics*, Vol. 10, 211-230 (2018)
11. Farve-Marinet, M., Camano, E. B., and Sarboch, J., *Experiments in Fluids*, 26, 97-106 (1999)
12. Ibrahim, E. A., Kenny, R. J., and Walker, N. B., *42nd AIAA/ASME/SAE/ASEE Joint Propulsion Conference,* Sacramento, California, USA, 2006
13. Wards, H. A., Kassab, S. Z., Elshorbagy, K. A., Elsaadawy, E, A., *Flow Measurement and Instumentation,*10, 1-14 (1999)
14. Lasheras, J. C., Villermaux, E., and Hopfinger, E. J., *Journal of Fluid Mechanics*, Vol. 357, 351-379 (1998)
15. Yang, B., Cuoco, F., and Oschwald, M., *Journal of Propulsion and Power*, Vol. 23, 763-771 (2007)

16. Oschwald, M., Naclerio, S., Yang, B., and Cuoco, F., *European Conference on Liquid Atomization and Spray Systems*, Como Lake, Italy, September 2008
17. Dahm, W. J. A., Frieler, C. E., and Tryggvason, G., *Journal of Fluid Mechanics,* Vol 241, 371-402 (1992)
18. Wicker, R. B., and Eaton, J. K., *AIAA Journal*, Vol. 32, Nol. 3 , 542-246 (1994)
19. Rehab, H., E. Villermaux, and Hopfinger, E. J., J*ournal of Fluid Mechanics*, Vol. 345, 345-375 (1997)
20. Villermaux, E., and Rehab, H., *Journal of Fluid Mechanics*, Vol. 425, 161-185 (2000)
21. Villermaux, E., *Journal of Propulsion and Power*, Vol. 14, No.5, 807-817 (1998)
22. Siamas, G. A., Jiang, X., and Wrobel L C., *Physics of Fluids*, 21 (2009)
23. Sadr, R., and Klewicki, J. C., *Physics of Fluids*, Vol. 15, 1233-1246 (2003)
24. Buresti, G., Talamelli A., and Petagna, P., *Experimental Thermal and Fluid Science*, Vol. 9, 135-146 (1994)
25. Baillor, F., Blaisot J, B., Boisdron G., and Dumouchel, *Journal of Fluid Mechanics*, Vol. 640, 305-342 (2009)
26. Gordillo, J. M., Perez-Saborid, M., Gañán-Calvo, A. M., *Journal of Fluid Mechanics*, Vol. 448, 23-51 (2001)
27. Roa, M., and Talley, D. G., *Journal of Propulsion and Power*, 1-13 (2018)
28. Roa, M., Forliti D. J., Badakhshan, A., Talley D. G., *28th Annual Conference on Liquid Atomization and Spray Systems*, Dearborn, Michigan, USA, 2016
29. Tsohas, J., Heister S. D., *Journal of Propulsion and Power*, Vol. 27, 793-810 (2011)
30. Locke, J. M., Roger, S. P., Woodward, R. D., and Santoro, R .J., *46th AIAA/ASME/SAE/ASEE Joint Propulsion Conference*, Nashville, Tennessee (2010)
31. Matsuyama, S., Shinjo, J., Ogawa, S., and Mizobuchi, Y., *49th AIAA Aerospace Sciences Meeting*, Orlando, Florida, USA (2011)
32. Smith, J. J., Bechle, M., Suslov, D., Oschwald, M., Haidn O, J., Schneider, G. M., *40th AIAA/ASME/SAE/ASEE Joint Propulsion Conference,* Fort Lauderdale, Florida, USA (2004)
33. Mayer, W., Schik, A., Schweitzer, C., Schaeffler, M., *AIAA Journal* (1996)
34. Mayer, W. O. H., *Experiments in Fluids,* 401-410 (1994)
35. Mayer, W., and Krülle, G., *28th AIAA/SAE/ASME/ASEE Joint Propulsion Conference,* Nashville Tennessee, USA (1992)
36. Mayer, W, and Tamura, H., *AIAA/ASME/SA/ASEE Joint Propulsion Conference,* San Diego, California, USA, (1995)
37. Mayer, W., Schik A., Schäffler, M., and Tamura, H., *Journal of Propulsion and Power*, Vol. 16, 823-828 (2000)
38. Mayer, W. O. H., Schik A. H. A., Vielle, B., Chauveau, C., Gökalp, I., Talley, D, G., and Woodward R. D., *Journal of Propulsion and Power*, Vol. 14, 835-842 (1998)
39. Hardi, J, S., Gomez Martinez, H. C., Oschwald, M., and Dally, B. B., *Journal of Propulsion and Power*, Vol. 30, 337-349 (2014)
40. Hardi, J, S., Beinke, S, K., Oschwald, M., and Dally, B. B., *Journal of Propulsion and Power*, Vol. 40, 991-1004 (2014)
41. Richecoeur, F., Scouflaire, P., Ducruix, S., Candel, S., *Journal of Propulsion and Power*, Vol. 22, 790-799 (2006)
42. Urbano, A., Selle, L., Staffelbach G., Cuenot, B., Schmitt, T., Ducruix, S., and Candel S., *Combustion and Flame*, 169, 129-140 (2016)
43. Richecoeur, F., Ducruix, S., Scouflaire, P., and Candel, S., *Acta Astronautica*,
44. Hakim, L., Schmitt, T., Ducruix, S., and Candel, S., *Combustion and Flame*, 3482-3502 (2015)
45. Masquelet, M., Menon, S., Jin, Y., and Friedrich, R., *Aerospace Science and Technology*, 466-474 (2006)
46. Farago and Chigier, *Atomization and Sprays*, Vol.2, 1992
47. Schmid, P. J. *Journal of Fluid Mechanics*, Vol 656, 2010

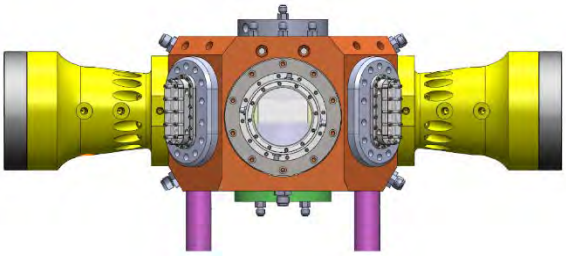

Figure 1. Assembly drawings of the combustion chamber.

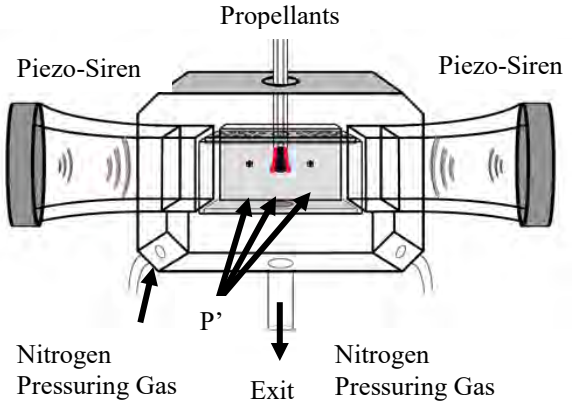

Figure 2. Inner details of the combustion chamber. P' is the location of the differential pressure transducers. The gray section in the middle is the optical windows used to complete the acoustic channel.

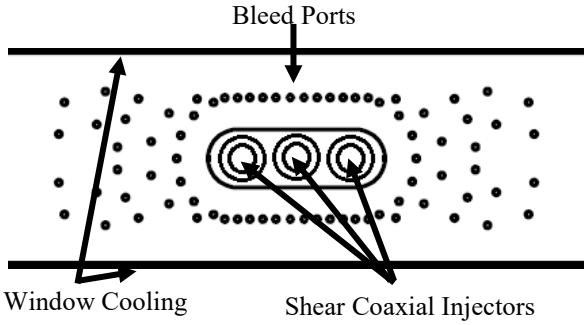

Figure 3. The injector faceplate with bleed ports, window film cooling, and the linear array injector in the center.

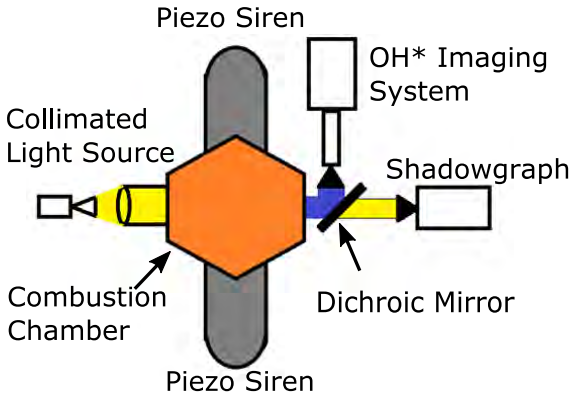

Figure 4. High speed, simultaneous imaging system layout.

J	Liquid Oxygen Temp (K)	Hydrogen Temp (K)	Oxygen Velocity (m/s)	Hydrogen Velocity (m/s)	Weber # (e3)	Reynolds Oxygen (e3)	Reynolds Hydrogen (e3)
0.15	133.5	289	4.1	27.6	65	75	2.4
0.5	136.1	288	4.1	34.9	114	87	3.5
1	128.1	282	3.9	54.3	330	82	5.1
2.2	130.8	287	3.2	89	827	58	7.6
4	133.5	289	2.76	104	1123	47	8.5

Table 1. Exit Conditions

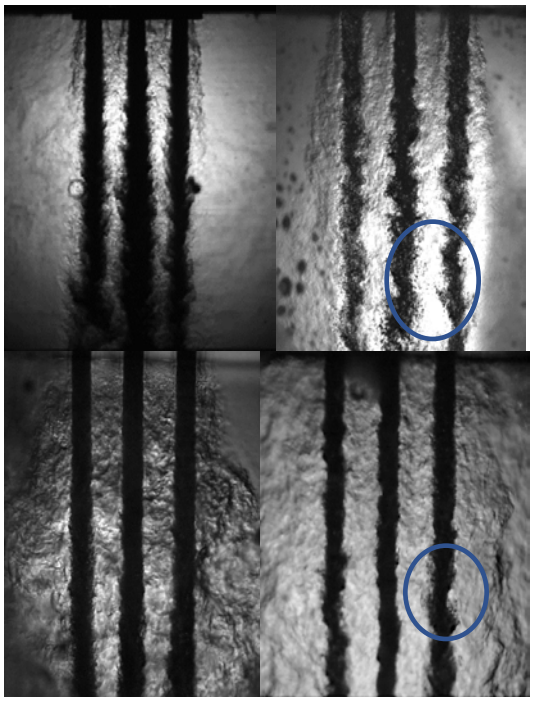

Figure 5. Instantaneous shadowgraph images of non-reacting (top row) and reacting (bottom row) flows. The right column is J=0.5 and the left column is J=4.0. The blue circles show droplets.

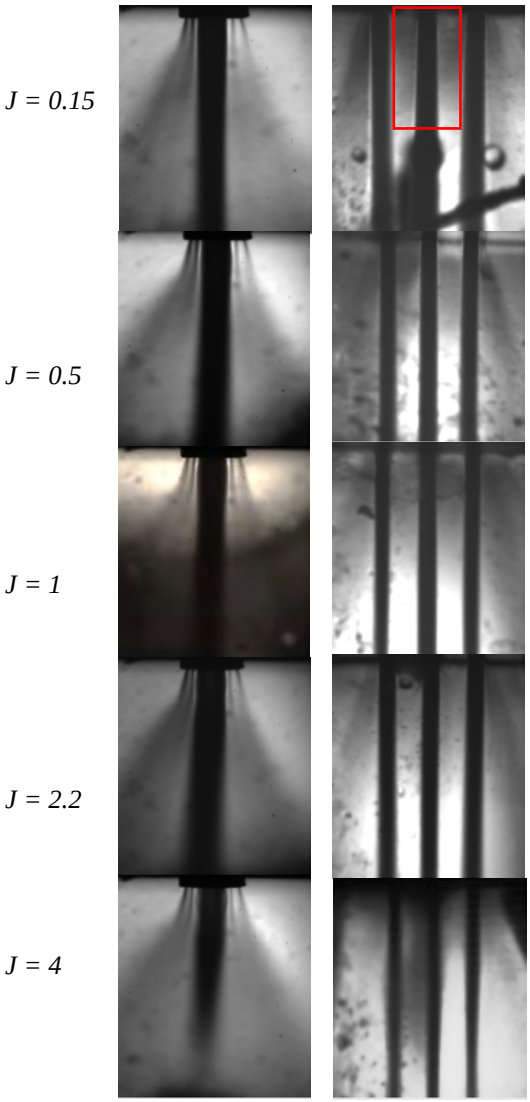

Figure 6. Shadowgraph averages for single and three elements. The red box is the field of view for the single element studies. The liquid oxygen jet breakup is shorter for the single element.

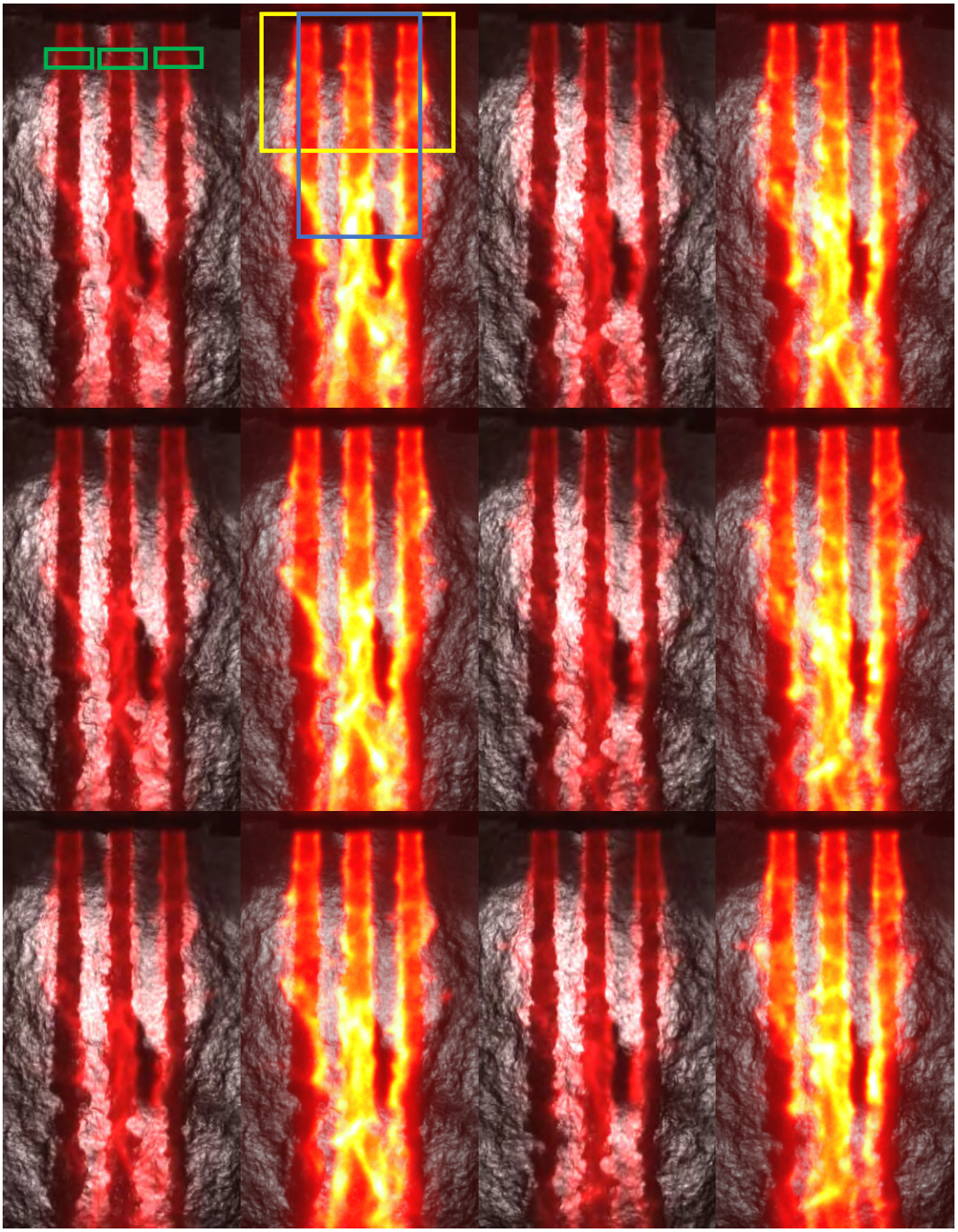

Figure 7. Side-to-side image pairs showing two methods of superimposing instantaneous shadowgraph and OH* emission images, wavelet fused (left image) and overlapped (right image). The pairs evolve sequentially in time, from top to bottom, then from left to right (six total times shown). The time separation between each frame is 0.16 milliseconds. The flames in the near nozzle region don't merge or interact. Each flame surrounds its corresponding liquid oxygen jet. At the locations of high OH* emission, waves form on the liquid oxygen jet. The green rectangles are the locations where the OH* emission fluctuations were recorded. The yellow and blue squares is where the DMD snapshots were taken for the OH* emission and shadowgraph, respectively.

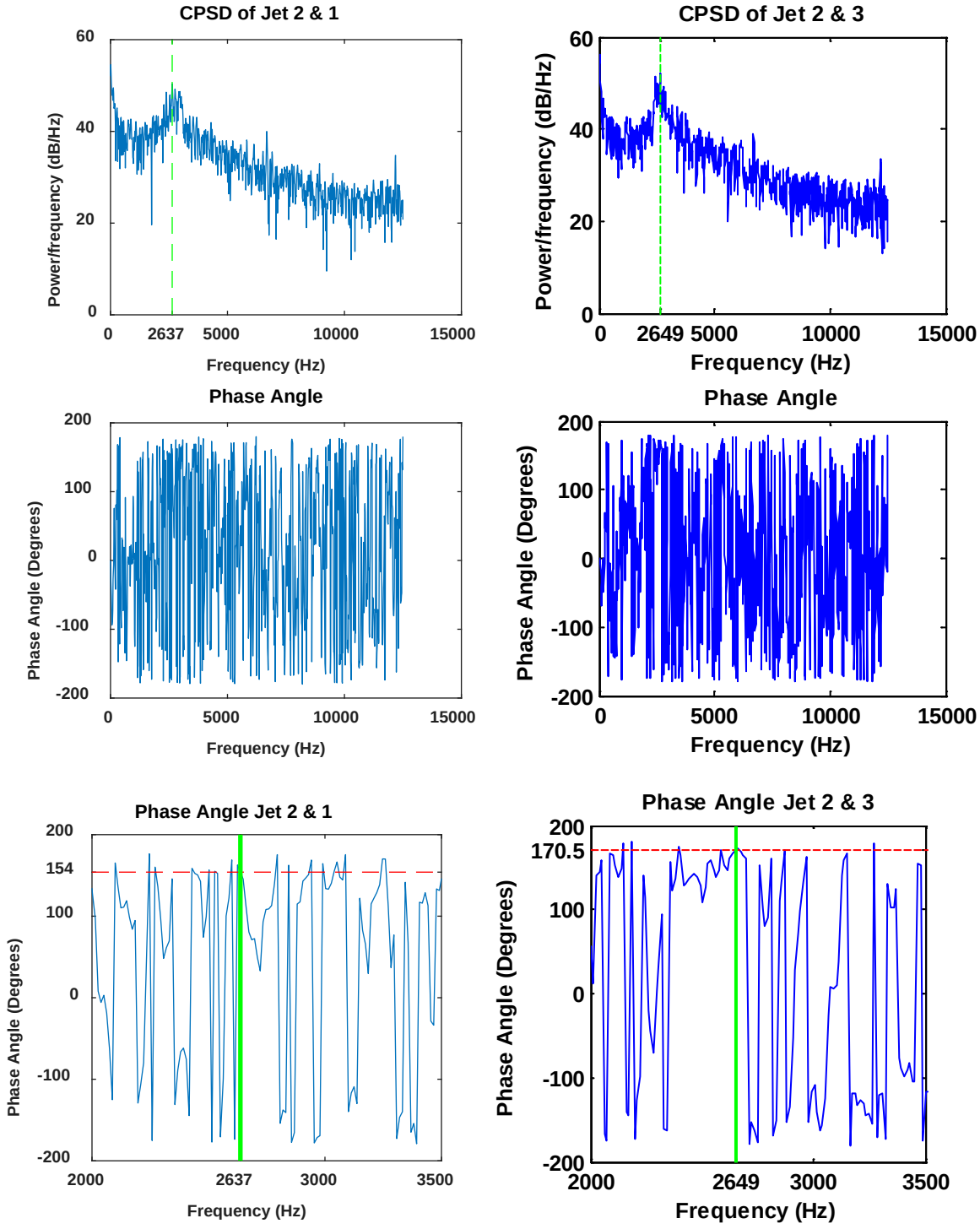

Figure 8. The cross power spectral density (CPSD) of the OH* fluctuations between (left column) Jet 2 and Jet 1, and (right column) between Jet 2 and Jet 3. The CPSD amplitudes are shown in the top row. Below each CPSD is the phase between both signals (middle row) along with the same phase information in a narrower frequency window (bottom row). The green line is the dominant frequency (dashed in the upper row and solid in the lower row), and the red dashed line is the maximum corresponding phase between both signals.

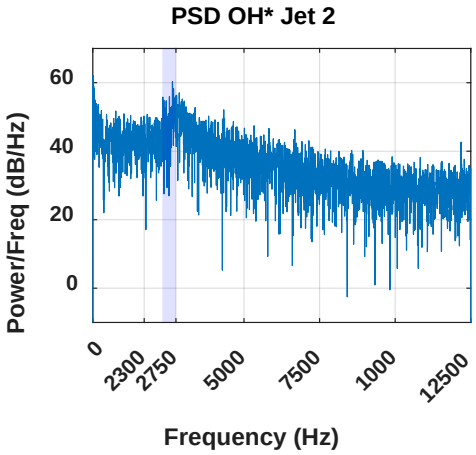

Figure 9. Power spectral density plot of Jet 2, with a shaded region between the frequencies of 2306 and 2756 Hz that occupies 25% of the total energy.

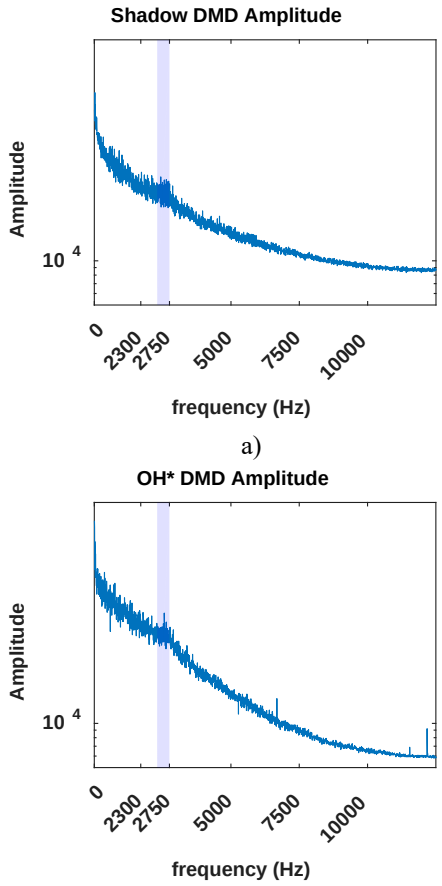

Figure 10. The DMD Mode Amplitude vs Frequency. The shaded region is the 25% occupied frequency from Jet2 for a) Shadowgraph and b) OH* emission.

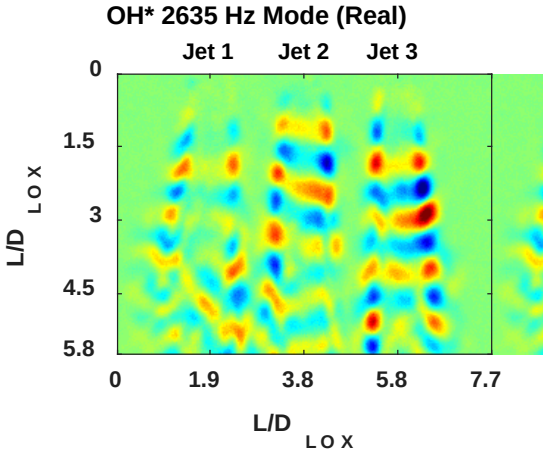

a)

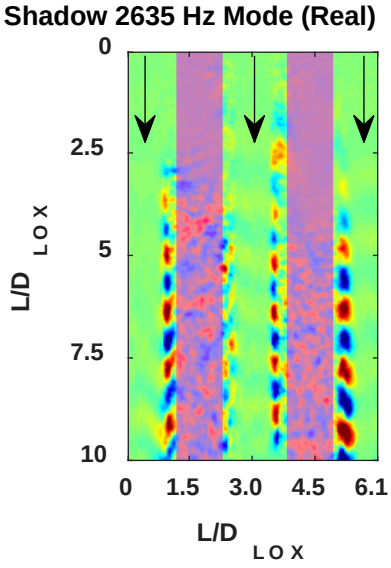

b)

Figure 11. The DMD spatial mode corresponding to the 2635 Hz frequency for: a) OH* emission and b) the shadowgraph. The alternating patterns indicate flame shedding events and surface waves on the liquid oxygen surface. The purple is the inter-injector spacing and the arrows point in the direction of the liquid oxygen jet flow.

AIAA Propulsion and Energy Forum
19-22 August 2019, Indianapolis, IN
AIAA Propulsion and Energy 2019 Forum

10.2514/6.2019-4108

Check for updates

Unsteady and Transversely Forced Dynamics of Two-Phase Multi-Element Shear Coaxial Flows

Mario Roa[1]
Sierra Lobo, Inc. Air Force Research Laboratory, Building 8451, Edwards AFB, Ca, 93524, USA

Douglas G. Talley[2]
Air Force Research Laboratory, Building 8451, Edwards AFB, Ca, 93524, USA

The unsteady dynamics and spectral content from a linear array of three LOX/hydrogen shear coaxial injectors was investigated at a high subcritical pressure using high speed imaging at different momentum flux ratios, and compared with single element flows. Two conditions were selected to be investigated under pressure node acoustic forcing. The injectors employed liquid rocket engine relevant propellants of gaseous hydrogen and liquid oxygen. High-speed shadowgraph images along with OH* chemiluminescence captured the unsteady hydrodynamic instabilities for each injector and the flame interactions. No lifted flames or group combustion was observed for any condition. The gas phases between the jets interacted within one or two diameters, but there was no evidence of interaction between the liquid phases except possibly through the intermediate gas phase. The single element and multi element flows exhibited qualitatively similar flame / jet / wave structure dynamics. Acoustic forcing near the unforced natural frequencies enhanced these dynamics and forced them to lock in to the acoustic frequency. A hypothesis is advanced that the acoustics might overwhelm any natural dynamics that would cause the jets to interact, and cause each jet to behave essentially as if it were independent of the others. However, further exploration will be needed to verify this hypothesis.

Downloaded by Doug Talley on August 21, 2019 | http://arc.aiaa.org | DOI: 10.2514/6.2019-4108

I. Introduction

Liquid rocket engines have been plagued with high frequency combustion instability from their inception [1]. Combustion instabilities in liquid rocket engines arise from complex interactions of acoustic waves coupling and causing oscillatory fluctuation of the volumetric heat release from the combustion process. Combustion instabilities can couple with the combustion chamber acoustics that can directly influence propellant atomization, mixing, flame interactions, and thus, heat release. Combustion instabilities can also be injector-coupled, where the acoustics from the chamber, propellant feed lines, or injector design drive mass-flow variations into the combustion chamber, causing periodic heat release and pressure fluctuations within the combustion chamber. The complexity of combustion instabilities, and the several potential origins from which they can arise, has usually required expensive trial and error testing to mitigate the severity of the instability in developing new engines [2]. Current efforts in predicting and designing future liquid rocket engines are being developed with computationally expensive models and validating them by using sub-scale liquid rocket engine experiments. This is a more favorable approach since it can potentially limit the amount of expensive development testing. In this effort, a detailed physical and dynamical understanding of the reacting flow from multiple injectors operating at the extreme liquid rocket engine environment is being sought.

Early experiments into understanding combustion instabilities have been documented progressively throughout the years [1-9], and so only the most recent research efforts are reviewed here. The current experimental efforts aimed at studying combustion instabilities are performed by constructing sub-scale combustion chambers that are naturally unstable [10-12] or by the actively driving the reacting flow with flow modulation [13-15] or acoustic drivers. Less extensively investigated is how a single injector's reacting flow field responds physically and dynamically in the presence of neighboring injectors. The few academic studies that have been tried are limited in what types of measurements possible in such extreme environments. In those studies where optical access is integrated into the

[1] Research Scientist, Sierra Lobo, Inc. 10 E. Saturn Blvd, Building 8451, Edwards, CA 935324, Member.
[2] Lead, Combustion Dynamic Group, AFRL/RQRC., 10 E. Saturn Blvd, Building 8451, Edwards, CA 935324, Associate Fellow

Distribution A: Approved for public release; distribution unlimited. PA #19376

This material is declared a work of the U.S. Government and is not subject to copyright protection in the United States.

experiment, the results typically consist of species selective emission from the flame and time resolved pressure measurements to deduce acoustic/flame interactions. More limited in these studies are quantitative measurements (e.g. temperature, velocity, density, *etc*.) and detailed temporal and spatial observations of how the shear flows from multiple injectors and flames interact under acoustic forcing. All of these are vital for the development of future computer models.

Studies performed at Purdue University [10-12] on combustion instabilities were carried out on naturally unstable combustors capable of transverse and longitudinal oscillations. Both the transverse instability combustor and the continuously variable resonance combustor are capable of producing self-sustaining transverse and longitudinal combustion instabilities, respectively. The transverse instability combustor, equipped with an optical viewing port, is a rectangular combustion chamber with multiple injectors capable of producing high-amplitude 1T or 2T mode instabilities. The high amplitude pressure oscillations are achieved by flowing different mixture ratios in separate injectors, with the center injector acting as the "study element" with optical access. Using high speed backlit imaging and CH* chemiluminescence, they observed that the CH* emission from the center injector was impeded. They observed this when an acoustic pressure wave of sufficient strength reached its maximum amplitude at the study element location. Comparing CFD results with the experimental CH* chemiluminescence, they observed the hydrocarbon fuel was impeded from exiting the injector due to the unsteady back pressure created by the natural instability. They also observed that the locations with the highest heat release corresponded well with the increases of CH* emission both temporally and spatially. This is also the case with the continuously variable resonance combustor, where the combustion instabilities were driven by changing the oxidizer tube length during experimental runs.

Hardi *et. al*. [13-15] employed flow modulation to study high frequency combustion instabilities. This experimental method produces pressure wave excitation of the combustion chamber's acoustic resonance modes by periodically blocking the exhaust from the combustion chamber by using a toothed wheel. The rotational speed determines the frequency and the location of the toothed wheel determines if transverse or longitudinal instabilities are created for a given experimental setup. Using this flow modulation technique, Hardi *et. al*. studied flame displacement and atomization from a multi-element gaseous hydrogen/liquid oxygen (LOX) shear coaxial injectors subjected to large amplitude pressure waves. Using the OH* emission from the flame, they employed a flame tracking technique to observe the flame displacement by a transverse acoustic forcing. They attributed the flame displacement created by the acoustic forcing to probably be due to the displacement of the propellants. Even though they collected back-lit imaging from the experiment, few observations were made on the propellant displacement behavior due to the vast amounts of density gradients in the reacting flow. The also observed changes in the breakup length of the LOX jet. When forced, the LOX jet length is on average shorter compared to an unforced LOX jet.

Concurrent computational studies performed by Candel *et al*. [16-20], Juniper *et. al.* [21], Sirignano *et. al* [22,23] and Harvazinski *et. al.* [24] have focused on comparing experimental results with computational models. These efforts focused on identifying flow features and the high pressure physics that lead to combustion instabilities that are otherwise too difficult to resolve and obtain from the experimental efforts. Large eddy simulations of liquid oxygen with a gaseous fuel (Hydrogen or Methane) carried out by Candel *et. al.* studied the effects acoustic forcing had on the flame and liquid oxygen jet geometry. Similar to previous experimental results, the liquid oxygen jet shortened and flattened due to the acoustic forcing. They also observed that depending on the acoustic forcing frequency, the flame could have either a flag flapping motion or be displaced in a quasi-periodic bulk fashion. Juniper *et. al.* studied the stability and sensitivity of a coaxial flow using linear models. This was accomplished by varying time and spatial scales for the hydrodynamic response to acoustic forcing. They observed that varying the degree of hydrodynamic instabilities greatly influences the regions of heat release and hence the overall thermo-acoustic instability cycle. Sirignano *et. al.* used linear models to study coaxial diffusion flames with and without acoustic forcing. This method used less costly computations to perform a parametric study on varying flow parameters (e.g. injector dimensions) and to observe trends within the flow field. Using a hybrid RANS/LES Distributed Eddy formulation, Harvazinski *et. al.* [24] studied the coupling between acoustics, hydrodynamics, and heat release of Purdue's continuously variable resonance combustor. They investigated the injector's exit conditions under stable and unstable conditions. The physical interactions of the hydrodynamic response of the injector to the acoustic forcing that led to the unsteady heat release are detailed in [24]. What was observed was that under unstable conditions, vortex shedding from the injector would carry with it unburned propellants and would mix and react rapidly when the incoming pressure wave reached the unburnt propellants, resulting in localized and rapid mixing and heat release.

Recent experimental single element studies by Roa *et.al.* [25-26] have highlighted several physical interactions between the hydrodynamics instabilities and acoustic forcing that have been missing from the previous experimental studies. Unlike the naturally unstable combustors or the flow modulated combustors, piezo-sirens were used to acoustically drive the reacting flow. This has the advantage of not introducing additional mean flow. The volume occupied by the reacting flow is kept small relative to the volume of the chamber. This ensures that heat release from

Distribution A: Approved for public release; distribution unlimited. PA #19376

Downloaded by Doug Talley on August 21, 2019 | http://arc.aiaa.org | DOI: 10.2514/6.2019-4108

the combustion is not allowed to form a feed-back loop and become naturally unstable. This method allows better control over how different pressure amplitudes affects the reacting flow. Using high speed shadowgraphs and OH* emission to study a gaseous hydrogen/liquid oxygen shear coaxial flame, they detailed the influence that shear layer hydrodynamics have on the downstream flow. They observed that when an annular hydrogen structure is formed by the outer shear layer, the annular structure would impinge and locally consume the liquid oxygen jet at a rapid rate. Spatially at the same location, there will be an increase in OH* emission, where they argued that the annular structure would increase the local heat transfer and vaporization, and hence locally consume the liquid oxygen jet. They observed that the annular hydrogen structure had the same shape and behavior as vortices formed and shed due to Kelvin-Helmholtz instabilities. When the same single element was subjected different levels of acoustic forcing amplitudes, they observed that the outer shear layer annular structure/vortex would "lock in" to the acoustic forcing frequency when the forcing amplitude was sufficiently high enough.

Using the same experimental chamber as [25-26], a three element, linear array of shear coaxial injectors was investigated for this paper. The linear injector array was studied with and without acoustic forcing. Using high speed shadowgraph and OH* chemiluminescence, this investigation focuses on the unsteady influence the two neighboring elements have on the center injector. This investigation identified the spectral behavior between the neighboring injectors and physical interactions between the acoustics and flow features in the near nozzle region. Spectral analysis of OH* emission and dyanmic mode decomposition on the high speed images were performed in order to identify the physical flow features that are influencing behavior of the center injector.

Downloaded by Doug Talley on August 21, 2019 | http://arc.aiaa.org | DOI: 10.2514/6.2019-4108

II. Experimental Setup

The multi-element shear coaxial injectors were tested using the previous high-pressure, windowed combustion chamber. The multi-element injector is an array of three elements with an annular gaseous hydrogen and center LOX jet. Figure 1 shows an assembly drawing of the windowed chamber. The main body of the outer chamber is shown in orange. Mounted on the orange chamber are a total of six windows, consisting of two large 101 mm (4 in) diameter round sapphire windows and four oblong windows angled at 45 degree offsets. The chamber is symmetric about the vertical center plane, so only three of the windows are shown in Figure 1. Only the two (diametrically opposed) round windows were used in this study. The round windows were used for high speed shadowgraphy and OH* chemiluminescence imaging, described further below. The gaseous hydrogen and liquid oxygen enter settling plenums that feed the linear injector array from the grey flange on top. The combustion gases exit from the green flange on the bottom. The combustion chamber uses nitrogen gas to achieve desired operating pressures independent of the combustion process. Pressurizing nitrogen is introduced into the sides of the combustion chamber, as shown in Figure 2. On either side of the main chamber are high pressure acoustic channels shown in yellow in Figure 1, which are connected to and held at the same pressure as the main chamber. Piezoelectric acoustic drivers are attached internally to the grey flanges on either end. There is no flow in the channels other than the flow induced by the acoustics when they are being operated.

Figure 2 shows a schematic of the internal configuration of the chamber acoustic channel. The acoustic channel constitutes an inner chamber. The inner chamber is connected to and is at the same pressure as the outer chamber and cannot itself sustain any pressure difference with the outer chamber. It does, however, focus the acoustics and limits hot combustion gases from exiting into the main chamber. The outer chamber and associated pressure-containing windows and window seals are therefore not exposed to potentially damaging high temperature combustion gases. The multi-element injector is located in the center of this inner chamber and at the top. The injector issues into the acoustic channel where two opposed flat windows are used as walls of the acoustic channel for visualization, measuring 76.2 mm (3 in) wide by 41.4 mm (1.63 in) high, shown in grey in Figure 2. Three dynamic pressure transducers are located in the rectangular inner windows to measure acoustic pressure fluctuations. These pressure transducers are also used to set up the standing wave from the piezo-sirens. In the vicinity of the multi-element coaxial injector, the inner cross section of the acoustic channel normal to the page is rectangular with 20.5 mm (0.81 in) wide (or 13 inner liquid oxygen injector diameters) and 35.5 mm high. The end-to-end length of the acoustic channel or piezo-siren to piezo-siren is 0.75 m, or 473 inner liquid oxygen post diameters. There is a round-to-rectangular transition from the acoustic drivers to the channel, but the transition is far enough away from the multi-element injector to not influence the present results.

The combustion chamber is pressurized using nitrogen gas from the two side inlets and does not rely on the combustion process to provide chamber pressure. This is accomplished by keeping the volume occupied by the flame small compared to the combined volume of the inner and outer chambers. This was done in order to maintain accurate control of the chamber pressure and to de-couple any thermo-acoustic interactions. In addition to the fuel and oxidant

Distribution A: Approved for public release; distribution unlimited. PA #19376

and pressurizing nitrogen, a separately controlled nitrogen bleed is introduced through round holes in a face plate surrounding the coaxial injector. The bleed suppresses the formation of a hot gas recirculation zone near the injector that can otherwise influence the dynamics of the reacting flow. The faceplate with the bleed holes is illustrate in Figure 3. The linear array of coaxial injectors is located in the center of the plate. The inner diameter of each liquid oxygen jet is 1.58 mm (0.0625in), with a LOX post thickness of 0.39 mm. The outer diameter of the hydrogen flow is 2.82 mm (0.11in). The center of each coaxial injector is separated 2.8 inner liquid oxygen diameters away from each other. This is a representative interelement spacing. The diameter of the bleed holes is 0.5 mm. The nitrogen bleed is regulated to a velocity of 0.08 m/s. Also in the faceplate are slots for window cooling. In order to avoid steam condensation that would otherwise obstruct the optical view to the reacting flow, the window cooling issued nitrogen gas at exit velocity of 5.7 m/s. Although the velocity from the window purge is high, the momentum flux ratio from a single element from the linear injector when compared to the bleed port and the window cooling is well over 104 and 15, respectively. Hence, the flow is expected in the near nozzle region to dominate and experience little influence from the both the bleed port and window cooling flows.

The bleed ports and window cooling manifolds were analyzed to determine the possible presence of acoustic resonances that might affect the dynamic results reported in this paper. The resonant frequencies were found to be many times lower than the frequencies associated with these results. The gas circuit of the annular fuel manifold (hydrogen) was similarly analyzed and also found not to be acoustically active for these experiments.

All flows were regulated and metered as high pressure gases with calibrated orifices. Following regulation and metering, the flows were subsequently chilled to the desired temperatures, for example to liquefy the gaseous oxygen, using heat exchangers cooled with liquid nitrogen. The pressurizing nitrogen gas and the other nitrogen flows were heated to 300 K to overcome the chilling effects due to Joule-Thompson expansion effects. Each element of the linear injector was designed to have straight passages for fully developed flows at the exit. The internal passages for the linear injector was designed to have injector length to exit diameter (L/D) of over 100. The Reynolds numbers of the fuel and oxygen exceeded 10^3 and are assumed to be turbulent. The pressure and temperature for both LOX and hydrogen were measured before entering the injector. The LOX jet was kept at 140 K, and the hydrogen gas was chilled prior to entering the injector. Some heat exchange occurred inside the injector internal passages due to the temperature difference. In order to minimize this heat exchange, the injector was pre-chilled. Before the hydrogen and LOX entered the injector, chilled gaseous nitrogen (at 140 K) was run through the LOX feed circuit for several minutes prior to combustion.

The chamber pressure used this study was 3.4 MPa (500 psia). This is considerably below the critical pressure of oxygen (4.97 MPa), so the oxygen is initially a liquid. When the acoustics were present, a standing wave was formed at a frequency of 2750 Hz with a wavelength of 0.13 m, which is much larger than the total length of the injector end to end. The phase of the standing wave was adjusted to correspond to a pressure node at the injector exit. To form the standing wave, a waveform generator, Keysight 33500B, was used to drive high voltage amplifiers, Trek PZD2000A, connected to individual piezo-sirens. The constant pressure amplitude of 13.78 kPa (2 Psi) was chosen for the acoustic forcing. The pressure amplitude and phase of the standing wave were measured and adjusted using three differential pressure transducers, Kulite XCL-100D, prior to ignition. The differential pressure transducers are located 20.5 mm away from the nozzle exit, with one located at the center of the injector and the other two 25.4 mm left and right from the center differential pressure transducer. Igniting the flows at this pressure proved to be non-trivial as most spark ignition methods do not work when a high pressure is established prior to ignition as in this experiment. The approach used was a hydrogen-air torch, ignited using an electrically heated hot wire.

The reacting flow was visualized simultaneously using high speed shadowgraphy and OH* chemiluminescence. The imaging arrangement is illustrated in Figure 4. The imaging systems captured the unsteadiness of the reacting flow at a framing rate of 50 kHz for the OH* and 25 kHz for shadowgraphs. Both systems recorded for a duration of 0.2 seconds, long enough to study the unsteady limit cycle aspects associated with these flows. The high speed shadowgraph optics were composed of a 7.6cm (3 inch) collimated light source, formed with a ThorLabs SL S202 broadband light source and a spherical 152 mm lens, imaged onto a Phantom Research v 1210 with an Nikon AF Micro Nikkor 200 mm lens. Simultaneously, OH* chemiluminescence was captured with Lambert Instruments HICATT imaged directly onto a Phantom Research v2511 camera. An UV lens (F/2.8 Cerco 2178) with a Semrock (PN FF02-320/40) optical filter were used to image the OH* emission. An external pulse generator (BNC Model 555) was used to synchronize the imaging system and set the frame rates. An IRIG time signal was used to synchronize the high-speed imaging systems to the data acquisition systems. A dichroic mirror was used to reflect the UV OH* emission from the flame onto the intensifier, while allowing the visible light to pass through for the shadowgraph images. The both imaging systems captured the over 14 LOX diameters from the nozzle exit.

Downloaded by Doug Talley on August 21, 2019 | http://arc.aiaa.org | DOI: 10.2514/6.2019-4108

Distribution A: Approved for public release; distribution unlimited. PA #19376

The gas-to-liquid momentum flux ratio $\left(J = \frac{\rho U_{Gas}^2}{\rho U_{Liquid}^2}\right)$ has been identified as a global parameter that on average, places the LOX jet into certain regimes of atomization and break up. Previous research has shown that if the momentum ratio is high by flowing the annular jet at order of magnitudes higher than the center jet, then the center liquid can be severely shortened, while the dynamics and flow physics downstream are highly turbulent and difficult to analyze. In order to understand the impact of the neighboring injector's unsteady nature and flame dynamics on the center injector flow and flame, five different J conditions were selected. Momentum flux ratios of 0.15, 0.5, and 1 were selected for this study by keeping the LOX jet flow constant and varying the hydrogen flow. For the remaining conditions, the hydrogen flow was fixed and the LOX flow was changed to achieve the desired J condition. The conditions *J* of 0.15 and 0.5 were acoustically forced at the pressure node condition. The flow conditions are presented in Table 1.

III. Results

Unforced Results

Shadowgraph images are shown in Figure 5 for both multi-element injection and single element injection operating at J of 0.15, with nearly similar hydrogen and LOX exit conditions as given in Table 1 for this value of J. Present in both the multi element and single element flows are large scale gas structures that surround and envelope the LOX jet(s) in the center. These structures have been noted by Roa and Talley [25] to behave as vortices due to a Kelvin-Helmholtz instability of the outer most shear layer. They are visible on either side of the LOX jet for the single element, and in the outer flows for the multi-element. For the multi-element flow, present within one to two LOX jet diameters between the elements is a highly turbulent flow where the hydrogen shear layers merge and combustion gases are present. Interaction occurs between the gas flows beginning at this location. In contrast, the single element turbulence encounters mainly the surrounding quiescent background gas. Compared with the gas phase, the liquid phases in the jets in the multi-element case do not appear to directly interact with each other, except possibly through the intermediate gas phase in a manner which is not obvious from the visualizations.

Figures 6 and 7 are images of shadowgraph and OH* emission for single element and multi element flows for all conditions tested. It should be noted that in the shadowgraph images, the single element images presented are not at the same field of view as the multi-element images; the first 8 LOX diameters are imaged for the single element, whereas the first 14 LOX diameters are imaged for the multi element. However, both data sets have similar flow characteristics that can be compared at these different fields of view. The spreading angle of the outer hydrogen jets from the multi element injector is observed to be similar to that of the single element injector. The LOX jet break up length of the single element injector consistently decreases as J increases, although this is explicitly evident only for J of 4 in Figure 6 due to the field of view in this figure. Although slightly obscured due to steam condensation, the multi-element shadowgraphs show that the LOX jets are intact for a longer length than the single element for the same condition. The LOX jets for both single and multi-elements also feature surface structures that travel downstream.

In Figure 7, consistent with past researcher's results, the flame is attached at the nozzle exit for both the single element and multi-element flows. No lifted flames or group combustion was observed for any condition. Consistent with the shadowgraph results, the single element flame becomes shorter as J is increased, while the multi-element has longer flame lengths at comparable J's. Also consistent is the fact that the single and the outer flame elements are observed to expand downstream, whereas the center flame is constrained with very little expansion observed. The flames for both single elements and multi elements feature wave-like structures that travel downstream. Roa and Talley [25] observed that the wave-like flame structures of single jets traveled downstream at a little more than the average velocity between the hydrogen and LOX jets. The wave-like flame structures for the multi element jets appeared to propagate significantly slower than for single elements at the same J.

These wave-like structures in the flame and the LOX jet have been observed and were previously noted to interact with each other and appear to be intricately linked. A sequential series of the instantaneous shadowgraph and OH* emission images is shown for the multi element at J of 0.5 in Figure 8. In Figure 8 the shadowgraph is wavelet fused (left columns) and overlaid (right columns) with its corresponding false colored OH* image. Present in the background of these images are many density gradients from the reacting flow, making the hydrogen jet difficult to visualize separately. Although each hydrogen jet is difficult to observe, the liquid oxygen jet is clearly visible. From Figure 8, each flame envelopes its own LOX jet in the near nozzle region and anchors at the LOX post tip. At different locations, high intensity OH* bands are observed to wrap around the LOX jet. The same bands were previously observed by Roa and Talley [25] in single element studies using the same propellant combinations. They observed that the annular hydrogen jet would shed Kelvin-Helmholtz wave structures that impinge on the LOX jet, similar to what can be seen in Figure 5. The shed structure would then locally consume the LOX jet and form a trough in the LOX jet column.

Distribution A: Approved for public release; distribution unlimited. PA #19376

Downloaded by Doug Talley on August 21, 2019 | http://arc.aiaa.org | DOI: 10.2514/6.2019-4108

Similarly, high intensity OH* emission bands are observed in Figure 8 for each flame, located along the troughs of the LOX jets. These troughs appear as surface wave structures on the LOX jet and are observed for each individual jet. These surface wave structures are highlighted in Figure 8, where higher intensity OH* emission is observed to curl along the same locations where the LOX jet exhibits surface troughs and displacement. These unsteady LOX/flame wave interactions were observed across all single and multi-elements conditions, albeit with varying sizes of wave structures and troughs.

One way that the center injector flame and flow can be influenced by its neighbors is through interaction occurring in the gas phase, particularly the interactions that take place when outer hydrogen shear layers for each jet merge and/or come in contact. Due to turbulence within the inter-element spacing, the hydrogen jets cannot be separately distinguished in the inter-element space. However, their influence can be indirectly inferred. Following the detailed events shown by Roa and Talley at the same locations where these annular structures form and impinge on the LOX jet, there should be an increase in OH* emission. These OH* emission fluctuations can be tracked and correlated among the three flames. In Figure 8, the interrogation area used to record the OH* emission fluctuations is shown in the green boxes in the upper left panel for the left, middle, and right jet flames, which from now on will be referred to as Jet 1, Jet 2, and Jet 3, respectively. The green boxes are placed roughly 1 LOX diameter downstream, where the hydrogen jets come in contact with each other based on visualizations of non-reacting flows. Within the interrogation area, the OH* emission was integrated for each frame with the temporal mean subtracted. Using a cross power spectral density calculation, the OH* emission fluctuations of Jet 2 (central element) is compared to its closet neighbors. Hence, the left side of the Jet 2 is compared to right side of Jet 1, and right side of Jet 2 is compared to the left side of Jet 3. The comparison is performed in this manner since it is assumed that interactions among the jets will occur mostly in the inter element spacing between the jets.

Figure 9 shows the cross power spectral density (CPSD) plots of Jet 2 analyzed with Jet 1, and of Jet 2 with Jet 3, for J of 0.15, 0.5, and 1. For all three conditions presented, there is a range of frequency peaks clustered together. It should be noted that there are also higher frequency peaks occurring around 8 kHz and 12 kHz, but further analysis revealed that these peaks are an artifact of the OH* imaging system and have no real physical correspondence to the flame results presented here. The *J* of 0.15 condition has the lowest frequency peaks at 1868 to 1892 Hz. For the higher *J* conditions, there is a shift to a higher frequency peaks as the hydrogen velocity increases. Unlike for *J* of 0.15 where the frequency peaks are close to each other, the remaining two conditions have peaks that are separated by 300 to 500 Hz. Regardless of the frequency gap separating the peak frequencies at the higher *J* conditions, the trend suggests that the flames share spectral content and the frequency shifts upwards as hydrogen exit velocity is increased. This indicates that although each individual jet and flame visually appears to behave as independent stream columns, there is an unsteady mechanism present that exhibits an influence near the nozzle exit that is responsible for the temporal flame fluctuations at similar frequencies for each jet.

Dynamic mode decomposition (DMD) on the OH* emission images was used to identify the unsteady behavior occurring within the inter-element space. In Figure 8, the yellow box is the area used in DMD analysis. 10,000 snapshots were used for a total elapsed time of 0.2 seconds at a 50 kHz frame rate. Figure 10 shows the DMD amplitude along with a selected mode. The mode shown corresponds to the highest frequency peak from both the DMD amplitude and the CPSD. For the *J* of 0.15, present in the DMD amplitudes is a frequency peak of 1877 Hz close to the peak frequencies found from the cross power spectral analysis. Examining the spatial mode at 1877 Hz, Jet 2 has a fluctuating pattern along both its edges. The fluctuating pattern is associated with the structures of the high intensity OH* emission bands that travel downstream. A similar mode pattern is observed at the right side of Jet 1 and the left side of Jet 3, with little or no organized pattern on the outer edges for these two jets. For the higher *J* of 0.5, the same pattern is observed where the organized structure is evident along the edges of the flames that are in the inter-element spacing, but less evident in the outer edges. For the *J* of 1, the mode pattern is less well organized, but still present. The wavelength of the structures within the inter-element spacing are observed to be of comparable size among the different jets. This suggests that the flames interact with some influence within the inter-element space that is not clearly present in the shadowgraph images. The J of 1 condition also has a bulk mode at 570 Hz present in both the CPSD and DMD analysis, which may indicate a weak chamber-coupled instability. Although present, this bulk mode is not observed to influence the trends and results presented in this paper.

Forced Results

The conditions *J* of 0.15 and 0.5 were selected to be acoustically forced at a pressure node/velocity antinode configuration. As stated previously, the pressure amplitude of 13.78 kPa (2 Psi) was selected, corresponding to velocity fluctuations of roughly 1 m/s. The forcing frequency was 2733Hz for *J* of 0.15, and 2750 Hz for J of 0.5. The forcing frequencies selected were near the natural frequencies obtained from the cross power spectral analysis of the

Distribution A: Approved for public release; distribution unlimited. PA #19376

Downloaded by Doug Talley on August 21, 2019 | http://arc.aiaa.org | DOI: 10.2514/6.2019-4108

unforced flow. Figure 11 shows an instantaneous image of the acoustically forced flow. From Figure 11, the LOX jet wavy structures have been enhanced and are highly organized close to the nozzle exit and far downstream for the *J* of 0.5 condition. For J of 0.5, the average transverse locations of the LOX jets appear to be unaffected by the transverse acoustic forcing. In other words, the jets do not appear to be fluctuating transversely as a total jet. However, the hydrogen jets are observed to fluctuate transversely as total jets. On the other hand, for *J* of 0.15, while the LOX jets also do not appear to fluctuate transversely as a total jet and the hydrogen jets also fluctuate transversely, for this lower J there does not appear to be significant LOX surface wave enhancement. In addition, the spreading of the outer hydrogen jets was more limited at J of 0.15 than at J of 0.5. Although the LOX jets acoustic wave enhancement is different for the two J's, similar high intensity OH*emission waves are also present along the edges of the LOX jets. Near the nozzle exit, these OH* waves are localized within the troughs of the LOX jet, and spread and diffuse further downstream. This is especially true for *J* of 0.5 condition. These results are consistent with the unforced results. The reason the acoustic enhancement is different for the two J's is not certain at present. It is speculated that the higher available hydrogen momentum for J of 0.5 may be more capable of amplifying surface irregularities than at J of 0.15.

Further analyzing the *J* of 0.5 condition, the cross power spectral analysis of the OH* fluctuations shows that the OH* fluctuations "lock-in" to the acoustic forcing. In Figure 12 the cross power spectral analysis from Jet 1 and Jet 2 shows that the forcing frequency of 2750 Hz is present for both flames. The same is true when comparing Jet 2 and Jet 3. Figure 13 shows the amplitudes of the DMD modes calculated. Strongly present is the forcing frequency along with higher harmonics, reinforcing the notion that the flame has coupled with the transverse forcing. Inspection of the spatial mode in Figure 14 reveals that the three jets have a similar zig-zag shape. An intriguing way this might be interpreted is that the acoustics has overwhelmed any natural dynamics that would cause the jets to interact, such that each jet behaves essentially as if it were independent of the others. It is further hypothesized that the dynamics of the LOX jet is largely controlled by the dynamics of the hydrogen jet. By coupling with the transverse acoustic forcing, the hydrogen jets are displaced in the direction of the time varying velocity field, in the same way for each hydrogen jet. As it displaces, each hydrogen jet impinges in the same way on each corresponding LOX jet, resulting in the annular structure/flame interactions previously noted, and dominates the flow behavior in the inter-element spacing.

The notion that the acoustics might overwhelm the natural dynamics that cause jet interactions is further supported by examining phase averaged shadowgraphs with respect to the acoustic forcing frequency. Figure 15 shows the phase averaged shadowgraphs of the multi-element and single element flows under transverse pressure node forcing at near similar conditions for the first three LOX diameters at J of 0.5. The single element was forced at 2773 Hz, and the multi element was forced at 2750 Hz. The LOX jet is observed to take on an S-shaped pattern, consistent with the zig-zag pattern present in the OH* DMD mode from Figure 14 and the instantaneous images in Figure 11. For the multi-element flow, the three jets appear to have the same curvature at the same locations. Although somewhat difficult to distinguish in the multi-element case, the hydrogen jet is observed to deflect, curl, and impinge on the LOX jet. While phase averaging may not reveal other unsteady aspects and interactions of the flow, it does also suggest that the acoustic forcing might override and dominate the natural dynamics and interactions present among the jets and possibly lead to each element behaving as if it were isolated from the others. Hence any dynamics and interactions that occur within the gas phase may be overwhelmed by the dynamics of the time varying velocity field that will control the flame/hydrogen wave structure interactions and the subsequent LOX surface waves. Further investigation will be needed to verify these hypotheses.

Downloaded by Doug Talley on August 21, 2019 | http://arc.aiaa.org | DOI: 10.2514/6.2019-4108

IV. Conclusions

The unsteady dynamics and spectral content from a linear array of three LOX/hydrogen shear coaxial injectors was investigated at a high subcritical pressure using high speed imaging at different momentum flux ratios, and compared with single element flows. Two conditions were selected to be investigated under pressure node acoustic forcing.

For the unforced conditions, the investigation revealed that each jet flame surrounded its own LOX jet and anchored at the LOX post tip. No group combustion or lifted flame was observed. In the gas phase, it was observed that the hydrogen shear layers and combustion gases interacted in the turbulent inter-element region, as close as one LOX jet diameter from the nozzle exit. Compared with the gas phase, the liquid phases in the jets did not appear to directly interact with each other, except possibly through the intermediate gas phase. From the shadowgraph results, it was observed that both the single element and outer hydrogen jets of the multi-element had similar spreading angles. However, the center flame appeared to be constrained, with little or no spreading of the flame observed. As with the single element studies, the individual jets from the multi-element injector demonstrated similar flame and wave structure dynamics. However, the flame waves for the multi element injector appeared to propagate downstream

Distribution A: Approved for public release; distribution unlimited. PA #19376

slower than for single element injectors. Spectral analysis within the inter-element spacing revealed that the neighboring flames shared similar frequencies. The shared frequency was only present when comparing the fluctuations along adjacent merging hydrogen shear layers. The dynamic mode decomposition showed that there are organized structures within the inter-element spacing and with diminished structures found on the outer edges of the outermost jets. Both the spectral analysis and the DMD showed that natural frequencies increased as hydrogen exit velocity increased.

For the acoustically forced cases, the hydrogen jets at both the momentum flux ratios investigated were found to fluctuate transversely with the acoustics, while the average LOX jet transverse positions did not. However, significant enhancement of the wavy structures on the LOX jets were observe for J of 0.5 but not at J of 0.15. When the wavy structures were present at J of 0.5, they were highly organized and persisted far downstream. Although the reason for the difference is not clear at present, it is speculated that the hydrogen jets for J of 0.5 may have enough momentum to augment the surface structures, whereas the hydrogen jets for J of 0.15 may not. Further research will be needed to understand the reason for this difference. Highly coupled dynamic wave structures in the flame and on the LOX jet were observed at both J's, similar to the unforced results. Spectral analysis of the DMD of the OH* emission for J of 0.5 showed that the flame coupled to the forcing frequency. A hypothesis was advanced that the acoustics might overwhelm any natural dynamics that would cause the jets to interact, and cause each jet to behave essentially as if it were independent of the others. The hypothesis is further supported by phase averaged shadowgraph images. It is further hypothesized that the dynamics of the LOX jets are largely controlled by the dynamics of the hydrogen jets. By coupling with the transverse acoustic forcing, the hydrogen jets are displaced in the direction of the time varying velocity field, in the same way for each hydrogen jet. As it displaces, each hydrogen jet impinges in the same way on each corresponding LOX jet. These hypotheses need to be further explored and confirmed by additional research.

Downloaded by Doug Talley on August 21, 2019 | http://arc.aiaa.org | DOI: 10.2514/6.2019-4108

References

[1] Ross, C. C., and Datner, P. P., "Combustion Instability in Liquid-Propellant Rocket Motors–A Survey," Selected Combustion Problems, edited by Hawthorne, W. R., Fabri, J., and D. B., Spalding, Butterworths Scientific, London, 1954, pp. 352–380.

[2] Oefelein, J. C., and Yang, V., "Comprehensive Review of Liquid- Propellant Combustion Instabilities in F-1 Engines," Journal of Propulsion and Power, Vol. 9, No. 5, 1993, pp. 657–677.

[3] Anderson, W. E., Ryan, H. M., and Santoro, R. J., "Combustion Instability Phenomena of Importance to Liquid Bi-Propellant Rocket Engine," 28th JANNAF Combustion Subcommittee Meeting, edited by Gannaway, M. T., Chemical Propulsion Information Agency (CPIA), Columbia, MD, 1991, pp. 99–112.

[4] Crocco, L., and Cheng, S.I., Theory of Combustion Instability in Liquid Propellant Rocket Motors, AGARDograph 8, Princeton Univ., Princeton, NJ, 1956, pp. 1–24.

[5] Harrje, D. T., and Reardon, F. H., "Liquid Propellant Rocket Combustion Instability," NASA Special Publ. SP-194, 1972.

[6] Culick, F. E. C., "Combustion Instabilities in Liquid-Fuelled Propulsion Systems," AGARD Conference Proceedings, NATO Paper 450, Neuilly sur Seine, France, 1988.

[7] Culick, F. E. C., "Unsteady Motions in Combustion Chambers for Propulsion Systems,"NATOAGARDograph AG-AVT-039, California Inst. of Technology, Pasadena, CA, 2006.

[8] Yang, V., and Anderson, W. E. (eds.), Liquid Rocket Engine Combustion Instability, Vol. 169, Progress in Astronautics and Aeronautics, AIAA, Washington, D.C., 1995.

[9] Natanzon, M. S., Combustion Instability, Vol. 222, Progress in Astronautics and Aeronautics, AIAA, Washington, D.C., 2008.

[10] Morgan C. J., Shipley, K. J., and Anderson, W. E., "Comparative Evaluation between Experiment and Simulation for a Transverse Instability," Journal of Propulsion and Power, Vol. 31, No. 6, 2015

[11] Pomeroy, B. R., Morgan, C., and Anderson, W. E., "Response of a Gas Centered Swirl Coaxial Injector to Transverse Instabilities," 47th AIAA/ ASME/SAE/ASEE Joint Propulsion Conference & Exhibit, AIAA Paper 2011-5698, 2011

[12] Yu. Y. C., Sisco, J. C., Rosen, S., Madhav, A., and Anderson W. E., "Spontaneous Longitudinal Combustion Instability in a Continuously Variable Resonance Combustor," Journal of Propulsion and Power, Vol. 28, No.5, 2012

[13] Hardi. J. S., Beinke, S. K., Oschwald, M.., and Dally, B. B., "Coupling of Cryogenic Oxygen-Hydrogen Flames to Longitudinal and Traverse Acoustic Instabilities," Journal of Propulsion and Power, Vol. 30, No. 4, 2014

[14] Gröning, S., Hardi. J. S., Suslov. D., and Oschwald. M., "Injector-Driven Combustion Instabilities in a Hydrogen/Oxygen Rocket Combustor," Journal of Propulsion and Power, Vol. 32, No. 3, 2016

Distribution A: Approved for public release; distribution unlimited. PA #19376

[15] Hardi. J. S., Oschwald. M., and Dally, B. B., "Study of Lox/H2 Spray Flame Response to Acoustic Exictation in a Rectangular Rocket Combustor," 49th AIAA/ ASME/SAE/ASEE Joint Propulsion Conference & Exhibit, AIAA Paper 2013-3781, 2013
[16] Hakim. L., Schmitt. T., Ducruix, S., and Candel S., "Dynamics of a Transcritical Coaxial Flame under High-Frequency Transverse Forcing: Influence of the Modulation Frequency on the Flame Response," Combustion and Flame, 162, 2015
[17] Urbano, A., Selle, L., Staffelbach, G., Cuenot, B., Schmitt, T., Ducruix, S., and Candel, S., "Exploration of Combustion Instability Triggering using Large Eddy Simulation of a Multiple Injector Liquid Rocket Engine," Combustion and Flame, 169, 2016
[18] Richecoeur, F., Ducriox, S., Scouflaire, P., and Candel, S., "Experimental Investigation on High-Frequency Combustion Instabilities in Liquid Rocket Engines," Acta Astronautica, 62, 2008
[19] Rey, C., Ducruix, S., Richecoeur, F., Scouflaire, P., Vingert, L., and Candel, S., "High Frequency Combustion Instabilities Associated with Collective Interactions in Liquid Propulsion," 40th AIAA/ ASME/SAE/ASEE Joint Propulsion Conference & Exhibit, AIAA Paper 2004-3518, 2004
[20] Richecoeur, F., Scouflaire, P., Ducruix, S., and Candel, S., "High-Frequency Transverse Acoustic Coupling in a Multiple-Injector Cryogenic Combustor," Journal of Propulsion and Power, Vol. 22, No. 4, 2006
[21] Magri. L., See, Y. C., Tammisola, O., Ihme, M., and Juniper, M. P., "Multiple-Scale Thermo-Acoustic Stability Analysis of a Coaxial Jet," Proceedings of the Combustion Institute, 36, 2017
[22] Popov, P. P., Sideris, A., and Sirignano, W. A., "Low-Probability Events Leading to Rocket Engine Combustion Instability," Journal of Propulsion and Power, Vol. 55, No. 3, 2017
[23] Sirignano, W. A., and Krieg, J., "Coaxial Jet Flame Subject to Long-Wavelength Acoustic Oscillations," Journal of Propulsion and Power, Vol. 32, No. 3, 2016
[24] Harvazinski, M. E., Huang, C., Sankaran, V., Feldman, T. W., Anderson, W. E., Merkle, C. L., and Talley, D. G., "Coupling Between Hydrodynamics, Acoustics, and Heat Release in a Self-Excited Unstable Combustor," Physics of Fluids, 27, 2015
[25] Roa, M., and Talley, D. G., "Wave Dynamic Mechanisms in Coaxial in Hydrogen/LOX Jet Flames," Journal of Propulsion and Power, Vol. 35, No. 2, 2019
[26] Roa, M., Forliti, D., Badakhshan, A., and Talley, D. G., "Acoustically Forced Coaxial Hydrogen/ Liquid Oxygen Flames," ILASS Americas 28th Annual Conference, 2016

Downloaded by Doug Talley on August 21, 2019 | http://arc.aiaa.org | DOI: 10.2514/6.2019-4108

Distribution A: Approved for public release; distribution unlimited. PA #19376

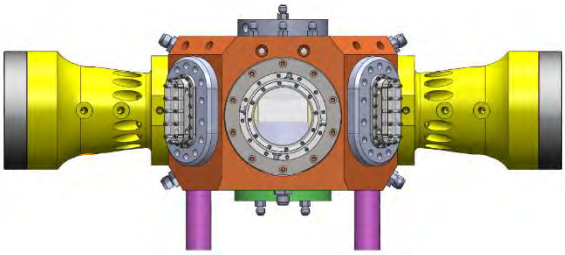

Figure 1. Assembly drawing of the combustion chamber.

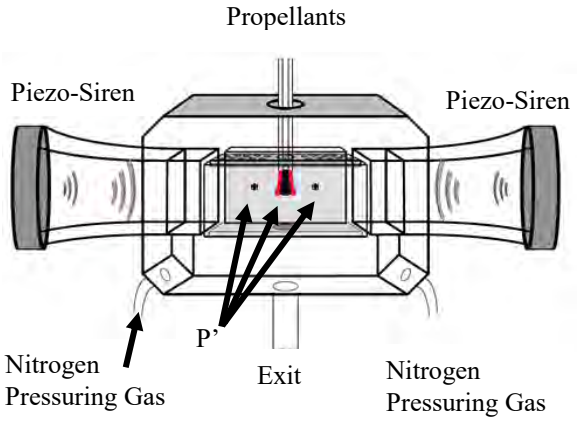

Figure 2. Inner configuration of the combustion chamber. P' is the location of the differential pressure transducers. The gray section in the middle is the optical windows used to complete the acoustic channel.

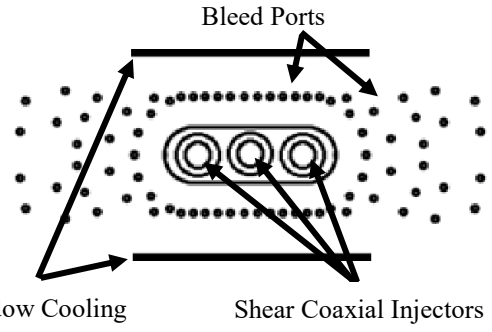

Figure 3. The injector faceplate with bleed ports, window film cooling, and the linear array injector in the center.

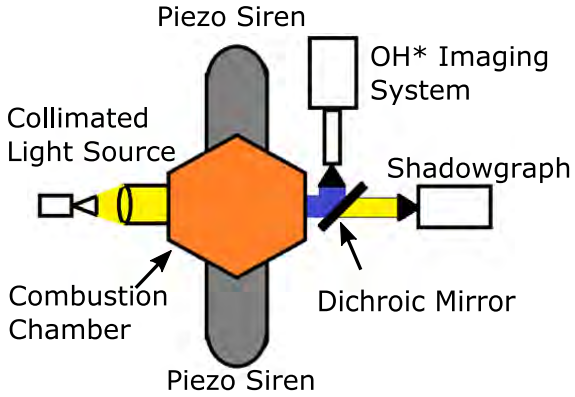

Figure 4. High speed, simultaneous imaging system layout.

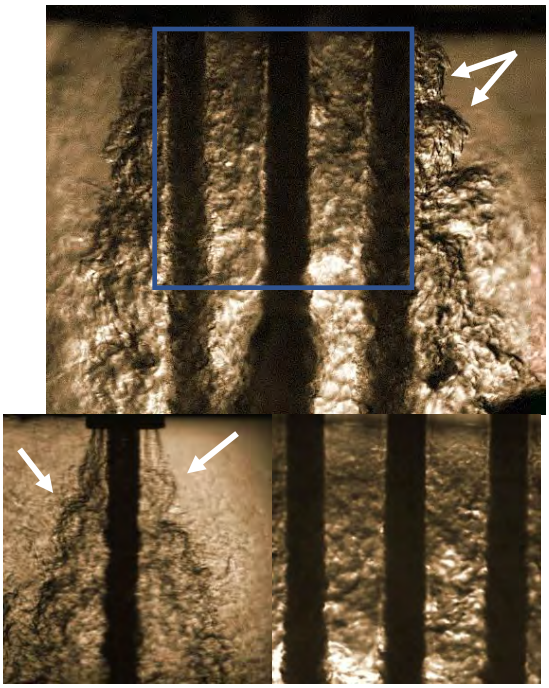

Figure 5. The top figure shows a shadowgraph image of the reacting flow. The blue box is the field of view for the single element comparison below. The bottom two figures show a comparison of single and multielement flows at the same physical size. Large scale structures are evident on the outer shear layers as indicated by the white arrows. The gas turbulence between the multielement jets begins interacting within one or two LOX jet diameters.

Downloaded by Doug Talley on August 21, 2019 | http://arc.aiaa.org | DOI: 10.2514/6.2019-4108

Distribution A: Approved for public release; distribution unlimited. PA # 19376

Table 1. Exit Conditions

J	Liquid Oxygen Temp (K)	Hydrogen Temp (K)	Oxygen Velocity (m/s)	Hydrogen Velocity (m/s)	Weber # ($x10^3$)	Reynolds Oxygen ($x10^3$)	Reynolds Hydrogen ($x10^3$)
0.15	133.5	289	4.1	27.6	65	75	2.4
0.5	136.1	288	4.1	34.9	114	87	3.5
1	128.1	282	3.9	54.3	330	82	5.1
2.2	130.8	287	3.2	89.1	829	58	7.6
4	133.5	289	2.7	104	1123	47	

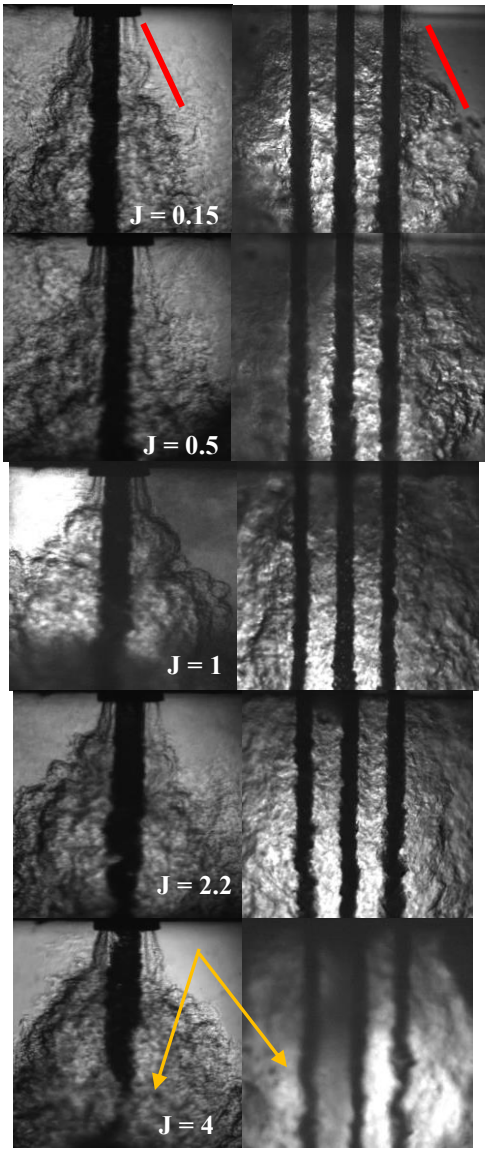

Figure 6. Spatial uncorrected shadowgraph images. There are comparable single element and outer element turbulence half-spreading angles for the hydrogen jet (red line). For the *J* of 4 condition, although slightly obscured by window fogging, the LOX jet is longer for the multi-element then the single element, as indicated by the yellow arrow arrows where the LOX jet is observed to break up.

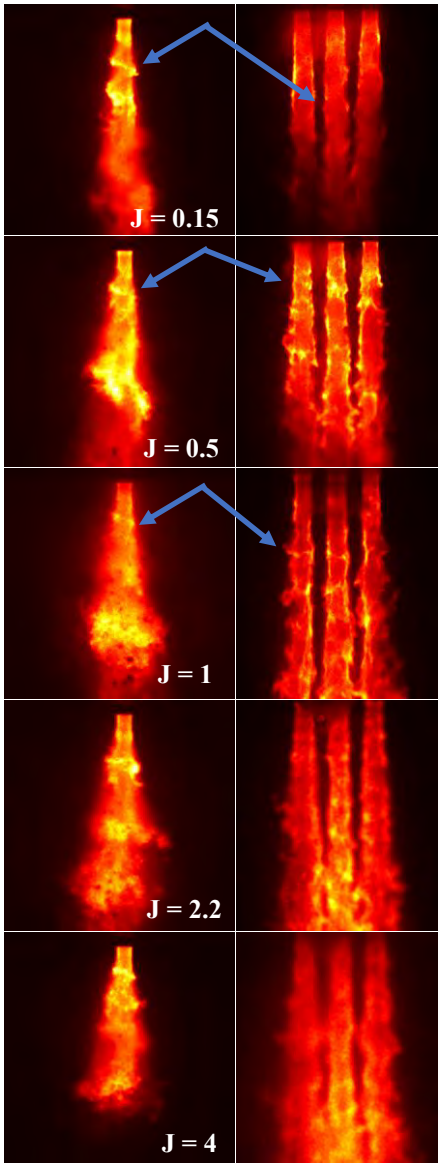

Figure 7. Flames are individually attached to each injector with no group combustion or lifted flames. Wave structures are present (arrows). Multi element flames are longer. The single element and outer flames spread outwards, while the multi-element center flame is more constrained. Camera sensitivities were not controlled, so the apparent OH* intensities cannot be compared.

Distribution A: Approved for public release; distribution unlimited. PA # 19376

Downloaded by Doug Talley on August 21, 2019 | http://arc.aiaa.org | DOI: 10.2514/6.2019-4108

Downloaded by Doug Talley on August 21, 2019 | http://arc.aiaa.org | DOI: 10.2514/6.2019-4108

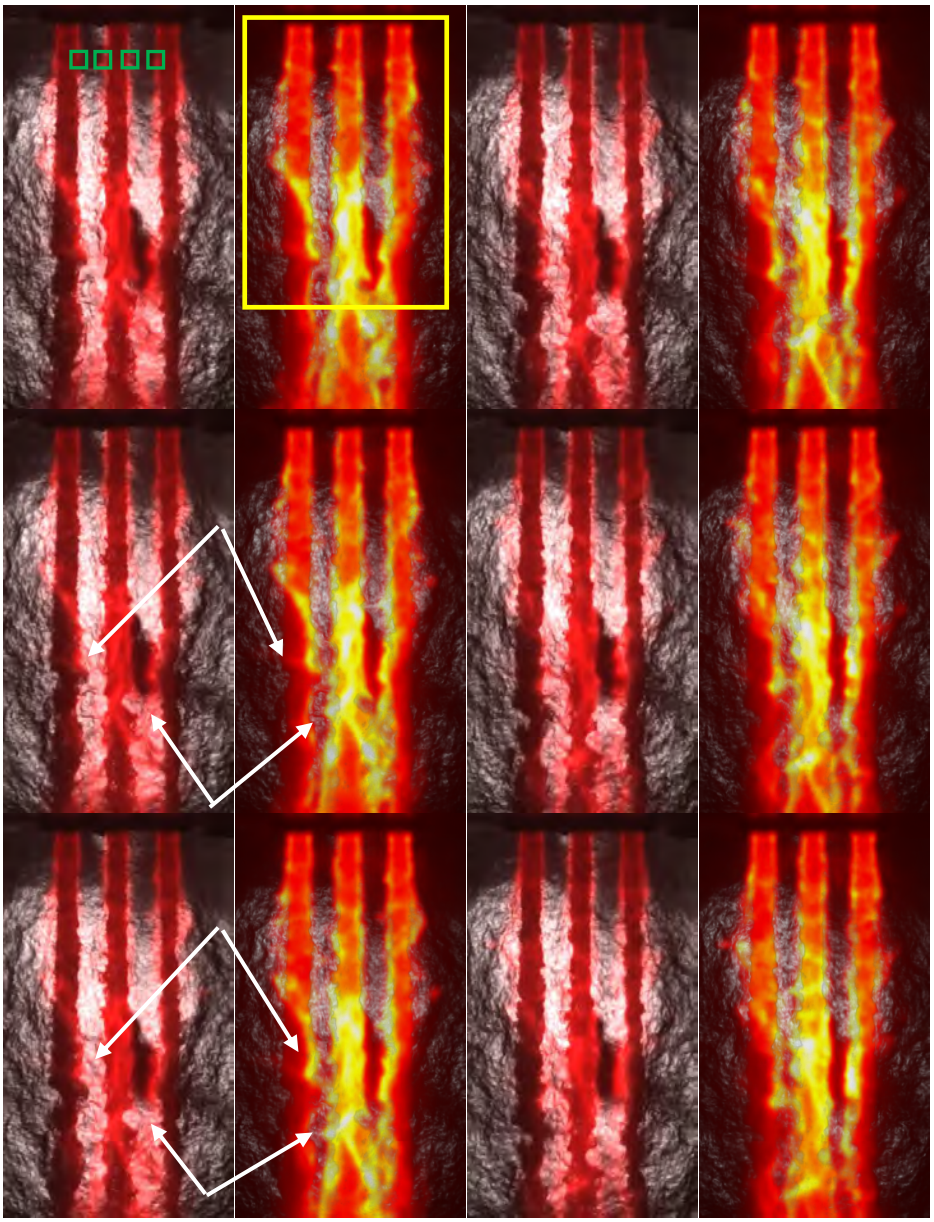

Figure 8. Side-to-side image pairs showing two methods of superimposing instantaneous shadowgraph and OH* emission images, wavelet fused (left image) and overlapped (right image). The pairs evolve sequentially in time, from top to bottom, then from left to right (six total times shown). The time separation between each frame is 40 microseconds. The flames in the near nozzle region are individually attached to their own exit and don't merge or lift. The green rectangles show the locations where the OH* emission fluctuations were recorded. The yellow square is where the DMD snapshots were taken for the OH* emission. The white arrows point the locations where LOX waves and high intensity OH* emission are present together.

Distribution A: Approved for public release; distribution unlimited. PA # 19376

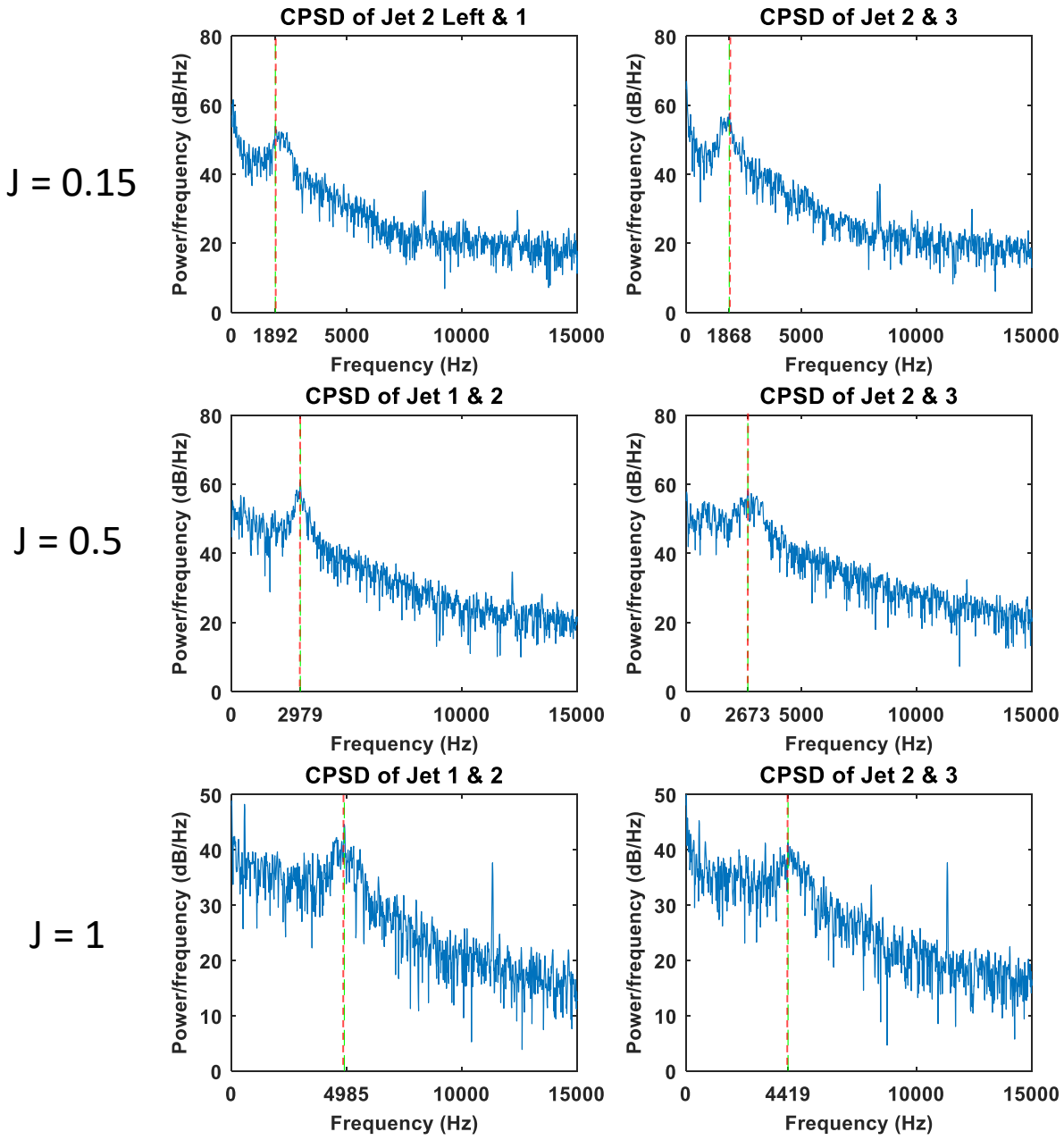

Figure 9. The cross power spectral density (CPSD) of the OH* fluctuations between (left column) Jet 2 and Jet 1, and (right column) between Jet 2 and Jet 3. The top row is the J of 0.15 condition, followed by J of 0.5 and then J of 1. Present in the CPSD plots are peak frequencies that are shared among the center flame's OH* fluctuations and its neighbor's, as shown by the dashed line. The frequency peak increases with J, or as hydrogen exit velocity increases.

Downloaded by Doug Talley on August 21, 2019 | http://arc.aiaa.org | DOI: 10.2514/6.2019-4108

Distribution A: Approved for public release; distribution unlimited. PA #19376

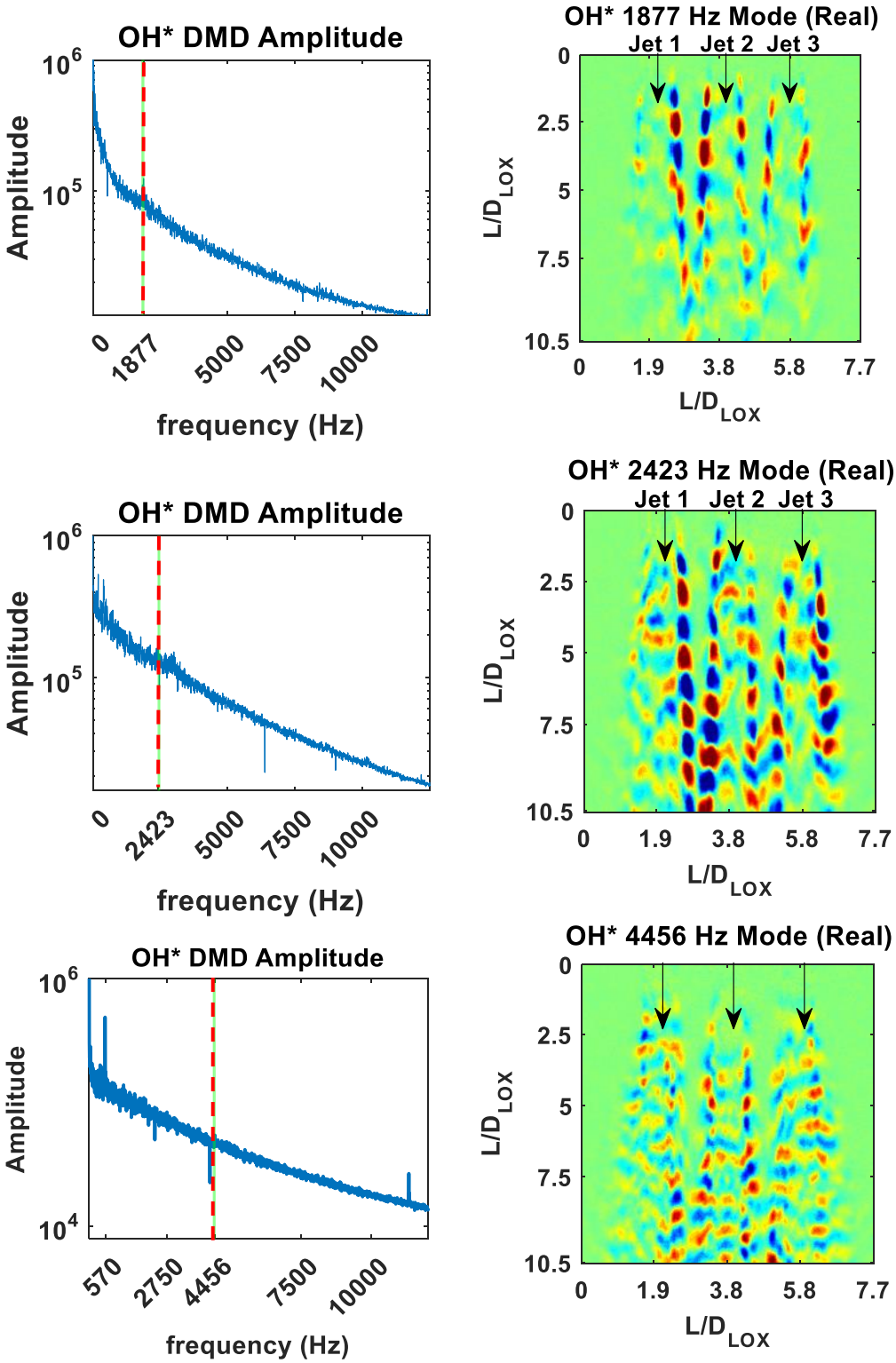

Figure 10. Shown are the dynamic mode decomposition amplitudes with the mode shape based on the frequency peak from the CPSD comparisons for the OH*. Slightly above the noise, the DMD amplitudes have similar frequency peaks as the OH* CPSD. The top row is for *J* of 0. 15, followed by 0.5 and 1. *J* of 1 exhibited a natural chamber mode instability at 570 Hz. At the frequencies peaks, J of 0.15 and 0.5 exhibit the same mode behavior, where the center jet's structure is correlated with the neighboring flame's structure. The effects are weaker for *J* of 1.

Distribution A: Approved for public release; distribution unlimited. PA #19376

Downloaded by Doug Talley on August 21, 2019 | http://arc.aiaa.org | DOI: 10.2514/6.2019-4108

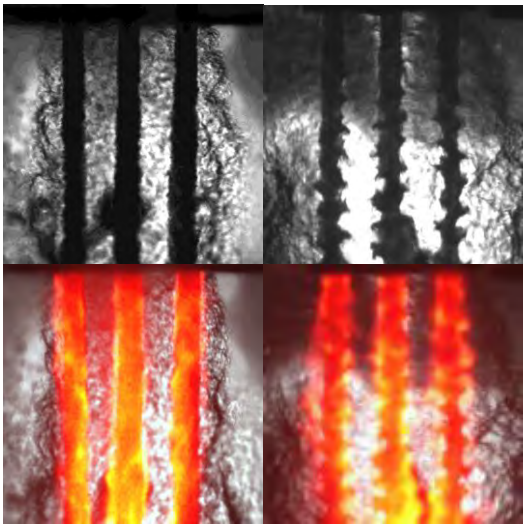

Figure 11. The acoustically forced *J* of 0.15 (left column) and 0.5 (right column) condition. The bottom row image is OH* emission overlapped on top of the shadowgraph image. The LOX jet structures are enhanced by the pressure node forcing for the *J* of 0.5 condition. The LOX jet for the *J* of 0.15 condition shows little influence from the acoustic forcing.

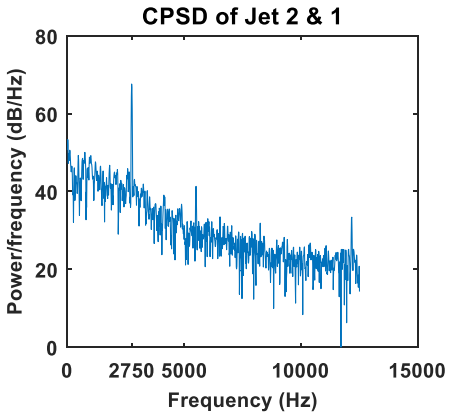

Figure 12. Cross power spectral density between the center flame and the left jet flame for *J* of 0.5 condition. The flame's natural observed frequency is overridden by the acoustic forcing frequency, which is higher than the flame's natural frequency.

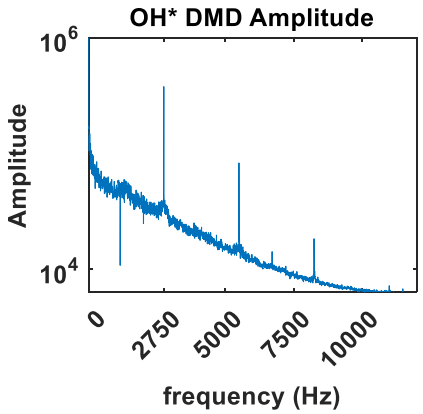

Figure 13. The DMD amplitude for the acoustically forced condition. All three jets have locked in to the acoustic forcing. Higher harmonics of the forcing frequency are present.

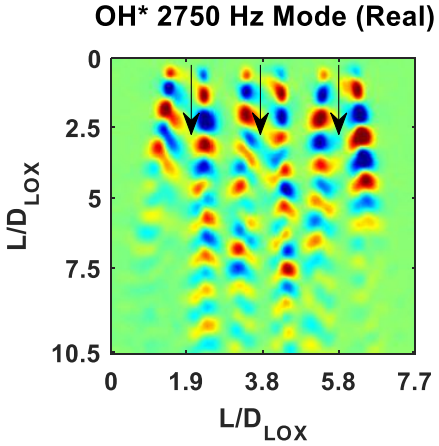

Figure 14. The DMD mode shape at the forcing frequency. The individual jets in the near nozzle region have the same shape and dynamics. The organized structures decay further downstream.

Distribution A: Approved for public release; distribution unlimited. PA #19376

Downloaded by Doug Talley on August 21, 2019 | http://arc.aiaa.org | DOI: 10.2514/6.2019-4108

Downloaded by Doug Talley on August 21, 2019 | http://arc.aiaa.org | DOI: 10.2514/6.2019-4108

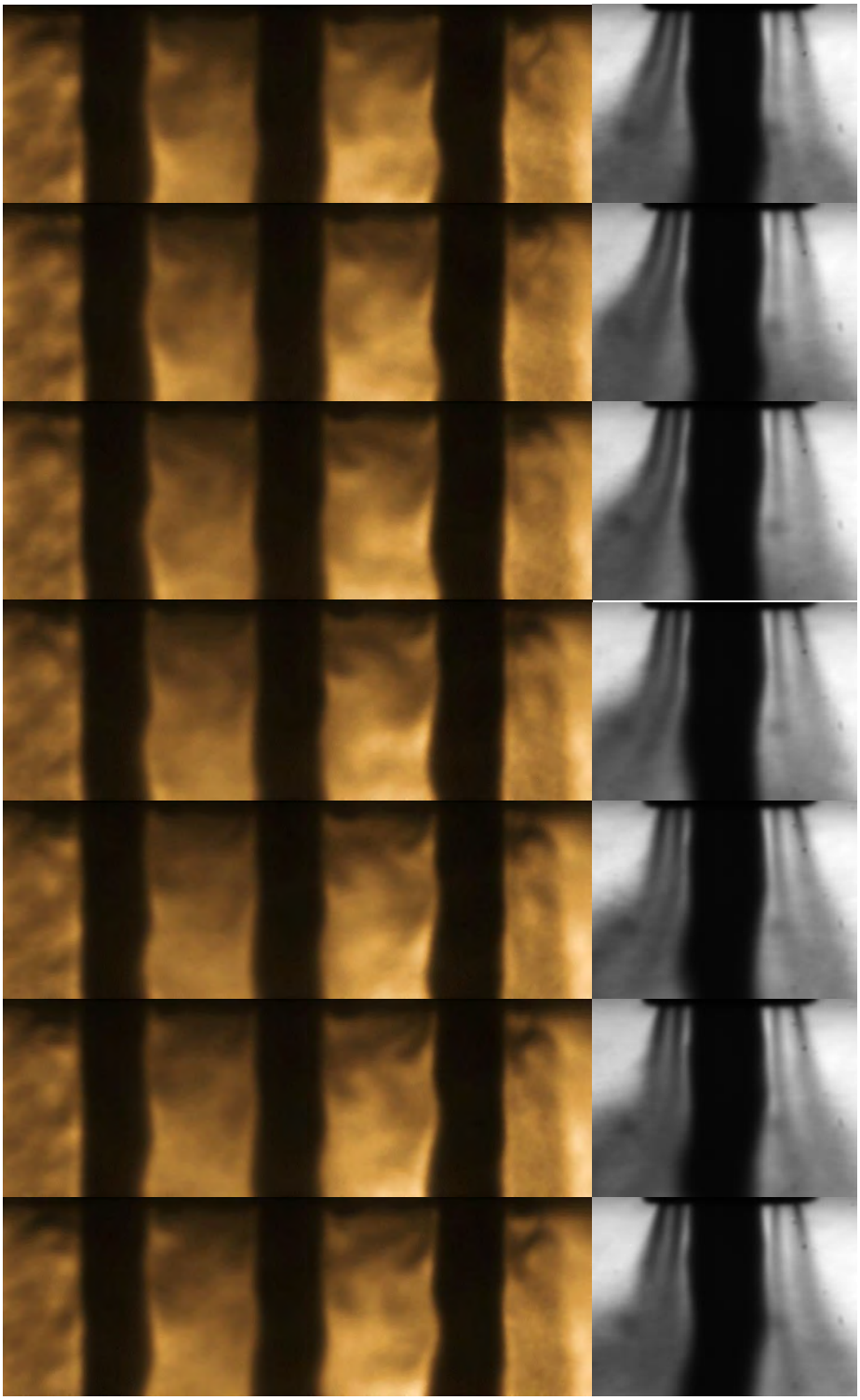

Figure 15. Phase averaged images of the shadowgraph. Multi-element (Left) and single element (Right) are presented for a complete cycle. The phase averages are taken with respect to the acoustic forcing frequency. It is observed in the phase average that the LOX jets developed a similar wavy pattern for multi element and single elements, indicating that the dynamics of each jet in a multi-element injector may be dictated separately by the acoustic forcing. Slight evidence of the hydrogen jet curling is present from the shadows surrounding the LOX jet in the multi-element case.

Distribution A: Approved for public release; distribution unlimited. PA #19376

AIAA SciTech Forum
6-10 January 2020, Orlando, FL
AIAA Scitech 2020 Forum

10.2514/6.2020-0422

Check for updates

Acoustic Forcing and Sensitivity of the Hydrodynamic Instabilities and Flame Dynamics from Hydrogen/LOX Shear Coaxial Flames

Mario Roa[1]
Sierra Lobo, Inc., Air Force Research Laboratory, Building 8451, Edwards AFB, Ca 93524, USA

Douglas G. Talley[2]
Air Force Research Laboratory, Building 8451, Edwards AFB, Ca, 93524, USA

Downloaded by Doug Talley on January 7, 2020 | http://arc.aiaa.org | DOI: 10.2514/6.2020-0422

An experimental investigation was performed to detail the hydrodynamic and flame interactions and their sensitivity to transverse acoustic forcing for shear coaxial flames. The experiment, performed using an optically accessible combustion chamber, investigated the dynamics of an annular gaseous hydrogen jet with a centeral liquid oxygen jet at high pressures. The hydrodynamic wave instabilities associated with the annular hydrogen jet were found to have dramatic effects that greatly influenced the physical features and the dynamics of the liquid oxygen jet. While varying the relative momentum flux between the hydrogen and liquid oxygen jets, high speed shadowgraph images captured the sensitivity of the annular hydrogen wave structures when subjected to the high frequency transverse acoustic forcing. Simultaneously, high speed OH* chemiluminescence images captured the flame's behavior when the annular structures coupled to the acoustic forcing. It was observed from the high speed images that when the annular hydrogen structures coupled with the acoustic forcing, it would enhance the wavy hydrogen jet structure/flame interactions that naturally occur when the flow is unforced. These interactions would also dominate the shape and breakup of the liquid oxygen jet, as well as the flame dynamics.

I. Nomenclature

DMD = Dynamic mode decomposition
J = Momentum flux ratio
LOX = Liquid oxygen

II. Introduction

High frequency combustion instabilities experienced by liquid rocket engines involves the interaction between resonant acoustic modes of the combustion chamber and unsteady heat release. These high frequency instabilities have detrimental effects on the performance of liquid rocket engines and can lead to catastrophic engine failure. Transverse combustion instabilities have been identified as the most harmful and damaging. Investigations into high frequency combustion instabilities have been carried out by several researchers [1-19]. Although great strides have been and continue to be made in experiments and modeling of combustion instabilities, there is still much to be desired in

[1] Research Scientist, Edwards AFRL/RQRC, and Member
[2] Research Physical Scientist, Edwards AFRL/RQRC, and Senior Member

This material is declared a work of the U.S. Government and is not subject to copyright protection in the United States.

understanding the pathways and mechanisms that lead to the coupling of resonant acoustic modes and unsteady heat release.

Experimental and computational efforts on shear coaxial injectors using a gaseous annular flow and a central cryogenic jet for liquid rocket engine applications have been carried out by Candel et al. [7-12], Mayer et al. [20-22], Yang et al. [23-25], and Talley et al.[18, 19, 26-28]. These efforts focused largely on characterizing and understanding the atomization, flame locations, and average global behavior with and without acoustic perturbations. These are reviewed in Roa and Talley [26]. Hardi et al. [4-6] investigated the atomization of liquid oxygen jets for reacting shear coaxial injectors in multi-element configurations. Their results compared the average LOX jet break up length to correlations developed by past researchers. They determined that the past correlations tended to underestimate the intact length of the LOX jet when the flow is reacting. For acoustic forcing, Hardi et al. employed a saw-toothed wheel to achieve high frequency, acoustic forcing up to peak amplitudes of 9% of the mean chamber pressure. Hardi et al. observed that the LOX jet break up length can decreased by as much as 30% when acoustically forced. Hardi et al. also observed that when the reacting flow is subjected to pressure node forcing, the flame is convectively displaced with the transverse acoustic velocity field.

Candel et al. performed both experimental and large eddy simulations on acoustically forced shear coaxial flows. They reported a change in the LOX jet from a cylindrical shape to a flattened fan shape when subjected to transverse acoustic modulations. Two possible causes were suspected for the change in shape. One of these, they argued, was that a suction effect caused by the acceleration of the flow around the LOX jet creates a non-uniform pressure on the surface of the LOX jet that results in the flattened shape. The other possible cause was the non-uniform acoustic radiation pressure impinging on the LOX jet. Neither possible cause was investigated further. Similar to the results of Hardi et al., the LOX jet break up length was shortened due to the transverse modulations. The flame length was also observed to shorten, correlating with the LOX jet break up length. By tracking changes in the OH* emission, Candel et al. argued that the locations of high heat released were displaced in the direction of the transverse forcing and were in phase. The large eddy simulations also showed that when the reacting flow was subjected to low frequency perturbations, the flame develops a flag-like motion, whereas the flow exhibits bulk motion when subjected to high frequency perturbations. Computational work carried out by Sirignano et al. [29-31] had success matching trends observed in the experiments conducted by Purdue [32,33]. The computational results by Juniper et al. [34-36] showed that combustion instabilities were easier to achieve when the hydrodynamics coupled with the acoustic forcing.

Researchers at Edwards AFRL [18, 19, 26-28] experimentally investigated the effects that transverse forcing has on non-reacting supercritical and sub-critical reacting shear coaxial reacting flows. Unlike the previous researchers mentioned earlier, the investigations subjected the injector flow to a transverse acoustic standing wave created by piezo-sirens. For the non-reacting experiments, gaseous and liquid nitrogen were used a propellant simulants. These studies reported differences between the cryogenic nitrogen jet break up at sub- and supercritical conditions. They observed a similar trend where the center liquid jet experienced a reduction in length or earlier breakup when subjected to transverse acoustic forcing. Under reacting conditions, the researchers investigated the receptivity of a single flame condition to increasing pressure amplitudes. They observed that at low pressure amplitudes, less than 1% of the mean chamber pressure, the reacting flow would couple with the acoustic flowing, but it did not necessarily override the natural dynamics of the reacting flow. Instead, larger amplitude forcing was required for the natural dynamics of the reacting flow to be overcome by the acoustics. It was not understood if the coupling was a linear or non-linear result. The researchers also explored the natural dynamics of non-forced jets and observed that the annular jet instabilities created in the injector region would dominant the downstream flow by shedding structures that would directly influence the flame and LOX jet behavior.

An experimental investigation was carried out here to explore the sensitivity of the annular hydrogen jet structures, the annular hydrogen flame, and the LOX jet to high frequency acoustic perturbations as a function outer-to-inner momentum flux ratio (J). To explore the sensitivity, J was varied by keeping one of the propellant's exit velocity constant and varying the other, and subjecting the reacting flow to near constant amplitude, pressure node acoustic forcing for all conditions investigated. High speeding imaging focused on the annular hydrogen jet's structure and dynamics, and on the influence the imposed acoustic forcing had on the resulting flow.

III. Experimental Methods

A shear coaxial injector was tested in a high-pressure, windowed combustion chamber equipped with piezo-sirens to acoustically force the reacting flow. The combustion chamber is a chamber-within-a-chamber design. The main outer body of the combustion chamber is designed with optical access and to operate at high pressures. An acoustic channel within the outer combustion chamber acts as the inner combustion chamber and is where the acoustic forcing

Downloaded by Doug Talley on January 7, 2020 | http://arc.aiaa.org | DOI: 10.2514/6.2020-0422

takes place. The injector is located in the middle of the acoustic forcing channel. A schematic is shown in Figure 1. Mounted on the chamber shown in orange are a total of six windows, consisting of two large 101 mm (4 in) diameter round sapphire windows and four oblong windows angled at 45 degree offsets. The chamber is symmetric about the vertical center plane, so only three of the windows are shown in Figure 1. The two oblong windows shown in Figure 1 are not used in this study but can be used for laser diagnostics like particle image velocimetry or planar laser induced fluorescence. Only the large 101 mm windows were used for high speed shadowgraphy and OH* chemiluminescence imaging. The optical set up for each are described further below.

The propellants enter the injector from the top of the combustion chamber. The volume occupied by the reacting flow is small compared to the volume of the combustion chamber. Nitrogen gas is introduced into the sides of the chamber, as shown in Figure 2, and is used to pressurize the combustion chamber. The combustion process itself is not used to achieve the pressures at which this experimental investigation was carried out. This was done in order to maintain accurate control of the chamber pressure and ensures that the combustion process does not enter a combustion instability limit cycle spontaneously. Combustion gases at the exit of the inner chamber mix with the pressurizing nitrogen and the gas mixture is diluted and cooled before it exits through a metering orifice (not shown) at the bottom of the outer chamber.

Figure 2 shows a schematic of the internal details of the chamber. The acoustic channels constitute the inner chamber and the injector and flame are located at the center. The inner chamber is connected to and is at the same pressure as the outer chamber and cannot itself sustain any pressure difference with the outer chamber. It does, however, focus the acoustics, driven by piezo-sirens attached at either end, and limits hot combustion gases from exiting into the main chamber. The outer chamber and associated pressure-containing windows and window seals are therefore not exposed to potentially damaging high temperature combustion gases. In the vicinity of the coaxial injector, the inner cross section of the acoustic channel normal to the page is rectangular, 20.5 mm (0.81 in) wide (or 6.8 inner LOX post diameters) and 35.5 mm high. The end-to-end length of the acoustic channel is 0.375 m or 268 LOX post diameters. There is a round-to-rectangular transition from the acoustic drivers to the channel, but the transition is far enough away from the coaxial injector that the geometric details are not important for this study.

Centered around the injector are two opposed flat windows in the walls of the acoustic channel for visualization, measuring 76.2 mm (3 in) wide by 41.4 mm (1.63 in) high. Three dynamic pressure transducers (Kulite XCL-100 25D) are located on one of the rectangular inner windows to measure the setup of a standing acoustic wave at a known frequency, phase, and pressure amplitude within the inner channel. The dynamic pressure transducers are located at the center in the middle of the viewing window, corresponding to 20.7 mm downstream of the injector exit. One transducer is located in the center of the acoustic channel along the exit of the injector and two other neighboring dynamic transducers located 25.4 mm (1 in) to the left and right of the center transducer. The two viewing windows have a nitrogen film over them to shield them from the combustion gases. In addition, a separately controlled nitrogen bleed is introduced through round holes in a face plate surrounding the coaxial injector on the upper wall of the inner chamber. The bleed suppresses the formation of a hot gas recirculation zone near the injector that can otherwise influence the dynamics of the reacting flow. The faceplate with the bleed holes is illustrate in Figure 3. The inner diameter of the center LOX jet is 1.4 mm, with a LOX post thickness of 0.38 mm. The outer diameter of the hydrogen flow is 2.82 mm, giving an exit area ratio of 1.68. The diameter of the bleed holes is 0.5 mm. The nitrogen bleed is regulated to a velocity of 0.05 m/s, as well as the window cooling, separately controlled, to a velocity of 0.05 m/s.

The purge and window cooling manifolds were analyzed to determine the possible presence of resonances that might affect the dynamic results reported in this paper. The resonant frequencies were found to be many times lower than the frequencies associated with these results. The gas circuit of the annular fuel manifold (hydrogen) and liquid oxygen were similarly analyzed and also found not to be acoustically active for these experiments and far away from the driving acoustic frequency used in this study.

The coaxial injector was designed to have straight passages resulting in fully developed flows at the exit, namely $\frac{L}{D} \geq 4.4Re^{1/6}$. For the given Reynolds numbers investigated an L/D of over 100 was used for both propellant circuits (the annular gap thickness was used as the length scale for the coaxial hydrogen). The pressure and temperature for both LOX and hydrogen were measured immediately upstream of entering the injector. The LOX jet was kept roughly at 140 K, and the hydrogen gas was chilled to 285 K prior to entering the injector. Some heat exchange occurred inside the injector internal passages due to the temperature difference. In order to minimize this heat exchange, the injector was pre-chilled. Before LOX entered the injector, liquid nitrogen ran through the LOX fed circuit for several minutes prior to combustion. The chamber pressure used in these studies was 4.13 MPa (600 psia). This is considerably below the critical pressure of oxygen, so the oxygen was initially a liquid. Igniting the flows at this pressure proved to be non-trivial as most spark ignition methods do not work when a high pressure is established prior to ignition as in this

Downloaded by Doug Talley on January 7, 2020 | http://arc.aiaa.org | DOI: 10.2514/6.2020-0422

experiment. The approach used was a hydrogen-air torch, ignited using a photoignition technique. See Badkahshan et al. [37] for details about the photoignition technique.

The reacting flow was visualized with simultaneous high speed shadowgraphy and OH* chemiluminescence. The imaging arrangement is illustrated in Figure 4. The imaging systems captured the unsteadiness of the reacting flow at a framing rate of 25 kHz. The high speed shadowgraph optics were composed of a 7.6cm (3 inch) collimated light source, formed with a ThorLabs SL S202 broadband light source and a spherical 152 mm lens, imaged onto a Phantom Research v 710 with an Infinity K2 long distance microscope lens. The shadowgraph setup allows for feautres of roughly 100 μm to be resolved. Simultaneously, OH* chemiluminescence was captured with Lambert Instruments HICATT imaged directly onto a Phantom Research v1210 camera. An UV lens (F/2.8 Cerco 2178) with a Semrock (PN FF02-320/40) optical filter were used to image the OH* emission. An IRIG time signal synchronized the high-speed imaging and data acquisition systems. A dichroic mirror was used to reflect the UV OH* emission from the flame onto the intensifier, while allowing the visible light to pass through for the shadowgraph images. The optical arrangement is shown in a schematic in Figure 4.

The gas-to-liquid momentum flux ratio ($J = \frac{\rho U_{Gas}^2}{\rho U_{Liquid}^2}$) has been identified as a global parameter that controls the atomization and breakup a liquid jet in two phase coaxial flows [38]; hence an investigation on the dynamic mechanism and sensitivity of reacting hydrogen/LOX coaxial jets to acoustic perturbations was principally studied by varying J. The momentum flux ratio was varied primarily by varying the hydrogen gas flow rate through the injector, while the oxygen flow rate was kept relatively constant for the J conditions less than or equal to 1. For the conditions greater than 1, the hydrogen gas flow was keep constant and the LOX flow rate dropped. Momentum flux ratios ranging from 0.12 to 3.54 were tested. Other flow parameters are presented in table 1. All flows were regulated and metered in a gaseous state using Porter mass flow meter (model 123) and needle valves for each individual circuit feeding the injector, bleed ports, and film cooling. After regulation and metering, the gaseous oxygen was subsequently chilled to the desired temperatures using heat exchangers cooled with liquid nitrogen. The pressurizing ambient gases were not temperature regulated and were supplied at room temperature. However, the presence of the LOX and the cooling liquid nitrogen usually produced chamber ambient temperatures that were somewhat below the room temperature. Chilling due to Joule-Thompson expansion effects was also observed.

The reacting flow was subjected to pressure node forcing (velocity anti-node). An example of the pressure trace measured by the high frequency Kulite pressure transducers is shown in Figure 5. The center transducer corresponding to the injector location is shown to experience only negligible pressure fluctuations, confirming the presence of a pressure node. A constant pressure amplitude at of 20.68kPa (3 Psi) at the transducers offset from the injector location was selected for all conditions, but to due to the influence of the flame this could not be precisely maintained. Hence the reacting flow was forced at a pressure amplitude of between 18.61 to 24.8 kPa (2.7 to 3.6 Psi), which corresponds to velocity fluctuations at the pressure node itself of between 1 to 1.5 m/s. The forcing frequency was 3008 Hz, corresponding to a wavelength of 0.12 m, which was much larger than the injector diameter.

IV. Results

For the three conditions where *J* was less than 1, the LOX jet exit velocity was kept constant and *J* was changed by increasing the hydrogen exit velocity. For the remaining conditions, hydrogen exit velocity was kept at roughly the maximum 80 m/s and the LOX jet flow exit velocity was lowered to achieve the desired value of *J*. The desired exit jet velocities were accomplished by varying the mass flowrate through the injector and the results are listed in Table 1. Figure 6 shows an example of an instantaneous image of the OH* chemiluminescence and shadowgraph captured for $J = 2.2$. The shadowgraph images focused on the near nozzle region up to 8 LOX diameters downstream of the nozzle exit. Due to limitations of the focal length of the UV lens, the field of view captured in the OH* chemiluminescence images was larger, roughly 19 LOX diameters from the nozzle exit. From Figure 6, present in the shadowgraph image are two gradient regions of the index of refraction referred to below as "density gradients," since they are related to gradients in the gas density. The gradients are roughly symmetric on average on either side surrounding the dark LOX jet. The outer most density gradient is the boundary of the annular hydrogen jet and the high pressure nitrogen. The inner most density gradient, the shadow closet to the inner LOX jet, is the boundary between the flame and hydrogen jet. It will be shown later that the flame is situated close the LOX jet in the near nozzle region, indicated by the locations of OH* emission. The OH* chemiluminescence image shown in Figure 6 features high intensity wavy OH* emission bands that go across the entire jet, which are located at the same locations of the hydrodynamic instabilities of the annular hydrogen jet.

Figure 7 shows a single phase averaged shadowgraph image each for different values of *J*. The phase averaged image was created by averaging across every 10th cycle of the 3008 Hz forcing cycle. For the lowest hydrogen exit

Downloaded by Doug Talley on January 7, 2020 | http://arc.aiaa.org | DOI: 10.2514/6.2020-0422

velocity, J = 0.12, the annular hydrogen structure is observed to be deflected by the acoustic forcing. After the hydrogen jet deflects, it impinges on the LOX jet which is clearly visible shown by the dark density gradients described earlier. At the same locations where the hydrogen structure impinges on the LOX jet, the LOX jet is locally consumed and develops a wavy pattern. This is the same behavior previously observed by Roa and Talley [26] for the unforced shear coaxial flames. These hydrodynamic instabilities and flame interactions are coupled to the acoustic forcing.

Figure 8 shows interactions between the acoustically coupled hydrodynamic structures and the flame and LOX jet. Figure 8 is a series of instantaneous images; a shadowgraph is to the left and to the right is the same shadowgraph image with the OH* emission image overlapped. In Figure 8 the hydrogen jet and flame are deflected towards the LOX jet, in the same direction as time varying velocity field. As it impinges on the LOX jet, there is an increase in OH* emission, indicating enhanced combustion which locally evaporates and consumes the LOX jet. As the LOX jet travels downstream, the high intensity OH* emission bands remain within the trough of the developed LOX jet wavy pattern. As the velocity field reverses direction, the annular structure is shed and convects downstream. This process repeats itself on either side, giving rise to the alternating wavy pattern the LOX jet exhibits in Figure 7 and the high intensity OH* emission alternating pattern in Figure 8.

The wavy pattern on the LOX jet persists for the J of 0.5 and 0.84 condition. Although the hydrogen jet structure behavior is not clear and appears to be absent from these two J conditions from the phase averaged images, the same mechanism is still present when the instantaneous images are reviewed. For the remaining J conditions, conditions 2.7 and 3.5, the phase averaged images of the LOX jet do not appear to be influenced by the acoustic forcing; however, the instantaneous images show this is not necessarily the case. Figure 9 shows a series of instantaneous images, similar to Figure 8, for J of 3.5. In this series of images, the LOX jet is observed to be initially deflected. At the same instant, the hydrogen jet starts to develop an annular structure. The creation of the annular structure is coupled with acoustic forcing. As the annular structure develops, it much larger in scale compared to the J of 0.12 condition and exhibits the same behavior of impinging onto the LOX jet. As it convects downstream it encounters the curved portion of the LOX jet and eventually breaks up the LOX jet. An increase in OH* emission intensity is observed where the hydrogen jet impinges. The annular structure is observed to be larger in size when hydrogen exit velocity is increased. It should be noted that the annular structures shed are not always the same size, unlike the J of 0.12 where all of the annular structures shed are of similar size. The difference in sizes has also be previous observed by Roa and Talley [26] for the unforced conditions. Both J of 2.7 and 3.5 exhibit similar LOX jet breakup behavior when an annular structure is shed, unlike the J of 0.5 and 0.84 where the LOX jet is always intact for the field of view investigated. The annular structure is observed to be always responsible for the developed wavy pattern observed on the LOX jet and its breakup.

Examining the phase average for the flame, a similar pattern of dynamics is observed when the flow is acoustically forced. Figure 10 shows the OH* emission phas averaged to the acoustic forcing frequency with the temporal mean subtracted. Unlike the shadowgraph phas averaged images, the OH* averages continue to show structure for the higher J value conditions. For all conditions, a zig-zag pattern is observed and is mostly coherent for the first 6 LOX diameters downstream of the injector exit, except for the J of 0.84 where the pattern persists further downstream. As described earlier, the zig-zag alternating pattern is a result of the hydrogen jet being displaced towards the LOX jet and causing a localized increase in OH*. This is indicated by the bright yellow portions and are located where the edges of the LOX jet would be. The size of the bright spots are larger as the hydrogen velocity increases. The dark regions directly opposite of the bright yellow portions is where the hydrogen jet is deflected away from the LOX jet. Although these regions are dark, the flame is still present as indicted by Figures 8 and 9 and should not be confused with an extinction of the flame locally. It should be noted that no flame extinction was ever noticed due to the acoustic forcing, but rather an enhancement of the natural hydrogen jet instabilities / flame interactions for unforced jets were observed when the flow was acoustically forced.

As mentioned earlier, the size of the annular hydrogen structure can vary largely, even within the same operating condition, similar to the results observed by Roa and Talley [26]. This distribution in size leads to observed differences in the break-up length of the LOX jet for the conditions investigated, the size of the bright flame regions in Figure 10, and how far the OH* bright spots travel downstream. The sensitivity of these structures to acoustic forcing can be analyzed using dynamic mode decomposition (DMD) on the OH* images. The OH* images were selected for DMD analysis because of their larger field of view compared to the shadowgraph images. Dynamic mode decomposition is a dimensionality reduction of a given time series data, where DMD computes a set of modes each with a unique oscillation frequency, decay/growth rate, and amplitude based its contribution to reconstructing the time series data. The larger the amplitude associated with a unique frequency, the more that mode contributes to the reconstruction of the original data. Figure 11 shows the DMD amplitude for all J conditions. For the DMD analysis, 5000 images or 0.2 seconds of data were used. In Figure 11, the flow is observed to be highly coupled to the acoustic forcing, with higher harmonics present. Although for the J of 2.7 and 3.5 shows strong coupling to the acoustic forcing, the third harmonic is not present, indicating a reduction in sensitivity of the flow to the acoustic forcing.

Downloaded by Doug Talley on January 7, 2020 | http://arc.aiaa.org | DOI: 10.2514/6.2020-0422

Figure 12 is the DMD spatial mode at the 3008 Hz forcing frequency. The same size and shape of the alternating pattern is observed when comparing them with the phase average. This indicates that an independent data analysis technique gave a similar result and therefore that the zig-zag flame pattern is a dominant flow feature. However, it should be understood that the DMD amplitude for the spatial modes at the forcing frequency for 3008 Hz, contribute less to the reconstruction of the original flow for the higher *J* values since the third harmonic is missing. The sensitivity of the flame to the acoustic forcing can also be observed in tracking the OH* structures downstream from the injector exit. Figure 13 tracks the bright OH* emission structures observed to occur when the hydrogen jet impinges on the LOX jet for 15 acoustic cycles. The method is described in [26]. From Figure 13, in particular for *J* of 0.12, it is observed that the jet is highly receptive to the acoustic forcing. From Figure 13, the OH* structures are highly organized and are separated by a time interval corresponding to the driving frequency of 3008 Hz. As *J* increases, the OH* structures are no longer created at the same time intervals and become more random. In fact, as *J* increases there are larger instants where no new OH* wave structures are created and cease to correspond to the 3008 Hz forcing frequency. This trend is indicative of a decrease in sensitivity to the acoustic forcing. It is also observed that the majority of the OH* wave structures persist roughly for the first 6 LOX jet diameters. It is speculated that, although the creation of the OH* wave structures becomes increasingly more random as *J* increases, the time varying velocity field (due to acoustic forcing) is able to limit the lifespan of the OH* wave structure. It is speculated that this is accomplished through a combination of flow features describe earlier with an increase in the LOX jet break-up events, as in the case for *J* of 3.5 (Figure 9). It is also possible that the coherency of the OH* structure is disrupted by displacing the OH* structure towards and away from the LOX jet for the first 6 LOX diameters. The latter would explain why the higher *J* values still shows a coupling to the acoustic forcing.

V. Conclusion

(in our earlier work ref[] ?)An experimental investigation was performed using high speed imaging to study how hydrodynamic instabilities and the flame interact in a shear coaxial flame. In this paper we study their sensitivity when subjected to transverse acoustic forcing at the same frequency and similar pressure amplitudes. The acoustically forced phase averaged shadowgraph images for all conditions showed differences in the LOX jet shape. An examination of the phase averaged shadowgraph images appeared to show that the higher momentum flux ratio conditions have reduced interactions with the acoustic forcing. However, the instantaneous images show that the annular hydrogen jet does in fact interact with the transverse forcing, except that the structures formed by the hydrogen jet are capable of breaking up the LOX jet. The naturally occurring hydrodynamic wave structure/flame interactions observed for unforced conditions appear to be enhanced by the acoustics. The phase averaged OH* emission images further support this argument, where the bright OH* emissions are detected when the hydrogen jet is deflected towards the LOX jet and a decrease in OH* emission is noted when the hydrogen jet is deflected away from LOX jet due to the time varying velocity field for all test conditions. The dynamic mode decomposition spatial mode of the OH* emission shows a similar behavior as the OH* phase averaged images where the size of OH* wave structures increase with *J* and are largely coherent for the first 6 LOX jet diameters. Examining the DMD amplitudes, all test conditions are observed to be coupled to the acoustic forcing, but a reduction in higher harmonics is noted as *J* increases. Plotting the OH* wave trajectories, a decrease of coupling to the acoustic forcing is perceived as *J* increases as the creation of new OH* waves become more random.

References

[1] Harvazinski, M. E., Huang, C., Sankaran, V., Feldman T. W., Anderson, W. E., Merkle, C. L., and Talley, D. G., "Coupling between hydrodynamics, acoustics, and heat release in a self-excited unstable combustor," *Physics of Fluids*, Vol. 27, Is. 4, 2015,
doi: 10.1063/1.4916673

[2] Harrje, D. T., and Reardon F. H., "Liquid Propellant Rocket Combustion Instability," NASA SP-194, Washington D.C., 1972

[3] Yang, V., and Anderson, W., "Liquid Rocket Engine Combustion Instability," *Progress in Astronautics and Aeronautics*, Vol. 169, AIAA, Washington, D. C., 1995

[4] Hardi, J. S., Camilo Gomez Martinez, H., and Oschwald, M., "Lox Jet Atomization Under Transverse Acoustic Oscillations", *Journal of Propulsion and Power*, Vol. 30, No. 2, 2014, pp. 337-349
doi: 10.2514/1.B34979

[5] Gröning, S., Hardi, J. S., Suslov, D., and Oschwald, M., "Injector-Driven Combustion Instabilities in a Hydrogen/Oxygen Rocket Combustor," *Journal of Propulsion and Power*, Vol. 32, No. 3, 2016, pp. 560-573
doi: 10.2514/1.B35768

Downloaded by Doug Talley on January 7, 2020 | http://arc.aiaa.org | DOI: 10.2514/6.2020-0422

[6] Hardi, J. S., Beinke, S. K., and Oschwald, M., "Coupling of Cyrogenic Oxygen-Hydrogen Flames to Longitudinal and Transverse Acoustic Instabilities," *Journal of Propulsion and Power*, Vol. 30, No.4, 2014, pp. 991-1004
doi: 10.2514/1.B35003
[7] Richecoeur, F., Scouflaire, P., Ducruix, S., Candel, S., "High-Frequency Transverse Acoustic Coupling in a Multiple-Injector Cryogenic Combustor," *Journal of Propulsion and Power*, Vol. 22, No. 4, 2006, pp. 790-799
doi: 10.2514/1.18539
[8] Richecoeur, F., Ducruix, S., Scouflaire, P., Candel, S., "Experimental Investigation of High-Frequency Combustion Instabilities in Liquid Rocket Engine," *Acta Astronautica*, Vol. 62, Is. 1, 2008, pp. 18-27
doi: 10.1016/j.actaastro.2006.12.034
[9] Richecoeur, F., Ducruix, S., Scouflaire, P., Candel, S., "Effect of Temperature Fluctuations on High Frequency Acoustic Coupling," *Proceedings of the Combustion Institute*, Vol. 32, 2009, pp. 1663-1670
doi: 10.1016/j.proci.2008.05.068
[10] Rey, C., Ducruix, S., Richecoeur, F., Scouflaire, P., Vingert, L., and Candel, S., "High Frequency Combustion Instabilities Associated with Collective Interactions in Liquid Propulsion," *AIAA/ASME/SAE/ASEE 40th Joint Propulsion Conference,* AIAA Paper 2004-3518, 2004
doi: 10.2514/6.2004-3518
[11] Méry, Y., Hakim, L., Scouflaire, P., Vingert, L., Ducruix, S., and Candel, S., "Experimental Investigation of Cryogenic Flame Dynamics Under Transverse Acoustic Modulations," *Comptes Rendus Mecanique*, Vol. 341, 2013, pp. 100-109
doi: 10.106/j.crme.2012.10.013
[12] Poinsot, T. J., Trouve, A. C., Veynante, D. P., Candel, S. M., and Esposito E. J., "Vortex-Driven Acoustically Coupled Combustion Instabilities," *Journal of Fluid Mechanics*, Vol. 177, 1987, pp. 265-292
doi: 10.1017/S0022112087000958
[13] Hakim, L., Schmitt, T., Ducruix, S., and Candel, S., "Dynamics of a Transcritical Coaxial Flame Under a High-Frequency Transverse Acoustic Forcing: Influence of the Modulation Frequency on the Flame Response," *Combustion and Flame*, Vol. 162, 21015, pp. 3482-3502
doi: 10.1016/j.combustflame.2015.05.022
[14] Urbano, A., Selle, L., Staffelbach, G., Cuenot, B., Schmitt T., Ducruix, S., and Candel, S., "Exploration of Combustion Instability Triggering using Large-Eddy Simulation of a Multiple Injector Liquid Rocket Engine," *Combustion and Flame*, Vol. 169, 2016, pp. 129-140
doi: 10.1016/j.combustflame.2016.03.020
[15] Hakim, L., Ruiz, A., Schmitt, T., Boileau, M., Staffelbach, G., Ducruix, S., Cuenot, B., and Candel S., "Large Eddy Simulations of Multiple Transcritical Coaxial Flames Submitted to a High-Frequency Transverse Acoustic Modulation," *Proceedings of Combustion Institute*, Vol. 35, 2015, pp. 1461-1468
doi: 10.1016/j.proci.2014.05.142
[16] Urbano, A., Douasbin, Q., Selle, L., Staffelbach, G., Cuenot, B., Schmitt, T., Ducruix, S., and Candel, S., "Study of Flame Response to Transverse Acoustic Modes from the LES of a 42-Injector Rocket Engine," *Proceedings of the Combustion Institute,* Vol. 36, 2017, pp. 2633-2639
doi: 10.1016/j.proci.2016.06.042
[17] Gonzalez-Flesca, M., Schmitt, T., Ducruix, S., and Candel, S., "Large Eddy Simulations of Transcritical Round Jet Submitted to Transverse Acoustic Modulations," *Physics of Fluids,* Vol. 28, 2016
doi: 10.1063/1.4948586
[18] Roa. M., Forliti, D. J., Badakhshan, A., and Talley, D. G., "Acoustically Forced Coaxial Hydrogen/Liquid Oxygen Jet Flames," 28th ILASS Americas, Dearborn, MI, 2016
[19] Forliti D. J., Badakhshan, A., Wegener, J. L., Leyva, I. A., and Talley, D. G., "The Response of Cyrogenic H2/O2 Coaxial Jet Flames to Acoustic Disturbances," *53rd AIAA Aerospace Sciences Meeting*, AIAA 2015-1607, Kissimmee, FL, 2015
doi: 10.2514/6.2015-1607
[20] Mayer, W., and Krülle, G., "Rocket Engine Coaxial Injector Liquid/Gas Interface Flow Phenomena," *Journal of Propulsion and Power*, Vol. 11, No. 3, 1995, pp. 513-518
doi: 10.2514/3.23872
[21] Mayer, W., and Tamura, H., "Flow Visualization of Supercritical Propellant Injection in a Firing LOX/GH2 Rocket Engine," *31st AIAA/ASME/SAE/ASEE Joint Propulsion Conference*, AIAA 1995-2433, San Diego, Ca, 1995
doi: 10.2514/6.1995-2433
[22]Mayer, W., Schik, A., Schäffler, M., and Tamura, H., "Injection and Mixing Processes in High-Pressure Liquid Oxygen/Gaseous Hydrogen Rocket Combustors" *Journal of Propulsion and Power,* Vol. 16, No. 5, 2000, pp. 823-828.
doi: 10.2514/2.5647
[23] Zong, N., and Yang, V., "A Numerical Study of High-Pressure Oxygen/Methane Mixing and Combustion of a Shear Coaxial Injector," *43rd AIAA Aerospace Sciences Meeting*, AIAA 2005-152, Reno, NV, 2005
doi: 10.2514/6.2005-152
[24] Oefelein, J. C., and Yang, V., "Modeling High-Pressure Mixing and Combustion Processes in Liquid Rocket Engines," *Journal of Propulsion and Power*, Vol. 14, No. 5, 1998, pp.843-857
doi: 10.2514/2.25349

Downloaded by Doug Talley on January 7, 2020 | http://arc.aiaa.org | DOI: 10.2514/6.2020-0422

[25] Zong, N., and Yang, V., "Cryogenic Fluid Jets and Mixing Layers in Transcritical and Supercritical Environments," *Combustion Science and Technology*, Vol. 178, No. 1-3, 2006, pp. 193-227
doi: 10.1080/00102200500287613
[26] Roa, M., and Talley, D. G., "Wave Dynamic Mechanisms in Coaxial Hydrogen/Liquid-Oxygen Jet Flames," *Journal of Propulsion and Power*, Vol. 35, No. 2, 2019, pp. 369-381
doi: 10.2514/1.B37079
[27] Hua, J C., Gunaratne G. H., Talley, G. D., Gord, J. R., and Roy, Sukesh, "Dynamic-mode Decomposition based Analysis of Shear Coaxial Jets with and without Transverse Acoustic Driving," *Journal of Fluid Mechanics*, Vol. 790, 2016, pp. 5-32
doi: 10.1017/jfm.2016.2
[28] Graham, J. J., Leyva, I. A., Rodriguez, J. I., and Talley D., "On the Effect of a Transverse Acoustic Field on a Flush Shear Coaxial Injector," 45th *AIAA/ASME/SAE/ASEE Joint Propulsion Conference,* AIAA 2009-5142, Denver, Co. 2009
doi: 10.2514/6.2009-5142
[29] Nguyen, T. M., Popov, P. P., and Sirignano, W. A., "Longitudinal Combustion Instability in a Rocket Engine with a Single Coaxial Injector," *Journal of Propulsion and Power*, Vol. 34, No. 2, 2018, pp. 354-373
doi: 10.2514/1.B36516
[30] Sirignano, W, A., and Krieg, J., "Coaxial Jet Flame Subject to Long-Wavelength Acoustic Oscillations," *Journal of Propulsion and Power*, Vol. 32, No. 3, 2016, pp. 743-754
doi: 10.2514/1.B35953
[31] Popov, P. P., Sideris A., and Sirignano, W. A., "Low-Probability Events Leading to Rocket Engine Combustion Instability," *Journal of Propulsion and Power*, Vol. 55, No. 3, 2017, pp. 919-929
doi: 10.2514/1.J055276
[32] Morgan, C. J., Shipley, K. J., Anderson W. E., "Comparative Evaluation Between Experiment and Simulation for a Transverse Instability," Vol. 31, No. 6, 2015, pp. 1696-1706
doi: 10.2514/1.B35759
[33] Feldman, T. W., Harvazinski, M. E., and Merkle, C. L., "Comparison between Simulation and Measurement of Self-Excited Combustion Instability," *48th AIAA/ASME/SAE/ASEE Joint Propulsion Conference*, AIAA Paper 2012-4088, July 2012
doi: 10.2514/6.2012-4088
[34]Li, L. K. B., and Juniper, M. P., "Lock-in and Quasiperiodicity in Hydrodynamically Self-Excited Flames: Experiments and Modelling," *Proceedings of the Combustion Institute*, Vol. 34, 2013, pp. 947-954
doi: 10.1016/j.proci.2012.06.022
[35] Magri, L., See. Y.-C., Tammisola, O., Ihme, M., and Juniper, M. P., "Multiple-scale Thermo-Acoustic Stability Analysis of a Coaxial Jet Combustor," *Proceedings of the Combustion Institute*, Vol. 36, 2017, pp. 3863-3871
doi: 10.1016/j.proci.2016.06.009
[36]Juniper, M. P., Li, L. K. B., Nichols, J. W., "Forcing of Self-Excited Round Jet Diffusion Flames," *Proceedings of the Combustion Institute,* Vol. 32, 2009, pp. 1191-1198
doi: 10.1016/j.proci.2008.05.065
[37]Badakshan, A. and Danczyk, S., "Ignition of Nanoparticles by a Compact Camera Flash," DTIC ADA614547, http://www.dtic.mil/dtic/tr/fulltext/u2/a614547.pdf
[39]Marinet, M. F., and Schettini, E. B. C., "The Density Field of Coaxial Jets with Large Velocity Ratio and Large Density Differences," *International Journal of Heat and Mass Transfer*, Vol. 44, No. 10, 2001, pp. 1913-1924
doi: 10.1016/S0017-9310(00)00240-4

Downloaded by Doug Talley on January 7, 2020 | http://arc.aiaa.org | DOI: 10.2514/6.2020-0422

Images, Tables, and Charts

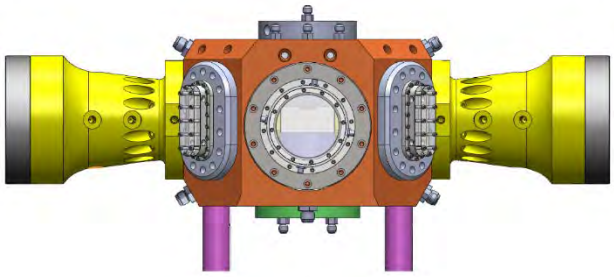

Fig. 1 Assembly drawing of the combustion chamber. The 101mm diameter center window provides a size reference.

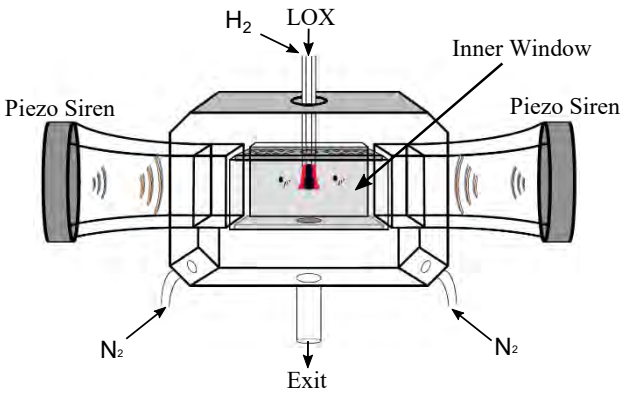

Fig. 2 Inner details of the combustion chamber.

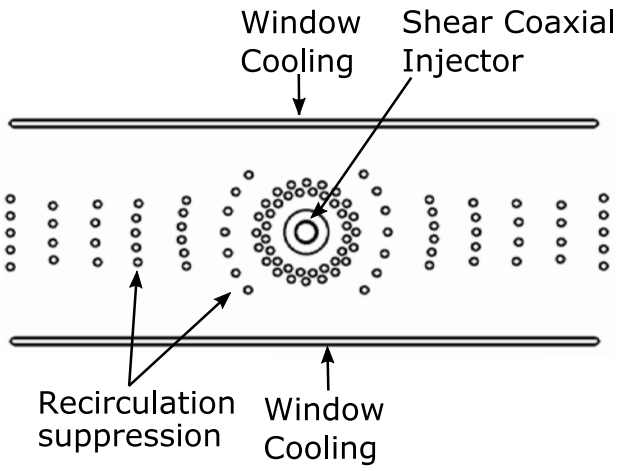

Fig. 3 The injector faceplate including recirculation suppression holes and window cooling slots.

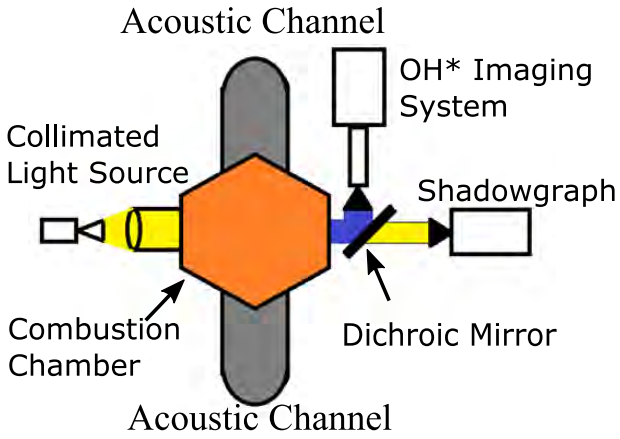

Fig. 4 High speed, simultaneous imaging system lay out.

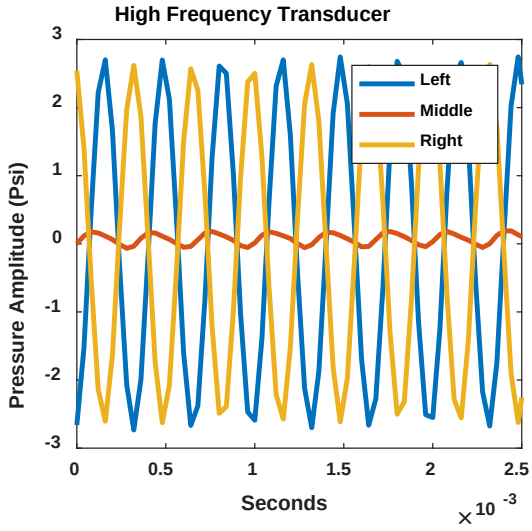

Fig. 5 The pressure trace measured by the three high frequency pressure transducers located within the window. The pressure trace is of the standing acoustic wave at a pressure node of frequency 3008 Hz.

Downloaded by Doug Talley on January 7, 2020 | http://arc.aiaa.org | DOI: 10.2514/6.2020-0422

Table 1 Operating Conditions

J	*LOX Injection Temp [K]*	*GH2 Injection Temp [K]*	*LOX Injection Bulk Velocity (m/s)*	*GH2 Injection Bulk Velocity (m/s)*	*Pressure Amplitude (Psi)*	*LOX Reynolds # ($x10^3$)*	*GH2 Reynolds # ($x10^3$)*
0.12	138	290	4.6	26.5	3	82.2	3.2
0.5	137	274	4.7	51.8	3	83.8	7.2
0.84	141	286	5.5	79.4	3.2	103.9	10
2.7	136	286	2.95	78.6	2.7	50.9	9.9
3.56	140	287	2.6	79	3.6	48.3	9.4

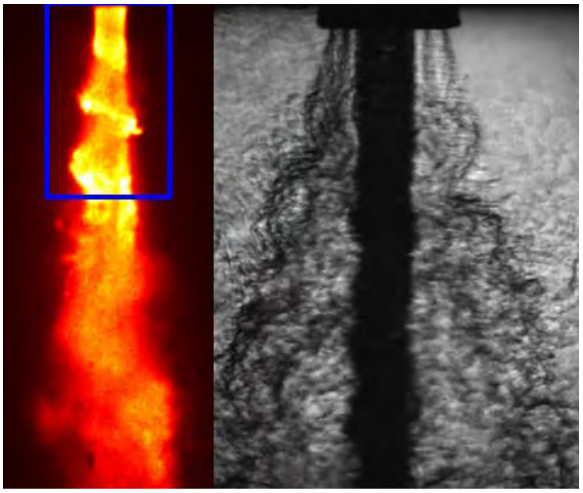

Fig. 6 An instantaneous OH* emission with it corresponding shadowgraph image. The blue box is the viewing area of the shadowgraph image. The shadowgraph focused on the near nozzle region.

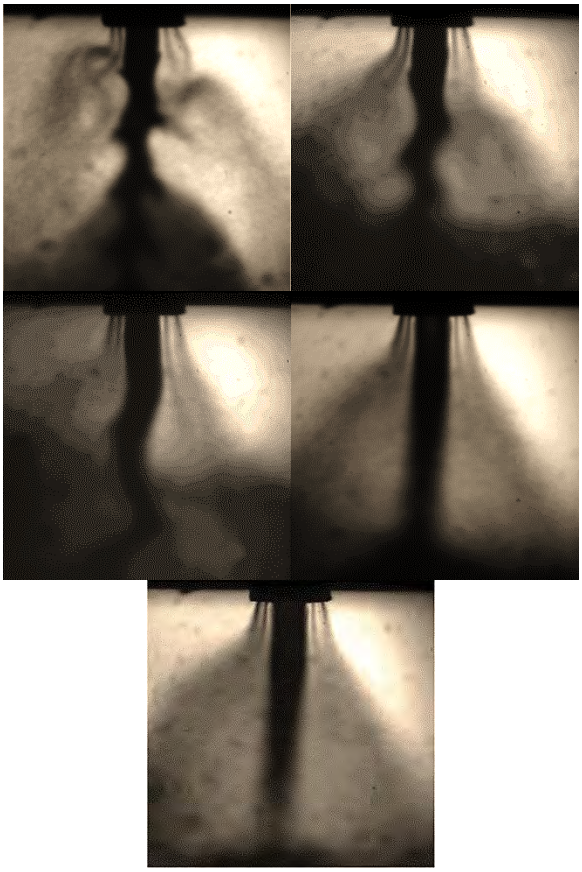

Fig. 7 Phase averaged shadowgraph images. The top row is the *J* of 0.12 and 0.5, followed by .8 and 2.7, and last is 3.5 condition. For the first three *J* conditions, the LOX jet is observed to develop an exaggerated wavy pattern. Some of the dark regions at the bottom of the figures, especially the conically shaped shadow for *J* = 0.12, are due to steam condensation on the windows.

Downloaded by Doug Talley on January 7, 2020 | http://arc.aiaa.org | DOI: 10.2514/6.2020-0422

Downloaded by Doug Talley on January 7, 2020 | http://arc.aiaa.org | DOI: 10.2514/6.2020-0422

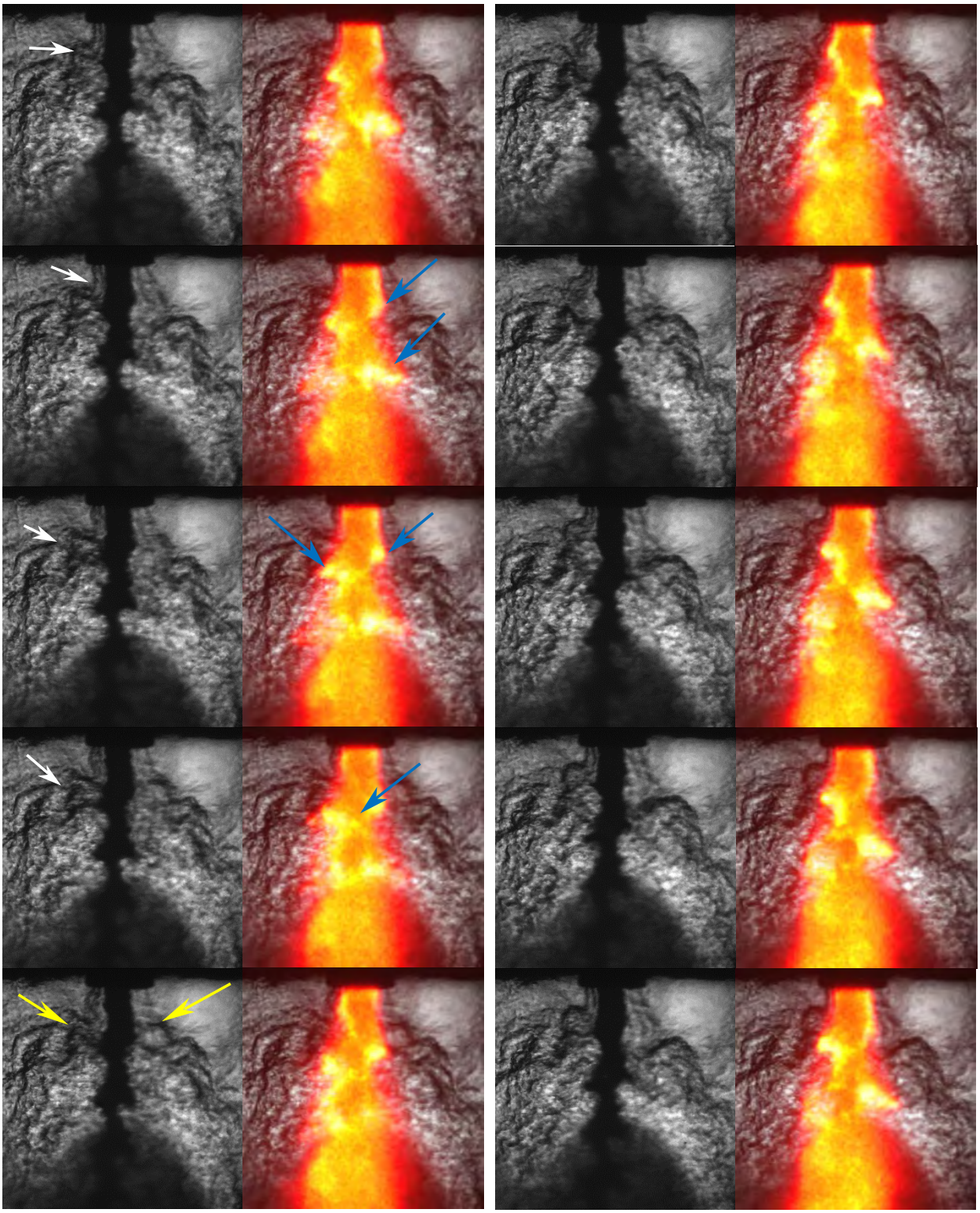

Fig. 8 Instantaneous images of the shadowgraph and OH* overlapped with the same shadowgraph image for *J* of 0.12. The series of images increases by 40 μs, progressing from top to bottom and from left to right. For the 10 images shown, a full cycle of acoustic forcing is displayed. The LOX jet is initially intact and deflected downstream. The formation of the large hydrogen structure is also observed (indicated by the white arrow) and travels downstream. As the annular structure convects downstream, it impinges on the LOX jet. These annular structures couple with the acoustic forcing. The higher intensity OH* emission, indicated by the blue arrows, is located where the annular structures form and impinge. The arrows point to where the annular structure separates due to the velocity reversing direction.

Downloaded by Doug Talley on January 7, 2020 | http://arc.aiaa.org | DOI: 10.2514/6.2020-0422

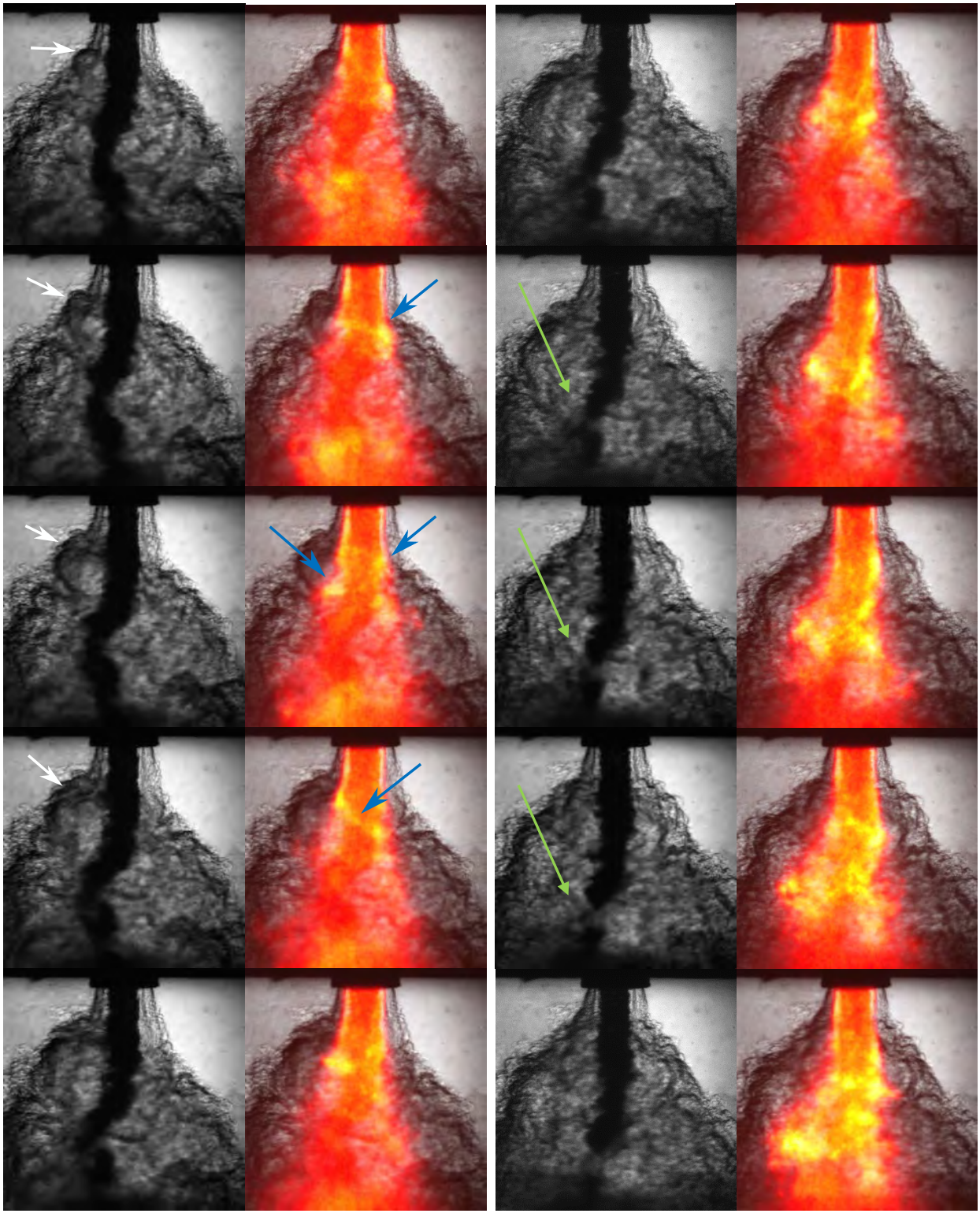

Fig. 9 Instantaneous images of the shadowgraph and OH* emission overlapped the same shadowgraph image for *J* of 3.56. The series images increase by 40 μs between each frame. For the 10 images shown, a full cycle of acoustic forcing is displayed. The LOX jet is initially intact and deflected downstream. The formation of the large hydrogen structure is also observed (indicated by the white arrow) and travels downstream. As the annular structure convects downstream, it impinges on the LOX jet and afterwards LOX jet breaks up. These annular structures couple with the acoustic forcing. The higher intensity OH* emission, indicated by the blue arrow, which is yellow in color, is located where the annular structures form and impinge. The breakup of the LOX jet is indicated by the green arrows.

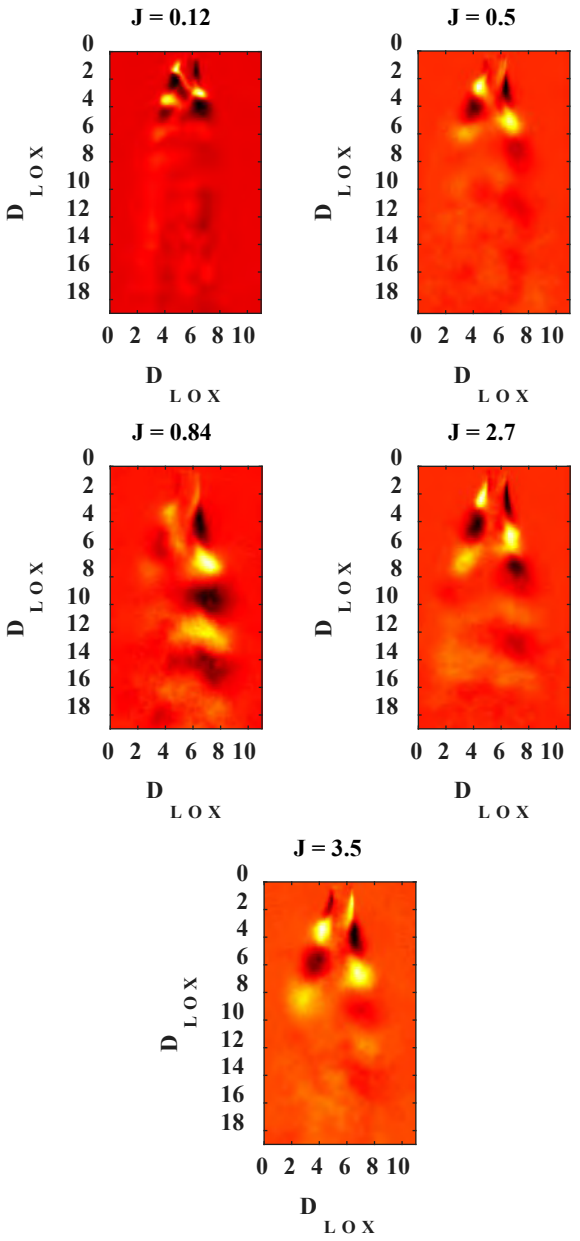

Fig. 10 OH* emission phase averaged images with the temporal mean subtracted. A zig-zag pattern is observed for all conditions. The bright yellow sections is the increased OH* emission observed when the acoustically forced hydrogen jet impinges onto the LOX jet.

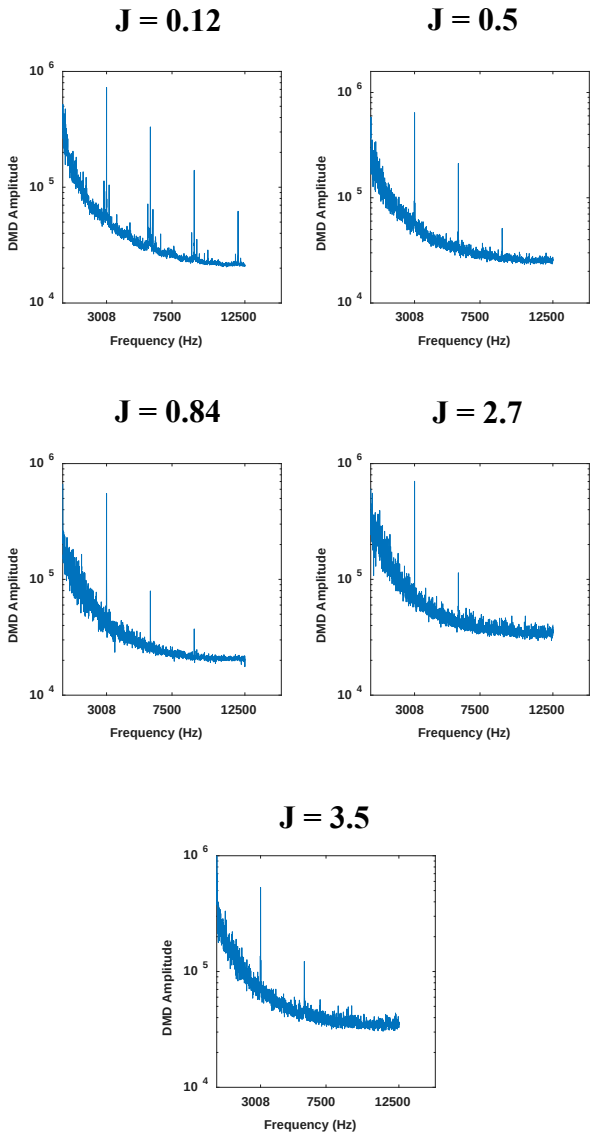

Fig. 9 Dynamic mode decomposition amplitudes for OH* emission images. The flame is strongly coupled with the acoustic forcing indicated by the higher harmonics of the forcing frequency. Stronger coupling is observed for the lower *J* values.

Downloaded by Doug Talley on January 7, 2020 | http://arc.aiaa.org | DOI: 10.2514/6.2020-0422

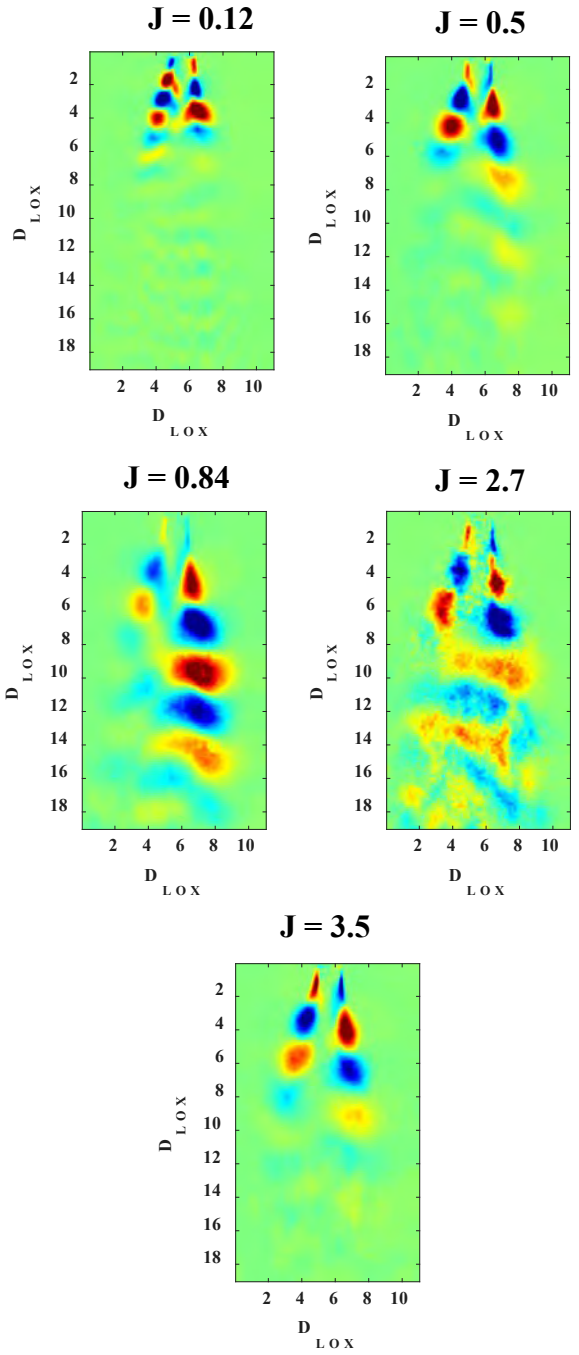

Fig. 10 Dynamic mode decomposition spatial mode of the OH* emission images at the forcing frequency. The spatial mode has the same features and pattern as the OH* phase averaged. Strong coupling is observed for the first 6 LOX jet diameters away from the downstream of the nozzle exit.

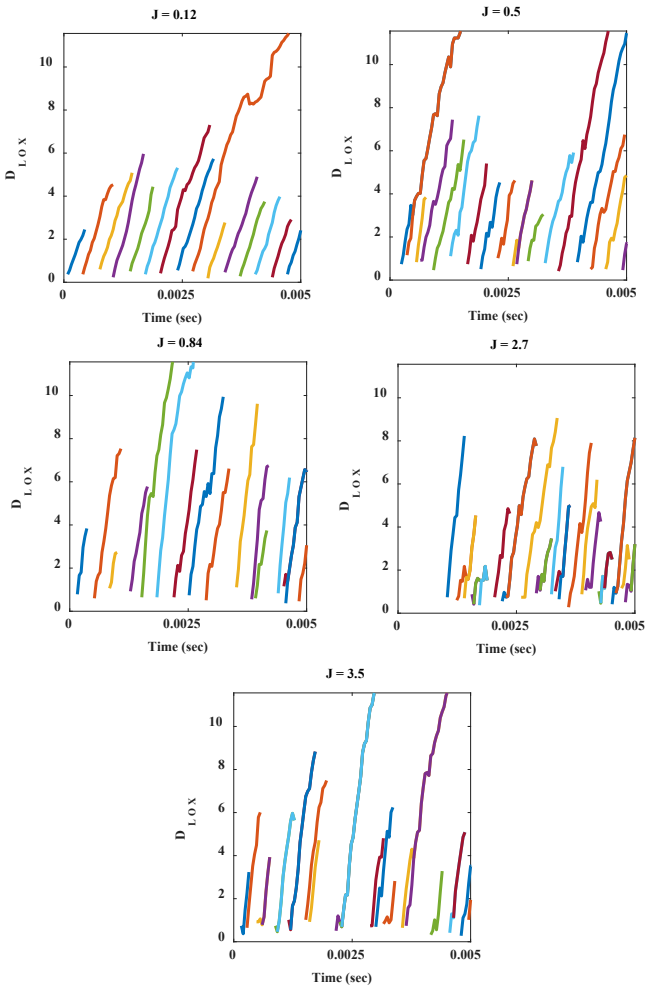

Fig. 113 OH* wave position plotted against time for 15 acoustic cycles. The different colors are different OH* waves. A large fraction of the OH* wave are observed to travel only for 6 LOX diameters downstream from the nozzle exit.

Downloaded by Doug Talley on January 7, 2020 | http://arc.aiaa.org | DOI: 10.2514/6.2020-0422

Propulsion and Energy Forum
July 25-27, 2016, Salt Lake City, UT
52nd AIAA/SAE/ASEE Joint Propulsion Conference

Cryogenic Impinging Jets Subjected to High Frequency Transverse Acoustic Forcing in a High Pressure Environment

Mario Roa[1]
Sierra Lobo, Inc. Air Force Research Laboratory, Building 8451, Edwards AFB, CA, 93524

S. Alexander Schumaker[2] and Douglas G. Talley[3]
Air Force Research Laboratory, Building 8451, Edwards AFB, CA, 93524

Downloaded by Doug Talley on September 19, 2016 | http://arc.aiaa.org | DOI: 10.2514/6.2016-5086

An experimental study has been conducted to explore the coupling between the impact waves created by impinging jets and high frequency acoustic pressure perturbations. High speed, backlit imaging was used to capture the physical response of impact waves present on impingement sheet formed by two like on like impinging jets. Dynamic mode decomposition was used to extract the natural frequencies of impact waves and isolate the spatial structures response present on the impingement sheet due to the transverse acoustic forcing. Chamber pressure and jet velocity were varied until impact waves became visually prominent. After impact waves became visually prominent, the impingement sheet was subjected to incremental pressure amplitudes in a pressure anti-node (PAN) and pressure node (PN) configurations. The results indicate that impact waves appear to vanish once a certain pressure amplitude is reached. When subjected to PAN forcing the impingement sheet size grows and decays and in-plane flapping is generated under a PN forcing.

Nomenclature

DMD = Dynamic Mode Decomposition
PAN = Pressure Anti-Node
PN = Pressure Node

I. Introduction

Impinging jet injectors are one of the many injectors type used for liquid propellant atomization in rocket engines[1-2]. Liquid rocket engines like the F-1 have successfully used like-on-like impinging jet injectors and are a preferred injector type for hypergolic and gelled-propellants[3-4]. Figure 1 shows a schematic of the flow field formed by a like-on-like impinging jets injector. In Figure 1 two cylindrical liquid jets strike each other at an angle 2Θ and form an impingement sheet. Impact waves or surface waves travel along the surface of the impingement sheet, detach, and form ligaments and droplets. These injectors are favored due to inherently simple design, potential high flow rate operation, and low manufacturing costs[1-2]. Although great operation success has been achieved with like on like impinging injectors, they do suffer from some major drawbacks. One such drawback is the high machining tolerance needed for like-on-like impingement of the two cylindrical jets. Another drawback, perhaps the most critical, is that rocket engine using impinging jets sacrifice performance in order to achieve an acceptable level of high frequency combustion instability[1].

[1]Research Scientist, Sierra Lobo, Inc. 10 E. Saturn Blvd, Building 8451, Edwards, CA 93524, Member
[2]Research Engineer, AFRL/RQRC., 10 E. Saturn Blvd, Building 8451, Edwards, CA 93524, Senior Member
[3]Lead, Combustion Dynamic Group, AFRL/RQRC., 10 E. Saturn Blvd, Building 8451, Edwards, CA 93524, Associate Fellow

This material is declared a work of the U.S. Government and is not subject to copyright protection in the United States.

Extensive experimental and theoretical studies have been performed on understanding the spray characteristics of these injectors, with particular attention given to the shape of the impingement sheet, the breakup length of liquid impingement sheet, and mean droplet size and distribution[4-8]. It has been well documented that the impingement sheet shows several physical characteristics depending on the operating Reynolds and Weber number[5, 9]. These physical characteristics or modes of the impingement sheet are: closed-rim, open-rim, and fully developed. Transition to either of these modes is dependent on jet velocity. Present on these modes are unstable hydrodynamic waves usually referred to as impact waves. It is theorized that these impact waves are the dominant mechanism in the impingement sheet breakup and atomization.

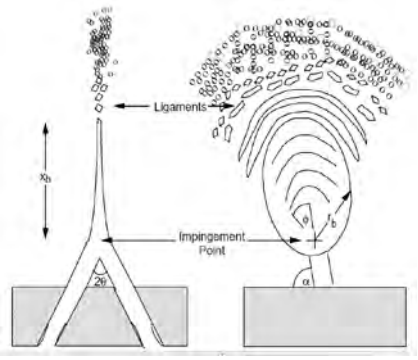

Figure 1. Schematic of typical like-on-like impinging jet injector. Figure is reproduced from Anderson[9].

Heidmann *et al*[4] and Dombrowski *et al*[5] performed extensive studies on impinging jets under atmospheric conditions. From these studies, two mechanisms were identified as the responsible mechanism to impingement sheet breakup. One mechanism is the superposition of aerodynamic waves. The second is when waves are produced at the point of impingement, which results in ripples[8] emanating from this point. These ripples are referred to as impact waves. Impact waves were observed even in near vacuum conditions and exhibit nonlinear behavior that cannot be fully predicted by linear stability theory. Heidmann *et al* arrived at these two breakup mechanisms by systemically studying the effect of orifice diameter, jet velocity, impingement angle, pre-impingement length, and jet viscosity by using different liquid combinations of glycerol and water. Heidmann *et al* concluded that jet velocity was the parameter of choice to describe the spray structures produced by the impinging jets. Guided by Heidmann *et al* results, Dombrowski *et al* studied the disintegrations of the impingement sheet. Their results show that the disintegration of the impingement sheet usually resulted from the formation of unstable waves, either aerodynamic or hydrodynamic in origin. Their results indicate there is a transition to when impact waves control breakup of the impingement sheet. This transition occurs when the liquid jets are above a critical Weber number. This critical Weber number when impact waves start to appear lies between 65 and 165[5, 9], defined as $We = \frac{\rho v^2 D}{\sigma}$, where ρ is the jet density, v is the jet velocity, D the jet diameter, and σ is the surface tension. It should be noted that Dombrowski *et al* results are dependent on the jets being either laminar or turbulent.

Anderson *et al*[10] performed experiments on impinging jets using water at atmospheric conditions to characterize the effect of impact waves on the atomization process. Anderson *et al* measured atomization frequency from the impingement sheet using high-speed videos. They did this by monitoring a fixed point in the high speed videos and checking if ligaments and droplets passed through. They discovered that impact waves are formed with a characteristic wavelength of about one jet diameter. The experimental results also suggested that impact waves seem to dominate the atomization process over most of the conditions relevant to rocket engines and are responsible for the atomization frequency. Although, these observations was made only when jet velocities were low. Anderson *et al* also reported that the experimental results are dependent if the jets are laminar or turbulent, similar to Dombrowski *et al*.

Chen *et al*[10] performed a numerical study on the physical mechanism of impact waves and mixing process, and atomization of impinging jets. Chen *et al* carried out his numerical studies by varying Reynolds number, surface tension, and impingement sheet thickness. Chen *et al* concluded that impact waves form when the impinging jets have a Strouhal value of 0.86. Their results show that impact waves are caused by the interfacial shear stress which form capillary waves on the either side of the impingement sheet.

A single like-on-like impinging jet injector, machined at relevant dimensions for liquid rockets engines, was studied under acoustic perturbations. Cryogenic nitrogen was used as the working fluid. The study focused on identifying the conditions when visibly impact waves were formed by the like-on-like injector at elevated pressures. After identifying where the impact waves were easily identified, dynamic mode decomposition (DMD) was used to extract the natural frequency associated with the impact waves. The same condition was then subjected to high frequency acoustic forcing with incremental pressure amplitudes in both the PAN and PN configurations. High speed backlit imaging was used to capture the effect of acoustic forcing has on the impact waves. DMD analysis was performed to identify the dominate mode frequencies and structures.

Downloaded by Doug Talley on September 19, 2016 | http://arc.aiaa.org | DOI: 10.2514/6.2016-5086

II. Experimental Set-up and Methods

The experiment was performed at Air Force Research Laboratory (AFRL), Edwards. A schematic of the experimental facility can be found in previous research conducted using shear coaxial injectors[12-13]. The same windowed pressure chamber from the previous shear coaxial injector studies was used for these studies. The impingement jet injector was manufacture as a cap disk that attaches to small reservoir. High machining tolerances were kept on the cap to ensure proper jet impingement. A drawing of the cap and reservoir is shown in Figure 2. The natural acoustic frequencies of the reservoir are 16 kHz longitudinally and 35 kHz radially, both are higher than the forcing frequencies that were used for these studies. The impinging jet injector selected for this study has a jet diameter of 0.5 mm (0.02 in) with a half angle between exit holes of 30 degrees. Cryogenic nitrogen was used as the working fluid. The injector has a flow passage length of l/d of 8 within the injector. After exiting the injector, the fluid travels a pre-impingement length of 2.3 jet diameters. The jet velocity was controlled by varying the mass flow rate fed into the reservoir. A Porter mass flow meter (model 123-DKASVDAA) was used to measure the gaseous nitrogen flow. The gaseous nitrogen then traveled to a liquid nitrogen heat exchanger, where the gaseous nitrogen was converted to liquid nitrogen before entering the injector. An E type thermocouple on a piezo-electric translating stage (AttoCube ANS Scanners) was used to measure the temperature of the liquid impingement sheet prior to testing to ensure the temperature of the liquid nitrogen emerging from the injector was at steady state condition. A xenon arc lamp was used to provide the illumination for the back lit images. A high speed Phantom v710 CMOS camera, set at 25 kHz frame rate, was used to capture impact waves from the impingement sheet.

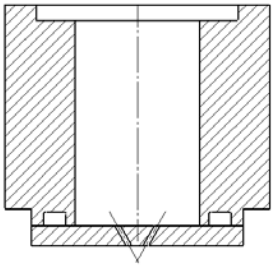

Figure 2. Drawing of the injector cap attached to the liquid nitrogen feed reservoir.

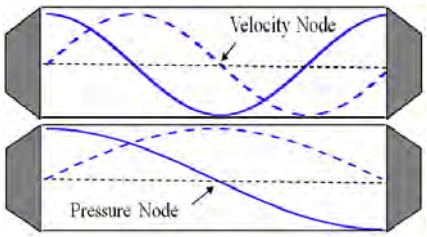

Figure 3. An instant in time of PAN and PN forcing. The solid line is the pressure fluctuations and the dash line is the velocity fluctuations. In PAN forcing, the injector experiences maximum and minimum pressure fluctuations. In PN forcing, the velocity fluctuations are maximum.

The acoustic waves used for the acoustic forcing portion of the study were generated by a Fluke 292 arbitrary waveform generator. The signal generator was then fed to two Trek PZD2000A high-voltage amplifiers that drove two piezo-sirens and generate a standing wave. The impingement sheet was then subjected to the acoustic forcing from the piezo-sirens tuned to the resonance chamber frequency for a PAN or PN configuration. Both the PAN and PN where centered at the middle of the impingement sheet. The shape of the PAN and PN forcing and be seen in Figure 3. For PAN forcing the pressure fluctuations are maximum and the velocity fluctuations are maximum for the PN forcing. Three differential pressure transducers (Kulite CCQ-093) were used to measure both the shape and amplitude of the acoustic forcing to ensure that a PAN and PN was achieved for each test condition. The chamber resonance for the PAN configuration was measured and driven at 2950 Hz and 3110 Hz for the PN. The impingement sheet was then subjected to incremental pressure amplitudes and the physical response was then visually recorded with the high speed camera. Dynamic mode decomposition (DMD), as outlined by Peter Schmid[14], was then used to extract the natural frequency of the impact waves in the unforced and forced conditions and their corresponding spatial response and structures.

III. Results

A. Velocity and Chamber Pressure Parametric Sweeps

For the first portion of the experiment, both jet velocity and chamber pressure were varied until visible impact waves became prominent on the impingement sheet. Impact waves appeared in a narrow range of conditions. Impact waves were observed at low jet velocities within the range of 2 to 5 m/s and at a chamber pressure of 1 to 1.37 MPa (150 to 200 PSIA) corresponding to jet Reynolds numbers of 7000 to 20000 and Weber numbers of 220 to 760, respectively. Figure 4 shows the spray formed by the impinging jets at several test conditions. Each column in Figure 4 corresponds to the same jet velocity of 5, 7, and 10 m/s. The first row in Figure 4 is at a chamber pressure

Downloaded by Doug Talley on September 19, 2016 | http://arc.aiaa.org | DOI: 10.2514/6.2016-5086

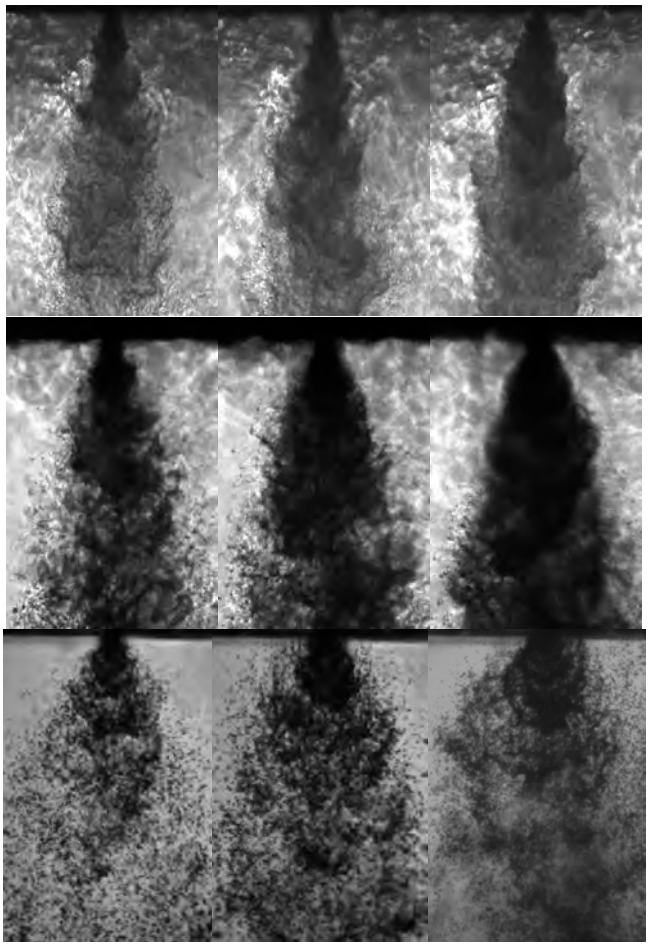

Figure 4. The spray formed by the impinging jets. Each column the jet velocity if the same of 5, 7, and 10 m/s. The first row of images was taken at a supercritical chamber pressure of 4.8 MPa (700 Psia), the second and third row at subcritical pressures of 2.5 MPa (375 Psia) and 1.37 MPa (200 Psia).

of 4.8 MPa (700Psia), above the supercritical pressure of nitrogen of 3.39 MPa (492 PSIA). The middle row and third row were taken at a subcritical chamber pressures of 2.5 MPa (375 PSIA) and 1.37 MPa (200 PSIA), respectively. At the supercritical chamber pressure a fine mist was formed regardless of the jet velocity and no evidence of impact waves was observed. As the chamber pressure is reduced to subcritical conditions, droplets and ligaments were observed to be shed off from the impingement sheet. No such identifiable droplets or ligaments were observed in the supercritical condition. As the jet velocity was increased for subcritical chamber pressure of 2.5 MPa, finer droplets were formed and eventually a dense mist was observed. A similar behavior was observed for the 1.37 MPa chamber pressure condition, but a dense mist similar to the 2.5 MPa and 10 m/s condition was never observed. It is apparent from these instantaneous images that there are different regimes of atomization for impinging jets which are dependent on several factors. At the supercritical condition it is possible that the aerodynamic forces on the cylindrical jets promptly atomize and form a fine mist or at these conditions the injection can no longer be regarded as an atomization or spray formation process. Further work will be require to understand how the interface between the low temperature jet and the supercritical nitrogen play a role, since the Weber number at these conditions approaches infinity and the mist formed is not as dense as the subcritical cases. At the subcritical conditions, chamber pressure or density ratio of the jet and the chamber gas plays a large role in promptly atomizing the impingement sheet, since it is evident that mist is formed at 10 m/s for the 2.5 MPa chamber pressure condition and not 1.37 MPa.

Downloaded by Doug Talley on September 19, 2016 | http://arc.aiaa.org | DOI: 10.2514/6.2016-5086

For the higher chamber pressure conditions above 1.4 MPa no discernible impact waves or frequencies were detected. It was only when the jet velocities were at 5 m/s and below and at 1.37MPa and below chamber pressures did impact waves became visually prominent. Figure 5 shows impact waves originating from the impingement point for the subcritical chamber pressures of 1 and 1.37 MPa at a constant jet velocity of 2 m/s. Similar to the higher jet velocity conditions, as the chamber pressure is increased, evidence of impact wave structures on the impingement sheet breaks down and a dense mist is formed. It was also observed that there was lack of structure at the lower chamber pressures, evident in the lowest chamber pressure shown in Figure 5. From low jet velocity conditions, chamber pressures between 1 and 1.37 MPa produced the most prominent impact waves, particularly at 1 MPa shown in Figure 5. Although from Figure 5 the chamber pressure condition at 1 MPa shows evidence of impact wave atomization, the chamber pressure of 1.37 MPa was selected for further analysis with a constant jet velocity at 2 m/s. Based on the jet diameter the jet Reynolds number was 7800 and a jet Weber of 270, meeting the critical Weber number criteria calculated by Heidmann *et al*. The jet exit temperature was kept at a constant 95 K.

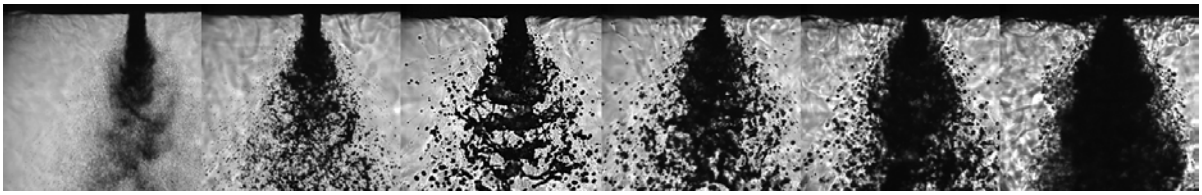

Figure 5. Instantaneous images of the flow field of the impingement sheet at a constant jet velocity of 2 m/s and increasing chamber pressure. From left to right the chamber pressure if 0.34, 0.68, 1, 1.37, 2.06, 2.75 MPa. A density ratio of jet over chamber of 165, 78, 53, 38, 25, 19.

B. Acoustic Forcing Results

Figure 6 is an instantaneous image of the impingement sheet without any acoustic forcing for a chamber pressure of 1.37 MPa and a jet velocity of 2 m/s. The impact waves and subsequent ligaments formed are shown to be emanating from the impingement sheet. This condition, with no acoustic forcing, served as a reference to compare to the acoustic forcing conditions. Dynamic mode decomposition was used to extract the natural frequencies of the impact waves emanating from the impingement sheet. The DMD analysis was apply to red square section shown in Figure 6. The DMD amplitude spectrum is shown below in Figure 7. Although no dominant mode was detected by the DMD analysis, the natural frequency of the corresponding to impact waves was measured to 4822 Hz, based on visually inspecting the spatial DMD modes.

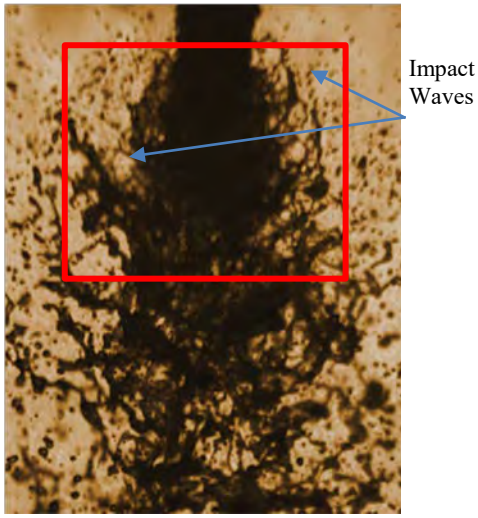

Figure 6. Instantaneous image of the impingement with impact waves emanating from the impingement sheet.

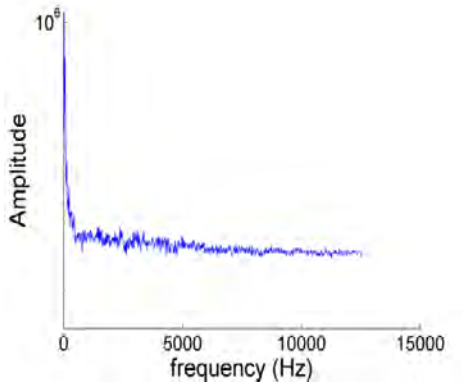

Figure 7. DMD amplitude spectrum from the no forcing base condition.

The DMD spatial mode corresponding to the impact waves for the base condition is shown in Figure 8. The alternating red and blue bands correspond to light intensity fluctuations due to dark liquid nitrogen impact waves passing on the exterior of the impingement sheet. It is currently suspected that variations in the impact wave's convective speeds or droplets shed along the exterior of the impingement sheet dampen the spectral content associated with impact waves and hence weak spectral frequency is picked up by the DMD analysis. The impact wave velocity is suspected because based on the high speed images, impact wave's velocity decelerates the further away they are from

Downloaded by Doug Talley on September 19, 2016 | http://arc.aiaa.org | DOI: 10.2514/6.2016-5086

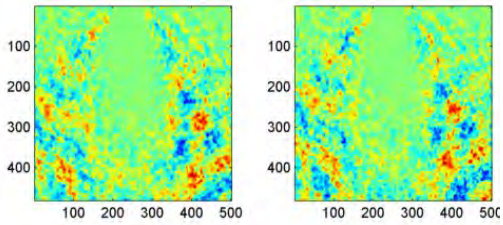

a) b)

Figure 8. DMD spatial for the base condition at 4822Hz. a) is the real portion and b) is the imaginary portion.

the impingement point. There is also a great degree of variation as to when the impact wave detach from the impingement sheet and is shed as ligaments. This variation of the breakup length of the impingement sheet seems to affect the impact wave velocity. A similar observation was made by Heidmann *et al* depending if the impingement sheet was closed or open rim. Heidmann *et al* also made an observation that the breakup length of the impingement sheet had a large variation in the fully develop mode and that the breakup length cannot be measured with any certainty. Similar mechanisms are likely responsible for the weak DMD amplitude of the impact waves since the impingement sheet in Figure 7 is in the fully developed regime, although further study will be needed to address the weak spectral strength.

Table 1 shows the acoustic test conditions with the pressure amplitude (P') the impingement sheet was subjected. Table 1 also has P' normalized to the dynamic pressure of the jets. For the PAN conditions, a total of 5 conditions were tested and a total of 4 conditions were tested for the PN configurations. For the PAN conditions, at the low P' (PAN 1 condition) acoustic forcing, the impingement sheet doesn't couple with the acoustic forcing. As P' is increased, the impingement sheet starts to couple with the acoustic forcing. This transition can be observed in the DMD amplitude spectrum shown in Figure 9. The corresponding DMD spatial mode is also shown. From Figure 9, PAN 1 condition is relatively unchanged when subjected to low P' PAN acoustic forcing. The DMD amplitude spectrum appears similar to the based unforced condition shown in Figure 7. The DMD spatial mode in Figure 9a also appears similar to the Figure 8 with the wave like pattern. Both PAN and the base condition have similar frequencies associated with the wave like pattern with frequencies of 4730 Hz and 4822 Hz, respectively, indicating this low level of acoustic forcing has little influence the dynamics of the impingement sheet and the frequency of the impact waves. The transition to where the impingement sheet couples with the acoustic forcing can be readily seen in the PAN 2 condition. Figure 9b shows the DMD amplitude spectrum with a peak centered at 2957 Hz, close to the acoustic forcing frequency of 2950 Hz. The DMD spatial mode, shown in Figure 9b, also demonstrates the transition with the impingement sheet. The alternating red and blue bands have grown larger and across the entire impingement sheet. This is different when from the base condition having the alternating bands only on exterior of the impingement sheet. What this transition seems to indicate that there is a coupling between the injector mass flow rate and the acoustic field. The impingement sheet under goes a surge of mass flow when the PAN forcing dips in the negative direction due to its sinusoid nature, it results in a temporally larger differential pressure This localized larger pressure differential drives a larger volume of mass flow through the injector. The impingement sheet also contracts in size when the PAN forcing is at its greatest and resulting in a small differential pressure between chamber and injector, thus restricting mass flow.

Table 1. Acoustic Test conditions with relevant parameters.

	No Forcing	**PAN 1**	**PAN 2**	**PAN 3**	**PAN 4**	**PAN 5**	**PN 1**	**PN 2**	**PN 3**	**PN 4**
P'(Psi)	0	1.75	2.97	4.5	6.6	11	1.5	2.7	6.2	7.6
P'/½ ρu^2	0	9.13	15.52	23.4	34.3	58.1	9.13	15.52	37.6	40

This coupling effect can be readily noticed for the PAN 5 condition, where the impingement sheet has fully coupled with the acoustic forcing. Both the DMD amplitude spectrum and spatial mode are shown in Figure 10. A strong peak centered at 2925 Hz, within less than 1% error of the acoustic forcing frequency of 2950Hz, is readily noticeable in Figure 10a, along with a higher harmonic. In Figure 10b demonstrates the large physical expansion and contraction of the impingement sheet, due to the surges of mass flow rates the injector is experiencing. It is at this condition that no traces of the impact waves were readily visible. Instead, what was observed was a large group of droplets shedding at the acoustic forcing frequency from the impingement sheet. This is indicative of a klystron effect, where faster moving fluid particles overtake slower liquid particles. This event is captured in the phase average images shown in Figure 11. The phased average images were false colored to best demonstrate both large group of droplets being shed and the klystron effect. As the pressure increases locally below the injector, there is a temporarily reduction in mass flow and jet velocity, afterwards the liquid jets

Downloaded by Doug Talley on September 19, 2016 | http://arc.aiaa.org | DOI: 10.2514/6.2016-5086

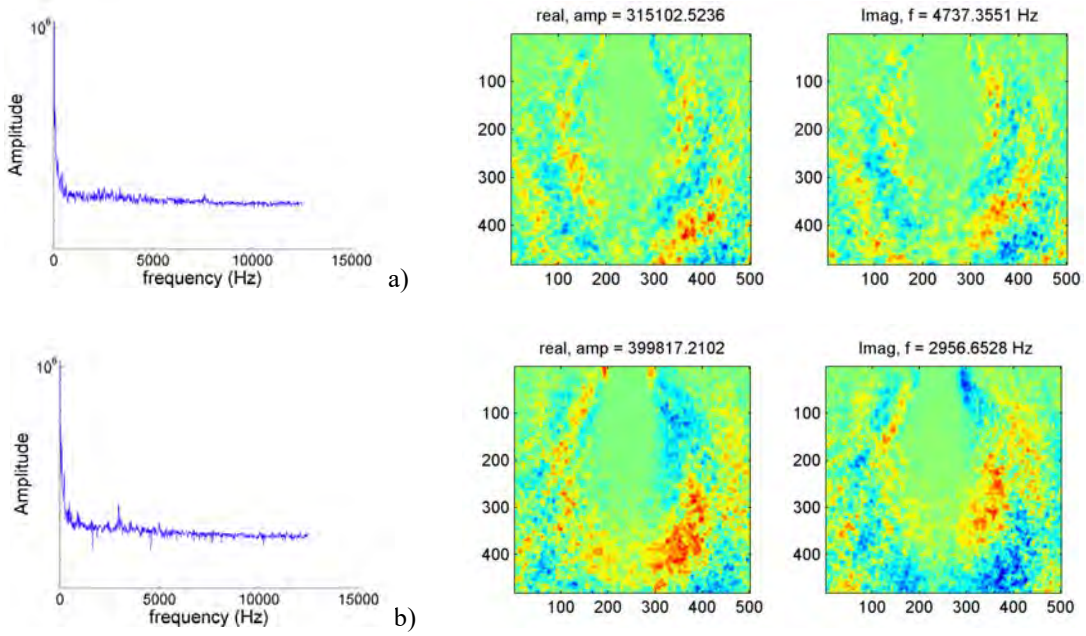

Figure 9. The DMD amplitude spectrum with the corresponding spatial mode. A) is the DMD amplitude spectrum and spatial mode for PAN 1 condition. B) is the DMD amplitude spectrum and spatial mode for PAN 2 condition.

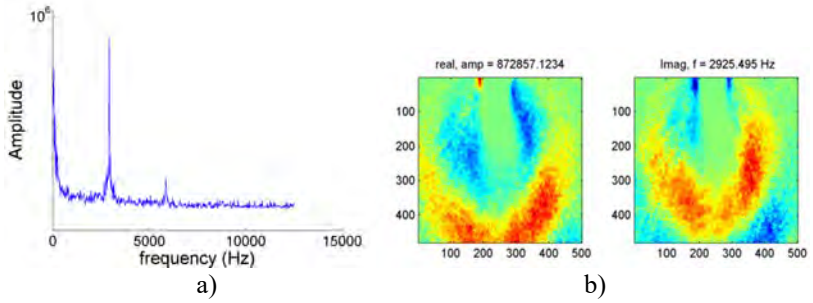

Figure 10. DMD output for PAN 5. A) is the DMD amplitude spectrum and b) is the corresponding spatial mode of 2925 Hz.

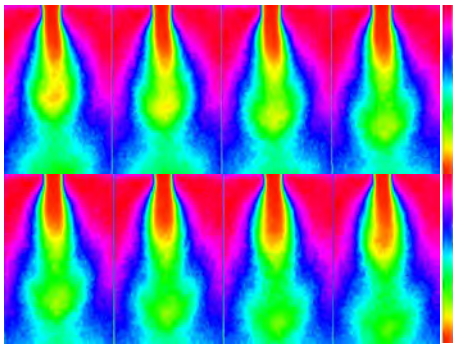

Figure 11. False colored, phased average images of the PAN 5 condition. A large small of liquid nitrogen is shown being shed off.

surge when the pressure amplitude dips. This dip in pressure temporally increases both the mass flow and jet velocity. This also gives the instantaneous images a "Christmas tree[15]" appearance (Appendix A). It is after when the pressure dips that the impingement sheet is observed to expand to its maximum width and shed large group of droplets. It is this condition where the atomization regime is dominant by the coupling of injector with the imposed acoustic field and not by impact waves. Based on observation of the high speed images no impact waves where formed when the injector fully couple with the acoustic field. A similar coupling between the propellant feed system and the acoustic field has been identified since the Apollo era[8].

For the PN conditions, the velocity fluctuations are maximum, unlike the PAN conditions where the pressure fluctuations are maximum. For the PN conditions coupling between the acoustic perturbations and impingement sheet occurred at a lower pressure

Downloaded by Doug Talley on September 19, 2016 | http://arc.aiaa.org | DOI: 10.2514/6.2016-5086

amplitude. Figure 12 demonstrates this coupling at a lower pressure amplitude. Shown in Figure 12 is the DMD spectrum and spatial mode for the PN 1 and PN 4 conditions. Unlike the PAN conditions, the velocity perturbations produce an in plane flapping motion of the impingement sheet. Both PN conditions spatial modes share the same characteristic shape. As the pressure amplitude is increased the in plane flapping motion becomes more pronounce as shown from Figure 12b for PN 4 condition. Although the PN spatial modes appear similar to the base case condition, fundamentally they represent a different mode of operation. In the base condition the alternating red and blue pattern are symmetric along the impingement sheet. This is physically representative of impact waves travelling down along the impingement sheet. In the PN forcing, the spatial modes have an alternating patterns that are asymmetrical. Physically what is occurring is that in a PN acoustic field the two cylindrical jets swing in phase with the velocity perturbations. As they swing, the impingement point is physically displaced and hence the impingement sheet is also displaced resulting in the in plane flapping motion.

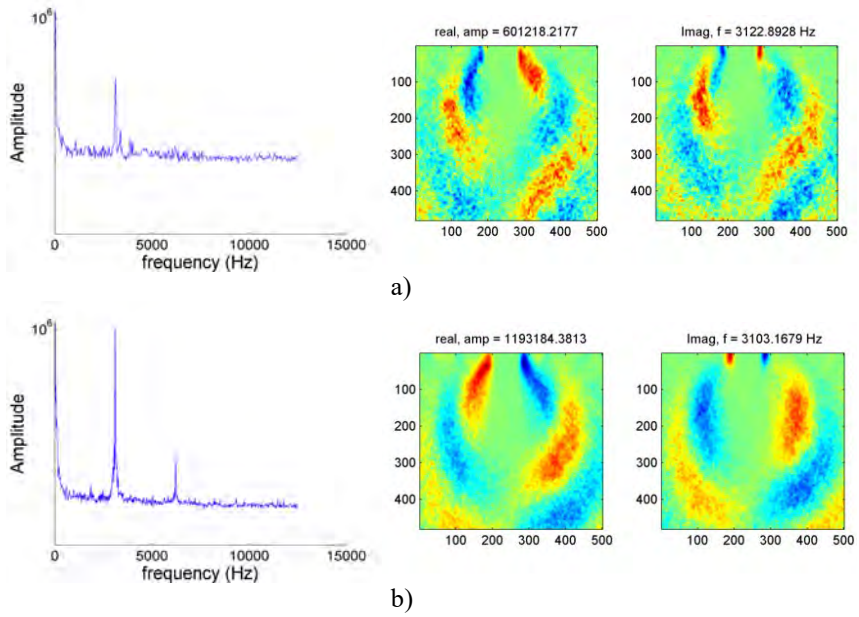

Figure 12. The DMD spectrum and spatial mode for a) PN 1 and b) Pan 4.

This in plane flapping motion is observed in the phased average images of PN 4 condition in Figure 13. Unlike the PAN forcing conditions where the cyclic mass flow variations produce a symmetric impingement sheet, PN forcing produces an S-shape curvature along the impingement sheet. S-shape curvature is indicative of the impingement point being periodically displaced. What was also observed was that ligaments would be shed in the direction of the incoming acoustic wave (Appendix A). This is a different mode of atomization when compared to the base condition. In the base condition the dynamic pressure of the liquid jets are used to overcome the surface tension force and atomize into droplets, but prior to becoming droplets, impact waves form on the impingement sheet and subsequently detach as ligaments and form droplets. Instead in a PN acoustic field, the edges of the impingement sheet are stripped off as ligaments and form a swig-swag pattern downstream. It is this mode of atomization that dominates the impingement sheet and not impact waves. Similar to PAN 5 condition, no impact waves were observed when the jets fully coupled with the acoustic field. It is believe that after a certain pressure amplitude associated with both PAN and PN acoustic forcing is reached, the impingement sheet is never fully developed, and hence limits any influence or traces of impact waves on the impingement sheet.

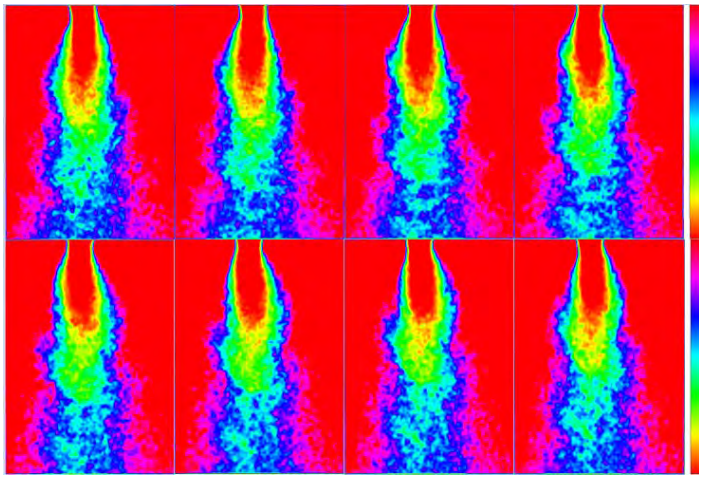

Figure 13. False colored, phased average images of the PN 4 condition. An in plane flapping is generated with PN forcing.

Downloaded by Doug Talley on September 19, 2016 | http://arc.aiaa.org | DOI: 10.2514/6.2016-5086

IV. Conclusion

Cryogenic nitrogen impinging jets were studied under a high pressure environment and subjected to an acoustic perturbations. High speed, backlit imaging was used to capture the physical response of the impact waves to the acoustic forcing present on impingement sheet form. For the first phase of the study**,** jet velocity and chamber pressure were varied until impact waves were visually prominent on the impingement sheet. Chamber pressures, up to 4.8 MPa, and jet velocity, 2 to 10 m/s, were investigated. It was observed that impact waves became visually prominent in a narrow range of chamber pressures and jet velocities, particularly when both jet velocity and chamber pressure are low. At supercritical pressures, no droplets or ligaments were ever observed to form, instead the flow field resemble a fine mist. In subcritical pressure both ligaments and droplets were observed to be shed from the impingement sheet. In the subcritical pressures there appears to be an influence of jet to chamber gas density ratio. It was observed for the same jet velocity a transition to a fully atomize, when a dense mist is formed, occurs sooner at higher chamber pressures.

After the conditions that led to impact waves being visually prominent were identified, dynamic mode decomposition was used to extract the natural frequencies of impact waves and isolate the spatial structures, both the unforced and force conditions at a constant chamber pressure and jet velocity. For the forces conditions the pressure amplitude was incrementally increased until the injector and the acoustic field fully coupled. The results indicate that impact waves influence appear to vanish once a certain pressure amplitude is reached. When subjected to PAN forcing the impingement sheet size grows and decays and a large group of droplets are shed. For the PN forced conditions, in-plane flapping is generated and ligaments are stripped of the impingement sheet.

Downloaded by Doug Talley on September 19, 2016 | http://arc.aiaa.org | DOI: 10.2514/6.2016-5086

References

[1]Anderson, W. E., Ryan, H. M., Pal, S., and Santoro, R. J., "Fundamental Studies of Impinging Liquid Jets," *30th Aerospace Sciences Meeting & Exhibit, AIAA Paper 92-0458, Reno, NV*.

[2]Anderson, W. E., Ryan, H. M., and Santoro, R. J., "Impinging Jet Injector Atomization," Liquid Rocket Combustion Instability, edited by V. Yang and W. E. Anderson, Progress in Astronautics and Aeronautics, vol. 169, AIAA, Washington D.C., 1995, pp. 215-246

[3]James, M. D., Kubal, T. D., Son, S. F., Anderson, W. E., and Poutpoint, T. L., " Calibration of an Impinging Jet Injector Suitbale for Liquid and Gelled Hypergolic Propellants," *45th AIAA/ASME/SAE/ASEE Joint Propulsion Conference & Exhibit*, Denver, Co, AIAA 2009-4882, 2009

[4]Fakhri, S., Lee, J. G., and Yetter, R. A., "Atomization and Spray Characteristics of Gelled-Propellant Simulants Formed by Two Impinging Jets," *45th AIAA/ASME/SAE/ASEE Joint Propulsion Conference & Exhibit*, Denver, Co, AIAA 2009-5241, 2009

[4] Heidmann, M. F., Priem, R. J., and Humphrey, J. C., "A Study of Sprays Formed by Two Impinging Jets," NACA TN-3835, 1957.

[5] Dombrowski, N., and Hooper, P. C., " A Study of the Sprays Formed Imping Jets in Laminar and Turbulent Flow," *Journal of Fluid Mechanics,* vol. 18, no. 3, 1964, pp. 392-400.

[6] Anderson, W. E., Ryan, H. M., and Santoro, R. J., "Impinging Jet Injector Atomization," Liquid Rocket Combustion Instability, edited by V. Yang and W. E. Anderson, Progress in Astronautics and Aeronautics, vol. 169, AIAA, Washington D.C., 1995, pp. 215-246

[7] Anderson, W. E., Ryan, H. M., Pal, S., and Santoro, R. J., "Spray Formation Processes of Impinging Jet Injectors," NASA Propulsion Engineering Research Center, vol. 2, N94-23042, 1993, pp.69-74.

[8] Li, R., and Ashgriz., "Characteristics of liquid sheets formed by two impinging jet," *Physics of Fluids*, Vol. 18, No. 8, 2006, pp. 087104-1, 087104-13

[9] Ciezki, H. K., Tiedt, T., Von Kampen, J., and Bartels, Nora., "Atomization Behavior of Newtonian Fluids with an Impinging Jet Injector in Dependence upon Reynolds and Weber Numbers" *41th AIAA/ASME/SAE/ASEE Joint Propulsion Conference and Exhibit*, Tucson, AZ, AIAA 2005-4477, 2005.

[10] Anderson, W. E., Ryan, H. M., and Santoro, R. J., "Impact Wave-Based Model of Impinging Jet Atomization," *Atomization and Sprays*, Vol. 16, No. 7, 2006, pp. 791-806

[11] Chen, X., Ma, D., and Yang, V., "Mechanism Study of Impact Wave in Impinging Jets Atomization," *50th AIAA Aerospace Sciences Meeting*, Nashville, TN, AIAA 2012-1089, 2012

[12] Teshome, S., Leyva, I. A., Talley, D, G., and Karagozian, A. R., "Cryogenic High-Pressure Shear-Coaxial Jets Exposed to Transverse Acoustic Forcing," *50th Aerospace Sciences Meeting*, Nashville, TN, AIAA2012-12665, 2012

[13] Graham, J. J., Leyva, I. A., Rodriguez, J. I., and Talley, D. G., "On the Effect of a Transverse Acoustic Field on a Flush Shear Coaxial Injector," *45th AIAA/ASME/SAE/ASEE Joint Propulsion Conference and Exhibit*, Denver, CO, AIAA 2009-5142, 2009

[14] Schmid, P. J., "Dynamic mode decomposition of numerical and experimental data," *Journal of Fluid Mechanics*, Vol. 656, 2010, pp. 5-28

[15]Harrje D. T., and Reardon, F. H., "Liquid Propellant Rocket Combustion Instability," NASA SP-194, 1972

V. Appendix A

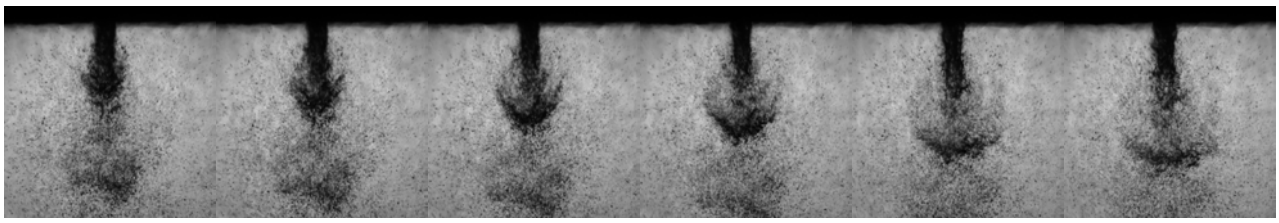

Figure A1. Instantaneous images of an acoustic cycle for the PAN 5 condition. A large group of droplets are shed and no impact waves were ever observed. The klystron effect produces the Christmas tree shape in the far left image.

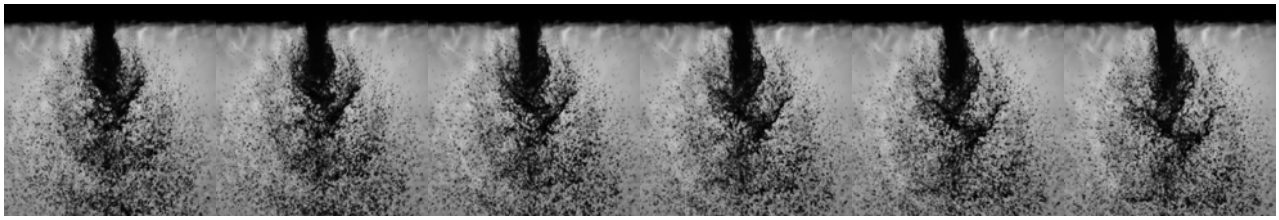

Figure A2. Instantaneous image of an acoustic cycle for the PN 4 condition. A swig-swag pattern of ligaments being shed off the impingement sheet can be observed in the downstream flow. No impact waves were ever observed in this condition.

Downloaded by Doug Talley on September 19, 2016 | http://arc.aiaa.org | DOI: 10.2514/6.2016-5086

AIAA SciTech Forum
9 - 13 January 2017, Grapevine, Texas
55th AIAA Aerospace Sciences Meeting

CrossMark
click for updates

A Study of Acoustic Forcing on Gas-Centered Swirl-Coaxial Reacting Flows

Mario Roa[1]
Sierra Lobo, Inc., Air Force Research Laboratory, Building 8451, Edwards AFB, CA, 93524

John W. Bennewitz[2]
UCLA, Air Force Research Laboratory, Building 8451, Edwards AFB, CA, 93524

Stephen Alexander Schumaker[3] and Douglas G. Talley[4]
Air Force Research Laboratory, Building 8451, Edwards AFB, CA, 93524

Downloaded by Doug Talley on May 1, 2017 | http://arc.aiaa.org | DOI: 10.2514/6.2017-1335

The reacting flow from a single gas-centered, swirl-coaxial injector was studied in an optically accessible, high-pressure chamber, with and without high-frequency acoustic perturbations. The gas-centered, swirl-coaxial injector employed liquid rocket engine relevant propellants of gaseous oxygen and RP-2. The reacting flow field behavior at an operating chamber pressure of 3.2 MPa and varying momentum flux ratios were investigated. High-speed shadowgraph images along with OH* and CH* chemiluminescence images were taken to capture the liquid fuel film, droplets, and flame response under acoustic excitation. For the acoustic forcing studies, low amplitude transverse standing waves typically below 5% of the chamber pressure were generated to simulate transverse combustion instabilities. Proper orthogonal decomposition and dynamic mode decomposition were performed on the high-speed shadowgraph and chemiluminescence images to detect the flame response to acoustic forcing, to which in-plane flapping motion was observed for acoustic forcing and rotating soot clouds were a large structures associated with the reacting flow field.

Nomenclature

DMD	=	Dynamic Mode Decomposition
GCSC	=	Gas-Centered Swirl-Coaxial Injector
J	=	Momentum Flux Ratio
PN	=	Pressure Node
POD	=	Proper Orthogonal Decomposition

I. Introduction

Gas-centered swirl-coaxial injectors (GCSC) have seen an increase in interest over the past decade for rocket engine applications[1-4]. These injectors combine features of the coaxial air-blast and pressure swirl atomizers. Similar to coaxial air blast atomizers, a shear layer is formed between the gaseous and liquid propellants. For these injectors, the liquid propellant is injected tangentially through the outer annulus, imparting a swirl onto the liquid similar to the pressure swirl atomizers. The resulting shear and tangential forces are responsible for atomizing the liquid propellant. This injector is ideally suited for oxygen-rich staged combustion cycles and has been used successfully in the Russian RD-180[5] rocket engines. Although, great operational success has been achieved with these injectors, there is very little

[1] Research Scientist, Sierra Lobo, Inc. 10 E. Saturn Blvd, Building 8451, Edwards, CA 935324, Member
[2] Postdoctoral Research Scholar, UCLA., 10 E. Saturn Blvd, Building 8451, Edwards, CA 935324, Senior Member
[3] Research Engineer, AFRL/RQRC., 10 E. Saturn Blvd, Building 8451, Edwards, CA 935324, Senior Member
[4] Lead, Combustion Dynamic Group, AFRL/RQRC., 10 E. Saturn Blvd, Building 8451, Edwards, CA 935324, Associate Fellow

Distribution A: Approved for public release; distribution unlimited. Clearance # 16597

This material is declared a work of the U.S. Government and is not subject to copyright protection in the United States.

understanding regarding the full modes of operation these injectors experience at rocket relevant conditions and their susceptibility to combustion instabilities.

Most of the related studies performed using GCSC injectors have been focused on the atomization process of the liquid fuel sheet, hydrodynamic instabilities, and spray characteristics. Researchers at the Air Force Research Laboratory (AFRL)[6-8] have developed physics-based scaling laws for GCSC injector design through extensive cold flow experimental studies with a parametric variation of physical dimensions such as cup recess length (L_c shown in Figure 1). It has been shown that the liquid sheet length prior to break-up scales strongly with the momentum flux ratio (J) of the two propellants. Lightfoot *et al.*[6-8] showed that the liquid sheet/film break up length reaches an asymptomatic value for a critical J value, hence any operating J value greater than the critical *will* result in the same film break up length. Experimental studies by Kim *et al.*[9] on the spray patterns for a GCSC injector performed at high pressures also identified J as the controlling parameter for the break up length. Schumaker *et.al.*[2] and Jeon *et al.*[10] studied the effect of the recess cup length L_c for GCSC injectors. They independently showed experimentally that L_c has very little effect on the film break-up length once a critical operating J value is reached. Eberhart *et al.*[11] investigated the the spray cone angle as a function of chamber pressure, observing that the cone angle from the swirling liquid sheet decreased with increasing chamber pressure.

As the bulk of the prior research has been focused on characterizing the spray pattern and design methodologies for GCSC injectors under cold flow conditions, there is very little understanding of how these injectors operate under reacting conditions. A numerical study by Muss *et al.*[12] demonstrated phenomenological differences between cold flow and hot-fire spray patterns, particularly droplet size. Pomeroy *et al.*[13] and Morgan *et al.*[14] studied the response of GCSC injectors to transverse instabilities, but no effort to characterize the flame in steady-state conditions was attempted as the combustion chamber produced a self-excited combustion instability.

This paper encompasses an experimental effort to describe the steady-state combustion behavior and the combustion response of a single GCSC injector under acoustic forcing conditions using high-speed imaging techniques. Varying momentum flux ratios were investigated for a single geometry GCSC injector to characterize steady-state operation, whereas one test condition was subjected to high-frequency, low amplitude transverse acoustic oscillations in a pressure node (PN) configuration for the forcing study. All experimental efforts were done at a high chamber pressure of 3.2 MPa, where simultaneous high-speed shadowgraph and OH*/CH* chemiluminescence images were taken to capture the flame behavior.

II. Experimental Setup

The GCSC injector was tested in the Combustion Stability Lab (EC-4) at Edwards AFRL CA, using RP-2 and gaseous oxygen. A detailed review of the complete system can be found in the work of Wegener *et al.*[15]. The system has since been upgraded to accommodate liquid hydrocarbon propellants. This test facility also has fuel systems capable of flowing gaseous fuels such as CH_4 and H_2 and/or cryogenic oxygen or gaseous oxygen. The facility is equipped with a Pacific Instruments data acquisition system that is used for diagnostic and system monitoring measurements. The GCSC propellants were ignited using a hydrogen/air torch at the operating chamber pressure with a capsule of nano-particulate additives photo-ignited by a Xenon flashbulb acting as a pre-ignition source for the torch. A detailed description for the ignition system can be found in the work of Badakshan *et al.*[16]

The experiment was performed within a high pressure, optically accessible combustor. A CAD rending of the windowed combustor is shown in Figure 2. This windowed combustor features a chamber within a chamber design, where the large outer windows are used to contain pressure and the small inner windows are used to contain the flame. The windowed combustor features two piezo-sirens positioned on either side of the injector that are capable of generating an acoustic standing wave to force the flame/injector flow. The combustor's two large windows are used for the various line-of-sight imaging techniques (e.g., shadowgraphy). The combustor also features off-axis windows for future laser diagnostics measurements like particle image velocimetry (PIV) and planar laser induced fluorescence (PLIF). The windowed chamber is pressurized using a continuous flowrate of nitrogen gas and is not affected by the combustion process, as the volume occupied by the flame is small relative to the volume of the pressurizing nitrogen gas. This helps sever the thermo-acoustic feedback loop, effectively isolating the flame from any potential chamber coupled combustion instabilities.

Three high-speed cameras, (Phantom v710, v1210, and v2512) were used for the simultaneous shadowgraph, OH*, and CH* chemiluminescence.. All three cameras were synchronized using an IRIG time signal, along with the system measurements from the Pacific Instruments data acquisition system. A schematic of the optical setup for the three high-speed imaging techniques is shown in Figure 3. For the shadowgraph system, a broadband collimated light travels through two dichroic mirrors. This collimated light first encounters a dichroic mirror coated to reflect 410 nm to 450 nm light, and transmit in the higher visible wavelengths, towards the Phantom v2512 for CH* chemiluminescence.

Distribution A: Approved for public release; distribution unlimited. Clearance # 16597

Downloaded by Doug Talley on May 1, 2017 | http://arc.aiaa.org | DOI: 10.2514/6.2017-1335

The CH* chemiluminescence 431 nm light is captured by a Lambert Instruments HiCATT intensifier with a Semrock filter (FF01-425/26). The reflective surface of this dichroic mirror rejected the blue light portion from the broadband collimated light away from the intensifier and hence there was no need to pre-color filter this light to avoid saturating the intensifier. The second dichroic mirror is coated to reflect the UV light for the OH* chemiluminescence and transmits visible light used for the shadowgraphy system. The OH* chemiluminescence was also imaged using a HiCATT intensifier with a Semrock filter (FF01-320/40). The shadowgraph camera was set to a gate of 7 μs, with the intensifiers gated at 110 ns for OH* and 500 ns for CH*. The cameras captured images at 1000 Hz for a one second of steady-state combustion. For the acoustically-forced conditions, the image capture rate of the shadowgraph and CH* systems was increased to 25 kHz for 0.2 seconds, while the OH* system was set to a lower frame rate to capture one second of the acoustically-forced flame.

As can be seen in Table 1, four test conditions were investigated with different J values of oxidizer-to-fuel momentum flux. For each test condition, the RP-2 flowrate was kept constant while the gaseous oxygen flow was varied to achieve different J values. The flowrates of RP-2 and gaseous oxygen were measured using a Siemens Coriolis mass flow meter (SITRANS FC) and Porter Thermal mass flow meter (Type 123), respectively. The windowed combustor was pressurized to 3.2 MPa using gaseous nitrogen prior to ignition. From these four conditions, Test 4 was selected to be acoustically forced. During these experiments, the piezo-sirens were operated 180° out-of-phase to form a standing wave pressure node (PN) condition in the vicinity of the reacting flow field, where a PN and corresponding velocity anti-node (VAN) was located at the injector location. Three differential pressure transducers (Kulite XCL-100) were mounted to one of the inner windows to measure the pressure amplitude, phase, and shape of the standing wave during testing. These inner windows were also coated with an oleophilic coating that spread RP droplets optical thin, thus not obscuring the view to the flame.

Table 1. Operating Conditions and Average Cone Angles

Test	$\dot{m}_{RP-2}(g/s)$	$\dot{m}_{ox}(g/s)$	Φ	J	P_c (MPa)	Left Side STD Θ	Right Side STD Θ
001	1.36	5	0.92	5.5	3.26	5.27	10.45
002	1.40	5.67	0.84	6.45	3.3	5.79	9.94
003	1.40	4.56	1.04	4.4	3.21	6.84	9.90
004	1.37	4.62	1	4.88	3.17	5.58	7.88

III. Results

A. Average Behavior

For each test condition, one second of steady-state flame operation was averaged using each optical method and can been seen in Figure 4. The vertical green line shown in this figure represents 10 mm of the flow field beginning at the nozzle exit plane. For the CH* averages, the view is partially blocked downstream by the differential pressure transducer used to characterize the standing wave for acoustic forcing studies. From both the CH* and OH* average images, it is observed that the flame is separated from the nozzle for each test condition. Great care must be taken in interpreting this behavior, since the average shadowgraph images show the flame is attached at the nozzle exit. By overlapping the CH* and shadowgraph average images, as shown in Figure 5, an apparent spatial offset exists between where the CH* is first observed and the flame at the injector exit present in the shadowgraph average. Related experiments done at AFRL show strong indications of burning in the cup recess. Those related experiments have shown decomposed fuel deposits on the injector face, significant heat flux into the injector and evolved injector face temperatures, which are all experimental findings indicating burning in this portion of the injector. Purdue University has also measured OH* and CH* directly in the injector. It is currently believed that the flame is anchored within the cup recess of the injector for these studies, and it is observed that combustion takes place in the near injector region and at times the chemiluminescence is obscured from view. It will be shown later from the instantaneous shadowgraph images that highly luminous pockets of reacting RP are observed to be attached to the nozzle exit, then are later obstructed from view by either a soot cloud or by the liquid RP sheet emanating from the nozzle.

From Figure 4, Tests 2 and 3 both show an asymmetric flame structure present in the average OH* and CH* images. This asymmetry is not fully understood since a consistent asymmetry is not present for the other two test conditions. In the X-ray radiography cold flow studies performed by Schumaker *et al.*[13], an asymmetry of the mass distribution in the swirling spray was observed at different operating conditions for a single injector. It is possible that

Distribution A: Approved for public release; distribution unlimited. Clearance # 16597

Downloaded by Doug Talley on May 1, 2017 | http://arc.aiaa.org | DOI: 10.2514/6.2017-1335

a similar mechanism is occurring during Tests 2 and 3, where greater concentrations of fuel are present at different spray locations, resulting in higher CH* and OH* concentrations at those locations.

There is also an asymmetry present in the cone angle formed by the spray. In Figure 6, the standard deviation of the shadowgraph images were used to measure the cone formed by the reacting flow field. The standard deviation images were chosen over the averages for the cone angle Θ measurement as there were more pronounced edge boundaries of the reacting flow field present in the standard deviation images. These cone angle measurements were performed by visual inspection and are presented in Table 1. As the cone angles significantly differ between the left and right spray edge boundaries for all test conditions, an unequal cone angle contributing to this asymmetry is observed. Further investigation will be necessary to address the physical mechanisms leading to this asymmetry.

B. Instantaneous Behavior

A time series of the instantaneous shadowgraph, CH*, and OH* images for Test 4 are shown in Figures 7, 8, and 9, respectively. In the shadowgraph and OH* images, a soot cloud can be viewed rotating about the gaseous oxygen core. The soot clouds corresponds to the dark regions in the flow field that obscure the view to the flame. As mentioned earlier, this soot cloud surrounds the oxygen core and blocks the view to the flame and its anchoring regions. Occasionally, highly luminous reacting pockets can been seen to attach to the injector exit in Figure 7. Given the CH* and OH* averages indicate the flame is separated from the nozzle but is visibly attached within the nozzle in the shadowgraph average and instantaneous images in Figure 7, it is vital that direct observation of the flame within the injector is needed to verify the flame's anchoring location.

The soot cloud near the injector droplet field obscuring the near field region of the flame is caused by the design of the injector. GCSC injectors are designed to have a fuel-rich outer layer that helps keep the injector face from overheating. In a multi-element configuration, this fuel flow across the injector is pushed downstream when fuel from neighboring elements meet in the interelement regimes. This creates a fuel-rich mixture that breaks down as it is heated, creating a soot cloud that can block light emission in the UV and visible spectrums.

Observation of the high-speed videos shows the soot cloud originates from the periphery of the swirling liquid sheet, which is consistent with a fuel-rich mixture breakdown being responsible for the soot formation. The soot cloud also rotates in the direction of the swirl and hence carries the angular momentum imparted by the swirl. The generated soot clouds convect at much slower velocity compared to the oxygen core and the flame. Unreacted fuel droplets are also observed to be shed from the periphery of the liquid sheet. Although droplets were observed in the flow field, the spatial resolution was not high enough to provide droplet statistics for these studies. The OH* chemiluminescence was also very diffusive compared to the other two viewing methods and it is not fully understood why this is the case at the moment. From the instantaneous CH* images, it was observed that the luminous zones were created in isolated pockets, indicating that the flame this not spatially continuous but instead reacts in isolated regions. These isolated pockets were observed to extend further downstream from the field of view and hence no flame length statistics were extracted for these studies.

C. Proper Orthogonal Decomposition

Proper orthogonal decomposition (POD) was select to study the large structures associated with the flame and rotating soot cloud present in the instantaneous images. Only the POD analysis for Test 4 will be discussed in greater detail as the results for the other test conditions yielded similar findings. The POD analysis decomposes a time series of images into spatially orthogonal structures, with each spatial mode having an energy and temporal component. A representation of the most dynamic flow features can be reconstructed by combining the most dominant POD modes[14]. This POD analysis was performed on the average image subtracted fluctuating component (i.e., instantaneous image minus the average image) for each optical method.

The energy associated with each mode from the shadowgraph, CH*, and OH* POD results are shown in Figure 10. From this analysis, there is no dominant mode present in the flow field, but instead the modal energies have a linear relationship. This indicates that reconstructing a representative flow field of the dynamic processes is only possible by combining hundreds of modes, as there are no truly dominant modes. This lack of dominant modes indicates that the rotating soot cloud is very chaotic and turbulent. Inspecting the certain spatial modes along with the fast Fourier transform (FFT) of the corresponding temporal mode, the rotation of the soot cloud about the oxygen core can be observed along with its physical spatial scales. This is given by the alternating red and blue pattern, which represents changes in light intensity caused by the soot cloud blocking the view to the flame. This pattern is independently detected with each optical viewing method, hence the soot cloud is a dominant flow field structure in these studies.

Distribution A: Approved for public release; distribution unlimited. Clearance # 16597

Downloaded by Doug Talley on May 1, 2017 | http://arc.aiaa.org | DOI: 10.2514/6.2017-1335

Multiple frequency peaks are present within the single spatial mode shown in Figure 11. These multiple frequency peaks indicate that the creation of the soot clouds and their rotation about the oxygen core is irregular. A similar observation can made by performing an FFT (shown in Figure 12) on the pixel intensity that is 15 inner injector diameters away from the nozzle exit. This location was chosen as it encompasses the average path taken by the soot clouds throughout the one second of high-speed images captured. From Figure 12, multiple frequencies are also present without a defined peak, similar to the POD temporal modes.

D. Acoustically Forced Results

For the acoustically forced studies, Test 4 was studied in greater detail. The injector was forced at six different chamber resonant frequencies, corresponding to PN excitation, spanning from 1920 Hz to 3430 Hz. For each of the six forcing frequencies, the standing wave pressure amplitude was set to 20.68 KPa (3 Psi). Using the definition of DMD decomposition, where

$$I(x,y,t) = Real(\sum_{j=1}^{N} A_j \exp(i2\pi f_j \Delta t)\, DM_j), \quad \text{Eq. 1}$$

$I(x,y,t)$ is the time series video, A_j is the amplitude or modal energy of component j, i is the imaginary number coefficient, f_j is the complex frequency of mode j, Δt is the time separation between each frame, and DM_j is the complex spatial mode j. In DMD, each spatial mode j has a unique complex frequency f. We can define the sensitivity of the reacting flow to the acoustic forcing by comparing the A_j relative to its neighboring spatial modes, as comparing A_j to its neighbors is similar to comparing frequency peaks from power density plots to its neighbors.

Figure 13 shows the A_j values for the unique frequencies of each DM_j, similar to a power density plot. The results for the shadowgraph high-speed video will be discussed further as the CH* DMD output yielded similar results. It should be noted that dynamic mode decomposition was not applied to the unforced conditions as temporal resolution for these experiments was not high enough as per the Nyquist criteria. For the forcing cases, however, the DMD analysis shows the strongest peaks relative to the neighboring spatial modes is strongest for 1920 Hz and 3060 Hz forcing. The shape of the spatial mode can be seen in Figure 14 for the forcing frequency 1920 Hz and 3060 Hz. For both frequencies, the acoustic perturbations impose the same shape to the flow, where the injector experiences in-plane flapping motion. The in-plane flapping is imposed onto the central gaseous oxygen flow, behaving almost as a single jet. The in-plane flapping motion is given by the yellow and blue bands directly across from each other right below the nozzle exit. The effect on the acoustic perturbations on the liquid film or droplets was not observed.

The in-plane flapping motion can be observed by viewing the temporal evolution of mode j at the forcing frequency f_j detected by the DMD analysis. The temporal evolution of the spatial mode throughout time can be created by using Eq.1. By selecting the mode j of interest and marching Δt in time, the time evolution of a specific mode can be created. The temporal evolution of mode j associated with 1920 Hz can be seen in Figure 15. The spatial mode was cropped to focus on the behavior near the nozzle exit. The red and blue pattern alternate along a given side of the gaseous oxygen core. This alternating pattern is due to the in-plane flapping motion of the gaseous oxygen core. The physical interpretation of this red and blue pattern is changes in light intensity associated with the flame along the oxygen core swaying side to side.

Summary and Conclusions

Although the results presented here cover a small amount of the vast physical processes associated with GCSC injectors, there are several findings from this experimental study. Among the findings are the following:

- Flame appears to be separated from the nozzle exit as shown in the CH* and OH* chemiluminescence average image, but attached in the shadowgraph images
- Depending on the operating J condition, the flame is asymmetric
- Cone angle formed by the flow is also asymmetric
- Soot cloud is created at the outer periphery of the swirling, liquid sheet
- Soot cloud is non-periodic in nature and rotates about the oxygen core, blocking the flame's chemiluminescence
- Soot cloud convects slowly compared to the oxygen core and the flame
- From the POD analysis, the lack of high energy modes and presence of the multiple strong frequency peaks indicate that the soot cloud is highly stochastic in its creation and rotation about the oxygen core

Distribution A: Approved for public release; distribution unlimited. Clearance # 16597

Downloaded by Doug Talley on May 1, 2017 | http://arc.aiaa.org | DOI: 10.2514/6.2017-1335

- The gaseous oxygen core behaves similar to a single jet under acoustic forcing
- From the DMD analysis, the GCSC injector has shown a sensitivity to the frequency of the external acoustic field

It is suspected that the sensitivity of the injector to the acoustic forcing can be due to injector geometry, but will have to be investigated further. Future work will be identifying if the momentum flux ratio dominants the dynamics of the reacting flow as it does for the cold flow studies. Given the limited range of *J* values tested here, no conclusions can presently be drawn regarding the influence the momentum flux ratio has on the reacting flow field. Sensitivity and its subsequent behavior to acoustic excitation under a pressure anti-node configuration will also be investigated. Combined, these future studies will extend the current knowledge of GCSC injectors.

ACKNOWLEDGMENTS

The authors would like to thank Randy Harvey (ERC, Inc.), Dr. Alireza Badakhshan (ERC Inc), and Dr. Rosa Padilla (UCLA Post Doctoral Researcher) for their help in setting up the test hardware and running the experiment. This work was funded by the Air Force Space and Missile Systems Center under the Combustion Stability Tool Development Program with Major Richard Paek as program manager.

Downloaded by Doug Talley on May 1, 2017 | http://arc.aiaa.org | DOI: 10.2514/6.2017-1335

References

[1]Canino, J., Heister, S., Sankara, V., and Zakharov, S., "Unsteady Response of Recessed-Post Coaxial Injectors", *41st AIAA/ASME/SAE/ASEE Joint Propulsion Conference and Exhibit, AIAA 2005*-4297, Tucson*, AZ, 2005*

[2]Schumaker, S. A., Danczyk, S, A. and Lightfoot, M .D .A., " Effect of Swirl on Gas-Centered Swirl-Coaxial Injectors", *47st AIAA/ASME/SAE/ASEE Joint Propulsion Conference and Exhibit, AIAA 2011-4297,* San Diego, 2011

[3]Lightfoot, M. D. A., Danczyk, S.A., and Talley, D.G. "Atomization in Gas-Centered Swirl-Coaxial Injectors,*" 19th ILASS Americas,* Toronto, Canada, 2006

[4]Schumaker, S.A., Danczyk, S.A., and Lightfoot, M.D.A. "Effect of Cup Length on Film Profiles in gas-Centered Swirl-Coaxial Injectors,*" 48th AIAA Aerospace Sciences Meeting,* 2010-368, Orlando, Fl, 2010.

[5]Dranovsky, M.L., "Combustion Instabilities in Liquid Rocket Engines: Testing and Development Practices in Russia,*" Progress in Astronautics and Aeronautics*, Vol. 221, 2007.

[6]Lightfoot, M. D. A,. Danczyk, S. A., and Talley, D. G., "A method to predict atomization performance in gas-centered swirl-coaxial injectors," Technical Paper No. AFRL-PR-ED-TP-2007-125

[7] Lightfoot, M. D. A,. Danczyk, S. A., and Talley, D. G., "Atomization rate of gas-centered swirl-coaxial injectors," Technical Paper No. AFRL-RZ-ED-TP-2008-074

[8]M. D. A. Lightfoot, S. A. Danczyk, and D. G. Talley, "Scaling of gas-centered swirl-coaxial injectors," Technical Report No. ADA502809

[9]Kim. J. G., Han, Y. M., Choi, H. S., and Yoon, Y., "Study on spray patterns of gas-centered swirl coaxial (GCSC) injectors in high pressure conditions" Aerospace Science and Technology, 27 (2013)

[10] Jeon, J., Hong, M., Han, Y. M., and Lee, S. Y., "Experimental Study on Spray Characteristics of Gas-Centered Swirl Coaxial Injectors," Journal of Fluids Engineering, (133) 2011

[11] Eberhart, C. J., Lineberry, D. M., and Moser, M. D., "Effects of Variable Chamber Pressure on Swirl Coaxial Injection: A Cold Flow Study," *46th AIAA/ASME/SAE/ASEE Joint Propulsion Conference and Exhibit*, AIAA 2010-368 Nashville, TN, July 2010.

[12] Muss, J. A., Johnson, C. W., Cheng., G. C., and Cohn, R. K., "Numerical Cold Flow and Combustion Characterization of Swirl Coaxial Injectors," *41th Aerospace Sciences Meeting*, Reno, NV, Jan 2003

[13] Pomeroy, B, R,. Sisco, J, C., Eckstein, J, R,. and Anderson, W. E., " Characterization of Gas-Centered Swirl-Coaxial Injector Stability in a Subscale Mutli-Element Combustor," *44th AIAA/ASME/SAE/ASEE Joint Propulsion Conference & Exhibit*, AIAA 2008-5249, Hartford, CT, 2008

[14] Morgan, C., Shipley, K. J., and Anderson W. E., "Comparative Evaluation Between Experimental and Simulation for a Transverse Instability," Journal of Propulsion and Power, (31) No 6 2015

[15] Wegener, J, L., Leyva, I. A., Forliti, D. J., and Talley, D. G., "Development of a Facility for Combustion Stability Experiments at Supercritical Pressure," *52nd AIAA Aerospace Sciences Meeting*, 2014-0317, National Harbor, MD, 2014

[16]Badakshan, A., Danczyk, S., Forliti, D., Levya, I., and Talley, D., "Nano-ignition Torch applied to cryogenic H2/O2 Coaxial Jet," *54th AIAA Aerospace Sciences Meeting*, 2016-0184, San Diego, Ca, 2016

Distribution A: Approved for public release; distribution unlimited. Clearance # 16597

[17] Schumaker, S. A., Kastengren, A. L., Lightfoot, M. D., Danczyk S. A., and Powell, C. F., "A study of Gas-Centered Swirl Coaxial Injectors Using X-ray Radiography," *12th Triennial International Conference on Liquid Atomization and Spray Systems,* Heidelberg, Germany, Sept 2-6, 2012

[18] Roy, S., Hua, J. C., Barnhill, W., Hunaratne, and Gord, J. R., " Deconvolution of reacting-flow dynamics using proper orthogonal and dynamic mode decompositions," Phys. Rev. E 91, 013001

Downloaded by Doug Talley on May 1, 2017 | http://arc.aiaa.org | DOI: 10.2514/6.2017-1335

Distribution A: Approved for public release; distribution unlimited. Clearance # 16597

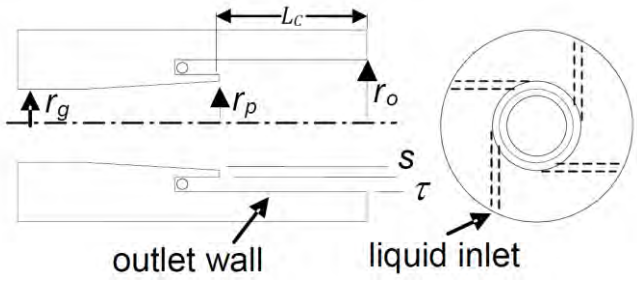

Figure 1. A schematic of a gas-centered swirl-coaxial injector, where r_g represents the initial gas radius, L_c the injector cup length, r_p the gas post radius at the end of the sheltering lip, r_o the outlet radius, S the step height and τ the initial film thickness.

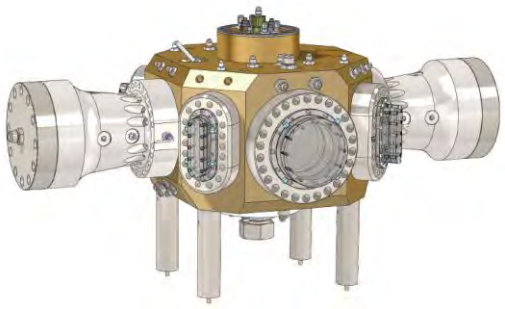

Figure 2. A CAD rending of the high pressure, windowed combustor.

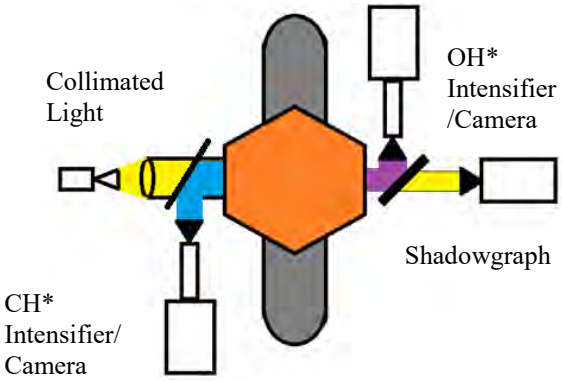

Figure 3. A schematic of the optical setup. A collimated light passed through two dichroic mirrors used for CH* and OH* chemiluminescence. The blue represents the 431nm CH* chemiluminescence, the purple 308nm OH* chemiluminescence, and the yellow the broadband collimated light for used for shadowgraph.

Downloaded by Doug Talley on May 1, 2017 | http://arc.aiaa.org | DOI: 10.2514/6.2017-1335

Distribution A: Approved for public release; distribution unlimited. Clearance # 16597
A-598

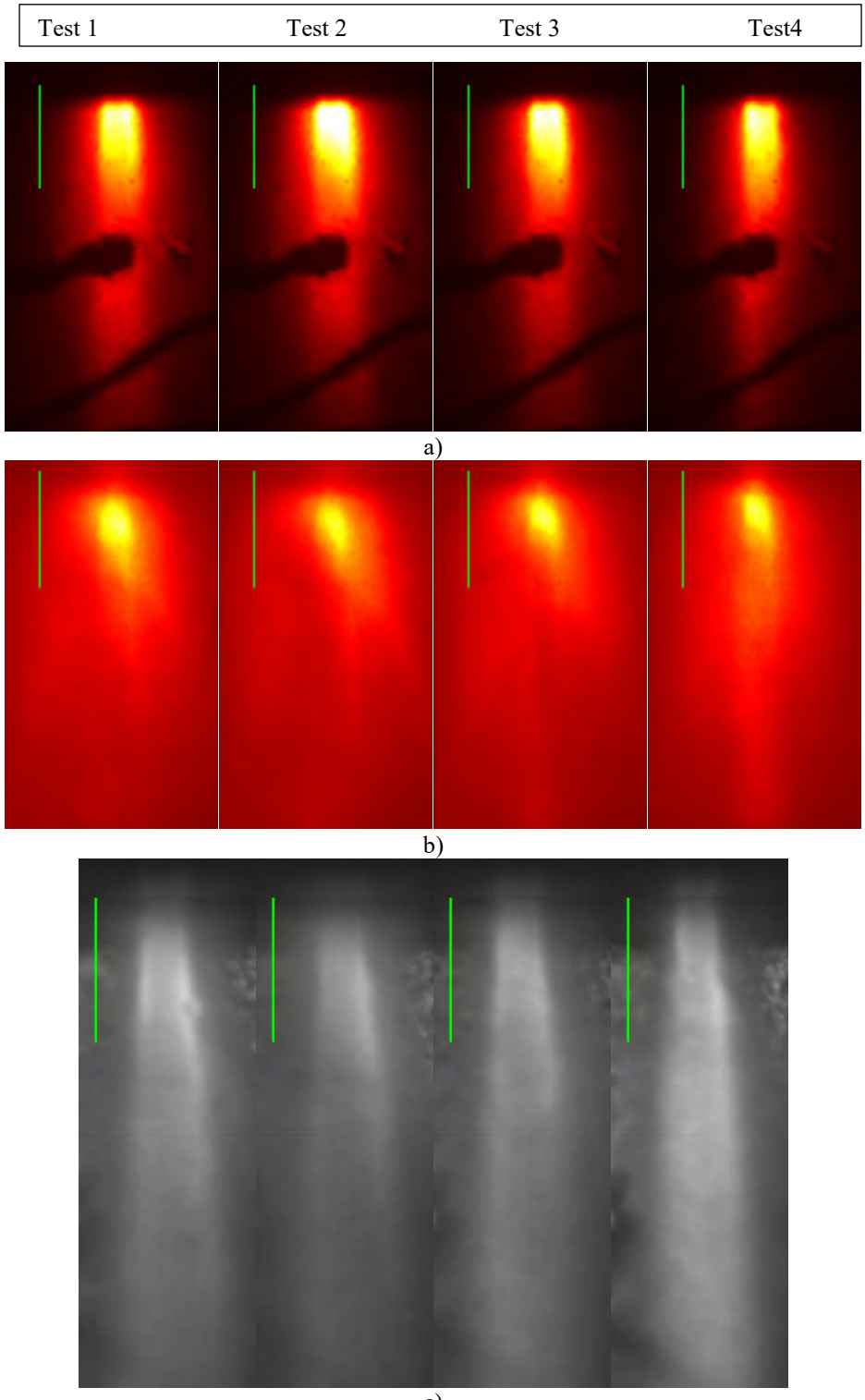

Figure 4 - (a) False color CH* average, (b) False color OH*average and (c) Shadowgraph average. The vertical green line is located at the nozzle exit plane and is 10 mm in length. Note that images are not at the same scale. From left to right, the averages are from Test 1, 2, 3, and 4, respectively.

Downloaded by Doug Talley on May 1, 2017 | http://arc.aiaa.org | DOI: 10.2514/6.2017-1335

Distribution A: Approved for public release; distribution unlimited. Clearance # 16597
A-599

Downloaded by Doug Talley on May 1, 2017 | http://arc.aiaa.org | DOI: 10.2514/6.2017-1335

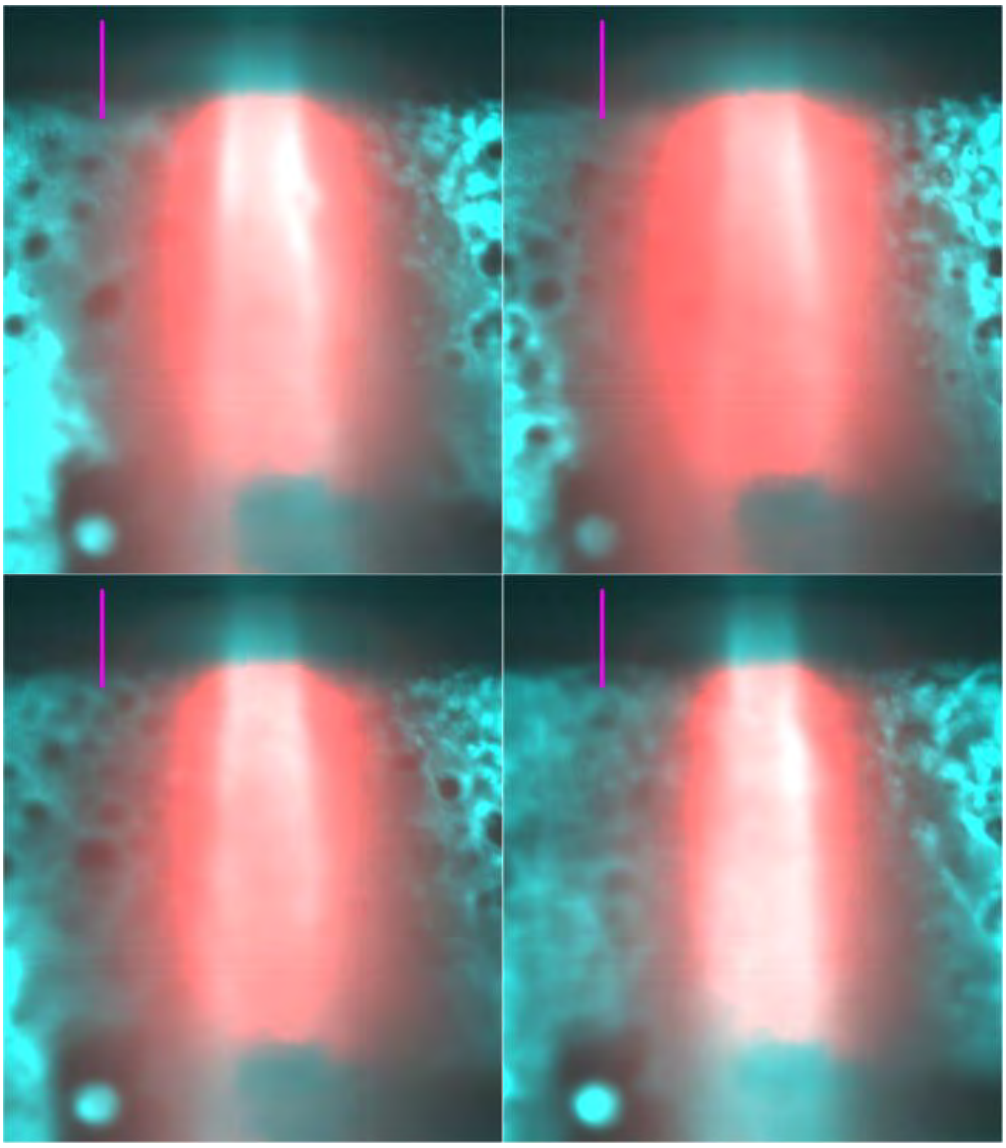

Figure 5 – Wavelet fused image of shadowgraph and CH* averages. The red represents the CH*, while the blue background represents the shadowgraph. The purple vertical line is 3 inner core diameters from the nozzle exit. Top row from left to right is Test 1, 2 and bottom row, left to right is Test 3 and4, respectively.

Distribution A: Approved for public release; distribution unlimited. Clearance # 16597
A-600

Downloaded by Doug Talley on May 1, 2017 | http://arc.aiaa.org | DOI: 10.2514/6.2017-1335

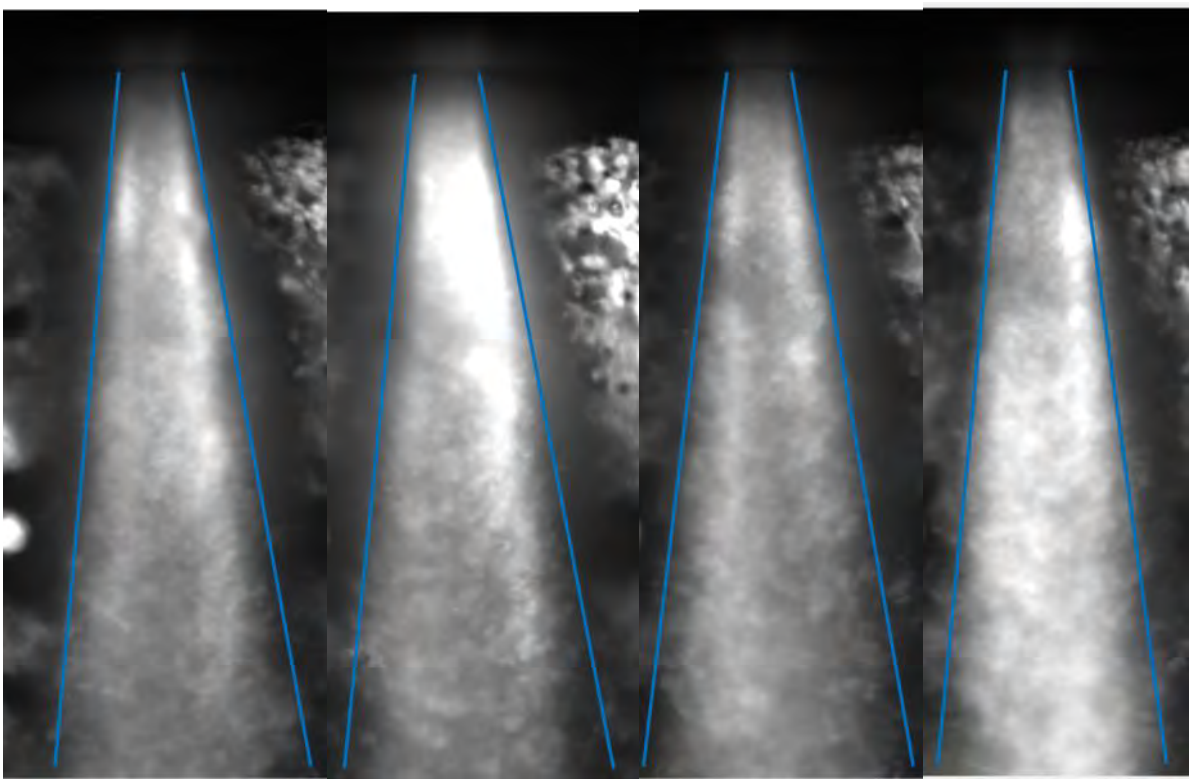

Figure 6 – Standard Deviation pixel intensity from the shadowgraph images. The blue represent the spread of the cone. From left to right is Test 1, 2, 3, 4, respectively.

Figure 7 – Time series of an instantaneous shadowgraph images. A dark soot cloud can be seen obstructing the view to the center core.

Distribution A: Approved for public release; distribution unlimited. Clearance # 16597

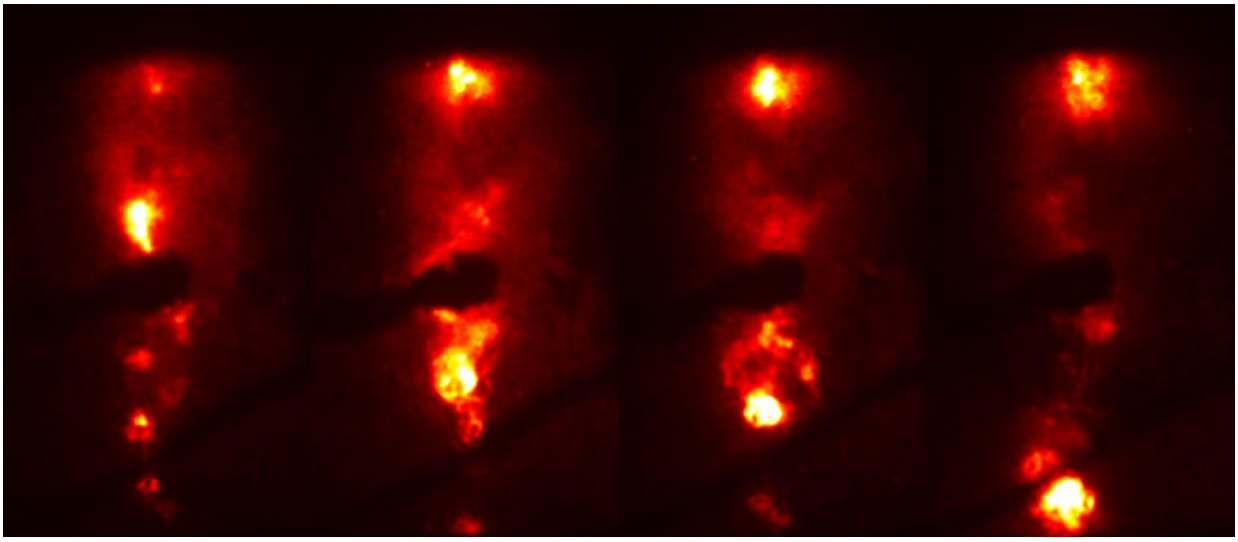

Figure 8 – Time series of an instantaneous CH* images. The flame is longer than the field of view. The differential pressure transducer is blocking part of the view.

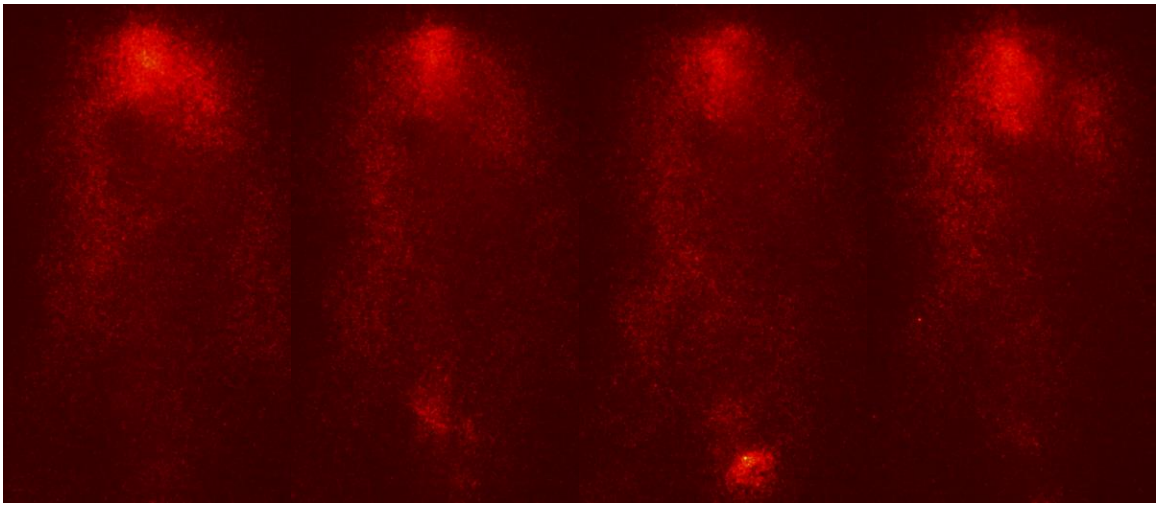

Figure 9 – Time series of an instantaneous OH* images. The flame is longer than the field of view and the soot cloud obstructs the same regions as the shadowgraph.

Downloaded by Doug Talley on May 1, 2017 | http://arc.aiaa.org | DOI: 10.2514/6.2017-1335

Distribution A: Approved for public release; distribution unlimited. Clearance # 16597

Downloaded by Doug Talley on May 1, 2017 | http://arc.aiaa.org | DOI: 10.2514/6.2017-1335

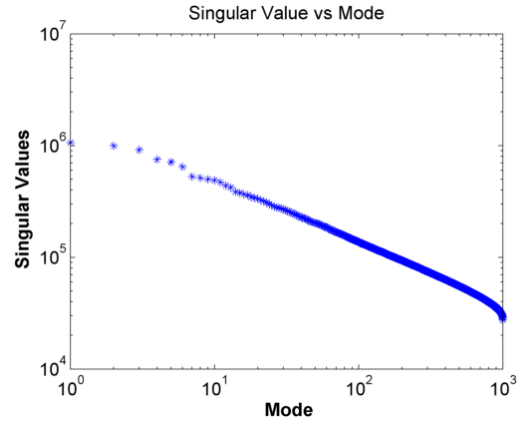

a)

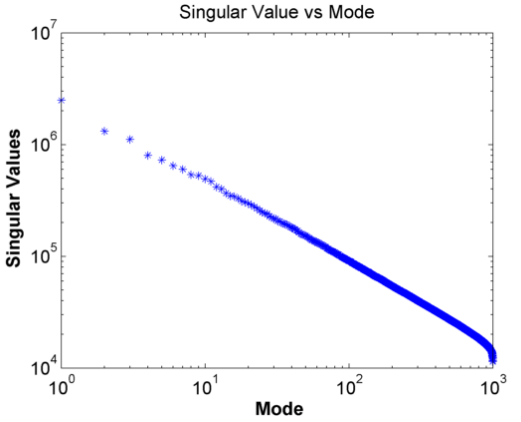

b)

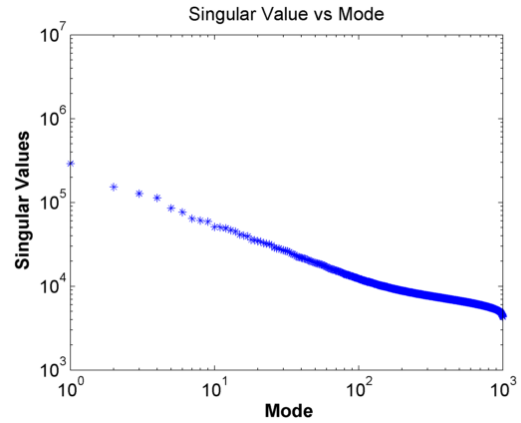

c)

Figure 10 – POD Energy values associated with each POD spatial mode. a) Shadowgraph, b) CH*, and c) OH*.

Distribution A: Approved for public release; distribution unlimited. Clearance # 16597
A-603

Downloaded by Doug Talley on May 1, 2017 | http://arc.aiaa.org | DOI: 10.2514/6.2017-1335

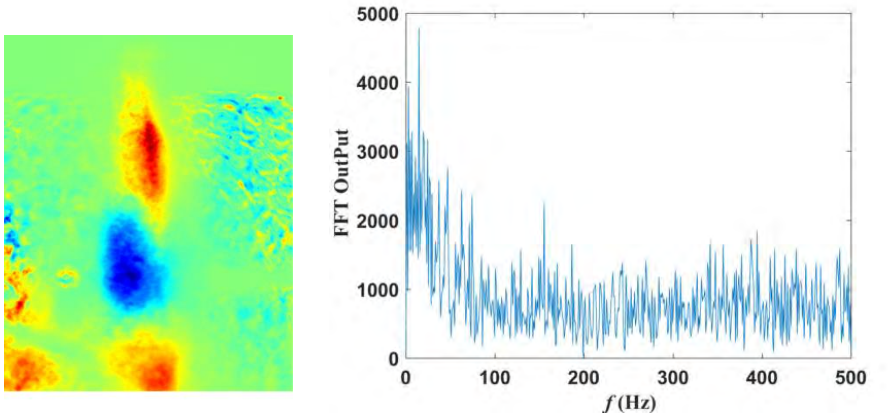

a)

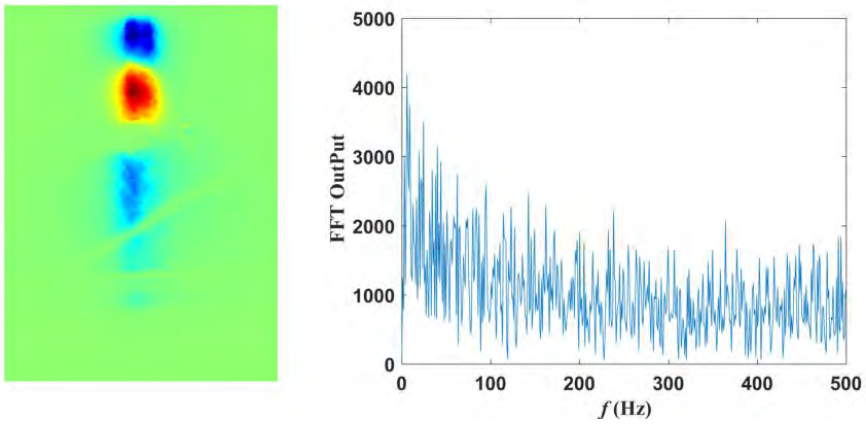

b)

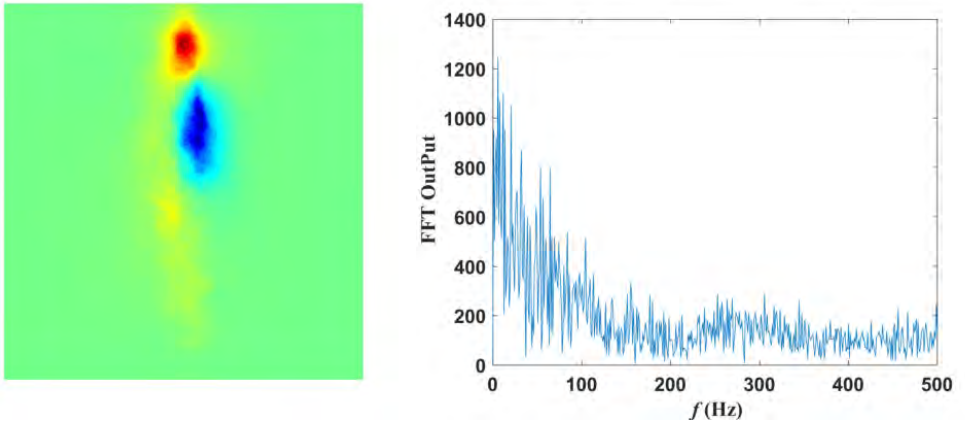

c)

Figure 11 – A POD Spatial mode and FFT of the corresponding temporal mode. A) Shadowgraph, B) CH*, and C) OH*. The alternating pattern is due to the soot cloud blocking the flame's chemiluminescence.

Distribution A: Approved for public release; distribution unlimited. Clearance # 16597
A-604

Downloaded by Doug Talley on May 1, 2017 | http://arc.aiaa.org | DOI: 10.2514/6.2017-1335

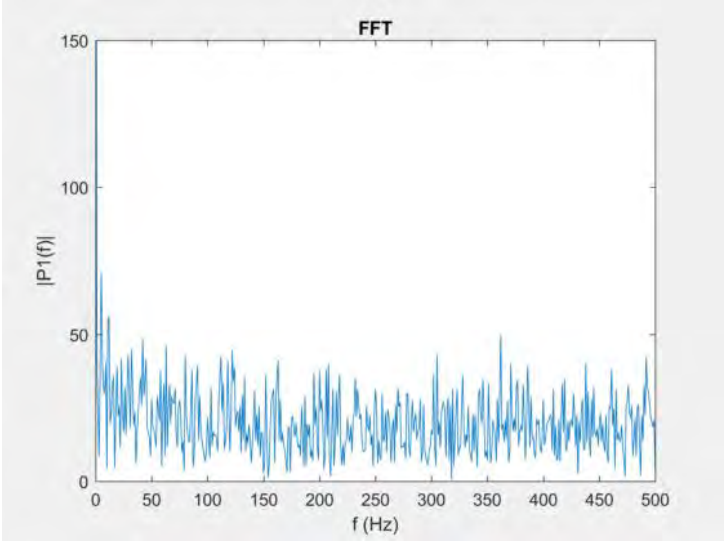

Figure 12 – A FFT of the pixel intensity from the shadowgraph images taken 15 oxygen diameters away from the nozzle exit.

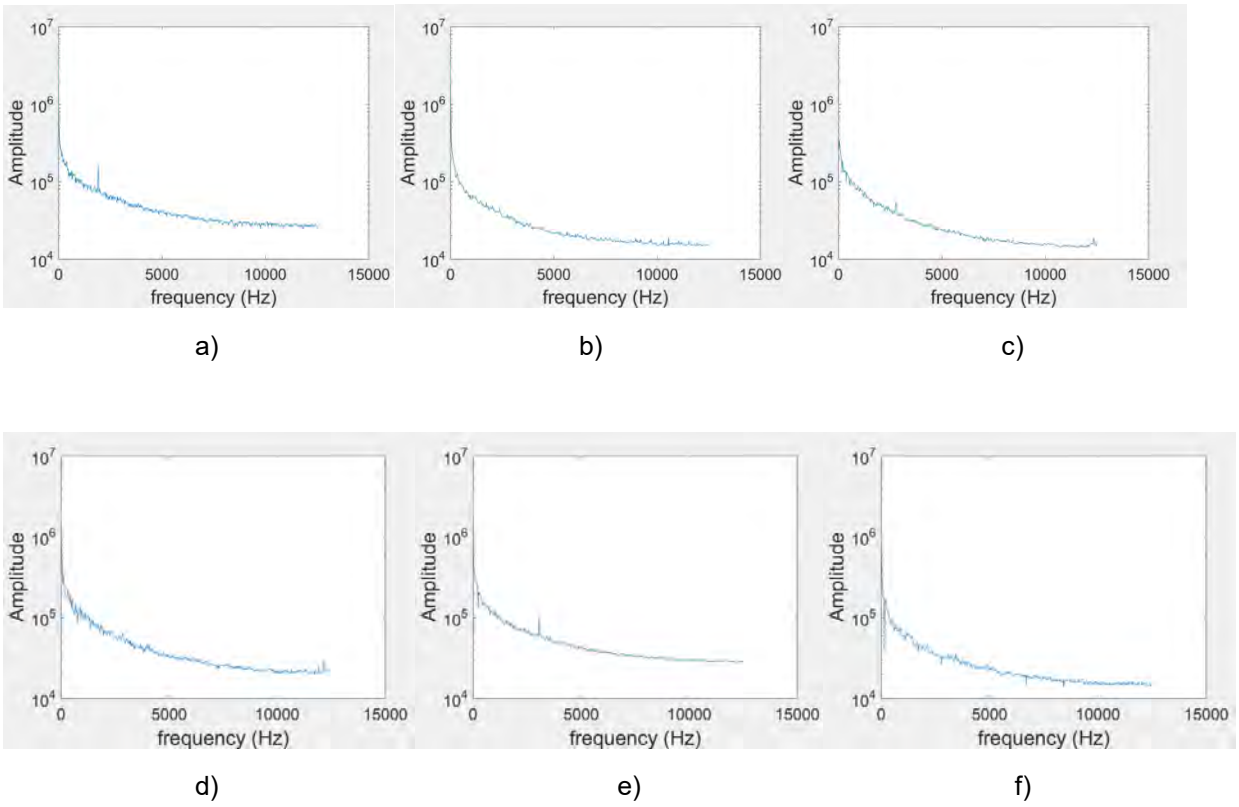

Figure 13 – The DMD amplitude *A* vs the frequency. a) is 1930 Hz, b) 2380 Hz, c) 2780 Hz, d) 2852 Hz, e) 3060 Hz, and f) 3430 Hz.

Distribution A: Approved for public release; distribution unlimited. Clearance # 16597
A-605

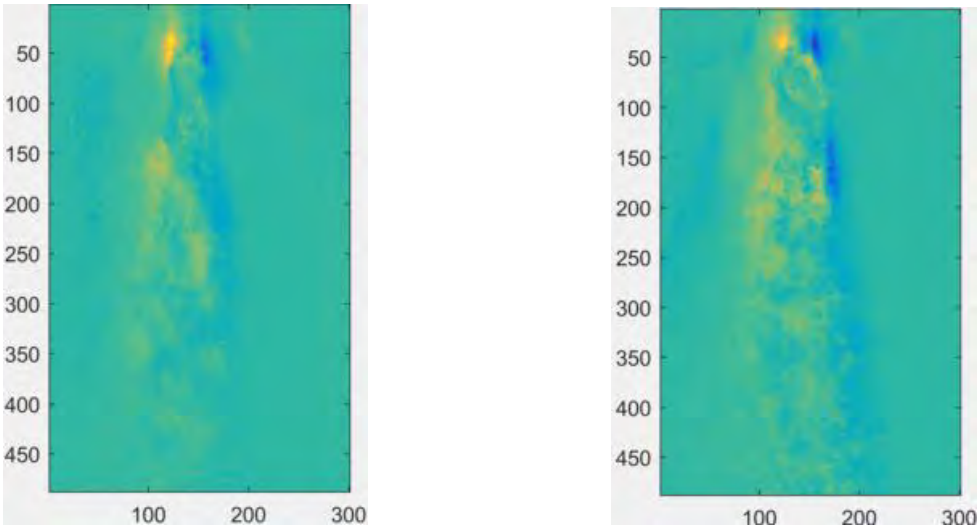

Figure 14 – The DMD spatial mode extracted from the high-speed shadowgraphy for a) 1920 Hz, and b) 3060 Hz. The alternating band is indicative of a in-plane flapping.

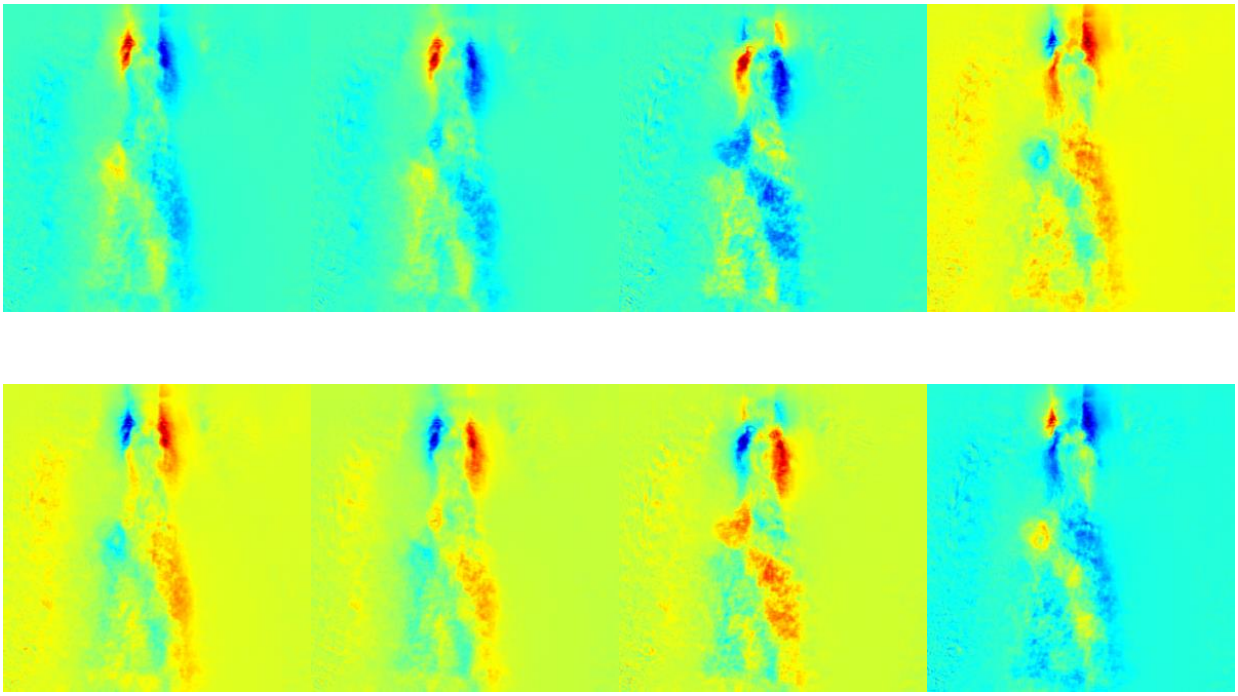

Figure 15 – The DMD spatial mode temporal evolution extracted from the high-speed shadowgraphy of the 1920 Hz acoustic perturbations. An in-plane flapping motion is indicative by the changing red and blue pattern.

Downloaded by Doug Talley on May 1, 2017 | http://arc.aiaa.org | DOI: 10.2514/6.2017-1335

Distribution A: Approved for public release; distribution unlimited. Clearance # 16597
A-606

10th U. S. National Combustion Meeting
Organized by the Eastern States Section of the Combustion Institute
April 23-26, 2017
College Park, Maryland

Combustion Characteristics of Hydrocarbon Droplets Induced by Photoignition of Aluminum Nanoparticles

Alireza Badakhshan[1,], John W. Bennewitz[2], Douglas G. Talley[3]*

[1]Engineering Research Corporation, Edwards AFB, Edwards, CA 93524
[2]Department of Mechanical and Aerospace Engineering, UCLA, Los Angeles, CA 90095
[3]Air Force Research Laboratory, Edwards AFB, Edwards, CA 93524
[*]Corresponding Author Email: alireza.badakhshan.2.ctr@us.af.mil

Abstract: Combustion of a wide range of hydrocarbon fuel droplets has been achieved through photoignition (PI) utilizing sub milligram of aluminum nanoparticles (Al NPs). For diesel fuel, a reliable ignition was made possible by mixing a solid oxidizer with the Al NPs. PI offers a fast (<5 ms) gasless reaction, a high ignition temperature (>2000 K), and a relatively short total ignition duration (80-150 ms). Droplets with a diameter of 1.4±0.1 mm were suspended from a 0.15 mm quartz fiber, then ignited through PI and in a few cases with a Ni-Cr heating wire. The burning rate constant *K* for ethanol, heptane, n-dodecane, kerosene (RP-2), Fischer−Tropsch, and diesel fuel #2 was found to be 0.83±0.01, 0.95±0.01, 0.90±0.01, 0.77±0.02, 0.99±0.01 and 0.71±0.05 mm^2/s, respectively. PI also allows the evaluation of ignition delays via high-speed imaging of the luminous flame. Ignition delays as short as 50 ms were observed that is much smaller than those achieved by conventional ignition methods at atmospheric pressure (>400 ms). The dramatically shorter ignition delay may be explained in part by the extremely fast local heating effect (estimated to exceed 10^5 K/s) and the high burning temperature of Al NPs in the vicinity of the droplet.

Keywords: Droplet Combustion, Burning Rate Constant, Ignition Delay, Photoignition

1. Introduction

The study of droplet burning is mostly focused either on single suspended droplets or free droplets, usually in a free fall. In either case, the burning of a single fuel droplet involves evaporation of the fuel at the surface of the droplet, which leads to a diffusion flame to form around the droplet as the fuel vapor reacts with the surrounding air. While in many sprays the flame regime encompasses the entire spray [1], characterizing the burning of single droplets is required to assist with modeling of such sprays [2]. Specifically, the fundamental processes that occur during the burning of individual droplets are pertinent to understanding combustion dynamics for multiphase reactive systems that are prone to self-excited combustion instabilities [3, 4].

Substantial experimental work has been devoted to the ignition of single droplet [5] and fuel spray [6] as well as the ignition delay in past decades [7-11]. However, a systematic study to correlate the stated combustion parameters to the type and the concentration of fuel additives for rocket relevant fuels is yet to be reported. The present experimental study has been focused on the determination of burning rate constants and the ignition delays for various hydrocarbon fuel droplets as important combustion metrics related to combustion dynamics, in preparation for the study of fuel additives.

Distribution Statement A: Approved for Public Release; Distribution is Unlimited. PA Clearance Number 17118

Another objective of this work was to study possible effects of a faster and hotter ignition approach on the combustion characteristics of suspended hydrocarbon fuel droplets. PI was selected as an alternative ignition method because it is much faster than any conventional approaches in droplet ignition, as will be described later in this paper. Another advantage of PI is the ease of its application for ignition at elevated pressures [12].

2. Experimental Details

In order to investigate combustion characteristics of hydrocarbon fuels, the suspended droplet approach was implemented. A fuel droplet with a nominal size of 1.4±0.1 mm was suspended from a 0.15 mm uncoated quartz fiber (see Fig. 1), from Polymicro Technologies Inc. In order to increase the retention of the fuel droplet on the fiber, a bead was generated at the end of each fiber through a heating process using an oxy-propane torch.

The burning of the fuel droplet was captured by a high-speed camera, model Phantom v7.1 from Vision Research Inc., imaging at 1,000 fps. In order to provide the proper contrast between the liquid droplet and background for image processing, a cluster of adjustable intensity white light emitting diodes (LED's) was implemented to provide sufficient backlighting to create shadowgraph images of the droplet burning process. The LED's were turned off for the evaluation of the ignition delay time of the droplet in order to observe the appearance of the flame.

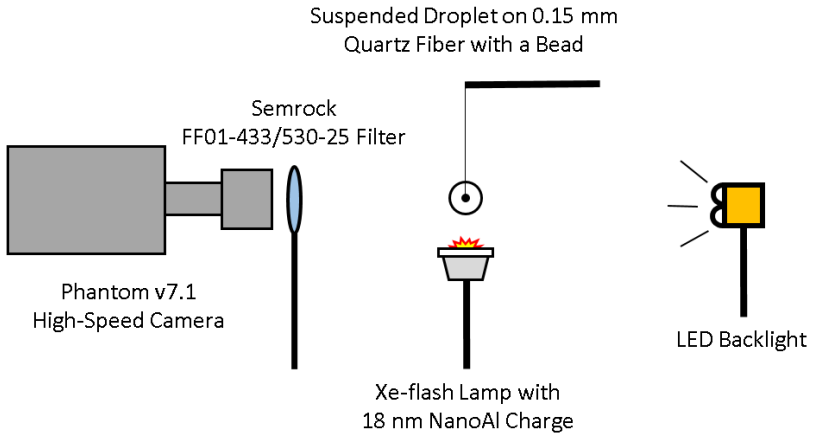

Figure 1: Schematic layout of suspended droplet experiment test facility consisting of the high-speed imaging configuration and the photoignition system.

Ignition System

For ignition, two different methods were implemented for the suspended droplets experiments, a conventional Ni-Cr heating wire and the PI system, which was the main ignition method in this work. To the best of our knowledge, this is the first report on the use of PI for ignition of fuel droplets. PI, takes advantage of photothermal heating from a Xe-flash and subsequent ignition of energetic nanostructures, in this case aluminum nanoparticles (Al NPs).

The PI system consisted of Xe-flash lamp, a photo-ignitable solid fuel mixture, and a transparent substrate to hold the fuel and to protect the flash bulb and its reflector from burning particles. The entire assembly was positioned directly underneath the droplet at a distance of ~7 mm, as shown in Fig. 1. The light source for PI was a compact Xe-flash lamp with a flash duration of ~1 ms and an energy output of ~1.4 J per flash. In order to achieve a relatively small ignition plume (~10 mm in size) that produced little or no gas, 0.3±0.2 mg of 18 nm Al NPs, from

NanoAmor, Houston, TX, were implemented as the energetic fuel for PI. Upon activating the Xe flash, micron size burning aggregates of Al NPs are ejected from the glass substrate initiating the combustion of the droplet.

PI has a few characteristics that sets it apart from other droplet ignition methods that makes it particularly attractive for the intended ignition application in this study. Generally, PI is fast acting (<5 ms) and has a relatively short total duration (<150 ms) compared to traditional droplet heating methods (>0.5 s), which is long compared to the typical burn duration of a droplet (>1.5 s). More specifically, PI of Al NPs takes place in the solid phase and at a high temperature (>2000K) [12] with a temperature ramp up on the order of 10^6 K/s [13]. PI produces numerous burning particles that rapidly surround the droplet and ignite pockets of combustible mixtures that may exist around the droplet.

3. Results and Discussion

The image processing method presented in Sevilla et al. [14] was developed to track the droplet diameter regression throughout its burning by fitting an ellipse around the droplet boundary. By properly tracking the droplet diameter regression, the average burning rate constant *K*, given by:

$$K = \frac{d}{dt}\left(d_{\text{eqvs}}\right)^2, \tag{1}$$

was calculated using the well-established D^2 law for burning fuel droplets [15]. For this study, the diameter used in the *K* calculation was the droplet diameter associated with the equivalent volume of a sphere as described by Struk et al. [16]. This equivalent diameter can be written as

$$d_{\text{eqvs}} = 2a^{2/3}b^{1/3}, \tag{2}$$

where *a* and *b* are the semi-major and minor axis lengths of the fitted ellipse.

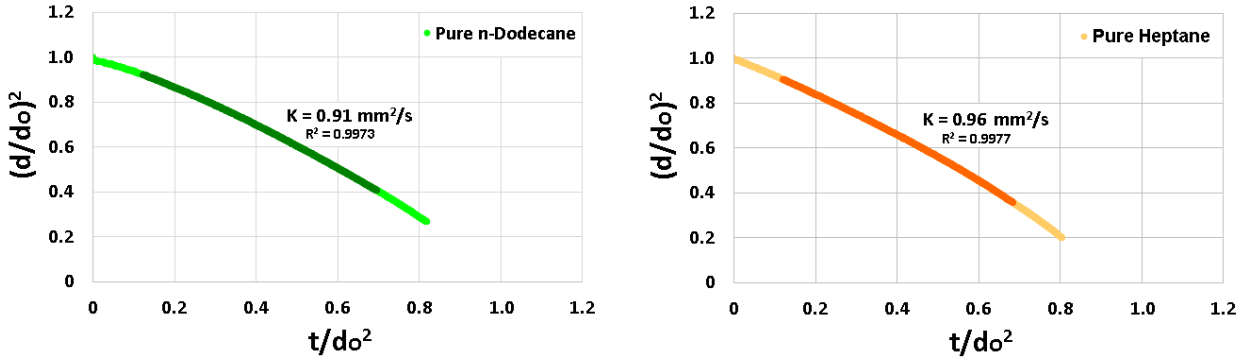

(a) (b)

Figure 2: Normalized droplet diameter regressions for pure (a) n-dodecane and (b) heptane.

The burning rate constant *K* is determined using 70% of the data centered around the midpoint as depicted by the darker section of each line to negate the transient effects at the beginning and end of the droplet burning process.

Figure 2 shows the examples of burning rate constants for n-heptane and n-dodecane. In each case part of the data from the beginning and the end of the burning process was eliminated from the calculation in order to avoid the transient effect that is often expected to interfere with the evaluation of *K*. A series of 10-15 droplet burning tests for the each hydrocarbon fuel have been performed in order to produce statistically reliable data for *K*. To quantify the uncertainty of *K* values, the Student's t-distribution for small sample size [17] was implemented to provide a 95% confidence interval on the reported values. A summary of these results is presented in Table 1 that shows the experimental burning rate constants and ignition delays for fuel droplets that were ignited by PI. RP-2 and diesel fuel #2 have the lowest average values of *K*, while Fischer−Tropsch Jet fuel (FT) has the highest. Also, the burning rate constant for ethanol was the same for both PI and ignition through a Ni-Cr heating wire (0.83 ± 0.02 mm^2/s),

Ignition delay is another parameter of interest in this study and unlike the burning rate, it is not as easy to come up with a direct estimate for its value through conventional ignition methods such as heating by a Ni-Cr wire. The problem is associated with the relatively slow heating process and the interference from the luminous background in most cases. The subjective definition of the ignition delay time is another source of uncertainty, where most generally it is defined as the time interval from introducing the droplet to the hot environment to the point that the combustion of the droplet is established [5]. As expected, the ignition delay is a function of the droplet temperature that may be strongly influenced by the ignition method.

Table 1: The burning rates and ignition delays for neat hydrocarbon fuel droplets

Fuel	**Initial Droplet Diameter, d_o (mm)**	**Burning Rate Constant, K (mm^2/s)**	**Ignition Delay (via PI) Based on Initial Flame (ms)**
Ethanol (by PI) (by heating wire)	1.30 ± 0.04	0.83 ± 0.01 0.83 ± 0.02	N/A (the blue flame is not luminous enough)
Heptane	1.40 ± 0.06	0.95 ± 0.01	60
n-Dodecane	1.51 ± 0.04	0.90 ± 0.01	120
Kerosene (RP-2)	1.34 ± 0.06	0.77 ± 0.02	70
FT	1.54 ± 0.04	0.99 ± 0.01	100
Diesel #2	1.57 ± 0.06	0.71 ± 0.05	110

While, the time from introducing the droplet to the hot environment applies to conventional methods, it does not directly apply in the PI process. Instead, the activation time of the Xe-flash was chosen as the beginning of the ignition process (t=0), followed by the appearance of burning Al NPs surrounding the droplet within ~5 ms. For most hydrocarbon fuel droplets a two-stage ignition is observed, where the first visible flame, here referred to as "initial flame", peaks within 50 -130 ms for different fuels. This is shown in Fig. 3(c), while still a few burning NPs may be present around the droplet, as seen within the field of view of the high-speed camera. For most fuels the initial flame which may be related to "cool flame" phenomenon [10,11] gradually diminishes, or even disappears in some cases, within another 50-100 ms, only to be replaced by the "primary flame" that remains visible as long as the fuel droplet burns.

Figure 3 shows snapshots from a high-speed movie for ignition and burning of a heptane droplet. The first frame in Fig. 3 indicates the peak of Xe-flash at t=0, where its high luminosity saturates the pixels of the image sensor within the entire field of view. Most burning particles in

Figs. 3(b) and 3(c) are by far much smaller than the droplet, i.e. << 1mm, but the out of focus particles in the image appear to be much larger than their actual size. In Table 1, the last column shows the estimated ignition delay time for each fuel except for ethanol, where the flame in not visible by the camera. The reported values are the best estimate and they clearly show relatively low ignition delays compared to what has been reported in the literature with traditional ignition methods [5]. A more detailed investigation of ignition delays for hydrocarbon fuel droplets is underway and will be reported subsequently.

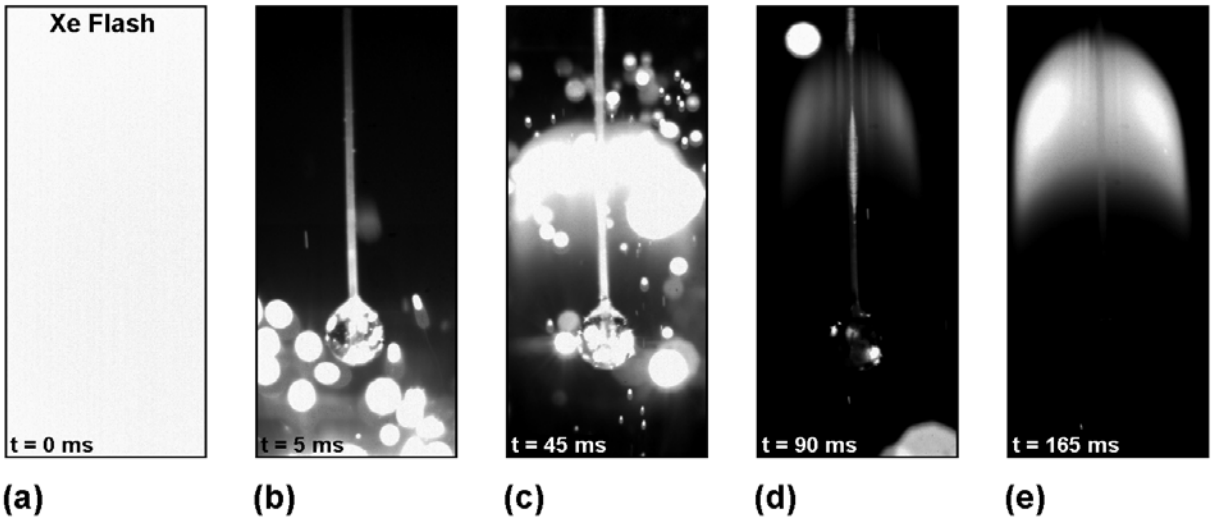

Figure 3: A time sequence of specific burning events for a heptane droplet, (a) the Xe-flash light covers the entire field of view, (b) burning Al NPs surround the droplet, (c) the initial flame is clearly visible, (d) The initial flame almost disappears, and (e) the primary flame gradually appears. The frame rate was 1,000 fps and the exposure time was ~ 0.98 ms.

4. Conclusion

In the present experimental study, the burning characteristics of various suspended hydrocarbon fuel droplets have been investigated utilizing photoignition (PI) of aluminum nanoparticles for the first time. PI is a fast acting (<5 ms), hot burning (> 2000 K), multi-spot ignition method with a relatively short burn duration (< 150 ms). The burning rate constant, *K,* for ethanol, heptane, n-dodecane, kerosene (rocket grade), Fischer−Tropsch jet fuel (FT), and diesel fuel #2, ignited with PI, was found to be 0.83±0.01, 0.95±0.01, 0.90±0.01, 0.77±0.02, 0.99±0.01 and 0.71±0.05 mm^2/s, respectively. Study of fuel droplets yielded burning rate constants with a maximum uncertainty of 0.02 mm^2/s, with the exception of uncertainty for diesel #2 that is 0.05 mm^2/s. Also, investigation of the high-speed images for fuel ignition by PI provided a lower and upper limit of ~50 to ~250 ms for the ignition delay of the stated hydrocarbon fuel droplets. These values are generally much smaller than the reported ignition delays for similar size droplets using conventional ignition methods at ambient pressure (typically > 400 ms), which may be explained in part by the extremely fast local heating effect (estimated to exceed 10^5 K/s) and the high burning temperature of Al NPs in the vicinity of the droplet. Quantification of the droplet burning rate constant *K* and the ignition delays creates the baseline for the continuation of this project that will be focused on the effect of different solid additives on the combustion characteristics of liquid hydrocarbon fuels for the possible control of combustion dynamics in liquid rocket engines.

5. Acknowledgement

Funding for this work has been provided by the Air Force Office of Scientific Research under a Grant for “The Design of Nanoenergetic Materials for Control of Combustion Dynamics”, with Dr. Mitat Birkan as the program manager.

6. References

[1] Sirignano, W.A., "Fuel Vaporization and Spray Combustion Theory", Progress in Energy and Combustion Science 9, (1983); 4, 291-322.
[2] Faeth, C.M., "Current Status of Droplet and Liquid Combustion", Progress in Energy and Combustion Science 3, (1977); 4, 191-224.
[3] Candel, S., Juniper, M., Singla, G., Scouflaired, P., and Rolon, C., "Structure and Dynamics of Cryogenic Flames at Supercritical Pressures", Combustion and Science Technology, (2006); 178, 161-192.
[4] Chehroudi, B., Davis, D.W., and Talley, D.G., "The Effects of Pressure and Acoustic Field on a Cryogenic Coaxial Jet", 42nd AIAA Aerospace Sciences Meeting and Exhibit, Paper AIAA-2004-1330, (2004).
[5] Aggarwal, S.K., “Single droplet ignition: Theoretical analyses and experimental findings” Progress in Energy and Combustion Science (2014); 45, 79-107, and references there in.
[6] Aggarwal, S.K., “A review of spray ignition phenomena: Present status and future research”, Progress in Energy and Combustion Science (1998); 24(6), 565–600.
[7] Saitoh, T., Ishiguro, S., Niioka, T., “An experimental study of droplet ignition characteristics near the ignitable limit”, Combust Flame (1982); 48, 27-32.
[8] Bergeron CA, Hallett WLH., “Ignition characteristics of liquid hydrocarbons as single droplets”, Can J Chem Eng (1989); 67, 142-149.
[9] Tanabe, M., Kono, M., Sato, J., Koenig, J., Eigenbrod, C., Rath, H.J., “Effects of natural convection on two-stage ignition of an n-dodecane droplet”, Proc Combust Inst (1994); 25, 933-940.
[10] Tanabe, M., Kono, M., Sato, J., Koenig, J., Eigenbrod, C., Dinkelacker, F., et al., “Two stage ignition of n-heptane isolated droplets”, Combust Sci Tech (1995); 108, 103-119.
[11] Wong, S.C., Hsu, T.S., Chang, J.C., “Validity of droplet ignition criterion derived assuming gas-phase quasisteadiness”, J. Propulsion Power (1996); 12(1), 18-25.
[12] Badakhshan, A., Danczyk, S., Forliti, D.J., Leyva, I.A., “Nano-ignition Torch Applied to Cryogenic H2/O2 Coaxial Jet”, 54th AIAA Aerospace Science Meeting, (AIAA 2016-0184), 2016).
[13] Ohkura, Y., Rao, P. M., Zheng, X., “Flash ignition of Al nanoparticles: Mechanism and applications”, Comb. and Flame (2011); 158(12), 2544-2548.
[14] Sevilla-Esparza, C.I., Wegener, J.L., Teshome, S., Rodriguez, J.I., Smith, O.I. and Karagozian, A.R., "Droplet Combustion in the Presence of Acoustic Excitation", Combustion and Flame, (2014); 6, 161, 1604-1619.
[15] Glassman, I., and Yetter, R.A., *Combustion: Fourth Edition*, Academic Press, Elsevier Inc., Burlington, MA, 2008.
[16] Struk, P.M., Ackerman, M., Nayagam, V., and Dietrich, D.L, "On Calculating Burning Rates During Fibre Supported Droplet Combustion", Microgravity Science and Technology (1998); 4(11) 144-151.
[17] Beckwith, T.G., Marangoni, R.D., and Lienhard V’s, *Mechanical Measurements: Sixth Edition*, Pearson Education Inc., Upper Saddle River, NJ, 2007.

Measurement of the Burning Rate and Ignition Delay for Various Hydrocarbon Fuel Droplets using Photothermal Ignition of Aluminum Nanoparticles

J. W. Bennewitz[1*], A. Badakhshan[2], S. A. Schumaker[3] and D. G. Talley[3]
[1]Department of Mechanical and Aerospace Engineering
University of California, Los Angeles
Los Angeles, CA 90095 USA

[2]Engineering Research Corporation
Edwards Air Force Base
Edwards, CA 93524 USA

[3]Edwards Air Force Base
Edwards, CA 93524 USA

Abstract

Combustion of a wide range of hydrocarbon fuel droplets has been achieved through photoignition (PI) utilizing sub milligram of aluminum nanoparticles (Al NPs). For diesel fuel, a reliable ignition was made possible by mixing a solid oxidizer with the Al NPs. PI offers a fast (<5 ms) gasless reaction, a high ignition temperature (>2000 K), and a relatively short total ignition duration (80-200 ms). Droplets with a diameter of 1.4±0.1 mm were suspended from a 0.15 mm quartz fiber, then ignited through PI and in a few cases with a Ni-Cr heating wire. The burning rate constant K for ethanol, heptane, n-dodecane, kerosene (RP-2), Fischer−Tropsch synfuel (FT), and diesel #2 was found to be 0.83±0.01, 0.95±0.01, 0.90±0.01, 0.77±0.02, 0.99±0.01 and 0.71±0.05 mm^2/s, respectively. PI also allows the evaluation of ignition delays via high-speed imaging of the luminous flame. Ignition delays as short as 50 ms were observed, which are much smaller than those achieved by conventional ignition methods at atmospheric pressure (>400 ms). The dramatically shorter ignition delay may be explained in part by the extremely fast local heating effect (estimated to exceed 10^5 K/s) and the high burning temperature of Al NPs in the vicinity of the droplet.

*Corresponding author: johnbennewitz@ucla.edu

Introduction

When studying combustion characteristics of liquid rocket fuels, it is customary to either investigate the combustion of liquid fuel droplets or the combustion of fuel sprays. However, the two are closely related to each other, as in a typical rocket combustion chamber, where the burning of droplets, droplet clusters, and fuel sprays occur simultaneously. The study of droplet burning is mostly focused either on single suspended droplets or free droplets, usually in a free fall. In either case, the conditions regarding the combustion of a single fuel droplet deviates from what is expected in typical liquid rocket engines (LRE's). This not only concerns the chamber pressure and temperature usually being much lower in a typical droplet study, but also the droplet ignition process and the related transient effects such as temperature ramp up, which is much slower than what takes place in LRE's. As a result, reported values of combustion parameters such as the burning rate constant and the ignition delay time obtained under typical experimental conditions may not entirely represent the combustion processes in LRE's. However, studying droplet combustion behavior provides a platform to fundamentally characterize the burning characteristics of fuels.

The burning of a single fuel droplet involves evaporation of the fuel at the surface of the droplet, which leads to a diffusion flame to form around the droplet as the fuel vapor reacts with the surrounding air. While in LRE's the flame regime encompasses the entire spray [1], characterizing the burning of single droplets is required to assist with the modeling of such sprays [2]. Specifically, the fundamental processes that occur during the burning of individual droplets are pertinent to understanding combustion dynamics for multiphase reactive systems that are prone to self-excited combustion instabilities [3, 4].

Another objective of this work was to study possible effects of a faster and hotter ignition approach on the combustion characteristics of suspended hydrocarbon fuel droplets. Photoignition (PI) was selected as an alternative ignition method because it is much faster than any conventional approach in droplet ignition, as will be described later in this paper. Another advantage of PI is the ease of its application for subscale test rocket engines at elevated pressures, as has been demonstrated recently [5].

Substantial experimental work has been devoted to the ignition of single droplets [6] and fuel sprays [7], as well as ignition delay in past decades [8-12]. However, a systematic study to correlate the stated combustion parameters for rocket relevant fuels using this ignition approach is yet to be reported. The present experimental study has been focused on the burning characteristics of various hydrocarbon fuels to quantify changes in important combustion metrics related to combustion dynamics. The objective of this study is to determine the burning rate constant and ignition delay of different hydrocarbon fuel droplets under ambient conditions ignited by PI.

It should be mentioned that this work is the first part of a larger project investigating the effects energetic fuel additives have on the combustion dynamics of hydrocarbon fuels at elevated pressures. By quantifying the burning rate constant K and the ignition delay of these hydrocarbon fuel droplets under ambient conditions, a baseline is created to compare against fuel additive data.

Experimental Details

In order to investigate various combustion characteristics of hydrocarbon fuels, the suspended droplet approach was implemented. A fuel droplet with a nominal size of 1.4±0.1 mm was suspended from a 0.15 mm uncoated quartz fiber (see Fig. 1), from Polymicro Technologies Inc. The droplets were first produced using a hypodermic needle and then mechanically transferred to the fiber. In order to increase the surface tension of the fuel droplet on the fiber, a bead was generated at the end of each fiber through a heating process using an oxy-propane torch once the polymer coating of the fiber was chemically removed. Each quartz fiber was used for a set of 10-15 identical experiments in order to generate statistically reliable data. The fiber was flame treated with a butane torch and mechanically cleaned in between tests as needed.

The burning of the fuel droplet was captured by a high-speed camera, model Phantom v7.1 from Vision Research Inc., imaging at 1,000 fps. In order to provide the proper contrast between the liquid droplet and background for image processing, a cluster of adjustable intensity white light emitting diodes (LED's) was implemented for sufficient backlighting to create shadowgraph images of the droplet burning process. A dual-band bandpass filter, Semrock FF01-433/530-25, was placed in front of the camera in order to limit the spectral spread of light reaching the high-speed camera during the burning of fuel droplets. The backlight was turned off during the evaluation of the droplet ignition delay time in order to observe the appearance of the flame that was indicative of the initiation of droplet combustion.

Ignition System

For ignition, two different methods were implemented for the suspended droplets experiments, a conventional Ni-Cr heating wire and the PI system, which was the main ignition method in this work. To the best of our knowledge, this is the first use of PI for the ignition of fuel droplets. PI, also known as flash ignition, takes advantage of photothermal heating from a Xe-

Fuel	Initial Droplet Diameter, d_o (mm)	Burning Rate Constant, K (mm^2/s)	Ignition Delay (via PI) Based on the Initial Flame (ms)
Ethanol (with PI)	1.30 ± 0.04	0.83 ± 0.01	N/A (the blue flame is not luminous
(with Ni-Cr coil)		0.83 ± 0.02	enough)
Heptane	1.40 ± 0.06	0.95 ± 0.01	60
n-Dodecane	1.51 ± 0.04	0.90 ± 0.01	120
Kerosene (RP-2)	1.34 ± 0.06	0.77 ± 0.02	70
Fischer−Tropsch (FT)	1.54 ± 0.04	0.99 ± 0.01	100
Diesel #2	1.57 ± 0.06	0.71 ± 0.05	110

Table 1. The burning rate constant and ignition delay for hydrocarbon fuel droplets.

flash and subsequent ignition of energetic nanostructures, in this case aluminum nanoparticles (Al NPs).

Unless otherwise stated, a miniature PI source designed to work for a millimeter size fuel droplet was used for the experiments reported this study. This ignition system consisted of Xe-flash lamp, a photo-ignitable solid fuel mixture, and a transparent substrate to hold the fuel and protect the flash bulb from burning particles. The entire assembly was positioned directly underneath the droplet at a distance of ~7 mm, as shown in Fig. 1. The light source for PI was a compact Xe-flash lamp with a flash duration of ~1 ms and an energy output of ~1.4 J per flash. In order to achieve a relatively small ignition plume (~10 mm in size) that produced little or no gas, 0.3±0.2 mg of 18 nm Al NPs were implemented as the energetic fuel for PI. Upon activating the Xe flash, micron size burning aggregates of Al NPs are ejected from the glass substrate, initiating the combustion of the droplet.

PI has a few characteristics that sets it apart from other droplet ignition methods. Generally, PI is fast acting (<5 ms) and has a short total duration (<250 ms) compared to traditional droplet heating methods (>0.5 s) and the typical burn duration of a droplet (>1.5 s). More specifically, PI of Al NPs takes place in the solid phase and at a high temperature (>2000 K) [5] with a temperature ramp up on the order of 10^5 K/s [13]. It also involves a burning process that produces no gas, which means any pressure wave that may be generated during the ignition of Al NPs minimally disturb the fuel droplet, as seen by the high-speed imaging. Instead, PI produces numerous burning particles that rapidly surround the droplet and ignite pockets of combustible mixtures that may exist locally around the droplet. The fast moving burning particles significantly increase the chance of a successful ignition, making PI quite suitable for hard-to-ignite fuels such as rocket grade kerosene (RP-2) and diesel fuel.

Results and Discussion

The image processing method presented in Sevilla et al. [14] was developed to track the droplet diameter regression throughout its burning by fitting an ellipse around the droplet boundary. Example images demonstrating the diameter tracking of an ethanol droplet is shown in Fig. 2(a), which is designated by the red ellipsoid outline of the droplet in each image.

By properly tracking the droplet diameter regression, the average burning rate constant K, given by

$$K = \frac{d}{dt}\left(d_{\mathrm{eqvs}}\right)^2, \tag{1}$$

was calculated using the well-established D^2 law for burning fuel droplets [15]. For this study, the diameter used in the K calculation was the droplet diameter associated with the equivalent volume of a sphere as described by Struk et. al. [16]. This equivalent diameter can be written as

$$d_{\mathrm{eqvs}} = 2a^{2/3}b^{1/3}, \tag{2}$$

where a and b are the semi-major and minor axis lengths of the fitted ellipse.

Utilizing this equivalent diameter, K was then determined using 70% of the data centered around the midpoint of the droplet burning event, as shown by the darker line in Fig. 2(b). This reduced the variability in the calculation of K due to any transient startup behavior immediately following ignition, as well as the end of the droplet lifetime when the droplet size became on the order of the quartz fiber.

Pure Hydrocarbon Fuel Droplet Baseline Results

A series of 10-15 droplet burning tests for the hydrocarbon fuels have been performed to produce statistically reliable data for K. A major objective of this study was to quantify and minimize the uncertainty in the K values, generating a robust baseline for burning

rates of various hydrocarbon fuels. To quantify the uncertainty of *K* values, the Student's t-distribution for small sample size [17] was implemented to provide a 95% confidence interval on the reported values. A summary of these results is presented in Table 1.

Table 1 shows the experimental burning rate constants and ignition delays for fuel droplets that were ignited by PI. RP-2 and diesel #2 have the lowest average values of *K*, while Fischer−Tropsch synfuel (FT) has the highest. Also, the burning rate constant for ethanol was the same for both PI and ignition through a Ni-Cr heating wire (0.83 ± 0.02 mm^2/s), which indicates that PI it is a viable method for initiation of combustion in fuel droplets.

Specific examples of the droplet diameter regression for n-dodecane and heptane are shown in Figs. 3(a) and 3(b), respectively. Similar to the droplet burning for ethanol, the droplet regression for these hydrocarbon fuels are mostly linear across the range that was used for the *K* calculation. However, less volatile fuels such as diesel #2 have a noticeable non-linear startup transient immediately following ignition, most likely associated with heating of the liquid fuel before the quasi-steady droplet burning phase begins. Hence, this justifies calculation of the burning rate constant based on the middle section of the droplet burning event as described previously. The experiments have yielded burning rate constants with very low statistical uncertainties, which provide a reliable baseline for discerning small changes in droplet burning rates for future studies.

Ignition delay was another parameter of interest in this study, and unlike the burning rate, it is not as easy to come up with a measured value through conventional ignition methods such as heating by a Ni-Cr wire. The problem is associated with the relatively slow heating process and the interference from the luminous background in most cases. The subjective definition of the ignition delay time is another matter, where most generally it is defined as the time interval from introducing the droplet to a hot environment to the point that the combustion of the droplet is established [6].

While the time from introducing the droplet to a hot environment applies to conventional methods involving furnace heating, it does not directly apply to the PI process. Instead, the activation time of the Xe-flash was chosen as the beginning of the ignition process (t = 0 ms), followed by the appearance of burning Al NPs surrounding the droplet within ~5 ms. For most hydrocarbon fuel droplets, two-stage combustion is observed where the first visible flame, here referred to as the "initial flame", peaks within 60-120 ms for different fuel droplets. This is shown in Fig. 4(c), while still a few burning NPs may be present around the droplet, as seen within the field of view of the high-speed camera. For most fuels, the initial luminous flame gradually diminishes, or even disappears in some cases within another 50-100 ms, eventually returning as the "primary flame" that is generally more luminous in most cases and remains visible as long as the fuel droplet burns.

Figure 4 shows snapshots from a high-speed movie for the ignition and burning of a heptane droplet. The first frame in Fig. 4 indicates the peak of the Xe-flash at t = 0 ms, where its high luminosity saturates the pixels of the image sensor within the entire field of view. It should be noted that most burning particles in Figs. 4(b) and 4(c) are by far much smaller than the droplet, i.e., << 1 mm, but the out-of-focus particles in the image appear to be much larger than their actual size. Though the exact timing of the stated flames are somewhat subjective, their presence is unmistakable by the growing luminosity in the cases where flames are observed. In Table 1, the last column shows the estimated time of the initial flame for each fuel except for ethanol. The reported values are the best estimate and they clearly show relatively short ignition delays compared to what has been reported in the literature [6]. A more detailed investigation of ignition delays for hydrocarbon fuel droplets is underway and will be reported subsequently.

The values of ignition delays obtained through the application of PI are substantially lower than the values that have been reported for these fuels utilizing conventional ignition methods [6], presumably due to the ignition method that was employed in each case. The large reduction in the ignition delay for PI may be explained in part by the extremely fast local heating effect (estimated to exceed 10^5 K/s) and the high burning temperature of Al NPs (> 2000 K) in the vicinity of the droplet. While the initial results indicate that the ignition method may have a sizable effect on the ignition delay and possibly some other combustion properties of a fuel droplet, a detailed experimental work on the effect of ignition method on the combustion characteristics of fuel droplets is needed to properly address these issues.

Conclusions

In the present experimental study, the burning characteristics of various suspended hydrocarbon fuel droplets have been investigated utilizing photoignition (PI) of aluminum nanoparticles for the first time. PI is a fast acting (<5 ms), hot burning (> 2000 K) ignition method with a relatively short burn duration (< 150 ms). The burning rate constant, *K*, for ethanol, heptane, n-dodecane, kerosene (rocket grade), Fischer−Tropsch synfuel (FT), and diesel #2 ignited with PI was found to be 0.83±0.01, 0.95±0.01, 0.90±0.01, 0.77±0.02, 0.99±0.01 and 0.71±0.05

mm^2/s, respectively. For these fuels, K was determined through high-speed imaging of the burning droplets at 1,000 fps, with the droplet diameter automatically tracked throughout the fuel burning process using edge-detection software. The study of the various fuel droplets yielded burning rate constants with a maximum uncertainty of 0.02 mm^2/s, with the exception being diesel #2 that had an uncertainty of 0.05 mm^2/s. Also, investigation of the high-speed images for fuel ignition by PI provided a lower and upper limit of ~50 to ~250 ms for the ignition delay of the various hydrocarbon fuel droplets. These values are generally much shorter than the reported ignition delays for similar size droplets using conventional ignition methods at ambient pressure (typically > 400 ms), which may be explained in part by the extremely fast local heating effect (estimated to exceed 10^5 K/s) and the high burning temperature of Al NPs in the vicinity of the droplet. Quantification of the droplet burning rate constant K and the ignition delay for these fuels provides a baseline for the continuation of this project that will be focused on the effect of different solid additives on the combustion characteristics of liquid hydrocarbon fuels.

Acknowledgements

Funding for this work has been provided by the Air Force Office of Scientific Research under a Grant for "The Design of Nanoenergetic Materials for Control of Combustion Dynamics", with Dr. Mitat Birkan as the program manager.

Nomenclature

a	semi-major axis length
b	semi-minor axis length
d_{eqvs}	droplet diameter with the equivalent volume of a sphere
d_o	initial droplet diameter
K	burning rate constant

References

1. Sirignano, W.A., *Progress in Energy and Combustion Science* 9(4):291-322 (1983).
2. Faeth, C.M., *Progress in Energy and Combustion Science* 3(4):191-224 (1977).
3. Candel, S., Juniper, M., Singla, G., Scouflaired, P., and Rolon, C., *Combustion and Science Technology* 178:161-192 (2006).
4. Chehroudi, B., Davis, D.W., and Talley, D.G., *42nd AIAA Aerospace Sciences Meeting and Exhibit*, Paper AIAA-2004-1330, 2004.
5. Badakhshan, A., Danczyk, S., Forliti, D.J., and Leyva, I.A., *54th AIAA Aerospace Science Meeting*, AIAA 2016-0184, 2016.
6. Aggarwal, S.K., *Progress in Energy and Combustion Science* 45:79-107 (2014) and reference within.
7. Aggarwal, S.K., *Progress in Energy and Combustion Science* 24(6):565-600 (1998).
8. Saitoh T, Ishiguro S, and Niioka T., *Combustion and Flame* 48:27-32 (1982).
9. Bergeron C.A., and Hallett W.L.H., *Canadian Journal of Chemical Engineering* 67:142-149 (1989).
10. Tanabe M., Kono M., Sato J., Koenig J., Eigenbrod C., and Rath Zarm H.J., *Proceedings of the Combustion Institute* 25:933-940 (1994).
11. Tanabe M., Kono M., Sato J., Koenig J., Eigenbrod C., Dinkelacker F., and Rath Zarm H.J., *Combustion and Science Technology* 108:103-119 (1995).
12. Wong S.C., Hsu T.S., Chang J.C., *Journal of Propulsion and Power* 12(1):18-25 (1996).
13. Ohkura, Y., Rao, P. M., Zheng, X., *Combustion and Flame* 158(12):2544-2548 (2011).
14. Sevilla-Esparza, C.I., Wegener, J.L., Teshome, S., Rodriguez, J.I., Smith, O.I. and Karagozian, A.R., *Combustion and Flame* 161(6):1604-1619 (2014).
15. Glassman, I., and Yetter, R.A., *Combustion: Fourth Edition,* Academic Press, Elsevier Inc., 2008, pp. 358-363.
16. Struk, P.M., Ackerman, M., Nayagam, V., and Dietrich, D.L, Microgravity Science and Technology 4(11):144-151 (1998).
17. Beckwith, T.G., Marangoni, R.D., and Lienhard V, J.H., *Mechanical Measurements: Sixth Edition,* Pearson Education Iinc., 2007, pp. 55-59.

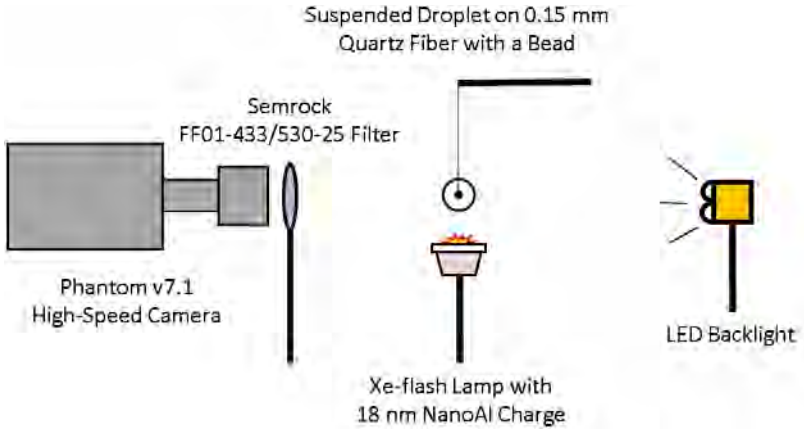

Figure 1. Schematic layout of the suspended droplet experiment test facility consisting of the high-speed imaging configuration and the photoignition system.

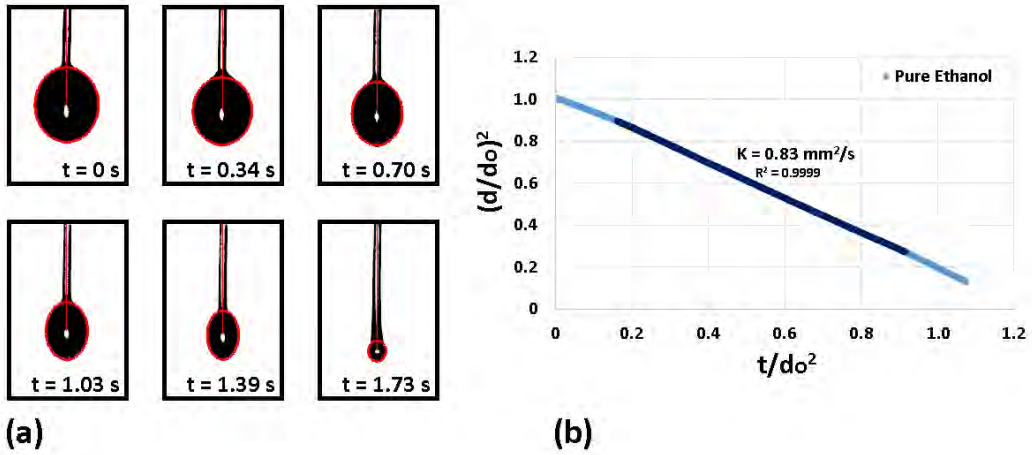

Figure 2. Time sequence of the droplet diameter edge detection for the burning ethanol droplet and (b) the corresponding normalized droplet diameter regression. The burning rate constant *K* is determined using 70% of the data around the midpoint as depicted by the darker line.

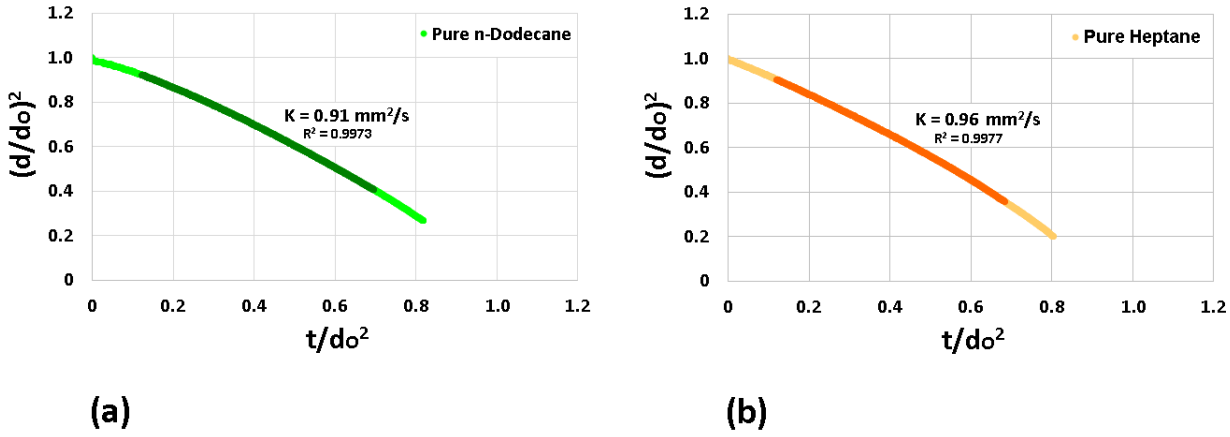

Figure 3. Normalized droplet diameter regressions for (a) n-dodecane and (b) heptane.

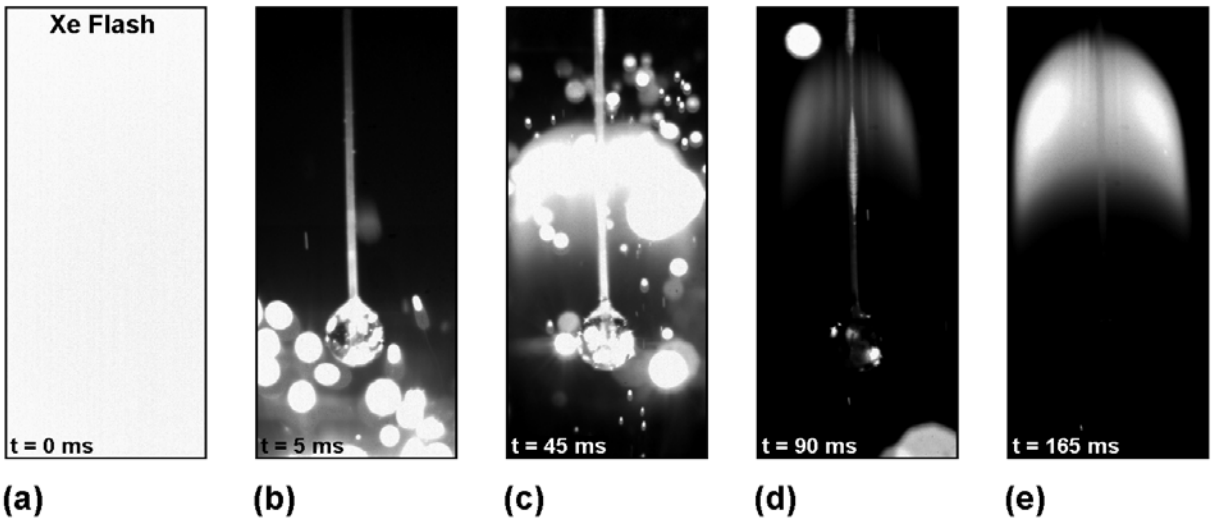

Figure 4. A time sequence of specific burning events for a heptane droplet, demonstrating (a) the Xe-flash light covering the entire field of view, (b) burning Al NPs surrounding the droplet, (c) the initial flame clearly visible, (d) the initial flame almost disappearing, and (e) the primary flame gradually appearing. The framing rate for this time sequence was 1,000 fps and the exposure time was ~ 0.98 ms.

AIAA SciTech Forum
8–12 January 2018, Kissimmee, Florida
2018 AIAA Aerospace Sciences Meeting

10.2514/6.2018-0672

Check for updates

Systematic Measurement of Hydrocarbon Fuel Droplet Burning Rate Constants and Ignition Delays

John W. Bennewitz*, Alireza Badakshan†
ERC Inc., Air Force Research Laboratory, Building 8451, Edwards AFB, CA, 93524

Douglas G. Talley‡
Air Force Research Laboratory, Building 8451, Edwards AFB, CA, 93524

This experimental study investigated droplet burning properties of ten common fuels including two alcohols, four simple hydrocarbons and four kerosene blends. Specifically, ignition delays and burning rate constants were quantified for each of these fuels using a combination of high-speed IR and visible imaging. Ignition delays measured using a short-duration plasma ignitor were 65 to 110 ms for all fuels except for hexadecane, which was 250 ms. Generally, the more volatile fuels with lower boiling temperatures had shorter ignition delays compared with the less volatile fuels. Burning rate constants, K, ranged from 0.74 to 0.94 mm^2/s, which were typically grouped by similarities in thermo-physical properties of the fuel types. It was found that the data reduction method had a sizeable effect on the burning rate constants for non-volatile simple hydrocarbons and kerosenes, varying up to 10%. Hence, a new data reduction approach for the burning rate constant was developed that automatically leads to the best-fit linear regression for the longest duration of droplet burning, and therefore best representing quasi-steady droplet burning processes. This K_β method and its simpler equivalent $K_{\mathrm{end},5,70}$ yielded burning rates that had small statistical uncertainty ($\approx$ 0.006 mm^2/s average) across each of the fuels and were associated with the highest coefficient of determination for all K measurement methods. Therefore, these two methods should be considered as viable options for improved droplet burning rate data reduction.

Nomenclature

a	=	semi-major axis length of the ellipsoidal droplet
b	=	semi-minor axis length of the ellipsoidal droplet
β	=	linear regression coefficient
c_p	=	specific heat capacity
$d_{\mathrm{eqvs.}}$	=	droplet diameter equivalent to the volume of a sphere
η	=	interval for the burning rate constant calculation
γ	=	offset for the burning rate constant calculation
Δh_c	=	heat of combustion
$\Delta h_{\mathrm{vap.}}$	=	heat of vaporization
K	=	burning rate constant
$K_{q,r,s}$	=	burning rate constant identifier where q is the reference location, r and s are the offset and interval
λ	=	thermal conductivity
MW	=	molecular weight
O/F	=	stoichiometric air-fuel ratio
R^2	=	coefficient of determination
ρ	=	mass density
$\tau_{\mathrm{drop.}}$	=	droplet burn time
$\tau_{\mathrm{ign.}}$	=	ignition delay
$T_{\mathrm{adia.}}$	=	adiabatic flame temperature
$\Delta\tau_\eta$	=	interval time

*Research Scientist, ERC Inc., 10 E. Saturn Blvd., Edwards, CA 93524. AIAA Member.
†Research Consultant, ERC Inc., 10 E. Saturn Blvd., Edwards, CA 93524. AIAA Member.
‡Lead, Combustion Dynamics Group, Air Force Research Laboratory, 10 E. Saturn Blvd., Edwards, CA 93524. Associate Fellow.

Distribution Statement A: Approved for Public Release; Distribution is Unlimited. PA Clearance #17745.

Copyright © 2018 by John W. Bennewitz, Alireza Badakhshan, Douglas G. Talley. Published by the American Institute of Aeronautics and Astronautics, Inc., with permission.

Downloaded by Doug Talley on January 10, 2018 | http://arc.aiaa.org | DOI: 10.2514/6.2018-0672

I. Introduction

The study of burning fuel droplets has been used as a basis of fundamental combustion studies for liquid rocket and air-breathing propulsion applications for decades [1–4]. The burning of an isolated droplet provides a convenient way to investigate condensed phase combustion processes. Evaporation of the liquid fuel at the droplet surface leads to a diffusion flame that encompasses the droplet as the fuel vapor reacts with the surrounding oxidizer. This causes the liquid fuel surface to continuously regress, reducing the droplet in size until the end of its lifetime. The rate at which this process occurs is primarily dependent on the thermodynamic properties of the fuel and is often used to quantify droplet burning through the well-established d-squared law [3–6].

The d-squared law states that during quasi-steady droplet burning, the square of the droplet diameter regresses linearly with time. However, this is an idealization which does not fully apply to many real droplets due to several effects, including droplet heating, multicomponent distillation, end-of-life processes such as microexplosions and suspending fiber interference, as well as non-quasisteady effects such as vapor accumulation [4, 7]. Nevertheless, it is useful to quantify results as "effective" burning rate constants. It is shown in the present study that there can be up to a 10% variation depending on how the burning rate constants are effectively measured. As the most direct implementation of the linear regression idea, here we report burning rate constants determined using a method that automatically determines the most linear part of the droplet diameter regression for the longest time. Accompanying correction factors from other commonly used methods to this method for a range of hydrocarbon fuels are also shown.

Recently, there has been substantial experimental work devoted to droplet studies involving the use of energetic additives to liquid fuel as burning rate modifiers [8–13]. As the base liquid fuels for these experiments have included alcohols (i.e., ethanol) and certain kerosene blends (i.e., Jet-A, JP-8), there is a need for baseline burning rate results of a variety of common pure fuels using a consistent approach (i.e., controlling the initial droplet size, experimental procedure, and data reduction method). Also, results from these studies indicated that augmentation of burning rates is possible up to approximately 20% for additive concentration ≤5 wt%, but is typically no greater than 10%. Our group currently is investigating the use of nanoenergetic additives as a method to garner control of combustion dynamics, and to date, has performed a series of suspended nanofuel droplet studies using various rocket relevant base fuels (e.g., RP-2). As the enhancements in droplet burning rate reported by the various research groups are measured using different methods, it was necessary to quantify the error attributed with the burning rate measurement method for a range of pure fuels to better interpret our results. Therefore, the current study presents droplet burning rate and ignition delay baseline data for a broad range of ten common hydrocarbon fuels, while also including a sensitivity study on the burning rate constant that encompasses all reasonable possibilities and commonly implemented methods. Through this process, a new approach to determine the droplet burning rate was developed that consistently provides a better measure of the "effective" droplet burning rate constant for all fuel types.

II. Experiment setup and data processing

The current study investigated droplet burning properties of various hydrocarbon fuels within an ambient air environment using the suspended droplet method. Droplets 1.35±0.05 mm in diameter were suspended from an uncoated 0.15 mm quartz fiber from Polymicro Technologies Inc., with a bead at the end (see Fig. 1). A bead was generated on the end of the quartz fiber through a heating process using an oxy-propane torch, which assisted with the retention of the droplet on the fiber during burning. Droplets were transferred to the quartz fiber mechanically using a hypodermic needle that would consistently dispense the same amount of fluid to create droplets of similar size for each test.

Droplet burning was captured with a backlit imaging system consisting of a Phantom v7.1 high-speed camera with white background illumination. The high-speed camera was fitted with a Nikon AF Micro Nikkor 200 mm lens and operated at 1,000 fps for the duration of the droplet lifetime (approximately 2 seconds), with a Semrock FF01-433/530-25 filter used to provide improved visibility of the droplet regression for sooting fuels. To provide the proper contrast between the liquid droplet and illuminated background for image processing, a 2X2 rectangular array of adjustable white light-emitting diodes (LED's) was implemented.

For tests examining the ignition behavior of these hydrocarbon fuels, infrared (IR) thermal imaging was used to clearly view the evolution of the reaction zone enveloping the droplet. This entailed substituting the Phantom v7.1 high-speed camera with a FLIR SC6800 mid-wave infrared (1.5–5.0 μm) camera imaging at 250 fps, or simultaneously imaging with both. To provide full-scale measurements and prevent saturation with the IR camera, a 0.6 neutral density filter was used in combination with a StingRay Optics SR1936-A01 50 mm lens.

Distribution Statement A: Approved for Public Release; Distribution is Unlimited. PA Clearance #17745.

Downloaded by Doug Talley on January 10, 2018 | http://arc.aiaa.org | DOI: 10.2514/6.2018-0672

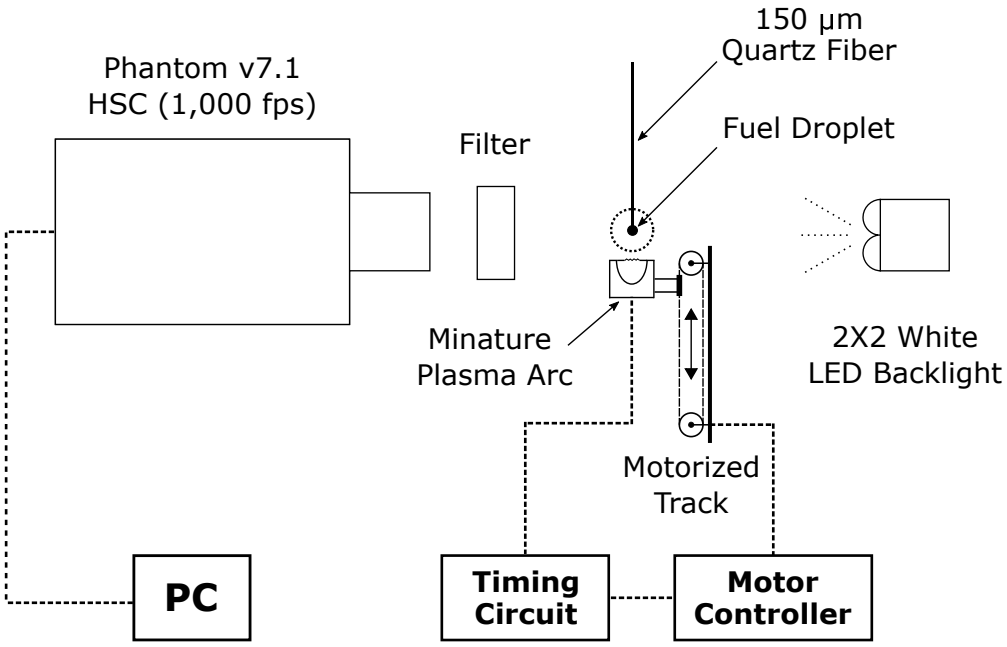

Fig. 1 Droplet experiment test facility consisting of the high-speed imaging configuration for the suspended fuel droplet and the plasma arc ignition system connected to the automated motorized track. For the ignition delay experiments, a FLIR SC6800 was used in place of the Phantom v7.1 or in tandem at a 45 degree offset angle.

A. Ignition System: Plasma Arc Ignitor

Droplets were ignited using a miniature plasma arc ignition (PAI) system, which consisted of a controllable duration plasma source that was scaled appropriately to the droplet length scale. The electrodes of the PAI system had a gap of 5 mm and were placed about 1 mm beneath the suspended droplet during the onset of ignition. The arc was found to be a periodic impulse with an exponential decay, where the plasma pulse duration was estimated to be on the order of a few microseconds and had a discharge repetition rate of 20,500 Hz.

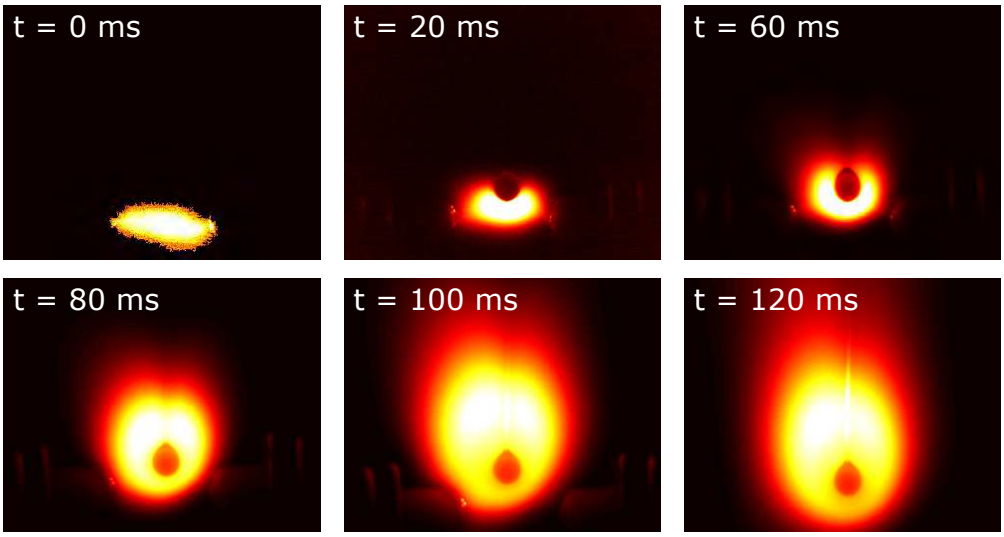

Fig. 2 Infrared thermographic images depicting the ignition sequence of an n-dodecane droplet using the plasma arc ignition system with a duration set to 100 ms.

Distribution Statement A: Approved for Public Release; Distribution is Unlimited. PA Clearance #17745.

Downloaded by Doug Talley on January 10, 2018 | http://arc.aiaa.org | DOI: 10.2514/6.2018-0672

The plasma arc ignitor was integrated with a custom built timing circuit and motor controller. The timing circuit allowed the total arc duration to be adjusted for reliable droplet ignition, where the motor controller automatically pulled the ignitor away from the droplet after the set arc duration. It was found that all hydrocarbon fuels investigated in this study were consistently ignited within 100 ms of arc duration, except for hexadecane, which required 250 ms. A typical sequence for droplet ignition can be seen in Fig. 2. This figure shows the entire ignition process occurred in 100 ms, where the reaction zone of the n-dodecane droplet grew and fully established by the time the ignitor was moved away from the droplet. This fast duration ignition method was chosen for this study as it acts only over a fraction of the total droplet lifetime, essentially isolating quasi-steady droplet burning from ignition effects. To the best of the authors' knowledge, this is the first study implementing the use of such an ignitor for investigating droplet burning. A detailed description of the PAI system and a comparison with other ignition methods is covered in another publication [14].

B. Droplet Burning Properties

With the fuels burned in the suspended droplet configuration, the two burning parameters investigated in this study are the burning rate constant K and ignition delay $\tau_{\text{ign.}}$. The burning rate constant is the governing parameter for quasi-steady droplet burning behavior, which comes from the well-known d^2-law [4–6], and is written as

$$K = \frac{d}{dt}(d_{\text{eqvs.}})^2. \tag{1}$$

In this study, the diameter used to determine K was the droplet diameter associated with the equivalent volume of a sphere as described by Struk et al. [15]. This equivalent diameter is given by

$$d_{\text{eqvs.}} = 2a^{2/3}b^{1/3}, \tag{2}$$

where a and b are the semi-major and minor axis lengths associated with the ellipsoidal droplet.

For each test, the droplet diameter was automatically tracked using a modified MATLAB$^{\text{TM}}$ script based on the work of Bennewitz et al. [16] and Sevilla-Esparza et al. [17]. This script takes the series of backlit images captured from the visible high-speed camera starting 200 ms after the ignitor is activated and fits an ellipse to the outer edge of the droplet for each image. With the outline of the droplet edge defined, the instantaneous equivalent diameter regression can then be determined using Eq. 2 for the entire droplet burn time, $\tau_{\text{drop.}}$. An example image sequence depicting the diameter tracking of a burning RP-2 droplet and its corresponding normalized d^2-regression can be seen in Fig. 3(a) and (b), respectively.

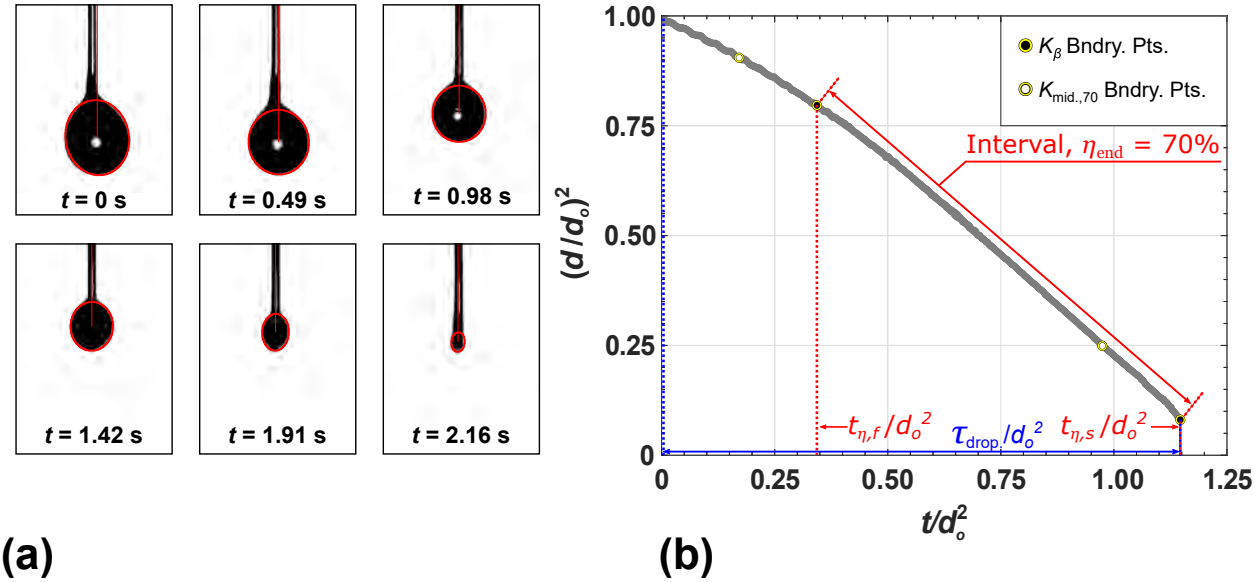

Fig. 3 Time sequence depicting the (a) droplet diameter edge detection of a burning RP-2 droplet outlined in red and the (b) corresponding normalized droplet diameter regression.

Downloaded by Doug Talley on January 10, 2018 | http://arc.aiaa.org | DOI: 10.2514/6.2018-0672

Distribution Statement A: Approved for Public Release; Distribution is Unlimited. PA Clearance #17745.

In multicomponent fuels such as RP-2 and non-volatile pure hydrocarbons, there can exist pronounced non-linear droplet diameter regression effects throughout the droplet burn time, as observed at the beginning of the burning RP-2 droplet in Fig. 3(b). Non-linear droplet burning behavior can include initial heating effects, multicomponent effects such as individual constituents exhibiting different burning behavior, as well as end-of-life effects such as microexplosions and suspension fiber influences [18]. When these behaviors are present, determining the proper portion of data to be used in the K calculation that is most representative of steady burning (i.e., most linear) is important, as this can have a significant effect on the reported K value.

In our previous work on pure hydrocarbon fuels [19], K was evaluated using 70% of the data centered around the midpoint of the droplet burn time, referred to as the $K_{\text{mid.,70}}$ approach. This was done to add consistency to the data reduction methodology and attempt to remove the effects of transient behavior. However, previously, there was no detailed sensitivity study performed to evaluate the $K_{\text{mid.,70}}$ approach and assess alternative techniques that may be more suitable as the "effective" burning rate constant for all fuels.

To address this point, K was calculated a multitude of different ways for a single set of data. A conceptual example depicting the diameter regression of a burning droplet exhibiting some non-linear effects is shown in Fig. 4, which specifies the parameters used to determine K. First, the three general data reduction schemes implemented for this study are shown: (1) beginning, (2) middle, and (3) end. As their names suggest, each denotes the reference location of the considered data set. Starting at these three reference points, the script separately calculated K for a range of specified intervals and offsets.

The offset γ is the amount of data that is discarded from both the start and finish of the droplet burn time ($t_{\alpha,s}$ and $t_{\alpha,f}$) to the beginning and end reference points ($t_{\eta,\text{beg.,s}}$ and $t_{\eta,\text{end.,s}}$). The offset is defined as a percentage of the entire burn time (i.e., $\gamma = X/Y$ in Fig. 4), and is applied to both ends of the test symmetrically. The interval η is the portion of data that is considered past the beginning and end reference points, namely $t_{\eta,\text{beg.,s}}$ to $t_{\eta,\text{beg.,f}}$ or $t_{\eta,\text{end.,s}}$ to $t_{\eta,\text{end.,f}}$, respectively. Similarly, the interval is given as a percentage of the two bounding reference points ($t_{\eta,\text{beg.,s}}$ and $t_{\eta,\text{end.,s}}$), where $\eta_{\text{beg.}} = B/Z$ and $\eta_{\text{end}} = E/Z$ in Fig. 4. For the cases starting in the middle of the droplet regression, only the interval $\eta_{\text{mid.}}$ was required, and therefore was given as a percentage of the total burn time (i.e., $\eta_{\text{mid.}} = M/Y$).

For each interval and offset, K was calculated by taking the corresponding amount of droplet diameter regression data and fitting a linear regression through the data and determining the slope. In this study, the notation for the burning rate constant is $K_{q,r,s}$, where q is the reference location (i.e., beginning, middle or end), and r and s are the offset and interval percentages, respectively. It should be noted that when the offset is 0%, r is omitted and the notation becomes $K_{q,s}$. By applying these definitions to actual data, examples of $K_{\text{end,70}}$ and $K_{\text{mid.,70}}$ are indicated in Fig. 3(b), where the boundary points for $K_{\text{end,70}}$ and $K_{\text{mid.,70}}$ are shown in black and white, respectively. A continuation of this example comparing the various K values attained is found in Section III.A.

In this study, the applied offset ranged from 0-15% from each side in increments of 2.5% for the cases with the beginning and end as the reference. For each offset, values of $K_{\text{beg.}}$ and K_{end} were calculated at each interval from 1-100% in increments of 1% by fixing $t_{\eta,\text{beg.,s}}$ and $t_{\eta,\text{end.,s}}$ and correspondingly varying $t_{\eta,\text{beg.,f}}$ and $t_{\eta,\text{end.,f}}$, respectively; this totaled 100 values each for $K_{\text{beg.}}$ and K_{end} at every offset and 700 separate values overall. Again, cases starting at the middle of the test required no applied offset, as all $K_{\text{mid.}}$ values were covered by intervals spanning from the 1-100%. These 1500 total cases were chosen to adequately cover all reasonable methods to determine K and reduce the overall number of redundant cases. A summary of the three data reduction schemes is presented in Table 1.

Table 1 Various data reduction schemes implemented for calculating the burning rate constant of a single set of data.

Scheme	Offset, γ	Interval, η	Total K Values
Beginning	0-15%, 2.5% increments	1-100%, 1% increments	700
Middle	0%	″	100
End	0-15%, 2.5% increments	″	700

Distribution Statement A: Approved for Public Release; Distribution is Unlimited. PA Clearance #17745.

Downloaded by Doug Talley on January 10, 2018 | http://arc.aiaa.org | DOI: 10.2514/6.2018-0672

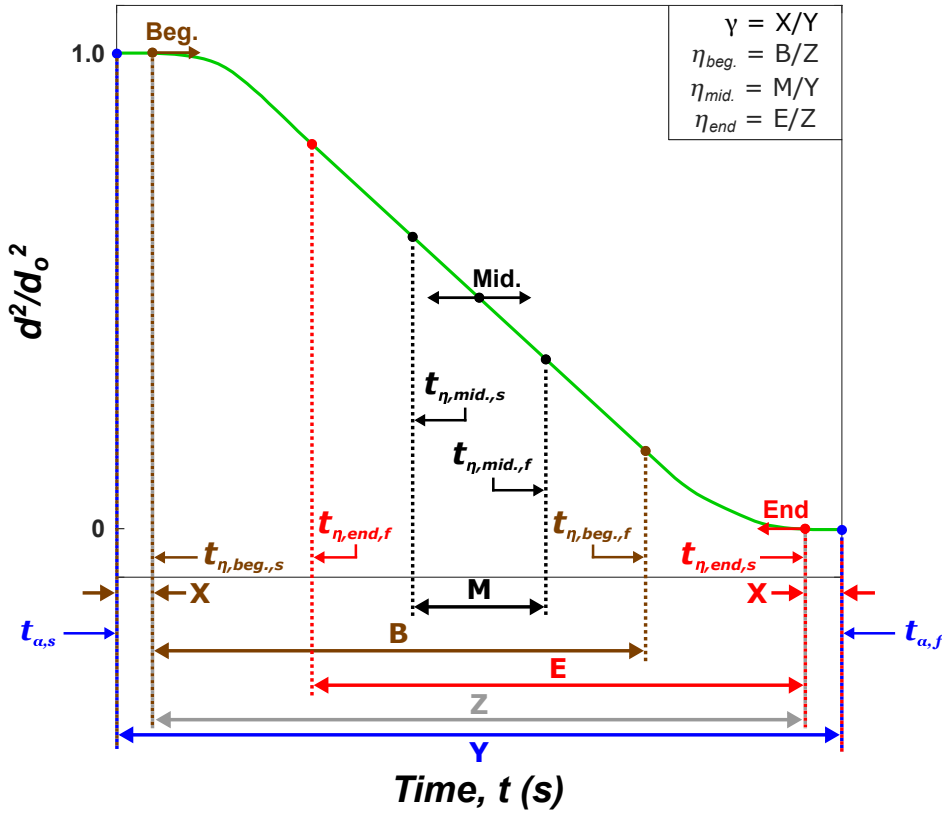

Fig. 4 Conceptual droplet diameter regression depicting some non-linear regression behavior and defining the offset γ and interval η for $K_{\text{beg.}}$, $K_{\text{mid.}}$, and K_{end}.

Ignition delay $\tau_{\text{ign.}}$ was the second parameter evaluated in this study. Igniting suspended droplets via the short-duration plasma arc provided a convenient platform to study ignition behavior due to its constant average output power and adjustable ignition duration. As the plasma arc produced minimal background light and heat [14], details of ignition and the development of the flame early in the droplet lifetime were readily captured. Typically, ignition delay is defined as the time separation between introducing the droplet to the (hot) ignition environment and the observation of the established flame [20]. While it is straightforward to define the first event, naturally there is some subjectivity associated with the second. In general, the fully-established flame is associated with an enveloping reaction zone around the droplet that is on the order of the droplet diameter [20]. For the various hydrocarbons studied, the flame originates beneath the droplet close to the ignitor location, and quickly grows to a maximum before slightly reducing in size at the start of steady burning. Therefore, $\tau_{\text{ign.}}$ was taken to be the time the ignitor is first activated to the time the droplet flame reaches an initial maximum size, which represents the upper limit of the ignition delay for each fuel.

To provide a consistent approach for $\tau_{\text{ign.}}$, the flame region was automatically tracked in the IR images using an image processing script. Example results for ethanol are shown, for reference, in Fig. 5. This depicts an image sequence of the tracked flame region along with nondimensionalized time traces of the flame pixel area $A_{\text{pxl.}}$ and integrated thermal radiance I, corresponding to $\tau_{\text{ign.}}$ = 68 ms. $A_{\text{pxl.}}$ is the number of pixels contained within the tracked flame region and is indicative of the reaction zone size, while I is the summation of the thermal radiance counts captured by the IR camera within the defined flame region. Although the ignition delays reported here were evaluated using the maximum flame pixel area, there is general agreement with the time associated with an initial maximum in integrated thermal radiance as well. Similar results for $\tau_{\text{ign.}}$ were produced using visible imaging, often simultaneous with the IR images. Visible imaging is reliant on the flame luminosity, which differs among the fuels in this study largely due to soot formation. Therefore, ignition delays from visible imaging were deemed to be less reliable than the IR results, leading to only the IR results being reported in this study.

Downloaded by Doug Talley on January 10, 2018 | http://arc.aiaa.org | DOI: 10.2514/6.2018-0672

Distribution Statement A: Approved for Public Release; Distribution is Unlimited. PA Clearance #17745.

Downloaded by Doug Talley on January 10, 2018 | http://arc.aiaa.org | DOI: 10.2514/6.2018-0672

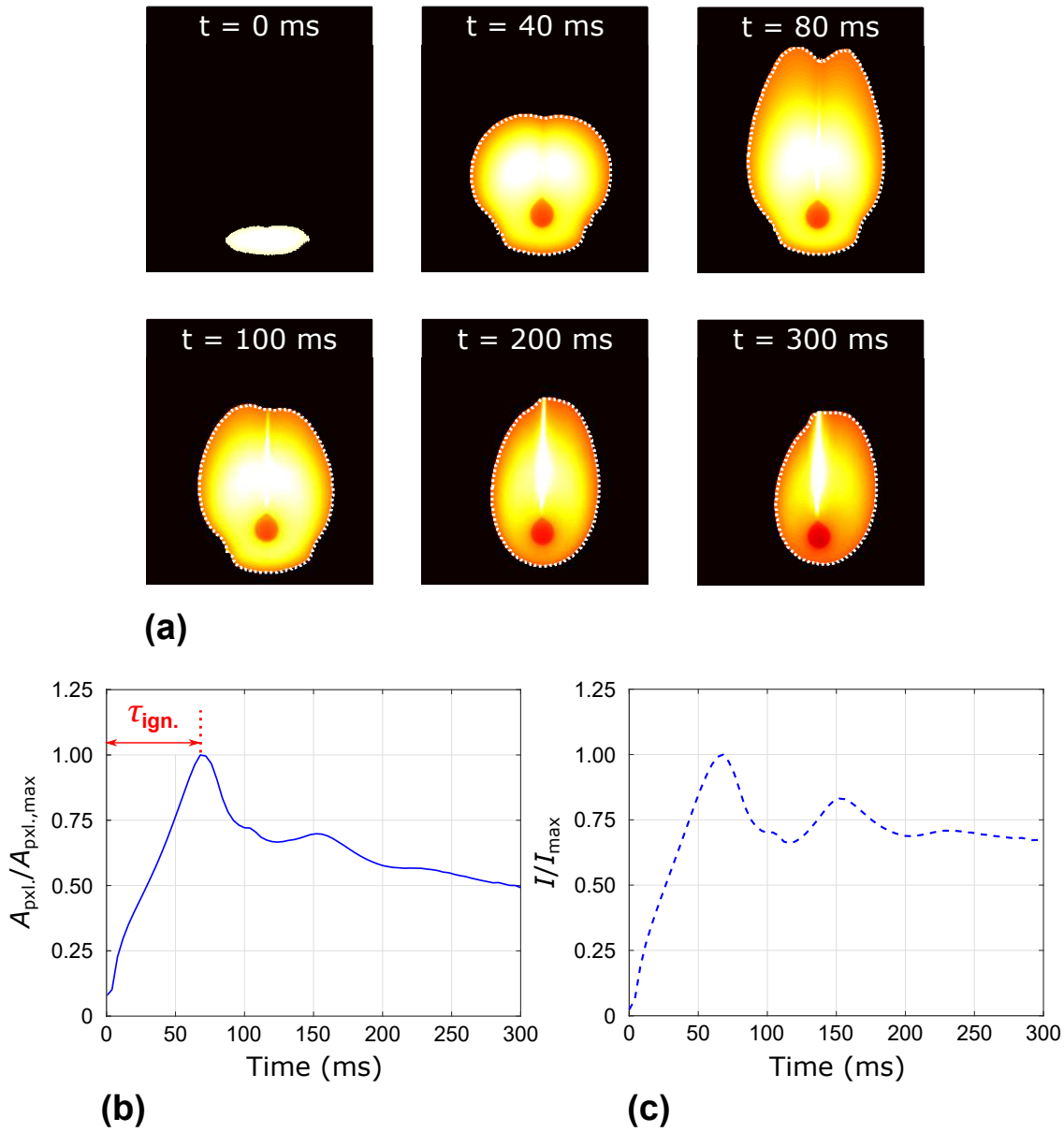

Fig. 5 Time sequence of the (a) ignition process of an ethanol droplet, with the corresponding (b) tracked pixel area of the flame and (c) integrated thermal radiance taken from the infrared images.

III. Results

Droplet burning properties were investigated for ten various hydrocarbon fuels, encompassing alcohols (i.e., ethanol, methanol), simple hydrocarbons (i.e., n-heptane, toluene, n-dodecane and hexadecane), and kerosene blends including rocket grade kerosene RP-2, diesel #2 and the aviation fuels JP-8 and its surrogate Fischer-Tropsch synfuel (FT). These fuels were chosen as they represent a large range of common hydrocarbons and alternative fuels implemented in rocket engine and air-breathing propulsion systems [21–23]. These three fuel types can be broadly classified by their thermo-physical properties, which are documented in Tables 2 and 3.

The thermodynamic characteristics of the two alcohols, while similar to each other, vary significantly from the other pure hydrocarbons and kerosene blends. Similar trends can be seen for the four pure hydrocarbons, with a notable difference in particular for the heats of vaporization $\Delta h_{vap.}$ and combustion Δh_c when compared to the alcohol fuels. Generally, there is some spread among these simple hydrocarbons in thermo-physical properties, which typically

Distribution Statement A: Approved for Public Release; Distribution is Unlimited. PA Clearance #17745.

Table 2 Thermodynamic characteristics of the pure hydrocarbon fuels [16, 24]

Fuel Property	Ethanol	Methanol	n-Heptane	Toluene	n-Dodecane	Hexadecane
Chemical Formula	C_2H_5OH	CH_3OH	C_7H_{16}	C_7H_8	$C_{12}H_{26}$	$C_{16}H_{34}$
Molecular Weight [kg/kmol]	46.07	32.04	100.21	92.14	170.34	226.45
Stoichiometric Air-Fuel Ratio, O/F	8.946	6.431	15.081	13.418	14.920	14.863
Specific Heat Cap.*, c_p [kJ/(kg-K)] [25]	2.44	2.50	2.24	1.70	2.21	2.21
Thermal Cond.*, λ [W/(m-K)] [26]	0.167	0.202	0.123	0.131	0.135	0.140
Mass Density*, ρ [g/cm^3] [26]	0.79	0.79	0.68	0.86	0.75	0.77
Boiling Temp., T_b [K] [26]	351	338	372	384	489	560
Vapor Pressure*, $P_{\text{vap.}}$ [kPa] [25]	7.9	16.9	6.1	3.8	1.5E-02	9.6E-05
Adiabatic Flame Temp., $T_{\text{adia.}}$ [K] [6]	2195	2150	2265	2317	2268	2269
Heat of Vapor.$^+$, $\Delta h_{\text{vap.}}$ [kJ/kg] [26]	837	1099	317	360	259	229
Heat of Comb.*, Δh_c [kJ/g] [26]	29.7	22.7	48.1	42.4	47.2	47.2
Energy Density, [kJ/cm^3]	23.5	17.9	32.7	36.5	35.4	36.3

* Calculated for T = 298 K and P = 101,325 Pa

\+ Calculated for $T = T_b$ and P = 101,325 Pa

span the range of values characteristic of the kerosene blends. This can be attributed to these simple hydrocarbons representing some of the lighter (e.g., n-heptane, toluene) and heavier (e.g., n-dodecane, hexadecane) constituents found in the various kerosene fuels. To investigate the effects of these different constituents further, the burning properties of a 50/50 wt% binary mixture of n-heptane and n-dodecane were also quantified. Finally, the kerosenes share similar properties to each other, with JP-8 and FT in particular in close agreement, which is the main reason Fischer-Tropsch has been authorized for use as a JP-8 replacement in Air Force applications [27].

A. Burning Rate Constant Sensitivity

The approach detailed in Section II.B was implemented to determine K using the data reduction schemes summarized in Table 1. To examine the sensitivity of the burning rate constant to the data reduction technique, the coefficient of determination R^2 was first calculated for each K value over the same data ranges for K. The coefficient of determination is a well-established parameter that indicates how well the linear regression fits the data, with a value that ranges from zero to one, where R^2 equaling one signifies a perfect fit [42]. Again consider the RP-2 example, where the droplet initially regressed slower than over the remaining $\approx$ 75% of its lifetime, which appeared to be more linear with a considerable steeper slope as shown in Fig. 3(b). Examining the R^2 distribution for this data set, there is a wide distribution of K values corresponding to high coefficients of determination (see Fig. 6(a)). Specifically, the burning rate constant varied from 0.57 to 1.0 mm^2/s for R^2 values above 0.997, which would initially indicate a very representative fit. Therefore, there is significant limitation to reporting solely the raw coefficient of determination value as a justification of the data reduction method in determining the burning rate constant. Examining this R^2 distribution of K further, there exists three distinct R^2 peaks for each of the beginning, middle, and end schemes corresponding to K equaling 0.659, 0.867, and 0.919 mm^2/s, respectively. The R^2 values associated with these peaks increase from 0.9986 to 0.9999 from beginning to end, consistent with droplet burning for RP-2 approaching linear regression behavior towards the end of the droplet burn time.

Downloaded by Doug Talley on January 10, 2018 | http://arc.aiaa.org | DOI: 10.2514/6.2018-0672

Distribution Statement A: Approved for Public Release; Distribution is Unlimited. PA Clearance #17745.

Table 3 Thermodynamic characteristics of the kerosene fuels [16, 24]

Fuel Property	RP-2	JP-8	FT	Diesel #2
Average Chemical Formula	$C_{11.74}H_{23.40}$ [28]	$C_{11}H_{21}$	$C_{12}H_{25}$	$C_{12}H_{23}$
Molecular Weight [kg/kmol]	164.60	153.29	169.34	167.32
Stoichiometric Air-Fuel Ratio, O/F	14.681	14.563	14.806	14.574
Specific Heat Cap.*, c_p [kJ/(kg-K)]	2.03† [29]	1.92	2.73	2.20 [30]
Thermal Cond.*, λ [W/(m-K)]	0.107 [28, 31]	0.115	9.35E-03	0.125 [32]
Mass Density*, ρ [g/cm^3]	0.80 [28, 33]	0.81	0.76	0.83 [32]
Boiling Temp., T_b [K]	438-498 [28]	413-573	448-633	453-613 [34]
Vapor Pressure*, $P_{\text{vap.}}$ [kPa]	5.7E-02 [28]	1.8E-01 [35]	21 [36]	7.7E-02 [37]
Adiabatic Flame Temp., $T_{\text{adia.}}$ [K]	-	2338 [38]	2338 [38]	2292 [39]
Heat of Vapor.+, $\Delta h_{\text{vap.}}$ [kJ/kg]	308† [40]	441	339	270 [30]
Heat of Comb.*, Δh_c [kJ/g]	44 [28, 41]	43	44	46.1 [30]
Energy Density, [kJ/cm^3]	35.2	34.8	33.4	38.3

* Calculated for T = 298 K and P = 101,325 Pa

\+ Calculated for $T = T_b$ and P = 101,325 Pa

† For $C_{12}H_{23.40}$

One drawback associated with only using the coefficient of determination to find a specific K that effectively represents quasi-steady burning is that this parameter does not account for the duration of the droplet burning considered. As the burning rate constant is an idealization used to describe the steady-state droplet burning rate, the effective K should be associated with the best linear fit spanning the longest duration of the droplet lifetime. Hence, it was necessary to introduce a new parameter referred to as the linear regression coefficient β, which equally weights the coefficient of determination and the amount of data considered. This is written as

$$\beta(i) = R^2(i)\left|\frac{\Delta t_\eta(i)}{\tau_{\text{drop.}}}\right|, \tag{3}$$

where $\tau_{\text{drop.}}$ is the total droplet burn time and $\Delta t_\eta(i) = t_{\eta,f}(i) - t_{\eta,s}(i)$ is the interval time associated with the specific case. It should be noted that $R^2(i)$ was rescaled in the beta calculation by applying a correction factor based on the percentage of $R^2(i)$ compared to the maximum R^2 value for all considered cases. Modifying R^2 in this fashion equally redistributed the values between zero and one for ease of identifying the maximum β, as the non-scaled R^2 values were all typically greater than 0.99. Therefore, the linear regression coefficient also ranges from zero to one, where the highest value corresponds to the K that is a best fit to the droplet regression data for the longest duration of droplet burning.

The β distribution for the RP-2 data set shows that all three data reduction schemes again converge to distinct maximums similar to the R^2 distribution (see Fig. 6(b)). Specifically, calculating K from the end of the test corresponds to significantly higher β values than those taken from the middle or beginning. In this study, K_β was found by averaging the top 5% of the K values according to β. Hence, K_β was 0.896 mm^2/s, with R^2 equaling 0.9993, which differed substantially from the previous $K_{\text{mid.,70}}$ approach at 0.831 mm^2/s and R^2 = 0.9962; this corresponds to a percent error of ≈ 7%, which demonstrates the data reduction methodology can play a large role in affecting the value of the calculated droplet burning rate. Therefore, it is critical for the measurement approach to be consistent and well-defined for reporting meaningful results.

Distribution Statement A: Approved for Public Release; Distribution is Unlimited. PA Clearance #17745.

Downloaded by Doug Talley on January 10, 2018 | http://arc.aiaa.org | DOI: 10.2514/6.2018-0672

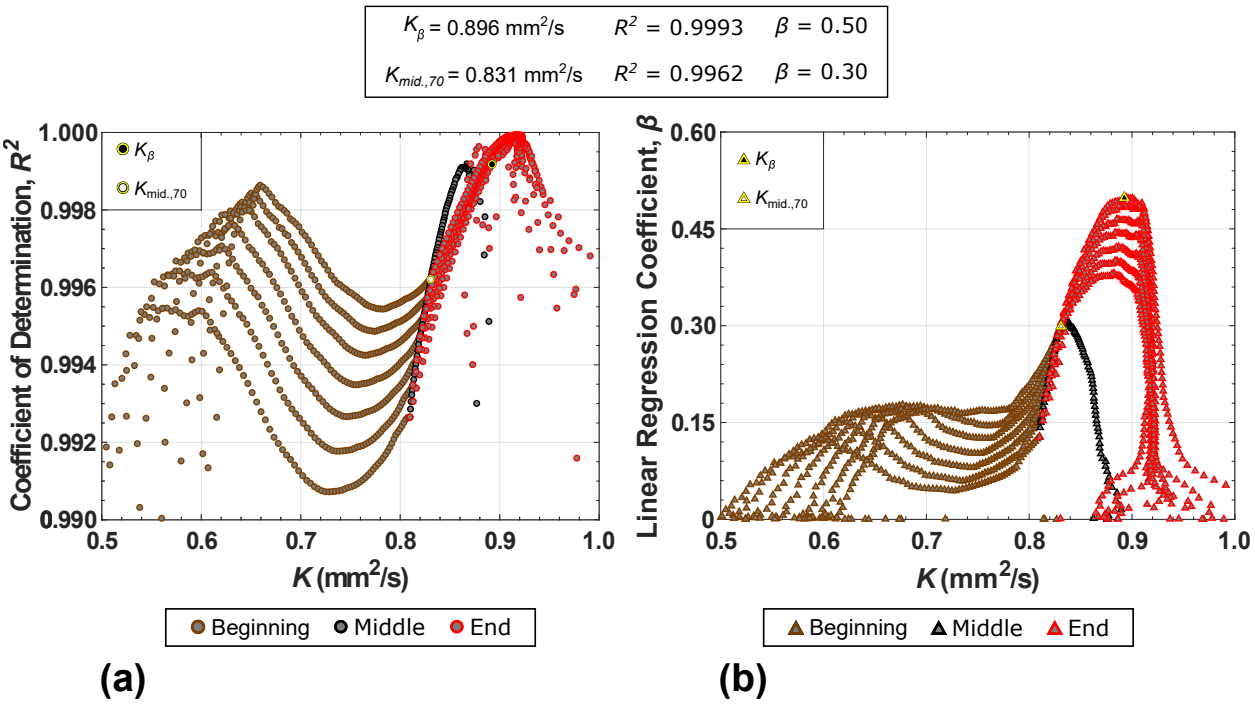

Fig. 6 Sensitivity of the droplet burning rate constant K for an RP-2 droplet, showing the (a) coefficient of determination R^2 and (b) linear regression coefficient β values for the various data reduction cases.

Performing the same R^2-β analysis for a volatile fuel (i.e., ethanol), although the droplet diameter regression is very linear (see Fig. 7(a)), K still appears to have a large variation for R^2, as shown in Fig. 7(b). The burning rate constant ranges approximately from 0.60 - 0.90 mm^2/s all with R^2 values greater than 0.997. However, unlike for RP-2, all three data reduction schemes broadly converge to a K value of about 0.75 mm^2/s for the highest R^2 values approaching 1.0.

The β distribution for this ethanol test shows all three data reduction schemes converge to a single well-defined peak at a maximum of β = 0.75, as indicated in Fig. 7(c). Specifically, K_β was 0.746 mm^2/s, with an R^2 of 0.9999. Comparing this result to $K_{\text{mid.,70}}$ showed very slight deviation, as $K_{\text{mid.,70}}$ = 0.744 mm^2/s with R^2 also being 0.9999. This is expected because the droplet diameter regression for this fuel happens to be very linear throughout its lifetime and thus, was fairly insensitive to the data reduction approach.

B. Burning Rate Constant Summary

Individual series of 15 droplet burning tests were performed for all ten hydrocarbon fuels, as well as the 50/50 wt% blend of n-heptane and n-dodecane, to produce statistically reliable data for K. To quantify the statistical uncertainty of K and remove outlying data, the Student's t-distribution for small sample size [43] along with Chauvenet's rejection criteria [42] were implemented to provide a 95% confidence interval on the reported values. The droplet burning rates for these fuels ranged from 0.74 to 0.94 mm^2/s, with the lowest K_β value for ethanol and the highest for n-heptane, as shown in Fig. 8(a). In general, the burning rate constants were grouped according to their thermo-physical properties, where the alcohol fuels exhibited the lowest K_β values and the more volatile simple hydrocarbons including n-heptane and toluene were on the upper end. The less-volatile hydrocarbons n-dodecane and hexadecane were in between and similar to the other complex hydrocarbons. The three aerospace kerosenes all were very similar to each other with $K_\beta \approx$ 0.89 mm^2/s and diesel #2 being lower at 0.85 mm^2/s.

Comparing the K_β results to $K_{\text{mid.,70}}$ (see Fig. 8(b)), the burning rate constant was generally insensitive to the data reduction approach for the more volatile fuels including the two alcohols, n-heptane, and toluene. However, there was significant deviation up to 10% for the less-volatile simple hydrocarbons and all four kerosene fuels, where $K_{\text{mid.,70}}$ was found to be consistently lower than K_β. Also, the statistical uncertainty associated with the K_β values was extremely small with the average being 0.006 mm^2/s for all fuels, as well as consistently higher R^2 values compared to $K_{\text{mid.,70}}$. Hence, the reported K_β values are shown to be more representative of the "effective" droplet burning rate across all fuel

Downloaded by Doug Talley on January 10, 2018 | http://arc.aiaa.org | DOI: 10.2514/6.2018-0672

Distribution Statement A: Approved for Public Release; Distribution is Unlimited. PA Clearance #17745.

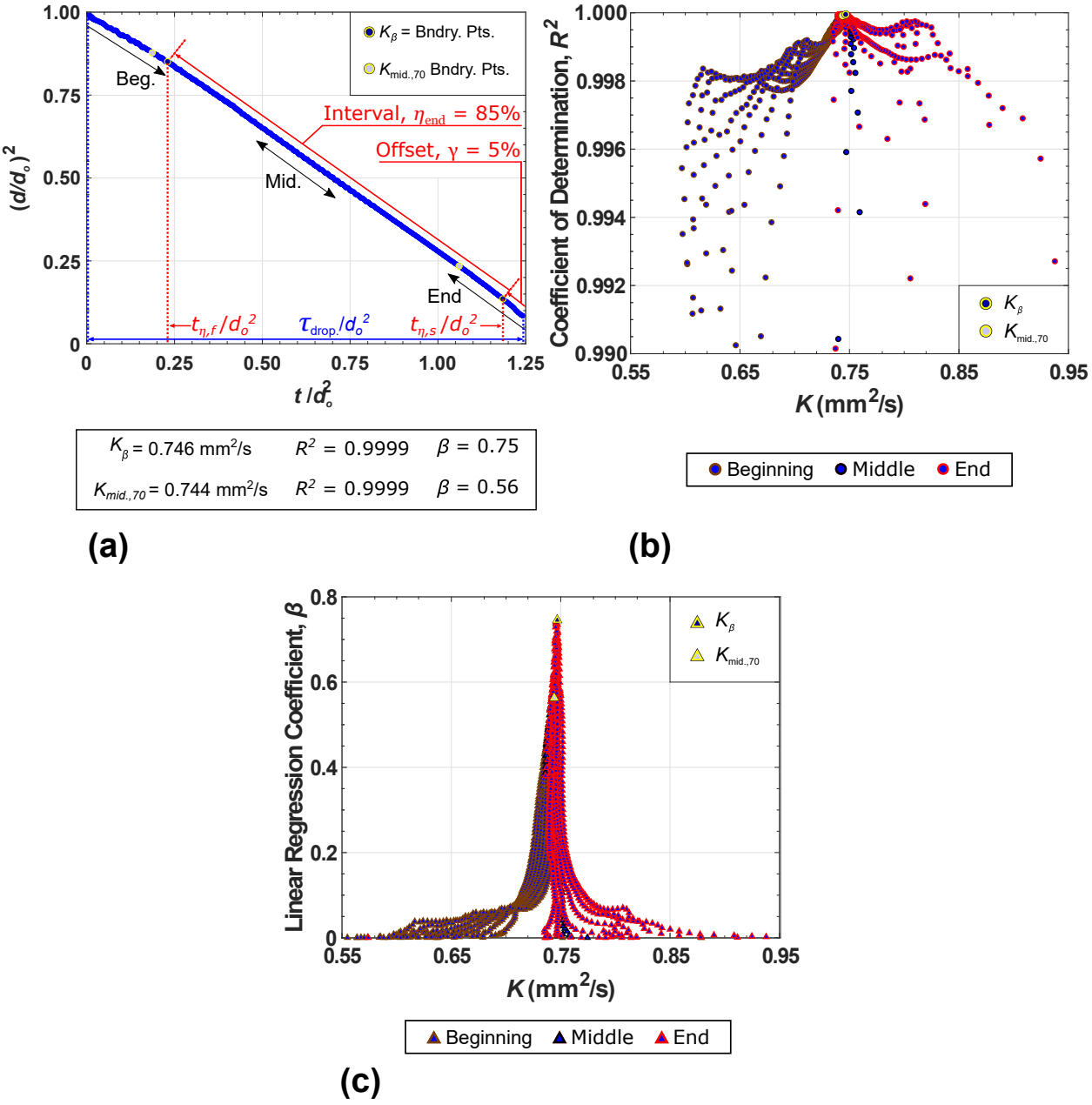

Fig. 7 Sensitivity of the droplet burning rate constant K for an ethanol droplet, depicting the (a) normalized droplet diameter regression and the corresponding (b) coefficient of determination R^2 and (c) linear regression coefficient β values for the various data reduction cases.

types. However, it is recognized that the process to quantify K_β is rather extensive, therefore, a simpler alternative was found by taking K_β as the accepted value and calculating the percent error for each of the 1500 cases in each test across all ten fuels. The percent errors calculated for the 1500 cases across each fuel test were then all averaged together and $K_{end,5,70}$ was found to be the best alternate that overall minimized the percent error to K_β.

As the burning rate constant has proven to be dependent on the data reduction method, there are some challenges in comparing results across different droplet studies found in the literature as often the approach to find K is not explicitly stated. However, there are some commonly implemented ways to determine K including $K_{mid.,70}$, $K_{mid.,80}$ [12, 44], and $K_{two-pt.}$ [11], which is based only on the initial droplet diameter and the droplet burn time. Using the pure fuel data

Distribution Statement A: Approved for Public Release; Distribution is Unlimited. PA Clearance #17745.

Downloaded by Doug Talley on January 10, 2018 | http://arc.aiaa.org | DOI: 10.2514/6.2018-0672

Downloaded by Doug Talley on January 10, 2018 | http://arc.aiaa.org | DOI: 10.2514/6.2018-0672

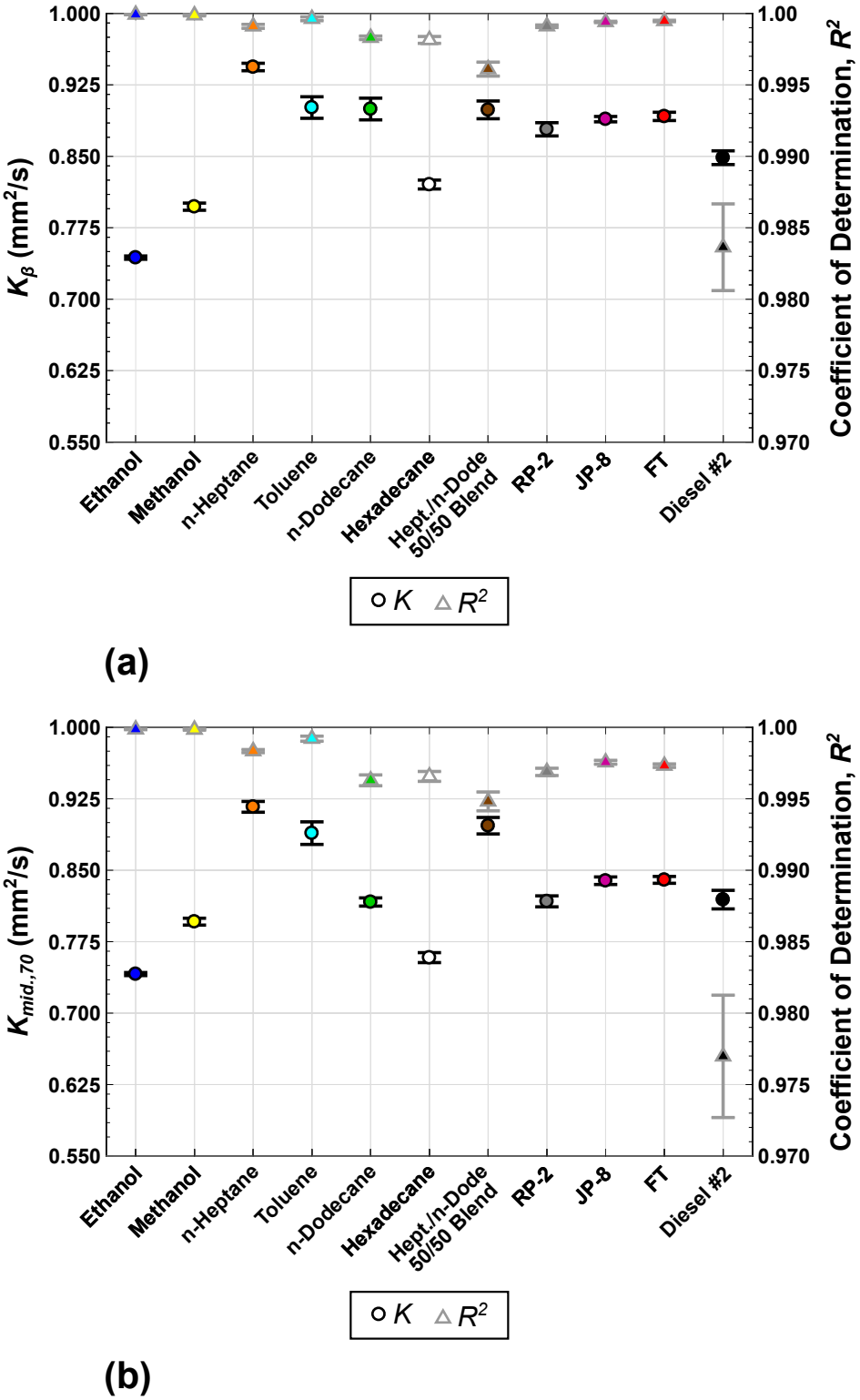

Fig. 8 Droplet burning rate constant K summary for the various hydrocarbon fuels using the (a) K_β and (b) $K_{\text{mid.},70}$ approaches.

Distribution Statement A: Approved for Public Release; Distribution is Unlimited. PA Clearance #17745.

Table 4 Summary of the average percent error and correction in K for the non-volatile fuels (excluding diesel #2) determined using the select approaches.

Approach, K_i	Average K Error %	Average R^2	Average Correction Factor, C_o
$K_{\text{mid.,70}}$	7.09	0.9969	1.071
$K_{\text{mid.,80}}$	7.69	0.9959	1.077
$K_{\text{two-pt.}}$	9.36	-	1.094
$K_{\text{end,5,70}}$	0.58	0.9989	1.006

collected in this study for the non-volatile fuels (excluding diesel #2), K was calculated using these different methods and compared to K_β, as summarized in Table 4. As expected, $K_{\text{two-pt.}}$ deviated by the largest margin of 9.36% as it is the coarsest method implemented, while $K_{\text{end,5,70}}$ was the closest to K_β at only 0.58% average error, while also having the same average R^2 value as K_β at 0.9989. Therefore, $K_{\text{end,5,70}}$ is a suitable alternative to K_β. A proposed correction factor C_o (see Table 4) could be used to find the equivalent K_β value, which takes the form $K_\beta \approx C_o K_i$. All of the correction factors for the four K methods were above one as they all are consistently lower than K_β. It should be noted that this correction factor is only required for fuels that have demonstrated a sensitivity to the data reduction approach as with the non-volatile hydrocarbon fuels and kerosenes.

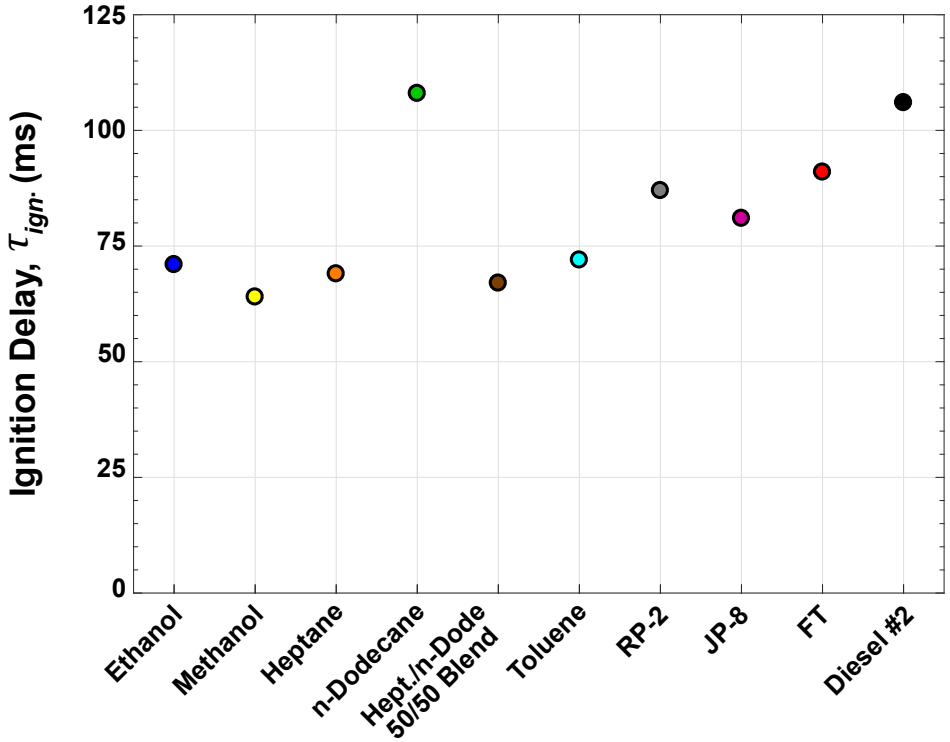

Fig. 9 Ignition delay $\tau_{\text{ign.}}$ summary for the various hydrocarbon fuels (excluding hexadecane) evaluated from the infrared thermal images.

C. Ignition Delay Summary

Ignition delays for these fuels were measured by taking an average of five identical ignition events and post-processing the IR images using the procedure described in Section II.B. It was found that $\tau_{\text{ign.}}$ ranged from 65 to 110 ms for all fuels except for hexadecane, which was much longer at 250 ms, as this fuel had an extremely low vapor pressure. Overall, these ignition delays measured using PAI were much shorter than other ignition delays reported in the literature (up to

Downloaded by Doug Talley on January 10, 2018 | http://arc.aiaa.org | DOI: 10.2514/6.2018-0672

≈ 5X) using arc furnace ignition [45–48], and thus produced ignition events that are much more sharply defined in time (see Ref. [14] for more detail). As shown in Fig. 9, ignition delays correlated closely with the fuel boiling temperature T_b (see Tables 2 and 3), where the more volatile fuels with the lowest boiling temperatures exhibit shorter ignition delays. For the 50/50 wt% n-heptane/n-dodecane blend, $\tau_{\text{ign.}}$ followed the volatile component, n-heptane, where $\tau_{\text{ign.}}$ was close to 70 ms for both. This behavior was also exhibited by the kerosene fuels as well, which is consistent with the lighter constituents vaporizing and burning earlier in the droplet lifetime of a multicomponent fuel [18, 49]. Finally, ignition delays for n-dodecane and diesel #2 were both approximately 110 ms, which supports some previous ignition work with n-dodecane as a proposed diesel surrogate for use in fundamental combustion studies [50, 51].

IV. Concluding Remarks

This experimental study investigated fuel droplet combustion properties for a variety of hydrocarbon fuels encompassing alcohols, simple hydrocarbons and kerosene blends. Considering the burning rate constant K and ignition delay $\tau_{\text{ign.}}$, K generally corresponded to the differences in thermophysical properties between the fuel types, while the trends for $\tau_{\text{ign.}}$ correlated with the fuel boiling temperature. One major observation in this study was that K was found to have a notable sensitivity to the data reduction method for non-volatile simple hydrocarbons and kerosenes, with deviations among typical approaches as large as 10% possible. Hence, the K_β approach was developed that automatically found the K associated with the most linear fit to the data for the longest duration of droplet burning. The newly reported K_β values for all fuels consistently corresponded to very small statistical uncertainty between fuel tests and higher R^2 values when compared to common methods (e.g., $K_{\text{mid.,70}}$). Therefore, the K_β approach was found to better represent steady droplet burning processes for the fuel investigated, and should be considered along with its simpler alternative $K_{\text{end.,5,70}}$ as potential options for improved droplet burning rate data reduction.

V. Acknowledgements

This work has been supported by the Air Force Office of Scientific Research (AFOSR) under the grant entitled "The Design of Nanoenergetic Materials for Control of Combustion Dynamics", with Dr. Mitat Birkan as program manager.

References

[1] Sirignano, W. A., *Fluid Dynamics and Transport of Droplets and Sprays*, 2nd ed., Cambridge University Press, Cambridge, NY, 2010.

[2] Harrje, D., "Liquid Propellant Rocket Combustion Instability," Tech. rep., National Aeronautics and Space Administration, 1972.

[3] Godsave, G., "Studies of the combustion of drops in a fuel spray - the burning of single drops of fuel,," *Symposium (International) on Combustion*, Vol. 4, No. 1, 1952, pp. 818–830. doi:http://dx.doi.org/10.1016/S0082-0784(53)80107-4.

[4] Law, C., and Williams, F., "Kinetics and Convection in the Combustion of Alkane Droplets," *Combustion and Flame*, Vol. 19, No. 3, 1972, pp. 393–405. doi:https://doi.org/10.1016/0010-2180(72)90009-0.

[5] Faeth, G. M., "Current Status of Droplet and Liquid Combustion,," *Progress in Energy and Combustion Science*, Vol. 3, No. 4, 1977, pp. 191–224. doi:http://dx.doi.org/10.1016/0360-1285(77)90012-0.

[6] Glassman, I., and Yetter, R., *Combustion*, 4th ed., Academic Press, San Diego, CA, 2008.

[7] Law, C. K., "Recent advances in droplet vaporization and combustion," *Progress in Energy and Combustion Science*, Vol. 8, No. 3, 1982, pp. 171–201.

[8] Basu, S., and Miglani, A., "Combustion and heat transfer characteristics of nanofluid fuel droplets: A short review," *International Journal of Heat and Mass Transfer*, Vol. 96, 2016, pp. 482–503. doi:http://dx.doi.org/10.1016/j.ijheatmasstransfer.2016.01.053.

[9] Pfeil, M. A., Rosen, S. C., Yu, Y. C., Anderson, W. E., and Son, S. F., "Effects of NanoAluminum on Droplet Combustion and Combustion Instabilities in a Single Element Rocket Combustor," *46th AIAA Joint Propulsion Conference & Exhibit*, Vol. Paper AIAA-2010-7154, July 2010.

[10] Pfeil, M. A., Groven, L. J., Lucht, R. P., and Son, S. F., "Effects of Ammonia Borane on the Combustion of an Ethanol Droplet at Atmospheric Pressure," *Combustion and Flame*, Vol. 160, No. 10, 2013, pp. 2194–2203. doi:http://doi.org/10.1016/j.combustflame.2013.04.014.

Distribution Statement A: Approved for Public Release; Distribution is Unlimited. PA Clearance #17745.

Downloaded by Doug Talley on January 10, 2018 | http://arc.aiaa.org | DOI: 10.2514/6.2018-0672

[11] Guerieri, P. M., DeLisio, J. B., and Zachariah, M. R., "Nanoaluminum/Nitrocellulose Microparticle Additive for Burn Enhancement of Liquid Fuels," *Combustion and Flame*, Vol. 176, 2017, pp. 220–228. doi:https://doi.org/10.1016/j.combustflame.2016.10.011.

[12] Sim, H., Plascencia, M. A., Vargas, A., Bennewitz, J. W., Smith, O. I., and Karagozian, A. R., "Effects of ALuminum Nanoparticle Additives on Liquid Fuel Droplet Combustion with and without Acoustic Excitiation," 10^{th} *U.S. National Combustion Meeting*, April 2017.

[13] Ghamari, M., and Ratner, A., "Combustion Characteristics of Colloidal Droplets of Jet Fuel and Carbon Based Nanoparticles,," *Fuel*, Vol. 188, No. 1, 2017, pp. 182–189. doi:http://dx.doi.org/10.1016/j.fuel.2016.10.040.

[14] Badakshan, A., Bennewitz, J. W., and Talley, D. G., "New Ignition Methods for Droplet Combustion Studies," *Combustion and Flame, Currently Under Review*, 2017.

[15] Struk, P. M., Ackerman, M., Nayagam, V., and Dietrich, D. L., "On calculating burning rates during fibre supported droplet combustion," *Microgravity Science and Technology*, Vol. 11, No. 4, 1998, pp. 144–151.

[16] Bennewitz, J. W., Valentini, D., Plascencia, M. A., Vargas, A., Sim, H. S., Lopez, B., Smith, O. I., and Karagozian, A. R., "Periodic Partial Extinction in Acoustically Coupled Fuel Droplet Combustion," *Combustion and Flame*, Vol. 189, 2018, pp. 46–61. doi:https://doi.org/10.1016/j.combustflame.2017.10.019.

[17] Sevilla-Esparza, C. I., Wegener, J. L., Teshome, S., Rodriguez, J. I., Smith, O. I., and Karagozian, A. R., "Droplet Combustion in the Presence of Acoustic Excitation," *Combustion and Flame*, Vol. 161, No. 6, 2014, pp. 1604–1619. doi:http://dx.doi.org/10.1016/j.combustflame.2013.12.012.

[18] Lefebvre, A. H., and McDonell, V. G., *Atomization and Sprays*, 2nd ed., CRC Press, Boca Raton, FL, 2017.

[19] Badakshan, A., Bennewitz, J. W., and Talley, D. G., "Combustion Characteristics of Hydrocarbon Droplets Induced by Photoignition of Aluminum Nanoparticles," 10^{th} *U.S. National Combustion Meeting*, April 2017.

[20] Aggarwal, S. K., "Single Droplet Ignition: Theoretical Analyses and Experiment Findings," *Progress in Energy and Combustion Science*, Vol. 45, 2014, pp. 79–107. doi:http://dx.doi.org/10.1016/j.pecs.2014.05.002.

[21] Turns, S. R., *An Introduction to Combustion: Concepts and Applications*, 8th ed., McGraw-Hill Higher Education, Boston, MA, 2000.

[22] Sutton, G. P., and Biblarz, O., *Rocket Propulsion Elements*, 8th ed., John Wiley & Sons, Inc., Hoboken, NJ, 2010.

[23] Erbschloe, D., "Air Force alternative fuels process paves way to future," Tech. rep., Air Force Air Mobility Command, Sapphire Energy Report, 2012.

[24] Sevilla-Esparza, C. I., "Oscillatory Flame Response in Acoustically Coupled Fuel Droplet Combustion," M.S. Thesis, University of California, Los Angeles, 2013.

[25] Linstrom, P., and Mallard, W., *NIST Chemistry WebBook, NIST Standard Reference Database Number 69*, National Institute of Standard and Technology, Gaithersburg, MD, 2017.

[26] Haynes, W., Lide, D. R., and Bruno, T. J., *CRC Handbook of Chemistry and Physics*, 97th ed., CRC Press, Boca Raton, FL, 2017.

[27] Karagozian, A. R., Dahm, W. J. A., Glasgow, E., Howe, R., Kroo, I., Murray, R., and Shyu, H., "Technology Options for Improved Air Vehicle Fuel Efficiency," Tech. Rep. SAB-TR-06-04, Air Force Scientific Advisory Board Report, 2006.

[28] Huber, M., Lemmon, E., Ott, L., and Bruno, T., "Preliminary Surrogate Mixture Models for the Thermophyscial Properties of Rocket Propellants RP-1 and RP-2," *Energy and Fuels*, Vol. 23, No. 6, 2009, pp. 3083–3088. doi:http://dx.doi.org/10.1021/ef900216z.

[29] Abdulagatov, I., and Azizov, N., "Heat capacity of rocket propellant (RP-1 fuel) at high temperatures and high pressures," *Fuel*, Vol. 90, No. 2, 2011, pp. 563–567. doi:https://doi.org/10.1016/j.fuel.2010.09.038.

[30] Heywood, J., *Internal Combustion Engine Fundamentals*, 1st ed., McGraw-Hill, Inc., New York, NY, 1988.

[31] Bruno, T. J., "The Properties of RP-1 and RP-2 MIPR F1SBAA8022G001," Tech. Rep. AFOSR-MIPR F1SBAA8022G001, National Institute of Standards and Technology, 2008.

Distribution Statement A: Approved for Public Release; Distribution is Unlimited. PA Clearance #17745.

Downloaded by Doug Talley on January 10, 2018 | http://arc.aiaa.org | DOI: 10.2514/6.2018-0672

[32] Kolev, N., *Multiphase Flow Dynamics 4: Turbulence, Gas Absorption and Release, Diesel Fuel Properties*, 2nd ed., Springer-Verlag Berlin Heidelberg, 2012.

[33] Outcalt, S., and Laesecke, A., "Thermophysical Properties Measurements of Rocket Propellants RP-1 and RP-2," *Journal of Propulsion and Power*, Vol. 25, No. 5, 2009, pp. 1032–1040. doi:https://doi.org/10.2514/1.40543.

[34] Rose, J., and Cooper, J., *Technical Data on Fuel*, 7th ed., Scottish Academic Press Ltd, 1977.

[35] NRC, *Permissible Exposure Levels for Selected Military Fuel Vapors*, National Academies Press (US), Washington DC, 1996.

[36] Kresnyak, S., and Giles, T., "Enhancement of Fischer-Tropsch Process for Hydrocarbon Fuel Formulation," *U.S. Patent*, , No. US 9-115-324-B2, 2015. doi:https://doi.org/10.1016/0010-2180(72)90009-0.

[37] EPA, *AP-42: Compilation of Air Emission Factors*, U.S. Environmental Protection Agency, Research Triangle Park, NC, 1995.

[38] Narayanaswamy, K., Pitsch, H., and Pepiot, P., "A component library framework for deriving kinetic mechanisms for multi-component fuel surrogates: Application for jet fuel surrogates," *Combustion and Flame*, Vol. 165, 2016, pp. 288–309. doi:http://doi.org/10.1016/j.combustflame.2015.12.013.

[39] Glaude, P., Fournet, R., Bounaceur, R., and Molière, M., "Adiabatic Flame Temperature from Biofuels and Fossil Fuels and Derived Effect on NOx Emissions," *Fuel Processing Technology*, Vol. 91, No. 2, 2010, pp. 229–235. doi:https://doi.org/10.1016/j.fuproc.2009.10.002.

[40] Chickos, J. S., and Zhao, H., "Measurement of the Vaporization Enthalpy of Complex Mixtures by Correlation-Gas Chromatography. The Vaporization Enthalpy of RP-1, JP-7, and JP-8 Rocket and Jet Fuels at T = 298.15 K," *Energy and Fuels*, Vol. 19, No. 5, 2005, pp. 2064–2073. doi:http://dx.doi.org/10.1021/ef050116m.

[41] Ott, L., Hadler, A., and Bruno, T., "Variability of The Rocket Propellants RP-1, RP-2, and TS-5: Application of a Composition- and Enthalpy-Explicit Distillation Curve Method," *Industrial and Engineering Chemistry Research*, Vol. 47, No. 23, 2008, pp. 9225–9233. doi:https://doi.org/10.1021/ie800988u.

[42] Taylor, J. R., *An Introduction to Error Analysis: The Study of Uncertainties in Physical Measurements*, 2nd ed., University Science Books, Sausalito, California, 1997.

[43] Beckwith, T. G., Roy D, M., and V, J. H. L., *Mechanical Measurements*, 6th ed., Pearson Prentice Hall, Upper Saddle River, NJ, 2007.

[44] Vargas, A., Sim, H., Plascencia, M. A., Smith, O. I., and Karagozian, A. R., "Effects of Aluminum Nanoparticles on Burning Liquid Fuel Droplets in a Quiescent Environment," 11th *Southern California Flow Physics Symposium*, April 2017.

[45] Saitoh, T., Ishiguro, S., and Niioka, T., "An experimental study of droplet ignition characteristics near the ignitable limit," *Combustion and Flame*, Vol. 48, 1982, pp. 27–32. doi:https://doi.org/10.1016/0010-2180(82)90113-4.

[46] Tanabe, M., Bolik, T., Eigenbrod, C., Rath, H., Sato, J., and Kono, M., "Spontaneous ignition of liquid droplets from a view of non-homogeneous mixture formation and transient chemical reactions," *Symposium (International) on Combustion*, Vol. 26, No. 1, 1996, pp. 1637–1643. doi:https://doi.org/10.1016/S0082-0784(96)80387-0.

[47] Dahyabhai, S., and Rathod, P., "An Experimental Investigation on Droplet Ignition of Bio-Diesel and its Blends," *International Journal of Advance Engineering and Research Development*, Vol. 1, No. 5, 2014, pp. 420–434.

[48] Javed, I., Baek, S., and Waheed, K., "Autoignition and combustion characteristics of heptane droplets with the addition of aluminium nanoparticles at elevated temperatures," *Combustion and Flame*, Vol. 162, No. 1, 2015, pp. 191–206. doi:http://dx.doi.org/10.1016/j.combustflame.2014.07.015.

[49] Williams, F. A., *Combustion Theory: The Fundamental Theory of Chemically Reacting Flow Systems*, 2nd ed., Benjamin/Cummings Publishing Company, Inc., Menlo Park, CA, 1985.

[50] Pickett, L. M., Genzale, C. L., Bruneaux, G., Malbec, L.-M., Hermant, L., Christiansen, C., and Schramm, J., "Comparison of Diesel Spray Combustion in Different High-Temperature, High-Pressure Facilities," *SAE International Journal of Engines*, Vol. 3, 2010.

[51] Som, S., Longman, D. E., Luo, Z., and Lu, T., "Three Dimensional Simulations of Diesel Sprays Using n-Dodecane as a Surrogate," *Fall Technical Meeting of the Eastern States Section of the Combustion Institute*, October 2011.

Distribution Statement A: Approved for Public Release; Distribution is Unlimited. PA Clearance #17745.

Downloaded by Doug Talley on January 10, 2018 | http://arc.aiaa.org | DOI: 10.2514/6.2018-0672

Combustion Science and Technology

ISSN: 0010-2202 (Print) 1563-521X (Online) Journal homepage: https://www.tandfonline.com/loi/gcst20

New ignition methods for droplet combustion studies

Alireza Badakhshan, John W. Bennewitz & Douglas Talley

To cite this article: Alireza Badakhshan, John W. Bennewitz & Douglas Talley (2018) New ignition methods for droplet combustion studies, Combustion Science and Technology, 190:7, 1302-1312, DOI: 10.1080/00102202.2018.1445726

To link to this article: https://doi.org/10.1080/00102202.2018.1445726

Published online: 20 Apr 2018.

Submit your article to this journal

Article views: 202

View related articles

View Crossmark data

Citing articles: 1 View citing articles

Full Terms & Conditions of access and use can be found at
https://www.tandfonline.com/action/journalInformation?journalCode=gcst20

COMBUSTION SCIENCE AND TECHNOLOGY
2018, VOL. 190, NO. 7, 1302–1312
https://doi.org/10.1080/00102202.2018.1445726

Taylor & Francis
Taylor & Francis Group

SHORT COMMUNICATION

Check for updates

New ignition methods for droplet combustion studies

Alireza Badakhshan[a], John W. Bennewitz[a], and Douglas Talley[b]

[a]ERC Inc., Edwards AFB, CA, USA; [b]Air Force Research Lab, Edwards AFB, CA, USA

ABSTRACT

Two new methods for igniting suspended droplets, namely Plasma Arc Ignition (PAI) and Photoignition (PI), were developed which offer relatively short ignition initiation times within 65–110 ms range for all fuels except hexadecane that is about 260 ms. The fuels included ethanol, methanol, n-heptane, n-dodecane, toluene, RP-2, JP-8, Fischer-Tropsch (FT), diesel #2, and hexadecane. The resulting average droplet ignition delays were up to an order of magnitude smaller than other methods for ignition of fuel droplets reported in the literature such as heated furnaces and ignition coils. The significant reduction in the ignition delay is most likely due to the substantially hotter ignition temperatures (≥2000 K) of these methods, which makes them more suitable for relatively well-defined ignition events and capable of igniting less volatile fuels such as diesel and hexadecane. To the best of our knowledge, this is the first report on the use of these techniques for the ignition of suspended fuel droplets.

ARTICLE HISTORY
Received 12 December 2017
Revised 21 February 2018
Accepted 22 February 2018

KEYWORDS
Plasma Arc Ignition; Droplet Ignition; Photoignition; Suspended Droplets; Flash Ignition; Ignition Delay; Hydrocarbon Fuel Droplets

1. Introduction

Substantial experimental work has been devoted to the ignition of a droplet as reported by Aggarwal (2014) in a review article, as well as earlier works reported by Saitoh et al. (1982), Wong et al. (1996), and Bergeron and Hallett (1989). The work by Tanabe et al. (1994) and Tanabe et al. (1995) is mostly concerned with what is described as two-stage droplet ignition. A report by Sazhin (2006) describes a model for droplet heating and evaporation leading to ignition and combustion of single droplets. Usually, ignition is achieved by introducing the droplet to a hot furnace or box, or placing it in the vicinity of a heated surface or object such as a nichrome wire heater, as described by Aggarwal (2014). This report shows that typical temperatures the droplets are exposed to are <1300 K for these ignition methods and the corresponding ignition delays are usually >0.5 s, which are relatively long compared to the total lifetime of a 1-mm diameter droplet (1–2 s). This can make it difficult to clearly distinguish droplet-burning processes affected by ignition transients from burning processes that occur after ignition transients have decayed. Quasi-steady droplet combustion theory, for example, does not consider the portion of droplet lifetime occupied by ignition transients at all. Moreover, droplet-burning rate constants for different fuels are often presented in the d-squared law format (square of droplet diameter as a function of time) even when the droplet combustion is not strictly quasi-steady. The latter tend to be useful only after the initial ignition transients have decayed.

Methods are described below to ignite droplets by exposing them to relatively higher temperatures (>2000 K) for a much shorter exposure time (~100 ms), which produce ignition

CONTACT Alireza Badakhshan douglas.talley.1@us.af.mil
Color versions of one or more of the figures in the article can be found online at www.tandfonline.com/gcst.
© 2018 Taylor & Francis

delays much shorter than the total droplet lifetimes (≥1.5 s for all fuels). It may be noted that the reduced ignition delays produced by these methods do not remove the effects of ambient properties, which are retained even after the initial ignition transients have decayed. The two ignition methods are plasma arc ignition (PAI) and photoignition (PI). They are evaluated below on a range of hydrocarbon fuel droplets, using a consistent suspended droplet experiment to be described in the next section.

2. Suspended droplet experiment

The suspended droplet approach implemented is illustrated in Figure 1. A fuel droplet with a nominal size of 1.35 ± 0.05 mm was suspended within an atmospheric pressure air environment from a 0.15 mm uncoated quartz fiber from Polymicro Technologies Inc. In order to increase the retention of the fuel droplet on the fiber, a bead was generated at its end through a heating process using an oxy-propane torch. The burning of the fuel droplet was imaged by an infrared (IR) camera, model SC6800 from Flir Inc., operated at 250 frames per second (fps), or a visible light Phantom v7.1 by Vision Research Corp. at 1000 fps. All the experiments were performed under ambient condition at about T = 298 K and P = 100 kPa. Figure 1 shows the experimental set up for the ignition of a suspended fuel droplet along with the PAI and PI system.

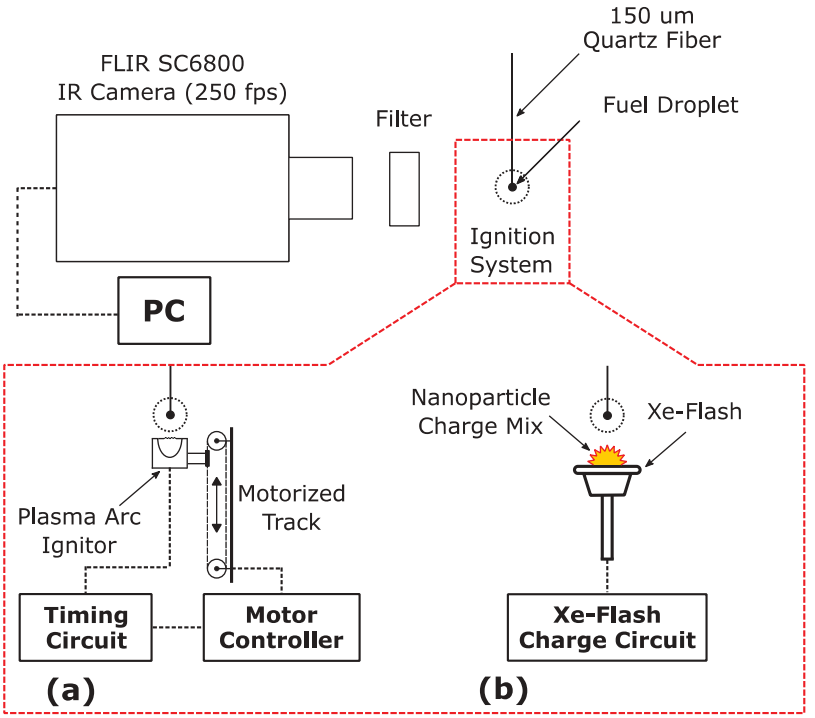

Figure 1. The experimental set up for the ignition of a suspended fuel droplet utilizing either the (a) plasma arc ignitor or (b) photoignition system.

3. Plasma arc ignition method

PAI in a spark plug configuration has been a standard in liquid fuel ignition in internal combustion engines and other combustion applications for decades. Also, Starikovskaya and Starikovskii (2010) and Starikovskaya et al. (2009) worked on the operational principle of various forms of plasma ignition, detailing the theoretical and experimental aspects of it over the past two decades. A spark plug, however, does not ignite a single suspended droplet mostly due to its short duration, which does not allow enough time for sufficient droplet heating and fuel evaporation.

A continuous spark source (2 mA at 10 kV) with 30 μs duration and 11 Hz repetition rate was tested by our group. It was found to be physically too intrusive in that it knocked the droplet off of the fiber and in some cases completely vaporized the droplet prior to ignition. It was found that a low-current plasma arc with adjustable duration was best suited to ignite suspended fuel droplets. The PAI system was built from the components of a commercially available unit from Tesla Coil Lighters™ that operates based on an open-cored Tesla transformer. The miniaturized arc plasma source was characterized by a low-current pulsed plasma arc on the order of 100 μA, somewhat similar to what was described by Schutze et al. (1998). The working voltage of the PAI is estimated to be close to 10 kV as described by Lou et al. (2007). A customized timing circuit provided an adjustable duration of the plasma arc within a wide range.

The electrodes for the PAI unit were designed so that the filament-like plasma region was 5 mm long and 1 mm in diameter. The Li-polymer rechargeable battery used in the PAI unit weighs 10 g and stores 3.5 kJ of energy (at 3.7 V and 380 mAh), which is comparable to an alkaline AAA battery weighing 12 g, storing 4 KJ (at 1.22 V and 1150 mAh). The PAI unit typically delivers power at a rate of 2 watt or 0.2 J per ignition event, which lasts 100 ms for all fuels except hexadecane, for which a longer ignition duration of 260 ms was required. Upon stable ignition, the PAI mechanism was physically removed from the vicinity of the droplet automatically along the motorized track as depicted in Figure 1(a).

The average temperature of the gas surrounding the plasma arc was estimated from thin-filament pyrometry (TFP) measurements to be about 2300 K. The same approach in pyrometry that has been described by Wu et al. (2017) has been adopted in this report. Also, a NASA report by Struk et al. (2003) describes various aspects of TFP with an estimated overall uncertainty of ≤50 K. The measurement system in this report was calibrated with a blackbody source at 1200°C (1473 K). The temperature of the 15 μm SiC fiber was 2020 ± 45 K taken by averaging 20 identical measurements and the radiation correction in this case would add about 300 K, as described by Ma et al. (2014). The low heat capacity and the longitudinal conductivity of the ultra-thin fiber is expected to have a negligible effect on the plasma (Oksanen et al., 1997). Based on the work of Schutze et al. (1998), the electron and gas temperature of the plasma are expected to converge at atmospheric pressure to around 3000 K. This is consistent with the average measured temperature of 2300 K for the rapidly pulsing plasma. Measurement of the pulse discharge operation of the PAI was performed through high-speed imaging at a rate of 300,000 fps utilizing a high-speed camera from Vision Research Corp, model # Phantom v1210. The pulse width was estimated to be a few microseconds and its repetition rate was 20.5 kHz.

Assuming that 50% of the plasma energy was absorbed by the droplet, it receives 0.1 J per ignition event. Table 1 lists the fuels studied along with their vapor pressure and enthalpy of

Table 1. Summary of the fuels that were used for this study and some of their properties.

Fuel of interest		Plasma arc ignition			Photo ignition	
Fuel type	Vapor pressure* (at Atm., 20–25° C) (kPa)	Enthalpy of vaporization 25°C (kJ/kg)**	Ignition duration (ms)	τ_{ign} (Ign. Delay) (ms)	Solid fuel to achieve ignition	Amount of solid fuel used (mg)
Ethanol	7.9	840	104 ± 2	71	n-Al (18 nm)	3 ± 2
Methanol	16.9	1100	104 ± 2	64	n-Al (18 nm)	3 ± 2
n-Heptane = A (C_7H_{16})	6.1	320	104 ± 2	69	n-Al (18 nm)	3
Toluene (C_7H_8)	4	350–410	104 ± 2	72	n-Al (18 nm)	3
n-Dodecane = B ($C_{12}H_{26}$)	1.5E-02	260	104 ± 2	108	n-Al+BKNO3	3 + 1
Hexadecane	**9.6E-05**	**230**	**260 ± 2**	**257**	**(no ignition)**	3 + 1 + 1
RP-2 (a rocket grade kerosene)	5.7E-02 (Huber et al., 2009)	300 or 308+ (Chickos et al., 2005)	104 ± 2	87	n-Al (18 nm)	3
JP-8 ($C_{11}H_{21}$) (Jet propellant)	1.8E-01 (NRC, 1996)	440	104 ± 2	81	n-Al+BKNO3	3 + 1
Fischer-Tropsch (FT) ($C_{12}H_{25}$) (Synth. Jet Fuel)	2.1E-02++ (Kresnyak and Giles, 2015)	340	104 ± 2	91	n-Al (18 nm)	3
Diesel #2	7.7E-02 (EPA, 1995 AP −42)	270	104 ± 2	106	n-Al+BKNO3 +Solid Rocket Fuel	3 + 1 + 1

* From Linstrom and Mallard (2017), calculated for T = 298 K and P = 101,325 Pa.
**From PubChem and references there in also from Haynes et al. (2017).
+: Calculated for T = *T-boil* and P = 101,325 Pa; ++: This value could not be verified by a second sources.

vaporization. For a suspended droplet of 1.35 mm diameter (1.3 μL or ~1 mg for most fuels), 0.1 J is enough energy to vaporize the outer surface of the droplet, leading to a successful ignition event. However, 0.1 J is far less than what is needed to heat up and vaporize the entire droplet prior to ignition, which was never observed in our experiments.

It was found that fuels with very low vapor pressure were relatively harder to ignite, so the duration of the plasma arc needed to be increased. To be consistent, the plasma arc duration was kept uniformly at 104 ms for all of the fuels except for hexadecane, where the arc duration of 260 ms was needed to achieve a consistent droplet ignition event. Table 1 suggests the determining factor in the ignitability of any fuel using PAI method correlates well with the vapor pressure of the fuel.

4. Photoignition method

Photoignition (also known as flash ignition) as described previously by Badakhshan and Danczyk (2014) is a photothermal effect that is induced by a flash of light (typically from a Xenon flash) in certain nanostructured materials. Ohkura et al. (2013) reported on photoignition of porous silicon films and Gilje et al. (2010) described the use of photoignition of graphene oxide foam for the patterning application through photo-thermal activation. Nano-aluminum (nAl) was selected as the main photoignition agent in this study similar to the report by Ohkura et al. (2011). The main advantages of aluminum in the photoignition process are its high burning temperature and "gasless" combustion in that the only products are heat and condensed phase aluminum oxide. Thus, physical and chemical interference such as keeping the droplet

suspended and influencing the ignition process by gaseous byproducts is minimized, except for the expansion of the surrounding air due to heating. In the ignition of JP-8 and diesel fuel, other solid fuels were added to the nAl, where their combustion produced relatively small amount of gas. The 18 nm passivated nAl samples used as the primary photoignition agent in this study were from NanoAmor Corp. PI with nAl as the main ignition agent has a particle ignition time of <5 ms and a burn temperature of >2000 K. This was measured by a fast pyrometer, model KGA 740-HS from Mikron Infrared Inc., with a response time of 10 μs, which was focused on a 1–2 mm spot on the bulk nAl sample. The stated temperature is in agreement with the value for burning nAl in air reported by Bazyn et al. (2007), while a report by Risha et al. (2007) indicated a burn temperature of 3500 K for nAl in air at atmospheric pressure. The burning nAl clusters in the ignition plume provides an ignition source with an estimated temperature between 2000–3000 K.

The miniature battery-operated PI unit uses a single AA or AAA battery to operate a compact Xe-flash bulb with 1 ms flash duration and 6 J/flash of optical energy. The measured optical fluence for the initiation of photoignition of nAl was about 0.3 J/cm^2. There were certain cases where additional solid fuel was used to increase the output energy and temperature of PI to achieve a more consistent ignition. For n-dodecane and JP-8, 1 mg of $BKNO_3$, which is an oxidizer with 20% boron, was added to the nAl sample to achieve ignition. For diesel #2, a third solid fuel was needed to induce ignition, namely 1 mg of granular solid rocket fuel that is comprised of a polymerized Al powder plus ammonium perchlorate as an oxidizer. However, PI was not able to ignite a hexadecane droplet, most likely due to the relatively low vapor pressure of this fuel. In all of these cases, the photo-ignitable solid was the 18 nm passivated nAl.

For the PI ignition of most fuel droplets, about 3 mg of nAl was used, estimated to contain 1 mg of Al metal and 2 mg of Al_2O_3 (Castronuovo et al., 2015). Aluminum powder is expected to generate 1680 kJ/mol of heat with a molar mass of 102 g/mol or 16 kJ/g, producing no more than 16 J per ignition event. Most of this energy is absorbed by the Al_2O_3 covering the metallic nAl. However, only about 1% of the total energy released needs to be absorbed by a 1.35 mm suspended droplet to vaporize an equivalent amount of fuel from the surface layer for successful ignition. Full treatment of the thermal processes involved and the evaluation of the minimum heat required for a sustained combustion event is beyond the scope of this communication. Two recent reports reported by Glushkov et al. (2016a, 2016b) describes the heat and mass transfer processes occurring with vaporization and chemical reaction during the interaction of a small hot particle with the fuel.

5. Results and discussion

Thermographic images of PAI and PI of an n-dodecane droplet are shown as examples in Figures 2 and 3, respectively. The top row of Figure 2 shows the plasma arc and its relative position with respect to the n-dodecane droplet. In this case, the electrodes of the PAI system are placed about 1 mm beneath the droplet for 100 ms, at which point the plasma is turned off and moved away. Typically, the flame continuously grows larger for the first 100 ms until it stabilizes to a fully established flame. The glowing vertical band appearing on the last image in Figure 2 is the supporting fiber.

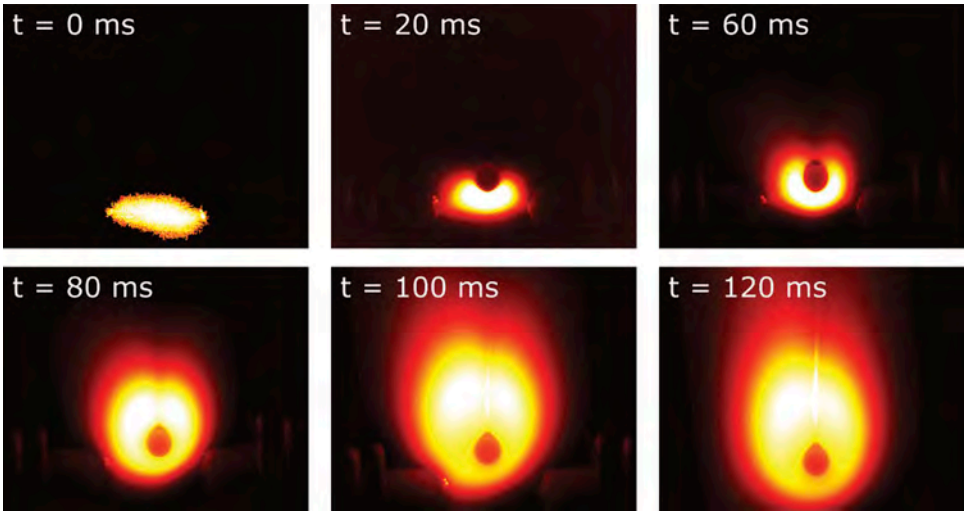

Figure 2. Plasma arc ignition of an n-dodecane droplet showing a fully established flame within 100 ms.

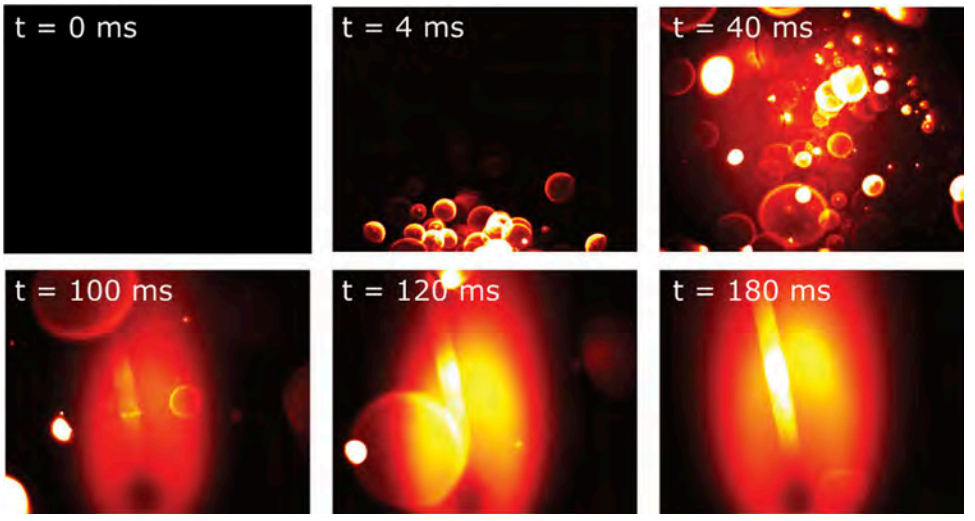

Figure 3. Photoignition of an n-dodecane droplet showing a fully established flame within 120 ms.

For the photoignition of n-dodecane in Figure 3, the nAl ignition charge was located 7 mm below the droplet. The droplet can be seen as the darker, spherical shape in the bottom row. The Xenon flash at $t = 0$ ms saturates the camera for visible imaging and is barely visible in IR imaging. The Xe-flash produces a shower of burning nAl clusters which appear to be large spheres, much larger than their actual sizes due to the clusters being out of focus. In Figure 3, one or more of the burning clusters ignite the droplet and the flame appears to be fully established at around 120 ms. The probability of ignition was >90% using PAI and >70% using PI. Beyond ignition probability, the two ignition methods were found to be generally comparable in performance, as they produced comparable ignition delay results (discussed

in the next section). PAI proved to be slightly faster and more capable of igniting fuel droplets with low vapor pressure. A notable difference between the two methods is the potential presence of atomic oxygen, radicals, and reactive species in the PAI arc as described by Starikovskaya and Starikovskii (2010), which would not be produced by the PI particles. The equivalent ignition delay results between the two methods, however, suggest a relative insensitivity to the presence of the plasma-generated reactive species, instead indicating that the dominant ignition mechanisms were thermal processes. It may be mentioned, however, that ignition delays determined by using PAI method could possibly be slightly shorter than those with PI, suggesting a minor involvement of the reactive species induced by the plasma. Alternatively, this difference may be related to the relatively small difference in the ignition temperature between the two methods. In any case, PAI offers clear advantages over PI except for ignition at elevated pressures (>15 atm) where PI has been applied up to 75 atm with a reasonable success rate as described by Badakhshan et al. (2016) and conversely, plasmas are difficult to form at high pressures.

6. Ignition delays

PAI and PI were used to evaluate the ignition delays of suspended droplets of ten different hydrocarbon fuels. PAI proved to be more convenient to use for a comparative study due to its constant average output power and its adjustable ignition duration, which is not the case for PI. Additionally, since the plasma arc produces almost no background light and heat, it was much easier to observe the details of ignition and the flame propagation at the early stage of the ignition event, as compared to photoignition. This is particularly useful for the study of fuels with relatively short ignition delays (e.g., <70 ms).

Care was taken to maintain the same experimental conditions and parameters for all fuels except for hexadecane that proved to be extremely difficult to ignite, most likely due to its extremely low vapor pressure. Using PI, it was not possible to ignite hexadecane, while JP-8, and diesel #2 where relatively harder to ignite. This is indicated in Table 1, which shows ignition delays that were determined for different fuels through the systematic analysis of IR imaging data for the PAI method. These results are compared with some arc furnace data in the literature, as shown in Figure 4. These ignition delays are for n-heptane (Saitoh et al., 1982), n-dodecane (Tanabe et al., 1996), kerosene (Javed et al., 2015), and diesel fuel (Dahyabhai and Rathod, 2014). The most widely used definition of ignition delay is the time separation between two events: (1) introducing the droplet to the ignition environment and (2) the observation of the established flame as described by Aggarwal (2014). In the current study, the ignition delay was defined as the time separation between the electronic initiating signal (either with PAI or PI) and the observation of the established flame through image analysis (see Bennewitz et al. (2018) for more detail).

The ignition delays shown in Figure 4 represent the upper limit of the ignition delay for each fuel, which are the result of averaging five identical ignition events. The uncertainty in the values of the ignition delays is no larger than the symbols used to represent the data in Figure 4. The values for the data for arc furnace ignition show a range for the reported results, where the lower values are associated with the highest furnace temperatures.

A similar set of data was produced using 1000 fps gray scale images in the visible, often in tandem with the IR images. Visible imaging relies in part on the luminosity of the flame that is particularly sensitive to soot formation, which is vastly different among the fuels

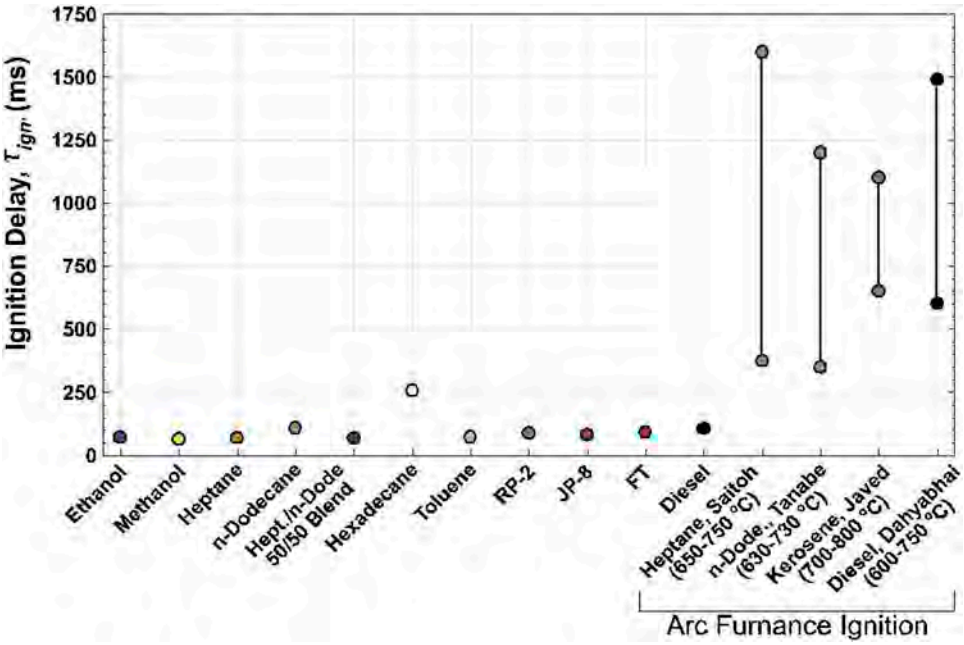

Figure 4. Ignition delays for all of the fuels obtained by PAI and IR imaging, as stated in Table 1. Ranges of other data for some of these fuels, represented by "Arc Furnace Ignition", are from published results.

used in this study. Therefore, ignition delays using visible imaging were judged to be less reliable across all fuels than using IR imaging. Thus, only the IR results are reported here. Visible imaging was used to track droplet diameter regression and their burning rates, and part of these findings was reported by Bennewitz et al. (2017).

The ignition delays inferred by analysis of the IR imaging data during the ignition process using either PAI or PI are 6 to 10 times shorter than other ignition delays reported in the literature, as represented in the arc furnace data. This is shown in Figure 4 and it should be noted that this does not imply that one set of results is more reliable than the other set. Instead, the difference merely signifies that the ignition delay is strongly dependent on the ignition method, as it is significantly influenced by the temperature of the ignition source. These results do suggest, however, that the methods presented here produce ignition events that are more sharply defined in time.

PI has some similarities to the hot object ignition method reported by Glushkov et al. (2016a, 2016b), which show similar trends in ignition delay with increased temperature that are consistent with the results in Figure 4. However, those studies were not performed on single droplets, but their modeling approach provides insight into the stated trend in the ignition delay.

7. Conclusions

A PAI and a PI system were used to ignite ten different hydrocarbon fuel droplets suspended on a fiber, including ethanol, methanol, n-heptane, n-dodecane, toluene, RP-2, JP-8, Fischer-Tropsch (FT), diesel #2, and hexadecane. PAI exposes the droplets to a hot plasma, while PI exposes the

droplets to a shower of hot particles undergoing "gasless" combustion. Compared to other ignition methods which operate at relatively low temperatures (<1300 K) and have relatively long ignition delays (>500 ms), PAI and PI methods use relatively higher temperatures (>2000 K) and therefore have shorter heating times and ignition delays (<100 ms in most cases). The resulting ignition delays were found to be up to an order of magnitude shorter than those measured by most other droplet ignition methods. These results suggest that the methods presented here produce ignition events that are more sharply defined in time and they are quite suitable for droplet combustion experiments.

Acknowledgment

We gratefully thank Dr. Rosa Padilla for help with thin-filament pyrometry and Dr. Mario Roa for assistance with the diagnostic imaging of the plasma arc ignition source.

Funding

This work was funded by the Air Force Office of Scientific Research (AFOSR), under Dr. Mitat Birkan, Project Officer.

References

Aggarwal, S.K. 2014. Single droplet ignition: theoretical analyses and experimental findings. *Prog. In Energy and Comb. Sci.*, **45**, 79.

Badakhshan, A., and Danczyk, S. (2014) Ignition of nanoparticles by a compact camera flash. *AFRL-RQ-ED-TR-2014-0029*, Air Force Research Laboratory (AFMC), Edwards Air Force Base, CA.

Badakhshan, A., Danczyk, S., Forliti, D., Leyva, I.A., and Talley, D.G., (2016) Nano-ignition torch applied to cryogenic H2/O2 coaxial jet, *54th AIAA Aerospace Sciences Meeting*, paper AIAA 2016-0184, San Diego, California, USA.

Bazyn, T., Glumac, N., Krier, H., Ward, T.S., Schoenitz, M., and Dreizin, E.L. 2007. Reflected shock ignition and combustion of aluminum and nanocomposite thermite powders. *Comb. Sci. Tech.*, **179**, 457.

Bennewitz, J.W., Badakhshan, A., and Talley, D. (2017) Combustion characteristics of hydrocarbon droplets induced by photoignition of aluminum nanoparticles, *10th US Nat. Comb. Meeting, College Park, MD.*, http://www.dtic.mil/docs/citations/AD1034441.

Bennewitz, J.W., Badakhshan, A., and Talley, D.G. (2018), Systematic measurement of hydrocarbon fuel droplet burning rate constants and ignition delays, 2018 AIAA SciTech Meeting Forum, Kissimmee, Florida.

Bergeron, C.A., and Hallett, W.L.H. 1989. Ignition characteristics of liquid hydrocarbon fuels as single droplets. *Canadian J. Of Chem. Eng.*, **67**, 142.

Castronuovo, L., Dunn-Rankin, L., and Garman, J. 2015. Photoignited aluminum nanopowder combustion in air. *J. Of Aero. Astro. Avia.*, **47**, 297.

Chickos, J.S., and Zhao, H. 2005. Measurement of the vaporization enthalpy of complex mixtures by correlation-gas chromatography. The vaporization enthalpy of RP-1, JP-7, and JP-8 rocket and jet fuels at T = 298.15 K. *Energy and Fuels*, **19**, 2064. doi:10.1021/ef050116m.

Dahyabhai, S.V., and Rathod, P.P. 2014. An experimental investigation on droplet ignition of bio-diesel and its blends. *Ijaerd*, **1**, 420.

EPA. 1995. *AP-42: Compilation of Air Emission Factors*, U.S. Environmental Protection Agency, Research Triangle Park, NC.

Gilje, S., Dubin, S.A., Badakhshan, A., Farrar, J., Danczyk, S.A., and Kaner, R.B. 2010. Photothermal deoxygenation of graphene oxide for patterning and distributed ignition *applications*. *Adv. Matt.*, **22**, 419.

Glushkov, D.O., Legros, J.C., Strizhak, P.A., and Zakharevich, A.V. 2016a. Heat and mass transfer at the ignition of vapors of volatile liquid fuels by hot metal core: experimental study and modelling. *Inter. J. Of Heat and Mass Transfer*, **92**, 1182.

Glushkov, D.O., Legros, J.C., Strizhak, P.A., and Zakharevich, A.V. 2016b. Experimental and numerical study of heat transfer and oxidation reaction during ignition of diesel fuel by a hot particle. *Fuel*, **175**, 105.

Haynes, W., Lide, D.R., and Bruno, T.J. 2017. *CRC Handbook of Chemistry and Physics*, 97th, CRC Press, Boca Raton, FL.

Huber, M., Lemmon, E., Ott, L., and Bruno, T. 2009. Preliminary surrogate mixture models for the thermophyscial properties of rocket propellants RP-1 and RP-2. *Energy and Fuels*, **23**, 6, 3083–3088. doi:10.1021/ef900216z.

Javed, I., Baek, S.W., and Waheed, K. 2015. Autoignition and combustion characteristics of heptane droplets with the addition of aluminum nanoparticles at elevated temperatures. *Comb. Flame*, **162**, 191.

Kresnyak, S., and Giles, T., (2015) Enhancement of Fischer-Tropsch process for hydrocarbon fuel formulation, *U.S. Patent*, No. US 9-115-324-B2, doi:10.1016/0010-2180(72)90009-0.

Linstrom, P., and Mallard, W. 2017. *NIST Chemistry Webbook, NIST Standard Reference Database 69*, National Inst. of Standard and Tech., Gaithersburg, MD.

Lou, G. et al. 2007. Ignition of premixed hyrocarbon-air flows by repetitively pulsed, nanosecond pulse duration plasma. *Proc. Comb. Inst.*, **31**, 3327.

Ma, B., Wang, G., Magnotti, G., Barlow, R.S., and Long, M.B. 2014. Intensity-ratio and color-ratio thin-filament pyrometry: uncertainties and accuracy. *Comb. Flame*, **161**, 908.

NRC. 1996. *Permissible Exposure Levels for Selected Military Fuel Vapors*, National Academies Press (US), Washington DC.

Ohkura, Y., Rao, P.M., and Zheng, X. 2011. Flash ignition of Al nanoparticles: mechanism and applications. *Comb. And Flame*, **158**, 2544.

Ohkura, Y., Weisse, J.M., Cai, L., and Zheng, X. 2013. Flash ignition of freestanding porous silicon films: effects of film thickness and porosity. *Nano Lett.*, **13**, 5528.

Oksanen, M., Scholz, R., and Fabbri, L. 1997. On the longitudinal thermal diffusivity of SiC-based fibres. *J. Of Mat. Sci. Lett*, **16**, 1092.

Risha, G.A., Son, S.F., Yetter, R.A., Yang, V., and Tappan, B.C. 2007. Combustion of nano-aluminum and liquid water. *Proc, Comb. Inst.*, **31**, 2029.

Saitoh, T., Ishiguro, S., and Niioka, T. 1982. An experimental study of droplet ignition characteristics near the ignitable limit. *Combust. Flame*, **48**, 27.

Sazhin, S.S. 2006. Advanced models of fuel droplet heating and evaporation, Prog. *Energy and Comb. Sci.*, **32**, 162.

Schutze, A. et al. 1998. The atmospheric-pressure plasma jet: a review and comparison to other plasma sources. *IEEE Trans. Plasma Sci.*, **26**, 1685.

Starikovskaya, S.M., Aleksandrov, N.L., Kosarev, I.N., Kindysheva, S.V., and Starikovskii, A.Y. 2009. Ignition with low-temperature plasma: kinetic mechanism and experimental verification. *High Eng. Chem.*, **43**, 213.

Starikovskaya, S.M., and Starikovskii, A.Y. 2010. *Plasma-Assisted Ignition and Combustion, Handbook of Comb*, Part 5, Wiley Online Library 2010 and references there in.

Struk, P., Dietrich, D., Valentine, R., and Feier, I. (2003) Comparisons of gas-phase temperature measurements in a flame using thin-filament pyrometry and thermocouples, *41st Aerospace Sciences Meeting and Exhibit*, Reno, Nevada, AIAA 2003–2853.

Tanabe, M., Bolik, T., Eigenbrod, C., Rath, H.J., Sato, J., and Kono, M. 1996. Spontaneous ignition of liquid droplets from a view of non-homogeneous mixture formation and transient chemical reactions. *Symp. Comb.*, **26**, 1637.

Tanabe, M., Kono, M., Sato, J., Koenig, J., Eigenbrod, C., and Dinkelacker, F. 1995. Two-stage ignition of n-heptane isolated droplets. *Comb. Sci. Tech.*, **108**, 103.

Tanabe, M., Kono, M., Sato, J., Koenig, J., Eigenbrod, C., and Rath, H.J. 1994. Effects of natural convection on two-stage ignition of an n-dodecane droplet. *Proc. Combust. Inst.*, **25**, 933.
Wong, S.C., Hsu, T.S., and Chang, J.C. 1996. Validity of droplet ignition criterion derived assuming gas-phase quasisteadiness. *J. Prop. Power*, **12**, 18.
Wu, F.H., Padilla, R.E., Dunn-Rankin, D., Chen, G.B., and Chao, Y.C. 2017. Thermal structure of methane hydrate fueled flames. *Proc. Of Comb. Inst.*, **36**, 4391.

COMBUSTION CHARACTERISTICS OF NEAT AND NANOPARTICLE FUELS OF HYDROCARBON DROPLETS: EFFECTS OF IGNITION METHOD AND NANOPARTICLE ADDITIVES

A. Badakhshan, J.W. Bennewitz
ERC Inc., Edwards AFB, CA

D.G. Talley
Air Force Research Laboratory, Edwards AFB, CA

ABSTRACT

The burning rate constant and the ignition delay of 10 neat hydrocarbon fuels were investigated under ambient conditions. The fuels included alcohols (ethanol and methanol), simple hydrocarbons (n-heptane, n-dodecane, toluene, and hexadecane) and kerosene blends (RP-2, JP-8, Fischer-Tropsch (FT), and diesel #2). For representative fuels of each category i.e. ethanol, heptane and RP-2, nanoparticle (NP) additives were used to modify the stated combustion characteristics of the resulting nanofuels. The main NP was aluminum with a nominal size of 80 nm and concentration of 0.5-5% by weight. In case RP-2, other NP additives such as MgO, $NaBH_4$, and graphene nanoplatelets were also used. In each case, a droplet with a nominal diameter of 1.35±0.15 mm was suspended from a 0.15 mm quartz fiber. The initiation of combustion was achieved either through a low-power plasma arc or a gasless photoignition system through ignition of 18 nm aluminum NPs by a compact Xe-flash. Each of these ignition methods offer a relatively short ignition duration <110 ms (except for hexane) and a very high ignition temperature >2000 K. For the neat fuels, the burning rate constants were between 0.74 to 0.94 mm^2/s, which is in general agreement with the previously reported values. The ignition delays for the fuel droplets that were evaluated by thermographic imaging found to be within 65-110 ms for all fuels except for hexadecane, which was about 260 ms. The stated range is considerably smaller than the previously reported values for ignition delays of any hydrocarbon fuel by other ignition methods (with T< 1300 K). For each nanofuel (fuel + NPs), a relatively moderate change in the burning rate constant was found due to NP additives, typically <10%. No significant change in ignition delays were found due to NP additives for the nanofuels that were studied.

INTRODUCTION

The combustion characteristics of various liquid fuels has been the subject of interest for many decades. This includes the study of fuel droplets as well as fuel sprays under different conditions. However, the much newer field of nanofuel (nanoparticles suspended in a fuel) research is a direct result of substantial successes of utilization of nanoparticles (NPs) in combustion science and in nanofluids, [1,2] and the improvements in performance of explosives and solid propellants that has been achieved by the addition of nanostructured energetic materials such as micron and sub-micron size aluminum additives to the polymer mix. [3]

Distribution Statement **A**: Approved for public release; distribution is unlimited. PA clearance number 19070.

The automotive industry has adopted NP additives for hydrocarbon fuels (HCFs), [4] with an interest in their catalytic effects for the reduction of tail pipe gas emission. [5] There are wide ranges of elemental and compound NPs as well as metallic alloys that are desirable liquid fuel additives due to their energetic properties, reactivity and/or catalytic effects. [6-9] Basically, NPs consist of 3-D clusters of NPs or 2-D sheets of atomic and molecular structure of inorganic materials that are nanometer size, typically 1-100 nm or even 1-1000 nm. Regardless of the definition, the most interesting properties of NPs are dictated by their relative size, which is best indicated by the surface to volume ratio of particles. Therefore, NPs with a nominal size of a few nanometers are expected to show a much higher reactivity or catalytic effect than NPs with a nominal size of say 100 nm.

It is generally true that for NPs the smaller the size the higher the reactivity, but for most NPs the surface layer is easily oxidized thus non-reactive. For example, in case of Al NPs elemental Al is covered by a self- terminating impenetrable native aluminum oxide shell that is expected to be anywhere between 4 to 10 nm think depending on the oxidation condition. [10] This means that only a fraction of the volume of each NP consists of Al. For instance, for Al NPs with a nominal size of 80 nm. On average only about 50% of the volume is Al and the rest of it is Al_2O_3 that is undesirable when the reactivity of Al NPs is of interest. NPs as additives have proven successful in many applications [2,3], however, impressive or even promising results that are applicable to LREs have yet to be reported.

There is an interest in utilizing nanostructured fuel additives for the control of combustion instability in LREs. This requires substantial background work in understanding the effects of nanostructured materials and nano-energetics as liquid fuel additives. One such background study includes the combustion characteristics of nanofuel droplets, which is the subject of interest in this article. This includes an evaluation of the effect of additives on certain combustion parameters including the burn rate constant and the ignition delay time.

Synthesis of NPs

This is a very wide topic and full treatment of the synthesis of NPs is beyond the scope of this article. Synthesis and application of NPs has been the subject of great interest to researchers in a wide range of disciplines including physics, chemistry, material science, engineering, biology, and medicine. Several comprehensive and specialized review articles on synthesis and applications of functional NPs have appeared in recent publications. [11-13]

However, our focus in this section will be limited to those aspect of synthesis of NPs that is directly related to nanofuels. There are two major approaches in synthesis of NPs and preparation of nano-suspensions, top down or bottom up. [14] One of the concerning issues in the synthesis of elemental NPs or metal alloys is the formation of oxide layers moments after the NPs have been formed or soon after they are exposed to environmental oxygen and moisture. In the case of Al NPs the relatively thick Al_2O_3 layer/shell is undesirable for the following reasons, (i) the surface layer of NPs is a very stable oxide unlike the highly reactive Al, (ii) it is an impenetrable shell with a very high melting temperature, far higher than that of Al and (iii) for smaller NPs say less than 80 nm, a relatively large percentage of the available material (depending on the size) is a nonenergetic substance.

Dispersion of NPs in Hydrocarbon Fuels

This involves creating a well-dispersed suspension of NPs in the fuel of choice, which for this research is either an alcohol, typically ethanol, a simple hydrocarbon such as heptane or n-dodecane, or a complex hydrocarbon such as rocket grade kerosene (RP) or a jet propellant (JP). In some cases, it may be necessary to perform some sort of surface treatment on the NPs such as passivation to counter balance the tendency of NPs to aggregate and form a much larger

cluster. Most often a surfactant is employed to reduce the surface tension and make NPs disperse in the liquid more effectively, to form a nano-suspension through formation of nanoclusters, and to stay suspended for a longer period. Much of the earlier work in this area has been performed on the suspension of poorly soluble drugs for drug delivery. [16, 17]

The aggregation process in a suspension is generally a very slow process and it is expected to severely hamper the reactivity of NPs by taking away the most important characteristic property of NPs, i.e. the extremely large surface to volume ratio of NPs. That is, the very specific property of NPs that gives them their unusually high reactivity, catalytic properties, as well as liquid phase properties such as increased heat transfer. The only exception concerning the loss of such desirable properties is when the NP aggregates are extremely porous, which is rarely the case and should not be assumed without due investigation. In fact, highly porous materials with nano-scale pores show high reactivity and catalytic properties that makes them behave more like NPs, unlike other mesoscale materials. [18]

The intricacies of dispersions of NPs in HCF have not received enough attention by researchers working on nanofuels, as judged by the lack of details about nano-dispersion in published reports. In fact, most NPs show a tendency to form sizable aggregates when they are introduced to most liquids. It is quite possible that NPs that are supplied by vendors as a powder are mostly in large clusters and it is often necessary to use sonication to break the NP clusters up while they are added to a liquid. Often the best practice is to use a powerful enough sonication probe/tip instead of an ultrasonic bath, which may be marginally effective in some cases. Even then, a sonication probe may not be able to break apart a strongly bonded cluster of NPs.

Typically, NPs in a “nanofuel” form relatively sizeable aggregates that are no more than a few micrometers. Such aggregates may stay suspended within the liquid long enough so that, the suspension passes the customary turbidity test. Most often, the quality of the NPs dispersion in HCF is merely judged by the turbidity of the liquid, which is how fast the solid particles settle at the bottom of a container. Such a test only reveals the extreme cases and it cannot be an indicator for a nano-suspension or any form of well-suspended NPs in the liquid. In most nanofuels that pass the turbidity test, while the weigh% of the added NPs is high enough, quite possibly most of NPs are “trapped” in larger clusters, so that the concentration of NPs and nanoclusters in the “nanofuel” ends up to be far less than what it takes to exhibit a noticeable NP-related effect.

Nano-dispersion is achieved when a majority of the suspended NPs are in relatively small clusters, each containing no more than a few hundred NPs. For example, for Al NPs with nominal size of 80 nm, we considered a reasonably good dispersion was achieved if most of the NPs clusters where smaller than about 500 nm, as revealed by particle size distribution measurement long after addition of NPs to the fuel and subsequent sonication. For most fuels in this study, a reasonably good dispersion was only achieved with the inclusion of a surfactant (typically < 5% by weight) along with the NPs.

An effective approach for the determination of a reasonably good dispersion of NPs in a liquid is through a series of periodic measurements of particle size distribution to obtain temporal evolution of the size distribution of NPs clusters in the liquid. Unfortunately, this approach proved to be ineffective when the additives have extremely large aspect ratio, as in the case for graphene nanoplatelets. Based on our experience, the optical detection system of the particle sizer consistently picked up the larger dimension of the platelets that is in microns and their smaller dimension that is in nanometer scale remained obscure, rendering the particle size distribution results meaningless.

Use of transmission electron microscopy (TEM) can be helpful in learning certain aspects of the dispersion of NPs in a liquid, but it has its own limitations. The main limitation stems from the fact that typical TEM measurements are performed on dry samples and the drying process usually introduces aggregation of NPs not to mention occasional impurities. However, TEM images usually reveal how densely the clusters are packed and if there exist substantial porosity within the clusters, assuming the drying process does not affect their porosity. As previously

mentioned, sufficiently porous NP clusters may retain the substantial reactivity of the NPs. A better approach may be to perform a cryogenic TEM imaging, which involves observation of a matrix of NP clusters within the frozen HCF, near liquid nitrogen temperature. However, this type of TEM, which is commonly used for biological samples is costly and may not be available to most researchers.

Formation of Nanofuel Droplets

The nanofuel droplets are often a suspended droplet that is formed at the end of a solid fiber or a capillary tube held by the surface tension. A somewhat less common practice is to create free droplets, often a steam of falling droplets, and study their burning properties while they are in motion. Burning properties of droplets of different sizes, typically 0.1-2 mm in diameter, have been have been reported in the literature. The common practice for a suspended droplet is to use a small diameter rod or fiber made of quartz or other materials such as SiC with a relatively high meting point.

The formation of a droplet at the end of the rod is greatly facilitated by producing a “bead” at the end of the rod, which may be achieved through melting of the end of the quartz rod by a high temperature flame such as an oxy-propane torch. Excellent results have been achieved with communication grade quartz optical fibers, 0.1, 0.15, and 0.2 mm in diameter. No appreciable change in the surface tension of the HCF was observed with any of the surfactants that were used in this study, i.e. Oleic Acid, Span 80, and bis(2-ethylhexyl) sulfosuccinate sodium salt (NaAOT). In this study, the diameter of the quartz fiber was 0.15 mm and the diameter of a typical nanofuel droplet was between 1.2-1.5 mm.

Ignition of Fuel Droplets

There are relatively few ignition methods for the initiation of combustion in HCF droplets of all kinds. The most common ignition methods are hot wire ignition and hotbox ignition. Occasionally a flame ignitor may be used, commonly in a miniature torch or in a small flat flame arrangement. The difference between various ignition sources boils down to two main parameters, (i) the temperature of the source that affects auto ignition of the droplet and (ii) amount of energy exchange and the speed of the heat exchange mechanisms between the ignition source and the fuel droplet as it influences the rate of vaporization.

Other parameter that effect ignition include the availability and mixing of gaseous oxidizer, proximity of the ignition source to the droplet and the geometrical spread of the source that may also be influential in the ignition process. For example, hotbox ignition and hot wire ignition tend to be among the slower methods, compared to say, flame ignitors, so that smaller droplets may be completely vaporized before they experience the combustion event.

There are ignition methods that are relatively much faster so that the droplet is subject to a substantially sharper temperature rise, potentially exceeding 10e5 K/s. We have recently introduced two new ignition methods, photo-ignition (PI) and plasma arc ignition (PAI). [19] Photo-ignition is based on the gasless micro explosion of aluminum NPs ejects burning Al NPs (with T > 2000 K) very close to the fuel droplet.

PAI takes advantage of a high frequency and low current plasma arc that can rapidly “heat up” a small spot on the edge of droplet leading to the combustion of a wide range of fuel droplets including hard-to-ignite fuels such as diesel and hexadecane. The gas temperature in PAI is estimated to exceed 3000 K and it is capable of igniting fuel droplets with an extremely low vapor pressure such as AF315E and vacuum pump oil within a small fraction of a second. AF M315E is a green monopropellant that was developed by the Air Force Research Laboratory as a hydrazine replacement for in-space applications. Details of these ignition methods and the results of their

applications are described in a recent publication. [19] Figure 1 shows the experimental set up for the study of combustions characteristics of suspended fuel droplets.

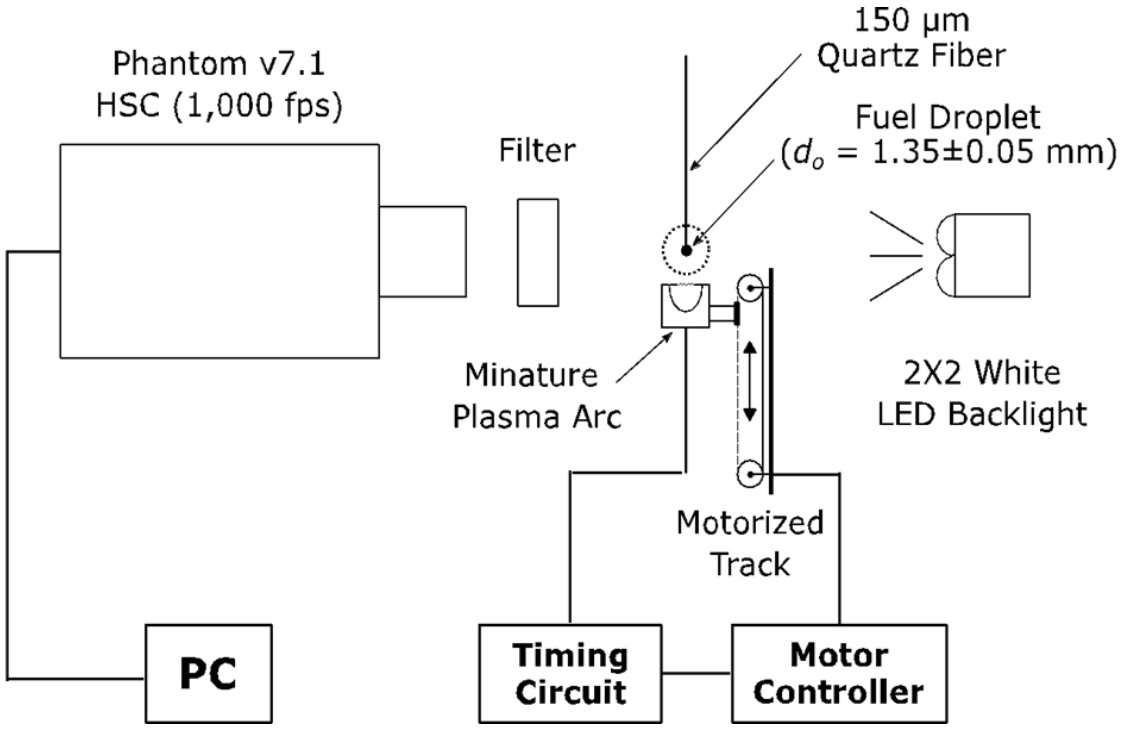

Figure 1 - Droplet experiment test facility consisting of the high-speed imaging configuration for the suspended fuel droplet and the plasma arc ignition system.

Burning Characteristics of Nanofuel Droplets

Most reports on the burning characteristics of HCF droplets are solely focused on the burning rate constant, *K*, of the droplet. It is usually assumed that *K* is a characteristic of a fuel. However, the evolution of the size and shape as well as turbulence or even movement of the fuel droplet along the fiber throughout the lifetime of the droplet may include the effects of other events that are associated with the droplet ignition and the subsequent burning process. [20, 21]

The fuel burning related events include, evaporation phase of the droplet, ignition process (one-stage vs. two-stage), low-temperature flame (aka cold flame) followed by a fully established flame and the accelerated burning towards the end of the burning process. Any of these may be influenced by the shape of the droplet, the size and the temperature of the pendent/fiber, as well as the type and concentration of the NPs in the fuel. For a simple and very volatile neat HCF, such as ethanol and heptane the burning process is less eventful and for compound HCF and nanofuels with relatively high loading of NPs the burning process is expected to be more involved.

In-light-of the above discussion, there are reasons to believe that the values of *K* that appears in the literature may be unintentionally influenced by certain parameters, which results in non-repeatable *K* values from lab-to-lab or from one experimental set up to the next. However, as it becomes clear in the following discussion, one important parameter in the evaluation of *K* has nothing to do with the approach in the experimentation or the measurement process. Instead, it is greatly influenced by the data reduction approach, which is covered in the following section.

There are a few potentially less influential parameters, some better-known, such as droplet

size or radiation absorption, as well as less talked about parameters such as change in surface tension due to additives and the surfactant or the duration and the temperature of the ignition source. Burning characteristics of droplets within the range of 0.1-2 mm have been reported in the literature. Smaller droplets have smaller mass and relatively larger surface to volume ratio, so they are easier to heat up and produce enough fuel vapor for initiation of the combustion, assuming they get a chance to experience combustion before they are completely evaporated.

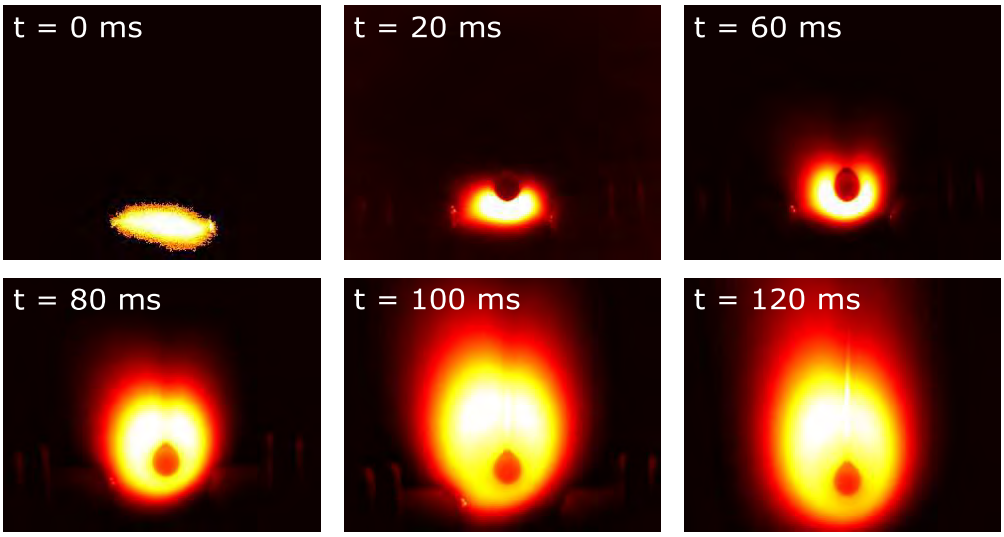

Figure 2- Infrared thermographic images depicting the ignition sequence of an n-dodecane droplet using the plasma arc ignition system with a duration set to 100 ms.

For any droplet size a nearly spherical droplet has a smaller surface area per volume than the more frequently observed elongated/ellipsoidal droplet of the same volume. Less surface area means less boundary layer, which may result in less evaporation and a relatively lower burning rate. Moreover, under the identical conditions (thermodynamic and ignition) the ignition delay may also be affected by the size and shape of the droplet.

Radiation absorption by nanofuel droplets is likely affected by the presence of solids in them. For example, the presence of a very small concentration of carbon-based nanoparticles such as carbon nanotubes and graphene nanoplatelets can substantially increase the radiation absorption of the liquid, [9] while Al NPs are routinely used to increase the thermal conductivity of nanofluid coolants. [2]

Evaluation of the Burn Rate Constant

Evaporation of the liquid fuel at the droplet surface leads to a diffusion flame that encompasses the droplet as the fuel vapor reacts with the surrounding oxidizer. This causes the liquid fuel surface to continuously regress, reducing the droplet in size until the end of its lifetime. The rate at which this process occurs is primarily dependent on the thermodynamic properties of the fuel and is often used to quantify droplet burning through the well-established d-squared law. [22-24]

The d-squared law states that during quasi-steady droplet burning, the square of the droplet diameter regresses linearly with time. However, this is an idealization, which does not fully apply to many real droplets due to several effects, including droplet heating, multicomponent distillation, end-of-life processes such as micro-explosions and possible interference from the

heated suspending fiber, as well as non-quasisteady effects such as fuel vapor accumulation. [22, 25] Nevertheless, it is useful to quantify results as “effective” burning rate constants. We recently reported burning rate constants for neat fuels, [26] that were determined using a method that automatically determines the most linear part of the droplet diameter regression for the longest time. We have shown that there can be up to a 10% variation depending on how the burning rate constants are effectively measured.

Recently, there has been substantial experimental work devoted to droplet studies involving the use of energetic additives to liquid fuel as burning rate modifiers. [9, 27-31] As the base liquid fuels for these experiments have included alcohols (i.e., ethanol) and certain kerosene blends (i.e., Jet-A, JP-8), there is a need for baseline burning rate results of a variety of common pure fuels using a consistent approach (i.e., controlling the initial droplet size, experimental procedure, and data reduction method). In addition, results from these studies indicated that augmentation of burning rates is possible up to approximately 20% for additive concentration of 5 wt%, but it is typically no greater than 10%.

One of our objectives was to investigate the use of nanoenergetic additives as a method of controlling combustion dynamics. Thus, we performed a series of suspended nanofuel droplet studies using various rocket relevant base fuels (e.g., RP-2). We reported on the droplet burning rate and ignition delay baseline data for a broad range of ten common hydrocarbon fuels, while also including a sensitivity study on the burning rate constant that encompasses all reasonable possibilities and commonly implemented methods. Through this process, a new approach to determine the droplet burning rate was developed that consistently provides a better measure of the “effective” droplet burning rate constant for all fuel types.

It was found that all HCFs under study were consistently ignited within about 100 ms of arc duration, except for hexadecane, which required about 260 ms. A typical sequence for droplet ignition can be seen in Fig. 2. In this figure the entire ignition process occurs within about 100 ms, where the reaction zone of the n-dodecane droplet grows and fully establishes by the time the ignitor is moved away from the droplet. The short duration ignition was only a fraction of the total droplet lifetime, essentially isolating quasi-steady droplet burning from ignition effects. To the best of our knowledge, this is the first study implementing the use of such an ignitor for investigating droplet burning. A detailed description of the PAI system and a comparison with other ignition methods has been covered in another publication. [19]

Droplet Burning Properties

In our previous work on pure hydrocarbon fuels, [19] K was evaluated using 70% of the data centered around the midpoint of the droplet burn time, referred to as the $K_{mid.,70}$ approach. This was done to add consistency to the data reduction methodology and attempt to remove the effects of transient behavior. However, after a detailed sensitivity study that was performed to evaluate alternative data reduction techniques we arrived at a more suitable approach as the “effective” burning rate constant evaluation method for all fuels.

To address this point, K was calculated a multitude of different ways for a single set of data. A conceptual example depicting the diameter regression of a burning droplet exhibiting some non-linear effects is shown in Fig. 3, which specifies the parameters used to determine K. First, the three general data reduction schemes implemented for this study are shown: (1) beginning, (2) middle, and (3) end. As their names suggest, each denotes the reference location of the considered data set. Changing the three variables x, y, and z covers all possible methods for determination of K from the provided data. Starting at these three reference points, the script separately calculated K for a range of specified intervals and offsets. More details of different approaches to calculate K is found in [26].

Ignition Delay in Nanofuel Droplets

Ignition delay time was the other important parameter that was evaluated in the study of nanofuel droplet burning. Igniting suspended droplets via the short-duration plasma arc provided a convenient platform to study ignition behavior due to its constant average output power and adjustable ignition duration. As the plasma arc produced minimal background light and heat. [14]

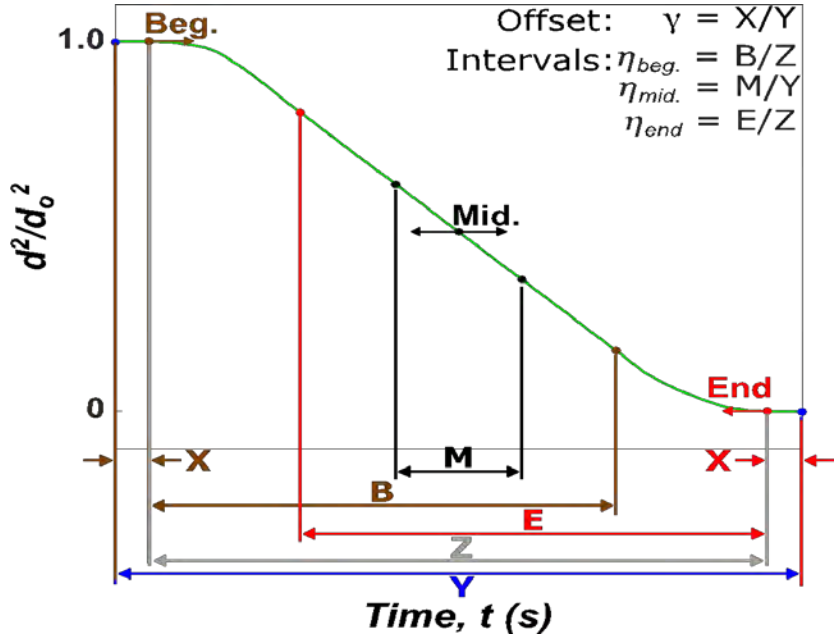

Figure 3- Schematic representation of different methods of calculating *K* for a range of specified offsets and intervals for three reference locations: the beginning, the mid-point and the end-point.

The details of ignition and the development of the flame early in the droplet lifetime were readily captured. Typically, ignition delay is defined as the time separation between introducing the droplet to the (hot) ignition environment and the observation of the established flame. [32] While it is straightforward to define the first event, naturally there is some subjectivity associated with the second. In general, the fully-established flame is associated with an enveloping reaction zone around the droplet that is on the order of the droplet diameter.

For the various hydrocarbons studied, the flame originates beneath the droplet close to the ignitor location, and quickly grows to a maximum before slightly reducing in size at the start of steady burning. Therefore, τ_{ign} was the time the ignitor is first activated to the time the droplet flame reaches an initial maximum size, which represents the upper limit of the ignition delay for each fuel.

To provide a consistent approach for the evaluation of the ignition delay, the flame region was automatically tracked in the IR images using an image processing script. Example results for ethanol are shown, for reference, in Fig. 4. Similar results for τ_{ign} were produced using visible imaging, often simultaneous with the IR images. However, visible imaging is reliant on the flame luminosity, which differs among the fuels in this study, largely due to soot formation. Therefore, evaluation of ignition delays through visible imaging were deemed to be less reliable than the IR results, leading to only the IR results being reported in this study.

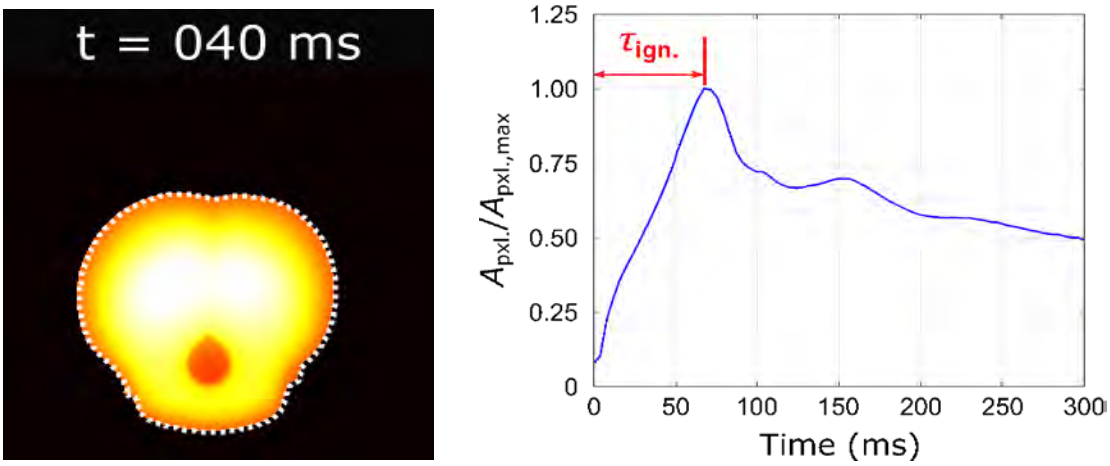

Figure 4 - The approach in calculating the ignition delay, τ_{ign}, (a) IR images (at 250 fps) was used to capture the temporal evolution of the enveloping droplet flame. (b) Flame region was tracked and τ_{ign} was determined as the time from the start of ignition to the droplet flame reaches an initial maximum size ($A_{\mathbf{pxl,\ max}}$).

Table 1 - Thermodynamic characteristics of the pure hydrocarbon fuels

Fuel Property	Ethanol	Methanol	n-Heptane	Toluene	n-Dodecane	Hexadecane
Chemical Formula	C_2H_5OH	CH_3OH	C_7H_{16}	C_7H_8	$C_{12}H_{26}$	$C_{16}H_{34}$
Molecular Weight [kg/kmol]	46.07	32.04	100.21	92.14	170.34	226.45
Stoichiometric Air-Fuel Ratio, O/F	8.946	6.431	15.081	13.418	14.920	14.863
Specific Heat Cap.*, c_p [kJ/(kg-K)]	2.44	2.50	2.24	1.70	2.21	2.21
Thermal Cond.*, λ [W/(m-K)]	0.167	0.202	0.123	0.131	0.135	0.140
Mass Density*, ρ [g/cm^3]	0.79	0.79	0.68	0.86	0.75	0.77
Boiling Temp., T_b [K]	351	338	372	384	489	560
Vapor Pressure*, $P_{vap.}$ [kPa]	7.9	16.9	6.1	3.8	1.5E-02	9.6E-05
Adiabatic Flame Temp., $T_{adia.}$ [K]	2195	2150	2265	2317	2268	2269
Heat of Vapor.$^+$, $\Delta h_{vap.}$ [kJ/kg]	837	1099	317	360	259	229
Heat of Comb.*, Δh_c [kJ/g]	29.7	22.7	48.1	42.4	47.2	47.2
Energy Density, [kJ/cm^3]	23.5	17.9	32.7	36.5	35.4	36.3

* Calculated for T = 298 K and P = 101,325 Pa

\+ Calculated for $T = T_b$ and P = 101,325 Pa

Table 2 - Thermodynamic characteristics of the kerosene fuels

Fuel Property	RP-2	JP-8	FT	Diesel #2
Average Chemical Formula	$C_{11.74}H_{23.4}$	$C_{11}H_{21}$	$C_{12}H_{25}$	$C_{12}H_{23}$
Molecular Weight [kg/kmol]	164.60	153.29	169.34	167.32
Stoichiometric Air-Fuel Ratio	14.681	14.563	14.806	14.574
Spec. Heat Cap.*, c_p [kJ/(kg-K)]	2.03†	1.92	2.73	2.20
Thermal Cond.*, λ [W/(m-K)]	0.107	0.115	9.35E-03	0.125
Mass Density*,ρ [g/cm^3]	0.80	0.81	0.76	0.83
Boiling Temp., T_b [K]	438-498	413-573	448-633	453-613
Vapor Pressure*, $P_{vap.}$ [kPa]	5.7E-02	1.8E-01	21	7.7E-02
Adiabatic FlameTemp., $T_{adia.}$ [K]	2406†	2338	2338	2292
Heat of Vapor.+, $\Delta h_{vap.}$ [kJ/kg]	308†	441	339	270
Heat of Comb.*, Δh_c [kJ/g]	44	43	44	46.1
Energy Density, [kJ/cm^3]	35.2	34.8	33.4	38.3

* Calculated for T = 298 K and P = 101,325 Pa

\+ Calculated for $T = T_b$ and P = 101,325 Pa

† For $C_{12}H_{23.40}$

RESULTS AND DISCUSSION

Burning Rate Constants

Droplet burning properties were investigated for ten various hydrocarbon fuels, encompassing alcohols (i.e., ethanol, methanol), simple hydrocarbons (i.e., n-heptane, toluene, n-dodecane and hexadecane), and kerosene blends including rocket grade kerosene RP-2, diesel #2 and the aviation fuels JP-8 and its surrogate Fischer-Tropsch synfuel (FT).

These fuels were chosen as they represent a wide range of common hydrocarbons and alternative fuels implemented in rocket engine and air-breathing propulsion systems. [33-35] The three fuel types can be broadly classified by their thermo-physical properties, which are documented in Tables 2 and 3.

The thermodynamic characteristics of the two alcohols, while similar to each other, vary significantly from the other pure hydrocarbons and kerosene blends. Similar trends can be seen for the four pure hydrocarbons, with a notable difference in particular for the heats of vaporization and heat of combustion when compared to the alcohol fuels. Generally, there is some spread among these simple hydrocarbons in thermo-physical properties, which typically span the range of values characteristic of the kerosene blends. This can be attributed to these simple hydrocarbons representing some of the lighter (e.g., n-heptane, toluene) and heavier (e.g., n-dodecane, hexadecane) constituents found in the various kerosene fuels.

To investigate the effects of these different constituents further, the burning properties of a

50/50 wt% binary mixture of n-heptane and n-dodecane were also quantified. Finally, different types of kerosene blends share similar properties to each other, with JP-8 and FT in particular being in close agreement, which is the main reason Fischer-Tropsch has been used as a JP-8 replacement in Air Force applications. [36].

Ignition Delays

Ignition delays for the stated eleven fuels were measured by taking an average of five identical ignition events and post-processing the IR images using the procedure described in [26]. It was found that the ignition delays covered a range from 65 to 110 ms for all neat fuels except for hexadecane that was 260 ms. The much longer ignition delay of this fuel is most likely due to its extremely low vapor pressure. Overall, the measured ignition delays using PAI were much shorter than other ignition delays reported in the literature using arc furnace ignition [37-40], thus produced ignition events that were much more sharply defined in time. [14]

As shown in Fig. 5, ignition delays correlated closely with fuel's boiling temperature T_b (see Tables 1 and 2), where the more volatile fuels with the lowest boiling temperatures exhibit shorter ignition delays. Understandably, for the 50/50 wt% n-heptane/n-dodecane blend, the ignition delay followed the more volatile component, n-heptane, where the ignition delay was close to 70 ms for both. This behavior was also exhibited by the kerosene blends as well, where lighter constituents vaporizing and burning earlier in the droplet lifetime of a multicomponent fuel. [41,42] Finally, ignition delays for n-dodecane and diesel #2 were both approximately 110 ms, which supports some previous ignition work with n-dodecane as a proposed diesel surrogate for use in fundamental combustion studies. [43,44]

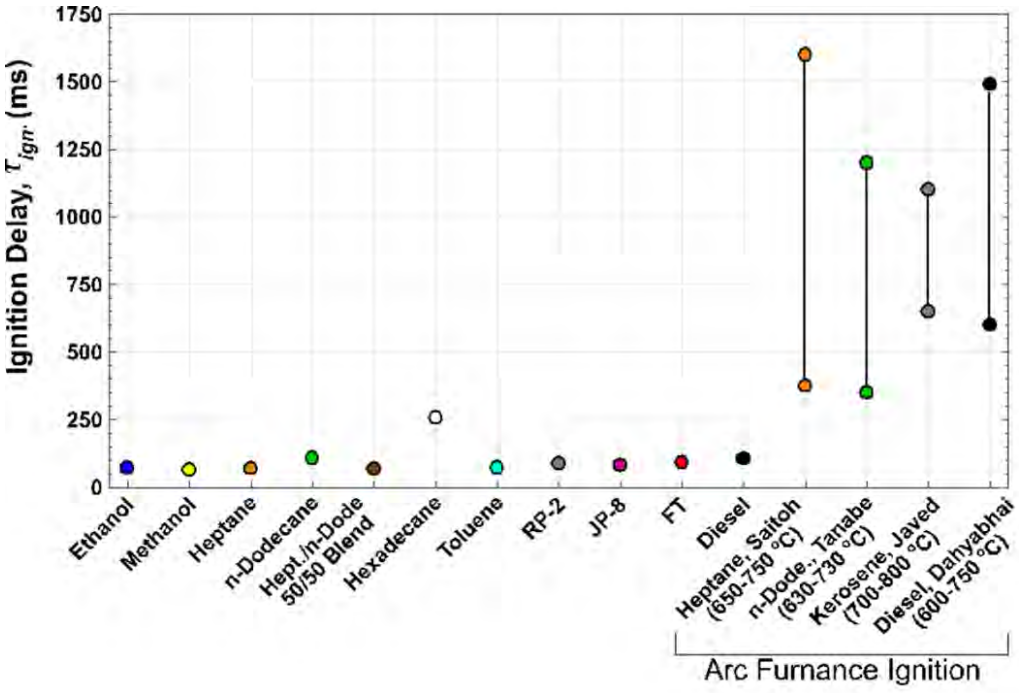

Figure 5 - Ignition delays τ_{ign} for various hydrocarbon fuels evaluated from the infrared thermal images. The reported ignition delays measured by conventional methods are also shown.

CONCLUSIONS

The combustion properties of fuel droplets were investigated for a variety of hydrocarbon fuels encompassing alcohols, simple hydrocarbons and kerosene blends. The burning rate constants *K* generally corresponded to the differences in thermophysical properties between the fuel types, while the trends for τ_{ign} correlated with the boiling temperature of the fuel. One major observation in this study was that *K* was found to have a notable sensitivity to the data reduction method for non-volatile simple hydrocarbons and kerosene blends. The deviations among typical approaches in the evaluation of K was found to be as large as 10%. Hence, the K_β approach was developed that automatically found the *K* associated with the most linear fit to the data for the longest duration of droplet burning. The K_β approach was found to better represent steady droplet burning processes for the investigated fuels, and should be considered along with its simpler alternative $K_{end.,5,70}$ as potential options for a more reliable data reduction methods for evaluation burning rate constant of suspended fuel droplets.

It is not clear how fuel additives may affect/influence combustion dynamics in a nanofuel droplet. Thermodynamic effects of fuel additives such as their effect on the energy content, heat absorption, and possibly rate of vaporization of the nanofuel droplets is one area that has been the subject of interest and needs to be looked at by theoretical combustion scientists. For instance, a recent report [9] revealed a relatively small increase in the burning rate constant of RP-2 to a very modest concentration (0.1 w%) of GNP in RP-2. They attributed this to an increase in radiative heat absorption by the nanofuel. They also reported that further increase in concentration to 1 w% reverses the trend and results in a very small decrease in the burning rate constant, *K*. While we were not able to reproduce their result for 0.1 w% concentration, we observed the small decrease (~5%) in *K* with 1-2 w% GNP in RP-2. Repeating the same set of experiments for ethanol and GNP produced similar results as RP-2. Based on the burn rate constant and ignition delay results, it is hard to conclude that low concentration (< 2%) of most energetic solids has a significant effect on the burning characteristic of nanofuels.

ACKNOWLEDGEMENTS

This work has been supported by the Air Force Office of Scientific Research (AFOSR) with Dr. Mitat Birkan as program manager.

REFERENCES

[1] Yetter, RA, Risha GA, Son, SF, ***Metal particle combustion and nanotechnology***, Proc Comb Inst. 32(2) (2009) pp. 1819-1838.

[2] Saidur, BR, Leong, KY, Mohammad, HA, ***A review on applications and challenges of nanofluids***, Renew. Sust. Energy Rev. 15 (2011) pp. 1646–1668.

[3] Armstrong RW, B. Baschung B, Booth DW, and Samirant M, ***Enhanced propellant combustion with nanoparticles***, *Nano Letters*, 3(2) (2003), pp 253–255

[4] Tyagi H, Phelan PE, Prasher R, Peck R, Lee T, Pacheco JR, Arentzen P., ***Increased hot-plate ignition probability for nanoparticle-laden diesel fuel***, Nano Lett 8(5) (2008), pp. 1410–1416.

[5] Basha SA and Gopal KR, ***A review of the effects of catalyst and additive on biodiesel production, performance, combustion and emission characteristics***, Ren. Sust. Engy, 16(1) (2012), pp 711-717.

[6] Jones M, Li CH, Afjeh A, Peterson GP., ***Experimental study of combustion characteristics of nanoscale metal and metal oxide additives in biofuel (ethanol)***,

Nanoscale Res Lett 6(1), (2011), pp. 246-9.
[7] Sabourin JL, Yetter RA, Parimi VS. ***Exploring the effects of nanostructured particles on liquid nitromethane combustion***, J Propul Power, 26(5) (2010), pp.1006–15.
[8] Sabourin JL, Dabbs DM, Yetter RA, Dryer FL, Aksay IA., ***Functionalized graphene sheet colloids for enhanced fuel/propellant combustion***, ACS Nano, 3(12), (2009) pp. 3945–54.
[9] Ghamari M. and Ratner A., ***Combustion characteristics of colloidal droplets of jet fuel and carbon based nanoparticles***, Fuel 188 (2017) pp. 182-189.
[10] RAI, A., PARK, K., ZHOU, L., and ZACHARIAH, M. R., ***Understanding the mechanism of aluminium nanoparticle oxidation***, Comb. Teor. Modeling 10(5) (2006) pp. 843-859.
[11] Lu, AH, Salabas EL, Schuth F, ***Magnetic Nanoparticles: Synthesis, Protection, Functionalization, and Application***, Chemie Intern. Ed. (2007), Wiley Online Lib.
[12] Tang, F, Li, L, Chen, D, ***Mesoporous Silica Nanoparticles: Synthesis, Biocompatibility and Drug Delivery***, Adv. Matt, 24(12), (2012) pp. 1504-1534.
[13] Mittal, AK, Chisti, Y, Banerjee UC, ***Synthesis of Metalic Nanoparticles using Plant Extracts***, Biotech. Adv. 31(2) (2013) pp 346-356.
[14] Biswas, A, Bayer, IS, Biris, AS, Wang, T, Dervishi, E, Faupel F, ***Advances in top–down and bottom–up surface nanofabrication: Techniques, applications & future prospects***, Adv. Colloid Inter Sci. 170 (1-2) (2012), pp. 2-17.
[15] Verma S, Gokhale R, Burgess DJ, ***A comparative study of top-down and bottom-up approaches for the preparation of micro/nanosuspensions***, Intern J of Pharma, 380, (2009), pp. 216-222.
[16] VR Patel, YK Agrawal, ***Nanosuspension: An approach to enhance solubility of drugs,*** J. Adv. Pharm. Technol Res. 2(2) (2011), pp 81-87.
[17] Chingunpituk J., ***Nanosuspension Technology for Drug Delivery***, Walailak J. of Sci Tech. 4(2) (2007), pp. 139-153.
[18] Tang, F, Li, L, Chen, D, ***Mesoporous Silica Nanoparticles: Synthesis, Biocompatibility and Drug Delivery***, Adv. Matt, 24(12), (2012) pp. 1504-1534.
[19] Badakhshan, A, Bennewitz JW, and Talley DG, ***New Ignition Methods for Droplet Combustion Studies***,, accepted for publication in J. Comb. Sci. & Tech. in March 2018.
[20] Verwey C, and Birouk M, ***Fuel vaporization: Effect of droplet size and turbulence at elevated temperature and pressure***, Combus. Flame 189, (2018) pp. 33-45.
[21] Bennewitz JW, et al., ***Periodic partial extinction in acoustically coupled fuel droplet combustion***, Combus. Flame 189, (2018) pp. 46-61.
[22] Law, C., and Williams, F., ***Kinetics and Convection in the Combustion of Alkane Droplets***, *Combustion and Flame*, Vol. 19, No. 3, (1972), pp. 393–405.
[23] Faeth, G. M., ***Current Status of Droplet and Liquid Combustion„" Progress in Energy and Combustion Science***, Vol. 3, No. 4, (1977), pp. 191–224.
[24] Glassman, I., and Yetter, R., *Combustion*, 4th ed., Academic Press, San Diego, CA, 2008.
[25] Law, C. K., ***Recent advances in droplet vaporization and combustion***," *Progress in Energy and Combustion Science*, Vol. 8, No. 3, (1982), pp. 171–201.
[26] Bennewitz, JW, Badakhshan A., and Talley DG, ***Systematic Measurement of Hydrocarbon Fuel Droplet Burning Rate Constants and Ignition Delays***", AIAA Aerospace Sciences Meeting Kissimmee, FL. (AIAA 2018-0672), (2018).
[27] Basu, S., and Miglani, A., ***Combustion and heat transfer characteristics of nanofluid fuel droplets: A short review***, *International Journal of Heat and Mass Transfer*, 96, (2016), pp. 482–503.
[28] Pfeil, M. A., Rosen, S. C., Yu, Y. C., Anderson, W. E., and Son, S. F., ***Effects of NanoAluminum on Droplet Combustion and Combustion Instabilities in a Single Element Rocket Combustor***, *46th AIAA Joint Propulsion Conference & Exhibit*, Vol. Paper

AIAA-2010-7154, (July 2010).

[29] Pfeil, M. A., Groven, L. J., Lucht, R. P., and Son, S. F., ***Effects of Ammonia Borane on the Combustion of an Ethanol Droplet at Atmospheric Pressure***," *Combustion and Flame*, 160(10), (2013), pp. 2194–2203.

[30] Guerieri, P. M., DeLisio, J. B., and Zachariah, M. R., ***Nanoaluminum/Nitrocellulose Microparticle Additive for Burn Enhancement of Liquid Fuels,*** *Combustion and Flame*, 176, (2017), pp. 220–228.

[31] Sim, H., Plascencia, M. A., Vargas, A., Bennewitz, J. W., Smith, O. I., and Karagozian, A. R., ***Effects of ALuminum Nanoparticle Additives on Liquid Fuel Droplet Combustion with and without Acoustic Excitiation***, 10th *U.S. National Combustion Meeting*, (April 2017).

[32] Aggarwal, S. K., ***Single Droplet Ignition: Theoretical Analyses and Experiment Findings***, *Progress in Energy and Combustion Science*, 45, (2014), pp. 79–107.

[33] Turns, S. R., ***An Introduction to Combustion: Concepts and Applications***, 8th ed., McGraw-Hill Higher Education, Boston, MA, (2000).

[34] Sutton, GP, and Biblarz, O., ***Rocket Propulsion Elements***, 8th ed., John Wiley & Sons, Inc., Hoboken, NJ, (2010).

[35] Erbschloe, D., ***Air Force alternative fuels process paves way to future***, Tech. rep., Air Force Air Mobility Command, Sapphire Energy Report, (2012).

[36] Karagozian, A. R., Dahm, W. J. A., Glasgow, E., Howe, R., Kroo, I., Murray, R., and Shyu, H., ***Technology Options for Improved Air Vehicle Fuel Efficiency***, Tech. Rep. SAB-TR-06-04, Air Force Scientific Advisory Board Report, (2006).

[37] Sioui, R., and Jr., L. R., ***The prediction of the burning constants of suspended hydrocarbon fuel droplets***, *Combustion and Flame*, 13(5), (1969), pp. 447–454.

[38] Vargas, A., Sim, H., Plascencia, M. A., Smith, O. I., and Karagozian, A. R., ***Effects of Aluminum Nanoparticles on Burning Liquid Fuel Droplets in a Quiescent Environment***," 11th *Southern California Flow Physics Symposium*, (April 2017).

[39] Saitoh, T., Ishiguro, S., and Niioka, T., ***An experimental study of droplet ignition characteristics near the ignitable limit,*** *Combustion and Flame*, 48, (1982), pp. 27–32.

[40] Tanabe, M., Bolik, T., Eigenbrod, C., Rath, H., Sato, J., and Kono, M., ***Spontaneous ignition of liquid droplets from a view of non-homogeneous mixture formation and transient chemical reactions***, *Symposium (International) on Combustion*, 26(1), (1996), pp. 1637–1643.

[41] Lefebvre, A. H., and McDonell, V. G., ***Atomization and Sprays***, 2nd ed., CRC Press, Boca Raton, FL, (2017).

[42] Dahyabhai, S., and Rathod, P., ***An Experimental Investigation on Droplet Ignition of Bio-Diesel and its Blends***, *International Journal of Advance Engineering and Research Development*, 1(5), (2014), pp. 420–434.

[43] Javed, I., Baek, S., and Waheed, K., ***Autoignition and combustion characteristics of heptane droplets with the addition of aluminium nanoparticles at elevated temperatures***," *Combustion and Flame*, 162(1), (2015), pp. 191–206.

[44] Williams, F. A., ***Combustion Theory: The Fundamental Theory of Chemically Reacting. Flow Systems***, 2nd Ed., Benjamin/Cummings Publishing Co, Inc., Menlo Park, CA, (1985).

JOURNAL OF PROPULSION AND POWER
Vol. 35, No. 4, July–August 2019

Systematic Measurement of Hydrocarbon Fuel Droplet Burning Rate Constants and Ignition Delays

John W. Bennewitz* and Alireza Badakhshan†
ERC, Inc., Edwards Air Force Base, California 93524
and
Douglas G. Talley‡
U.S. Air Force Research Laboratory, Edwards Air Force Base, California 93524

DOI: 10.2514/1.B37195

In this experimental study, a new data reduction approach was developed for measuring droplet burning rate constants that automatically finds the most linear part of the *d*-squared curve for the longest period of time. The approach, here called K_β, was developed in response to the observation that burning rate constants can vary by up to 10%, depending on the reduction approach used, especially for fuel types such as nonvolatile simple hydrocarbons and kerosenes. To evaluate this new method, burning rate constants were measured for 10 fuels, including two alcohols, four simple hydrocarbons and four kerosene blends. The measured rates ranged from 0.74 to 0.94 mm^2/s, typically grouped by similarities in thermophysical properties of the fuel types. Notably, K_β and its simpler equivalent $K_{end,5,70}$ yielded burning rates with small statistical uncertainty ($\approx$0.006 mm^2/s average) across all fuels and were associated with the highest coefficient of determination for all K measurement approaches, indicating that these two methods are viable options for improved consistency in measuring burning rate constants. In addition, a systematic method is presented for measuring ignition delays τ_{ign} using a short-duration plasma source for ignition. The ignition delays ranged from 65 to 110 ms for most fuels, correlating well with the fuel boiling temperature. Combined, this work provides baseline data and data reduction tools suitable for future droplet combustion studies.

Downloaded by Doug Talley on August 19, 2019 | http://arc.aiaa.org | DOI: 10.2514/1.B37195

Nomenclature

A	=	semimajor axis length of the ellipsoidal droplet, mm
A_{flm}	=	flame area, mm^2
B	=	semiminor axis length of the ellipsoidal droplet, mm
b_χ	=	standard type-B uncertainty for a specific parameter χ
c_p	=	specific heat capacity, $kJ/(kg \cdot K)$
d_{eqac}	=	droplet diameter equivalent to the area of a circle, mm
d_{eqas}	=	droplet diameter equivalent to the surface area of a sphere, mm
d_{eqvs}	=	droplet diameter equivalent to the volume of a sphere, mm
d_{ss}	=	side-to-side droplet diameter, mm
F_{ij}	=	matrix defined by Eq. (19)
H	=	height of an individual pixel, mm
H_{tot}	=	total height of image field of view, mm
I	=	integrated thermal radiance, $W/(m^2 \cdot sr)$
i	=	specific image indicator or matrix row element
j	=	matrix column element
K	=	burning rate constant, mm^2/s
$K_{q,r,s}$	=	burning rate constant identifier, where q is the reference location, and r and s are the offset and interval, mm^2/s
m	=	total number of data points
N_H	=	total number of horizontal pixels within the image field of view
N_V	=	total number of vertical pixels within the image field of view
$n_{HP,i}$	=	number of horizontal pixels comprising the droplet minor axis length in a specific image i
$n_{VP,i}$	=	number of vertical pixels comprising the droplet major axis length in a specific image i
O/F	=	stoichiometric air/fuel ratio
P_{vap}	=	vapor pressure, kPa
R^2	=	coefficient of determination
s_χ	=	standard type-A uncertainty for a specific parameter χ
T_b	=	boiling temperature, K
T_{ad}	=	adiabatic flame temperature, K
U_χ	=	expanded uncertainty for a specific parameter χ
u_χ	=	combined standard uncertainty for a specific parameter χ
W	=	width of an individual pixel, mm
W_{tot}	=	total width of image field of view, mm
Z_{ij}	=	matrix defined by Eq. (18)
α_{ij}	=	matrix containing the linear regression coefficients
β	=	linear regression coefficient
γ	=	offset for the burning rate constant calculation
Δh_c	=	heat of combustion, kJ/g
Δh_{vap}	=	heat of vaporization, kJ/kg
$\Delta\tau_\eta$	=	interval time, s
η	=	interval for the burning rate constant calculation
λ	=	thermal conductivity, $W/(m \cdot K)$
ρ	=	mass density, kg/m^3
τ_{drop}	=	droplet burn time, s
τ_{ign}	=	ignition delay, s
ϕ	=	number of pixels along major or minor axis length defining the droplet edge

Presented as Paper 2018-0672 at the 2018 AIAA Aerospace Sciences Meeting, Kissimmee, FL, 8–12 January 2018; received 3 May 2018; revision received 18 January 2019; accepted for publication 9 February 2019; published online 8 April 2019. This material is declared a work of the U.S. Government and is not subject to copyright protection in the United States. All requests for copying and permission to reprint should be submitted to CCC at www.copyright.com; employ the eISSN 1533-3876 to initiate your request. See also AIAA Rights and Permissions www.aiaa.org/randp.

*Research Scientist, 10 E. Saturn Blvd., Building 8451. Member AIAA.
†Research Consultant, 10 E. Saturn Blvd., Building 8451. Member AIAA.
‡Lead, Combustion Dynamics Group, 10 E. Saturn Blvd., Building 8451. Associate Fellow AIAA.

I. Introduction

THE study of burning fuel droplets has been used as a basis of fundamental combustion studies for liquid rocket and airbreathing propulsion applications for decades [1–4]. The burning of an isolated droplet provides a convenient way to investigate condensed phase combustion processes. Evaporation of the liquid fuel at the droplet surface leads to a diffusion flame that encompasses the droplet as the fuel vapor reacts with the surrounding oxidizer. This causes the liquid fuel surface to continuously regress, reducing

the droplet in size until the end of its lifetime. The rate at which this process occurs is primarily dependent on the transport and thermodynamic properties of the liquid fuel and surrounding ambient gas, and it is often used to quantify droplet burning through the well-established d-squared (d^2) law [3–6].

The d-squared law states that, during quasi-steady droplet burning, the square of the droplet diameter regresses linearly with time. However, this is an idealization that does not fully apply to many real droplets due to several effects, including droplet heating, multicomponent distillation, end-of-life processes such as micro-explosions, and suspending fiber interference, as well as non-quasi-steady effects such as vapor accumulation [4,7]. Nevertheless, it is useful to quantify results as "effective" burning rate constants, which is a well-established method used to compare experimental results for both single-component [3,4,8–10] and multicomponent fuels [3,11–14]. Aside from being an established practice in experimental studies, approximating the burning rate for both of these fuel types in this manner is suitable in computer simulations in which a more detailed model of droplet behavior might not be affordable. Specifically, a linear regression approximation of the burning rate for a multicomponent fuel should be capable of capturing larger differences in droplet behavior, such as the variance between droplets composed of lighter average multicomponent fuels and those composed of heavier average multicomponent fuels. Therefore, it is necessary to quantify effective droplet burning rates using a consistent unified approach. It is shown in the present study that there can be up to a 10% variation, depending on the way the burning rate constants are evaluated. As the most direct implementation of the linear regression idea, here, we report burning rate constants quantified using a method that automatically determines the most linear part of the droplet diameter regression for the longest time of droplet burning. Justification for adopting this method and accompanying correction factors from other commonly used approaches to this method for a range of hydrocarbon fuels are also shown subsequently. A detailed uncertainty analysis for the measured burning rates is also provided, based upon the work of Shaw and Yu [15].

Recently, there has been substantial experimental work devoted to droplet studies involving the use of energetic additives to liquid fuel as burning rate modifiers [12,13,16–19]. As the base liquid fuels for these experiments have included alcohols (i.e., ethanol) and certain kerosene blends (e.g., Jet-A, JP-8), there is a need for baseline burning rate results of a variety of common pure fuels using a consistent approach (i.e., controlling the initial droplet size, experimental procedure, and data reduction method). Also, results from these studies indicated that the augmentation of burning rates is possible up to approximately 20% for $\leq$5 wt% additive concentration, but it is typically no greater than 10%. Our group currently is investigating the use of nanoenergetic additives as a method to garner control of combustion dynamics and, to date, has performed a series of suspended nanofuel droplet studies using various rocket relevant base fuels (e.g., RP-2). As the enhancements in droplet burning rate reported by the various research groups were measured using different methods, it was necessary to quantify the error attributed with the burning rate measurement method for a range of pure fuels to better interpret our results. Therefore, the current study presents droplet burning rate and ignition delay baseline data for a broad range of 10 common hydrocarbon fuels while also including a sensitivity study on the uncertainties associated with the evaluation methods of the burning rate constant that encompasses all reasonable possibilities and commonly implemented approaches. Through this process, a new method to determine the droplet burning rate is developed that consistently provides a better measure of the effective droplet burning rate constant for all fuel types.

II. Experiment Setup and Data Processing

The current study investigates droplet burning properties of various hydrocarbon fuels within an ambient air environment using the suspended droplet method. Droplets 1.35 ± 0.05 mm in diameter are suspended from an uncoated 0.15 mm quartz fiber from Polymicro Technologies, Inc., with a bead at the end (see Fig. 1). A nominal 0.20 mm bead is generated on the end of the quartz fiber through a heating process using an oxypropane torch, which assists with the retention of the droplet on the fiber during burning. Droplets are transferred to the quartz fiber mechanically using a hypodermic needle that consistently dispenses the same amount of fluid to create droplets of similar size for each test.

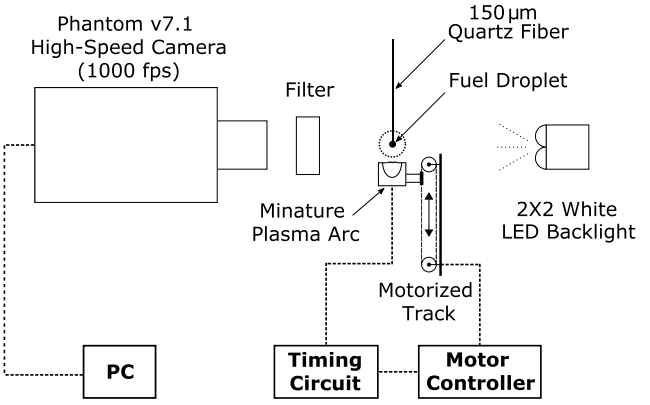

Fig. 1 Droplet experiment test facility consisting of the high-speed imaging configuration and the plasma arc ignition system connected to the automated motorized track.

Droplet burning is captured with a backlit imaging system consisting of a Phantom v7.1 high-speed camera with white background illumination. The high-speed camera is fitted with a Nikon AF Micro Nikkor 200 mm lens and operated at 1000 frames per second (FPS) for the duration of the droplet lifetime (approximately 2 s), with a Semrock FF01-433/530-25 filter used for improved visibility of the droplet regression for sooting fuels. To provide the proper optical contrast between the liquid droplet and the illuminated background for image processing, a 2×2 rectangular array of adjustable-intensity white light-emitting diodes (LEDs) is implemented.

For tests examining the ignition behavior of the various hydrocarbon fuels, infrared (IR) thermal imaging is used to clearly view the evolution of the reaction zone enveloping the droplet. This entailed substituting the Phantom v7.1 high-speed camera with a FLIR SC6800 midwave infrared (1.5–5.0 μm) camera imaging at 250 FPS, or simultaneously imaging with both. To provide full-scale measurements and prevent saturation with the IR camera, a 0.6 neutral density filter is used in combination with a StingRay Optics SR1936-A01 50 mm lens.

A. Ignition System: Plasma Arc Ignitor

Droplets are ignited using a miniature plasma arc ignition (PAI) system, which consists of a controllable duration plasma source that is scaled appropriately to the droplet length scale. The electrodes of the PAI system have a gap of 5 mm and are placed approximately 1 mm beneath the suspended droplet during the onset of ignition. The plasma arc is a periodic impulse with an exponential decay, where the high-temperature plasma pulse duration is estimated to be on the order of a few microseconds with a discharge repetition rate of 20.5 kHz.

The plasma arc ignitor is integrated with a custom-built timing circuit and motor controller. The timing circuit allows the total arc duration to be adjusted for reliable droplet ignition, for which the motor controller automatically pulls the ignitor away from the droplet after the set arc duration. All hydrocarbon fuels investigated in this study were consistently ignited within 100 ms of arc duration, except for hexadecane, which required approximately 260 ms. A typical sequence for droplet ignition can be seen in Fig. 2. This figure shows the entire ignition process occurred within 100 ms, for which the reaction zone of the n-dodecane droplet grew and was fully established by the time the ignitor moved away from the droplet. This fast-duration ignition method was chosen for this study because it acts only over a fraction of the total droplet lifetime, essentially isolating quasi-steady droplet burning from ignition effects. To the

Downloaded by Doug Talley on August 19, 2019 | http://arc.aiaa.org | DOI: 10.2514/1.B37195

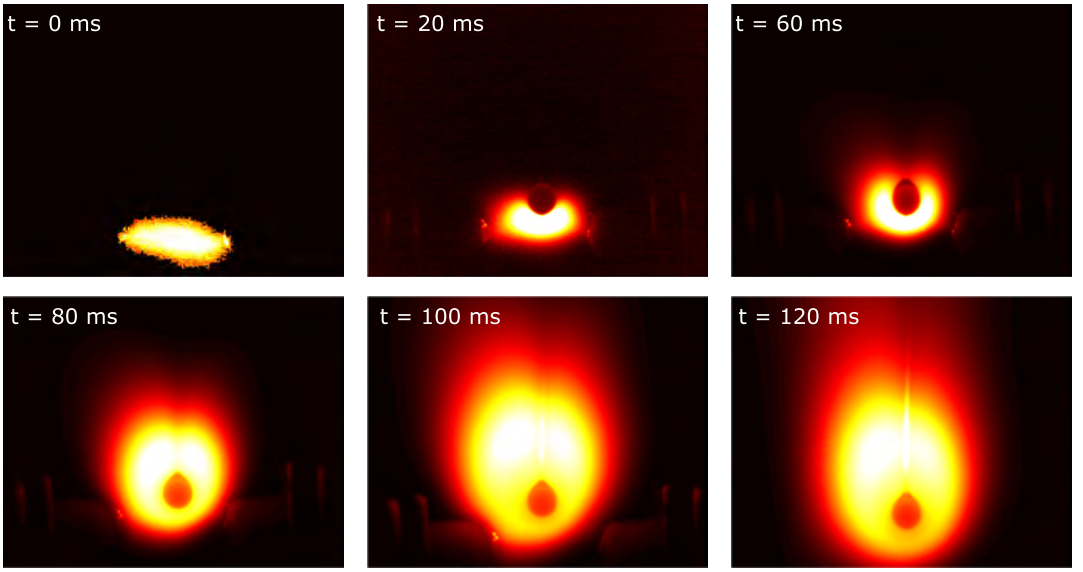

Fig. 2 Infrared thermographic images depicting the ignition sequence of an n-dodecane droplet using the plasma arc ignition system with a duration set to 100 ms.

Downloaded by Doug Talley on August 19, 2019 | http://arc.aiaa.org | DOI: 10.2514/1.B37195

best of the authors' knowledge, this is the first study implementing the use of such an ignitor for investigating droplet burning. A detailed description of the PAI system and a comparison with other ignition methods is covered in a related publication [20].

B. Droplet Burning Properties

As the fuels are burned in the suspended droplet configuration, the two burning parameters investigated in this study are the burning rate constant K and ignition delay τ_{ign}. The burning rate constant is the governing parameter for quasi-steady droplet burning behavior, which comes from the well-known d^2 law [4–6], and is written as

$$K = -\frac{\mathrm{d}}{\mathrm{d}t}(d_{eqvs})^2 \tag{1}$$

In this study, the diameter used to determine K is the droplet diameter associated with the equivalent volume of a sphere as described by Struk et al. [21]. This equivalent diameter is given by

$$d_{eqvs} = 2A^{1/3}B^{2/3} \tag{2}$$

where A and B are the semimajor and minor axis lengths associated with the ellipsoidal droplet.

For each test, the droplet diameter was automatically tracked using a script based on the work of Bennewitz et al. [14] and Sevilla-Esparza et al. [22]. This script takes the series of backlit images captured from the visible high-speed camera starting 200 ms after the ignitor is activated and fits an ellipse to the outer edge of the droplet for each image. With the outline of the droplet edge defined, the diameter regression history is created using Eq. (2) for the entire droplet burn time τ_{drop}. To first quantify the error associated with the droplet tracking algorithm, synthetic data following a known regression were created to assess the diameter fitting method. The synthetic image data included a perfectly spherical droplet of a representative initial size in the image field of view that followed a completely linear d-squared regression for approximately 2 s, ending at 10% of the original size. The outputs from the tracking algorithm and the analytical solution are extremely close to one another throughout the entire droplet lifetime, which are shown in Fig. 3 to be perfectly linear. The percent error for the droplet tracking script averages only 1.3% of the analytical solution across the droplet lifetime, therefore confirming that this approach provides reliable droplet diameter tracking for evaluating the burning rate constant.

For the burning rate constant calculation, there are multiple diameter definitions that can be applied to report measurements [8,21,23], which may introduce varying amounts of uncertainty. To quantify this sensitivity, the d-squared percent error for the synthetic data was determined using three alternative droplet diameter definitions, including the side-to-side diameter ($d_{ss} = 2B$), the equivalent area of a circle ($d_{eqac} = \sqrt{4AB}$), and the equivalent area of a sphere:

$$\left(d_{eqas} = \sqrt{2B^2 + \frac{2AB\sin^{-1}(\epsilon)}{\epsilon}}, \quad \text{where } \epsilon = \sqrt{\frac{A^2 - B^2}{A^2}}\right)$$

Overall, the d-squared percent error is fairly similar across the four diameter definitions (see Table 1), ranging from 1.27 to 1.33%.

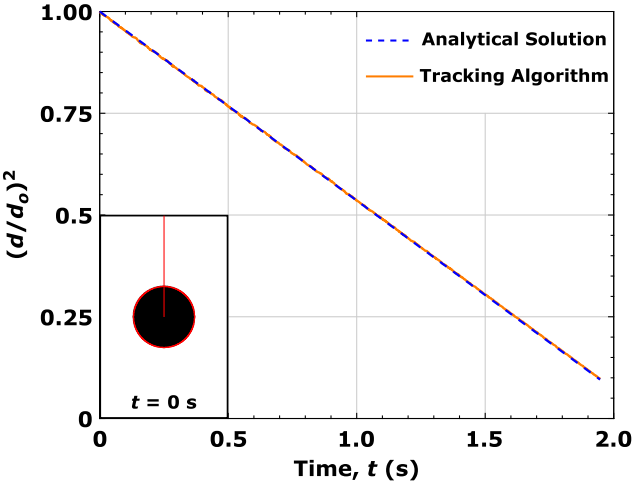

Fig. 3 Diameter regression history for synthetic data comparing the analytical solution (dashed blue) to the output from the tracking algorithm (orange).

Table 1 Summary of the average percent error for the d-squared regression and burning rate constant using the selected diameter definitions

Diameter definition	Average d-squared error %	$K_{end,5,70}$ error %
d_{eqvs}	1.33	0.69
d_{ss}	1.27	0.65
d_{eqac}	1.36	0.71
d_{eqas}	1.33	0.69

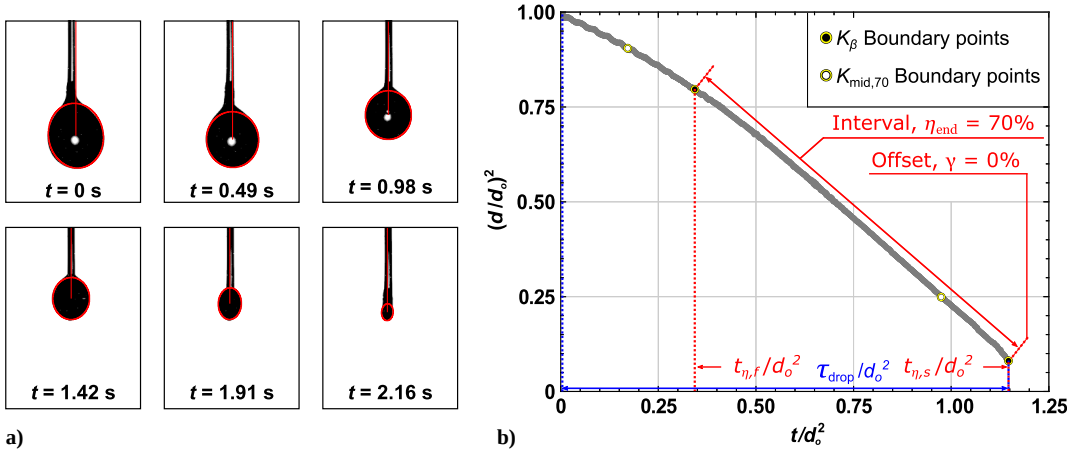

Fig. 4 Time sequence depicting the a) droplet diameter edge detection of a burning RP-2 droplet and the b) corresponding normalized droplet diameter history.

Additionally, the percent error associated with the burning rate constant is also small, ranging from 0.65 to 0.71%. Therefore, there is no significant variation in the regression properties due to the diameter definition for a perfectly spherical droplet. However, there is a larger sensitivity in the burning rate among these droplet definitions for ellipsoidal droplets, as shown for the RP-2 droplet in Sec. III.A.

An example image sequence depicting the diameter tracking of a burning RP-2 droplet and its corresponding normalized d^2-regression history can be seen in Figs. 4a and 4b, respectively. In multicomponent fuels such as RP-2 and nonvolatile pure hydrocarbons, there can exist pronounced nonlinear droplet regression effects throughout the droplet burn time, as observed at the beginning of the burning RP-2 droplet in Fig. 4b. Nonlinear droplet burning behavior can include initial heating effects, multicomponent effects such as individual constituents exhibiting different burning behaviors, as well as end-of-life effects such as microexplosions and suspension fiber influences [24]. When these behaviors are present, determining the most suitable portion of data to be used in the K calculation that is most representative of steady burning (i.e., most linear) is important because this can have a significant effect on the reported K value.

In our previous work on pure hydrocarbon fuels [25], K was evaluated using 70% of the data centered around the midpoint of the droplet burn time, referred to here as the $K_{mid,70}$ approach. This was done to add consistency to the data reduction methodology and attempt to remove the effects of transient behavior. However, previously, there was no detailed sensitivity study performed to evaluate the $K_{mid,70}$ approach and assess alternative techniques that may be more suitable as the effective burning rate constant for all fuels.

To address this point, K is calculated a multitude of different ways for a single set of data. A conceptual example depicting the diameter regression history of a burning droplet exhibiting nonlinear effects is shown in Fig. 5, in which the curvature is exaggerated for illustration purposes compared to typical droplet results. Figure 5 specifies the parameters used in this work to determine K. First, the three overall data reduction schemes implemented for this study are shown: 1) beginning, 2) middle, and 3) end. As their names suggest, each denotes the reference location of the considered part of the dataset. Starting at these three reference points, the script separately calculates K for a range of specified intervals and offsets.

The offset γ is the amount of data that is discarded from both the start and finish of the droplet burn time ($t_{\alpha,s}$ and $t_{\alpha,f}$) to the beginning and end reference points ($t_{\eta,\mathrm{beg},s}$ and $t_{\eta,\mathrm{end},s}$). The offset is defined as a percentage of the entire burn time (i.e., $\gamma = X/Y$ in Fig. 5), and it is applied to both ends of the dataset symmetrically. The interval η is the portion of data that is considered past the beginning and end reference points, namely, $t_{\eta,\mathrm{beg},s}$ to $t_{\eta,\mathrm{beg},f}$ or $t_{\eta,\mathrm{end},s}$ to $t_{\eta,\mathrm{end},f}$, respectively. Similarly, the interval is given as a percentage of the two bounding reference points ($t_{\eta,\mathrm{beg},s}$ and $t_{\eta,\mathrm{end},s}$), where $\eta_{beg} = B/Z$ and $\eta_{end} = E/Z$ in Fig. 5. For the cases starting in the middle of the droplet regression, only the interval η_{mid} is required, and therefore is given as a percentage of the total burn time (i.e., $\eta_{mid} = M/Y$).

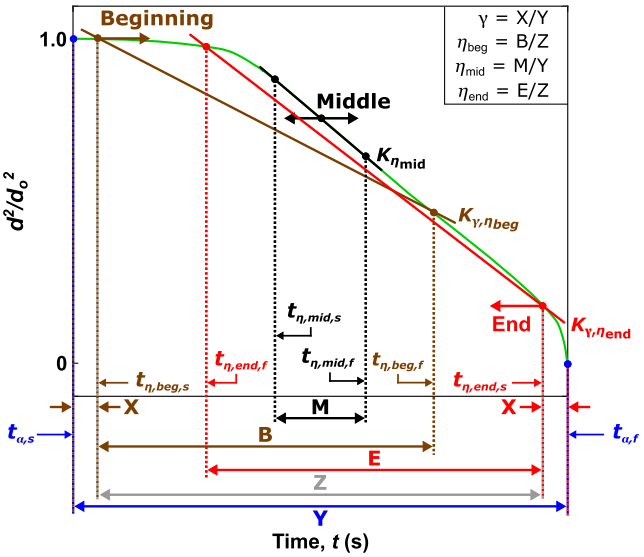

Fig. 5 Conceptual droplet regression history depicting exaggerated nonlinear behavior (for illustration purposes) and defining the offset γ and interval η for K_{beg}, K_{mid}, and K_{end}.

For each interval and offset, K is calculated by taking the corresponding amount of droplet diameter regression data, fitting a linear regression through the data, and determining the slope. In this study, the notation for the burning rate constant is $K_{q,r,s}$, where q is the reference location (i.e., beginning, middle, or end), and r and s are the offset and interval percentages, respectively. It should be noted that, when the offset is 0%, r is omitted and the notation becomes $K_{q,s}$. By applying these definitions to experimentally produced data, examples of $K_{end,70}$ and $K_{mid,70}$ are indicated in Fig. 4b, in which the boundary points for $K_{end,70}$ and $K_{mid,70}$ are shown in black and white, respectively. A continuation of this example comparing the various K values attained is found in Sec. III.A.

In this study, the applied offset ranges from 0 to 15% from each side in increments of 2.5% for cases with the beginning and end as the reference. For each offset, values of K_{beg} and K_{end} are calculated at each interval from 1 to 100% in increments of 1% by fixing $t_{\eta,\mathrm{beg},s}$ and $t_{\eta,\mathrm{end},s}$ and correspondingly varying $t_{\eta,\mathrm{beg},f}$ and $t_{\eta,\mathrm{end},f}$, respectively; this resulted in 100 values each for K_{beg} and K_{end} at every offset and 700 separate values overall. Again, cases starting at the middle of the test require no applied offset because all K_{mid} values are covered by intervals spanning from 1 to 100%. These 1500 total cases adequately cover all reasonable methods to determine K and reduce the overall number of redundant cases. A summary of the three data reduction schemes is presented in Table 2.

Downloaded by Doug Talley on August 19, 2019 | http://arc.aiaa.org | DOI: 10.2514/1.B37195

Table 2 Various evaluation schemes implemented for calculating the burning rate constant of a single set of data

Scheme	Offset γ	Interval η	Total K values
Beginning	0–15%, 2.5% increments	1–100%, 1% increments	700
Middle	0%	〃	100
End	0–15%, 2.5% increments	〃	700

Ignition delay τ_{ign} is the other parameter evaluated in this study. Igniting suspended droplets via the short-duration plasma arc provides a convenient platform to study ignition behavior, due to its constant average output power, adjustable ignition duration, and consistent temperature [20]. This approach is chosen because it reduces the effects of the ignition system on the measured ignition delay results and creates consistent experimental conditions. As the plasma arc produces minimal interference from background light and heat [20], details of the ignition and the development of the flame early in the droplet lifetime were readily captured. Typically, ignition delay is defined as the time separation between introducing the droplet to the (hot) ignition environment and the observation of the established flame [26]. Although it is straightforward to define the first event, naturally, there is some subjectivity associated with the second. In general, the fully established flame is characterized by an enveloping reaction zone surrounding the droplet that is on the order of the droplet diameter [26]. For the various hydrocarbons in this study, the flame originates beneath the droplet close to the ignitor location, and it quickly grows to a maximum before slightly reducing in size at the start of steady burning. Therefore, τ_{ign} is chosen to be the time the ignitor is first activated to the time the droplet flame reaches an initial maximum size, which represents the upper limit of the ignition delay for each fuel.

To provide a consistent approach for τ_{ign}, the flame region was automatically tracked in the IR images using an image processing script. Example results for ethanol are shown, for reference, in Fig. 6. This depicts an image sequence of the tracked flame region along with nondimensionalized temporal histories of the flame pixel area A_{flm} and integrated thermal radiance I, corresponding to $\tau_{ign} = 68$ ms. A_{flm} is the number of pixels contained within the tracked flame region and is indicative of the reaction zone area, whereas I is the summation of the thermal radiance counts captured by the IR camera within the defined flame region. Although the ignition delays reported here are evaluated using the maximum flame pixel area, there is general agreement with the time associated with an initial maximum in integrated thermal radiance as well. Similar results for τ_{ign} were produced using visible imaging: often simultaneous with the IR images. Visible imaging relies on the flame luminosity, which differs among the fuels in this study largely due to soot formation. Therefore, ignition delays from visible imaging were deemed to be less reliable than the IR results, leading to only the IR results being reported in this study.

Downloaded by Doug Talley on August 19, 2019 | http://arc.aiaa.org | DOI: 10.2514/1.B37195

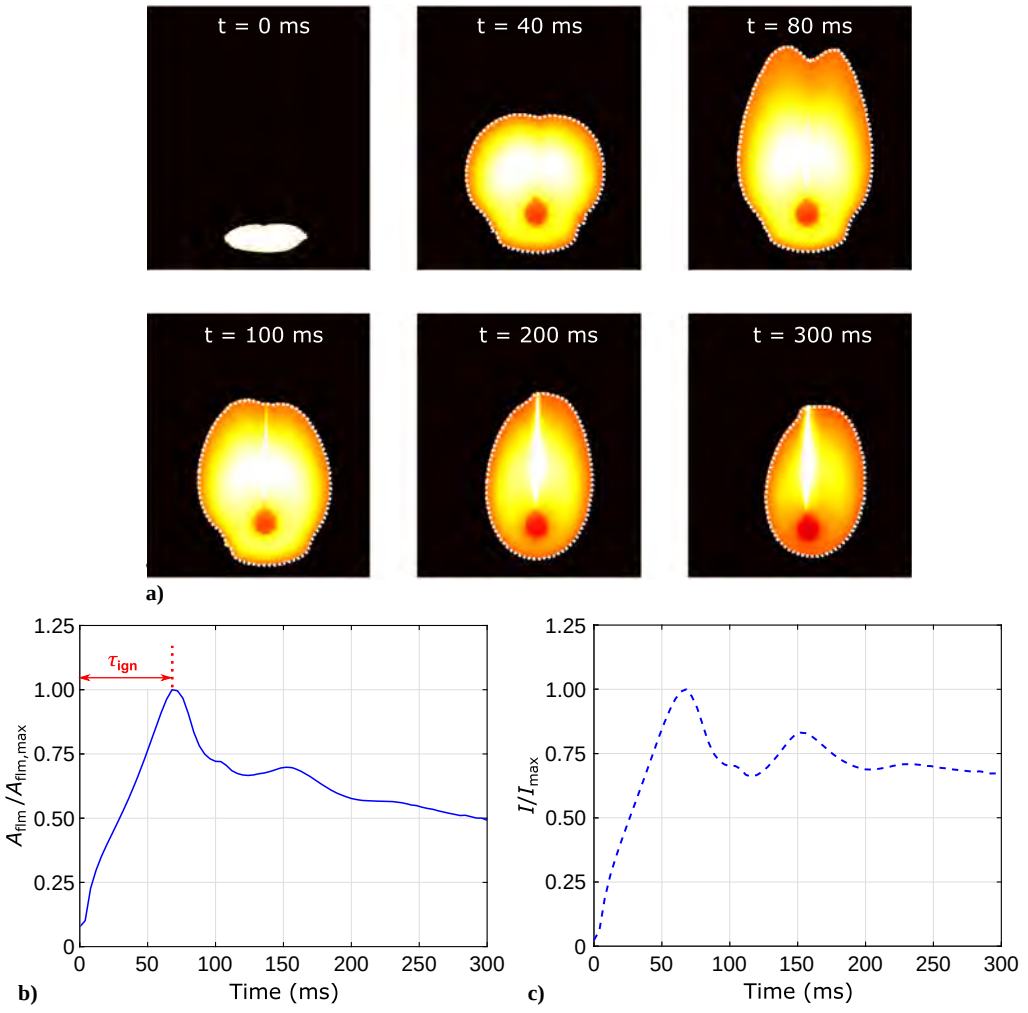

Fig. 6 Time sequence of the a) ignition process of an ethanol droplet with the corresponding b) flame area and c) integrated thermal radiance temporal histories.

Downloaded by Doug Talley on August 19, 2019 | http://arc.aiaa.org | DOI: 10.2514/1.B37195

III. Results

Droplet burning properties were investigated for 10 various hydrocarbon fuels, encompassing alcohols (i.e., ethanol and methanol); simple hydrocarbons (i.e., n-heptane, toluene, n-dodecane, and hexadecane); and kerosene blends including rocket-grade kerosene RP-2, diesel no. 2, and aviation fuel JP-8 and its surrogate Fischer–Tropsch (FT) synfuel. These fuels were chosen because they represent a large range of common hydrocarbons and alternative fuels used in rocket-engine and airbreathing propulsion systems [27–29,30]. These three fuel types can be broadly classified by their thermophysical properties, which are documented in Tables 3 [14,31–33] and 4 [14,34–47].

The thermodynamic characteristics of the two alcohols, although similar to each other, vary significantly from the other pure hydrocarbons and kerosene blends. Similar trends can be seen for the four pure hydrocarbons, with a notable difference in particular for the heats of vaporization Δh_{vap} and combustion Δh_c when compared to the alcohol fuels. Generally, there is some deviation among these simple hydrocarbons in thermophysical properties, which typically spans the range of values characteristic of the kerosene blends. This can be attributed to these simple hydrocarbons representing some of the lighter (e.g., n-heptane and toluene) and heavier (e.g., n-dodecane and hexadecane) constituents found in the various kerosene fuels. To investigate the effects of multiple constituents further, the burning properties of a 50/50 wt % binary mixture of n-heptane and n-dodecane were also quantified. Finally, the kerosenes share similar properties to each other, with JP-8 and FT in particular in close agreement, which is the main reason Fischer–Tropsch has been authorized for use as a JP-8 replacement in U.S. Air Force applications [30].

A. Burning Rate Constant Sensitivity

The approach detailed in Sec. II.B was implemented to determine K using the evaluation schemes summarized in Table 2. To examine the sensitivity of the burning rate constant to the data reduction technique, first, the coefficient of determination R^2 associated with each K value was calculated over the same data ranges for K. The coefficient of determination is a well-established parameter that indicates how well a linear regression fits the data, with a value that ranges from zero to one, where $R^2 = 1$ signifies a perfect fit [48]. Again, consider the RP-2 example from Sec. II.B, in which the droplet initially regresses slower than over the remaining three-quarters of its burn time, which appears to be more linear with a notable steeper slope, as shown in Fig. 4b. Examining the R^2 distribution for this dataset, there is a wide distribution of K values corresponding to high coefficients of determination (see Fig. 7a). Specifically, the burning rate constant varies from 0.57 to 1.0 mm^2/s for R^2 values above 0.997, which initially indicate that any of these K values spanning this entire range (i.e., encompassing all K values for typical hydrocarbons) provide a good fit that well represents the data. Therefore, there is significant limitation to solely reporting the coefficient of determination value as a justification for using a specific burning rate constant evaluation method. Examining this R^2 distribution of K further, there exists three distinct R^2 peaks for each of the beginning, middle, and end schemes corresponding to K equaling 0.659, 0.867, and 0.919 mm^2/s, respectively. The R^2 values associated with these peaks increase from 0.9986 to 0.9999 from beginning to end, which is consistent with droplet burning for RP-2 approaching linear regression behavior toward the end of the droplet burn time.

One drawback associated with only using the coefficient of determination to find a single K value that effectively represents

Table 3 Thermodynamic characteristics of the pure hydrocarbon fuels [14,31]

Fuel property	Ethanol	Methanol	n-heptane	Toluene	n-dodecane	Hexadecane
Chemical formula	C_2H_5OH	CH_3OH	C_7H_{16}	C_7H_8	$C_{12}H_{26}$	$C_{16}H_{34}$
Molecular weight, kg/kmol	46.07	32.04	100.21	92.14	170.34	226.45
Stoichiometric air/fuel ratio, O/F	8.946	6.431	15.081	13.418	14.920	14.863
Specific heat capacity[a] c_p, kJ/(kg · K) [32]	2.44	2.50	2.24	1.70	2.21	2.21
Thermal conductivity[a] λ, W/(m · K) [33]	0.167	0.202	0.123	0.131	0.135	0.140
Mass density[a] ρ, g/cm^3 [33]	0.79	0.79	0.68	0.86	0.75	0.77
Boiling temperature T_b, K [33]	351	338	372	384	489	560
Vapor pressure[a] P_{vap}, kPa [32]	7.9	16.9	6.1	3.8	1.5E-02	9.6E-05
Adiabatic flame temperature T_{ad}, K [6]	2195	2150	2265	2317	2268	2269
Heat of vaporization[b] Δh_{vap}, kJ/kg [33]	837	1099	317	360	259	229
Heat of combustion[a] Δh_c, kJ/g [33]	29.7	22.7	48.1	42.4	47.2	47.2
Energy density, kJ/cm^3	23.5	17.9	32.7	36.5	35.4	36.3

[a]Calculated for $T = 298$ K and $P = 101,325$ Pa.
[b]Calculated for $T = T_b$ and $P = 101,325$ Pa.

Table 4 Thermodynamic characteristics of the kerosene fuels [14,31]

Fuel property	RP-2	JP-8	FT	Diesel no. 2
Average chemical formula	$C_{11.74}H_{23.40}$ [34]	$C_{11}H_{21}$	$C_{12}H_{25}$	$C_{12}H_{23}$
Molecular weight, kg/kmol	164.60	153.29	169.34	167.32
Stoichiometric air/fuel ratio, O/F	14.681	14.563	14.806	14.574
Specific heat capacity[a] c_p, kJ/(kg · K)	2.03[c] [35]	1.92	2.73	2.20 [36]
Thermal conductivity[a] λ, W/(m · K)	0.107 [34,37]	0.115	9.35E-03	0.125 [38]
Mass density[a] ρ, g/cm^3	0.80 [34,39]	0.81	0.76	0.83 [38]
Boiling temperature T_b, K	438-498 [34]	413-573	448-633	453-613 [40]
Vapor pressure[a] P_{vap}, kPa]	5.7E-02 [34]	1.8E-01 [41]	21 [42]	7.7E-02 [43]
Adiabatic flame temperature T_{ad}, K	2406[c]	2338 [44]	2338 [44]	2292 [45]
Heat of vaporization[b] Δh_{vap}, kJ/kg	308[c] [46]	441	339	270 [36]
Heat of combustion[a] Δh_c, kJ/g	44 [34,47]	43	44	46.1 [36]
Energy density, kJ/cm^3	35.2	34.8	33.4	38.3

*Calculated for $T = 298$ K and $P = 101,325$ Pa.
[b]Calculated for $T = T_b$ and $P = 101,325$ Pa.
[c]For $C_{12}H_{23.40}$.

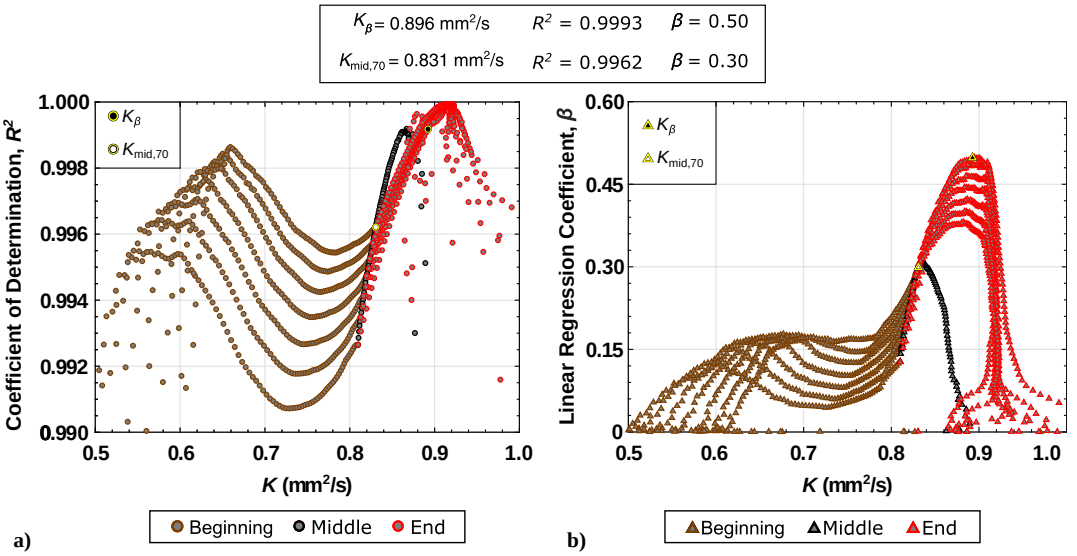

Fig. 7 Sensitivity of the burning rate constant K for an RP-2 droplet showing the a) coefficient of determination R^2 and b) linear regression coefficient β values.

Downloaded by Doug Talley on August 19, 2019 | http://arc.aiaa.org | DOI: 10.2514/1.B37195

quasi-steady burning is that this parameter does not account for another consequential parameter: the duration of the droplet burning considered. As the burning rate constant is an idealization used to describe an effective steady-state droplet burning rate, the effective K should be associated with the best linear fit spanning the longest duration of the droplet lifetime. Hence, it is necessary to introduce a new parameter referred to as the linear regression coefficient β, which equally weights the coefficient of determination and the fraction of the burn duration. This is written as

$$\beta(i) = R^2(i)\left|\frac{\Delta t_\eta(i)}{\tau_{\text{drop}}}\right| \tag{3}$$

where τ_{drop} is the total droplet burn time, and $\Delta t_\eta(i) = t_{\eta,f}(i) - t_{\eta,s}(i)$ is the interval time associated with the fraction of the burn duration. It should be noted that $R^2(i)$ is rescaled in the beta calculation by applying a correction factor based on the percentage of $R^2(i)$ as compared to the maximum R^2 value for all considered cases. Modifying R^2 in this fashion equally redistributes the values between zero and one for ease of identifying the maximum β because the nonscaled R^2 values are all typically greater than 0.99. Therefore, the linear regression coefficient also ranges from zero to one, where the highest value corresponds to the K that is the best fit to the droplet regression data for the longest duration of droplet burning.

The β distribution for the RP-2 dataset shows that all three evaluation schemes again converge to distinct maximums similar to the R^2 distribution (see Fig. 7b). Specifically, K_{end} corresponds to significantly higher β values than either K_{mid} or K_{beg}. In this study, K_β is found by averaging the top 5% of the K values according to β. Hence, K_β is 0.896 mm^2/s, with R^2 equaling 0.9993, which differs substantially from the previous $K_{\text{mid},70}$ approach at 0.831 mm^2/s and $R^2 = 0.9962$; this corresponds to a 7% deviation, demonstrating the data reduction methodology can play a large role in affecting the value of the reported droplet burning rate. Therefore, it is critical for the evaluation approach to be consistent and well defined for reporting meaningful results.

Additionally, although the beta distribution is used in this study to report a single effective burning rate constant, it can also illustrate the degree of nonlinearity present. This is achieved by observing the local variation in K centered around the maximum β value, with a larger variation indicating a higher degree of nonlinearity. This approach can also be used to determine the burning rate during specific times throughout the droplet lifetime starting at the beginning, middle, or end. This may be useful during instances in which nonlinear effects are of noteworthy interest in understanding the droplet burning processes, such as for a multicomponent fuel or nanofuel.

The burning rate constant for the RP-2 droplet was also calculated using the other previously described droplet diameter definitions. This is summarized in Table 5, which shows a larger K deviation for this droplet than for the perfectly spherical synthetic data in Sec. II.B. This is primarily due to the suspended droplet appearing ellipsoidal in shape throughout its lifetime. Overall, K_β ranges from 0.875 to 0.926 mm^2/s, depending on which droplet diameter definition is implemented. Specifically, the burning rate constant associated with the equivalent volume of a sphere d_{eqvs} is closest to the average of this range, supporting its use within this study.

Nonlinear droplet regression behavior is not only exhibited by kerosene fuels, but it is occasionally observed in other fuels as well, such as the simple hydrocarbon n-dodecane, as depicted in Fig. 8a. Similar to RP-2, the diameter of the n-dodecane droplet regresses slower at the beginning of the test, becoming more linear and regressing faster for the last two-thirds of the droplet burn time. As this test exhibited more nonlinear behavior than RP-2, the R^2 distribution (see Fig. 8b) again has three regions corresponding to the evaluation schemes but with broader distributions across the K range, corresponding to 0.64 to 1.10 mm^2/s for R^2 values above 0.997. Similarly, the β values for this test shown in Fig. 8c are highest for K_{end}, where K converges to a peak, albeit slightly more broad than for RP-2. This corresponds to K_β being 0.911 mm^2/s, whereas $K_{\text{mid},70}$ is 0.819 mm^2/s, producing a maximum deviation in K across all fuels at 10% when comparing these two approaches.

Performing the same $R^2 - \beta$ analysis for a volatile fuel (i.e., ethanol), although the droplet diameter regression is very linear (see Fig. 9a), K still exhibits a large variation for R^2, as shown in Fig. 9b. The burning rate constant ranges approximately from 0.60 to 0.90 mm^2/s, all with R^2 values greater than 0.997. However, unlike for RP-2 and n-dodecane, all three data reduction schemes broadly converge to a K value of about 0.75 mm^2/s for the highest R^2 values approaching 1.0.

The β distribution for this ethanol test shows all three evaluation schemes converge to a single well-defined peak at a maximum of

Table 5 K_β summary for the RP-2 droplet using the four droplet diameter

Diameter definition	K_β, mm^2/s
d_{eqvs}	0.896
d_{ss}	0.926
d_{eqac}	0.875
d_{eqas}	0.889

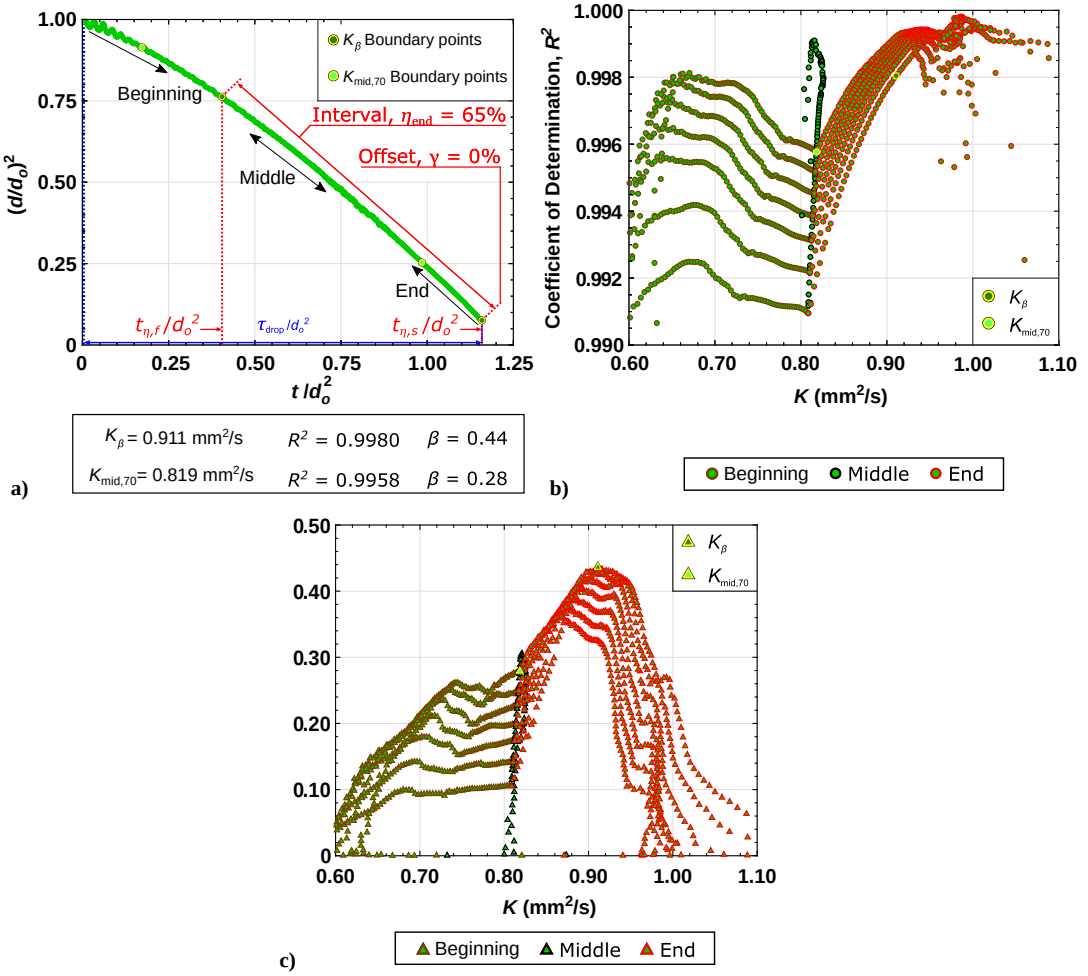

Fig. 8 ***K*** **sensitivity for an n-dodecane droplet depicting the a) regression history, the b) coefficient of determination R^2, and c) linear regression coefficient β values.**

$\beta = 0.75$, as indicated in Fig. 9c. Specifically, K_β is 0.746 mm^2/s, with an R^2 of 0.9999. Comparing this result to $K_{mid,70}$ shows a very slight deviation, as $K_{mid,70} = 0.744$ mm^2/s with R^2 also being 0.9999. This is expected because the droplet diameter regression for this fuel happens to be notably more linear throughout its lifetime as compared with RP-2 and n-dodecane, and hence is fairly insensitive to the data reduction approach. Nevertheless, the β distribution for all of these fuels reduces the range of K values centered around the maximum β value as compared to the R^2 distribution, providing a more pronounced visual indication of the effective K value.

B. Burning Rate Constant Summary

A series of 15 identical droplet burning tests were performed for each of the 10 hydrocarbon fuels, as well as the 50/50 wt % blend of n-heptane and n-dodecane, to produce statistically reliable data for K. To quantify the statistical uncertainty of K and remove outlying data, the Student's t distribution for a small sample size [49] along with Chauvenet's rejection criteria [48] are implemented to provide a 95% confidence interval on the reported values. An example set of K_β values for the 15 ethanol tests is presented in Fig. 10. This shows the test-to-test variation for both K_β and R^2 is extremely small across all of the tests, with only a single outlying data point (circled in red) being discarded. As a result, this experimental and evaluational approach for K permits the experimental uncertainty for the reported K_β values to be significantly reduced.

The droplet burning rates for all of these fuels range from 0.74 to 0.94 mm^2/s, where the lowest K_β value is for ethanol and the highest for n-heptane, as shown in Fig. 11a. In general, the burning rate constants are grouped according to their thermophysical properties, for which the alcohol fuels exhibit the lowest K_β values and the more volatile simple hydrocarbons including n-heptane and toluene are on the upper end. The less volatile hydrocarbons of n-dodecane and hexadecane have K_β values that are in between the two extremes and similar to the other complex hydrocarbons. The three aerospace kerosenes all are very similar to each other with $K_\beta \approx 0.89$ mm^2/s and diesel no. 2 being lower at 0.85 mm^2/s. Also appearing in this figure are K values of five fuels selected from the literature for suspended droplets of similar initial size burning in atmospheric air under normal gravity; these include an alcohol (ethanol) and volatile (n-heptane) and nonvolatile (n-dodecane) simple hydrocarbons, as well as two kerosenes (JP-4 and diesel). It can be seen that, for all of these fuels, the burning rate constants are within the reasonable range of the K values reported in this study, providing validation of the current approach.

Comparing the K_β results to $K_{mid,70}$ (see Fig. 11b), the burning rate constant is generally insensitive to the evaluation method for the more volatile fuels including the two alcohols, n-heptane, and toluene. However, there is significant deviation up to 10% for the less volatile simple hydrocarbons and all four kerosene fuels, where $K_{mid,70}$ is found to be consistently lower than K_β. Also, the statistical uncertainty associated with the K_β values is extremely small, with the average being 0.006 mm^2/s for all fuels, as well as higher R^2 values associated with K_β compared to $K_{mid,70}$. Hence, the reported K_β values are shown to be more representative of the effective droplet burning rate across all fuel types. However, it is recognized that the process to quantify K_β is rather extensive; therefore, a simpler alternative was found by taking K_β as the accepted value and calculating the percent error for each of the 1500 cases in each test across all 10 fuels. The percent errors calculated for the 1500 cases across each fuel test were then all averaged together, and $K_{end,5,70}$ was found to be the best alternate that overall minimized the percent error

Downloaded by Doug Talley on August 19, 2019 | http://arc.aiaa.org | DOI: 10.2514/1.B37195

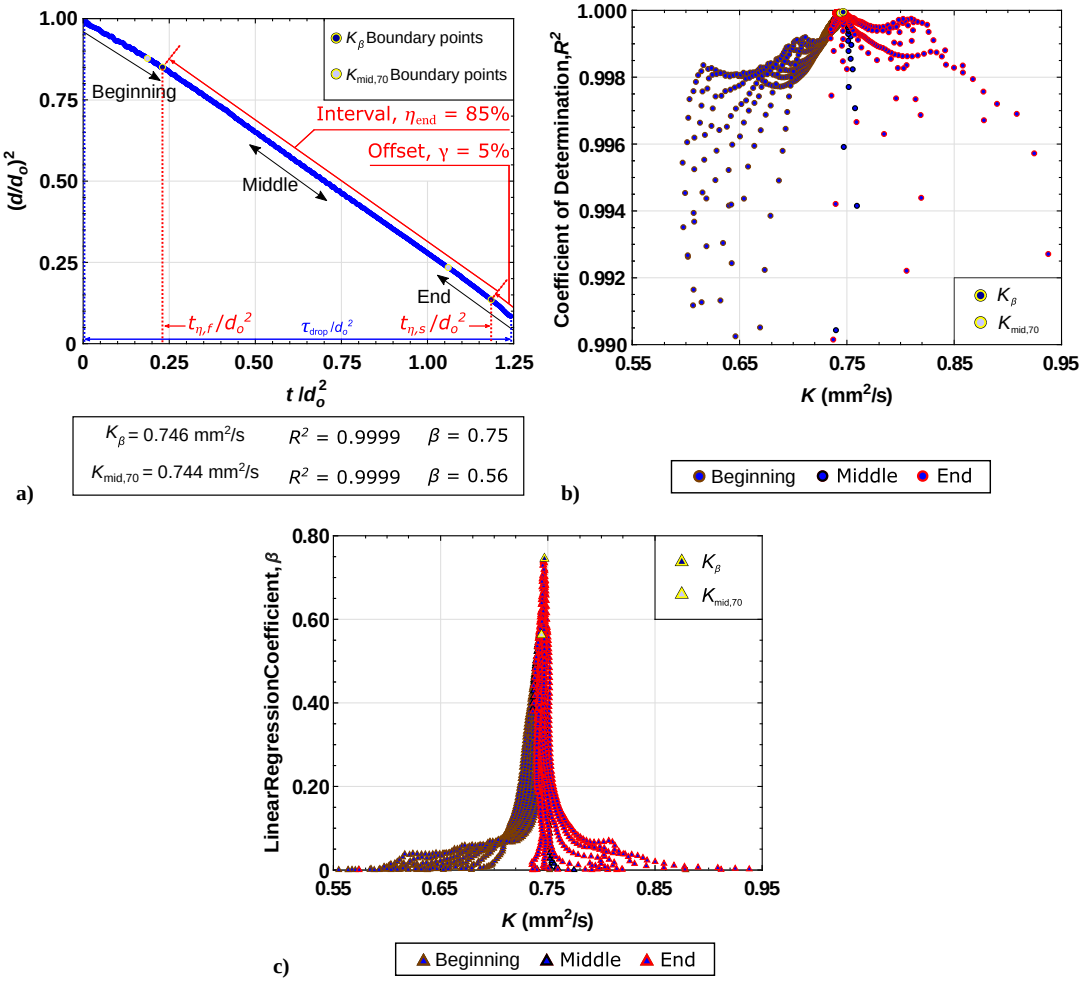

Fig. 9 ***K*** **sensitivity for an ethanol droplet depicting the a) regression history, b) the coefficient of determination R^2, and c) linear regression coefficient β values.**

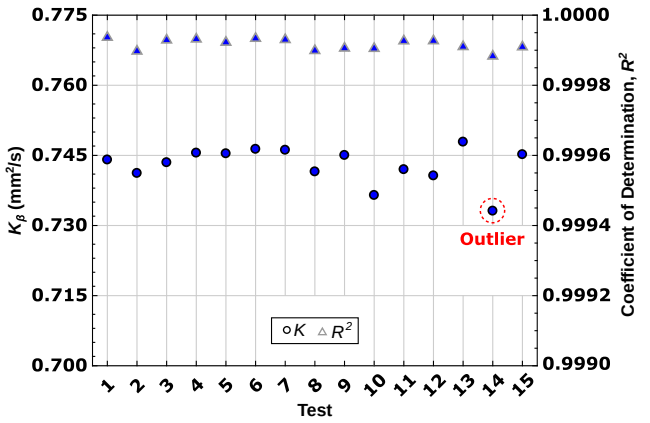

Fig. 10 Burning rate constant summary for ethanol, depicting typical test-to-test variation of K_β and R^2.

with respect to K_β. $K_{end,5,70}$ being the individual K closest corresponding to the best-fit linear regression for the longest duration of droplet burning in all fuels is consistent with the observed behavior that the droplet regression typically becomes more linear toward the latter portion of the burn time (indicative of steady burning) while also removing end-of-life droplet nonlinearities involving suspension fiber influences present within $\gamma = 5\%$.

As the burning rate constant has proven to be dependent on the evaluation method, there are some challenges in comparing results across different droplet studies found in the literature because, often, the K determination approach is not explicitly stated. However, there are some commonly implemented ways to evaluate K, including $K_{mid,70}$, $K_{mid,80}$ [19,50], and K_{two-pt} [18], which is based only on the initial droplet diameter and burn time. Using the pure fuel data collected in this study for the nonvolatile fuels (excluding diesel no. 2), K was calculated using these different methods and compared to K_β, as summarized in Table 6. As expected, K_{two-pt} deviates by the largest margin of 9.36% because it is the coarsest method implemented, whereas $K_{end,5,70}$ is the closest to K_β with only a 0.58% average error while also having the same average R^2 value as K_β at 0.9989. Therefore, this shows $K_{end,5,70}$ is a suitable alternative to K_β. A proposed correction factor C_o (see Table 6) can be used to find the equivalent K_β value, which takes the form of $K_\beta = C_o K_i$. All of the correction factors for the four K methods are above one because they all are consistently lower than K_β. It should be noted that this correction factor is only required for fuels that have demonstrated a sensitivity to the evaluation method as with the nonvolatile hydrocarbon fuels and kerosenes.

C. Uncertainty Analysis

To quantify the error associated with the droplet burning results, an uncertainty analysis was performed for both the droplet regression data as well as the burning rate constant. This analysis was done using the approach by Shaw and Yu [15]. By defining $Y = d^2_{eqvs}$, the standard combined uncertainty associated with the droplet diameter for a given image i is

$$u_{Y_i} = (s^2_{Y_i} + b^2_{Y_i})^{1/2} \tag{4}$$

where s_{Y_i} and b_{Y_i} are the standard type-A and -B uncertainties, respectively [51]. The standard type-A uncertainty accounts for the

Downloaded by Doug Talley on August 19, 2019 | http://arc.aiaa.org | DOI: 10.2514/1.B37195

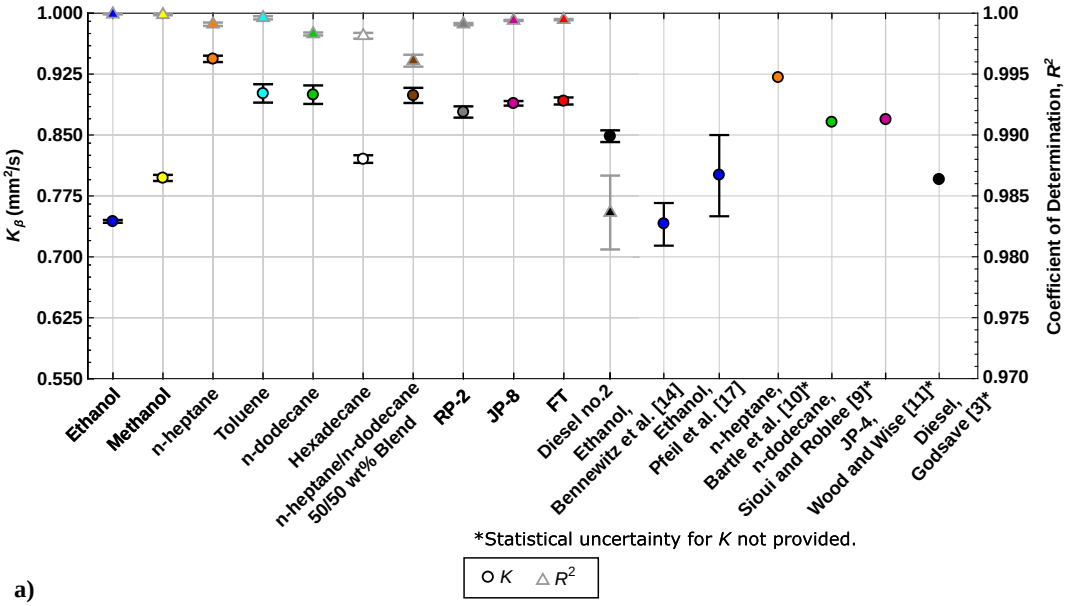

a)

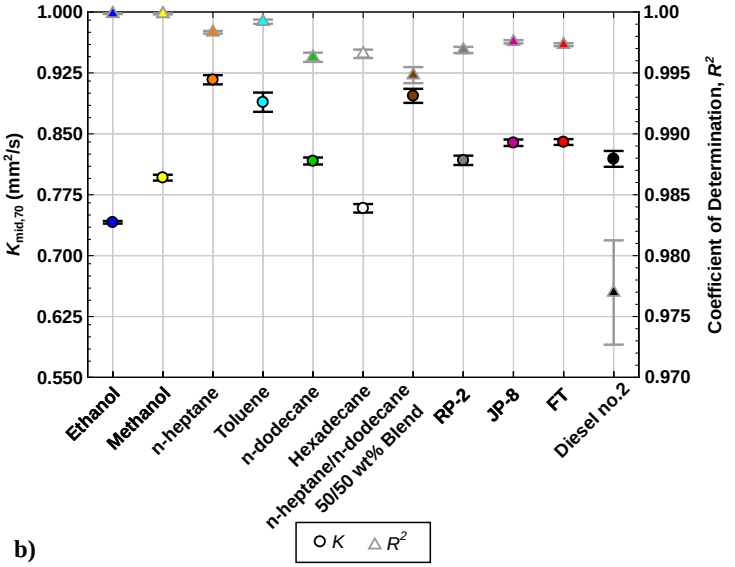

b)

Fig. 11 Hydrocarbon fuel droplet burning rate constant K summary using a) K_β and b) $K_{mid,70}$ with other values taken from various references for comparison [3,9–11,14,17].

error due to the linear regression used to quantify K, whereas the type-B uncertainty is associated with the error introduced by the diameter tracking method. The standard type-B uncertainty b_{Y_i} is written using the Taylor series expansion method for the d_{eqvs} definition in Eq. (2), yielding

$$b_{Y_i}^2 = \left(\frac{\partial Y_i}{\partial A_i}\right)^2 b_{A_i}^2 + \left(\frac{\partial Y_i}{\partial B_i}\right)^2 b_{B_i}^2 + 2\left(\frac{\partial Y_i}{\partial A_i}\frac{\partial Y_i}{\partial B_i}\right) b_{A_iB_i} \tag{5}$$

Through differentiation of Eq. (2), Eq. (5) simplifies to

$$b_{Y_i}^2 = Y_i^2\left(\left(\frac{2}{3A_i}\right)^2 b_{A_i}^2 + \left(\frac{4}{3B_i}\right)^2 b_{B_i}^2 + \frac{16 b_{A_iB_i}}{9A_iB_i}\right) \tag{6}$$

where the covariance term $b_{A_iB_i}$ is modeled as $b_{A_iB_i} = b_{A_i} b_{B_i}$ [15,51].

Within the ellipsoidal droplet, A_i is essentially the number of vertical pixels $n_{VP,i}$ contained along the major axis multiplied by the individual height of a pixel H (i.e., $A_i = n_{VP,i}H$). Again using the Taylor series approach, b_{A_i} is

$$b_{A_i}^2 = \left(\frac{\partial A_i}{\partial n_{VP,i}}\right)^2 b_{n_{VP,i}}^2 + \left(\frac{\partial A_i}{\partial H}\right)^2 b_H^2 + 2\left(\frac{\partial A_i}{\partial n_{VP,i}}\frac{\partial A_i}{\partial H}\right) b_{n_{VP,i}H} \tag{7}$$

Differentiating the terms in Eq. (7) using the definition for A_i and simplifying yields

$$b_{A_i}^2 = A_i^2\left(\frac{b_{n_{VP,i}}^2}{n_{VP,i}^2} + \frac{b_H^2}{H^2} + \frac{2b_{n_{VP,i}H}}{n_{VP,i}H}\right) \tag{8}$$

where $b_{n_{VP,i}H} = b_{n_{VP,i}} b_H$ [15,51].

The height of an individual pixel is the vertical distance spanning the entire image divided by the total number of vertical pixels N_V

Table 6 Summary of the average percent error and correction in K for the nonvolatile fuels (excluding diesel no. 2) determined using selected approaches

Approach K_i	Average K error %	Average R^2	Average correction factor C_o
$K_{mid,70}$	7.09	0.9969	1.071
$K_{mid,80}$	7.69	0.9959	1.077
K_{two-pt}	9.36	— —	1.094
$K_{end,5,70}$	0.58	0.9989	1.006

Downloaded by Doug Talley on August 19, 2019 | http://arc.aiaa.org | DOI: 10.2514/1.B37195

(i.e., $H = H_{\text{tot}}/N_V$). For the imaging configuration used in the droplet burning experiments, the image resolution is 800×600 and the physical field of view is $W_{\text{tot}} = 5.94 \pm 0.018$ mm by $H_{\text{tot}} = 4.46 \pm 0.014$ mm. This was determined at a 95% confidence interval using the 150 μm fiber diameter as a reference across 30 droplet burning tests. Assuming $b_{H_{\text{tot}}} = \frac{U_{H_{\text{tot}}}}{2} = 0.007$ mm, the type-B uncertainty for the individual pixel height is expressed as $b_H = U_{H_{\text{tot}}}/2N_V$ [15].

The number of pixels along the major axis of the droplet $n_{\text{VP},i}$ is a function of the pixel height as well as the discretization of the spatial coordinates and image grayscale sensitivity at the droplet edge [15]. As a result, the type-B uncertainty for $n_{\text{VP},i}$ can be written as

$$b^2_{n_{\text{VP},i}} = \left(\frac{\partial n_{\text{VP},i}}{\partial H}\right)^2 b^2_H + b^2_{\text{sd}} + b^2_{\text{gd}} \tag{9}$$

where b^2_{sd} and b^2_{gd} are the type-B uncertainties associated with the spatial and grayscale sensitivities. Assuming the number of vertical pixels within the droplet and pixel height are inversely proportional [15], Eq. (9) becomes

$$\frac{b^2_{n_{\text{VP},i}}}{n^2_{\text{VP},i}} = \frac{b^2_H}{H^2} + \frac{b^2_{\text{sd}} + b^2_{\text{gd}}}{n^2_{\text{VP},i}} \tag{10}$$

The combined discretization uncertainties encompass tracking errors that arise at the droplet edge. As defined by Shaw and Yu [15], these edge effects can be quantified by considering variations in the number of diffuse pixels ϕ that constitute the droplet periphery. Specifically for our droplet tracking method, ϕ is the number of pixels along either the major or minor axis length that define the droplet edge. The combined discretization error is then determined using the assumption $(b^2_{\text{sd}} + b^2_{\text{gd}})^{1/2} \approx \phi_i/4$ [15]. With this assumption, Eq. (10) is now

$$\frac{b^2_{n_{\text{VP},i}}}{n^2_{\text{VP},i}} = \frac{b^2_H}{H^2} + \frac{\phi^2}{16n^2_{\text{VP},i}} \tag{11}$$

It is noted that the backlit imaging scheme used in this study significantly reduces uncertainty at the droplet edge. Therefore, from visual inspection of multiple droplet burning tests, it was found that ϕ equaling one is reasonable.

The same procedure for b_{A_i} is carried out to determine the type-B error associated with the minor axis length b_{B_i}. Similarly, B_i is the number of horizontal pixels $n_{\text{HP},i}$ comprising the minor axis of the droplet multiplied by the width of an individual pixel W (i.e., $B_i = n_{\text{HP},i}W$). Applying the same Taylor series method for b_{B_i} and simplifying yields

$$b^2_{B_i} = B^2_i\left(\frac{b^2_{n_{\text{HP},i}}}{n^2_{\text{HP},i}} + \frac{b^2_W}{W^2} + \frac{2b_{n_{\text{HP},i}W}}{n_{\text{HP},i}W}\right) \tag{12}$$

where $b_{n_{\text{HP},i}W} = b_{n_{\text{HP},i}}b_W$.

As with the pixel height, the individual pixel width is the horizontal distance of the image frame divided by the total number of horizontal pixels N_H (i.e., $W = W_{\text{tot}}/N_H$). Again, assuming $b_{W_{\text{tot}}} = U_{W_{\text{tot}}}/2 = 0.009$ mm, the type-B pixel width error is $b_W = U_{W_{\text{tot}}}/2N_H$.

The uncertainty in the number of pixels comprising the minor axis of the droplet $n_{\text{HP},i}$ is affected by the pixel width and the same discretization effects existing at the droplet edge. Therefore, $b^2_{n_{\text{HP},i}}$ is

$$\frac{b^2_{n_{\text{HP},i}}}{n^2_{\text{HP},i}} = \frac{b^2_W}{W^2} + \frac{\phi^2_i}{16n^2_{\text{HP},i}} \tag{13}$$

The type-A uncertainty for the regression history data s_{Y_i} is due to the deviation of the linear regression fit to the experimental data. The linear regression $\hat{Y}_i$ is

$$\hat{Y}(t) = \alpha_1 t + \alpha_0 \tag{14}$$

which causes s_{Y_i} to be the sum of square error divided by the data degree of freedom [52]. This is written as

$$s^2_{Y_i} = \left(\frac{1}{m-2}\right)\sum_{i=1}^{m}(Y_i - \hat{Y}_i)^2 \tag{15}$$

where m is the total number of data points.

Along with determining the combined uncertainty of the droplet regression data u_{Y_i}, the total uncertainty associated with the burning rate constant u_{K_i} is calculated using

$$u_{K_i} = (s^2_{K_i} + b^2_{K_i})^{1/2} \tag{16}$$

To quantify the type-A and -B uncertainties for the burning rate constant, a modification to the method developed by Shaw and Yu [15] was used to account for the linear regression model. This first entails writing the matrix α_{ij} for the optimized coefficients used for the linear regression Eq. (14) as

$$[\alpha] = [Z][Y] \tag{17}$$

where

$$[Z] = ([F]^T[F])^{-1}[F]^T \tag{18}$$

and

$$[F] = \begin{bmatrix} (t_1 - t)^0 & (t_1 - t) \\ (t_2 - t)^0 & (t_2 - t) \\ \cdot & \cdot \\ \cdot & \cdot \\ \cdot & \cdot \\ (t_n - t)^0 & (t_n - t) \end{bmatrix} \tag{19}$$

In this form, the instantaneous values for the regression data and burning rate constant at time t are then expressed as

$$\hat{Y}_i = \hat{d}^2_i = \alpha_0 = \sum_{i=1}^{m} Z_{1i}Y_i \tag{20}$$

and

$$K_i = -\alpha_1 = \sum_{i=1}^{m} Z_{2i}Y_i \tag{21}$$

where K_i is constant throughout the steady droplet burn period due to the imposed linear fit model.

With $\hat{Y}_i$ and K_i in this form, s_{K_i} and b_{K_i} can be written as

$$s^2_{K_i} = \sum_{i=1}^{m}\sum_{j=1}^{m}\frac{\partial K_i}{\partial Y_i}\frac{\partial K_i}{\partial Y_j}s_{Y_iY_j} = \sum_{i=1}^{m}\sum_{j=1}^{m} Z_{2i}Z_{2j}s_{Y_iY_j} \tag{22}$$

and

$$b^2_{K_i} = \sum_{i=1}^{m}\sum_{j=1}^{m}\frac{\partial K_i}{\partial Y_i}\frac{\partial K_i}{\partial Y_j}b_{Y_iY_j} = \sum_{i=1}^{m}\sum_{j=1}^{m} Z_{2i}Z_{2j}b_{Y_iY_j} \tag{23}$$

where $s_{Y_iY_j} = s_{Y_i}s_{Y_j}$ and $b_{Y_iY_j} = b_{Y_i}b_{Y_j}$ [15].

Upon calculating the total uncertainties u_{Y_i} and u_{K_i} using Eqs. (4) and (16) for all of the droplet burning tests, it was found that the droplet regression uncertainty decreases throughout the course of the

Downloaded by Doug Talley on August 19, 2019 | http://arc.aiaa.org | DOI: 10.2514/1.B37195

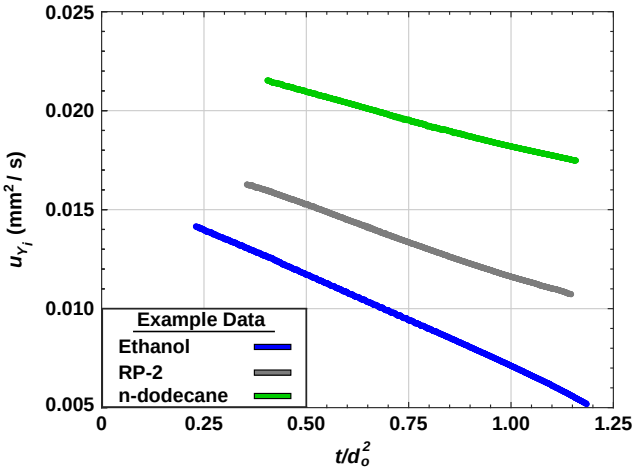

Fig. 12 u_{Y_i} total uncertainty for the ethanol, RP-2, and n-dodecane example droplet burning tests.

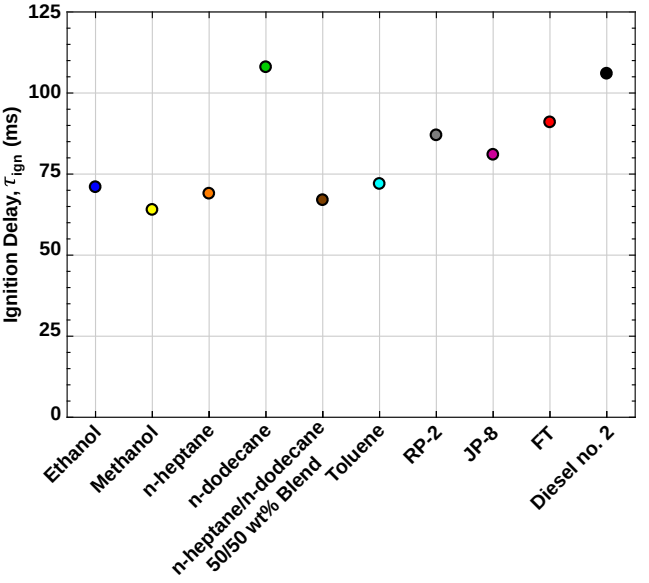

Fig. 13 Ignition delay τ_{ign} summary for the various hydrocarbon fuels (excluding hexadecane) evaluated from the infrared thermal images.

droplet lifetime, whereas the burning rate uncertainty is constant (due to $K_i = K_\beta$). This trend is evident in the three droplet burning tests in Fig. 12, which depicts u_{Y_i} for the respective data ranges used to determine K_β. All of the three fuels demonstrate similar trends for u_{Y_i} during the quasi-steady burning portion, where u_{Y_i} is highest for n-dodecane and lowest for ethanol. This is mainly due to the error associated with the linear fit deviation to the experimental data s_{Y_i}. Therefore, fuels with more nonlinearity present within the droplet regression history will have higher uncertainty.

To compare the total uncertainties for all fuels, Table 7 summarizes the average uncertainty parameters for Y_i and K. These parameters were determined by averaging the uncertainties across the quasi-steady burning portion for the 15 tests of each fuel. For these fuels, u_Y ranges from 0.005 to 0.060 mm^2, where u_Y typically is less than 5% of the droplet diameter during droplet burning. Regarding the burning rate constant, u_K averages 0.006 mm^2/s across all fuels, which is generally less than 1% of the K_β values. As a result, the reported burning rate constants are shown to have extremely small uncertainty for all fuels, further validating the current approach.

D. Ignition Delay Summary

Ignition delays for these fuels were measured by taking an average of five identical ignition events and postprocessing the IR images using the procedure described in Sec. II.B. It was found that τ_{ign} ranges from 65 to 110 ms for all fuels except for hexadecane, which is much longer at about 260 ms, because this fuel has an extremely low vapor pressure. Overall, the ignition delays measured using PAI are much shorter than other ignition delays reported in the literature (up to an order of magnitude) using arc furnace ignition [53–56], and thus produce ignition events that are much more sharply defined in time (see Ref. [20] for more detail). As shown in Fig. 13, ignition delays correlate closely with the fuel boiling temperature T_b (see Tables 3 and 4), for which the more volatile fuels with the lowest boiling temperatures exhibit shorter ignition delays. This trend is consistent with other ignition delay results reported for various pure hydrocarbons using arc furnace ignition [57,58], which provides validation for the current τ_{ign} definition and measurement approach. Uncertainty estimates for these measurements are not larger than the symbols used in the figure. For the 50/50 wt % n-heptane/n-dodecane blend, τ_{ign} corresponds to the volatile component n-heptane, with τ_{ign} close to 70 ms for both fuels. This is consistent with the work of Khan et al. [59], which reported that the ignition delay for a multicomponent fuel correlates with the lighter, more volatile constituents using arc furnace heating at the investigated temperatures from 850 to 1000 K. Similar behavior is also exhibited by the kerosene fuels for our study, which is consistent with the lighter constituents vaporizing and burning earlier in the droplet lifetime of a multicomponent fuel [24,60]. Finally, ignition delays for n-dodecane and diesel no. 2 are both approximately 110 ms, which supports some previous ignition work with n-dodecane as a proposed diesel surrogate for use in fundamental combustion studies [61,62].

Table 7 Summary of the average total uncertainties for the regression history data u_Y and burning rate constant u_K

Fuel	$u_{Y_{min}}$, mm^2	$u_{Y_{max}}$, mm^2	u_Y/Y_i average	u_K average, mm^2/s
Ethanol	0.005	0.015	0.011	0.005
Methanol	0.008	0.016	0.010	0.005
n-heptane	0.011	0.017	0.019	0.007
Toluene	0.008	0.015	0.015	0.006
n-dodecane	0.015	0.022	0.025	0.006
Hexadecane	0.015	0.019	0.027	0.006
n-heptane/n-dodecane 50/50 wt % blend	0.028	0.032	0.040	0.006
RP-2	0.010	0.018	0.023	0.006
JP-8	0.009	0.015	0.016	0.006
FT	0.009	0.015	0.017	0.006
Diesel no. 2	0.058	0.060	0.077	0.006

IV. Conclusions

This experimental study develops data analysis tools and generates baseline fuel droplet combustion properties for 10 various hydrocarbon fuels encompassing alcohols, simple hydrocarbons, and kerosene blends. One major observation in this study is that the burning rate constant K has a notable sensitivity to the evaluation method for nonvolatile simple hydrocarbons and kerosenes, with deviations among typical K approaches as large as 10% possible. Hence, the K_β method was developed that automatically finds the K associated with the most linear fit to the data for the longest duration of droplet burning. The newly reported K_β values along with its simpler alternative $K_{end,5,70}$ for all fuels range from 0.74 to 0.94 mm^2/s, which consistently correspond to very small statistical uncertainty among fuel tests (≈0.006 mm^2/s average) and higher R^2 values when compared to other common methods (e.g., $K_{mid,70}$ and $K_{mid,80}$). A detailed uncertainty analysis also reveals that the total error associated with these burning rates is less than 1% of the K values. As a result, K_β and $K_{end,5,70}$ are suitable options for improved consistency in evaluating droplet burning rates. Additionally, reported K values for these fuels correspond to differences in their thermophysical properties, providing validation for the two K evaluation methods. This work also indicates that, for fuels exhibiting appreciable amounts of regression nonlinearities (i.e., deviating from idealized droplet behavior), there

Downloaded by Doug Talley on August 19, 2019 | http://arc.aiaa.org | DOI: 10.2514/1.B37195

are limitations to using a single effective burning rate to adequately describe their burning processes. Nevertheless, this is still currently common practice for both pure and multicomponent fuels. Therefore, the K_β and $K_{\text{end},5,70}$ methods essentially minimize these nonlinearities to provide an effective burning rate constant that is most representative of idealized droplet burning. Finally, this work presents a systematic approach for measuring ignition delays τ_{ign} with a controllable short-duration plasma arc ignitor. Ignition delays range from 65 to 110 ms for all fuels except for hexadecane, which was 260 ms. Generally, τ_{ign} correlates well with the fuel boiling temperature across all of the investigated fuels, validating the ignition delay measurement method.

Acknowledgments

This work was funded by the U.S. Air Force Office of Scientific Research under Mitat Birkan as Project Officer.

References

[1] Sirignano, W. A., *Fluid Dynamics and Transport of Droplets and Sprays*, 2nd ed., Cambridge Univ. Press, Cambridge, NY, 2010, p. 24. doi:10.1017/CBO9780511529566

[2] Harrje, D., "Liquid Propellant Rocket Combustion Instability," NASA TR NASA-SP-194, 1972.

[3] Godsave, G., "Studies of the Combustion of Drops in a Fuel Spray—The Burning of Single Drops of Fuel," *Symposium (International) on Combustion*, Vol. 4, No. 1, 1953, pp. 818–830. doi:10.1016/S0082-0784(53)80107-4

[4] Law, C., and Williams, F., "Kinetics and Convection in the Combustion of Alkane Droplets," *Combustion and Flame*, Vol. 19, No. 3, 1972, pp. 393–405. doi:10.1016/0010-2180(72)90009-0

[5] Faeth, G. M., "Current Status of Droplet and Liquid Combustion," *Progress in Energy and Combustion Science*, Vol. 3, No. 4, 1977, pp. 191–224. doi:10.1016/0360-1285(77)90012-0

[6] Glassman, I., and Yetter, R., *Combustion*, 4th ed., Academic Press, San Diego, CA, 2008, pp. 358–359. doi:10.1016/b978-0-12-088573-2.x0001-2

[7] Law, C. K., "Recent Advances in Droplet Vaporization and Combustion," *Progress in Energy and Combustion Science*, Vol. 8, No. 3, 1982, pp. 171–201. doi:10.1016/0360-1285(82)90011-9

[8] Kumagai, S., and Isoda, H., "Combustion of Fuel Droplets in a Vibrating Air Field," *Symposium (International) on Combustion*, Vol. 5, No. 1, 1955, pp. 129–132. doi:10.1016/S0082-0784(55)80019-7

[9] Sioui, R., and Roblee, L. H. S., Jr., "The Prediction of the Burning Constants of Suspended Hydrocarbon Fuel Droplets," *Combustion and Flame*, Vol. 13, No. 5, 1969, pp. 447–454. doi:10.1016/0010-2180(69)90083-2

[10] Bartle, K., Fitzpatrick, E., Jones, J., Kubacki, M., Plant, R., Pourkashanian, M., Ross, A., and Williams, A., "The Combustion of Droplets of Liquid Fuels and Biomass Particles," *Fuel*, Vol. 90, No. 3, 2011, pp. 1113–1119. doi:10.1016/j.fuel.2010.10.054

[11] Wood, B. J., and Wise, H., "Measurement of the Burning Constant of a Fuel Drop," *Journal of Applied Physics*, Vol. 28, No. 9, 1957, Paper 1068. doi:10.1063/1.1722910

[12] Ghamari, M., and Ratner, A., "Combustion Characteristics of Colloidal Droplets of Jet Fuel and Carbon Based Nanoparticles," *Fuel*, Vol. 188, No. 1, 2017, pp. 182–189. doi:10.1016/j.fuel.2016.10.040

[13] Pfeil, M. A., Rosen, S. C., Yu, Y. C., Anderson, W. E., and Son, S. F., "Effects of NanoAluminum on Droplet Combustion and Combustion Instabilities in a Single Element Rocket Combustor," *46th AIAA Joint Propulsion Conference & Exhibit*, AIAA Paper 2010-7154, July 2010. doi:10.2514/6.2010-7154

[14] Bennewitz, J. W., Valentini, D., Plascencia, M. A., Vargas, A., Sim, H. S., Lopez, B., Smith, O. I., and Karagozian, A. R., "Periodic Partial Extinction in Acoustically Coupled Fuel Droplet Combustion," *Combustion and Flame*, Vol. 189, March 2018, pp. 46–61. doi:10.1016/j.combustflame.2017.10.019

[15] Shaw, B., and Yu, F., "ISS Droplet Combustion Experiments—Uncertainties in Droplet Sizes and Burning Rates," *Microgravity Science and Technology*, Vol. 26, No. 2, 2014, pp. 89–99. doi:10.1007/s12217-014-9377-x

[16] Basu, S., and Miglani, A., "Combustion and Heat Transfer Characteristics of Nanofluid Fuel Droplets: A Short Review," *International Journal of Heat and Mass Transfer*, Vol. 96, May 2016, pp. 482–503. doi:10.1016/j.ijheatmasstransfer.2016.01.053

[17] Pfeil, M. A., Groven, L. J., Lucht, R. P., and Son, S. F., "Effects of Ammonia Borane on the Combustion of an Ethanol Droplet at Atmospheric Pressure," *Combustion and Flame*, Vol. 160, No. 10, Oct. 2013, pp. 2194–2203. doi:10.1016/j.combustflame.2013.04.014

[18] Guerieri, P. M., DeLisio, J. B., and Zachariah, M. R., "Nanoaluminum/Nitrocellulose Microparticle Additive for Burn Enhancement of Liquid Fuels," *Combustion and Flame*, Vol. 176, Feb. 2017, pp. 220–228. doi:10.1016/j.combustflame.2016.10.011

[19] Sim, H. S., Plascencia, M. A., Vargas, A., Bennewitz, J. W., Smith, O. I., and Karagozian, A. R., "Effects of Aluminum Nanoparticle Additives on Liquid Fuel Droplet Combustion with and Without Acoustic Excitation," *10th U.S. National Combustion Meeting*, U.S. Sections of the Combustion Inst. No. 3C09, April 2017.

[20] Badakshan, A., Bennewitz, J. W., and Talley, D. G., "New Ignition Methods for Droplet Combustion Studies," *Combustion Science and Technology*, Vol. 190, No. 7, 2018, pp. 1302–1312. doi:10.1080/00102202.2018.1445726

[21] Struk, P. M., Ackerman, M., Nayagam, V., and Dietrich, D. L., "On Calculating Burning Rates During Fibre Supported Droplet Combustion," *Microgravity Science and Technology*, Vol. 11, No. 4, 1998, pp. 144–151.

[22] Sevilla-Esparza, C. I., Wegener, J. L., Teshome, S., Rodriguez, J. I., Smith, O. I., and Karagozian, A. R., "Droplet Combustion in the Presence of Acoustic Excitation," *Combustion and Flame*, Vol. 161, No. 6, 2014, pp. 1604–1619. doi:10.1016/j.combustflame.2013.12.012

[23] Dattarajan, S., Lutomirski, A., Lobbia, R. B., Smith, O. I., and Karagozian, A. R., "Acoustic Excitation of Droplet Combustion in Microgravity and Normal Gravity," *Combustion and Flame*, Vol. 144, Nos. 1–2, 2006, pp. 299–317. doi:10.1016/j.combustflame.2005.07.013

[24] Lefebvre, A. H., and McDonell, V. G., *Atomization and Sprays*, 2nd ed., CRC Press, Boca Raton, FL, 2017, pp. 237–239. doi:10.1201/9781315120911

[25] Badakshan, A., Bennewitz, J. W., and Talley, D. G., "Combustion Characteristics of Hydrocarbon Droplets Induced by Photoignition of Aluminum Nanoparticles," *10th U.S. National Combustion Meeting*, U.S. Sections of the Combustion Inst. No. 1E06, April 2017.

[26] Aggarwal, S. K., "Single Droplet Ignition: Theoretical Analyses and Experiment Findings," *Progress in Energy and Combustion Science*, Vol. 45, Dec. 2014, pp. 79–107. doi:10.1016/j.pecs.2014.05.002

[27] Turns, S. R., *An Introduction to Combustion: Concepts and Applications*, 8th ed., McGraw–Hill Higher Education, Boston, MA, 2000, pp. 362–421.

[28] Sutton, G. P., and Biblarz, O., *Rocket Propulsion Elements*, 8th ed., Wiley, Hoboken, NJ, 2010, pp. 259–260.

[29] Erbschloe, D., "Air Force Alternative Fuels Process Paves Way to Future," U.S. Air Force Air Mobility Command, Sapphire Energy TR, 2012.

[30] Karagozian, A. R., Dahm, W. J. A., Glasgow, E., Howe, R., Kroo, I., Murray, R., and Shyu, H., "Technology Options for Improved Air Vehicle Fuel Efficiency," U.S. Air Force Scientific Advisory Board TR SAB-TR-06-04, 2006.

[31] Sevilla-Esparza, C. I., "Oscillatory Flame Response in Acoustically Coupled Fuel Droplet Combustion," M.S. Thesis, Univ. of California, Los Angeles, 2013.

[32] Linstrom, P., and Mallard, W., *NIST Chemistry WebBook: NIST Standard Reference Database Number 69*, National Inst. of Standard and Technology, Gaithersburg, MD, 2017.

[33] Haynes, W., Lide, D. R., and Bruno, T. J., *CRC Handbook of Chemistry and Physics*, 97th ed., CRC Press, Boca Raton, FL, 2017, pp. 3-236, 3-246, 3-290, 3-294, 3-346, 3-514, 5-67, 6-144, 6-145, 6-147, 6-152, 6-256, 6-257, 6-258. doi:10.1201/9781315380476

[34] Huber, M., Lemmon, E., Ott, L., and Bruno, T., "Preliminary Surrogate Mixture Models for the Thermophysical Properties of Rocket Propellants RP-1 and RP-2," *Energy and Fuels*, Vol. 23, No. 6, 2009, pp. 3083–3088. doi:10.1021/ef900216z

Downloaded by Doug Talley on August 19, 2019 | http://arc.aiaa.org | DOI: 10.2514/1.B37195

[35] Abdulagatov, I., and Azizov, N., "Heat Capacity of Rocket Propellant (RP-1 Fuel) at High Temperatures and High Pressures," *Fuel*, Vol. 90, No. 2, 2011, pp. 563–567. doi:10.1016/j.fuel.2010.09.038

[36] Heywood, J., *Internal Combustion Engine Fundamentals*, 1st ed., McGraw–Hill, New York, 1988, p. 915.

[37] Bruno, T. J., "The Properties of RP-1 and RP-2 MIPR F1SBAA8022G001," Air Force Office of Scientific Research TR AFOSR-MIPR F1SBAA8022G001, 2008.

[38] Kolev, N., *Multiphase Flow Dynamics 4: Turbulence, Gas Absorption and Release, Diesel Fuel Properties*, 2nd ed., Springer–Verlag, Berlin, 2012, p. 317. doi:10.1007/978-3-642-20749-5

[39] Outcalt, S., and Laesecke, A., "Thermophysical Properties Measurements of Rocket Propellants RP-1 and RP-2," *Journal of Propulsion and Power*, Vol. 25, No. 5, 2009, pp. 1032–1040. doi:10.2514/1.40543

[40] Rose, J., and Cooper, J., *Technical Data on Fuel*, 7th ed., Scottish Academic Press, Edinburgh, Scotland, 1977, p. 282. doi:10.1016/0016-2361(77)90090-4

[41] *Permissible Exposure Levels for Selected Military Fuel Vapors*, National Academies Press, Washington, D.C., 1996, p. 15. doi:10.17226/9133

[42] Kresnyak, S., and Giles, T., "Enhancement of Fischer-Tropsch Process for Hydrocarbon Fuel Formulation," U.S. Patent No. 9-115-324-B2, 2015. doi:10.1016/0010-2180(72)90009-0

[43] *AP-42: Compilation of Air Emission Factors*, U.S. Environmental Protection Agency Rept. AP-42, Research Triangle Park, NC, 1995, p. 63, Chap. 7.

[44] Narayanaswamy, K., Pitsch, H., and Pepiot, P., "A Component Library Framework for Deriving Kinetic Mechanisms for Multi-Component Fuel Surrogates: Application for Jet Fuel Surrogates," *Combustion and Flame*, Vol. 165, March 2016, pp. 288–309. doi:10.1016/j.combustflame.2015.12.013

[45] Glaude, P., Fournet, R., Bounaceur, R., and Molière, M., "Adiabatic Flame Temperature from Biofuels and Fossil Fuels and Derived Effect on NOx Emissions," *Fuel Processing Technology*, Vol. 91, No. 2, 2010, pp. 229–235. doi:10.1016/j.fuproc.2009.10.002

[46] Chickos, J. S., and Zhao, H., "Measurement of the Vaporization Enthalpy of Complex Mixtures by Correlation-Gas Chromatography: The Vaporization Enthalpy of RP-1, JP-7, and JP-8 Rocket and Jet Fuels at $T = 298.15$ K," *Energy and Fuels*, Vol. 19, No. 5, 2005, pp. 2064–2073. doi:10.1021/ef050116m

[47] Ott, L., Hadler, A., and Bruno, T., "Variability of the Rocket Propellants RP-1, RP-2, and TS-5: Application of a Composition- and Enthalpy-Explicit Distillation Curve Method," *Industrial and Engineering Chemistry Research*, Vol. 47, No. 23, 2008, pp. 9225–9233. doi:10.1021/ie800988u

[48] Taylor, J. R., *An Introduction to Error Analysis: The Study of Uncertainties in Physical Measurements*, 2nd ed., Univ. Science Books, Sausalito, CA, 1997, p. 217.

[49] Beckwith, T. G., Marangoni, R. D., and Lienhard, V. J. H., *Mechanical Measurements*, 6th ed., Pearson, Upper Saddle River, NJ, 2007, pp. 57–61.

[50] Sim, H. S., Plascencia, M. A., Vargas, A., Bennewitz, J. W., Smith, O. I., and Karagozian, A. R., "Effects of Inert and Energetic Nanoparticles on Burning Liquid Ethanol Droplets," *Combustion Science and Technology*, Aug. 2018. doi:10.1080/00102202.2018.1509857

[51] Coleman, H. W., and Steele, G. W., *Experimentation, Validation, and Uncertainty Analysis for Engineers*, 4th ed., Wiley, Hoboken, NJ, 2018, p. 15, 167. doi:10.1002/2F9781119417989

[52] Shaw, B. D., *Uncertainty Analysis of Experimental Data with R*, Taylor and Francis, Boca Raton, FL, 2017, p. 111.

[53] Saitoh, T., Ishiguro, S., and Niioka, T., "An Experimental Study of Droplet Ignition Characteristics Near the Ignitable Limit," *Combustion and Flame*, Vol. 48, Jan. 1982, pp. 27–32. doi:10.1016/0010-2180(82)90113-4

[54] Tanabe, M., Bolik, T., Eigenbrod, C., Rath, H., Sato, J., and Kono, M., "Spontaneous Ignition of Liquid Droplets from a View of Non-Homogeneous Mixture Formation and Transient Chemical Reactions," *Symposium (International) on Combustion*, Vol. 26, No. 1, 1996, pp. 1637–1643. doi:10.1016/S0082-0784(96)80387-0

[55] Dahyabhai, S., and Rathod, P., "An Experimental Investigation on Droplet Ignition of Bio-Diesel and Its Blends," *International Journal of Advance Engineering and Research Development*, Vol. 1, No. 5, 2014, pp. 420–434.

[56] Javed, I., Baek, S., and Waheed, K., "Autoignition and Combustion Characteristics of Heptane Droplets with the Addition of Aluminium Nanoparticles at Elevated Temperatures," *Combustion and Flame*, Vol. 162, No. 1, 2015, pp. 191–206. doi:10.1016/j.combustflame.2014.07.015

[57] Bergeron, C. A., and Hallett, W. L. H., "Ignition Characteristics of Liquid Hydrocarbon Fuels as Single Droplets," *The Canadian Journal of Chemical Engineering*, Vol. 67, No. 1, 1989, pp. 142–149. doi:10.1002/cjce.v67:1

[58] Faeth, G. M., and Olson, D. R., "The Ignition of Hydrocarbon Fuel Droplets in Air," SAE Technical Paper Series, SAE International TP 680465, Warrendale, PA, 1968, pp. 1793–1802. doi:10.4271/680465

[59] Khan, Q. S., Baek, S. W., and Ghassemi, H., "On the Autoignition and Combustion Characteristics of Kerosene Droplets at Elevated Pressure and Temperature," *Combustion Science and Technology*, Vol. 179, No. 12, 2007, pp. 2437–2451. doi:10.1080/00102200701484605

[60] Williams, F. A., *Combustion Theory: The Fundamental Theory of Chemically Reacting Flow Systems*, 2nd ed., Benjamin/Cummings Publ., Menlo Park, CA, 1985, p. 68.

[61] Pickett, L. M., Genzale, C. L., Bruneaux, G., Malbec, L.-M., Hermant, L., Christiansen, C., and Schramm, J., "Comparison of Diesel Spray Combustion in Different High-Temperature, High-Pressure Facilities," *SAE International Journal of Engines*, Vol. 3, No. 2, 2010, pp. 156–181. doi:10.4271/2010-01-2106

[62] Som, S., Longman, D. E., Luo, Z., and Lu, T., "Three Dimensional Simulations of Diesel Sprays Using n-Dodecane as a Surrogate," *Fall Technical Meeting of the Eastern States Section of the Combustion Institute*, U.S. Sections of the Combustion Inst., Oct. 2011.

G. Richards
Associate Editor

Downloaded by Doug Talley on August 19, 2019 | http://arc.aiaa.org | DOI: 10.2514/1.B37195

Combustion Science and Technology

ISSN: 0010-2202 (Print) 1563-521X (Online) Journal homepage: https://www.tandfonline.com/loi/gcst20

Combustion Characteristics of Suspended Hydrocarbon Fuel Droplets with Various Nanoenergetic Additives

John W. Bennewitz, Alireza Badakhshan & Douglas G. Talley

To cite this article: John W. Bennewitz, Alireza Badakhshan & Douglas G. Talley (2020): Combustion Characteristics of Suspended Hydrocarbon Fuel Droplets with Various Nanoenergetic Additives, Combustion Science and Technology, DOI: 10.1080/00102202.2020.1729756

To link to this article: https://doi.org/10.1080/00102202.2020.1729756

Published online: 24 Feb 2020.

Submit your article to this journal

View related articles

View Crossmark data

Full Terms & Conditions of access and use can be found at
https://www.tandfonline.com/action/journalInformation?journalCode=gcst20

COMBUSTION SCIENCE AND TECHNOLOGY
https://doi.org/10.1080/00102202.2020.1729756

Taylor & Francis
Taylor & Francis Group

Check for updates

Combustion Characteristics of Suspended Hydrocarbon Fuel Droplets with Various Nanoenergetic Additives

John W. Bennewitz[a], Alireza Badakhshan[b], and Douglas G. Talley[a]

[a]Combustion Devices Branch, Air Force Research Laboratory, Edwards AFB, California, USA; [b]ERC Inc, Edwards AFB, California, USA

ABSTRACT

The burning process of multiple liquid fuels with various nanoenergetic additives is investigated experimentally in the suspended droplet configuration. Specifically, the burning rate constant K and ignition delay τ_{ign} are measured for two base fuels, rocket grade kerosene (RP-2) and ethanol, with seven energetic additives; the investigated additives include aluminum (Al), magnesium oxide (MgO), graphene, graphene nano-platelet (GNP), as well as numerous soluble additives including ammonia borane (AB), ammonium nitrate (NaAN) and sodium borohydride ($NaBH_4$), all of which do not exceed 6 wt.% loading concentration. Results from these experiments show that in general, there is not a significant modification to the steady burning rate for these nanofuel combinations (averaging $< 10\%$) for the loading concentrations considered. Instead, the additives exhibit a majority of particle burning during the end of the droplet lifetime, which generally are short-lived events that do not affect the overall K. This is illustrated by calculating the instantaneous burning rate $\widetilde{K}$ for these nanofuels, where $\widetilde{K}$ is 2% to 18% higher than pure fuels during the last half of the droplet burn time depending on the additive type. Similarly, nanofuel ignition delays generally only exhibit modest changes for a majority of the investigated combinations, causing only a $\pm 5\%$ change on average. However, two nanofuels consisting of ethanol with 5 wt.% soluble ammonia borane and RP-2 with 1 wt.% suspended graphene do exhibit increases in τ_{ign} of approximately 20 and 30%, respectively. These nanofuel compounds also exhibit substantial qualitative combustion behavioral changes including flame color changes and micro-droplet shedding events for ethanol with ammonia borane, as well as a notable reduction in the average burning rate of 20% for RP-2 with graphene. Therefore, these two nanofuel combinations may be candidates for further study as a means to garner control of combustion dynamics in a reacting liquid rocket spray environment.

ARTICLE HISTORY
Received 7 October 2019
Revised 11 February 2020
Accepted 11 February 2020

KEYWORDS
Nanofuel droplets; droplet combustion; energetic additives; burning rate; ignition delay

Introduction

Heterogeneous mixtures incorporating a pure liquid base fuel with metallic fuel additives have been a topic of interest in propulsion applications dating back to the 1940s, primarily due to the potential for significantly increased energy densities and overall performance increases. The earliest known study of heterogeneous mixtures for rocket applications was performed by Heinz Mueller's group of Bavarian Motor Works (BMW) (Clark 2018),

CONTACT John W. Bennewitz john.bennewitz.1@us.af.mil Air Force Research Laboratory, 10 E. Saturn Blvd, Edwards AFB, California, USA

© 2020 Taylor & Francis Group, LLC

which investigated both aluminum and magnesium powders suspended separately in diesel fuel. Unfortunately, these engines suffered from very low performance due to incomplete additive burning, yielding overall chamber pressures lower than 1/3 of the desired level (Clark 2018). However, more recently, this research area has garnered renewed interest through the use of metalized nanoparticles (i.e., particles less than 1 μm) as the suspended additives. Essentially, nanoparticles (NP's) consist of three-dimensional clusters or two-dimensional sheets of atomic and molecular structure of inorganic materials that are nanometer size, typically 1 to 100 nm or even 1 to 1000 nm. Overall, nanoparticles offer a significantly large surface area to volume ratio compared to particles on the micron scale and above, which theoretically correspond to much higher reactivity. This interest resurgence is mostly a direct result of substantial successes of nanoparticle utilization in the fields of combustion science and nanofluids (Saidur, Leong, and Mohammad 2011; Yetter, Risha, and Son 2009), which have demonstrated improvements in performance of explosives and solid propellants through the addition of various nanostructured energetic materials such as micron and sub-micron size aluminum additives to polymer mixtures (Armstrong et al. 2003).

Expanding upon the research started by BMW during the 1940s, the automotive industry has since adopted NP additives for hydrocarbon fuels (Tyagi et al. 2008), with an interest in their catalytic effects for the reduction of tail pipe gas emission (Basha and Gopal 2012). There are wide ranges of elemental and compound NP's, as well as metallic alloys that are desirable liquid fuel additives due to their energetic properties, reactivity and/or catalytic effects (Ghamari and Ratner 2017; Jones et al. 2011; Sabourin et al. 2009; Sabourin, Yetter, and Parimi 2010). Research into biodiesel nanoadditives has successfully demonstrated the use of manganese oxide (MnO), cobalt oxide, and cerium oxide functionalized carbon nanotubes in various nanobiodesel blends to reduce carbon monoxide (CO) emissions through an oxidation catalysis process (Mehregan and Moghiman 2018; Mirzajanzadeh et al. 2015). However, it should be noted that while there is evidence to support nanoadditives as a means to reduce harmful emissions, certain researchers did not observe any significant difference between the amount of CO emission for neat biodiesel and blends with nanoparticles (Soudagar et al. 2018).

For propulsion applications, fundamental droplet combustion studies with nanoenergetic additives as burning rate modifiers have been investigated by numerous research groups using a variety of liquid base fuels and additive combinations (Ghamari and Ratner 2017; Guerieri, DeLisio, and Zachariah 2017; Javed, Baek, and Waheed 2015; Pfeil et al. 2010; Pfeil et al. 2013; Sim et al. 2018). In these experiments, varying levels of burning rate modification were observed, including increases in differing amounts from small variations (Pfeil et al. 2010; Pfeil et al. 2013), to moderate (Sim et al. 2018), or even a decrease (Guerieri, DeLisio, and Zachariah 2017), depending on the additive type (i.e., solid or soluble) and base fuel. In general, results from these studies indicate that the augmentation of burning rates is possible up to approximately 15% for ≤ 5 wt.% additive concentration, but it is typically no greater than 10%. Effects on nanofuel droplet ignition delay τ_{ign} have also been reported (Javed, Baek, and Waheed 2015; Kim, Baek, and Yoon 2016), which also show either an increase (Kim, Baek, and Yoon 2016) or decrease (Javed, Baek, and Waheed 2015; Kim, Baek, and Yoon 2016) depending on the nanofuel combination and ambient conditions, i.e., temperature and pressure, of the surrounding environment.

Aside from overall performance benefits, there is interest in using nanostructured fuel additives to control combustion dynamics in liquid rocket engines (LRE's). As detrimental thermo-acoustic instabilities are excited due to in-phase coupling between oscillatory chamber pressure and unsteady heat release from combustion, it is theorized that nanoenergetic additives can affect this coupling to potentially lead to a damping effect. One experimental study investigating the addition of a soluble additive ammonia borane (AB), NH_3BH_3, into ethanol was studied in a model LRE combustor (Pfeil, Son, and Anderson 2014). Compared to pure ethanol, it was found that there existed an axial bimodal heat release distribution throughout the combustor present with ethanol and AB at 6 wt.%. While this spatial relocation of the heat release did alter flame-acoustic coupling within the chamber, unfortunately, the ethanol with ammonia borane nanofuel actually caused the engine to become more unstable across various injector configurations than operating with neat ethanol (Pfeil, Son, and Anderson 2014). Nevertheless, this demonstrated the potential for significantly altering the combustion dynamic processes within the combustor during operation.

Another experimental study investigating the flame-acoustic coupling of a nanofuel was recently investigated in the continuously-fed burning droplet geometry (Sim et al. 2019). The investigated nanofuel mixture consisted of ethanol and the non-soluble additive nanoaluminum (nAl) up to 3 wt.% loading. Overall, it was found that nAl addition increased the degree of flame-acoustic coupling (i.e., Rayleigh index G) in the presence of a velocity antinode up to 45% on average during sustained oscillatory combustion. Also, the mean strain rate attributed to periodic partial extinction (PPER) phenomena (Bennewitz et al. 2018) that occurs at higher amplitude forcing was shown to increase up to 44% with the addition of nAl, as well as delaying the onset of PPER for lower frequency forcing at 332 Hz (Sim et al. 2019). This further indicates the possibility of altering the flame-acoustic coupling with the use of energetic nanoparticles.

In order to lay the foundation for developing a nanofuel that can garner control of combustion dynamics, substantial background work in understanding the effects of nanostructured materials and nano-energetics as rocket relevant liquid fuel additives is first required. One fundamental approach is to study the combustion characteristics of suspended nanofuel droplets, as this provides a suitable means to investigate condensed phase combustion (Godsave 1953; Law and Williams 1972; Sirignano 2010). Therefore, the focus of this experimental study is to investigate the effect of various nanoadditives using two rocket relevant base fuels in the suspended droplet geometry to discern changes in the burning rate constant K and ignition delay time τ_{ign}.

The emphasis in this study is on relatively low loading of nanoenergetics (< 1 wt.% for solids, < 6 wt.% for solubles), in consideration of the fairly low tolerance many engine systems have for elevated particulate levels, due to concerns over particulate accumulation leading to potential clogging or failure of engine components. For example, the military specification for rocket grade kerosene only permits a maximum of 1 mg/L of solid particulates for delivered fuel, or only about 10^{-4} wt.% (USAF 2006). Thus, even the relatively low loading levels considered in this paper are still orders of magnitude larger than the current specification. The implementation of even these loadings would therefore as a minimum requires a reexamination of current fuel specifications, and beyond that it could also require a substantial redesign of engine system components.

The investigated base fuels in this study include ethanol and rocket grade kerosene (RP-2), with solid nanoadditives including aluminum (Al), magnesium oxide (MgO), graphene, graphene nano-platelet (GNP), and the soluble additives ammonia borane, ammonium nitrate (NaAN) and sodium borohydride ($NaBH_4$). The three main solid additives aluminum, graphene nano-platelet, and magnesium oxide mainly target modifying transport and thermodynamic fuel properties in various ways. Specifically, aluminum has shown to increase overall heat release of the reacting system through the increase of the flame temperature (Sim et al. 2018; Tanvir and Qiao 2015) and heat of combustion (Sim et al. 2018). Additionally, the increased thermal conductivity of aluminum-based nanofuels (Pfeil et al. 2010; Sim et al. 2018; Tanvir and Qiao 2015) has also shown a benefit to droplet burning. Graphene nano-platelet has similarly demonstrated an increase in internal heat transfer within the liquid droplet due to increased thermal conductivity (Ghamari and Ratner 2017), as well as increased heat absorption through radiation due to the darkened nature of GNP (Ghamari and Ratner 2017). Magnesium oxide has previously exhibited the ability to provide a quality dispersion in nonpolar fuels (Bello et al. 2015), which makes it desirable from a flow system infrastructure and storability standpoint for a reactive system. In addition, MgO has shown increased diffusive behavior in kerosene fuels, leading to similar diffusive timescales compared to aluminum and much shorter radiative timescales (Bello et al. 2015).

Regarding the soluble additives, ammonia borane is unique in that it provides a mechanism for internal hydrogen gas generation to occur during droplet burning, as the dissociation temperature for ammonia borane is lower than the boiling point of its base fuel (ethanol) (Pfeil et al. 2013, 2014). This hydrogen gas generation causes an increase in the chemical kinetic rates (Pfeil et al. 2013), and can potentially help mitigate the onset of combustion instabilities in a reactive system (Yu et al. 2008). Ammonia borane addition has also shown to increase overall heat release through increased flame temperature, heat of combustion and thermal conductivity (Pfeil et al. 2013, 2014). In total, 10 nanofuel combinations are studied in the present work for loading concentrations under 6 wt.%. Generally, most nanofuel combinations at these loading concentrations do not exhibit large changes in global droplet burning properties but show an increase in the instantaneous burning rate toward the end of the droplet lifetime. Both ethanol with 5 wt.% AB and RP-2 with 1 wt.% graphene demonstrate the largest changes to droplet burning, permitting them to be suitable for further investigation in a reacting liquid nanofuel spray.

Nanofuel creation

Synthesis and dispersion of nanoparticles is an expansive topic and full treatment is beyond the scope of this article. Synthesis and application of NP's have been the subject of great interest to researchers in a wide range of disciplines including physics, chemistry, material science, engineering, biology, and medicine. Several comprehensive and specialized review articles on the synthesis and applications of functional NP's have appeared in recent publications (Lu, Salabas, and Schüth 2007; Mittal, Chisti, and Banerjee 2013; Tang, Li, and Chen 2012). However, the focus in the following two sections will be limited to the aspects of synthesis and dispersion of nanoparticles that are directly related to liquid nanofuels.

Synthesis of nanoparticles

There are two major approaches regarding the synthesis of NP's and preparation of nano-suspensions, designated as either top-down or bottom-up nanofabrication (Biswas et al. 2012). Top-down nanofabrication involves starting from a larger piece of material and etching away to produce nanoparticles, whereas the bottom-up fabrication process builds nanostructures from subcomponents on the molecular level through an additive procedure (Biswas et al. 2012). One issue encountered in the synthesis of elemental NP's or metal alloys is the formation of oxide layers immediately after the NP's have been formed or soon after they are exposed to environmental oxygen and moisture (Meziani et al. 2009). For example, in the case of aluminum NP's, the relatively thick Al_2O_3 layer/shell is undesirable for three reasons: (i) the surface layer of NP's is a very stable oxide unlike the highly reactive Al, (ii) it is an impenetrable shell with a very high melting temperature, far higher than that of Al and (iii) for smaller NP's (e.g., less than 80 nm), a relatively large percentage of the available material (depending on the size) is nonenergetic (i.e., significantly reducing the large surface area to volume ratio).

The use of transmission electron microscopy (TEM) is crucial in revealing structural details of the solid nanoparticles prior to dispersion into the liquid fuel. This illustrates the average particle size and distribution compared to the manufacturer specified size. In addition, TEM images usually reveal how densely the clusters are packed and if there exists substantial porosity within the structures, assuming the drying process does not significantly affect porosity. Overall, TEM encompasses a quality assessment of the raw nanoparticles. Example TEM images for 80 nm aluminum (see Figure 1) taken from two separate batches from the same vendor demonstrate large discrepancies in the nanostructures. To generate these images, sonication of the samples containing ethanol with aluminum nanoparticles is first performed for 10 min, after which the nanofuel mixture is exposed to atmospheric conditions to permit all liquid to evaporate. In these images, it is apparent that batch #1 (Figure 1(a)) contains uniformly spherical particles that are below 100 nm and on average approximate the specified 80 nm size. Batch #2 however, has severely different nanostructures that include large irregularities in both shape and porosity (Figure 1(b)). Nanostructure aggregates largely exceeding 100 nm are present, often with serrated structural boundaries in lieu of spherically smooth edges. As batch #2 contains particles of such poor quality, only aluminum NP's from batch #1 are used for testing in the current study. However, this illustrates the importance of performing TEM on all purchased raw nanoparticles to ensure their quality.

TEM views of two other types of nanoparticles including 20 nm magnesium oxide and 5 to 7 μm graphene nano-platelet display different structural characteristics to aluminum (see Figure 2). Magnesium oxide shows a combination of both spherical and elliptical shaped particles, which on average appear to be 20 nm in size (Figure 2(a)). This is shown in greater detail in the zoomed view on the right, which displays nanoparticles that are more ovular and have less defined edges than the spherical nAl particles. Graphene nano-platelet (Figure 2(b)) are nanostructures comprised in a multi-layered sheet geometry that is approximately 5 to 7 μm in size with under 30 layers per structure. Unlike the other particle types, GNP has sharp-edge boundaries that have well-defined corners throughout the nanoclusters. These three main solid particle types are selected as the droplet burning modifiers due to their drastically differing size and structure.

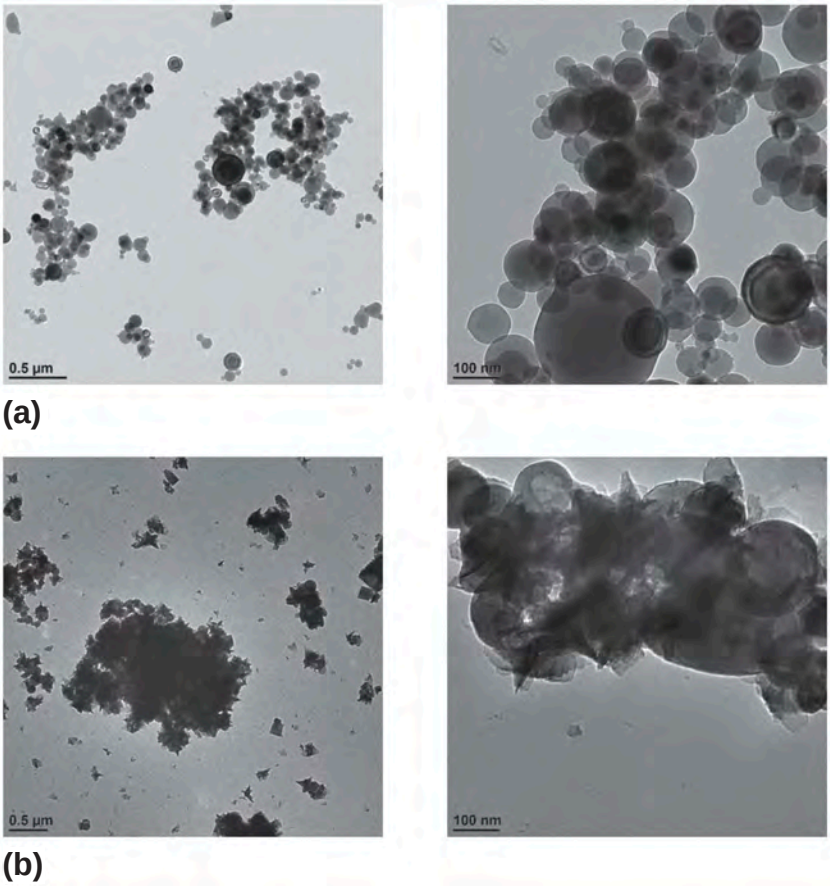

Figure 1. Transmission electron microscopy images of 80 nm aluminum particles after sonication from the same vendor in two separate batches, with (a) batch #1 showing well-defined spherical structures within the desired size range and (b) batch #2 exhibiting non-spherical agglomerates substantially higher than 100 nm in size. It should be noted that the 0.5 μm scale images are shown on the left and the 100 nm reduced scale images are on the right.

Dispersion of nanoparticles within liquid fuel

Dispersion and proper suspension of solid nanoparticles within a liquid base fuel are crucial to nanofuel performance. This involves creating a well-dispersed suspension of NP's in the fuel of choice, which for this study is either an alcohol, i.e., ethanol, or a complex hydrocarbon, i.e., rocket grade kerosene (RP-2). Both the base fuel and nanoadditive type affect the strategy to adequately disperse and suspend the solid particles. Most often, a surfactant is employed to reduce the surface tension and make NP's disperse in the liquid more effectively, in effect creating a nano-suspension through the formation of nanoclusters that stays suspended for a longer period. Much of the earlier work in this area has been performed on the suspension of poorly soluble drugs for drug delivery (Agrawal and Patel 2011; Chingunpituk 2007). As ethanol is a polar fuel, a surfactant is not necessary to create the nano-suspension, while RP-2 always requires a surfactant for

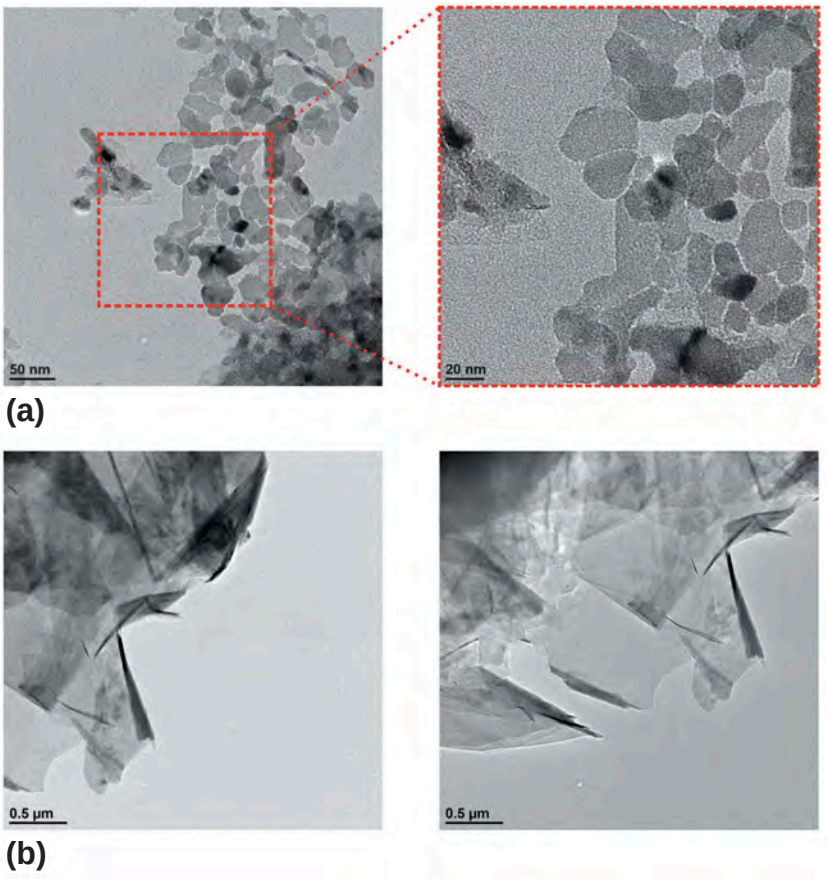

Figure 2. Transmission electron microscopy images of (a) 20 nm magnesium oxide at a 50 nm scale (left) and a zoomed view at a 20 nm scale outlined in red (right), along with two views of (b) graphene nano-platelet (GNP). Both nanostructure types are imaged after 10 min of sonication in ethanol and once all of the liquid is evaporated.

proper suspension. Surfactants including a sugar-based type called Span 80, oleic acid (OA), as well as the sodium-based sodium bis(2-ethylhexyl) sulfosuccinate (NaAOT) all have shown to be effective at nanoparticle suspension in nonpolar fuels (Bello et al. 2015; Ghamari and Ratner 2017; Javed, Baek, and Waheed 2015). Aside from the use of surfactants, in certain cases it is necessary to perform surface treatment on the NP's such as passivation to counter-balance the tendency of NP's to aggregate and form a much larger cluster (Guerieri et al. 2015).

The aggregation process in a suspension is generally very slow but severely reduces the reactivity of NP's by removing the most important characteristic property of NP's, i.e., the extremely large surface area to volume ratio (Deng et al. 2016). Specifically, this is what permits NP's to have extremely high reactivity, advantageous catalytic properties, as well as affect liquid phase properties such as increased thermal conductivity. The only exception concerning the loss of such desirable properties is when the NP aggregates are extremely porous, which is rare and should not be assumed without due investigation.

However, highly porous materials with nano-scale pores have shown high-reactivity and catalytic properties that makes them behave more like NP's, unlike other mesoscale materials (Tang, Li, and Chen 2012).

The intricacies of NP dispersions in liquid fuels for propulsion applications have not received significant attention up until now, due to the lack of details about nano-dispersion in published reports. In fact, most NP's show a tendency to form sizable aggregates when introduced to most liquids. It is quite possible that NP's supplied by vendors as powder are mostly in large clusters well exceeding 500 nm, which is the reason the sonication process is required to properly break down the NP clusters within a liquid. Typically, the use of a high-powered sonication probe/tip is recommended instead of an ultrasonic bath, which may only be marginally effective in some cases. It should be noted that even with ultrasonication using a probe, it may not be able to break apart a strongly bonded cluster of NP's.

Typically, the formed NP aggregates are relatively large in size and can grow up to a few micrometers (Anton, Benoit, and Saulnier 2008), making it difficult to achieve a stable nano-dispersion (Hwang et al. 2008). Such aggregates may stay suspended within the liquid long enough so that the suspension passes a standard turbidity test, which denotes how fast solid particles settle at the bottom of a container. In addition, the quality of the NP's dispersion in fuels is most often solely judged by the turbidity of the liquid. Such a test only reveals the extreme cases of suspension settling and it cannot be used as an indication for the quality of a nano-suspension or any form of well-suspended NP's in the liquid. For most nanofuels that pass the turbidity test, although the loading concentration of the added NP's is high enough, it is possible that most NP's are contained in larger clusters, causing the concentrations of NP's and nanoclusters to be much less than what is required to cause a noticeable NP-related effect. Agglomeration effects such as these have been noted as a reason behind the variation in the droplet burning rates observed among various research groups using the same additive (Guerieri, DeLisio, and Zachariah 2017).

Proper nano-dispersion is achieved when a majority of the suspended NP's are in relatively small clusters, with each structure containing no more than several hundred NP's (Hwang et al. 2008). For example, nanofuels used in this study with nominally 80 nm Al NP's are shown to have a reasonably good dispersion when most of the nano-clusters are smaller than approximately 500 nm, as revealed by particle size distribution measurements using a zetasizer instrument taken long after the NP's were added to the fuel and subsequent sonication. For RP-2, a good dispersion is only achieved with the inclusion of a surfactant, typically < 5 wt.% with the NP's.

An effective approach to determine a reasonably good dispersion of NP's in a liquid is through a series of periodic measurements of particle size distribution to obtain temporal evolution of the size distribution of nanoparticle clusters in the liquid. However, this approach proved to be ineffective with additives of very large aspect ratio, as with graphene nano-platelet. For GNP, the optical detection system of the zetasizer instrument consistently detects the larger platelet dimensions on the micron scale while leaving the smaller features on the nanometer scale obscured, not permitting an accurate account of the total particle size.

While TEM is helpful in learning aspects of the dispersion quality of NP's in liquid, it has its own limitations. The main limitation stems from the fact that typical TEM measurements are performed on dry samples and the drying process usually introduces

aggregation of NP's, as well as occasional impurities. A better approach is to perform cryogenic TEM imaging, which involves observation of a matrix of NP clusters within the frozen base fuel, near liquid nitrogen temperature. However, this type of TEM, which is commonly used for biological samples, is costly and may not be available to most researchers. Nevertheless, it is important to characterize the quality of both the raw nanoparticles and their suspension within the liquid fuel prior to experimentation.

Experiment setup

The test facility used to investigate the burning characteristics of various nanofuel droplets is the same as our previous works (Badakhshan, Bennewitz, and Talley 2018; Bennewitz, Badakhshan, and Talley 2019). It allows suspended droplets to be automatically ignited and imaged throughout their entire burn time (see Figure 3). For each experiment, a droplet is suspended from an uncoated quartz fiber from Polymicro Technologies, Inc. that is 150 μm in diameter; the formation of a droplet on the fiber is greatly facilitated by producing a "bead" at the fiber end, which is achieved through melting the tip by a high-temperature flame using an oxy-propane torch. It should be noted that no appreciable change in the surface tension of the hydrocarbon fuel is observed with any of the surfactants in this study, i.e., Span 80, oleic acid, and NaAOT; this is indicated by the droplets of the same initial size staying suspended on the supporting fiber. The fiber bead is nominally 200 μm and the diameter of a typical nanofuel droplet range between d = 1.2 to 1.5 mm. A hypodermic needle capable of repeatably dispensing the same amount of fluid is used to transfer the droplet onto the fiber as a means to generate droplets of similar initial size.

Direct high-speed visible imaging of the burning droplet is performed using a Phantom v7.1 camera with a Nikon AF Micro Nikkor 200 mm lens. Images are recorded at a rate of 1000 fps for the droplet lifetime (typically 2 s), which are backlit using a 2 × 2 square array

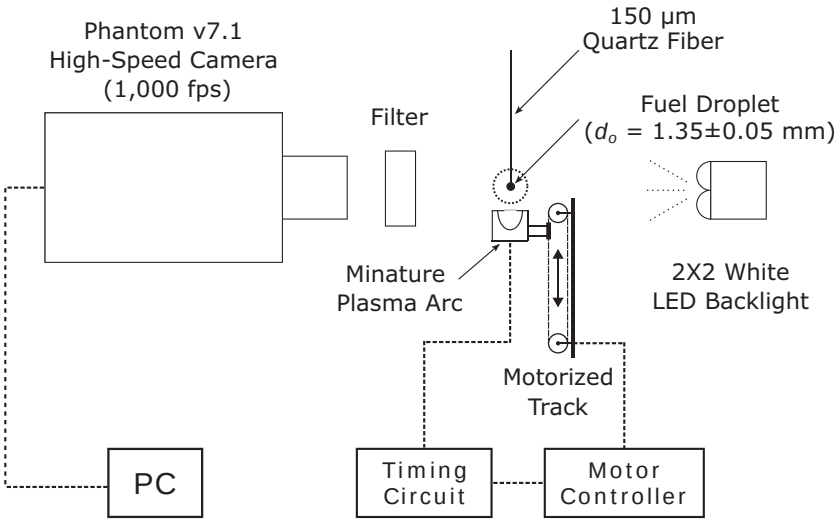

Figure 3. Droplet experiment test facility schematic consisting of the high-speed imaging configuration and the plasma arc ignition (PAI) system connected to the automated motorized track.

of adjustable-intensity white light-emitting diodes (LEDs) to capture the droplet diameter regression. Certain heavily sooting droplets require a Semrock FF01-433/530-25 filter for droplet imaging to provide increased droplet visibility. Also, in certain experiments where the ignition process is studied, the Phantom camera is replaced by a FLIR SC6800 midwave infrared (1.55.0 μm) camera imaging at 250 fps with a StingRay Optics SR1936-A01 50 mm lens and 0.6 neutral density filter.

The suspended droplet is ignited using a custom-built miniature plasma arc ignition (PAI) system detailed in previous work (Badakhshan, Bennewitz, and Talley 2018). It is a controllable duration plasma source that has two electrodes spaced 5 mm apart and are placed approximately 1 mm beneath the droplet prior to ignition. PAI takes advantage of a high-frequency and low current plasma arc that can rapidly heat a localized spot on the edge of droplet, leading to the ignition of a wide range of fuel droplets including hard-to-ignite fuels such as diesel and hexadecane (Badakhshan, Bennewitz, and Talley 2018). The ignitor is positioned on a motorized track that is connected to an adjustable timing circuit. During a test, the plasma source is first positioned underneath the droplet and activated for a set firing duration. Once the plasma is finished discharging, the unit is automatically pulled away from the droplet. For all nanofuels used in this study, droplets are consistently ignited with a 100 ms arc discharge duration.

Droplet burning characteristics

As with our previous droplet work (Bennewitz, Badakhshan, and Talley 2019), the two burning properties investigated in this study are the burning rate constant K and ignition delay τ_{ign}. These two parameters have become the standard in experimental droplet studies for both single-component (Bartle et al. 2011; Bennewitz et al. 2018; Godsave 1953; Kumagai and Isoda 1955; Law and Williams 1972; Sioui and Roblee 1969) and multicomponent pure fuels (Bennewitz et al. 2018; Ghamari and Ratner 2017; Godsave 1953; Pfeil et al. 2010; Wood and Wise 1957), as well as various nanofuels (Ghamari and Ratner 2017; Javed, Baek, and Waheed 2015; Kim, Baek, and Yoon 2016; Pfeil et al. 2010; Pfeil et al. 2013; Sim et al. 2018); they provide quantifiable measures of both the quasi-steady burning and ignition processes, which offer insight into underlying mechanisms that can affect flame-acoustic coupling within an LRE combustor.

Burning rate constant

The droplet burning rate provides a measure of the rate at which the droplet diameter regresses throughout quasi-steady combustion. It comes from the well-established d-squared law (Faeth 1977; Glassman and Yetter 2008; Law and Williams 1972), which states that the droplet diameter squared regresses linearly with time and is written as

$$K = -\frac{d}{dt}(d_{\text{eqvs}})^2. \tag{1}$$

For this study, the droplet diameter definition used to quantify K is based on an equivalent volume of a sphere (Struk et al. 1998) given by

$$d_{\text{eqvs}} = 2A^{1/3}B^{2/3}, \tag{2}$$

where A and B are the semimajor and minor axis lengths of the two-dimensional projected ellipsoidal droplet. This droplet definition is implemented as K calculated using d_{eqvs} was shown in a previous work (Bennewitz, Badakhshan, and Talley 2019) to produce results with low uncertainty closest to the average upon comparing various droplet diameter definitions for hydrocarbon fuels.

In order to determine the burning rate constant, an automated image processing technique is implemented to track the droplet d-squared temporal regression; this takes the high-speed visible backlit images starting 200 ms after ignition and fits an ellipse to the droplet's outer edge in each image. By processing synthetic image data with a known linear regression using this automated procedure, this approach has been previously shown to be sufficiently robust as it provides less than 1.5% deviation on average (Bennewitz, Badakhshan, and Talley 2019). Using the droplet diameter temporal history, the burning rate can then be evaluated.

As the d-squared law is an idealization describing steady droplet burning, in reality, certain phenomena including droplet heating, multicomponent distillation effects, and vapor accumulation (Law 1982; Law and Williams 1972) can cause deviations from linear d-squared droplet regression behavior. Nevertheless, reporting "effective" droplet burning rates is useful in describing steady burning processes. To provide K values that are the most direct implementation of the linear regression idea, our previously developed K evaluation method (Bennewitz, Badakhshan, and Talley 2019) is implemented. This approach automatically determines the burning rate based upon the most linear portion of the d-squared regression for the longest period of droplet burning. This approach has successfully shown to provide K values with small statistical and total uncertainties (Bennewitz, Badakhshan, and Talley 2019) for a large range of hydrocarbon fuels exhibiting varying degrees of nonlinear regression behavior. Therefore, this evaluation method is adopted for the current study.

A final consideration for nanofuel droplet combustion is end-of-life processes that can contain a notable amount of additive burning and particle expulsion events. For the traditional solid nanofuels investigated in this work, a majority of the particle burning events take place as essentially "char" combustion, where there is a significantly higher amount of solid additives left compared to the liquid base fuel. In order to be consistent with the burning droplet theory, reporting burning rates as defined by the d-squared law is only appropriate when there is a perfectly spherical or ellipsoidal droplet that is not significantly distorted. Therefore, the image processing approach implemented here addresses this by only considering the droplet regression data until there ceases to be a reduction in the liquid droplet size, as when there are predominantly only solids present, different physical mechanisms begin to dominate and cause the d-squared law to no longer apply. Once there is no liquid fuel left, i.e., denoted by a constant diameter output from the droplet tracking algorithm, all data past this point is removed to report the burning rates.

Ignition delay

Ignition delay time τ_{ign} is the other parameter used in this study to quantify droplet burning behavior that may influence combustion dynamics within a reacting spray. Typically, τ_{ign} is defined as the time separation between introducing the droplet to a hot ignition environment and the observation of the established flame, which denotes the start

of quasi-steady droplet burning (Aggarwal 2014). Previously, many droplet ignition experiments have used arc furnace heating or an ignition coil (i.e., nichrome wire) for combustion initiation, which is generally slow acting. Also, on occasion a flame ignitor may be used, commonly in a miniature torch or small flat flame arrangement. Nevertheless, the differences between various ignition sources primarily can be attributed to two main parameters, (i) the temperature of the source inducing auto-ignition of the droplet and (ii) amount of energy exchange and speed of the heat exchange mechanisms between the ignition source and the fuel droplet, as it influences the rate of vaporization. Other parameters that affect ignition include the availability and mixing of the gaseous oxidizer, proximity of the ignition source to the droplet, and the geometrical spread of the heating source.

The short-duration plasma arc provides a convenient method to systematically study droplet ignition behavior due to its constant average power and adjustable ignition duration, while simultaneously producing minimal background light and heat detected by infrared imaging. The gas temperature for PAI is estimated to exceed 3000 K and the delivered power is at a rate of 2 W or 0.2 J per ignition event of 100 ms duration (Badakhshan, Bennewitz, and Talley 2018). In addition, the short-duration ignition is only active during a fraction of the total droplet lifetime, which isolates quasi-steady droplet burning from the ignition process. As PAI provides repeatable ignition events for all investigated nanofuels, it is used in this study for the ignition experiments.

Ignition delay values are evaluated using the same approach developed in our previous work (Bennewitz, Badakhshan, and Talley 2019). This method automatically tracks the flame region growth from the IR images throughout the ignition process to the start of quasi-steady burning. Example data for a pure ethanol droplet is shown in Figure 4, where the flame region size grows to an initial maximum that then reduces in size at the start of steady burning. Therefore, τ_{ign} is defined as the time duration between the ignitor activation to the time the droplet flame reaches an initial maximum size (i.e., τ_{ign} = 68 ms for this example), representing an upper limit of the ignition delay for each fuel (see Figure 4(b)).

Burning characteristics of Nanofuel droplets

Droplet burning for a range of nanofuel combinations is investigated to identify candidates that exhibit substantial changes in the quantitative burning properties and qualitative burning characteristics (i.e., unsteady burning, micro-droplet shedding, etc.). The base fuels ethanol and RP-2 encompass an alternative fuel and common kerosene blend relevant to propulsion systems (Erbschloe 2012; Sutton and Biblarz 2010; Turns 2000). Ethanol is a non-sooting alcohol that is a convenient base fuel for energetic additive investigation due to no additional surfactant being required for adequate particle suspension, and its compatibility with the soluble additive ammonia borane. In addition, ethanol has the lowest burning rate K of the base fuel candidates studied in our previous work (Bennewitz, Badakhshan, and Talley 2019), primarily due to the significant differences of its heats of combustion Δh_c and vaporization Δh_{vap} compared to other simple hydrocarbons and kerosene blends. RP is the other selected base fuel, as it is a standard kerosene for rocket propulsion applications (Clark 2018; Heister et al. 2019; Sutton and Biblarz 2010).

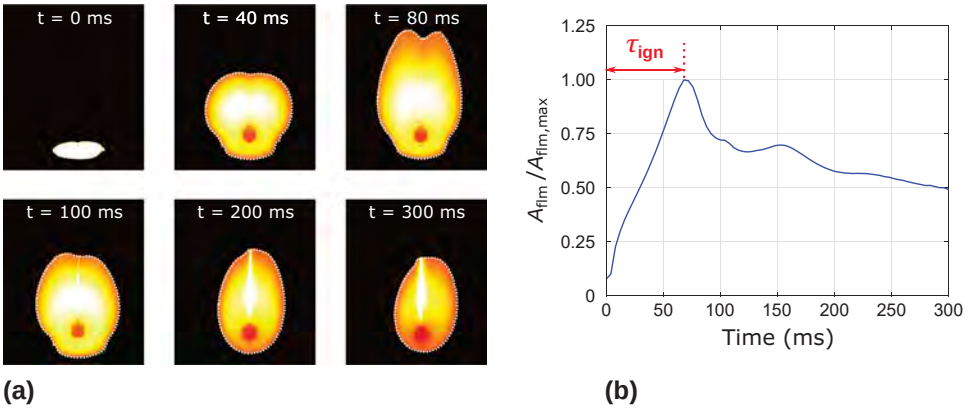

Figure 4. Time sequence of the (a) ignition process for an ethanol droplet taken from infrared imaging, with the corresponding (b) flame area temporal history establishing the ignition delay definition τ_{ign}.

Burning rate

The droplet burning rate constants for both neat RP-2 and ethanol are summarized in Table 1. These effective K values are taken through averaging 15 pure droplet experiments for each fuel and evaluating the burning rate with the previously described approach. A detailed uncertainty analysis for these burning rate measurements is presented in our other work (Bennewitz, Badakhshan, and Talley 2019). As can be seen in Table 1, ethanol has a 15% lower average burning rate than RP-2. Using this evaluation method, both pure fuels have coefficients of determination R_K^2 exceeding 0.999 and uncertainties less than ± 0.006 mm^2/s, denoting the suitability of this K evaluation approach.

Each nanofuel combination investigated in the present study has a minimum of five droplet burning tests conducted to produce statistically reliable results. The Student's t-distribution (Beckwith and Roy 2007) for small sample sizes and Chauvenet's rejection criteria (Taylor 1997) are used together to report a 95% confidence interval on the burning rates. Prior to studying the effects of nanoparticle addition to liquid base fuels, burning rate measurements are taken for RP-2 with various surfactants (see Figure 5). The three surfactants Span 80, oleic acid, and NaAOT at varying concentrations up to 10 wt.% are considered, as this is the maximum used in this study and not commonly exceeded in similar nanofuel droplet experiments. All presented droplet burning rates in this study are normalized by the average K_o of the corresponding neat base fuel shown in Table 1. In addition, all presented error bars for the normalized burning rates correspond to the experimental uncertainty generated from the small sample statistical analysis. For all surfactant types, there is a notable reduction in K approaching 10 to 20% when the loading concentration is large, i.e., exceeding 5 wt.%. However, with less than 5 wt.% Span

Table 1. Summary of the baseline droplet burning parameters K_o and $\tau_{ign,o}$ for the investigated neat fuels, along with the average total uncertainty u_K (Bennewitz, Badakhshan, and Talley 2019).

Fuel	K_o (m m^2/s)	u_{K_o} Avg. (mm^2/s)	$\tau_{ign,o}$ (ms)	
Ethanol	0.744	0.005	0.999	71
RP-2	0.878	0.006	0.999	87

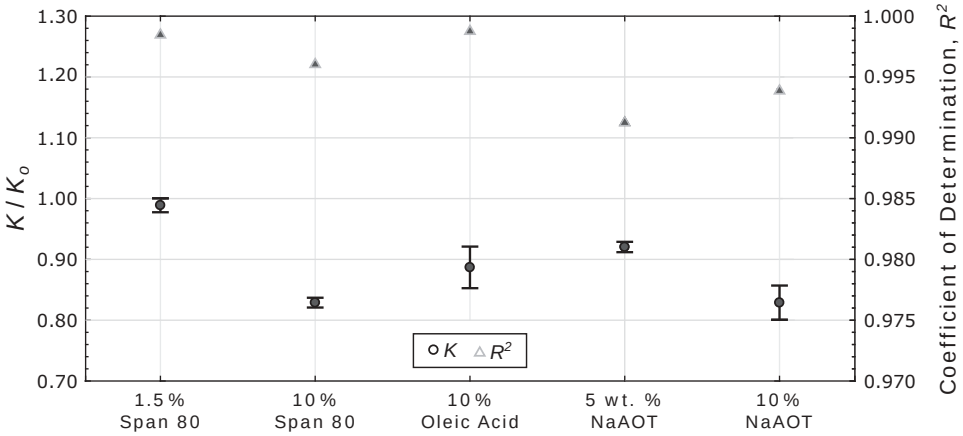

Figure 5. Normalized droplet burning rate constant K/K_o for RP-2 with various surfactants including Span 80, oleic acid and sodium bis(2-ethylhexyl) sulfosuccinate (NaAOT). It should be noted that K_o is the burning rate constant of neat RP-2. The left axis of this plot shows the normalized burning rate (●) and the right axis is the corresponding coefficient of determination (▲).

80, the burning rate is mostly unaffected compared to pure RP-2. Therefore, the amount of surfactant should ideally be minimized and limited to not exceed 5 wt.% concentration if possible to create an adequate nano-suspension. If exceeding 5 wt.% loading is required, surfactant effects on K need to be taken into account.

Influenced by the works of Ghamari and Ratner (Ghamari and Ratner 2017) using graphene nano-platelet in Jet-A and Pfeil et al. (Pfeil et al. 2013) with ammonia borane soluble in ethanol, three nanofuel combinations are investigated with ethanol as the base fuel (see Figure 6). The first ethanol nanofuel contains suspended GNP at varying loading concentrations from 0.2 to 1.0 wt.%, as results from Ghamari and Ratner's experiments reported a 7% maximum increase for very small GNP loading (i.e., 0.1 wt.%) (Ghamari and Ratner 2017). It should be noted that the increase in K reported by Ghamari and Ratner is not attributed to active particle burning, but rather the increased thermal conductivity and radiative heat absorption increase due to the "darkened" nanofuel. Our results for ethanol with GNP do not show any significant change in the burning rate from 0.2 to 1.0 wt.% GNP addition. Similarly, there is no active particle burning of GNP throughout the droplet lifetime, except for occasional reacting particle expulsion events during final droplet burnout. For ethanol with ammonia borane, Pfeil et al. initially reported a 16% increase in K for a maximum of 6 wt.% AB addition, as that is the maximum solubility amount in ethanol. During our testing, there is a notable change in flame color, with the existence of transient micro-droplet shedding events throughout droplet burning, as well as foaming effects at the end of fuel burning. These physical changes to the steady burning process cause the reported burning rate to have much higher uncertainty than the other nanofuels. Specifically, K/K_o is 1.02 $\pm$ 0.06, showing inconclusive results regarding a definitive change in the average burning rate. Finally, a combination of GNP and AB in ethanol is evaluated, to potentially use the micro-droplet shedding associated with the AB to act as a transport mechanism for the GNP particles to

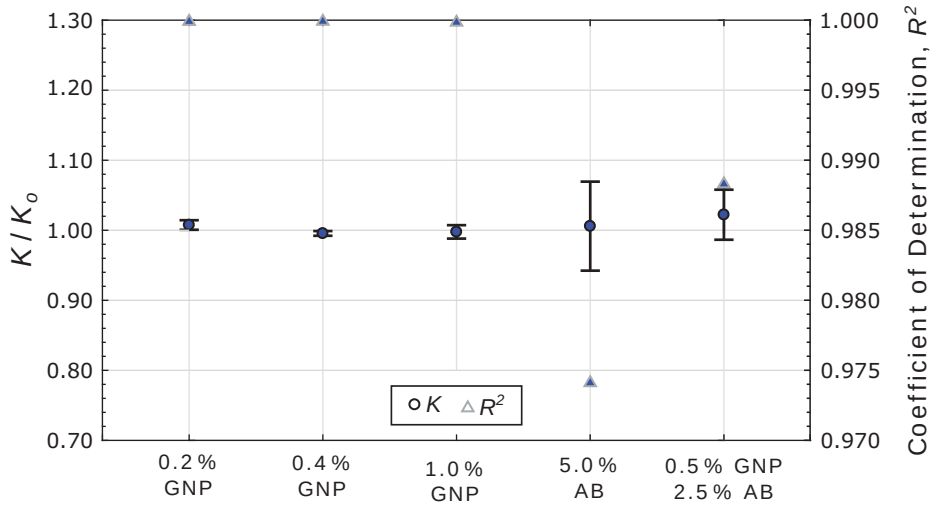

Figure 6. Normalized droplet burning rate constant K/K_o for ethanol with various nanoenergetic additives including graphene nano-platelet (GNP) and ammonia borane (AB) at varying loading wt.% concentrations. It should be noted that K_o is the burning rate constant of neat ethanol. The left axis of this plot shows the normalized burning rate (●) and the right axis is the corresponding coefficient of determination (▲).

the reaction zone to induce particle oxidation. During droplet burning, this did occur to some degree during the micro-droplet shedding events; this produces a subtle effect in the burning rate, where the average K is slightly increased by 2 to 3% over pure ethanol.

Similarly, graphene nano-platelet addition to RP-2 is also investigated for loading concentrations ranging from 0.1 to 1.0 wt.%, as shown in Figure 7. For all of these tests, Span 80 is the surfactant used at a constant 1.5 wt.% to create an adequate nano-suspension, in the same fashion as Ghamari and Ratner (Ghamari and Ratner 2017). Comparing the average burning rate to pure fuel, RP-2 with solely surfactant addition (shown at 0 wt.% GNP in Figure 7) is only slightly reduced, whereas the varying amounts of GNP addition largely have minimal effect with only a small 2-3 % maximum increase observed for 0.50 wt.% GNP. In the work of Ghamari and Ratner, the maximum increase in the burning rate of 7% is reported for 0.10 wt.% graphene nano-platelet addition, which reverses the trend for higher loading concentrations up to 1 wt.%. Again, their work suggests that particle burning is not the primary mechanism responsible for the increase in the average droplet burning rate, but rather enhancements of the heat transfer to the liquid droplet through increased thermal conductivity and higher radiative heat absorption due to the darkened nature of the fluid with GNP addition. This is generally consistent with our qualitative observations during RP-2 with GNP droplet burning, as the majority of graphene nano-platelet reaction takes place at the very end of the droplet lifetime through primarily char combustion, i.e., similar to Ghamari and Ratner (Ghamari and Ratner 2017). Therefore, our results also suggest that the small burning rate enhancement observed for low loading concentration GNP is not due to the chemical reaction of the nanoparticles, but rather the alterations of the transport properties of the liquid droplet.

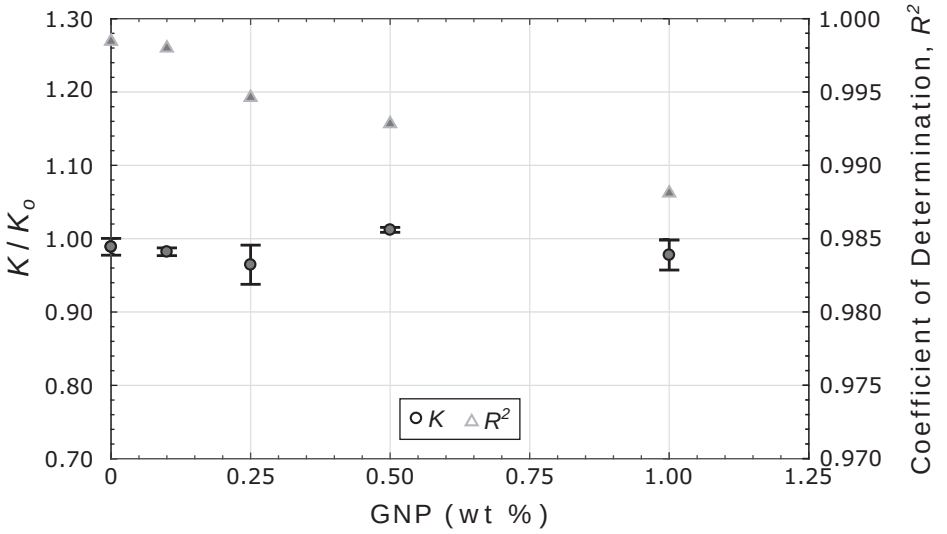

Figure 7. Normalized droplet burning rate constant K/K_o for RP-2 with graphene nano-platelet (GNP) at varying loading wt.% concentrations up to 1 wt%. It should be noted that K_o is the burning rate constant of neat RP-2. The left axis of this plot shows the normalized burning rate (●) and the right axis is the corresponding coefficient of determination (▲).

Magnesium oxide (MgO) suspended in RP-2 using Span 80 at varying loading concentrations is also investigated. This is based upon the work of Bello et al. (Bello et al. 2015), which characterized droplet burning for RP-2 with varying amounts of 20 nm MgO addition ranging between 0 to 1 wt.%, suspended using oleic acid. In this work, a significantly large increase in the quasi-steady droplet burning rate is reported, where a maximum of 270X increase above neat RP-2 is exhibited for 0.50 wt% MgO. However, it should be noted that the process used to quantify the droplet burning rate is not specified, making it difficult to reconcile whether this notably large increase is attributed to physical phenomena or due to the K evaluation method. For our experiments, Span 80 is chosen as the surfactant due to its ability to lengthen the duration of MgO particle suspension compared to oleic acid, based upon measurements using a combination of nanofuel turbidity and particle size distributions taken at varying times after sonication. During testing, the same 10:1 surfactant-to-additive ratio is also followed similarly to Bello et al. (Bello et al. 2015). Results from these tests do not show a substantial increase in the average burning rate (see Figure 8). By fixing the surfactant-to-additive ratio, the maximum surfactant addition is 10 wt.%, which itself (i.e., without additive addition) decreases K by approximately 15%. Comparing this to the maximum loading concentration of 1 wt.% MgO and 10 wt.% Span 80, there is only a slight K increase of 1 to 2%. Aside from this, it should be noted that the maximum increase in the burning rate of 5% is achieved with 0.25 wt.% MgO and 2.5 wt.% Span 80. This follows a similar trend to Bello et al. (Bello et al. 2015), which reports maximum burning rates between 0.25 and 0.50 wt.% MgO addition.

Aside from investigating additives for RP-2 that are based on previous studies, multiple series of tests are conducted using different additives that have yet to be explored. The first uses

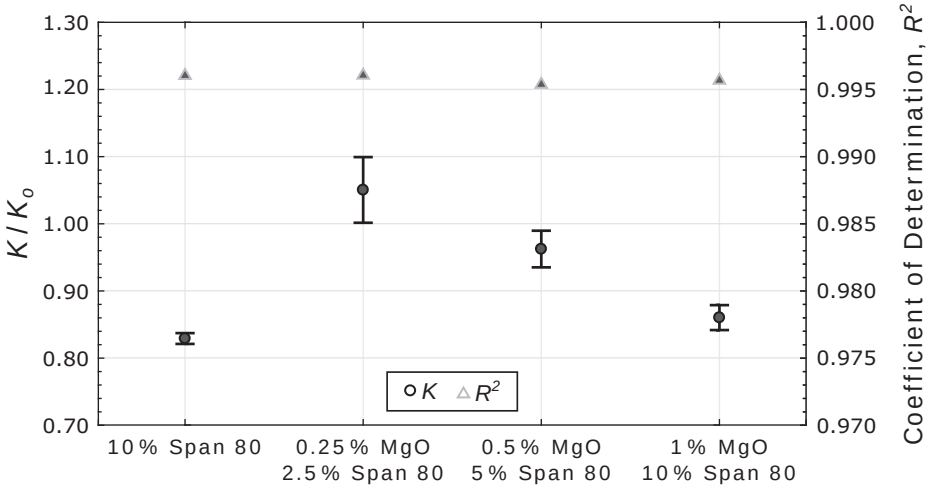

Figure 8. Normalized droplet burning rate constant K/K_o for RP-2 with magnesium oxide (MgO) at varying loading concentrations up to 1 wt.%, with a fixed 10:1 ratio of additive to Span 80 surfactant. It should be noted that K_o is the burning rate constant of neat RP-2. The left axis of this plot shows the normalized burning rate (●) and the right axis is the corresponding coefficient of determination (▲).

80 nm aluminum, which has shown some evidence as a useful burning rate modifier in other simple hydrocarbon fuels (Sim et al. 2018). For these tests, Span 80 is again used as the surfactant to produce a suitable suspension at a fixed 1.5 wt.%. With the maximum 1 wt.% nAl addition, there is no appreciable change in K (see Figure 9), again only exhibiting momentary char burning of the solid nanoparticles at the end of the droplet lifetime. Two soluble sodium-based compounds including ammonium nitrate (NaAN) and borohydride ($NaBH_4$) are also considered, similar to ammonia borane addition to ethanol. As with the ethanol and AB experiments, the soluble additive RP-2 tests use the maximum soluble concentration within RP-2 for both compounds, i.e., 6 wt.%. Similarly to the other additive combinations with RP-2, there is no significant change in the average burning rate observed. However, there is notably large uncertainty for the $NaBH_4$ experiments. This is attributed to internal gas generation that is also present during the previous soluble tests, which causes qualitative changes in droplet burning with occasional microdroplet shedding events throughout the droplet lifetime.

Finally, the droplet burning rate is quantified for RP-2 with stabilized graphene at two concentrations using oleic acid, as shown in Figure 10. RP-2 with the highest concentration level of 1 wt.% graphene causes a notable 20% reduction in K, with reasonably low uncertainty. When the concentration of graphene is reduced to a substantially lower level of 0.1 wt.%, the droplet burning rate becomes essentially equivalent to neat RP-2. Thus, the nanofuel mixture at 1 wt.% does modify the droplet burning rate sufficiently, but does not lead to a desired enhancement. However, it may be a suitable nanofuel candidate to alter the flame-acoustic coupling within a liquid injection spray.

The effective burning rate results largely show that the various nanoadditives for the two base fuels augment the burning rate only modestly, none of which exceed 10% for the additive loading concentrations levels of interest, i.e., less than 6 wt.%. While other research groups have reported increases in K exceeding 10%, they mostly do not exceed a 20% maximum. Aside from the nanofuel suspension issues mentioned in Section 2 that may unintentionally

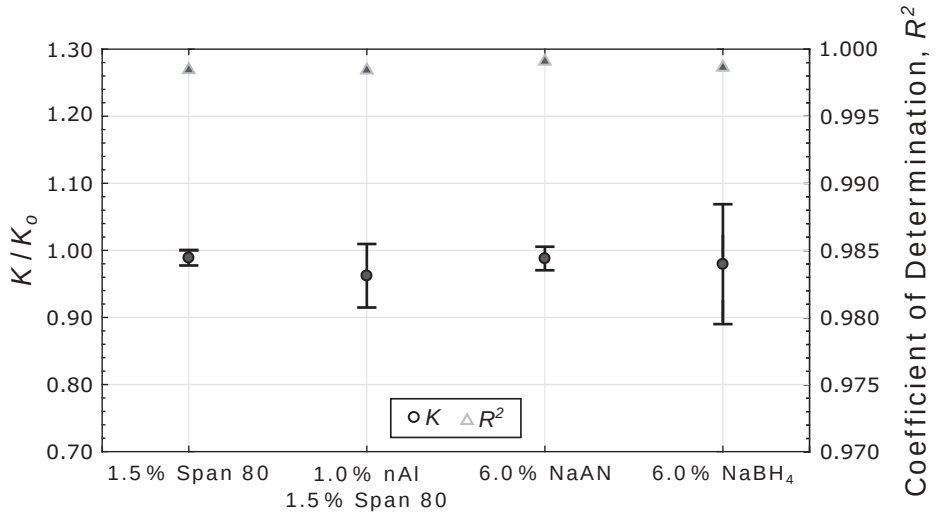

Figure 9. Normalized droplet burning rate constant K/K_o for RP-2 with various energetic compounds including nanoaluminum (nAl) and the sodium-based compounds ammonium nitrate (NaAN) and borohydride ($NaBH_4$). It should be noted that K_o is the burning rate constant of neat RP-2. The left axis of this plot shows the normalized burning rate (●) and the right axis is the corresponding coefficient of determination (▲).

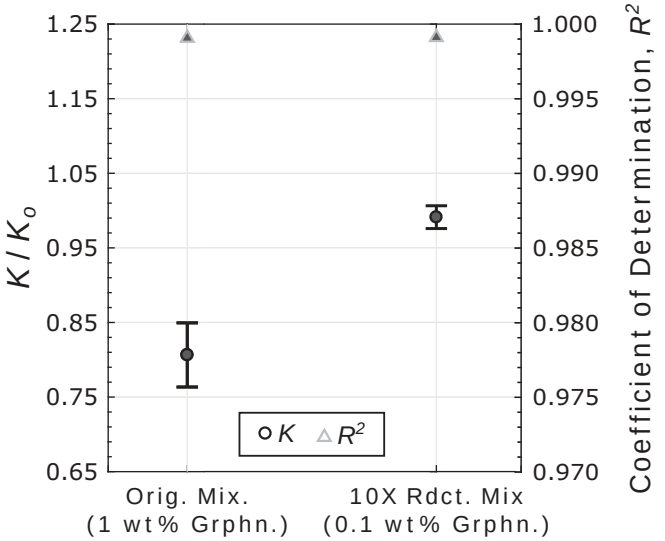

Figure 10. Normalized droplet burning rate constant K/K_o for RP-2 with graphene suspended at loading amounts up to 1 wt.% using oleic acid as a surfactant. It should be noted that K_o is the burning rate constant of neat RP-2. The left axis of this plot shows the normalized burning rate (●) and the right axis is the corresponding coefficient of determination (▲).

influence K values in the literature, the evaluation method used to quantify the burning rate has alone been shown to cause variations up to 10% if a standardized approach is not implemented (Bennewitz, Badakhshan, and Talley 2019). As the method in this study has

been shown to produce minimal statistical uncertainty and the highest coefficient of determination across a variety of 10 various hydrocarbons (including both base fuels in this study), the evaluation uncertainty effects on our reported average K values are minimized.

Instantaneous burning rate

As nanoadditive chemical reaction tends to occur during the end of droplet burning, the instantaneous burning rate $\widetilde{K}$ is calculated throughout the droplet lifetime to determine if the nanoadditives affect end-of-life burning substantially. $\widetilde{K}$ is determined by taking the d-squared regression temporal history and calculating the numerical derivative using the procedure outlined in the work of Chartrand (Chartrand 2011). This approach is suited to determine the numerical derivative of noisy data in situations where traditional finite difference schemes provide an unacceptable level of noise; it is based on total variation regularization, which permits a reduction in the noise amplification inherent to the numerical derivative calculation. The total variation regularization is essentially a penalty that accounts for the total deviation of the input data, and the regularization parameter α provides weighting of this penalty in the minimizer function for the numerical derivative calculation (Chartrand 2011). Essentially, α is a smoothing filter for the calculated numerical derivative, balancing the noise and solution accuracy. A lower level of α will capture the bulk mean solution, whereas a higher α contains a larger amount of fluctuations within the solution. As suggested by Chartrand, a sensitivity analysis is performed for varying levels of α from 10^{-1} to 10^{-5}. Results from this analysis for a pure ethanol droplet show that $\alpha = 10^{-1}$ provides a continuously smooth temporal history of $\widetilde{K}$ based on the d-squared droplet regression (see Figure 11(a)), essentially capturing the bulk solution. To ensure the accuracy of the approach, the d-squared droplet regression data is reconstructed through taking the antidifferentiated numerical derivative of $\widetilde{K}$ and then comparing it to experimental data. As shown in Figure 11(b), the reconstructed d-squared regression data follows the actual experimental data extremely closely, which yields only an average of 0.52% percent error. As such, this approach

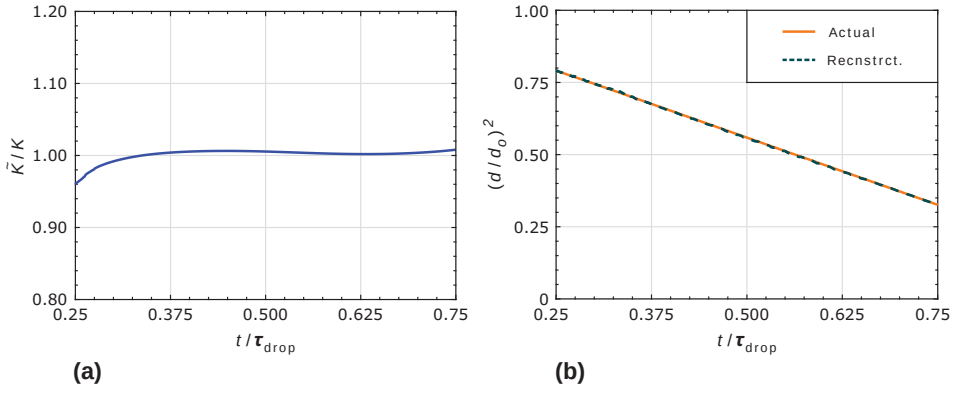

Figure 11. Example data for a pure ethanol droplet showing the (a) instantaneous burning rate $\widetilde{K}$ and the (b) reconstructed d-squared droplet regression from the antidifferentiated numerical derivative. It should be noted that K is the average burning rate constant for ethanol and τ_{drop} is the droplet lifetime.

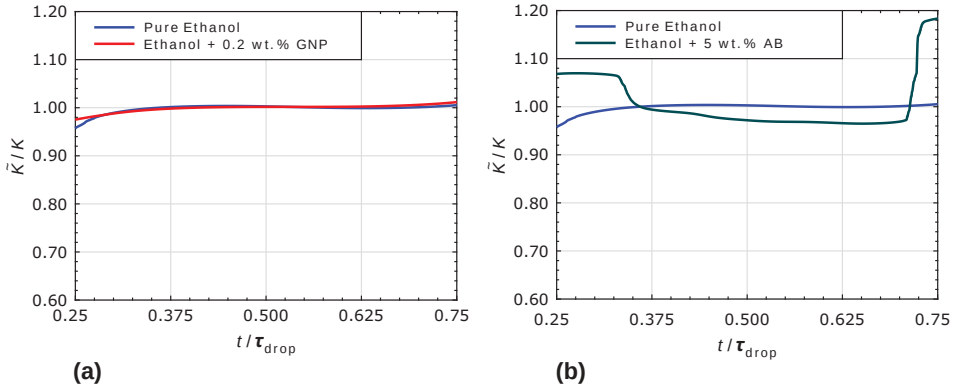

Figure 12. Normalized instantaneous burning rate $\widetilde{K}/K$ for ethanol with various nanoadditives including (a) 0.2 wt.% GNP and (b) 5 wt.% AB. It should be noted that K is the average burning rate constant and τ_{drop} is the droplet lifetime of the respective fuel/nanofuel.

provides a reasonable estimate of the instantaneous burning rate. It should be noted that a constant $\alpha = 10^{-1}$ value is used for all of the tests to adequately track the global changes in K throughout the droplet lifetime. Also, this numerical derivative approach contains some inherent numerical uncertainties at the temporal solution boundaries, therefore, only $\widetilde{K}$ solutions between $0.25 < t/\tau_{drop} < 0.75$ are shown.

The two main additives with ethanol as the base fuel are graphene nano-platelet and ammonia borane. Example $\widetilde{K}$ data is shown in Figure 12 for two representative tests at the respective concentrations yielding the largest increase in the average burning rate. It should be noted that the instantaneous burning rate $\widetilde{K}$ data is normalized using the average burning rate K of the respective nanofuel combination. For 0.2 wt.% GNP addition (Figure 12(a)), the instantaneous burn rate is mostly equivalent to pure ethanol during the steady-state mid-portion of the droplet lifetime, with a slight increase over pure ethanol near the end. Specifically, there is an approximate 1-2% increase by $t/\tau_{drop} = 0.75$. Overall, ethanol with 5 wt.% ammonia borane displays the largest qualitative change in burning characteristics for all ethanol nanofuels. Although the average K does not exhibit a substantial increase, the statistical uncertainty is large at $\pm 6\%$. This can be attributed to the large $\widetilde{K}$ variations throughout droplet burning (see Figure 12(b)). In this test, $\widetilde{K}$ is very close to that of pure ethanol during the steady mid-life burning and rapidly increases past $t/\tau_{drop} = 0.70$. During this period, $\widetilde{K}$ approaches an 18% increase, providing another indication that this nanofuel combination is effective at altering droplet combustion characteristics.

The same analysis is done for various RP-2 nanofuel combinations. Example data for four representative tests are shown in Figure 13, including GNP, nAl, MgO, and NaAN nanofuels for loading concentrations corresponding to the maximum average burning rate. All four of these additive types cause an increase in $\widetilde{K}$ by $t/\tau_{drop} = 0.75$ to varying degrees up to 8%. This rise begins at varying points depending on the additive, with 0.5 wt.% GNP starting at $t/\tau_{drop} = 0.40$ and 0.25 wt.% MgO and 6.0 wt.% NaAN at $t/\tau_{drop} = 0.50$. $\widetilde{K}$ for RP-2 with 1.0 wt.% nAl and 1.5 wt.% Span 80 is consistently 2 to 6% higher than pure RP-2 after the droplet's mid-life point.

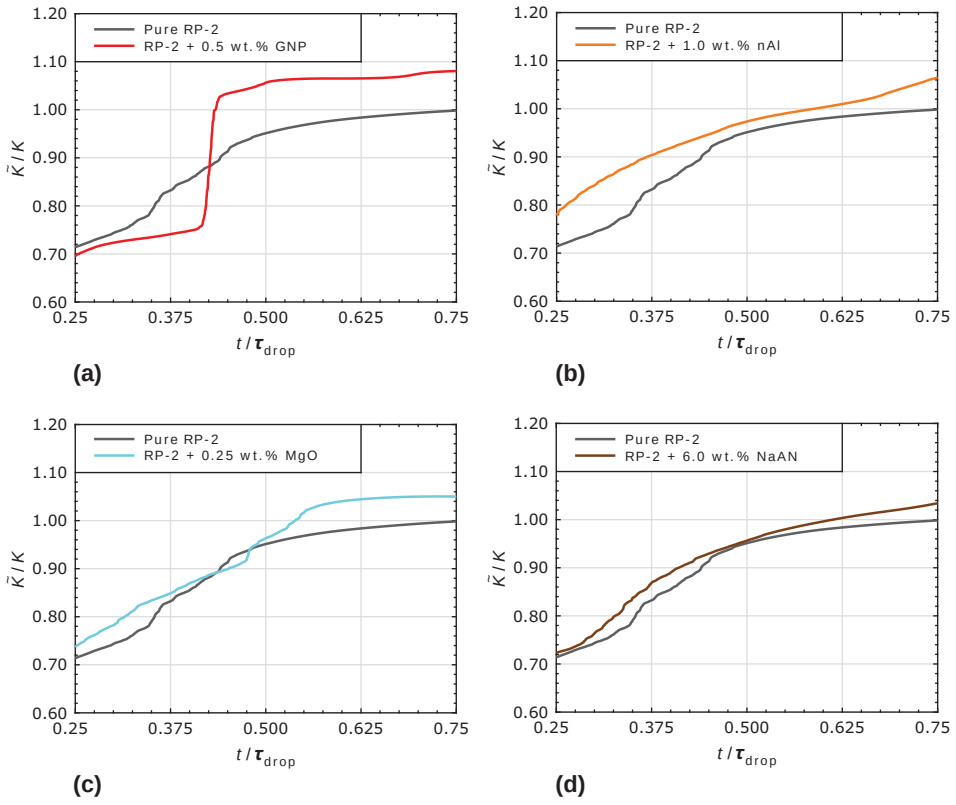

Figure 13. Normalized instantaneous burning rate $\widetilde{K}/K$ for RP-2 with various nanoadditives including (a) 0.5 wt.% GNP, (b) 1.0 wt.% nAl, (c) 0.25 wt.% MgO and (d) 6 wt.% NaAN. It should be noted that K is the average burning rate constant and τ_{drop} is the droplet lifetime of the respective fuel/nanofuel.

Finally, RP-2 with 0.25 wt.% MgO and 2.5 wt.% Span 80 yields a sustained 5% maximum increase over pure RP-2 for $0.50 < t/\tau_{drop} < 0.75$.

Results from this analysis show that the additives do begin to primarily affect the burning rate toward the end of the droplet lifetime. This is consistent across a majority of the nanofuel combinations, which exhibit increases in $\widetilde{K}$ from 2 to 18%. However, as these increases are not sustained throughout the entirety of the droplet burn time, average burn rates are not substantially enhanced compared to the pure base fuels.

Ignition delay

Ignition delays for six nanofuel combinations are measured by taking an average of five identical ignition events and post-processing the IR images using the procedure described in our previous work (Bennewitz, Badakhshan, and Talley 2019). All of the nanofuel ignition delays are normalized using the neat fuel baseline $\tau_{ign,o}$ for comparison (see Table 1). Ignition delays defined using this approach are found to correlate closely with liquid boiling temperature for the previously investigated pure hydrocarbon fuels (Bennewitz, Badakhshan, and Talley 2019), essentially providing validation to this experimental method. Four nanofuel combinations with ethanol are considered, with two additional mixtures using RP-2. In

general, ignition delays for the solid additives in ethanol and RP-2 remain within $\pm 5\%$ of the pure fuel (see Figure 14). This is expected as these additives do not show any evidence of particle reaction during the onset of droplet combustion, but rather at the end of droplet burning. However, it is notable that the soluble nanofuel ammonia borane in ethanol exhibits a fairly large increase in ignition delay approximating 20%. This is consistent with the location of maximum unsteady heat release for ethanol with ammonia borane in the work of Pfeil et al. (M. A. Pfeil, Son, and Anderson 2014) being pushed downstream in their laboratory scale rocket combustor. Aside from this, RP-2 with 1 wt.% graphene exhibits the largest increase in τ_{ign} approaching 30%.

Thermoacoustic instabilities are typically associated with a feedback cycle among oscillatory velocity u', pressure p' and heat release q' with the combustor of a reactive system. Growth of the instability occurs when the maximum amplitude oscillatory pressure and heat release are in-phase with one another both spatially and temporally, as per the well-known Rayleigh criterion (Rayleigh 1878). To dampen an instability, designed suppression techniques generally attempt to either reduce the amplitude of the oscillatory pressure or heat release, or decouple p' and q' (Harrje 1972). Increasing the ignition delay time for the reacting system could potentially cause the location of maximum heat release to be spatially shifted downstream, away from the pressure anti-node (maximum p' amplitude) that is inherently located at the injection head. This can lead to a decoupling of the maximum p' and q' to help mitigate the onset of a thermoacoustic instability. Therefore, as both the ethanol with 6 wt.% ammonia borane and RP-2 with 1 wt.% graphene nanofuel combinations significantly

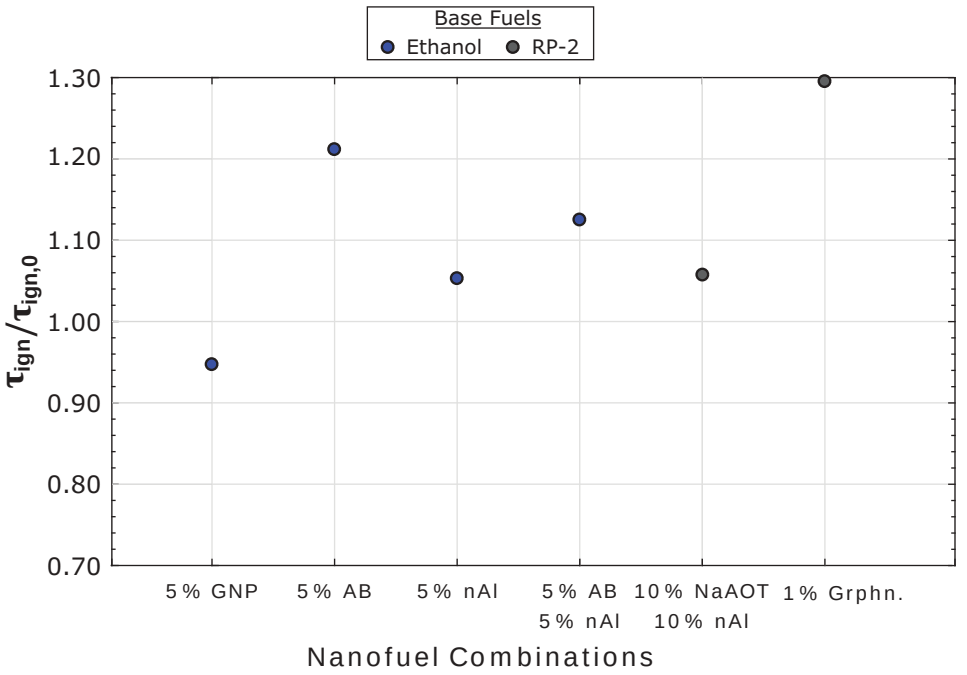

Figure 14. Normalized ignition delay $\tau_{ign}/\tau_{ign,o}$ for both ethanol (blue) and RP-2 (gray) nanofuel combinations using various additive types at different wt.% loading concentrations. It should be noted that $\tau_{ign,o}$ is the ignition delay of the respective neat base fuel.

lengthen the ignition delay in the suspended droplet geometry, they may be capable of altering the flame-acoustic coupling in a combustor.

Concluding remarks

Droplet combustion parameters for a variety of nanofuel combinations are investigated experimentally in this study. The emphasis in this study is on relatively low loadings of nanoenergetics in consideration of the fairly low tolerance many engine systems have for elevated particulate levels. Two rocket relevant base fuels RP-2 and ethanol are considered, with multiple solid nanoadditives including aluminum (Al), magnesium oxide (MgO), graphene, graphene nano-platelet (GNP), as well as the soluble additives ammonia borane (AB), ammonium nitrate (NaAN) and sodium borohydride ($NaBH_4$). Two series of experiments are performed for these nanofuels, aimed to separately measure the burning rate constant K and ignition delay τ_{ign}. Based on the effective burning rate results, it is difficult to conclude that low concentration (< 6 wt.%) of most energetic solids has a significant effect on the steady-state burning characteristics of nanofuels. A similar conclusion can be made for a majority of the traditional solid nanoadditives regarding ignition delay, which generally only causes a $\pm 5\%$ change. However, instantaneous burning rates on average do show an increase above average K values at the end of the droplet lifetime during times where additive reaction typically occurs. Also, the ignition delay for ethanol with 5 wt.% ammonia borane, as well as RP-2 with 1 wt.% graphene is lengthened 20 to 30% compared to pure fuel, indicating they may be capable of altering flame-acoustic coupling. Therefore, these two nanofuel combinations may be considered for investigation in a reactive liquid nanofuel spray. Overall, the results from this study show that a majority of traditional solid additive nanofuels cause only subtle changes to the global droplet burning parameters for the additive concentration levels relevant for propulsion applications, making it challenging to easily identify promising nanofuel candidates for future liquid propulsion studies.

Acknowledgments

The authors would like to acknowledge Dr. Hyung Sub Sim for performing the TEM of the various nanoparticles, as well as Professor Ann Karagozian and her research group for their insight into certain aspects of this work regarding burning nanofuel droplets.

Funding

This work has been supported by the Air Force Office of Scientific Research (AFOSR) with Dr. Mitat Birkan as program manager.

References

Aggarwal, S. K. 2014. Single droplet ignition: Theoretical analyses and experimental findings. *Prog. Energy Combust. Sci.* 45:79–107. doi:10.1016/j.pecs.2014.05.002.

Agrawal, Y., and V. Patel. 2011. Nanosuspension: An approach to enhance solubility of drugs. *J. Adv. Pharm. Technol. Res.* 2 (2):81. doi:10.4103/2231-4040.82950.

Anton, N., J.-P. Benoit, and P. Saulnier. 2008. Design and production of nanoparticles formulated from nano-emulsion templates—a review. *J. Controlled Release* 128 (3):185–99. doi:10.1016/j.jconrel.2008.02.007.

Armstrong, R. W., B. Baschung, D. W. Booth, and M. Samirant. 2003. Enhanced propellant combustion with nanoparticles. *Nano Lett.* 3 (2):253–55. doi:10.1021/nl025905k.

Badakhshan, A., J. W. Bennewitz, and D. Talley. 2018. New ignition methods for droplet combustion studies. *Combust. Sci. Technol.* 190 (7):1302–12. doi:10.1080/00102202.2018.1445726.

Bartle, K., E. Fitzpatrick, J. Jones, M. Kubacki, R. Plant, M. Pourkashanian, and A. Williams. 2011. The combustion of droplets of liquid fuels and biomass particles. *Fuel* 90 (3):1113–19. doi:10.1016/j.fuel.2010.10.054.

Basha, S. A., and K. R. Gopal. 2012. A review of the effects of catalyst and additive on biodiesel production, performance, combustion and emission characteristics. *Renewable Sustainable Energy Rev.* 16 (1):711–17. doi:10.1016/j.rser.2011.08.036.

Beckwith, T. G., and D., . M. Roy. 2007. *Mechanical measurements*. 6th ed. Upper Saddle River, NJ: Pearson Prentice Hall.

Bello, M. N., M. L. Pantoya, K. Kappagantula, W. S. Wang, S. A. Vanpalli, D. J. Irvin, and L. M. Wood. 2015. Reaction dynamics of rocket propellant with magnesium oxide nanoparticles. *Energy & Fuels* 29 (9):6111–17. 12.1021/acs.energyfuels.5b00905.

Bennewitz, J. W., A. Badakhshan, and D. G. Talley. 2019. Systematic measurement of hydrocarbon fuel droplet burning rate constants and ignition delays. *J. Propul. Power* 35 (4):690–703. doi:10.2514/1.b37195.

Bennewitz, J. W., D. Valentini, M. A. Plascencia, A. Vargas, H. S. Sim, B. Lopez, … A. R. Karagozian. 2018. Periodic partial extinction in acoustically coupled fuel droplet combustion. *Combust. Flame* 189:46–61. doi:10.1016/j.combustflame.2017.10.019.

Biswas, A., I. S. Bayer, A. S. Biris, T. Wang, E. Dervishi, and F. Faupel. 2012. Advances in top–down and bottom–up surface nanofabrication: Techniques, applications & future prospects. *Adv. Colloid Interface Sci.* 170 (1–2):2–27. doi:10.1016/j.cis.2011.11.001.

Chartrand, R. 2011. Numerical differentiation of noisy, nonsmooth data. *ISRN Appl. Math.* 2011:1–11. doi:10.5402/2011/164564.

Chingunpituk, J. 2007. Nanosuspension technology for drug delivery. *Walailak J. Sci. Technol.* 4 (2):139–53.

Clark, J. D. 2018. *Ignition!: An informal history of liquid rocket propellants*. New Brunswick, N.J.: Rutgers University Press.

Deng, X., Z. Huang, W. Wang, and R. N. Davé. 2016. Investigation of nanoparticle agglomerates properties using monte carlo simulations. *Adv. Powder Technol.* 27 (5):1971–79. doi:10.1016/j.apt.2016.06.029.

Erbschloe, D. 2012. *Air force alternative fuels process paves way to future* (Tech. Rep.). Air Force Air Mobility Command, Sapphire Energy Report. doi:10.1094/PDIS-11-11-0999-PDN.

Faeth, G. 1977. Current status of droplet and liquid combustion. *Prog. Energy Combust. Sci.* 3 (4):191–224. doi:10.1016/0360-1285(77)90012-0.

Ghamari, M., and A. Ratner. 2017. Combustion characteristics of colloidal droplets of jet fuel and carbon based nanoparticles. *Fuel* 188:182–89. doi:10.1016/j.fuel.2016.10.040.

Glassman, I., and R. Yetter. 2008. *Combustion*. 4th ed. San Diego, CA: Academic Press.

Godsave, G. 1953. Studies of the combustion of drops in a fuel spray—the burning of single drops of fuel. *Symp. (Int.) Combust.* 4 (1):818–30. doi:10.1016/s0082-0784(53)80107-4.

Guerieri, P. M., S. DeCarlo, B. Eichhorn, T. Connell, R. A. Yetter, X. Tang, Z. Hicks, K. H. Bowen, and M. R. Zachariah. 2015. Molecular aluminum additive for burn enhancement of hydrocarbon fuels. *J. Phys. Chem. A* 119 (45):11084–93. doi:10.1021/acs.jpca.5b08580.

Guerieri, P. M., J. B. DeLisio, and M. R. Zachariah. 2017. Nanoaluminum/nitrocellulose microparticle additive for burn enhancement of liquid fuels. *Combust. Flame* 176:220–28. doi:10.1016/j.combustflame.2016.10.011.

Harrje, D. 1972. *Liquid propellant rocket combustion instability (Tech. Rep.)*. National Aeronautics and Space Administration.

Heister, S. D., W. E. Anderson, T. L. Pourpoint, and R. J. Cassady. 2019. *Rocket propulsion*. 1st ed. Cambridge, UK: Cambridge University Press.

Hwang, Y., J.-K. Lee, J.-K. Lee, Y.-M. Jeong, S. Ir Cheong, Y.-C. Ahn, and S. H. Kim. 2008. Production and dispersion stability of nanoparticles in nanofluids. *Powder Technol.* 186 (2):145–53. doi:10.1016/j.powtec.2007.11.020.

Javed, I., S. W. Baek, and K. Waheed. 2015. Autoignition and combustion characteristics of kerosene droplets with dilute concentrations of aluminum nanoparticles at elevated temperatures. *Combust. Flame* 162 (3):774–87. doi:10.1016/j.combustflame.2014.08.018.

Jones, M., C. H. Li, A. Afjeh, and G. Peterson. 2011. Experimental study of combustion characteristics of nanoscale metal and metal oxide additives in biofuel (ethanol). *Nanoscale Res. Lett.* 6 (1):246. doi:10.1186/1556-276x-6-246.

Kim, D. M., S. W. Baek, and J. Yoon. 2016. Ignition characteristics of kerosene droplets with the addition of aluminum nanoparticles at elevated temperature and pressure. *Combust. Flame* 173 (nov):106–13. doi:10.1016/j.combustflame.2016.07.033.

Kumagai, S., and H. Isoda. 1955. Combustion of fuel droplets in a vibrating air field. *Symp. (Int.) Combust.* 5 (1):129–32. doi:10.1016/s0082-0784(55)80019-7.

Law, C. 1982. Recent advances in droplet vaporization and combustion. *Prog. Energy Combust. Sci.* 8 (3):171–201. doi:10.1016/0360-1285(82)90011-9.

Law, C., and F. Williams. 1972. Kinetics and convection in the combustion of alkane droplets. *Combust. Flame* 19 (3):393–405. doi:10.1016/0010-2180(72)90009-0.

Lu, A.-H., E. Salabas, and F.Schüth. 2007. Magnetic nanoparticles: Synthesis, protection, functionalization, and application. *Angew. Chem. Int. Ed.* 46 (8):1222–44. doi:10.1002/anie.200602866.

Mehregan, M., and M. Moghiman. 2018. Effects of nano-additives on pollutants emission and engine performance in a urea-SCR equipped diesel engine fueled with blended-biodiesel. *Fuel* 222 (jun):402–06. doi:10.1016/j.fuel.2018.02.172.

Meziani, M. J., C. E. Bunker, F. Lu, H. Li, W. Wang, E. A. Guliants, … Y.-P. Sun. 2009. Formation and properties of stabilized aluminum nanoparticles. *ACS Appl. Mater. Interfaces* 1 (3):703–09. doi:10.1021/am800209m.

Mirzajanzadeh, M., M. Tabatabaei, M. Ardjmand, A. Rashidi, B. Ghobadian, M. Barkhi, and M. Pazouki. 2015. A novel soluble nano-catalysts in diesel–biodiesel fuel blends to improve diesel engines performance and reduce exhaust emissions. *Fuel* 139 (jan):374–82. doi:10.1016/j.fuel.2014.09.008.

Mittal, A. K., Y. Chisti, and U. C. Banerjee. 2013. Synthesis of metallic nanoparticles using plant extracts. *Biotechnol. Adv.* 31 (2):346–56. doi:10.1016/j.biotechadv.2013.01.003.

Pfeil, M., S. Rosen, Y. Yu, W. Anderson, and S. Son 2010. Effects of NanoAluminum on droplet combustion and combustion Instabilities in a single element rocket combustor. In *46th AIAA/ASME/SAE/ASEE joint propulsion conference & exhibit*. American Institute of Aeronautics and Astronautics, Nashville, TN. July doi:10.2514/6.2010-7154

Pfeil, M. A., L. J. Groven, R. P. Lucht, and S. F. Son. 2013. Effects of ammonia borane on the combustion of an ethanol droplet at atmospheric pressure. *Combust. Flame* 160 (10):2194–203. doi:10.1016/j.combustflame.2013.04.014.

Pfeil, M. A., S. F. Son, and W. E. Anderson. 2014. Influence of ammonia borane on the stability of a liquid rocket combustor. *J. Propul. Power* 30 (2):290–98. doi:10.2514/1.b34950.

Rayleigh, J. 1878. The explanation of certain acoustical phenomena. *Nat.* 18:319–21. doi:10.1038/018319a0.

Sabourin, J. L., D. M. Dabbs, R. A. Yetter, F. L. Dryer, and I. A. Aksay. 2009. Functionalized graphene sheet colloids for enhanced fuel/propellant combustion. *ACS Nano* 3 (12):3945–54. doi:10.1021/nn901006w.

Sabourin, J. L., R. A. Yetter, and V. S. Parimi. 2010. Exploring the effects of nanostructured particles on liquid nitromethane combustion. *J. Propul. Power* 26 (5):1006–15. doi:10.2514/1.48579.

Saidur, R., K. Leong, and H. Mohammad. 2011. A review on applications and challenges of nanofluids. *Renewable Sustainable Energy Rev.* 15 (3):1646–68. doi:10.1016/j.rser.2010.11.035.

Sim, H. S., M. A. Plascencia, A. Vargas, J. W. Bennewitz, O. I. Smith, and A. R. Karagozian. 2018. Effects of inert and energetic nanoparticles on burning liquid ethanol droplets. *Combust. Sci. Technol.* 191 (7):1079–100. doi:10.1080/00102202.2018.1509857.

Sim, H. S., M. A. Plascencia, A. Vargas, and A. R. Karagozian. 2019. Acoustically forced droplet combustion of liquid fuel with reactive aluminum nanoparticulates. *Combust. Sci. Technol.* 1–25. doi:10.1080/00102202.2019.1593971.

Sioui, R., and L. Roblee. 1969. The prediction of the burning constants of suspended hydrocarbon fuel droplets. *Combust. Flame* 13 (5):447–54. doi:10.1016/0010-2180(69)90083-2.

Sirignano, W. A. 2010. *Fluid dynamics and transport of droplets and sprays*. 2nd ed. Cambridge, NY: Cambridge University Press.

Soudagar, M. E. M., -N.-N. Nik-Ghazali, M. A. Kalam, I. Badruddin, N. Banapurmath, and N. Akram. 2018. The effect of nano-additives in diesel-biodiesel fuel blends: A comprehensive review on stability, engine performance and emission characteristics. *Energy Convers. Manage.* 178 (dec):146–77. doi:10.1016/j.enconman.2018.10.019.

Struk, P. M., M. Ackerman, V. Nayagam, and D. L. Dietrich. 1998. On calculating burning rates during fibre supported droplet combustion. *Microgravity. Sc.i Technol.* 11 (4):144–51.

Sutton, G. P., and O. Biblarz. 2010. *Rocket propulsion elements*. 8th ed. Hoboken, NJ: John Wiley & Sons, Inc.

Tang, F., L. Li, and D. Chen. 2012. Mesoporous silica nanoparticles: Synthesis, bio- compatibility and drug delivery. *Adv. Mater.* 24 (12):1504–34. doi:10.1002/adma.201104763.

Tanvir, S., and L. Qiao. 2015. Effect of addition of energetic nanoparticles on droplet- burning rate of liquid fuels. *J. Propul. Power* 31 (1):408–15. doi:10.2514/1.b35500.

Taylor, J. R. 1997. *An introduction to error analysis: The study of uncertainties in physical measurements*. 2nd ed. Sausalito, California: University Science Books.

Turns, S. R. 2000. *An introduction to combustion: Concepts and applications*. 8th ed. Boston, MA: McGraw-Hill Higher Education.

Tyagi, H., P. E. Phelan, R. Prasher, R. Peck, T. Lee, J. R. Pacheco, and P. Arentzen. 2008, may. Increased hot-plate ignition probability for nanoparticle-laden diesel fuel. *Nano Lett.* 8 (5):1410–16. doi:10.1021/nl080277d.

USAF. 2006. *Detail specification: Propellant, rocket grade kerosene*. (Tech. Rep. No. MIL- DTL-25576E) United States Air Force.

Wood, B. J., and H. Wise. 1957. Measurement of the burning constant of a fuel drop. *J. Appl. Phys.* 28 (9):1068–1068. doi:10.1063/1.1722910.

Yetter, R. A., G. A. Risha, and S. F. Son. 2009. Metal particle combustion and nanotechnology. *Proc. Combust. Inst.* 32 (2):1819–38. doi:10.1016/j.proci.2008.08.013.

Yu, Y., S. Koeglmeier, J. Sisco, and W. Anderson. 2008. Combustion instability of gaseous fuels in a continuously variable resonance chamber (CVRC). July doi:10.2514/6.2008-4657.

AFRL-RQ-ED-TR-2020-0026
Primary Distribution of this Report:

RQR
AFRL R&D Case Files
Completed Interim and Final Tech Reports Repository

AFRL/RQ Technical Library
6 Draco Drive
Edwards AFB, CA 93524-7130

Johns Hopkins University
Whiting School of Engineering
ATTN: Mary T. Gannaway/FSO
10630 Little Patuxent Pkwy, Suite 202
Columbia, MD 21044-3286

Defense Technical Information Center
(1 Electronic Submission via STINT)
Attn: DTIC-ACQS
8725 John J. Kingman Road, Suite 94
Ft. Belvoir, VA 22060-6218